

65th Annual Conference of the South African Institute of Physics

SAIP

Conference Proceedings

Edited by
Prof Aletta Prinsloo



2021



PROCEEDINGS EDITOR-IN-CHIEF: Prof Aletta Prinsloo, University of Johannesburg

PUBLISHER: The South African Institute of Physics

SAIP COPYRIGHT NOTICE:

Copyright 2021 by the South African Institute of Physics (SAIP)

The Proceedings of SAIP2021, the 65th Annual Conference of the South African Institute of Physics (SAIP), will be available electronically only on the SAIP website www.saip.org.za.

Permission to make digital or hard copies of part or all of this work for personal or classroom use is granted without fee provided that copies are not made or distributed for profit or commercial advantage and that copies bear this notice and the full citation on the first page. Abstracting with credit is permitted. To copy otherwise, to republish, to post on servers, or to distribute to lists, requires specific permissions and/or a fee.

Request permissions from the SAIP Office,

Tel. +27 (0)12 841 2655 / 2627,

Fax +27 (0)86 648 8474,

E-mail info@saip.org.za.

ISBN: 978-0-620-97693-0

SAIP2021

Proceedings of SAIP2021

**The 65th Annual Conference of the South African Institute of
Physics (Virtual Conference)**

Hosted by the North-West University

20 July 2021 to 30 July 2021

**Edited By
Prof Aletta Prinsloo**

Table of contents

Editorial	<i>Page: 1</i>
Message from The Conference Organizers	<i>Page: 3</i>
Conference, Divisions, and Editorial Board details	<i>Page: 4</i>
Editorial Board	<i>Page: 6</i>
List of Reviewers	<i>Page: 8</i>
DIVISION A – DIVISION FOR PHYSICS OF CONDENSED MATTER AND MATERIALS	<i>Page: 12</i>
63Cuq+ and 197Auq+ ion beam induced sputtering of ITO coated glass thin films at 0.1 MeV/u – 0.6 MeV/u SIMS energies	<i>Page: 13</i>
Theoretical Modeling of High Entropy Alloys	<i>Page: 19</i>
Spin-imbalances in non-magnetic nano-systems: Using non-equilibrium Green's function DFT to model spin-selective phenomena mediated by spin-orbit coupling.	<i>Page: 25</i>
Characterization of P3HT-CNT thin films for photovoltaic solar cell applications	<i>Page: 31</i>
Computational Studies of Pentlandite Mineral: Structural and Dynamical Properties Probed by Molecular Dynamics	<i>Page: 37</i>
Computational modelling studies of pentlandite (Fe4Ni5S8)(111) surface: Oxidation and hydration	<i>Page: 43</i>
Effect of oxygen adsorption on the electronic properties of Li/MO2 (M= Ti, V, Mn) surfaces	<i>Page: 49</i>
Physical properties of the layered structure compound Ce3Os4Al12	<i>Page: 55</i>
Evaluating the evolution of Ti5 cluster in LiCl medium	<i>Page: 60</i>
Influence of duration of annealing on thermoluminescence of natural quartz annealed at 1000 °C	<i>Page: 65</i>
DIVISION B – NUCLEAR, PARTICLE AND RADIATION PHYSICS	<i>Page: 71</i>
The derivation of preliminary reference levels for natural radioactivity in drinking water surrounding nuclear sites	<i>Page: 72</i>
An investigation of over-training within semi-supervised machine learning models in the search for heavy resonances at the LHC	<i>Page: 78</i>
Analysis of UOC for nuclear forensics using Scanning Electron Microscope	<i>Page: 85</i>
South African contribution towards the ATLAS Tile Calorimeter PreProcessor	<i>Page: 91</i>
Understanding two same-sign and three leptons with b-jets in four top quark events at the LHC	<i>Page: 96</i>
The use of Semi-supervision in the search for heavy resonances with the Zγ final state at the LHC	<i>Page: 102</i>
Background decomposition in Zγ events used in the search for high-mass resonances	<i>Page: 108</i>
Search for Zγ high-mass resonances using the ATLAS detector	<i>Page: 114</i>
Re-designing a radiation-tolerant low voltage power supply for the ATLAS Tile Calorimeter Phase-II Upgrade	<i>Page: 120</i>

Search for heavy resonances in the $+ - + -$ final state in association with missing transverse energy using pp collisions at $s = 13$ TeV with the ATLAS detector	Page: 126
The replacement and refurbishment of Gap Scintillator Counters for the ATLAS Tile Calorimeter Phase I Upgrade	Page: 132
Quality assurance testing of the ATLAS Tile-Calorimeter Phase-II upgrade low-voltage power supplies	Page: 138
Search for a heavy pseudo-scalar decaying into a Z boson and another heavy scalar boson leading to four lepton final states in pp collisions at $s = 13$ TeV with the ATLAS detector	Page: 199
The anatomy of the multilepton anomalies at the LHC and a candidate for a singlet scalar	Page: 151
A compact neutron spectrometer for neutrons produced by cosmic rays	Page: 157
Machine learning approach for the search of resonances with topological features at the Large Hadron Collider	Page: 163
Measurement of the photoabsorption cross section of ^{24}Mg .	Page: 169
A search for tWZ production in the trilepton channel using Run 2 data from the ATLAS experiment	Page: 174
Statistical correlations impacting a top quark mass measurement in 13 TeV proton-proton collision data from the ATLAS detector	Page: 180
Simplified Template Cross Section measurements of the V ($H \rightarrow b\bar{b}$) process with the ATLAS detector at $\sqrt{s} = 13$ TeV	Page: 187
Simulation of the strip sub-detectors in the Inner Tracker of the ATLAS detector	Page: 193
Search for a heavy di-photon resonance in association with b-jets with the ATLAS detector at the LHC	Page: 199
Transfer reactions to populate the Pygmy Dipole Resonance (PDR) in ^{96}Mo	Page: 206
Search for the non-resonant Higgs-pair production in $\ell^+\ell^-\ell^+\ell^-$ final state at $s = 13$ TeV in the ATLAS detector	Page: 210
Search for a heavier Higgs like boson and a dark force boson using ATLAS experimental data.	Page: 217
Activity Concentration Measurement of Naturally-Occurring Radionuclides in Various Vegetation plots in Rustenburg, South Africa	Page: 223
Investigation of the relation between limit of detection and solid angle by measuring standard radioactive sources with a $\text{LaBr}_3:\text{Ce}$ detector	Page: 229
An estimation for the 4γ branching ratio of positronium using $\text{LaBr}_3:\text{Ce}$ scintillator detectors	Page: 235
The possible use of Fibre Optic Sensors in Pressurized Water Reactors	Page: 241

DIVISION C - PHOTONICS

Page: 247

Nuclear translocation of Map Kinase and release of basic fibroblast growth factor following photobiomodulation at 660 nm in diabetic wounded cells

Page: 248

A comparison between photobiomodulation at 830 nm and 660 nm on differentiation in diabetic human skin fibroblast cells

Page: 253

Facilitating iADMSC Differentiation into Neuronal Cells by Photobiomodulation Using Visible and Near-Infrared Wavelengths

Page: 259

Increasing efficiency of photodynamic therapy in in vitro cultured colorectal cancer cells by improved photosensitizer uptake

Page: 265

Targeted Photodynamic Diagnosis of In Vitro Cultured Colorectal Cancer Cells

Page: 272

Photobiomodulated Differentiation of Adipose-derived Stem Cells into Osteoblasts.

Page: 278

Dicoma anomala enhances the zinc phthalocyanine tetrasulphonic acid (ZnPcS4) mediated photodynamic therapy in breast cancer cells

Page: 284

Effects of photodynamic therapy on A375 Melanoma cells using aluminium phthalocyanine photosensitizer

Page: 290

Inhibition of Lung Cancer Migration and Invasion Using a Gold Nano Photosensitizer Conjugate

Page: 296

DIVISION D – ASTROPHYSICS & SPACE SCIENCE

Page: 302

Kinematics and star formation histories of brightest cluster galaxies

Page: 303

Probing dark matter in the Madala model using radio observations

Page: 310

Diffusing assumptions in astroparticle physics

Page: 316

Studying patched spacetimes for binary black holes

Page: 322

Simulating the enrichment of cosmological gas: incorporating a new chemical enrichment model in Simba

Page: 328

Galaxy evolution in the local universe: studying the complete local-volume groups sample (CLOGS)

Page: 334

A study of the lobes of the radio galaxy Hydra A using MeerKAT observations

Page: 340

Optical emission line properties of some little-known Narrow Line Seyfert 1 galaxies

Page: 345

SALT spectroscopy to measure the abundances of gas-rich galaxies in Fornax A

Page: 352

Spatio-kinematics of the massive star forming region NGC6334I during an episodic accretion event

Page: 358

Optical spectropolarimetry monitoring of flaring blazars	Page: 364
Investigating the orbital parameters of the gamma-ray binary HESS J0632+057	Page: 370
A multi-band view on the evolution of group centralgalaxies	Page: 375
Potential of the MeerKAT telescope to detect the stimulated decay of axion-like particles	Page: 380
Dark coupling: cosmological implications of interacting dark energy and dark matter fluids	Page: 386
The Effect of Dark Matter During the Cosmic Dawn	Page: 392
Remote Sensing of Aerosol Optical Depth (AOD) over Pretoria, South Africa	Page: 398
Daily global solar radiation estimation using artificial intelligence approach	Page: 405

DIVISION E – PHYSICS FOR DEVELOPMENT, EDUCATION AND OUTREACH

Polarising questions in the Force Concept Inventory	Page: 411
Classification of sound conceptions	Page: 412
Grade 11 Physical Sciences learners’ perceptions of scientific inquiry	Page: 418
Music, context-based inquiry, and computer simulation as engagement strategy	Page: 424
Science teachers’ beliefs about the impact of 4IR on their classroom practices	Page: 430
Quantum technology: A potential tool for development in Africa	Page: 436
The global Gender Gap project: fair treatment, and some recommendations for South Africa	Page: 442
South Africa and the joint data-backed study of publication patterns of the Global Gender Gap project	Page: 448
Inaugural Quantum Computing School in Lesotho: Its impact and the Lessons Learnt	Page: 454
Leveraging Artificial Intelligence and Quantum Machine Learning for economic growth in Africa	Page: 460
Evolution of the 3rd Year Physics Major Project at WITS	Page: 467
Modular logic gate emulator for on-line laboratory	Page: 473
The South African Institute of Physics (SAIP) Benchmark Statement and physics graduate preparedness: A case study of the University of the Western Cape	Page: 478

DIVISION F – APPLIED PHYSICS

The development of a real-time Monitoring system for the ATLAS Tile Calorimeter Phase-II Upgrades	Page: 484
Integration of the ALTI module in the ATLAS Tile Calorimeter system	Page: 490
Quality control software development for testing the next generation of upgraded low voltage power supplies for the ATLAS Tile Calorimeter	Page: 491
Programming the load readout board micro-controllers used in the development of aBurn-In test bench for the ATLAS TileCal Phase-II Upgrade	Page: 497
The characterization and functionality of the interface boards used in the burn-in test station for the ATLAS Tile Calorimeter Low Voltage Power Supplies Phase-II upgrade	Page: 503

A Burn-in test station for the ATLAS Tile-calorimeter low-voltage power supply transformer-coupled buck converters	Page: 523
Heat Transfer Enhancement of a Thermal Interface Material for Heat Sink Applications Using Carbon Nanotubes	Page: 530
Digital data acquisition system for neutron metrology	Page: 536
Development of ¹⁸ F Radiochemistry for Positron Emission Particle Tracking (PEPT)	Page: 542
Solar irradiance in Gauteng during the 2020 COVID-19 lockdown– can we detect decreased aerosol loading?	Page: 548
Enhancing Zinc Oxide gas sensing device for microcontroller application	Page: 554
A new fast neutron facility for materials analysis at UCT	Page: 560
Enhancing PEPT: high delity analysis with augmented detection	Page: 566
Plasma Diagnostics of Miniaturised DC Glow Discharge Thruster Concept	Page: 572
Performance analysis of thin-film photovoltaic (PV) technologies in an embedded generation network	Page: 578
Evaluation of PV power forecasting models using temperature data	Page: 584
An experimental study of a combined solar cooking and thermal energy storage system for domestic applications	Page: 590

DIVISION G – THEORETICAL AND COMPUTATIONAL PHYSICS

Fitting the relic density with dimension-five contributions	Page: 598
Quasinormal modes in the large angular momentum limit: an inverse multipolar expansion analysis	Page: 599
Generating function approach to Open Quantum Walks	Page: 605
GHZ state generation via projected squeezed states with dephasing	Page: 611
Investigating a New Approach to Quasinormal Modes: Physics-Informed Neural Networks	Page: 617
Random number generation using IBM quantum processors	Page: 624
Effect of Ti content on the magnetic and mechanical properties of B2 FeCo alloy: a DFT study	Page: 630
Bianchi Type-V model in Rn-gravity: A dynamical systems approach	Page: 636
Three-party reference frame independent quantum key distribution with an imperfect source	Page: 644
B and D meson Suppression and Azimuthal Anisotropy in a Strongly Coupled Plasma at $\sqrt{s_{NN}} = 5.5$ TeV	Page: 650
Factorisation in Heavy Ion Collisions	Page: 656
	Page: 663

Cosmological Models in Gravitational Scalar-Tensor Theories

Page: 674

Corrigenda to The Proceedings of SAIP2021

Page: 675

Effect of Gold Nanoparticle-Hypericin Mediated Photodynamic Therapy in MCF-7 Breast Cancer Cells.

Page: 676

Comparison of Indoor Radon Levels measured with three different Detectors (Passive and Active)

Page: 682

On the advantages of relative phase Toffoli gates

Page: 689

Editorial

North-West University (NWU) became the first institute to host the annual South African Institute of Physics (SAIP) conference virtually. Against the backdrop of the ongoing limitations due to the Covid-19 pandemic NWU successfully ran a memorable virtual 65th conference in the series of SAIP. Some papers from this online meeting are collected in this peer-reviewed volume. Submissions for the proceedings of SAIP2021 were handled by an Editorial Board headed by an Editor-in-Chief and Associate Editors with responsibility for submissions in different subject tracks.

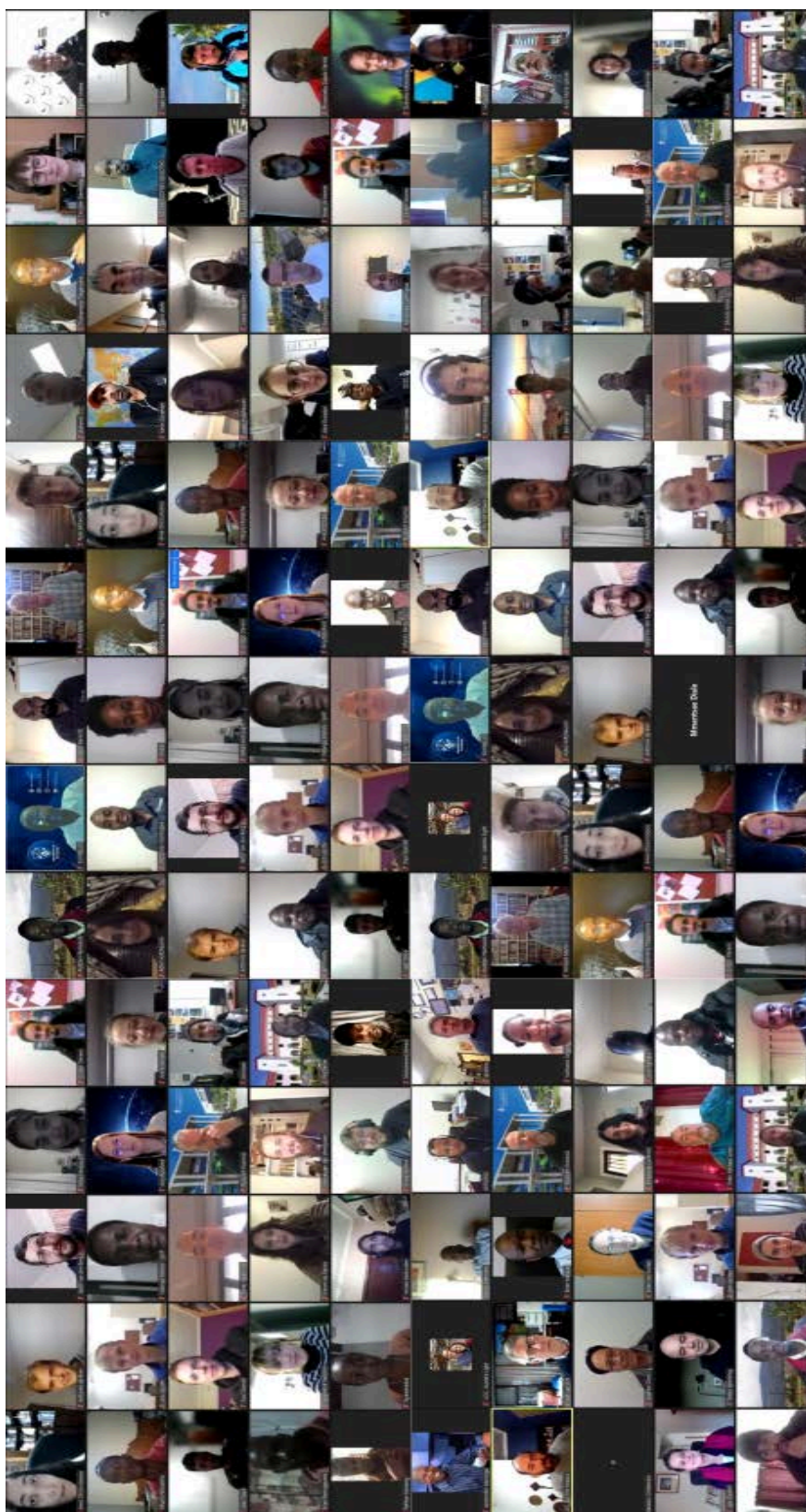
The Editor Board of the SAIP2021 Proceedings received 123 manuscripts for consideration by the deadline of 30 August 2021. A total of 112 of these manuscripts met the relevant criteria and were submitted to a full peer-review process involving 177 individual reviewers (some reviewed more than one manuscript). The style of these proceedings is that of the (British) Institute of Physics Conference Series, similar to the styling used in previous SAIP Proceedings.

Authors were requested to ensure that the defined layout were adhered to in their submitted pdf documents. At the start of the reviewing process, an initial layout review was conducted by the Associate Editors on each manuscript. It was noted that there were small deviations between the layout templates available in MSWord and Latex – both of these formats were accepted by the Associate Editors. Manuscripts that deviated considerably from the specified layout specifications, while still broadly appropriate in their composition, were referred back to the authors for major layout corrections before being forwarded to knowledgeable content reviewers as a second step in the review process. This year the Editorial Board aimed to reduce the time between the submissions and publication, with the authors being informed of the outcome of their submissions before the closure for the December holiday.

The publication of the SAIP Proceedings are highly dependent on the efficiency of the Associate Editors and the goodwill of Reviewers from the scientific community in South Africa. The Editor-in-Chief wishes to acknowledge the hard work of the Associate Editors who spent much time considering the papers and reviewer reports in order to ensure that acceptable academic standards were met during peer-review for the proceedings to be credible. The majority of the content reviews received were done with great care and diligence and to the highest standards. The Editorial Board wishes to voice their sincere thanks to the participating Reviewers for their pro bono work, specifically to those Reviewers that read more than one paper. The meticulous reviewing process described above has ensured that these proceedings contain thoroughly peer-reviewed manuscripts of a high professional standard, which report on novel work that has not been published elsewhere.

The Editor-in-Chief also wishes to recognise and thank Mr Mokhine from the SAIP offices for his support and help in preparing these proceedings. His technical skills were essential throughout the entire process and his patient assistance much appreciated.

Finally, the Editorial Board wishes to thank all of the authors for submitting their research work to this proceedings to undergo the rigorous review process. It is our sincere hope that the final product offered here constitutes a due outcome of their hard work.



Delegates to the 2021 South African Institute of Physics Virtual Conference.

Message from The Conference Organizers

The 65th South African Institute of Physics (SAIP) Annual Conference will always be remembered as the first virtual SAIP conference. We, as the LOC from the North-West University, are proud of the initiative, as well as the innovative solutions adopted to make this new conference format feasible during the most trying of times. This would, however, not have been possible without all the conference participants who, by engaging actively on new and unfamiliar platforms, made this conference a success.

We would like to thank all participants who submitted papers to the conference proceedings, editors and reviewers for assistance with the peer-review process, and especially Prof Aletta Prinsloo for her guidance as editor-in-chief. During the conference, a lot of excellent science was presented and discussed, and we hope that this proceedings volume archives these new discoveries and insights for future generations.

Eugene Engelbrecht (SOC Chair) and Du Toit Strauss (LOC Chair)

Conference, Divisions, and Editorial Board details

SAIP2021 Conference Chairperson

Du Toit Strauss

Local organising Committee

Eugene Engelbrecht

Lente Dryer

Amare Abebe

Christo Venter

Manny Mathuthu

Patrick Oyirwoth

Elanie van Rooyen

Bruno Letarte

Ashleigh Pieterse

Miriam Lemmer

Ruhann Steyn

Lynndle Square

James Chibueze

Rhyme Setshedi

Stefan Ferreira

Gerard Moerdyk

Tebogo Kupi

Sumari Hattingh

Markus Boettcher

Naomi Mokhine

Bruce Mellado (Wits)

Brian Masara (SAIP office)

Tebogo Mokhine (SAIP office)

SAIP2021 Division Chairs

Division for Physics of Condensed Matter and Materials

Rudolph Erasmus, University of the Witwatersrand

Division for Nuclear, Particle, and Radiation Physics

Rudolph Nchodu, iThemba LABS

Bruce Mellado, University of the Witwatersrand

Division for Photonics

Pieter Neethling, Stellenbosch University

Division for Astrophysics & Space Science

Zama Katamzi, South African National Space Agency

Brian Van Soelen, University of the Free State

Division for Physics for Development, Education and Outreach

Sam Ramaila, University of Johannesburg

Division for Applied Physics

Phil Ferrer, University of Witwatersrand

Division for Theoretical and Computational Physics

Allan Cornell, University of Johannesburg

SAIP2021 Editorial Board

Editor-in-Chief

Aletta Prinsloo, University of Johannesburg

Associate Editors

Division for Physics of Condensed Matter and Materials	Charles Sheppard, University of Johannesburg
Division for Nuclear, Particle, and Radiation Physics	Mukesh Kumar, University of Witwatersrand
Division for Photonics	John Bosco Habarulema, Sansa
Division for Astrophysics	Christo Venter, North West University
Division for Space Science	John Bosco Habarulema, Sansa
Division for Physics for Development, Education and Outreach	Grace Phalwane, Sefako Makgatho Health Sciences University
Division for Applied Physics	Andrew Venter, Necsa
Division for Theoretical and Computational Physics	Will Horowitz, University of Cape Town

Editorial Board

Proceedings of SAIP2021

Editor-in-Chief

Aletta Prinsloo

Aletta Prinsloo is a Professor of Physics in the Department of Physics at the University of Johannesburg. She is an NRF rated research physicist in the field of experimental solid state physics. Her research is focused on the magnetism of chromium-based bulk alloys, thin films and nanomaterials.

Associate Editors

Division for Applied Physics: Prof AM Venter

Andrew Venter is the head of the Diffraction Section (Neutron and X-ray) at Necsa SOC Ltd. and has an Adjunct Professor appointment within the MC Centre for Applied Radiation Science and Technology of the North-West University. He is a NRF rated researcher with specialities in the application of diffraction techniques in powder diffraction (nuclear and magnetic systems) and residual stress investigation of materials.

Division for Astrophysics: Prof C Venter

Christo Venter is a Professor of Physics in the School of Physical and Chemical Sciences and the Director of the Centre for Space Research at the North-West University. He is an NFR B-rated scientist in the field of Gamma-ray Astronomy. His research focuses on pulsars, pulsar wind nebulae, globular clusters and cosmic rays.

Division Theoretical and Computational Physics: Prof WA Horowitz

Will Horowitz is an Associate Professor of Physics at the University of Cape Town. Among other honours, Prof Horowitz has received the Claude Leon Merit Award for Early-Career Researchers and the Meiring Naudé Medal for Outstanding Early Career Contributions to Science from the Royal Society of South Africa. Prof Horowitz research explores the non-trivial emergent many-body properties of the strong force using the methods of perturbative quantum field theory and the AdS/CFT correspondence.

Division for Physics for Development, Education and Outreach: Dr MG Phalwane

Grace Phalwane is a Dental Doctor and Health Professions Educationalist in the Department of Community Dentistry at the Sefako Makgatho Health Sciences University. Her research interest is focused on the Service Learning (SL), Problem-Based Learning (PBL) and Inter-Professional Education (IPE).

Division for Nuclear, Particle and Radiation Physics: Dr M Kumar

Mukesh Kumar is a Lecturer of Physics in the School of Physics at the University of the Witwatersrand. He is an NRF Y-rated research physicist in the field of high energy particle physics. His research is focused on Higgs boson, top quark, and dark matter physics at the Large Hadron Collider (CERN) including the future e-p and e+e⁻ colliders. He is a member of TileCal Speaker committee for ATLAS detector at CERN.

Division for Photonics and Space Science: Dr J Bosco Habarulema

John Bosco Habarulema is a research physicist at the South African National Space Agency. He is a B2-rated research scientist by the National Research Foundation in the field of Space Physics. His research interests include ionospheric modelling and characterisation using various approaches including machine learning; ionospheric electrodynamics; and studies of Atmospheric Gravity Waves especially during geomagnetic storms.

Division for Physics of Condensed Matter and Materials: Prof CJ Sheppard

Charles Sheppard is an Associate Professor and a member of the Cr Research Group in the Physics Department at the University of Johannesburg. His current research interest focuses on the various physical properties observed in bulk Cr alloys, Cr thin films, and chrome oxide magnetic nano-materials.

List of Reviewers

Andrew Forbes - Wits University.

Abdulrafiu Raji - UNISA.

Aggrey Mwesigye - University of Calgary, Canada.

Alan Cornell - University Of Johannesburg.

Alberto Valero - CERN.

Aletta Prinsloo - University of Johannesburg.

Amare Abebe - North West University.

Andrew Venter - Necsa SOC Ltd.

Andy Buffler - University of Cape Town.

Anslyn John - Stellenbosch.

Bidhubhusan Sahu - KIIT University.

Bincy Susan Jacobs - University of Johannesburg.

Bo Liu - IHEP..

Bonex Mwakikunga - CSIR.

Brian van Soelen - University of Free State.

Buyi Sondezi - University of the Witwatersrand.

Carel Wagner - Necsa SOC Ltd.

Carlos Solans Sanchez - CERN.

Christian Engelbrecht - University of Johannesburg.

Simon Ellingsen - School of Natural Sciences at the University of Tasmania.

Christian Engelbrecht - University of Johannesburg.

Christine Steenkamp - University of Stellenbosch.

Da Xu - CERN.

Daniel Wamwangi - University of the Witwatersrand.

Danil Groenewald - South African Astronomical Observatory.

Deepak Kar - Wits University.

Deon Marais - Necsa SOC Ltd.

Derck Smits - Emeritus.

Dimitrios Tsimpis - Institut de Physique des deux Infinis de Lyon.

Du Toit Strauss - North West University.
Ed Elson - University of the Western Cape.
Emanuela Carleschi - University of Johannesburg.
Fernando Carrio - CERN.
Bonex Mwakikunga - CSIR.
Carel Wagner - Necsa SOC Ltd.
Daniel Wamwangi - University of the Witwatersrand.
Deon Marais - Necsa SOC Ltd.
Emanuela Carleschi - University of Johannesburg.
Francisco Torralba - University Of Cape Town.
Frederik Vorster - Nelson Mandela University.
Garreth Kemp - University of Johannesburg.
Geoff Beck - Wits University.
Gianni Bernardi - SKA.
Graham Daniels - Necsa SOC Ltd.
Gurthwin Bosman - University of Stellenbosch.
Gyula I. G. Jzsa - Rhodes University.
Hartmut Winkler - University of Johannesburg.
Heidi Abrahamse - University of Johannesburg.
Henri Marais - North West University.
Malili Matshaba - University of Limpopo.
Henric Wilkens - Cern, University of the Witwatersrand.
Hing Tong Cho - Tamkang University.
Ilani Loubser - North West University.
Ilya Sinayskiy - University of Kwazulu-Natal.
Ismail Akhalwaya - IBM.
Iurii Sushch - North West University.
Iyabo Usman - Wits University.
Jaco van der Walt - Necsa SOC Ltd.
Jalal Abdallah - Cern, University of the Witwatersrand.

James Chibueze - North West University.
James Keaveney - University of Cape Town.
John Carter - University of the Witwatersrand.
Kenda Knowles - Rhodes University.
Kenny Uren - North West University.
Ketevi Adikle Assamagan - BNL.
Konstantinos Zoubos - University of Pretoria.
Lei Zhang - CERN.
Lerothodi Leeuw - UWC/CERN.
Luca Panizzi - Uppsala University.
Makhamisa Senekane - University of Johannesburg.
Malili Matshaba - University of Limpopo.
Manny Mathuthu- North West University.
Marco Mariola - University of Kwazulu-Natal.
Markus Bottcher - North West University.
Matt Hilton - University of Kwazulu-Natal.
Moses Mogotsi -South African Astronomical Observatory.
Mudhahir Al-Ajmi - Sultan Qaboos University.
Nicolette Houreld - University of Johannesburg.
Nigel Bishop - Rhodes University.
Nukri Komin - Wits University.
Marco Mariola - University of Kwazulu-Natal.
Oliver Fischer - University of Liverpool.
Pankaj Mohanty - University of Johannesburg.
Patience Pmthunsikufa - CSIR.
Peane Maleka - iThemba LABS, Cape Town.
Pete Jones - iThemba LABS, Cape Town.
Peter Dunsby - University Of Cape Town.
Phil Ferrer - Department of Physics, University of the Western Cape.
Pieter Meintjes - University of Free State.
Rachid Mazini - CERN.

Rian Prinsloo - Necsa Limited.

Richard Britto - University of Free State.

Rituparno Goswami - University of Kwazulu-Natal.

Robert Lindsay - University of the Western Cape.

Xifeng Ruan - Wits University.

Robert Warmbier - University of Johannesburg.

Roberto Franceschini - INFN and Rome 3 University.

Rosalind Skelton - South African Astronomical Observatory.

Roy Maartens - University of the Western Cape.

Rustem Ospanov - CERN.

Sahal Yacoob - University of Cape Town.

Saturnin Ombinda - Lemboumba - CSIR.

Shimaa AbuZeid - Cern, University of the Witwatersrand.

Siegfried Förtsch - iThemba LABS.

Simon Connell - KIIT University.

Simon Ellingsen - School of Natural Sciences at the University of Tasmania.

Somnath Bhattacharyya - Wits University.

Stephan Woodborne - iThembaLABS.

Thomas Konrad - University of Kwazulu-Natal.

Thulani Hlatshwayo - University of Pretoria.

Thuto Mosuang - University of Limpopo.

Tjaart Krüger - University of Pretoria.

Tom Leadbeater - University of Cape Town.

Vishana Naicker - North West University.

Wade Naylor - Immanuel Lutheran College.

Xifeng Ruan - Wits University.

Yaquan Fang - IHEP, UCAS.

Zina Ndabeni - University of Cape Town.

**DIVISION A –
PHYSICS OF CONDENSED
MATTER AND MATERIALS**

$^{63}\text{Cu}^{q+}$ and $^{197}\text{Au}^{q+}$ ion beam induced sputtering of ITO coated glass thin films at 0.1 MeV/u – 0.6 MeV/u SIMS energies

G T Mafa^{1,2}, T P Sechogela¹ and M Msimanga^{1,2}

¹ Department of Physics, Tshwane University of Technology, Private Bag X680, Pretoria, 0001, South Africa

² iThemba LABS TAMS, National Research Foundation, Private Bag 11, WITS, 2050, Johannesburg, South Africa

Email: Granttshepo02@gmail.com

Abstract. Ion beam induced sputtering in matter is of interest for fundamental ion-atom interaction studies. It is also important for practical applications such as ion beam materials analysis techniques like Secondary Ion Mass Spectrometry at MeV ion energies (MeV SIMS). Theoretical descriptions of nuclear sputtering yields due to keV projectile ions are generally in good agreement with experimental data, but this is not the case for electronic sputtering yields using heavy projectile ions. There is thus a need for experimental data to improve existing theoretical models that describe electronic sputtering due to MeV ions. This work presents results of thin film sputtering yield measurements carried out using the Elastic Recoil Detection Analysis technique (ERDA). Measurements were carried out to determine the electronic sputtering yield in Indium Tin Oxide (ITO) due to $^{63}\text{Cu}^{q+}$ and $^{197}\text{Au}^{q+}$ MeV ion beams over an ion velocity range of 0.1 MeV/u - 0.6 MeV/u. The UV-Vis characterization technique was also used to determine the changes in the optical properties of the conducting oxide films due to heavy ion beam irradiation. Results show that reduction in thickness of the ITO film is attributed to the preferential sputtering of oxygen from the surface. The measured sputtering yield data were found to decrease with increasing ion fluence in the ITO target material for both Au and Cu ion beams. The optical band gap was found to decrease only slightly from 3.99 eV (for pristine) to 3.93 eV with increasing ion fluence. The results, in general, indicate that heavy ion beams irradiation can be used as an effective tool to induce surface modifications in thin films by dense electronic excitation.

1. Introduction

The sputtering of atoms from a solid thin film by heavy ion beam bombardment is of practical interest in areas related to materials analysis and modification, and for understanding the fundamentals of heavy ion interaction with matter.

Sputtering of ions in matter has been studied extensively over the years [1,2]. Although a lot of research on sputtering yields induced by ion-target nuclei collisions at keV energies has been done in this field, this has not been the case for sputtering yields induced by interactions between high energy (MeV) projectile ions and orbital electrons of target atoms. Nuclear sputtering yields at keV energies can be predicted fairly accurately by existing sputtering theories [3] for practical applications in the traditional keV SIMS technique for instance. SIMS is a mass spectrometry technique that involves

bombarding the surface of a sample with a beam of accelerated ions and analyzing the secondary ions produced by the ion bombardment [4]. The predictive accuracy of existing models for electronic sputtering due to MeV ions is still inadequate for many practical applications, thus more experimental data is needed for the improvement and validation of theory. In this work we present experimental sputtering yield results in thin films due to heavy ion beam bombardment in the context of possible applications in MeV SIMS.

Sputtering occurs when a solid target sample is subjected to irradiation with energetic ions resulting in particles being ejected from the surface. The projectile particle loses energy to the target via two mechanisms, which are central aspects in the theory of ion-matter interaction: inelastic electronic losses (ionization, electron-electron collisions, electronic excitation, and charge transfer) and elastic nuclear collisions (atom-atom collisions and conserved kinetic energy) [3]. The energy of the incident ions determines which energy loss will be dominant. At low projectile energies (< 100 keV/nucleon) the dominant mode of ion-target interaction is through nuclear collision cascades, which lead to nuclear sputtering. As the projectile energy increases, its energy loss tends to be mostly due to interaction with the electron cloud of the target atom than with the nucleus, this leads to electronic sputtering.

The removal rate of surface atoms due to ion bombardment is quantified by the sputtering yield, Y , which is defined as the average number of atoms removed from the surface per incident ion [5]:

$$Y = \frac{\text{average number of atoms removed}}{\text{number of incident ions}} \quad (1)$$

The definition of sputtering yield implies that the average number of atoms removed is proportional to the number of incident ions. The sputtering yield is strongly dependent on the energy of the incident ions, the masses of the ions and target atoms, the experimental geometrical conditions (e.g., ion incidence angle) and the binding energy of atoms in the solid.

2. Experimental Method

Ion beam induced sputtering yield measurements were performed using the Time of Flight (ToF-ERDA) set up located on the zero-degree line of the 6 MV Tandem accelerator at iThemba LABS-TAMS, Gauteng. The ToF-Energy spectrometer, shown in the schematic in Figure 1, detects atoms forward recoiled from the target sample by the incident beam. Coincident measurement of the ToF and Energy allows for recoil atoms to be separated according to atomic mass, and so it then becomes possible to determine elemental spectra, from which depth profiles can be calculated [6].

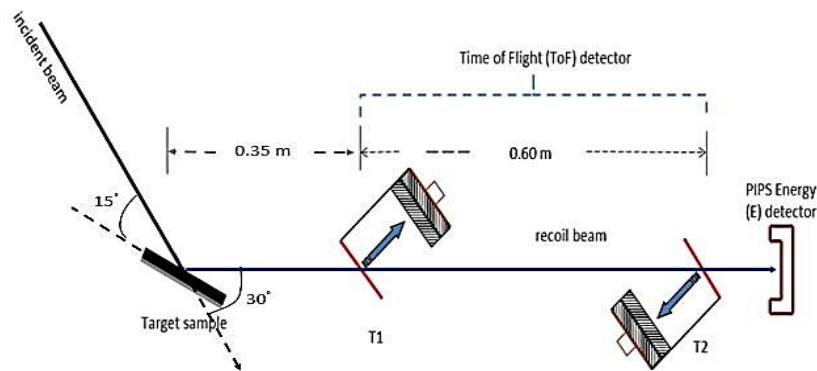


Figure 1. A schematic representation of the ToF-ERDA telescope configuration at iThemba LABS-TAMS [7].

Indium Tin Oxide (ITO)-on-glass samples of thickness ~ 32 nm (or $\sim 253 \times 10^{15}$ atoms/cm²) were used in the irradiation measurements. The samples were mounted on a stainless-steel ladder located at the

center of a target chamber. The pressure in the chamber was maintained at 2×10^{-6} mbar during the measurements. The targets were placed at a tilted grazing incidence angle of 15° , with respect to the beam. The samples were uniformly irradiated for different irradiation times using three sets of energies for the Au^{q+} (20, 30 and 40 MeV) and Cu^{q+} (18, 27 and 34 MeV) collimated beams. The acceleration voltage, obtainable beam current for different charge states and the desired incident ion energy determines the ion charge state that eventually comes through to the experimental station. The ToF-Energy detector telescope used for the detection and identification of recoil ions is set at a forward scattering angle of 30° to the initial beam direction [8]. Measurements were carried out at an existing installation of the ERDA technique set up at iThemba LABS TAMS, where the ToF detector is at a fixed angle of 30° . The original choice of 30° was based on kinematic considerations to prevent flooding of the detector by forward scattered incident ions during routine Heavy Ion ERD thin film analysis [7].

A two-dimensional spectrum of ToF versus Energy was generated for the different incident ion energies used. The spectra gave well separated bands of the different elements present in the films, as shown in Figure 2. The spectra were analyzed to obtain depth profile information using a Heavy Ion ERDA software called Potku [9].

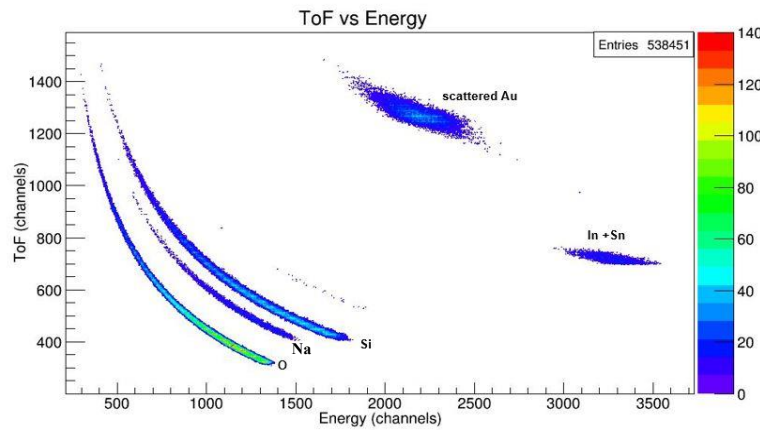


Figure 2. ToF-Energy scatter plot of an ITO film-coated glass substrate measured using a 40 MeV Au^{8+} incidence beam.

The beam fluence ϕ was calculated from the irradiation time t , beam current I and the beam spot area A on the target [8]:

$$\phi = \frac{It}{qeA} \quad (2)$$

where q is the ionic charge and e is the electron charge (1.602×10^{-19} C). The reduction in the thickness of the films due to sputtering was determined in terms of areal concentration from the Potku calculated depth profiles and the sputtering yield rate was determined from the slope of a graph of film thickness versus beam fluence.

The pristine and irradiated thin films were also subjected to Ultraviolet Visible measurements (LAMBDA 365 PerkinElmer Spectrophotometer) to investigate the changes in the optical band gap.

3. Results and Discussion

3.1. Sputtering Yields of ITO/Glass

For beam induced sputtering yield measurements, the irradiation fluence was extended beyond normal ERDA analysis measurement times to obtain a measurable decrease in the thickness of the ITO film.

Figure 3 depicts the change in atomic concentration of ITO as fluence is varied, as measured with a 30 MeV Au^{7+} ion beam. As the beam fluence increases, the atomic concentration of oxygen decreases, as a result of oxygen atoms being sputtered from the ITO film. A similar comparison for atomic concentrations of indium and tin (In + Sn) shows fairly constant concentrations with increasing beam fluence, this is interpreted as an indication of insignificant sputtering of the In + Sn atomic species. The above-observed results of the relative decrease in O concentrations and constant In + Sn concentrations with increasing fluence, indicates a case of preferential sputtering; whereby oxygen atoms are sputtered at a higher rate than either In or Sn atoms.

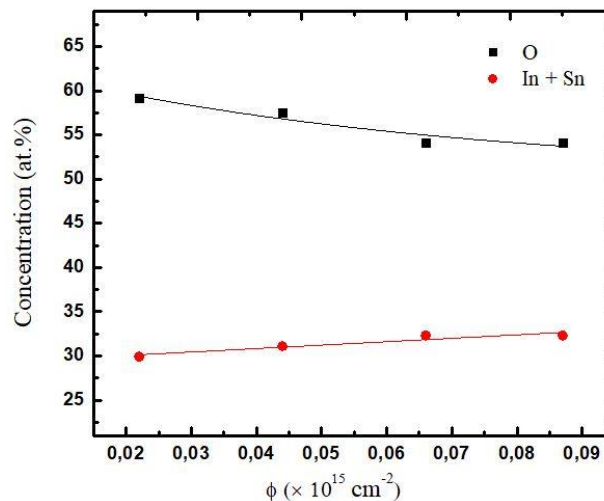


Figure 3. Concentrations of O and In + Sn in the ITO/glass thin film at different sputtering fluences measured using a 30 MeV Au^{7+} ion beam.

Figures 4 and 5 shows plots of sputtering yields of oxygen as a function of incident Au and Cu ion beam fluence, respectively. The sputtering yield was obtained from the change in areal concentration against the ion fluence i.e., dividing the content of an element at two points in the initial part of the plot by the corresponding fluence values. The sputtering yield of oxygen by incident Au and Cu ions decreases with increasing ion fluence for the measured fluence range, as shown in both figures. Similar behaviour of a decrease in the sputtering yield with an increase in bombarding fluence was recently reported by Mammeri *et al.* [10], in the case of Bismuth thin films irradiated by swift Cu^{q+} heavy ions over the 10 to 26 MeV range and ion beam fluences of approximately $10^{13} - 10^{15}$ ions/ cm^2 . The decrease in the sputtering yields with increasing ion fluence can be attributed to the inelastic collisions causing changes in the ITO film thickness under heavy ion irradiation, due to large deposited electronic energy density.

Two different trends are also observed for sputtering yields versus beam fluence, obtained by the different Au and Cu beams as shown in Figures 4 and 5; for Au beam irradiations it can be noted that the sputtering yield rate shows a steep drop at low fluences and then tends to flatten as the fluence increases and for Cu beam irradiations the sputtering yield rate decreases gradually at first and then shows a steep drop as the fluence increases. Comparing the sputtering yields obtained by both Au and Cu beams, it can be noted that the sputtering yields for Au ions are larger than that of Cu ions. This can be explained in terms of the velocity effect based on the inelastic thermal spike model [11], which states that the relationship between the electronic sputtering yield is directly proportional to the area of the ion damage zone. The velocities of the Au ions are approximately 2.6 times smaller than that of Cu ions, thus lower velocity ions deposit high energy density resulting in a high ion damaged zone and higher sputtering yields.

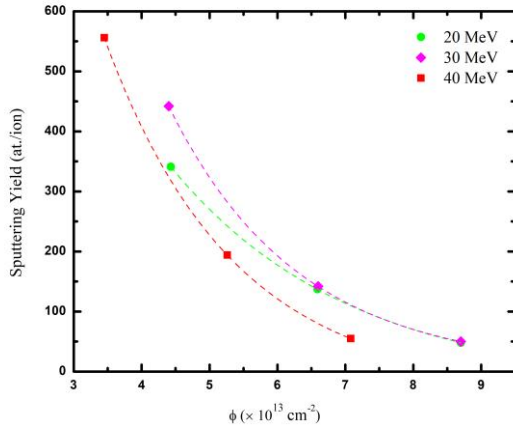


Figure 4. Sputtering yields versus ion fluence of O atoms from ITO/Glass thin films irradiated by 20, 30 and 40 MeV Au^{q+} ions.

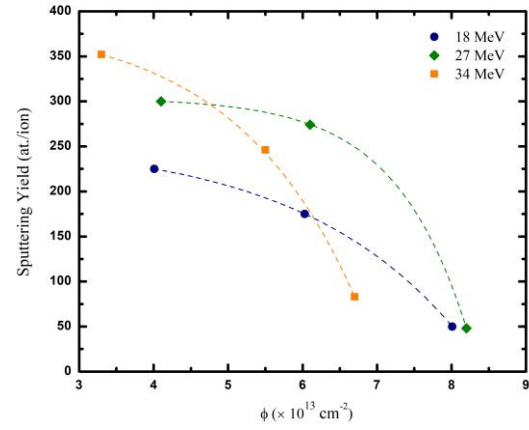


Figure 5. Sputtering yields versus ion fluence of O atoms from ITO/Glass thin films irradiated by 18, 27 and 34 MeV Cu^{q+} ions.

3.2. Secondary Irradiation Effects

Ultraviolet-Visible Spectroscopy (UV-Vis) was used to study the secondary irradiation effects of ITO thin films in comparison to unirradiated ITO thin films. Figures 6 and 7 shows the plots of $(\alpha h\nu)^2$ versus $(h\nu)$ for Au and Cu ion irradiated films, respectively. The value of the optical band gap is obtained by a method of extrapolating (Tauc's extrapolation) the linear part of the plot which intersects the x-axis at zero absorption, this gives the energy band gap. A slight decrease in the energy band gap of the Au and Cu irradiated films is seen from Figures 6 and 7. The energy band gap of the ITO thin films irradiated by 40 MeV Au^{8+} ions was slightly reduced from a pristine band gap value of 3.99 eV to 3.93 eV and those irradiated by 34 MeV Cu^{7+} ions slightly reduced from 3.99 eV to 3.95 eV with increases in ion fluences, this was concluded to be an insignificant reduction in the band gaps.

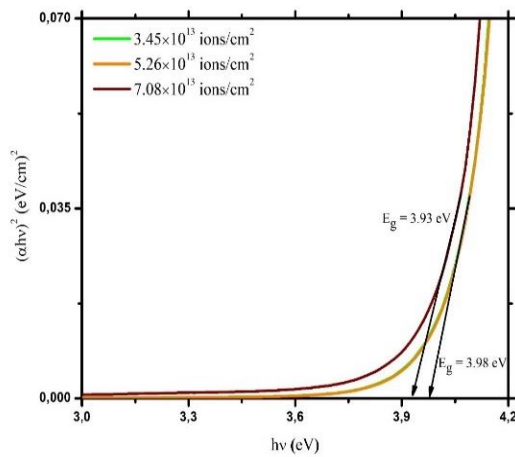


Figure 6. Plot of $(\alpha h\nu)^2$ versus Photon energy ($h\nu$) for 40 MeV Au^{8+} ion irradiated ITO films coated glass substrate.

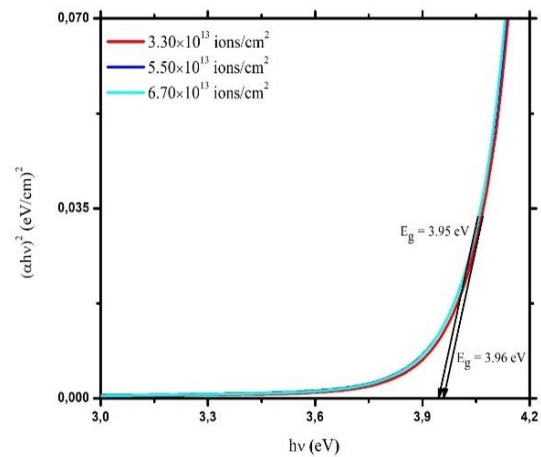


Figure 7. Plot of $(\alpha h\nu)^2$ versus Photon energy ($h\nu$) for 34 MeV Cu^{7+} ion irradiated ITO films coated glass substrate.

4. Conclusion

Sputtering and secondary irradiation effects studies on ITO thin films were carried out. The reduction in thicknesses of the ITO films was attributed to the preferential sputtering of oxygen from the surface, as a consequence of weakly bonded oxygen atoms in the crystal lattice of the film. Electronic sputtering yields decrease with increasing ion fluences for both Au and Cu ion beams. The sputtering yields were found to be in the range of $10^1 - 10^2$ atoms/ion. The observed oxygen sputtering yields from the ITO thin films irradiated by Au ions were higher as compared to those irradiated by Cu ions. An insignificant decrease in the optical band gap as a function of ion fluence confirms that no changes in the optical properties occurred.

5. Acknowledgments

We acknowledge the Tshwane University of Technology and NRF for their financial support. The authors also acknowledge iThemba LABS-TAMS, South Africa, for providing infrastructural resources to this project.

References

- [1] Arnoldbik W M, Tomozeiu N and Habraken F H P M 2003 *Nucl. Instruments Methods Phys. Res. Sect. B Beam Interact. with Mater. Atoms.* **203** 151–157
- [2] Madito M J, Terblans J J, Swart H C and Mtshali C B 2020 *South African J. Sci. Technol.* **39** 40–45
- [3] Sigmund P 2012 *Nanofabrication by Ion-Beam Sputtering: Fundamentals and applications* (Singapore: Pan Stanford Publishing) pp 1–40
- [4] Fearn S 2015 *An Introduction to Time-of-Flight Secondary Ion Mass Spectrometry (TOF-SIMS) and its Applications to Materials Science* (USA: Morgan & Claypool) pp 1–6
- [5] Sigmund P 1969 *Phys. Rev.* **184** 383–416
- [6] Nastasi M, Mayer J W and Wang Y 2014 *Ion Beam Analysis Fundamentals and Applications* (New York: CRC Press) pp 79–100
- [7] Msimanga M 2010 PhD Thesis University of Cape Town
- [8] Mavhungu H, Msimanga M and Hlatshwayo T 2015 *Nucl. Instruments Methods Phys. Res. Sect. B Beam Interact. with Mater. Atoms.* **349** 79–84
- [9] Arstila K *et al.* 2014 *Nucl. Instruments Methods Phys. Res. Sect. B Beam Interact. with Mater. Atoms.* **331** 34–41
- [10] Mammeri S, Msimanga M, Dib A, Ammi H and Pineda-Vargas C A 2018 *Surf. Interface Anal.* **50** 328–334
- [11] Wang Z G, Dufour C, Cabeau B, Dural J, Fuchs G, Paumier E, Pawlak F and Toulemonde M 1996 *Nucl. Instruments Methods Phys. Res. Sect. B Beam Interact. with Mater. Atoms.* **107** 175–180

Theoretical Modelling of High Entropy Alloys

V Nolting

Vaal University of Technology, Private Bag X021, Vanderbijlpark 1911, South Africa

E-mail: volkmarn@vut.ac.za

Abstract. High entropy alloys (HEA) containing Co, Fe, Ni have recently enjoyed considerable attention in the physical and material sciences due to their interesting mechanical and magnetic properties that are further enhanced by the additive manufacturing technique often used to process them. HEAs are theoretically difficult to describe as they often form amorphous structures and the Bloch theorem is not applicable. In this article the method of the effective medium is used and the corresponding many body problem is solved self-consistently within the coherent potential approximation. The mixing entropy of HEAs is explained using an optimization approach. The complex micro and multi-phase structures are due to many body effects that are discussed from a calculation of the quasiparticle density of states. It turns out that these many body effects are most significant if the n components of the alloy are present at about equal proportions. Using alternatively a lattice gas model to represent the disordered alloy the existence of a second order phase transition is confirmed; the transition temperature is calculated. Heat capacity and entropy are evaluated as a function of temperature T . It is shown that the results of the two model calculations are in qualitative agreement with one another and must thus be regarded as good and reliable.

1. Introduction

High entropy alloys (HEA) have been studied since 2003 [1] mainly due to their exceptional mechanical properties, i.e. high yield and ultimate strengths, high structural and phase stability, good corrosion resistance, and high hardness. These properties make high entropy alloys suitable for high temperature applications, e.g. gas turbines in the aerospace industry. They are also routinely used in boat structures, racing car bodies, spaceships, and other constructions of a challenging nature. High entropy alloys are novel or composite materials with about equal proportions of several metals. The basic idea is to create a multi-element single phase solid solution alloy. This feature makes HEAs different to conventional alloys which consist of a primary component with small amounts of additional elements added. Examples for such conventional alloys are bronze (88% Cu and 12% Sn) and carbon steel (96% Fe and 4% C). On the other hand, in high entropy alloys additional elements may be added to Fe to form a new material with properties very much different to those of the individual components. As each HEA can be modified by minor variations in the choice of added elements, the possible number of new alloy bases is vast [2]. Elements with different crystal structures are mixed with the possibility to form various new phases. An example is the single phase CoCrFeNi high entropy alloy which forms an f.c.c. crystal lattice even though Ni, Fe, and Co on their own all crystallize in different lattice structures. To form single phase structures a homogeneous distribution of elements is useful but not necessary [3]. Due to their high mixing entropy high entropy alloys often form multi-phase or even amorphous structures. In the CoCrCuFeNi alloy complex microstructures are observed consisting of amorphous regions and

magnetic nanoparticles forming a superparamagnetic phase. Other alloys exhibit a gap in the density of states near the Fermi level which makes them interesting due to their electronic and magnetic properties as Kondo insulators [4]. Possible applications as soft magnetic materials are suggested.

High entropy alloys are conveniently produced using the additive manufacturing technology [5]. To prevent component failure a structure and design evaluation known as structural health monitoring SHM [6] can then be performed for a risk based analysis and quality assurance. The aim of the article is to get to a better understanding of the material properties of high entropy alloys. It is organized as follows. In the next section the theory on elementary excitations in disordered alloys is presented and a many body problem is formulated. In Section 3 results are presented for the mixing entropy of an ideal solid solution consisting of n components. The discussion of the quasiparticle density of states reveals that many body effects are most prominent for near equal component concentrations, i.e. $c_\alpha = 1/n$ for all α . These many body effects are ultimately responsible for the microstructure and thus the mechanical properties of high entropy alloys. In Section 4 the lattice gas model is applied to disordered alloys. Conclusions are drawn in Section 5.

2. Theory

The perfectly periodic solid is invariant with respect to translational symmetry operations so that the one particle contribution of the Hamiltonian becomes diagonal in \mathbf{k} -space. The Bloch theorem may then be applied to reduce the total many body problem to that of a microscopic unit cell determined by the lattice structure. On the other hand, for disordered systems, e.g. alloys, the Bloch theorem is not applicable. For reasons of simplicity we consider a substitutional alloy consisting of several compounds with similar bandstructure. Additionally we restrict the calculation to a one band model to obtain the model Hamiltonian in the formalism of 2nd quantization

$$\mathbf{H} = \mathbf{H}_0 + \mathbf{H}_p = \sum_{ij\sigma} T_{ij} a_{i\sigma}^\dagger a_{j\sigma} + \sum_{i\sigma} \eta_{i\sigma} a_{i\sigma}^\dagger a_{i\sigma}. \quad (1)$$

Here the term \mathbf{H}_0 denotes a one electron contribution describing the hopping of an electron with spin σ from lattice site \mathbf{R}_j to lattice site \mathbf{R}_i . The corresponding hopping integrals are related to the Bloch energies via

$$T_{ij} = \frac{1}{N} \sum_{\mathbf{k}} \epsilon(\mathbf{k}) e^{i\mathbf{k} \cdot (\mathbf{R}_i - \mathbf{R}_j)}. \quad (2)$$

The perturbation \mathbf{H}_p arises from different atom types with atomic energy level η occupying the lattice site \mathbf{R}_i . It is this part of the Hamiltonian that is responsible for many body effects. The Hamiltonian of Eq. (1) represents the simplest model to describe electrons in a multicomponent alloy. It contains no electron-electron interaction and only depends on the concentrations of different alloy components. It, however, includes electrons interacting with the local lattice potential via the Bloch energies.

To determine \mathbf{H}_p the method of the effective medium [7] may be used. The potential of the fictitious medium is chosen so that the corresponding many body problem can be solved exactly. The perturbation part of the Hamiltonian then describes the deviation of the local potential from that of the effective medium. As this is not known, it is varied until the quasiparticles are not scattered any more at the local potential. This implies that the many body problem becomes an effective one particle problem and the corresponding self-energy

$$\mathbf{M}_\sigma(\mathbf{k}, E) = 0. \quad (3)$$

Alternatively, for the calculation of the one electron Green function $\mathbf{G}_{\mathbf{k}\sigma}(E)$ a configuration average can be performed where for a given set of component concentrations c_α an average over all possible distributions of atoms is calculated. The coherent potential approximation CPA [8] describes a self-consistent calculation where the self-energy $\mathbf{M}_\sigma(\mathbf{k}, E)$ becomes \mathbf{k} -independent, i.e.

$$\mathbf{M}_\sigma(\mathbf{k}, E) = \mathbf{M}_\sigma(E). \quad (4)$$

The self-energy $\mathbf{M}_\sigma(E)$ contains the contributions of the perturbation \mathbf{H}_p , i.e. deviations of the atomic energy levels from the ideal periodic solid. Within the CPA the configuration averaged one particle Green function becomes

$$\langle G_{k\sigma}(E) \rangle = \frac{\hbar}{E - \varepsilon(k) + \mu - M_{\sigma}(E)}. \quad (5)$$

The quasiparticle density of states then follows from the \mathbf{k} -summation

$$\rho_{\sigma}(E) = -\frac{1}{N\pi} \text{Im} \sum_{\mathbf{k}} \frac{1}{E - \varepsilon(\mathbf{k}) - M_{\sigma}(E)} = -\frac{1}{\pi} \text{Im} \int_{-\infty}^{+\infty} \frac{\rho_0(x)}{E - x - M_{\sigma}(E)} dx. \quad (6)$$

In the second step of Eq. (6) the \mathbf{k} -summation is replaced by an integral over the free Bloch density of states that can be chosen in such a way to conveniently represent interacting particle systems. Numerical evaluations are presented in the next section.

3. Results

Section 3 contains both analytical and numerical evaluations regarding the mixing entropy and the quasiparticle density of states of high entropy alloys. The corresponding results are presented, discussed, and compared with those of other authors.

3.1 The mixing entropy

The mixing entropy ΔS for an ideal solid solution consisting of n components is given as

$$\Delta S = -R \sum_{\alpha=1}^n c_{\alpha} \ln c_{\alpha}. \quad (7)$$

Here R denotes the universal gas constant and c_{α} the concentration of components of type α . For the case $n = 2$ Eq. (7) simplifies to

$$\Delta S = -R (c \ln c + (1 - c) \ln(1 - c)). \quad (8)$$

The mixing entropy ΔS attains a maximum value if

$$\frac{d(\Delta S)}{dc} = -R \ln\left(\frac{c}{1-c}\right) = 0. \quad (9)$$

From Eq. (9) follows that $c = 1/2$. If the components are present in equal proportions, then ΔS is maximized with

$$(\Delta S)_{\max} = R \ln n. \quad (10)$$

The result of Eq. (10) agrees with reference [9] suggesting that with larger values of n the formation of random solid solutions in a multi element alloy system becomes more likely. However, the importance of a high mixing entropy with regard to an energy minimum is reduced with decreasing temperature.

3.2. The Quasiparticle Density of States

Eq. (6) is numerically evaluated for a binary alloy consisting of two components with concentrations c_A and $c_B = 1 - c_A$. Corresponding results are depicted in Fig 1 below. The pure crystal is described by the undisturbed density of states with centres of gravity at energies $E = 0.5$ and $E = 1.5$ respectively. Moving away from this trivial situation the densities $\rho(E)$ start overlapping and additionally become more and more deformed. If the centres of gravity are far enough apart, then at intermediate concentrations $c_A = c_B = 1/2$ a band splitting is observed. This band splitting is a typical many body effect which becomes more significant when the chemical potential falls into the band gap. In that case the alloy becomes semiconducting with interesting electronic and magnetic phenomena present like hybridization of localized and conduction electrons, mixed valence states, spin glass behavior, and superparamagnetism. Such phenomena are indeed observed in high entropy alloys. Similar results to those presented in Fig 1 below are also reported in reference [10].

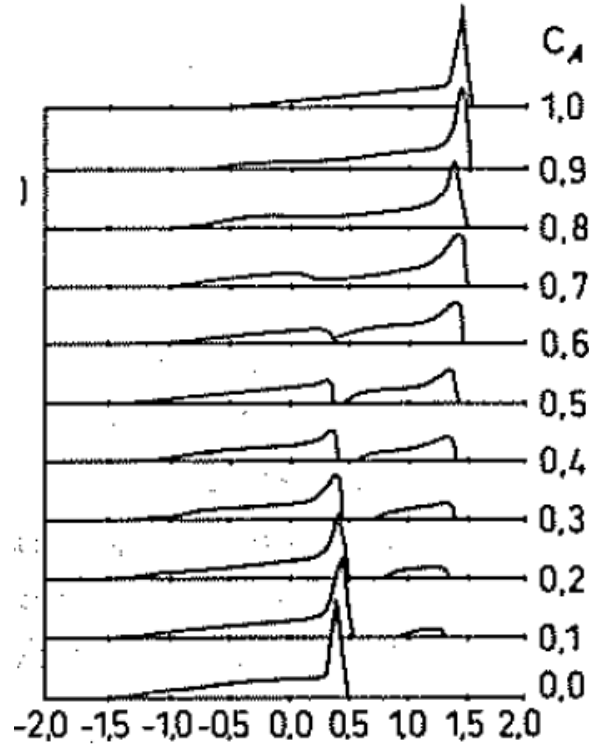


Figure 1. Density of states $\rho(E)$ as a function of energy E for a binary alloy AB plotted for different component concentrations c_A .

4. The Lattice Gas Model

The lattice gas model [11] is applied to describe respectively liquids, disordered alloys, and magnetic systems (Ising model). The total volume V is subdivided into microscopic cells of volume ΔV that are either occupied or unoccupied. One then distinguishes between two situations:

- (1) There are large regions that are either completely occupied or unoccupied. Such a phase separation occurs for temperatures $T \leq T_C$.
- (2) The occupied cells are statistically distributed over the entire volume V . This vapor phase is realized at temperatures $T > T_C$.

The coexistence line between the phase separated system and the homogeneous system is obtained from the ratio of atoms in the liquid state. This ratio is temperature dependent and described by the implicit equations

$$\begin{aligned} r(T) &= \tanh\left(\frac{\alpha r(T)}{T}\right), \\ T_C &= \frac{z w}{2 k_B}. \end{aligned} \quad (11)$$

The transition temperature depends on the number of nearest neighbours z and the interaction energy w between molecules. Similar expressions for T_C are also obtained from other models of phase transitions, e.g. molecular field approximation of Heisenberg model. A numerical evaluation of Eq (11) yields the results of Fig 2 below.

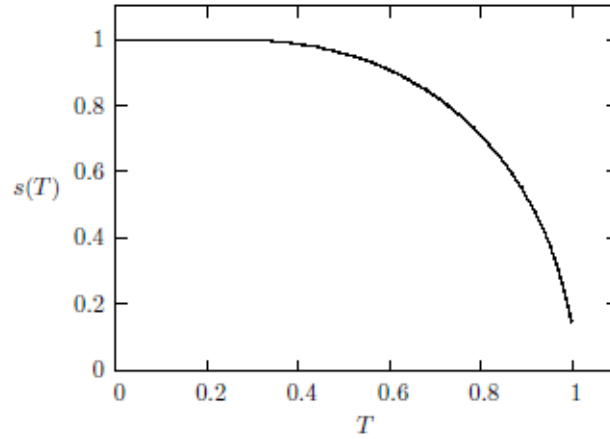


Figure 2. Ratio of atoms $r(T)$ ($= s(T)$) in the liquid state as a function of temperature T .

At $T = 0$ all atoms are in the liquid state, i.e. $r(T = 0) = 1$. With increasing temperature more and more atoms become vaporized and $r(T)$ continuously decreases as a function of T . At the transition temperature $r(T = T_c) = 0$ as all atoms are vaporized; the corresponding phase transition is of second order. This is further confirmed with the discussion of the heat capacity

$$C_V = \frac{x^2}{(\cosh x)^2}, \quad (12)$$

where $x = \frac{\alpha}{T}$ and the entropy $S(T)$ as a function of temperature T . Corresponding results are depicted in Figures 3 and 4 below. As a response function the heat capacity has a peak at the critical temperature T_c ; such peaks are typical for 2nd order phase transitions. The entropy $S(T)$ reaches saturation in the high temperature limit where

$$S(T) \rightarrow N k_B \ln 2. \quad (13)$$

For a binary alloy this is identical to the result of Eq. (10) above. On the other hand, in the low temperature limit

$$S(T = 0) = 0. \quad (14)$$

This is in agreement with the 3rd law of thermodynamics. Furthermore, at the critical temperature T_c the entropy function is continuous as expected for a 2nd order phase transition.

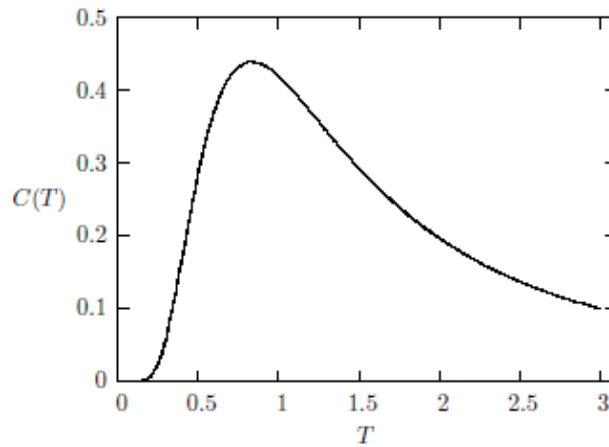


Figure 3. Heat capacity $C_V(T)$ as a function of temperature T .

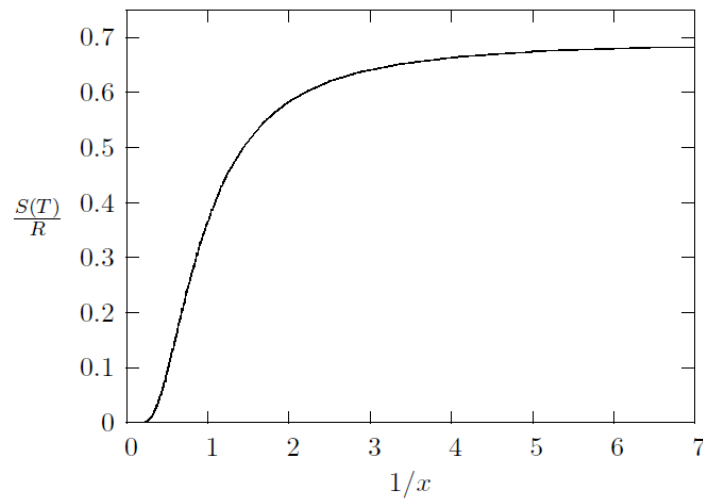


Figure 4. Entropy $S(T)$ as a function of temperature T .

5. Conclusions

In this work high entropy alloys are theoretically described using the method of the effective medium; the corresponding many body problem is solved within the coherent potential approximation CPA. The mixing entropy ΔS attains a maximum value for equal distribution of alloy components. The quasiparticle density of states QDOS shows many body effects in exactly the same region of concentrations. From the lattice gas model the critical temperature T_c for phase separation is calculated. The existence of a 2nd order phase transition is confirmed.

References

- [1] Popescu G et al 2016 *Materials Science and Engineering* 133
- [2] Miracle D B 2019 *Nature Communications* 10
- [3] Feng He et al 2017 *Scripta Materialia* **131**, 42
- [4] Kulkarni R et al 2018 *J Alloys and Compounds* **746**, 194
- [5] Cui W et al 2017 *Proceedings of 28th Annual Int Solid Freeform Fabrication Symposium* 712
- [6] Boller C 2013 Asia Pacific Conference on Non- Destructive Testing APCNDT, Mumbai
- [7] Wang M and Pan N 2008 *Materials Science and Engineering* 63
- [8] Yonezawa F and Morigaki K 1973 *Prog Theoretical Physics Suppl* 53
- [9] Yeh J W et al 2004 *Adv Engineering Mat.* **6**, 299
- [10] Nolting W 2017 *Theoretical Physics* 7, Springer
- [11] Yang C N and Lee T D 1952 *Phys Rev* **87**, 404

Spin-imbalances in non-magnetic nano-systems: Using non-equilibrium Green's function DFT to model spin-selective phenomena mediated by spin-orbit coupling.

W. Dednam^{1,2}, Linda A. Zotti³, S. Pakdel⁴, E. B. Lombardi¹ and J. J. Palacios⁵

¹ Department of Physics, Science Campus, University of South Africa, Private Bag X6, Florida Park 1710, South Africa

² Departamento de Física Aplicada and Unidad Asociada CSIC, Universidad de Alicante, Campus de San Vicente del Raspeig, E-03690 Alicante, Spain.

³ Departamento de Física Teórica de la materia condensada, Universidad Autónoma de Madrid, Cantoblanco, Madrid 28049, Spain

⁴ Department of Physics, Technical University of Denmark: Kongens Lyngby, Hovedstaden, Denmark

⁵ Departamento de Física de la Materia Condensada, Universidad Autónoma de Madrid, Cantoblanco, Madrid 28049, Spain

E-mail: dednaw@unisa.ac.za

Abstract. Heavy transition metals are frequently used as electrodes and substrates in scanning tunneling microscopy experiments. In the constricted low dimensional systems that occur in such experiments, typically under conditions of non-zero bias voltage, spin-imbalance may develop even in non-magnetic atomic- and nano-systems. This phenomenon arises as a result of spin selective effects mediated by spin-orbit coupling. It is important to not only understand the emergence of the spin imbalance, but also to model associated properties such as spin-polarized electron transport in these systems. Conventional theoretical approaches cannot model these effects because they usually neglect spin-orbit coupling. Therefore, to model spin-imbalance in the electronic transport of constricted nano-systems, such as in atomically sharp transition metal electrode tips or surfaces, as well as in organic molecules bridging the electrode tips, we have implemented spin-orbit coupling as a post-self-consistent correction in atomic orbital basis density functional theory within the non-equilibrium Green's function formalism. Our method takes advantage of optimized Gaussian orbital basis sets and effective core potentials and one-shot transport calculations with steady convergence and charge transfer properties compared to other similar approaches. We apply this method to a selected number of sample constricted low dimensional systems where spin-imbalance is important by performing density functional transport calculations. This permits us to demonstrate that incorporation of spin-orbit coupling is essential to understanding emergent spin-imbalance in molecular electronics, while in certain instances, the consideration of the applied bias is also important to the manifestation of spin imbalance phenomena in heavy transition metal electrodes and substrates.

1. Introduction

Spintronics is a promising field in which the electron's spin is used to process and store information as an improvement on the present use of its charge to accomplish those same tasks [1]. Recently, spin-orbit coupling (SOC) has been proposed as an explanation for spin-polarized currents in molecular junctions [2, 3, 4, 5], which, in the simplest possible arrangement, consist of two nano-sized transition metal electrodes bridged by freely-suspended chiral organic molecules (molecules which have non-superimposable mirror images), typically in the scanning tunneling microscope (STM) setup [6, 7]. In practical applications, spin-selective molecular nano-junctions could serve, for example, as spin-current rectifiers in novel spintronic molecular devices, due to the so-called chirality induced spin selectivity (CISS) effect.

There still exists, however, a controversy surrounding the exact origin of the CISS effect: is it due to spin-locking along the twisting chiral molecule in which orbit moments on the molecule's atoms favour the transport of one spin orientation over another [2], or does the molecule inherit SOC from the heavy transition metal electrodes such that spin-filtering rather take places at the interface between metal electrode and molecule [3, 4, 5]? To answer this question from a theoretical perspective, it is at the very least necessary to model SOC properly and conveniently in electronic transport calculations based on density functional theory (DFT), since comparisons with experiment are usually accomplished via such calculations [7, 8, 9]. SOC transport calculations are possible in many DFT codes, but convergence may be intractable for nano-systems involving more than a few tens of (heavy transition metal) atoms. In this work, we present one-shot DFT electronic transport calculations based on the non-equilibrium Green's function (NEGF) method [8] using Gaussian-type orbital (GTO) basis sets that have been fitted to high quality SOC bands.

2. Models

In 2018, Pakdel et al. [10] found that if a GTO basis set describes the band structure of a material well in the absence of SOC, then adding SOC as a correction in a post self-consistent-field (SCF) step gives good SOC bands, when compared to a reference method that produces very high quality bands such as VASP [11], Wien2k [12], Quantum Espresso [13] or OpenMX [14, 15, 16, 17]. Pakdel et al.'s method [10] and our recent improvements thereupon are described very briefly below.

The Dirac-Kohn-Sham Hamiltonian can be written, to lowest order, as the standard atomic SOC matrix because the radial and angular components of the wave functions in atomic-orbital based DFT, such as the GTOs used by CRYSTAL14 [18] or GAUSSIAN09 [19] are orthogonal:

$$\xi_{ij}(r) \mathbf{L} \cdot \mathbf{S} = [\xi_{ij} \langle l_i; m_{l_i}; s | \mathbf{L} \cdot \mathbf{S} | l_j; m_{l_j}; s' \rangle], \quad (1)$$

where:

$$\xi_{ij} = \frac{e^2}{2m_e c^2} \int_0^\infty \frac{1}{r} \frac{dV_{\text{eff}}(r)}{dr} R_i(r) R_j^*(r) r^2 dr. \quad (2)$$

In equation (2), $V_{\text{eff}}(r) = -\frac{Z}{r}$ is the effective nuclear potential [10], with Z the atomic number. $R_i(r)$ are the radial (un)contracted gaussian-type orbitals (CGTOs). Only CGTOs on the same atom and of the same shell type ($L = 1, 2$ or 3) contribute to the integral because SOC is an intra-atomic phenomenon [10]. However, for CGTO basis sets with pseudopotentials, Pakdel et al. found that a single multiplicative correction to ξ_{ij} was needed in order to account for the correct effective charge in $V_{\text{eff}}(r)$ due to the lack of nodal structure near the nucleus in pseudopotentials. Here, we make two minor modifications to improve the above implementation. We use the following modified Yukawa screening potential:

$$V_{\text{eff}}(r) = \begin{cases} \frac{-(Z-1) \left[\exp\left(-\frac{\ln Z}{r_c} r\right) + 1 \right]}{r} & r \leq r_c \\ \frac{-1}{r} & r > r_c \end{cases} \quad (3)$$

where r_c is a cutoff, typically the size of an atomic radius ($\sim 2.5 - 3.0$ a.u.). Instead of the single global multiplicative factor used in ref. [10], we implement a multiplicative factor for each shell type ($L = 1, 2$ or 3) to account for the fact that the radial SOC coefficients of different shells are usually multiples of each other [20].

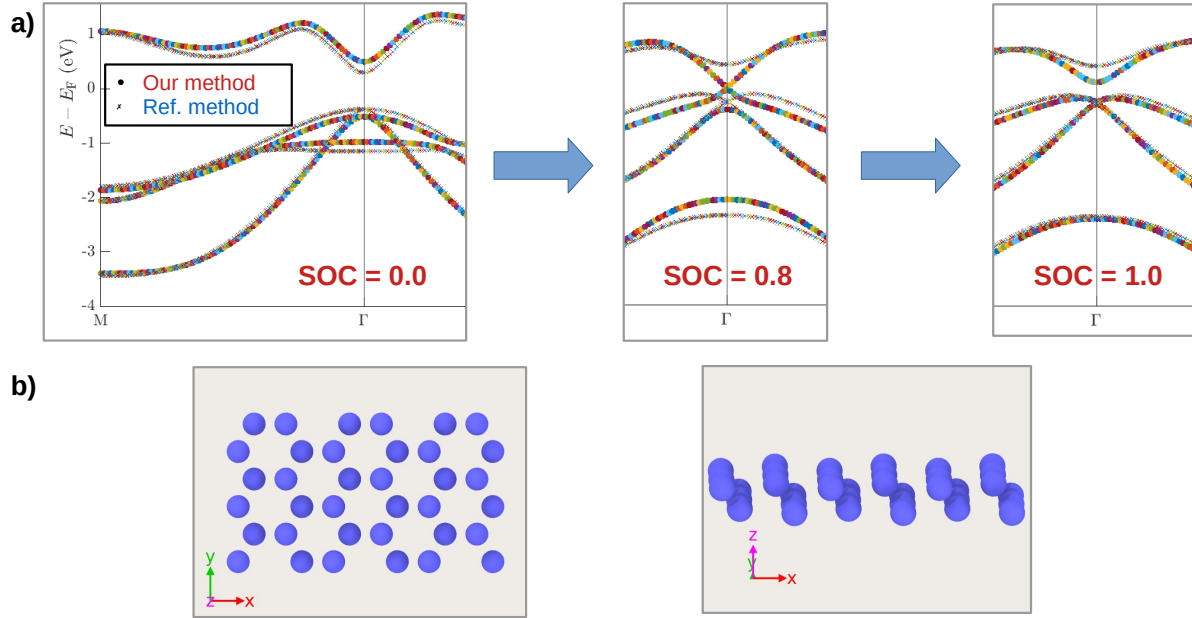


Figure 1. (Colour online) a) Example of adding spin-orbit coupling as a post-SCF correction in DFT calculations of the bands of a solid material, for b) Bismuth (111) bilayers. Solid markers are our method and the fainter crosses correspond to the reference method. The same lattice parameters were used in both methods as in ref. [10]: $a = 4.33$ Å and $c = 1.74$ Å in symmetry group $P\bar{3}m1$ of the Hermann-Mauguin classification or space group 164 in the International Tables of Crystallography.

3. Results and discussion

To verify that adding SOC as a correction in a post-SCF step gives good SOC bands, we use Bi(111) bilayers (see figure 1 b)) as a test system and compare our calculations using **CRYSTAL14** on one hand, and **OpenMX** as reference method, on the other, given the very good agreement between **OpenMX** and **Wien2k** [21, 22].

In Bi(111) bilayers, starting without SOC in the left panel of figure 1 a), the band gap must evolve first into a Dirac cone at the Γ point (SOC=0.8 in the middle panel of figure 1 a)) and then open up again as SOC is increased to 1.0 in a so-called “band inversion” in the rightmost panel of figure 1 a). We used the high quality basis set from ref. [23] for Bi and the Perdew-Burke-Ernzerhof (PBE) generalized-gradient approximation (GGA) exchange correlation functional in our **CRYSTAL14** calculation of the bands in the absence of SOC, resulting in reasonable agreement with our reference method, using the **Bi8.0-s4p4d3f2** basis set and **Bi_PBE19** pseudopotential in **OpenMX**. We also used very large k meshes ($81 \times 47 \times 1$) in multiples of 3 to correctly capture the electronic structure at the Γ point. In going from SOC=0.0 to SOC=1.0, we only tuned the multiplicative factor empirically for the bands of p -orbital ($L = 1$ shell) character because only

they contribute to SOC ± 4 eV about the Fermi energy. Thus, in figure 1, SOC=0.8 corresponds to using a $L = 1$ multiplicative factor $\text{SOCFAC}_P = 270.0$ and SOC=1.0, to $\text{SOCFAC}_P = 350.0$.

The ultimate goal of fitting SOC corrected bands to a reference method is to choose high quality basis sets that can be used in DFT electronic transport calculations where transition metal elements, sometimes with strong SOC, are used as the electrodes. We therefore need high quality GTO basis sets for metals such Au, Ag and Cu, which are used in experiments [24, 25]. For the sake of brevity, we present only the SOC-corrected bands for two extreme cases (see figure 2): face-centred cubic (FCC) Cu using an all-electron basis set [26] (all multiplicative factors set equal to 1.0) and FCC Au using the high quality pseudopotential basis set reported in ref. [23]. The latter required larger per-shell multiplicative factors, $\text{SOCFAC}_P = 260.0$, $\text{SOCFAC}_D = 40.0$ and $\text{SOCFAC}_F = 10.0$ for the $L = 1, 2, 3$ shells respectively. The same lattice parameters were used in our and the reference methods: 3.63 Å in the case of Cu and 4.05 Å for Au [23]. As basis sets and pseudopotentials in `OpenMX`, we used Cu6.0H-s3p3d3f1 and Cu_PBE19H for Cu and Au7.0-s2p2d2f1 and Au_PBE19 for Au.

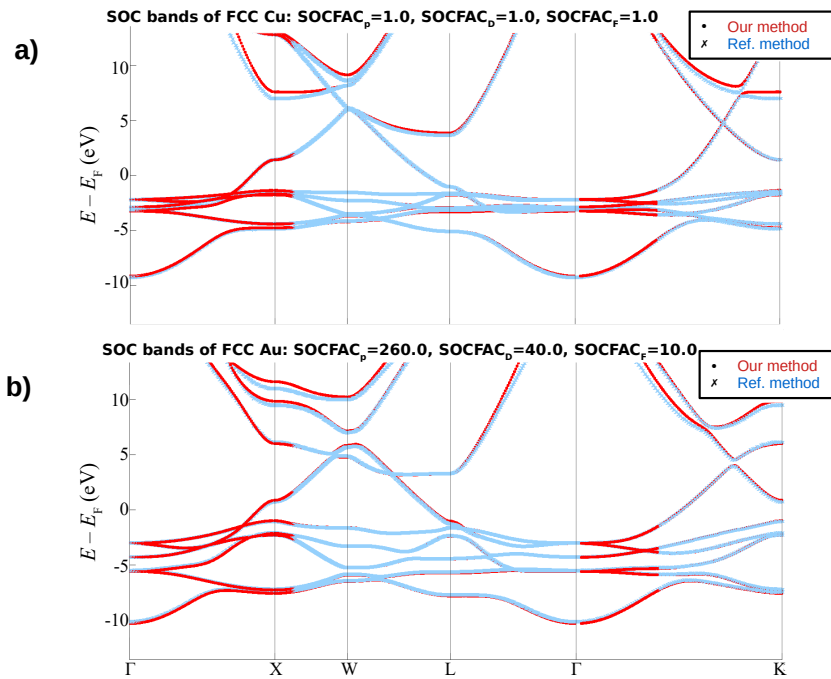


Figure 2. (Colour online) a) SOC-corrected bands for face-centred cubic Cu obtained using the all-electron basis set reported in ref. [26] in `CRYSTAL14` (red solid markers) and the reference method `OpenMX` (light blue crosses) b). SOC-corrected bands for FCC Au obtained using the pseudopotential basis set reported in ref. [23] in `CRYSTAL14` (red solid markers) and the reference method `OpenMX` (light blue crosses). Notice that per-shell multiplicative SOC factors much larger than 1 were needed to get a good empirical fit in the case of Au.

Figure 3 illustrates two simple example applications of our post-SCF electronic transport implementation of SOC. For this, we use the code Atomistic NanoTransport (`ANT.Gaussian`) [27, 28, 29]. It interfaces with `Gaussian09` [19] to perform a scalar-relativistic, spin-unrestricted calculation of the transport. The SOC correction has been implemented in `ANT.Gaussian` and is freely available online [30]. The advantage of using `ANT.Gaussian` over other density functional theory (DFT) codes with a self-consistent SOC electronic transport capability, is that the calculation requires just one step unlike most of the other codes in which a one-dimensional

electrode model is used [31, 32]. Moreover, our method displays better convergence properties compared to other codes in the absence of SOC, such as our reference method `OpenMX` [33, 32].

The structure in figure 3 a) was taken directly from the online supplementary material of ref. [4]. For Au and Cu, we used the basis sets referred to previously. For Ag, a pseudopotential basis set giving good agreement with the reference method and similar to that of Au was used [34]. As expected, the polarization in the molecule generally increases as the metal becomes heavier and the intra-atomic SOC interaction becomes larger.

In figure 3 b), we show the manifestation of the classical spin-Hall effect in an unreconstructed surface of Au(111). Broken inversion symmetry in thin samples or exposed surfaces of heavy transition elements leads to the lateral separation of spins of roughly opposite orientation under non-zero bias, 0.1 and 0.5 V, even in non-magnetic materials [35].

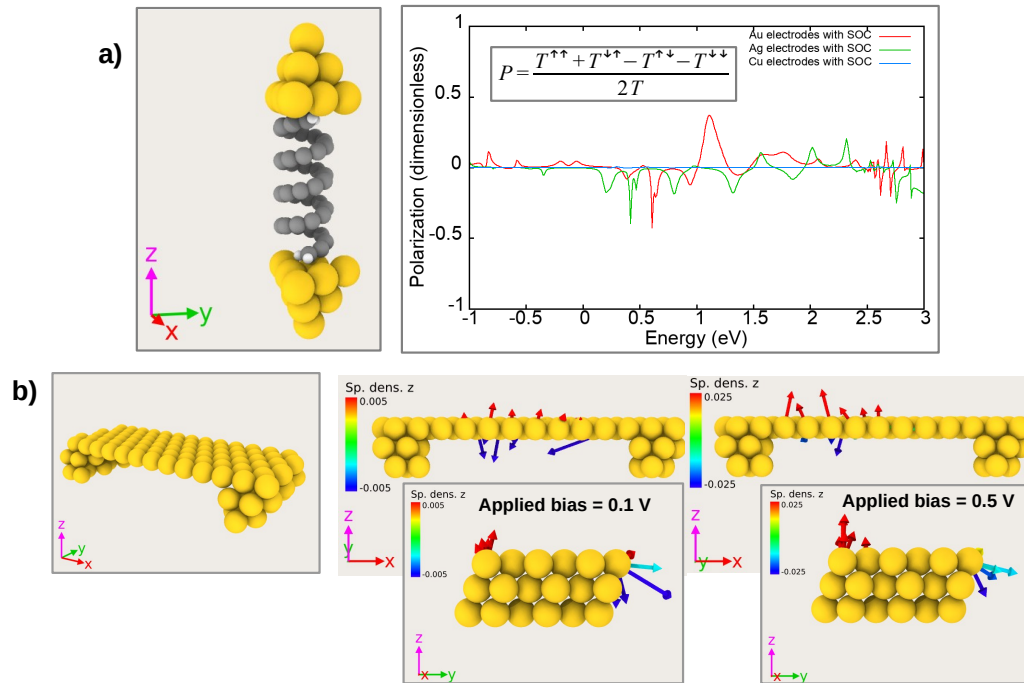


Figure 3. (Colour online) a) Polarization (P) of the helicene molecule sandwiched between Au, Ag or Cu electrodes (left) as a function of energy, calculated at zero bias voltage from the spin-resolved transmission $T^{\sigma,\sigma'}$, where $\sigma, \sigma' = \{\uparrow, \downarrow\}$. b). Spin densities along the z direction in the Au "table" shown on the left and calculated at bias voltages of 0.1 and 0.5 V, respectively. Under non-zero bias, the classical spin Hall effect manifests as the lateral separation, along the transport direction, of spins of approximately opposite orientation.

4. Conclusion

We have presented a post self-consistent field implementation of spin-orbit coupling in density functional theory calculations on transition metals using Gaussian type local orbitals. The ability of such basis sets to correctly reproduce the electronic structure of the metals is established by comparing spin-orbit-coupling corrected bands with those generated by a fully self-consistent implementation of the spin-orbit interaction. The transferrability of the basis sets to density functional theory electronic transport calculations was established by performing simple test calculations to reproduce phenomena that are known to trace their origins to spin-orbit coupling: (i) chirality induced spin selectivity of organic molecules under zero bias and

(ii) the manifestation, under non-zero bias, of the classical spin Hall effect in a thin non-magnetic Au(111) surface. The advantage of our method is that the calculation is one-shot, i.e., requires only one step and also exhibits superior convergence properties compared to other fully-relativistic self-consistent implementations. In future work, we will implement SOC-corrected band fitting for magnetic systems and composite materials.

Acknowledgments

The computational results contained in this work would also not have been possible without access to the high performance computing (HPC) facility at Unisa, and the supercomputing facility in the Department of Applied Physics at the University of Alicante.

References

- [1] Joshi V K 2016 *Engineering Science and Technology, an International Journal* **19** 1503–1513
- [2] Dalum S and Hedegård P 2019 *Nano Letters* **19** 5253–5259
- [3] Zöllner M S, Varela S, Medina E, Mujica V and Herrmann C 2020 *Journal of Chemical Theory and Computation* **16** 2914–2929
- [4] Zöllner M S, Saghatchi A, Mujica V and Herrmann C 2020 *Journal of Chemical Theory and Computation* **16** 7357–7371
- [5] Liu Y, Xiao J, Koo J and Yan B 2021 *Nature Materials* **20** 638–644
- [6] Binnig G, Rohrer H, Gerber C and Weibel E 1982 *Phys. Rev. Lett.* **49**(1) 57–61
- [7] Agraït N, Yeyati A L and Van Ruitenbeek J M 2003 *Physics Reports* **377** 81
- [8] Cuevas J C and Scheer E 2010 *Molecular Electronics* (Singapore: World Scientific)
- [9] Requist R, Baruselli P P, Smogunov A, Fabrizio M, Modesti S and Tosatti E 2016 *Nat. Nanotechnol.* **11** 499
- [10] Pakdel S, Pourfath M and Palacios J J 2018 *Beilstein J. Nanotechnol.* **9** 1015
- [11] Kresse G and Furthmüller J 1996 *Computational Materials Science* **6** 15–50
- [12] Blaha P, Schwarz K, Madsen G, Kvasnicka D and Luitz J 2001 *Wien2k: An augmented plane wave+ local orbitals program for calculating crystal properties* (Karlheinz Schwarz, Techn. Universität Wien, Austria) ISBN 3-9501031-1-2
- [13] Giannozzi P *et al.* 2009 *J. Phys.: Condens. Matter* **21** 395502
- [14] Ozaki T 2003 *Phys. Rev. B* **67**(15) 155108
- [15] Ozaki T and Kino H 2004 *Phys. Rev. B* **69**(19) 195113
- [16] Ozaki T and Kino H 2005 *Phys. Rev. B* **72**(4) 045121
- [17] Ozaki T *et al.* 2017 OpenMX (Open source package for Material eXplorer) ver. 3.8 URL <http://www.openmx-square.org/>
- [18] Dovesi R *et al.* 2014 *Int. J. Quantum Chem.* **114** 1287
- [19] Frisch M J *et al.* Computer code GAUSSIAN09, Revision C.01, Gaussian, Inc. Wallingford, CT, 2009
- [20] Barreateau C, Spanjaard D and Desjonquères M C 2016 *Comptes Rendus Physique* **17** 406
- [21] Lejaeghere K *et al.* 2016 *Science* **351**
- [22] Ozaki T 2019 Delta gauge of OpenMX with the database (2019) URL https://t-ozaki.issp.u-tokyo.ac.jp/vps/_pao2019/Delta_Factor/index.html
- [23] Laun J and Bredow T 2021 *Journal of Computational Chemistry* **42** 1064–1072
- [24] Sabater C, Dednam W, Calvo M R, Fernández M A, Untiedt C and Caturla M J 2018 *Phys. Rev. B* **97** 075418
- [25] Calvo M R, Sabater C, Dednam W, Lombardi E B, Caturla M J and Untiedt C 2018 *Phys. Rev. Lett.* **120**(7) 076802
- [26] Ruiz E, Lluell M and Alemany P 2003 *Journal of Solid State Chemistry* **176** 400–411
- [27] Palacios J J, Pérez-Jiménez A J, Louis E and Vergés J A 2001 *Phys. Rev. B* **64**(11) 115411
- [28] Palacios J J, Pérez-Jiménez A J, Louis E, SanFabián E and Vergés J A 2002 *Phys. Rev. B* **66**(3) 035322
- [29] Louis E, Vergés J A, Palacios J J, Pérez-Jiménez A J and SanFabián E 2003 *Phys. Rev. B* **67**(15) 155321
- [30] Palacios J J *et al.* Computer code ANT.Gaussian, with SOC corrections Available from <https://github.com/juanjosepalacios/ANT.Gaussian>
- [31] Jacob D and Palacios J J 2011 *The Journal of Chemical Physics* **134** 044118
- [32] Zotti L A and Pérez R 2017 *Phys. Rev. B* **95**(12) 125438
- [33] Ozaki T, Nishio K and Kino H 2010 *Phys. Rev. B* **81** 035116 ISSN 1098-0121
- [34] Laun J, Vilela Oliveira D and Bredow T 2018 *Journal of Computational Chemistry* **39** 1285–1290
- [35] Jungwirth T, Wunderlich J and Olejník K 2012 *Nature Materials* **11** 382–390

Characterization of P3HT-CNT thin films for photovoltaic solar cell applications

Seithati Qotso^{1*}, Pontsho Mbule² and Bakang Mothudi²

¹Department of Electrical Engineering, CSET, University of South Africa, Johannesburg, 1710, South Africa

²Department of Physics, CSET, University of South Africa, Johannesburg, 1710, South Africa

*E-mail: qotsoas@gmail.com / mbuleps1@unisa.ac.za

Abstract. This work report on the structure, morphology, optical and electrical properties of few-walled carbon nanotubes (FWCNT) as electron acceptor in the active layer of organic solar cell devices. FWCNT were dissolved in chlorobenzene and incorporated with pristine P3HT-conjugated polymer at different ratios (1:1-1:4) and systematically the effects on the structure, morphology, optical and photoluminescence were investigated. The XRD results exhibits the cubic structure, UV-Vis showed improvement in absorption which gives a better opportunity for enhanced efficiency in organic solar cells. PL results showed that all samples are quenching the P3HT intensity giving a large possibility of the charge separation in the photoactive layer and FESEM showed the disordered nanotubes.

1. Introduction

The global share of photovoltaic (PV) technologies in energy production still remains marginal today and is likely to remain this way for a long period of time especially in the poor developing countries [1]. The evidence of the limited global impact of PV is marked by the increasing market share of fossil fuels in the generation of electricity [2]. Carbon nanotubes (CNT) have emerged as one of the leading additives for improving the thermoelectric properties of organic materials due to their unique structure and excellent electronic transport properties [3]. CNT are the most commonly used and effective material among numerous fillers. They can provide conductive paths when embedded in polymer matrix since CNT possess excellent electrical conductivity and high charge mobilities [3]. These CNT can be divided into three (3) types: single walled carbon nanotubes (SWCNT), few walled carbon nanotubes (FWCNT) and multi walled carbon nanotubes (MWCNT) [4]. The high conductivity of CNT is due to the availability of free electrons owing to sp² hybridized carbon atoms of the hexagonal graphite plane [5]. The electrical behavior of SWCNT can be determined by their chirality, either metallic or semiconductor [6], however, MWCNT is metallic if at least one sheet has a metallic chirality [7]. Comparing the CNT, FWCNT are known for their remarkable electronics properties [8], conductivity and field emission is stronger [9]. Jung et al. [10] incorporated FWCNT with different conducting polymers including poly(3 – hexylthiophene) (P3HT) for thermoelectric properties. They also reported the highest thermal conductivity when FWCNT incorporated with P3HT compared to other conducting

polymers. Khan et al. [11] used MWCNT mixed with P3HT as a photoactive layer for organic solar cells. In their findings, they reported the photoelectrical conversion efficiency (PCE) of 2.35%.

Recently, organic electronics based on conducting polymers have been intensively investigated due to their interesting band gap and they can also be easily used to fabricate thin films [11]. These conducting polymers have been applied in organic light emitting diodes (OLED), organic gas sensors (OGS) and organic solar cells (OSC) amongst others [12-16]. Poly(3 – hexylthiophene) P3HT is a conjugated electron donor polymer that is commonly used in solar cells, due to its good electro-optical properties, ease of process and synthesis [18–22] and it has been seen as the pillar in the development of future nanostructured polymer solar cells [23]. (P3HT) has been mostly applied in organic solar cells due to its narrow band gap (1.93-1.95 eV) that enable it to absorb a large energy spectrum [17]. In this study, P3HT-FWCNT at different ratios were investigated for the purpose of improving P3HT absorption and conductivity for applications in organic solar cells.

2. Experimental Procedure

Few walled carbon nanotube (FWCNT) and poly(3 – hexylthiophene) (P3HT) were purchased from Sigma Aldrich used in this study without further purification. FWCNT was dissolved in chlorobenzene using the ultrasonic bath for 30 minutes and P3HT was also dissolved in chlorobenzene and stirred on the magnetic stirrer for 24 hours. P3HT was incorporated in FWCNT at different ratios, the composites were stirred on the magnetic stirrer for 3 hours. The thin films were prepared by using a pipette to drop-cast the solution onto the ultrasonically cleaned borosilicate glass substrate and thereafter the film was then allowed to dry at room temperature. The thin films were then characterized using X-ray diffraction (XRD), ultraviolet to visible (UV-Vis/NIR) spectrophotometer and photoluminescence (PL) spectroscopy, field emission scanning electron microscopy (FE-SEM) and current-voltage (I-V) characterization.

3. Results and discussion

3.1. X-ray diffraction Analysis

Figure 1 shows the XRD results of the thin films prepared using the drop-cast method. The results show a clear cubic structure for all the samples. Furthermore, it clearly shows that by increasing the FWCNT-P3HT ratio, the intensity of the [302] peak decreases. The decrease in [302] intensity clearly shows that P3HT covers the surface of the FWCNT. The results shows that 1:1 ratio is more crystalline than other samples, and therefore the composite (1:1) are further studied by other techniques such as UV/Vis/NIR, SEM among others. The average crystallite size were found to be 19, 18, 16, 15 and 10 for FWCNT and P3HT-FWCNT at different ratios, respectively. The average crystallite sizes were calculated using the Scherrer equation [25]:

$$D = \frac{k\lambda}{\beta \cos\theta}$$

Where D is the crystallite size (nm), k is the Scherrer constant (0.9), λ is the wavelength of the x-ray source (0.15406 nm), β (radians) is the full width at half maximum and θ is the peak position in radians. It is clear that as the diffraction peaks broaden the crystallite size decreases.

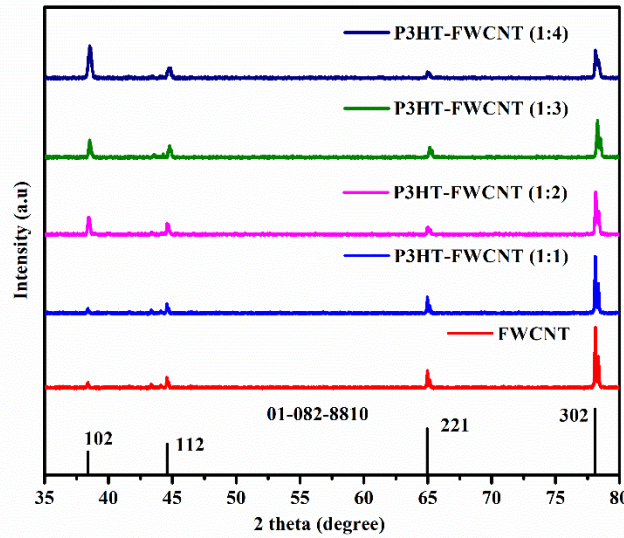


Figure 1: XRD patterns of FWCNT, P3HT, P3HT-FWCNT at different ratios.

3.2. UV-Vis Analysis

The absorption spectra of the prepared samples were investigated at room temperature using UV/Vis/NIR spectrophotometer in the wavelength region of 250 to 800 nm. Figure. 2 (a) shows the normalized absorption spectra P3HT and P3HT-FWCNT at different ratios. P3HT-FWCNT at different ratios show an improved absorption efficiency. The results clearly show that P3HT-FWCNT (1:1) has the highest absorption compared to other composites. This is expected to improve the electrical conductivity and may lead to the enhanced efficiency in photovoltaic solar cell. The spectra shows that the samples have peaks at different positions (530 and 636 nm), and these positions are attributed π - π^* transitions of P3HT [26]. The optical bandgap was extrapolated from the linear portion of the Tauc's plot [27]:

$$Ah\nu = A(h\nu - E_g)^{1/2}, \quad (1)$$

where A is the constant, $h\nu$ is the photon energy (h =Planck's constant and ν is frequency of a photon) and a is the absorption coefficient. The estimated optical bandgap was obtained by extrapolating from the linear portion of the Tauc's plot as shown in figure 3 (b) with P3HT having 1.8 eV. The estimated bandgap for FWCNT was found to be 2.7 eV and 1.8-1.9 eV for P3HT-FWCNT at different ratios.

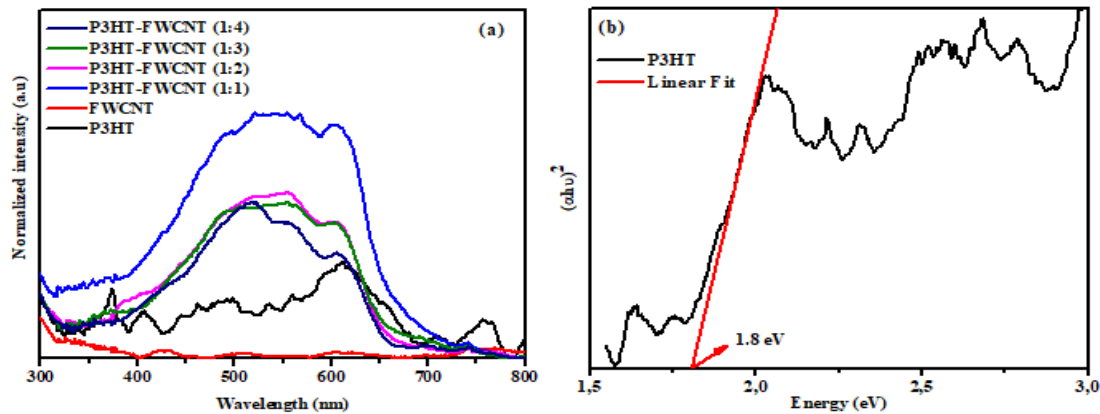


Figure 2: Normalized absorption spectra of (a) FWCNT, P3HT and P3HT-FWCNT at different ratios (b) P3HT Tauc's plot.

3.3. Photoluminescence Analysis

The PL measurements shown in Figure 3 (c) were carried out to observe the charge transfer between the donor-acceptor pair. The emission spectra were compared to that of P3HT. The PL results clearly shows PL quenching of the emission spectra, and this may be attributed to the presence of FWCNT. This confirms that charge transfer between P3HT and FWCNT was successful. This quenching is attributed to the position of P3HT LUMO and work function of FWCNT which are close to each other [28]. This phenomenon can be further explained by the strong π - π interaction between P3HT chains and FWCNT, through which the photoinduced electrons are efficiently separated and transferred and excitonic combination is avoided [29,30]. This makes it energetically favourable for electrons transfer from P3HT LUMO to FWCNT which suggest a strong electronic interaction between P3HT chains and FWCNT. These results correspond with UV/Vis/NIR results. The spectra shows that the samples have peaks at different positions (636 and 690 nm), and these positions are attributed to the pure electronic transition in the regioregular P3HT [31]. The results shows that P3HT-FWCNT (1:1) quenches the PL intensity even more showing a charge transfer between donor-acceptor materials and therefore reducing the electron-hole recombination. This P3HT-FWCNT (1:1) has a strong PL quenching effect which leads to a large possibility of charge separation in the photoactive layer.

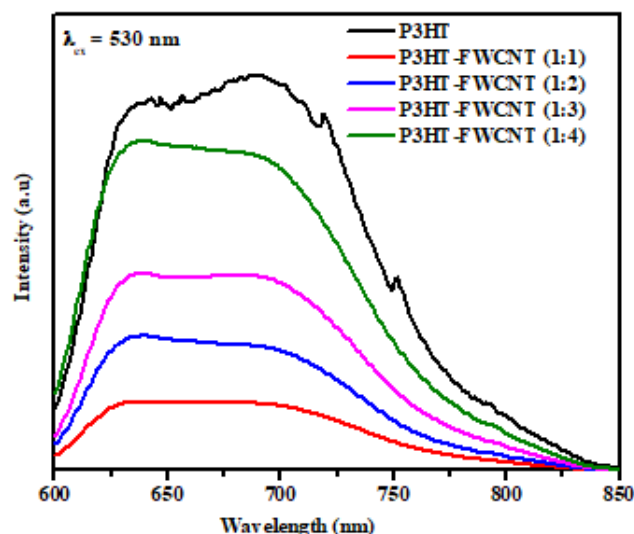


Figure 3: Emission spectra of pristine P3HT, and P3HT-FWCNT at different ratios.

3.4. FESEM Analysis

The FESEM images in figure 4 (a), (b) and (c) shows the morphology of the organic P3HT, nanotubes and disordered nanotubes, respectively. CNT performance in general is still not as impressive as expected due to some issues such as nanotube entanglement, non-alignment, and metallic impurities [32]. According to Danish et al. [32] these issues may lead to the decrement in hole mobility and increment in recombination pathways. However, in this study the aim is to search for the composite which has the strongest PL quenching effect which indicates the highest possibility of the charge separation in photoactive layer. Prior to choosing an appropriate composition in the composite used for photoactive layer, we also investigated PL properties of pristine P3HT and composite film, and therefore 1:1 is expected to improve the electrical conductivity of P3HT.

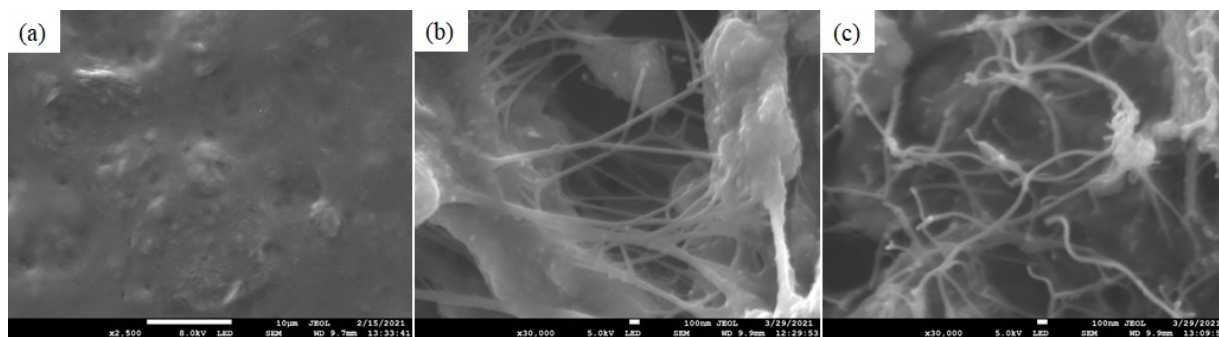


Figure 4: (a) P3HT (b) FWCNT (c) P3HT-FWCNT (1:1).

4. Conclusion

In summary, the interaction between FWCNT and P3HT have been studied. The XRD confirmed the cubic structure and that no other diffraction peaks other than those of FWCNT. UV-Vis showed improvement in absorption which gives a better opportunity for enhanced efficiency in organic solar cells. PL results showed that all samples are quenching the P3HT intensity giving a large possibility of the charge separation in the photoactive layer and FESEM showed the disordered nanotubes.

References

- [1] Rwenyagila E.R 2017 *Int. J. Photoenergy*. 1–12.
- [2] Grossiord N, Kroon M.J, R, Andriessen, Blom P.W.N 2012 *Org. Electron.* **13** 432–456.
- [3] Qu S, Wang, Chen M. Y, Yao Q and Chen L 2018 *RSC Adv.* **8** 33855–33863.
- [4] McEuen P.L, Fuhrer M.S and Park H 2002 *IEEE Trans. Nanotechnol.*, **1** 78–85.
- [5] Inmuddin, Shakeel N, Ahamed M.I, Kanchi S and Kashmery H.A 2020 *Nature research*, **10** 5052.
- [6] Dekker C, 1999 *Phys Today*, **52** 22 – 28.
- [7] Stavarache L, Lepadatu A, Teodorescu V.S, Ciurea M.L, Lancu V, Dragoman M, Kostantinidis G, Buiculescu R, 2011 *Nanoscale Res. Lett.* **6** 88.
- [8] Feng Y, Zhang H, Hou Y, McNicholas T.P, Yuan D, Yang S, Ding L, Feng W and Liu J 2008 *ASC Nano*, **2** 1634–1638
- [9] Ma M, Miao Z, Zhang D, Du X, Zhang Y, Zhang C, Lin J and Chen Q 2015 *Biosens. Bioelectron.* **64** 477–484.
- [10] Jung J, Suh E.H, Jeong Y.J, Yang H.S, Lee T and Jang J, 2019 *ASC Appl. Mater. Interfaces*, S1–S14.
- [11] Khanh T.S.T, Nam N.P.H and Dinh N. N 2020 *J. Mater. Sci: Chem. Eng*, **8** 1-10.
- [12] Zhang M, Hofle S, Czolk J, Mertens A, Colsmann A, 2015 *Nanoscale*, **7** 20009 – 20014.
- [13] Luo D, Chen Q.B, Liu B and Qui Y 2019 *Polymers*, **11** 384.
- [14] Li G, Zhu R, Yang Y, 2012 *Nature Photonics*, **6** 153 – 161.
- [15] Gao Y. Y, Wang Z, Yue G.T, Yu X, Liu X.S, Yang G, Tan F.R, Wei Z.X and Zhang W.F 2019 *Solar RRL*, **3** 1900012.
- [16] Zhang Z.J, Miao J.H, Ding Z.C, Kan B, Lin B.J, Wan X.J, Ma W, Chen Y.S, Long X.J, Dou C.D, Zhang J.D, Liu J and Wang L.X 2019 *Nat. Commun.* **10** 3271.
- [17] Ren S, Chang L.Y, Lim S.K, Zhao J, Smith M, Zhao N, Bulovic V, Bawendi M and Gradecak S 2011 *Nano Letters*, **11** 3998–4002.
- [18] Haucha J. A, Schilinskya P, Choulisa S. A, Childersb R, Bielea M and Brabeca C. 2008 *J. Sol. Energy Mater. Sol. Cells* **92** 727 – 731
- [19] Treat N.D, et al., 2011 *Adv. Energy Mater.* **1** 82 – 89.
- [20] Liu C, Holman Z.C and Kortshagen U.R 2009 *Nano Lett.* **3** – 6.
- [21] Greene L.E, Law M, Yuhas B.D and Yang P 2007 *J. Phys. Chem. C Lett.* **18**.
- [22] Chen D, Nakahara A, Wei D, Nordlund D and Russell T.P 2011 *Nano Lett.* 561 – 567.

- [23] Dennler D, Scharber M.C and Brabec C.J 2009 *Adv mater* **21** 1323 – 1338.
- [24] Ahmad M, Foroughi M and Monish M.R, 2012 *WJNSE*. **2** 154 – 160.
- [25] Cullity B.D, Elements of X-ray Diffraction (2nd Ed), Addison Wesley, 1956, pp 284-285.
- [26] Huiling T, Xian L, Yadong J, Guangzhong X and Xiaosong D 2015 *Sensors*. **15** 2086 – 2103.
- [27] Oh H, Krantz J, Litzov I, Stubhan T, Pinna L, Brabec C.J 2011 *Sol Energy Mater Sol Cells*, **95** 2194 – 2199.
- [28] Lee J. M, Park J. S, Lee S. H, Kim H, Yoo S and Kim S. O 2011 *Adv. Mater.* **23** 629 – 633.
- [29] Cheng F.Y, Imin P, Maunders C, Botton G and Adronov A 2008 *Macromolecules*, **41** 2304 – 2308.
- [30] Jin H.D, Zheng F, Xu W.L, Yuan W.H, Zhu M.Q and Hao X.T 2014 *J.Phys. D: Appl. Phys* 505502.
- [31] Al-Gaashani R, Radiman S, Daud A. R, Tabet N and Al-Douri Y 2013 *Ceram. Int.* **39** 2283 – 2292.
- [32] Danish K, Zahid A, Danyal A, Manoj K.P, Idris K, 2021 *Ain Shams Eng. J*, **12** 897 – 900.

Computational Studies of Pentlandite Mineral: Structural and Dynamical Properties Probed by Molecular Dynamics

M A Mehlape¹, S P Kgalema and P E Ngoepe

Materials Modelling Centre, School of Physical and Mineral Sciences, University of Limpopo, South Africa, Private Bag, X1106, SOVENGA, 0727

E-mail: mofuti.mehlape@ul.ac.za

Abstract. Pentlandite is a major precious metals-bearing mineral and plays a very important role in mining. Precious metal ores co-exists with base metals either as solid-solution and intergrowths, hence rendering its detailed understanding important for efficient extraction of these precious metals. In order to extract the precious metals from the ores effectively it is necessary to study and understand structural and physical properties, of pentlandite mineral in detail. This work relates to problems in applied areas such as mineralogy, geophysics and geochemistry, whereby phase transition is modified by impurities, so there is the additional concern of the effect of temperature. Computational modelling technique, molecular dynamics (MD) is applied to investigate structural and physical properties of nickel rich pentlandite ($\text{Fe}_4\text{Ni}_5\text{S}_8$). Radial distribution functions (RDFs) and mean square displacement (MSD) are used to establish the effect of temperature on the pentlandite mineral. The MD results are found to compare well with the experimental results.

1. Introduction

The Bushveld Complex has the largest concentration of platinum group elements (PGEs) and these are ruthenium (Ru), rhodium (Rh), palladium (Pd), osmium (Os), iridium (Ir), and platinum (Pt) [1]. Pentlandite minerals are known to host such precious metals, either as solid solutions or as intergrowths [2] and in order to achieve high recoveries of such metals it is necessary to float pentlandites efficiently, particularly in reefs that are less explored, such as the platreef. These PGEs exist in different structures and they could form pentlandite structure ($\text{Fe}_4\text{Ni}_5\text{S}_8$), which makes them significant sulphide minerals. Owing to their high concentration in the Bushveld Complex, it draws much attention in investigating their structure and dynamic properties. In order to extract the precious metals from the ores effectively it is necessary to study, and understand structural and dynamical properties of pentlandites in detail. Notwithstanding their significance in mineralogy, experimental studies on pentlandites are not as abundant as those of pyrites and metal oxide minerals. Moreover, computational modelling investigations probed by molecular dynamics (MD) simulations are also very scarce. There is a need to choose appropriate interatomic potentials for the MD simulation, which might be impossible to get readily available potentials for the material at hand from literature. Here, we present a new set of interatomic potentials for MD simulations of pentlandite ($\text{Fe}_4\text{Ni}_5\text{S}_8$) mineral. The derived interatomic potentials of $\text{Fe}_4\text{Ni}_5\text{S}_8$ were validated by the accurate determination of structure and elastic constants. Furthermore, the potential model yields a melting temperature that is close to the experimental value.

¹ To whom any correspondence should be addressed.

1.1. Pentlandite, (FeNi)₉S₈ structure

Pentlandite ((Fe,Ni)₉S₈) has a space group of *Fm3m* symmetry and a chemical formula of M₉S₈ (M is a metal). The cation sites may be occupied by Fe and Ni. The structure consists of approximately close-packed alternating layers of sulphur and metal atoms. The cations are distributed across 32 tetrahedral sites in a cube cluster arrangement, each bonded to 4 sulphur anions, and 4 octahedral sites joining the

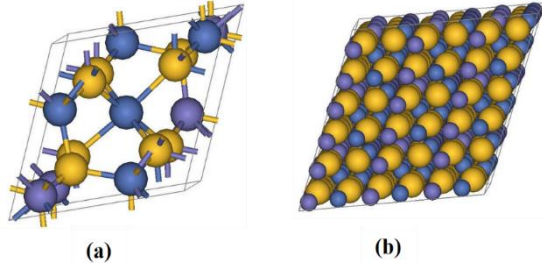


Figure 1. Snapshots of (a) Primitive Unit Cell of Fe₄Ni₅S₈ and (b) The initial configuration of a 3x3x3 supercell of Fe₄Ni₅S₈ used in the MD calculations, where yellow spheres represent Sulphur, blue spheres represent iron and purple spheres represent nickel.

cube clusters, each bonded to 6 sulphur anions. Of the 32 sulphur atoms, 24 occupy 5- coordinate “face capping” sites, capping the faces of the cube clusters, and the remaining 8 sulphur anions occupy 4-coordinate sites “linking” the cube clusters [3]. Figure 1 shows (a) the primitive unit cell and (b) the initial configuration of a 3x3x3 supercell of Fe₄Ni₅S₈ constructed using BIOVIA Materials Studio [4].

2. Computational Details

2.1. Molecular dynamics simulations setup

The study is based on atomistic simulation of pentlandite structure (Fe₄Ni₅S₈). The atomistic simulation method uses interatomic potential functions to describe the total energy of a system in terms of atomic coordinates. The static energy minimization code, General Utility Lattice Program (GULP) [5] was used to derive interatomic potentials. The molecular dynamics (MD) simulations are performed to calculate the properties of 3x3x3 supercell of Fe₄Ni₅S₈ using GULP as implemented in BIOVIA Materials Studio. MD simulation were run for 500 ps and equilibrated for 100 ps. Temperature is controlled by the canonical ensemble (NVT) constant number of particles (N), volume (V), temperature (T). Temperature is controlled by a Nose-Hoover thermostat [6] and the equation of motion were integrated using the Verlet Leapfrog algorithm [7] with a time step of 1 fs. The constant temperature and volume simulations were performed over the temperature range of 300 K to 1500 K with 100 K increments. In this work, we consider the approximation for describing the pentlandite structure (Fe₄Ni₅S₈), which is the rigid ion model potential. This is an empirical approach and relies on a set of parameters, which were modified using cobalt pentlandite potentials (Co₉S₈) [8]. The potential models can accurately describe the bulk and surface structure properties, lattice constants, and elastic properties of sulphides [9], oxides [10], and other pentlandite structures [11].

2.2. Representation of interatomic potentials

The MD calculations in this work are based on the Born ionic model [12] of a solid and parameters were derived for short range interactions represented by the Buckingham potential, Morse potential and three body terms.

2.2.1. Buckingham Potential.

In the Buckingham potential, the repulsive term is replaced by an exponential term and potential takes the form:

$$U(r_{ij}) = A_{ij} e^{-r_{ij}/\rho_{ij}} - \frac{C_{ij}}{r_{ij}^6}, \quad (1)$$

where A_{ij} and ρ_{ij} are parameters that represent the ion size and hardness, respectively, while C_{ij} describe the attractive interaction and r_{ij} is the distance between ion i and ion j . The first term is known as the Born-Mayer potential and the attraction term (second term) was later added to form the Buckingham potential. For the cation-anion interactions, the attractive term is ignored due to the very small

contribution of this term to the short-range potential, or, alternatively, the interaction is subsumed into the A and ρ parameters.

2.2.2. Morse Potential.

The Morse potential is used to model the interactions between covalently bonded atoms and has the form:

$$U(r_{ij}) = D_{ij} \left(1 - e^{(-B_{ij}(r_{ij}-r_0))} \right)^2 - D_{ij}, \quad (2)$$

where D_{ij} is the bond dissociation energy, r_0 is the equilibrium bond distance, and B_{ij} is a function of the slope of the potential energy well. The Coulombic interactions between covalently bonded atoms are often partially or totally ignored as the Morse potential already contains the attractive component of the interaction between neighbours.

2.2.3. Three-Body Potential.

A further component of the interactions of covalent species is the bond-bending term, which is added to take into account the energy penalty for deviations from the equilibrium value. Hence, this potential describes the directionality of the bonds and has a simple harmonic form:

$$U(\theta_{ijk}) = \frac{1}{2} k_{ijk} (\theta_{ijk} - \theta_0)^2, \quad (3)$$

where k_{ijk} is the three-body force constant, θ_0 is equilibrium angle and θ_{ijk} is the angle between two interatomic vectors $i-j$ and $i-k$. The interatomic potentials used for this study are given in Table 1.

Table 1. Interatomic potential parameters for the pentlandite $\text{Fe}_4\text{Ni}_5\text{S}_8$ as derived in the present study.

Interatomic potential parameters			
Charges			
Ions			
Nickel (Ni)	0.40		
Iron (Fe)	0.40		
Sulphur (S)	-0.45		
Buckingham potential			
S-S	1130.533064	0.184528	20.0
Morse potential			
	$A_{ij}(eV)$	$\rho_{ij}(\text{\AA})$	$C_{ij}(eV\text{\AA})$
Fe-S	3.0	1.47	2.20
Ni-S	3.0	1.90	2.20
Three body potential			
	$D_{ijk}(eV)$	$r_0(\text{\AA})$	$\alpha_{ij}(eV)$
Fe-S-S	2.82	109.503	
S-Fe-Fe	0.89	109.503	
S-Ni-Ni	2.30	109.503	
Ni-S-S	1.72	109.503	
S-Fe-Ni	1.60	109.503	

3.1. Results and discussion

In this section, the results from both the bulk properties and molecular dynamics (MD) simulations of $\text{Fe}_4\text{Ni}_5\text{S}_8$ are presented. In Section 3.1, the interatomic potentials are validated by calculating the bulk properties, which includes lattice constants, bond lengths and elastic constants. In section 3.2, we present MD simulations, which include structural and dynamical properties of $\text{Fe}_4\text{Ni}_5\text{S}_8$.

3.1. Bulk Properties

The derived interatomic potentials given in Table 1 have been applied successfully to $\text{Fe}_4\text{Ni}_5\text{S}_8$. The potential models are developed to simplify the complexity of the quantum mechanical computations. The accuracy of the derived interatomic potentials was first checked by comparing the known experimental and calculated data. To validate our potential models we start by showing the properties

that were obtained from our derived potentials i.e., lattice constants, bond lengths and elastic constants. The properties calculated from the derived potential model are in good agreement with those from DFT calculations. The lattice constants, bond lengths and elastic constants of Fe₄Ni₅S₈ are listed in Table 2.

Table 2. Lattice constants, bond lengths and elastic constants of Fe₄Ni₅S₈

	Potential Model	Density Functional Theory (DFT)
Lattice Parameter (Å)		
a	7.015	7.012
b	6.855	7.039
c	6.976	7.024
Volume (Å ³)	238.236	237.358
Density of Cell (g/cm ³)	5.390	5.410
Bond Length (Å)		
Fe-S	2.11	2.22
Ni-S	2.09	2.20
Fe-Fe	2.45	2.50
Ni-Ni	2.49	2.53
S-S	3.27	3.22
Elastic Constant (GPa)		
<i>C</i> ₁₁	205.50	207.8
<i>C</i> ₁₂	100.72	102.38
<i>C</i> ₄₄	49.40	47.07
Bulk Modulus (GPa)	131.35	137.31

3.2. Structural and dynamical properties

RDF is an important parameter to describe the structural characteristics of solid, amorphous and liquid states [13]. It defines the probability of finding an atom in a distance ranging from *r* to *r*+*dr* (*dr* is the step of calculation) and is expressed as:

$$g(r) = \frac{V \sum_{i=1}^{N_i} n_i(r)}{N^2 4\pi r^2 dr}, \quad (4)$$

where *V* and *N* are the volume and total number of atoms of the system, *N_i* is the number of atoms around *i*th atom and *n_i(r)* is the corresponding atom number in the sphere shell ranging from *r* to *r* + *dr* at the radius *r*. Figure 2 shows the radial distribution functions (RDFs) for the Fe₄Ni₅S₈ supercell at various temperatures, from 300 K to 1500 K. From the radial distribution function plots we observe that at lower temperatures of 300 K there are several sharp peaks, implying a well-ordered structure. However, as we increase the temperature the peaks become broader and their number decreases, showing that the structure is experiencing the phase transition from a solid phase to a liquid phase. This happens mainly at the temperature of 1300 K, wherein the arrangement of atoms is fading and the peaks are broad, which corresponds to the structure melting. This agrees with the experimental melting temperature of Fe₄Ni₅S₈, which is approximately 1255 K [14]. Figure 3 shows the snapshots for 3x3x3 supercell structure of Fe₄Ni₅S₈ simulated at various temperatures. From the pictures we observe that there is a phase transition from a lower temperature to a higher temperature. At temperatures 300 K to 900 K, the structure is still well maintained showing crystallinity. However, as we increase the temperature to 1300 K, we observe that the structure loses its crystallinity, as the regular arrangement of atoms disappears. It can be seen that the arrangement of atoms has completely disappeared at a temperature of 1300 K, which is in agreement with the variation trend of the RDF results described above.

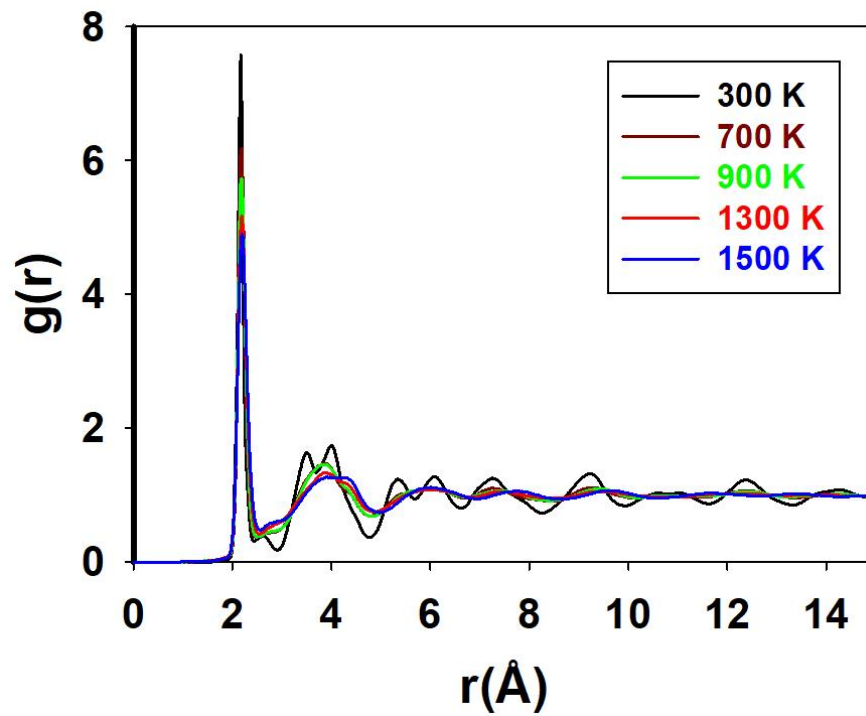


Figure 2. The radial distribution functions (RDFs) of $\text{Fe}_4\text{Ni}_5\text{S}_8$ at various temperatures

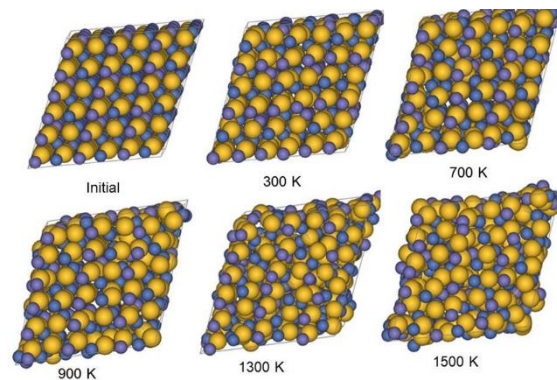


Figure 3. Structural changes of $\text{Fe}_4\text{Ni}_5\text{S}_8$ structure after MD simulations at various temperatures.

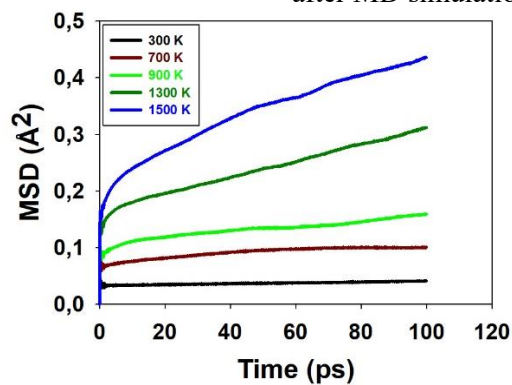


Figure 4. The variation of MSD of $\text{Fe}_4\text{Ni}_5\text{S}_8$ with time at various temperatures.

Mean square displacement (MSD) refers to the square of the average displacement of particles in a certain period of time [15]. MSD in MD simulations show that the position and the direction of the motion of particles keep changing, especially at high temperatures. Figure 4 shows the total MSD as a function of time at different temperatures from 300 K to 1500 K. From the MSD of $\text{Fe}_4\text{Ni}_5\text{S}_8$, at lower temperatures of 300 K to 900 K, it predicts that the mobility of atoms within the structure is less. As temperature is increased to 1300 K and 1500 K the mobility of atoms in the pentlandite structure increases. At a simulation time of around 100 picoseconds, the mobility of atoms is more at higher temperatures, which is between 1300 K and 1500 K. The same temperature range was observed through the RDFs in Figure 2. Figure 4, demonstrate that after initial diffusion for a period of time, the ions quickly reached the stable stage and then maintained a relatively stable diffusion level. A linear relationship is observed between MSD and simulation time.

4. conclusion

Molecular dynamics simulations were performed with the aim of investigating the dynamic and structural properties of pentlandite structure. The melting of the structure was observed through the radial distribution function (RDFs). At low temperature (300 K) the RDFs have many and sharp peaks, however, at higher temperature (1300 K) the RDFs curve are relatively smooth and does not exhibit any defined peaks, indicative of structural change from solid to liquid phase. Furthermore, through the mean-squared displacement (MSD), the results show that MSD increases with temperature and atoms are able to move more at high temperature. MSD increases with time in all investigated temperatures and there is a linear relationship between MSD and simulation time.

Acknowledgements

The computations were performed at the Materials Modelling Centre (MMC), University of Limpopo and at the Centre for High Performance Computing (CHPC), Cape Town. We also acknowledge the National Research Foundation (NRF) for funding.

References

- [1] O'Connor T C and Shackleton N J 2013 *Platin. Met. Rev.* **57** 302
- [2] Wang Q and Heiskanen K 1990 *Int. J. Miner. Process.* **29** 99
- [3] Hoodless R C, Moyes R B and Wells P B 2006 *Catal. Today* **114** 377
- [4] BIOVIA, Materials Studio, (20.1.051), Dassault Systemes, San Diego, 2020
- [5] Gale J D 1997 *J. Chem. Soc., Faraday Trans.* **93** 629
- [6] Nosé S 1990 *J. Phys.:Condens. Matter.* **2** 115
- [7] Verlet L 1967 *Phys. Rev.* **159**, 98
- [8] Mehlae M A 2013 *PhD Thesis*. University of Limpopo
- [9] Sithole H M, Ngoepe P E and Wright K 2003 *Phys. Chem. Miner.* **30** 615
- [10] Maphanga R R, Ngoepe P E and Parker S C 2009 *Surf. Sci.* **603** 3184
- [11] Mehlae M A, Ngoepe P E and Parker S C 2013 Proceedings of SAIP 98-103 Available online at <http://events.saip.org.za>
- [12] Born M and Huang K. 1954 *Dynamical Theory of Crystal Lattices 1st edition*. Oxford: University Press
- [13] Zhanga X, Lia B, Liu H X, Zhao G H, Yanga Q L, Chenga X M, Wong C H, Zhang Y M and Lime C W J 2019 *Appl. Surf. Sci.* **465** 871
- [14] Kitakaze A and Sugaki A 2004 *Can. Mineral.*, **42** 17
- [15] Wang G, Cui Y, Li X, Yang S, Zhao J, Tang H and Li X 2020 *Minerals*, **10** 149

Computational modelling studies of pentlandite ($\text{Fe}_4\text{Ni}_5\text{S}_8$) (111) surface: Oxidation and hydration

S T Ntobeng¹, P P Mkhonto, M A Mehlape and P E Ngoepe

Materials Modelling Centre, University of Limpopo, Private Bag X1106, Sovenga, 0727, South Africa

Email: thapeloasegoarihle@gmail.com

Abstract. Minerals are exposed to atmospheric oxidation and hydration during ore grinding, as such the interaction of oxygen and water on mineral surface aid as a tool to determine the oxidation behaviour and wettability. In this study we employed the computational density functional theory (DFT) to investigate the adsorption of oxygen molecule and water molecule on the nickel-rich pentlandite ($\text{Fe}_4\text{Ni}_5\text{S}_8$) (111) surface. The oxidation preferred the bridging on Fe and Ni atoms (Fe-O₂-Ni) with exothermic adsorption energy of -262 kJ.mol^{-1} , which resulted from the initial Ni-peroxide adsorption. The hydration showed a strong exothermic interaction of H₂O with Fe than Ni and suggested that water adsorb on the pentlandite surface through the Fe atoms. This study predicts the oxidation and hydration behaviour of pentlandite mineral and suggested that the oxidation weathering of pentlandite will occur preferentially on the Fe atoms sites.

1. Introduction

Pentlandite ($\text{Fe,Ni}_9\text{S}_8$) is an iron-nickel sulphide with Ni:Fe ratio of close to 1:1 [1], and is regarded as a principal source of nickel [2]. Minerals are susceptible to oxidation and weathering overtime and thus investigation of oxidation behaviour is of paramount. Naturally, atmospheric oxidation of minerals results in oxide formation. There is still a lack in oxidation behaviour of pentlandite from computational aspects, in particular investigation of different oxidation mechanisms.

Xiong *et al.* [3] recently investigated the oxidation behaviour of (010) and (001) surfaces of pentlandite and it was reported that the Fe atoms in pentlandite migrated to the surface and were preferentially oxidized to form a thin layer of Fe_2O_3 . Similar prediction was made by Mkhonto *et al.* on pentlandite (110) surface [4]. An interesting phenomenon was observed by Xiong *et al.* where the oxygen molecule adsorptions preferred the bridging sites (Fe-Ni and Fe-Fe) on the surfaces and were the most favourable adsorption sites [3]. It appears that oxidation products are unconventional of the pentlandite composition, where both Iron-rich and Nickel-rich pentlandite give out almost the same products [5].

The hydration of minerals plays a crucial role in understanding the hydrophilicity and hydrophobicity of minerals. In particular during wet grinding, minerals tend to break differently compared to dry grinding. Furthermore, the oxidation of minerals involves water where dissociation

¹ To whom any correspondence should be addressed.

occurs resulting in formation of Fe–OOH on the mineral surface [6]. Waterson *et al.* has previously reported a strong interaction of water with Fe atoms than Ni atoms [7].

In this paper, we investigated the effects of oxidation and hydration adsorption on the nickel-rich pentlandite (Fe₄Ni₅S₈) (111) surface using the density functional theory (DFT) calculations.

1.1. Bulk pentlandite(Fe₄Ni₅S₈) properties

The pentlandite structure is defined by a space group of *Fm-3m* (225) [8]. An important aspect of the pentlandite structure is the presence of three metal-metal bond extending from each tetrahedral cation to form essential isolated cube cluster of tetrahedral cation, Rajamani and Prewitt [9] and Vaughan and Craig [10]. The conventional unit cell of the pentlandite structure has a cubic close-packed arrangement of sulphide ions include 36 tetrahedral holes and 32 octahedral holes and has 68 atoms. In the nickel-rich pentlandite (Fe₄Ni₅S₈) the octahedral sites are occupied by Ni atoms, while the tetrahedral sites are evenly distributed by Fe and Ni atoms. We have found that the (Fe₄Ni₅S₈) pentlandite structure relaxed to lattice parameters of 9.947 Å. Our model is based on previously determined pentlandite bulk structure by Lu and Yu [11]; where the Fe and Ni distributes in heterogeneous (Fe–Ni) bonding as shown in figure 1a.

2. Computational methodology

The *ab-initio* density functional theory (DFT) [12, 13] method was employed to explore the interaction of oxygen molecule and water molecule onto nickel-rich pentlandite (111) surface. The plane-wave (PW) pseudopotential method with generalized gradient approximation of Perdew-Burke-Ernzerhof (GGA-PBE) within the CASTEP (Cambridge Serial Total Energy Package) [14] code were adopted for all calculations. A plane wave energy cut-off of 400 eV was used with k-points of 5×5×5 for the bulk and 5×5×1 for the surface as proposed by Monkhorst-Pack [15]. The (111) surface was used in this study and previously similar surface was investigated by Waterson *et al.* [7]. The surface energies are calculated using equation (1):

$$E_{\text{surface}} = \frac{E_{\text{slab}} - (n_{\text{slab}})(E_{\text{bulk}})}{2A} \quad (1)$$

where the surface slab area is A , E_{slab} is the total slab energy, n is the number of atoms in the slab, and E_{bulk} is the total bulk energy per atom. The lowest positive surface energy indicates a stable surface.

The strength of surface interaction with adsorbates (O₂ and H₂O) was calculated from equation (2):

$$E_{\text{adsorption}} = E_{\text{system}} - (E_{\text{adsorbate}} + E_{\text{surface}}) \quad (2)$$

where the energy of the surface slab and the adsorbate is E_{system} , the energy of the clean surface slab is E_{surface} , and the isolated adsorbates energy is $E_{\text{adsorbate}}$. The positive energy of adsorption corresponds to the endothermic process. The negative energy of adsorption corresponds to the process of exothermic adsorption and indicates a strong interaction between the adsorbate and the surface.

Now, in order to calculate the adsorption energies, the energy of the free O₂ and H₂O molecules were relaxed in a cubic box of 10 Å with similar oxygen ultrasoft pseudopotential, cut-off energy, at gamma point k-points and other equivalent precision parameters as in the surface calculations.

3. Results and discussion

3.1. Structural relaxation of pentlandite (Fe₄Ni₅S₈) (111) surface

The (111) surface was cleaved from the relaxed bulk pentlandite structure and the calculated surface energy is given in table 1. The (111) surface is composed of two slabs of repeating bulk thickness, with each slab containing seven layers (figure 1b). The slab thickness of pentlandite was previously investigated and reported that the 14 layers was sufficient for adsorption [7]. The supercell (111)

surface of 2×2 was adopted. The surface was fully relaxed before adsorption allowing only the atomic position to relax. After surface relaxation, we noted a slight change on the surface, where the Ni atoms relaxed inwards, while the Fe atoms relaxed outwards. Mkhonto *et al.* and Xiong *et al.* [4, 3] previously reported this behaviour.

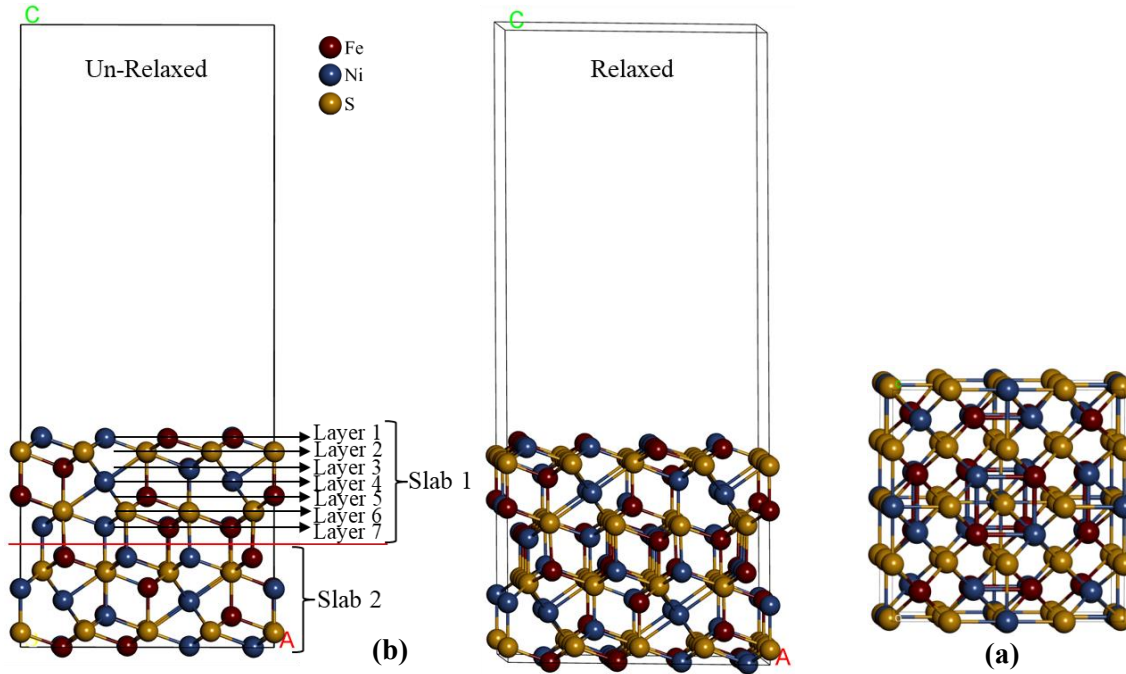


Figure 1: Crystal structures: (a) bulk nickel-rich ($\text{Fe}_4\text{Ni}_5\text{S}_8$) pentlandite and (b) side view of the un-relaxed and relaxed (111) $\text{Fe}_4\text{Ni}_5\text{S}_8$ surface.

3.2. $\text{Fe}_4\text{Ni}_5\text{S}_8$ (111) surface oxidation

The oxygen molecule adsorption on the $\text{Fe}_4\text{Ni}_5\text{S}_8$ (111) surface was performed on different adsorption sites namely: Ni-peroxide ($\text{Ni}-\text{O}_2$), Fe-peroxide ($\text{Fe}-\text{O}_2$), Ni-superoxide ($\text{Ni}-\text{O}_2^-$), Fe-superoxide ($\text{Fe}-\text{O}_2^-$) and Ni-bridge ($\text{Ni}-\text{O}_2-\text{Ni}$). Each O_2 adsorption mode was allowed to relax to its preferential bonding site and we observed different behaviour of the oxygen molecule on the surface. The most exothermic adsorption was Ni-peroxide with adsorption energy of -262 kJ.mol^{-1} as shown in table 1. We presented the un-relaxed and relaxed structures to identify the changes after relaxation.

Table 1: Calculated surface energy of $\text{Fe}_4\text{Ni}_5\text{S}_8$ (111) surface and adsorption energies of oxygen and water molecules

Surface	Fe ₄ Ni ₅ S ₈ Surface energy (J.m ⁻²)		
(111)	0.92		
Oxidation		Hydration	
Adsorption modes	E _{adsorption} (kJ.mol ⁻¹)	Adsorption modes	E _{adsorption} (kJ.mol ⁻¹)
Fe-Peroxide	-188	Fe-Top	-53
Ni-Peroxide	-262	Ni-Top	-22
Ni-Superoxide	-253		
Fe-Superoxide	-168		
Ni-Ni-Bridge	-122		

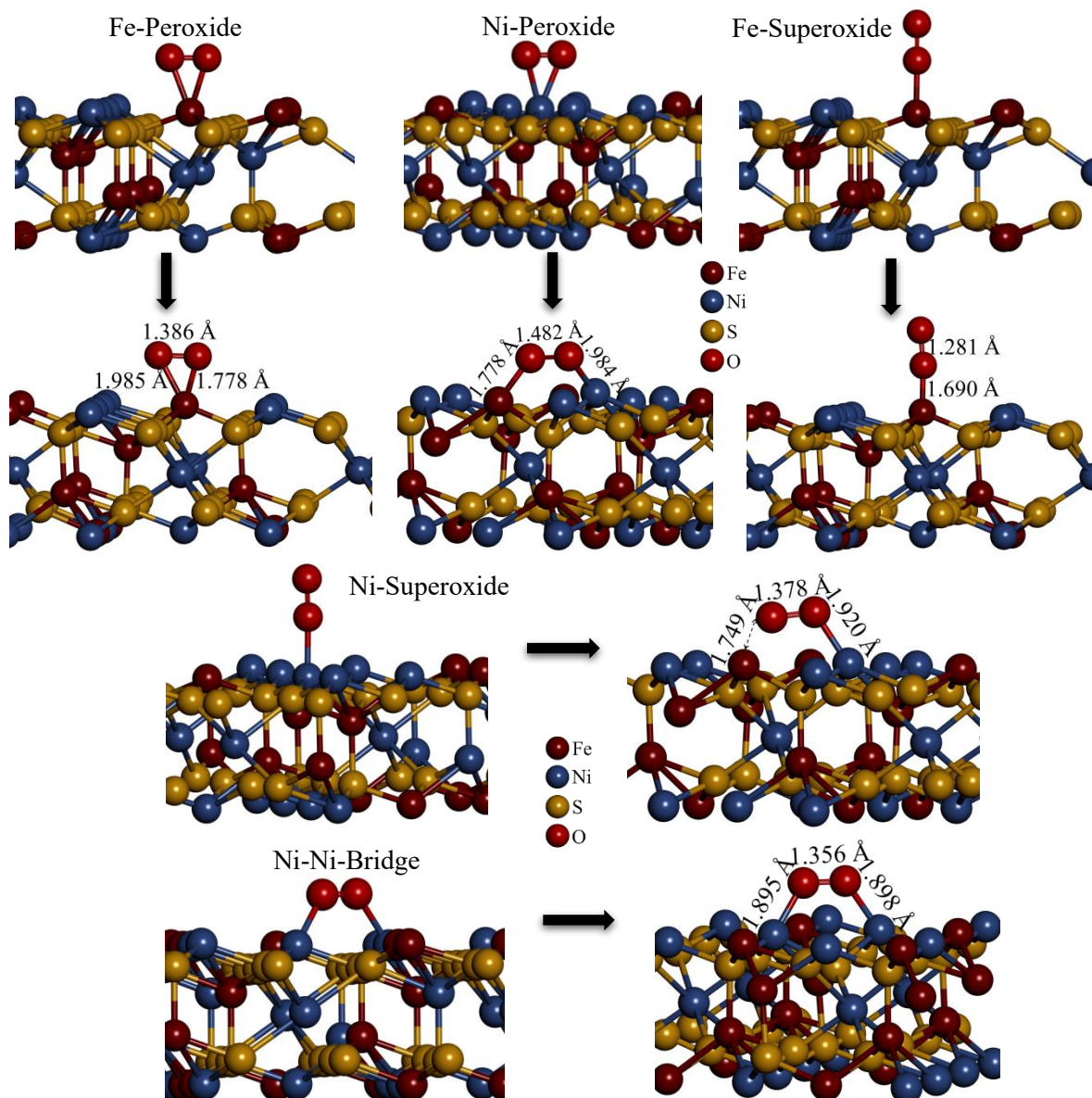


Figure 2: Adsorption sites of Oxygen molecule on the $\text{Fe}_4\text{Ni}_5\text{S}_8$ (111) surface.

The adsorption of O_2 in figure 2 (Ni-peroxide) showed that, the O_2 molecule moves and a bridge bond on Fe and Ni atoms ($\text{Fe}-\text{O}_2-\text{Ni}$), which suggested the preferential oxidation of Fe atom. The adsorption on Fe-peroxide and Fe-superoxide did not change the bonding mode. It is noted that Ni-superoxide resulted in oxygen molecule bending towards Fe atoms giving a distance of $\text{Fe}-\text{O} = 1.749 \text{ \AA}$, although the bond was not created. This resulted in adsorption energy close to that of Ni-peroxide (leading to $\text{Fe}-\text{O}_2-\text{Ni}$). It was found that the $\text{Ni}-\text{O}_2-\text{Ni}$ bridge was weaker amongst the adsorption sites (-122 kJ.mol^{-1}). In all adsorptions, except for Fe-superoxide the oxygen molecule ($\text{O}-\text{O}$) bond length stretched to over 1.300 \AA , which indicated a weakened bond due to electron transfer from the d-orbital to the unoccupied orbital of oxygen molecules.

3.3. $\text{Fe}_4\text{Ni}_5\text{S}_8$ (111) surface hydration

The interaction of water (H_2O) with nickel-rich (111) pentlandite surface was tested on Fe-top ($\text{Fe}-\text{OH}_2$) and Ni-top ($\text{Ni}-\text{OH}_2$). Table 1 shows that the Fe atom gave the most exothermic adsorption energy than Ni atom, suggesting that the Ni-rich pentlandite is more hydrophilic on Fe atoms and thus,

the most preferred adsorption site for H₂O on the (111) surface. This is in line with previous report of water interaction with Ni-Pn and Fe-Pn [7]. In order to examine the structural bonding mode of the H₂O on the (111) surface, we present the un-relaxed and relaxed structures.

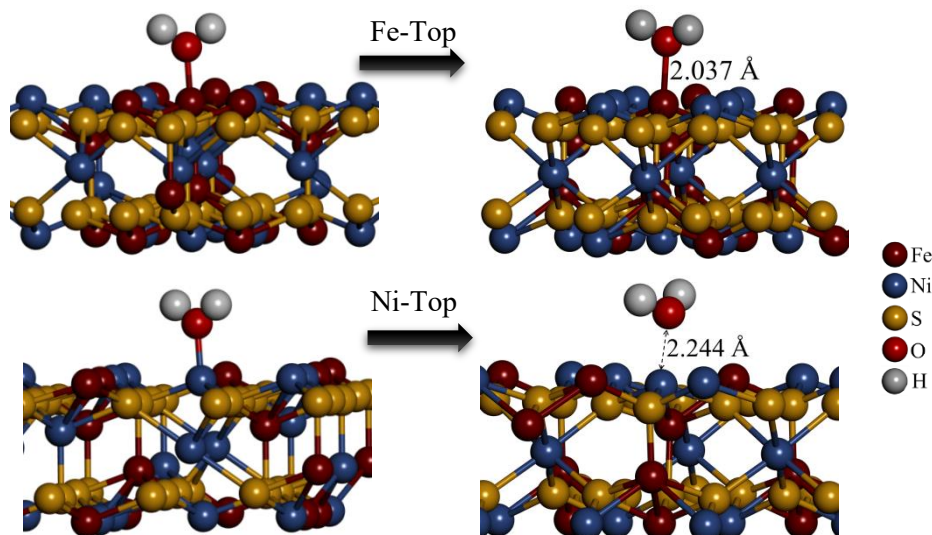


Figure 3: Adsorption sites of water molecule on the Fe₄Ni₅S₈ (111) surface.

We observed that figure 3, indicates the adsorption of water on Fe-top did not change the orientation. The adsorption of H₂O on Ni-top resulted in water relaxing upwards leaving a distance of Ni---OH₂ = 2.244 Å. In addition, we found that the Fe-OH₂ (2.037 Å) bond length was shorter than for Ni-OH₂ (2.244 Å), indicating the strong interaction between Fe and water molecule. The O-H bond length for Fe-top was approximately equal to that of Ni-top (0.980 Å). The water molecules resulted in bond angles of 107.69° on Fe-top and 106.34° on Ni-top.

4. Conclusion

In this study the oxidation and hydration of Fe₄Ni₅S₈ (111) surface was investigated using the *ab-initio* DFT method. The adsorption of oxygen and water molecule on the (111) surface of nickel-rich pentlandite were tested on different adsorption sites, preferably the Ni and Fe atoms. We found that the oxidation preferred the Ni-peroxide mode, which resulted in bridging on Fe and Ni atoms (Fe-O₂-Ni). This bonding was the most exothermic with adsorption energy of -262 kJ.mol⁻¹ and therefore signifying preferential oxidation of Fe atoms. In the case of hydration of (111) surface, we observed that the water adsorb strongly on iron (-53 kJ.mol⁻¹) as compared to nickel (-22 kJ.mol⁻¹) and complimented by the bond length after surface relaxation. This study demonstrated that the oxidation and hydration behaviour of pentlandite mineral. Moreover, the oxidation by weathering of pentlandite is found to occur spontaneously on the Fe sites.

Acknowledgements

This work was performed at the Materials Modelling Centre (MMC), University of Limpopo. The resources for computing at the Centre for High Computing (CHPC) are acknowledged and the National Research Foundation (NRF) for financial aid.

References

- [1] Legrand D L, Bancroft G M and Nesbitt H W 2005 Oxidation of pentlandite and pyrrhotite surface at pH 9.3: Part 1. Assignment of XPS spectra and chemical trends *Am. Miner.* **90** 1042–1054.

- [2] Knop O, Huang C H, Woodhams F and Cabri L J 1989 Platinum-group elements: Mineralogy, geology and recovery *Can. Inst. Min. Metall. CIM Special* **23** 199–217.
- [3] Xiong X, Lu X, Li G, Cheng H, Xu Q and Li S 2018 Energy dispersive spectrometry and first principles studies on the oxidation of pentlandite *Roy. Soc. Chem.* **20** 12791–12798.
- [4] Mkhonto P P, Chauke H R and Ngoepe P E 2015 Ab initio studies of O₂ adsorption on (110) Nickel-rich Pentlandite (Fe₄Ni₅S₈) *Miner.* **5** 665–678.
- [5] Merape G *Fundamental Electrochemical Behaviour of Pentlandite* Masters Thesis, University of Pretoria, Pretoria.
- [6] Kelebek S and Nanthakamar B 2007 Characterization of stockpile oxidation of pentlandite and pyrrhotite through kinetic analysis of their flotation *Int. J. Miner. Process.* **84** 69–80.
- [7] Waterson C N, Sindt J O, Cheng J, Tasker P A and Morrison C A 2015 First-Principles Study on Ligand Binding and Positional Disorder in Pentlandite *J. Phys. Chem.* **119** 25457–2546.
- [8] Geller S 1962 Refinement of the crystal structure of Co₉S₈ *Acta Crystallogr.* **15** 1195–1198.
- [9] Rajamani V and Prewitt C T 1973 Crystal chemistry of natural pentlandites *Can. Minera.* **12** 178–187.
- [10] Vaughan D J and Craig J R 1978 Mineral Chemical Of metal sulphides *Cambridge Earth science series, Cambridge University Press* 493–512.
- [11] Lu L and Yu S 2019 Metal distribution in iron-nickel sulfide mineral pentlandite: First-principles study *Chem. Phys. Letters* **736** 136786: 1–7.
- [12] Hohenberg P and Kohn W 1965 Inhomogeneous electron gas *Phys. Rev. B* **136** 864–871.
- [13] Kohn W and Sham L J 1965 Self-consistent equations including exchange and correlation effects. *Phys. Rev.* **140** 1133–1138.
- [14] Clark S J, Segall M D, Pickard C J, Hasnip P J, Probert M, Refson K and Payne M C 2005 First principles methods using CASTEP *Z. Kristallogr.* **220** 567–570.
- [15] Monkhorst H F and Park J D 1976 Special points for Brillouin-zone integrations *Phys. Rev. B* **13** 5188–5192.

Effect of oxygen adsorption on the electronic properties of Li/MO₂ (M= Ti, V, Mn) surfaces

Percy Ngobeni, Phuti Ngoepe and Khomotso Maenetja

Material Modelling Centre, University of Limpopo, Private Bag x1106, Sovenga, 0727, South Africa.

Email: percy.ngobeni@ul.ac.za

Abstract: Lithium-air batteries, based on their high theoretical specific energy, are a particularly attractive technology for electrical energy storage. However, they suffer from the production of unstable discharge products which leads to capacity fading of the battery. Several catalysts have been used to improve Oxygen Reduction Reaction (ORR) and Oxygen Evolution Reaction (OER) which will yield stable discharge product. In this study, Density functional theory (DFT) is employed to investigate the relative stability of electronic properties of oxygen adsorption on Li/MO₂ (110) surfaces. Electronic properties such as band structures and density of states (DOS) are investigated on different configurations (dissociated, peroxy on Li, peroxy on Li-M, and peroxy on M) as oxygen is adsorbed on Li/MO₂. The electronic band structures were calculated to check the conductivity of the systems. The DOS was calculated to check the stability of the system by comparing how each system behaves along the Fermi level. These findings are important in improving the cycling performance of Li-air batteries and give insight into the reactivity of Li/MO₂ (110) surfaces.

1. Introduction

Metal-air batteries offer advantageous properties, such as high hypothetical energy and control densities, low working temperature, low cost, and fabric recyclability [1]. Lithium-air batteries are seen by numerous researchers as a potential next-generation innovation in energy capacity with the most elevated hypothetical energy density of all battery devices. The permeable cathode helps with the dissemination of O₂ gas so that it can be transported to the electrolyte-electrode interface as much as conceivable from the lithium-air battery. Li-air is based on either aqueous or nonaqueous electrolyte for which the negative anode is lithium metal, and the positive anode comprises porous carbon as a catalyst [2].

Various studies have employed metal oxides as catalyst for Li-air batteries [3,4]. Transition metal oxides such as MnO₂ has been considered as potential electrocatalysts for bi-functional oxygen terminals due to their high catalytic activity and uncommon disintegration stability for Li-air batteries [5]. The previous study gives insights in understanding charge transfer responses that create the potential distinction within the battery from the Li adatom to the surface M (Mn, Ti, and V) to have lithium-air batteries that are productive [6]. The surface free energies for the most stable composition for the oxidation on the lithiated surfaces of the metal oxides (MnO₂, TiO₂, VO₂) are calculated for different configurations. The oxygen adsorption is examined though in this study we utilize the examined oxygen adsorption on the Li/MO₂ to check the electronic stability of all produced configurations.

2. Methodology

The oxygen adsorption of the Li/MO₂ (110) calculations were performed utilizing the density functional theory (DFT) within the generalized gradient approximation (GGA) utilizing the Perdew, Barker, and Ernzerhof (PBE) exchange-correlation functional [7]. The number of plane waves was chosen by the cut-off kinetic energy of 500 eV and the Brillouin zone examining a plan of Monkhorst-Pack with 6x6x1 k-points work was utilized for the integration inside the reciprocal space for all the (110) surfaces. From the surface calculations the number of k-points was adapted to achieve a similar sampling density in a reciprocal space. Gaussian smearing with a width of 0.05 eV was utilized to progress the convergence amid geometry optimizations.

3. Results and discussion

3.1. Electronic properties overview

The number of states at each energy level, which are accessible to be occupied, is called the density of states (DOS). A zero DOS of an energy level suggests that no states can be possessed. It could be a valuable numerical concept permitting integration about the electron energy to be utilized rather than the integration over the Brillouin zone. Furthermore, the DOS is regularly utilized for quick visual investigation of the electronic structure. The closest band over the bandgap is called the conduction band, and the closest band below the bandgap is called the valence band [8]. In metal or semimetals, the Fermi level is inside of one or more allowed bands. In semimetals, the groups are commonly referred to as "conduction band" or "valence band" depending on whether the charge transport is more electron-like or hole-like, by closeness to semiconductors. In different metals, the bunches are not one or the other electron-like nor hole-like and are frequently sensibly called "valence bunches" as they are made of valence orbitals [9].

3.2. Electronic band structures

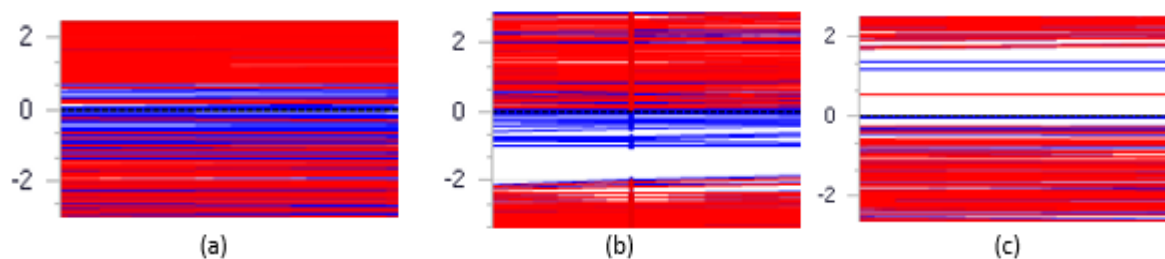


Figure 1. Electronic band structures of (a) (LiMn₄O₉)₄, (b) (LiV₄O₉)₄, and (c) (LiTi₄O₉)₄ dissociated surfaces.

The calculated band structure for (LiMn₄O₉)₄ and (LiTi₄O₉)₄ reveals the presence of a direct gap of 0.007 eV and 0.547 eV respectively, which signifies that the systems are semiconductors. However, there is an absence of an electronic band gap for (LiV₄O₉)₄ at the fermi level thus the structure is metallic.

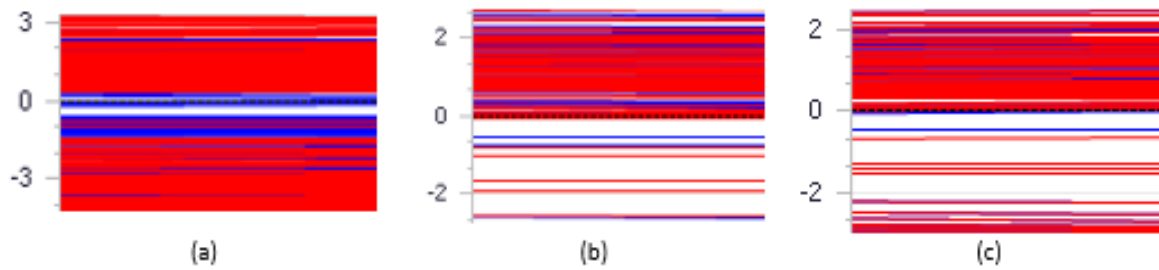


Figure 2. Electronic band structures of (a) $(\text{LiMn}_4\text{O}_9)_4$, (b) $(\text{LiV}_4\text{O}_9)_4$, and (c) $(\text{LiTi}_4\text{O}_9)_4$ peroxo on Li.

The calculated electronic band structures from all the systems $(\text{LiMn}_4\text{O}_9)_4$, $(\text{LiTi}_4\text{O}_9)_4$, and $(\text{LiV}_4\text{O}_9)_4$ affirm a nonappearance of a gap at the Fermi level. Consequently, all the systems are metallic.

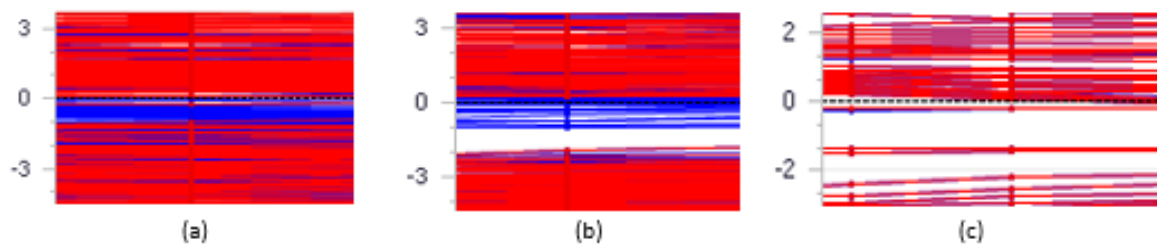


Figure 3. Electronic band structures of (a) $(\text{LiMn}_4\text{O}_9)_4$, (b) $(\text{LiV}_4\text{O}_9)_4$, and (c) $(\text{LiTi}_4\text{O}_9)_4$ peroxo on Li-M.

The calculated electronic band structures from all the systems $(\text{LiMn}_4\text{O}_9)_4$, $(\text{LiTi}_4\text{O}_9)_4$, and $(\text{LiV}_4\text{O}_9)_4$ validates an absence of a gap at the Fermi level. Subsequently, all the systems are metallic.

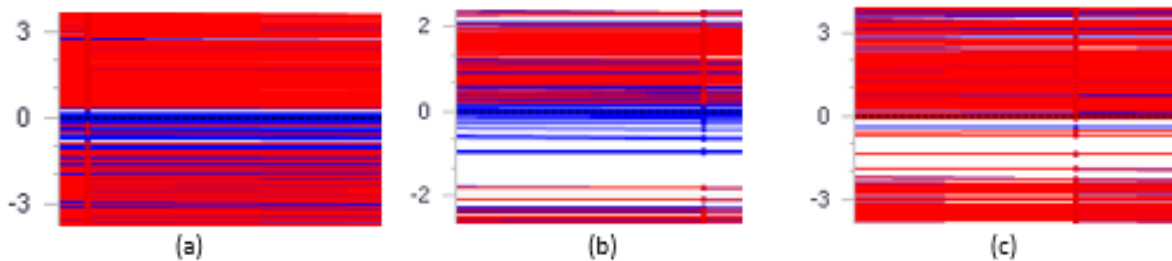


Figure 4. Electronic band structures of (a) $(\text{LiMn}_4\text{O}_9)_4$, (b) $(\text{LiV}_4\text{O}_9)_4$, and (c) $(\text{LiTi}_4\text{O}_9)_4$ peroxo on M.

The calculated band structure for $(\text{LiMn}_8\text{O}_{16})_4$ illustrates the presence of a direct gap at the Fermi level of about 0.035 eV, as a result, the system is a semiconductor. Moreover, there is a nonappearance of an electronic bandgap at the Fermi level for both $(\text{LiTi}_8\text{O}_{16})_4$ and $(\text{LiV}_8\text{O}_{16})_4$ thus the systems are metallic.

The focus of the band structure shown above is mainly at the Fermi level, and other gaps outside the Fermi level are not considered. The conductivity of the material was determined based on the interaction of electron orbitals at the Fermi level. Systems obtained with metallic behavior displayed orbital overlap at the Fermi level, but systems with bandgap less than 3 eV near the Fermi level have been established as semiconductors.

3.3. Density of states (DOS)

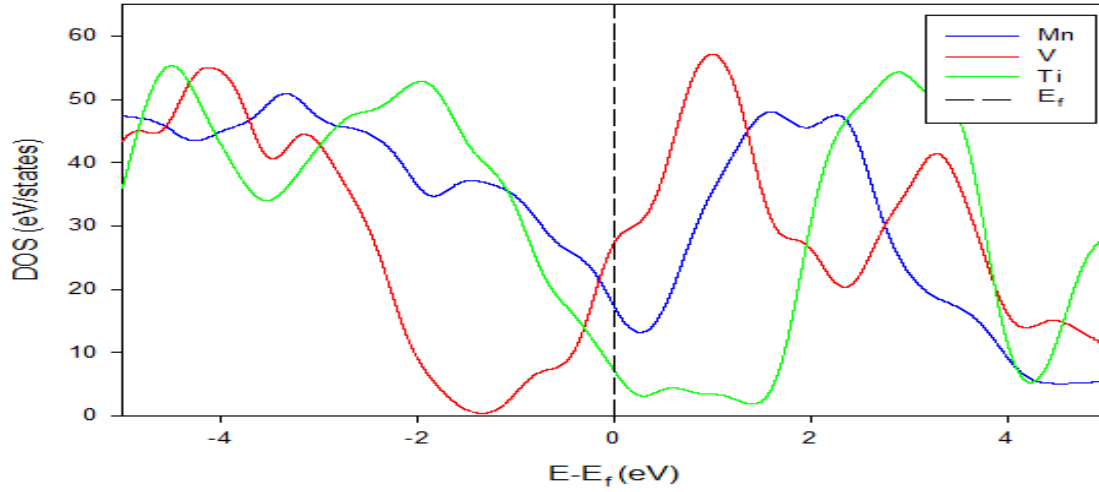


Figure 5. Comparison of the total density of states for the dissociated surfaces.

From figure 5, we observe that near E_f the DOS peak of $(\text{LiV}_4\text{O}_9)_4$ has a higher DOS which suggest the least stability of the system. However, $(\text{LiTi}_4\text{O}_9)_4$ has a lower density of states compared to the other structures near E_f . It is clear that $(\text{LiTi}_4\text{O}_9)_4$ is the most stable compared to $(\text{LiV}_4\text{O}_9)_4$ and $(\text{LiMn}_4\text{O}_9)_4$, the stability trend can be written as $(\text{LiTi}_4\text{O}_9)_4 > (\text{LiMn}_4\text{O}_9)_4 > (\text{LiV}_4\text{O}_9)_4$. However, low Fermi energy for $(\text{LiTi}_4\text{O}_9)_4$ and $(\text{LiMn}_4\text{O}_9)_4$ has been concluded to have a lower catalytic effect for Li-air batteries, since both systems has low number of DOS at the Fermi level.

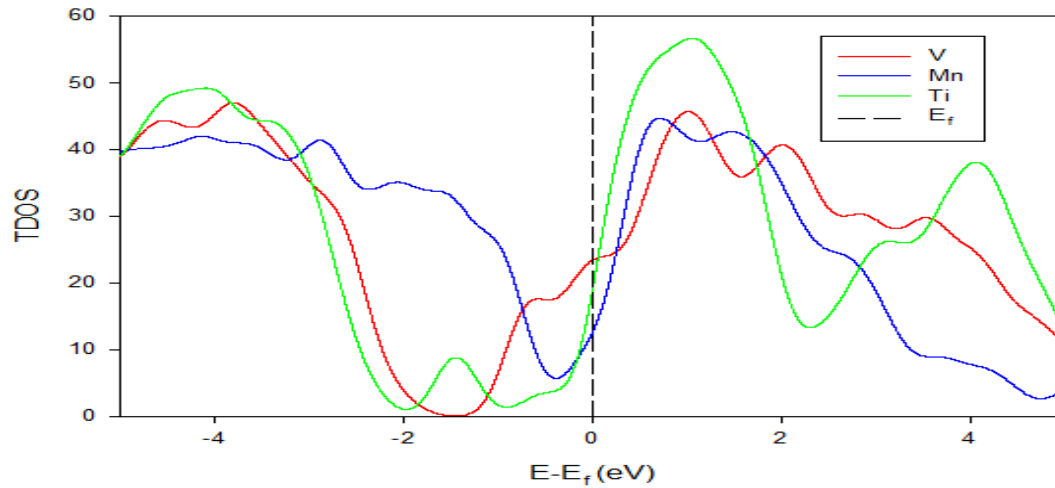


Figure 6. Comparison of the overall density of states for the Peroxo on Li surfaces.

Figure 6 shows the total density of states (TDOS) for $(\text{LiMn}_4\text{O}_9)_4$, $(\text{LiTi}_4\text{O}_9)_4$, and $(\text{LiV}_4\text{O}_9)_4$ surfaces. We notice that towards E_f the DOS peak of $(\text{LiMn}_4\text{O}_9)_4$ has a lower density of states which agrees that it is the most stable structure. Furthermore, we notice that $(\text{LiTi}_4\text{O}_9)_4$ and $(\text{LiV}_4\text{O}_9)_4$, both have a higher density of states at E_f compared to $(\text{LiMn}_4\text{O}_9)_4$. The DOS for $(\text{LiV}_4\text{O}_9)_4$ has a higher density of states at E_f , indicating that it is the least stable structure. The stability trend can be written as $(\text{LiMn}_4\text{O}_9)_4 > (\text{LiTi}_4\text{O}_9)_4 > (\text{LiV}_4\text{O}_9)_4$. In any case, low Fermi energy for $(\text{LiTi}_4\text{O}_9)_4$ and $(\text{LiMn}_4\text{O}_9)_4$ has been concluded to have a lower catalytic impact for Li-air batteries.

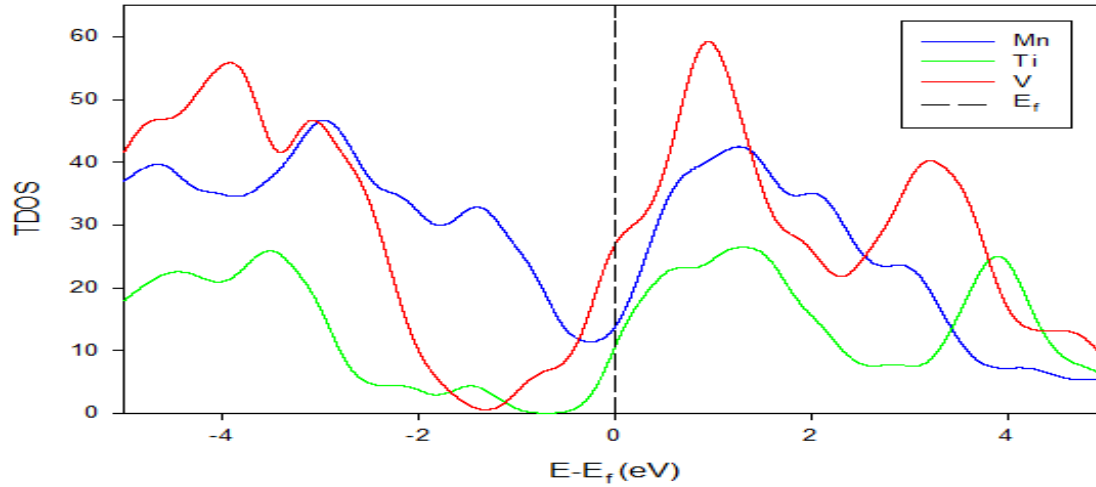


Figure 7. Comparison of the full density of states for Peroxo on Li-M surfaces.

The total density of states (TDOS) for $(\text{LiMn}_4\text{O}_9)_4$, $(\text{LiTi}_4\text{O}_9)_4$, and $(\text{LiV}_4\text{O}_9)_4$ surfaces is observed above in figure 7. We notice that along with E_f the DOS peak of $(\text{LiMn}_4\text{O}_9)_4$ has a lower density of states which agrees that it is the most stable structure with a slight shift towards the conduction band. Furthermore, we notice that $(\text{LiTi}_4\text{O}_9)_4$ and $(\text{LiV}_4\text{O}_9)_4$, both have a higher density of states at E_f compared to $(\text{LiMn}_4\text{O}_9)_4$. The shift from the valence band from both $(\text{LiTi}_4\text{O}_9)_4$ and $(\text{LiV}_4\text{O}_9)_4$ to the conduction band is observed. The DOS for $(\text{LiV}_4\text{O}_9)_4$ has a higher density of states at E_f , indicating that it is the least stable structure. The stability trend can be written as $(\text{LiMn}_4\text{O}_9)_4 > (\text{LiTi}_4\text{O}_9)_4 > (\text{LiV}_4\text{O}_9)_4$. However, low Fermi energy for $(\text{LiTi}_4\text{O}_9)_4$ and $(\text{LiMn}_4\text{O}_9)_4$ has been concluded to have a lower catalytic impact for Li-air batteries.

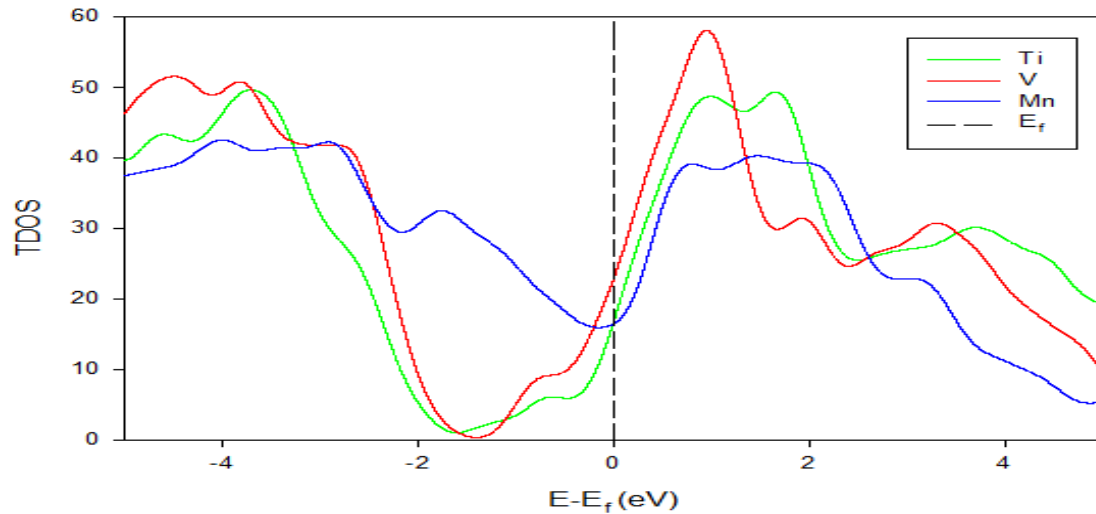


Figure 8. Comparison of the overall density of states for the Peroxo on M surfaces.

The total density of states (TDOS) for $(\text{LiMn}_4\text{O}_9)_4$, $(\text{LiTi}_4\text{O}_9)_4$, and $(\text{LiV}_4\text{O}_9)_4$ surfaces is displayed in figure 8 above. We note that near E_f the DOS peak of $(\text{LiMn}_4\text{O}_9)_4$ has a lower density of states which agrees that it is the most stable. However, we notice that $(\text{LiTi}_4\text{O}_9)_4$ and $(\text{LiV}_4\text{O}_9)_4$, both have higher density of states at E_f compared to $(\text{LiMn}_4\text{O}_9)_4$. The shift from the valence band from both $(\text{LiTi}_4\text{O}_9)_4$ and $(\text{LiV}_4\text{O}_9)_4$ to the conduction band is observed. The DOS for $(\text{LiV}_4\text{O}_9)_4$ has a higher density of states at E_f , suggesting that it is the least stable structure. The stability trend can be written as $(\text{LiMn}_4\text{O}_9)_4 >$

$(\text{LiTi}_4\text{O}_9)_4 > (\text{LiV}_4\text{O}_9)_4$. However, low Fermi energy for $(\text{LiTi}_4\text{O}_9)_4$ and $(\text{LiMn}_4\text{O}_9)_4$ has been concluded to have a lower catalytic impact for Li-air batteries.

After successful adsorption with oxygen at the Li/MO₂, there are arrangements produced (dissociated, peroxo on Li, peroxo on Li-M, and peroxo on M). Configurations such as peroxo on Li, peroxo on Li-M, and peroxo on M yielded the same trend of stability when observing the density of states with $(\text{LiMn}_4\text{O}_9)_4$ found to have less density of states at the Fermi level in all arrangements obtained, followed by the $(\text{LiTi}_4\text{O}_9)_4$ frameworks. The final one from the observed results is $(\text{LiV}_4\text{O}_9)_4$ with a high density of states at the Fermi level, the electronic band structures compare well with the density of states. The behavior of the frameworks is characterized by how the frameworks are associated with the Fermi level, which ordinarily results in finding a way of classifying the metallic, semiconductor, and insulator behavior.

4. Conclusion

The electronic properties were effectively obtained from the DFT using the Vasp and CASTEP codes. The k-points used throughout the calculations are 6x6x1 for all the (110) surface systems. The electronic properties such as the electronic band structures and the density of states were successfully obtained for the clean (110) surfaces. Oxygen adsorption on the Li/MO₂ resulted in configurations such as the dissociated, peroxo on Li, peroxo on Li-M, and peroxo on M. The stability of these specified arrangements was distinguished by how much contribution each system makes to the fermi level. The high density of states means the system is less stable compared to the one with a low density of states at the Fermi level. However, from all the configurations mentioned above $(\text{LiTi}_4\text{O}_9)_4$ and $(\text{LiMn}_4\text{O}_9)_4$ are found to have lower catalytic impact due to low fermi energy contributions. The electronic band structures compared well with the energy of states. These discoveries are critical in progressing the cycling execution of Li-air batteries and provide understanding into the reactivity of Li/MO₂ (110) surfaces.

5. References

- [1] Tahir M, Pan L, Idrees F, Zhang X, Wang L, Zou J, and Wang Z L 2017 Electrocatalytic oxygen evolution reaction for energy conversion and storage: A comprehensive review *Nano Energy* **37** 126-157
- [2] Cheong K Y, Impellizzeri G, and Fraga M A 2018 Emerging materials for energy conversion and storage *Elsevier*
- [3] Geng D, Ding N, Andy Hor T S, Chien S W, Liu Z, Wu D, Sun X, and Zong Y 2016 From Lithium-Oxygen to Lithium-Air Batteries: Challenges and opportunities *Adv. Energy Mater.* **9** 1502164
- [4] Bruce P G, Freunberger S A, Hardwick L J and Tarascon J M 2012 Li-O₂ and Li-S batteries with high energy storage *Nature Materials*. **11** 19-29
- [5] Li Q, Cao R, Cho J and Wu G 2014 High-Performance Direct Methanol Fuel Cells with Precious-Metal-Free Cathode *Phys. Chem. Chem. Phys.* **16** 13568
- [6] Maenetja K P 2017 Density functional theory study of (110) β -MnO₂, β -TiO₂ and β -VO₂ surface in metal-air batteries *Unive of Limp thesis*
- [7] Abrahams S C and Bernstein J L 1971 Rutile: Normal Probability Plot Analysis and Accurate Measurement of Crystal Structure *Chem. Phys.* **55** 3206
- [8] Du X, Huang J, Zhang J, Yan Y, Wu C, Hu Y, Yan C, Lei T, Chen W, Fan C, and Xiong J 2018 Modulating Electronic Structures of Inorganic Nanomaterials for Efficient Electrocatalytic Water Splitting *A Journal of the German chemical society* **58** 4484-4502
- [9] Choy T S, Naset J, Chen J, Hershfield S, and Stanton C 2000 A data of fermi surface in virtual reality modelling language (VRML) *Bull. Amer. Phys. Soc.* **45** 36-42

Physical properties of the layered structure compound $\text{Ce}_3\text{Os}_4\text{Al}_{12}$

RF Djoumessi¹, BN Sahu¹ and AM Strydom¹

¹Highly Correlated Matter Research Group, Physics Department, University of Johannesburg, PO Box 524, Auckland Park 2006, South Africa

E-mail: redrissed@uj.ac.za

Abstract. In this work, we report on the structural and physical properties of polycrystalline $\text{Ce}_3\text{Os}_4\text{Al}_{12}$ synthesized by the argon arc-melting technique. The Rietveld refinement of powder X-ray diffraction patterns confirm that $\text{Ce}_3\text{Os}_4\text{Al}_{12}$ crystallizes in the hexagonal $\text{Gd}_3\text{Ru}_4\text{Al}_{12}$ -structure type with space group $P6_3/\text{mmc}$. The temperature dependent dc-magnetic susceptibility and specific heat data reveals that the compound undergoes a ferromagnetic type of ordering below 3 K. The study may contribute towards a better understanding of the physics in distorted Kagomé structure compounds, since in a frustrated lattice system such as this, there are strict constraints imposed upon the occurrence of long-range magnetic order and the magnetic order parameter.

1. Introduction

$\text{R}_3\text{T}_4\text{X}_{12}$ type of compounds are of particular interest among intermetallics because the crystal structure contains layers as well as triangular and distorted Kagomé lattice features [1, 2, 3]. The arrangement of the atoms carrying magnetic moments at the vertices of the structure and the competition between ferro- and antiferromagnetic interactions can lead to the appearance of magnetic frustration phenomena. Several studies have been done on Ru-based compounds in this series of aluminides. In these Ru-based compounds, a ferromagnetic behavior is observed in the light rare-earth based compounds (Pr and Nd) [2, 3, 4] while an antiferromagnetic behavior is observed in the heavy rare-earth ones (Gd, Tb, Dy and Yb) [5, 6, 7]. For instance, in $\text{Gd}_3\text{Ru}_4\text{Al}_{12}$, geometrical frustration together with the formation of ferromagnetic trimers due to the long-range RKKY interaction is observed at low temperatures [5]. Moreover, a skyrmion lattice with large topological Hall effect has been experimentally observed in the same material [8]. Skyrmions have good potential for information carriers in spintronic devices and frustration is a route towards enhanced skyrmion stability even in systems with a ferromagnetic ground state [9]. In $\text{Pr}_3\text{Ru}_4\text{Al}_{12}$, a magnetic moment instability in the presence of crystal electric fields is observed [2]. Despite the number of studies carried out in the $\text{R}_3\text{Ru}_4\text{Al}_{12}$ series, no physical and magnetic properties have been reported yet on Os-based compounds (except on $\text{Gd}_3\text{Os}_4\text{Al}_{12}$) synthesized for the first time by Niermann [10]. This work is the first report on physical properties of $\text{Ce}_3\text{Os}_4\text{Al}_{12}$.

2. Synthesis and experimental details

A polycrystalline sample was synthesized by arc-melting stoichiometric amounts of high-purity (99.99 mass % purity or better) elements (Ce, Os and Al) under argon atmosphere in an Edmund Buhler arc-melting furnace. After melting, the sample was annealed in a resistance furnace at 900°C for two weeks and finally water quenched. Dc-magnetic susceptibility, isothermal magnetization and specific heat measurements were performed using a commercial Dynacool physical properties measurement system from Quantum Design, USA. The measurements were carried out in the temperature range between 1.8 K to 300 K and fields up to a maximum value of 9 T.

3. Results and Discussion

The powder x-ray diffraction spectrum of this sample (see Fig. 1) was successfully refined on the basis of the hexagonal $\text{Gd}_3\text{Ru}_4\text{Al}_{12}$ structure type with P63/mmc space group. The structure was refined to $R_{\text{wp}} = 6.84\%$, $R_p = 4.49\%$ and $R_{\text{exp}} = 0.98$. The obtained lattice parameters are $a = 0.889(1)$ nm and $c = 0.953(1)$ nm. These values are in good agreement with an earlier report [10]. The refined atomic positions are reported in table 1.

The crystal structure may be described as a layered structure. The Ce atoms occupy only one site in the Ce_3Al_4 layer. The Ru atoms share two sites and the Al atoms occupy two different sites in the Os_4Al_8 puckered layer (see Fig. 2). The Ce atoms are arranged as a distorted Kagomé net with different sizes of triangles leading to two slightly different nearest-neighbour Ce-Ce distances.

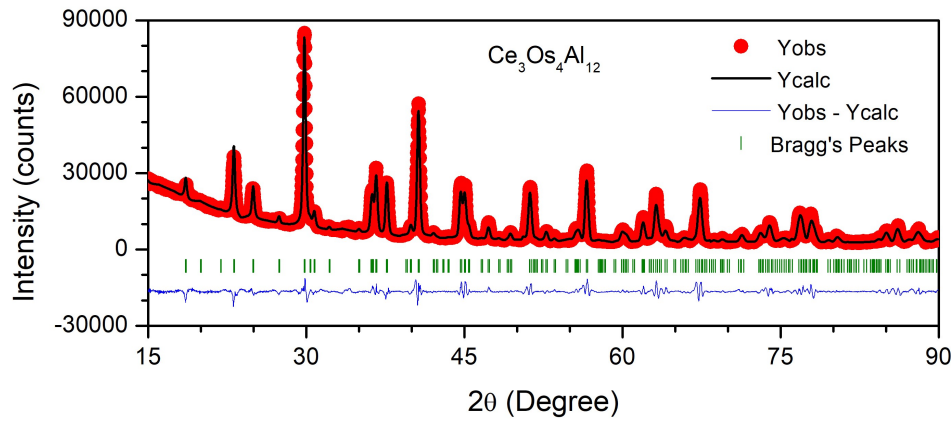


Figure 1. (a) Layered representation of the crystal structure of $\text{Ce}_3\text{Os}_4\text{Al}_{12}$ with Ce (Orange spheres), Os (blue spheres) and Al (green). (b) The Ce_3Al_4 layer showing the distorted Kagomé nets.

The main panel of Fig. 3 represents the dc-magnetic susceptibility $\chi(T)$ of $\text{Ce}_3\text{Os}_4\text{Al}_{12}$ measured in a magnetic field of 0.1 T. The data are obtained in a field-cooled protocol (cooling of the sample from 300 K to 2 K). $\chi(T)$ exhibits a modified Curie-Weiss behavior described by equation (1) from 300 K down to 50 K:

$$\chi(T) = \chi_0 + C/(T - \theta_P), \quad (1)$$

where χ_0 is the temperature independent susceptibility, C is the Curie-Weiss constant, and θ_P is the paramagnetic Weiss temperature. From the least-squares fit of equation (1) to the data, we obtained an effective magnetic moment (μ_{eff}) of $0.54 \mu_B/\text{Ce}$ ion which is less than one quarter

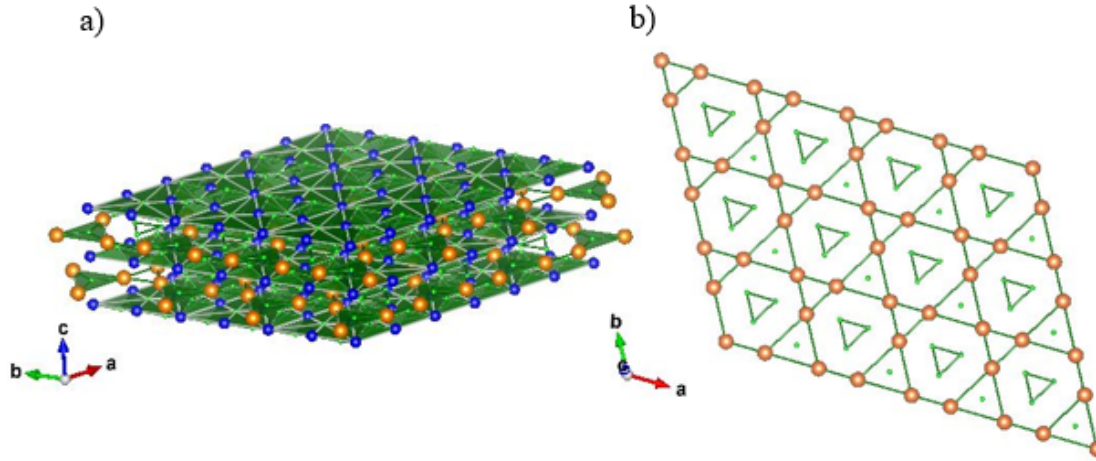


Figure 2. (a) Layered representation of the crystal structure of $\text{Ce}_3\text{Os}_4\text{Al}_{12}$ with Ce (Orange spheres), Os (blue spheres) and Al (green). (b) The Ce_3Al_4 layer showing the distorted Kagomé nets.

Table 1. Crystallographic details of $\text{Ce}_3\text{Os}_4\text{Al}_{12}$.

Atom	Wyckoff	x	y	z	Occupancy
Ce	6h	0.19174	0.38348	0.25000	0.19211
Os ₁	6g	0.50000	0.00000	0.00000	0.30492
Os ₂	2a	0.00000	0.00000	0.00000	0.11893
Os ₃	6h	0.00000	0.00000	0.25000	0.11893
Al ₁	12k	0.16523	0.33046	0.57419	0.42748
Al ₂	6h	0.53125	0.12953	0.25000	0.02533
Al ₃	4f	0.33333	0.66667	0.02753	0.19764
Al ₄	2b	0.00000	0.00000	0.25000	0.05803

of the theoretical value of a free trivalent Ce ion ($2.54 \mu_B$) in $\text{Ce}_3\text{Os}_4\text{Al}_{12}$. This suggests either an itinerant character or a strong crystal field effect of the 4f-electrons in $\text{Ce}_3\text{Os}_4\text{Al}_{12}$. The paramagnetic Weiss temperature is found to be $\theta_p = +5.3$ K with the positive sign indicating the dominance of ferromagnetic interactions in the high temperature region. The kink observed around the transition temperature $T_c = 3$ K (see inset (a) of Fig. 3) is a sign of a short-range order-like transition. Isothermal magnetization at temperatures between 2 K and 20 K is presented in the inset (b) of Fig. 3. Broad curvatures are observed below 6 K. The saturation magnetization at 2 K and in 9 T is only about $0.06 \mu_B/\text{Ce}$ ion which is less than 5% of the full saturation value compared to the free ion saturation value $2.16 \mu_B/\text{Ce}$. The quasi-linear behavior above 6 K indicates a paramagnetic state.

The main panel of Fig. 4 represents the specific heat of $\text{Ce}_3\text{Os}_4\text{Al}_{12}$ and $\text{La}_3\text{Os}_4\text{Al}_{12}$ as function of temperature. The high temperature region resembles the behavior of a normal metal. Inset (a) of Fig 4 represents the low-temperature region. The blue symbols represent the magnetic 4f contribution to the specific heat obtained by subtracting the specific heat of $\text{La}_3\text{Os}_4\text{Al}_{12}$ from that of $\text{Ce}_3\text{Os}_4\text{Al}_{12}$. The kink observed around the transition temperature $T_c = 3$ K is a sign of a short-range order-like transition. Inset (b) shows the 4f contribution to the entropy per Ce as a function of temperature. The magnetic contribution released at T_c is about $0.6 \text{ J/mole}_{\text{Ce}} \cdot \text{K}^2$ which is about 10% of the value $R \ln 2$ expected for a doublet ground

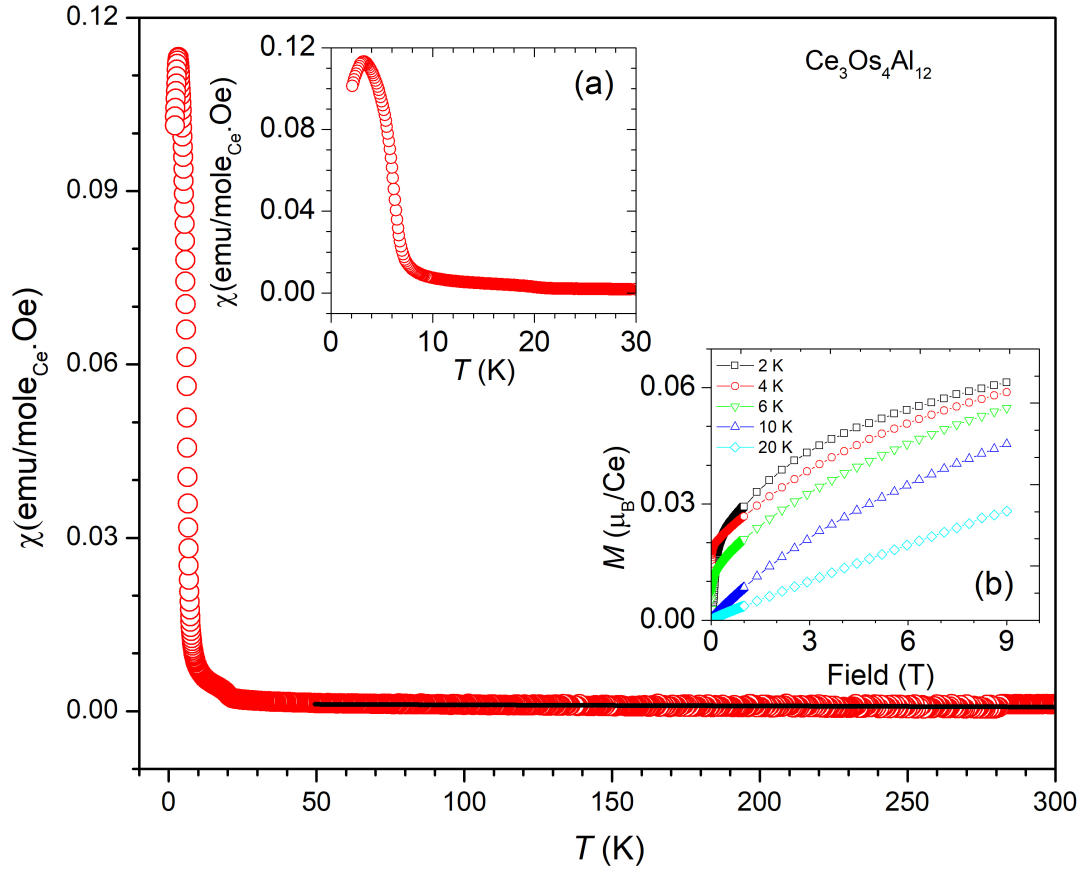


Figure 3. Main panel: magnetic susceptibility of $\text{Ce}_3\text{Os}_4\text{Al}_{12}$ measured in a constant dc-magnetic field of 0.1 T. The black line represents the least-squares fit of the modified Curie-Weiss relation (see equation 1). Inset (a) highlights the low-temperature region. Inset (b) represents the isothermal magnetization at temperatures between 2 K and 20 K.

state of the crystal field split multiplet of trivalent Ce. Inset (c) of Fig 4 represents the specific heat $C_{4f}(T)/T$ vs T^2 . $C_{4f}(T)/T$ at $T \rightarrow 0$ reaches $0.4 \text{ J/mol}_{\text{Ce}} \cdot \text{K}^2$ which is enhanced by a factor of 100 above that of an ordinary metal [11]. This points to a large residual 4f-electron entropy in the low-temperature limit which is likely caused by strong electron correlations in the Ce compound.

4. Conclusion

$\text{Ce}_3\text{Os}_4\text{Al}_{12}$ is a new example of a layered distorted Kagomé structure with possible effects of the geometric frustration. The $\chi(T)$ and $C_p(T)$ data confirm the presence of weak magnetic order. Further magnetic studies are needed to describe in detail the nature of the phase transition observed in $\text{Ce}_3\text{Os}_4\text{Al}_{12}$.

4.1. Acknowledgments

RFD thanks OWSD and SIDA for fellowships towards her PhD studies. B. Sahu thanks Global Excellence and Stature (UJ-GES) fellowship, University of Johannesburg. AMS thanks the URC/FRC of UJ and the SA-NRF (93549) for financial support.

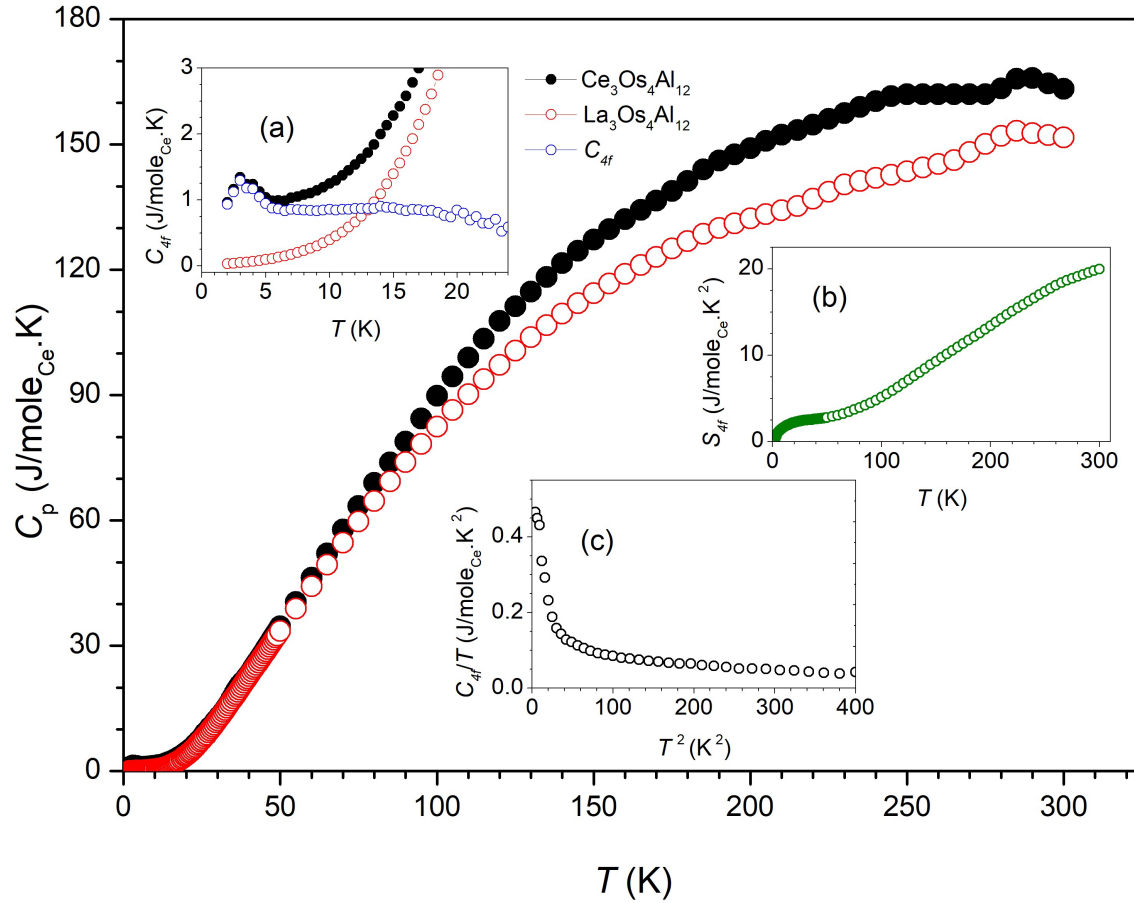


Figure 4. Main panel: Specific heat of $\text{Ce}_3\text{Os}_4\text{Al}_{12}$ and $\text{La}_3\text{Os}_4\text{Al}_{12}$ against temperature. Inset (a) represents the low-temperature region. The blue symbols represent the 4f-electron contribution to the specific heat of $\text{Ce}_3\text{Os}_4\text{Al}_{12}$ obtained by subtracting the specific heat of $\text{La}_3\text{Os}_4\text{Al}_{12}$ from that of $\text{Ce}_3\text{Os}_4\text{Al}_{12}$. Inset (b) shows the 4f contribution to the entropy per Ce as a function of temperature. Inset (c) illustrates $C_{4f}(T)/T$ vs T^2 .

References

- [1] Ge W, Michioka C, Ohta H and Yoshimura K 2014 *Solid State Communications* **195** 1–5
- [2] Henriques M, Gorbunov D, Andreev A, Fabrèges X, Gukasov A, Uhlarz M, Petříček V, Ouladdiaf B and Wosnitza J 2018 *Physical Review B* **97** 014431
- [3] Gorbunov D, Henriques M, Andreev A, Gukasov A, Petříček V, Baranov N, Skourski Y, Eigner V, Paukov M and Prokleška J 2014 *Physical Review B* **90** 094405
- [4] Gorbunov D, Henriques M, Andreev A, Eigner V, Gukasov A, Fabrèges X, Skourski Y, Petříček V and Wosnitza J 2016 *Physical Review B* **93** 024407
- [5] Nakamura S, Kabeya N, Kobayashi M, Araki K, Katoh K and Ochiai A 2018 *Physical Review B* **98** 054410
- [6] Upadhyay S K, Iyer K K and Sampathkumaran E 2017 *Journal of Physics: Condensed Matter* **29** 325601
- [7] Nakamura S, Toyoshima S, Kabeya N, Katoh K, Nojima T and Ochiai A 2015 *Physical Review B* **91** 214426
- [8] Hirschberger M, Nakajima T, Gao S, Peng L, Kikkawa A, Kurumaji T, Kriener M, Yamasaki Y, Sagayama H and Nakao H 2019 *Nature Communications* **10** 1–9
- [9] Von Malottki S, Dupé B, Bessarab P F, Delin A and Heinze S 2017 *Scientific Reports* **7** 1–10
- [10] Niermann J and Jeitschko W 2002 *Zeitschrift für anorganische und allgemeine Chemie* **628** 2549–2556
- [11] Kittel C, McEuen P and McEuen P 1996 *Introduction to Solid State Physics* vol 8 (Wiley New York)

Evaluating the evolution of Ti_5 cluster in LiCl medium

A F Mazibuko¹, P E Ngoepe and H R Chauke

Materials Modelling Centre, University of Limpopo, Private bag x1106, Sovenga, 0727, South Africa

E-mail: andile.mazibuko@ul.ac.za

Abstract. Titanium can be produced as both a metal and in powder form. It finds applications in various industries such as in medicine and aerospace, where the fabrication of components with excellent corrosion and high-temperature performance are significant. The titanium metal also plays a significant role in the titanium production process due to its desirable physical and chemical properties. Also, this process occurs in the presence of alkali metal and alkali earth metal salt mediums. Recent experimental studies are focusing on developing the lithiothermic part of the titanium formation process. However, the process happens quickly and is difficult to trace. In this study, classical molecular dynamic calculations were performed to understand the evolution of the small titanium Ti_5 cluster within the LiCl medium. The DL_POLY code was used to evaluate the temperature dependence of the structure. It was found that the cluster maintains its trigonal bipyramid geometry at the temperature range of 100 K – 2000 K. Furthermore, the cluster was observed to show elongation patterns. The results of this study might give us more insight into the growth and evolution of titanium in salt mediums.

1. Introduction

Transition metal clusters have attracted a lot of attention worldwide due to their useful chemical and physical properties such as corrosion resistance and ductility [1]. Several studies on transition metal clusters, such as palladium (Pd) and titanium (Ti) have been carried out [1,2]. These studies reported that the properties of small metal clusters may differ significantly from those of bulk structures. However, they can emulate the behavior of either the metal particle or crystal defects in supported crystals [2]. An increment in the cluster size results in the gradual evolution of properties towards the bulk structure and creates new prospects for sustainable materials [3].

Titanium clusters form a fundamental point in understanding the electronic structure and geometry of the bulk Ti structure and small titanium clusters are reported to elucidate bulk-like electronic structures [4]. Zhao et al. [5] used DFT to investigate the electronic and structural properties and found that Ti clusters follow a pentagonal growth behavior that favors close-packed structures. In other work, Sun et al. [6] reported on the icosahedral, octahedral-, and tetrahedral- sequences being some of the size-dependent growth patterns. These structures or geometries can be attained by either adding or removing atoms from specific basic motif or positions. They also reported that the n clusters with 7, 13 and 15 atoms are magic numbers or stable clusters, with unique configurational geometries [6].

In this paper, we use molecular dynamics and density functional theory to gain understanding and knowledge on the titanium formation processes at a fundamental level. Titanium metal/powder production is significant in various industries, particularly the aerospace and medical industries. Firstly, we report on the geometry and evolution of the interaction of Ti_5 cluster with LiCl medium. Secondly,

the thermodynamic properties particularly the entropy and Gibbs free energy for Ti_5/LiCl system are briefly described. The Ti_5 cluster is one of the magic number clusters reported in literature and may provide insight into the behavior of small clusters in salt mediums. Finally, the rest of the paper is organized in the following manner: section 2 provides computational details; the geometry of the Ti_5 cluster and thermodynamic properties of the Ti_5/LiCl system are presented and discussed in Section 3; and lastly, the conclusion is provided.

2. computational details



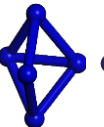
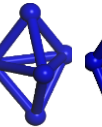
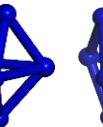
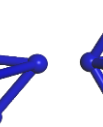
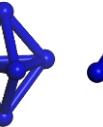
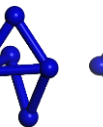
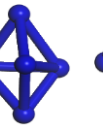
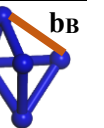
The Knowledge-Led Master code (KLMC) was employed to develop the Ti_5 nanocluster, using the genetic algorithm (GA) module. It has proven to accurately locate local and global minima on the potential energy surface to predict the structure of metallic clusters or their alloys. The Ti_5 cluster was then validated using the General Utility Lattice Program (GULP) [7], which is used in performing various types of simulations on materials employing boundary conditions unique to the type of material. Molecular dynamics simulations were performed using DL_POLY code [8,9]. The code can be used to understand the structure, reactivity and stability of materials and it is recommended for simulating large systems. A radial cut-off of 9.95 Å was used in a simulation of 221 atoms of the Ti_5/LiCl system. The time step was set at 1e^{-6} ns and the thermal data was computed every 120 000 steps while increasing the temperature from 100 to 2000 K. Furthermore, an NVT ensemble employing the Nosé-Hoover thermostat and barostat was run for 50000 steps to bring the system to equilibrium.

3. results and discussion

3.1. Effect of LiCl on the Ti_5 nanocluster.

Table 1 shows the Ti_5 nanocluster geometry in the presence of LiCl medium at different temperatures. This was to investigate how LiCl may influence the evolution of Ti_5 as the temperature is increased. We note that the cluster maintains its ground state trigonal bipyramid geometry at all temperatures. However, there is elongation of Ti-Ti bonds from $b_A = 2.673$ Å (low temperature, 0 K) to $b_B = 2.933$ Å (high temperature, 2000 K). This may be due to the strong interaction of Li-Ti. The observed elongation of Ti-Ti bonds is similar to the reported work by Henderson et al. [10] for rutile and geikielite structures.

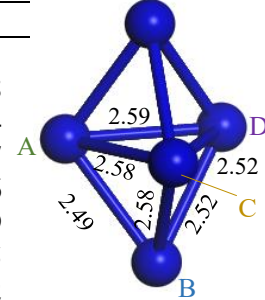
Table 1. The geometry of Ti_5 after interactions with LiCl medium. The Ti-Ti bond length is represented as b_A (0 K) and b_B (2000 K).

Ground state	100 K	300 K	600 K	900 K	1100 K	1300 K	1600 K	1900 K	2000 K
									

The elongation of bonds can also be seen by the absence of bonds between Ti atoms at 100 K, 300 K, 1100 K, 1600 K and 2000 K. Notably, the bond increases along A-D for 100 K and 300 K. At high temperature, the bond elongation is along A-B and A-C (1600 K); A-C (1900 K) and along A-C and B-D for 2000 K (see table 2). The bond distances are indicated in the figure inserted in table 2. This observation suggests that the interaction of Ti_5 cluster with LiCl medium resulted in the elongation of the cluster.

Table 2. The calculated Ti-Ti bond length of Ti_5/LiCl system at different temperatures, the bond length and sites A, B, C and D are indicated on the nanocluster (insert on the right of the table). The pure theoretical value [11] and Ti_5 (GULP) are added for comparison.

		Ti-Ti bond length (Å)					
Bond site		A-D	A-B	A-C	B-C	B-D	C-D
Theor.		2.59	2.49	2.58	2.58	2.52	2.54
Ground state		2.528	2.458	2.528	2.458	2.458	2.528
Calc.	100 K	2.927	2.660	2.917	2.825	2.820	2.854
	300 K	3.125	2.744	3.006	2.752	2.770	2.857
	600 K	2.863	2.684	2.772	2.805	2.708	2.876
	900 K	2.775	2.455	2.928	2.862	2.708	2.829
	1100 K	2.655	2.625	2.940	2.809	2.786	2.875
	1300 K	2.867	2.506	2.845	2.765	2.847	2.742
	1600 K	2.722	2.977	2.908	2.424	2.633	2.812
	1900 K	2.781	2.709	3.034	2.571	2.472	2.821
	2000 K	2.847	2.862	3.428	2.753	2.933	2.919



3.2. Thermodynamic properties.

We investigated the thermodynamic properties of the Ti_5/LiCl system, particularly the entropy and Gibbs free energy. Firstly, we calculated the entropy to measure the atom disorder and randomness to understand the effect of temperature. Secondly, the Gibbs free energy was estimated to determine the equilibrium conditions of the system.

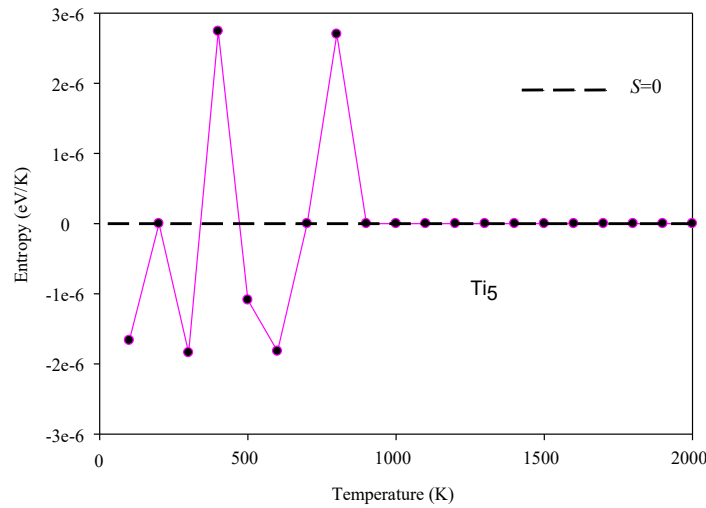


Figure 1. The entropy for the Ti_5/LiCl system. The dashed line indicates zero entropy.

Figure 1 depicts the entropy of the Ti_5/LiCl system at various temperatures. Note that a positive entropy indicates an increase in disorder whilst a negative entropy indicates a decrease in the disorder of atoms [12]. The Ti_5/LiCl system shows an increase in the disorder of atoms at 400 K and 800 K. At 200 K, 700 K and in the temperature range of 900 K – 2000 K; the entropy is zero which suggests that the atoms are ordered.

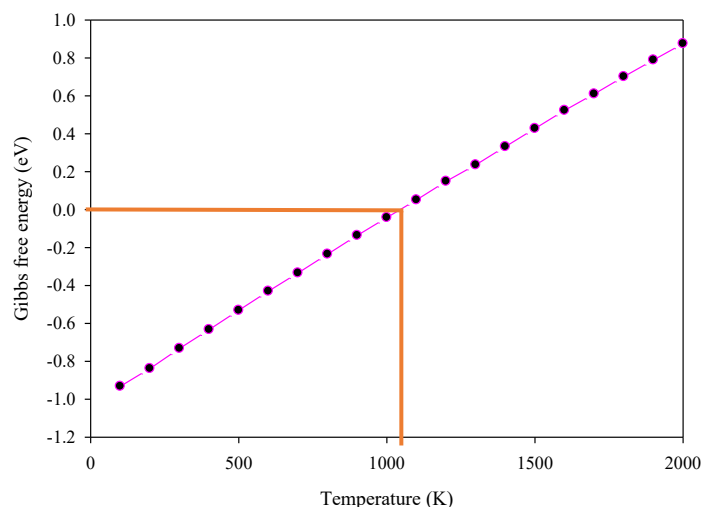


Figure 2. Gibbs free energy for the Ti_5/LiCl system. The orange vertical and horizontal lines indicate the region where the system is favorable.

The system was further characterized using the Gibbs free energy as shown in figure 2. It is observed that the figure depicts a linear increase in the Gibbs free energy as the temperature is increased. We note that the Gibbs free energy values are negative at 100 K – 1050 K. This suggests that reactions between the Ti_5 cluster with LiCl are exothermic (spontaneous). The calculated entropy and Gibbs free energy results can be taken as a prediction study for future investigation.

4. Conclusion

We investigated the effect of LiCl on the Ti_5 titanium cluster at different temperatures. Molecular dynamics results showed that the cluster maintains its ground state trigonal bipyramid geometry at all temperatures. However, the Ti-Ti bond lengths of the Ti_5 nanocluster increase. The observations suggested that interaction of Ti_5 cluster with LiCl medium result in the elongation of the cluster. Entropy results showed that at higher temperatures (900 K – 2000 K) the Ti_5/LiCl system depicts a degree of ordering in the atoms. Furthermore, the Gibbs free energy indicated that reactions are favorable (spontaneous) below 1050 K and spontaneity decrease as the temperature is increased above 1050 K. Moreover, the findings suggest that lithium chloride promotes elongation to the size of the Ti_5 nanocluster and might be a potential medium for evaluating the growth of small titanium clusters in titanium production.

Acknowledgements

The work was carried out at the Materials Modelling Centre (MMC), University of Limpopo. We acknowledge the National Research Foundation for financial assistance and funding from the Royal Society Advanced Fellowship Newton Grant (NA140447). The authors also wish to recognize the support of the South African Research Chair initiative of the Department of Science and Technology.

References

- [1] Lazauskas T, Sokol A A, Buckeridge J, Catlow C R A, Escher S G E T, Farrow M R, Mora-Fonz D, Blum V W, Phaahla T M, Chauke H R, Ngoepe P E and Woodley S M 2018 *Phys. Chem. Chem. Phys.* **20** (20) 13962
- [2] Estiu G L and Zerner M C 1994 *J. Phys. Chem.* **98** (18) 4793
- [3] Nava P, Sierka M and Ahlrichs R 2003 *Phys. Chem. Chem. Phys.* **5** (16) 3372
- [4] Fernando A, Weerawardene K L D M, Karimova N V and Aikens C M 2015 *Chem. Rev.* **115**

- (12) 6112
- [5] Zhao J, Qiu Q, Wang B, Wang J and Wang G 2001 *Solid State Commun.* **118** (3) 157
 - [6] Sun H, Ren H, Wu Z and Xu N 2015 *Comput. Theor. Chem.* **1062** 74
 - [7] Gale J D 1997 *J. Chem. Soc.* **93** 629
 - [8] Smith W and Todorov I T 2006 *Mol. Simul.* **32** (12-13) 935
 - [9] Todorov I T, Smith W, Trachenko K and Dove M T 2006 *J. Mater. Chem.* **16** (20) 1911
 - [10] Henderson C M B, Knight K S and Lennie A R 2009 *The Open Mineralogy Journal* **3** 1
 - [11] Castro M, Liu S R, Zhai H J and Wang L S 2003 *J. Chem. Phys.* **118** (5) 2116
 - [12] Jha D K 2004 Textbook of thermodynamics Discovery Publishing House New Delhi

Influence of duration of annealing on thermoluminescence of natural quartz annealed at 1000 °C

D E Folley¹, M L Chithambo

Department of Physics and Electronics, Rhodes University,
PO Box 94 Grahamstown 6140, South Africa

E-mail: damilolafolley@gmail.com

Abstract. The influence of duration of annealing on thermoluminescence of natural quartz annealed at 1000 °C is reported. The study looks at samples annealed for 10 and 60 min. A glow curve measured at 1 °Cs⁻¹ after beta irradiation to 50 Gy for the sample annealed for 10 min shows seven peaks at 68, 130, 176, 276, 300, 360, and 416 °C labelled I through VII. The sample annealed for 60 min has five peaks at 70, 128, 176, 234, and 308 °C labelled I-V respectively. A study of dosimetric features and kinetic analysis was carried out on the two prominent peaks, peak I and III for both samples. The electron trap responsible for peak I depletes faster at high duration of annealing between irradiation and measurement. In contrast, the electron trap for peak III was more stable for both samples. Kinetic analysis shows that peak I is a first-order peak and peak III a non-first-order peak. The activation energy obtained using the initial rise, whole glow peak, and curve fitting methods is ~0.95 eV for peak I and ~1.20 eV for peak III. In particular, the kinetic parameters obtained for both peaks decrease with annealing time. This suggests that the duration of annealing at 1000 °C has an effect on the trap parameters of natural quartz.

1. Introduction

Quartz is the second most abundant mineral after feldspar and is used widely in retrospective dosimetry and luminescence dating. Its use as a natural dosimeter in a variety of applications is well documented [1-10]. When quartz is heated at elevated temperatures, it undergoes phase transitions, namely at 573 °C and 870 °C [11, 12]. Several studies have shown that annealing improves the luminescence sensitivity of quartz. Bøtter-Jensen et al. [13] showed that annealing of quartz prior to irradiation can significantly increase its luminescence sensitivity. The significant increase, which occurs between the first two phase inversion temperatures, is attributed to alteration in the concentration of recombination centres [14]. Further work also shows that annealing affects the luminescence lifetimes [15, 16] and radioluminescence emission bands [17] of quartz.

There are for quartz, numerous studies on thermoluminescence (TL) reported in the literature. The so-called “110 °C peak” has been the peak of interest for most thermoluminescence investigations. The shape and kinetic parameters of this peak vary by a narrow range for all quartz samples even after extreme conditions of irradiation and heating [18]. Recent work (e.g. [2, 3]) has shown that annealing has little effect on the kinetic parameters of the “110 °C” peak of natural quartz at 800 °C. However, the influence of duration of annealing on thermoluminescence of natural quartz is yet to be investigated in

¹ To whom any correspondence should be addressed.

greater detail. In his work, Chithambo [19] showed that lifetimes increase with annealing time for natural quartz annealed at 1000 °C in studies using time-resolved optical stimulation. This response of lifetimes to annealing is the motivation for the current investigation on the same quartz using thermoluminescence.

In this work, we investigated the influence of duration of annealing on thermoluminescence of natural quartz annealed at 1000 °C, that is beyond the second phase inversion temperature. Dosimetric features and kinetic analysis were carried out on the two prominent peaks of the samples annealed at 1000 °C for 10 and 60 min.

2. Experimental details

Natural sedimentary quartz of grain size 90 – 250 µm commercially available from BDH Ltd (UK) was used. The samples were annealed at 1000°C for 10 minutes and another for 1 hour. The quartz was annealed to remove any remanent signal and to improve its sensitivity to thermal stimulation. The same quartz annealed at 1000 °C has been used previously for thermoluminescence and luminescence lifetimes investigations [4, 19]. Experiments were performed using a RISØ TL/OSL DA-20 Luminescence Reader. The luminescence was detected by an EMI 9235QB photomultiplier tube through a 7 mm Hoya U-340 filter. Samples were irradiated at room temperature using a $^{90}\text{Sr}/^{90}\text{Y}$ β source at a rate of 0.10 Gys⁻¹. All measurements were carried out at a heating rate of 1°Cs⁻¹ unless otherwise stated. The same sample mass of 30 mg was used throughout.

3. Results and discussion

3.1. General features of glowcurves

Figure 1 shows glow curves measured at 1°Cs⁻¹ from samples of natural quartz annealed at 1000 °C for 10 minutes (solid symbols) and 60 minutes (open symbols). The samples were irradiated to 50 Gy. The intensity of the sample annealed for 10 min is higher than that annealed for 60 min. For ease of reference, the samples annealed for 10 min and 60 min will be referred to as samples A and B respectively. The glow curves show four peaks for each sample as can also be seen in the inset. An intense peak (labelled I) was recorded at 68 and 70 °C for samples A and B respectively. Secondary peaks labelled II, III, and IV were recorded at 130, 176 and 276 °C respectively for sample A. In comparison, the peaks II, III, and IV are at 128, 176, and 308 °C respectively for sample B. The position of each of these peaks was verified using the thermal cleaning technique.

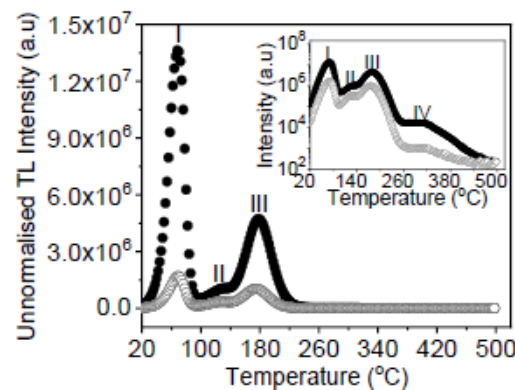


Figure 1. Thermoluminescence glow curves of natural quartz annealed at 1000 °C for 10 min (solid symbols) and 60 min (open symbols) measured at 1 °Cs⁻¹ following irradiation to 50Gy. The inset shows the same curves on a semilogarithmic plot which reveals the presence of peak IV.

3.1.1. Resolution of peaks by thermal cleaning.

To determine the exact number of peaks in the glow curve and to obtain a clear rising edge of the individual peaks, the thermal cleaning technique [20] was used. In the method, an irradiated sample is heated to a temperature just beyond the final temperature of each peak that needs to be removed. In this

way, the electron traps responsible for such peak(s) are emptied. The sample is then cooled and reheated to a final temperature to record the whole glow curve. By adopting the procedure, sample A heated in turn to 100, 140, 250, 350, and 400 °C following irradiation to 50 Gy each time revealed the positions of peaks II, III, IV, V, VI, and VII as 130, 176, 276, 300, 360, and 416 °C respectively. Similarly, for sample B, the procedure revealed peaks II, III, IV, and V at 128, 176, 234, and 308 °C respectively following irradiation to 50 Gy each time and preheating to 95, 140, and 240 °C. In comparison, an unannealed sample of the same mass irradiated to the same dose showed six peaks at 72, 122, 174, 254, 280, and 416 °C [3]. The relevant plots for this method are available as *supplementary information*. Thus, the thermal cleaning technique revealed that thermoluminescence of sample A consists of seven peaks, whereas that of sample B consists of five peaks. The difference in the number of peaks for both samples can be ascribed to the influence of annealing.

3.2. Dosimetric features

For a material to be considered a good dosimeter, its luminescence signal should be properly reproducible, ideally not fade or if so only slowly. These dosimetric features were studied on peaks I and III, the two most prominent peaks of the annealed quartz. These peaks are well defined compared to other peaks in the glow curves.

3.2.1. Fading.

Fading of a TL signal occurs as a result of the escape of electrons from an electron trap between irradiation and measurement. This causes the TL intensity to decrease or fade between irradiation and measurement. For this study, the intensities of peaks I and III were monitored for different durations between irradiation and measurement up to 5 hours. Figure 2 shows the change of TL intensity with delay for peak I measured after a dose of 50 Gy. The intensity decreases with delay. The data were fitted with the function:

$$f(t) = I_0 \exp\left(-\frac{t}{\tau}\right), \quad (1)$$

from which the mean lifetime τ was evaluated as 7784 s (half-life = 5395s) and 4686 s (half-life = 3248 s) for samples A and B respectively. The result shows that lifetime decreases with duration of annealing. Galloway [15] has also reported that lifetimes in natural quartz decrease when the annealing temperature is increased beyond 600 °C. For peak III (graph omitted), the intensity was constant with delay between irradiation and measurements implying that the electron trap corresponding to peak III is stable. Thomas and Chithambo [5] have also reported a similar occurrence of stable intensity with delay for peak III for the same unannealed quartz irradiated to 10 Gy after a 20 h delay.

3.3. Assessing the order of kinetics

3.3.1. Influence of dose on peak position.

The order of kinetics of peaks I and III was assessed by studying the dependence of peak position T_m on dose. For a first-order peak, T_m is independent of dose, whereas T_m decreases with dose for a second-order peak [21]. Peak I was determined to be independent of irradiation between 10 and 300 Gy at 68.5 ± 0.6 °C for sample A and at 69.9 ± 0.3 °C for sample B. The results show that peak I for both samples follows first-order kinetics. This agrees with the findings for peak I for the same unannealed natural quartz reported by Folley and Chithambo [3]. Literature (e.g. [6-8]) shows that peak I generally referred to as the “110 °C peak” is a first-order peak for all quartz samples. Figure 3 shows the variation of position of peak III with dose for samples A (solid symbols) and B (open symbols). The position of peak III decreases with dose for both samples in a staircase manner, from which T_m is independent of dose at different levels of the decrease. That the position of peak III is independent of dose at different levels could imply that the peak for both samples is general order peak. In contrast, the position of peak III for an unannealed sample was reported to be independent of dose by Thomas and Chithambo [5] implying that annealing influences the change of its order of kinetics from first-order to non-first-order.

3.4. Kinetic analysis

In order to determine the kinetic parameters of peaks I and III, kinetic analysis was carried out using the initial rise, whole glow-peak, variable heating rate, and curve fitting methods. Several methods were

used in evaluating the kinetic parameters in order to corroborate the results. Kinetic analysis will only be reported for the annealed quartz. These results will be compared with the analysis of peak I reported by Folley and Chithambo [3] for the same unannealed quartz irradiated to 50 Gy and of peak III by Thomas and Chithambo [5] for a dose of 10 Gy. This is necessary for monitoring the influence of annealing on the kinetic parameters of the investigated peaks. For completeness, we also compare our values with ones from the literature.

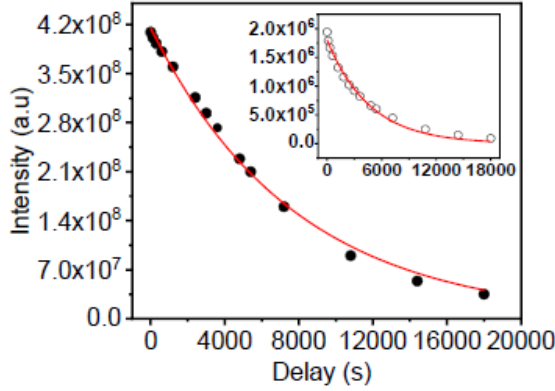


Figure 2. The variation of TL intensity with delay between irradiation and measurements for peak I. The inset shows data for sample B. The line passing through the data points is a fit of equation (1).

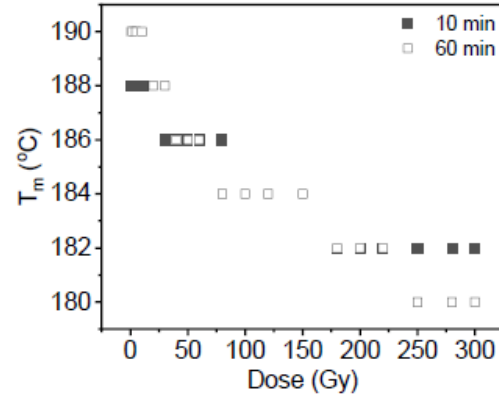


Figure 3. The influence of dose on the position of peak III for the samples annealed for 10 min (solid squares) and 60 min (open squares).

3.4.1. Initial rise method.

Peaks I and III were first analysed using the initial rise method, applicable to the clear rising edge of a glow peak whose intensity and temperature are related as:

$$I = C' \exp\left(-\frac{E}{kT}\right), \quad (2)$$

where E is the activation energy, k is Boltzmann's constant, and C' is a constant.

Plots of $\ln I$ against $1/kT$ for the initial rise portions of the peaks are shown in Figure 4. The activation energy of peak I for sample A (solid circles) was evaluated as 0.934 ± 0.004 eV. This value is consistent with 0.93 ± 0.03 eV for similar peak of an unannealed quartz reported by Folley and Chithambo [3] using the same method. The value of the activation energy is also in agreement with 0.92 eV reported by Mebhah et al. [9] for the same 110 °C peak of unannealed fired quartz irradiated to 10 Gy. In comparison, the activation energy for peak I for sample B (open circles) was evaluated as 0.904 ± 0.004 eV and agrees with 0.90 ± 0.01 eV reported by Yazici and Topaksu [10] for an unannealed quartz. This shows that annealing has minimal effect on the activation energy of peak I. Similarly, for peak III, the activation energy was determined to be 1.18 ± 0.01 eV and $E = 1.10 \pm 0.01$ eV for samples A (solid squares) and B (open squares) respectively. In comparison, the values of E for peaks I and III for sample B are slightly less than those obtained for sample A. An increase in the duration of annealing did not cause a significant increase in the activation energy.

3.4.2. Whole glow peak method.

The whole glow peak method was further used to determine the activation energy E , order of kinetics b , and frequency factor of peaks I and III. The method is best suited for a well-isolated glow peak whose area A under the glow peak is related to the order of kinetics b by:

$$\ln\left(\frac{I}{A^b}\right) = \ln\left(\frac{s'}{\beta}\right) - \left(\frac{E}{kT}\right), \quad (3)$$

where β is the heating rate, s' is the effective pre-exponential factor [20]. For first-order kinetics, s' becomes the frequency factor. Graphs of $\ln\left(\frac{I}{A^b}\right)$ against $\frac{1}{kT}$ for different values of b were plotted to determine the best choice for b . For peak I in sample A, this was determined as $b = 1.1$ ($R^2 = 0.99$) and as $b = 1.2$ ($R^2 = 0.999$) for peak I for sample B. For peak III, $b = 1.2$ and $b = 1.1$ for samples A

and B respectively. These values of b suggest that the peaks are of first-order kinetics. The activation energy for peak I for sample A was found as $E = 0.96 \pm 0.01$ eV. This is consistent with 0.95 ± 0.01 eV for the same quartz annealed for 60 minutes implying that the duration of annealing did not affect the activation energy of peak I. The values obtained for the activation energy for samples A and B as described are in good agreement with 0.98 ± 0.01 eV for unannealed quartz [3] implying that annealing has little effect on the activation energy. For peak III, $E = 1.09 \pm 0.01$ eV for sample A and $E = 1.02 \pm 0.01$ eV for sample B. The activation energy decreases with the duration of annealing. However, the value obtained for sample A compares favourably with 1.06 ± 0.01 eV [8] for peak III for the unannealed quartz, suggesting that annealing has little effect on the activation energy. The frequency factors obtained from the intercept of the plots for peak I are $1.5 \times 10^{13} \text{ s}^{-1}$ for sample A and $8.5 \times 10^{12} \text{ s}^{-1}$ for sample B. Similarly, for peak III, the frequency factor was evaluated as $1.1 \times 10^{11} \text{ s}^{-1}$ and $6.5 \times 10^{10} \text{ s}^{-1}$ for samples A and B respectively. The frequency factors for both peaks also decreases with the duration of annealing. The relevant plots for this method are available as *supplementary information*.

3.4.3. Curve fitting method.

Peaks I and III extracted from thermal cleaning were fitted using the expression:

$$I(T) = I_m b^{\frac{b}{b-1}} \exp\left(\frac{E(T-T_m)}{kTT_m}\right) \left[(b-1) \left(1 - \frac{2kT}{E}\right) \frac{T^2}{T_m^2} \exp\left(\frac{E(T-T_m)}{kTT_m}\right) + 1 + (b-1) \frac{2kT_m}{E} \right]^{-\frac{b}{b-1}}, \quad (4)$$

where I_m is the maximum peak intensity, and other parameters remain as defined previously [22].

The goodness of fit was tested by the so-called figure of merit (FOM) defined as:

$$FOM = \frac{\sum_p |y_{exp} - y_{fit}|}{\sum_p y_{fit}} \times 100\%, \quad (5)$$

where y_{exp} and y_{fit} represent the experimental intensity data and the values of the fitting function, respectively [23]. A fit is acceptable if $FOM \leq 3.5\%$ [23, 24].

The frequency factor was calculated by substituting the values of E and T_m into the expression:

$$s = \frac{\beta E}{kT_m^2} \exp\left(\frac{E}{kT_m}\right), \quad (6)$$

where all parameters maintain their meanings.

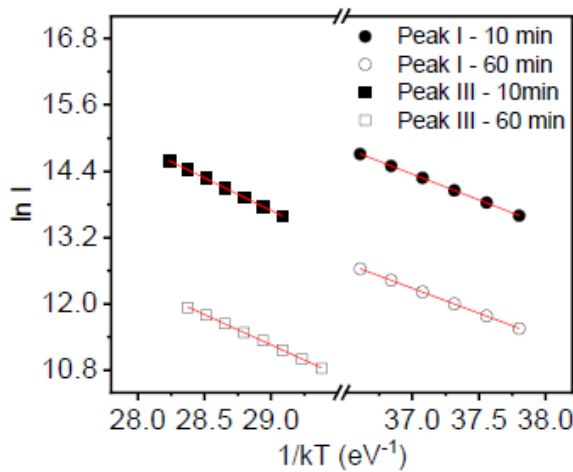


Figure 4. A plot of $\ln I$ against $1/kT$ for peak I and peak III using the initial rise method.

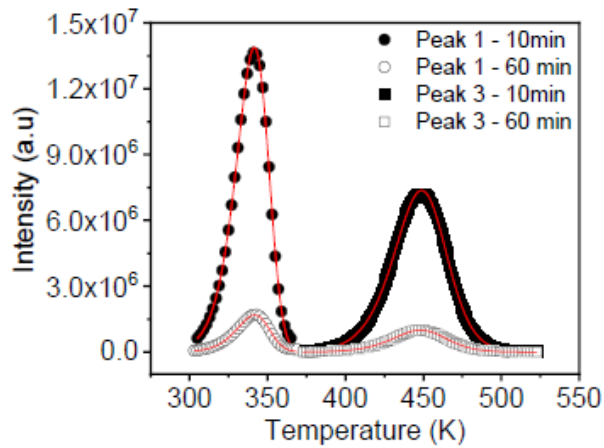


Figure 5. Curve fitting for peaks I and III. The solid lines through data points are the best fits of equation (4).

Figure 5 shows the best fit obtained for peaks I and III. The kinetic parameters determined for peak I are $E = 1.01 \pm 0.01$ eV and $b = 1.14 \pm 0.02$ with $FOM = 0.21\%$ for sample A whereas $E = 1.04 \pm 0.02$ eV and $b = 1.22 \pm 0.04$ with $FOM = 0.48\%$ for sample B. Here, the activation energy of sample A is only slightly lower than that of B implying that the duration of annealing has little effect on the activation energy of peak I. For peak III, $E = 1.23 \pm 0.01$ eV and $b = 1.46 \pm 0.01$ with $FOM = 0.36\%$ for sample A. These values are in good agreement with $E = 1.204 \pm 0.004$ eV and $b = 1.50 \pm$

0.01 with $FOM = 0.33\%$ for sample B. The E values obtained for peaks I and III for both annealed samples are consistent with literature values (e.g. $E = 1.01 \pm 0.01$ eV [3], $E = 1.00$ eV [6], $E = 1.22$ eV [6], $E = 1.21 \pm 0.02$ eV [8]). The values of b suggest that peak I for both samples follow first-order kinetics whereas peak III is of general-order kinetics. This agrees with the findings from the dose dependence of peak position method. The FOM values show that the curve fits are reliable. The frequency factor for peak I was calculated as 7.7×10^{13} and $2.0 \times 10^{14} \text{ s}^{-1}$ for samples A and B respectively. For peak III, $s = 4.5 \times 10^{12} \text{ s}^{-1}$ for sample A and $s = 2.0 \times 10^{12} \text{ s}^{-1}$ for sample B. These values are of the correct order of magnitude being consistent with the Debye vibration frequency.

4. Conclusion

The influence of annealing on thermoluminescence of natural quartz has been investigated through various methods of kinetic analysis. Peaks I and III, the two prominent peaks of the samples annealed for 10 and 60 min were analysed for kinetic parameters. We found that the thermoluminescence intensity decreases with the duration of annealing for both peaks. Lifetimes also decreases with annealing time. The activation energy and frequency factor obtained for both peaks using various methods decrease with the duration of annealing. This implies that the duration of annealing at 1000 °C has an effect on the trap parameters of natural quartz.

References

- [1] Preusser F, Chithambo M L, Götte T, Martini M, Ramseyer K, Sendezera E, Susino G J and Wintle A G 2009 *Earth Sci. Rev.* **97** 184–214
- [2] Yüksel M, Dogan T, Unsal E, Portakal Z G, Akca S, Yegingil Z and Topaksu M 2016 *Lumin.* **31(8)**1513-8
- [3] Folley D E and Chithambo M L 2018 *Radiat. Meas.* **120** 53-8
- [4] Folley D E 2020 *Dynamics of stimulated luminescence in natural quartz: Thermoluminescence and phototransferred thermoluminescence* (Unpublished PhD thesis)
- [5] Thomas S, Chithambo M L 2018 *J. Lumin.* **204** 603-8
- [6] Kitis G, Pagonis V, Carty H and Tatsis E 2002 *Radiat. Prot. Dosim.* **100** 225-8
- [7] Chithambo M L 2014 *J. Lumin.* **151** 235–43
- [8] Thomas S and Chithambo M L 2018 *J. Lumin.* **197** 406-411
- [9] Mebhah D, Imatoukene D, Lounis-Mokrani Z and Kechouane M 2009 *J. Lumin.* **129(12)**1615-18
- [10] Yazici A N and Topaksu M 2003 *Journal of Physics D: Applied Physics* **36(6)** 620
- [11] Schilles T, Poolton N, Bulur E, Bøtter-Jensen L, Murray A, Smith G, Riedi P and Wagner G 2001 *J. Phys. D: Appl. Phys.* **34** 722
- [12] Gribble C D 2012 *Optical mineralogy: principles and practice* (Springer Science & Business Media)
- [13] Bøtter-Jensen L, Agersnap Larsen N, Mejdahl V, Poolton N R J, Morris M F and McKeever S W S 1995 *Radiat. Meas.* **24(4)** 535-41
- [14] Poolton N R J, Smith G M, Riedi P C, Bulur E, Bøtter-Jensen L, Murray A S and Adrian M 2000 *J. Phys. D: Appl. Phys.* **33(8)** 1007
- [15] Galloway R B 2002 *Radiat. Meas.* **35(1)** 67-77
- [16] Chithambo M L and Ogundare F O 2009 *Radiat. Meas.* **44** 453-57
- [17] Pagonis V, Chithambo M L, Chen R, Chruścińska A, Fasoli M, Li S H, Martini M and Ramseyer K 2014 *J. Lumin.* **145** 38-48
- [18] Pagonis V, Tatsis E, Kitis G, Drupieski C 2002 *Radiat. Prot. Dosim.* **100** 373-6
- [19] Chithambo M L 2015 *Radiat. Meas.* **81** 198–204
- [20] McKeever S W S 1985 *Thermoluminescence of solids* (Cambridge University Press)
- [21] Chen R, McKeever S W S 1997 *Theory of thermoluminescence and related phenomena* (World Scientific)
- [22] Kitis G 2001 *J. Radioanalyt. Nucl. Chem.* **3** 697–703
- [23] Balian H G and Eddy N W 1977 *Nucl. Instrum. Meth.* **145** 389 –95
- [24] Gartia R K and Singh L L 2011 *Radiat. Meas.* **46** 664 –8

**DIVISION B –
NUCLEAR, PARTICLE AND
RADIATION PHYSICS**

The derivation of preliminary reference levels for natural radioactivity in drinking water surrounding nuclear sites

Thato B Molokwe

National Nuclear Regulator: Centre for Nuclear Safety and Security, Pretoria,
Gauteng, 0028, South Africa

E-mail: Tmolokwe@nnr.co.za

Abstract. The mandate of the National Nuclear Regulator (NNR) is to protect the people, property and environment from radiological damage, through the establishment of safety standards and regulatory practices. The NNR aims to establish criteria for drinking water in the vicinity of authorised nuclear facilities and is currently involved with projects to establish the levels of radioactivity in drinking water in the vicinity of authorised nuclear sites. The study seeks to derive preliminary reference levels based on the principles established by the World Health Organisation (WHO). The Annual Limit on Intake (ALI) was calculated for different age groups. The calculations were performed using the dose conversion factors provided by the International Atomic Energy Agency (IAEA) in the General Safety Regulations (GSR Part 3). The calculated ALI results for infant, child and adult age groups are presented. The calculated ALI could be used as preliminary reference levels during the assessment of the radioactivity status of baseline data that is currently being collected.

1. Introduction

The major sources of public exposure to natural radiation are cosmic and terrestrial radiation, inhalation of air/dust containing radionuclides and ingestion of radionuclide contaminated water or food [1]. Therefore, the risk to human health (public) could be presented in numerous pathways, one of which is through the ingestion of water containing radionuclides. The National Nuclear Regulator (NNR) is currently involved with projects to establish the radioactivity of drinking water in the vicinity of authorised nuclear facilities. The objective of conducting these projects is to ultimately establish regulatory criteria for the radioactivity of drinking water in the vicinity of authorised and legacy sites.

The establishment of safety standards and regulatory practices supports the NNR in carrying out its mandate. The mandate of the NNR is to protect the people, property and environment from radiological damage [2]. South Africa is a member state of the International Atomic Energy Agency (IAEA) [3]. The IAEA is an independent intergovernmental organisation that develops nuclear safety standards for the protection of human health and the environment from ionising radiation [4]. Consequently, the NNR considers these standards when establishing its safety standards and regulatory practices. Requirement 51 of the IAEA's General Safety requirements state that "the regulatory body or other relevant authority shall establish reference levels for exposure due to radionuclides in commodities" such as drinking water. In addition, the requirements state that the regulatory body/relevant authority should consider the guideline levels for water containing radionuclides published by the World Health Organisation [3].

Therefore, the principles of the World Health Organization should be used as a basis during the development of national guideline levels for radionuclides in drinking water.

As a way to assist the NNR with establishing regulatory criteria for radioactivity in drinking water, the radiological baseline of drinking water in areas surrounding authorised nuclear sites needs to be established. Before this can be done, it is important to first establish preliminary reference levels, which will be used to assess the radioactivity levels in collected samples later on. The study seeks to derive preliminary reference levels for the infant, child and adult age groups based on the current international best practice. In addition the study aims to, assess the differences of the derived reference levels across the above-mentioned age groups. These reference levels will inform whether the water resource from which the sample was collected could pose a radiological threat to human health if ingested or not.

2. Method

The Annual Limit on Intake (ALI) was calculated for the infant, child and adult age groups based on the principles established by the WHO. The ALI through ingestion is the intake of a given radionuclide by a reference person which would result in a committed dose that is equal to the relevant dose limit [5]. The assumption that is made is that the calculated preliminary radionuclide reference levels are applicable for water under standard conditions for temperature and pressure. ALI was calculated for commonly detected radionuclides in drinking water sources in the vicinity of Naturally Occurring Radioactive Materials (NORM) producing mines and legacy mine sites.

2.1. Determining commonly detected radionuclides in drinking water sources in the vicinity of NORM-producing mines and legacy mine sites.

There are three main decay series in the natural environment, U-238, Th-232 & U-235 [6]. Therefore, all the radionuclides of these decay series have the potential of being present in water resources surrounding regulated nuclear sites (surface water and groundwater). The study also took into consideration the limitations of laboratory measurement techniques in analysing all these radionuclides.

2.2. Drinking water consumption rates.

The daily water consumption rates of the adult (>17 years), children (1-17 years) and infant (<1 year) age groups are presented in table 1 [7]. These were rates converted to annual consumption rates. For the adult age group, the average consumption rate of an adult male and adult female was used.

Table 1. Consumption rates of infant, children and adults adapted from [7].

Category	Daily Consumption Rate (L/d)	Annual Consumption rate (L/yr)
Adult	Male	2.723
	Female	2.129
Children	0.431	157.315
Infant	0.327	119.355

2.3. Calculation of Annual Limit on Intake.

The Annual Limit of Intake is calculated using equation (1) obtained from the WHO drinking water guidelines [8].

$$ALI = \frac{IDC}{(U \times Dc)} \quad (1)$$

Where;

IDC – annual dose to the whole body ($\mu\text{Sv/yr}$), in this the IDC of 0.0001 (Sv/yr)

ALI – concentration of radionuclide in water, which in this case is the ALI (Bq/L)

U – annual consumption rate (L/yr)

Dc – ingested dose coefficient (Sv/Bq)

3. Results

The calculated ALI for the infant, child and adult age groups are presented in table 2, table 3 and table 4. The differences in calculated ALI for the same radionuclide in the infant, child and adult age groups are within the same order of magnitude. This suggests that the derived radionuclide reference levels for different age groups give rise to a similar dose due to ingestion. However, the WHO recommends that dose assessments may be introduced for infants and children in cases of prolonged contamination of the water source [8].

Table 2. Calculated ALI for an infant.

Infant (<1 yr)				
Radionuclide	Individual Dose Criterion (IDC) - (Sv/yr)	Ingestion Dose Coefficient (Dc) - (Sv/Bq)	Annual Consumption Rate (U) - (L/yr)	Annual Limit on Intake (Bq/L)
U-232	0.0001	2.5E-06	119	0.34
Pb-210	0.0001	8.4E-06	119	0.10
U-235	0.0001	3.5E-07	119	2.39
Th-230	0.0001	4.1E-06	119	0.20
Ra-226	0.0001	4.7E-06	119	0.18
Po-210	0.0001	2.6E-05	119	0.03
Th-227	0.0001	3.0E-07	119	2.79
Ra-223	0.0001	5.3E-06	119	0.16
Ra-224	0.0001	2.7E-06	119	0.31
K-40	0.0001	6.2E-08	119	13.51
Tritium	0.0001	1.2E-10	119	6981.97
I-132	0.0001	3.0E-09	119	279.28
I-133	0.0001	4.9E-08	119	17.10
Cs-134	0.0001	2.6E-08	119	32.22
Cs-136	0.0001	1.5E-08	119	55.86
Co-60	0.0001	5.4E-08	119	15.52
Te-131	0.0001	9.0E-10	119	930.93
U-234	0.0001	3.7E-07	119	2.26
Cs-137	0.0001	2.1E-08	119	39.90
I-131	0.0001	1.8E-07	119	4.65
La-140	0.0001	2.0E-08	119	41.89
I-135	0.0001	1.0E-08	119	83.78
Te-132	0.0001	4.8E-08	119	17.45
Nb-95	0.0001	4.6E-09	119	182.14
U-238	0.0001	3.4E-07	119	2.46
U-235	0.0001	3.5E-07	119	2.39

Table 3. Calculated ALI for a child.

Child (1-17 yr)				
Radionuclide	Individual Dose Criterion (IDC) - (Sv/yr)	Ingestion Dose Coefficient (Dc) - (Sv/Bq)	Annual Consumption Rate (U) - (L/yr)	Annual Limit on Intake (Bq/L)
U-232	0.0001	6.5E-07	157	0.98
Pb-210	0.0001	2.4E-06	157	0.26
U-235	0.0001	8.9E-08	157	7.14
Th-230	0.0001	3.0E-07	157	2.12
Ra-226	0.0001	9.7E-07	157	0.66
Po-210	0.0001	4.4E-06	157	0.14
Th-227	0.0001	3.6E-08	157	17.66
Ra-223	0.0001	6.2E-07	157	1.03
Ra-224	0.0001	3.7E-07	157	1.72
K-40	0.0001	2.0E-08	157	31.78
Tritium	0.0001	7.3E-11	157	8707.77
I-132	0.0001	1.2E-09	157	529.72
I-133	0.0001	2.1E-08	157	30.27
Cs-134	0.0001	1.6E-08	157	39.73
Cs-136	0.0001	5.9E-09	157	107.74
Co-60	0.0001	1.5E-08	157	42.38
Te-131	0.0001	3.3E-10	157	1926.26
U-234	0.0001	9.2E-08	157	6.91
Cs-137	0.0001	1.1E-08	157	57.79
I-131	0.0001	9.2E-08	157	6.91
La-140	0.0001	6.6E-09	157	96.31
I-135	0.0001	4.3E-09	157	147.83
Te-132	0.0001	1.5E-08	157	42.38
Nb-95	0.0001	1.7E-09	157	373.92
U-238	0.0001	8.4E-08	157	7.57
U-235	0.0001	8.9E-08	157	7.14

Table 4. Calculated ALI for an adult.

Adult (>17 yr)				
Radionuclide	Individual Dose Criterion (IDC) - (Sv/yr)	Ingestion Dose Coefficient (Dc) - (Sv/Bq)	Annual Consumption Rate (U) - (L/yr)	Annual Limit on Intake (Bq/L)
U-232	0.0001	3.3E-07	885	0.34
Pb-210	0.0001	6.9E-07	885	0.16
U-235	0.0001	4.7E-08	885	2.40
Th-230	0.0001	2.1E-07	885	0.54
Ra-226	0.0001	2.8E-07	885	0.40
Po-210	0.0001	1.2E-06	885	0.09
Th-227	0.0001	8.8E-09	885	12.84
Ra-223	0.0001	1.0E-07	885	1.13
Ra-224	0.0001	6.5E-08	885	1.74
K-40	0.0001	6.2E-09	885	18.22
Tritium	0.0001	4.2E-11	885	2690.34
I-132	0.0001	2.9E-10	885	389.64
I-133	0.0001	4.3E-09	885	26.28
CS-134	0.0001	1.9E-08	885	5.95
Cs-136	0.0001	3.0E-09	885	37.66
Co-60	0.0001	3.4E-09	885	33.23
Te-131	0.0001	8.7E-11	885	1298.79
U-234	0.0001	4.9E-08	885	2.31
Cs-137	0.0001	1.3E-08	885	8.69
I-131	0.0001	2.2E-08	885	5.14
La-140	0.0001	2.0E-09	885	56.50
I-135	0.0001	9.2E-10	885	122.82
Te-132	0.0001	3.8E-09	885	29.74
Nb-95	0.0001	5.8E-10	885	194.82
U-238	0.0001	4.5E-08	885	2.51
U-235	0.0001	4.7E-08	885	2.40

4. Conclusions

The above results show that the differences in calculated ALI values for individual radionuclides across all ages are insignificant (within the same order of magnitude). Therefore, it is recommended that the NNR use calculated ALI for adults as preliminary reference levels during the assessment of the radioactivity status of baseline data that is currently being collected. However, if the water source undergoes prolonged contamination dose assessments for infants and child age groups may be introduced.

5. References

- [1] Canadian Nuclear Safety Commission 2019 *Introduction to radiation*. Accessed 18 July 2019. <http://nuclearsafety.gc.ca/eng/resources/radiation/index.cfm>
- [2] National Nuclear Regulator 2020 *Our roles and Functions*. Accessed 15 June 2020. <https://nnr.co.za/about-us/our-role-and-functions/>
- [3] International Atomic Energy Agency 2014 *Radiation Protection and Safety of Radiation Sources: International Basic Safety Standards (GSR Part 3)*
- [4] International Atomic Energy Agency 2021 *The IAEA mission statement*. Accessed 20 August

2021. <https://www.iaea.org/about/mission>
- [5] International Atomic Energy Agency 2019 *IAEA safety glossary : 2018 edition* p 128-129
 - [6] Kim G 2011 Measurement and application of radium and radon in the environment. *Journal of Analytical Science & Technology* **2** p A115-A119
 - [7] Fakhri Y, Oliveri G, Ferrante M, Bay A, Avazpour M, Moradi B, Zamdsalimi Y, Amirhajeloo L R, Langarizadeh G and Keramati H 2016 *Assessment of concentration of radon 222 and effective dose; Bandar Abbas city (Iran) citizens exposed through drinking tap water*. *International Journal of Pharmacy & Technology* **8** p 10782-10793
 - [8] World Health Organization 2017 *Guidelines for drinking water-water quality: Fourth edition incorporating the first addendum*. p 203-218

An investigation of over-training within semi-supervised machine learning models in the search for heavy resonances at the LHC

Benjamin Lieberman¹, Joshua Choma¹, Salah-Eddine Dahbi¹, Bruce Mellado^{1,2} and Xifeng Ruan¹

¹School of Physics and Institute for Collider Particle Physics, University of the Witwatersrand, Johannesburg, Wits 2050, South Africa

²iThemba LABS, National Research Foundation, PO Box 722, Somerset West 7129, South Africa

E-mail: benjamin.lieberman@cern.ch

Abstract. In particle physics, semi-supervised machine learning is an attractive option to reduce model dependency in searches beyond the Standard Model. Over-training of the model must be investigated when using semi-supervised techniques to train machine learning models for searches for new bosons at the Large Hadron Collider. In the training of classification models, fake signals can be generated due to over-fitting. The extent of false signals generated in semi-supervised models requires further analysis and therefore the probability of such situations occurring must be quantified on a case-by-case basis. This investigation of $Z\gamma$ resonances is performed using toy Monte Carlo samples normalised to mimic ATLAS data in a background-plus-signal region. Performing multiple runs, using random toy Monte Carlo samples, the probability of false signals being produced through over-training is investigated. The distribution of significance, of fake signals being generated using semi-supervised techniques, is found to form the positive side of a normal distribution for all background rejections and can therefore be said to be under control.

1. Introduction

In 2012 the ATLAS and CMS collaborations reported on the observation of a Higgs boson with a mass of 125 GeV [1, 2]. The Standard Model (SM) was completed by the discovery of the Higgs boson. The SM however, is not able to explain a number of phenomena that display substantial experimental evidence, such as Dark Matter, the origin of neutrino mass, the matter-anti-matter asymmetry, and a number of theoretical problems. These experimental discrepancies with the SM motivate the search for new bosons.

A 2HDM+ S model, where S is a singlet scalar, was used in Ref. [3, 4] to explain some features of the Run 1 Large Hadron Collider (LHC) data. Here the heavy scalar, H , decays predominantly into SS, Sh , where h is the SM Higgs boson. The model predicts the emergence of multi-lepton anomalies that have been verified in Refs. [5, 6, 7, 8], where a possible candidate of S has been reported in Ref. [9]. The model can elaborate on multiple anomalies in astrophysics, if it is complemented by a Dark Matter candidate [10]. It can be further extended to account for anomalies, including the anomaly reported by Fermilab, in the $g - 2$ muon experiment [11, 12, 13]. For a full review of anomalies, see Ref. [14].

The above mentioned motivates for the searches of heavy scalar resonances. We choose to investigate the search of $H \rightarrow Z\gamma$ with $Z \rightarrow \ell\ell$ and $\ell = e, \mu$. This is done using semi-supervision with topological features, as suggested in Ref. [15]. Semi-supervised learning is a machine learning technique where a model is trained on partially labelled data in order to reduce training biases. In this paper we focus on the potential over-training entailed in the use of semi-supervision when confronting side-bands and the signal region using a neural network.

1.1. $Z\gamma$ Dataset

In this study we use the simulated Higgs like heavy scalar decaying to $Z\gamma$ ($pp \rightarrow H \rightarrow Z\gamma$) events, where $Z \rightarrow e^+e^-$ or $Z \rightarrow \mu^+\mu^-$. The simulated $Z\gamma$ dataset was produced using truth particles and particle reconstruction by ATLAS full simulation. The objects of analysis are electrons, muons, photons, jets and b -jets. The simulated non-resonant $Z\gamma$ dataset is used as it is the dominant background, representing more than 90% of the total background. This is therefore an ideal dataset to evaluate the extent of false signals generated during the Machine Learning (ML) training as any signals found within the dataset are a product of over-training and/or fluctuations within the phase space. Further details on the $Z\gamma$ dataset, including production mechanisms, are described in Ref. [16]. The important features selected and used for this analysis are the invariant mass, $m_{\ell\ell\gamma}$; invariant di-jet mass, m_{jj} ; pseudo-rapidity of leading and sub-leading jets, η_{j1}, η_{j2} ; number of jets, N_j ; number of leptons, N_ℓ ; number of b -jets, N_{bj} ; transverse energy, E_T^{miss} ; transverse energy significance, $\sigma_{E_T^{miss}}$ and the following difference in the azimuthal angles, $\Delta\Phi(ForwardJets, E_T^{miss})$, $\Delta\Phi(LeadingJet, E_T^{miss})$, $\Delta\Phi(LeadingJet, Z\gamma)$, $\Delta\Phi(Z\gamma, E_T^{miss})$. Example feature distributions are shown in Figure 1.

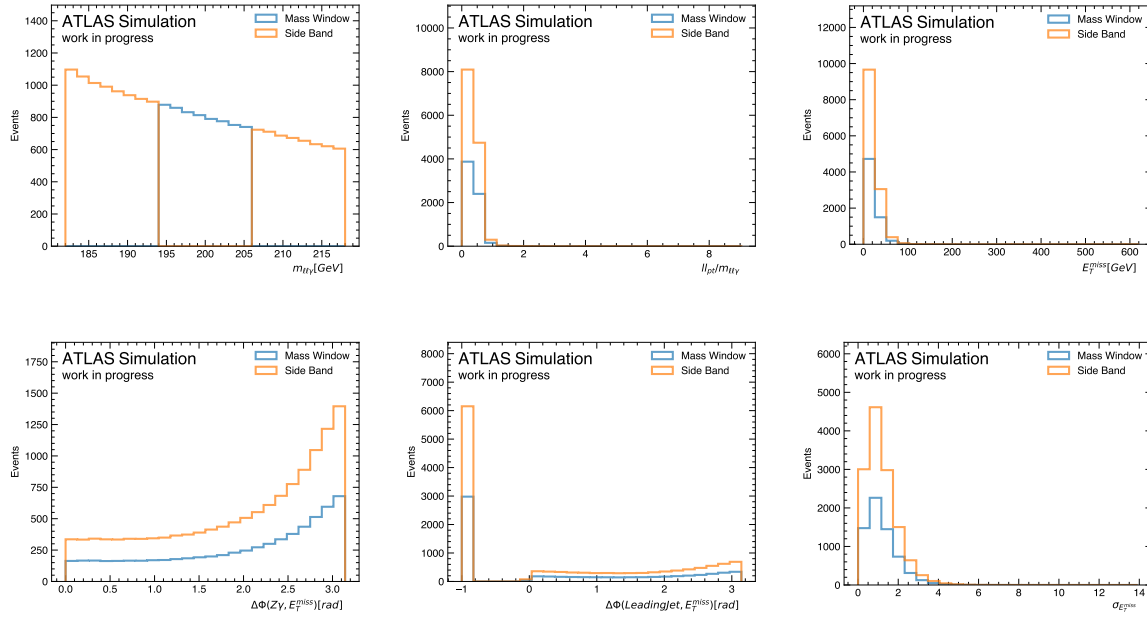


Figure 1: $Z\gamma$ dataset important feature distributions.

1.2. Semi-Supervised Machine Learning

In high energy physics, fully-supervised ML methods are frequently used as binary classifiers. The model is trained on labelled data where each event, \vec{x}_i , has a corresponding target/label,

$y_i \in \{0, 1\}$. The model can therefore be understood to be trained on two sample types, a signal sample, with label 1, and background sample, with label 0. For each given event, \vec{x}_i , the model generates a an output response, $\hat{y}_i \in (0, 1)$. Model training therefore aims to minimise the difference between the targets and the responses by using a loss function, usually in the form of binary cross-entropy:

$$\ell(y, \hat{y}) = -y \cdot \log \hat{y} + (1 - y) \cdot \log(1 - \hat{y}), \quad (1)$$

The minimising of the loss function to find the optimum solution in full-supervision ML can therefore be described using the following equation:

$$f_{full} = \underset{f: \mathbb{R}^n \rightarrow [0,1]}{\operatorname{argmin}} \sum_{i=1}^N \ell(y_i, \hat{y}_i), \quad (2)$$

In semi-supervised models Ref. [17], the model is trained on partially labelled datasets. This means that the model is trained on one sample of pure background, labelled 0, and one unlabeled sample made up of a mixture of signal and background events, labelled 1. Therefore as apposed to full-supervised methods, Eq. 2, the semi-supervised method can be described using the following equation:

$$f_{semi} = \underset{f: \mathbb{R}^n \rightarrow [0,1]}{\operatorname{argmin}} \sum_K \ell \left(\frac{1}{|K|} \sum_{i \in K} \hat{y}_i, y_K \right), \quad (3)$$

where K denotes the batches of training data and y_K is the signal ratio in each batch.

The quantification of uncertainties propagated within ML methods is vital in sub-atomic physics analysis as it allows both an understanding of the accuracy of any predictions made and exposes the level of validity of any ML based discoveries. The uncertainties in fully supervised techniques used in particle physics are well defined and extensively researched [18], however the uncertainties propagated in semi-supervised techniques have not been quantified to the same extent. This research therefore focuses on measuring the uncertainties, represented as fake signals, produced in the training of semi-supervised models within a given phase space.

2. Methodology

A benchmark centre of mass of 200 GeV is selected and each data sample is divided into a mass-window of 194 to 206 GeV and side-bands from 194 to 182 GeV and from 206 to 218 GeV. The model is trained on $Z\gamma$ events, with sample 0 and sample 1 consisting of events within the side-band and mass-window region respectively. As neither sample contains signal, there is no significant separation expected, in the model output, between the mass-window and side-band samples.

2.1. Deep Neural Network Model

The Binary Decision Tree (BDT), Multi-Layer Perceptron (MLP) and Deep Neural Network (DNN) classification models were compared. The area under the Receiver Operating Characteristic (ROC) curve is used to evaluate the classifier performance and the Kolmogorov-Smirnov test is used to measure over-training of the models. The DNN is selected as the optimum classifier as it showed the best classification score and lowest over-training. As the model is being used as a binary classifier, the cross-entropy loss (Eq. 1) is used as the loss function during training.

The DNN architecture implemented in this study consists of an input layer (360 neuron), four hidden layers (180, 180, 90, 180 neuron respectively) and an output layer with a single

neuron. The input and hidden layers use the rectified linear unit (ReLU) activation function and the output layer uses the sigmoid activation function. A learning rate of $1 \cdot 10^{-3}$ is used with a learning decay of $3 \cdot 10^{-4}$. The model is run for 8 epochs using a batch size of 1.

2.2. Toy Monte Carlo Sample Generation

In order to evaluate the over-training of the DNN model, the model must be run on a large number of statistically unique samples. To this end a toy Monte Carlo (MC) generator is used to extract random batches of events from the $Z\gamma$ simulated dataset. Each batch of events is normalised, using the corresponding event weights, to mimic data produced at the ATLAS experiment. Each sample contains approximately 45500 side-band events and 23000 mass-window events, labelled 0 and 1 respectively. Therefore the toy MC generator is used to produce a single random normalised sample for each given run of the model.

2.3. Evaluating Over-training on Invariant Mass

In order to calculate the significance of false signals being generated, the following steps are applied to each toy MC sample generated.

- (i) The DNN model is trained on the given sample using events within the side-band and mass-window regions as sample 0 and sample 1 respectively. Once trained the DNN output, in the form of a response distribution (example in Figure 2), is generated.
- (ii) Batches of 50, 60, 70, 80 and 90% of the total events are taken from the response distribution. Each batch is extracted by starting at the response distribution's maximum, 1, and moving towards the minimum, 0, until the required percentage of events are collected. The events of each batch are then mapped to their corresponding invariant mass.
- (iii) The invariant mass, $m_{\ell\ell\gamma}$, distribution of each batch is then analysed in terms of the mass-window and side-band. This is done by fitting an exponential function and an exponential + Gaussian function to each batch's invariant mass distribution:

$$f(x) = n_0 \cdot e^{ax+bx^2}, \quad (4)$$

$$g(x) = n_0 \cdot e^{ax+bx^2} + n_1 \cdot e^{\frac{(x-\mu)^2}{2\sigma^2}}, \quad (5)$$

where n_0 , a , b and n_1 are constants produced in the fit; μ is the mean (fixed at centre of mass) and σ is the standard deviation (as calculated by the fit). The exponential function, Eq. 4, is therefore used to describe the background, in the side-band and mass-window, and the Gaussian function, Eq. 5, is used to define signal, within the mass window. An example of the invariant mass distribution fits is shown in Figure 3.

2.4. Significance Calculation

The significance of fake signals generated, in the mass-window, due to over training can be quantified as the difference between the log-likelihoods of the two functions. The following steps are implemented:

- (i) The log-likelihood can be calculated using a Poisson probability mass function, p_X , on the first n terms of the invariant mass distribution $\{X_n\}$. The probability mass function of a term x_i is:

$$p_X(x_i) = e^{-\lambda} \frac{\lambda^{x_i}}{x_i!}, \quad (6)$$

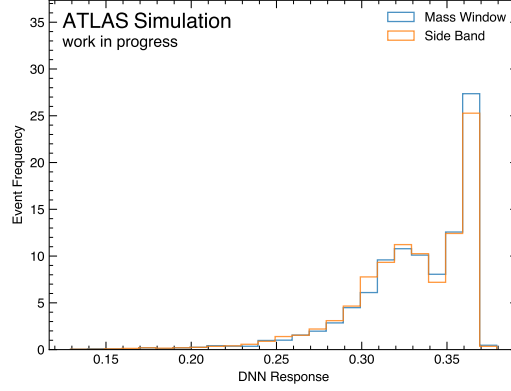


Figure 2: Example DNN response distribution output from a single toy MC sample.

where λ is the parameter of interest. The likelihood function, L , and log-likelihood, $\ln(L)$, can therefore be calculated as follows:

$$L(\lambda; x_1, x_2, \dots, x_n) = \prod_{i=1}^n e^{-\lambda} \frac{\lambda^{x_i}}{x_i!}, \quad (7)$$

$$\ln L(\lambda; x_1, x_2, \dots, x_n) = -n\lambda - \sum_{i=1}^n \ln(x_i!) + \ln(\lambda) \sum_{i=1}^n x_i. \quad (8)$$

- (ii) The log-likelihood of the two functions can then be used to calculate the model's uncertainty significance for the given run:

$$S_k = \sqrt{2 \cdot (\ln L_{eg} - \ln L_e)}, \quad (9)$$

where S_k is the Significance for the k^{th} run and L_{eg} and L_e are the log-likelihoods of the exponential + Gaussian function and the Exponential function, respectively.

- (iii) Repeating the process with statistically random toy MC samples a number of times (initially 500 times) will produce the statistical deviations in significance of fake signals being generated. The uncertainty generated, within the semi-supervised model, can therefore be quantified. As the samples are limited by the MC statistics, the number of runs is limited to 500.

3. Results

3.1. Invariant Mass Distribution with Cuts

In order to analyse false signals generated in the training of the model, the DNN is trained and the output response distribution analysed, for each toy MC sample. An example of the response distribution produced in a single run can be seen below in Figure 2.

Background rejection batches, containing 50, 60, 70, 80 and 90% of the total events, are extracted from the DNN response distribution and mapped to their corresponding invariant masses. An example of the number of events extracted for each background rejection, in a single run, is shown in Table 1. The fit functions, Eq. 4 and 5, are applied to each invariant mass distribution in order to expose the extent of fake signals generated. Examples of the 60 and 80% background rejections, for a single run, are shown in Figure 3.

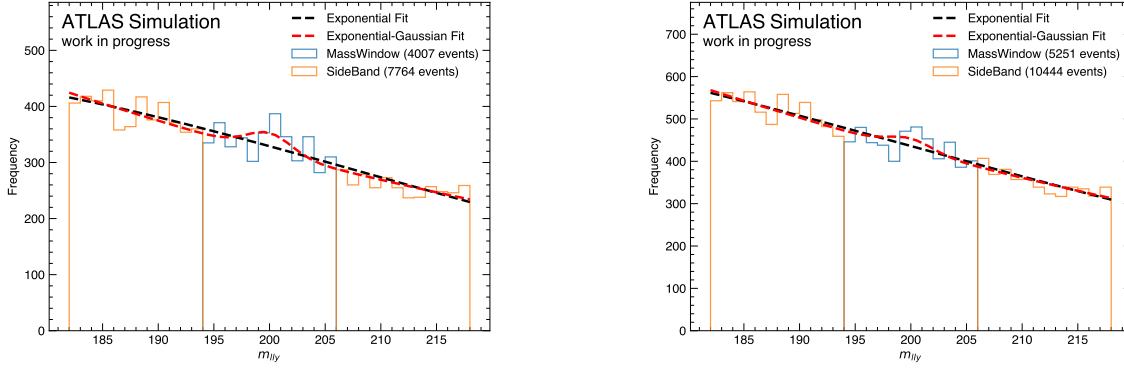


Figure 3: Example $m_{\ell\ell\gamma}$ distributions of 60% and 80% background rejections, for a single run.

3.2. Significance Distributions

For each background rejection, of a given run, the significance is calculated using the difference in the log-likelihoods of the fit functions, Eq. 9. Therefore for each background rejection, of a given run, the significance is calculated. The breakdown of background rejections and corresponding significance for an example run is shown in Table 1.

Table 1: Example of the number of events and corresponding significance, related to each background rejection, for a single run.

% Events	Mass-window events	Side-band events	Significance (σ)
50	3347	6462	1.80
60	4007	7764	2.85
70	4642	9091	2.15
80	5251	10444	1.87
90	5841	11816	1.36

Repeating this methodology on multiple toy MC samples, produces significance distributions for each background rejection. These significance distributions can therefore be used to quantify the extent of false signals produced in the model. The results below, in Figure 4, demonstrate examples of the significance distributions produced when the model is run on 500 toy MC samples.

4. Conclusions

The investigation into quantifying the uncertainty generated, through the over-training of semi-supervised techniques, using $Z\gamma$ resonances was performed using pure background toy MC generated samples and a semi-supervised DNN model. The invariant mass distributions for various background rejections was used to measure the fake signals produced by the model. This in turn was quantified through the calculated significance for the background rejections of each run. The significance distributions produced on 500 samples, Figure 4, form the positive side of a normal distribution for all background rejections. The significance distributions therefore verify

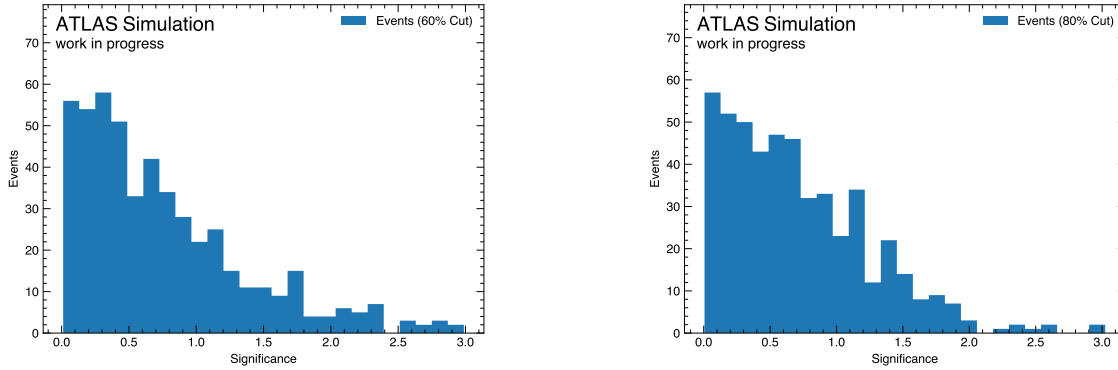


Figure 4: Significance distribution, for 60% and 80% background rejection, for 500 runs.

that the extent of fake signals generated, does not refute any scientific observations made using the semi-supervised technique. The study however is limited by the MC statistics produced using full simulation and future research should consider adopting generative models to increase the size and statistics of the dataset used for analysis.

References

- [1] Aad G *et al.* (ATLAS) 2012 *Phys. Lett. B* **716** 1–29 (*Preprint* 1207.7214)
- [2] Chatrchyan S *et al.* (CMS) 2012 *Phys. Lett. B* **716** 30–61 (*Preprint* 1207.7235)
- [3] von Buddenbrock S, Chakrabarty N, Cornell A S, Kar D, Kumar M, Mandal T, Mellado B, Mukhopadhyaya B and Reed R G 2015 (*Preprint* 1506.00612)
- [4] von Buddenbrock S, Chakrabarty N, Cornell A S, Kar D, Kumar M, Mandal T, Mellado B, Mukhopadhyaya B, Reed R G and Ruan X 2016 *Eur. Phys. J. C* **76** 580 (*Preprint* 1606.01674)
- [5] von Buddenbrock S, Cornell A S, Fadol A, Kumar M, Mellado B and Ruan X 2018 *J. Phys. G* **45** 115003 (*Preprint* 1711.07874)
- [6] Buddenbrock S, Cornell A S, Fang Y, Fadol Mohammed A, Kumar M, Mellado B and Tomiwa K G 2019 *JHEP* **10** 157 (*Preprint* 1901.05300)
- [7] von Buddenbrock S, Ruiz R and Mellado B 2020 *Phys. Lett. B* **811** 135964 (*Preprint* 2009.00032)
- [8] Hernandez Y, Kumar M, Cornell A S, Dahbi S E, Fang Y, Lieberman B, Mellado B, Monnagotla K, Ruan X and Xin S 2021 *Eur. Phys. J. C* **81** 365 (*Preprint* 1912.00699)
- [9] Crivellin A, Fang Y, Fischer O, Kumar A, Kumar M, Malwa E, Mellado B, Rapheeha N, Ruan X and Sha Q 2021 (*Preprint* 2109.02650)
- [10] Beck G, Kumar M, Malwa E, Mellado B and Temo R 2021 (*Preprint* 2102.10596)
- [11] Sabatta D, Cornell A S, Goyal A, Kumar M, Mellado B and Ruan X 2020 *Chin. Phys. C* **44** 063103 (*Preprint* 1909.03969)
- [12] Abi B *et al.* (Muon g-2) 2021 *Phys. Rev. Lett.* **126** 141801 (*Preprint* 2104.03281)
- [13] Aoyama T *et al.* 2020 *Phys. Rept.* **887** 1–166 (*Preprint* 2006.04822)
- [14] Fischer O *et al.* 2021 *Unveiling hidden Physics Beyond the Standard Model at the LHC* (*Preprint* 2109.06065)
- [15] Dahbi S E, Choma J, Mokgatitwane G, Ruan X, Lieberman B, Mellado B and Celik T 2021 *International Journal of Modern Physics A* ISSN 1793-656X URL <http://dx.doi.org/10.1142/S0217751X21502419>
- [16] Aad G *et al.* (ATLAS) 2019 *ATLAS-CONF-2019-034*
- [17] Dery L M, Nachman B, Rubbo F and Schwartzman A 2017 *Journal of High Energy Physics* **2017** 1–11
- [18] Abdughani M, Ren J, Yang J M and Zhao J 2019 *Communications in Theoretical Physics* **71** 955

Analysis of UOC for nuclear forensics using Scanning Electron Microscope

V Uushona¹, N D Mokhine², M Mathuthu², I Shuro³, T G Kupi^{2, 4}

¹ National Radiation Protection Authority of Namibia

² Centre for Applied Radiation Science and Technology, North-West University, Mafikeng Campus, Corner of Albert Luthuli and University Drive, Mmabatho, 2745

³ Electron Microscope Laboratory, North-West University, Potchefstroom Campus, 11 Hoffman Street, Potchefstroom, 2531

⁴ Unit for Environmental Sciences and Management, North-West University, Potchefstroom Campus, 11 Hoffman Street, Potchefstroom, 2531

E-mail: dikeledi.mokhine@gmail.com

Abstract

Nuclear forensics involves the analysis of nuclear material for possible provenance determination using various analytical tools that are available for such analysis. In this study, Scanning Electron Microscopy (SEM) combined with Electron Dispersion Spectrometer (EDS), were used to determine the signatures of uranium ore concentrates (UOCs) samples for nuclear forensic applications. SEM and SEM / EDS provided substantial information on the UOC's morphology and elemental composition. Distinct qualitative and quantitative difference are present for the different UOC's. The UOC's surface consists of agglomeration made up of homogenous spherical particles, irregular shaped particles and plate like bulky particles. Average particle size ranged between 0.1 – 0.2 μm . EDS analysis of all the samples showed they contained a consistent 70 weight % of uranium and a stoichiometric formula closest to the molecule of UO_4 . This technique can thus be used to distinguishing and fingerprinting UOC's originating from different mine.

1. Introduction

Nuclear forensics is a new discipline of forensic science. It is defined as *the examination of nuclear or other radioactive material, or of evidence that is contaminated with radionuclides, in the context of legal proceedings under international or national law related to nuclear security* [1]. Nuclear forensics provides material signature such as isotopic abundances, elemental concentrations, physical and chemical forms, morphology and physical dimensions that may be used to link a material, either nuclear or other radioactive (non-nuclear, such as those used for medical imaging), to individuals, locations, or processes, date of production and on the intended use [2, 3].

The Uranium Ore concentrate (UOC), commonly known as yellow cake is the main component in the uranium fuel cycle production. It is produced by various process which involves crushing, grinding and leaching the uranium ores or recovered as a by-product of other products, such as copper or phosphoric acid. Several cases involving theft of UOC's are recorded in the IAEA incident trafficking database [4]. Morphological signature is a comparatively new topic in nuclear forensics and refers to the size, crystalline structure and shape of particles. It is complementary signature to isotopic and elemental compositions [5]. The particle shape parameter is one of the most useful morphological characteristics for material differentiation [6].

The focus for much of the development and success of nuclear forensic investigation is to provide rapid capability for the characterisation of materials in scenarios where a bulk quantity has been

discovered or seized. A Scanning Electron Microscopy (SEM) equipped with Electron Dispersive Spectrometry (EDS) has the capability to provide one of the most rapid and reliable microscopy- based direct analytical techniques for measuring particle size, morphology and composition, however it requires accurate sample preparation [7]. EDS can also provide rapid qualitative analysis of elemental composition with a sampling depth of 1–2 microns, whilst x-rays might also be used to represent maps or line profiles, showing the elemental distribution in a sample surface [8].

SEM has been successfully applied in nuclear forensics to investigate the shape, appearance and particle size of various nuclear material from the nuclear fuel cycle [6, 9, 10]. Morphology of uranium pellets intended for the graphite moderate reactor was identified [11], high enrich uranium power origin was identified [12] and at the Munich airport, a sample consisting in a mixture of uranium and plutonium analysed by SEM revealed different grain sizes, leading to the conclusion that the materials were coming from different processes of formation [13]. The aim of the study was to resolve nuclear forensics signatures based on morphology and compositional analysis of the UOC's samples from Namibia and South Africa uranium mines.

2. Materials and Method

Three (3) UOC samples were obtained from Uranium mines in Namibia and South Africa. The powdered samples were mounted on an aluminium stub using double sided carbon tape. The mounted sample were coated with carbon to enhance conductivity and prevent charge build-up during SEM imaging. Secondary electron images of the samples were obtained in an FEI Quanta FEG 250 field emission gun SEM operating at an accelerating voltage of 15 kV. Oxford Energy Dispersive Spectrometer (EDS) operating with the Inca software was used for the compositional analysis. The quantitative measurement of the imaged morphological features was performed using Image J 1.52 a software and the distribution plotted in excel.

3. Results and Discussions

3.1 Morphology Characteristics

In an attempt to identify forensic signatures indicative of the origin of the material, qualitative as well as quantitative SEM image analysis of surface characteristics of the UOC's were carried out. The respective SEM images of the samples can be seen in Figures 1A – C below. Each row of images represents a sample taken at different levels of magnification X 13 000, 50 000 respectively. The UOC from mine A consists of massive agglomerates made up of homogenous spherical particles of size range 0.050 – 0.234 μm .

The UOC from mine B is a heterogeneous matrix consisting of spherical particles sandwiched between plates like bulky particles of size in range 0.041-0.799. The third UOC from Mine C shows the finest textures homogenous spherical particles in the range of 0.037-0.115. The morphological structures are summarised in Table 1.

The order of particle size is as follow: Mine A > Mine B > Mine C meaning Mine C has smallest particle sizes. The particles size distribution of the UOC's is shown in Figure 2 a – c. There is notable difference in the texture, size and shape of the particles from the different mines, this is mainly attributed to the different processing mechanism such as dissolution, extraction, ion exchange and precipitation [3].

Table 1: Summary of the morphology characteristics.

Mine ID	Texture	Average particle size (nm)
A	Homogenous spherical particles	92 \pm 9.10
B	Heterogeneous platelets spherical particles	89 \pm 8.45
C	Homogenous fine grained particles	69 \pm 6.45

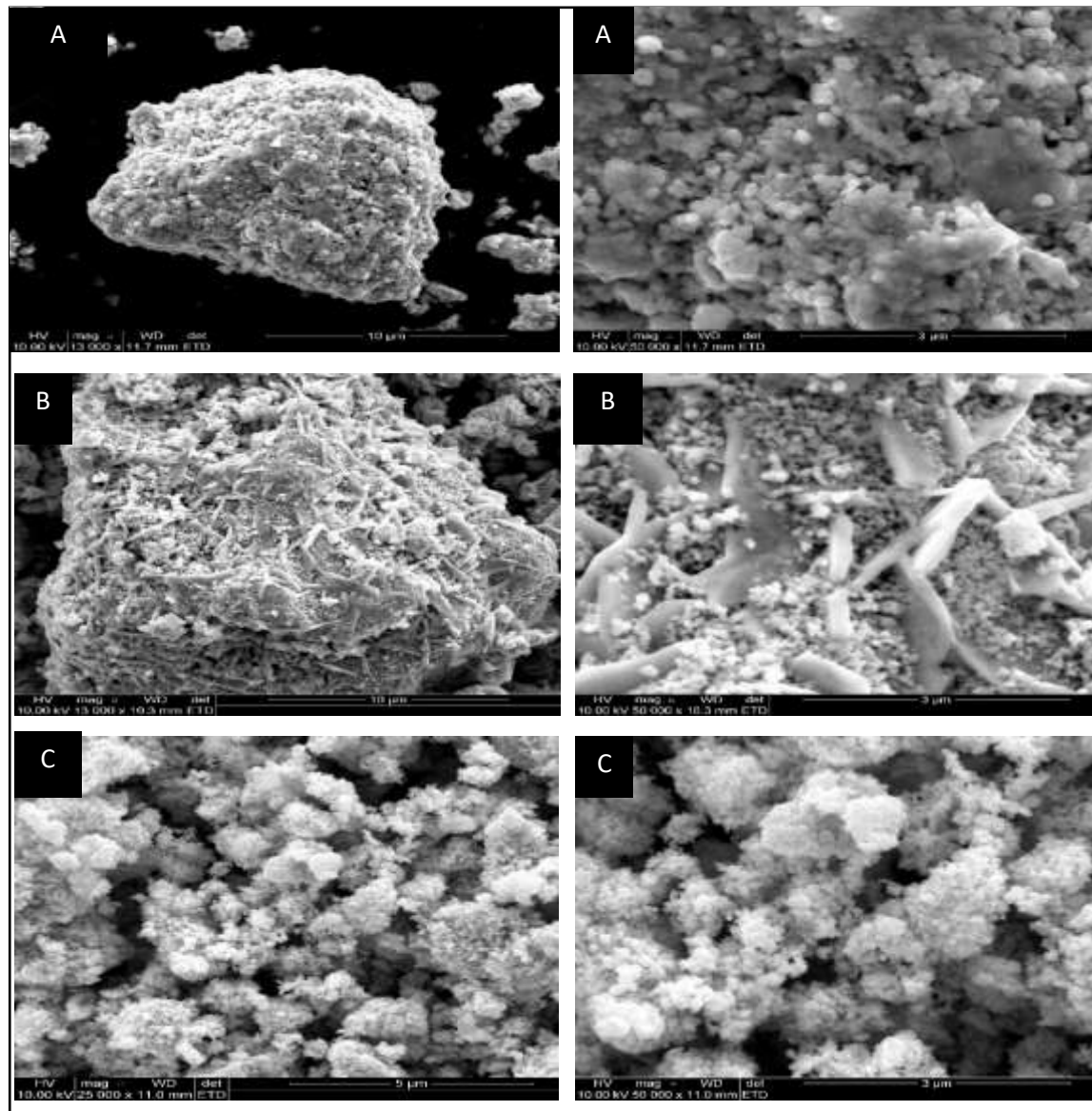


Figure 1: A-B-C SEM morphology images.

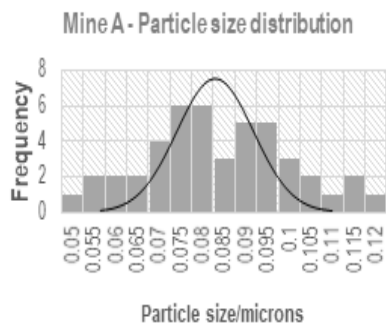


Figure 2.1: SEM images, histogram distributions and lognormal fits of mine A

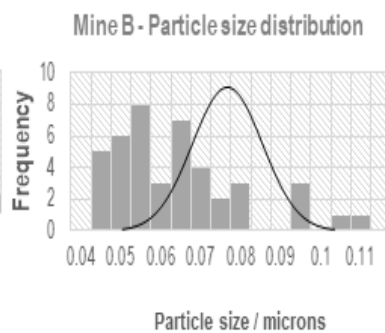


Figure 2.2: SEM images, histogram distributions and lognormal fits of mine B

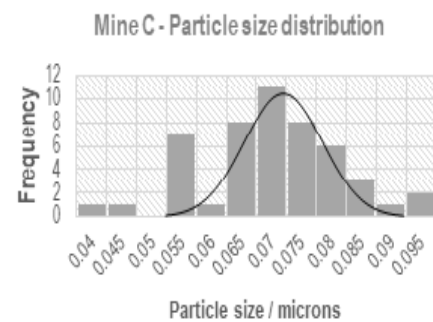


Figure 2.3: SEM images, histogram distributions and lognormal fits of mine C

There is difference in the particle size distributions as seen in Figure 2 above. Mine A particles shows almost symmetric distribution where most of the observed particles close to the mean $0.1\ \mu\text{m}$. Few particles are further away from the mean in both directions, Mine B distribution is skewed to the right most particle size is between 0.05 and $0.09\ \mu\text{m}$. Mine C particles are left-skewed as most of the particle size clustered on the left side of the histogram. The differences in the distribution indicate that the mean particle size are different and distinct for each mine.

3.2 Elemental composition

Elemental composition was performed with the EDS and the obtained spectrums are depicted in Figures 3.1- 3.3 below. The major peaks observed were those of U and O, C with some minor peak of Na. The element carbon on the spectrums is a result of carbon coating prior to the analysis. Mine A contains additional element impurities Na which is due to the processing mechanism of the mine.

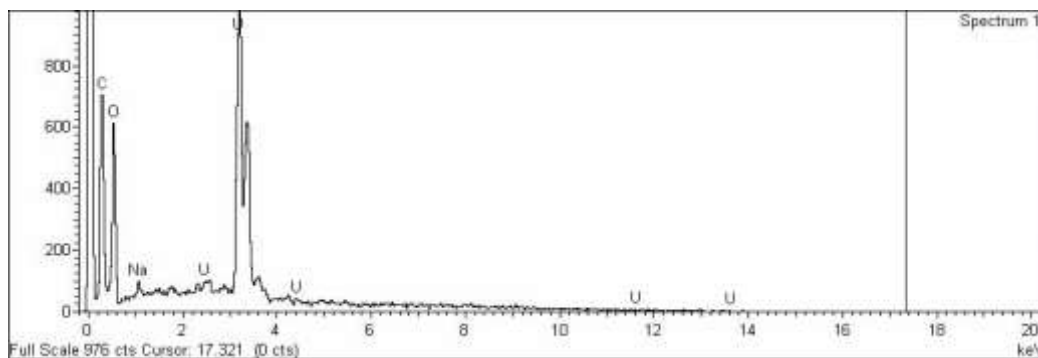


Figure 3.1: EDS spectrum of mine A, UOC.

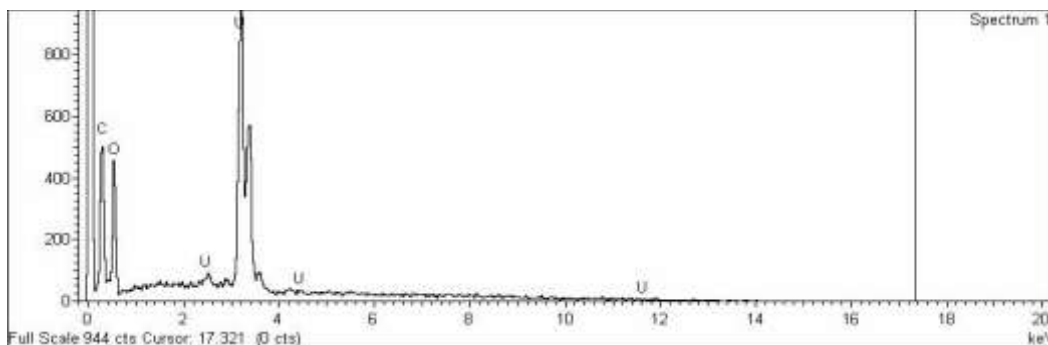


Figure 3.2: EDS spectrum of mine B, UOC.

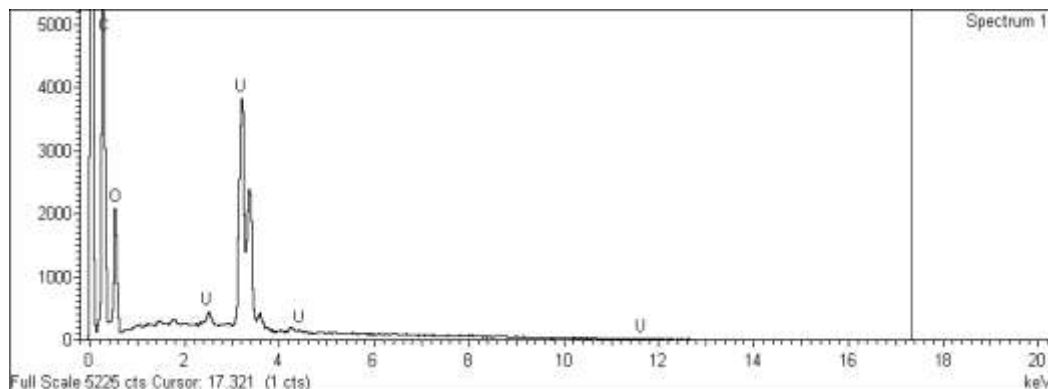


Figure 3.3: EDS spectrum of mine C, UOC.

Results of the semi quantitative analysis of the UOC's using SEM / EDS are shown in Table 2.

Table 2: Elemental composition (weight (wt. %) and atomic (at %)).

Mine ID	U		O		Na		Formulae
	wt%	at%	wt%	at%	wt%	at%	Based on at% ratio
Mine A	73.84						
	\pm	$16.1 \pm$	$25.32 \pm$	$81.98 \pm$	$0.85 \pm$	$1.92 \pm$	
	0.68	0.50	0.77	0.77	0.11	0.28	UO ₄
Mine B	77.64						
	\pm	$18.92 \pm$	$22.36 \pm$	$81.08 \pm$			
	0.21	0.18	0.21	0.18	-	-	UO ₄
Mine C	76.56						
	\pm	$18.02 \pm$	$23.44 \pm$	$81.98 \pm$			
	0.63	0.53	0.63	0.53	-	-	UO ₄

The results of wt % confirm that the samples of the mine are Uranium Oxide compounds constituting on over 70% of Uranium. The at% ratio analysed are closest to the molecules of UO₄ which constitute of 20%U and 80% O.

4. Conclusion

It has been demonstrated that SEM is a useful tool for possible signature of UOC origin assessment. The morphology analysis was able to distinguish particle's texture, shape and size of the UOCs indicative that they are of different mines. Impurities related to the production process were observed from the EDS results and the weight percentage indicates samples contains 70% of uranium. Future work would be to use a more quantitative approach to investigate if there are any crystalline difference between such samples.

Acknowledgement

Authors acknowledge the financial assistance provided by the International Atomic Energy Agency [research grant no. CRP2300].

References

- [1] IAEA, *Nuclear Forensics in Support of Investigations*, Vienna: IAEA, 2015
- [2] E. Keegan, M. J. Kristo, K. Toole, R. Kips, and E. Young, "Nuclear Forensics: Scientific Analysis Supporting Law Enforcement and Nuclear Security Investigations," *Analytical Chemistry*, vol. 88, no. 3, pp. 1496-505, Feb 2 2016
- [3] K. Mayer, M. Wallenius, and Z. Varga, "Interviewing a Silent (Radioactive) Witness through Nuclear Forensic Analysis," *Analytical Chemistry*, vol. 87, no. 23, pp. 11605-10, Dec 1 2015
- [4] IAEA. "Incident of nuclear and other radioactive material out of Regulatory Control, 2017 Fact sheet." <https://www.iaea.org/sites/default/files/17/12/itdb-factsheet-2017.pdf> (accessed 09 January, 2019)
- [5] S. A. Ray.I.L.F, Wallenius, M, "The concept of a microstructural fingerprintfor the characterization of samples in nuclear forensic science," in *International Conference on Advance in Destructive Analysis for Environmental Monitoring and Nuclear Forensics*, 2002

- [6] Y. Kimura, N. Shinohara, and T. Matsumoto, "Study on nuclear forensics signatures of nuclear source materials and irradiated nuclear fuels for material discrimination," in *6th Asia-Pacific Symposium on Radiochemistry*, Jeju Island, Korea, 2017
- [7] N. B. Ghomrasni, C. Chivas-Joly, L. Devoille, J.-F. Hochepped, and N. Feltin, "Challenges in sample preparation for measuring nanoparticles size by scanning electron microscopy from suspensions, powder form and complex media," *Powder Technology*, vol. 359, pp. 226-237, 2020
- [8] S. E. Shaban, N. M. Ibrahim, S. A. El-mongy, and E. E. Elshereafy, "Validation of scanning electron microscope (SEM), energy dispersive X-ray (EDX) and gamma spectrometry to verify source nuclear material for safeguards purposes," *Journal of Radioanalytical and Nuclear Chemistry*, vol. 296, no. 3, pp. 1219-1224, 2012
- [9] E. Keegan *et al.*, "Nuclear forensic analysis of an unknown uranium ore concentrate sample seized in a criminal investigation in Australia," *Forensic Science International*, vol. 240, pp. 111-21, Jul 2014
- [10] I. J. Schwerdt *et al.*, "Nuclear forensics investigation of morphological signatures in the thermal decomposition of uranyl peroxide," *Talanta*, vol. 176, pp. 284-292, Jan 1 2018
- [11] K. Mayer, M. Wallenius, and T. Fanghänel, "Nuclear forensic science—From cradle to maturity," *Journal of Alloys and Compounds*, vol. 444-445, pp. 50-56, 2007/10/11/ 2007
- [12] M. Wallenius, K. Mayer, and I. Ray, "Nuclear forensic investigations: Two case studies," *Forensic Science International*, vol. 156, no. 1, pp. 55-62, 2006/01/06/ 2006
- [13] M. Wallenius, "Nuclear forensic investigations with a focus on plutonium," *Journal of alloy and Compound*, 2007.

South African contribution towards the ATLAS Tile Calorimeter PreProcessor

M G D Gololo¹, F C Argos¹ and B Mellado^{1,2}

¹ School of Physics and Institute for Collider Particle Physics, University of the Witwatersrand, Johannesburg, Wits 2050, South Africa

² iThemba LABS, National Research Foundation, PO Box 722, Somerset West 7129, South Africa

E-mail: `mpho.gift.doctor.gololo@cern.ch`

Abstract. Four major experiments for the High Luminosity Large Hadron Collider (HL-LHC) are upgraded to accommodate an increase in luminosity. ATLAS (A Toroidal LHC ApparatuS) is one of these four major experiments and it is upgraded to investigate a wide range of physics. The ATLAS detector is the largest and a general-purpose particle detector. The Tile Calorimeter (TileCal) is part of the ATLAS detector and is the central hadronic calorimeter. The detector is divided into one long barrel and two extended barrels. The main aim of the TileCal Phase-II upgrade is to completely redesign the on- and off-detector electronics. The TileCal PreProcessor (TilePPr) is one of the off-detector electronics and it is responsible for processing the detector data with a total data bandwidth of 40 Tbps. The University of the Witwatersrand is contributing 24 % to the total design and production of boards towards the TilePPr. The TilePPr is made up of numerous modules and the University of the Witwatersrand is responsible for TileCal GbE Switch and TileCoM modules.

1. Introduction

The Large Hadron Collider (LHC) collides proton beams at four interaction points where main experiments are located [1]. These are; ATLAS (A Toroidal LHC ApparatuS)[2], CMS (Compact Muon Solenoid)[3], ALICE (A Large Ion Collider Experiment)[4] and LHCb (Large Hadron Collider beauty)[5]. A major upgrade to the High Luminosity Large Hadron Collider (HL-LHC) will increase the instantaneous luminosity by a factor 5 compared to the operation of the LHC during Run 2. The complete redesign of replacement of on- and off-detector electronics for the ATLAS Tile Calorimeter Phase II upgrade is due to: radiation and time aging of the electronics; compatibility with full digital TDAQ and trigger processing at 40 MHz (L0) and; to fulfill Phase II radiation requirements. The new readout strategy for HL-LHC will transmit digitized data to the off-detector electronics at the HL-LHC frequency (40 MHz), which is approximately 40 Tbps to read out the entire detector.

2. ATLAS TileCal Pre-Processor for the Phase-II upgrades

Figure 1 shows the proposed redesign for the ATLAS Tile Calorimeter electronic readout chain where the on-detector electronics sends digitized data to off-detector electronics. The off-detector

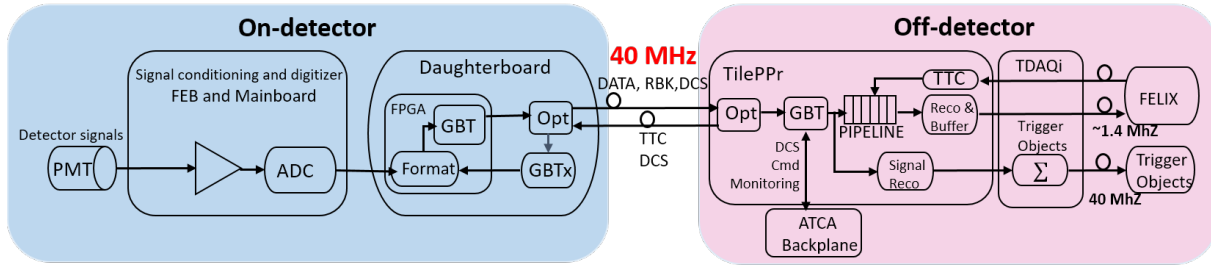


Figure 1. The ATLAS Tile Calorimeter electronic readout chain[6].

electronics receives these digital data using GBT protocol at the HL-LHC frequency, stores and processes these data in the Tile PreProcessor (TilePPr) modules. Figure 2 shows the components of the TilePPr which includes an ATCA Carrier Board, four Compact Processing Modules (CPM) and a Trigger and Data Acquisition Interface (TDAQi) module. The TDAQi provides preprocessed data to the ATLAS calorimeter and muon trigger systems. The TilePPr also includes mezzanine modules such as the TileCal Gigabit Ethernet (GbE) Switch, TileCal Computer on Module (TileCoM) and the Intelligent Platform Management Controller (IPMC). All the off-detector electronics are housed inside Advanced Telecommunication Computing Architecture (ATCA) shelves that can be controlled through remote communication. The IPMC is used for control and monitoring of the ATCA Carrier Base Board.

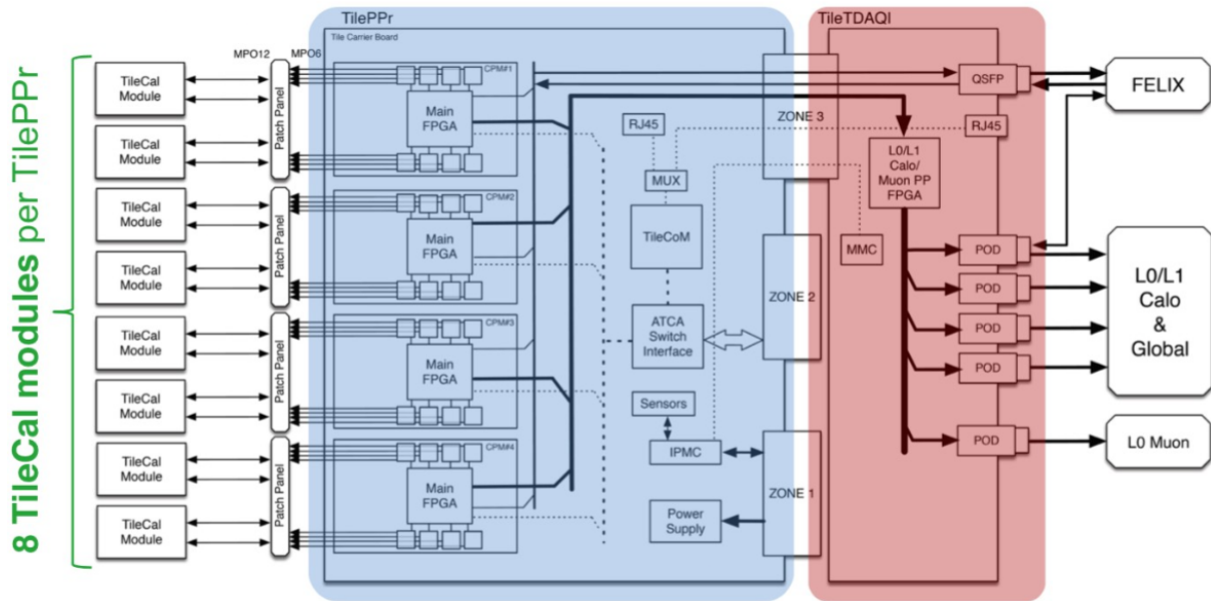


Figure 2. The ATLAS TileCal PreProcessor [7].

3. The South african contribution

3.1. Production of boards

The University of the Witwatersrand and iThemba labs are contributing towards production of boards from state-of-the-art companies in South Africa. The two mezzanine modules, TileCoM and TileCal Gigabit Ethernet (GbE) Switch, introduced in Section 2 are produced from South African companies. Figure 3 shows the TileCal GbE Switch, that will interconnect all the

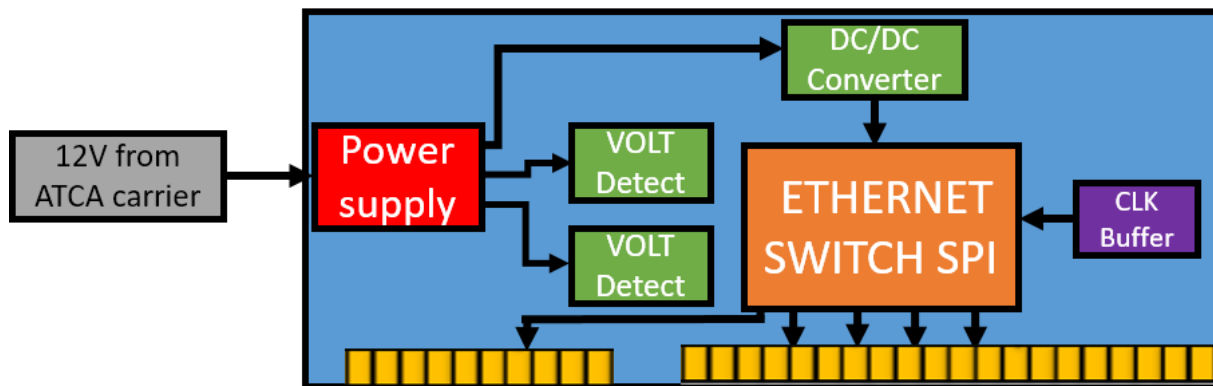


Figure 3. The TileCal Gigabit Ethernet switch card.

components in the TilePPr with an external ethernet network through the ATCA Base Interface located in the Zone 2 backplane on the shelf. The main component of this module is the Broadcom(R) BCM5396 which is a 16-port GbE switch with 16 1.25G-SerDes/SGMII port interfaces for connecting to external Gigabit PHYs or fiber modules. The Tile GbE switch provides communication to the CPMs and TDAQi.

This module consists of the interface connector to communicate with external components connectors and power regulators responsible for stepping down the 12V input voltage to the required voltages. Six boards have been produced from South African companies and these modules have been tested with the TilePPr modules. The produced TileCal GbE switch module has passed electrical and communication tests with TilePPr modules. The TileCoM functionalities detailed in subsection 3.2 are implemented and tested with TileCal GbE switch module and other TilePPr modules.

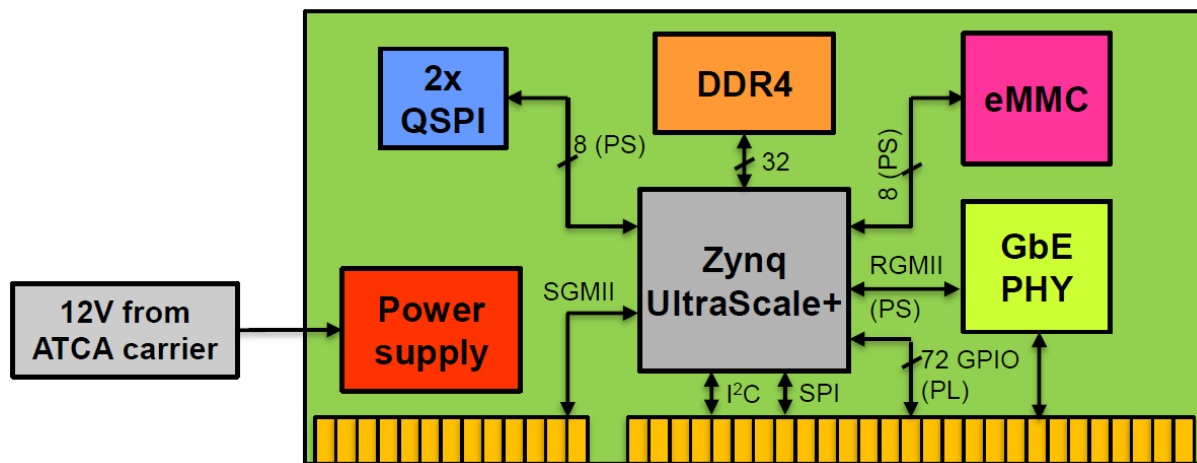


Figure 4. The TileCal Computer On Module (TileCoM).

Figure 4 shows the TileCoM architecture with connection interfaces to the ATCA carrier. The TileCoM main components are the Zynq UltraScale + ZU2CG and 2GB DDR4. All the interface components are used for the main functionalities of the TileCoM. The TileCoM will receive 12V power supply from the ATCA carrier to power all the components. The DC/DC regulators are used to step-down the voltage to supply other components that are on the board.

The Transmission Control Protocol (TCP) and the Internet Protocol (IP) are used to remotely connect to the TileCoM and implement the main functionalities. The Inter-Integrated Circuit (I²C) protocol is used to interface with the ATCA temperature and voltage sensors for monitoring purposes. The TileCoM reads these temperatures and voltages, and send them to DCS through a GbE port.

3.2. Software implementation for TileCoM functionalities

The three main functionalities of the TileCoM involves remote programming, interface with TDAQ[8] and integration with the Detector Control System (DCS)[9]. The remote programming application is used to remotely program all the FPGAs on the ATLAS TileCal Phase II upgrades electronic readout chain. The interface with TDAQ is used to monitor and control the data acquisition on the TilePPr. Lastly, the integration with DCS functionality is used to remotely control and monitor the health status of the readout modules. All these functionalities are implemented in the software application level of the embedded linux running on TileCoM. TileCoM drivers are developed to integrate with the TileCoM hardware and the rest of the ATLAS TileCal Phase II upgrades electronic readout chain. The Extensible Markup Language (XML) is used as a lightweight data-interchange format to read data from the electronic readout chain.

The Open Platform Communications United Architecture (OPC-UA) projects are part of the DCS TileCoM functionality that is used to control and monitor the readout electronic chain. This DCS TileCoM functionality is divided into two projects. The first OPC-UA project focuses on only reading the Xilinx Analog to Digital Values from the TileCoM. This project was successfully integrated and tested with the SCADA system of the DCS to remotely acquire sensor data. The second OPC-UA project is currently in process of implementation and involves software integration with the CPM on the ATCA carrier board.

3.3. Progress status of the South African contribution

Figure 5 shows a Gant Chart with the projects for the South African contribution towards the TilePPr for 2021. All the projects are on schedule in terms of production and developments of software applications. The final design of the TileCoM involves integration tests with the TilePPr and TDAQ FPGAs. This project will commence on the last quarter of 2021 together with the production of TileCoM boards by South African companies.

The plan for the year 2022 on-wards is to perform electrical and communication tests on the TileCoM boards produced in South Africa. This will commence early 2022 and will involve testing the TileCoM as well as integration tests with the other ATLAS TileCal Phase II upgrade electronic readout chain boards.

4. Conclusion

Current work at CERN involves progressing towards Phase II upgrades to accommodate an increase in the instantaneous luminosity by a factor 5 compared to the current operation of the LHC. The University of the Witwatersrand and iThemba labs are contributing towards the off-detector electronics. This contribution involves software developments and production of boards by South African companies. The University of the Witwatersrand has produced six fully functional TileCal GbE Switch boards.

The first OPC-UA software development project has been completed and integrated successfully with the SCADA systems of the DCS. The ATLAS TileCal note is a document that contains all the details about the TileCoM and it is currently under review. The production of TileCoM boards as well as the development of the second project for the OPC-UA will commence on the last quarter of 2021. All the projects of the South African contribution are on schedule.

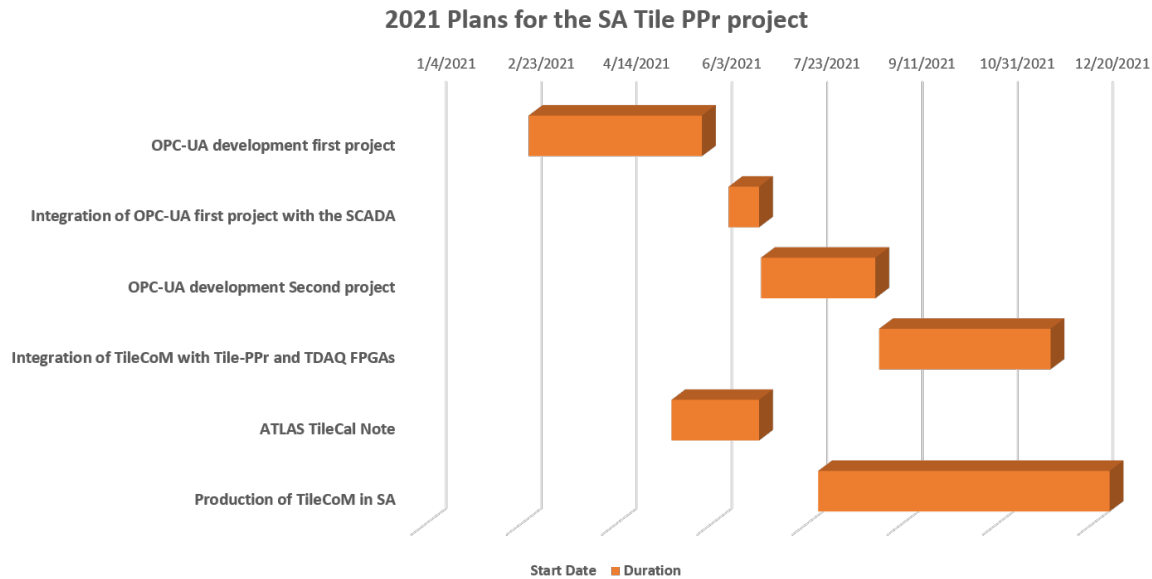


Figure 5. Progress status of the South African contribution towards TilePPr.

References

- [1] Benedikt 2004 *LHC Design Report* (Geneva: CERN)
- [2] Collaboration 2012 *Letter of Intent for the Phase-II Upgrade of the ATLAS Experiment* (Geneva: CERN)
- [3] Ressegotti M 2019 *Overview of the CMS Detector Performance at LHC Run 2* 9
- [4] Vyvre P V 2014 *Performance of the ALICE Experiment at the CERN LHC* 108
- [5] Collaboration 2014 *LHCb Detector Performance* 83
- [6] Santurio E V 2020 *Performance of the ATLAS Hadronic Tile Calorimeter Demonstrator system for the Phase-II upgrade facing the High-Luminosity LHC era.* 4
- [7] Argos F C and Valero A 2019 *The PreProcessor Module for the ATLAS Tile Calorimeter at the HL-LHC* 4
- [8] Xiaoguang Y 2019 *TileCal TDAQ interface module for the Phase-II Upgrade of the ATLAS Tile Calorimeter* 4
- [9] Martins F 2016 *The ATLAS Tile Calorimeter DCS for Run 2*

Understanding two same-sign and three leptons with b -jets in four top quark events at the LHC

Thuso Mathaha¹, Abhaya Kumar Swain¹, Mukesh Kumar¹,
Xifeng Ruan¹, Bruce Mellado^{1,2}

¹School of Physics and Institute for Collider Particle Physics, University of the Witwatersrand, Johannesburg, Wits 2050, South Africa

²iThemba LABS, National Research Foundation, PO Box 722, Somerset West 7129, South Africa

E-mail: thuso.stephen.mathata@cern.ch

Abstract. The top quark is the heaviest known elementary particle of the Standard Model (SM) of particle physics and, therefore, it is expected to have large couplings to hypothetical new physics in many models beyond the SM (BSM). Various studies have predicted the presence of multi-lepton anomalies at the LHC. One of those anomalies is the excess production of two same-sign leptons and three isolated leptons in association with b -jets. These are reasonably well described by a 2HDM+ S model, where S is a singlet scalar. Both the ATLAS and CMS experiments have reported sustained excesses in these final states. This includes corners of the phase-space where production of top quark pairs in association with a W boson contributes to. Here, we investigate the production of two same-sign and three leptons from the production of four top quark final states. Our focus is on understanding the differences between the SM and BSM production mechanisms of four top quarks from $t\bar{t}A$ ($A \rightarrow t\bar{t}$) using Machine Learning techniques with twelve discriminating kinematic variables.

1. Introduction

The exploration of a Higgs boson (h) at the Large Hadron Collider (LHC) by ATLAS [1] and CMS [2] Collaborations has opened a new window of opportunity for the community of particle physics. The measured properties relating to the Higgs boson have illustrated the compatibility with those predicted by the Standard Model (SM) [3, 4]. Be that as it may, the possibility of the existence of additional scalar bosons is not excluded provided that their mixing with the SM Higgs boson is adequately small. Subsequently with the higher luminosity, the focus has shifted towards understanding the couplings of the Higgs boson to the SM particles and searching for new particles. Thus, leaving no stone unturned to search for new particles/interactions at the LHC. In doing so the LHC has already reported a few prelusive hints/anomalies in its current data which needs immediate attention. In this context a scalar singlet S was introduced in conjunction with a 2HDM model in Ref. [5, 6] to explain some features of the Run 1 LHC data, referred to as the 2HDM+ S model. The model predicts the emergence of multi-lepton anomalies that have been verified in Refs. [7, 8, 9, 10], where a possible candidate of S has been reported in Ref. [11]. The model can further elaborate on multiple anomalies in astro-physics if it is complemented by a candidate of a Dark matter [12]. It can be easily extended [13] to account for the 4.2σ anomaly $g - 2$ of the muon [14, 15].

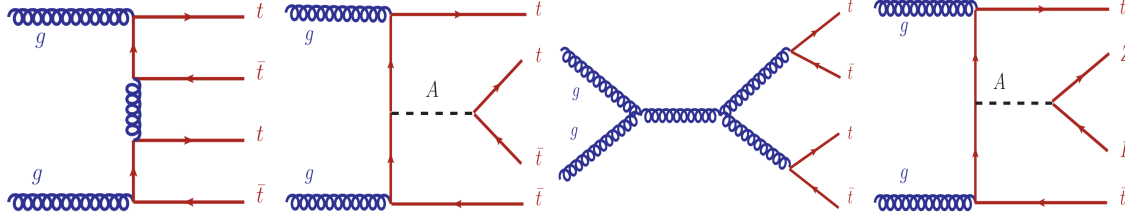


Figure 1. The Feynman diagram for the four top quarks production at the leading order in QCD.

The large coupling of the top quark with the SM Higgs boson exposes it to multiple new particles as well as new interactions predicted in various physics in BSM. Thus, studying rare processes involving the top quarks are of high interest. The four top quark production has been observed recently by both ATLAS [16] and CMS [17] collaborations and it is one of the rare processes predicted by the SM. In this study we require two same-sign leptons (2LSS) or events with at least three leptons (3L) to be present in the final state. Although the branching fractions for these channels are relatively small, it delivers promising results owing to its clean nature and small background contribution from the SM. The addition of a Higgs-doublet to the SM resulted in the scalar spectrum being populated with two CP-even (h, H), one CP-odd (A) and charged scalar bosons (H^\pm), thus leaving room to study the characteristics of the scalar spectrum. Our interest is to investigate the CP-odd scalar in the 2HDM+ S model, by studying the production of A in association with two top quarks and its decay of $A \rightarrow t\bar{t}$ channels. The relevant Feynman diagrams are shown in Fig. 1.

2. The Model

In order to understand the results reported by ATLAS [16], we have considered a 2HDM extended with a real singlet scalar [6, 18], Φ_S , we kept the notation same as in Ref. [6] and name this model as 2HDM+ S . The potential of the model is given by:

$$\begin{aligned}
 V(\Phi_1, \Phi_2, \Phi_S) = & m_{11}^2 |\Phi_1|^2 + m_{22}^2 |\Phi_2|^2 - m_{12}^2 (\Phi_1^\dagger \Phi_2 + h.c.) \\
 & + \frac{\lambda_1}{2} (\Phi_1^\dagger \Phi_1)^2 + \frac{\lambda_2}{2} (\Phi_2^\dagger \Phi_2)^2 + \lambda_3 (\Phi_1^\dagger \Phi_1) (\Phi_2^\dagger \Phi_2) \\
 & + \lambda_4 (\Phi_1^\dagger \Phi_2) (\Phi_2^\dagger \Phi_1) + \frac{\lambda_5}{2} [(\Phi_1^\dagger \Phi_2)^2 + h.c.] \\
 & + \frac{1}{2} m_S^2 \Phi_S^2 + \frac{\lambda_6}{8} \Phi_S^4 + \frac{\lambda_7}{2} (\Phi_1^\dagger \Phi_1) \Phi_S^2 + \frac{\lambda_8}{2} (\Phi_2^\dagger \Phi_2) \Phi_S^2.
 \end{aligned} \tag{1}$$

Here the Φ_1 and Φ_2 are the $SU(2)_L$ Higgs doublets and Φ_S is the singlet field. The first three lines correspond to the potential for the 2HDM and the last line is the contribution from the singlet field. In order to avoid the tree-level FCNC's, all the quarks of a given charge must couple to a single Higgs doublet, which can be done by imposing a Z_2 symmetry and it is softly broken by the m_{12}^2 term. Moreover, if we extend the Z_2 symmetry to the Yukawa sector it guarantees the absence of FCNC at tree level. Here, we consider a case where the real singlet field acquires a vacuum expectation value (vev) with a Z_2 symmetry. In other words, if this symmetry is respected then the singlet scalar becomes a viable dark matter candidate. In this study we set $m_{12}^2 \neq 0$ in the 2HDM+ S potential, Eqn. 1, which corresponds to a soft breaking of the Z_2 symmetry. Since we do not consider explicit CP violation, we assume λ_i to be real. Minimising the potential with the three Higgs fields and assuming the $vevs$ of the fields $\Phi_1 \rightarrow v_1/\sqrt{2}$, $\Phi_2 \rightarrow v_2/\sqrt{2}$ and $\Phi_S \rightarrow v_S$, the three minimisation conditions are:

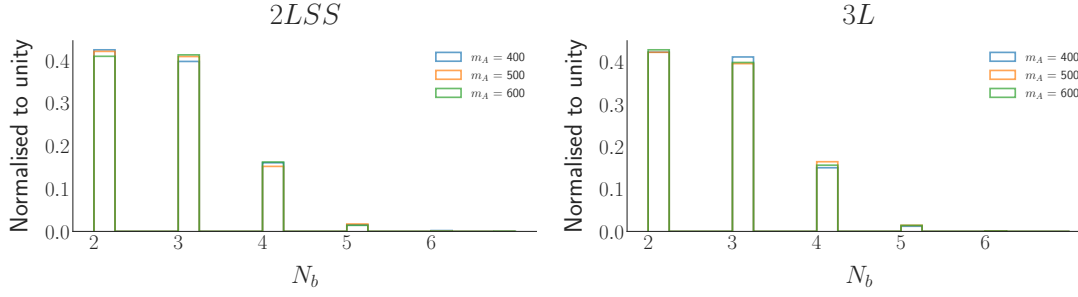


Figure 2. The b -jet multiplicity in events from $pp \rightarrow t\bar{t}A \rightarrow t\bar{t}t\bar{t}$ production for three values of m_A with the event selection applied in Ref. [16]. The graphs on the left (right) correspond to two same-sign (three) leptons.

$$\frac{\partial V}{\partial[v_1, v_2, v_S]} = 0. \quad (2)$$

With these conditions on the fields are:

$$m_{11}^2 = -\frac{1}{2}(v_1^2\lambda_1 + v_2^2\lambda_{345} + v_S^2\lambda_7) + \frac{v_2}{v_1}m_{12}^2, \quad (3)$$

$$m_{22}^2 = -\frac{1}{2}(v_2^2\lambda_2 + v_1^2\lambda_{345} + v_S^2\lambda_8) + \frac{v_2}{v_1}m_{12}^2, \quad (4)$$

$$m_S^2 = -\frac{1}{2}(v_1^2\lambda_7 + v_2^2\lambda_8 + v_S^2\lambda_6), \quad (5)$$

where $\lambda_{345} = \lambda_3 + \lambda_4 + \lambda_5$.

3. Deep Neural Networks

Deep Neural Networks (DNN) are considered a powerful tool for big data problems when using machine learning. They have been applied to a variety of problems, essentially classifications of various types and to Artificial Intelligence complex systems needed at CERN when searching for new physics. Large data sets with various kinematics are produced by the multipurpose detectors at the LHC from the proton-proton collisions. To get information from the data, different mechanisms are used to process the multi-dimensional space.

DNNs make use of multiple processing layers to determine patterns within large data sets, through each layer learning from the input data and subsequently passing on the information to the next layer. The data flow in DNNs is in one direction, from the input layer to the output layer with the connections between the layers being fed forward, while the output results are obtained using back propagation.

In our study we have engineered three separate DNN models that will be used to separate the SM production of four top quarks from the BSM production, as we have evaluated the heavy pseudo scalar A with three different masses, $m_A = 400, 500, 600$ GeV. The best working hyper parameters for the DNNs were used to build DNNs that provided efficient results for the classification task.

4. Results

We perform a Monte-Carlo simulation of pp collisions at the LHC. The events corresponding to the signal and SM backgrounds are generated using **Madgraph5** [19] with the **NNPDF3.0** parton distribution functions [20]. The UFO model files required for the Madgraph analysis have been obtained from **FeynRules** [21] after a proper implementation of the model. Following this partonlevel analysis, the parton showering and hadronization are performed using

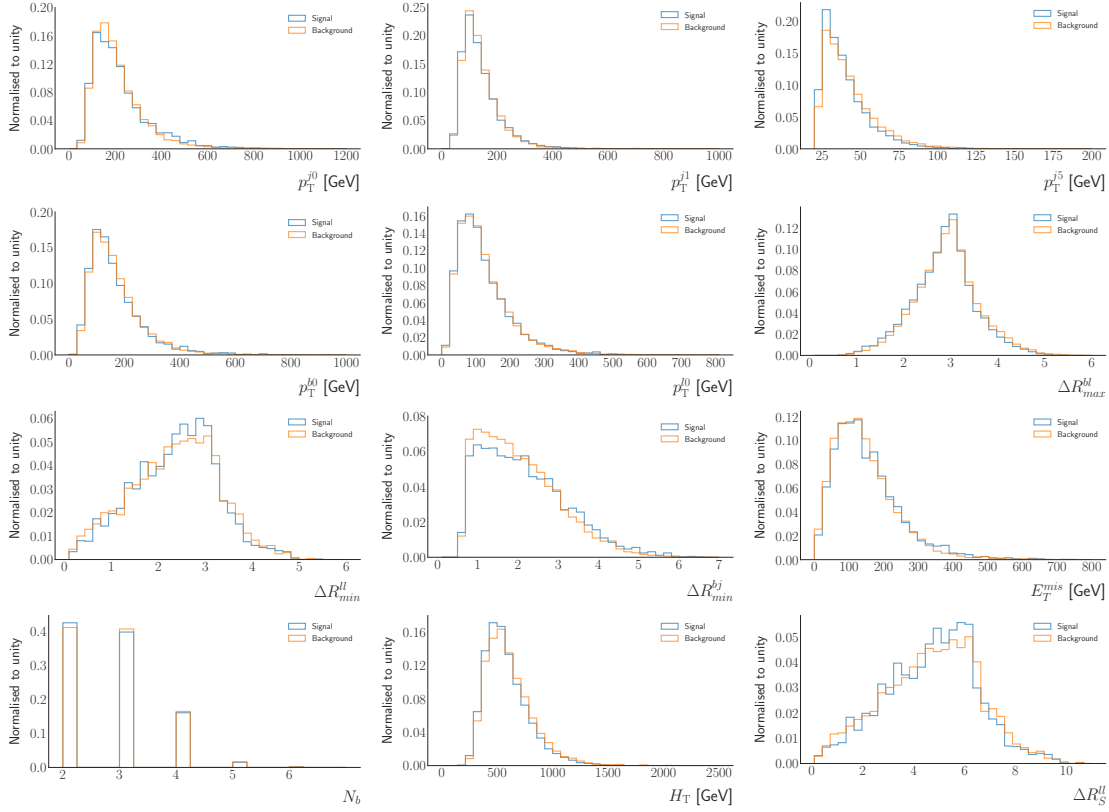


Figure 3. The distributions of the input variables used to train the DNN for two same-sign leptons. The BSM signal corresponds to $m_A = 400$ GeV.

Pythia [22]. We use Delphes(v3) [23] for the corresponding detector level simulation after the showering/hadronization.

The event selection documented in Ref. [16] is used here. The DNN used in this study is a binary classification algorithm which categorizes between 0 and 1, with 0 being associated with the SM production of four top quarks while 1 is associated with BSM production. The signature that will be used to explain the results reported by ATLAS in Ref. [16] with b -jets follows the production mechanism $pp \rightarrow t\bar{t}A \rightarrow t\bar{t}t\bar{t}$. This gives rise to an excess of multi-lepton final states associated with b -tagged jets in the two channels of interest. In order to illustrate the excess of b -tagged jets in the final state of the signature that we are studying, distributions of the b -tagged jets for the two channels are shown in Fig. 2.

The discriminating features used to train the DNN in order to perform a classification between the SM and BSM four top quark productions are displayed in Fig. 3. This includes the total number of b -tagged jets, N_b , the leading lepton transverse momentum, p_T^{l0} , the missing transverse energy, E_T^{mis} , the leading jet transverse momentum, p_T^{j0} , the second leading jet transverse momentum, p_T^{j1} , the sixth leading jet transverse momentum, p_T^{j5} , the leading b -tagged jet transverse momentum, p_T^{b0} , the minimum distance defined as $\Delta R = \sqrt{(\Delta\eta)^2 + (\Delta\phi)^2}$ between two leptons out of all possible pairs, $\Delta R_{min}^{\ell\ell}$, the scalar sum of transverse momenta over all leptons and jets excluding the leading jet, H_T , the sum of the distances between two leptons for all possible pairs, $\Delta R_S^{\ell\ell}$, the maximum distance between a b -tagged jet and a lepton among all possible pairs ΔR_{max}^{bl} , and the minimum distance between a jet and a b -tagged jet among all possible pairs ΔR_{min}^{bj} . From the distributions of these input variables we are able to see that

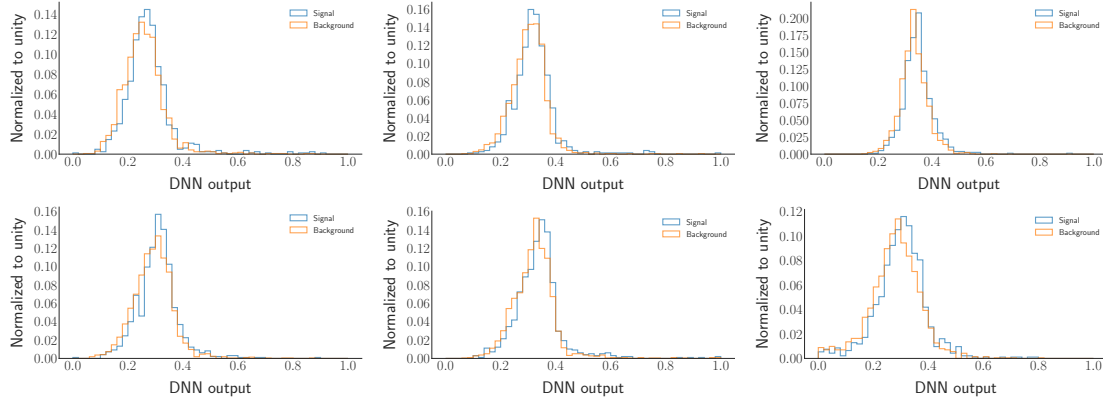


Figure 4. The DNN output distributions for the three mass ranges for two channels of interest. The first row represents SS and the second row represents 3L. The first column is for $m_A=400$ GeV, the second column is for $m_A=500$ GeV and the third column is for $m_A=600$ GeV.

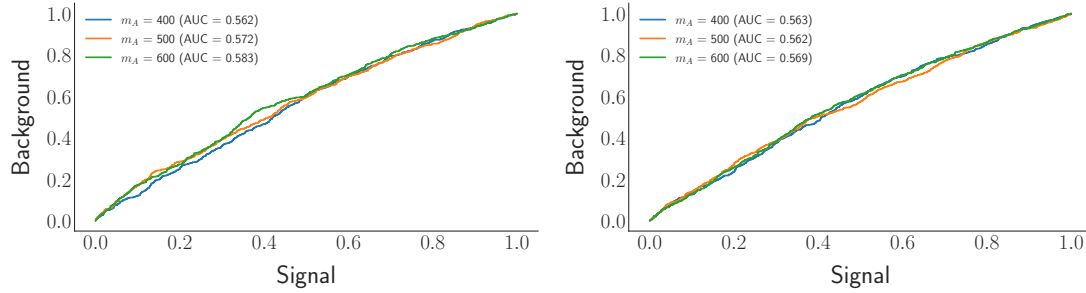


Figure 5. The ROC curves obtained from the DNN models for signal and background. The graphs correspond to 2LSS (left) and 3L (right).

there is no significant discrimination between the background and the signal.

The DNN was set to the best hyper parameters and output distributions obtained from the model for testing data are shown in Fig. 4. From the output distributions of the DNN, we see that the SM four top quark and BSM four top quark productions are not far from each other, thus making it difficult to separate the two. This is further illustrated by the ROC (receiving operating characteristic) curves displayed in Fig. 5 whose AUC (area under curve) are barely above 50%. The ROC curves are obtained with the corresponding test data samples, which were not used in the training of the DNNs.

5. Summary and Conclusion

We have studied the four top quark production at the center of mass $\sqrt{s} = 13$ TeV at the LHC with two categories of multi-lepton channels: two same-sign leptons and three leptons. After using a number of kinematic variables, we notice that there is no significant discrimination between the four top quark production in the SM and that of the BSM model used here ($pp \rightarrow t\bar{t}A \rightarrow t\bar{t}t\bar{t}$). A multivariate analysis is performed with a DNN using twelve features, where no significant discrimination between the SM and BSM four top quark signals. This is illustrated by the AUCs of the ROC curves being marginally higher than 50%. Hence, we are predicting that the BSM signal should be seen as an elevation of the measured four top cross-section.

References

- [1] Aad G *et al.* (ATLAS) 2012 *Phys. Lett. B* **716** 1–29 (*Preprint* 1207.7214)
- [2] Chatrchyan S *et al.* (CMS) 2012 *Phys. Lett. B* **716** 30–61 (*Preprint* 1207.7235)
- [3] Chatrchyan S *et al.* (CMS) 2013 *Phys. Rev. Lett.* **110** 081803 (*Preprint* 1212.6639)
- [4] Aad G *et al.* (ATLAS) 2013 *Phys. Lett. B* **726** 120–144 (*Preprint* 1307.1432)
- [5] von Buddenbrock S, Chakrabarty N, Cornell A S, Kar D, Kumar M, Mandal T, Mellado B, Mukhopadhyaya B and Reed R G 2015 (*Preprint* 1506.00612)
- [6] von Buddenbrock S, Chakrabarty N, Cornell A S, Kar D, Kumar M, Mandal T, Mellado B, Mukhopadhyaya B, Reed R G and Ruan X 2016 *Eur. Phys. J. C* **76** 580 (*Preprint* 1606.01674)
- [7] von Buddenbrock S, Cornell A S, Fadol A, Kumar M, Mellado B and Ruan X 2018 *J. Phys. G* **45** 115003 (*Preprint* 1711.07874)
- [8] Buddenbrock S, Cornell A S, Fang Y, Fadol Mohammed A, Kumar M, Mellado B and Tomiwa K G 2019 *JHEP* **10** 157 (*Preprint* 1901.05300)
- [9] von Buddenbrock S, Ruiz R and Mellado B 2020 *Phys. Lett. B* **811** 135964 (*Preprint* 2009.00032)
- [10] Hernandez Y, Kumar M, Cornell A S, Dahbi S E, Fang Y, Lieberman B, Mellado B, Monnakgotla K, Ruan X and Xin S 2021 *Eur. Phys. J. C* **81** 365 (*Preprint* 1912.00699)
- [11] Crivellin A, Fang Y, Fischer O, Kumar A, Kumar M, Malwa E, Mellado B, Rapheeha N, Ruan X and Sha Q 2021 (*Preprint* 2109.02650)
- [12] Beck G, Kumar M, Malwa E, Mellado B and Temo R 2021 (*Preprint* 2102.10596)
- [13] Sabatta D, Cornell A S, Goyal A, Kumar M, Mellado B and Ruan X 2020 *Chin. Phys. C* **44** 063103 (*Preprint* 1909.03969)
- [14] Abi B *et al.* (Muon g-2) 2021 *Phys. Rev. Lett.* **126** 141801 (*Preprint* 2104.03281)
- [15] Aoyama T *et al.* 2020 *Phys. Rept.* **887** 1–166 (*Preprint* 2006.04822)
- [16] Aad G *et al.* (ATLAS) 2020 *Eur. Phys. J. C* **80** 1085 (*Preprint* 2007.14858)
- [17] Sirunyan A M *et al.* (CMS) 2020 *Eur. Phys. J. C* **80** 75 (*Preprint* 1908.06463)
- [18] von Buddenbrock S, Cornell A S, Iarilala E D R, Kumar M, Mellado B, Ruan X and Shrif E M 2019 *J. Phys. G* **46** 115001 (*Preprint* 1809.06344)
- [19] Alwall J, Frederix R, Frixione S, Hirschi V, Maltoni F, Mattelaer O, Shao H S, Stelzer T, Torrielli P and Zaro M 2014 *JHEP* **07** 079 (*Preprint* 1405.0301)
- [20] Ball R D *et al.* (NNPDF) 2015 *JHEP* **04** 040 (*Preprint* 1410.8849)
- [21] Alloul A, Christensen N D, Degrande C, Duhr C and Fuks B 2014 *Comput. Phys. Commun.* **185** 2250–2300 (*Preprint* 1310.1921)
- [22] Sjostrand T, Mrenna S and Skands P Z 2006 *JHEP* **05** 026 (*Preprint* hep-ph/0603175)
- [23] de Favereau J, Delaere C, Demin P, Giammanco A, Lemaître V, Mertens A and Selvaggi M (DELPHES 3) 2014 *JHEP* **02** 057 (*Preprint* 1307.6346)

The use of Semi-supervision in the search for heavy resonances with the $Z\gamma$ final state at the LHC

Joshua Choma^{1,*}, Salah-Eddine Dahbi¹, Bruce Mellado^{1,2}, Xifeng Ruan¹

¹ School of Physics and Institute for Collider Particle Physics, University of the Witwatersrand, Johannesburg, Wits 2050, South Africa.

² iThemba LABS, National Research Foundation, PO Box 722, Somerset West 7129, South Africa

E-mail: *naalamotse.joshua.choma@cern.ch

Abstract. Unlike supervised learning which is known to assume a full knowledge of the underlying model, semi-supervised learning, weak supervision in particular allows with partial knowledge to extract new information from data. The objective of this study is to set up the search for heavy resonances at the electroweak scale with topological requirements. These resonances could be produced with different production mechanisms. In this case we will be focusing on the searches for new resonances in the $Z\gamma$ final state using the Monte Carlo simulated signal samples for 139 fb^{-1} of integrated luminosity for Run 2, collected at the LHC. The weak supervised learning approach will be implemented, which will then be compared to the performance of the full supervision approach.

1. Introduction

Large Hadron Collider (LHC) at CERN produces a very large amount of data, which is computationally intensive and requires super-computing abilities to process. This data is generated through proton-proton collisions, pp , at the ATLAS detector at high energies. The collisions at the LHC produce particles which physicists have been studying in search for a new physics beyond the Standard Model (BSM). For the probability of the BSM events to be produced, the particles have to be accelerated at extremely high energy and high luminosity.

Machine learning (ML), deep learning, in particular, comes across as one of the tools to use in this type of analysis because of its ability of handling complex and high dimensionality data. The application of ML to high energy physics started in the 1990s, used for analysis and which later developed into event identification and reconstruction in the 2010s [1]. There are quite a number of ML algorithms which have been used in physics which include support vector machines, boosted decision trees, kernel density estimation and artificial neural networks.

For the longest time ML has been following two most commonly known learning paradigms, namely, supervised and unsupervised learning. Supervised learning is known to assume full knowledge of the model since it is trained on labelled data. On the other hand, in unsupervised learning, the learning takes place without labels. The algorithm is expected to learn from itself by finding similarities in the data and assigning them to the same output unit. Weak supervision

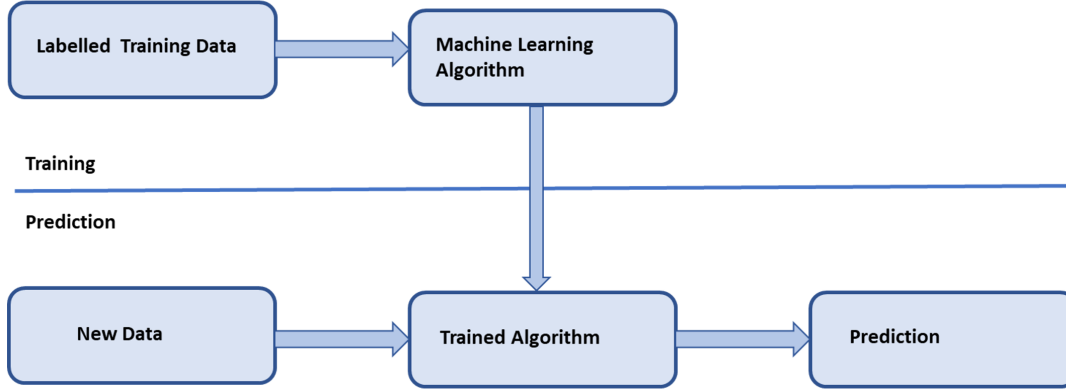


Figure 1: Schematic representation of supervised learning.

in addition to these two, it is a new paradigm that allows extraction of information with partial knowledge of the data.

The focus on this research is to search for resonances using $H \rightarrow Z\gamma$ in the final states in predefined categories shown in Table 1 where H is a Higgs-like scalar. The purpose of this study is to scan from 200 - 900 GeV to verify the ability of the proposed methodology, which will further be used to prepare a search for new phenomena in high mass in $Z\gamma$ final states at the LHC. As this is an ongoing study, this paper will present and focus more on the mass point of 200 GeV.

The rest of this paper is organised as follows: Section 2 discusses the ML techniques, Section 3 presents data selection and data preprocessing, while Sections 4 and 5 concludes this work and gives a brief discussion, respectively.

2. Machine Learning

This section gives a brief description of the methodology implemented in this study. Two ML techniques in the form of full supervised learning and weak supervised learning have been implemented and evaluated for the purpose of events classification. This is done to train the algorithm to learn what the signal and background events look like. These techniques have been implemented in conjunction with deep neural networks (DNNs) [2].

2.1. Full Supervised Learning

Full supervised classification is one of the most popular learning paradigms of ML. The name dictates that the dataset should come with labels. Each example \vec{x}_i comes with a label $y_i \in \{0, 1\}$ in a case of binary classification task. Figure 1 shows a schematic representation of full steps involved in supervised learning. The purpose of this approach is to learn a mapping from x to y while minimising the loss function (see equation 2) which can be in a form of binary cross-entropy:

$$\ell(y, \hat{y}) = -y \cdot \log \hat{y} + (1 - y) \cdot \log(1 - \hat{y}), \quad (1)$$

where \hat{y} is the model output and y is the target output. The loss function is given by [3]:

$$f_{full} = \operatorname{argmin}_{f: \mathbb{R}^n \rightarrow [0,1]} \sum_{i=1}^N \ell(y_i, \hat{y}_i), \quad (2)$$

where f is the predictor function, \hat{y}_i is the i^{th} model output, y_i is the corresponding target output and ℓ is the loss for a single example [4]. For this task, the training data contains labelled signal

Table 1: Yield for the considered processes normalised to the expected events yields and signal injection rates for VBF, ggH, ZH and WH signal samples for 139 fb^{-1} of integrated luminosity for Run 2.

Process	Selection	Sideband Region	Signal Region	Signal
ggH	Inclusive	13175	6444	160
ZH & WH	$MET_{sig} > 2.5 \text{ GeV}$	808	394	40
ZH & WH	$N_{jets} \geq 2 \text{ GeV}; 60 < m_{jj} < 120 \text{ GeV}$	839	414	40
VBF	$N_{jets} \geq 2 \text{ GeV}; \Delta\eta_{jj} > 2 \text{ GeV}; m_{jj} > 300 \text{ GeV}$	498	245	30

and background events, with 1 and 0 used as the labels, respectively. This is done to ensure that the algorithm is able to generalize on an unseen data to make predictions. This learning paradigm requires a large amount of labelled data, especially when applied on a deep learning algorithm.

2.2. Weak Supervised Learning

Unlike supervised learning, semi-supervised learning, weak supervision in particular allows with partial knowledge to extract new information from the data. This is different from supervised learning which is known to assume a full knowledge of the underlying model. Weak supervised learning is less expensive compared to supervised learning since it takes less time manually labelling the data. Weak supervised learning enables the model to learn from data with imprecise labels [5], it is for this reason that it is regarded as cheap form of supervision [6, 7]. These benefits sparked a lot of interest from researchers in high energy physics [3]. The most commonly known types of weak supervision come in three ways, namely, *incomplete*, *inexact*, and *inaccurate* supervision [8]. The names are self-explanatory, *i.e.* *incomplete* supervision comes with incomplete labels, *inaccurate* supervision with inaccurate labels and *inexact* supervision for coarse-grained labels [8].

3. Data Selection and Preparation

This work explores the separation power of weak supervision technique in comparison with full supervision. The performance of these two techniques will be tested on ATLAS Monte Carlo samples. This corresponds to simulated non-resonant $Z\gamma$ dataset, as it is the dominant background, representing more than 90% of the total background. The signal in this research represents the simulated Higgs-like to $Z\gamma$ final state [9]. Data preprocessing plays a fundamental role in ML and has a significant influence on the performance of ML methods [10, 11, 12]. The data is normally scaled to the intervals of $[0, 1]$ and $[-1, 1]$ to ensure that features have the same degree of influence [13]. This ensures that the values use a common scale however, the difference in the ranges is not distorted. For this study MinMax scaler was used to normalize the data. MinMax scaler is defined by:

$$x'_i = \frac{x_i - \min(x)}{\max(x) - \min(x)} \quad (3)$$

where x_i is the i^{th} entry/record for the variable x , x'_i is the rescaled entry, whereas $\min(x)$ and $\max(x)$ represent the minimum and maximum entries, respectively. Table 1 shows the number of expected events yields for both sideband and signal region for all predefined categories for this mass point. The width of the $Z\gamma$ invariant mass for the sideband region is defined as 12% of center mass of the resonance Higgs-like signal while the signal region is 6%. Different signal production mechanisms (WH , ZH , ggH and VBF) were injected, these injected numbers are

Table 2: Maximum significance for different background rejections from the weak supervised learning DNN response distribution.

Category	Max Significance	Background Rejection (%)
Inclusive	1.97	0
$MET_{sig} > 2.5$ GeV; ZH	3.65	99
$MET_{sig} > 2.5$ GeV; WH	2.87	99
$N_{jets} \geq 2$ GeV; $60 < m_{jj} < 120$ GeV; ZH	1.91	30
$N_{jets} \geq 2$; $60 < m_{jj} < 120$ GeV; WH	1.88	0
$N_{jets} \geq 2$ GeV; $\Delta\eta_{jj} > 2$ GeV; $m_{jj} > 300$ GeV	2.31	90

defined by 2σ , where σ is the statistical uncertainty of the background in the signal region, given by:

$$\sigma = \sqrt{B_{MW}} \quad (4)$$

where B_{MW} represents the number of background events in the mass window region. The signal region for this mass is defined as $194 < m_{\ell\ell\gamma} < 206$ GeV whereas the sideband is between $182 < m_{\ell\ell\gamma} < 194$ GeV and $206 < m_{\ell\ell\gamma} < 218$ GeV.

Throughout this research, background events in the sideband region will be represented by sample 1. Sample 2 is made up of the background and the signal in the mass window region.

4. Results

A python API, Keras library with Tensorflow backend [14] was used for DNNs configurations. DNNs with four hidden layers of 200 nodes each and a single output node have been configured and implemented for this study. All of the hidden layers of the DNN used ReLu for an activation function and a sigmoid for the output layer. The input layer consists of 17 neurons, representing the kinematic features of the dataset. The separation power of the two techniques in conjunction with DNNs was evaluated using an ROC curve (receiver operating characteristic curve). Figure 2 shows the ROC curves for all the predefined categories with their respective signal injection. The performance in this case is measured by the area under the curve (AUC). Figure 3 (a) shows the DNN distribution plot from the weak supervised learning model when tested with pure signal and background. This is the selected plot for the VBF ($N_{jets} \geq 2$ GeV, $\Delta\eta_{jj} > 2$ GeV, $m_{jj} > 300$ GeV) category. This response distribution was further used to calculate the significance based on background rejection using the following equation:

$$\text{significance} = \frac{S}{\sqrt{S+B}} \quad (5)$$

where S is the number of signal events and B is the number of background events. Significance in this case can be regarded as the maximum ratio of signal to noise that is produced by the DNN classifier. The results of this significance are shown in Figure 3(b). The maximum significance together with the background rejection in terms of percentages are recorded in Table 2 for all categories. The two categories, inclusive and $N_{jets} \geq 2$ GeV; $60 < m_{jj} < 120$ GeV, WH show to have a maximum significant at 0% background and this is due to having no clear separation between background and signal.

5. Discussion and Conclusion

In this study, we proposed the search for new resonances beyond the standard model using machine learning techniques, weak supervision and full supervision in particular. These learning

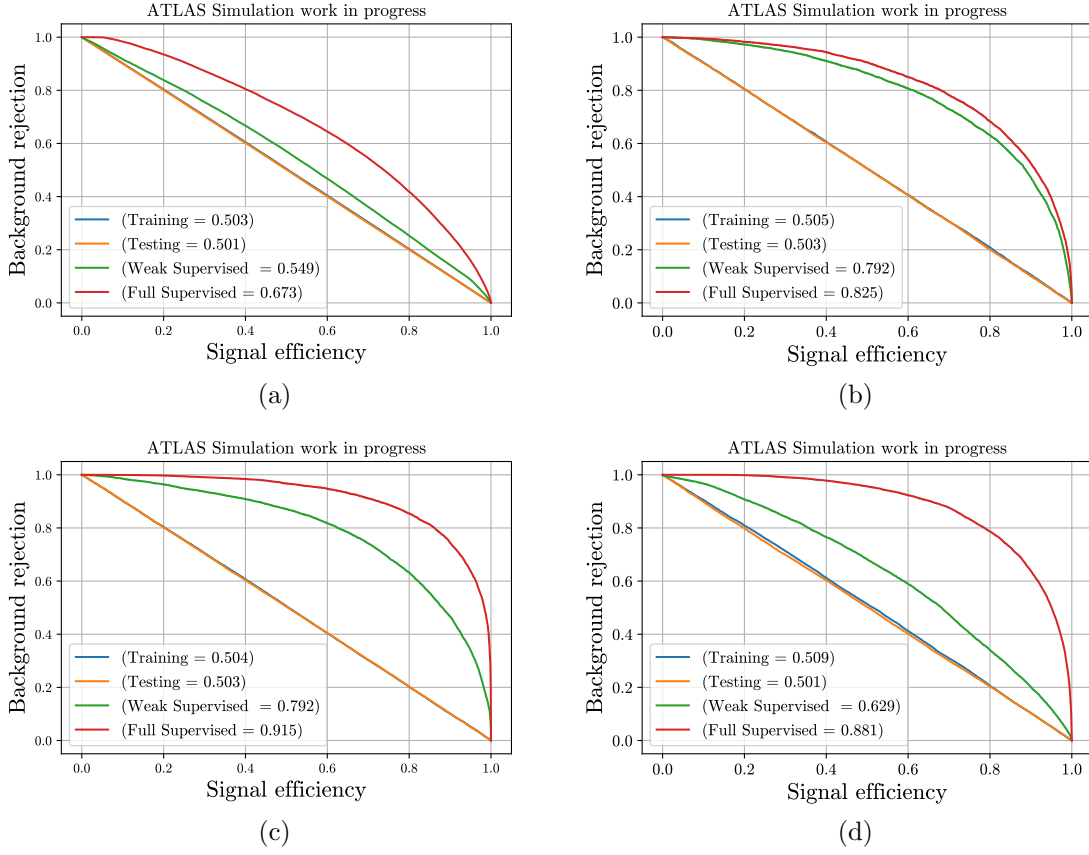


Figure 2: ROC curves showing weak supervising learning and full supervised learning results. Training and testing represent results for sample 1 and sample 2: (a) Inclusive, (b) $N_{jets} \geq 2$ GeV, $\Delta\eta_{jj} > 2$ GeV, $m_{jj} > 300$ GeV, (c) $MET_{sig} > 2.5$ GeV, WH and $N_{jets} \geq 2$ GeV, $60 < m_{jj} < 120$ GeV, ZH .

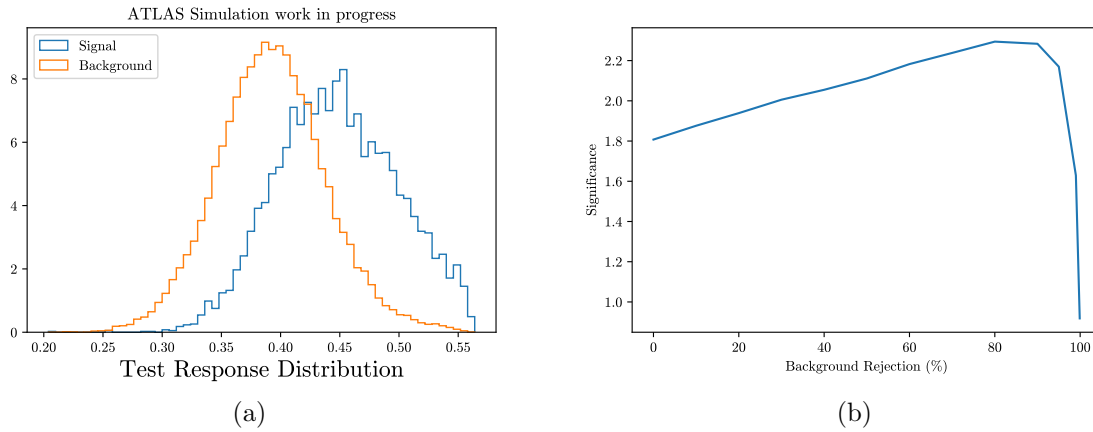


Figure 3: The two plots show the results for the VBF ($N_{jets} \geq 2$ GeV, $\Delta\eta_{jj} > 2$ GeV, $m_{jj} > 300$ GeV) category: (a) DNN response distribution for the weak supervised learning model, (b) significance calculated based on background rejection from the response distribution.

paradigms were used in conjunction with deep neural networks algorithm. The search was done in the $Z\gamma$ final state. The performance of the full supervision approach was compared to weak supervision. ROC curves were used as an evaluation metric to compare the two approaches. Based on this, it can be seen that the performance of weak supervision is reasonable and depends on the event configuration (see Figure 2) in comparison to full supervision for all categories. This is in agreement with the study carried out on the mass point of 105 GeV [2]. The study is used to setup for search for new phenomena in high-mass final states for the LHC.

References

- [1] Albertsson K, Altoe P, Anderson D, Andrews M, Espinosa J P A, Aurisano A, Basara L, Bevan A, Bhimji W, Bonacorsi D *et al.* 2018 *Journal of Physics: Conference Series* vol 1085 (IOP Publishing) p 022008
- [2] Dahbi S e, Choma J, Mellado B, Mokgatitswane G, Ruan X, Celik T and Lieberman B 2020 *arXiv preprint arXiv:2011.09863*
- [3] Dery L M, Nachman B, Rubbo F and Schwartzman A 2017 *Journal of High Energy Physics* **2017** 1–11
- [4] Cheong S Cs 229 project report: Weakly supervised classifiers with adversarial training in high-energy physics
- [5] Dehghani M, Zamani H, Severyn A, Kamps J and Croft W B 2017 *Proceedings of the 40th International ACM SIGIR Conference on Research and Development in Information Retrieval* pp 65–74
- [6] Han J, Zhang D, Cheng G, Guo L and Ren J 2014 *IEEE Transactions on Geoscience and Remote Sensing* **53** 3325–3337
- [7] Zhang F, Du B, Zhang L and Xu M 2016 *IEEE Transactions on Geoscience and Remote Sensing* **54** 5553–5563
- [8] Zhou Z H 2018 *National Science Review* **5** 44–53
- [9] Choi S, Muhlleitner M and Zerwas P 2013 *Physics Letters B* **718** 1031–1035
- [10] Zhang S, Zhang C and Yang Q 2003 *Applied artificial intelligence* **17** 375–381
- [11] Huang J, Li Y F and Xie M 2015 *Information and software Technology* **67** 108–127
- [12] Keung J, Kocaguneli E and Menzies T 2013 *Automated Software Engineering* **20** 543–567
- [13] Angelis L and Stamelos I 2000 *Empirical software engineering* **5** 35–68
- [14] Abadi M, Agarwal A, Barham P, Brevdo E, Chen Z, Citro C, Corrado G S, Davis A, Dean J, Devin M, Ghemawat S, Goodfellow I, Harp A, Irving G, Isard M, Jia Y, Jozefowicz R, Kaiser L, Kudlur M, Levenberg J, Mané D, Monga R, Moore S, Murray D, Olah C, Schuster M, Shlens J, Steiner B, Sutskever I, Talwar K, Tucker P, Vanhoucke V, Vasudevan V, Viégas F, Vinyals O, Warden P, Wattenberg M, Wicke M, Yu Y and Zheng X 2015 TensorFlow: Large-scale machine learning on heterogeneous systems software available from tensorflow.org URL <https://www.tensorflow.org/>

Background decomposition in $Z\gamma$ events used in the search for high-mass resonances

N P Rapheeha¹, X Ruan¹, G Mokgatitswane¹, S Dahbi¹ and B Mellado^{1,2}

¹ School of Physics and Institute for Collider Particle Physics, University of the Witwatersrand, Johannesburg, Wits 2050, South Africa

² iThemba LABS, National Research Foundation, PO Box 722, Somerset West 7129, South Africa

E-mail: ntsoko.phuti.rapheeha@cern.ch

Abstract. The study presents the measurement of purity of $Z\gamma$ and Z +jet background events in the search for high-mass $Z\gamma$ resonances. The study uses events where the Z boson decays into a pair of oppositely charged electrons or muons. The events used consist of 139 fb^{-1} of proton-proton collision data at $\sqrt{s} = 13 \text{ TeV}$, recorded by the ATLAS detector at the CERN's Large Hadron Collider. The measured purity of $Z\gamma$ events depends on the parameter R that gives the correlation between the isolation and identification criteria for jets faking photons in the Z +jet events. A data-driven method that uses $\gamma\gamma$ events collected with the same detector conditions as the $Z\gamma$ events is used to determine the value of R in various bins of the photon transverse momentum. The results are compared against values obtained by computing R using a Z +jet Monte Carlo sample and a data-driven method that uses $Z\gamma$ events to estimate R .

1. Introduction

Many theories of physics Beyond the Standard Model, BSM, predict the existence of new high-mass states that can be observed as experimental signatures at the CERN's Large Hadron Collider. One of such models predicts the existence of a heavy scalar boson H which may participate in the electroweak symmetry breaking or decaying predominantly into a part of lighter scalar boson, S [1–5].

In collider searches for H decaying into the $Z\gamma$ final state the dominant background events are expected to originate the production of non-resonant $Z\gamma$ events and the subleading background contribution from the production of a Z boson in association with jets. The Z boson decays into a pair of leptons, $\ell\ell$, $\ell = e, \mu$ where e and μ are electron and a muon, respectively. In the $Z\gamma$ events, the photon candidate is a prompt photon, which is characterised by a narrow energy cluster in the electromagnetic calorimeter and it is usually well isolated from hadronic activity. In the Z +jet background events, one jet is misidentified as a photon. The misidentified photon candidate is mainly from the decay of neutral meson, typically a π^0 , carrying a large fraction of the initial parton energy and producing an energy cluster in the electromagnetic calorimeter. The produced energy cluster has non-negligible leakage in the hadronic calorimeter. It is not isolated from hadronic activity as other particles in the same jet deposit energy in the calorimeters near the photon candidate. The photon isolation and identification, ID, variables can therefore be used to estimate the contributions of $Z\gamma$ and Z +jet events in the collected $Z\gamma$ data.

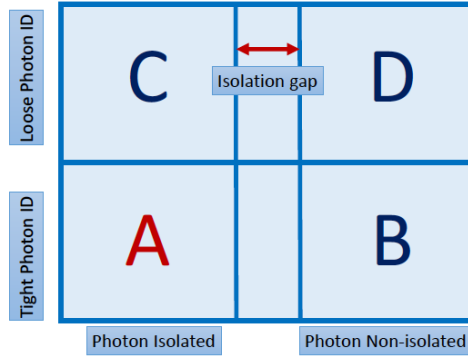


Figure 1. Definition of the ABCD regions based on photon ID and isolation.

The composition of the selected dataset is measured using the data-driven method exploited in the Run 1 SM $h \rightarrow Z\gamma$ (2D-sideband method) with prompt photons in the final state [6] and where h is the SM Higgs boson. The total background yields a smooth $Z\gamma$ invariant mass distribution which can be described by an analytic function. Knowledge of the background composition is very important in performing spurious signal studies, where the bias on the signal yield caused by choice of a particular background function is quantified [7].

1.1. Data-driven background composition estimation with the 2D-sideband method

The 2D-sideband is a counting method that relies on the definition of a two dimensional plane, as shown in Fig 1.1, based on the isolation and identification variables of the prompt photon candidate of the selected $\ell\ell\gamma$ triplet [7]. One region (A) with enhanced $Z\gamma$ contribution and three control regions (B,C, D) enriched with Z +jet events are defined in this plane as follows:

- Tight and isolated region (A): the photon candidates are well isolated from hadronic activity and pass the tight selection criteria.
- Tight but non-isolated region (B): the photon candidates are not isolated from the hadronic activity but pass the tight selection criteria.
- Non-tight, isolated region (C): the photon candidates are isolated from the hadronic activity (as in region A) but fail the tight identification criteria but pass some looser identification criteria.
- Non-tight, non-isolated region (D): the photon candidates are non-isolated (as in region B) and pass the same identification requirements of region C.

These four regions are populated with the events passing all the object selection requirements of the analysis except the photon identification and isolation requirements. Region A corresponds to the signal region used in the final measurement.

The $Z\gamma$ yield, $N_A^{Z\gamma}$, in region A is estimated from the number of events in data in the four regions, N_k^{data} ($k \in \{A, B, C, D\}$), through the relation:

$$N_A^{Z\gamma} = N_A^{\text{data}} - (N_B^{\text{data}} - c_B N_A^{Z\gamma}) \frac{(N_C^{\text{data}} - c_C N_A^{Z\gamma})}{(N_D^{\text{data}} - c_D N_A^{Z\gamma})} R^{Zj}, \quad (1)$$

where $c_k \equiv \frac{N_k^{Z\gamma}}{N_A^{Z\gamma}}$ are signal leakage fractions that are extracted from the simulated $Z\gamma$ sample and:

$$R^{Zj} \equiv \frac{N_A^{Zj} N_D^{Zj}}{N_B^{Zj} N_C^{Zj}}, \quad (2)$$

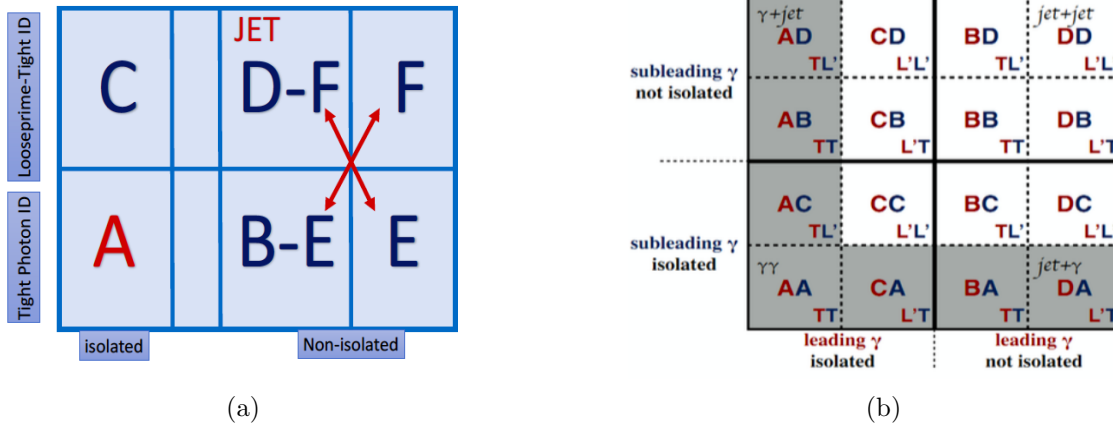


Figure 2. (a) Definition of the EF regions to directly obtain R^{Zj} directly from data. (b) Definition of the 16 regions used in the 2x2D-sideband method of estimating purity of $\gamma\gamma$ events.

quantifies the correlation between the isolation and identification variables for the jets faking photons in Z +jet events ($R^{Zj} = 1$ in the case of vanishing correlations). The correlation parameter cannot be measured directly from data since it requires background events to fall into the signal region. The parameter R^{Zj} can be obtained from the Z +jet full Monte Carlo, MC, simulated sample, to validate the obtained value of R^{Zj} , data-driven methods are devised.

2. Methodology

2.1. Data-driven estimation of R using $Z + \gamma$ events

The R^{Zj} is estimated by defining two new non-isolated regions called region "E" and region "F", as illustrated in Fig. 2(a). The region E is extra tight, while region F is extra loose as compared to region D. These two regions are defined so that the R^{Zj} from Eq. 2 can be estimated directly from data instead of MC, Eq. 2 becomes Eq. 3:

$$R^{\text{data}, Z\gamma} = \frac{N_{B-E}^{\text{data}} N_F^{\text{data}}}{N_{D-F}^{\text{data}} N_E^{\text{data}}}. \quad (3)$$

The following event selection was used to select $Z\gamma$ events used in the estimation of $R^{\text{data}, Z\gamma}$. The reconstructed $\ell\ell\gamma$ system is required to have an invariant mass greater than 130 GeV and less than 2500 GeV. The invariant mass of the reconstructed $\ell\ell$ candidates is required to be within 15 GeV of the Z boson pole mass. The photon candidate is required to have a minimum p_T of 40 GeV. The tight photon identification and the FixedCutLoose isolation requirements were used for the identification and isolation requirements [8].

A sample of Z +jet events was simulated at next-to-leading order, NLO, in quantum chromodynamics using POWHEG [9] showered with PYTHIA8 [10] event generators. The CT10 [11] parton distribution function, PDF, set was in the matrix element. To model the non-perturbative effects, the AZNLO set of tuned parameters [12] alongside the CTEQ6L1 PDF set [13] are used. The MC sample will be used to compute R^{Zj} , as per Eq. 2. The event selection used to select $Z\gamma$ events was used in selecting the Z +jet events.

2.2. Data-driven estimation of R using $\gamma\gamma$ events

To verify the accuracy of the purity computed with $R^{\text{data}, Z\gamma}$ estimated with Eq. 3, a new data driven method is used. The main idea of the method is to use an X +jet sample, where X is

a well defined object, in order to estimate R in the same regions as ones used to define R^{Zj} in Eq. 2. A $\gamma\gamma$ data sample composed of two real photons, 1 real photon and a hadronic jet and two hadronic jets is used. Each photon candidate is classified as either belonging to a category A, B, C or D, depending on whether it fails or passes the identification criteria, as shown in Fig. 2(b). The two candidates are considered sequentially; the 2D-sideband method is first applied to the photon candidate with a leading photon transverse momentum, p_T , to extract events for which the leading p_T candidate is a true photon and then the method is applied to the subleading p_T photon candidate knowing that the leading photon is tightly identified and well isolated. This results in 16 orthogonal regions, shown in Fig. 2(b).

A X + jet sample is formed by fixing either the leading or subleading photon to be well isolated and passing the tight identification requirement to be X . To obtain the desired X +jet sample from the $\gamma\gamma$ data sample, pure $\gamma\gamma$ events are subtracted from the data sample. The number of X +jet events in a region of interest is given by:

$$N_j^{\text{data}} = N_j^{\text{data}} - N_j^{\text{M.C}} \times k - \text{factor}, \quad (4)$$

where j is a region of interest and $k\text{-factor} = N_{AA}^{\text{data}} \times \frac{\text{purity}}{N_{AA}^{\text{MC}}}$. The purity of $\gamma\gamma$ events is computed using the 2 \times 2D-sideband method used in ATLAS studies [14]. The method performs a data-driven background evaluation by extrapolating the background from the control regions defined in the sidebands of isolation and identification variables in which the photons either pass or fail the Tight ID criteria or fail the isolation selection. The purity of $\gamma\gamma$ events is computed in a region where both the leading and subleading photons are well isolated and identified. The regions used in the 2 \times 2D-sideband method are shown in Fig. 2 (b).

The data driven correlation parameter in a case where the leading p_T photon candidate is classified as being tight and isolated, $X = \gamma$, is computed as:

$$R^{\gamma+jet} = \frac{N_{AA}^{\gamma+jet}/N_{AB}^{\gamma+jet}}{N_{AC}^{\gamma+jet}/N_{AD}^{\gamma+jet}}. \quad (5)$$

In the case where the subleading p_T photon candidate is selected as X the correlation parameter is defined as:

$$R^{jet+\gamma} = \frac{N_{AA}^{jet+\gamma}/N_{BA}^{\gamma+jet}}{N_{CA}^{\gamma+jet}/N_{DA}^{\gamma+jet}}. \quad (6)$$

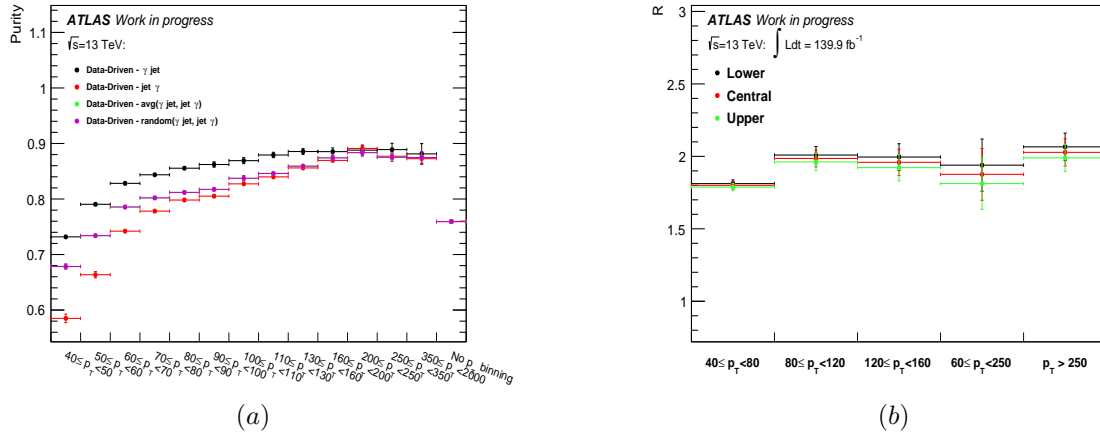
The following event selection was used to select $\gamma\gamma$ events used to compute $R^{\text{data},\gamma\gamma}$. The photon pairs are required to have a reconstructed invariant mass between 130 GeV and 2500 GeV. The leading photon is required to have a minimum p_T of 40 GeV and the subleading photon has a minimum p_T of 30 GeV. The photon isolation and identification requirements are the same as the ones used for $Z\gamma$ events.

3. Results

The values of R obtained using the data-driven $Z\gamma$ method and the Z +jet MC are summarised in Table 1. The obtained values of $R^{\text{data},\gamma\gamma}$ will depend on whether leading or subleading photon in the $\gamma\gamma$ data sample was selected as X when forming a X +jet sample. To eliminate potential bias on the selection of X will be done at random. Figure. 3 (a) shows purities obtained when the leading photon is selected as X (X +jet), the subleading photon selected as X (jet+ X) and when the selection between either photon is done randomly. It is noted that the $\gamma\gamma$ purity obtained when the X candidate is selected at random is the same as the average between X +jet and jet+ X purities. The purity obtained by selection X at random is used to compute values of $R^{\text{data},\gamma\gamma}$.

Table 1. Estimated values of R obtained using the data-driven ABCDEF method, MC Z +jet events and the data-driven $\gamma\gamma$ events.

p_T^γ bin [GeV]	$R^{\text{data}, Z\gamma}$	$R^{Zj}(Z+\text{jet MC})$	$R^{\text{data}, \gamma\gamma}$
$40 \leq p_T < 80$	1.36 ± 0.03	1.30 ± 0.04	1.80 ± 0.04
$80 \leq p_T < 120$	1.21 ± 0.06	1.55 ± 0.13	1.99 ± 0.08
$120 \leq p_T < 160$	1.28 ± 0.11	1.70 ± 0.27	1.96 ± 0.13
$160 \leq p_T < 250$	1.53 ± 0.16	1.96 ± 0.44	1.88 ± 0.24
$p_T > 250$	1.27 ± 0.20	1.60 ± 0.52	2.03 ± 0.13

**Figure 3.** (a) di-photon purity at different photon p_T bins. (b) The R parameter computed using the central value of $\gamma\gamma$ purity \pm the statistical uncertainty of the purity.

The measured purity of $\gamma\gamma$ events has a significant impact of the computed value of $R^{\text{data}, \gamma\gamma}$. Fig. 3(b) shows the values of $R^{\text{data}, \gamma\gamma}$ using the central values of the $\gamma\gamma$ purity, lower and upper values of purity. The lower and upper values of the $\gamma\gamma$ purity are obtained by subtracting or adding the statistical uncertainty of $\gamma\gamma$ purity from the central value. The largest difference between R values computed using the central of purity and the values computed using lower and upper values is propagated as the systematic uncertainty of $R^{\text{data}, \gamma\gamma}$. The $R^{\text{data}, \gamma\gamma}$ values obtained using the $\gamma\gamma$ events are summarised in Table 1. The reported uncertainties of $R^{\text{data}, \gamma\gamma}$ consist of the statistical uncertainty and the systematic uncertainty.

The comparison between R values obtained using the three different samples is shown in Figure 4 (a). In the low mass region, where the photon p_T is less than 80 GeV, the R value computed with the $e^+e^- Z$ +jet MC is much closer to the one computed using the ABCDEF method. As the photon p_T increases, going to higher $Z\gamma$ masses, the R value computed with the Z +jet MC gets closer to R computed with the $\gamma\gamma$ data-driven method.

The comparison of the purity in each photon p_T bin using the different methods of computing R is shown in Figure 4 (b). It can be seen that value of R used does not impact the measured purity that much. It can be seen that as the photon p_T increases the value of purity obtained using the $\gamma\gamma$ data-driven method gets closer to the value obtained using R from the MC.

4. Conclusions

The background decomposition study in search for $Z\gamma$ events that can decay from a potential heavy scalar resonance has been performed. The purity of $Z\gamma$ events in data was measured using

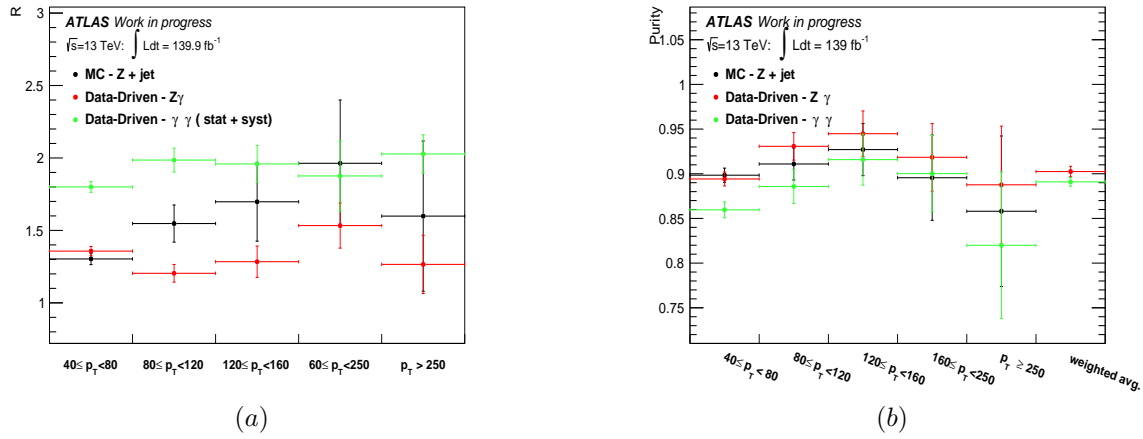


Figure 4. (a) Computed R values in different photon p_T bins. (b) The observed $Z\gamma$ purity using R values computed using the different methods in different photon p_T bins.

R computed with a data-driven method that uses $\gamma\gamma$ events, a data-driven method that uses $Z\gamma$ events and Z +jet MC. It was observed that the purity obtained using R^{Zj} computed with the Z +jet MC and $R^{\text{data},Z\gamma}$ to be comparatively the same for photons with p_T less than 80 GeV. As the photon p_T increases above 80 GeV the purity of $Z\gamma$ measured with R^{Zj} obtained with the Z +jet MC gets closer to the purity calculated with $R^{\text{data},\gamma\gamma}$ obtained from the data-driven $\gamma\gamma$ method. The three methods of estimating R resulted in the measured $Z\gamma$ that is relatively the same, except for the minor differences highlighted above.

References

- [1] von Buddenbrock S, Chakrabarty N, Cornell A S, Kar D, Kumar M, Mandal T, Mellado B, Mukhopadhyaya B and Reed R G 2015 (*Preprint* 1506.00612)
- [2] von Buddenbrock S, Chakrabarty N, Cornell A S, Kar D, Kumar M, Mandal T, Mellado B, Mukhopadhyaya B, Reed R G and Ruan X 2016 *Eur. Phys. J. C* **76** 580 (*Preprint* 1606.01674)
- [3] Buddenbrock S, Cornell A S, Fang Y, Fadol Mohammed A, Kumar M, Mellado B and Tomiwa K G 2019 *JHEP* **10** 157 (*Preprint* 1901.05300)
- [4] Hernandez Y, Kumar M, Cornell A S, Dahbi S E, Fang Y, Lieberman B, Mellado B, Monnakgotla K, Ruan X and Xin S 2021 *Eur. Phys. J. C* **81** 365 (*Preprint* 1912.00699)
- [5] von Buddenbrock S, Ruiz R and Mellado B 2020 *Phys. Lett. B* **811** 135964 (*Preprint* 2009.00032)
- [6] ATLAS Collaboration 2011 *Phys. Rev. D* **83**(5) 052005
- [7] ATLAS Collaboration 2020 Recommendations for the Modeling of Smooth Backgrounds Tech. rep. CERN Geneva
- [8] ATLAS Collaboration 2019 *Journal of Instrumentation* **14** P12006–P12006 (*Preprint* 1908.00005)
- [9] Alioli S, Nason P, Oleari C and Re E 2008 *Journal of High Energy Physics* **2008** 060–060 (*Preprint* 0805.4802)
- [10] Sjostrand T, Mrenna S and Skands P Z 2008 *Computer Physics Communications* **178** 852–867 ISSN 0010-4655 (*Preprint* 0710.3820)
- [11] Lai H L, Guzzi M, Huston J, Li Z, Nadolsky P M, Pumplin J and Yuan C P 2010 *Phys. Rev. D* **82** 074024 (*Preprint* 1007.2241)
- [12] ATLAS Collaboration 2014 *JHEP* **09** 145 (*Preprint* 1406.3660)
- [13] Pumplin J, Stump D R, Huston J, Lai H L, Nadolsky P M and Tung W K 2002 *JHEP* **07** 012 (*Preprint* hep-ph/0201195)
- [14] ATLAS Collaboration 2012 *Phys. Rev. D* **85**(1) 012003

Search for $Z\gamma$ high-mass resonances using the ATLAS detector

G Mokgatitswane¹, S Dahbi¹, N P Rapheeha¹, B Mellado^{1,2} and X Ruan¹

¹ School of Physics and Institute for Collider Particle Physics, University of the Witwatersrand, Johannesburg, Wits 2050, South Africa

² iThemba LABS, North, Empire Road, Braamfontein 2000, Johannesburg

E-mail: gaogalalwe.mokgatitswane@cern.ch

Abstract. This study presents a search for high-mass resonances in the $Z\gamma$ final states. The search is performed using the Monte Carlo simulated signal samples of mass from 200 GeV up to 5 TeV, corresponding to an integrated luminosity of 139 fb^{-1} dataset recorded by the ATLAS experiment in proton-proton collisions during the LHC Run 2. Only the leptonic decay of the Z boson to a lepton-antilepton pair $\mu^+\mu^-$ is considered. The analysis search for a localized excess in the invariant mass distribution of reconstructed final state over a smoothly-falling background emanating from Standard Model processes. The characterization of signal shape for the mass spectrum from gluon fusion production mode is modelled by a double-sided crystal ball function form and the background shape modelling is performed using analytic functions of different orders. The systematic uncertainties are incorporated, which arise from several experimental sources and on the possible bias (spurious signal) on the fitted signal yield due to the choice of background function.

1. Introduction

The discovery of new boson consistent with the Standard Model (SM) Higgs Boson h by the ATLAS and CMS experiments [1,2] at the Large Hadron Collider (LHC) opened a wide range of research focus to studying the nature of the Higgs boson and allows to investigate a wide scope of physical phenomena. This includes theoretical modelling of Higgs boson production processes and searches for physics Beyond the Standard Model (BSM) which might be discovered with large dataset from the LHC.

A 2HDM+ S model, where S is a singlet scalar, was used in Ref. [3,4] to explain some features of the Run 1 LHC data. Here the heavy scalar, H , decays predominantly into SS, Sh , where h is the SM Higgs boson. The model predicts the emergence of multi-lepton anomalies that have been verified in Refs. [5–8], where a possible candidate of S has been reported in Ref. [9]. The model can further elaborate on multiple anomalies in astro-physics if it is complemented by a candidate of a Dark matter [10]. It can be easily extended [11] to account for the muon $g-2$ anomaly (see Ref. [12] for a review of anomalies). This further motivates searches for heavy resonances decaying into $Z\gamma$.

The study aims at developing a search for high-mass $Z\gamma$ resonances of mass from 200 GeV up to 5 TeV. Here we consider a hypothetical heavy scalar H decaying to $Z\gamma$ ($H \rightarrow Z\gamma$) as shown in Fig. 1, where only events in which the Z boson decays to di-electrons or di-muons are used. The

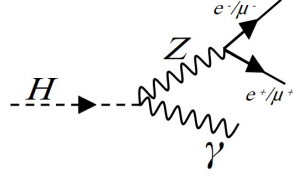


Figure 1: A schematic Feynman diagram of the decay of a heavy scalar H .

$Z\gamma$ channel is considered because a Higgs like boson (H) can have relatively higher possibility of decaying into a $Z\gamma$ final state in comparisons with the di-photon final state. In addition, its vertex is well reconstructed than di-photon events, hence making it possible to search for excesses.

However, the resonances which are searched for can not be easily extracted since they are overlayed by background processes with similar signatures. These backgrounds originate from non-resonant $Z\gamma$ events, either from initial state radiation (diboson production in the t , u channels), from final-state-radiation in radiative Z boson decays ($Z \rightarrow \ell\ell\gamma$) or from parton-to-photon fragmentation. Furthermore, the production of a Z boson in association with jets, followed by a $Z \rightarrow \ell\ell$ decay and misidentification of a jet as a photon also form part of the background. For other backgrounds, the contribution from $t\bar{t}$ and W/Z are expected to be much smaller and thus they are neglected.

For this study, it is therefore imperative to understand well, the yield of both signal and background events. In order to achieve this, the signal and background modelling is performed using the Double Sided Crystal Ball function (DSCB) and analytic functional forms of a different order, respectively. Systematic uncertainties are also included to account for possible residual mismodelling effects. The study is focusing on the di-muon channel as the first part of the actual full analysis.

2. Signal and Background samples

The Monte Carlo (MC) samples of $Z \rightarrow \mu^+\mu^-$ used in this analysis correspond to 2015-18 data condition. These samples are generated using a next-to-leading order (NLO) MC generator POWHEG [13] interfaced to the PYTHIA8 parton shower model [14], with the CT10 parton distribution functions (PDFs) in the matrix element [15]. The AZNLO set of tuned parameters [16] was used in conjunction with CTEQ6L1 PDF set [17] for modelling of non-perturbative effects. The background samples are generated from full simulated $Z\gamma$ with SHERPA [18,19], and Z +jet events obtained through data-driven method by reversing one photon (2D-sideband method) [20].

2.1. Event selection

For this analysis we select photon and muon candidates [18,21]. The preselected photons are required to have transverse momentum above 15 GeV and those reconstructed within regions of the calorimeter affected by read-out or high-voltage failures are rejected (loose identification requirement). After preselection of photons, the following stringent selections are required:

- Isolation from hadronic activity using “FixedCutLoose” working point. It is based on the energy in a cone and defined as: $E_T^{iso}|_{\Delta R=0.2} < 0.065 \times p_T$ GeV (calorimeter isolation) and $p_T^{iso}|_{R_{max}=0.2} < 0.05 \times p_T$ GeV (track isolation).
- The relative photon p_T over $m_{\ell\ell\gamma}$ is required to be over 0.27 GeV.

The di-lepton mass is required to be $76.18 < m_{\ell\ell} < 106.18$ GeV.

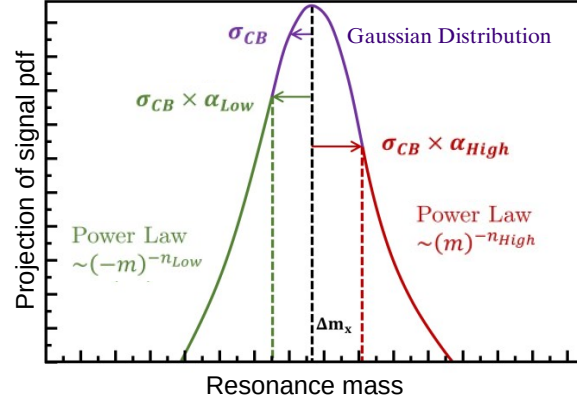


Figure 2: The Double-Sided Crystal Ball function definition.

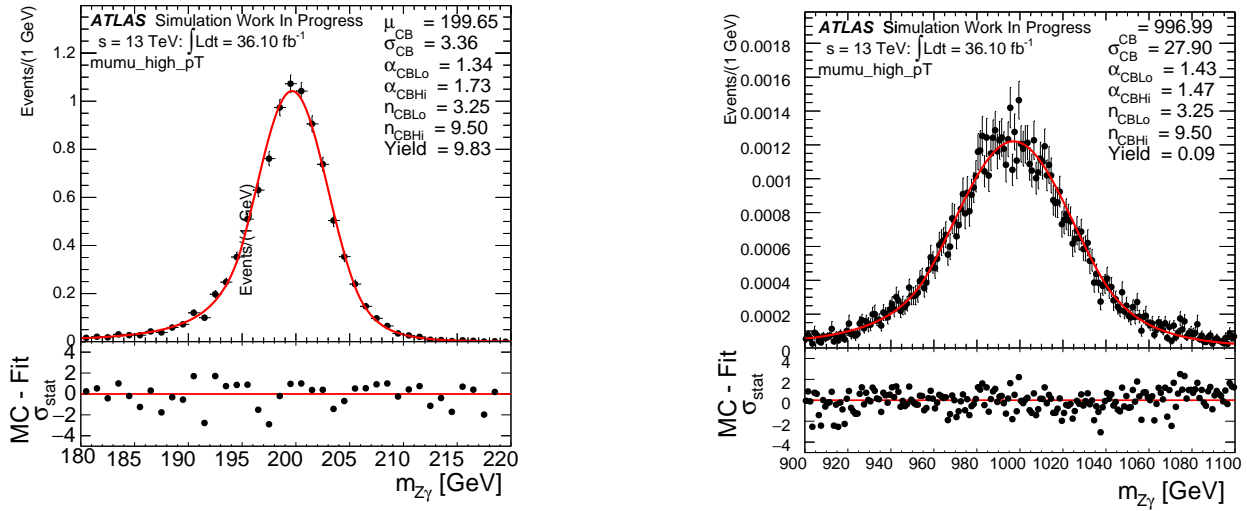


Figure 3: Results of individual fit of DSCB parameters.

3. Signal parameterisation

Characterisation of the $Z\gamma$ invariant mass distribution for high mass resonances is found to be well modelled with a Double-Sided Crystal Ball function (DSCB). The shape and parameters definition of DSCB are shown in Fig. 2.

The DCSB function consists of a core Gaussian with power-law tails on both sides of the mode of the distribution. It is defined as:

$$N. \begin{cases} e^{-t^2/2}, & \text{if } -\alpha_{Lo} \leq t \leq \alpha_{Hi} \\ \frac{e^{0.5\alpha_{Lo}^2}}{[\frac{\alpha_{Lo}}{n_{Lo}}(\frac{\alpha_{Lo}}{n_{Lo}} - \alpha_{Lo} - t)]^{n_{Lo}}}, & \text{if } t < -\alpha_{Lo} \\ \frac{e^{0.5\alpha_{Hi}^2}}{[\frac{\alpha_{Hi}}{n_{Hi}}(\frac{\alpha_{Hi}}{n_{Hi}} - \alpha_{Hi} + t)]^{n_{Hi}}}, & \text{if } t > \alpha_{Hi}, \end{cases} \quad (1)$$

where $t = \Delta m_x / \sigma_{CB}$, $\Delta m_x = m_x - \mu_{CB}$, N is the normalisation parameter, μ_{CB} is the peak of the Gaussian distribution, σ_{CB} represents the width of Gaussian part of the function, while $\alpha_{Lo}(\alpha_{Hi})$ is the point where the Gaussian becomes a power-law on low (high) mass side and $n_{Lo}(n_{Hi})$ is the exponent of the power-law. The results of the DSCB fits are shown in Fig. 3 for signal mass points $m_X = 200$ GeV and 1000 GeV.

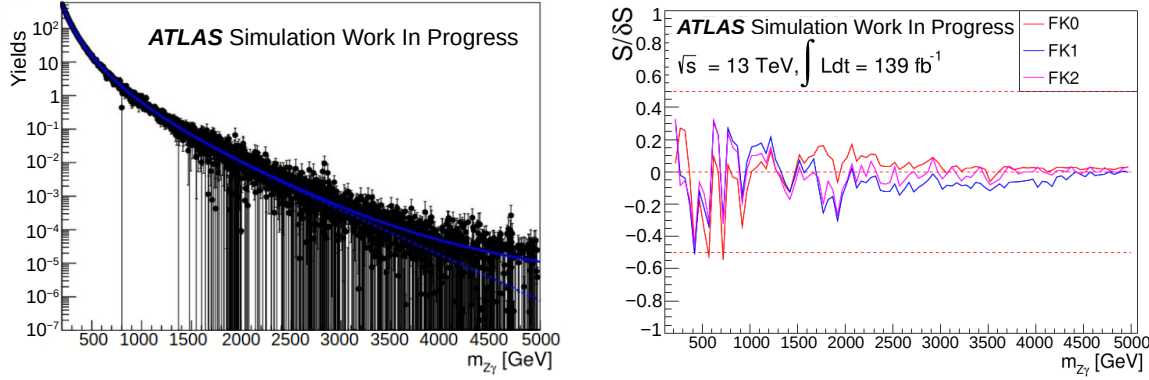


Figure 4: Fitting on the background template [200,5000] GeV with S+B function (left) and Ratio of the fitted spurious signal yield to its uncertainty for the background models as a function of mass for each functional form (right).

4. Background modelling

To estimate the background functional shape, a background template is required which consists of the $Z\gamma$ and Z +jet processes [22]. The template is prepared by combining the background using MC normalised to 90% of data in the signal region ($Z\gamma$ events) and 10% of reverse photon identification data in the control region (Z +jet events) [20]. Here we use the template to find the suitable function to describe background in the data, which gives a small bias on the signal yield (spurious signal) compared to the expected uncertainty from the background fluctuations. The bias over its uncertainty ($S/\delta S$) is expected to be less than 50%.

4.1. Spurious signal

The spurious signal, caused by the choice of a particular background parameterisation is evaluated by fitting a high statistics background sample (template) with a signal plus background model [22]. A scan (20 GeV step) of the existence of fake signal is performed across the m_X window (200 GeV-5000 GeV). Functional forms of different order, of up to third order exponential polynominal are used for modelling:

$$f_k(x; b, a_k) = (1 - x)^b x^{\sum_{j=0}^k a_j \log(x)^j}, \quad (2)$$

where $x = \frac{m_{\ell\ell\gamma}}{\sqrt{s}}$, $k = 0, 1, 2$ noted as FK0, FK1 and FK2, respectively, and the b parameter is usually set either to 1/3. Figure 4 (left) shows a mass spectrum of a three-body invariant mass distribution ($m_{\ell\ell\gamma}$), of up to 5000 GeV fitted with signal plus background model. Figure 4 (right) shows the maximum ratio of fitted spurious signal yield to its uncertainty.

5. Systematic uncertainty

5.1. Systematic uncertainty on the signal $m_{\ell\ell\gamma}$ distribution

The systematic uncertainties due to the modelling of the signal invariant mass distribution, have been estimated. For the invariant mass of $Z\gamma$ system, the main sources of systematic uncertainties on signal modelling are e/γ resolution, e/γ energy scale, muon momentum scale or resolution variations.

For the simulated signal MC samples used in this study, the $m_{\ell\ell\gamma}$ distribution is recomputed after varying the former uncertainty sources by $\pm 1\sigma$, where σ is its uncertainty provided by the Muon Combined Performance Working Group (MCP). Systematic uncertainties on the mass position and mass resolution are summarized in Tables 1 and 2, respectively.

Table 1: Summary of systematic uncertainty on signal position (μ_{CB}).

Source	Uncertainty on <i>Signal position</i> (%)
e/γ energy scale (all)	(0.38,-0.38)
Muon sagitta resolution bias	(0.00, 0.00)
Muon sagitta angle (ρ)	(0.00, 0.00)
Muon scale	(-0.05,0.05)

Table 2: Summary of systematic uncertainty on signal resolution (σ_{CB}).

Source	Uncertainty on <i>Signal resolution</i> (%)
e/γ energy resolution (all)	(2.06,-1.43)
Muon inner detector	(3.35,-2.89)
Muon spectrometer	(2.25,-3.86)

5.2. Systematic uncertainty on the signal efficiency

Table 3 summarizes the systematic uncertainty on the signal efficiency, which is estimated by varying the trigger, reconstruction, isolation and identification scale factors of the leptons by $\pm 1\sigma$. The dominant uncertainty is from muon reconstruction efficiency. There is p_T -dependent systematic taking into account the extrapolation of the Z efficiency measurements towards very high p_T . According to the MCP, the increase in uncertainty may well be compatible with expectations, depending on the campaign and the kinematics of the events looked at. However, this is not considered a limiting factor for the analysis.

Table 3: Summary of systematic uncertainty on signal efficiencies for $\mu\mu$ channel.

Source	Uncertainty on <i>Signal efficiency</i> (%)
Muon isolation efficiency (stat.)	(0.59, -0.59)
Muon isolation efficiency (sys.)	(0.45,-0.39)
Muon reconstruction efficiency (stat.)	(0.13, -0.13)
Muon reconstruction efficiency (sys.)	(15.86,-15.76)
Muon reconstruction efficiency (stat. lowpt)	(0.03,-0.04)
Muon reconstruction efficiency (sys. lowpt)	(0.05, -0.05)
Muon efficiency (ttva stat.)	(0.14, -0.13)
Muon efficiency (ttva sys.)	(0.15, -0.14)
Muon efficiency (trig. stat. uncertainty)	(0.00, 0.00)
Muon efficiency (trig. sys. uncertainty)	(0.00, 0.00)
Photon ID efficiency uncertainty	(0.75, -0.75)
Photon isolation efficiency uncertainty	(1.33, -1.33)
Photon trigger efficiency uncertainty	(0.00, 0.00)
Pile-up	(0.99, -1.76)

6. Conclusion

The aim of this study was to search for high-mass $Z\gamma$ resonances in 200-5000 GeV mass range, using the Monte Carlo simulated signal samples corresponding to an integrated luminosity of 139 fb^{-1} dataset recorded by the ATLAS experiment in proton-proton collisions during the LHC Run 2. The signal and background modelling have been performed using Double Sided Crystal Ball function and functional forms of up to third order exponential polynominal, respectively. The systematic uncertainties which arise from several experimental sources have been estimated as well as on the possible bias (spurious signal) on the fitted signal yield due to the choice of background function. The analysis is ongoing and aiming at setting up the statistical interpretation.

References

- [1] Aad G *et al.* (ATLAS) 2012 *Phys. Lett. B* **716** 1–29 (*Preprint* 1207.7214)
- [2] Khachatryan V *et al.* 2017 *Journal of High Energy Physics* **2017** 076
- [3] von Buddenbrock S, Chakrabarty N, Cornell A S, Kar D, Kumar M, Mandal T, Mellado B, Mukhopadhyaya B and Reed R G 2015 (*Preprint* 1506.00612)
- [4] von Buddenbrock S, Chakrabarty N, Cornell A S, Kar D, Kumar M, Mandal T, Mellado B, Mukhopadhyaya B, Reed R G and Ruan X 2016 *Eur. Phys. J. C* **76** 580 (*Preprint* 1606.01674)
- [5] von Buddenbrock S, Cornell A S, Fadol A, Kumar M, Mellado B and Ruan X 2018 *J. Phys. G* **45** 115003 (*Preprint* 1711.07874)
- [6] Buddenbrock S, Cornell A S, Fang Y, Fadol Mohammed A, Kumar M, Mellado B and Tomiwa K G 2019 *JHEP* **10** 157 (*Preprint* 1901.05300)
- [7] von Buddenbrock S, Ruiz R and Mellado B 2020 *Phys. Lett. B* **811** 135964 (*Preprint* 2009.00032)
- [8] Hernandez Y, Kumar M, Cornell A S, Dahbi S E, Fang Y, Lieberman B, Mellado B, Monnakgotla K, Ruan X and Xin S 2021 *Eur. Phys. J. C* **81** 365 (*Preprint* 1912.00699)
- [9] Crivellin A, Fang Y, Fischer O, Kumar A, Kumar M, Malwa E, Mellado B, Rapheeha N, Ruan X and Sha Q 2021 (*Preprint* 2109.02650)
- [10] Beck G, Kumar M, Malwa E, Mellado B and Temo R 2021 (*Preprint* 2102.10596)
- [11] Sabatta D, Cornell A S, Goyal A, Kumar M, Mellado B and Ruan X 2020 *Chin. Phys. C* **44** 063103 (*Preprint* 1909.03969)
- [12] Fischer O *et al.* 2021 *Unveiling hidden Physics Beyond the Standard Model at the LHC* (*Preprint* 2109.06065)
- [13] Alioli S, Nason P, Oleari C and Re E 2008 *Journal of High Energy Physics* **2008** 060–060
- [14] Sjöstrand T, Mrenna S and Skands P 2008 *Computer Physics Communications* **178** 852–867
- [15] Lai H L, Guzzi M, Huston J, Li Z, Nadolsky P M, Pumplin J and Yuan C P 2010 *Phys. Rev. D* **82**(7) 074024
- [16] Aad G *et al.* 2014 *Journal of High Energy Physics* **2014**
- [17] Pumplin J, Stump D R, Huston J, Lai H L, Nadolsky P and Tung W K 2002 *Journal of High Energy Physics* **2002** 012–012
- [18] Aad G *et al.* (ATLAS Collaboration) 2011 *Phys. Rev. D* **83**(5) 052005
- [19] Gleisberg T, Höche S, Krauss F, Schönherr M, Schumann S, Siegert F and Winter J 2009 *Journal of High Energy Physics* **2009** 007–007
- [20] P N Rapheeha, X Ruan, G Mokgatitswane, S Dahbi and B Mellado 2021 *Background decomposition in $Z\gamma$ events used in the search for high-mass resonances* (to be published in the 2021 SAIP book of proceedings)
- [21] Aad G *et al.* 2019 *Journal of Instrumentation* **14** P12006–P12006
- [22] Aad G *et al.* (ATLAS Collaboration) 2020 Recommendations for the Modeling of Smooth Backgrounds Tech. rep. CERN Geneva

Re-designing a radiation-tolerant low voltage power supply for the ATLAS Tile Calorimeter Phase-II Upgrade

E K Nkadimeng¹, R P Mckenzie¹, R van Rensburg¹, N Njara¹, T Lepota¹, O Mouane¹ and B Mellado^{1,2}

¹ School of Physics and Institute for Collider Particle Physics, University of the Witwatersrand, Johannesburg, Wits 2050, South Africa

² iThemba LABS, National Research Foundation, PO Box 722, Somerset West 7129, South Africa

E-mail: edward.khomotso.nkadimeng@cern.ch

Abstract. Power Electronics used in high-energy physics experiments at the Large Hadron Collider more specifically the ATLAS detector, are custom built and have to work reliably in the presence of ionizing radiation and an ever present magnetic field. In many such applications, owing to cost constraints, components that are radiation-hard by design are often used for such systems. Moreover, design complexity, verification effort, and scalability issues in centralized structures can impede performance improvement in monolithic designs. We demonstrate the steps followed for upgrading and re-designing a radiation tolerant low voltage power supply for a large scale operation and the considerations made for such a design. This includes measurements taken at component level, system level, and radiation tests done using the newly upgraded low voltage power supply. The upgraded low voltage power supplies will power the next generation of Front-End electronics of the Tile calorimeter in HL-LHC era.

1. Introduction

The Large Hadron Collider accelerator at CERN [1], will be upgraded to deliver an instantaneous luminosity up to $7.5 \times 10^{34} \text{ cm}^{-2} \text{ s}^{-1}$. The increase in integrated luminosity will correspond to an average of 200 simultaneous proton-proton interactions per bunch crossing. The ATLAS TileCal which covers the central region of the ATLAS experiment is a sampling calorimeter using iron as the absorber and plastic scintillator as the active material and divided longitudinally into three cylindrical barrels. The partition scheme of the barrels consists of two central long barrel segments and shorter extended barrel segments at each end [1, 2]. Each partition is comprised of 64 wedge-shaped segment modules. The Phase-II upgrade program of the TileCal system aims to satisfy the HL-LHC requirements and will be compatible with the new Trigger Data Acquisition (TDAQ) architecture, able to transfer full data to the off-detector electronics optically at 40 MHz [1]. The Tile Calorimeter front-end electronics (drawers) are powered by 256 LVBOXes. Each LVBOX contains eight 200W DC/DC single-output modules transforming 200 VDC input into +10V low voltage output. Each LVBOX is water cooled, contains the so called ELMB Motherboard, ELMB module, the 200 VDC distribution Fuse-Board, integrated cable set for connections, and chassis. The ELMB incorporates CAN Bus protocol for

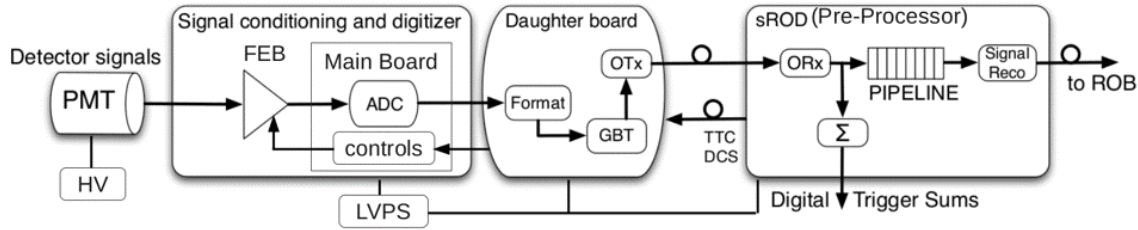


Figure 1: Upgraded TileCal readout architecture [2].

communication. It enables to monitor behavioural parameters of each DC/DC buck convertor, such as I_{in} , I_{out} , V_{in} , V_{out} , two on board temperatures. In order to evaluate the new readout architecture and the technology choices of the implementation, completely new on-detector and off-detector electronics are being developed, aiming to compensate for increased trigger rates and high-performance data acquisition.

2. Power and readout architecture

The low voltage power distribution system for TileCal provides power to the front-end electronics that reside on-detector as seen in figure 1. It is a three-stage power system. The bulk +200 VDC power supplies will be sourced in USA15, and distributed to the low voltage power supplies (LVPS) that reside inside "finger" of each module, just outside of each electronics drawer. These low voltage power supplies are also called "finger low voltage power supplies," (fLVPS). The fLVPS uses switching "Buck Converter" technology to convert the high voltage, low current power provided from the bulk source, into the low voltages required by the various sub circuits in the upgraded front-end electronics. The use of switching technology improves the efficiency of the power conversion, as opposed to the use of linear supplies. Upgraded fLVPS units will utilize identical LVPS bricks. Each of the new bricks produces +10 VDC as output. This is distributed to the front-end circuits, and the power is converted again using point-of-load (POL) regulators to the voltage levels needed by the local circuits. The interface in the fLVPS utilizes the ELMB, which is a standard for slow controls in ATLAS. The second part of the control system is based on the sub-system of small power supplies, called the AUXBoard which are placed in USA15 as bulk 200V DC power supplies. There is one AUXBoard for four fLVPS. New aspects of the upgrade design is to improve the performance, and adapt to the new requirements and interfaces of the upgrade. In the present system, the eight bricks that reside in the fLVPS supplies each provide power for specific circuitry in the drawer. They all use the same basic design, but are configured for the circuitry that they service, resulting in eight different types. In the new design, all eight bricks have the same specifications and performance requirements.

3. Functional description and specification of power supply

The basic topology of the brick is a transformer-coupled buck converter as used in the previous designs. The LVPS is centered around the LT1681 [4] controller chip with its dual transistor forward convertor (see figure 2) able to produce the drive pulse at the frequency of 300 KHz with an output duty factor that can vary from a few percent up to a maximum of 45%. The pulse width is controlled by a feedback circuit based on the values of the output voltage of the brick. This input permits us to ensure continuous-mode operation at the nominal voltages and currents. The signal from the LT1681 is sent to the Metal Oxide Semiconductor Field Effect Transistors (MOSFETs) drivers [2,3,5]. These are transistor drivers that have sufficient current and voltage drive, to drive the high-side and low-side power.

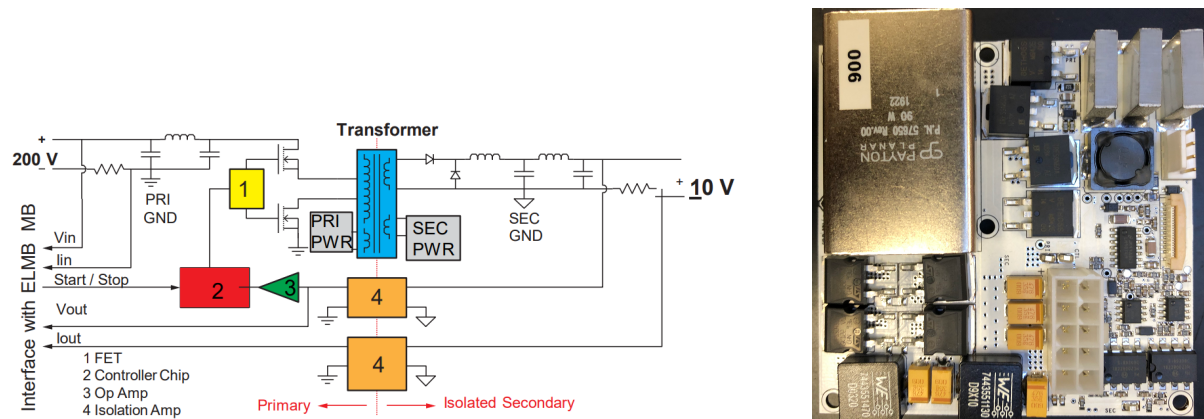


Figure 2: LVPS block diagram control system illustrating the LT1681 forward controller operating at 300 kHz [2] (Left) and University of the Witwatersrand low voltage power supply brick (right).

Both the high-side and low-side transistors turn on for the duration that the output clock is in the high state, and both are in the off state when the clock is low. When the MOSFETs conduct, current flows through the primary windings of the transformer, which transfers energy to the secondary windings. A buck converter [2,3] is implemented on the secondary side of the transformer and converts the signal to a constant voltage for the output. The output side also contains an additional LC (Inductor and Capacitor) stage for noise filtering. Voltage feedback, for controlling the output voltage, is provided by the opto-isolators [5]. This component processes the electrical signal converting it into digital signal at the input stage and transmitting it through pulsed light signal to the output, where it is converted back to an electrical analog signal. The signal is transmitted maintaining the input and output electrically insulated from each other. The design also incorporates two shunt resistors for measuring the output current, the voltage for which is also fed back using an opto-isolator.

The brick has three types of built-in protection circuitry as part of the design, namely the over voltage protection (OVP), over current protection (OCP) which are on the primary side. The third protection circuitry is the over temperature protection (OTP), which monitors the temperatures of the low-side transistor on the primary side. This circuit is integrated in the LT1681 design. When one protection circuit is triggered an 'off' signal is sent to the LT1681 which stops the brick immediately. The ELMB inside the LVBOX is used for digitization of monitored values from the bricks and ELMB send them via CANBUS to DCS. In particular, the ELMB monitors two temperatures on the primary side of the brick both close to the input of over temperature protection of the LT1681 and the output values.

The Printed Circuit Board (PCB) layout is a 6 layer board with dimensions of 80.26 mm by 80.26 mm and has mounting holes for attachment to the cooling plate inside the LVPS box. A shielded transformer following our custom specifications is used to step down an alternating high voltage produced from the forward controller to a lower an alternating voltage for DC-DC regulation. Ceramic cylinders made from Aluminium Oxide, called thermal posts, are used to transfer heat from brick components to the cooling plate. The metallized cylinders have one metallized face, which will be in contact with the pad of the switches and diodes on the PCB.

Parameter	Value
Threshold for Stable Load	2.3 A
Over Voltage Protection	12.5 V
Over current Protection	7 A
Duty Cycle at Nominal Load	> 45 %
Frequency at Nominal Load	300 kHz
Efficiency at Nominal Load	75 %
Input Current at Nominal Load	0.2 A
Over Temperature Protection	72 °C

Table 1: Specification parameters used to ensure uniformity of individual bricks in the test station software.

4. Improvements on the latest LVPS brick

The primary goals are to improve noise performance, reliability, and tolerance to Total Ionizing Dose (TID), Neutron Ionizing Event Loss (NIELs), single-event upset (SEU), while retaining the physical layout, interface to the detector control system, and other infrastructure.

4.1. Real-time monitoring of Low Voltage Power Supply

The brick measures six analog signals and sends them to the ELMB motherboard, which includes input voltage and current, output voltage and current, and the temperature readings from two points on the brick (primary and secondary side switches), measured using thermistors. Custom PC based software was synthesized to perform and monitor the LVPS brick and the tests are graphically displayed and recorded onto file these [4]. Testing ensures that LVPS bricks meet the criteria listed in Table 1. The feasibility of the design regarding the electrical parameters of specification was verified using a test-station [5] that was assembled at the University of the Witwatersrand. Various tests determine whether the protection circuitry of the LVPS is functioning correctly. Built-in protection circuitry are assessed for over current protection (at 10.5 A) and over temperature protection (at 70°C), in addition over voltage protection (at 12 V).

4.2. Thermal Management

In the upgraded design the ceramic posts utilize the same material which is the Aluminum Oxide (Al_2O_3) material to provide thermal coupling. The ceramic posts provide sufficient heat dissipation and can be seen from the two dimensional temperature maps of a +10 V brick operating at 2.3A which are shown in Figure 3, the old version of the power supply which had significantly lower efficiency MOSFET (left) and new upgraded version with high efficiency MOSFETs (right). Even if the obtained improvement are clear, there are two zones, where the location of the converter LT1681 and the location of the FET driver, that still show a very high temperature during operation. For this reason, these chips at the bottom side are coupled to the plate with the application of the Bergquist gap-pad for further reduction of the temperature to the two critical components responsible for heat generation of the power supply.

4.3. Radiation test results

Extensive radiation test campaigns have been on going for close to 5 years. We mostly attempt in finding candidates with acceptable degradation with Total Ionizing Dose (TID) and Neutron Ionizing event loss (NIELs). The Cobalt-60 gamma tests were performed at the CC60 facility

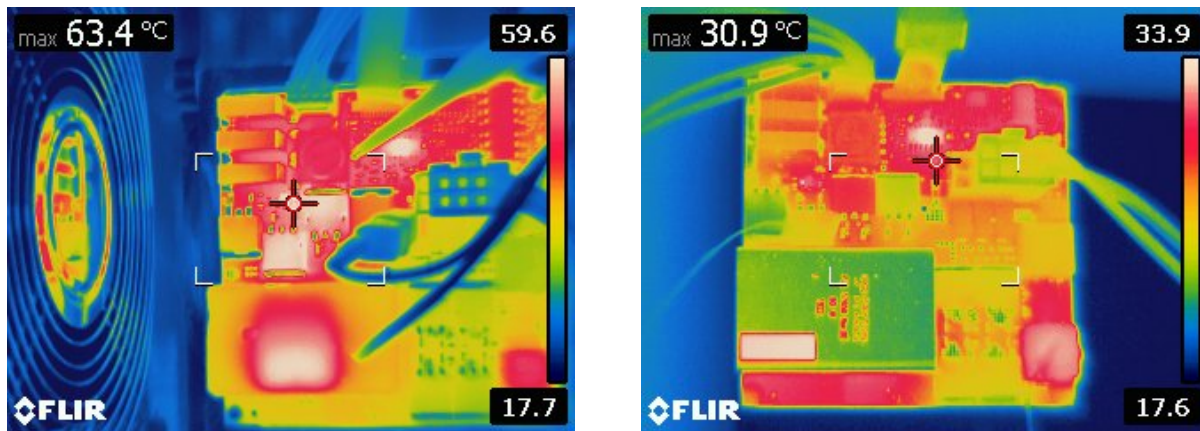


Figure 3: Two dimensional temperature maps of a + 10 V brick operating at 2.3 A with thermal coupling with Aluminum Oxide thermal coupling. These maps have been obtained with the application of a Bergquist gap-pad on the LT1681 and FET drivers. Thermal reading of the previous 8.1.0 version of the power supply (left) and the Thermal reading of current 8.4.2 version of the power supply (right).

at CERN. All irradiation sessions were performed with a dose rate of 3.75 Gy/hr. We placed the test set up (the power supplies and interface PCBs) at about approximately 75 cm from the CC60 source to ensure we receive a maximum dose close to 500 Gy at the center. There were no hard failures of bricks during the TID irradiation study. No transient event phenomena occurred during gamma irradiation, in the power supplies. All the bricks were running and monitored during up to end of the tests with only an output voltage drop of 1 mV/Gy. Since the accepted range of output voltage is 8 to 12 V from the point of load regulators, this drop is completely acceptable due to wide range of input voltage for our front end electronics. Parameters showed expected behaviour as a function of time for output voltage as shown in (Figure 4) and the output current in (Figure 4) both over a 12 hour duration.

5. Overall performance and reliability analysis

The overall performance of the tested low voltage power supplies must meet the stringent specifications of the ATLAS Phase-II LVPS project. Testing is based on two testing stations, both followed by debug and repair sessions. The sessions address protection and monitor circuits and are separated by the burn-in which aims at having the bricks working under stress conditions. At the end of the checkout procedure all the bricks must match the design parameters within the allowed ranges before checkout. Quality control testing at Wits University is ongoing and test benches are operable. The LVPS prototype guarantees over 80.5% efficiency at 2.3 A nominal load and +10V input and able to withstand harsh environments from the overall design.

6. Summary and Outlook

We have built and tested the LVPS bricks which are manufactured in South Africa and tested at Wits University. The reliability and stability of the system has been visibly improved with respect to the previous prototype produced at Wits University with key improvements being the thermal management and slow deviations of the monitored voltages. The project is well on track. More improvements are expected with the final design to include a decrease in clock jitter and stability in output noise and in the clock frequency. Expectedly, no gamma radiation related malfunctioning was detected. The LVPS progress of the ATLAS TileCal have been presented in several meetings and reviews. Further analysis of the LVPS bricks can be used to

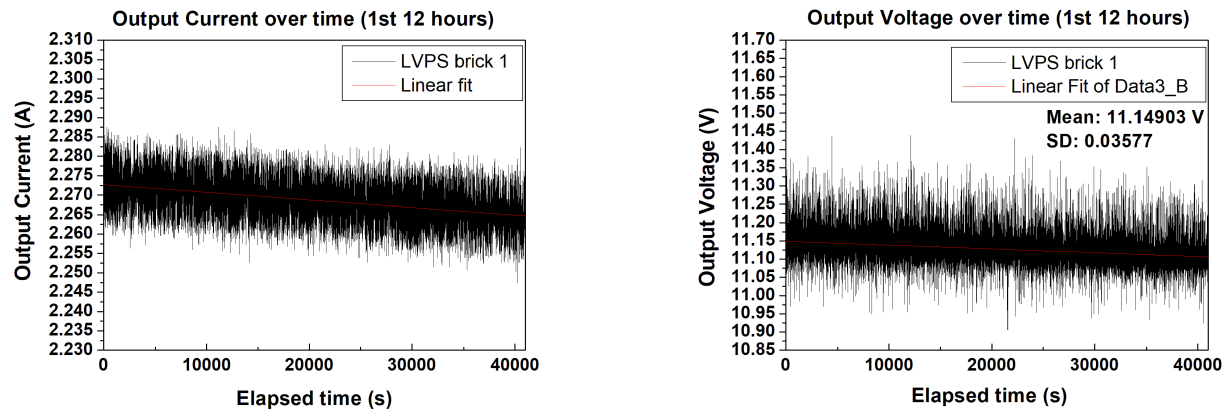


Figure 4: Output Current (A) and output voltage (V) of the LVPS monitored during irradiation testing at the CC60 facility.

gain detailed insight in what causes variations in detector response. Once a brick passes the Quality Assurance tests it will be sent to CERN for installation inside an LVBOX.

References

- [1] ATLAS Collaboration. (2008) The ATLAS Experiment at the CERN Large Hadron Collider. JINST. vol **3** p 150.
- [2] Ryan Mckenzie et al. (2021) The ATLAS Tile Calorimeter performance and its upgrade towards the High Luminosity Large Hadron Collider. Technical report. p 1-4.
- [3] Nkadimeng E et al. (2019) *Proc. SAIP Conf. (Venda)* p 257 - 262
- [4] Lepota T et al. (2019) *Proc. SAIP Conf. (Venda)* p 251 - 256
- [5] LT1681 datasheet, *Technical datasheet* p 1 - 16
- [6] Nkadimeng E and Mellado B. (2020) *Proc. Int. Conf. on Particle Physics and Astrophysics (Moscow)* JPCS Ser. **201** p 589

Search for heavy resonances in the $\ell^+\ell^-\ell^+\ell^-$ final state in association with missing transverse energy using pp collisions at $\sqrt{s} = 13$ TeV with the ATLAS detector

H Tlou¹, A Fadol^{1,2}, B Mellado^{1,3}, O Mtintsilana¹ and X Ruan¹

¹ School of Physics and Institute for Collider Particle Physics, University of the Witwatersrand, Johannesburg, Wits 2050, South Africa

² Institute of High Energy Physics, Chinese Academy of Sciences, Beijing, 100049, China

³ iThemba LABS, National Research Foundation, PO Box 722, Somerset West 7129, South Africa

E-mail: humphry.tlou@cern.ch

Abstract. Search for the presence of a new heavy resonance produced via gluon-gluon fusion and decaying to the four-lepton (4ℓ) final state, in association with missing transverse energy (E_T^{miss}), with $\ell = e, \mu$. The search uses 2015–2018 proton-proton collision data at $\sqrt{s} = 13$ TeV, corresponding to an integrated luminosity of 139 fb^{-1} , collected by the ATLAS detector at the Large Hadron Collider at CERN. The data is interpreted in terms of two models, firstly the $R \rightarrow SH \rightarrow 4\ell + E_T^{\text{miss}}$, where R is a scalar boson, which decays to two lighter scalar bosons (S and H). The S decays to a pair of neutrinos (E_T^{miss}) and the H decays into 4ℓ , through ZZ bosons. The second model is the $A \rightarrow Z(\nu\nu)H(ZZ) \rightarrow 4\ell + E_T^{\text{miss}}$, where A is considered to be a CP-odd scalar which decays to a CP-even scalar H and the Z boson. The Z boson decays to a pair of neutrinos, and the H decays to the 4ℓ final state. The discovery of the Standard Model (SM) Higgs boson imposes questions as to whether there is physics beyond the SM or not. The 4ℓ and the rich E_T^{miss} on the final states, give rise to activities of physics beyond the SM in which we investigate in this search.

1. Introduction

In 2012, two of the Large Hadron Collider (LHC) experiments, A Toroidal LHC Apparatus (ATLAS) and the Compact Muon Solenoid (CMS), independently led to the discovery of the Higgs boson [1, 2]. Its properties are compatible with the Standard Model (SM) Higgs boson. Many studies have been conducted, towards understanding the Higgs boson's properties and couplings to SM particles. Studies are being conducted beyond the SM (BSM), in search for new scalars which may participate in electroweak symmetry breaking. ATLAS and CMS collaborations are actively conducting these searches in various channels. This study is an effort to search for a heavy scalar in the four-lepton (4ℓ , where $\ell = e, \mu$) final state in association with missing transverse energy (E_T^{miss}). The study is highly motivated by the multi-lepton anomalies observed at the LHC and one possible interpretation is the existence of a new scalar [3, 4]. The search focuses on the high mass region of the heavy bosons where the 4ℓ invariant mass ($m_{4\ell}$) is greater than 200 GeV. The data is interpreted in terms of two models,



Figure 1: The Feynman diagrams for the $R \rightarrow SH \rightarrow 4\ell + E_T^{\text{miss}}$ model (left) and the $A \rightarrow Z(\nu\nu)H(ZZ) \rightarrow 4\ell + E_T^{\text{miss}}$ model (right).

Table 1: Summary of MC generators used to model signal and background processes, accuracy in Quantum ChromoDynamics (QCD) and the Parton Distribution Function (PDF) set.

Process	Generator	QCD accuracy	Tune and PDF set
$R \rightarrow SH \rightarrow 4\ell + E_T^{\text{miss}}$	Pythia8 [7]	NLO	A14 NNPDF23LO
$A \rightarrow Z(\nu\nu)H(ZZ) \rightarrow 4\ell + E_T^{\text{miss}}$	MadGraph5+Pythia8 [7, 8]	NLO	A14 NNPDF23LO
$q\bar{q} \rightarrow ZZ^*$	Sherpa+MePs [9, 10]	NLO (0- and 1-jet), LO (2- and 3-jet)	NNPDF30NNLO [11]
$gg \rightarrow ZZ^*$	Sherpa+OpenLoops [9, 12]	LO (0- and 1-jet)	NNPDF30NNLO [11]
$q\bar{q} \rightarrow ZZ^*$ (EW)	Sherpa [9, 10]	LO	NNPDF30NNLO [11]
$ZZZ(4\ell 2\nu, 6\ell 0\nu)$	Sherpa [9, 10]	NNLO	NNPDF30NNLO [11]
$WZZ(5\ell 1\nu)$	Sherpa [9, 10]	NNLO	NNPDF30NNLO [11]
$WWZ(4\ell 2\nu)$	Sherpa [9, 10]	NNLO	NNPDF30NNLO [11]
$t\bar{t}V$ ($V = W/Z$)	MadGraph5+Pythia8 [7, 8]	LO	A14 NNPDF23LO
$t\bar{t}$	Powheg-Box+Pythia8 [7, 13]	NNLO+NNLO	A14 NNPDF23LO
$WZ \rightarrow 3\ell 1\nu$	Powheg-Box+Pythia8 [7, 13]	NNLO	CT10NLO, AZNLOCTEQ6L1 [11]
Z +Jets	Sherpa+Comix+OpenLoops+MePs [9, 10]	NLO (0- and 2-jet), LO (3- and 4-jet)	NNPDF30NNLO [11]

the $R \rightarrow SH \rightarrow 4\ell + E_T^{\text{miss}}$ [3] and the $A \rightarrow Z(\nu\nu)H(ZZ) \rightarrow 4\ell + E_T^{\text{miss}}$ [3, 5, 6] models, where heavy resonances are produced via gluon-gluon fusion. Figure 1 (left) represents the $R \rightarrow SH \rightarrow 4\ell + E_T^{\text{miss}}$, where R is a scalar boson that decays to two lighter scalar bosons, S and H . The mass of S is fixed to 160 GeV and S decays to the SM neutrinos (E_T^{miss}). The scalar H , decays to a pair of Z bosons, which further decays into 4ℓ . To further explore regions with jet activities in the Two-Higgs-doublet scenario, the $A \rightarrow Z(\nu\nu)H(ZZ) \rightarrow 4\ell + E_T^{\text{miss}}$ model is introduced. Figure 1 (right) depicts the $A \rightarrow Z(\nu\nu)H(ZZ) \rightarrow 4\ell + E_T^{\text{miss}}$ model, where A is a CP-odd scalar which decays to a CP-even scalar H and a Z boson. The Z boson decays to neutrinos and the H decays to a pair of Z bosons, which further decay to 4ℓ . The search uses 2015–2018 proton-proton collision data at $\sqrt{s} = 13$ TeV corresponding to an integrated luminosity of 139 fb^{-1} . Signal and background samples are simulated using Monte Carlo (MC) generators according to ATLAS detector configurations. Table 1 summarises the MC generators for signal and background processes and PDF sets used in both signal and background simulation. MC samples are used in the signal optimisation, signal and background parametrisation, to estimate the systematic uncertainties and statistics.

2. Object and event selection

This study requires four charged leptons in the final state and the missing transverse momentum. Table 2 summarises the object requirements and event selection. Electrons are reconstructed by matching the Inner Detector (ID) track to a cluster of energy in the electromagnetic calorimeter. The final track-cluster matching is performed after the tracks have been fitted with a Gaussian-sum filter to account for bremsstrahlung energy losses. The reconstruction of muons requires the matching of the track in the muon spectrometer (MS) to the track in the ID. If a complete track is present in both the MS and ID, the matching is performed through a global fit. The fit uses

Table 2: Summary of physics objects and event selection requirements. The lepton pairs are given by m_{12} and m_{34} .

Physics Objects
ELECTRONS
Loose likelihood criteria applied for electrons with track hit in innermost layer, $E_T > 7 \text{ GeV}$ and $ \eta < 2.47$ Constraint of the interaction point is: $ z_0 \cdot \sin \theta < 0.5 \text{ mm}$ (if track of ID is present)
MUONS
Candidate reconstruction with "loose" identification for $p_T > 5 \text{ GeV}$ and $ \eta < 2.7$ Calo-tagged muons with $p_T > 15 \text{ GeV}$ and $ \eta < 0.1$, segment-tagged muons with $ \eta < 0.1$ Stand-alone and forward ID tracklets restricted to the $2.5 < \eta < 2.7$ region Muon candidates with $p_T > 5 \text{ GeV}$ for combined, stand-alone (with ID hits) and segment-tagged muons. Constraint of the interaction point is: $ d_0 < 1 \text{ mm}$ and $ z_0 \cdot \sin \theta < 0.5 \text{ mm}$ (if track of ID is present)
JETS
anti- k_T jets reconstruction with <i>bad-loose</i> identification, $p_T > 30 \text{ GeV}$ and $ \eta < 4.5$ Require jets with $p_T < 60 \text{ GeV}$ and $ \eta < 2.4$, to pass the pile-up jet rejection at 92% working point (jet-vertex-tagger score > 0.59) Require jets with $p_T < 50 \text{ GeV}$ and $ \eta < 2.5$, to pass the forward pile-up jet rejection at 90% working point
<i>b</i> -TAGGING
A <i>b</i> -tagging weight is applied with the MV2_c10 algorithm [14] to the previously selected jets with $ \eta < 2.5$
OVERLAP REMOVAL
Remove jets within a cone of radius (ΔR) < 0.2 of an electron or $\Delta R < 0.1$ of a muon
Event Selection
QUADRUPLLET SELECTION
Require at least a single quadruplet of leptons composed of two pairs of the same-flavour and opposite-charge, fulfilling these requirements: <ul style="list-style-type: none"> p_T thresholds for the three leading leptons in the quadruplet should be: 20, 15 and 10 GeV Each quadruplet to consist of at most 1 calo-tagged, stand-alone or forward ID muon tracklets <ul style="list-style-type: none"> Require the mass for the leading di-lepton to be: $50 < m_{12} < 106 \text{ GeV}$ Require the mass for the sub-leading di-lepton to be: $m_{\text{threshold}} < m_{34} < 115 \text{ GeV}$ All pairs of leptons in the quadruplet to have $\Delta R(\ell, \ell') < 0.10$ and remove the quadruplet if alternative same-flavour and opposite-charge di-lepton gives $m_{\ell\ell} < 5 \text{ GeV}$. Keep all quadruplets passing this selection
ISOLATION
– Remove the contribution from other leptons of the quadruplet
IMPACT PARAMETER SIGNIFICANCE
– Apply impact parameter significance cut to all leptons of the quadruplet to suppress the background from heavy-flavour hadrons

the hit information from the MS (combined muon) and ID, else the momentum is determined from the ID, and the MS track segment is used as the identification (segment-tagged muon). The reconstruction of jets is performed using the anti- k_T algorithm with a radius parameter $R = 0.4$ [15]. The particle flow (PFlow) objects are used as inputs to the **FastJet** package [16]. In PFlow, the removal of clusters is based on the expected energy being deposited by tracks during jet reconstruction. Prior to jet-finding, the topo-cluster pseudorapidity (η) and ϕ are recomputed with respect to the primary vertex position rather than the detector origin. E_T^{miss} is the imbalance of visible momenta in the plane transverse to the beam axis. It is calculated as the negative sum of the momenta of all identified physics objects (electrons, muons, jets) and the "soft term", that accounts for unclassified soft tracks and calorimeter clusters. This study uses the track-based soft term E_T^{miss} . The combined information from the ID and the calorimeter is used in reducing the effect of pile-up, which degrades the E_T^{miss} performance. The soft term is calculated using the momentum of the tracks associated with the primary vertex, whereas the hard objects have their momentum being computed at the calorimeter level, to include the momentum measurements for neutral particles. After object reconstruction, an overlap-removal

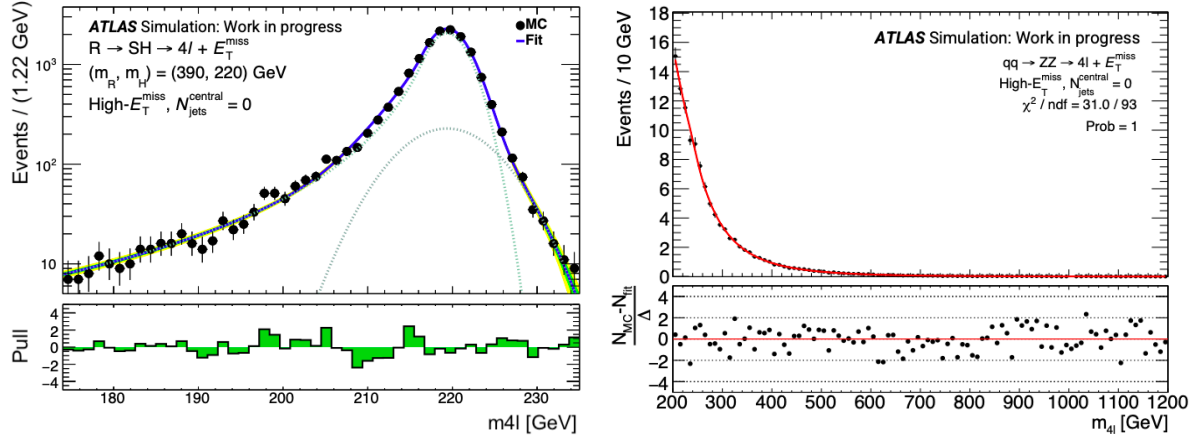


Figure 2: Distribution of the $m_{4\ell}$ for fitting the CB + G PDF (see text) to (390,220) GeV signal mass point for the $R \rightarrow SH \rightarrow 4\ell + E_T^{\text{miss}}$ model (left). Distribution of the $m_{4\ell}$ for an analytical function fit (solid line) to the $qqZZ$ background MC simulation (dots) (right).

procedure is applied to all selected objects to remove ambiguities resulting from objects being reconstructed by several algorithms.

3. Signal optimisation

After the pre-selection described in Section 2, an additional selection depending on the signal model is applied, where the optimisation is quantified by the significance (Z_{Sig}) formula:

$$Z_{\text{Sig}} = \frac{S}{\sqrt{B}}, \quad (1)$$

where S and B represent the signal and background events respectively. Both the signal and the background are considered for $m_{4\ell} > 200$ GeV. The optimisation of the signal is considered for both models with events categorisation. Table 3 summarises the optimal cuts, their representation and Z_{Sig} of each applied cut for the $A \rightarrow Z(\nu\nu)H(ZZ) \rightarrow 4\ell + E_T^{\text{miss}}$ model. The combined Z_{Sig} is obtained by the quadrature sum of all the categories per model after pre-selection. The combined Z_{Sig} is 4.2σ for the $A \rightarrow Z(\nu\nu)H(ZZ) \rightarrow 4\ell + E_T^{\text{miss}}$ model and 6.9σ for the $R \rightarrow SH \rightarrow 4\ell + E_T^{\text{miss}}$ model, where a different signal mass point $(m_A, m_H) = (390, 220)$ GeV is used for calculating the yields.

Table 3: The expected yields for a signal mass point $(m_A, m_H) = (330, 220)$ GeV and Z_{Sig} calculated from the MC simulation at an integrated luminosity of 139 fb^{-1} .

	Signal	$qqZZ$	$ggZZ$	$qqZZ(EW)$	$t\bar{t}V$	VVV	$Z + jets$	WZ	$t\bar{t}$	Z_{Sig}
Pre-selection	60.3 ± 0.1	2492.8 ± 4.4	347.4 ± 0.7	32.7 ± 0.3	38.7 ± 0.5	19.0 ± 0.1	12.2 ± 6.5	5.0 ± 0.3	2.7 ± 0.2	2.5
High- E_T^{miss} & $N_{\text{jets}}^c = 0$	6.1 ± 0.0	113.1 ± 1.2	27.4 ± 0.2	0.5 ± 0.0	1.2 ± 0.1	7.4 ± 0.1	0.9 ± 0.3	1.9 ± 0.2	0.6 ± 0.1	1.1
Low- E_T^{miss} & $N_{\text{jets}}^c = 0$	1.8 ± 0.0	174.6 ± 1.1	34.4 ± 0.2	0.5 ± 0.0	0.1 ± 0.0	0.8 ± 0.0	1.8 ± 1.5	0.5 ± 0.1	0.1 ± 0.0	0.3
High- E_T^{miss} & $N_{\text{jets}}^c \geq 1$	3.1 ± 0.0	12.4 ± 0.3	2.6 ± 0.1	0.4 ± 0.0	4.0 ± 0.2	4.7 ± 0.1	0.1 ± 0.0	0.7 ± 0.1	0.6 ± 0.1	1.4
Low- E_T^{miss} & $N_{\text{jets}}^c \geq 1$	4.6 ± 0.0	42.5 ± 0.5	8.3 ± 0.1	1.2 ± 0.0	1.2 ± 0.1	1.5 ± 0.0	0.1 ± 0.0	0.3 ± 0.1	0.2 ± 0.1	1.4
$N_{b\text{-jets}} \geq 1$	9.1 ± 0.1	67.2 ± 0.5	7.9 ± 0.1	2.4 ± 0.1	30.0 ± 0.4	0.6 ± 0.0	0.1 ± 0.0	0.2 ± 0.1	0.9 ± 0.1	1.9
$ m_{jj}^c - m_Z < 20 \text{ GeV}$	6.7 ± 0.0	43.2 ± 0.3	7.2 ± 0.1	2.1 ± 0.1	0.2 ± 0.0	0.2 ± 0.0	0.2 ± 0.2	0.0 ± 0.0	0.0 ± 0.0	2.0
$ m_{jj}^c - m_Z > 20 \text{ GeV}$	12.8 ± 0.1	191.0 ± 0.6	27.2 ± 0.2	14.6 ± 0.2	1.1 ± 0.1	1.1 ± 0.0	1.0 ± 0.8	0.3 ± 0.1	0.1 ± 0.0	1.9
$N_{\text{jets}}^c = 1$	12.6 ± 0.1	529.2 ± 2.0	82.2 ± 0.3	9.1 ± 0.2	0.7 ± 0.1	1.6 ± 0.0	0.3 ± 0.4	0.6 ± 0.1	0.2 ± 0.1	1.1
Total significance										4.2

4. Signal and background parametrisation

MC simulation is used to parametrise the reconstructed $m_{4\ell}$ distribution of both backgrounds and signals shapes. In signal parametrisation, the narrow-width signal models of $R \rightarrow SH \rightarrow 4\ell + E_T^{\text{miss}}$ and $A \rightarrow Z(\nu\nu)H(ZZ) \rightarrow 4\ell + E_T^{\text{miss}}$ models are modelled using a Crystal ball (CB) plus Gaussian (G) functions. The sum of these functions is described as:

$$P_{\text{signal}}(m_{4\ell}) = f_{\text{CB}} \times \text{CB}(m_{4\ell}; \mu, \sigma_{\text{CB}}, \alpha_{\text{CB}}, n_{\text{CB}}) + (1 - f_{\text{CB}}) \times \text{G}(m_{4\ell}; \mu, \sigma_{\text{G}}). \quad (2)$$

Both CB and G functions peak at a mean value of $m_{4\ell}(\mu) = m_H$ which is the reconstructed $m_{4\ell}$ of (m_R, m_H) and (m_A, m_H) signal mass points. The resolution of the $m_{4\ell}$ distribution is affected by σ_{CB} and σ_{G} parameters. The tail position of the non-Gaussian distribution is adjusted using the α_{CB} parameter, while its slope is handled by the n_{CB} parameter. The relative normalisation between the Gaussian and Crystal ball functions is taken care of by f_{CB} parameter. The $P_{\text{signal}}(m_{4\ell})$ function is fitted to simulated signal samples to determine the values of the function's parameters. For simplicity and to avoid lower statistics, the CB + G PDF fit is performed to the inclusive lepton channel only, to extract the parameter shown in Eq. 2. Figure 2 (left) shows the CB+G PDF fit to $R \rightarrow SH \rightarrow 4\ell + E_T^{\text{miss}}$. This is one of the sixty five signal mass points for $R \rightarrow SH \rightarrow 4\ell + E_T^{\text{miss}}$ and the PDF fit is performed for all categories. The $m_{4\ell}$ shape of the backgrounds is obtained from MC simulation and parametrised using an empirical function. Four background templates are used as $qqZZ$, $ggZZ$, VVV and other, which is a combination of WZ , $q\bar{q} \rightarrow ZZ(EW)$ and $t\bar{t}$ backgrounds. Each of the background template is fitted with an analytical function for $m_{4\ell}$ in the range of 200-1200 GeV, as follows:

$$f_{qqZZ, ggZZ, VVV, \text{other}}(m_{4\ell}) = H(m_0 - m_{4\ell})f_1(m_{4\ell})C_1 + H(m_{4\ell} - m_0)f_2(m_{4\ell})C_2, \quad (3)$$

where:

$$f_1(m_{4\ell}) = \left\{ \frac{1}{2} + \frac{1}{2} \text{erf} \left(\frac{m_{4\ell} - a_1}{a_2} \right) \right\} \cdot \frac{1}{1 + \exp \left(\frac{m_{4\ell} - a_1}{a_3} \right)}, \quad (4)$$

$$f_2(m_{4\ell}) = (1 - m_{4\ell})^{b_1} \cdot m_{4\ell}^{(b_2 + b_3 \cdot \ln(m_{4\ell}))}, \quad C_1 = \frac{1}{f_1(m_0)}, \quad C_2 = \frac{1}{f_2(m_0)}, \quad (5)$$

where f_1 models the ZZ threshold around $2m_Z$ and f_2 describes the high mass tail. The a_i and b_i are shape parameters obtained by fitting the $m_{4\ell}$ distribution for each category. The transition between functions f_1 and f_2 is given by m_0 and it is performed by the Heaviside step function $H(x)$ around $m_0 = 260$ GeV for $qqZZ$, $ggZZ$ and VVV , and $m_0 = 240$ GeV for other backgrounds. The transition point is determined by optimising the function's smoothness. C_1 and C_2 are used to ensure the continuity of the function around m_0 . Figure 2 (right), shows the High- E_T^{miss} and $N_{\text{jets}}^{\text{Central}} = 0$ category with MC simulation fitted with Eq. 3, for the $qqZZ$ background. All background processes are also fitted for each category and for both models.

5. Statistical procedure and upper limits

The upper limits on the cross section times the branching ratio for a heavy resonance are obtained as a function of m_H with the Confidence Limits (CL_s) procedure. The limits are obtained using the unbinned profile likelihood fits, using $m_{4\ell}$ as the discriminant. The profile likelihood is the product of a Poisson term, representing the probability for observing n events and a weighted sum of both signal and background probability distribution functions (PDFs), which are evaluated at all observed events. The PDFs are given by $f_{S_M}(m_{4\ell})$ and $f_B(m_{4\ell})$ and normalisations by S_M and factor B :

$$\mathcal{L}(m_{4\ell}^1, \dots, m_{4\ell}^n | \sigma_M) = \text{Pois}(n | S_M + B) \left[\prod_{i=1}^n \frac{S_M f_{S_M}(m_{4\ell}^i) + B f_B(m_{4\ell}^i)}{S_M + B} \right], \quad (6)$$

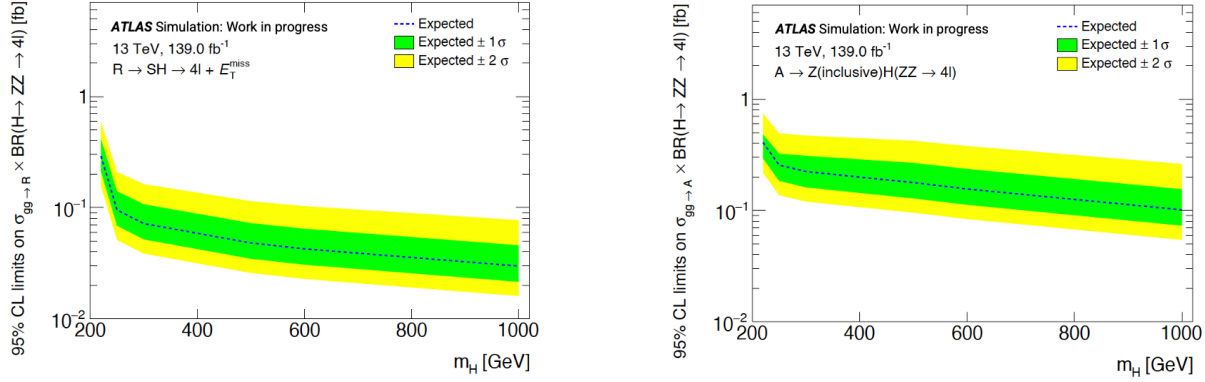


Figure 3: Expected upper limits at 95% confidence level on the $\sigma_M \times \text{BR}(H \rightarrow ZZ \rightarrow 4\ell)$ for a heavy resonance have been set for both models.

The parameters of interest (POI) in the fit enter the likelihood inside the expected signal yield S_M , where the POI is the product of the first two parameters:

$$S_M = \sigma_M \times \text{BR}(H \rightarrow ZZ \rightarrow 4\ell) \times (A \times E) \times \int L dt, \quad (7)$$

where $A \times E$ is the signal acceptance, and the integral is the integrated luminosity of the dataset. The CL_s are used for calculating the upper limits for both the $R \rightarrow SH \rightarrow 4\ell + E_T^{\text{miss}}$ and $A \rightarrow Z(\nu\nu)H(ZZ) \rightarrow 4\ell + E_T^{\text{miss}}$ models as seen in Figure 3.

6. Conclusions

The search for new heavy resonances based on the multi-lepton anomalies observed at the LHC is performed. The $R \rightarrow SH \rightarrow 4\ell + E_T^{\text{miss}}$ and $A \rightarrow Z(\nu\nu)H(ZZ) \rightarrow 4\ell + E_T^{\text{miss}}$ models are used to interpret the data. The search uses 2015–2018 proton-proton collision data at $\sqrt{s} = 13 \text{ TeV}$, corresponding to an integrated luminosity of 139 fb^{-1} . The signal optimisation is computed and the combined Z_{Sig} is 6.9σ for the $R \rightarrow SH \rightarrow 4\ell + E_T^{\text{miss}}$ model and 4.2σ for the $A \rightarrow Z(\nu\nu)H(ZZ) \rightarrow 4\ell + E_T^{\text{miss}}$ model. Expected upper limits have been set for both models.

References

- [1] Aad G *et al.* (ATLAS) 2012 *Phys. Lett. B* **716** 1–29 (*Preprint* 1207.7214)
- [2] Chatrchyan S *et al.* (CMS) 2012 *Phys. Lett. B* **716** 30–61 (*Preprint* 1207.7235)
- [3] von Buddenbrock S, Chakrabarty N, Cornell A S, Kar D, Kumar M, Mandal T, Mellado B, Mukhopadhyaya B, Reed R G and Ruan X 2016 *Eur. Phys. J. C* **76** 580 (*Preprint* 1606.01674)
- [4] Buddenbrock S, Cornell A S, Fang Y, Fadol Mohammed A, Kumar M, Mellado B and Tomiwa K G 2019 *JHEP* **10** 157 (*Preprint* 1901.05300)
- [5] von Buddenbrock S, Cornell A S, Iarilala E D R, Kumar M, Mellado B, Ruan X and Shrif E M 2019 *J. Phys. G* **46** 115001 (*Preprint* 1809.06344)
- [6] Dorsch G C, Huber S J, Mimasu K and No J M 2014 *Phys. Rev. Lett.* **113** 211802 (*Preprint* 1405.5537)
- [7] Sjöstrand T, Ask S, Christiansen J R, Corke R, Desai N, Ilten P, Mrenna S, Prestel S, Rasmussen C O and Skands P Z 2015 *Comput. Phys. Commun.* **191** 159 (*Preprint* 1410.3012)
- [8] Alwall J, Herquet M, Maltoni F, Mattelaer O and Stelzer T 2011 *JHEP* **06** 128 (*Preprint* 1106.0522)
- [9] Gleisberg T *et al.* 2009 *JHEP* **02** 007 (*Preprint* 0811.4622)
- [10] Höche S, Krauss F, Schumann S and Siebert F 2009 *JHEP* **05** 053 (*Preprint* 0903.1219)
- [11] Ball R D *et al.* (NNPDF) 2015 *JHEP* **04** 040 (*Preprint* 1410.8849)
- [12] Cascioli F *et al.* 2014 *JHEP* **01** 046 (*Preprint* 1309.0500)
- [13] Alioli S, Nason P, Oleari C and Re E 2010 *JHEP* **06** 043 (*Preprint* 1002.2581)
- [14] Aad G *et al.* (ATLAS) 2016 *JINST* **11** P04008 (*Preprint* 1512.01094)
- [15] Cacciari M, Salam G P and Soyez G 2008 *JHEP* **2008** 063–063 (*Preprint* 0802.1189)
- [16] Cacciari M, Salam G P and Soyez G 2012 *Eur. Phys. J. C* **72** 1896 (*Preprint* 1111.6097)

The replacement and refurbishment of Gap Scintillator Counters for the ATLAS Tile Calorimeter Phase I Upgrade

G Mokgatitswane¹, T J Lepota¹ and B Mellado^{1,2}

¹ School of Physics and Institute for Collider Particle Physics, University of the Witwatersrand, Johannesburg, Wits 2050, South Africa

² iThemba LABS, North, Empire Road, Braamfontein 2000, Johannesburg

E-mail: gaogalalwe.mokgatitswane@cern.ch

Abstract. We report on the replacement of E3 and E4 scintillators (Crack) and refurbishment of Minimum Bias Trigger Scintillator (MBTS) counters as part of Phase I upgrade of the Tile Calorimeter of the ATLAS experiment during the long shutdown 2. The Crack and MBTS counters, situated between the central and extended Tile Calorimeter barrels, are used for correcting the electromagnetic energy responses and for providing inputs to the trigger, respectively. During the LHC Run 2 data-taking period in 2015-2018, the Crack and MBTS scintillators have deteriorated by radiation and had to be replaced with more radiation-hard scintillators and optimised geometry for Run 3. The Phase I upgrade has been ongoing since the beginning of the LHC LS2. The upgrade activities which were finalized with a strong contribution from South Africa consisted of the re-design of the Crack and MBTS detector modules, their assembly, qualification and characterization using radioactive sources (strontium-90 and cesium-137), as well as their installation on the ATLAS detector. The University of the Witwatersrand was previously involved in the radiation qualification and selection of the scintillator material to be used in the counter production.

1. Introduction

During Phase I upgrade of the ATLAS Experiment, the Tile Calorimeter (TileCal) completely replaced the Crack and MBTS scintillators since they were degraded by high levels of radiation (up to 10^3 Gy/year) during the LHC Run 2 data-taking period spanning 2015-2018 [1]. Prior to the first run of the LHC at centre-of-mass energy of 7 TeV of proton-proton (pp) head-on collision (Run 1), radiation background simulations were conducted to identify and quantify the detrimental effects of these backgrounds on the performance of detector components. The general-purpose Monte Carlo particle transport programs FLUKA [2] and GEANT3-CALOR (GCALOR) [3] were used to predict the background radiation in ATLAS. It was predicted that the sub-detector components in close proximity to the beam axis would receive higher radiation dose rates.

The MBTS counters were originally intended to operate only in the early running of the LHC, where the vast majority of crossings would not result in large pile-up. Thus, the counters would serve to provide a trigger to discriminate beam-beam interactions from beam-gas interactions. Originally, there were no TileCal electronic channels available for the MBTS counter

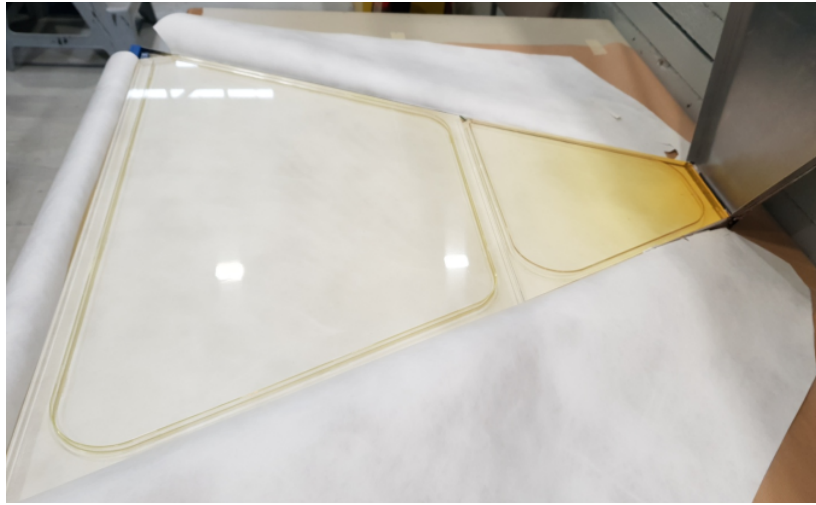


Figure 1. A photograph of one of the MBTS counters after irradiation (Run 2).

readout. To create the needed channels, one-eighth of the Crack counters were removed from the detector, and the light signals from the MBTS counters were connected to the optical cables originally used for the missing Crack counters. Later, for Run 2, additional channels were made available by the merging of the light signals from adjacent E1 counters, and the missing Crack scintillators were replaced.

Figure 1 shows one sector of the MBTS counter, where intense radiation damage is indicated by the yellowing of the scintillator (loss of up to 95% of the light yield). The radiation dose at the inner radius was of the order of 20 MRad. The Crack counters are located at a lower rapidity, but in the case of E4, in a region corresponding to electromagnetic shower max. This position results in a higher radiation dose, but an accurate sampling of the energy deposited by electrons and photons in this region is crucial for improving the energy resolution degraded by the material present.

2. Crack and MBTS geometry optimisation and scintillating materials used in counter production

2.1. Crack counters

The Crack counters were extended from a maximum pseudo-rapidity coverage from up to 1.6 to up to 1.72 (see Figure 2), motivated by the need to improve the e/γ energy resolution in this extended range. This is supported by multivariate analysis (MVA) calibration of the reconstructed electron energy in the extended range [4], which shows a significant improvement in the energy resolution (see Figure 3). Based on simulation and rate studies, the decision was made to have the E3 section cover the rapidity range from 1.2 to 1.6, and to then use the freed-up E4 channels to cover the region from 1.6 to 1.72. The rate in the old E3 counter (1.2–1.4) was significantly smaller than in the old E4 counter (1.4–1.6), so combining the two rapidity regions in the same readout did not seriously affect the performance. This results in reasonable rates for both the new E3 and E4 counters.

A new Crack counter is composed of a radiation hard and high-performing PolyvinylToluene (PVT) based plastic scintillator (EJ-208). It has a long emission spectrum (435 nm) which provides additional resistance to radiation damage. The wavelength shifting (WLS) Y-11 optical fibers (high light yield) are used to collect light emitted by the scintillating tiles (blue to green shifters), which is then transported by clear optical fiber cable to the photomultiplier tubes in

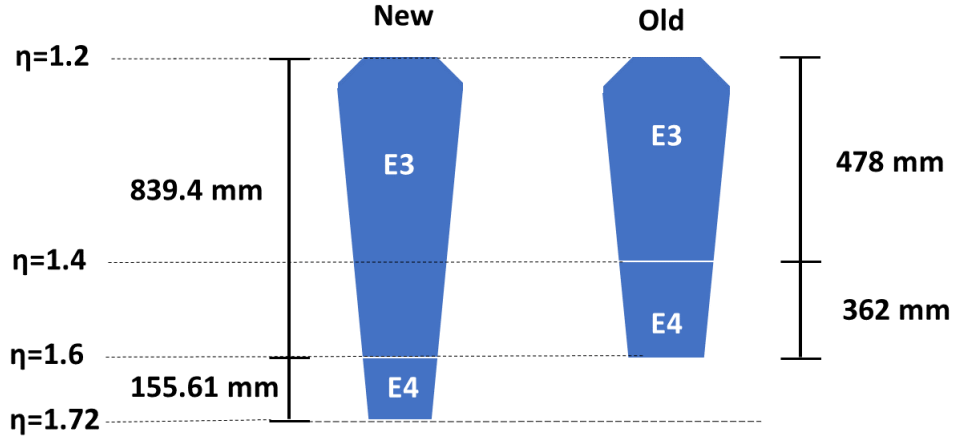


Figure 2. Sketch of the geometry of old Crack scintillation counter vs. the geometry of the new counters.

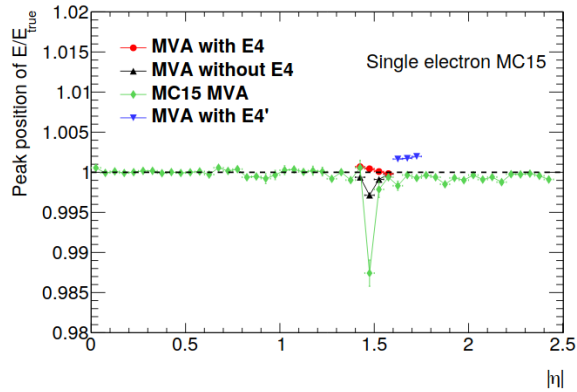


Figure 3. Resolution as a function of pseudorapidity for electrons [4].

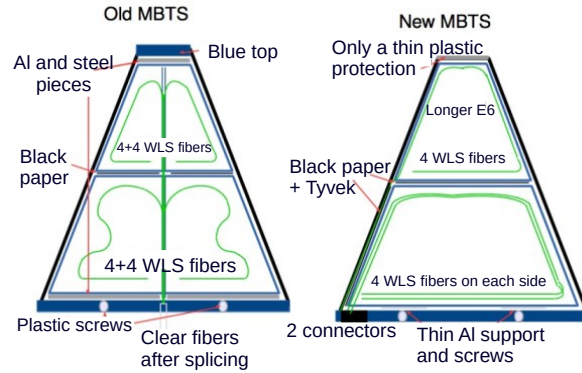


Figure 4. MBTS geometry optimisation.

the TileCal girder.

2.2. Minimum Bias Trigger Scintillators (MBTS)

During the studies of potential radiation hard plastic scintillator, it was found that commercially available plastic scintillators would still succumb to high doses in the MBTS region and hence degrade. In order to counterbalance the degradation effect, several optimisations were proposed. The first optimisation was the replacement of one 20 mm thick scintillator plate with a sandwich of four 5 mm scintillators, each wrapped individually with Tyvek (a material made of 100% high-density polyethylene, acting as a diffuser).

One reason for using thin plates was to allow for oxygen diffusion into the scintillators, which plays a vital role in annealing of radiation induced optical color centers. This phenomenon improves light transmission and therefore helps in recovery of scintillator slabs after exposure to high energy particles. The second optimisation was the placement of the WLS fibres in the grooves on both sides of the large (outer) plates, to improve the light collection properties, as opposed to several fibres in the same groove on one side [5] (see Figure 4)



Figure 5. Assembly of a Crack counter.

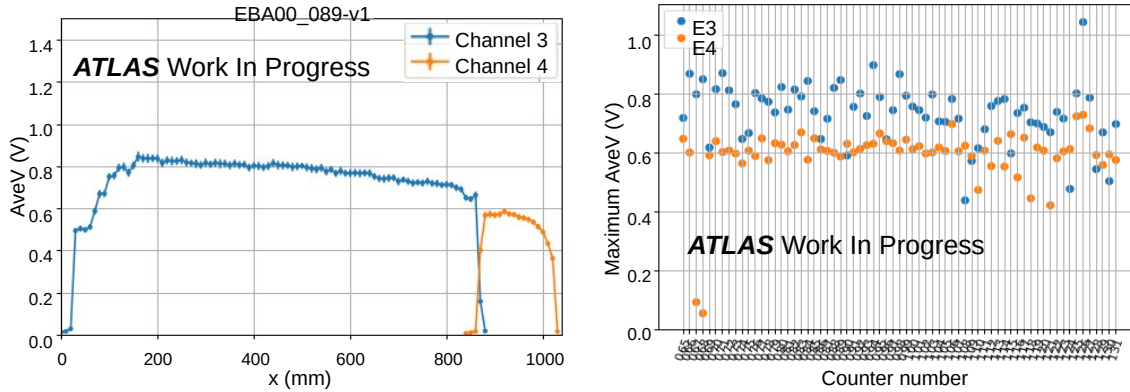


Figure 6. Fine scan (10 mm step) of EBA-089 counter (left) and the highest signal output for all EBA counters (right).

3. Assembly of Crack and MBTS counters

A Tyvek was used to wrap each scintillator slab [5], together with their corresponding coupled WLS optical fibers. Tyvek is specially designed to trap the scintillation light through internal reflection and also provides mechanical protection. The wrapped slabs were then placed inside the aluminium cover constructed to house the scintillator slabs, providing mechanical protection as well as eliminating the possibilities of light leakage. Figure 5 is shown a Crack counter being assembled. A standard assembly procedure was followed for both counters.

4. Qualification and characterization of assembled counters

Prior to installation of the assembled counters on the ATLAS detector, their quality had to be assured. The certification and characterization was performed using ^{90}Sr and ^{137}Cs radioactive sources located at CERN B175 laboratory [6].

4.1. ^{90}Sr tests

The E3 and E4 segments of the counter were tested using ^{90}Sr scans. The experimental setup comprised of a light-tight scan box containing a photomultiplier tube (PMT), a high voltage source to supply the PMT with 700 V, clear optical fiber cable (6 fibers) to connect the counter to the PMT, a digital multimeter for readout, ^{90}Sr β -electron source of 25 MBq activity and recording system to record the data [6].

The E3 and E4 segments of the counter were both evaluated to check for any possible light leaks. Prior to performing ^{90}Sr scans, the pedestal was measured where the signal across the PMT was read without ^{90}Sr source on the counter segments. After measuring the pedestal, the source was then introduced and moved along the x -axis of the counter while taking the reading in each step. Figure 6 shows a plot of PMT average voltage (aveV) response versus source position (x) on the scintillator and the maximum aveV output for all EBA counters (right).

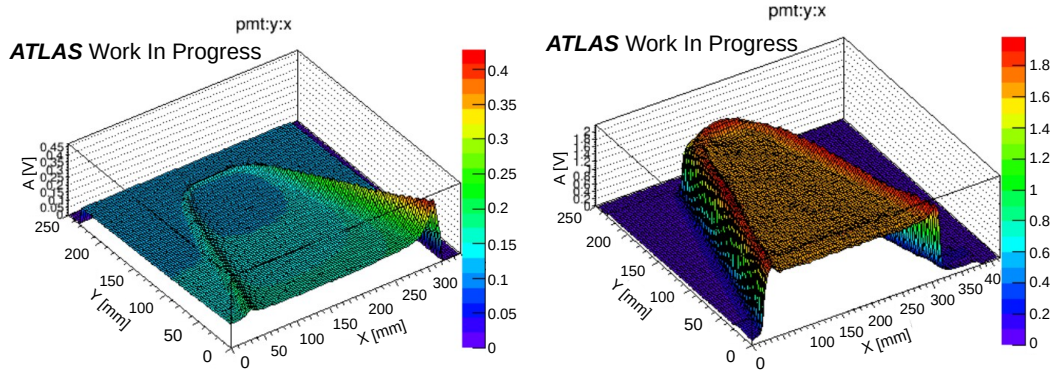


Figure 7. ^{90}Sr 2D scans of the old inner MBTS UPS923A with 4x old WLS Y-11 fibres (left) and new inner MBTS EJ200 with 1x new WLS Y-11 (right).

The low response of E4 segments for counters 67 and 68 (special counters) is because of using orange fibers for readout. Orange fibers attenuate more light due to short light attenuation length ($> 1.5\text{ m}$) in comparison with green fibers ($> 3.5\text{ m}$), hence the response was expected. The performance of orange fibers would be studied during Run 3 and compared with green fibers.

4.2. ^{90}Sr scanning of new and old inner MBTS scintillators

The assessment of the performance of old and new inner MBTS scintillators from the C-Side of ATLAS was conducted by testing their response to a ^{90}Sr β -electron source. The signal generated by the PMT was measured as a function of radiation source position and a 2D scan of signal was measured in the x and y direction over the inner MBTS scintillator. Figure 7 shows 2D scans of a 20 mm thick old inner MBTS UPS923A with 4x old WLS Y-11 green fibres (left) and a new inner MBTS EJ200 scintillator with 1x new WLS Y-11 green fibre (right). According to the results, response of the old scintillator to ^{90}Sr was low in comparison with the new EJ200 scintillator, which was attributed to degradation undergone by the old scintillators during Run 2. However, the old WLS Y-11 fibres appeared to be less damaged since their response was comparable to that of new fibres.

4.3. ^{137}Cs tests

The MBTS counters were evaluated using the ^{137}Cs system from a spare extended barrel (EB) module. The ^{137}Cs γ source of 250 MBq activity embedded in the metal capsule is transported by liquid flow inside the tubes passing towards the MBTS counter [7]. The counter was attached to the edge of EB module, where the tubes are going out of the calorimeter module.

When a source approaches the counter, photons with the energy $E_\gamma=0.662\text{ MeV}$ excite light emission in the scintillating slabs and that allows a measurement of the optical quality of the slabs and fibres. The inner (E6) and outer (E5) counters were each connected to PMT2 and PMT14, respectively, using a clear optical fibre cable (3 m). Figure 8 shows plots of ADC counts versus trigger (after subtracting the pedestal) as the source travels towards the MBTS counter (left) and a zoomed peak showing the maximum ADC count value for the inner counter (right).

The maximum ADC counts for inner and outer counters were calculated by taking the integral of the peaks. The limits for integration on the x -axis (trigger) were defined by fixing the threshold at 50 ADC counts. Since the speed of ^{137}Cs source travelling through the tube would differ from run to run, the maximum ADC integral value obtained was divided by width of the peak to get an average value. Figure 9 shows the relative maximum ADC integral and average values versus ϕ position of the MBTS detector modules for side C of ATLAS.

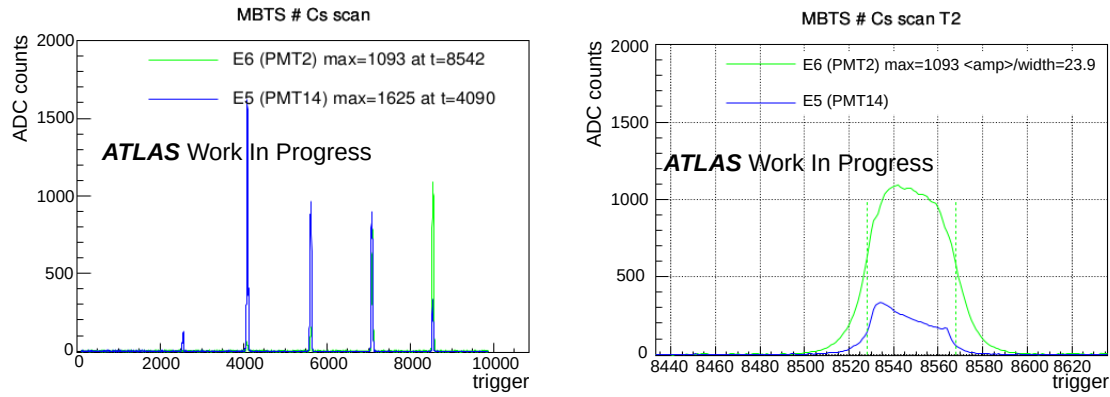


Figure 8. Signal response of the inner and outer MBTS counters to ^{137}Cs source.

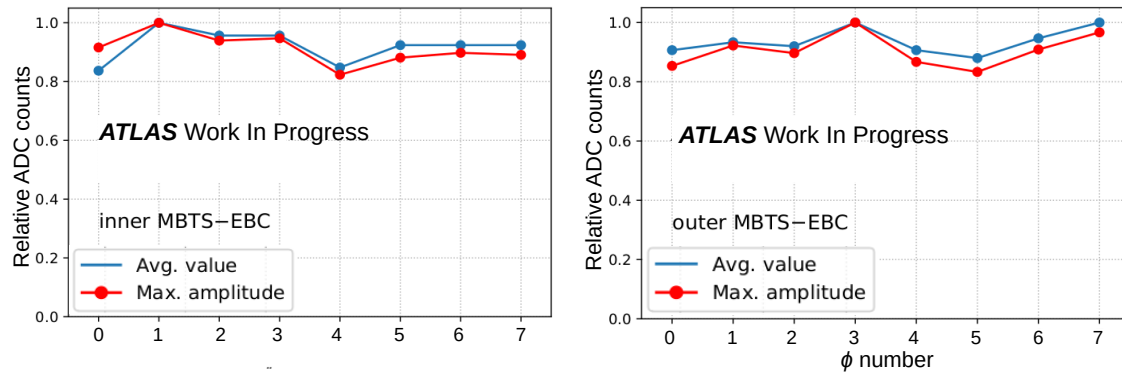


Figure 9. Relative ADC counts of maximum amplitude and average for side-C inner counters (left) and outer counters(right).

5. Conclusion

The Phase I upgrade at CERN commenced since the beginning of LHC long shutdown 2 where the TileCal was completely replacing and refurbishing the E3 and E4 and MBTS counters. These counters were degraded by high radiation levels during the LHC Run 2 and had to be replaced with high-performing and more radiation hard scintillator prior to Run 3. Both counters have undergone several improvements with respect to LHC Run 1 and Run 2 to maximise the light yield and their performance efficiency. Phase I upgrade was completed with a strong contribution from South Africa.

References

- [1] Aad G *et al.* (ATLAS) 2011 Letter of Intent for the Phase-I Upgrade of the ATLAS Experiment Tech. rep. CERN Geneva (CERN-LHCC-2011-012)
- [2] Ferrari A, Sala P R, Fassò A and Ranft J 2005 *FLUKA: A multi-particle transport code (program version 2005)* CERN Yellow Reports: Monographs (Geneva: CERN)
- [3] Zeitnitz C and Gabriel T 1994 *Nucl. Instrum. Meth. A* **349** 106–111
- [4] Durglishvili A 2020 Ph.D. thesis CERN (CERN-THESIS-2020-110)
- [5] Scheu S, Kaspar H, Robmann P, van der Schaaf A and Truol P 2006 *Nucl. Instrum. Meth. A* **567** 345–349
- [6] Baranov V *et al.* 2018 *Nucl. Instrum. Methods Phys. Res. B* **436** 236–243
- [7] Blanchot G *et al.* 2020 *J. Instrum.* **15** 03017

Quality assurance testing of the ATLAS Tile-Calorimeter Phase-II upgrade low-voltage power supplies

R Mckenzie¹, E Nkadimeng¹, R Van Rensburg¹, T Lepota¹, N Njara¹
and B Mellado^{1,2}

¹University of the Witwatersrand, School of Physics and Institute for Collider Particle
Physics, Johannesburg, South Africa

² iThemba LABS, National Research Foundation, PO Box 722, Somerset West 7129, South
Africa

E-mail: ryan.peter.mckenzie@cern.ch

Abstract. The TileCal is a sampling calorimeter that forms the central region of the hadronic calorimeter of the ATLAS experiment. This detector is to undergo its Phase-II upgrade during Long-Shutdown 3, in the years from 2025 to mid-2027, in preparation for the start of operation of the HL-LHC. The TileCal phase-II upgrade consists of numerous elements such as the LVPSs which reside on-detector. A total of 256 LVPSs provide the TileCal on-detector electronics with +10 V DC power. An individual LVPS consist of a metallic box which contains an Embedded Local Monitoring Board attached to a motherboard, a fuse board, and eight transformer-coupled buck converters (Bricks) which are mounted to a cooling plate. Access to the Bricks is limited to only once per year due to their location within the inner-barrel. If a Brick experiences a failure it can be offline for up to a year resulting in the front-end electronics that it services being offline for this extended period as well. Therefore, the reliability of the Bricks is a key concern that needs to be addressed during their production. South Africa has committed to the production of 1024 Bricks which constitutes half of all the Bricks required. In order to ensure the reliability of these Bricks, once installed on-detector, quality assurance testing is implemented. These proceedings will provide an overview of the TileCal Phase-II upgrade, the motivation, and application for quality assurance testing of the Bricks, the development of the required apparatus as well as preliminary results.

1. Introduction

The TileCal is a sampling calorimeter that forms the central section of the Hadronic calorimeter of the ATLAS experiment [1]. It performs several critical functions within ATLAS such as the measurement and reconstruction of hadrons, jets, hadronic decays of τ -leptons and missing transverse energy. It also contributes to muon identification and provides inputs to the Level 1 calorimeter trigger system.

The detector is located in the pseudorapidity region $|\eta| < 1.7$ ¹ and is partitioned into in a central barrel, known as Long Barrel, which is itself partitioned into two barrel regions (LBA and LBC). Two Extended Barrels (EBA and EBC) are located on either side of the Long Barrel. Each

¹ The pseudorapidity (η) is defined in terms of the polar angle θ as $\eta = -\ln \tan(\theta/2)$.

current using six gains. A FENICS also contains two calibration systems, namely the charge injector system utilized for physics signal readout calibration, and the current injection system for the integrator readout. A Main Board (MB) is located within each MD of the TileCal. A single MB interfaces with twelve FENICS and one Daughter Board (DB). A MB digitizes the low- and high-gain signals received from the FENICS, which are then sent to its associated DB. The DBs are the primary interface between the on- and off-detector electronics and are mounted atop every MB. A DB transmits detector data to the off-detector electronics, receives and distributes the LHC clock, configurations, as well as slow-control commands. The High Voltage (HV) distribution system provides regulated HV power to the PMTs. It consists of off-detector HV Remote-boards that provide the primary HV, received from adjacent HV supply boards to the passive Bus-boards located within the MDs of all modules via 100m long cables. These Bus-boards then distribute the HV power to the HVADs. The three stage Low-Voltage (LV) system provides LV power to the Front-End electronics located within the SDs. The first stage of the LV system resides off-detector and is comprised of Auxiliary boards, that provide on/off control of the individual Bricks within a Low Voltage Power Supply (LVPS), as well as 200 V DC power supplies. A LVPS, of which one is located on the end of every SD, is comprised of eight transformer-coupled buck converters (Bricks) that function to step down the 200 V DC, received from the off-detector power supplies to 10 V DC. The 10 V DC power is then routed to point-of-load regulators which perform the final stepping down to that required by the local circuitry within the SDs. There is also an Embedded Local Monitoring Board (ELMB), that digitizes the signals received from the Bricks which are then sent to the Detector Control System (DCS) [3].

3. The Low-voltage power supply Bricks

A Phase-II Brick, of which there will be a total of 2048 within TileCal, provides a nominal output current of 2.3 A. These Bricks are of an iterative design with the latest version being the V8.4.2. As we can observe in Figure 2, at the centre of its design is the LT1681 controller chip [4]. It is dual transistor forward synchronous controller from Linear Technologies that operates at a fundamental frequency of 300 kHz. The LT1681 output clock pulse width is controlled via two inputs, the first of which is a slow feedback path that monitors the feedback voltage with a bandwidth of approximately 1 kHz. The second input is a fast feedback path that monitors the current through the low-side transistor on the primary side. The output clock is sent to the FET drivers, which perform the switching on the primary side. The design utilizes synchronous switching, That is, both the high-side and low-side transistors turn on and conduct for the duration that the output clock is in the high state, and both are off when the clock is in the low state. When the FETs conduct, current flows through the primary windings of the transformer, which then transfers energy to the secondary windings. The buck converter is implemented on the secondary side of the transformer. The output side also contains an additional inductor-capacitor stage for the filtering of noise. Voltage feedback for controlling the output voltage is provided.

Table 1. V8.4.2 Brick protection circuitry trip parameters

Protection circuitry	Trip parameters
Over voltage protection	11.50 V - 12.00 V
Over current protection	10.24 A - 10.75 A
Over temperature protection	70 °C \geq

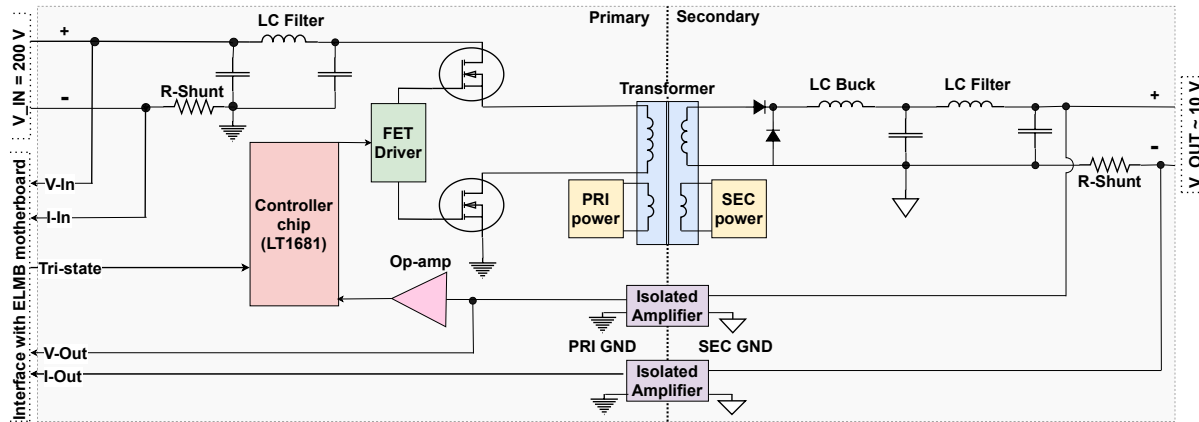


Figure 2. An updated functional block diagram of a Brick [2].

A Brick measures six analog signals and sends them to the ELMB motherboard, which include input voltage and current, output voltage and current, and the temperature readings from two points on the brick (primary and secondary side switches). In-built protection circuitry is also present in the Brick design in the form of over-voltage protection, over-current protection, and over-temperature protection. The purpose of this in-built protection is to initiate a trip if any of the trip criteria in Table 1 are met. This serves to limit damage to both the Brick as well as the electronics to which it provides power.

4. Quality assurance testing

Quality assurance testing plays a key role in the manufacturing process of electronics that require a high degree of reliability, as in the case of the Bricks. The emphasis placed on the reliability of the Bricks is due to their location within the inner-barrel of ATLAS which results in limited access on the order of once per year. Therefore a failed Brick and the electronics to which it provides power can be offline for up to a year. To prevent this outcome a quality assurance testing procedure illustrated in Figure 3 was developed. The procedure consists of four distinct steps namely the Visual inspection, Initial testing, Burn-in and Final testing steps.

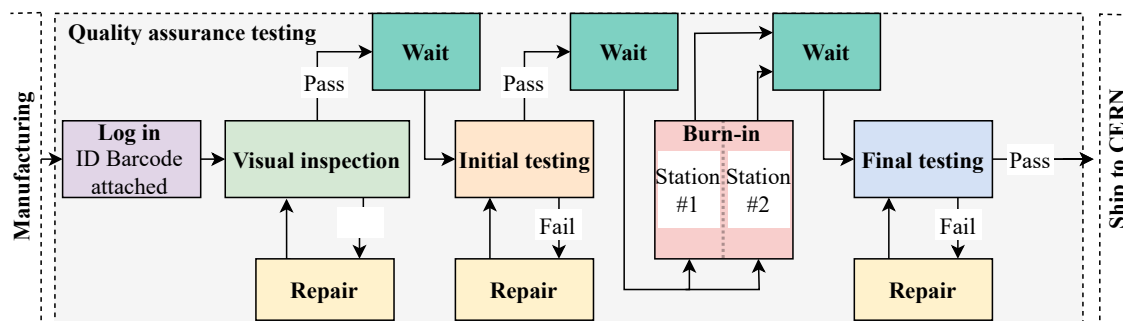


Figure 3. The quality assurance testing procedure for the Brick production.

4.1. Visual inspection

The Visual inspection step functions to detect macroscopic manufacturing defects. Automated visual inspection is undertaken at the assembly house. However, this inspection is performed

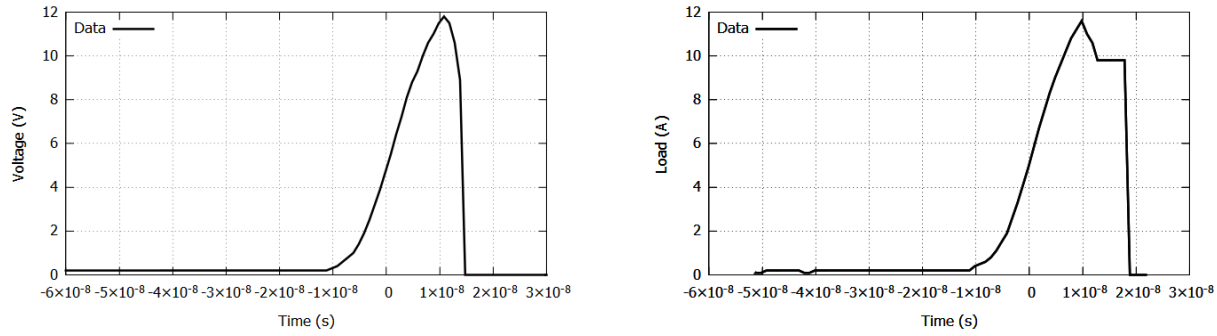


Figure 4. Brick over-voltage protection test data illustrating a pass (left). Brick over-current protection test data illustrating a failure (right). Data taken using a V8.4.2 Brick.

prior to the manual attachment of the thermal posts and the manual soldering of the transformer and connectors to the Bricks. Due to this an additional visual inspection is undertaken by a Brick quality assurance expert upon arrival at the testing facility.

4.2. Initial/Final testing

Initial testing and Final testing make use of the same testing apparatus and procedure. They are differentiated by having occurred either before or after Burn-in testing, respectively. Both of these tests serve to ensure that the Bricks are operating within their design parameters by assessing various performance metrics. Examples of some of these metrics are the maximum startup delay, minimum output voltage, over-voltage trip point and over-current trip point. These tests are facilitated by the Initial/Final test station. The operating principle of this test station is to emulate the required input and output stages that a Brick requires for operation while piggybacking off of the Bricks inbuilt analogue monitoring hardware to monitor its performance. The input stage consists of a 200 V DC power supply which provides the input power for the Brick to step-down as well a low-voltage power supply which is used to send the Brick enable signal to power it on via a custom Interface board. The Interface board is also used to interface between the Brick and a National Instruments data-acquisition card for the transfer of the analog data to a PC for display and recording on a custom LabVIEW control program. The output stage consists of a dummy-load which converts the stepped down power received from the Brick into heat to be dissipated. An oscilloscope is used to measure the output clock frequency of the LT1681 controller chip by attaching a probe to a via which is itself connected to the output clock pin. The Initial/Final test station is fully operational with preliminary testing having occurred. In Figure 1, we can observe two of the multiple tests undertaken during the automated testing procedure. These are the over-voltage trip point and over-current trip point tests which make use of the parameters stated in Table 1. We can observe that the Brick tested passed the over-voltage trip point test with a trip having been initiated at 11.6 V. This as opposed to the over-current trip point test which was failed with a trip only having been initiated at 11.6 A. An undesirable latency period at 9.8 A can also be observed.

4.3. Burn-in testing

Burn-in testing is an active means by which the reliability of the Bricks can be increased once installed on-detector. It is a form of accelerated aging which is used to address the high failure rate experienced by electronics during their early life as can be seen in Figure 5. Failures experienced in this region are known as infant mortality failures. These failures occur due to unavoidable manufacturing inconsistencies at both the device and component levels.

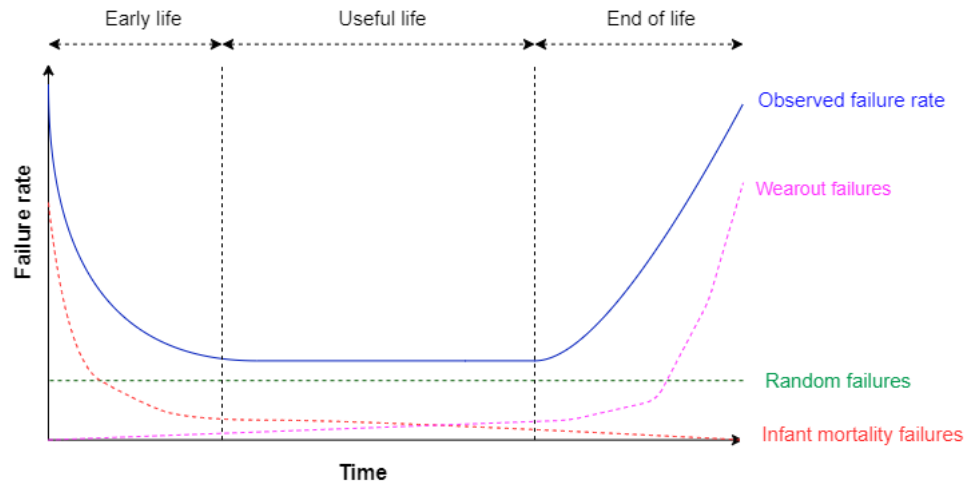


Figure 5. A generalized Bathtub-curve illustrating the failure rate as a function of time as experienced by electronic components.

Burn-in testing is used to artificially age the Bricks towards the useful life region, in which a lower constant failure rate is experienced before they are installed within the TileCal. By causing Bricks that would fail prematurely within the TileCal to rather fail during Burn-in testing increases the reliability of the Brick population once installed on-detector. This is achieved by subjecting the Bricks to a Burn-in cycle within a custom Burn-in apparatus in which they experience sub-optimal operating conditions which function to stimulate failure mechanisms within the Bricks. A Burn-in cycle consists of an 8-hour endurance run of the Bricks at a load of 5 A and an operating temperature of around 60° C which is twice the expected nominal on-detector operating temperature..

A custom Burn-in test station has been developed to undertake the Burn-in of eight Bricks per cycle. The station consists of a Main-board which multiplexes with the eight Brick-interface boards and the two Dummy-load boards as well as allowing for serial communication with the custom control and monitoring LabVIEW software.

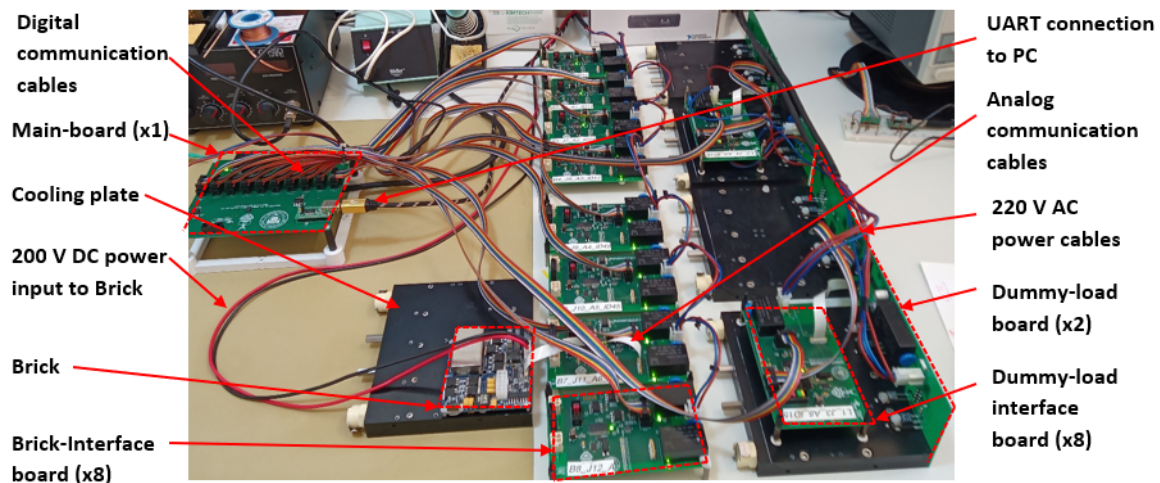


Figure 6. Calibration and fault finding of a Burn-in stations electronics before final integration with the chassis and cooling system.

A Brick-interface board provides the on/off control of a Brick and an analog to digital converter for the conversion of the analog data received from the Bricks measurements hardware. The custom Dummy-load boards provide a programmable load to be placed on the Bricks. The heat generated by the Dummy-load boards as well as the Bricks, due to power conversion inefficiency, is extracted by means of water cooled plates. An external DC input power supply for the Bricks as well as a water chiller form part of the test station.

5. Conclusions

The Contribution of South Africa to the TileCal Phase-II upgrade was described, with the quality assurance testing of Bricks to be produced being emphasized. The Bricks in-built protection circuitry was provided. Motivation for quality assurance testing of the Bricks was provided with the distinct Visual inspection, Initial testing, Burn-in testing and Final testing steps having been covered in detail. The custom testing apparatus was described and preliminary Initial testing data was presented and explained.

References

- [1] The ATLAS Experiment at the CERN Large Hadron Collider (ATLAS Collaboration) 2008 *JINST* **3** S08003. 437 p also published by CERN Geneva in 2010 URL <https://cds.cern.ch/record/1129811>
- [2] The ATLAS Tile-Calorimeter (ATLAS Collaboration) 2017 *published by CERN Geneva* **3** pg 87 – pg 156 URL <https://cds.cern.ch/record/2285583>
- [3] R Mckenzie (ATLAS Collaboration) 2021 *published by CERN Geneva* URL <https://cds.cern.ch/record/2778343?ln=en>
- [4] Analog Devices 2021 URL <https://www.analog.com/media/en/technical-documentation/data-sheets/1681f.pdf>

Search for a heavy pseudo-scalar decaying into a Z boson and another heavy scalar boson leading to four lepton final states in pp collisions at $\sqrt{s} = 13$ TeV with the ATLAS detector

Onesimo Mtintsilana¹, Abdualazem Fadol^{1,2}, Humphry Tlou¹, Bruce Mellado¹ and Xifeng Ruan¹

¹ School of Physics and Institute for Collider Particle Physics, Wits, Johannesburg, Wits 2050, South Africa

² Institute of High Energy Physics Chinese Academy of Sciences, 19B Yuquan Road, Shijingshan District, Beijing

³ iThemba LABS, National Research Foundation, PO Box 722, Somerset West 7129, South Africa

E-mail: onesimo.mtintsilana@cern.ch

Abstract. A current study showed that a simplified model predicting a 270 GeV heavy scalar (H) that decays to a Standard Model (SM) Higgs boson in association with a 150 GeV scalar singlet (S) may accommodate numerous anomalous multi-lepton observations in proton-proton (pp) collisions at the Large Hadron Collider (LHC). With this in mind, the purpose of this article is to provide a search for a heavy resonance pseudo-scalar, A , which decays into a Z boson and another heavy scalar boson, H . The $H \rightarrow SS$ decay mode will be investigated with at least four leptons in the final state, using a data sample corresponding to an integrated luminosity of 139 fb^{-1} from pp collisions at $\sqrt{s} = 13$ TeV.

1. Introduction

The discovery of a Higgs-like scalar [1, 2] at the Large Hadron Collider (LHC) has offered up a new window of opportunity for particle physics. Following its discovery, many studies have been done to better understand the boson's couplings to particles in the Standard Model (SM) and beyond Standard Model (BSM), as well as to search for new bosons. So far, conclusive proof for any of these BSM hypotheses has proved elusive. Many dedicated investigations are being undertaken within the LHC experimental collaborations to look for such evidence. Recently, in an effort uncover evidence of BSM physics, the ATLAS experiment conducted a model-independent study [3] in events involving three or four leptons.

Simple extensions of the SM include the two-Higgs doublet models (2HDM) [4, 5], which require the inclusion of an additional Higgs-doublet. Due to this additional doublet, the scalar spectrum contains two CP-even (h, H) scalar bosons, one CP-odd (A), and charged (H^\pm) scalar bosons. However, as shown in Ref. [6, 7], a 2HDM alone cannot incorporate certain characteristics of the data. An early 2015 research looked at the potential of a heavy scalar, H , being

consistent with various LHC Run 1 measurements [8]. Following a discussion of the results in Ref. [8] the next step was to investigate the idea of introducing a scalar mediator S (rather than utilizing effective vertices), so that H might decay to Sh , SS , and hh [6]. The S was supposed to have globally re-scaled Higgs-like couplings, allowing for constant branching ratios (BRs). In this configuration, particularly in light of the observations in Ref. [9], which ruled out a 100% branching ratio of S into Dark Matter, multi-lepton final states became a focus. These couplings are supposed to be suppressed by some undefined BSM physics, resulting in a Higgs-like hierarchy of relative couplings to the SM particles. Although S is not generated directly with a large cross section, its BRs should be identical to those of an SM-like Higgs boson with a larger mass. This significantly decreases the model's number of free parameters. If this is the case, then when the mass of S approaches $\sim 2m_W$, it should decay more strongly to W and Z boson pairs. As a result of the gauge boson decays, S becomes a source of many leptons. The potential of embedding H into a 2HDM was also explored, with the model's permitted parameter space stated in Ref. [6, 10]. Furthermore, a predicted set of possible search channels for the new scalars was demonstrated. Several of these predictions have been tested and elaborated upon in Ref. [11, 12]. As such, the BSM scenario discussed in Ref. [11] is of special importance here.

The parameters of the model were fixed in 2017 in order to further investigate outcomes with more data and new final states while minimizing biases and look-elsewhere effects. This includes assigning the scalar masses to $m_H = 270$ GeV and $m_S = 150$ GeV, treating S as an SM Higgs-like scalar, and assuming that the decays $H \rightarrow Sh, SS$ are dominant. Excesses in opposite sign di-leptons, same-sign di-leptons, and three leptons were reported in Ref. [13], with and without the presence of b-tagged hadronic jets. Furthermore, CMS and ATLAS have reported $t\bar{t}$ and $Zb\bar{b}$ final state [14] excesses that may be interpreted with $m_A \approx 600$ GeV using the aforementioned model. As a result, the 2HDM+S model with the parameters derived in Ref [12] may accommodate the LHC excesses reported in Ref. [15]. Additional excesses in the Zh spectrum and the production of three leptons plus two b-tagged jets can be explained without changing these parameters, assuming $m_A \approx 600$ GeV. The conclusions from these studies further reinforce the relevance of multi-lepton final states in the search for new bosons.

Due to the impossibility of analyzing all possible final states that may contain potential for discovery, we shall build on the phenomenology found in Ref. [6, 12]. We present an introduction to a study of the production of A via the gluon-gluon fusion (ggF) mode and its decay into the AZH channel, taking into account the decay mode $H \rightarrow SS$. This configuration results in the final state containing four leptons.

2. $A \rightarrow ZH \rightarrow 4\ell$ search

The model described in Ref. [6] is a 2HDM with an additional real singlet Φ_s , and it serves as the foundation for our formalism. We will build on the phenomenology given in Ref. [11] and focus is on the production of A via the ggF mode and its decay into $A \rightarrow ZH \rightarrow 4\ell$ channel as shown in Figure 1. In the scenario considered here, Z decays further into two opposite-sign leptons, while the other two leptons are produced by the HSS decay mode, in which one of the S 's decays to a positively charged lepton and the other to a negatively charged lepton. The resulting kinematics of the decay of $A \rightarrow ZH$, where $m_A > m_Z + m_H$ and $H \rightarrow SS$, have been explored in Ref. [11].

For the purpose of interpreting the $H \rightarrow SS$, H denotes the heavy Higgs boson with mass $m_H = 270$ GeV, S and Z are considered to have fixed masses of 150 GeV and 91.190 GeV, respectively. The masses were chosen based on the best-fit values obtained from previous research [11, 8]. Fixing these parameters based on the outcomes of entirely different data-

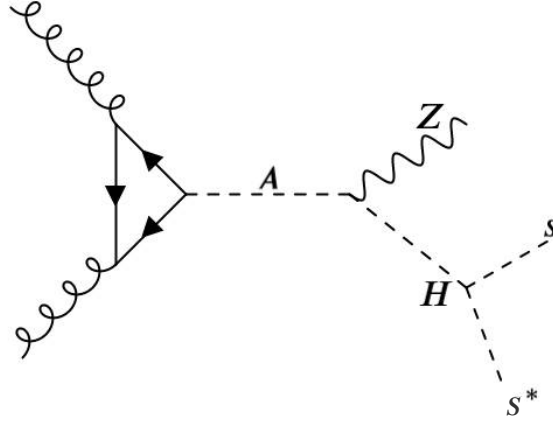


Figure 1. The representative Feynman diagram for the production mode of A and its subsequent decay to SS via gluon fusion (ggF) production mode.

Table 1. This table outlines the preselection cuts applied.

	Trigger
	At least 1-lepton matched to triggering-lepton Each lepton must have $p_T^l > 10$ GeV Events with SFOS require $m_\mu > 12$ GeV
Preselection	Require exactly four leptons with total charge equal zero Leptons require loose identification and isolation criteria $ \eta^e < 2.47$, excluding $1.37 < \eta^e < 1.52$ $ \eta^\mu < 2.5$
Categories	1-SFOS

sets allows us to prevent possible bias in adjusting the masses to reproduce data excesses. As a result, because no additional masses are considered, a "look elsewhere effect" is not required to quantify a global relevance in fits.

The mass of H was calculated using data from the LHC Run 1 experiment, which included distortions in the Higgs boson spectrum [16], searches for di-Higgs and di-boson resonances [16], and measurements on the rate of top associated Higgs production [16]. Likewise, the mass of S is set at 150 GeV based on the best-fit point in the statistical study described in Ref. [11].

3. Monte Carlo samples

The data used in this study corresponds to the entire Run II of the LHC. This was collected by the ATLAS detector between 2015 and 2018 at $\sqrt{s} = 13$ TeV with stable beam conditions and all detector systems running normally. The data sample has an integrated luminosity of 139.0 fb^{-1} after data-quality requirements. Madgraph5_aMC@NLO [17] interfaced with PYTHIA 8 [18] is used for the showering and hadronisation with A14 tune NNPDF23LO PDF set [19] and EvtGen was used to simulate B-hadron decays. Background processes such $q\bar{q} \rightarrow ZZ, q\bar{q} \rightarrow ZZ(EW), VVV$ and $Z+\text{jets}$ are simulated with SHERPA 2.2.2 and the NNPDF30NNLO parton distribution function (PDF) set. POWHEG-BOX v2 with NNPDF30NNLO PDF set was used to produce the $t\bar{t}$ events.

Table 2. Summary of the yield calculations for different background categories.

	$qqZZ$	$ggZZ$	$qqZZEW$	$Z + jets$	VVV	ttV	tt	WZ	Total
4ℓ	4228.96	25.99	107.34	5645.82	31.28	435.29	2651.21	110.18	13236.10
1-SFOS	104.50	0.36	1.32	896.55	13.89	213.31	1312.53	53.14	2595.64
1-SFOS & $ m_z - m_{34} < 15$ GeV	75.34	0.30	0.83	705.45	12.82	170.48	273.84	36.75	1275.81
1-SFOS & $ m_z - m_{34} > 15$ GeV	29.20	0.06	0.49	191.10	1.07	42.83	1038.69	16.39	1319.83

4. Event Selection

The preselection cuts used are shown in Table 1. In general in HZZ , each channel four-lepton candidates are generated by identifying a lepton-quadruplet composed of two same-flavour, opposite-sign lepton pairs (SFOS), as reported in Ref [20]. However, for the purposes of our analysis, we solely examine 1-SFOS events. We eliminate all 2-SFOS events and only examine the following pairings: $e\mu 2e/e\mu 2\mu$. Each electron must have a $p_T > 7$ GeV and be measured in the $|\eta| < 2.47$ pseudorapidity range. The highest- p_T lepton in the quadruplet must satisfy $p_T > 20$ GeV, and the second lepton in p_T order must have $p_T > 15$ GeV. If assigning leptons to pairs is ambiguous, only one quadruplet per channel is chosen by keeping the quadruplet with the invariant mass of the lepton pairings closest (leading pair) and second closest (subleading pair) to the Z boson mass, with invariant masses referred to as m_{12} and m_{34} , respectively. m_{12} must satisfy $50 \text{ GeV} < m_{12} < 106 \text{ GeV}$ and m_{34} must satisfy $50 \text{ GeV} < m_{34} < 115 \text{ GeV}$ in the chosen quadruplet.

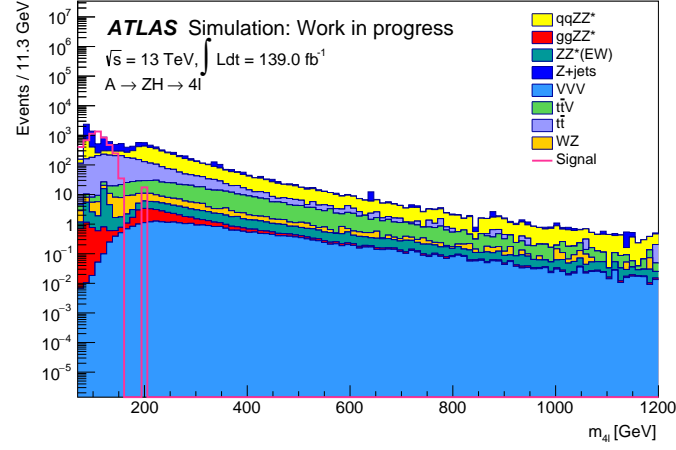
5. Results

Before one begins to construct a model to separate signal and background, it is important to check that the MC simulation with which the model is constructed, actually reflects the true distributions of the data. This section will present the results for both signal and background events. The preceding section's set of event selection cuts are used to assist us identify the signal events and determine how much of the background is needed to be removed while avoiding inadvertently removing signal events. Figure 2 shows the transverse mass ($m_{4\ell}$) and the transverse momentum ($p_T^{4\ell}$) distribution for the four leptons for both the signal and background events.

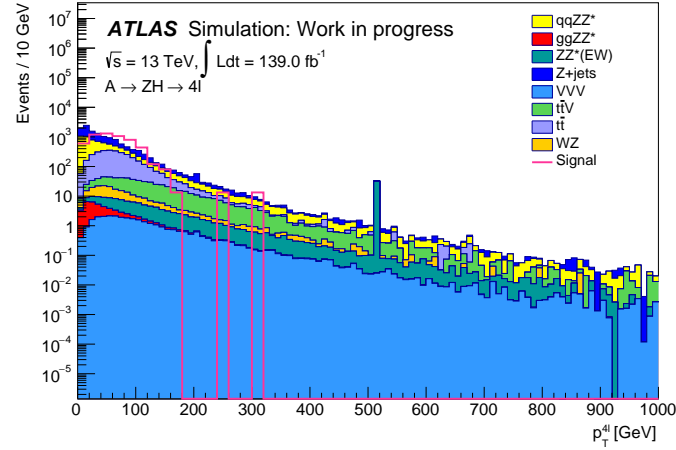
In order to separate the signal from the different background concentrations, more complex techniques will have to be introduced and applied to each category to deal with specific background events that need to be separated. As seen in Table 2, the concentrations for certain processes are different per category, with the Z +jets background being dominant. The events are tested for 1-SFOS ($e\mu 2e/e\mu 2\mu$) and also with a cut in the m_Z ($|m_z - m_{34}| < 15$) GeV and also outside the m_Z ($|m_z - m_{34}| > 15$) GeV mass window. Outside the m_Z mass window we are looking for lepton pairs ($m_{\ell\ell}$) from other processes other than the Z boson. It is worth noting that, owing to the lepton pairing technique used here, m_{34} is the leading lepton pair rather than the well-known m_{12} .

Additionally, the event yields were computed after the aforementioned standard selection criteria are applied. The signal events are generated to provide the event topology with a lepton pair decaying from the associated Z boson and at least another two same sign or different flavor leptons. The background yields were either obtained from MC for the ZZ continuum, or using data driven techniques for the reducible contributions, as described previously.

Table 2 shows that the total number of events generated for the background, after the 4ℓ selection is 13236.10. When the 1-SFOS cut is implemented, the number of events decreases



(a)



(b)

Figure 2. Signal and background events for the transverse momentum ($p_T^{4\ell}$) and transverse mass ($m_{4\ell}$) of the 4ℓ respectively.

by about 80%, as expected. This is because the events with two Z candidates will be removed, while events with a Z boson candidate and a non-Z boson pair will be kept.

6. Conclusion

The BSM scenario presented in this article introduces a search for a heavy pseudo-scalar decaying into a Z boson and another heavy scalar boson leading to four lepton final states in pp collisions at $\sqrt{s} = 13$ TeV with the ATLAS detector. This is an attempt to explain a number of features of the Run 1 data, which persist in the Run 2 data as explained in Ref. [?].

MC simulation samples are used to model the background and signal processes for this search. The decay process analysed was the $gg \rightarrow A \rightarrow ZH$.

The decay $A \rightarrow ZH$ leads to interesting final states, as pointed out earlier. For the sake of

simplicity, here we considered the case where S decays to 2ℓ and Z to the other 2ℓ pairs.

A comparison of the 4ℓ between the background and signal has been shown. The background study shows after the exact 1-SFOS selection the major background will be significantly suppressed, while the features of part of the signal will be kept. The study is still on going to optimise the parameter spaces for the signal production.

Acknowledgments

Onesimo Mtintsilana acknowledges the funding support by the National Research Fund (NRF).

References

- [1] Englert F and Brout R 1964 *Phys. Rev. Lett.* **13** 321–323
- [2] Higgs P W 1964 *Phys. Rev. Lett.* **13**(16) 508–509
- [3] Aad G *et al.* (ATLAS) 2021 (*Preprint* 2107.00404)
- [4] Lee T D 1973 *Phys. Rev. D* **8** 1226–1239
- [5] Branco G C, Ferreira P M, Lavoura L, Rebelo M N, Sher M and Silva J P 2012 *Phys. Rept.* **516** 1–102 (*Preprint* 1106.0034)
- [6] von Buddenbrock S, Chakrabarty N, Cornell A S, Kar D, Kumar M, Mandal T, Mellado B, Mukhopadhyaya B, Reed R G and Ruan X 2016 *Eur. Phys. J. C* **76** 580 (*Preprint* 1606.01674)
- [7] Kumar M, von Buddenbrock S, Chakrabarty N, Cornell A S, Kar D, Mandal T, Mellado B, Mukhopadhyaya B, Reed R G and Ruan X 2016 *61st Annual Conference of the South African Institute of Physics* pp 507–511 (*Preprint* 1608.03466)
- [8] von Buddenbrock S, Chakrabarty N, Cornell A S, Kar D, Kumar M, Mandal T, Mellado B, Mukhopadhyaya B and Reed R G 2015 (*Preprint* 1506.00612)
- [9] Aaboud M *et al.* (ATLAS) 2017 *Phys. Rev. D* **96** 112004 (*Preprint* 1706.03948)
- [10] von Buddenbrock S and Mellado B 2019 *64th Annual Conference of the South African Institute of Physics* (*Preprint* 1909.04370)
- [11] von Buddenbrock S, Cornell A S, Fadol A, Kumar M, Mellado B and Ruan X 2018 *J. Phys. G* **45** 115003 (*Preprint* 1711.07874)
- [12] von Buddenbrock S, Cornell A S, Iarilala E D R, Kumar M, Mellado B, Ruan X and Shrif E M 2019 *J. Phys. G* **46** 115001 (*Preprint* 1809.06344)
- [13] Buddenbrock S, Cornell A S, Fang Y, Fadol Mohammed A, Kumar M, Mellado B and Tomiwa K G 2019 *JHEP* **10** 157 (*Preprint* 1901.05300)
- [14] Sirunyan A M *et al.* (CMS) 2020 *JHEP* **04** 171 (*Preprint* 1908.01115)
- [15] Aaboud M *et al.* (ATLAS) 2018 *Phys. Lett. B* **783** 392–414 (*Preprint* 1804.01126)
- [16] Aad G *et al.* (ATLAS) 2014 *JHEP* **09** 112 (*Preprint* 1407.4222)
- [17] Alwall J, Herquet M, Maltoni F, Mattelaer O and Stelzer T 2011 *JHEP* **06** 128 (*Preprint* 1106.0522)
- [18] Sjöstrand T *et al.* 2015 *Comput. Phys. Commun.* **191** 159–177 (*Preprint* 1410.3012)
- [19] Ball R D *et al.* (NNPDF) 2015 *JHEP* **04** 040 (*Preprint* 1410.8849)
- [20] Aad G *et al.* (ATLAS) 2021 *Eur. Phys. J. C* **81** 332 (*Preprint* 2009.14791)

The anatomy of the multilepton anomalies at the LHC and a candidate for a singlet scalar

B Mellado

School of Physics and Institute for Collider Particle Physics, University of the Witwatersrand, Johannesburg, Wits 2050, South Africa
iThemba LABS, National Research Foundation, PO Box 722, Somerset West 7129, South Africa

E-mail: bmellado@mail.cern.ch

Abstract. In this presentation an account of the multi-lepton (electrons and muons) anomalies at the LHC is given. These include the excess production of opposite sign leptons with and without b-quarks, including a corner of the phase-space with a full hadronic jet veto; same sign leptons with and without b-quarks; three leptons with and without b-quarks, including also the presence of a Z . Excesses emerge in corners of the phase space where a range of SM processes dominate, indicating that the potential mismodeling of a particular SM process is unlikely to explain them. A procedure is implemented that avoids parameter tuning or scanning the phase-space in order to nullify potential look-else-where effects or selection biases. The internal consistency of these anomalies and their interpretation in the framework of a simplified model are presented. Motivated by the multi-lepton anomalies, a search for narrow resonances with $S \rightarrow \gamma\gamma, Z\gamma$ in association with light jets, b -jets or missing transverse energy is performed. The maximum local (global) significance is achieved for $m_S = 151.5 \text{ GeV}$ with 5.1σ (4.8σ), which is obtained by letting branching ratios of S float. Those can be constrained by combining with the multi-lepton excesses, where the combined significance is greater than 5σ .

1. Introduction

The discovery of a Higgs boson (h) [1, 2, 3, 4] at the Large Hadron Collider (LHC) by ATLAS [5] and CMS [6] has opened a new chapter in particle physics. Measurements of its properties so far indicate that this 125 GeV boson is compatible with those predicted by the Standard Model (SM) [7, 8]. However, this does not exclude the possible existence of additional scalar bosons as long as the mixing with the SM Higgs is sufficiently small.

One of the implications of a 2HDM+ S model, where S is a scalar SM singlet, is the production of multiple-leptons through the decay chain $H \rightarrow Sh, SS$ [9], where H is the heavy CP-even scalar and h is the SM Higgs boson. Excesses in multi-lepton final states were reported in Ref. [10].¹ In order to further explore results with more data and new final states while avoiding biases and look-else-where effects, the parameters of the model were fixed in 2017 according to Refs. [9, 10]. This includes setting the scalar masses to $m_H = 270 \text{ GeV}$, $m_S = 150 \text{ GeV}$, treating S as a SM Higgs-like scalar and assuming the dominance of the decays $H \rightarrow Sh, SS$. Excesses in opposite sign di-leptons, same-sign di-leptons, and three leptons, with and without the presence

¹ Here we use "anomalies" and "excesses" interchangeably. These are defined as deviations in the data from predictions by the SM after taking into account experimental and theoretical uncertainties.

of b -tagged hadronic jets were reported in Ref. [11, 12]. Interestingly, the model can explain anomalies in astro-physics (the positron excess of AMS-02 [13] and the excess in gamma-ray fluxes from the galactic centre measured by Fermi-LAT [14]) if it is supplemented by a Dark Matter candidate [15] and can be easily extended to account for $g - 2$ of the muon [16] (for a review of anomalies see Ref. [17]).

2. The simplified model

Here, we succinctly describe the model used to describe the multi-lepton anomalies observed in the LHC data and with which to interpret the above mentioned excesses in astrophysics. The formalism is comprised of a model of fundamental interactions interfaced with a model of cosmic-ray fluxes that emerge from DM annihilation. The potential for a two Higgs-doublet model with an additional real singlet field Φ_S (2HDM+S) is given as in Ref. [9]:

$$\begin{aligned} V(\Phi) = & m_{11}^2 |\Phi_1|^2 + m_{22}^2 |\Phi_2|^2 - m_{12}^2 (\Phi_1^\dagger \Phi_2 + \text{h.c.}) + \frac{\lambda_1}{2} (\Phi_1^\dagger \Phi_1)^2 + \frac{\lambda_2}{2} (\Phi_2^\dagger \Phi_2)^2 \\ & + \lambda_3 (\Phi_1^\dagger \Phi_1) (\Phi_2^\dagger \Phi_2) + \lambda_4 (\Phi_1^\dagger \Phi_2) (\Phi_2^\dagger \Phi_1) + \frac{\lambda_5}{2} [(\Phi_1^\dagger \Phi_2)^2 + \text{h.c.}] + \frac{1}{2} m_S^2 \Phi_S^2 \\ & + \frac{\lambda_6}{8} \Phi_S^4 + \frac{\lambda_7}{2} (\Phi_1^\dagger \Phi_1) \Phi_S^2 + \frac{\lambda_8}{2} (\Phi_2^\dagger \Phi_2) \Phi_S^2. \end{aligned}$$

The fields Φ_1, Φ_2 in the potential are the $SU(2)_L$ Higgs doublets. The first three lines in Eq. 1 are the contributions of the real 2HDM potential. The terms of the last line are contributions of the singlet field Φ_S . To prevent the tree-level flavour changing neutral currents we consider a Z_2 symmetry which can be softly broken by the term $m_{12}^2 \neq 0$. After the minimisation of the potential and Electro-Weak symmetry breaking, the scalar sector is populated with three CP even scalars h, H and S , one CP odd scalar A and charged scalar H^\pm . For more details of this model and associated interactions' Lagrangians and parameter space we refer to Refs. [9, 18]. Further, we consider interactions of S with three types of DM candidates χ_r, χ_d and χ_v with spins 0, 1/2 and 1, respectively:

$$\mathcal{L}_{int} = \frac{1}{2} M_{\chi_r} g_{\chi_r}^S \chi_r \chi_r S + \bar{\chi}_d (g_{\chi_d}^S + i g_{\chi_d}^P \gamma_5) \chi_d S + g_{\chi_v}^S \chi_v^\mu \chi_{v\mu} S,$$

where g_{χ_i} and M_{χ_i} are the coupling strengths of DMs with the singlet real scalar S and masses of DM, respectively.

3. Anatomy of the multilepton anomalies

We give a succinct description of the different final states and corners of the phase-space that are affected by the anomalies. As discussed in the introduction the anomalies are reasonably well captured by a 2HDM+S model. Here, H is predominantly produced through gluon-gluon fusion and decays mostly into $H \rightarrow SS, Sh$ with a total cross-section in the range 10-25 pb [11]. Due to the relative large Yukawa coupling to top quarks needed to achieve the above mentioned direct production cross-section, the production of H in association with a single top-quark. These production mechanisms together with the dominance of $H \rightarrow SS, Sh$ over other decays, where S behaves like a SM Higgs-like boson, lead to the a number of final states that can be classified into several groups of final states. Three are the groups of final states where the the excesses are statistically compelling: opposite sign (OS) leptons ($\ell = e, \mu$); same sign (SS) and three leptons (3ℓ) in association with b -quarks; SS and 3ℓ without b -quarks. In the sections below a brief description of the final states is given with emphasis on the emergence of new excesses in addition to those reported in Refs. [10, 11, 12], when appropriate. The new excesses reported here are not the result of scanning the phase-space, but the result of looking at pre-defined final states and corners of the phase-space, as predicted by the model described above.

Table 1. Summary of the status of the multi-lepton anomalies at the LHC, where $\ell = e, \mu$.

Final state	Characteristics	SM backgrounds	Significance
$\ell^+\ell^- + b\text{-jets}$	$m_{\ell\ell} < 100 \text{ GeV}$, low $b\text{-jet}$ mult.	$t\bar{t}, Wt$	$> 5\sigma$
$\ell^+\ell^- + \text{jet veto}$	$m_{\ell\ell} < 100 \text{ GeV}$	W^+W^-	$\approx 3\sigma$
$\ell^\pm\ell^\pm, 3\ell + b\text{-jets}$	Moderate H_T	$t\bar{t}W^\pm, t\bar{t}t\bar{t}$	$> 3\sigma$
$\ell^\pm\ell^\pm, 3\ell, n_b = 0$	In association with h	$W^\pm h, (WWW)$	4.2σ
$Z(\rightarrow \ell\ell)\ell, n_b = 0$	$p_{TZ} < 100 \text{ GeV}$	ZW^\pm	$> 3\sigma$

3.1. Opposite sign di-leptons

The production chain $pp \rightarrow H \rightarrow SS, Sh \rightarrow \ell^+\ell^- + X$, is the most copiously multi-lepton final state. Using the benchmark parameter space in Ref. [18], the dominant of the singlet are $S \rightarrow W^+W^-, b\bar{b}$. This will lead to OS leptons with without b -quarks. The most salient characteristics of the final states are such that the di-lepton invariant mass $m_{\ell\ell} < 100 \text{ GeV}$ where the bulk of the signal is produced with low b -jet multiplicity, $n_b < 2$ [11]. The dominant SM background in events with b -jets is $t\bar{t} + Wt$. The b -jet and light-quark of the signal is significantly different from that of top-quark related production mechanisms. As a matter of fact, excesses are seen when applying a full jet veto, top-quark backgrounds become suppressed and where the dominant backgrounds is non-resonant W^+W^- production [10, 19, 20].² A review of the NLO and EW corrections to the relevant processes can be found in Refs. [11, 20], where to date the $m_{\ell\ell}$ spectra at low masses remains unexplained by MC tools. A measurement of the differential distributions in OS events with b -jets with Run 2 data further corroborates the inability of current MC tools to describe the $m_{\ell\ell}$ distribution [22]. A summary of deviations for this class of excesses is given in Table 1.

3.2. SS and 3ℓ with b -quarks

The associated production of H with top quarks lead to the anomalous production of SS and 3ℓ in association with b -quarks with moderate scalar sum of leptons and jets, H_T . The elevated $t\bar{t}W^\pm$ cross-section measured by the ATLAS and CMS experiments can be accommodated by the above mentioned model [11, 23]. Based on a number of excesses involving Z bosons, in Ref. [18] it was suggested that the CP -odd scalar of the 2HDM+ S model could be as heavy as $m_A \approx 500 \text{ GeV}$, where the two leading decays would be $A \rightarrow t\bar{t}, ZH$. The cross-section for the associated production $pp \rightarrow t\bar{t}A$ with $A \rightarrow t\bar{t}$ would correspond to $\approx 10 \text{ fb}$. This is consistent with the elevated $t\bar{t}t\bar{t}$ cross-section reported by ATLAS and CMS [24, 25, 26]. The combined significance of the excesses related to the cross-section measurements of $t\bar{t}W^\pm$ and $t\bar{t}t\bar{t}$ surpass 3σ , as detailed in Table 1. The ATLAS collaboration has reported a small excess in the production of four leptons with a same flavor OS pair consistent with a Z boson, where the four-lepton invariant mass, $m_{4\ell} < 400 \text{ GeV}$ [27]. This excess can also be accommodated by the production of $A \rightarrow ZH$.

3.3. SS and 3ℓ without b -quarks

The production chain $pp \rightarrow H \rightarrow SS, Sh$ can give rise to SS and 3ℓ events, where b -jet activity would be depleted compared to production mechanism considered in Sec. 3.2. The potential impact on the measurement of the production of the SM Higgs boson in association with a W

² The CMS experiment presented the comparison of the yields in the data to a MC [21]. The MC does not describe simultaneously the di-lepton invariant mass and transverse momentum. As such, for the purposes of this study this data set is inconclusive, where we encourage the CMS experiment to provide differential measurements similar to those performed by ATLAS in Ref. [19].

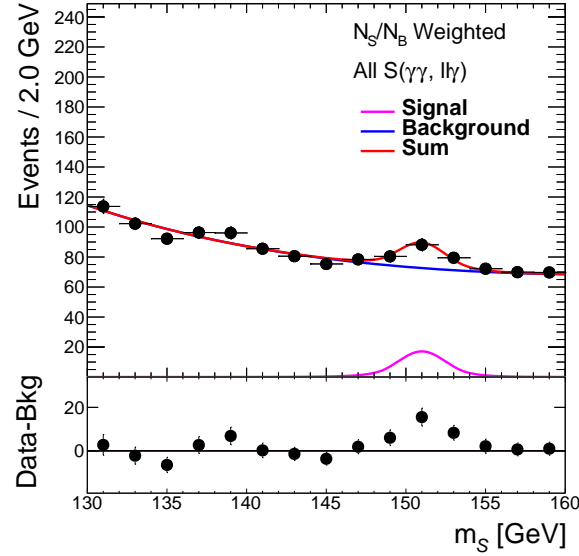


Figure 1. Combination of fits to all the categories in the $\gamma\gamma$ and $Z\gamma$ spectra (see text). The data points are S/B weighted.

boson and other measurements in the context discussed here was reported in Ref. [28]. A survey of available measurements of the signal yield of the Wh production was performed in Ref. [12]. A deviation of 3.8σ with respect to the Wh yield in the SM in corners of the phase-space predicted by the simplified model. The CMS experiment has recently reported the signal strength of the Vh , $V = Z, W^\pm$ production with the $h \rightarrow W^+W^-$ decay for low and high V transverse momentum [29]. The signal strength for Vh with the V transverse momentum, $p_{TV} < 150$ GeV, where the BSM signal is concentrated, is $2.65^{+0.69}_{-0.64}$. In addition CMS has also reported a large signal strength in the third di-jet bin optimised for Wh in the search for the $h \rightarrow Z\gamma$ decay of $\mu = 12.3^{+3.7}_{-3.5}$ [30]. This brings the combination to $\mu = 2.43 \pm 0.34$, or a 4.2σ effect. In order to reconcile observed excesses in Secs. 3.1 and 3.2 with the ones described here, it is necessary to assume the dominance of the $H \rightarrow SS$ decay over $H \rightarrow Sh$ [12]. Another important prediction of the simplified model is the elevated WWW cross-section. The ATLAS experiment reports a signal strength of 1.66 ± 0.28 [31].³ The latter includes the $Wh \rightarrow WWW^*$ production, hence it is not added to the combination due to partial double counting. Another final state of interest is the production of ZW^\pm events where Z transverse momentum, $p_{TZ} < 100$ GeV with depleted b -jet activity. Excesses were reported in Ref. [11]. The CMS experiment has recently reported an important excess in events with 3ℓ in association with one and two jets used for the measurement of $Zh, h \rightarrow W^+W^-$ production, where ZW^\pm is the dominant background [29]. As the analysis of the excess in the context of the simplified model described here is in progress, the significance of this excess is not added to the combination reported in Table 1.

4. Candidate of Singlet Scalar

The multi-lepton anomalies described here seem to be relatively well accommodated by 2HDM+S model with a sizeable direct production of $H \rightarrow SS, Sh$. This motivates the search

³ CMS [32] pursues a different approach compared to the more inclusive selection performed by ATLAS. For instance, the requirement that the azimuthal separation between the vector of the three leptons and the missing transverse energy be greater than 2.5 rad and other requirements suppress the contribution from the BSM signal considered here.

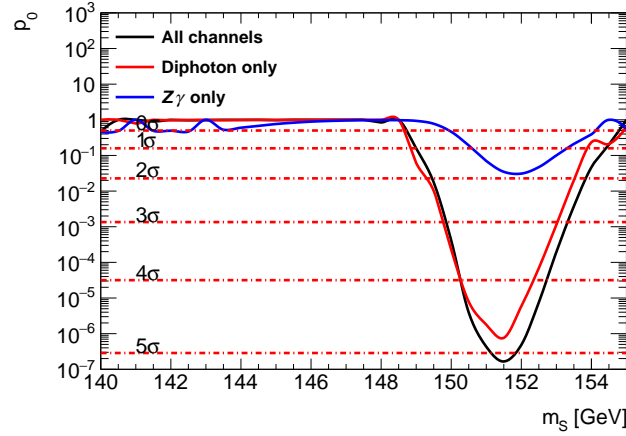


Figure 2. The combined local p -value (right) as a function of m_S using inputs described in Ref. [33].

for narrow resonances pertaining to $S \rightarrow \gamma\gamma, Z\gamma$ in association with light jets, b -jets or missing transverse energy. A survey of all publicly available data is performed [33] in the mass range motivated by the multi-lepton anomalies, in particular the di-lepton invariant mass spectra of the excesses. The region of interest is in the range $130 < m_S < 160$ GeV. Figure 1 displays the signal to background weighted combination of the mass spectra, where the red curve displays the combined fit. The signal normalisation in each of the categories is allowed to float. Figure 2 shows the local p -value distribution in the range 140-155 GeV. The upper and lower bounds of the search are determined by the availability of data reported by the experiments. The lowest local p -value is achieved for $m_S = 151.5$ GeV corresponding to 5.1σ . Taking into account the look-else-where effect the global significance in the range 140-155 GeV is 4.8σ . The above mentioned local significance is obtained by letting branching ratios of S float. Those can be constrained by combining with the multi-lepton excesses, where the combined significance is greater than 5σ .

Searches for $H \rightarrow SS^{(*)}, Sh \rightarrow \gamma\gamma b\bar{b}, \tau^+\tau^- b\bar{b}$ in asymmetric configurations, not performed by the experiments before, are well motivated [33]. Each experiment with the combined Run 2 and Run 3 data sets could achieve a 7σ effect with the $H \rightarrow SS^{(*)}\gamma\gamma b\bar{b}$ search [33].

The current results on the production of $hh \rightarrow \gamma\gamma b\bar{b}, \tau^+\tau^- b\bar{b}$ do not exclude the expected cross-section for $H \rightarrow Sh$. This is motivated by the fact that $Br(S \rightarrow b\bar{b}, \tau^+\tau^-) \ll Br(h \rightarrow b\bar{b}, \tau^+\tau^-)$ and that the mass resolution is better than the mass difference between h and S . Similarly, the limits set by CMS on $H \rightarrow Sh \rightarrow b\bar{b}, \tau^+\tau^-$ [34] are not strong enough to exclude the production rate of $H \rightarrow Sh$ as determined from Ref. [12].

Interestingly, as the LEP experiments reported a mild excess (2.3σ) in the search for a scalar boson (S') [35] using the process $e^+e^- \rightarrow Zh(\rightarrow b\bar{b})$ at 98 GeV for the invariant $b\bar{b}$ mass, asymmetric $\gamma\gamma b\bar{b}$ final states could also originate from the decay $H \rightarrow SS'$. This is further supported by the CMS result reporting similar excesses with Run 1 data and 35.9fb^{-1} of Run 2 data [34], with a local significance of 2.8σ at 95.3 GeV. In this context searches for $H \rightarrow S^{(l)}(\rightarrow \gamma\gamma, b\bar{b})S(\rightarrow \text{invisible})$ are well motivated.

5. Conclusions

This proceedings provide an update of the multi-lepton anomalies at the LHC since Ref. [11], where new data and final states and corner of the phase-space predicted by the 2HDM+ S model display excesses with respect to the SM. A summary of the multi-lepton anomalies is given in Table 1. Motivated by the fact that the $H \rightarrow SS, Sh$ decay describes reasonably well the multi-

lepton anomalies a search for narrow resonances with $S \rightarrow \gamma\gamma, Z\gamma$ in association with light jets, b -jets or missing transverse energy is performed. The maximum local (global) significance is achieved for $m_S = 151.5 \text{ GeV}$ with 5.1σ (4.8σ), which is obtained by letting branching ratios of S float. Those can be constrained by combining with the multi-lepton excesses, where the combined significance is greater than 5σ .

References

- [1] Higgs P W 1964 *Phys. Lett.* **12** 132–133
- [2] Englert F and Brout R 1964 *Phys. Rev. Lett.* **13** 321–323
- [3] Higgs P W 1964 *Phys. Rev. Lett.* **13** 508–509
- [4] Guralnik G S, Hagen C R and Kibble T W B 1964 *Phys. Rev. Lett.* **13** 585–587
- [5] Aad G *et al.* (ATLAS) 2012 *Phys. Lett. B* **716** 1–29 (*Preprint* 1207.7214)
- [6] Chatrchyan S *et al.* (CMS) 2012 *Phys. Lett. B* **716** 30–61 (*Preprint* 1207.7235)
- [7] Chatrchyan S *et al.* (CMS) 2013 *Phys. Rev. Lett.* **110** 081803 (*Preprint* 1212.6639)
- [8] Aad G *et al.* (ATLAS) 2013 *Phys. Lett. B* **726** 120–144 (*Preprint* 1307.1432)
- [9] von Buddenbrock S, Chakrabarty N, Cornell A S, Kar D, Kumar M, Mandal T, Mellado B, Mukhopadhyaya B, Reed R G and Ruan X 2016 *Eur. Phys. J. C* **76** 580 (*Preprint* 1606.01674)
- [10] von Buddenbrock S, Cornell A S, Fadol A, Kumar M, Mellado B and Ruan X 2018 *J. Phys. G* **45** 115003 (*Preprint* 1711.07874)
- [11] Buddenbrock S, Cornell A S, Fang Y, Fadol Mohammed A, Kumar M, Mellado B and Tomiwa K G 2019 *JHEP* **10** 157 (*Preprint* 1901.05300)
- [12] Hernandez Y, Kumar M, Cornell A S, Dahbi S E, Fang Y, Lieberman B, Mellado B, Monnakgotla K, Ruan X and Xin S 2021 *Eur. Phys. J. C* **81** 365 (*Preprint* 1912.00699)
- [13] Aguilar M *et al.* (AMS Collaboration) 2019 *Phys. Rev. Lett.* **122**(4) 041102 URL <https://link.aps.org/doi/10.1103/PhysRevLett.122.041102>
- [14] Ackermann M, Ajello M, Albert A, Atwood W B, Baldini L, Ballet J, Barbiellini G, Bastieri D, Bellazzini R, Bissaldi E and *et al* 2017 *The Astrophysical Journal* **840** 43 ISSN 1538-4357 URL <http://dx.doi.org/10.3847/1538-4357/aa6cab>
- [15] Beck G, Kumar M, Malwa E, Mellado B and Temo R 2021 (*Preprint* 2102.10596)
- [16] Sabatta D, Cornell A S, Goyal A, Kumar M, Mellado B and Ruan X 2020 *Chin. Phys. C* **44** 063103 (*Preprint* 1909.03969)
- [17] Fischer O *et al.* 2021 (*Preprint* 2109.06065)
- [18] von Buddenbrock S, Cornell A S, Iarilala E D R, Kumar M, Mellado B, Ruan X and Shrif E M 2019 *J. Phys. G* **46** 115001 (*Preprint* 1809.06344)
- [19] Aaboud M *et al.* (ATLAS) 2019 *Eur. Phys. J. C* **79** 884 (*Preprint* 1905.04242)
- [20] von Buddenbrock S and Mellado B 2019 *64th Annual Conference of the South African Institute of Physics* (*Preprint* 1909.04370)
- [21] Sirunyan A M *et al.* (CMS) 2020 *Phys. Rev. D* **102** 092001 (*Preprint* 2009.00119)
- [22] Aad G *et al.* (ATLAS) 2020 *Eur. Phys. J. C* **80** 528 (*Preprint* 1910.08819)
- [23] von Buddenbrock S, Ruiz R and Mellado B 2020 *Phys. Lett. B* **811** 135964 (*Preprint* 2009.00032)
- [24] Sirunyan A M *et al.* (CMS) 2020 *Eur. Phys. J. C* **80** 75 (*Preprint* 1908.06463)
- [25] Aad G *et al.* (ATLAS) 2020 *Eur. Phys. J. C* **80** 1085 (*Preprint* 2007.14858)
- [26] Aad G *et al.* (ATLAS) 2021 (*Preprint* 2106.11683)
- [27] Aad G *et al.* (ATLAS) 2021 (*Preprint* 2107.00404)
- [28] Fang Y, Kumar M, Mellado B, Zhang Y and Zhu M 2017 *Int. J. Mod. Phys. A* **32** 1746010 (*Preprint* 1706.06659)
- [29] Siruyan A M *et al* (CMS) Tech. rep. CERN CMS-PAS-HIG-19-017
- [30] Siruyan A M *et al* (CMS) Tech. rep. CERN CMS-PAS-HIG-19-014
- [31] Aad *et al.* (ATLAS) 2021 Tech. rep. CERN ATLAS-CONF-2021-039
- [32] Sirunyan A M *et al.* (CMS) 2020 **125** 151802 (*Preprint* 2006.11191)
- [33] Crivellin A, Fang Y, Fischer O, Kumar A, Kumar M, Malwa E, Mellado B, Rapheeha N, Ruan X and Sha Q 2021 (*Preprint* 2109.02650)
- [34] Sirunyan A M *et al.* (CMS) 2019 *Phys. Lett. B* **793** 320–347 (*Preprint* 1811.08459)
- [35] Barate R *et al.* (LEP Working Group for Higgs boson searches, ALEPH, DELPHI, L3, OPAL) 2003 *Phys. Lett. B* **565** 61–75 (*Preprint* hep-ex/0306033)

A compact neutron spectrometer for neutrons produced by cosmic rays

E Jarvie¹, A Buffler¹, T Hutton¹, Z Ndabeni^{1,3}, R Nndanganeni² and C Vandevoorde³

¹ Department of Physics University of Cape Town, ² South African National Space Agency, ³ iThemba LABS

E-mail: JRVERI002@myuct.ac.za

Abstract. A compact neutron spectrometer consisting of a 6x6x50 mm³ plastic scintillator with pulse shape discrimination (PSD), a silicon photomultiplier and digital data acquisition has been developed. Results from the first characterisation measurements with this device using neutrons up to 14.1 MeV are discussed. The spectrometer showed good quality pulse shape discrimination and energy resolution. Work to optimise the detector and characterise it up to 100 MeV is currently ongoing.

1. Introduction

Cosmic radiation interacting with our atmosphere produces a host of secondary particles through spallation [1][2]. At aviation altitudes the radiation field is made up predominantly of fast neutrons in the energy range 1-100 MeV [3], as seen in figure 1. The neutron energy spectrum and dose rate at these altitudes is well studied in regular conditions, and several computational models exist to calculate these values [4]. However, these codes are relatively unverified in the Southern Hemisphere, and very little observational data exists during space weather events such as solar flares and coronal mass ejections since they are fairly rare and unpredictable. These events cause an increase in ionizing radiation which not only provides increased biological risk to air crew and passengers [5], but also increases the risk of soft errors in aircraft electronics [6]. In order to better understand the effect of space weather events on our atmosphere and risks associated with flying during such events, more observational data need to be acquired.

Currently, Tissue Equivalent Proportional Counters (TEPCs) are the standard instrument for air crew dose measurements [8], however these devices do not provide spectroscopic information and therefore do not provide neutron-specific dose. As the radiation field at aviation altitudes is comprised 40% of neutrons [2] this is a problem. Neutron spectroscopy in a mixed radiation field requires a device capable of discriminating between neutron and gamma ray events. In some organic scintillators this can be done using a technique known as pulse shape discrimination (PSD). Typically, spectroscopic measurements of neutrons are made with organic liquid scintillators due to their high quality PSD capabilities, however these detectors and their associated electronics are bulky, and are toxic and fire hazards. We discuss the characterisation of the first prototype of a compact neutron spectrometer intended for studying the neutron field in an aviation scenario. The device consisting of a plastic scintillator capable of PSD, silicon

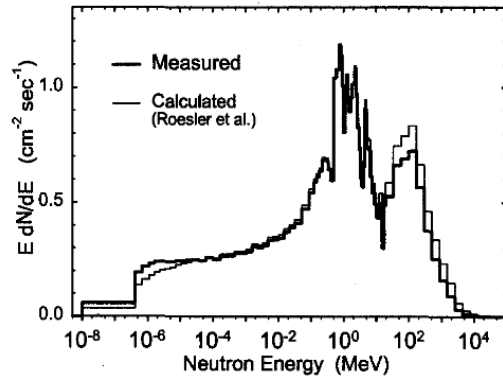


Figure 1. Neutron energy spectrum at an altitude of 20 km at 54°N, 117°W. The darker line is the measured spectrum by Goldhagen et al.[3] and the lighter line is the calculated spectrum at the same location produced by Roesler et al. [7].

photomultipliers and digital data acquisition, has been designed to be compact, robust and safe to operate on board aircraft.

2. Experimental setup

The prototype device consisted of a 6x6x50 mm³ slab of EJ276 plastic scintillator [9] coupled to a SensL C-series silicon photomultiplier (SiPM) [10] in a light tight polylactic acid plastic (PLA) casing, seen in figure 2, operated with an external power supply of 28.5 V. The signals produced by the detector were acquired digitally using a CAEN DT5730 digitiser [11] and custom open source software developed at UCT [12]. The EJ276 plastic scintillator was chosen since it is capable of PSD, is well characterised [13] and can be produced in any shape or size. The scintillator was wrapped in a reflective material in order to improve light collection from the scintillator. Since the intention is for this device to be operated on board commercial aircraft all features of the spectrometer were also chosen to make it safe to operate on board aircraft and pass through airport security checks without issues. The gamma ray and neutron response of the detector was characterised up to 4.3 MeV and 14.1 MeV respectively at the n-lab in the Department of Physics at UCT. Gamma ray characterisation was performed using ¹³⁷Cs, ²²Na and ⁶⁰Co sources and the neutron characterisation was performed using a 2.2 GBq americium beryllium (AmBe) source and 14.1 MeV neutrons from a D-T sealed tube neutron generator (STNG).

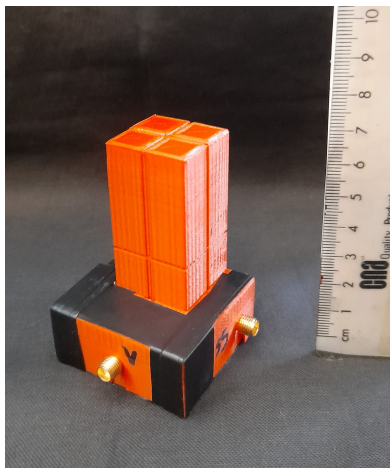


Figure 2. The prototype neutron detector scaled with a ruler measuring in centimetres.

3. Results and Analysis

Results from the prototype detector are compared to those of a reference detector (EJ301 liquid scintillator) which is commonly used for neutron spectroscopy. The fluorescence given off by scintillators is made up of a fast decaying and a slow decaying component. The ratio of light given off in each component, and therefore the shape of the pulse, depends on the nature of the excited particle [14]. Pulse shape discrimination uses this property to distinguish between gamma ray and neutron events since they interact through different mechanisms.

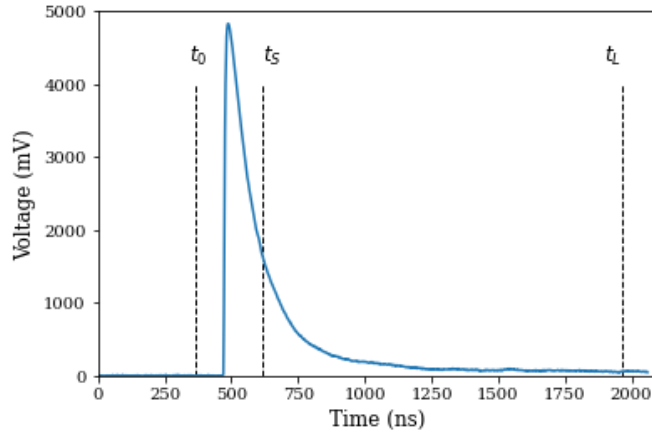


Figure 3. Typical pulse output from the prototype detector showing the starting time t_0 , short time interval t_S and long time interval t_L .

In this work the charge comparison method of PSD was implemented. The starting time, t_0 , for each pulse was chosen such that it was 80 ns before the peak of the pulse. It should be noted that using methods such as constant fraction discrimination (CFD) [12] or e-folding would be better approaches and will be implemented further in future work. The pulse was then integrated over a short time interval $[t_0; t_S]$ to produce Q_S – the short integral, and a long time interval $[t_0; t_L]$ to obtain Q_L – the long integral. The time t_L was chosen to occur at $t_0 + 1600$ ns so that the entire pulse is included and t_S was chosen to be $t_0 + 250$ ns such that the quality of the separation of pulses was optimised. As with the definition of t_0 , the definition of t_L would benefit from being determined using methods such as CFD. The chosen time intervals in relation to a typical pulse are shown in figure 3.

In the charge comparison method the pulse shape parameter S is determined through the following relation:

$$S = k \frac{Q_S}{Q_L} + c \quad (1)$$

where k and c are constants used to appropriately scale S . The gamma ray sources (^{22}Na , ^{137}Cs , ^{60}Co) were used for scaling Q_L to light output L , which has the units of MeV_{ee} (electron equivalent). Figures 4 and 5 show number of counts as a function of S and L for the AmBe source and STNG respectively. The loci associated with recoiling electrons from Compton scattering events of gamma-rays (e) and protons recoiling from n-p elastic scattering of neutrons (p) are well separated over the full range of L .

The separation between the distributions of S for two pulse classes events is quantified by the figure of merit (FoM). If the proton (p) and electron (e) recoil distributions are Gaussian the FoM can be defined in terms of the mean (μ) and full width half maximum (FWHM) such that

$$\text{FoM} = \frac{|\mu_e - \mu_p|}{\text{FWHM}_e + \text{FWHM}_p}. \quad (2)$$

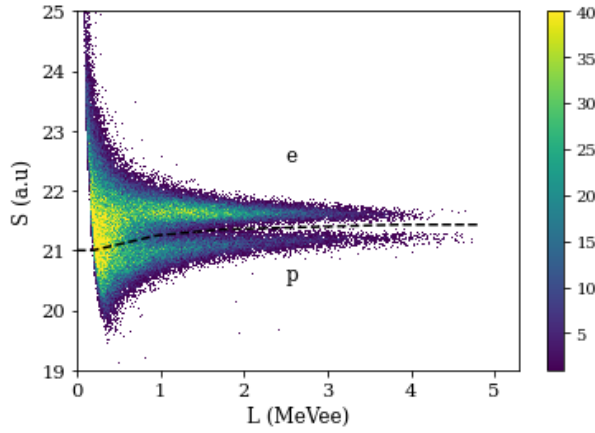


Figure 4. Counts as a function of L and S for events in the prototype detector when exposed to the AmBe source. The loci associated with neutron (e) and gamma ray (p) events are indicated and the events were separated along the dashed line.

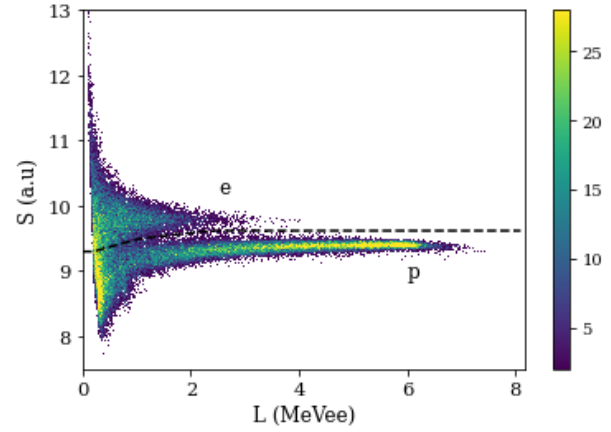


Figure 5. Counts as a function of L and S for events in the prototype detector when exposed to the STNG. The loci associated with neutron (e) and gamma ray (p) events are indicated and the events were separated along the dashed line.

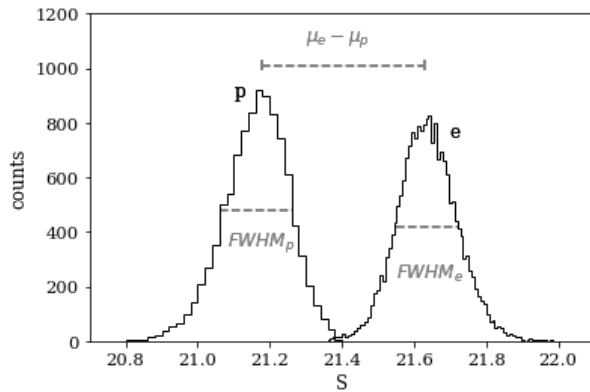


Figure 6. Counts as a function of pulse shape S for $1.9 < L < 5.0 \text{ MeV}_{ee}$ from the measurements of the AmBe source with the prototype detector. The gamma ray (e) and neutron (p) events are indicated.

The prototype detector has a FoM of 1.2 ± 0.4 over the light output range $1.9 < L < 7.7 \text{ MeV}_{ee}$, this is lower than that of the reference detector which has a FoM of 2.5 ± 0.2 over the same light output range. Despite the comparatively lower quality, a FoM > 1 is considered acceptable for the intended purpose of the detector.

To obtain spectroscopic information from the data the neutron light output spectra (LOS) were unfolded using the MAXED and GRAVEL algorithms [15]. The unfolding process utilises minimization algorithms which find the optimum combination of response functions required to produce the measured LOS provided. From this the algorithm can infer the energy spectrum of the radiation field. In order to unfold the measured LOS for the prototype detector the spectrum had to be scaled to match the response function of the EJ301 detector since there no response functions exist for the prototype.

Figures 7 and 8 show the comparison of the AmBe light output and energy spectra for the prototype and reference detectors. In figure 8 the energy spectra have peaks at the same energies, however show some differences in fluence which results in the spectra having slightly different shapes, particularly towards lower energies. This is seen in the LOS in figure 7 at low L where there is a separation between the two spectra.

Similarly, figures 9 and 10 show the light output and energy spectra for measurements of the 14.1 MeV neutrons from the STNG. In figure 10 the 14.1 MeV energy spectra clearly agree well on the position of the energy peak, however there are two distinct discrepancies in the spectra. At high energies ($\sim 15 - 16.5$ MeV) the spectrum produced by prototype has some extra contributions which is due to event pile-up in the prototype. This feature is seen in the LOS in figure 9 as a slightly longer tail at roughly 8.2 MeV_{ee} . The small bump at 11 MeV_{ee} in the energy spectrum from the prototype detector is due to the response function used having a slightly different shape to the measured LOS. The difference in shape, which is seen at around 6.5 MeV_{ee} in the LOS, is because the response function used is for a larger detector in which multiple scatter occurs. Since the prototype is very small there are no double scatter events.

Overall, the energy spectra of the two detectors agree well in terms of key features such as position of energy peaks. All of the differences in the unfolded energy spectra can be corrected by producing a response matrix for the prototype detector and using it for the unfolding.

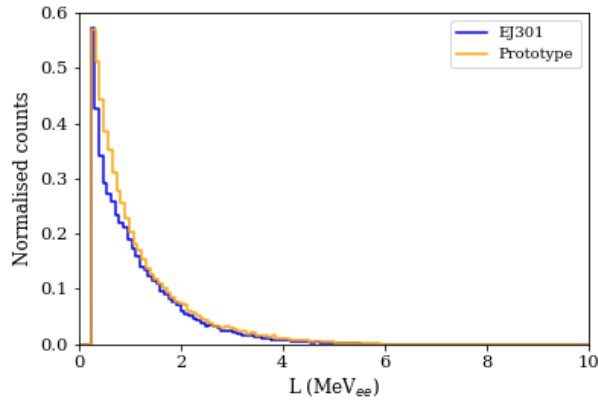


Figure 7. AmBe neutron light output spectrum for EJ301 reference detector and prototype detector.

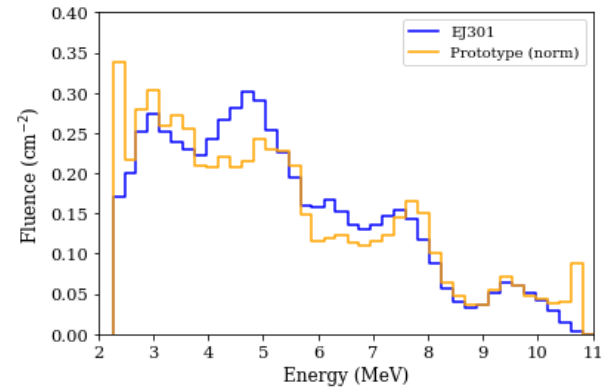


Figure 8. Unfolded AmBe neutron energy spectrum for the EJ301 reference detector and prototype detector.

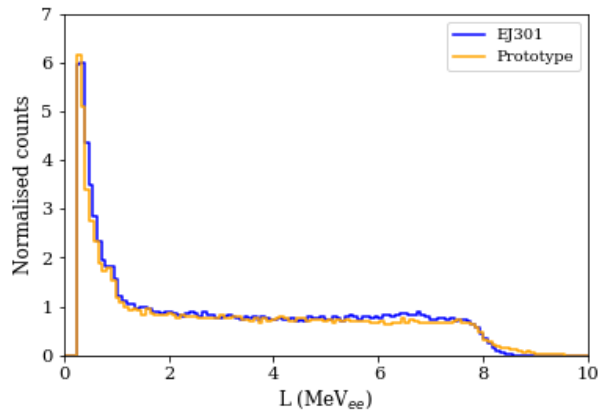


Figure 9. STNG (14.1 MeV) neutron light output spectrum for EJ301 reference detector and prototype detector.

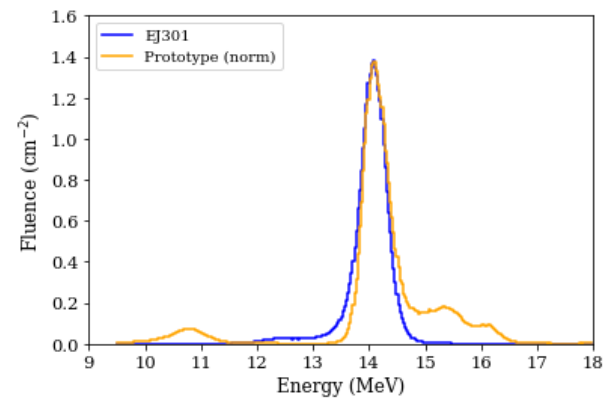


Figure 10. Unfolded STNG neutron (14.1 MeV) energy spectrum for the EJ301 reference detector and prototype detector.

The relative efficiency of the prototype detector was determined by comparing the detected

neutron rate to that measured in the EJ301 detector for the same source conditions. From Table 1 it is clear that the prototype has a lower efficiency comparison to the reference detector, however this is expected for a detector of this size since the scintillator is smaller. The energy peak resolution for the 14.1 MeV neutrons is comparable for the two detectors, which implies that the prototype is capable of high quality spectroscopy. In the work done previously by Comrie [12] a detector consisting of a EJ299-33 plastic scintillator of the same dimensions coupled to two SiPMs was presented. In comparison to this detector system the prototype does not perform as well, with a lower efficiency and FoM, however it is suggested in Comrie's work that the addition of the second SiPM improved both of these characteristics significantly.

Table 1. Comparison of the EJ301 reference and prototype detectors for relative neutron efficiency of both sources and 14.1 MeV energy peak resolution.

	EJ301	Prototype
Relative neutron efficiency (AmBe)	1.00	0.38
Relative neutron efficiency (STNG)	1.00	0.15
14.1 MeV energy peak resolution	1.64 ± 0.09	1.63 ± 0.08

4. Conclusions and future work

Overall the compact spectrometer shows promise. However improvements to the design and characterisation at higher energies are needed. Work is currently underway to improve and optimise the design of the detector presented using GEANT4 simulations. In addition to this, the next detector design will likely feature two SiPMs in order to improve light collection which will improve detection efficiency and PSD quality. The updated detector will be characterised with neutrons over the full energy range of interest at the UCT n-lab (1-14 MeV), AMANDE fast neutron facility at the IRSN in France (1-20 MeV) and iThemba LABS fast neutron facility (30-100 MeV). Measurements will also be made in real in-flight scenarios on both local and international flights.

Acknowledgments

This work is supported by the National Research Foundation (South Africa) and the South African National Space Agency.

References

- [1] Grieder P 2001 *Cosmic Rays at Earth: Researcher's reference manual and data book* (Elsevier)
- [2] Buffler A 2019 Neutrons in space Tech. rep. Seminar at South African National Space Agency
- [3] Goldhagen P, Clem J and Wilson J 2004 *Rad. Prot. Dosim.* **110** 387
- [4] Clem et al 2004 *Rad. Prot. Dosim.* **110** 423–428
- [5] Lynge E 2001 *International journal of epidemiology* **30** 830–832
- [6] W Tobiska et al 2015 *Space weather* **13** 202–210
- [7] Roesler S, Heinrich W and Schraube H 2002 *Radiat. Prot. Dosim.* **98** 367–388
- [8] Bilski P, Olko P and Horwacik T 2004 *Nukleonika* **49** 77–83
- [9] Eljen technologies, products <https://eljentechnology.com/products/plastic-scintillators/ej-276>
- [10] Sensl c-series data sheet <https://sensl.com/downloads/ds/DS-MicroCseries.pdf>
- [11] Caen desktop digitizers <https://www.caen.it/desktop-digitizers/>
- [12] Comrie A 2016 *A new compact neutron spectrometer* Ph.D. thesis University of Cape Town
- [13] Buffler A, Comrie A, Smit F and Wortche H 2015 *IEEE Transactions on nuclear science* **62** 1422–1428
- [14] Knoll G 2010 *Radiation Detection and Measurement* (Wiley)
- [15] Reginatto M, Goldhagen P and Neumann S 2002 *Nucl. Instr and Meth. A* **476** 242–246

Machine learning approach for the search of resonances with topological features at the Large Hadron Collider

S E Dahbi¹, J Choma¹, B Mellado^{1,2}, G Mokgatitswane¹, X Ruan¹
and B Lieberman¹

¹School of Physics and Institute for Collider Particle Physics, University of the Witwatersrand, Johannesburg, Wits 2050, South Africa.

²iThemba LABS, National Research Foundation, PO Box 722, Somerset West 7129, South Africa.

E-mail: salah_eddine.dahbi@cern.ch

Abstract. We propose a new approach to search for new resonances beyond the Standard Model (SM) of particle physics in topological configurations using Machine Learning techniques. This involves a novel classification procedure based on a combination of weak-supervision and full-supervision in conjunction with Deep Neural Network algorithms. The performance of this strategy is evaluated on the production of SM Higgs boson decaying to a pair of photons inclusively and exclusive regions of phase space, for specific production modes at the Large Hadron Collider (LHC), namely through the gluon-gluon fusion, the fusion of weak vector bosons, in associated production with a weak vector boson, or in association with a pair of top quarks. After verifying the ability of the methodology to extract different Higgs signal mechanisms, a search for new phenomena in high-mass diphoton final states is setup for the LHC.

1. Introduction

After the discovery of a Higgs boson (h) [1, 2, 3] at the Large Hadron Collider (LHC) by the ATLAS [4] and CMS [5] experiments, a number of anomalies have been identified based on discrepancies in the production of leptons at these experiments [6]. These anomalies join a number of phenomena that represent a significant experimental evidence, such as Dark Matter, the origin of neutrino mass, the matter-anti-matter asymmetry, in addition to a number of theoretical problems [7].

Machine Learning (ML) can play a significant role in solving these problems, by searching for resonances in corners of the phase-space that are either unexplored or poorly covered by the cut-based analysis strategy. Therefore, in this paper we extend the applications of machine learning in high energy physics to the search for new physics at the LHC, using weak supervision learning with topological requirements. The approach is intended to identify different phase-space of the resonances, since they are expected to be generated with different production mechanisms at the LHC and it is adequate to extract more subtle signals in the data without relying on a specific model of the signal with a particular set of parameters. We have organised this paper as follows: section 2 describes the simulation of both background and signal processes of the production

of the SM Higgs boson decaying to a pair of photons at the LHC, as a benchmark. Section 3 briefly introduces weak supervision learning classification and the used deep neural network (DNN) architecture. The performance of the weak supervision classification will be evaluated in section 4. Section 5 proposes an approach for the search for new physics, where weak supervision learning is restricted to the topological configurations of the phase space, such as number of b -tagged jets, number of leptons, vector boson fusion topology, etc... Finally, section 6 summarises the study with suggestions and prospects for the future search of resonances at the LHC.

2. SM Higgs datasets and event selection

The performance of the ML classifier, described in section 3, is tested on simulated Higgs to di-photon ($pp \rightarrow h \rightarrow \gamma\gamma$) events as a benchmark. We focus on the proton-proton collisions at the LHC with a centre-of-mass energy of 13 TeV. Background and signal Samples were produced using **MadGraph5_aMC@NLO** 2.6.7 with Next-to-Leading Order accuracy in QCD [8]. The parton showering and hadronization were simulated with **PYTHIA** 8.2 [9] using ATLAS A14 event tuning and NNPDF2.3 LO parton distribution function set [10]. Events were processed with **Delphes** 3 [11], which provides an approximate fast simulation of the current ATLAS experiment. Events of interest were simulated by imposing a set of generator-level cuts, where the transverse momentum of the photons is required to be greater than 25 GeV and the di-photon invariant mass to be between 105 and 160 GeV. Hadronic jets were reconstructed using the anti- k_t algorithm [12] with the radius parameter, $R = 0.4$, as implemented in the **FastJet** 3.2.2 [13] package. Jets with $p_T > 30$ GeV and $|\eta| < 4.7$ are considered. In addition, jets originating from bottom quarks are identified as b -jets with b -tagging algorithms [14]. Reconstructed jets overlapping with photons, electrons or muons in a cone of size $R = 0.4$ are removed. Electrons and muons are required to have $p_T > 25$ GeV and $|\eta| < 2.5$. Finally, an inclusive event selection of at least two photons, that have $p_T > 25$ GeV and $|\eta| < 2.37$, is applied. The reconstructed di-photon invariant mass spectra, $m_{\gamma\gamma}$, for signal and background are shown in figure 1.

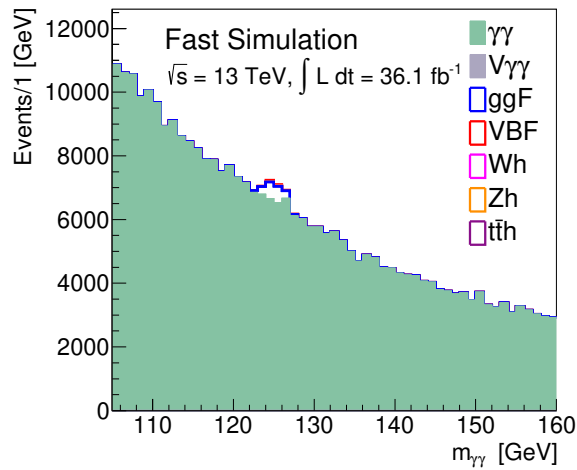


Figure 1. Di-photon invariant mass spectrum at 13 TeV of proton-proton collision, corresponds to an integrated luminosity of 36.1 fb^{-1} . The different production mode of the Standard Model Higgs boson samples, are normalised to the cross sections times the di-photon decay branching ratio.

3. Weak supervision classification and DNN architecture

The main purpose of supervised learning is to train a model on fully labelled data where each training example \vec{x}_i comes with a label $y_i \in \{0, 1\}$, in a case of binary classification task. The model is trained to minimise the loss function which can be in a form of binary cross-entropy:

$$\ell(y, \hat{y}) = -y \cdot \log \hat{y} + (1 - y) \cdot \log(1 - \hat{y}), \quad (1)$$

where \hat{y} is the model output and y is the target output (1 for signal and 0 for background). In the case of weak supervision [15], the learning phase during this paradigm takes place on partially/weakly labelled data set [16]. These weakly labelled data is then used by the classifier for the training. Contrariwise of the the full supervision (see equation 1), weak supervision uses the following equation:

$$f_{weak} = \operatorname{argmin}_{f: \mathbb{R}^n \rightarrow [0,1]} \sum_K \ell \left(\frac{1}{|K|} \sum_{i \in K} \hat{y}_i, y_K \right), \quad (2)$$

where K denotes training data batches and y_K is the signal ratio in each batch. The performance of weak supervision was compared to that of full supervision in [18] and weak supervision achieved reasonable results, despite knowing only a fraction of the labels.

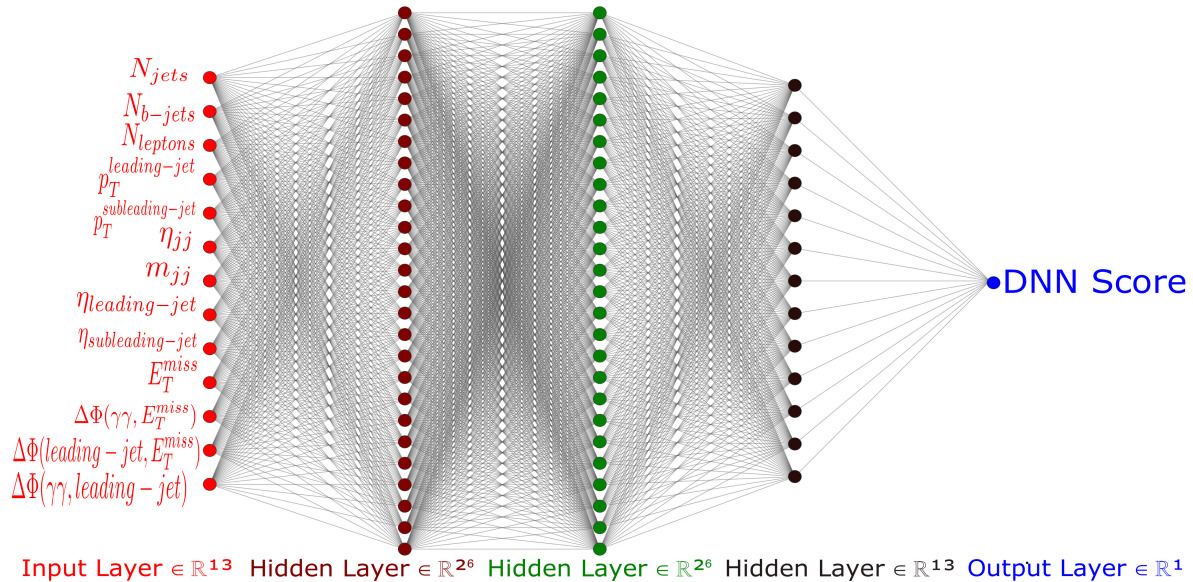


Figure 2. DNN architecture for the classification of events as background or signal in this study, with the "Layout=TANH|26,TANH|26,TANH|13,LINEAR" configuration.

Events from the simulated dataset are classified using a DNN algorithm, as implemented in the package ROOT [19] and the TMVA [20] data processing framework. The DNN architecture implemented in this study consists of an input layer, three hidden layers and an outer layer. The input layer consists of 13 neurons, which represent the kinematic features of the dataset. The three hidden layers are made up of 26, 26 and 13 neurons, respectively. The output layer consists of a single neuron. Two activation functions are used here: a hyperbolic tangent for the hidden layers, and a sigmoid function for the output layer. Since we are dealing with a binary classification problem, where the events are classified as signal or background, the cross-entropy (see equation 1) is used as a loss function. The training of the classifier is divided into

three stages. The first stage begins with a learning rate of 10^{-2} and a momentum of 0.9. In order to avoid overtraining the classifier, the weights are regularised using the $L2$ option, which multiplies a scaling factor of 10^{-3} to the norms of the weight matrices. For the second training stage, learning rate and momentum are reduced to 10^{-3} and 0.5, respectively. For the final training phase, the learning rate is set to 10^{-2} and the momentum to 0.3. Figure 2 describes the network topology and the input variables used in this study.

4. Weakly supervised learning for the classification of the SM Higgs boson

For the weak supervised learning study on the Higgs production mechanisms, the signals and background processes are mixed in the Higgs invariant mass window of 120 GeV to 130 GeV. The sideband contains only pure background in the region between 105 GeV and 160 GeV, excluding the signal mass window. The purpose of this procedure is to evaluate the ML algorithm's ability to classify a signal from an unknown mixture of signal and background, with respect to pure background in the sideband. According to the receiver operator characteristic (ROC) analysis results shown in figure 3, it is evident that weak supervision is capable of separating different signal candidates. However, the signal and background classification is not satisfactory when compared to full supervised learning (see table 1). Given these points, weak supervision seems to be inefficient due the complexity of the phase-space explored here. For that reason a guided weak supervision method with topological requirements is introduced. This will be discussed explicitly in section 5.

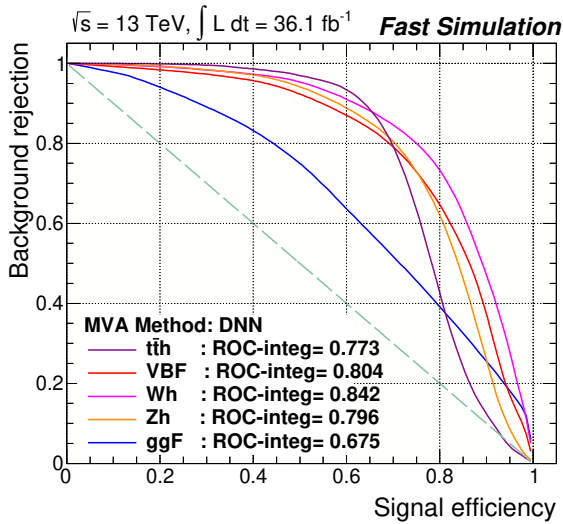


Figure 3. Weakly supervised ROC curves, using DNN classifier for different Higgs production mechanisms.

Table 1. Comparison of the integral of the ROC curve response from different supervised learning methods.

Process	Full Supervision	Weak Supervision
ggF	0.780	0.675
VBF	0.965	0.804
Wh	0.951	0.842
Zh	0.936	0.796
tth	0.997	0.773

5. Weak supervision learning with topological requirements

The performance of the weak supervised learning seems to be inefficient to separate different signal candidates, due the complexity of the phase-space explored here. Therefore there is a need to implement the method that we refer to as the guided weak supervision method. In guided weak supervision, the training is restricted to the topological signatures derived from selected production mechanisms. The effectiveness of this methodology is evaluated and verified on the VBF, Wh and $t\bar{t}h$ production mechanisms. The results are quantified and compared to the inclusive weak supervision in table 2.

The SM Higgs boson production mode through VBF represents the second largest cross section at the LHC. The VBF mechanism in the SM entails the scattering of two quarks, leading to two hard jets in the forward and backward regions of the ATLAS detector with high di-jet invariant mass, m_{jj} . These topological characteristics can be exploited by the DNN to distinguish VBF from backgrounds and other production mechanisms. In this context, the VBF topology is defined as events with at least two jets. This is followed by a signal significance scan using m_{jj} and the pseudorapidity separation between the two leading jets, $\Delta\eta_{jj}$. We use the signal significance scan to maximise the relative contribution of the VBF production mechanism and minimise the background yield as much as possible.

A similar test is performed on the associated production of Higgs boson, with a W gauge boson, where the neural networks are trained separately with two topological features from the Wh final states. This includes leptonic and hadronic decays of the W boson. The performance of weak supervision classification also experiences improvements with topological requirements and is able to isolate the Wh process.

In addition, the guided weak supervision is tested on the production of the Higgs boson in association with top-antitop quarks. Since the relative contribution of the top-antitop quark to the total Higgs boson production is less than 1%, it becomes challenging to extract this signal process. Most prominently, this is found to be the case for weak supervision. However, the test is performed by requiring two topological characteristics, representing a fully hadronic (at least two central jets) and semi-leptonic (at least one b -jets and one lepton) decays of top quark from $t\bar{t}h$ process.

Table 2. Summary of the ROC integrals for VBF, Wh and $t\bar{t}h$ with different topological requirements, compared to inclusive weak supervision learning.

Process	Weak Supervision	ROC Integral
VBF	Inclusive	0.804
	$N_{jets} \geq 2, \Delta\eta_{jj} > 0, m_{jj} > 1000 \text{ GeV}$	0.951
	$N_{jets} \geq 2, \Delta\eta_{jj} > 0, m_{jj} > 800 \text{ GeV}$	0.881
	$N_{jets} \geq 2, \Delta\eta_{jj} > 0, m_{jj} > 600 \text{ GeV}$	0.912
	$N_{jets} \geq 2, \Delta\eta_{jj} > 0, m_{jj} > 400 \text{ GeV}$	0.873
Wh	Inclusive	0.842
	Hadronic	0.907
	Leptonic	0.902
$t\bar{t}h$	Inclusive	0.773
	$N_{b-jets} \geq 1, N_{leptons} \geq 1$	0.880
	$N_{b-jets} \geq 2$	0.950

6. Discussion and conclusions

Machine learning may play a significant role in the deeper exploration of the phase-space available at the LHC. We introduce signatures and loose topological requirements before the implementation of weak supervised training. The impact on the signal efficiency and background rejection, in this approach, is evaluated for the different production mechanisms, where significant improvements are observed with respect to the implementation of weak supervision inclusively. This is referred to as guided weak supervision. While weak supervision, as setup here, has the advantage of not relying on a model for the signal it is necessary to restrict the phase-space where the sideband and the signal region are confronted with each other. While signature and topological requirements are driven by physics considerations, the search is not biased by the phenomenology of a model with a particular set of parameters.

The performance of the approach has been evaluated with the SM Higgs boson as a benchmark. The signatures and topologies used here in principle can be used in the search for heavier or lighter SM Higgs-like bosons. Provided that the topological requirements are loose enough, these can be used for more generic searches of bosons. For instance, it is well motivated to apply weak supervision in the presence of a b -tagged jet, while requiring a maximum amount of jets in order to remove potential signals in association with top quarks. This can be extended to other types of searches, such as search for resonances in multi-particle cascades.

Acknowledgments

The authors are grateful for support from the South African Department of Science and Innovation through the SA-CERN program and the National Research Foundation for various forms of support. The authors are also indebted to the Research Office of the University of the Witwatersrand for grant support.

References

- [1] P. W. Higgs, Phys. Lett. **12**, 132-133.
- [2] F. Englert and R. Brout, Phys. Rev. Lett. **13**, 321-323.
- [3] P. W. Higgs, Phys. Rev. Lett. **13**, 508-509.
- [4] G. Aad *et al.* [ATLAS], Phys. Lett. B **716**, 1-29, [arXiv:1207.7214 [hep-ex]].
- [5] S. Chatrchyan *et al.* [CMS], Phys. Lett. B **716**, 30-61, [arXiv:1207.7235 [hep-ex]].
- [6] S. von Buddenbrock, R. Ruiz and B. Mellado, Phys. Lett. B **811**, 135964, [arXiv:2009.00032 [hep-ph]].
- [7] S. Troitsky, Phys. Usp. **55** (2012), 72-95 [arXiv:1112.4515 [hep-ph]].
- [8] J. Alwall, R. Frederix, S. Frixione, V. Hirschi, F. Maltoni, O. Mattelaer, H. S. Shao, T. Stelzer, P. Torrielli and M. Zaro, JHEP **07**, 079, [arXiv:1405.0301 [hep-ph]].
- [9] T. Sjöstrand, S. Ask, J. R. Christiansen, R. Corke, N. Desai, P. Ilten, S. Mrenna, S. Prestel, C. O. Rasmussen and P. Z. Skands, Comput. Phys. Commun. **191**, 159-177, [arXiv:1410.3012 [hep-ph]].
- [10] R. D. Ball, V. Bertone, S. Carrazza, C. S. Deans, L. Del Debbio, S. Forte, A. Guffanti, N. P. Hartland, J. I. Latorre and J. Rojo, *et al.* Nucl. Phys. B **867**, 244-289, [arXiv:1207.1303 [hep-ph]].
- [11] J. de Favereau *et al.* [DELPHES 3], JHEP **02**, 057, [arXiv:1307.6346 [hep-ex]].
- [12] M. Cacciari, G. P. Salam and G. Soyez, JHEP **04**, 063, [arXiv:0802.1189 [hep-ph]].
- [13] M. Cacciari, G. P. Salam and G. Soyez, Eur. Phys. J. C **72**, 1896, [arXiv:1111.6097 [hep-ph]].
- [14] L. Vacavant [ATLAS], PoS **2008LHC**, 064.
- [15] L. M. Dery, B. Nachman, F. Rubbo and A. Schwartzman, JHEP **05**, 145, [arXiv:1702.00414 [hep-ph]].
- [16] Patrini, Giorgio and Nielsen, Frank and Nock, Richard and Carioni, Marcello, International conference on machine learning, arXiv:1602.02450, pages:708–717.
- [17] Junwei Han, Dingwen Zhang, Gong Cheng, Lei Guo, Jinchang Ren, IEEE Transactions on Geoscience and Remote Sensing, **53**, 6, 3325–3337, 2014, IEEE.
- [18] T. Cohen, M. Freytsis and B. Ostdiek, JHEP **02**, 034 [arXiv:1706.09451 [hep-ph]].
- [19] R. Brun and F. Rademakers, Nucl. Instrum. Meth. A **389**, 81-86.
- [20] J. Therhaag [TMVA Core Developer Team], AIP Conf. Proc. **1504**, no.1, 1013-1016 (2012)

Measurement of the photoabsorption cross section of ^{24}Mg .

J A C Bekker^{1,2} L Pellegri^{1,2} M Wiedeking^{1,2} P Adsley^{1,2} R Neveling¹, L M Donaldson¹

¹SSC Laboratory, iThemba LABS, P.O. Box 722, Somerset West 7129, South Africa.

²School of Physics, University of the Witwatersrand, Johannesburg 2050, South Africa.

E-mail: 1390529@students.wits.ac.za

Abstract. Accurate nuclear data is a key factor in determining the suitability and reliability of many theoretical nuclear models and large-scale calculations. One of the main ingredients of these calculations is how nuclei respond to an electromagnetic field. The excitation of the isovector giant dipole resonance (GDR) is of particular importance in both nuclear structure studies as well as being the main mode of interaction of ultra-high-energy cosmic rays with the extra-galactic medium en route to Earth. This study investigates the photoabsorption cross section in the region of the GDR in ^{24}Mg through the use of proton inelastic scattering and the equivalent virtual photon method. The K600 spectrometer at the iThemba LABS facility was used to obtain high resolution, low background $^{24}\text{Mg}(p,p')^{24}\text{Mg}^*$ inelastic scattering data. The virtual photon absorption method is described and the (p,p') spectrum that will be converted from a double-differential cross section to a photoabsorption cross section is presented.

1. Introduction

The field of nuclear astrophysics is littered with examples of calculations that require accurate experimental inputs to replicate and describe physical systems [1]. One of the pertinent examples of these calculations is a simulation of the propagation of ultra-high-energy cosmic rays (UHECR) that break up through absorption of the Lorentz-boosted cosmic microwave background, which requires input from hundreds of nuclei below mass 56 [2]. Obtaining all of the necessary quantities for all of these nuclei is unfeasible; however, some of the nuclei are of much greater importance and dominate these processes and model validations. This project aims at extracting the total photoabsorption cross section in the energy region of the isovector giant dipole resonance (IVGDR) for one of the keystone nuclei in this calculation: ^{24}Mg . This is done through relativistic Coulomb excitation of the IVGDR in ^{24}Mg , which falls in the energy region from 16-23 MeV, along with the use of the virtual photon absorption technique [3]. An exhaustive amount of E1 gamma transitions occur through this channel and it is a strong indicator of the reaction mechanism through which the energy and mass composition of the UHECR will be modified during the propagation path.

2. Experimental Methods

The K600 magnetic spectrometer at iThemba LABS is one of the few facilities in the world that can deliver high-resolution, low-background spectra for 0° measurements[4] and is shown in

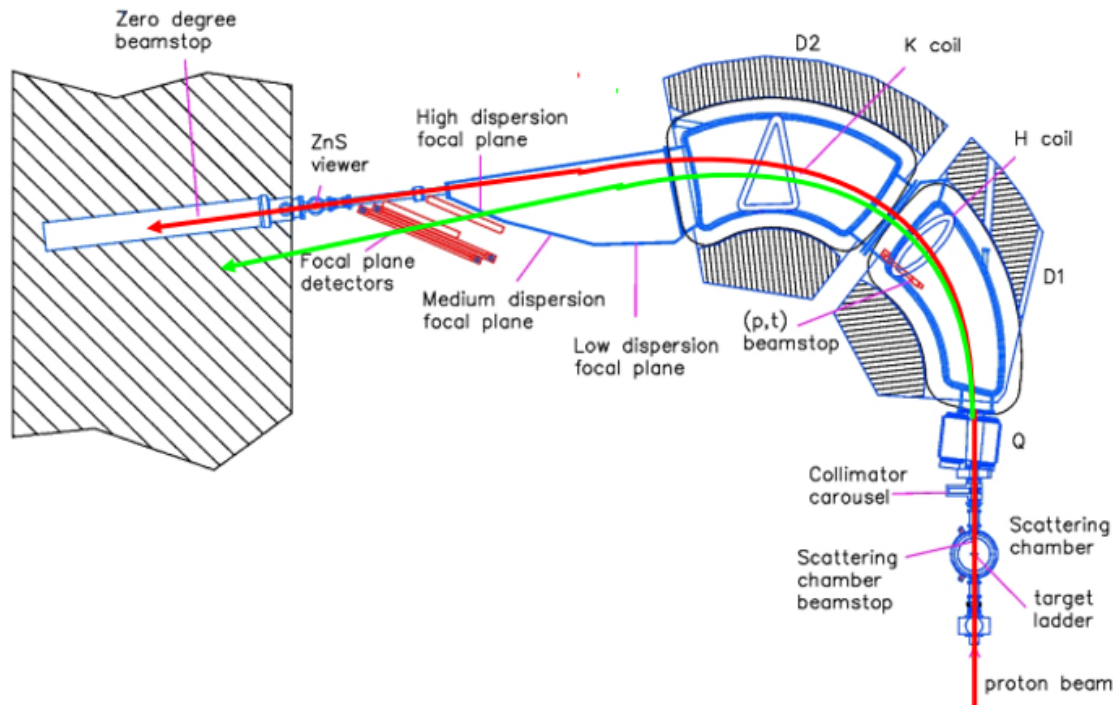


Figure 1. Schematic diagram of the K600 magnetic spectrometer at zero degrees mode.[4]

Fig. 1. The separated sector cyclotron (SCC) accelerates protons to 200 MeV and they are then transported to the target chamber using a series of magnets and beamlines. The unreacted beam is separated from the reacted beam using a magnetic spectrometer consisting of two dipoles, a quadrupole and two trim coils. The focal-plane detectors consists of two paddle scintillator detectors and two multi-wire drift chambers. The spectrometer is used in high-dispersion mode, where the focal plane angle of the detectors corresponds to a scattering angle between 0° and 2° . The ^{24}Mg target was hot rolled in argon atmosphere to a thickness of 2mm and an areal density of $2.1\text{mg}/\text{cm}^2$.

3. Theoretical Considerations

The use of 200 MeV protons at 0° scattering angle allows one to access a reaction system that greatly favours the IVGDR E1 excitation via Coulomb interaction. This is convenient because it limits the interference between the nuclear and Coulomb interactions, thus eliminating the arduous process of disentangling different contributions to the spectrum. One of the methods used to characterise and calculate the Coulomb excitation of the nucleus is virtual-photon production method, which recasts the electromagnetic interaction between the projectile and the target as a spectrum of virtual photons that are absorbed by the target [6]. The calculation of virtual photon production in this work was done using a code provided by Carlos Bertulani based on the methods described in reference [3]. This approach allows the equivalent photoabsorption cross section to be extracted from the double-differential cross section obtained in the experiment

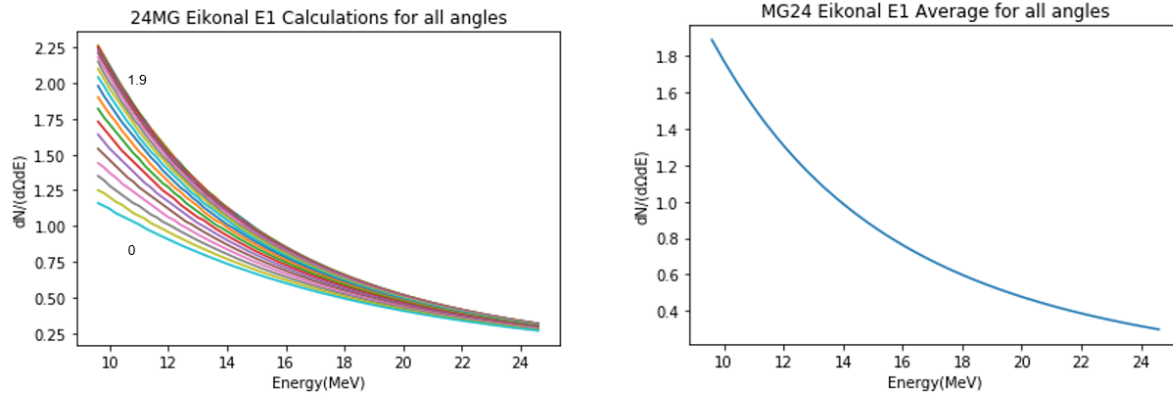


Figure 2. The Calculated number of virtual photons produced in the angular range of the K600 spectrometer. This is used in conjunction with the double differential cross section calculation to calculate the total E1 photoabsorption.

in the following way:

$$\frac{d^2\sigma}{d\Omega dE_\gamma} = \frac{1}{E_\gamma} \frac{dN_{E1}\sigma_\gamma^{\pi\lambda}}{d\Omega}(E_\gamma). \quad (1)$$

Here $\frac{dN_{E1}}{d\Omega}$ represents the amount of E1 virtual photons that are produced per solid angle, $\frac{d^2\sigma}{d\Omega dE_\gamma}$ is the double differential cross-section and E_γ is the energy of the γ . The model used to calculate the virtual-photon production is the Eikonal model and its main advantage over the semi-classical model is that it does not exhibit asymptotic behaviour at small angles, which is crucial to the implementation of the method at 0° . The number of virtual photons produced is calculated at regular intervals between 0° and 2° as can be seen in the left panel of Fig. 2. The right panel of Fig. 2 shows the weighted average of all of these calculations[3]. The photoabsorption cross section is calculated by dividing the double differential cross section by the right panel of Fig.2 and multiplying the result by the energy at each energy, thus solving for $\sigma_\gamma^{\pi\lambda}$ in Eqn. 1.

4. Results

The double differential cross section is calculated using the following formula:

$$\frac{d^2\sigma}{d\Omega d\sigma} = \frac{10^{27} \cdot N_c}{N_0 \cdot \rho \cdot D \cdot \Delta\Omega \cdot \Delta E \cdot \epsilon_{tot}} \quad (2)$$

Where:

- N_0 is the amount of protons incident on the target.
- N_c is the number of counts in a bin.
- ρ is the areal density of the target nucleus.
- $\Delta\Omega$ is the solid angle of the detector used in the K600 and has a value of 3.41 msr.
- ΔE is the energy bin of the histogram.
- ϵ_{tot} is the efficiency of the VDC's used in the K600.
- D is the alive time of the electronics used.

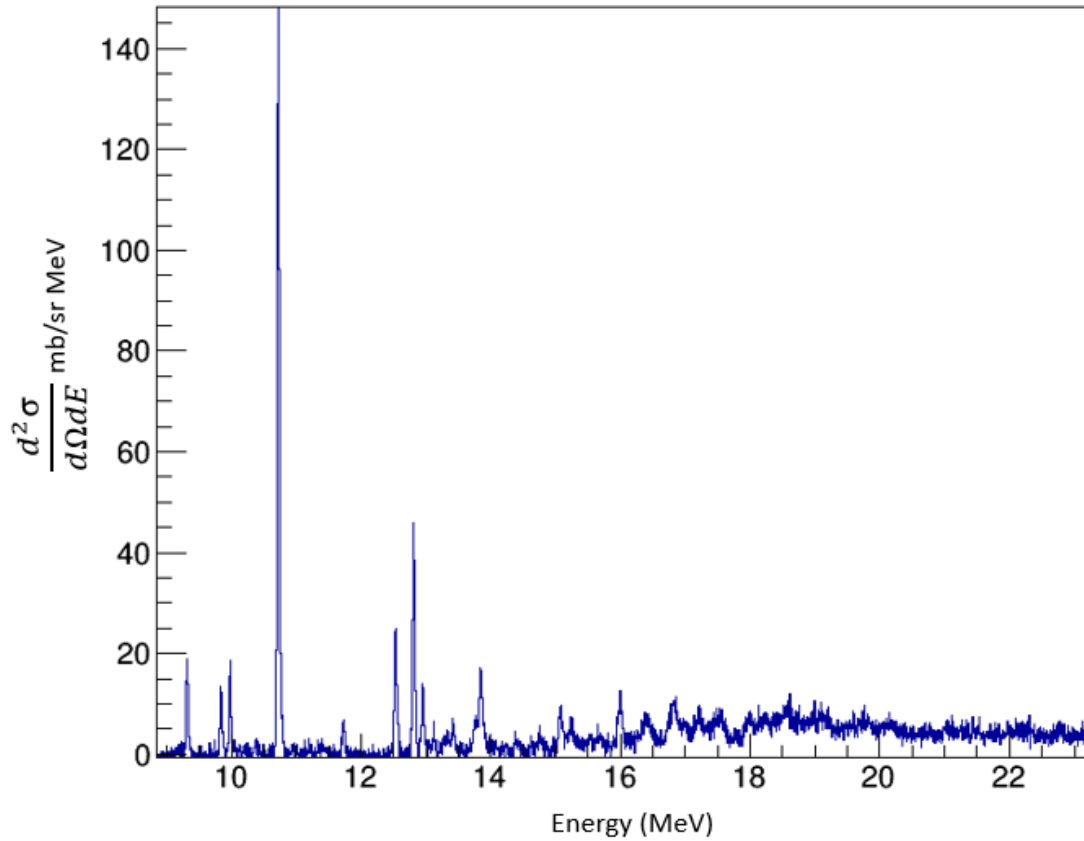


Figure 3. The Extracted double-differential cross section using the procedures described in sections 2 and 3.

The final result of the processes describe above are in the process of being calculated from the double-differential cross-section shown in Fig. 3. Still present in this spectrum is the background from higher multipoles and quasi-free particle scattering. The quantification of these backgrounds requires a rigorous DWBA calculation to estimate the relative strength of the isoscalar giant quadrupole resonance in the area of interest $16 < E_x < 23$ MeV and to account for other higher energy, higher multipolarity contributions. After the calculation has been finalised a meaningful comparison can be made to a previous (γ, abs) spectrum obtained by Dolbilkin *et al*[6] and systematic calculations made using the RIPL database[7].

Acknowledgments

This work is based on the research supported in part by the National Research Foundation (NRF) of South Africa grant number 118846.

References

- [1] Bernstein L A, Brown D A, Koning D A, Rearden B T, Romano C E, Sonzogni A A, Voyles A S, Younes W 2019, " Our Future Nuclear Data Needs" *Annual Review of Nuclear and Particle Science* 2019 **69:1**, 109-136.
- [2] Boncioli D, Fedynitch A, Winter W 2017 *Nuclear Physics Meets the Sources of the Ultra-High Energy Cosmic Rays*. Sci Rep **7**, 4882 .
- [3] Bertulani C A 2009, Theory and Applications of Coulomb Excitation. 2009, **0908.4307**, *arXiv*.
- [4] Neveling, R, et al 2011 "High energy-resolution zero-degree facility for light-ion scattering and reactions at iThemba LABS." *Nuclear Instruments and Methods in Physics Research Section A: Accelerators, Spectrometers, Detectors and Associated Equipment* 654.1 : 29-39.
- [5] von Neumann-Cosel P, Tamii 2019 A Electric and magnetic dipole modes in high-resolution inelastic proton scattering at 0°. *Eur. Phys. J. A* **55**, **110**
- [6] Dolbilkin B S 1966 "Gamma-ray absorption of ^{19}F , ^{24}Mg , and ^{40}Ca in the 10-30 MeV region." *In: Izv. Akad. Nauk SSSR, Ser. Fiz.*, **30**: 349-58.
- [7] Koning A J 2019 "TENDL: Complete Nuclear Data Library for Innovative Nuclear Science and Technology". *Nuclear Data Sheets* 155. Special Issue on Nuclear Reaction Data, pp. 1–55

A search for tWZ production in the trilepton channel using Run 2 data from the ATLAS experiment

Benjamin Warren

PhD student, Department of Physics, University of Cape Town, Rondebosch 7701, South Africa

E-mail: wrrben001@myuct.ac.za

Abstract. A search for tWZ production using events containing three leptons from Run 2 ATLAS proton-proton collision data with a centre of mass energy of 13 TeV will be presented. An event selection scheme was developed using simulation to select tWZ events and to broadly suppress background events. Events were then separated into mutually-exclusive regions of phase space to increase the amount of tWZ events compared to background events, and to calibrate the modelling of the backgrounds. Background events were further suppressed through the use of Gradient Boosted Decision Tree (GBDT) machine learning algorithms. An event-level GBDT was used to distinguish between tWZ and all backgrounds. Using the output score of the event-level GBDT, a maximum likelihood fit, blind to data in the Signal Region, was used to estimate the signal strength, μ , of tWZ production, where nuisance parameters were assigned to theoretical and experimental systematic uncertainties. A signal strength of $\mu = 1.20^{+1.37}_{-1.29}$ was determined with an expected significance of 0.77σ , and an expected upper limit on μ of $2.61^{+2.25}_{-1.21}$ was also determined. These preliminary blinded results show that the search has the potential to put the strongest ever constraint on tWZ production, but does not have the potential to observe tWZ production as predicted by the Standard Model.

1. Introduction

The Standard Model (SM) of particle physics describes the current understanding of the fundamental components of matter and three of the four fundamental forces. It has thus far stood up to every experimental test to which it has been subjected, and with the discovery of the Higgs Boson [1, 2] in 2012, the last major piece of the SM has been confirmed. However, even with the success of the SM, it is unable to address some unanswered questions about matter and forces in the universe. Gravity is not included in the SM, there is no explanation for why the Higgs boson mass seems to arise from very precise cancellations of different contributions [3], and there is no explanation for dark matter [4]. The current goal of particle physics is to search for solutions to these problems by testing the predictions of the SM in the hope of finding hints of Beyond the SM (BSM) physics that could provide solutions to these problems.

The Large Hadron Collider (LHC) is capable of colliding particles at high energies that have never been attained in a lab environment, and is capable of producing collisions at rates far higher than previously achieved. Due to its high energy and high collision rate capabilities, the LHC can produce a significant number of top quarks. This is of interest because as the heaviest elementary particle, the top quark serves as a unique probe in searches for BSM physics at high energies [5]. Furthermore, the ATLAS detector [6] is one of two general purpose experiments at

the LHC designed to collect pp collision data that can be used to test the properties of the top quark.

A search is presented for a rare and unobserved production process of a top quark produced in association with a W boson and a Z boson (tWZ production) using run 2 data from the ATLAS detector at the LHC. This is done with the goal of constraining the electroweak couplings of the top quark since these serve as interesting probes of BSM physics [5]. The Signal Region (SR), which is the region where the measurement of the cross section is performed, remains blind to run 2 data as this search is part of an ongoing ATLAS analysis and one does not want to be biased by looking at the data in the SR before all other aspects of this analysis are in place.

2. tWZ production and backgrounds in the trilepton channel

In order to reduce the number of background events in the search for tWZ production, a trilepton decay channel was chosen. In Figure 1, an example Feynman diagram of this decay channel is shown. This channel was chosen because in the case of less than three leptons, hadronic background processes dominate to such an extent as to make it impossible to make a measurement of tWZ production in these channels. The trilepton and four lepton channels were considered for further study and the trilepton channel was chosen because it offered manageable background production processes and offered reasonable statistical power.

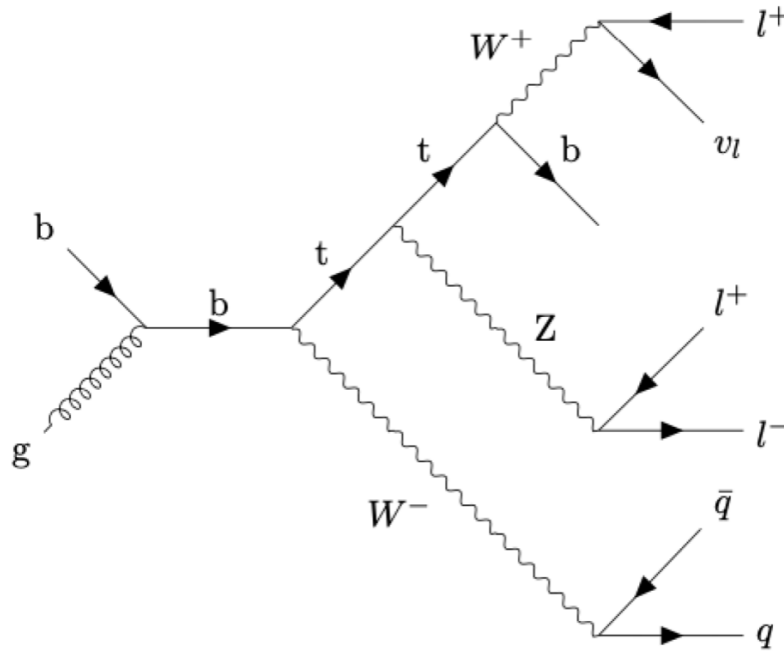


Figure 1. An example Feynman Diagram is shown for tWZ production in the trilepton channel.

In the trilepton search, the WZ and $t\bar{t}Z$ production processes are the dominant source of background events. In order to reduce these backgrounds, as well as other smaller backgrounds, kinematic selections and Machine Learning algorithms were used. This is necessary because of the similar decay products being produced by these processes in the trilepton channel, as well as the much larger cross sections of these processes when compared to tWZ production.

Before trying to distinguish between these two processes and tWZ production, one must check that these processes are well modelled. This is done using a Control Region (CR) for each of these main process. The CRs are also used to constrain these backgrounds in the fit. In Figure 2, the SR for tWZ production and the CRs for WZ and $t\bar{t}Z$ are shown. The simulation for the dominant backgrounds and smaller backgrounds are shown by stacked coloured histograms, and the Run 2 data is shown by the black dots in the two CRs. A normalized distribution of tWZ events is shown by a dotted black line and this shows that tWZ production is most abundant in the SR as desired. The simulation and data agree within uncertainty. This implies that the simulation is well modelled by the data and because these regions are enhanced in the main backgrounds, this implies that these main backgrounds are well modelled by simulation.

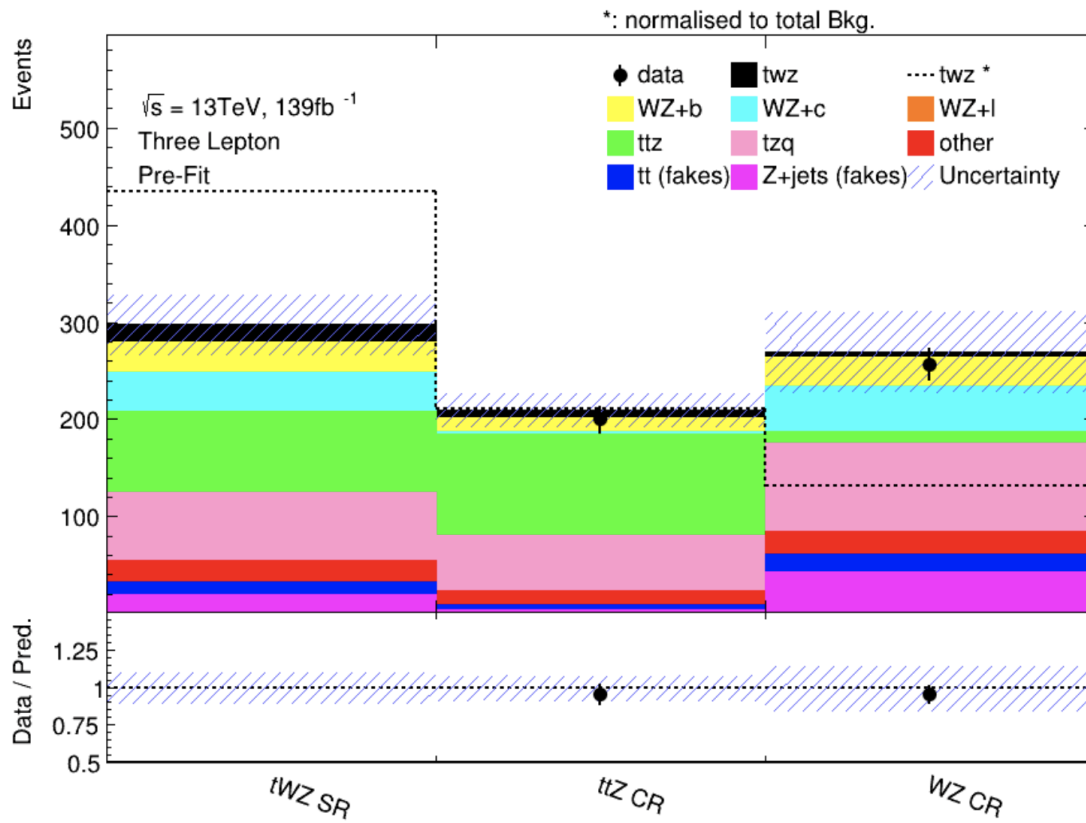


Figure 2. The tWZ SR, WZ CR, and the $t\bar{t}Z$ CR are shown. The SR is blind to data and Run 2 data is shown in the CRs.

3. Event-level GBDT

In this search, an event-level Gradient Boosted Decision Tree (GBDT) is used to distinguish between tWZ production and its main backgrounds. A GBDT is a machine learning algorithm that is trained on several input features to learn the differences between tWZ and the backgrounds. The chosen input features contain information that is useful for making this distinction. In this case, the input features were kinematics of objects in the event, and high level variables that made use of key differences between tWZ production and the main backgrounds.

After training on the input features, the event-level GBDT gives output scores for events based on the values of the features. A score closer to 0 is deemed to be more like a background event, and a score closer to 1 deemed to be more like a signal event. In Figure 3, the output for simulation in the tWZ SR is shown, with the normalized number of signal events shown by a dotted line. According to this figure, the event-level GBDT is effectively distinguishing between tWZ production and the main backgrounds since the dotted line shows more events with higher scores.

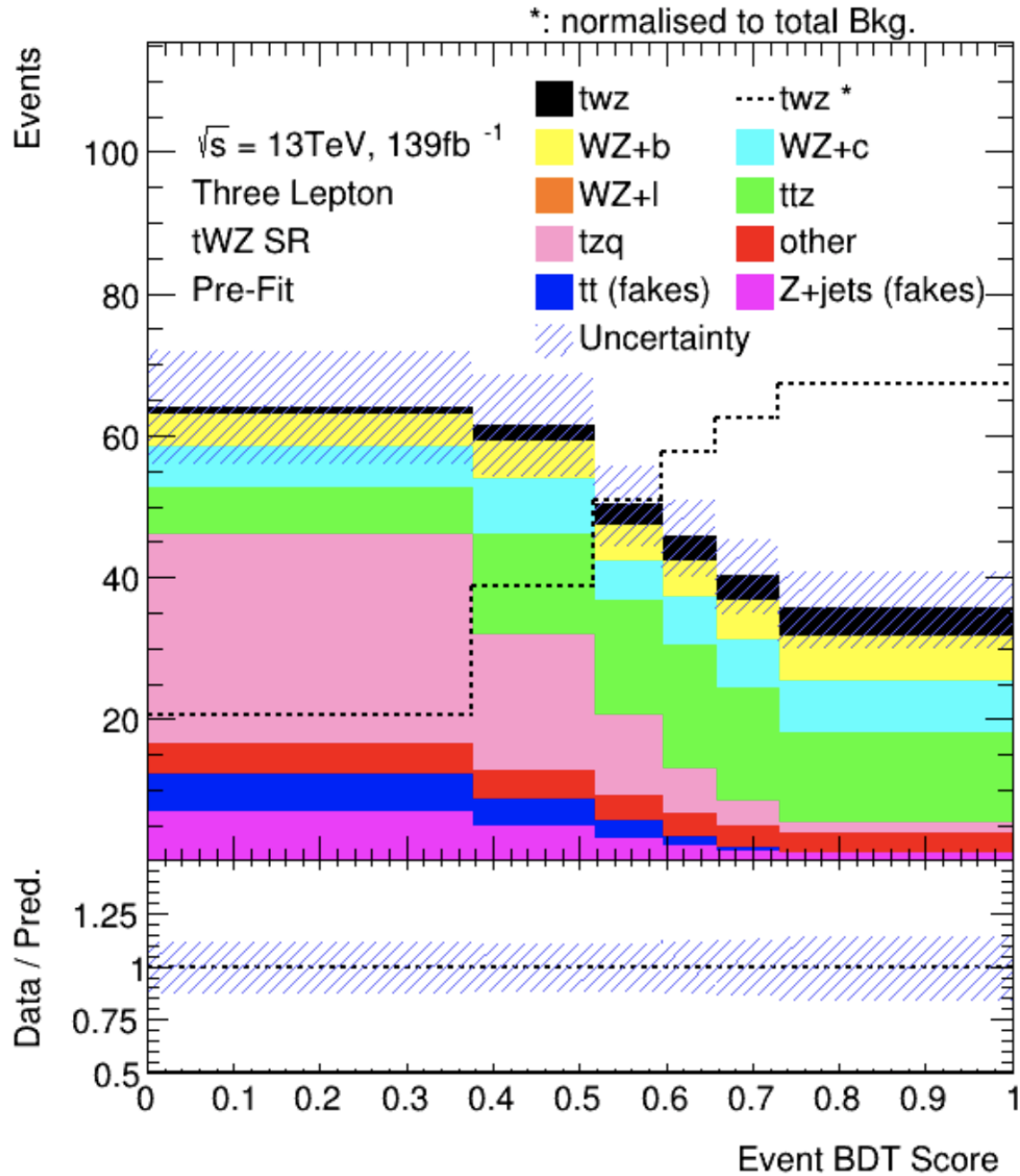


Figure 3. A histogram of the event-level GBDT scores is shown for simulation. A normalized distribution of tWZ events is shown by a dotted line.

4. Results

The signal strength, μ , of a process is the observed cross section divided by the SM prediction of the cross section (σ_{obs}/σ_{SM}). This is used easily see any deviations from the SM prediction. The signal strength of tWZ production is determined using the TRexFitter framework [7] for binned template profile likelihood fits. To determine the signal strength, event-level GBDT score histograms are used in the tWZ SR and the CRs. Since this search is blind in the SR, a dataset constructed from a background-only fit in the CR, is used in the SR to give a more accurate estimation of the sensitivity of this search.

Using the TRexFitter framework [7], a signal strength of $\mu = 1.20^{+1.37}_{-1.29}$ is determined with an expected significance of 0.77σ . This value is not at the 3σ level required in particle physics to constitute evidence. Therefore, an expected upper limit is placed on the signal strength as a measure of the sensitivity of the current setup. An expected upper limit of $2.61^{+2.25}_{-1.21}$ was determined.

From this fit, the main systematic uncertainties can be determined. In Figure 4, a ranking plot of the main systematic uncertainties are shown with those having the greatest impact appearing at the top. Based on this figure, the normalization uncertainties on the cross sections of WZ and $t\bar{t}Z$ production still have the greatest impact on this measurement, and a future measurement would greatly benefit from further suppressing these backgrounds. However, this measurement is strongly statistically limited and would benefit more from Run 3 data from the ATLAS detector.

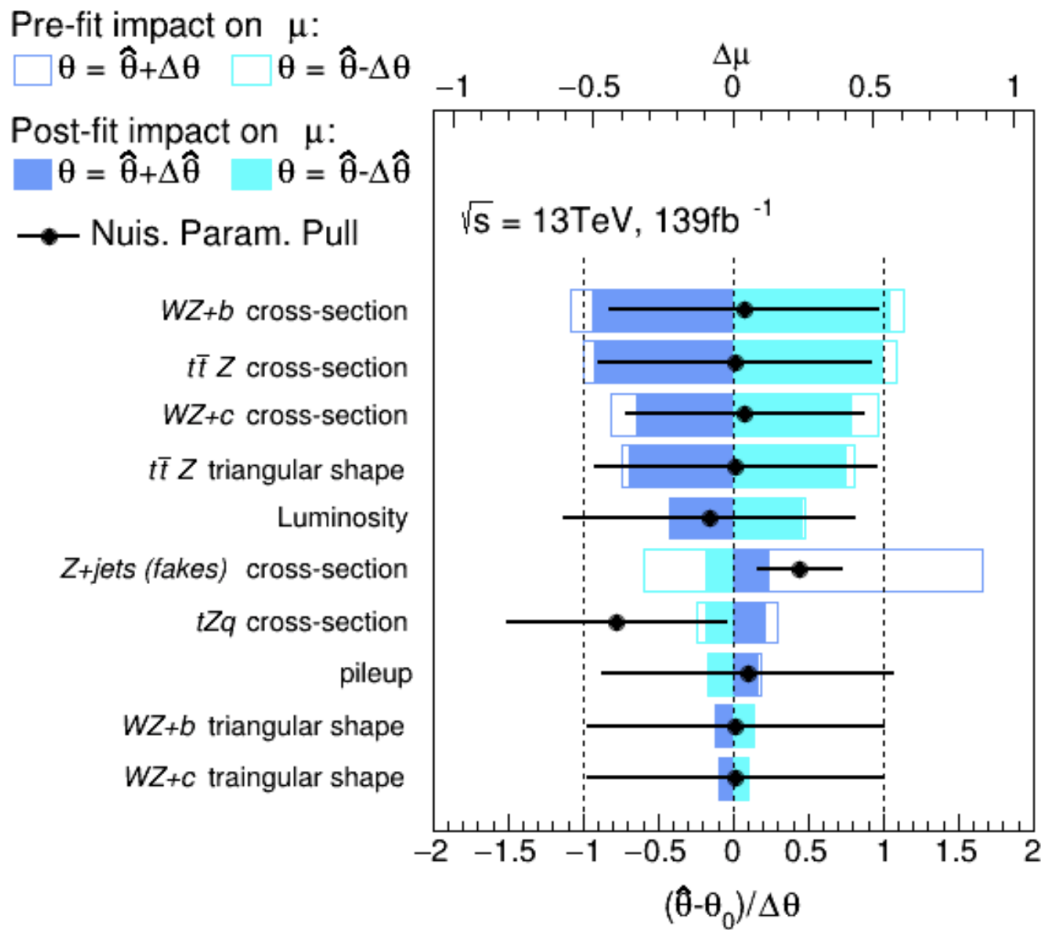


Figure 4. A ranking plot of the main systematic uncertainties ordered by impact is shown.

5. Conclusion

In the search for tWZ production in the trilepton channel, data and simulation from the Full Run 2 dataset of the ATLAS detector was used. An event selection scheme was applied to select tWZ events and to broadly suppress background events. Signal and Control Regions were chosen to perform this search and check the modelling of the background processes. Then GBDTs were used to suppress the main backgrounds.

A signal strength of $\mu = 1.20^{+1.37}_{-1.29}$ was determined with an expected significance of 0.77σ , as well as an expected upper limit of $2.61^{+2.25}_{-1.21}$. Given these expected results, one expects to be able to put the tightest limits ever on this rare and interesting production process.

References

- [1] Georges Aad et al. “Observation of a new particle in the search for the Standard Model Higgs boson with the ATLAS detector at the LHC”. In: *Phys. Lett. B* 716 (2012), pp. 1–29. DOI: 10.1016/j.physletb.2012.08.020. arXiv: 1207.7214 [hep-ex].
- [2] S. Chatrchyan et al. “Observation of a new boson at a mass of 125 GeV with the CMS experiment at the LHC”. In: *Physics Letters B* 716.1 (2012), 30–61. ISSN: 0370-2693. DOI: 10.1016/j.physletb.2012.08.021. URL: <http://dx.doi.org/10.1016/j.physletb.2012.08.021>.
- [3] Gian Francesco Giudice. “Naturally Speaking: The Naturalness Criterion and Physics at the LHC”. In: *Perspectives on LHC Physics* (2008), 155–178. DOI: 10.1142/9789812779762_0010. URL: http://dx.doi.org/10.1142/9789812779762_0010.
- [4] Vera C. Rubin. “One Hundred Years of Rotating Galaxies”. In: *Publications of the Astronomical Society of the Pacific* 112.772 (2000), pp. 747–750. DOI: 10.1086/316573. URL: <https://doi.org/10.1086/316573>.
- [5] Fabio Maltoni, Luca Mantani, and Ken Mimasu. “Top-quark electroweak interactions at high energy”. In: *Journal of High Energy Physics* 2019.10 (2019). ISSN: 1029-8479. DOI: 10.1007/jhep10(2019)004. URL: [http://dx.doi.org/10.1007/JHEP10\(2019\)004](http://dx.doi.org/10.1007/JHEP10(2019)004).
- [6] The ATLAS Collaboration et al. “The ATLAS Experiment at the CERN Large Hadron Collider”. In: *Journal of Instrumentation* 3.08 (2008), S08003–S08003. DOI: 10.1088/1748-0221/3/08/s08003. URL: <https://doi.org/10.1088/1748-0221/3/08/s08003>.
- [7] Michele Pinamonti and Loic Valery. *TRExFitter*. URL: <https://trexfitter-docs.web.cern.ch/trexfitter-docs/>.

Statistical correlations impacting a top quark mass measurement in 13 TeV proton-proton collision data from the ATLAS detector

Kevin Nicholas Barends¹, Sahal Yacoob

Department of Physics, University of Cape Town, Private Bag X3, Rondebosch 7701, South Africa

E-mail: ¹brnkev010@myuct.ac.za

Abstract. The top quark is the heaviest particle in the Standard Model and reducing the uncertainty of the top quark mass directly speaks to/ affects precision tests of the consistency with the Standard Model, where breaks from this consistency would point to the existence of more massive particles beyond the Standard Model. Since the top quark decays before hadronizing, either the kinematic properties of the decay products or measurements of the rate of the top quark production have been used to measure the mass of the top quark. The majority of measurements consider various decay modes of the W boson with no specification on the decay of the b-quark when utilizing the kinematic properties of the decay products. These measurements are predominantly limited by uncertainties related to the reconstruction of jets. However, there is a top quark decay mode which is largely independent of the aforementioned uncertainty which requires large amounts of data due to its low production rate. This decay mode includes a J/ψ meson originating from a b-hadron and a semi-leptonic decay of the W boson. The invariant mass reconstructed from the J/ψ meson and lepton is sensitive to the top quark mass. This paper describes a maximum likelihood approach to extract the top quark mass from a probability density function, pdf, while studying the impact of the correlations between each of the pdf parameters.

1. Introduction

The top quark is one of the most interesting fundamental particles in the Standard Model (SM) because the top mass impacts many areas within the SM and in new physics Beyond the SM (BSM) [1–3]. The current average Monte Carlo (MC) top mass of 172.26 ± 0.30 GeV [4] was determined by combining the kinematics of the top quark’s decay products, i.e. jets [5] and leptons. These jets and leptons originated from a primary decay of the top quark (i.e. into a W boson and a b quark) which has a branching fraction of $95.7 \pm 3.4\%$ [4]. There are other ways to measure the top mass which takes advantage of top quark cross section measurements [2], as well as different ways to quote the top mass depending on the renormalization scheme [6].

The largest source of uncertainty associated to top mass measurements using jet kinematics is jet reconstruction [7–10]. There are however different top quark decay modes that depend less on jet reconstruction and may produce a more precise top mass measurement. The decay mode of interest consists of a lepton originating from a W boson and two oppositely charged muons decaying from a J/ψ meson which originated from the b quark. This decay mode is largely independent of the jet reconstruction uncertainty. Due to the large amount of data

recorded by the Large Hadron Collider (LHC) during 2015-2018 [11], this decay mode can now be probed [12].

The invariant mass reconstructed from the lepton from the W boson and two oppositely charged muons from the J/ψ (i.e. three lepton system) is sensitive to the top mass [13]. This paper describes a maximum likelihood approach to extract the top quark mass from a probability density function (pdf) while studying the impact of the correlations between each of the pdf parameters using simulated proton-proton collision data at $\sqrt{s} = 13$ TeV, corresponding to an integrated luminosity of 139 fb^{-1} [14, 15].

2. ATLAS Detector

ATLAS [16] is a general-purpose detector designed to capitalize on the full potential of the LHC [11]. The magnet system consists of a superconducting solenoid surrounding the Inner Detector (ID) and three large superconducting toroids, one barrel and two end-caps, arranged azimuthally symmetric outside the calorimeters and within the Muon Spectrometer (MS). The ID performs precise particle reconstruction and identification of the collision point over $|\eta| < 2.5$, while the calorimeters measure the energy and position of particles over $|\eta| < 4.9$. The MS surrounds the calorimeters and identifies and measures muon up to $|\eta| < 2.7$. These components are integrated with a Trigger and Data Acquisition system and a computing system which selects events which consist of high transverse momenta particles or large missing transverse energy, and stores them for further analysis.

3. Event Selection

The $\ell + J/\psi$ top quark decay signature requires the W boson to decay leptonically into either an electron or a muon, at least 1 b-tagged jet and two oppositely charged muons with an invariant mass around that of a J/ψ meson (i.e. $3096.900 \pm 0.006 \text{ MeV}$). To enhance the selection of a lepton originating from a real W boson, a quantity known as the transverse mass of the W boson, $m_T(\text{lepton}, E_T^{\text{miss}}) = \sqrt{2p_T(\text{lepton})E_T^{\text{miss}}(1 - \cos(\phi(\text{lepton}) - \phi(E_T^{\text{miss}})))}$, was used. This quantity combines the kinematics of the lepton and the missing transverse energy (which represents the transverse kinematics of the neutrino). The kinematic requirements to extract the $\ell + J/\psi$ top quark decay signature is summarized in Table 1, where the definitions of the different observables can be found in reference [17–20]. The background estimation of this event selection can be found in [21].

Table 1. A table with the kinematic criteria for $t \rightarrow \ell + J/\psi$ events is shown.

Description	Kinematic criteria
Electron (Muon) selection	Exactly 1 lepton with $p_T > 25 \text{ GeV}$, $ \eta < 2.5$ $ \Delta z_0 \sin \theta < 0.5 \text{ mm}$, $ d_0 /\sigma_{d_0} < 5$ (3), isolation Gradient
Jet selection	At least 1 b-tagged jets with $p_T > 25 \text{ GeV}$ & $ \eta < 2.5$
Missing transverse momentum selection	$E_T^{\text{miss}} > 20 \text{ GeV}$
Real W boson selection	$m_T(\text{lepton}, E_T^{\text{miss}}) > 40 \text{ GeV}$
J/ψ muon selection	$p_T > 2.5 \text{ GeV}$ if $ \eta < 1.3$, $p_T > 3.5 \text{ GeV}$ if $1.3 < \eta < 2.5$
J/ψ selection	$p_T > 8 \text{ GeV}$, $ y < 2.1$, $2.9 < m(\mu^+\mu^-) < 3.3 \text{ GeV}$, $\tau > 0 \text{ ps}$

4. Building the model to extract the top mass

The top mass can be extracted using a maximum likelihood method with the invariant mass of the three-lepton system. Several top quark pair events were simulated within ATLAS using

different top quark masses (i.e. 169, 171, 172, 172.25, 172.5, 172.75, 173, 174 and 176 GeV). The three-lepton mass distribution can be modelled by the sum of a Gaussian [22], representing the signal component, and a Gamma distribution [22], representing the background component. The signal component originates from pairing the lepton from the W and the two-oppositely charged muons from the J/ψ from the same top quark, whereas the background component originates from pairing the leptons from different top quarks as well as from possible non-correlated backgrounds [13].

4.1. Parameter correlations

The parameter values in the pdf can be determined by fitting over the three-lepton mass distribution from the different top masses. Figure 1 shows the data distribution with the pdf fit over the $m_{\text{top}} = 172$ GeV (a) and $m_{\text{top}} = 172.5$ GeV (b) $t\bar{t}$ MC samples. The y-axis shows the number of raw events while accounting for the different detector effects. The relationship of these parameters to the top mass can then be determined to form a pdf that is solely dependent on the top mass. However, these parameters are correlated to some degree (see Table 2) and could affect the model.

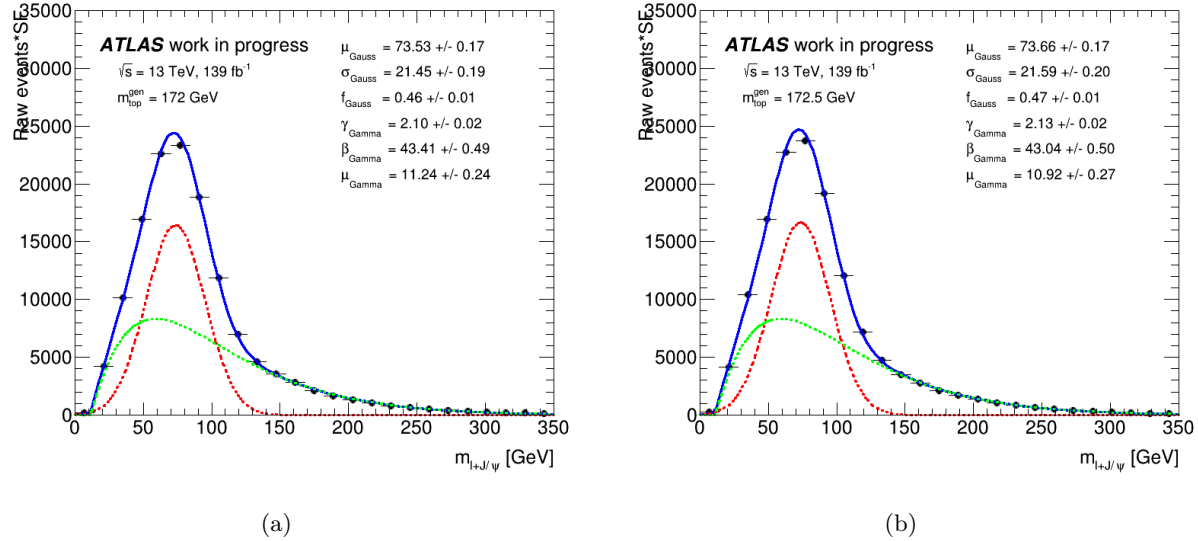


Figure 1. The three-lepton mass distribution showing the pdf fit (blue) with the signal (red) and background (green) over the $m_{\text{top}} = 172$ GeV (a) and $m_{\text{top}} = 172.5$ GeV (b) $t\bar{t}$ MC samples. The y-axis shows the number of raw events while accounting for the different detector effects.

Determining the relationships between each parameter and the top mass can be done by fitting a straight line. However, this does not account for the correlations between the different parameters. A χ^2 function that incorporates the different correlations by using the inverse of the covariance matrix as discussed in G. Cowan - Statistical data analysis [23] and is shown below

$$\chi^2(\theta) = \sum_{i,j=1}^N (y_i - \lambda(x_i; \theta))(V^{-1})_{ij}(y_j - \lambda(x_j; \theta)) \quad (1)$$

Table 2. A table showing the correlation strengths between the pdf parameters after fitting over the $m_{top} = 172.5$ GeV $t\bar{t}$ MC sample.

Parameters	μ_{Gauss}	σ_{Gauss}	$fraction_{Gauss}$	γ_{Gamma}	β_{Gamma}	μ_{Gamma}
μ_{Gauss}	1	-0.37	-0.37	-0.10	-0.11	-0.23
σ_{Gauss}	-0.37	1	0.83	-0.41	0.58	0.63
$fraction_{Gauss}$	-0.37	0.83	1	-0.52	0.73	0.57
γ_{Gamma}	-0.10	-0.41	-0.52	1	-0.92	-0.72
β_{Gamma}	-0.11	0.58	0.73	-0.91	1	0.66
μ_{Gamma}	-0.23	0.63	0.57	-0.72	0.66	1

where y_i are the measured parameter values, $\lambda(x_i; \theta)$ are the expected values (or straight line equations), and V_{ij}^{-1} is the inverse of the covariance matrix. The straight line equations take the form $parameter = a(m_{top}-172.5)+b$. The various values for a and b can be found in Table 3 for the different parameters with and without accounting for the correlations. Without considering the correlations, all the parameters except the fraction of Gaussian shows top mass dependence. The Gamma's parameter's were not expected to have any top mass dependency. However, including the correlations removed the top mass dependence in the Gamma's parameters, and only the Gaussian's parameters show a top mass dependence.

Table 3. A table showing the parameter relationships as a function of the top mass with and without accounting for the parameter correlations.

Parameter	Without correlations	With correlations
μ_{Gauss}	$a = 0.502 \pm 0.031$	$a = 0.538 \pm 0.028$
	$b = 73.765 \pm 0.060$	$b = 73.775 \pm 0.059$
σ_{Gauss}	$a = 0.187 \pm 0.030$	$a = 0.171 \pm 0.024$
	$b = 21.447 \pm 0.059$	$b = 21.437 \pm 0.058$
$fraction_{Gauss}$	$a = 0.00002 \pm 0.00002$	$a = -0.00003 \pm 0.00002$
	$b = 0.462 \pm 0.002$	$b = 0.459 \pm 0.003$
γ_{Gamma}	$a = 0.004 \pm 0.004$	$a = -0.0001 \pm 0.0001$
	$b = 2.111 \pm 0.007$	$b = 2.101 \pm 0.009$
β_{Gamma}	$a = 0.1660 \pm 0.0784$	$a = -0.0015 \pm 0.0016$
	$b = 43.613 \pm 0.160$	$b = 43.542 \pm 0.208$
μ_{Gamma}	$a = -0.065 \pm 0.028$	$a = 0.0014 \pm 0.007$
	$b = 9.691 \pm 0.062$	$b = 9.789 \pm 0.078$

4.2. Testing the performance of the model

The parameter relationships can be substituted into the pdf yielding a pdf with only the top mass as a parameter. The pdf will then determine the top mass which best fits the data distribution. However, the performance of the model has to be tested. This was done by performing a pull study which tests the bias and error coverage of the fit. The pull is defined by the measured value minus the true value divided by the error in the measured value and is Gaussian in shape. The pull mean describes the bias in the measured value while the pull width describes the accuracy in the error. For no bias and an accurate error estimation, the pull mean and width must be consistent with 0 and 1 within standard deviation (or 1σ), respectively.

In order to create a pull distribution, 5000 pseudo-datasets were randomly generated by inserting the true mass value into the pdf and fitting the pdf over each pseudo-data to obtain the measured value and error of the top mass. Figure 2 shows the pull distributions without (a) and with (b) accounting for the correlations when the true mass values is $m_{\text{top}} = 172.5$ GeV. A Gaussian was fit over the pull distribution to determine the pull mean and width. This was done for the nine different top mass values to estimate the pull mean and width as a function of the top mass.

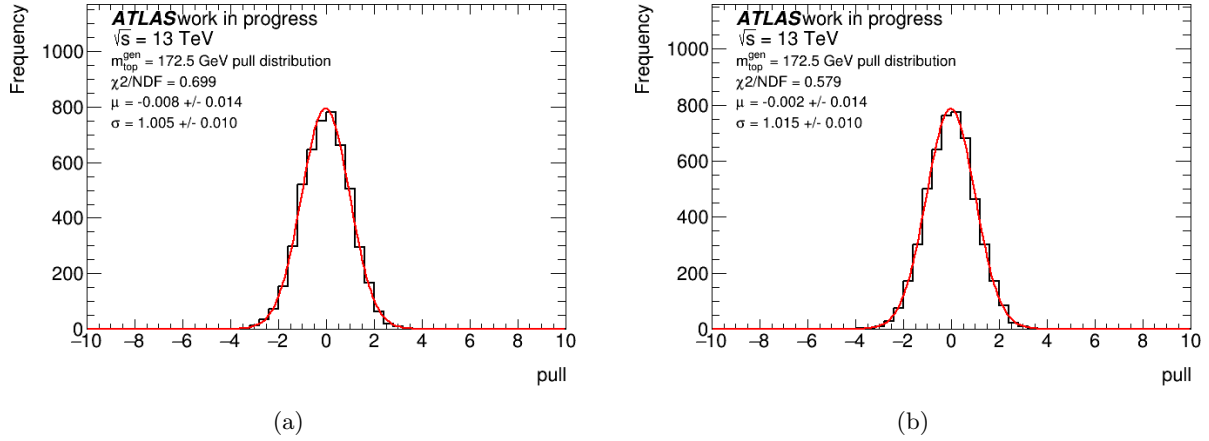


Figure 2. The pull distribution without (a) and with (b) accounting for the various parameter correlations in the pdf when using $m_{\text{top}} = 172.5$ GeV as the true top mass value. The red line shows a Gaussian fit over the distribution.

Figure 3 shows the pull mean without (a) and with (b) accounting for the parameter correlations as a function of the top mass. The expected pull mean of the model is not consistent with 0 within 1σ when not considering, but is consistent with 0 within 1σ when considering the parameter correlations. This shows that without considering the parameter correlations, the model would have produced a bias in the measured value. Figure 4 shows the pull width without (a) and with (b) accounting for the parameter correlations as a function of the top mass. The expected pull width of the model is not consistent with 1 within 1σ when not considering, but is consistent with 1 within 1σ when considering the parameter correlations. This shows that without considering the parameter correlations, the model would have underestimated the error in the measured value.

5. Conclusion

Measuring the MC mass of the top quark using the $\ell+J/\psi$ decay signature reduces the dependency on jet reconstruction. The three-lepton mass distribution is sensitive to the top mass which can be determined using a maximum likelihood approach. This maximum likelihood approach contains a pdf that consists of a Gaussian (signal) and a Gamma function (background). The parameters from the Gaussian and Gamma functions are correlated in the pdf. Not accounting for these statistical correlations in the parameters would have produced a bias and underestimated the uncertainty in the top mass measurement in data. After accounting for these parameter correlations, the model showed to have no bias and accurately estimates the uncertainty in the top mass measurement.

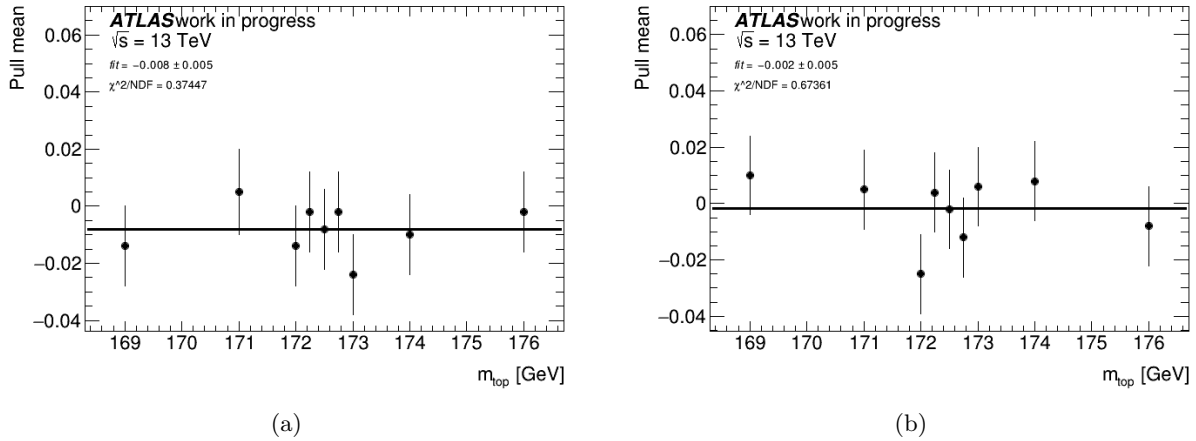


Figure 3. The pull mean as a function of the top mass without (a) and with (b) accounting for the parameter correlations. The solid black line represents the expected pull mean of the model and the value can be found on the top left of the figure.

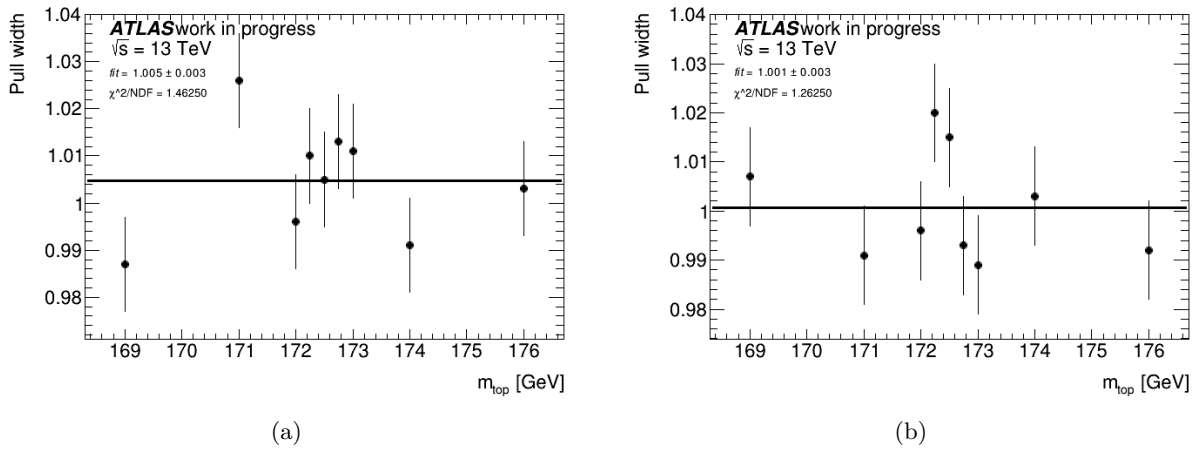


Figure 4. The pull width as a function of the top mass without (a) and with (b) accounting for the parameter correlations. The solid black line represents the expected pull width of the model and the value can be found on the top left of the figure.

6. Acknowledgements

I would like to thank the NRF for their financial support and Dr Sahal Yacoob, Dr James Keaveney, Assist. Prof. Tim Andeen, and Prof. Peter Onyisi for their guidance and continuous support.

7. References

- [1] Heinemeyer S, Kraml S, Porod W and Weiglein G 2003 *JHEP* **09** 075 (*Preprint* hep-ph/0306181)
- [2] Cortiana G 2016 *Rev. Phys.* **1** 60–76 (*Preprint* 1510.04483)
- [3] Degraess G *et al.* 2012 *JHEP* **08** 098 (*Preprint* 1205.6497)
- [4] Patrignani C *et al.* (Particle Data Group) 2016 *Chin. Phys.* **C40** 100001
- [5] Seymour M H 1995 *AIP Conf. Proc.* **357** 568–587. 20 p URL <https://cds.cern.ch/record/283896>
- [6] Melnikov K and Ritbergen T v 2000 *Phys. Lett.* **B482** 99–108 (*Preprint* hep-ph/9912391)
- [7] Sirunyan A M *et al.* (CMS) 2017 *Eur. Phys. J.* **C77** 354 (*Preprint* 1703.02530)

- [8] Aaboud M *et al.* (ATLAS) 2016 *Phys. Lett.* **B761** 350–371 (*Preprint* 1606.02179)
- [9] Khachatryan V *et al.* (CMS) 2016 *Phys. Rev.* **D93** 072004 (*Preprint* 1509.04044)
- [10] Tevatron E W G and Aaltonen T (CD and D0) 2016 (*Preprint* 1608.01881)
- [11] Voss R and Breskin A (eds) 2009 *The Large Hadron Collider* URL <https://home.cern/>
- [12] Khachatryan V *et al.* (CMS) 2016 *JHEP* **12** 123 (*Preprint* 1608.03560)
- [13] Behar S and Rozen Y Top Mass Determination from J/Psi - lepton correlation Tech. rep. CERN Geneva
- [14] Avoni G *et al.* 2018 *JINST* **13** P07017
- [15] Aaboud M *et al.* (ATLAS) 2016 *Eur. Phys. J.* **C76** 653 (*Preprint* 1608.03953)
- [16] Aad G *et al.* (ATLAS) 2008 *JINST* **3** S08003
- [17] Aad G *et al.* (ATLAS) 2016 URL <http://cds.cern.ch/record/2157687>
- [18] Aad G *et al.* (ATLAS) 2016 *Eur. Phys. J.* **C76** 292 (*Preprint* 1603.05598)
- [19] Cacciari M, Salam G P and Soyez G 2008 *JHEP* **04** 063 (*Preprint* 0802.1189)
- [20] Aad G *et al.* (ATLAS) 2015 URL <https://cds.cern.ch/record/2037697>
- [21] Barends, K SU/2019 in *The Proceedings of SAIP2019* 117–122
- [22] Verkerke W and Kirkby D P 2003 *eConf* **C0303241** MOLT007 [,186(2003)] (*Preprint* physics/0306116)
- [23] Cowan G 1998 *Statistical data analysis* ISBN 978-0-19-850156-5

Simplified Template Cross Section measurements of the $V(H \rightarrow b\bar{b})$ process with the ATLAS detector at $\sqrt{s} = 13$ TeV

Ryan Justin Atkin, Sahal Yacoob

Department of Physics, University of Cape Town, Private Bag X3, Rondebosch 7701, Cape Town, South Africa

E-mail: rjatin93@gmail.com

Abstract. Presented are the studies of the production of the Standard Model Higgs boson in association with a W or a Z boson, where the Higgs boson decays to $b\bar{b}$ and the W/Z bosons decay leptonically. The data used is the full Run-2 ATLAS dataset, corresponding to 139 fb^{-1} of integrated luminosity, which was collected in proton-proton collisions at a centre of mass energy of $\sqrt{s} = 13$ TeV. At this energy, the $H \rightarrow b\bar{b}$ decay has a branching fraction of $\sim 58\%$, so this study allows the probing of the dominant Higgs boson decay mode. This production mode also provides the best sensitivity to the WH and ZH interactions and allows the study of the Higgs boson at high transverse momentum, both of which are important for the interpretation of the Higgs boson measurements in Effective Field Theories. The focus of the latest round of this analysis is to measure the cross-sections using the Simplified Template Cross Section method. Here, the cross sections are measured as a function of the W/Z boson transverse momentum in different fiducial volumes based on kinematic selections. In particular, the jet p_T selections are studied to see if any improvements can be achieved by tightening the selections.

1. Introduction

The dominant decay of the Higgs boson is to two bottom quarks ($H \rightarrow b\bar{b}$), with a branching fraction of $\sim 58\%$ at $\sqrt{s} = 13$ TeV [1]. However, when searching for these events with the dominant Higgs boson production mode of gluon-gluon fusion, the multi-jet backgrounds are too large. Therefore, if we instead look at the production of the Higgs boson in association with a vector boson V (W/Z boson), we can use the leptonic decays of the vector bosons to help reduce those backgrounds [2]. A Feynman diagram of this process is given in Figure 1. This production and decay mode provides the best sensitivity of the Higgs coupling to the W/Z bosons and allows the study of the Higgs boson at high transverse momentum. This sensitivity and high momentum are important for the interpretation of the Higgs boson measurements in Effective Field Theories (EFTs) [2]. Since b -hadrons are the only down-type hadrons that can be effectively identified, this decay mode also allows the study of the Yukawa coupling of the Higgs boson to the down-type quarks.

This paper will discuss the work going into improving the Simplified Template Cross Section (STXS) measurements in the $V(H \rightarrow b\bar{b})$ analysis by tightening the jet transverse momentum selections. The previous analysis [2] found no discrepancies in the cross sections between the Standard Model and the data. The ATLAS detector is described in Section 2 and the event

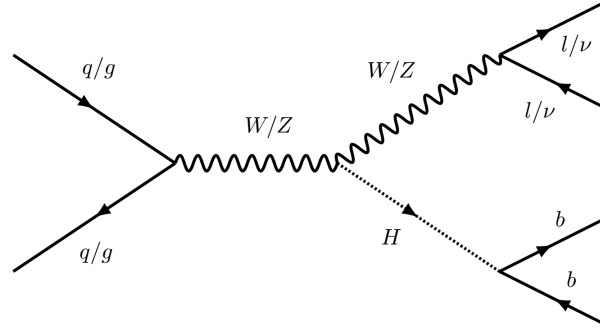


Figure 1. Feynman diagram for the $V(H \rightarrow b\bar{b})$ process. The W boson can only be produced by the quark initiated process due to charge conservation, while the Z boson can be produced via quark or gluon annihilations. The W/Z boson emits a Higgs boson which subsequently decays into a bottom anti-bottom quark pair. The Z boson then decays leptonically into two leptons or two neutrinos, while the W boson decays leptonically into a lepton and neutrino.

selections in Section 3. The STXS are explained in Section 4, with the new jet selections and results in Sections 5 and 6 respectively.

2. The ATLAS detector

The ATLAS detector[3], located at the Large Hadron Collider[4] at CERN, is an all-purpose particle detector with almost 4π coverage around the interaction point. The detector uses cylindrical coordinates (r, ϕ) in the transverse plane, with ϕ being the azimuthal angle around the z -axis. The pseudorapidity is defined as $\eta = -\ln(\tan \frac{\theta}{2})$, where θ is the polar angle and the distance in (η, ϕ) coordinates is defined as $\Delta R = \sqrt{(\Delta\phi)^2 + (\Delta\eta)^2}$. A convenient variable used is the transverse momentum $p_T = |p| \sin(\theta)$.

The detector is layered, with the inner layer being the Inner Detector (ID) used to track charged particles and calculate their momenta, and covers the pseudorapidity range $|\eta| < 2.5$. This is surrounded by a 2 T superconducting solenoid which bends the charged particles to allow for momenta and charge measurements. Following this are the electromagnetic and hadronic calorimeters used to measure the energy of the particles, covering the pseudorapidity range $|\eta| < 4.9$. The final layer is the Muon Spectrometer (MS) and superconducting toroidal magnets. The MS performs the same function as the ID but solely for muons, and the tracking covers the pseudorapidity range $|\eta| < 2.7$.

3. Event selections

The final objects for the $V(H \rightarrow b\bar{b})$ process contains leptons (e/μ) and two b -jets. For the Z boson production, there is either the 0-lepton decay ($Z \rightarrow \nu\nu$) or the two lepton decay ($Z \rightarrow ll$). The W boson only has a one lepton decay ($W^\pm \rightarrow l^\pm\nu$). This analysis is split into three channels based on these leptonic decays of the vector bosons. For this paper, the focus will be on the 0-lepton channel. Since neutrinos are undetected in the ATLAS detector, a lepton veto is applied to the events to ensure we have no reconstructed leptons in the final state. The events are then split by the p_T of the vector boson (p_T^V), since the sensitivity is higher at larger p_T^V . In the 0-lepton channel, the missing transverse momentum (E_T^{miss}) is used for p_T^V as this accounts for the neutrino p_T . The resultant p_T^V regions are $150 < E_T^{miss} < 250$, $250 < E_T^{miss} < 400$ and $E_T^{miss} > 400$, with the split at 400 being new for this round of the analysis.

Events are then further split by the number of jets in the event, which are reconstructed using the anti- k_T algorithm[5] with a radius parameter of $R = 0.4$. For the 0-lepton channel, there

Table 1. Some of the main selections for the analysis in the zero lepton channel.

Selection	selection
Leptons	0 leptons
p_T^V regions	$150 < p_T^V < 250$ $250 < p_T^V < 400$ $p_T^V > 400$
Jet p_T	> 20 GeV for central jets ($ \eta < 2.5$) > 30 GeV for forward jets ($2.5 < \eta < 4.5$)
b -jets	Exactly 2
Leading b -tagged jet p_T	> 45 GeV
Jet categories	Exactly 2 / Exactly 3 / Exactly 4

are the 2-jet, 3-jet and 4-jet regions, with 4-jet being new for this round of the analysis. The jets need to pass a p_T selection of 20 GeV if the jet is central ($|\eta| < 2.5$) or 30 GeV if forward ($2.5 < |\eta| < 4.5$). A neural-network based tagging algorithm (DL1r [6]) is applied to the central jets to identify the b -jets, and tuned to an average b -tagging efficiency of 70%. Exactly two b -tagged jets are required, with the addition of the highest p_T b -tagged jet having a p_T larger than 45 GeV. A summary of these selections is given in Table 1.

4. Simplified Template Cross Section

Usually when cross section measurements are performed, the differential cross section is calculated using the entire phase space possible within the detector. However, for this analysis a Simplified Template Cross Section (STXS)[7] measurement is performed which calculates the cross section in smaller predefined kinematic regions. This reduces the theoretical uncertainties directly folded into the measurement, and helps isolate certain BSM effects in each region. A diagram for the STXS regions of the $V(\rightarrow\text{leptons})H$ process is shown in Figure 2. These are the regions that could possibly be studied and are defined by the theorists. They are split by vector boson production, p_T^V and the number of additional jets above the two tagged jets. Due to experimental and statistical constraints, not all of these regions are used and some have to be merged. For example, in the previous round of the analysis [2], the five resultant regions were; WH with $150 < p_T^V < 250$ and $p_T^V > 250$, and ZH with $75 < p_T^V < 150$, $150 < p_T^V < 250$ and $p_T^V > 250$. In this round of the analysis, we are looking at splitting both the WH and ZH , $150 < p_T^V < 250$ regions into zero and greater than zero additional jets regions, for which the split can be seen in Figure 2, resulting in seven regions.

Important for this paper is that when the STXS theoretical calculations are performed, the particle-level b -jets are selected to have $p_T > 20$ GeV, while all other particle-level jets have $p_T > 30$ GeV. This is different to the reconstruction level selections which require all the central jets to have $p_T > 20$, and only the forward jets have $p_T > 30$ GeV.

5. Optimising jet selections

The focus of the previous round of this analysis was to maximise the overall VH significance. In this round, the focus is on improving the STXS measurements. As part of this improvement, we are looking at changing the jet p_T selections at reconstruction level, as shown in Table 1, to match more closely with the theoretical selections as described in Section 4. The two possible scenarios are to increase only the non-tagged central jet p_T cuts to 30 GeV, or to increase all central jet p_T cuts to 30 GeV. The main motivation for the second option over the first is that it would simplify the implementation, and so this scenario will be the focus of this paper. The hope is that increasing the jet p_T cuts will improve the correlation between the particle-level regions

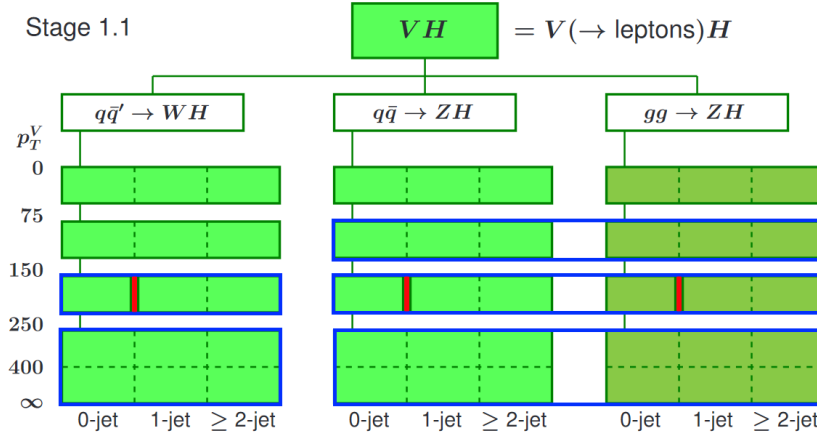


Figure 2. Diagram of the regions used in the STXS scheme for the $V(\rightarrow \text{leptons})H$ production [7]. The dashed lines show the theoretically possible regions that can be studied. However, due to limited statistics and the ability of the detector, some of the regions experimentally can't be used or need to be merged. This leaves with us with five regions, defined by the blue boxes; WH with $150 < p_T^V < 250$ and $p_T^V > 250$, and ZH with $75 < p_T^V < 150$, $150 < p_T^V < 250$ and $p_T^V > 250$. The red lines show the additional splits studied for this paper, giving seven regions.

(hereby referred to as STXS truth regions) and the reconstruction regions, i.e., that an event that falls in the truth region of no additional jets (only the two tagged jets) and $150 < p_T^V < 250$ also falls in the reconstruction region of two jets (only the two tagged jets) and $150 < p_T^V < 250$. The improved correlations should then increase the significance in the STXS fit and reduce the uncertainties on the cross section measurements.

6. Results

In order to study the correlation between the regions, or bins, we can look at matrices like that shown in Figure 3. In this plot, the y -axis has the nine reconstruction bins (three n -jet regions each with three p_T^V regions), while the x -axis has the STXS truth bins. The entries are the relative fraction of each reconstruction bin in each of the truth bins, in percentage, so the rows add up to 100%. Ideally the main diagonal would all be 100%, but due to uncertainties in the reconstruction, many events lie off this diagonal. As can be seen for the nominal case in Figure 3, with no change in the jet p_T cuts, the correlations improve for increasing p_T^V and decrease for increasing number of jets. The worst directly correlated bin (4-jet and $150 < p_T^V < 250$) only has 16.7% correlation.

For the case where all the central jet p_T cuts have been increased to 30 GeV, the matrix is shown in Figure 4. Clearly increasing the cut has improved the correlations overall. All the 2-jet bins have decreased slightly by about 3.75%, although they did start off a lot higher than the other bins. It's nice to see that the worse the correlation in the bin was, the larger the improvement. So for the worst bin discussed earlier, there is an improvement in the correlation by 118%, with the other 4-jet bins improving by 80-100% and the 3-jet bins improving by 32-45%.

So for events with more than two jets, increasing the jet p_T improves the STXS correlations, but it slightly decreases in the 2-jet regions. Unfortunately, the 2-jet regions dominant in statistics and correlations. It is therefore possible that the benefits of the increased cuts will only be seen when the final STXS bins used for the fit are split into the zero and greater than zero additional jets regions, as explained in Section 4. Without the split it is possible that the 2-jet regions

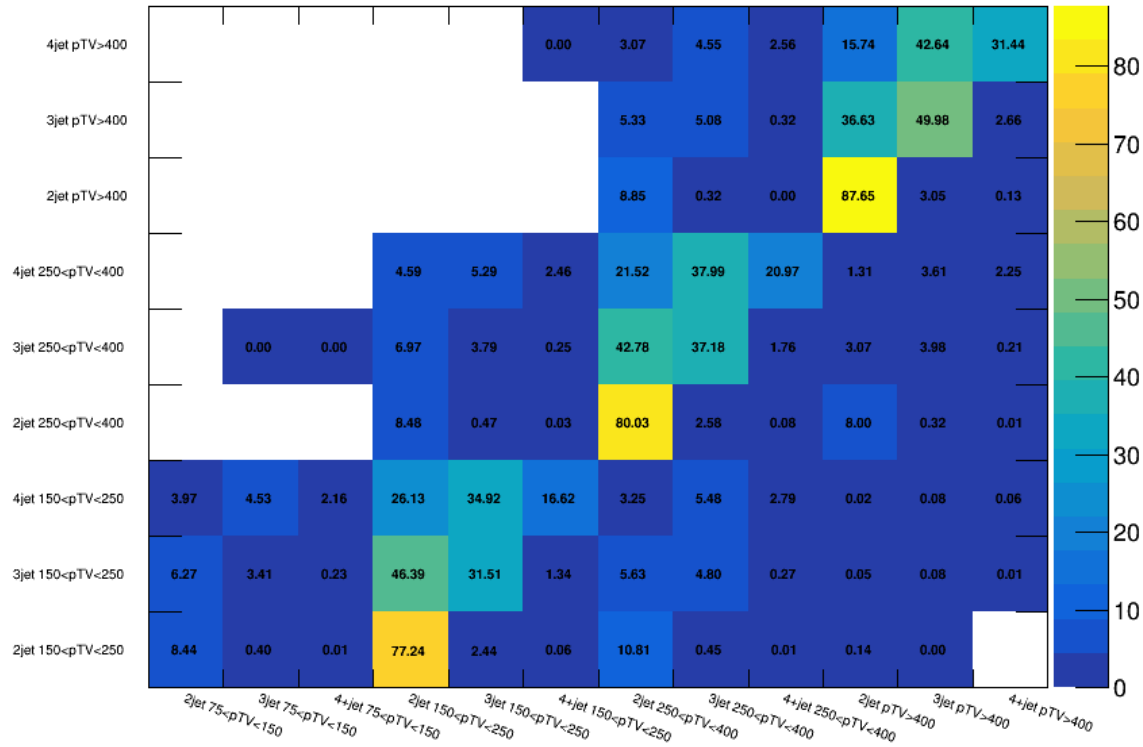


Figure 3. The correlation matrix comparing the nine reconstruction bins (y -axis) to the STXS truth bins (x -axis) for the nominal case. The bin values are the relative fractions in percent of each reconstruction bin in each truth bin, so the rows add up to 100%. The direct correlations between the reconstruction and particle-level bins lie on the diagonal from the bottom bin fourth from the left up to the top right bin. The reconstruction bins are defined by the number of jets in the event, while the truth bins are defined by the number of additional jets above the two b -tagged jets in the event.

dominate and the improvements in the higher jet regions is lost. As part of the next steps in this study, the full maximum likelihood fit will be performed in the STXS bins both with the increased cuts and with the extra split in the different number of jets.

7. Conclusion

The production of the Standard Model Higgs boson in association with a W or a Z boson, where the Higgs boson decays to $b\bar{b}$ and the W/Z bosons decay leptonically, is an important process due to the W/Z boson couplings to the Higgs boson and the decay of the Higgs boson in its dominant decay channel to two bottom quarks. This process is being studied in the framework of the Simplified Template Cross Section (STXS) and possible improvements over the previous round are being explored. One of the ways for this is to increase the jet p_T cuts at reconstruction level to match more closely to the cuts applied at the STXS truth level.

By increasing the p_T cuts of all the central jets from 20 GeV to 30 GeV, an overall improvement in the correlation between the reconstruction and STXS truth bins is observed. In particular, the regions with 3 jets improve by 32-45% while the 4-jet regions improve by 80-118%. There is a very slight decrease in the 2-jet region of about 3.75%, but these regions started off with high correlations. Future work would be to perform the full maximum likelihood fit in the STXS bins

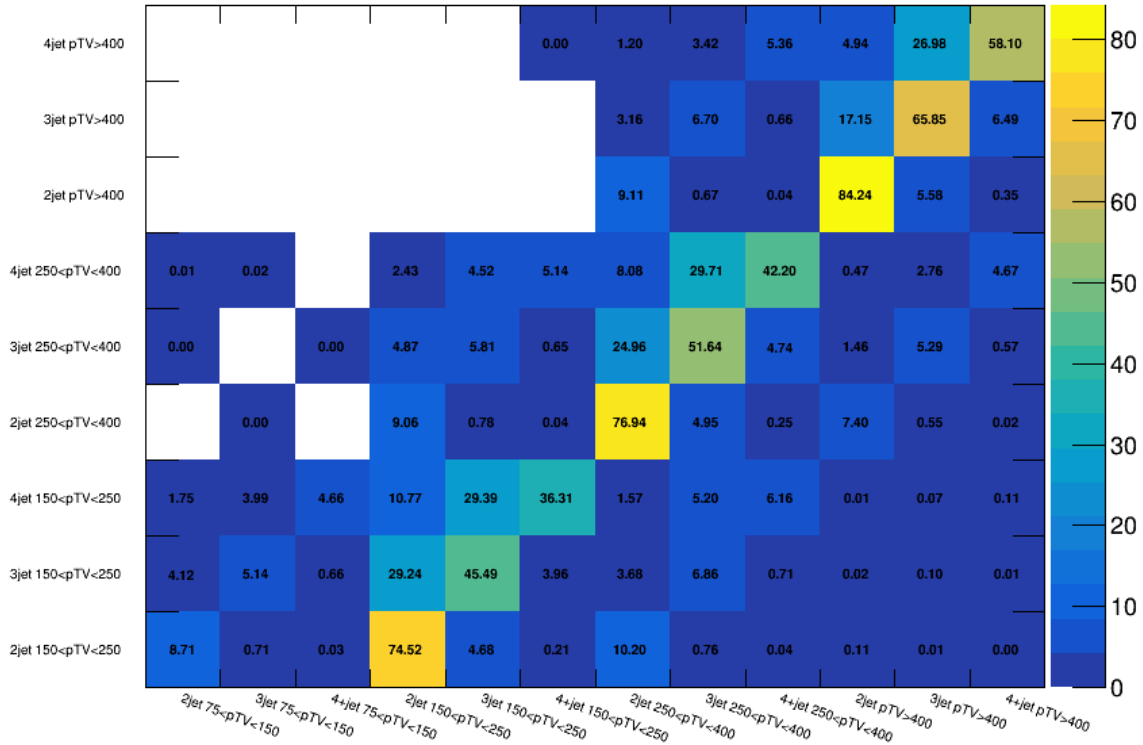


Figure 4. The correlation matrix comparing the nine reconstruction bins (y -axis) to the STXS truth bins (x -axis) for the increased jet p_T cut scenario. The bin values are the relative fractions in percent of each reconstruction bin in each truth bin, so the rows add up to 100%. The direct correlations between the reconstruction and truth bins lie on the diagonal from the bottom bin fourth from the left up to the top right bin. The reconstruction bins are defined by the number of jets in the event, while the truth bins are defined by the number of additional jets above the two b -tagged jets in the event.

to determine if the increased jet p_T cuts improve the significances as well, and if increasing the cuts would still be beneficial if the fit is not split by the number of jets in the events.

References

- [1] D de Florian et al. Handbook of LHC Higgs Cross Sections: 4. Deciphering the Nature of the Higgs Sector. 2016.
- [2] ATLAS Collaboration. Measurements of WH and ZH production in the $H \rightarrow b\bar{b}$ decay channel in pp collisions at 13 TeV with the ATLAS detector. *Eur. Phys. J. C*, 81(2):178, 2021.
- [3] ATLAS Collaboration. The ATLAS Experiment at the CERN Large Hadron Collider. *Journal of Instrumentation*, 3(08):S08003, 2008.
- [4] L Evans and P Bryant. LHC Machine. *Journal of Instrumentation*, 3(08):S08001, 2008.
- [5] M Cacciari, G P Salam, and G Soyez. The anti-kt Jet Clustering Algorithm. *JHEP*, 0804(063), 2008.
- [6] ATLAS Collaboration. ATLAS b -jet identification performance and efficiency measurement with $t\bar{t}$ events in pp collisions at $\sqrt{s} = 13$ TeV. *Eur. Phys. J. C*, 79(11):970, 2019.
- [7] N Berger et. al. Simplified template cross sections - stage 1.1, 2019. arXiv:1906.02754 [hep-ph].

Simulation of the strip sub-detectors in the Inner Tracker of the ATLAS detector

Ryan Justin Atkin, Sahal Yacoob

Department of Physics, University of Cape Town, Private Bag X3, Rondebosch 7701, Cape Town, South Africa

E-mail: rjatin93@gmail.com

Abstract. In the beginning of 2025, the Large Hadron Collider (LHC) will be shutdown in order for the final upgrades to the High Luminosity LHC (HL-LHC) to commence. This will almost quadruple the amount of collisions in the LHC, increasing the amount of data the detectors will have to deal with. Since the detectors were not designed to operate at these levels, they will also need an upgrade to deal with the increased radiation, data rates and amount of particles travelling through the detectors. One of the most extensive upgrades to the ATLAS detector will be the replacement of the current Inner Detector (ID) with an all silicon semiconductor based Inner Tracker (ITk). However, not only will the actual detector be upgraded, but the simulation of the detector will also need to be updated to match this new version. An accurate simulation of the detector is important since this is what is used to convert the outputs of the theoretical calculations (be it Standard Model (SM) or Beyond the Standard Model (BSM)) into a format that can be directly compared with the data coming from the experiment. Presented is some of the work behind updating the simulation of the strip detector in the ITk, from the sensors to the support structures and shielding components.

1. Introduction

With new physics searches pushing the limits of the current Large Hadron Collider (LHC) [1] and its detectors, an upgrade of the LHC to the High Luminosity LHC (HL-LHC) [2] has been planned. The principal upgrade will occur during the third Long Shutdown (LS3) starting at the beginning of 2025 and ending in 2027 [3]. The upgrade will increase the instantaneous luminosity to an ultimate value of $\mathcal{L}_{ins} = 75 \text{ nb}^{-1} \cdot \text{s}^{-1}$ [3], around 7.5 times the design luminosity. This will result in a total integrated luminosity of around $\mathcal{L} = 4000 \text{ fb}^{-1}$ after the 10 years of operation and up to an average of $\mu = 200$ collisions per bunch crossing. These improvements will greatly increase the statistics available for analysis while at the same time exceeding the current detectors' design capabilities with respect to pile-up management and radiation tolerance. Therefore the detectors will require an upgrade themselves. In particular, the ATLAS detector's main upgrades (phase-2 upgrades as laid out in the Letter of Intent (LoI) [4]) will occur during LS3. The focus will be on upgrading the current tracking Inner Detector (ID) to the full silicon semiconductor Inner Tracker (ITk) [3]. The purpose of the ID upgrade is to improve the tracking resolution as well as to cope with the higher occupancy environment and radiation doses.

Table 1. Some specifications of the ITk strip detector.

	no. Sensors	no. Chips	Channels [$\times 10^6$]	Radial coverage [mm]	$ z $ coverage [mm]
Barrel	10976	162624	~ 38	399 \rightarrow 1000	0 \rightarrow 1375
Endcap	6912	96768	~ 22	385 \rightarrow 968	1512 \rightarrow 2850
Total	17888	259392	~ 60	385 \rightarrow 1000	0 \rightarrow 2850

1.1. ITk

The current ID was designed to deal with an average of 23 proton-proton collisions per bunch crossing, not the expected 200 during the HL-LHC phase [3]. The current resolution of the ID would make pattern recognition difficult and provide a poor track finding efficiency in the higher occupancy environment. The ITk will be a full silicon semiconductor tracker divided into the strip detector (elongated read-outs capable of measuring 1 spatial co-ordinate) and the pixel detector (small read-outs capable of measuring 2 spatial co-ordinates). Both of these detectors are further split into the barrel (central region, $|\eta| < 1.8^1$) and endcap (forward region, $|\eta| > 1.8$) detectors. The tracking pseudorapidity range will be increased from $|\eta| < 2.5$ to $|\eta| < 4$, which will be important for electro-weak and new physics searches, as well as improving missing transverse momentum resolution and pile-up jet rejection [3].

The strip barrel has 4 layers of sensors, with the inner two layers being the short strip modules and the outer two layers the long strip modules. The strip endcap has 6 disks each side of the barrel, with the modules arranged in 6 rings. Some extra specifications of the strip detector are shown in Table 1, and a diagram comparing the current ID to the ITk is shown in Figure 1.

2. ITk strip modules

The strip sensors will be planar, n-in-p type silicon semiconductors with elongated readout strips (ranging from 19 mm to 60.2 mm in length) [3]. A module is a composite device composed of a power board and one or two hybrids (kapton board with read-out chips) glued to a sensor. An image of a barrel short strip module and an endcap module showing the sensor and hybrids is given in Figure 2. In the barrel the strips are placed parallel to the beam axis and in the endcaps the strips are placed radially pointing towards the beam axis. As the strips are only capable of measuring 1 spatial co-ordinate, the combination of strip sensors on either side of a stave or petal (the local support structures that hold the modules in the barrel and endcap respectively) allows for the measurement of the second spatial co-ordinate. The sensors on either side are placed at slight angles to each other (40 mrad in the endcap and 52 mrad in the barrel), allowing the strips to cross over at points which are used to get the 2D measurement [3]. Each readout chip reads 128 strips from two rows of strips, totalling 256 channels per chip. The chips provide a 1-bit digital output that only stores a yes or no if the charge collected in a strip is over a predefined threshold charge, hence the name ATLAS Binary Chips (ABCs).

3. Simulation

Apart from having the physical detector, a simulation of the ITk is also very important. Before the detector is running, the simulation is required to estimate its performance and test its viability. The simulation can also be used to check if the engineering designs work, making sure everything fits and that the amount of material is not too much. The simulations are created using a software that interfaces with the Geant4 package [5]. Geant4 is a C++ based program

¹ The ATLAS detector uses cylindrical coordinates (r, ϕ) in the transverse plane, with ϕ being the azimuthal angle around the z -axis. The pseudorapidity is defined as $\eta = -\ln(\tan(\frac{\theta}{2}))$, where θ is the polar angle.

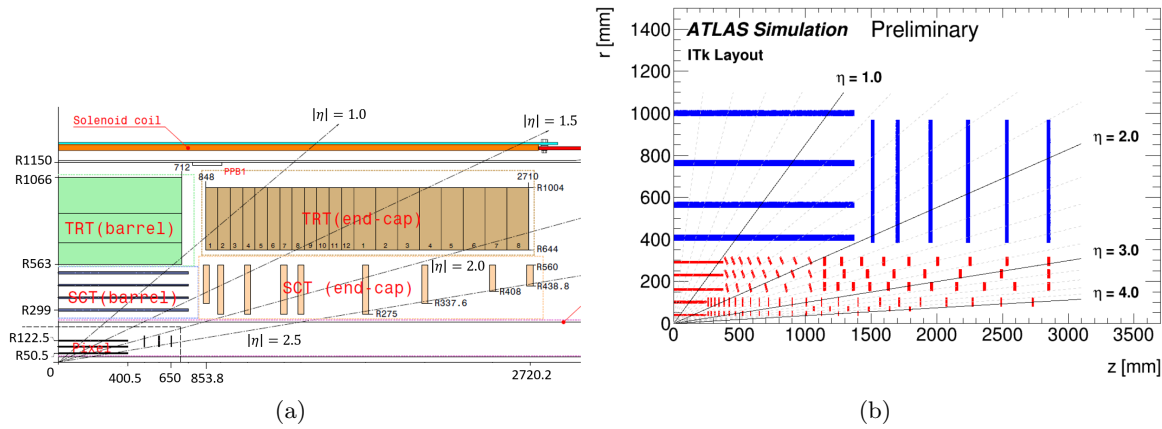


Figure 1. A diagram of the current ATLAS Inner Detector (a)[6] and the future ATLAS Inner Tracker (b)[7]. The Transition Radiation Tracker (TRT) is not present in the ITk as this type of detector would become saturated in the high luminosity environment. In (b), the blue shows the positions of the strip sensors while the red shows the position of the Pixel sensors. The increase in the pseudorapidity range (η) is also noticeable.

that simulates how particles interact with matter and is used by the ATLAS collaboration to model the full ATLAS detector. Once the detector is running, the simulation is important for producing the Monte Carlo simulated samples that are used to compare our theories to the data collected from the detector. Since our theories are all mathematically based, and our data from the detector is essentially just electronic signals, we need a way to convert our theories into a format that matches what we get from the detector. A simulation of the detector estimates how the theoretically produced particles would interact with the material in the detector and emulates how the data acquisition systems would convert those interactions into electronic signals.

As the ITk is still being built, there are often changes and finalisations to the original design laid out in the Letter of Intent [4]. One of the more recent updates was in the strip module Final Design Report in 2019, which finalised the strip module designs. From this, the dimensions and shapes of the strip module components were improved in the simulation, as well as an update to the material descriptions. The result of these can be seen in Figure 3. The main updates were to the hybrids and powerboard. One thing that is obvious is the lack of chips in the simulation, but this is explained in Section 5. Some simplifications in terms of the shapes can also be seen, particularly for the endcap module. This is because the gain from a more accurate description is not worth the increased computational cost.

4. Support Structures

Apart from updating the modules, there are also the support structures that need to be updated in the simulation. These are basically the skeleton of the ITk that either provide the structure that houses the modules and electronics, or provide protection from excessive radiation damage. A major update to the ITk outer cylinder was performed, which is the outer most structural support. It went from a uniform carbon fibre cylinder to a thinner carbon fibre cylinder, with flanges and titanium mount pads. The effect of this change can be seen in the X_0 measurements in Figure 4. Looking at the outer cylinder component, overall it has reduced, except for a few peaks that are located where the new flanges and mount pads are.

Another update was to the polymoderators. These are polyethylene cylinders around the ITk

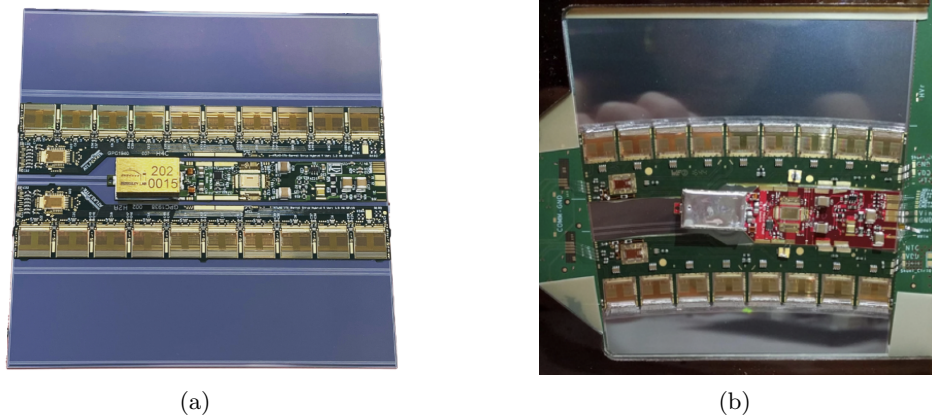


Figure 2. An image of a barrel short strip module (a) and an endcap module (b). The metallic is the silicon sensor, with the middle PCB and box object being the powerboard and DCDC converter respectively. The PCBs on either side of the powerboard are the hybrids housing the ABC readout chips and the hybrid controller chips (the smaller chip on the left of the hybrids). Both sensors have four rows of strips, hence two hybrids, and in both pictures the strips essentially run vertically.

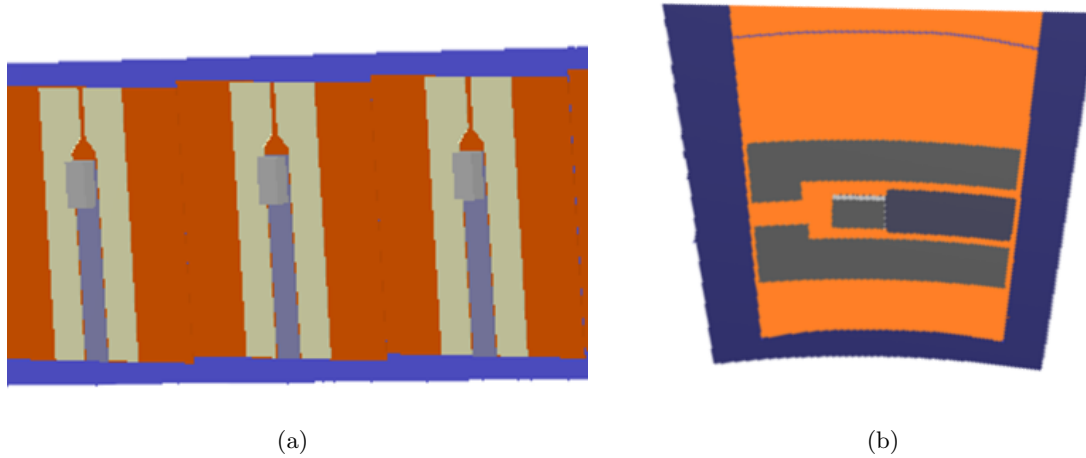


Figure 3. A visualisation of a barrel short strip module (a) and an endcap module (b) from the simulation. The orange is the sensor, on which are the hybrids and powerboards. The blue is the stave (a) and petal (b). Noticeably absent are the chips which is discussed in Section 5.

that help protect against neutrons that back-scatter from the calorimeters which could cause excessive damage to the sensors. The moderators' widths were slightly increased and they got an extra structural layer. This increase in material is shown in Figure 4 where the moderator component has slightly increased uniformly across pseudorapidity.

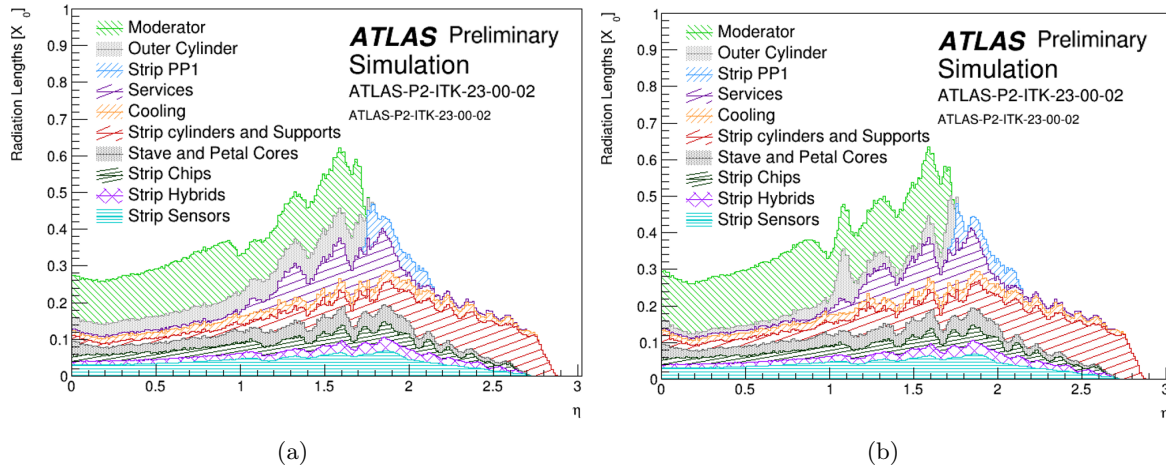


Figure 4. Plots of the Radiation Lengths of each of the components in the strip detector before the updates (a) and after the updates (b) as a function of the pseudorapidity (η). Radiation length X_0 is the mean distance a high-energy electron will travel before it is left with e^{-1} of its energy due to bremsstrahlung radiation.

5. Computational Improvements in Simulation

In simulations, it is not only important to have an accurate description of what is being tested, but for them to also be computationally efficient. There's no point in having a simulation that is a few percent more accurate but uses far more memory and CPU time to complete its calculations.

5.1. Simulation of readout chips

One of the first things we checked to improve computational cost was the simulation of the strip module chips. As can be seen in Table 1, there are almost 260000 chips that need to be created in the strip detector alone. We decided to try remove the chip objects from the simulation, but still included their material in the hybrids. This reduced the number of objects but kept the amount of material the same. While this had negligible impact on the radiation lengths, it did reduce the memory usage quite a bit and the CPU time a little bit, as is shown in Table 2.

5.2. Redefining compound volumes

The next test was more on the side of the simulation structure than the detector. When defining a composite object comprised of multiple objects, e.g., the strip module, this can be done with either an assembly volume or a logvol object. In the assembly volume, one of the objects is chosen as a reference and the other objects are placed in reference to it, resulting in a grouping of objects whose reference point is defined by the reference object. In the logvol, the different components are placed within a "mother" volume, and the reference point becomes that of the mother volume. Due to how the simulation tracks the particles and how it determines what object the particle is in, the logvol has a better memory and CPU time usage. We tried looking at changing the module descriptions from the assembly volumes to logvols. This resulted in a large reduction in memory usage and CPU time, which can be seen in Table 2. After both the chip and volume change, there is a reduction of almost 76% in the memory usage and 71% in the CPU time for the entire ITk.

Table 2. Summary of the computational cost for the strip detector. Shown is the memory and CPU time required for the voxelisation of the detector components.

Location	Memory [MB]			CPU time [s]		
	Original	Chip update	Chip+volume update	Original	Chip update	Chip+volume update
Barrel 3	314	212 (-32%)	67 (-79%)	25.96	21.71 (-16%)	6.64 (-74%)
Barrel 2	280	199 (-29%)	54 (-81%)	17.96	16.02 (-11%)	4.69 (-74%)
Barrel 1	239	145 (-39%)	48 (-80%)	14.75	11.25 (-24%)	3.95 (-73%)
Barrel 0	181	82 (-55%)	21 (-88%)	10.67	6.17 (-42%)	1.62 (-85%)
Endcaps	131	66 (-50%)	20 (-85%)	5.9	4.10 (-31%)	1.82 (-69%)
ITk Total	1184	743 (-37%)	279 (-76%)	79	63.00 (-20%)	23.00 (-71%)

6. Conclusion

Due to the HL-LHC upgrade, the ATLAS detector will require an upgrade to cope with the new high pile-up environment. But apart from the physical detector, an accurate simulation is also required for predictions of performance, and for the correct modelling of the Monte Carlo generated samples used to compare theory to data.

The simulation requires constant updates as the latest designs and new engineering specifications come out. Some of the updates to the strip detector of the ITk were to the descriptions of the modules and support structures. This has brought those objects closer to their true descriptions. Also the computational cost of the simulation was improved by removing some volumes and changing how the modules are defined in the code. There are still parts of the ITk that need to be updated in the simulation, e.g., the inner support structures and the electronics and cooling, but these will only be done when the latest engineering specifications are available.

Some studies were performed with these updates, but the results have not been made public yet so could not be shown in this paper. However, the ITk simulation is performing as good, and in some cases, better than the current ATLAS Inner Detector despite the more complicated reconstruction environment.

References

- [1] L Evans and P Bryant. LHC Machine. *Journal of Instrumentation*, **3**(08):S08001, 2008.
- [2] I B Alonso and L Rossi. HiLumi LHC Technical Design Report: Deliverable: D1.10. Technical Report CERN-ACC-2015-0140, Nov 2015.
- [3] ATLAS Collaboration. Technical Design Report for the ATLAS Inner Tracker Strip Detector. Technical Report CERN-LHCC-2017-005. ATLAS-TDR-025, CERN, Geneva, Apr 2017.
- [4] ATLAS Collaboration. Letter of Intent for the Phase-II Upgrade of the ATLAS Experiment. Technical Report CERN-LHCC-2012-022. LHCC-I-023, CERN, Geneva, Dec 2012.
- [5] Geant4 Collaboration. GEANT4: A Simulation toolkit. *Nucl. Instrum. Meth.*, A506:250–303, 2003.
- [6] ATLAS Collaboration. The ATLAS Experiment at the CERN Large Hadron Collider. *Journal of Instrumentation*, **3**(08):S08003, 2008.
- [7] Expected Tracking Performance of the ATLAS Inner Tracker at the HL-LHC. Technical report, CERN, Geneva, Mar 2019. <https://cds.cern.ch/record/2669540>.

Search for a heavy di-photon resonance in association with b-jets with the ATLAS detector at the LHC

E. Shrif¹, X. Ruan¹, S. Dahbi¹ and B. Mellado^{1,2}

¹ School of Physics and Institute for Collider Particle Physics, University of the Witwatersrand, Johannesburg, Wits 2050, South Africa

² iThemba LABS, National Research Foundation, PO Box 722, Somerset West 7129, South Africa

E-mail: shrif.esra@gmail.com

Abstract. A search for a heavy resonance decaying into di-photon in association with at least one b -jet in the mass range, 180–1600 GeV is performed using 139 fb⁻¹ of $\sqrt{s} = 13$ TeV pp collision data taken by the ATLAS detector at the Large Hadron Collider. A Higgs boson like heavy scalar X produced with top quarks, b quarks or Z boson decaying into $b\bar{b}$ are examined. Three models are tested in this search. Limits at 95% confidence level on the production cross-section times branching fraction to di-photon are set.

1. Introduction

Many proposals for theories beyond the Standard Model (SM), include the prediction of new massive bosons. Examples are, the graviton models [1] and the two-Higgs-doublet models (2HDM) [2], that address the large difference between the electroweak and gravitational scales. It is therefore well-motivated to extend the upper limit of the Higgs boson search mass range as much as possible above $m_H = 160$ GeV. The analyses presented here search for a heavy resonance decaying into two photons and produced in association with at least a b quark. Similar analyses have been performed by ATLAS [3] and CMS [4] in the $\mu^+\mu^-$ and $b\bar{b}$ final states. Three production modes are tested in this search, the $t\bar{t}X$, $b\bar{b}X$ and the ZX , where the Z boson decays into two b quarks, and X is assumed to be a Higgs like heavy resonance. The Feynman diagrams for these modes are shown in Fig. 1. The search examines the diphoton invariant mass spectrum from 130 GeV to 1.6 TeV with one b tagged jet, two b tagged jets and one b tagged jet plus one lepton final states. This analysis uses 139 fb⁻¹ data taken from ATLAS experiment during 2015–2018 with the centre of mass energy at 13 TeV. Limits at 95% confidence level (CLs) on the production cross-section times branching ratio to diphoton final state are set on the resonance range from 180 GeV to 1.6 TeV. Only the narrow width assumption is tested.

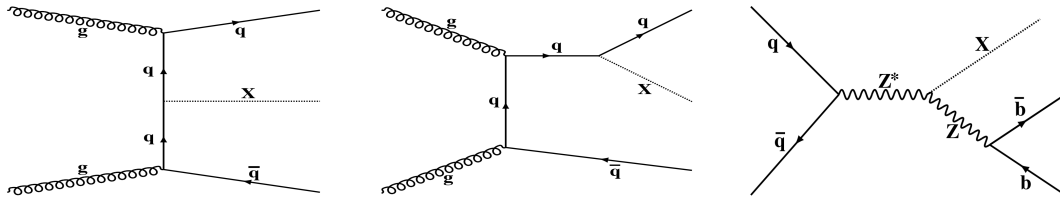


Figure 1: Feynman diagrams for the signal processes, with q refers to top or bottom quark.

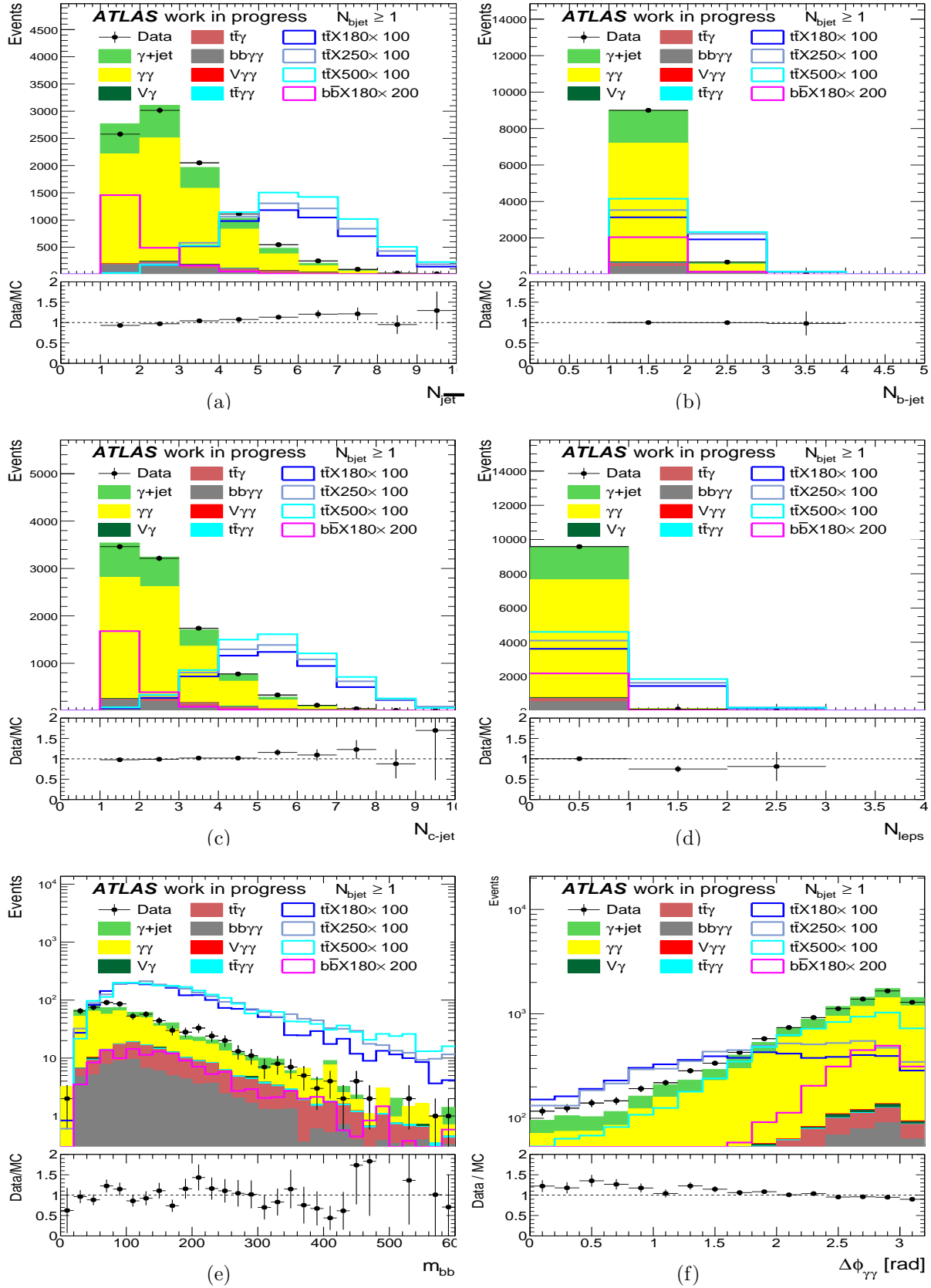


Figure 2: Kinematic distributions comparing the data to MC (after pre-selection and in the control region that $130 < m_{\gamma\gamma} < 160$ [GeV]). The multiplicity of jet (a), b -jet (b) and central jet (c). Number of leptons (d), the invariant mass of the two leading b -jets (e) and $\Delta\phi(\gamma\gamma)$ (f).

2. Samples and event pre-selection

Signal and background samples are simulated using Monte Carlo (MC) generators according to ATLAS detector configurations. MADGRAPH [5] generator, at next-to-leading order in QCD, is used to produce the $t\bar{t}X$ signal samples. Parton showering and hadronization are simulated using the PYTHIA8 [6]. The $t\bar{t}X$ and ZX signals samples are generated and showered using PYTHIA8 at leading order in QCD. The dominant background samples used here are the SM diphoton production and γ jet; contributions also come from $V\gamma$, $V\gamma\gamma$, $t\bar{t}\gamma\gamma$, $t\bar{t}\gamma$ and $b\bar{b}\gamma\gamma$, where V stands for Z or W boson. The dataset used in this analysis encompasses all data that was recorded with the ATLAS detector, between 2015 and 2018, in pp collisions with an integrated luminosity of 140 fb^{-1} at a centre-of-mass energy of $\sqrt{s} = 13 \text{ TeV}$.

In the pre-selections, events are selected with two identified and isolated photons invariant mass $m_{\gamma\gamma} > 130 \text{ GeV}$. The transverse momentum p_T of the leading and sub-leading photon are required to be greater than 40 GeV, and 30 GeV, respectively. Events should also have at least one b -tagged jets. The working point chosen is set at 77% b -tagged jet selection efficiency [7]. Figure 2 shows the kinematic distributions corresponding to different variables, just after the pre-selections. The agreement between data and total background is reasonable within the statistical uncertainties.

3. Optimization

The optimization is performed based on the pre-selection, We use the $t\bar{t}X$ sample with $m_X = 180 \text{ GeV}$, $b\bar{b}X$ with $m_X = 180 \text{ GeV}$ and ZX with $m_X = 200 \text{ GeV}$ as the signal sample for optimization. All background samples are mixed and normalised to 140 fb^{-1} for the optimization. For $t\bar{t}X$, we chose to optimize on the variables N_{cjet} and $\Delta\phi_{\gamma\gamma}$ due to the best performance comparing to other variables, like missing transverse momentum and transverse momentum of the two photon system. Events are split into three regions, namely, leptonic ($N_{leps} \geq 1$ and $N_{bjet} \geq 1$), Zero leptons with exactly one b -tagged jet or at least two b -tagged jet. In each region, events are further split into four bins by making a two dimension scan on $\Delta\phi_{\gamma\gamma}$ and N_{cjet} . For the ZX model, we optimize using the variable m_{bb} and $\Delta\phi_{\gamma\gamma}$ in the two b -jet region, where m_{bb} is the invariant mass of the two leading b -jets. While we only use the number of central jets for the $b\bar{b}X$ optimization. The significance is calculated using the formula S/\sqrt{B} , where S and B are the signal and background events, respectively. Table 1 shows a summary of the optimized results for $t\bar{t}X$ and ZX models. Based on these optimization results as well as the $b\bar{b}X$ results, the events are categorized in Table 2.

Table 1: The optimization results for the $t\bar{t}X$ model with $m_X = 180, 250 \text{ GeV}$ for each region (left) and for the ZX model with $m_X = 200 \text{ GeV}$ in the two b -jet region (right).

	Region	N_{cjet}	$\Delta\phi(\gamma\gamma)$	Significance	$ZX200$			
					$\Delta\phi(\gamma\gamma)$	$m_{bb}(\text{high})$	$m_{bb}(\text{low})$	Significance
ttX180	1l1b	3	1.2	2.75	1.6	105	65	0.284
	0l1b	6	2.4	1.26	2.0	105	65	0.289
	0l2b	5	2.0	1.80	2.4	105	65	0.294
ttX250	1l1b	6	1.2	5.94	2.8	105	70	0.281
	0l1b	6	2.0	2.00	3.2	105	65	0.262
	0l2b	6	2.4	3.18				

Table 2: The definition of each category, for different models and mass range.

	Category index	Cuts
Preselection		Photon $m_{\gamma\gamma} > 130$ GeV & $p_T > 40, 30$ GeV & $N_{bjet} \geq 1$
$m_{\gamma\gamma}$ in 160-1600 GeV		
bbX Categories	1	$N_{cj} = 1$
	2	$N_{cj} \geq 2$
$m_{\gamma\gamma}$ in 160-600 GeV		
$t\bar{t}X$ Categories	3	$N_{bj} \geq 1$ & $N_{leps} \geq 1$ & $N_{cj} \geq 4$
	4	$N_{bj} \geq 1$ & $N_{leps} \geq 1$ & $N_{cj} < 4$
	5	$N_{bj} \geq 2$ & $N_{leps} = 0$ & $N_{cj} \geq 5$ & $\Delta\phi_{\gamma\gamma} < 2$
	6	$N_{bj} \geq 2$ & $N_{leps} = 0$ & $N_{cj} \geq 5$ & $\Delta\phi_{\gamma\gamma} > 2$
	7	$N_{bj} \geq 2$ & $N_{leps} = 0$ & $N_{cj} < 5$
	8	$N_{bj} = 1$ & $N_{leps} = 0$ & $N_{cj} \geq 6$ & $\Delta\phi_{\gamma\gamma} < 2.4$
	9	$N_{bj} = 1$ & $N_{leps} = 0$ & $N_{cj} \geq 6$ & $\Delta\phi_{\gamma\gamma} > 2.4$
	10	$N_{bj} = 1$ & $N_{leps} = 0$ & $N_{cj} < 6$
ZX Categories	11	$N_{bj} \geq 2$ & $m_{bb} > 65$ & $m_{bb} < 105$ & $\Delta\phi_{\gamma\gamma} < 2.4$
	12	$N_{bj} \geq 2$ & $m_{bb} > 65$ & $m_{bb} < 105$ & $\Delta\phi_{\gamma\gamma} > 2.4$
	13	$N_{bj} \geq 2$ & ($m_{bb} < 65$ & $m_{bb} > 105$)
	14	$N_{bj} = 1$
$t\bar{t}X, ZX$ for $m_{\gamma\gamma}$ in 600-900 GeV		
	14	$N_{bj} = 1$
	15	$N_{bj} \geq 2$
$t\bar{t}X, ZX$ for $m_{\gamma\gamma}$ in 900-1600 GeV		
	0	$N_{bjet} \geq 1$

4. Signal and background modelling

To model the heavy scalar signal shape, we use a functional form that is the double-sided Crystal Ball function (DSCB) [8], consisting of a Gaussian central part extended by asymmetric power-law tails on both sides. The DSCB function modelling method is described in detail in [9, 10]. The DSCB shape is fitted to the signal distributions of the di-photon invariant mass spectrum for different mass points m_X , yielding a set of DSCB parameters for each category. As an example, Figure 4a, shows the result of a single fit of the DSCB function (lines) for a $t\bar{t}X$ signal sample with mass point $m_X = 180$ GeV for the category 3. The DSCB parameter σ_{CB} , the width of the Gaussian core (representing the detector resolution) and α are then parametrised as a function of m_X for each process for the all categorizes using linear functions. For instance, Figure 4b shows σ_{CB} for the $t\bar{t}X$ category 3 with all the signal mass points, where σ_{CB} increases for the signals at higher mass points. For simplicity, the ns for each model are set to the fixed value.

To estimate the signal yield, we parameterize the acceptance times efficiencies using a variety of analytic functions (linear, exponential functions of different-order or polynomials). The maximum difference between the predicted acceptance times efficiency and the MC points is treated as the systematic uncertainty. We only use the maximum difference within the mass range where the category is used. For example, we only use the maximum difference below $m_X = 700$ GeV for category 3-13. The statistical uncertainty of the MC samples is also taken into account.

To build up the background model, the diphoton purity is estimated by the 2×2D sideband method with at least one b-jet selection. The method uses the information of photon ID and

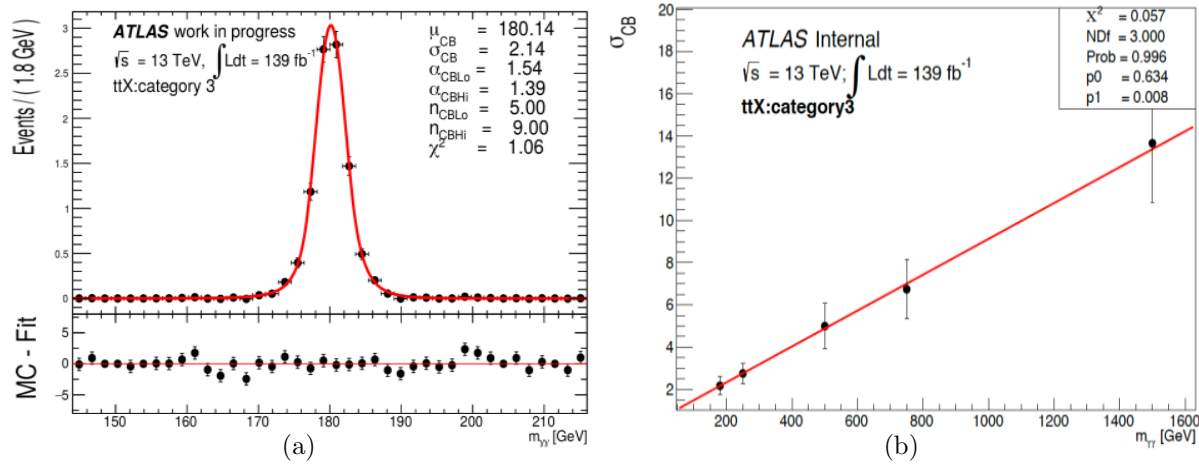


Figure 3: (a) Fit of the $m_{\gamma\gamma}$ for $t\bar{t}X$ with $m_X = 180$ GeV to a DSCB in category-3 and (b) Resolution of the resonance peak as a function $m_{\gamma\gamma}$ for $t\bar{t}X$ in category-3.

isolation variables to measure the fraction of the diphoton events from the data. More details of the method are found in Ref. [11]. The $\gamma\gamma$ and γ jet purity is estimated, and the measured purity is shown in Table 3. The uncertainty on the background modelling is parameterized using so called spurious signal. There are several functional forms to describe the background shape in large mass range. They are the different orders of the so called Dijet fit functions [12]: $f_k(x; b, \{a_k\}) = (1-x)^b x^{\sum_{j=0}^k a_j \log(x)^j}$, $k = 0, 1, 2$, noted as FK0, FK1 and FK2. The envelopes of the absolute spurious signals are obtained in each category. They are parametrised between 160-1500 GeV with a second polynomial exponential function with a constant term, as Figure 4 shows. F-test is used to decide which functional form to be used in each category. For instance, the function FK2 is selected for category-0.

Table 3: Purities with 2×2D sideband method with at least one b -jet selection.

	$\gamma - jet, jet - \gamma$ fraction	jet-jet fraction	$\gamma\gamma$ purity
$m_{\gamma\gamma} > 130$ GeV	0.18 ± 0.01	0.02 ± 0.00	0.80 ± 0.01
$180 \text{ GeV} < m_{\gamma\gamma} < 700$ GeV	0.20 ± 0.01	0.02 ± 0.00	0.78 ± 0.01
$m_{\gamma\gamma} > 700$ GeV	0.15 ± 0.06	0.02 ± 0.02	0.83 ± 0.07

5. Uncertainties and results

Both the experimental and theoretical uncertainties are used in obtaining the result of this analysis. As the background shapes are described by fitting in the data, the uncertainties except the spurious signal, which is discussed as previous section, are estimated on the signal samples only. The systematic uncertainties are implemented via nuisance parameters in the profiled likelihood fit. A summary of the experimental and theoretical uncertainties is given in Table 4 in terms of the relative impact on the number of events from the signal for the most sensitive category. The fits are performed on each mass points for each model. The CL_s limits on the production cross-section times the branching fraction $X \rightarrow \gamma\gamma$ are set to each of the model as a function of mass, as shown in Figure 5.

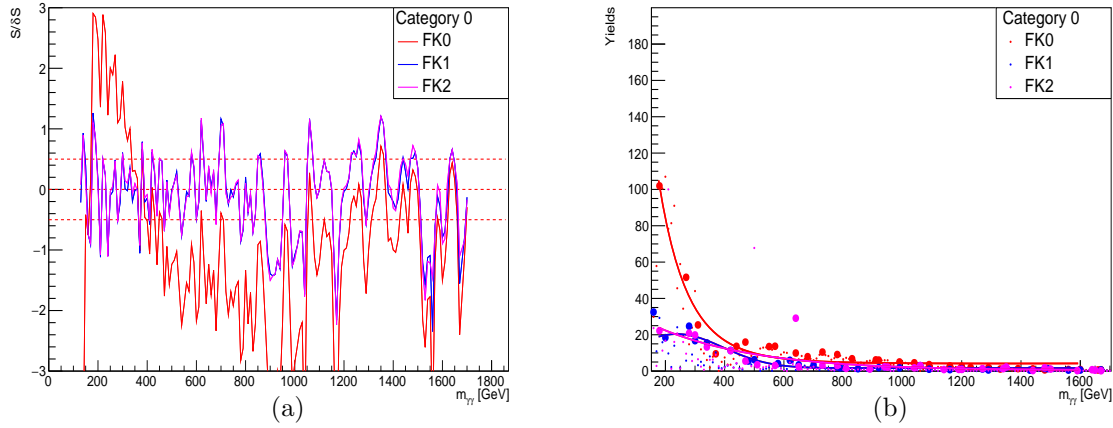


Figure 4: (a) The N_{spurious} envelop for each functional form for the $t\bar{t}X$ category 1 and (b) The $N_{\text{spurious}}/\delta N_{\text{spurious}}$ as a function of mass for each functional using background in category-1.

Table 4: Summary of the systematic uncertainties.

	Source	Signal uncertainty (%)
Experimental	Luminosity	1.7
	Trigger efficiency	1.0
	Vertex selection (inclusive cat.)	< 0.01
	Photon identification efficiency	0.6–1.5
	Photon identification efficiency due to fast simulation	2.0
	Photon isolation efficiency	0.6–1.5
	Photon energy resolution	0.6
	Pile-up reweighting	2.0–7.4
	Photon energy scale	0.3
	Signal efficiency interpolation	1.3–9
Theoretical	Factorization and renormalization scale in migration	1–7
	PDF+ α_S in migration	1–5
	PS, hadronization	3.0
	ISR, FSR, Multi-parton interactions	3.0–10.0

6. Summary

An analysis to search for new heavy resonance in di-photon channel is presented. Three models are tested in this search: $t\bar{t}X$, $b\bar{b}X$ and ZX . The expected 95% confidence level limits are set on the production cross-section times the branching fraction for the decay of the resonance into di-photon as a function of m_X . The mass range of the hypothetical resonances considered is between 180 GeV and 1.6 TeV depending on the final state the model considered.

Acknowledgment

E. Shrif would like to acknowledge the financial support of the Schlumberger Foundation, Faculty for the Future.

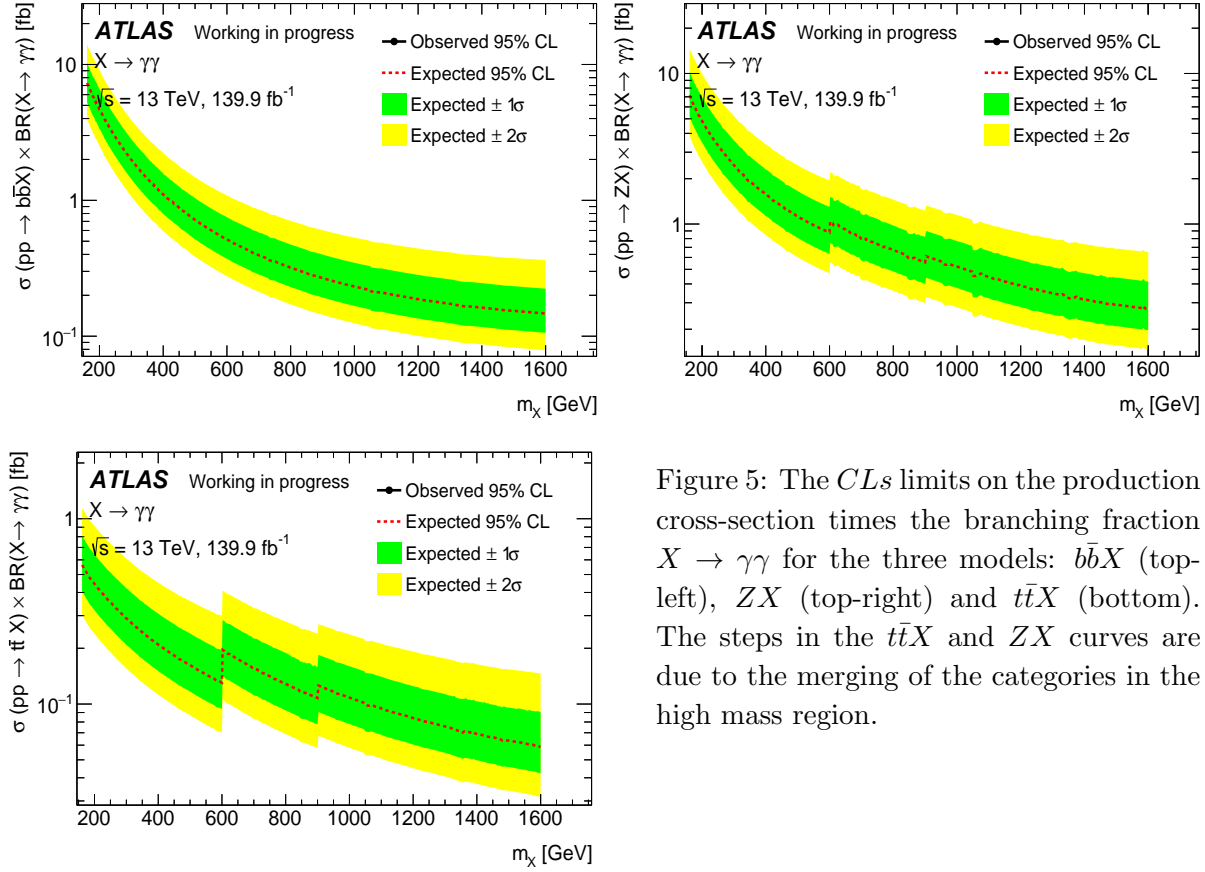


Figure 5: The CLs limits on the production cross-section times the branching fraction $X \rightarrow \gamma\gamma$ for the three models: $b\bar{b}X$ (top-left), ZX (top-right) and $t\bar{t}X$ (bottom). The steps in the $t\bar{t}X$ and ZX curves are due to the merging of the categories in the high mass region.

References

- [1] H. Davoudiasl, J. L. Hewett and T. G. Rizzo, (2000) [Phys. Rev. Lett. **84**, 2080](#).
- [2] G. C. Branco, P. M. Ferreira, L. Lavoura, M. N. Rebelo, M. Sher and J. P. Silva, *Phys. Rept.* **516**, 1-102 (2012) [[arXiv:1106.0034](#)].
- [3] ATLAS Collaboration, *JHEP* **07**, 117 (2019) [[arXiv:1901.08144](#)].
- [4] CMS Collaboration, *JHEP* **08**, 113 (2018) [[arXiv:1805.12191](#)].
- [5] Alwall J, Frederix R, Frixione S, Hirschi V, Maltoni F, Mattelaer O, Shao H S, Stelzer T, Torrielli P and Zaro M, *JHEP* **1407**, 079 (2014) [[arXiv:1405.0301](#)].
- [6] Sjostrand T, Mrenna S and Skands P Z, *Comput. Phys. Commun.* **178**, 852 (2008) [[arXiv:0710.3820](#)].
- [7] ATLAS Collaboration, (2017) [[ATL-PHYS-PUB-2017-013](#)].
- [8] Oreglia M, Appendix D. PhDthesis, Univ. Stanford, [[SLAC-0236 \(1980\)](#)].
- [9] ATLAS Collaboration, *Phys. Rev. D* **90**, no.11, 112015 (2014) [[arXiv:1408.7084](#)].
- [10] ATLAS Collaboration, *JHEP* **09**, 001 (2016) [[arXiv:1606.03833](#)].
- [11] Carminati L *et al.* (2012) [[ATL-COM-PHYS-2012-592](#)].
- [12] CDF Collaboration, *Phys. Rev. D* **79**, 112002 (2009) [[arXiv:0812.4036](#)].

Transfer reactions to populate the Pygmy Dipole Resonance (PDR) in ^{96}Mo

T C Khumalo^{1,2}, L Pellegrini^{1,2}, M Wiedeking^{1,2}, F Cappuzzello^{3,4}, M Cavallaro³,
D Carbone³, R Neveling¹, A Spatafora^{3,4}

¹Themba LABS, Old Faure Road, Faure, Cape Town, South Africa

²University of the Witwatersrand, 1 Jan Smuts Avenue, Braamfontein, Johannesburg, South Africa

³INFN Laboratori Nazionali del Sud, Catania, Italy

⁴Universita di Catania, Catania, Italy

¹E-mail: 2397687@students.wits.ac.za

Abstract. This paper presents a study that attempts to probe the nature of the pygmy dipole resonance (PDR). In particular, the single-particle or the collective nature of these dipole states by exploiting the sensitivity of one-particle transfer reactions to excite single-particle states. The measurements on transfer reactions (p,d) and (d,p) were performed on two different targets ^{97}Mo and ^{95}Mo , respectively to populate the ^{96}Mo residual nucleus. The proton and deuteron beam energies used were 25 MeV and 10 MeV for the (p,d) and (d,p) reaction channels, respectively. The ejectiles were detected, identified and momentum-analyzed by the MAGNEX spectrometer and its focal-plane detector. The data reduction process of the (p,d) reaction will be presented together with some preliminary results.

1. Introduction

The Pygmy Dipole Resonance (PDR), is widely described as a concentration of electric dipole states (1^-) around the neutron separation energy (S_n), has thus far only been observed in neutron-rich nuclei. Bracco *et al.* [1] and Savran *et al.* [2] recently conducted detailed reviews on the PDR, outlining the progress made in the study of dipole excitation. Macroscopically, the PDR was interpreted using the hydrodynamical model as an oscillation of a neutron skin against a proton-neutron core.

In an attempt to describe the PDR microscopically and, among the different models used, the quasi-particle random phase approximation (QRPA), the relativistic quasi-particle random phase approximation (RQRPA) and the quasi-particle phonon model (QPM) have been found to best describe the PDR when compared to available experimental results. Significant amount of work has also been done experimentally to study the PDR in order to understand its nature. Previous studies show that the PDR is very probe sensitive and, therefore, two different types of experiments conducted on the same nucleus might give complimentary information on the nature of the PDR. The interpretation of this excitation mode is not yet clear and lately the collectivity of these states has also been put under scrutiny. At an attempt to interpret this dipole excitation mode some theoretical studies [3, 4] found that although the low-lying states cannot be considered as collective as the Giant Dipole Resonance states, they also cannot be described as a single p-h configuration. The response of the PDR to an isovector operator calculated using RPA theoretical models, does not show a clear collective nature since the several particle-hole configurations do not contribute coherently to the pygmy state wave function. Contrarily, there are other studies

[5,6] where single-particle behaviour of the PDR strength is predicted due to an observed strong fragmentation which could be influenced by single-particle shell effects.

Experimentally, inelastic scattering of high-energy protons (p, p') [7] and real photons (γ, γ') [8] have been used as probes for PDR studies on ^{96}Mo . However, these are not selective thus to investigate properly the single-particle(hole) nature of this dipole response a more selective probe is required. Direct reactions, specifically stripping and pickup transfer reactions, owing to their selectivity for exciting single-particle (hole) states, were thus considered in this work.

2. Experimental Method

Stripping (d,p) and pickup (p,d) reactions were performed on ^{95}Mo and ^{97}Mo targets respectively, in order to examine the single-particle/hole configurations of ^{96}Mo . The targets used had aerial density of 0.6 mg/cm^2 and 0.4 mg/cm^2 for the (d,p) and (p,d) reactions, respectively. The 10-MeV deuteron and 25-MeV proton beams were delivered by the 14MV- Tandem accelerator which is installed at the INFN-LNS in Catania, Italy. The beams impinged on the ^{95}Mo and ^{97}Mo targets, respectively, to excite ^{96}Mo . The choice of the beam energies was influenced by the enhanced single-particle selectivity of direct reactions at this energy range [9]. The data were collected for approximately 234 hours at a beam current ranging between 0.9 nA and 5 nA for both reactions. The MAGNEX magnetic spectrometer and its focal-plane detection system was used to detect the reaction products [10]. The data were collected at three different angular settings, namely 10° , 17° and 24° in order to allow the measurement of the angular distribution of the scattered particles and deduce the spin/parity of the excited states. The magnetic field settings were adjusted to measure a wide excitation-energy region, up to 8 MeV.

3. The data reduction process

The data reduction process for the three angular settings has been completed for the pickup reaction on the ^{97}Mo target. The initial step was to identify the deuterons and this information was obtained through the combination of the energy loss (ΔE) measurement by the deuterons in the gaseous region of the detector and the focal-plane horizontal position (X_f) with the residual energy (E_{res}) in the silicon detectors. Once the deuterons were selected, the quality of the PID process was checked using the horizontal angle (Θ_f) and the focal-plane horizontal position (X_f) measurement as seen in Figure 2 for the low-energy regions of the focal- plane. The vertical position calibration of the focal plane was performed which allowed accurate extraction of the vertical position (Y_f) and the vertical angle (Φ_f) for the events of interest. Since MAGNEX is a large-acceptance spectrometer with a vertical acceptance of $\pm 125 \text{ mrad}$ [10] and a horizontal acceptance $-90 - 110 \text{ mrad}$ [10], ray-reconstruction is important to correct for high-order aberrations.

To initiate the reconstruction process, a direct transport 10^{th} -order matrix was created using COSY-INFINITY [11] with the final phase space parameters as input (X_f , Y_f , Θ_f , Φ_f). A correction of the rigidity (Bp), quadrupole field (BQ) and the boundary coefficients of the entrance of the dipole magnet was also included. A set of events was then created using Monte Carlo-based techniques which are included in the COSY-INFINITY as to test the quality of the reconstruction. These events were compared to the experimental data as seen Figure 2. The obtained transport matrix was then inverted and applied to the experimental data to extract the initial phase space parameters such as the excitation energy (E_x) and the scattering angle (Θ_{lab}). Once extracted, the next step was to analyze the ^{96}Mo excitation-energy spectrum to identify peaks and compare with data from Cochavi *et al.* [12] so as to ensure that the energy-calibration was correct and to compare the cross-section angular distributions of the lower-energy region states before extending to the PDR region which is our region of interest. The MAGNEX magnetic spectrometer allows

particle identification with energy resolution of ($\Delta E/E \sim 1/1000$) [10]. However, the energy loss in the target can also affect the final energy resolution. The preliminary estimation of the energy resolution for the pickup reaction (p,d) is ~ 40 -keV FWHM for the 17° angular setting dataset.

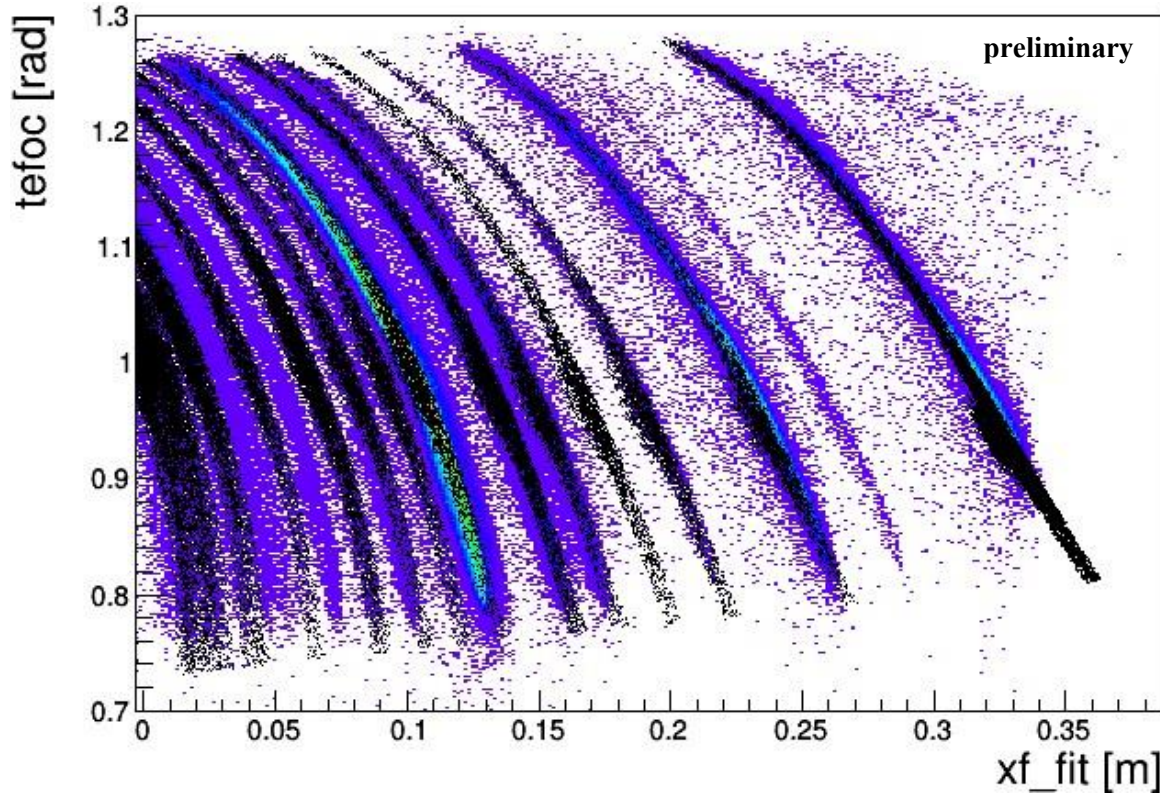


Figure 2: The horizontal angle (Θ_f) versus horizontal focal-plane position representation (X_f) where the 10° experimental data is represented in blue and the COSY INFINITY [11] simulations are represented in black. For the low-energy region of the focal plane, the experimental data and the simulations overlay. This representation is also used as quality check for the ray-reconstruction procedure.

4. Conclusion & future work

A study that seeks to examine the collective/ single-particle nature of the PDR was presented. Where the experimental setup and data optimization were presented. The current status of the study was also discussed. For future work and currently underway, the differential cross section for all the states identified will be calculated. Angular distributions of the scattered particles will be used to determine the spin and parity of the observed states. The results will be compared to theoretical predictions and other experimental data available for ^{96}Mo .

5. Acknowledgements

This work is based on the research supported in part by the National Research Foundation (NRF) of South Africa grant number 118846

References

- [1] Bracco A, Lanza E G and Tamii A 2019 *Progress in Particle and Nuclear Physics* **106** 360–433
- [2] Savran D, Aumann T, Zilges A 2013 *Progress in Particle and Nuclear Physics* **70** 210–45
- [3] Lanza E G, Catara F, Gambacurta D, Andrés M V and Chomaz Ph 2009 *Physical Review C* **79** 5
- [4] Roca-Maza X, Pozzi G, Brenna M, Mizuyama K and Colò G 2012 *Physical Review C* **85** 2
- [5] Reinhard P-G and Nazarewicz W 2010 *Physical Review C* **81** 5
- [6] Gambacurta D, Grasso M and Catara F 2011 *Physical Review C* **84** 3
- [7] Martin, D., von Neumann-Cosel, P., Tamii, A., Aoi, N., Bassauer, S., Bertulani, C., Carter, J., Donaldson, L., Fujita, H. and Fujita, Y., *et al.* 2017. Test of the Brink-Axel Hypothesis for the Pygmy Dipole Resonance. *Physical Review Letters*, **119** 18.
- [8] Rusev, G., Schwengner, R., Beyer, R., Erhard, M., Grosse, E., Junghans, A., Kosev, K., Nair, C., Schilling, K. and Wagner, A., *et al.* 2009. Enhanced electric dipole strength below particle-threshold as a consequence of nuclear deformation. *Physical Review C*, **79** 6.
- [9] Feshbach H and Henley E M 1992 *Physics Today* **45** 12 84–5
- [10] Cavallaro M, Agodi C, Brischetto G A, Calabrese S, Cappuzzello F, Carbone D, Ciraldo I, Pakou A, Sgouros O, Soukeras V, *et al.* 2020 *Nuclear Instruments and Methods in Physics Research Section B: Beam Interactions with Materials and Atoms* **463** 334–8
- [11] Makino K and Berz M 1999 *Nuclear Instruments and Methods in Physics Research Section A: Accelerators, Spectrometers, Detectors and Associated Equipment* **427** 1-2 338–43
- [12] Cochavi S, Moalem A, Ashery D, Alster J, Bruge G and Chaumeaux A 1973 *Nuclear Physics A* **211** 1 21–8

Search for the non-resonant Higgs-pair production in $\ell^+\ell^-\ell^+\ell^-$ final state at $\sqrt{s} = 13$ TeV in the ATLAS detector

Abdualazem Fadol^{1, 2}, Yaquan Fang², Bruce Mellado¹ and Xifeng Ruan¹

¹ School of Physics and Institute for Collider Particle Physics, University of the Witwatersrand, Johannesburg, Wits 2050, South Africa

² Institute of High Energy Physics, University of Chinese Academy of Sciences, 19B Yuquan Road, Shijingshan District, Beijing 100049, China

E-mail: amohammed@aims.ac.tz

Abstract. A search for the non-resonant production of a pair of the Standard Model Higgs boson h via gluon fusion, $gg \rightarrow hh$, is performed. Each Higgs boson decays to either $2W$, $2Z$ or 2τ , leading to $4\ell + X$ in the final state. The ℓ could be an electron or a muon, and X is missing transverse energy or jets. The search uses Monte Carlo samples at a centre-of-mass energy of 13 TeV generated according to the ATLAS detector configurations with an integrated luminosity of 139 fb^{-1} . The expected upper limit on the cross-section times the Standard Model (SM) Higgs pair branching ratio is found to be 49.22 times the SM prediction.

1. Introduction

A new era has emerged in High Energy Physics after the ATLAS [1] and CMS [2] experiments discovered a new scalar boson. Various measurements have been performed to confirm the compatibility of the new particle with the Higgs boson, h , which is predicted by the Standard Model (SM) [3, 4]. The SM predicted the existence of the non-resonant Higgs pair production and Higgs self-coupling. A search using 36.1 fb^{-1} datasets in the $hh \rightarrow WW^{(*)}WW^{(*)}$ showed no significant excess above the considered SM background is found [5]. However, the Higgs pair production is significantly enhanced by altering the Higgs boson self-coupling [6] or in extended Higgs sectors scenarios [7].

With the current 139 fb^{-1} dataset, one expects the sensitivity of the Higgs pair production to improve. In addition, including channels with a small branching ratio is expected to enhance the exploration. This study analyses the non-resonant Higgs pair production via gluon fusion, which subsequently decay to 4ℓ ($\ell = e$, or μ) final state. Each of the two Higgs bosons decays to $2W$, $2Z$ or 2τ , leading to $4\ell + X$, where X could either be missing transverse energy or jets. The combination of the Higgs decay products is shown in Figure 1 with their branching fractions. There are nine possible permutations, namely— $4W$, $4Z$, 4τ , $2W2Z$, $2Z2W$, $2W2\tau$, $2\tau2W$, $2Z2\tau$ or $2\tau2Z$. About 25% of the hh events are expected to come from the $hh \rightarrow 4W$, 20% from $hh \rightarrow 2Z2W$, and 11% from $hh \rightarrow 2W2\tau$. Other hh events such as $hh \rightarrow 4Z$, $hh \rightarrow 4\tau$, and $hh \rightarrow 2Z2\tau$ are expected to be less than 10%. Only Monte Carlo (MC) simulations are used in the analysis for the signal optimisation with an integrated luminosity of 139 fb^{-1} .

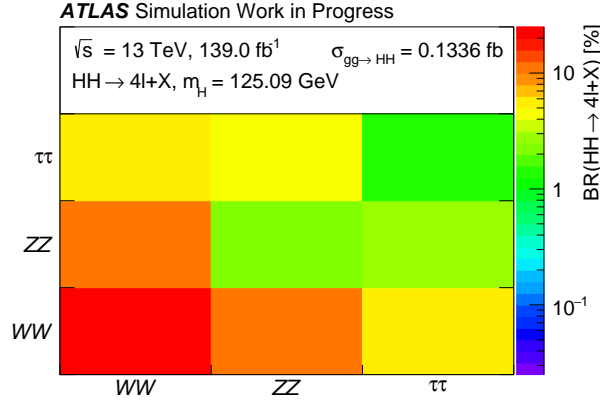


Figure 1. Di-Higgs decay modes and the calculated branching fraction of Di-Higgs to four leptons and X at the reconstruction level. The assumed Higgs mass is 125.09 GeV and the Higgs pair production cross-section in gluon fusion is 0.1336 fb.

This paper is organised as follows, MC samples used in the analysis are described in section 2. The event selection and analysis strategy are explained in section 3 and section 4, respectively. Systematic uncertainties included in the analysis are discussed in section 5. Section 6 shows the statistical procedure, results and discussion. Finally, the conclusion is given in section 7.

2. Monte Carlo samples

MC simulation according to the ATLAS experiment configuration is used. The samples are generated in three campaigns to emulate the 2015 - 2016, 2017 and 2018 data taking periods. The combination of all campaigns together matches up to an integrated luminosity of 139 fb⁻¹. Non-resonant, $gg \rightarrow hh$, signal and $t\bar{t}V$ background samples are generated at NLO using MADGRAPH5_AMC@NLO [8] interfaced with PYTHIA 8 [9] for the hadronisation. Background processes such as $q\bar{q} \rightarrow ZZ$, $q\bar{q} \rightarrow ZZ$ (EW), VVV ($V = Z/W^\pm$) and Z +jets are simulated using SHERPA 2.2.2 [10] with NNPDF30NNLO [11] parton distribution function (PDF) set. The $t\bar{t}$ events were generated using POWHEG-BOX v2 [12] with NNPDF30NNLO PDF set. PYTHIA 8 was used as an interface for the showering and hadronisation with A14 NNPDF23LO tune, and EVTGEN [13] was used to simulate B-hadron decays. POWHEG-BOX v2 and PYTHIA 8 were used for the generation and hadronisation of the WZ process.

3. Event selection

Electrons must be within the inner tracking detector system ($|\eta| < 2.47$ excluding the $1.37 < |\eta| < 1.52$ region) and have transverse energy $E_T > 7$ GeV. Muons are required to be inside $|\eta| < 2.7$ scope of the muon spectrometer, and have transverse momentum $p_T > 5$ GeV. Events are selected if they only contain exactly four leptons with $p_T^\ell > 10$ GeV, and a total charge sum equal to zero. Events are required to pass single- and di-lepton trigger [14], and at least one of the lepton candidate need to be matched to the trigger. After choosing four isolated leptons, events are classified further according to the number of lepton pairs. Events must have two same-flavour and opposite charges (2-SFOS) lepton pairs such as $4e$, 4μ and $\mu 2e$. In addition to events with one or zero same-flavour opposite charges pairs (1-SFOS or 0-SFOS), for instance, $e\mu\mu\mu$ and $e\mu e\mu$. The 0-SFOS events are combined with 1-SFOS (0/1-SFOS) due to the low statistics. In each quadruplet, the p_T of the leading lepton has to be higher than the succeeding one. The quadruplets are selected based on matching the invariant mass of the second lepton pairs m_{Z_2} to be closest to the Z boson mass, and the first lepton pair were taken as m_{Z_1} . Events

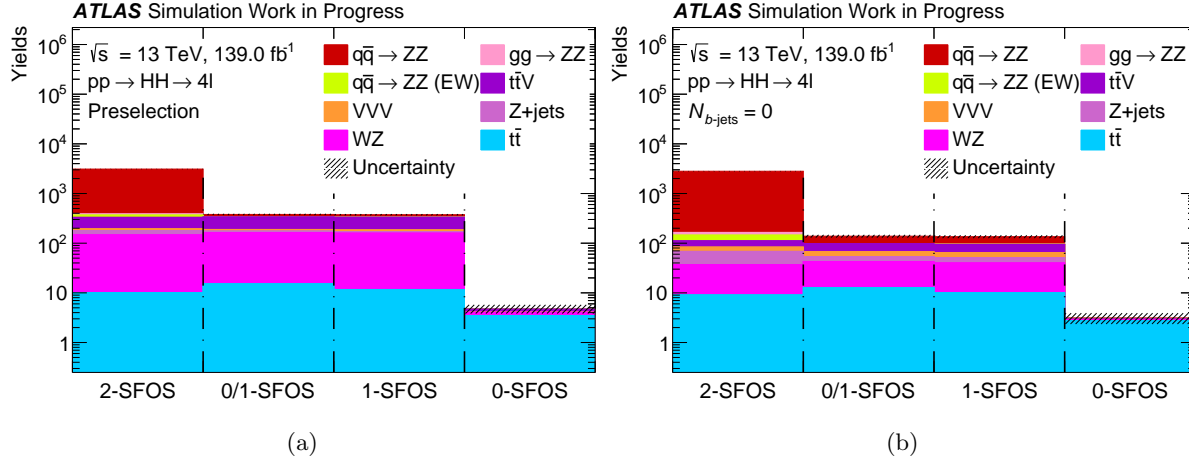


Figure 2. The expected background yields for MC simulation after the (a) preselection and (b) $N_{b\text{-jets}} = 0$ for the 2-SFOS, 1-SFOS, 0/1-SFOS and 0-SFOS categories.

carrying one or more b -jets are vetoed to suppress top related backgrounds further. Figure 2 shows the yield for each background component with and without the b -jet veto for 2-SFOS, 1-SFOS, 0-SFOS, and 0/1-SFOS categories.

4. Analysis strategy

A boosted decision tree (BDT) based on the Multivariate analysis package (TMVA) [16] is used to separate the $hh \rightarrow 4\ell + X$ signal from the background. Events are divided equally into two sets; the first half is used for training the BDT algorithm. And the other half is employed to test the performance of the method. Table 1 shows the unweighted events of the signal and backgrounds for 0/1-SFOS and 2-SFOS categories after the b -veto.

Sixteen variables are used as inputs to the BDT, including the four leptons invariant mass. The correlation between features is shown in Figure 3. Some of the variables have a high correlation; for instance, the first lepton momentum is correlated with the scalar sum of leptons. Table 2 summarises the description of each variable, its ranking and the separation power. The best- and worst-ranked variable are labelled 1 and 16, respectively. The invariant mass of the second lepton pair has the best ranking in 0/1-SFOS, while the invariant mass of the first lepton

Table 1. Unweighted events for the signal and backgrounds component in each category used in the training and testing. Events are shown after vetoing the b -jets.

	0/1-SFOS	2-SFOS
$q\bar{q} \rightarrow ZZ$	21675	1528977
$q\bar{q} \rightarrow ZZ$ (EW)	375	28806
$gg \rightarrow ZZ$	2966	256910
$t\bar{t}V$	11031	10105
VVV	18467	57908
Z +jets	69	116
WZ	328	276
$t\bar{t}V$	92	68
$hh \rightarrow 4\ell + X$	4340	3781

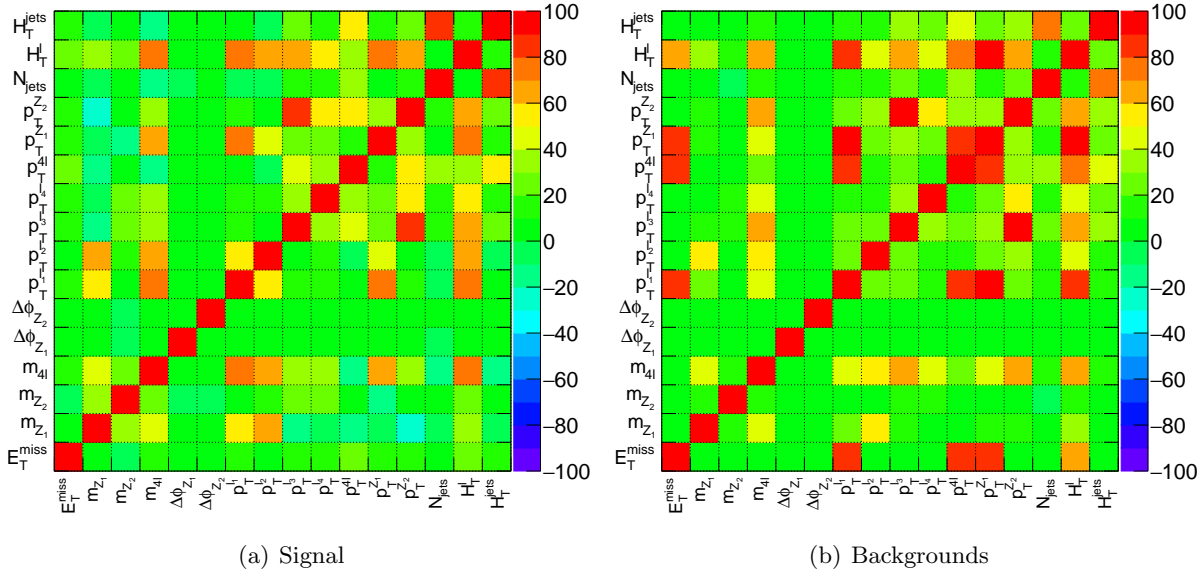


Figure 3. The correlation between input features for signal and background of the 2-SFOS category.

pair is the best in 2-SFOS. A comparison between BDT and other MVA methods is illustrated in Figure 4(a) for 2-SFOS. It shows that the Receiver operating characteristic (ROC) curve for the BDT is better. Figure 4(b) shows the ROC curve for the 0/1-SFOS and 2-SFOS categories.

Table 2. Input features used for the training and their ranking and separation power for 2-SFOS and 0/1-SFOS category. The higher the percentage value of the separation power, the better the ranking—the best-ranking start from 1 to the worst-ranked 16.

Input variable	Description	0/1-SFOS		2-SFOS	
		Rank	Separation	Rank	Separation
E_T^{miss}	Missing transverse energy	11	4.56%	2	37.82%
m_{Z_1}	Invariant mass of the first lepton pair	16	2.16%	1	52.44%
m_{Z_2}	Invariant mass of the second lepton pair	1	26.31%	4	30.88%
$m_{4\ell}$	Four-lepton invariant mass	4	6.10%	5	16.93%
$\Delta\phi_{Z_1}$	The azimuthal angle between the first lepton pair	2	11.52%	7	15.75%
$\Delta\phi_{Z_2}$	The azimuthal angle between the second lepton pair	6	5.73%	9	9.99%
$p_T^{\ell_1}$	p_T of the first lepton	3	7.35%	12	5.36%
$p_T^{\ell_2}$	p_T of the second lepton	8	5.16%	13	5.25%
$p_T^{\ell_3}$	p_T of the third lepton	13	3.82%	15	3.74%
$p_T^{\ell_4}$	p_T of fourth lepton	14	2.58%	10	6.17%
$p_T^{4\ell}$	p_T of the four-lepton system	7	5.49%	3	31.66%
$p_T^{Z_1}$	p_T of the first lepton pair	12	4.29%	16	3.02%
$p_T^{Z_2}$	p_T of the second lepton pair	15	2.29%	11	6.11%
N_{jets}	Number of the jets	10	4.61%	8	15.05%
H_T^{ℓ}	Scalar sum of the leptons p_T	5	5.95%	14	4.41%
H_T^{jets}	Scalar sum of the jets p_T	9	2.16%	6	16.92%

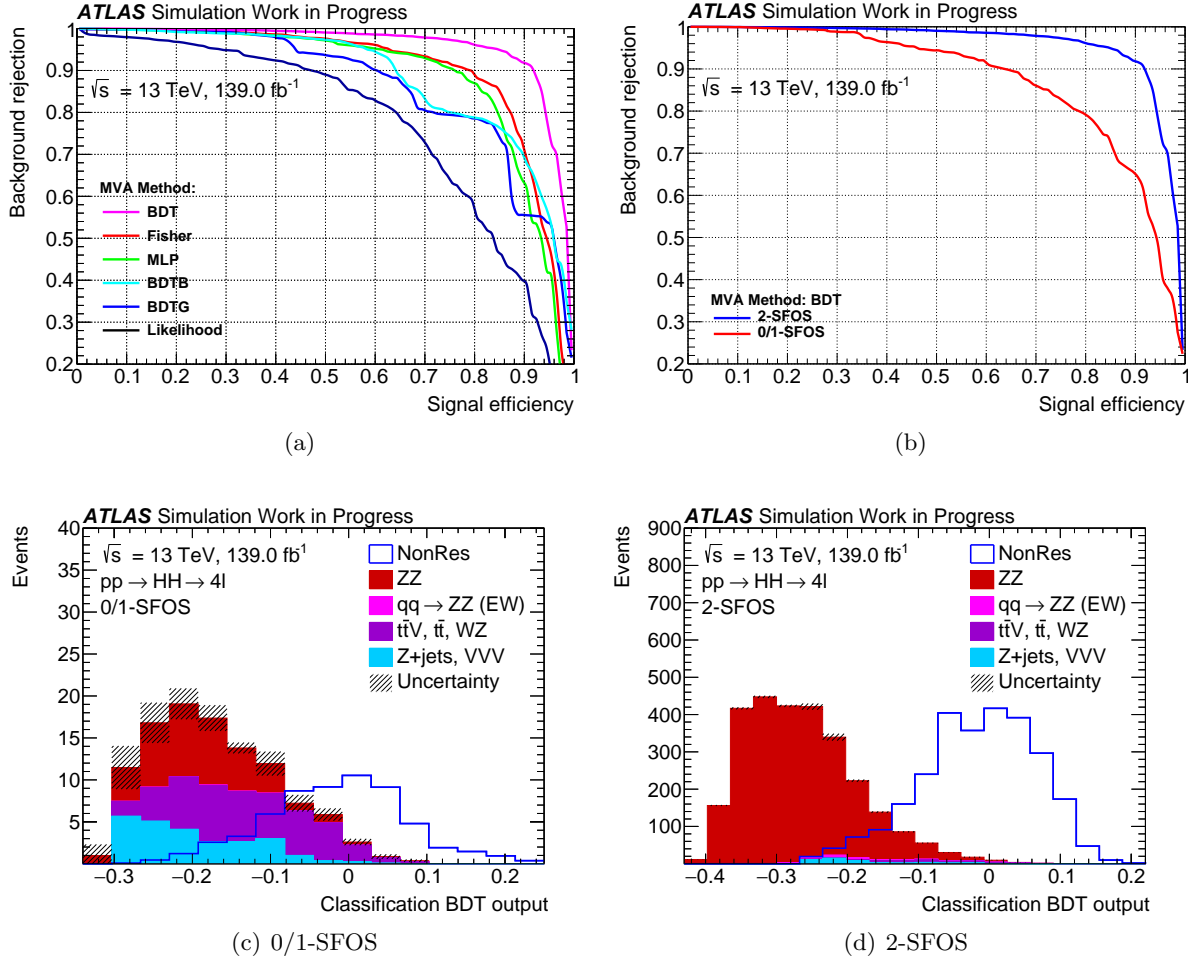


Figure 4. The BDT classification output of the signal and background captured after the training and the resulting weight application. The Receiver operating characteristic (ROC) curve showing the background rejection as a function of the signal efficiency for (a) different MVA algorithms and (b) the BDT for both 2-SFOS and 0/1-SFOS categories.

The area under the curve (AUC) is found to be 95.9% (87.4%) for 2-SFOS (0/1-SFOS). Finally, the classification of the BDT output is shown for 0/1-SFOS and 2-SFOS signal regions in Figures 4(c) and 4(d), respectively.

5. Systematic uncertainties

A global uncertainty of $\pm 1.7\%$ [15] on the total integrated luminosity of the data reported between 2015 and 2018 is considered. In addition, theoretical uncertainties on the signal's cross section are considered. For examples, $\pm 2.1\%$ uncertainty on the PDF and α_S , and $^{+2.2\%}_{-5.0\%}$ from the QCD scale. Other experimental systematic uncertainties are not included in the analysis, like the lepton energy scale and resolution, etc.

6. Statistics and results

Statistical analysis is performed using the profile-likelihood-ratio test statistic [17]. A simultaneous fit on the 0/1-SFOS and 2-SFOS signal regions using background only Asimov data is carried. Since the invariant mass of the 4-lepton is included during the training, the classification BDT output is utilised as a discriminant. A bin transformation method was used

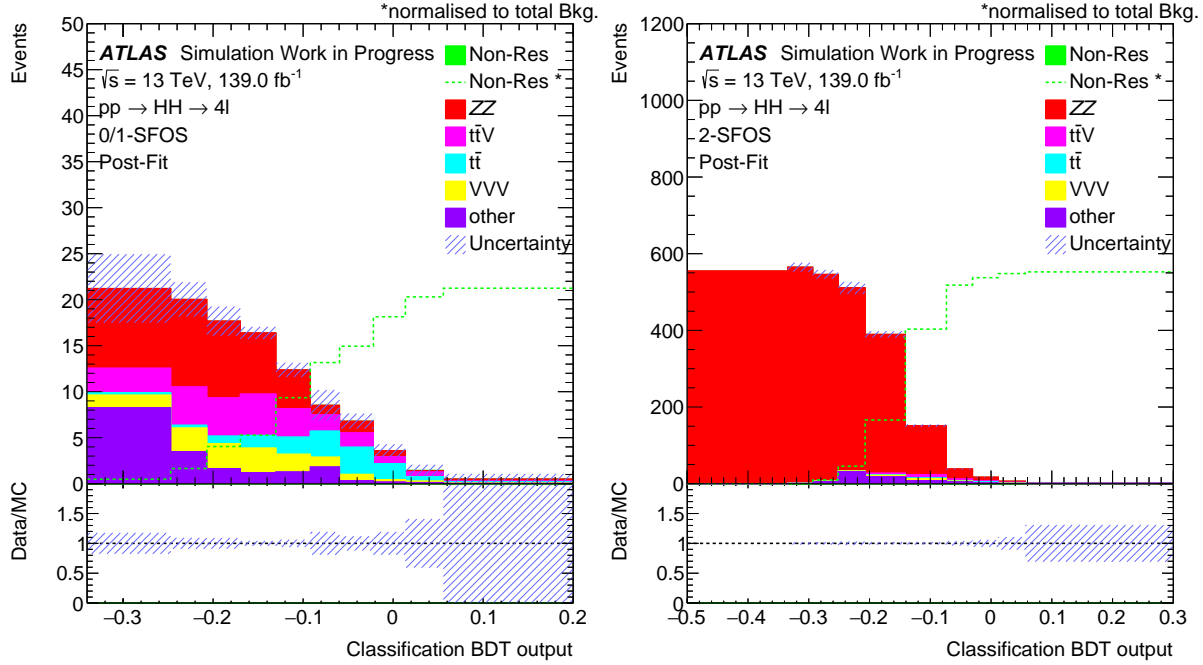


Figure 5. The classification BDT output fitted to background only Asimov data for 0/1-SFOS (left) and 2-SFOS (right) signal regions.

to avoid bins with low statistics. Figure 5 shows the post-fit result after the background only Asimov data fit. The $q\bar{q} \rightarrow ZZ$ and $g g \rightarrow ZZ$ backgrounds normalisation is set to free during the fit. The CL_s approach is used to set-up an upper limit on the cross-section times the branching ratio of the Higgs pair production. The upper limit is found to be as follows:

$$L_{-1\sigma, -2\sigma}^{+1\sigma, +2\sigma} = 49.22_{-13.75, -22.80}^{+35.4, +72.18}$$

7. Conclusion

A search for the non-resonant SM Higgs pair production via gluon fusion in the four-lepton channel is performed. The data used in the analysis is coming from MC simulation with an integrated luminosity equivalent to 139 fb^{-1} . The expected upper limit at 95% CL_s on cross-section times the non-resonant Higgs pair branching ratio is found to be 49.22 times the SM prediction.

Acknowledgments

Abdualazem Fadol acknowledges the funding support by the CAS-TWAS President's PhD Fellowship Programme.

References

- [1] ATLAS Collaboration 2012 *Phys. Lett. B* **716** 1-29 arXiv:1207.7214 [hep-ex]
- [2] CMS Collaboration 2012 *Phys. Lett. B* **716** 30-61 arXiv:1207.7235 [hep-ex]
- [3] ATLAS Collaboration 2015 *Eur. Phys. J. C* **75** no.10 476 arXiv:1506.05669 [hep-ex]
- [4] CMS Collaboration 2015 *Phys. Rev. D* **92** no.1 012004 arXiv:1411.3441 [hep-ex]
- [5] ATLAS Collaboration 2019 *JHEP* **05** 124 arXiv:1811.11028 [hep-ex]
- [6] Baur U, Plehn T and Rainwater D L 2002 *Phys. Rev. Lett.* **89** 151801-4 arXiv:0206024 [hep-ph]
- [7] von Buddenbrock S, Chakrabarty N, Cornell A S, Kar D, Kumar M, Mandal T, Mellado B, Mukhopadhyaya B, Reed R G and Ruan X 2016 *Eur. Phys. J. C* **76** no.10 580 arXiv:1606.01674 [hep-ph]

- [8] Alwall J, Herquet M, Maltoni F, Mattelaer O and Stelzer T 2011 *JHEP* **06** 128 arXiv:1106.0522 [hep-ph].
- [9] Sjöstrand T, Ask S, Christiansen J R, Corke R, Desai N, Ilten P, Mrenna S, Prestel S, Rasmussen C O and Skands P Z 2015 *Comput. Phys. Commun.* **191** 159–177 arXiv:1410.3012 [hep-ph]
- [10] Gleisberg T, Hoeche S, Krauss F, Schonherr M, Schumann S, Siegert F and Winter J 2009 *JHEP* **02** 007 arXiv:0811.4622 [hep-ph].
- [11] Ball R D *et al* 2015 *JHEP* **04** 040 arXiv:1410.8849 [hep-ph]
- [12] Alioli S, Nason P, Oleari C and Re E 2010 *JHEP* **06** 043 arXiv:1002.2581 [hep-ph]
- [13] Lange D J 2001 *Nucl. Instrum. Meth. A* **462** 152–155
- [14] ATLAS Collaboration 2017 *Eur. Phys. J. C* **77** no.5 317 arXiv:1611.09661 [hep-ex]
- [15] ATLAS Collaboration 2019 Luminosity determination in pp collisions at $\sqrt{s} = 13$ TeV using the ATLAS detector at the LHC *ATLAS-CONF-2019-021*
- [16] Hocker A, Speckmayer P, Stelzer J, Therhaag J, von Toerne E, Voss H, Backes M, Carli T, Cohen O and Christov A 2007 arXiv:physics/0703039 [physics.data-an]
- [17] Cowan G, Cranmer K, Gross E and Vitells O 2011 *Eur. Phys. J. C* **71** 1554 Erratum: 2013 *Eur. Phys. J. C* **73** 2501

Search for a heavier Higgs like boson and a dark force boson using ATLAS experimental data.

X.G Mapekula

University of Johannesburg, Johannesburg, Department of Mechanical Engineering, Corner Kingsway and University Road, Johannesburg, South Africa.

E-mail: xmapekul@cern.ch

Abstract. This paper presents the search for the Higgs boson, with mass 125 GeV, decaying to two new intermediate states and then into four lepton final states, $H \rightarrow Z_d Z_d \rightarrow 4l$. The analysis is conducted using the Run 2 data set from pp collisions collected with the ATLAS detector corresponding to a total integrated luminosity of 140fb^{-1} at a centre of mass energy of $\sqrt{s} = 13\text{TeV}$. A study on modifying the signal region has been conducted, assuming a broader width on the Z_d . It was found that the broader signal region has a minimal effect on the local p-value.

1 Introduction

Astronomers have made several observations in the cosmos which point to the existence of dark matter. These include observations of Einstein rings, which form as a result of gravitational lensing [1]. In addition, astronomers have observed discrepancies between the theoretical and observed radial velocities of spiral galaxies [2]. Both of these observations, among others, point to the existence of dark matter in the cosmos. However, the Standard Model (SM) is unable to explain the occurrence of dark matter [3]. The Higgs boson could be a portal into the dark sector that appears in many extensions of SM. The dark sector would provide candidates for the dark matter observed in the universe. The proposed search overlaps with a well studied SM process $H \rightarrow ZZ^* \rightarrow 4l$.

A dark sector would appear by adding a broken $U(1)_d$ gauge symmetry coupled to the SM through mixing with the hypercharge gauge boson via the kinetic mixing parameter. [4, 5]. The SM Higgs boson may mix with the dark sector Higgs boson if the introduction of a dark Higgs breaks the $U(1)_d$ gauge symmetry. The Higgs portal coupling parameter κ controls this mixing in this scenario. The lighter partner of the extended sector, which would also decay via the dark sector would be the observed Higgs, providing candidates for dark matter that account for both direct and indirect astronomical observations [6].

The published Run 2 results of the search for the Higgs boson decaying to four leptons via two Z_d bosons using pp data at $\sqrt{s} = 13\text{ TeV}$ with an integrated luminosity of 36.1 fb^{-1} collected at the ATLAS experiment [7] are presented in this paper [8]. In this search, we consider the Z_d bosons that decays to muon and electron same flavor pairs, where the final states include $4e$, $2e2\mu$, and 4μ . We emphasise the adjustment made to a previous event selection cut in the signal region which yielded a slight excess of 13 observed events for a background of 7.7 ± 0.1 in the 2015+6+7 iteration of the analysis.

Section 2 gives a brief description of the ATLAS detector together with a description of the triggers, pre-selection, event selection criteria and Monte Carlo simulation of the signal and background used in the analysis. Section 3 describes contributions of various processes to the background together with systematics uncertainties. Section 4 describes the results of the analysis while Section 5 presents the conclusion of the paper.

2 Experimental Setup

The ATLAS detector is a general purpose physics detector that has a cylindrical geometry which is symmetric and covers almost 4π solid angle.

The events must contain one primary vertex [9] where the transverse momentum of two or more track must be $p_T > 400$ MeV. Tracks that have too much noise in the calorimeter are rejected according to a cleaning criteria. In addition, the events have to adhere to the event selection criteria outlined in Table 1 where m_{12} and m_{34} are the leading and sub-leading dilepton pair masses, respectively.

Table 1: Summary of the event selection [8].

Object	$H \rightarrow Z_d Z_d \rightarrow 4\ell$
QUADRUPLET SELECTION	<ul style="list-style-type: none"> -Require at least one quadruplet of leptons consisting of two pairs of same-flavor opposite-charge leptons - Three leading-p_T leptons satisfy $p_T > 20$ GeV, 15 GeV, 10 GeV. - At least three muons are required to be reconstructed by combining ID and MS tracks in the 4μ channel. - Leptons in the quadruplet responsible for firing at least one trigger - $\Delta R(\ell, \ell') > 0.10$ (0.20) for all same (different) flavor leptons in the quadruplet
QUADRUPLET RANKING	-Select quadruplet with smallest $\Delta m_{\ell\ell} = m_{12} - m_{34} $
EVENT SELECTION	<ul style="list-style-type: none"> -Reject event if: <ul style="list-style-type: none"> $(m_{J/\Psi} - 0.25 \text{ GeV}) < m_{12,34,14,23} < (m_{\Psi(2S)} + 0.30 \text{ GeV})$ $(m_{\Upsilon(1S)} - 0.70 \text{ GeV}) < m_{12,34,14,23} < (m_{\Upsilon(3S)} + 0.75 \text{ GeV})$ - $m_{34}/m_{12} > 0.85$ - $115 \text{ GeV} < m_{4\ell} < 130 \text{ GeV}$ - $10 \text{ GeV} < m_{12,34} < 64 \text{ GeV}$ - $5 \text{ GeV} < m_{14,32} < 75 \text{ GeV}$ for $4e$ and 4μ channels

Simulated event samples generated using Monte Carlo are used to estimate the SM background and model the signal process which are then passed through a simulation of the ATLAS detector which uses GEANT4 [10, 11]

2.1 Signal

The Hidden Abelian Higgs Model (HAHM) is used to generate the $H \rightarrow Z_d Z_d \rightarrow 4\ell$ signal process [12] in MADGRAPH5 [13] interfaced with PYTHIA8 [14] to model the parton shower, hadronisation and underlying event. The mass of the Z_d is varied between 15 GeV and 60 GeV for different signal hypotheses in steps of 5 GeV for the process $H \rightarrow Z_d Z_d \rightarrow 4\ell$. The production mode under consideration for the Higgs is gluon-gluon-Fusion (ggF) where the mass of the Higgs is set to $m_H = 125$ GeV. The next-to-next-to-next-to-leading-order (N3LO) cross-section of the samples is normalized to $\sigma_{SM}(ggF) = 48.58$ pb as recommended in [15].

2.2 Backgrounds

- $H \rightarrow ZZ^* \rightarrow 4\ell$: Higgs that are produced through ggF [16] are simulated using POWHEG-BOX v2 MC event generator [17] while vector boson fusion (VBF) [18] and vector boson (VH) [19] processes are simulated using the PDF4LHC NLO PDF set [20]. For Higgs production through heavy quark pair annihilation, MADGRAPH5_AMC@NLO [21] is used to simulate the events while CT10nlo PDF set [22] for $t\bar{t}H$ and the NNPDF23 PDF set [23] for $b\bar{b}H$. PYTHIA8 [24] is used to model the ggF, VBF, VH , and $b\bar{b}H$ production mechanisms for the $H \rightarrow ZZ^* \rightarrow 4\ell$ decay process and the AZNLO parameter set for modelling parton showering, hadronisation and multiple parton interactions. HERWIG++ [25] and the UEEE5 parameter set [26] are used to model $t\bar{t}H$ showering.
- $ZZ^* \rightarrow 4\ell$: SHERPA 2.2.2 was used to model the non-resonant SM $ZZ^* \rightarrow 4\ell$ processes for quark anti-quark annihilation [27–29], using the NNPDF3.0 NNLO PDF set. GG2VV interfaced with PYTHIA8 was used to model the loop induced gg initiated ZZ^* production. Double counting was avoided by omitting the s-channel H diagrams using the CT10 PDFs. The latter process, which received large QCD corrections at NLO, was it was calculated at LO. Therefore, the sample was multiplied by an NLO/LO K-factor of 1.70 ± 0.15 [30]. This background contributes approximately 30% of the total background prediction.
- VVV/VBS are modeled using SHERPA 2.1 with the CT10 PDFs. These processes have cross-sections proportional to α^6 at leading order (LO) which include triboson production and vector boson scattering. This leads to four lepton final states that include two additional particles (electrons and muons or quarks). Some duplicates in this background are avoided by subtracting Higgs production through VBF from the estimates obtained with this generator. This background accounts for approximately 17% of the total prediction for the background of the high and low mass selections respectively.
- $Z + (t\bar{t}/J/\psi/\Upsilon) \rightarrow 4\ell$: The Z boson produced via a quarkonium state ($b\bar{b}$ or $c\bar{c}$) that decays to four leptons are simulated using PYTHIA8 with the NNPDF 2.3 PDFs while $t\bar{t}H$ background was generated with POWHEG-BOX interfaced to PYTHIA6 [31] for parton shower and hadronisation and underlying event.
- **Other Background** Jets can be misidentified as leptons which are produced by $Z + \text{jets}$ $t\bar{t}$ and WZ that decay to less than four prompt leptons but include jets. $Z + \text{jets}$ processes are modeled using SHERPA 2.2, while the production of $t\bar{t}$ is generated with POWHEG-BOX interfaced to PYTHIA6 [31] for parton shower and hadronisation. In addition, POWHEG-BOX interfaced to PYTHIA8 and the CTEQ6L1 is used to model the WZ production.

3 Analysis procedure

3.1 Original signal region cut

The previous MSR cut was defined in [8], used the narrow width mentioned in the HAHM model. This kinetic mixing parameter ϵ and the vector boson width are related with a scaling $\Gamma_{Z_d} \sim \epsilon$, where the point (Γ_{Z_d}, ϵ) corresponds to the mass $m_{Z_d} = 20$ GeV. In order to have maximal kinetic mixing, the kinetic mixing parameter $\epsilon = 0.03$ which corresponds to prompt decay of the dark vector boson having masses in the range $10 \text{ GeV} < m_{Z_d} < 50 \text{ GeV}$. This then gives the broadest expectation of the vector boson width to be $\Gamma_{Z_d} < 0.025 \text{ MeV}$. Since this width is too narrow for the detector to observe, the observed width would be the detector resolution. Figure

1 shows a scatter plot for the Run 2 [32] data taking where the previous signal region cut was used.

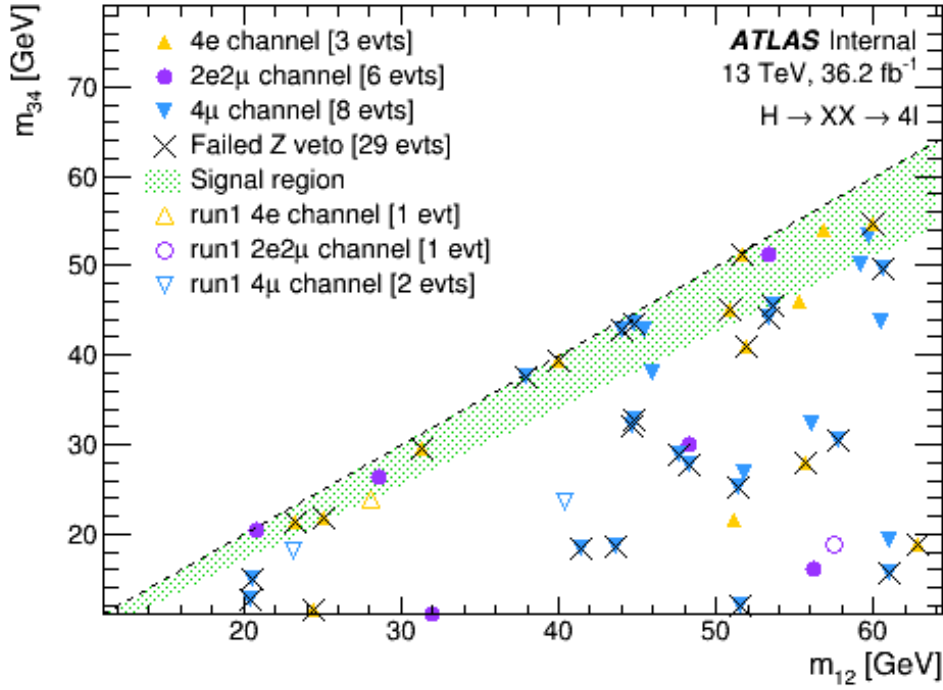


Figure 1: Scatter plot of the m_{12} vs m_{34} plane in the HM search. The shaded region represents events that are admitted in the previous MSR. The crossed out events indicated those that failed the Z boson veto cut. The 2015-6 in the previous MSR ($m_{34}/m_{12} > 0.85$) were internally unblinded [8].

The detector's lepton energy resolutions over the region of interest are given by $\Delta E_e \sim 3.5\%$ and $\Delta E_\mu \sim 3.8\%$. A 2σ window would then correspond to 13 GeV(14%) for electrons and 10 GeV(11.2%) for muons. Therefore, the m_{34}/m_{12} wedge cut listed in Table 1 corresponds to 15% for both electrons and muons when reconstructing dilepton masses. This cut seems to be optimal in the context of broadening the MSR.

3.2 Broadening the signal region cut

We observed in the previous iteration of the analysis [33] that the expected background in the MSR had few events for low Z_d masses. We therefore tested the sensitivity of the signal strength parameter μ_d to different width values of the MSR for various Z_d masses. We found that the local significance has a weak dependence on the MSR width for low masses m_{Z_d} . However, dependence grew stronger for values where $m_{Z_d} > 35$ GeV which indicates that we can modulate the MSR according to the background shape such that the cut could be 3.5σ at 10 GeV and decrease as the background increases so that it reverts to the previous MSR cut of 2.0σ where the background is most prominent, giving rise to a new MSR cut [8] expressed by Equation 1

$$m_{34} > 0.85m_{12} - 0.1125 \times f(m_{12}) \times m_{12} \quad (1)$$

where $f(m_{12})$ is the modulating function constructed using the parametrically fitted background shape. This new cut is represented by the new MSR shape shown in Figure 2

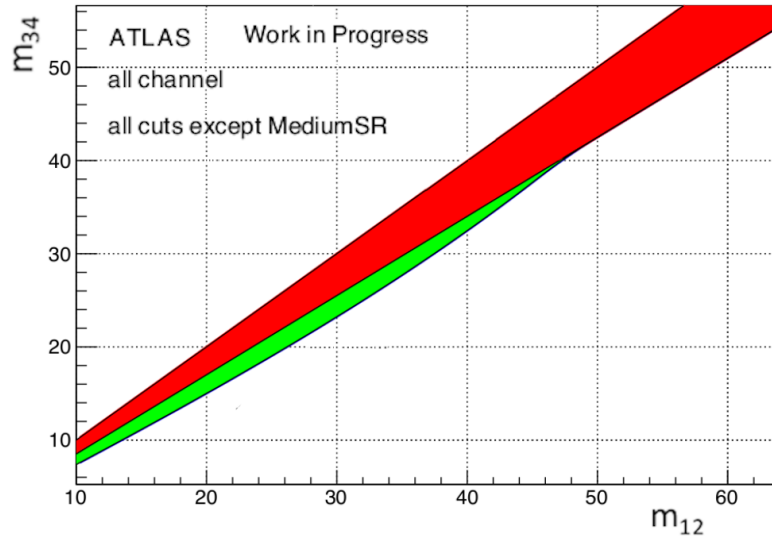


Figure 2: The new signal region is shown by green region while the old signal region is shown by the red region.

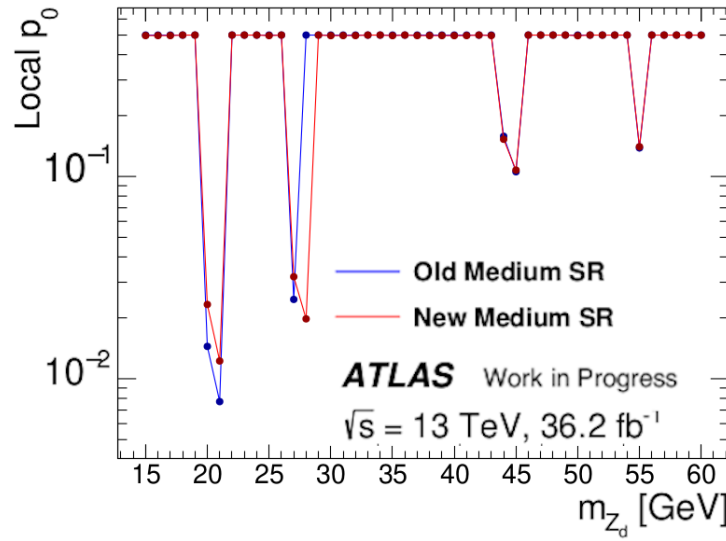


Figure 3: The old (blue) and the new (red) local p_0 value over the high-mass m_{Z_d} range.

4 Results

We tested the new signal region's impact on discovery by calculating the local p_0 value over the high-mass m_{Z_d} range with 2015-6 signal and data distributions in the i) new signal region and ii) old signal region. Figure 3 shows the p-values for the old signal region (blue) and the new signal region (red). The local p-value increases at around 20 GeV due to an increase in background events. The discrepancy between the new and old p-value at 28 GeV is due to convergence failure in the asymptotic calculator when calculating the p-value for the old signal region. Therefore, it is evident that the impact of the new signal region on the local p-value is minimal. However, for new data in the forthcoming analysis, the new MSR cut should enhance the p_0 sensitivity.

5 Conclusion

We presented a dedicated search for the exotic decays of the SM Higgs boson of mass 125 GeV decaying to two dark vector bosons which decay to two leptons each in this proceedings article. Particular emphasis was placed on re-optimizing the MSR. A modulated MSR shape was constructed with a 3.5σ width at 10 GeV, where the background has vanishingly few events and decreases to the original 2.0σ width at 49.64 GeV where there is much background present. It was subsequently found that the new MSR has a minimal effect on the local p-value for the present dataset. This new re-optimized signal region will be unblinded in order to quantify the amount of signal yield that is observed as a result of it and its effect on the statistical limits on various parameters of interest. It is expected that the new MSR will accommodate more signal after unblinding and thus have a more pronounced effect on the local p-value.

References

- [1] Massey R, Kitching T and Richard J 2010 The dark matter of gravitational lensing (*Preprint* 1001.1739) URL <https://iopscience-iop-org.ezproxy.cern.ch/article/10.1088/0034-4885/73/8/086901/pdf>
- [2] Zwicky F 1933 *Helv. Phys. Acta* **6** 110–127
- [3] Shears T 2012 *Trans. R. Soc. A* **370** 805–817 URL http://nobelprize.org/nobel_prizes/physics/laure
- [4] Curtin D, Essig R, Gori S and Shelton J 2015 *J. High Energy Phys.* **2015** 1–45 ISSN 10298479 (*Preprint* 1412.0018)
- [5] Curtin D, Essig R, Gori S, Jaiswal P, Katz A, Liu T, Liu Z, McKeen D, Shelton J, Strassler M, Surujon Z, Tweedie B and Zhong Y M 2014 *Phys. Rev. D - Part. Fields, Gravit. Cosmol.* **90** ISSN 15502368 (*Preprint* 1312.4992) URL <http://exotichiggs.physics>
- [6] Clowe D *et al.* 2006 *Astrophys. J.* **648** L109–L113 (*Preprint* astro-ph/0608407)
- [7] 2005 *Phys. Rev. Lett.* **95** ISSN 00319007 URL <https://cds.cern.ch/record/391176/files/cer-0317330.pdf>
- [8] Aad G *et al.* (ATLAS) 2021 (*Preprint* 2110.13673)
- [9] ATLAS Collaboration 2015 Vertex Reconstruction Performance of the ATLAS Detector at $\sqrt{s} = 13$ TeV ATL-PHYS-PUB-2015-026 URL <https://cds.cern.ch/record/2037717>
- [10] ATLAS Collaboration 2010 *Eur. Phys. J. C* **70** 823 (*Preprint* 1005.4568)
- [11] S Agostinelli *et al.*, (GEANT4 Collaboration) 2003 *Nucl. Instrum. Meth. A* **506** 250–303
- [12] Gopalakrishna S, Jung S and Wells J D 2008 *Phys. Rev. D* **78** 055002 (*Preprint* 0801.3456)
- [13] Alwall J, Herquet M, Maltoni F, Mattelaer O and Stelzer T 2011 *JHEP* **06** 128 (*Preprint* 1106.0522)
- [14] Sjöstrand T, Mrenna S and Skands P Z 2008 *Comput. Phys. Commun.* **178** 852–867 (*Preprint* 0710.3820)
- [15] Andersen J R *et al.* (LHC Higgs Cross Section Working Group) 2013 Handbook of LHC Higgs Cross Sections: 3. Higgs Properties (*Preprint* 1307.1347)
- [16] Hamilton K, Nason P, Re E and Zanderighi G 2013 *JHEP* **10** 222 (*Preprint* 1309.0017)
- [17] Nason P 2004 *JHEP* **11** 040 (*Preprint* hep-ph/0409146)
- [18] Nason P and Oleari C 2010 *JHEP* **02** 037 (*Preprint* 0911.5299)
- [19] Luisoni G, Nason P, Oleari C and Tramontano F 2013 *JHEP* **10** 083 (*Preprint* 1306.2542)
- [20] Butterworth J *et al.* 2016 *J. Phys. G* **43** 023001 (*Preprint* 1510.03865)
- [21] Alwall J, Frederix R, Frixione S, Hirschi V, Maltoni F, Mattelaer O, Shao H S, Stelzer T, Torrielli P and Zaro M 2014 *JHEP* **07** 079 (*Preprint* 1405.0301)
- [22] Lai H L, Guzzi M, Huston J, Li Z, Nadolsky P M, Pumplin J and Yuan C P 2010 *Phys. Rev. D* **82** 074024 (*Preprint* 1007.2241)
- [23] RD Ball *et al.*, (NNPDF Collaboration) 2013 *Nucl. Phys. B* **867** 244–289
- [24] Sjöstrand T, Mrenna S and Skands P Z 2008 *Comput. Phys. Commun.* **178** 852–867 (*Preprint* 0710.3820)
- [25] Bahr M *et al.* 2008 *Eur. Phys. J. C* **58** 639–707 (*Preprint* 0803.0883)
- [26] Seymour M H and Siodmok A 2013 *JHEP* **10** 113 (*Preprint* 1307.5015)
- [27] Gleisberg T *et al.* 2009 *JHEP* **02** 007 (*Preprint* 0811.4622)
- [28] Gleisberg T and Hoeche S 2008 *JHEP* **12** 039 (*Preprint* 0808.3674)
- [29] Cascioli F, Maierhofer P and Pozzorini S 2012 *Phys. Rev. Lett.* **108** 111601 (*Preprint* 1111.5206)
- [30] Caola F, Melnikov K, Rötsch R and Tancredi L 2015 *Phys. Rev. D* **92** 094028 (*Preprint* 1509.06734)
- [31] Sjöstrand T, Mrenna S and Skands P Z 2006 *JHEP* **05** 026 (*Preprint* hep-ph/0603175)
- [32] The ATLAS Collaboration 2018 *J. High Energy Phys.* **2018** ISSN 10298479 (*Preprint* 1802.03388) URL <https://arxiv.org/pdf/1802.03388.pdf>
- [33] The ATLAS Collaboration 2018 *J. High Energy Phys.* **2018** 20186 **2018** 1–51 ISSN 1029-8479 URL <https://link.springer.com/article/10.1007%2FJHEP06%282018%29166>

Activity Concentration Measurement of Naturally-Occurring Radionuclides in Various Vegetation plots in Rustenburg, South Africa

P O Olagbaju^{1*}, O B Wojuola¹ and M V Tshivhase²

¹ Department of Physics, North-West University, Mafikeng Campus, Mmabatho, South Africa

² Centre for Applied Radiation Science and Technology, North-West University, Mafikeng Campus, Mmabatho, South Africa

E-mail: olagbajupetero@gmail.com

Abstract. Globally, radiation level varies from one region to another due to the differences in the geological and mineralogical composition, and on the industrial and agricultural activities in each region. The aim of this study is to assess soil radioactivity level in different vegetational plots in Rustenburg which is associated with mining, industrial and agricultural practices in the North-West province of South Africa. In this study, the activity concentration of naturally-occurring radionuclides in beetroots (BRS), leeks (LKS), mints (MTS), onion (ONS), parsley (PSS) and wheat (WTS) plots were measured using broad-energy germanium (BEGe) detector, and correlation matrix was used to study the relationship between the radiological level in all the vegetation plots studied. The mean activity concentration of (^{238}U , ^{232}Th , and ^{40}K) was observed to be (25.15 ± 1.14 Bq/kg, 21.04 ± 9.49 Bq/kg and 90.20 ± 3.76 Bq/kg), (11.48 ± 0.68 Bq/kg, 6.77 ± 0.18 Bq/kg and 51.30 ± 4.96 Bq/kg), (23.63 ± 1.35 Bq/kg, 15.45 ± 0.28 Bq/kg and 105.10 ± 7.74 Bq/kg), (11.29 ± 0.76 Bq/kg, 8.08 ± 0.19 Bq/kg and 45.26 ± 13.78 Bq/kg), (23.08 ± 1.50 Bq/kg, 19.52 ± 0.30 Bq/kg and 99.69 ± 6.19 Bq/kg) and (11.78 ± 0.75 Bq/kg, 8.32 ± 0.38 Bq/kg and 89.25 ± 11.86 Bq/kg) for soil collected in BRS, LKS, MTS, ONS, PSS and WTS plots respectively. These were observed to be lower than the world average values of 30 Bq/kg, 35 Bq/kg and 400 Bq/kg reported by United Nation Scientific Committee on the Effects of Atomic Radiation [1], for ^{238}U , ^{232}Th and ^{40}K respectively. Radium equivalent activity, which is the weighted sum of the activity concentration of ^{238}U , ^{232}Th , and ^{40}K in measured soil samples, was found to be below the world's average value of 370 Bq/Kg, which show that the study area is safe for living and agriculture purposes. Weak correlation of radium equivalent activities was observed only in beetroot-wheat and leeks-parsley. This suggests different influence of plant types on soil radionuclides and thus affect their choice for phytoremediation purpose.

1. Introduction

Humans are continuously exposed to ionizing radiation from natural and anthropogenic sources. Naturally-occurring radionuclides originate from rock and mineral weathering as a result of volcanic eruption, erosion [1]. They contribute about 96% of the total radiation exposure to humans [1, 2]. Anthropogenic activities such as mining, industrial, and agricultural practices have been reported to enhance the concentration of naturally-occurring radionuclides in the soil. Their migration into non-contaminated areas via erosion, atmospheric deposition, penetration into environmental media pose significant radiological risk to human health [3].

Soil serves as a direct source of radionuclides, leading to the contamination of agricultural products, which represent an ingestion pathway of radionuclides to man [4, 5]. Soil radioactivity varies from one region to another depending on the geological and anthropogenic condition of each region, and is also influenced by the parent rock and its formation process [6, 7]. Since soil serves as indicator to environmental radiological contamination, the knowledge of soil radioactivity level is essential in environmental monitoring and protection, as it can be used to predict changes in environmental radioactivity caused by human activities [1].

South Africa, which has one of the most diverse and comprehensive crop farming systems, is long associated with mining and industrial activities resulting in radioactive waste littered in farmlands and communities [8]. Mine tailings and industrial wastes are major source of contamination in the environment, and their accumulation in soil, air, water, and agricultural products via the atmospheric deposition, groundwater sources and surface water body, represent a direct and indirect exposure pathway for incorporating into the human food chain. Therefore, this study aims to measure the activity concentrations of natural radionuclides (^{238}U , ^{232}Th , and ^{40}K) in different vegetational plots, and to investigate the relationship between various plots and soil radioactivity.

2. Materials and Methods

2.1. Sample collection, preparation, and measurement

Soil samples were randomly collected from seven vegetational plots. At each sampling point, four soil samples were collected with a hand trowel, mixed to form a homogenous composite sample. Soil samples were collected at a depth of about 20 cm to avoid the effect of plant cycling of radionuclides. They were transferred to the laboratory in well-labelled polythene bags, where they were processed for measurement, as described by [9, 10]. Collected soil samples were air-dried to remove moisture contents, crushed into fine powered using an electric grinder, and sieved using a 2 mm mesh screen to obtain a fine-grained homogenous soil sample. The fine-grained homogeneous sample was packed and sealed into well-labelled airtight containers to prevent the escape of ^{220}Rn and ^{222}Rn . The sealed soil samples were stored for about four weeks to allow secular radioactive equilibrium between thorium, radium and short-lived decay products before measurement at the Centre for Applied Radiation Science and Technology (CARST), North-West University South Africa [4].

Activity concentration of naturally-occurring radionuclides in soil was measured using broad-energy germanium detector (BEGe), with relative efficiency of 60%, a resolution of 2.0 keV for 1332 keV gamma-ray emission of ^{60}Co and necessary efficiency and energy calibration. Each sample was counted for 43,200 seconds, for the determination of the activity concentrations of ^{238}U using the 295.2 keV (19.7%) and 351.9 keV (38.9%) gamma-rays from ^{214}Pb and the 609.3 keV (43.3%), 1120.3 keV (15.7%) and 1764.5 keV (15.1%) gamma-rays from ^{214}Bi , and activity concentration of ^{232}Th using 238.6 keV (44.6%) from ^{212}Pb and 338.3 keV (11.4%), 911.6 keV (27.7%) and 969.1 keV (16.6%) gamma ray of ^{228}Ac , while the activity concentration of ^{40}K was determined using its 1460 keV gamma-line [11]. The activity concentrations $C(\text{Bq/kg})$ of the radionuclides were calculated using equation (1), as given by [10, 11]:

$$C(\text{Bq/kg}) = KC_n \quad (1)$$

where C_n is the count rate under the corresponding peak, $K = \frac{1}{\epsilon \rho_\gamma M_s}$ is the efficiency of the detector at specific gamma-ray energy, ρ_γ is the absolute transition probability of the specific gamma-ray, M_s is the sample mass. The minimum detectable activity of ^{40}K was 0.0189 Bq, while ^{238}U and ^{232}Th gamma energy line were not detected in the background spectrum.

2.2. Radiation indices measurements

Absorbed dose rate (ABDR) in air at 1 m from terrestrial sources of gamma radiation is estimated using the measured activity concentration of ^{238}U , ^{232}Th and ^{40}K by applying concentration-to-dose conversion factors of 0.462, 0.604 and 0.0417 respectively [1]

$$ABDR (nGy/hr) = 0.462C_U + 0.604C_{Th} + 0.0417C_K \quad (2)$$

Annual effective dose equivalent was estimated using the conversion coefficient of 0.70 Sv/Gy from absorbed dose in air to effective dose received by adults and 0.2 as the outdoor occupancy factor and 8760 hr [11]

$$AEDE (mSv/yr) = ABDR (nGy/hr) \times 8760 \times 0.2 \times 0.70 \times 10^{-6} \quad (3)$$

The annual gonadal equivalent dose (AGED) equivalent due to specific activities of ^{238}U , ^{232}Th , and ^{40}K was estimated using the formula given by [12]

$$AGED (\mu\text{Sv/yr}) = 309C_U + 4.18C_{Th} + 0.314C_K \quad (4)$$

Excess lifetime cancer risk (ELCR), used to estimate the probability of developing cancer over a lifetime at a given exposure level [12] is calculated using:

$$ELCR = AEDE (mSv/yr) \times D_L(yr) \times RF(Sv^{-1}) \times 10^{-3} \quad (5)$$

where, AEDE is the annual effective dose equivalent, D_L is the average duration of life (estimated to be 70 years), RF is the Risk Factor (Sv^{-1}) which is given as 0.05 for stochastic by ICRP [13].

External hazard index is used to quantify the effect of radon, a progeny of radium, and its short-lived products to the respiratory organs. It is estimated using equation 6, and must be less than unity for the radiation hazard to be negligible [12].

$$H_{ex} = \frac{C_{Ra}}{370} + \frac{C_{Th}}{259} + \frac{C_K}{4810} \quad (6)$$

3. Results and Discussion

The activity concentration of naturally-occurring radionuclides in sampled plots, which include beetroot plot (BRS), leek plot (LKS), mint plot (MTS), onion plot (ONS), parsley plot (PSS) and wheat plot (WHTS) are presented in table 1. The results obtained for activity concentration of naturally-occurring radionuclides in all the measured plots were observed to be lower than the world average recommended values of 30 Bq/kg, 35 Bq/kg and 400 Bq/kg for ^{238}U , ^{232}Th and ^{40}K , respectively [1]. The prevailing activity concentration of potassium in all sample soils can be attributed to its abundance in nature, agricultural practices that involve the use of organic and inorganic fertilizer containing potassium [14]. The high concentration of ^{238}U to ^{232}Th is attributed to the presence of uranium-bearing minerals associated with mining regions, which is predominant in the study area [15]. The variation observed in the activity concentration of each radionuclide is attributed to differences in radionuclides solubility and mobility [16].

The relationship between radium equivalent activity, which is used to express the weighted sum of ^{226}Ra (^{238}U), ^{232}Th , and ^{40}K , was investigated for the sampled plots using Pearson correlation. From table 2, a weak positive correlation can be observed between radium equivalent activity in beetroot-wheat, and leeks-parsley. Pearson correlation of radium equivalent activity among other vegetational plots show poor correlation coefficients. This observation suggests the varying influence of plant types on soil radionuclides, affecting choice of plant for phytoremediation purpose.

Table 1: Activity concentration of naturally-occurring radionuclides of soil in the selected area.

Sample code	Parameters	^{238}U (Bq/kg)	^{232}Th (Bq/kg)	^{40}K (Bq/kg)	Ra_{eq} (Bq/kg)
BRS	Maximum	29.56±1.19	23.23±0.33	112.70±4.69	69.46
	Minimum	20.71±1.25	19.10±0.31	52.48±3.76	55.72
	Average	25.15±1.14	21.04±9.49	90.20±5.94	62.18±3.95
LKS	Maximum	14.75±0.67	8.154±0.20	68.08±3.30	30.55
	Minimum	8.87±0.63	5.37±0.22	34.52±3.43	21.04
	Average	11.48±0.68	6.77±0.18	51.30±4.96	24.92±3.36
MTS	Maximum	30.99±1.44	20.94±0.34	149.10±4.98	66.93
	Minimum	12.75±0.24	12.35±0.24	57.98±6.38	45.09
	Average	23.63±1.35	15.45±0.28	105.10±7.74	53.81±6.50
ONS	Maximum	18.35±0.97	10.53±0.21	97.03±4.61	35.95
	Minimum	6.06±0.59	6.79±0.17	45.26±13.78	22.64
	Average	11.29±0.76	8.08±0.19	70.42±10.06	28.26±4.78
CMR	Maximum	25.35±1.31	18.38±0.28	133.50±2.60	50.79
	Minimum	10.78±0.69	10.16±0.22	26.48±4.46	32.66
	Average	16.14±0.85	13.68±0.25	70.52±6.56	41.13±5.45
PSS	Maximum	26.79±0.89	21.87±0.31	134.40±5.82	64.09
	Minimum	17.91±5.14	13.84±0.25	58.46±4.96	52.53
	Average	23.08±1.50	19.52±0.30	99.69±6.19	58.67±3.45
WHTS	Maximum	18.78±0.85	10.02±0.71	128.90±3.33	43.04
	Minimum	7.13±0.59	7.08±0.18	62.79±10.40	23.26
	Average	11.78±0.75	8.32±0.38	89.25±11.86	30.55±6.16
UNSCEAR [1]		35	30	400	370

Table 2: Correlation coefficient of radium equivalent in vegetational plots.

	BRTS	LKS	MTS	PSS	ONS	WHTS
BRTS	1.00					
LKS	-0.47	1.00				
MTS	-0.81	0.15	1.00			
PSS	-0.35	0.58	0.28	1.00		
ONS	-0.43	0.23	-0.10	-0.07	1.00	
WHTS	0.66	-0.54	-0.57	-0.07	0.02	1.00

3.1. Radiological hazards

The average absorbed dose rates estimated from the activity concentration of ^{238}U , ^{232}Th and ^{40}K , for beetroot, leeks, mints, onion, parsley and the uncultivated plot is 28.11 nGy/hr, 11.46 nGy/hr, 24.66 nGy/hr, 13.05 nGy/hr, 18.68 nGy/hr, 26.64 nGy/hr and 14.22 nGy/hr respectively. Absorbed dose rate obtained for all vegetational plots is found to be lower than the world's average value of 60 nGy/hr recommended by United Nations Scientific Committee on the Effect of Atomic Radiation [1]. Table 3 shows the average annual effective dose equivalent (AEDE), excess lifetime cancer risk (ELCR), annual gonadal dose equivalent (AGDE) and external hazard due to gamma ray emission from naturally-occurring radionuclide from all investigated plots. Similarly, they are observed to be below the world average value of 1 mSv/yr, 2.90×10^{-4} , 300 $\mu\text{Sv/yr}$ and unity, for annual effective dose equivalent, excess lifetime cancer risk, annual gonadal dose equivalent and external hazard index respectively, indicating that the study area is safe for living and agricultural purposes.

Table 3: Average radiological dose and hazard indices of soil in various vegetational plots.

Plots	ABDR (nGy/hr)	AEDE (mSv/yr)	ELCR	Hex	AGED ($\mu\text{Sv/yr}$)
BRS	28.11	0.03	1.21×10^{-4}	0.17	122.78
LKS	11.46	0.01	4.91×10^{-5}	0.07	67.87
MTS	24.66	0.03	1.06×10^{-4}	0.15	122.74
ONS	13.05	0.02	5.59×10^{-5}	0.08	73.71
CMR	18.68	0.02	8.01×10^{-5}	0.11	88.75
PSS	26.64	0.03	1.14×10^{-4}	0.16	119.34
WHTS	14.22	0.02	6.08×10^{-5}	0.08	81.15
UNSCEAR [1]	60.00	1.00	2.90×10^{-4}	1.0	300.00

4. Conclusion

Agricultural practices play an essential role in environmental radioactivity level, posing a significant exposure scenario to farmers and human food chains. The radiological impact of agrochemicals in soil was estimated using soil radioactivity measured in different vegetational plots in Rustenburg, South Africa. In all sampled soil, the activity concentration of naturally-occurring radionuclides was observed to increase in order of $^{40}\text{K} > ^{238}\text{U} > ^{232}\text{Th}$. The prevailing activity concentration of potassium in all sampled soil is attributed to its abundance in nature, agricultural practices that involve the use of organic and inorganic fertilizer containing potassium. Observed high concentration of ^{238}U to ^{232}Th is a result of the presence of uranium-bearing minerals associated with mining regions. The overall variation observed in the concentration of measured radionuclides is attributed to differences in their solubility and mobility [17].

However, radiological parameters such as absorbed dose rate, annual effective dose equivalent, excess lifetime cancer risk, external hazard index, estimated are found to be below recommended level. Thus, the study indicates the study area is safe for living and agricultural purposes. Notwithstanding, regular monitoring of soil radioactivity is recommended due to the presence of mines in the farming vicinity and the use of various agrochemicals, which contribute significantly to soil radioactivity.

References

- [1] UNSCEAR. Sources and effects of ionizing radiation. Journal of Radiological Protection. 2000;21(1):83.
- [2] Akpan AE, Ebong ED, Ekwok SE, Eyo JO. Assessment of radionuclide distribution and associated radiological hazards for soils and beach sediments of Akwa Ibom Coastline, southern Nigeria. Arabian Journal of Geosciences. 2020;13(15):1-12.
- [3] Andersson KG. Migration of radionuclides on outdoor surfaces. Radioactivity in the Environment. 2009;15:107-46.
- [4] IAEA-TECDOC-566. The Use of Gamma Ray Data to Define the Natural Radiation Environment. International Atomic Energy Agency Vienna; 1990.
- [5] Ilori AO, Chetty N. Soil-to-crop transfer of natural radionuclides in farm soil of South Africa. Environmental Monitoring and Assessment. 2020;192(12):1-13.
- [6] Gad A, Saleh A, Khalifa M. Assessment of natural radionuclides and related occupational risk in agricultural soil, southeastern Nile Delta, Egypt. Arabian Journal of Geosciences. 2019;12(6):1-15.
- [7] Guidotti L, Carini F, Rossi R, Gatti M, Cenci RM, Beone GM. Gamma-spectrometric measurement of radioactivity in agricultural soils of the Lombardia region, northern Italy. Journal of environmental radioactivity. 2015;142:36-44.
- [8] Kamunda C, Mathuthu M, Madhuku M. An assessment of radiological hazards from gold mine tailings in the province of Gauteng in South Africa. International Journal of environmental research and public health. 2016;13(1):138.
- [9] Ogundele LT, Oluwajana OA, Oguntimehin AC, Inuyomi SO. Heavy metals, radionuclides activity and mineralogy of soil samples from an artisanal gold mining site in Ile-Ife, Nigeria: implications on human and environmental health. Environmental Earth Sciences. 2021;80(5):1-15.
- [10] Olagbaju P, Okeyode I, Alatishe O, Bada B. Background radiation level measurement using hand held dosimeter and gamma spectrometry in Ijebu-Ife, Ogun State Nigeria. International Journal of Radiation Research. 2021;19(3):591-8.
- [11] Ibikunle SB, Arogunjo AM, Ajayi OS. Characterization of radiation dose and soil-to-plant transfer factor of natural radionuclides in some cities from South-Western Nigeria and its effect on man. Scientific African. 2019;3:e00062.
- [12] Avwiri G, Osimobi J, Agbalagba E. Natural Occurring Radionuclide Variation with a Soil Depth Profile of Udi and Ezeagu Local Government Areas of Enugu State, Nigeria. Facta Universitatis-Series: Working and Living Environmental Protection. 2013;10(1):53-60.
- [13] Taskin H, Karavus M, Ay P, Topuzoglu A, Hidiroglu S, Karahan G. Radionuclide Concentrations in Soil and Lifetime Cancer Risk due to Gamma Radioactivity in Kirklareli, Turkey. Journal of Environmental Radioactivity. 2009;100(1):49-53.
- [14] Ahmed NK, El-Arabi AGM. Natural radioactivity in farm soil and phosphate fertilizer and its environmental implications in Qena governorate, Upper Egypt. Journal of Environmental Radioactivity. 2005;84(1):51-64.
- [15] Ugbede FO, Osahon OD, Akpolile AF. Natural radioactivity levels of ^{238}U , ^{232}Th and ^{40}K and radiological risk assessment in paddy soil of Ezillo rice fields in Ebonyi State, Nigeria. Environmental Forensics. 2021:1-16.
- [16] Absar N, Abedin J, Rahman MM, Miah M, Hossain M, Siddique N, et al. Radionuclides Transfer from Soil to Tea Leaves and Estimation of Committed Effective Dose to the Bangladesh Populace. Life. 2021;11(4):282.
- [17] Kritsanawanit R, Sahoo S, Arae H, Fukushima M. Distribution of ^{238}U and ^{232}Th in selected soil and plant samples as well as soil to plant transfer factors around Southern Thailand. Journal of Radioanalytical and Nuclear Chemistry. 2015;303(3):2571-7.

Investigation of the relation between limit of detection and solid angle by measuring standard radioactive sources with a LaBr₃:Ce detector

F van Niekerk^{1,3}, S R Johnson² and P Jones³

¹Department of Physics, University of Stellenbosch, South Africa

²Department of Physics, University of Cape Town, South Africa

³Department of Subatomic Physics, iThemba LABS, Somerset West, South Africa

fvaniekerk@tlabs.ac.za

Abstract. A 2''×2'' LaBr₃:Ce detector was used to measure ambient background radiation, as well as the radiation of two standard sources with different activities, ²²Na and ⁶⁰Co. The sources have been measured at increasing distances from the detector to investigate the relation between a point-source solid angle and the detection limit of each radiation source. Results obtained during the study indicated a relation between source activity and the solid angle to such an extent that a detection limit can be extrapolated for sources with different activities, also considering background radiation. It was further shown that the solid angle is source independent.

1. Introduction

Over several years gamma-ray spectrometry has been limited to the use of NaI:Tl and Ge-based detectors. More recent development introduced the LaBr₃:Ce detector as an alternative detection device for several reasons. These include a more than two-fold better peak resolution compared to NaI:Tl detectors [7], a high light yield with > 65000 photons/MeV [5], and good detection efficiency [1]. No liquid nitrogen cooling is required, and the device lends itself as very practical in terms of ex-situ measurements due to its light weight and mobility [4]. Radiation is present everywhere in the natural environment due to naturally occurring radioactive materials (NORM) in the Earth's crust as well as in the atmosphere. Sources of this radiation are the ²³⁸U and ²³²Th decay series, and radioactive ⁴⁰K [2]. This results in background radiation that must be corrected for during experimental radiation measurements, data interpretation and the calculation of actual source activities and detection limits, especially when measurements are done in terrestrial environments. This work forms part of a broader scope of research where the LaBr₃:Ce detector will be utilised as a mobile unit to investigate in-situ radiation in various environmental regions. The relation between source activity and the solid angle relative to the detector surface is important during the determination of radiation detection limits.

2. Experimental

Radiation measurements related to this study were performed inside a vault (at iThemba LABS, Cape Town) constructed with building materials such as concrete. The vault is designed and shielded from

the outside environment as such that the radiation present will be from the building material of the vault itself. No significant variation in background radiation is expected. It is important to note that the detector position inside the vault is fixed which further emphasise no expected change in background radiation. Radiation sources and background measurements were done using a LaBr₃:Ce detector with a 2"×2" crystal. The detector was energy calibrated using three standard sources with known gamma-ray energies: ²²Na, ⁶⁰Co and ¹⁵²Eu. One background measurement inside the vault was performed for 10 minutes. Two standard sources, ²²Na and ⁶⁰Co, were measured at various distances from the detector. These distances were correlated with a solid angle value (Ω) where $\Omega = A/r^2$. The symbol A represents the detector surface area, and r represents the point-source distance between the detector and radiation source being measured [3]. Each source was measured for 10 minutes.

3. Results and discussion

Data obtained during the measurements of each source at various distance from the detector are summarised in table 1.

Table 1. Data for ²²Na and ⁶⁰Co: Total = total peak counts, Peak = background corrected counts.

r (mm)	Ω (Sr)	Total	Peak	Background	Total	Peak	Background
		511 keV ²² Na			1274 keV ²² Na		
228	0,038989 (0,20)	543386 (737)	501400 (708)	41986 (205)	128100 (358)	120757 (348)	7353 (86)
545	0,006824 (0,083)	114367 (338)	107107 (327)	7260 (85)	26430 (163)	23132 (152)	3297 (57)
2275	0,000392 (0,020)	12530 (112)	5875 (77)	6635 (81)	2491 (50)	1009 (32)	1482 (38)
2675	0,000283 (0,017)	9566 (98)	4341 (66)	5228 (72)	1796 (42)	665 (26)	1131 (34)
4330	0,000108 (0,010)	5828 (76)	1906 (44)	3922 (63)			
r (mm)	Ω (Sr)	1173 keV ⁶⁰ Co			1333 keV ⁶⁰ Co		
175	0,066182 (0,25)	32017 (179)	24779 (157)	7238 (85)	25926 (161)	22098 (149)	3828 (62)
560	0,006463 (0,080)	6021 (78)	2897 (54)	3124 (56)	3783 (62)	2103 (46)	1680 (41)
775	0,000337 (0,018)	3304 (57)	1302 (36)	2002 (45)	2234 (47)	1014 (32)	1220 (35)

For each peak the number of counts appear as a Gaussian distribution around the centroid of the peak. Measurement of the peak area was be done by a summation of the number of counts in each channel considered to be part of the peak, referred to as the region of interest (ROI). For background correction, channels were selected at both the lower and higher energy sides of each peak, just outside the ROI. The sum of the background counts in both regions were divided by the number of channels which gave an indication of the mean number of background counts for each channel. The sum of the counts for all channels in the ROI was determined, followed by the subtraction of the mean number of background counts in the same region. The result of this is a background corrected net peak area. Except for NORM's, also contributing to background counts is the Compton continuum associated with each radiation source. This continuum intensity is directly proportional to source activity, and the solid angle. Using the ⁶⁰Co source as example, this is illustrated in figure 1.

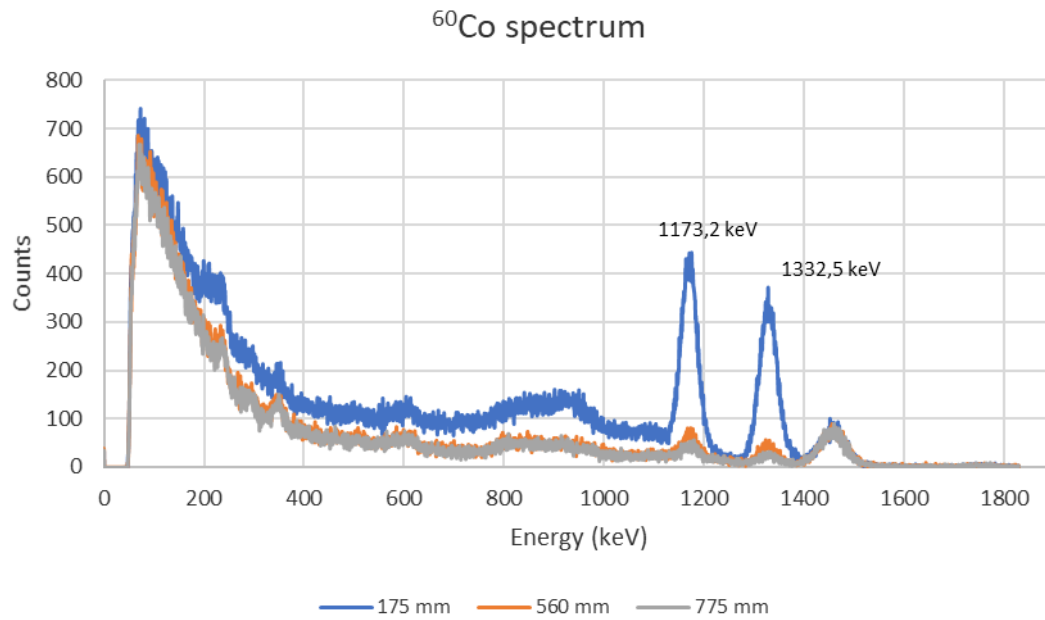


Figure 1. ^{60}Co spectrum with the source measured at increasing distances from the detector.

The results summarised in table 1 were used to determine a first order response between source activity and the solid angle. It can be assumed that the number of counts measured is directly proportional to the source activity, and the solid angle (distance between point-source and detector surface) as a first order function: Total counts = $b(\Omega) + c$. These correlations are summarised in table 2. The plots are shown in figure 2.

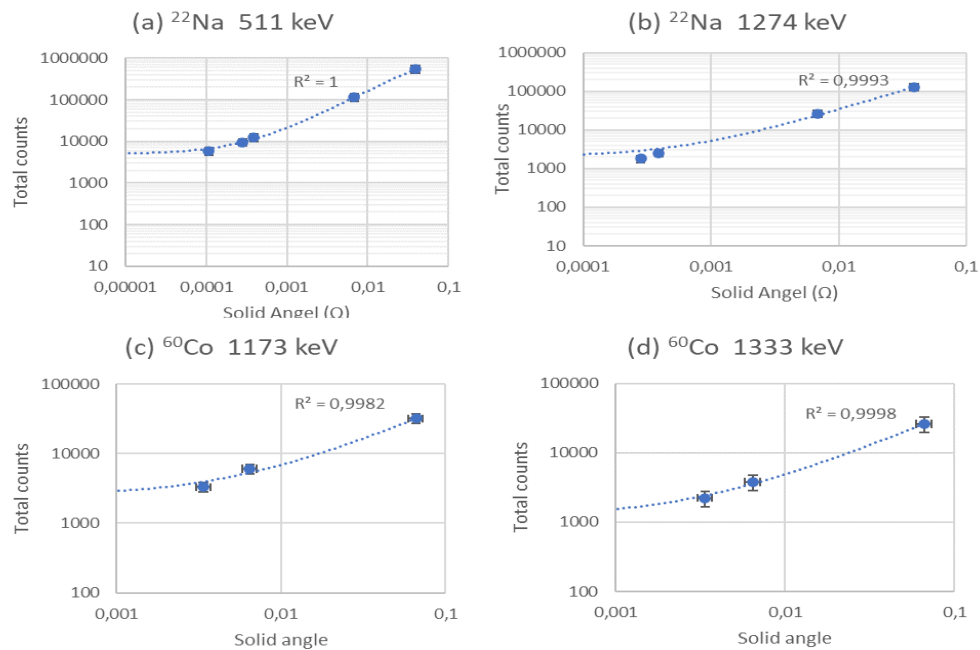


Figure 2. Plots for ^{22}Na 511 keV (a), 1274 keV (b) and ^{60}Co 1173 keV (c), 1333 keV (d).

Table 2. Response curves for ^{22}Na and ^{60}Co .

Source/Energy	Activity (kBq)	C (Slope error)	b	R
^{22}Na 511 keV	375.2	1.376×10^7 (59505)	8915	1
^{22}Na 1274 keV	375.2	3.244×10^6 (225080)	2001	0.9993
^{60}Co 1173 keV	47.48	1.118×10^6 (656)	2445	0.9982
^{60}Co 1333 keV	47.48	9.359×10^5 (9410)	1162	0.9998

The regression value (R) confirms the linear proportionality between the number of counts and the solid angle. Using these equations, it is possible to calculate the number of peak counts at any selected source activity. This should give an indication in terms of counts detected as a function of solid angle and source activity. The results are summarised in table 3.

Table 3. Calculated peak counts for different solid angles and activities.

511 keV		Ω			
Activity (kBq)	0,0389895	0,0068238	0,0003916	0,0002832	0,0001081
376	545583 (739)	102840 (321)	14305 (120)	12814 (113)	10403 (102)
300	437107 (661)	83855 (290)	13216 (115)	12026 (110)	10102 (101)
200	294377 (543)	58875 (243)	11782 (109)	10989 (105)	9706 (99)
100	151646 (389)	33895 (184)	10349 (102)	9952 (100)	9311 (96)
50	80280 (283)	21405 (146)	9632 (98)	9433 (97)	9113 (95)
10	23188 (152)	11413 (107)	9058 (95)	9019 (95)	8955 (95)
5	16052 (127)	10164 (101)	8987 (95)	8967 (95)	8935 (95)
0	8915 (94)	8915 (94)	8915 (94)	8915 (94)	8915 (94)
1274 keV		Ω			
Activity (kBq)	0,0389895	0,0068238	0,0003916	0,0002832	0,0001081
376	128548 (359)	24149 (155)	3272 (57)	2920 (54)	2352 (48)
300	102969 (321)	19672 (140)	3015 (55)	2735 (52)	2281 (48)
200	69313 (263)	13782 (117)	2677 (52)	2490 (50)	2188 (47)
100	35657 (189)	7891 (89)	2339 (48)	2246 (47)	2094 (46)
50	18829 (137)	4946 (70)	2170 (47)	2123 (46)	2048 (45)
10	5367 (73)	2590 (51)	2035 (45)	2025 (45)	2010 (45)
5	3684 (61)	2296 (48)	2018 (45)	2013 (45)	2006 (45)
0	2001 (45)	2001 (45)	2001 (45)	2001 (45)	2001 (45)

1173 keV Activity (kBq)	Ω			1333 keV Activity (kBq)	Ω		
	0,066182	0,0064631	0,0033745		0,066182	0,0064631	0,0033745
47	9785 (99)	3162 (56)	2819 (53)	47	7304 (85)	1762 (42)	1475 (38)
40	8692 (93)	3055 (55)	2764 (53)	40	6389 (80)	1672 (41)	1429 (38)
30	7130 (84)	2903 (54)	2684 (52)	30	5082 (71)	1545 (39)	1362 (37)
20	5568 (75)	2750 (52)	2604 (51)	20	3776 (61)	1417 (38)	1295 (36)
10	4007 (63)	2598 (51)	2525 (50)	10	2469 (50)	1290 (36)	1229 (35)
5	3226 (57)	2521 (50)	2485 (50)	5	1815 (43)	1226 (35)	1195 (35)
0	2447 (49)	2445 (49)	2445 (49)	0	1163 (34)	1162 (34)	1162 (34)

From this data a limit of detection can be estimated for each line: For ^{22}Na 511 keV at roughly 10000 counts and for ^{22}Na 1274 keV at roughly 3000 counts. At these values, counts from the source become indistinguishable from background counts. These values correlate well with the intercept values obtained for each line as summarised in table 3. By scaling these b-coefficients for 511 keV and 1274 keV on the same plot, a limit of detection at each solid angle can be extrapolated, as shown in figure 3.

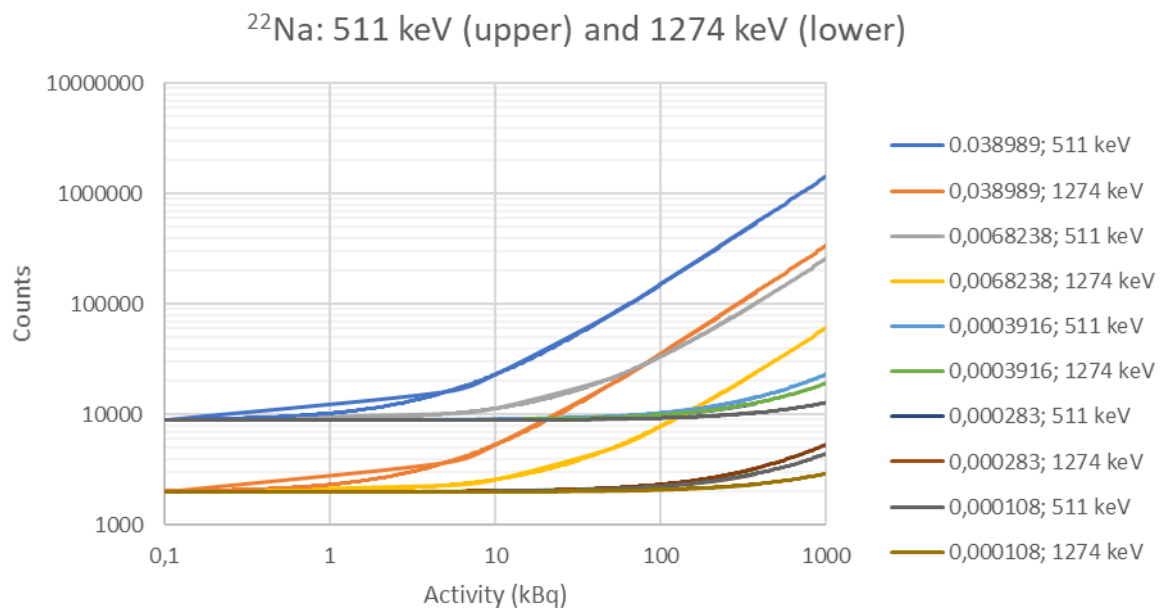


Figure 3. Scaled plots for ^{22}Na at 511 keV and 1274 keV

In the same way, limits of detection can be estimated for ^{60}Co 1173 keV at roughly 2000 counts and for ^{60}Co 1333 keV at roughly 3000 counts. This allows for the calculation of a detection limit in terms of activity at a specific solid angle. Results obtained are summarised in table 4.

Table 4. Limit of detection expressed as activity at specific solid angles.

Distance (mm)	Solid angle (Ω)	511 keV	1274 keV
		LD Activity (kBq)	LD Activity (kBq)
228	0,03899	0.761 (0,87)	0.761 (0,87)
545	0,006824	4.35 (2.1)	4.35 (2.1)
2275	0,0003916	75.7 (8.7)	75.7 (8.7)
2675	0,0002832	104.7 (10.2)	104.7 (10.2)
4330	0,0001081	274.3 (16.6)	274.3 (16.6)
mm	Ω	1173 keV	1333 keV
		LD Activity (kBq)	LD Activity (kBq)
175	0,06618	0,415 (0,64)	0,420 (0,65)
560	0,006463	4,25 (2,1)	4,30 (2,1)
775	0,003375	8,14 (2,85)	8,32 (2,9)

4. Conclusion

This investigation showed that the extrapolation of activity detection limits for different radiation sources - taking into consideration background counts, source activity and the distance between the detector and a point source (solid angle), and measurement time - is possible. When measurements are done in terrestrial environments it is most likely that the main source of radiation will be NORM's, hence the predominant source of background radiation. The intensity of this radiation is also regional-dependent as it will differ from one location to another. It is worthy to mention that the results obtained during this study is related to the specific experimental conditions such as the environment where the measurements were taken, the detector used, and counting time. Data obtained during terrestrial measurements will vary. For example, longer measurement times (compared to the 10 minutes during this study) might yield lower detection limits. This emphasises the importance of being able to estimate a limit of detection in terms of source activity, as well as optimising measurement time should there be some other source of radiation present, other than NORM's. By using two different radiation sources during this research, it is also evident that the activity limit of detection is source independent.

References

- [1] Drescher A, Yoho M, Landsberger S, Durbin M, Biegalski S, Meier D and Schwantes J 2017 Gamma-gamma coincidence performance of LaBr₃:Ce scintillation detectors vs HPGe detectors in high count-rate scenarios *Appl. Radiat. and Isot.*, **122** 116-120
- [2] James M E 2013 *Physics for radiation protection* 3rd ed. Wiley-VCH Verlag GmbH & Co. KGaA
- [3] Knol G F *Radiation detection and measurement* 3rd ed. John Wiley & Sons, Inc.
- [4] Ntalla E, Markopoulos A, Karfopoulos K, Potiriadis C, Clouvas A and Savidou A 2020 Development of a semi-empirical calibration method by using a LaBr₃(Ce) scintillation detector for NORM sample analysis *HNPS Adv. Nucl. Phys.* **27** 199-202
- [5] Quarati F G A, Owens A, Dorenbos P and De Haas J 2011 High energy gamma ray spectroscopy with LaBr₃ scintillation detectors *Nucl. Instrum. Methods Phys. Res.* **629** (1) 157-169
- [6] Rosson R, Lahr J and Khan B 2011 Radiation background in a LaBr₃(Ce) gamma-ray scintillation detector www.health-physics.com.
- [7] Zeng M, Zeng Z and Cang J 2014 A Prototype of LaBr₃:Ce in situ Gamma-Ray Spectrometer for Marine Environmental Monitoring *Technol. Instrumentation in Particle Phys.* June 2014

An estimation for the 4γ branching ratio of positronium using $\text{LaBr}_3\text{:Ce}$ scintillator detectors

S Johnson^{1,2}, T Leadbeater¹ and P Jones²

¹ Department of Physics, University of Cape Town, Private Bag X3, Rondebosch, 7701, South Africa

² Department of Subatomic Physics, iThemba LABS, PO Box 722, Somerset West, 7129, South Africa

E-mail: sjohnson@tlabs.ac.za

Abstract. An approximation for the branching ratio of the four-photon decay of parapositronium ($\text{BR}_{4\gamma}$) was measured using a multi-gamma-ray spectrometer. For the first time in such measurements, the spectrometer consisted of an array of eight identical $\text{LaBr}_3\text{:Ce}$ scintillator detectors, each of which combines good energy resolutions (5% and 10% at 511 keV for the signals from the eighth dynode and anode of the photomultiplier tube, respectively) with an excellent timing resolution (~ 300 ps). Through simplifying assumptions that neglected the background corrections and efficiency normalisations for each of the 2γ and 4γ decays, a first order approximation of $\text{BR}_{4\gamma}$ was determined as the ratio between measured 4γ events ($N_{4\gamma}$) and measured 2γ events ($N_{2\gamma}$), such that $\text{BR}_{4\gamma} \sim \frac{N_{4\gamma}}{N_{2\gamma}} = 4.8 (19) \times 10^{-7}$. This measured value of $\text{BR}_{4\gamma}$ differs from previous measurements and accepted literature values by a factor of 3.

1. Introduction and background

Positrons (e^+) are the positively-charged anti-particles of electrons (e^-). Due to the prevalence of electrons in matter, free positrons are often not observed to exist for prolonged periods of time (since they quickly undergo annihilation). Following emission from a decay, a positron travelling through a medium will undergo a series of collisions with bound electrons, causing it to thermalise. Once sufficiently thermalised, the positron will undergo either one of two processes: direct annihilation with an electron of opposing spin, or it will form an exotic atom known as positronium (Ps). Ps is a quasi-stable system consisting of an electron and a positron. After a finite period of time, the two particles annihilate to produce an even or odd number of gamma-rays (depending on the relative spin states of each particle, as well as the governing energy, momentum, and charge conservation laws). Similar to that of hydrogen, the ground state of Ps has two varieties: parapositronium (p-Ps), which is a singlet state with total spin $S = 0$, and orthopositronium (o-Ps), which is a triplet state with total spin $S = 1$. The Ps state can be considered non-relativistically as the product of an orbital wave function and a spin vector given as,

$$\Psi_{n,l,m}(\mathbf{r})|S, S_z\rangle. \quad (1)$$

The orbital wave function in Equation (1) is the wave function of the hydrogen atom (with the electron mass replaced by the reduced mass of the e^+e^- pair), where n , l , and m are the usual principle ($n \in \mathbb{Z} \leq 0$), orbital ($0 \leq l < n - 1$) and magnetic ($m \leq l$) quantum numbers,

respectively. The spin vectors are linear combinations of products of those of the individual particles, of which there are four possible:

$$\begin{aligned}
 |S = 1, S_z = 1\rangle &= |\uparrow\rangle|\uparrow\rangle \\
 |S = 1, S_z = 0\rangle &= \frac{1}{\sqrt{2}} (|\uparrow\rangle|\downarrow\rangle + |\downarrow\rangle|\uparrow\rangle) \\
 |S = 1, S_z = -1\rangle &= |\downarrow\rangle|\downarrow\rangle \\
 |S = 0, S_z = 0\rangle &= \frac{1}{\sqrt{2}} (|\uparrow\rangle|\downarrow\rangle - |\downarrow\rangle|\uparrow\rangle)
 \end{aligned} \tag{2}$$

The first three expressions describe the possible spin states of o-Ps (triplet), while the last expression describes the spin state of p-Ps (singlet). The selection rule that governs the e^+e^- annihilation [1, 2] is particularly important in understanding the decay modes of Ps. As a direct consequence from the selection rule and the energy, momentum, and charge conservation laws, it can be shown that p-Ps must decay into an even number of photons (two or more), while o-Ps must decay into an odd number (three or more). This is shown succinctly by Harpen [3].

The ultimate aim of this study is to demonstrate the measurement feasibility of the four photon branching ratio of p-Ps using an array of eight identical $2 \times 2''$ Lanthanum Bromine ($\text{LaBr}_3:\text{Ce}$) detectors. For these measurements, locally-produced ^{22}Na sources of various activities were used as positron emitters. It should be noted that ^{22}Na has a β^+ decay branching ratio of 90.3% [4], which makes it a suitable candidate for producing Ps.

2. Experimental set-up

2.1. Detector assembly

Measurements of the gamma radiation emitted from ^{22}Na radioactive sources of various activities were performed with the gamma-ray spectrometer. The gamma-ray spectrometer (see Figure 1) consisted of an array of eight $\text{LaBr}_3:\text{Ce}$ (5%) detectors (labelled as D1-D8), which were arranged in a planar geometry. These detectors were manufactured by Saint-Gobain, and each consists of a $2 \times 2''$ $\text{LaBr}_3:\text{Ce}$ scintillation crystal lattice which is attached to a Hamamatsu R2083 PMT. A ^{22}Na source was placed symmetrically at the centre of the detector array, such that it was equidistant at 12 cm from the face of each detector. The source was placed on a plastic stand, which ensured that it was situated in the same plane as the centre of each detector. Based on the cylindrical geometry of each detector, and the equidistant source-to-detector distance, the solid angle subtended between the source and each detector was determined to be 1.0838 (1)% of 4π steradians. Due to the symmetry of the set-up and isotropic nature of the source, the accumulative solid angle for the eight-detector system is 8.671 (3)% of 4π steradians.

2.2. Electronics and data acquisition system

As seen in Figure 1, the electronics (including the high voltage (HV) supply, the XIA Pixie-16 module and the CPU) were all housed in a crate and NIM bin. Each detector was powered by an HV power supply, and the detectors photomultiplier tube (PMT) anodes were integrated with a model 474 ORTEC pre-amplifier to provide the signals. The operating voltages for each detector were chosen such that the detectors were gain-matched, and the data was then re-binned post-acquisition through energy calibration. The signals generated at the anode (*fast signal*) and eighth dynode (*slow signal*) of the PMT were pre-amplified, and the resulting output signals were transmitted to the XIA Pixie-16 module using RG175/lemon connectors and RG58 cables, respectively. The XIA Pixie-16 module is a 16-channel digital signal processor which samples the waveform data at 500 MHz [5]. Each of the 16 channels of the Pixie-16 module can be operated independently for data acquisition. Each channel is gated using a Channel Gate Input which

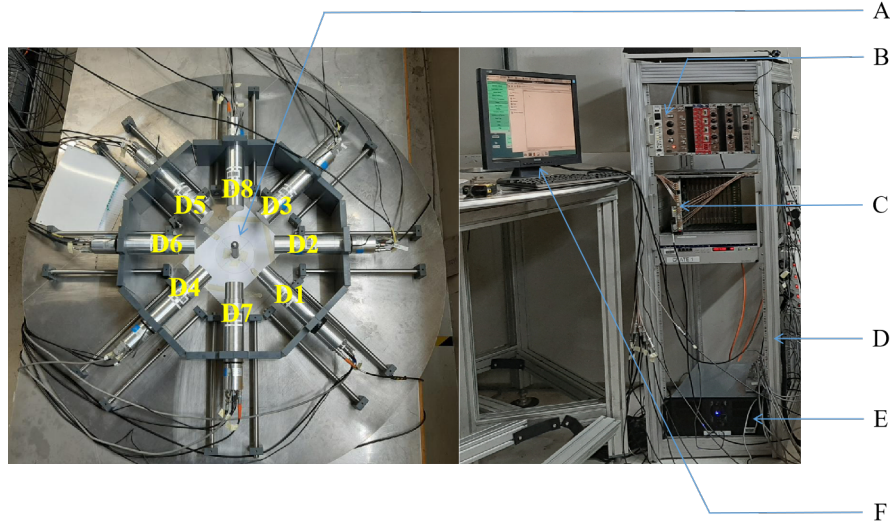


Figure 1. Eight LaBr₃:Ce detectors (D1-D8) are situated in a planar geometry. The associated electronics of the detector system are also shown. (A = ²²Na source, B = High voltage supply, C = Pixie-16, D = Crate and NIM bin, E = CPU and F = PC display).

ranges from 0-15. Each of the slow signals of detectors D1-D8 respectively, were connected to channels 0-7. Each of the fast signals of detectors D1-D8 respectively, were connected to channels 8-15. The digital signal processing (DSP) parameter settings for both the slow and fast signals were selected such that the measured energy resolutions were minimised to 5% and 10% at 511 keV for each detector, respectively. The software used for the data acquisition was the Multi Instance Data Acquisition System (or MIDAS) [6, 7]. MIDAS was able to access all of the recorded data from the hardware electronics through a single Peripheral Component Interconnect (PCI) bridge (PXI-8360). The data was recorded in list-mode and written to network storage for offline analyses. Each recorded event consisted of an event ID, timestamp (48-bit), CFD time (16-bit), and (calibrated) energy (16-bit) [5]. The measurement had an accumulative run time of 5.16×10^6 s, which is comparable to the run time of similar experiments performed by Yang *et al.* (2.02×10^7 s [1]) and Vetter & Freedman ($9.45 (1) \times 10^5$ s [8]). There were approximately 4.85×10^{11} total events (~ 12.5 TB of data) recorded at an average acquisition rate of 2.4 MB/s.

3. Data processing, analyses and results

3.1. Data reduction

Due to the large amount of data acquired during the measurement process, a filtering method was a necessary implementation. The object of the data reduction is to identify the events corresponding to both two and four photon decays, and separate each from the background events. The sorting code for the data defines the energy (E_c) and time (T_c) windows that were used to filter between various detected interactions. These windows act as logical filters which allow for the data to be categorised with specific energy and timing requirements. Specifically, the two filtering conditions that all potential Ps annihilation events must pass include:

- the sum energy of the detected photons in the event must sum to 1022 keV (so that events correspond to the real mass of the annihilating e^+e^- pair). The sum energy window E_c is set such that $|\sum_{i=1}^n E_i - 1022 \text{ keV}| < E_c = 80 \text{ keV}$.
- the detected photons must be detected in coincidence within a time window $T_c = 2 \text{ ns}$ i.e. the arrival times of each photon must occur within 2 ns of detection.

The width values for E_c and T_c for each detector in the detector array were selected such that the number of accepted 4γ events are maximised, while minimising background events from accidental interactions. These widths correspond to approximately 7σ of their respective peaks with a confidence level limit greater than 99%.

3.2. Multiplicity spectra

Figure 2 shows the multiplicity plots (T_c -gated and T_c - E_c -gated) that were generated through a data sorting code. The sorting code runs through each pair of detectors to determine whether the recorded events meet the timing and/or energy requirements defined by E_c and T_c . When sorting the data, the T_c -gated plot only applies the T_c filtering condition, while the T_c - E_c -gated plot applies both the T_c and E_c filtering conditions. A typical run through the sorting code to generate the multiplicity spectra is summarised below:

- The time difference between events in detectors j and $k \geq j + 1$ is determined such that the time difference peak is centred at some constant offset $t > 0$ (which is later set to 0 ns).
- If the time difference lies within the pre-defined time window T_c , a counter (denoted m_1) is incremented by 1. As the sorting code runs through each pair of detectors, m_1 will therefore be incremented by the number of detector pairs which have events measured in coincidence.
- The events in each detector j and k are checked for whether they correspond to the annihilation photon energy. If they lie within the energy window E_c , then a separate counter (denoted m_2) is incremented by 1. m_2 will be incremented by the number of detector pairs which have events corresponding to both the timing and energy requirements.
- After the sorting code has run through each pair of detectors, the values of m_1 and m_2 are binned separately, which generates two different multiplicity plots. The plot that bins m_1 values (T_c -gated plot) shows the multiplicity for coincident gamma-ray events, while the plot that bins m_2 (T_c - E_c -gated plot) shows the multiplicity for coincident events measured at the energy of the annihilation photon.
- This algorithm is repeated until all of the recorded data is processed.

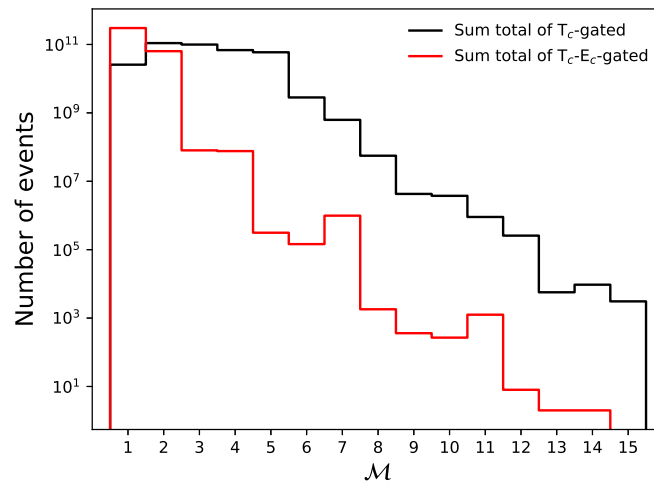


Figure 2. \mathcal{M} is shown for the contributions of both the T_c -gated (black), and T_c - E_c -gated (red) spectra. T_c -gated shows the filtered data using the time window $T_c = 2$ ns, while T_c - E_c -gated shows the filtered data using both the energy and time windows $E_c = 80$ keV and $T_c = 2$ ns.

Clearly the sorting code sorts measured events into detector pair multiplicities (which is denoted as \mathcal{M} in Figure 2). As such, the nature of this sorting allows for the use of the binomial formula,

$$\binom{n}{k=2} = \frac{n!}{k!(n-k)!} = \frac{n!}{2(n-2)!}, \quad (3)$$

where $k = 2$ because the code sorts the events into multiplicities of detector pairs. Equation (3) provides a relation between the number of detectors that detected an event to the bin number \mathcal{M} in which the event was placed. Hence, the case of $n = 2$ would correspond to the number of counts recorded between any two detectors, and is calculated as $\binom{2}{2} = 1$. This shows that a pair of detectors has a multiplicity of $\mathcal{M} = 1$, and so all 2γ events will be recorded in bin number 1 of the T_c - E_c -gated plot. Excluding accidental background interactions, the majority of these 2γ events ($\sim 60\%$ for most materials [9]) are resultant from direct annihilation, while the rest arise from the 2γ decay of Ps. For ease of reference, the counts corresponding to $\mathcal{M} = 1$ in the T_c - E_c -gated plot are denoted as $N_{2\gamma} = 3.02 (21) \times 10^{11}$. For the case of four detectors, $n = 4$, and so Equation (3) becomes $\binom{4}{2} = 6$. So the case of four detectors has a multiplicity of $\mathcal{M} = 6$, and hence, all possible 4γ events (the majority of which are from the 4γ decay of Ps) will be recorded in bin number 6 of the T_c - E_c -gated plot. For ease of reference, the counts corresponding to $\mathcal{M} = 6$ in the T_c - E_c -gated plot are denoted as $N_{4\gamma} = 1.45 (55) \times 10^5$. The values of $N_{2\gamma}$ and $N_{4\gamma}$ are used for the 4γ branching ratio calculation in the following section. The counts corresponding to other \mathcal{M} values are resultant from other detector multiplicities that are not of interest to this work. There are two types of uncertainties considered for the counts of the multiplicity spectra in Figure 2. These include the uncertainty from the coincident counting of event multiplicities (statistical), and the selection of window filter values for E_c and T_c (systematic). The statistical uncertainty was found to be several orders of magnitude smaller than the systematic uncertainty. It should also be mentioned that the relatively long measurement period of this work (~ 1433 hours) reduces the statistical noise of the measurement, and hence, the systematic uncertainty is the main contribution to the uncertainties shown in $N_{2\gamma}$ and $N_{4\gamma}$.

3.3. Calculations and discussion

Vetter & Freedman [8] determined the 4γ branching ratio of p-Ps (denoted $\text{BR}_{4\gamma}$) using,

$$\text{BR}_{4\gamma} = \frac{(N_{4\gamma} - B_{4\gamma})\epsilon_{2\gamma}}{N_{2\gamma}\epsilon_{4\gamma}}. \quad (4)$$

where $N_{n\gamma}$ represents the number of $n\gamma$ events observed, $B_{4\gamma}$ is the expected number of 4γ background events, and $\epsilon_{n\gamma}$ is the detection efficiency of the detector array for $n\gamma$ annihilations. Equation (4) is derived from the ratio between the number of detected 4γ events with the number of detected 2γ events (both normalised with their respective detection efficiencies). Lastly, the correction term $B_{4\gamma}$ accounts for the accidental detections of 4γ background events. In the previous section, the values for $N_{2\gamma}$ and $N_{4\gamma}$ were highlighted as key results from the T_c - E_c -gated plot of Figure 2. In order to complete the calculation of Equation (4), values for $B_{4\gamma}$, $\epsilon_{2\gamma}$ and $\epsilon_{4\gamma}$ must be estimated. From previous measurements of $\text{BR}_{4\gamma}$, Adachi *et al.* [10], Yang *et al.* [1], and Vetter & Freedman [8] evaluated these quantities (or similar) by performing Monte Carlo detector simulations for their respective experiments. Such simulations are beyond the scope of the current work, and is suggested as follow up. However, a suitable estimate for $\text{BR}_{4\gamma}$ can be obtained using this work's measured values for $N_{2\gamma}$ and $N_{4\gamma}$. At its most fundamental level, Equation (4) is the ratio between the number of detected 4γ events with the number of detected 2γ events. Neglecting the secondary considerations of 4γ background subtraction and efficiency normalisations, a suitable 'first order' approximation for $\text{BR}_{4\gamma}$ can be obtained as,

$$\text{BR}_{4\gamma} \sim \frac{N_{4\gamma}}{N_{2\gamma}} = 4.8 (19) \times 10^{-7}. \quad (5)$$

While this result is not a true measurement of $\text{BR}_{4\gamma}$, it does seem to be a fairly promising estimation. The accepted value for $\text{BR}_{4\gamma}$ is given by $\text{BR}_{4\gamma, \text{theory}} = 1.4388 (21) \times 10^{-6}$ [11], which is a factor of 3 larger than the estimate. From similar measurements of previous publications, Vetter & Freedman [8] found $\frac{N_{4\gamma}}{N_{2\gamma}} \sim 5 \times 10^{-9}$, while Adachi *et al.* [10] found $\frac{N_{4\gamma}}{N_{2\gamma}} \sim 5 \times 10^{-8}$. The discrepancies observed between these ratios are expected. The experimental set-up of this work and each of the aforementioned publications differ significantly (different detectors, detector geometries, and radioactive sources), which would suggest that the 2γ and 4γ detection efficiencies for each set-up would then also likely differ. Therefore, different measurements for $\frac{N_{4\gamma}}{N_{2\gamma}}$ will be found depending on the experimental set-up. As a consequence, there is no apparent method to quantify the quality of the $\text{BR}_{4\gamma}$ estimation from this work.

4. Summary and further work

The aim of this study was to demonstrate the measurement feasibility of the four photon branching ratio of p-Ps (denoted $\text{BR}_{4\gamma}$) using the experimental set-up described in Section 2. A complete calculation of $\text{BR}_{4\gamma}$ was not performed, since key factors from Equation (4) (specifically $B_{4\gamma}$, $\epsilon_{2\gamma}$ and $\epsilon_{4\gamma}$) were not evaluated. However, the key results of $N_{2\gamma}$ and $N_{4\gamma}$ were obtained through the generation of multiplicity spectra that allowed for the separation of the data into a binned distribution. The ratio between the values of $N_{4\gamma}$ and $N_{2\gamma}$ allowed for an order of magnitude to be estimated for $\text{BR}_{4\gamma}$ given by,

$$\text{BR}_{4\gamma} \sim 5 (2) \times 10^{-7}.$$

This estimation was compared to the accepted value, and was found to differ by a factor of 3. The most obvious limitation of this work is the lack of a final measurement result for $\text{BR}_{4\gamma}$. An improvement, therefore, would be to evaluate the factors $B_{4\gamma}$, $\epsilon_{2\gamma}$ and $\epsilon_{4\gamma}$ using Monte Carlo simulations for this work's experimental set-up. Factoring in these additional results using Equation (4) will allow for a complete calculation to be performed, and will provide a conclusive measurement of $\text{BR}_{4\gamma}$ (comparable to the literature values quoted).

References

- [1] Yang J, Chiba M, Hamatsu R, Hirose T, Matsumoto T and Yu J 1996 *Physical Review A* **54** 1952
- [2] Wolfenstein L and Ravenhall D G 1952 *Physical Review* **88** 279–282
- [3] Harpen M D 2003 *Medical Physics* **31** 57–61
- [4] Bé M M, Chisté V, Dulieu C, Mougeot X, Browne E, Chechev V, Kuzmenko N, Kondev F, Luca A, Galán M, Nichols A, Arinc A and Huang X 2010 *Table of Radionuclides (Monographie BIPM-5 vol 5)* (Pavillon de Breteuil, F-92310 Sèvres, France: Bureau International des Poids et Mesures) ISBN 92-822-2234-8
- [5] LLC X 2005 User's manual digital gamma finder (dgm) pixie-16 URL http://www.phys.utk.edu/expnuclear/LeRIBSS/Pixie16_UserManual1.0.6.pdf
- [6] Jones P 2013 ithemba labs annual report URL https://tllabs.ac.za/wp-content/uploads/pdf/annual_reports/Annual_Report_2013_small.pdf
- [7] Midas website URL <http://npg.dl.ac.uk/MIDAS/>
- [8] Vetter P A and Freedman S J 2002 *Physical Review A* **66** 052505
- [9] Castellaz P, Siegle A and Stoll H 2002 *Journal of Nuclear and Radiochemical Sciences* **3** R1–R7
- [10] Adachi S, Chiba M, Hirose T, Nagayama S, Nakamitsu Y, Sato T and Yamada T 1994 *Physical Review A* **49** 3201–3208
- [11] Vetter P A 2004 *Modern Physics Letters A* **19** 871–885

The possible use of Fibre Optic Sensors in Pressurized Water Reactors

B G Maqabuka¹, L Bedhesi², E Chinaka², S H Connell¹, G Daniels²,
P Naidoo¹, D Nicholls¹, F Pieterse¹, J Slabber³

¹University of Johannesburg, Johannesburg, Mechanical Engineering, South Africa.

²South African Nuclear Energy Corporation, Pelindaba, South Africa

³Department of Mechanical Engineering, Pretoria University, South Africa

E-mail: bmaqabuka@uj.ac.za

Abstract. Fibre Optic Sensors (FOS) are fibres with optionally a specific preparation or functional coating, which endows them sensitivity to various environmental parameters. The sensor is designed for extreme environments. Specifically, the environment of a nuclear reactor core, where the dose may be 2 GGy in two weeks of operation. The technologies considered are based on Fibre Bragg Gratings (FBGs), and also Long Period Gratings (LPGs). Using sense-region-gratings written into the fibre, one can measure length changes at the sensor with 1 pico-meter precision. There is growing interest in optical fibre based sensors for application in nuclear reactors because of their intrinsic attributes, such as package compactness, high bandwidth, multiplexing, ability to measure remotely in real time, and immunity to most electromagnetic perturbations. In-core, real-time, on-line and multi-parameter information gathering sensors throughout the nuclear power system could have the potential to improve efficiency and subsequently lower the overall cost of the nuclear power systems. In addition, the safety case would be greatly enhanced. FOS are presented as a remarkable new opportunity for sensing, especially in all kinds of extreme environments, and they represent a niche opportunity in the context of nuclear energy generally (PWR, BWR). In-core, on-line technology for sensing temperature, dose, water level and other parameters can enable instantaneous Reactor State knowledge enabling novel reactor operations and management. This paper discusses the current state of our experimental and theoretical programme.

1. Introduction

There is growing interest in the nuclear industry in optic fibre technology for both data communication and sensing applications. Optic fibre applications are found in a wide range of sectors such as in civil engineering structures, accelerators, etc. Events that took place in Japan in 2011, the Fukushima earthquake disaster, have highlighted the need for more research in radiation protection and nuclear safety to improve safety in the current and future nuclear power plants. South Africa operates two pressurized water reactors at Koeberg Nuclear Power station, which contributes about 5% of the country's electricity to the national grid [1]. This nuclear station was built in the 1970s; such novel technology would provide additional real-time in-core monitoring systems for the various critical parameters in the nuclear reactor. In addition to the reactor safety, accurate real-time measurements at multiple points and locations such as measurements of temperature, neutron dose levels, water levels and other parameters would allow enhanced power output from the nuclear reactor, and that would have tremendous economic benefits for the country. Traditional sensors such as thermocouples for temperature and fission fragment detectors for neutron flux have a limitation in that one may have indirect

measurements, sensing by a proxy not at the optimal positions and at all times, and working with a limited amount of sensor data. A single cable fibre can be multiplexed with tens of sensors, and in some cases, continuously sense along its length, thus equivalent to several 10 000s sensors. It can generate a continuous stream of data as a time series, e.g. temperature and neutron flux time differential mapping. Such detailed mapping would ensure that there are no hot spots occurring within the nuclear reactor.

Optic fibres potentially offer a wide range of advantages for safe operation and control of nuclear power reactors. Optic fibre sensors exhibit a number of attractive features more advantageous than their electronic counterparts: i) there is no need to power them or use with amplifiers, ii) they require small cable size and weights, which makes it easy to place in normally inaccessible areas, iii) one cable can be adapted to measure multiple environmental parameters, iv) allow for large scale multiplexing without electronics, v) and their remote sensing ability limits radiation exposure risks to workers. A nuclear reactor environment is characterised by the presence high electromagnetic interference and radiation levels, which can cause serious deterioration in the performance of the conventional sensors. Fibre optic sensors can be designed to withstand harsh nuclear reactor environments where the dose may be 2 GGy within two weeks of operation. Silica is a low Z non-metallic material, its introduction into a controlled reactor area would result in insignificant production of secondary waste. In this work, we report on the current state of our experimental and theoretical programme at Nuclear Energy Corporation of South Africa (Necsa) in Pretoria.

2. In-fibre based sensors

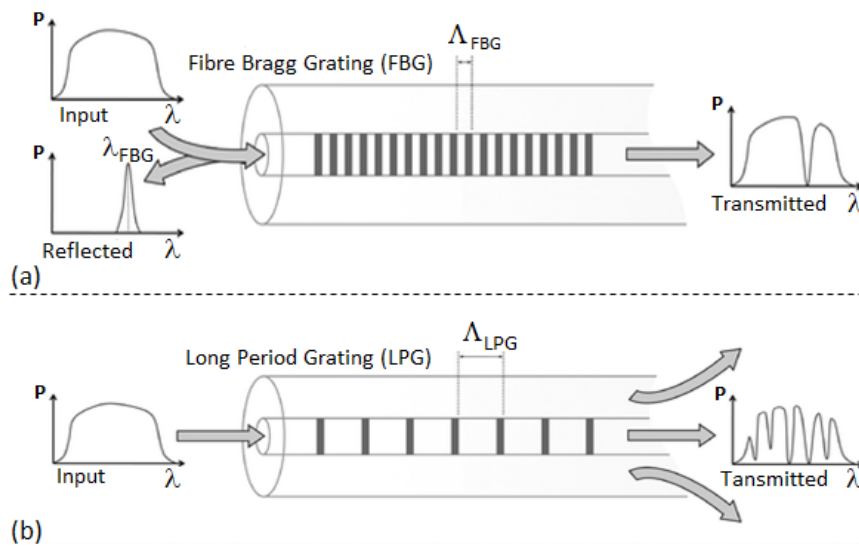


Figure 1. Schematic diagram of (a) Fibre Bragg Grating and (b) Long Period Grating written in a silica core fibre [2].

In-fibre gratings, shown in figure 1, are created by inducing periodic modulation of the refractive index in the fibre core formed by a spatially periodic exposure to intense light or other suitable radiation [3–5]. They are classified into two types based upon the period of grating.

The Fibre Bragg Grating (FBG), shown in figure 1(a) has a grating period of about $1\ \mu\text{m}$ [6]. A FBG behaves as a wavelength selective filter which reflects light signals at a specific wavelength, known as the Bragg wavelength (λ_B) that is strictly dependent on the fibre effective refractive index (n_{eff}) and the grating pitch Λ of the FBG:

$$\lambda_B = 2 \cdot n_{eff} \cdot \Lambda \quad (1)$$

The sensing qualities of a FBG are evident from this equation, any changes to the period Λ and/or the refractive index of the grating n_{eff} will be reflected by a shift in the Bragg wavelength λ_B . In a Fibre Bragg Grating sensor, the information on the measured parameter (temperature or strain) is wavelength-encoded and therefore insensitive to radiation-induced losses. The fractional Bragg wavelength shift for a temperature change ΔT is given by

$$\frac{\Delta \lambda_B}{\lambda_B} = (\alpha + \xi) \Delta T \quad (2)$$

where α is the thermal expansion coefficient, about $0.5 \times 10^{-6}/^\circ\text{C}$ [7] at room temperature and ξ represents the thermo-optic coefficient, about $10^{-5}/^\circ\text{C}$ [8]. FBGs are inherently sensitive to temperature and strain. In order to make them sensitive to other parameters, one needs to apply specialised coatings to the fibre. The coating converts the measured response into a strain on the fibre section that contains the gratings.

A Long Period Grating (LPG) has a longer grating period than an FBG, in the range $100\ \mu\text{m}$ – $1\ \text{mm}$. The LPG shown in figure 1 (b), the transmitted spectrum has valleys due to resonant energy losses by the cladding when there is power coupling between the fundamental guided core mode and co-propagating cladding modes. Each mode coupling happens at a distinct wavelength, where the so-called phase matching condition is satisfied:

$$\lambda_B = (n_{eff} - n_{clad}^i) \cdot \Lambda \quad (3)$$

where n_{eff} is the effective refractive index of the propagating core mode at wavelength λ , n_{clad}^i is the refractive index of the i th cladding mode and Λ is the period of the LPG. The n_{clad} can collectively include the optical coupling of the cladding to the functional coating and the environment beyond the functional coating. The centre wavelengths of the attenuated bands in the transmitted spectrum are sensitive to the period of the LPG, the length of the LPG and to the refractive index of the local environment [9]. The increased sensitivity to functional coating and the environment through this optical coupling and the increased complexity of the transmitted spectrum endow LPG technology with a wider range of designer capability and sensitivity. LPGs have a wider scope as “designer” sensors, in terms of what can be sensed, how it can be tuned for the particular application, and the enhanced sensitivity.

3. Radiation hardness tests for the optic fibres at SAFARI-1

Initial tests for FOS radiation hardness are carried out in a Material Test Reactor (MTR) at Necsa. A MTR should induce more damage to the fibres than a power reactor because it has a much higher ratio of fast-to-thermal neutrons. This makes it more appropriate for such tests and validation of new materials and sensors than a strictly regulated power reactor. Necsa operates a 20 MW MTR known as SAFARI-1 [10]. It is a light water-cooled, beryllium reflected, pool-type research reactor.

It has various in-core and ex-core radiation facilities with varying neutron flux levels. For these radiation hard studies, we have selected an in-core position with high neutron flux levels. This position is accessed by a pneumatically delivered capsule system. The neutron flux is well characterised using the OSCAR-4 deterministic reactor calculation code system [11]. For an

Table 1. Total fluences possible as a function of irradiation time with the SAFARI-1 reactor [10].

Total Fluence (n/cm²)	2.42×10^{20}	4.84×10^{20}	7.26×10^{20}	9.68×10^{20}
No. of days	28 days	56 days	84 days	112 days

assumed neutron flux value of 1.00×10^{14} n/cm²-s, the overall expected fluences as a function of irradiation time in the SAFARI-1 reactor are given in table 1.

For current measurements at Necsa SAFARI-1 reactor, we selected single mode type fibres with no Bragg gratings as an initial assessment of the fibre's ability to survive the high radiation and temperature environment; fibres with inner core diameter of $\varphi = 7\mu\text{m}$, a cladding layer of $\varphi = 125\mu\text{m}$ and with the coated layer of $\varphi = 245\mu\text{m}$. The four types of fibres selected, coated and non-coated are UV treated resin coated, acrylate coated, polyimide coated and a naked fibre. Samples of 10 cm lengths for each type of fibre were irradiated. They were placed and sealed in the 2 cm diameter aluminium irradiation capsules. The irradiations will be done in steps up to an accumulated neutron fluence (i.e. n.v.t.) of $\sim 10^{20}$ n/cm² or a total ionising dose of about 12 GGy. In this measurement, we want to look at the mechanical and optical changes in the fibres prior- and post-irradiation.

Similar studies testing irradiation hardness of different optic fibres have been conducted in other Materials Test Reactors (MTR) or Power Reactors (PR) elsewhere [12–14]. The highest dose reached at 16 GGy and neutron fluence 1.30×10^{20} n/cm² [12]. These studies indicate that the silica component of the fibre does become damaged, but slowly enough and in a systematic way. One expects that with appropriate understanding of the time dependant dose induced changes, one may still deploy the fibre effectively and with significant cost-benefits.

4. Optic fibre simulation calculations

Preparatory calculations were performed for a selection of the fibre types for the fibre irradiation damage study. An important aspect is activation studies of the fibre during the irradiation and assessment of the cool-down period. This is a necessary safety control before insertion of material into the SAFARI-1 MTR. Simulation analysis of the optic fibres was done using MCNP6.2 [15] and FISPACT-II [16] to study the level of activity induced on the fibres after irradiation and the extent of radiation damage.

MCNP results

Results from MCNP calculations show very low neutron and gamma heating, therefore the samples can be irradiated in the usual isotope production rigs without any modifications or deviation from the standard operating procedures. The neutron damage as represented by the Damage Per Atom (DPA) also show very low damage to the sample material [17].

FISPACT-II results

The results from FISPACT show that the amount of induced activity after irradiation is about 1.5 Ci, which goes down to about 0.5 Ci within 24 hours. The dose rate starts at about 1.05×10^{-6} Sv/h after irradiation and goes down within 24 hrs, see figure 2. This is the case for the period after 28 days, 56 days and 84 days irradiation intervals [17].

The simulation results show that the irradiation of the fibre optic samples in the SAFARI-1 reactor will not cause any significant damage to the samples. No long-lived radioisotopes producing high ionizing radiation are populated. It will be safe to handle the samples after a 2-day cool-off period without using specialised equipment.

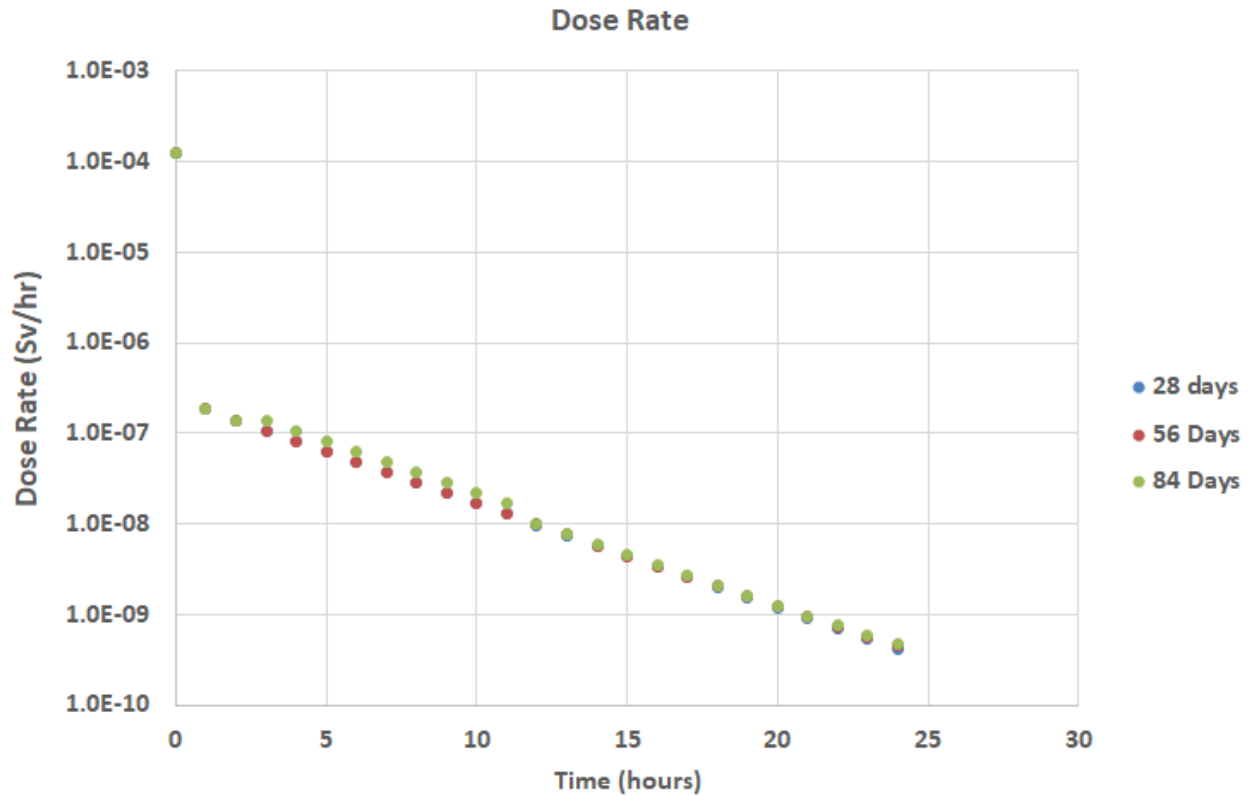


Figure 2. Expected dose rate after 28 days, 52 days and 84 days of irradiation.

5. FOS deployment to a PWR in Koeberg

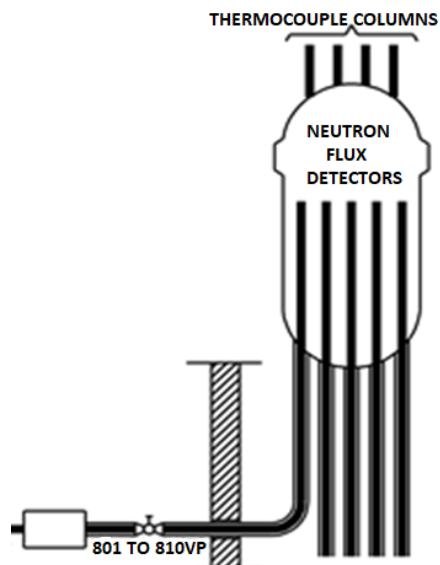


Figure 3. A schematic diagram of a PWR showing provision for regular insertion of sensors into the core.

The goal of this project is ultimately to deploy these optic fibre sensors to a PWR like in Koeberg. The Koeberg nuclear reactor has been operating for more than 30 years. Routine measurements that are done with the reactor like neutron flux measurements are carried out using a thimble sized fission fragment detector. The detector is inserted via a manifold through a blind tube system from outside the radiation shield zone into the pressure vessel of the reactor core. PWRs like in Koeberg already have about 40 built-in blind-tube penetrations into the reactor core. These blind access tubes into the reactor core could be used as access points for fibres. The fibres could be conveniently inserted into the core with little retrofit to the reactor vessel. A schematic diagram of the manifold system outside of the shielding and access to the in-core blind tube penetrations which could accommodate the fibres on a short to medium term basis is shown in figure 3.

6. Conclusions

The safety and reliability of nuclear power plants could be improved through the implementation of advanced sensing technologies like fibre optic sensors. Optic fibres can withstand the harsh radiation environment in nuclear reactors for significant time periods, for even months. The optic fibres can be innovatively adapted to measure a wide range of parameters critical for efficient nuclear reactor operation. Results from current samples being irradiated at SAFARI-1 reactor at Necsa should help us to determine the best fibres to use for further sophisticated tests, leading to in-situ readout of light attenuation and FBG/LPG performance. Simulation results using FISPACT-II show that it will be safe to handle the samples within a 24 hr period after irradiation. FOS are remarkable new opportunity for sensing, especially in all kinds of extreme environment. They represent a niche opportunity in the context of nuclear energy generally especially with nuclear reactors like PWR and BWR.

References

- [1] Koeberg nuclear power station <https://www.eskom.co.za> accessed: 2021-07-01
- [2] Jovanovic N, Fuerbach A, Marshall G, Ams M and Withford M 2012 *Fibre grating inscription and applications* (Topics in applied physics vol 123) pp 197–225
- [3] Hill K O and Meltz G 1997 *Journal of Lightwave Technology* **15**
- [4] Othenos A 1999 *Fiber Bragg Gratings* (Norwood and London: ArtechHouse)
- [5] Berruti G, Consales M, Giordano M, Sansone L, Petagna P, Buontempo S, Breglio G and Cusano A 2013 *Sensors and Actuators B* **177** 94–102
- [6] Vengsarkar A, Lemaire P, Judkins J, Bhatia V, Erdogan T and Sipe J 1996 *Journal of Lightwave Technology* **14** 58–65
- [7] Fernando G F, Webb D J and Ferdinand P 2002 *Optica-Fiber Sensors; MRS Bulletin* 359–64
- [8] Malitson I H 1965 *J. Opt. Soc. Am.* **55** 1205–09
- [9] Bhatia V 1999 *Optics Express* **4** 457–66
- [10] South African Nuclear Energy Corporation: (NECSA) <https://www.necsa.co.za/services/safari1> accessed: 2021-07-02
- [11] Stander G, Prinsloo R H, Muller E and Tomasevic D I 2008 *Proc. of the Int. Conf. on the Physics of Reactors* 1179–87
- [12] Cheymol G, Long H, Villard J F and Brichard B 2008 *IEEE Trans. Nucl. Sci* **SS(4)** 2252–8
- [13] Remy L, Cheymol G, Gusarov A, Morana A, Marin E and Girard S 2016 *IEEE Trans. Nucl. Sci.* **63(4)** 2317–22
- [14] Zaghoul A S M, Wang M, Huang S, Hnatovsky C, Grobnc D, Mihailov S, Li M, Carpenter D, Hu L, Daw J, Laffont G, Nehr S and Chen K P 2018 *Opt. Expr.* **26** 11775–86
- [15] Werner J C, Bull J S, Solomon C J, Brown F B, McKinney G W, Rising M E, Dixon D A, Martz R L, Hughes H G, Cox L J, Zukaitis A J, Armstrong J C, Forster R A and Casswell L 2018 MCNP Version 6.2 release notes
- [16] Fleming M, Stainer T and Gilbert M 2018 The FISPACT-II User Manual
- [17] Maqabuka B G, Bedhesi L, Chinaka E, Connell S H, Daniels G, Naidoo P, Nicholls D, Pieterse F and Slabber J 2021 *10th CIGRE Southern African Regional Conference 2nd-4th November 2021 Johannesburg, South Africa* [to be published]

DIVISION C - PHOTONICS

Nuclear translocation of Map Kinase and release of basic fibroblast growth factor following photobiomodulation at 660 nm in diabetic wounded cells

P Kasowanjete, N N Houreld¹ and H Abrahamse

Laser Research Centre, Faculty of Health Sciences, University of Johannesburg, P.O. Box 17011, Doornfontein, South Africa, 2028

E-mail: nhoureld@uj.ac.za

Abstract. Mitogen-activated protein kinase (MAPK) signalling is one of the best characterised signal transduction pathways in cell biology and is involved in wound healing processes. Photobiomodulation (PBM) has been used to induce physiological changes and has been shown to improve wound healing processes, however the underlying molecular and cellular mechanisms of action remain largely unexplained. The purpose of this study was to determine the effect of PBM at 660 nm on nuclear translocation of MAPK and release of basic fibroblast growth factor (bFGF) in diabetic wounded fibroblast cells *in vitro*. This was evaluated by irradiating cells at a wavelength of 660 nm with 5 J/cm² and incubating them for 24 and 48 h. Non-irradiated cells (0 J/cm²) served as controls. b-FGF was measured by the Enzyme Linked Immunosorbent Assay (ELISA) and translocation of phosphorylated MAPK was assessed by immunofluorescence. PBM of diabetic wounded cells showed an increased release of bFGF and translocation of MAPK in irradiated cells at 24 and 48 h as compared to non-irradiated cells. The findings of this study showed that PBM is capable of inducing the release of bFGF and activation of MAPK in diabetic wound cells *in vitro*, thus facilitating wound healing under diabetic conditions.

1. Introduction

Diabetes Mellitus (DM) is a chronic metabolic disease characterised by hyperglycaemia due to the absence or insufficient production of insulin, or an inability of the body to properly use insulin (insulin resistance). According to the International Diabetes Federation (IDF), DM is a global health burden with 463 million cases seen in adults between the ages of 20 to 79 (9.3%). South Africa has a prevalence rate of 12.7% [1]. Diabetic complications are due to high levels of glucose and protein glycation. Major complications include angiopathy, neuropathy, cardiovascular diseases, and retinopathy. Approximately 15% of diabetic patients experience lower limb complications, including chronic non-healing ulcers, largely due to neuropathy and angiopathy [2]. These ulcers commonly necessitate lower extremity amputation, often resulting in a poor-quality of life and the untimely death of the patient [3]. Globally, it has been estimated that every 30 seconds a diabetic patient loses a limb or part thereof due to amputation [1].

The normal wound healing process involves four sequential biological overlapping phases namely, homeostasis, inflammation, reepithelization, and tissue remodelling. The expected timeframe for

¹ To whom any correspondence should be addressed.

successful wound healing is three months, however once this time is exceeded due to conditions such as diabetes, the wound is considered to be chronic [4]. This delay in the wound healing process has been linked to a reduction in cellular processes due to a decrease in cell migration and proliferation, as well as a lack of growth factor and collagen synthesis [5].

The closure and repair process of wounds following tissue damage employs a series of molecular and cellular activities that aim to restore the injured tissue. The regulation and redirection of the wound healing process is mainly achieved by the presence of growth factors and cytokines [6]. It is well known that the activities of growth factors are deficient in diabetic wounds because of a reduction in their production and/or an increased rate of their elimination. Fibroblast growth factor (FGF) is one such growth factor, which has considerable effects on tissue repair and regeneration. There are 22 members of the FGF family, and basic FGF (bFGF or FGF2) has been shown to regulate cell proliferation, migration, and differentiation [7]. FGF interacts with their corresponding receptor, FGFR in the presence of heparan sulphate (HS) as a cofactor. This binding triggers the formation of the ternary FGF-FGFR-HS complex which in turn activates the FGFR intracellular kinase domain through the phosphorylation of a tyrosine residue. The activated domain is coupled to intracellular signalling pathways, including the Ras/ mitogen-activated protein kinase (MAPK) pathway [6]. MAPK is one of the best characterised signal transduction pathways, and an important bridge in cell biology that plays a crucial role in transducing signals from the extracellular milieu to the cell nucleus where specific genes are activated for cell growth, division, and differentiation that leads to improved wound healing [6].

Photobiomodulation (PBM) utilises non-ionised, low powered light sources (including lasers and light emitting diodes) with wavelengths typically in the visible red or near infrared (NIR) spectrum to promote physiological changes and render therapeutic benefits without causing damage [8,9]. The principle of PBM is based on the absorption of light by a chromophore which stimulates the biological system in an organism to speed up and activate an array of cellular processes that results in downstream physiological effects facilitating the process of wound healing, and concomitantly reducing pain, inflammation, and oedema [9,10]. Studies have shown that PBM at 660 nm increases the production of growth factors and the expression of genes that play an important role in wound healing [11-13]. PBM has also been used to treat a variety of conditions and has been found to be beneficial in the treatment of diabetic wounds [5, 9]. This study aimed to determine the effect of PBM at 660 nm on the nuclear translocation of MAPK and release of bFGF in diabetic wounded cells *in vitro*.

2. Materials and methods

This study used commercially purchased human skin fibroblast cells (WS1, ATTC® CRL-1502™). Ethical clearance was obtained from the University of Johannesburg, Faculty of Health Sciences Research Ethics Committee (REC-487-2020). A diabetic cell model was achieved by continuously growing cells in minimum essential media (MEM) containing an additional 17 mM D-glucose (MEM already contains glucose at a basal concentration of 5.6 mM, thus cells are grown in 22.6 mM D-glucose) [13-15]. Cells were seeded in 3.4 cm diameter tissue culture plates (6×10^5) and incubated overnight. A wound was created via the central scratch assay using a sterile 1 mL pipette to create a cell-free zone in the confluent monolayer of cells. After creating the cell-free zone, cells were incubated for 30 min before irradiation in order to allow them to adapt [14]. The effect of PBM on nuclear translocation of MAPK and release of bFGF in a diabetic wounded cell model was evaluated by irradiating cells at a wavelength of 660 nm with a fluence of 5 J/cm² (table 1), while non-irradiated (0 J/cm²) cells served as the control. A fluence of 5 J/cm² has been used extensively by the research group *in vitro* as an optimal fluence at a wavelength of 660 nm [12,14]. Cells were irradiated in the dark to eliminate the interference of surrounding light. The laser light was directed to the cells via fibre optics from above with the culture dish lid off in 1 mL of culture media.

Nuclear translocation of ERK1/2(MAPK) was detected by immunofluorescence whereby cells that were grown on coverslips placed in 3.4 cm diameter tissue culture plates were fixed with 4% paraformaldehyde. Following 15 min of incubation at room temperature cells were permeabilised with 0.1% Triton-X 100 in phosphate buffered saline (PBS). Thereafter, non-specific antibody binding was

blocked in 1% Bovine Serum Albumin (BSA) in PBS. MAPK was first labelled with 1:250 primary antibody (anti-Map kinase, activated (diphosphorylated ERK-1&2) antibody, mouse monoclonal; Sigma Aldrich, M9692). The primary antibody was detected using a 1:100 fluorescently labelled secondary antibody (Goat Anti-mouse IgG, H&L, FITC conjugate, Sigma Aldrich, 12-506). Nuclei were counterstained with 1 $\mu\text{g/mL}$ 4',6-diamidino-2-phenylindole (DAPI). Slides were observed under a fluorescent microscope (Carl Zeiss, Axio Observer Z1).

Table 1. Laser parameters.

Variables	Diode laser
Wavelength (nm)	660
Fluence (J/cm^2)	5
Power output (mW)	100
Power density (mW/cm^2)	11
Spot size (cm^2)	9.1
Irradiation time	7 min 57 s
Energy (J)	47.7

The release of bFGF into the culture media was analysed using a solid-phase sandwich Enzyme-Linked Immunosorbent Assay (ELISA) kit according to the manufacturers' details (Invitrogen, Human FGF basic ELISA Kit, Thermo Fisher Scientific, KHG0021). Absorbance was read at 450 nm using the VICTOR Nivo™ Multimode Plate Reader (PerkinElmer).

Experiments were conducted three times ($n=3$). ELISA results were statistically analysed using SigmaPlot version 13.0 (Systat Software, Inc.). Differences between groups was determined using the student t-test and each independent variable was considered statistically significant when $P < 0.05$.

3. Results and discussion

Immunofluorescent results in irradiated (5 J/cm^2) diabetic wounded cells showed strong translocation of MAPK as compared to control cells at 24 h (figure 1). At 48 h post-irradiation there was little translocation of MAPK with some localisation around the nucleus.

bFGF ELISA results showed a significant increase in bFGF released into the surrounding media in irradiated cells (5 J/cm^2) at 24 h ($P < 0.05$) (figure 2), while at 48 h there was a significant decrease ($P < 0.01$) (figure 3). Fibroblasts migrate into the wound site and start to release growth factors [16]. The binding of bFGF to its receptor (FGFR) leads to activation of the MAPK signalling pathway, and hence translocation of MAPK. The cells then start to participate in the process of wound healing, such as reducing wound size by contraction. The increase in bFGF at 24 h correlates with the increased MAPK translocation seen in the fluorescent images. The decrease seen in bFGF at 48 h may be due to the consumption of bFGF by the cells through paracrine signalling. The decrease in bFGF at 48 h also corresponds with the decrease seen in MAPK translocation at 48 h.

Other studies using PBM have found an increase in bFGF. A similar study conducted by our research group on fibroblast cells cultured under hyperglycaemic conditions found that PBM at a wavelength of 632.8 and 830 nm irradiated with a fluence of 5 J/cm^2 increased bFGF [13,14]. In another study, human skin fibroblast cells cultured under hyperglycaemic conditions and irradiated at the same wavelength of 632.8 nm once a day for three days at a fluence of 1 J/cm^2 also showed increased release of bFGF [17]. Human gingival fibroblast cells grown under normal conditions and irradiated at a wavelength of 780 nm and a fluence of 2-3 J/cm^2 showed increased production and secretion of FGF [18]. A wounded rat animal model irradiated at a wavelength of 660 nm and a fluence of 2.4 J/cm^2 showed that PBM

plays a critical role in diabetic wound healing by stimulating the release of essential growth factors (bFGF and FGF) [19].

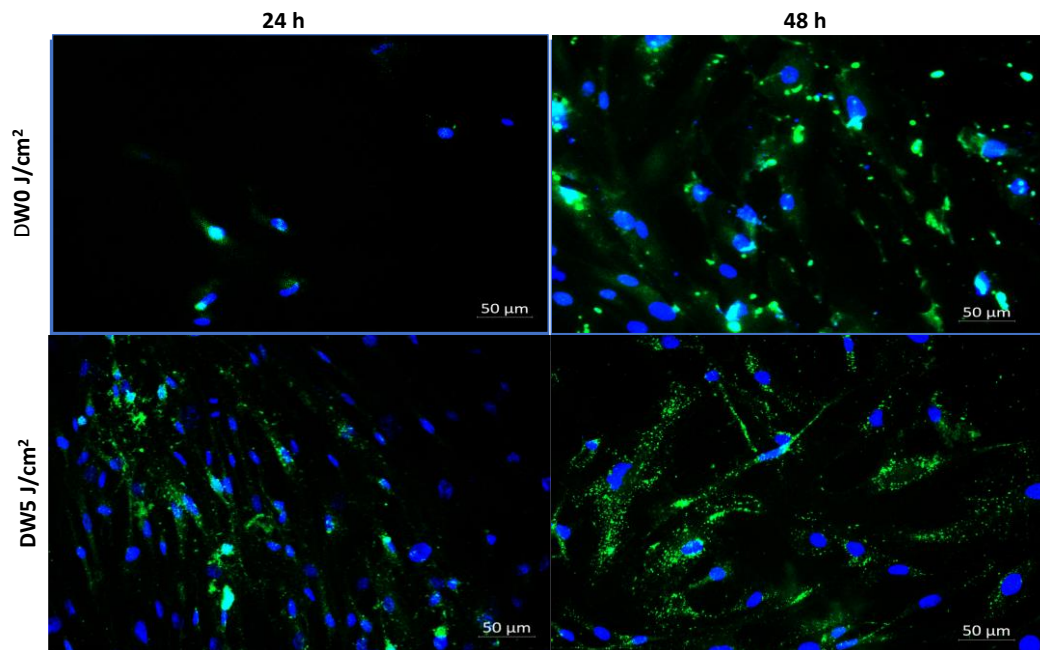


Figure 1. Diabetic wounded (DW) fibroblast cells were irradiated at 660 nm with 5 J/cm² and incubated for 24 or 48 h. Control cells were not irradiated (0 J/cm²). MAPK was fluorescently labelled with FITC (green) and nuclei stained with DAPI (blue). Irradiated cells showed nuclear translocation of MAPK, particularly 24 h post-irradiation (magnification 200x).

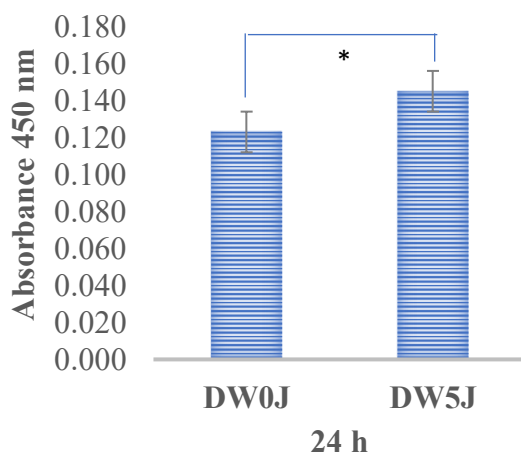


Figure 2. Basic Fibroblast Growth Factor (bFGF) analysed at 24 h in non-irradiated diabetic wounded (DW 0 J/cm²) control and irradiated diabetic wounded (DW 5 J/cm²) cells. Statistical significance is shown as *P<0.05, (±SEM).

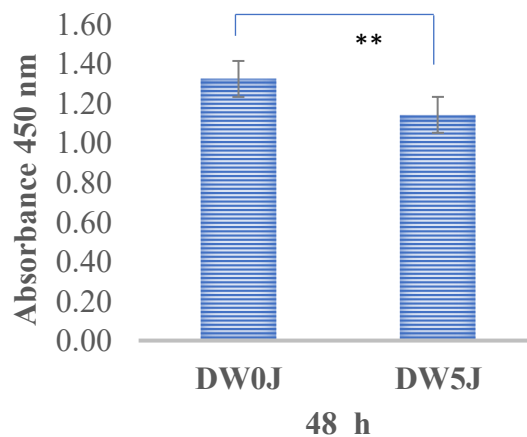


Figure 3. Basic Fibroblast Growth Factor (bFGF) analysed at 48 h in non-irradiated diabetic wounded (DW 0 J/cm²) and irradiated diabetic wounded (DW 5 J/cm²) cells. Statistical significance is shown as **P<0.01, (±SEM).

4. Conclusion

This study aimed to determine the effect of PBM at 660 nm with 5 J/cm² on nuclear translocation of MAPK and release of bFGF in diabetic wounded cells. The findings of this study showed that PBM at 660 nm and a fluence of 5 J/cm² promoted the release of bFGF *in vitro* at 24 h under hyperglycaemic conditions. PBM promoted nuclear translocation of MAPK, and hence activation of the MAPK signalling pathway. These results may explain the downstream effects seen in response to PBM, including increased proliferation and migration. Further studies into the effects of 660 nm on the MAPK pathway are warranted.

Acknowledgments

This work is based on the research supported by the South African Research Chairs Initiative of the Department of Science and Technology (DST) and National Research Foundation (NRF) of South Africa (Grant No 98337), as well as grants received from the University of Johannesburg (URC), the African Laser Centre (ALC) (student scholarship), the NRF Competitive Programme for Rated Researchers, and Council for Scientific and Industrial Research (CSIR) - National Laser Centre (NLC) Laser Rental Pool Program. All lasers were supplied and set up the NLC.

References

- [1] International Diabetes Federation, IDF 2019 *Diabetes Atlas*, 9th edition, available from <https://www.diabetesatlas.org/en/> Accessed on 26/04/21
- [2] Zhang C, Ponugoti B, Tian C, Xu F, Tarapore R, Batres A, Alsadun S, Lim J, Dong G and Graves D T 2015 *J. Cell. Biol.* **209** 289-303
- [3] Järbrink K, Ni G, Sönnnergren H, Schmidtchen A, Pang C, Bajpai R and Car J 2017 *Syst. Rev.* **6**, 15
- [4] Rajendran N K, Dhilip Kumar S S, Houreld N N and Abrahamse H 2019 *J. Cell. Commun. Signal.* **13** 151- 62
- [5] Houreld N N 2014 *Scientific World Journal* **2014** 398412
- [6] Ornitz DM and Itoh N 2015 *Wiley Interdiscip. Rev. Dev. Biol.* **4** 215–66
- [7] Yun Y-R, Won J E, Jeon E, Lee S, Kang W, Jo H, Jang J-H, Shin U S and Kim H-W 2010 *J. Tissue Eng.* **2010** 218142
- [8] Anders J J, Arany P R, Baxter G D and Lanzafame R J 2019 *Photobiomodul. Photomed. Laser Surg.* **37** 63-5
- [9] Houreld N N 2019 *Appl. Sci.* **9** 5114
- [10] Dompe C et al. 2020 *J. Clin. Med.* **9** 1724
- [11] Phillip V P, Chang T Y, Ryan B and Baxter D 2011 *Photomed. Laser Surg.* **29** 285-304
- [12] Jere S W, Houreld N N and Abrahamse H 2018 *J. Photochem. Photobiol. B.* **179** 74–83
- [13] Houreld N N and Abrahamse H 2008 *Lasers Med. Sci.* **23** 11–8
- [14] Houreld N N and Abrahamse H 2010 *Diabetes Technol. Ther.* **12** 971–8
- [15] Ayuk S M, Houreld N N and Abrahamse H 2012 *Diabetes Technol. Ther.* **14** 1110–7
- [16] Tracy L E, Minasian R A and Caterson E J 2016 *Adv. Wound Care* **5** 119-36
- [17] Esmaelinejad M and Bayat M 2013 *J. Cosmet. Laser Ther.* **15** 310–7
- [18] Castro T N S, Martignago C C S, Assis L, de Alexandria F E D, Rocha J C T, Parizotto N A and Tim C R 2020 *Lasers Med. Sci.* **35** 939-47
- [19] Damante C A, De Micheli G, Miyagi S P, Feist I S and Marques M M 2009 *Lasers Med. Sci.* **24** 885-91

A comparison between photobiomodulation at 830 nm and 660 nm on differentiation in diabetic human skin fibroblast cells

O A Oyebo¹ and N N Houreld

Laser Research Centre, Faculty of Health Sciences, University of Johannesburg,
P.O. Box 17011, Doornfontein, South Africa, 2028

E-mail: daramzjay09@gmail.com

Abstract. Different studies have proposed the efficacy of photobiomodulation (PBM) at different wavelengths (830 and 660 nm) to stimulate wound repair in diabetic cells. The TGF- β 1/Smad cascade has proven to be an effective signalling pathway in differentiating fibroblasts into myofibroblasts. This study aims to compare the effects of both wavelengths on cellular viability and expression of fibroblast differentiation markers in WS1 fibroblast cells. The cells were modelled into groups; normal (N), normal wounded (NW) and diabetic wounded (DW). At 830 nm and 660 nm, cells were irradiated with 5 J/cm², while control cells were without irradiation (0 J/cm²). At 24 and 48 h post-irradiation cell viability was investigated using the Trypan blue exclusion assay, while transforming growth factor-beta (TGF- β 1) and p-Smad2/3 was ascertained using ELISA. Immunofluorescence was used to observe the presence of alpha smooth muscle actin (α -SMA). There was a significant increase in cell viability in the irradiated models using both wavelengths. A wavelength of 830 nm elicited a slight increase in TGF- β 1 compared to 660 nm in diabetic wounded cells, while both wavelengths had no effect on p-Smad2/3. Both wavelengths were successful in initiating the differentiation of fibroblasts into myofibroblasts in diabetic wounded cells with no difference between wavelengths.

1. Introduction

Diabetes mellitus (DM) remains a complex metabolic disorder, with symptoms that progress to diverse micro and macro- complications. Presently, over 463 million cases of diabetes have been recorded globally [1]. This implies that 1 in 11 people worldwide currently have diabetes. The number of diabetes cases is estimated to increase to 700 million by 2045 (51% increase) [1]. In South Africa, the prevalence of diabetes surged from 5.5% to 9% within 2000 and 2010, making the country the second highest with respect to mean health care expenditure in the African region [2].

A rise in blood glucose levels occurs in diabetes due to insulin resistance which then leads to energy starvation and inadequate utilisation of sugar in peripheral organs. Hyperglycaemia has been implicated in the slow healing of wounds seen in diabetic patients with chronic foot ulcers [3, 4]. As a result, the quality of life of diabetic patients is often impacted negatively, not only because of their limited mobility and increased risk of death from limb amputations, but also due to the treatment costs that would have been incurred. Globally, reports indicate that a lower limb amputation occurs in

¹ To whom any correspondence should be addressed.

diabetic patients every 30 seconds [5]. New and potent modalities are therefore required to accelerate the healing process of diabetic wounds to reduce the risk of amputation and increase the quality of life of patients.

There is an urgent need to identify effective ways to accelerate the wound healing process, thereby reducing the global burden of diabetic wounds. Light (including lasers) can be used to speed up healing in a process called photobiomodulation (PBM), but the activation of specific and important cellular pathways in response to PBM must be identified to make the treatment more lucrative [6]. PBM is a non-invasive and painless therapy and can be used singly or jointly with other treatment strategies to speed up the healing of diabetic wounds. The positive influence of PBM on wound healing at *in vitro* level has been reported in earlier studies using stem cells, keratinocytes, fibroblasts, mast cells, osteoblasts, and others [7, 8]. *In vitro* PBM (adopting wavelengths of 630 to 830 nm with a fluence from 2 to 5 J/cm²) on diabetic cells has elicited positive responses to induce effective wound healing [9, 10, 11].

The inflammatory phase of wound healing becomes defective in diabetes, leading to downregulation of growth factors, including transforming growth factor beta-1 (TGF- β 1) [6] and alteration of differentiation of cells (such as fibroblasts) necessary for wound closure [7]. Usually, fibroblast cells cover the wound area differentiating into extra domain-A fibronectin (EDA-FN) expressing proto-myofibroblasts, which finally differentiate into alpha smooth muscle actin (α -SMA) expressing myofibroblasts which aids in wound contraction through the Smad pathway. The Smad3 cascade remains a novel and unexplored area in response to PBM.

This study aims to compare the influence of PBM at different wavelengths (830 nm and 660 nm) on cellular viability and presence of fibroblast differentiation markers in normal and diabetic WS1 fibroblast cells.

2. Materials and Methods

A commercially purchased human skin fibroblast cell line (WS1, ATCC® CRL-1502™) was cultured aseptically in line with the supplier's protocol. Three models, namely normal (N), normal wounded (NW) and diabetic wounded (DW) were used. Diabetic cells were attained by continually growing the cells in complete MEM (minimal essential media) containing D-glucose (17 mMol/L) to achieve and maintain hyperglycaemia [12]. Cells (6×10^5) were transferred into 3.4 cm diameter culture plates. To achieve a wound, a scratch was created with a sterile 1 mL pipette on a confluent monolayer of cells [13]. Irradiation occurred at 830 nm and 660 nm using a diode laser at a fluence of 5 J/cm² while non-irradiated cells (0 J/cm²) served as controls. Laser parameters used are recorded in table 1.

Post-irradiation, incubation of cells was done for 24 and 48 h. The viability of the cells was ascertained using the Trypan blue exclusion assay. The human TGF- β 1 ELISA kit (Whitehead Scientific, R&D Systems, DY240) was utilized to quantify the amount of released TGF- β 1 in the culture medium while the phosphorylated-Smad2/3 (Ser423/425) ELISA kit (Thermo Fisher Scientific, Invitrogen, 85-86192) was used to determine the phosphorylation (and hence activation) of Smad2/3 in the cells. Both experiments were done using the ELISA kits' protocols, and colorimetric reactions were quantified spectrophotometrically at 450 nm (Victor3 multiplate reader; Perkin-Elmer).

Immunofluorescence was performed by fixing cells at room temperature on a coverslip with 4% paraformaldehyde for 15 min followed by permeabilization with 0.5% triton X-100 in phosphate buffered saline. The first labelling of cells was done with anti-human alpha-Smooth Muscle Actin (Whitehead Scientific, R&D Systems, MAB1420) a primary antibody, followed by a washing step. Then the second labelling was done using a fluorescently tagged secondary antibody (Anti-mouse IgG NL557 conjugated secondary antibody; Whitehead Scientific, Novus Biological, NL007). Post-washing, counter staining of the nuclei was done with 1 μ g/mL 4',6-diamidino-2-phenylindole (DAPI) followed by mounting onto a slide and viewing on the Carl Zeiss Axio Z1 Observer using Zen imaging software.

Samples were analysed three times ($n=3$) and statistical analysis was done using SPSS version 27. The student t-test and One-way ANOVA was used to determine statistical differences and results were considered significant when $p < 0.05$.

Table 1. Laser parameters.

Variables		
Wavelength (nm)	830	660
Light source	Diode laser	Diode laser
Wave emission	Continuous wave	Continuous wave
Spot Size (cm ²)	9.1	9.1
Power Output (mW)	105	100
Power density (mW/cm ²)	11.54	11
Irradiation time	7 min 13 s	7 min 34 s
Energy density (J/cm ²)	5	5
Energy (J)	45.5	45.4

3. Results and Discussion

The high costs associated with the treatment of diabetic wounds causes a strain on the global expenditure on diabetes. In diabetes, slow healing of wounds occurs due to a decrease in the production of collagen; the main content in the extracellular matrix (ECM) [14, 15]. The migration of fibroblast cells to the wound area during the normal wound healing process induces cytokine and growth factor secretion in the ECM [15]. Research has shown that PBM is effective in increasing the rate of diabetic wound healing through stimulation of cellular processes with little side effects. This could be through the increased expression of α -SMA. Application of red (660 nm) and near-infrared (830 nm) laser in PBM has emerged as a promising technique for speeding up the wound healing process, minimising pain, and improving skin function due to direct wound penetration and modulation of biochemical pathways [16].

Results show an increase in cell viability in the tested models (figure 1). This shows the success of PBM using both wavelengths in promoting cell viability, as has been shown in other studies [17, 18]. In N cells, irradiation at 830 nm elicited an increase in cellular viability compared to 660 nm after 24 h ($p < 0.001$) and 48 h ($p < 0.05$). There was no substantial variance in viability of the NW cells upon comparison of both wavelengths at 24 and 48 h. However, the DW cells irradiated at 830 nm exhibited a considerable increase in viability ($p < 0.01$) in comparison to the same cells irradiated at 660 nm at 48 h.

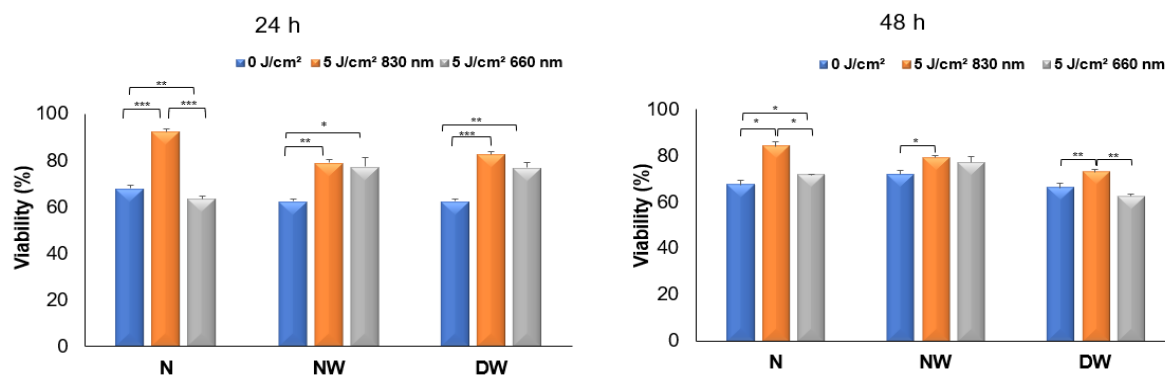


Figure 1. Cellular viability (%), assessed via the Trypan blue exclusion assay. Viability was determined in non-irradiated (0 J/cm²) and irradiated (5 J/cm² at 830 nm and 660 nm) normal (N), normal wounded (NW), and diabetic wounded (DW) cells, and analysed 24 and 48 h post-irradiation. Statistical significance is presented as * $P < 0.05$, ** $P < 0.01$ and *** $P < 0.001$ (\pm SEM).

In comparison to irradiation at 830 nm, irradiation at 660 nm resulted in a considerable ($p < 0.05$) increase in p-Smad 2/3 levels at 24 and 48 h in all the tested cell models (figure 2). This could suggest that irradiation at 660 nm might have initiated the activation of the Smad signalling pathway which was not noticed using the 830 nm. Interestingly, irradiation at 830 nm showed an increase in TGF- β 1 compared to 660 nm (table 2). This might be due to differentiation occurring before 24 h in the 660 nm irradiated cells, thereby causing the cells to use up more TGF- β in a paracrine fashion. TGF- β has been reported to increase the wound healing process by stimulating the production of collagen by fibroblast cells [19].

The immunofluorescence results using 660 nm showed an increase in the presence of α -SMA at 24 and 48 h post-irradiation compared to using 830 nm (figure 3). In skin contraction, during wound healing, myofibroblasts yield α -SMA to signify full fibroblast differentiation [20, 21]. Studies have shown that PBM using both wavelengths can trigger the release of α -SMA during wound healing [22, 23].

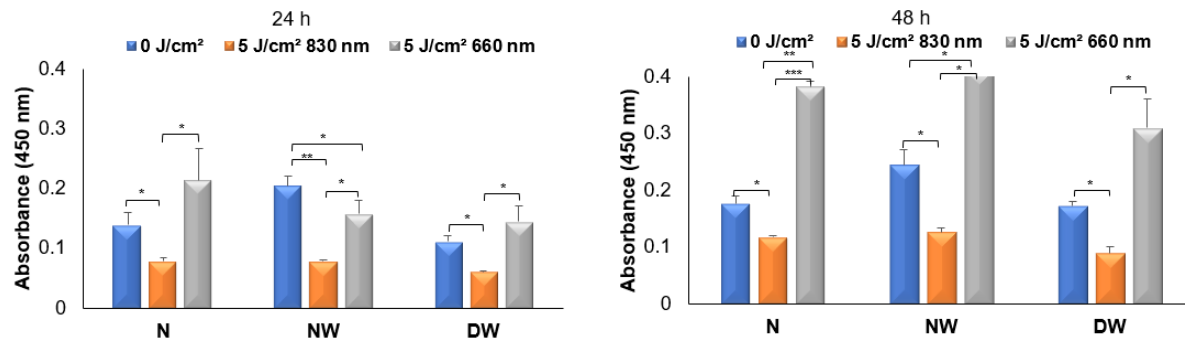


Figure 2. The presence of p-Smad2/3 was monitored using ELISA at 24 and 48 h in normal (N), normal wounded (NW) and diabetic wounded (DW) WSI fibroblast cells irradiated with an 830 nm and 660 nm laser at 5 J/cm² while the control group was not irradiated (0 J/cm²). Statistical significance is presented as * $P < 0.05$, ** $P < 0.01$ and *** $P < 0.001$ (\pm SEM).

Table 2. The presence of TGF- β 1 was measured using ELISA at 24 and 48 h in normal (N), normal wounded (NW) and diabetic wounded (DW) WSI fibroblast cells irradiated with an 830 nm and 660 nm laser at 5 J/cm² while control group was not irradiated cells (0 J/cm²).

	24 h			48 h		
	Control (0 J/cm ²)	5 J/cm ² 830 nm	5 J/cm ² 660 nm	Control (0 J/cm ²)	5 J/cm ² 830 nm	5 J/cm ² 660 nm
N	0.81 \pm 0.03	1.49 \pm 0.07**††	0.02 \pm 0.0006***	0.85 \pm 0.02	1.81 \pm 0.01***†††	0.03 \pm 0.007***
NW	0.74 \pm 0.04	1.48 \pm 0.07**††	0.02 \pm 0.002**	0.87 \pm 0.01	1.63 \pm 0.02***†††	0.02 \pm 0.0005***
DW	0.62 \pm 0.01	1.37 \pm 0.03***†††	0.021 0.0002***	0.76 \pm 0.005	1.73 \pm 0.02***†††	0.02 \pm 0.001***

Statistical significance as compared to the control is shown as ** $P < 0.01$ and *** $P < 0.001$, † signifies statistical difference between irradiation at 830 nm (5 J/cm²) and irradiation at 660 nm (5 J/cm²) (\pm SEM).

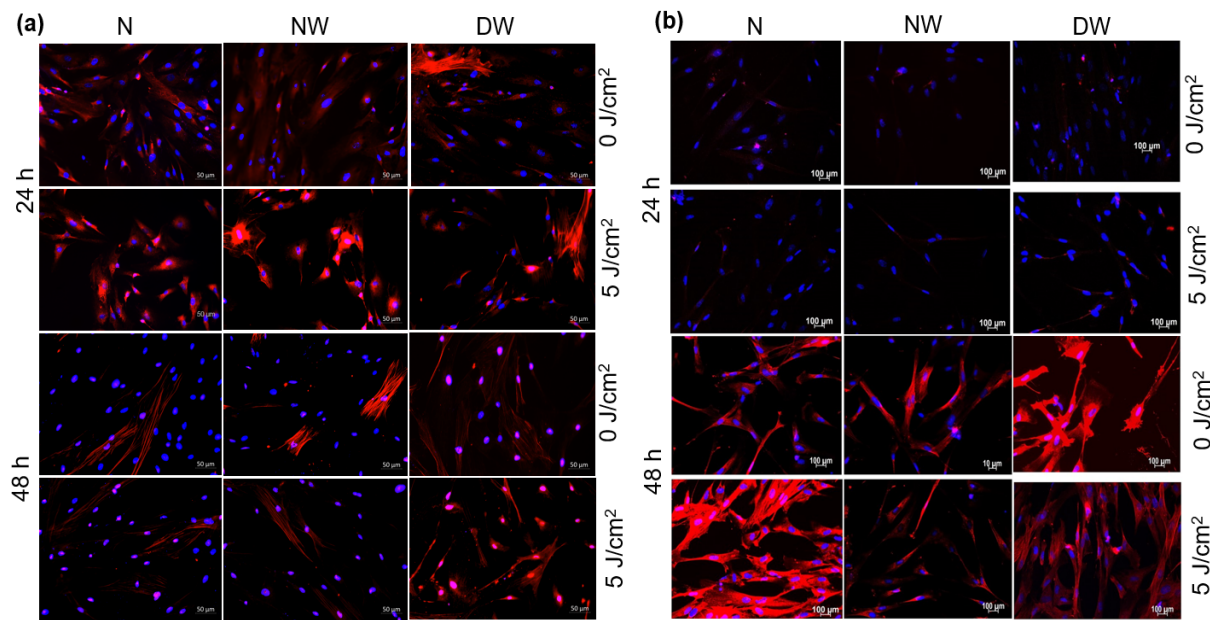


Figure 3. (a) Irradiation at 830 nm and (b) 660 nm wavelengths in normal (N), normal wounded (NW) and diabetic wounded (DW) cells irradiated at a fluence of 5 J/cm² and control cells (0 J/cm²). Cells were incubated for 24 and 48 h and stained for α -SMA (red). Counterstaining of nuclei was done with DAPI (blue), magnification (x200).

4. Conclusion

The study was aimed at comparing the influence of PBM at 830 nm and 660 nm on differentiation of N, NW and DW fibroblasts into myofibroblasts 24 and 48 h after irradiation. The results discussed showed that PBM at both wavelengths influenced the cells in comparison with the non-irradiated cells. There was an increase in the presence of p-Smad and α -SMA when using a wavelength of 660 nm in comparison with 830 nm. This difference may be due to the fact that the process of differentiation occurred faster at 660 nm (than at 830 nm) and could be the reason for the low presence of TGF- β 1 (at 660 nm) which could have already been used up by the cells during differentiation. Both wavelengths are equally successful in *in vitro* wound healing assays. More experiments (probably *in vivo* experiments) need to be done before we can justify the bases for a better wavelength.

Acknowledgments

This work is based on the research supported by the South African Research Chairs Initiative of the Department of Science and Technology and the National Research Foundation of South Africa (Grant No. 98337), and the CSIR (Council for Scientific and Industrial Research)—NLC (National Laser Centre) Laser Rental Pool Program (grant number LREHA01) as well as funding received from the University Research Committee, University of Johannesburg, South Africa. The authors would also like to appreciate Ms Dimakatso R. Mokoena whose masters research using the 660 nm laser was reported for this study.

References

- [1] International Diabetes Federation, IDF 2019 *Diabetes Atlas*, 9th edition, Available from www.diabetesatlas.org, Accessed on 21/03/21
- [2] Manyema M, Veerman J L, Chola L, Tugendhaft A, Labadarios D and Hofman K 2015 *PLoS One* **11** 0143050
- [3] Javed F, and Romanos G E 2019 *Periodontol.* **81** 57–63

- [4] Mekala K C, and Bertoni A G 2020 Academic press *Elsevier* 49–58
- [5] Raghav A, Khan Z A, Labala R K, Ahmad J, Noor S and Mishra B K 2018 *Ther. Adv. Endocrinol. Metab.* **9** 29–31
- [6] Houreld N N, Sekhejane P R, and Abrahamse H 2010 *Lasers Surg. Med.* **42** 494–502
- [7] Mokoena D, Dhilip Kumar S S, Houreld N N and Abrahamse H 2018 *J. Photochem. Photobiol. B Biol.* **189** 138–44
- [8] Houreld N N, 2014 *Sci. World J.* **2014** 398412
- [9] Oyeboode O, Houreld N N and Abrahamse H 2021 *Cell Biochem. Funct.* **39** 596–612
- [10] Ayuk S M, Houreld N N and Abrahamse H 2014 *Int. J. Photoenergy* **2014** 604518
- [11] Mokoena D R, Houreld N N, Dhilip Kumar S S and Abrahamse H 2020 *Lasers Surg. Med.* **52** 671–81
- [12] Houreld N N and Abrahamse H 2007 *Laser Chem.* **2007** 80536
- [13] Chen Z J, Yang J P, Wu B M and Tawil B 2014 *J. Dev. Biol.* **2** 198–209
- [14] Huang Y, and Kyriakides T R 2020 *Matrix Biol. Plus* **6** 100037
- [15] Qing C, 2017 *Chinese J. Traumatol.* **20** 189–93
- [16] Yadav A, and Gupta A 2017 *Photodermatol. Photoimmunol. Photomed.* **33** 4–13
- [17] Houreld N N, Masha R T and Abrahamse H 2021 *Lasers Surg. Med.* **44** 429–34
- [18] Jere S W, Houreld N N and Abrahamse H 2018 *J. Photochem. Photobiol. B Biol.* **179** 74–83
- [19] Szymanska J, *et al.* 2013 *J. Physiol. Pharmacol.* **64** 387–91
- [20] Li B, and Wang J H C 2011 *J. Tissue Viability* **20** 108–20
- [21] Midgley A C, Rogers M, Hallett M B, Clayton A, Bowen T, Phillips A O and Steadman R 2013 *J. Biol. Chem.* **288** 14824–38
- [22] Ribeiro M A G, Albuquerque R L C, Ramalho L M P, Pinheiro A L B, Bonjardim L R and Da Cunha S S 2009 *Photomed. Laser Surg.* **27** 49–55
- [23] Keshri G K, Gupta A, Yadav A, Sharma S K and Singh S B 2016 *PLoS One* **11** 0166705

Facilitating iADMSC Differentiation into Neuronal Cells by Photobiomodulation Using Visible and Near-Infrared Wavelengths

Madeleen Jansen van Rensburg¹, Anine Crous², and Heidi Abrahamse^{2*}

^{1/2} Laser Research Centre, Faculty of Health Sciences, University of Johannesburg, PO Box 17011, Johannesburg 2028, South Africa

*Email: habrahamse@uj.ac.za

Abstract. The central nervous system (CNS) of mammals is limited in its repair and regeneration in the event of injury due to trauma or neurodegeneration, therefore, optimization of its regeneration capabilities is necessary. Studies have shown that this issue may be addressed through the transdifferentiation of adipose-derived stem cells (ADMSCs) into neuronal cells. This process has not been efficiently achieved with chemical and biological inducers; this study explored possible optimization through the addition of photobiomodulation (PBM). PBM uses low intensity light to stimulate intracellular processes and has been known to increase cell proliferation and aid in stem cell differentiation. This *in vitro* research aimed to differentiate ADMSCs with growth factors and chemical inducers and subsequently measure the optimization effects that PBM had on differentiation. PBM was applied as single use at a low energy density, at visible and near-infrared (NIR) wavelengths. Characterization of immortalized ADMSCs (iADMSCs) with flow cytometry was used in identifying a CD marker and early and late neuronal markers. After this, biochemical analysis was performed to observe reactive oxygen species (ROS) production, cytotoxicity, proliferation, and viability. The outcome of this study indicated that PBM is beneficial to the differentiation process, however, prior induction at a longer incubation period is needed. Findings from this research serves as contribution toward validating stem cell technology for application in *in vivo*, pre-clinical and clinical research settings. Furthermore, an optimized protocol using differentiation media and PBM should be established for *in vivo* and clinical research, that specifically targets neuronal regeneration.

1. Introduction

Neurological diseases and illnesses present a task for therapy and rehabilitation, because of the limited ability for the nervous system to repair itself. Adipose-derived mesenchymal stem cells (ADMSCs) are more flexible than any adult stem cells and can be differentiated into non-mesodermal tissues, including neurons [1]. Differentiating ADMSCs into specific neuronal lineage cells allows us to transplant the correct cell type into the nervous system. To differentiate ADMSCs into active neurons several methodologies are being studied and evaluated. Limited success has been achieved in altering ADMSC's cellular structure and operational state to become identical with neuroglial cells [2]. Photobiomodulation (PBM) has been effectively implemented not only to enhance the viability and development of ADMSCs, but also as a potential enhancer of ADMSC differentiation [3, 4]. In this *in vitro* study, we

examined current neuro-differentiation methodologies along with the use of PBM, for differentiation of ADMSCs into neuronal lineages.

ADMSCs display plasticity and showcase the ability to transdifferentiate into multiple phenotypes, such as osteoblasts and neurons [5]. ADMSCs are abundantly available and easily sourced through surgeries that are not as invasive when compared to the harvesting of bone-marrow stem cells [6]. This process of differentiation can be triggered by exposing ADMSCs to growth factors or chemical inducers specific for the lineage in need [6-8]. The use of these factors upregulates in vitro potential of cells to differentiate [6]. Studies have met some success in differentiating ADMSCs into neuronal cell types with inducers forskolin, 3-isobutyl-1-methylxanthine, and basic fibroblast factor (bFGF) [9, 10]. Potentially, ADMSCs may be applied clinically to aid in the repair of mechanical brain injuries or neurodegenerative diseases [11].

Applying laser light to tissue to up- or downregulate the metabolism of cells is called PBM. The increase or decrease in metabolism is dependent on the parameters of the laser light [3]. Laser parameters include the wavelength that spans the visible and near-infrared (NIR) spectrum, ranging from 400-1100 nm, and fluence which is measure in J/cm² [3, 4]. Fluence, or energy density, is dependent on dosage, and has been determined to be effective at 3-5 J/cm². Below 3 J/cm² little to no effects are observed, and above 5 J/cm² often results in a biphasic dosage response [4, 12]. PBM applied at wavelengths within the visible spectrum of light has resulted in an increase in differentiation in osteoblasts from ADMCSs [13, 14]. The aim of this study was to evaluate the effects of PBM on iADMSC transdifferentiation into neuronal-like cells.

2. Materials and Methods

Immortalized ADMSCs (iADMSCs) (ASC52Telo; ATCC) were characterized through flow cytometry by identifying protein markers including stem cell marker CD44, neuronal early marker, neuron specific enolase (NSE) and late marker, microtubule associated protein 2 (MAP2). The iADMSCs were seeded at a density of 1×10^5 in 35 mm treated petri dishes and incubated overnight for attachment in neuronal induction media. The cells were treated with PBM using 825 nm near-infrared (NIR), 525 nm green (G), or the combination of both wavelengths at 5 J/cm². Cells that were not seeded in induction media nor treated with PBM served as a standard, and cells that were seeded in induction media but not exposed to PBM served as a control group. Post PBM exposure, cells were incubated 24 h, 48 h, and 7 days. Laser parameters are indicated in Table 1. The following formula was used to determine PBM irradiation time:

$$mW / cm^2 = \frac{mW}{\pi r^2}$$

$$W / cm^2 = \frac{mW / cm^2}{1000}$$

$$Time \text{ (seconds)} = \frac{J/cm^2}{W/cm^2}$$

Table 1. Laser Parameters

	Near infra-red (NIR)	Green (G)
Wavelength (nm)	825	525
Type	Diode	Diode
Emmision	CW	CW
Power (mW)	100	574
Power density (mW/cm²)	10.394	59.66
Fluence (J/cm²)	5	5
Time of irradiation (s)	8 min 1 sec	1 min 23 sec
Spot size (cm²)	9.62	9.62

The CytoTox 96® non-radioactive cytotoxicity assay was performed to determine the amount of lactate dehydrogenase (LDH) released from the cells, this was measured with a spectrophotometer. Reactive oxygen species (ROS) production was determined with the Fluorometric Intracellular Ros Kit (Sigma-Aldrich, MAK143) and subsequently measure with a spectrophotometer. The percentage viability was measured using a Trypan blue assay. The CellTiter-Glo® ATP Luminescence assay was used to determine the ATP generated in each experiment; this was then measured spectrophotometrically. Significant differences between experimental groups were designated as $p < 0.05$ (*), $p < 0.01$ (**) and $p < 0.001$ (***). All experiments were performed $n=4$.

3. Results

3.1. Characterization

Flow cytometry characterisation was used to detect the expression of stem cell and neuronal markers, where detection is represented by a histogram peak. An increased percentage to the right or right shift is indicative of increased expression and a left shift a decrease. Analysis (Figure 1) revealed that green and NIR-green laser light was the most effective in reducing stem-ness, as seen by the left shift in CD44 expression, indicating its effectivity in transdifferentiation. This study demonstrates the effectiveness of introducing green laser light to decrease stem-ness for transdifferentiation purposes. The right shift in early (NSE) and late (MAP2) neuronal markers 7 days post PBM treatment, albeit in very small percentages, is indicative of the iADMSCs being directed towards a neuronal fate.

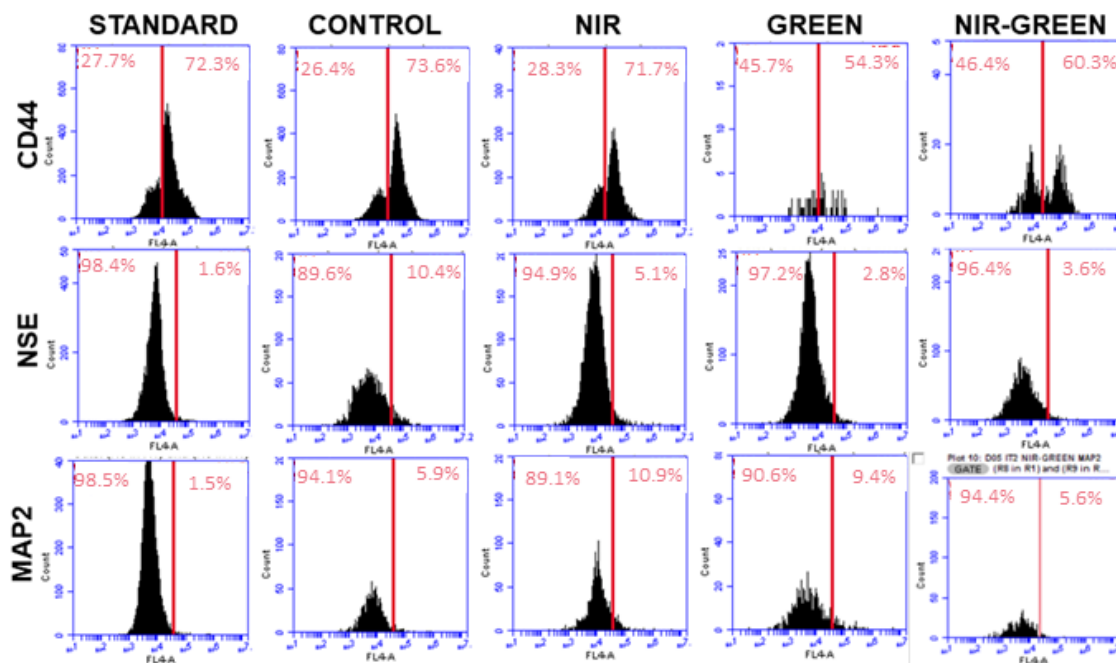


Figure 1. Flow cytometry characterization of stem cell marker CD44, early neuronal marker: Neuronal Specific Enolase (NSE), and late neuronal marker Microtubule-associated protein 2 (MAP2). A shift to the right of the red line indicated an increase in protein marker expression, whereas a shift to the left of the redline indicated a decrease in marker expression.

3.2. Cytotoxicity

Results showed an increase in LDH production in NIR and combination wavelengths 24 h following PBM treatment (Figure 2A). A significant increase was observed in all PBM treated experimental groups 48 h post PBM. NIR and green PBM significantly increased LDH concentration 7 days post irradiation. Although significant compared to the standard and control, these increases are not indicative of detrimental concentrations when compared to the positive control representing 100 percent toxicity and cell death.

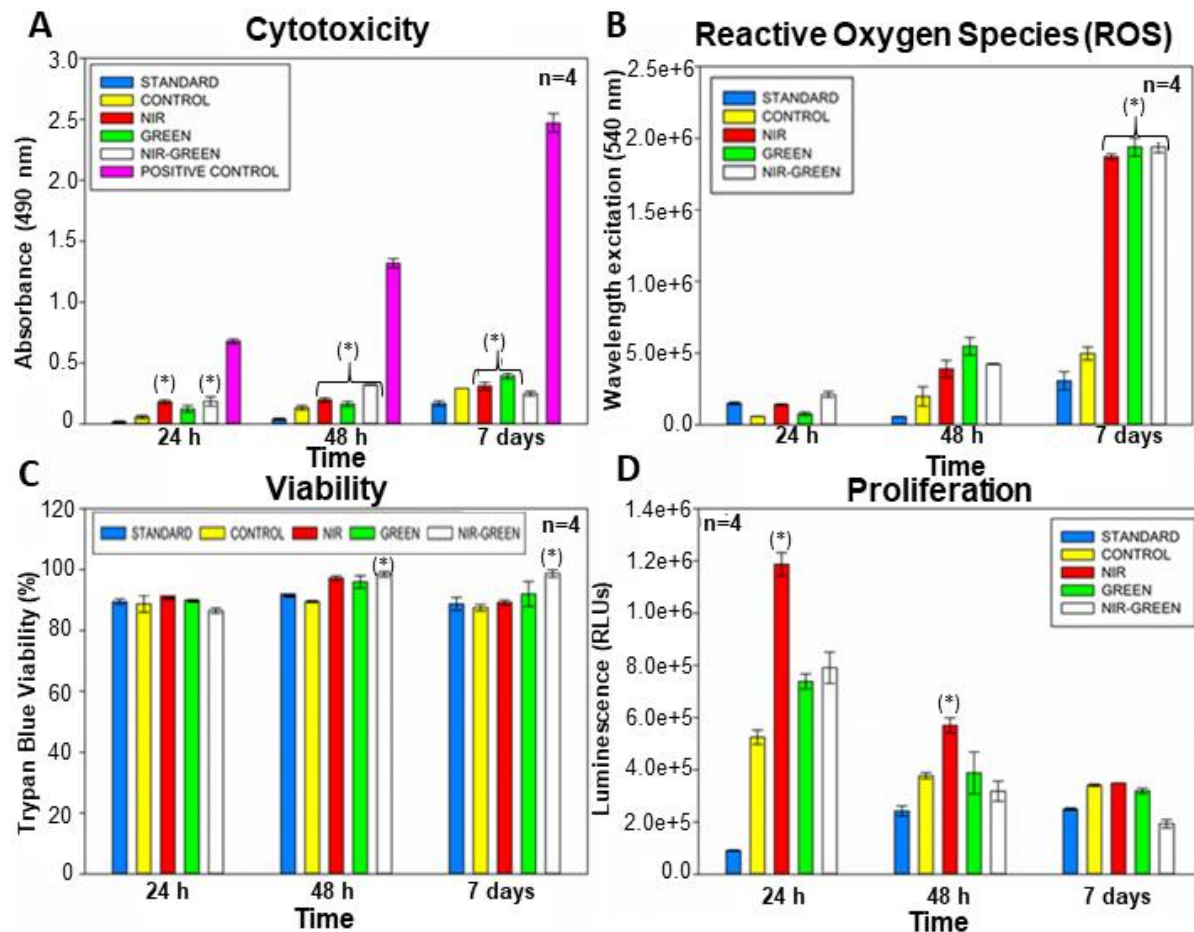


Figure 2. A. Cytotoxicity Lactate dehydrogenase (LDH) cytotoxicity assay. B. Reactive oxygen species (ROS) assay. C. Viability Trypan blue viability assay. D. Proliferation ATP luminescence assay.

3.3. Reactive oxygen species (ROS)

Increases in ROS activity is noted using NIR and concurrent PBM at 24 hours, and for all PBM groups at 48 hours albeit insignificant (Figure 2B). ROS production significantly increased in all PBM treated experimental groups 7 days post PBM exposure indicative of directing stem cell fate. As the increase in ROS was not detrimental to the cells as indicated by the viability results.

3.4. Viability

Biochemical analysis showed a consistency in percentage viability in the cells 24 h, 48 h, and 7 days post-PBM exposure (Figure 2C).

3.5. Proliferation

A significant increase in ATP was noted in the experimental group treated with NIR PBM 24 h and 48 h post PBM exposure (Figure 2D). PBM did not significantly increase proliferation 7 days post PBM exposure, however this can be due to the energy of the cells being redirected for differentiation rather than proliferation.

4. Discussion and Conclusion

Research has attempted to differentiate ADMSCs into multiple stem cell types, such as osteogenic or neuronal cells [5]. It has also been determined that these stem cells contribute to the repairing of damaged tissue cells. This study showed the ability of iADMSCs to differentiate into cells that carry neuronal cell markers and morphologically resemble premature neurons. This study also revealed that the differentiation process may be upregulated with PBM. Studies have been done to measure the effects of PBM on ADMSCs, however, the practice of consecutive wavelengths to exploit differentiation and proliferation has not been explored in great depth [3, 5], and can thus be considered a novel concept.

Analysis by flow cytometry revealed that the stem cell marker CD44, was maintained in most of the experimental groups. This suggests that large subpopulations of iADMSCs had not transdifferentiated. However, green and NIR-green PBM showed a significant decrease in CD44 marker expression, this is indicative of the cells losing their stemness and transitioning into a neuronal fate, as previous studies using ADMSC for differentiation into various cell lineages also indicated a decrease in stem cell marker expression [22]. This study showcases that the addition of green laser, with or without consecutive use, decreases cell stemness. Furthermore, it was seen that PBM facilitate differentiation of ADMSCs into neuronal like cells due to late neuronal marker detection seen 7 days post PBM treatment. Also, it is suggested to allow longer incubation periods for the cells to transdifferentiate which should bring about a greater increase in early and late neuronal marker expression [16].

Analysis of biochemical assays revealed that viability was maintained and remained unaffected regardless of treatment applied to the iADMSCs, therefore PBM does not have a detrimental effect on *in vitro* iADMSCs [3, 18]. The proliferation assays revealed a steady decrease in ATP production that was overall negligible. This decrease did not prove detrimental when comparing this to the cytotoxicity and viability results, perhaps indicating that cells are using their energy to differentiate rather than proliferate [19]. An assay to determine the amount of lactate dehydrogenase (LDH) released by the cell indicated significant increases by NIR and NIR-G groups 24 h post PBM, all three PBM groups 48 h post PBM, and in NIR and G PBM groups 7 days post PBM treatment. Nevertheless, when these significant increases are compared to the positive control of each period, the upregulation in LDH did not induce apoptosis. Finally, ROS studies showed that ROS concentrations increased as the population increases. Samples treated with PBM showed a significant upregulation in ROS production, however this was not detrimental to the cells when compared to the cytotoxicity studies and the viability results. A similar increase in ROS has been observed by Hu *et al* where the upregulation was tied to directing the stemness fate of the cells [20]. It should also be noted that an increase in ROS concentration is observed in neuronal developmental research and neuronal functionality studies [21].

In conclusion, the results of this study indicate that iADMSCs incubated for 7 days in media supplemented with chemical inducers and irradiated with PBM showed an upregulation in transdifferentiation. This is similar to previous research where G PBM upregulated differentiation and various wavelengths were not detrimental to cells. This study indicated that the addition of PBM prepared the cells for differentiation signified by the increase in ROS production observed in the PBM treated experimental groups. Green PBM shows significant potential for increasing the differentiation rate as seen in the decrease of CD44, indicating a loss of stem-ness at a faster rate than that of the other groups. Further studies will include incubating cells for a longer period prior to exposing cells to PBM to determine whether the goal of producing functional neuronal cells can be achieved.

References

- [1] Bajek A, Gurtowska N, Olkowska J, Kazmierski L, Maj M and Drewa T 2016 *Archivum Immunologiae et Therapiae Experimentalis* **64** 443-54
- [2] George S, Hamblin M R and Abrahamse H 2018 *Photomedicine and Laser Surgery* **36** 230-40
- [3] Mvula B, Mathope T, Moore T and Abrahamse H 2008 *Lasers in Medical Science* **23** 277-82
- [4] Wang Y, Huang Y-Y, Wang Y, Lyu P and Hamblin M R 2017 *Biochimica et Biophysica Acta- General Subjects* **1861** 441-9
- [5] Van Rensburg M J, Abrahamse H and Crous A 2020 *Current Stem Cell Research & Therapy*
- [6] Zuk P A, Zhu M, Mizuno H, Huang J, Futrell J W, Katz A J, Benhaim P, Lorenz H P and Hedrick M H 2001 *Tissue Engineering* **7** 211-28
- [7] Ateş G B, Ak A, Garipcan B and Gülsoy M 2018 *Lasers in Medical Science* **33** 1591-9
- [8] George S, Hamblin M R and Abrahamse H 2020 *Lasers in Surgery and Medicine* **52** 1032-40
- [9] Jang S, Cho H H, Cho Y B, Park J S and Jeong H S 2010 *BMC Cell Biology* **11**
- [10] Thompson R, Casali C and Chan C 2019 *Scientific Reports* **9** 1-10
- [11] Guy R and Offen D 2020 *Biomolecules* **10** 1320
- [12] Ateş G B, Ak A, Garipcan B and Gülsoy M 2020 *Cytotechnology* **72** 247-58
- [13] Fekrazad R, Asefi S, Eslaminejad M B, Taghiar L, Bordbar S and Hamblin M R 2019 *Lasers in Medical Science* **34** 115-26
- [14] Rosenberg N, Gendelman R and Noofi N 2020 *FEBS Open Bio* **10** 1276-87
- [15] Ge Y and Fuchs E 2018 *Nature Reviews Genetics* **19** 311-25
- [16] Ashjian P H, Elbarbary A S, Edmonds B, DeUgarte D, Zhu M, Zuk P A, Lorenz H P, Benhaim P and Hedrick M H 2003 *Plastic Reconstructive Surgery* **111** 1922-31
- [17] Wang Y, Huang Y-Y, Wang Y, Lyu P and Hamblin M R 2016 *Scientific Reports* **6** 33719
- [18] Nurković J, Zaletel I, Nurković S, Hajrović Š, Mustafić F, Isma J, Škevin A J, Grbović V, Filipović M K and Dolićanin Z 2017 *Lasers in Medical Science* **32** 151-60
- [19] Birket M J, Orr A L, Gerencser A A, Madden D T, Vitelli C, Swistowski A, Brand M D and Zeng X 2011 *Journal of Cell Science* **124** 348-58
- [20] Hu C, Zhao L, Peng C and Li L 2018 *Journal of Cellular Molecular Medicine* **22** 5196-207
- [21] Oswald M C, Garnham N, Sweeney S T and Landgraf M 2018 *FEBS Letters* **592** 679-91
- [22] Moraes, D.A., Sibov, T.T., Pavon, L.F., Alvim, P.Q., Bonadio, R.S., Da Silva, J.R., Pic-Taylor, A., Toledo, O.A., Marti, L.C., Azevedo, R.B. and Oliveira, D.M., 2016. *Stem cell research & therapy*, 7(1), pp.1-14.

Increasing efficiency of photodynamic therapy in in vitro cultured colorectal cancer cells by improved photosensitizer uptake

N W Nkune, C A Kruger and H Abrahamse

Laser Research Centre, Faculty of Health Sciences, University of Johannesburg, P.O. Box 17011, Doornfontein 2028, South Africa.

E-mail: cherier@uj.ac.za

Abstract. Colorectal cancer (CRC) is a fatal malignancy with limited therapeutic options and its incidence is on the rise in recent years. Photodynamic therapy (PDT) has emerged as a promising minimally invasive therapeutic modality that employs three fundamentals to induce tumour damage: a photosensitizer (PS), light of a specific wavelength and molecular oxygen. However, PDT has shown undesirable lack of specificity for tumour cells. The aim of this study was to develop a multicomponent nanoparticle-antibody (ZnPcS₄– AuNP-PEG5000-SH-NH₂ - Anti-GCC Ab) based system that is capable of enhanced ZnPcS₄ PS delivery within in vitro cultured CRC cells (CaCo-2) to increase the efficiency of PDT. The final conjugate was successfully synthesized and characterized to confirm the efficient binding of the antibody and PS to functionalized gold nanoparticle surfaces. Immunofluorescent results noted that the multicomponent PS nanoconjugate was able to enhance PS uptake in CRC cells, with far more significant cytotoxic responses post-PDT, when compared to PS administration alone. These findings suggest that this synthesized nano-antibody carrier could possibly enhance the in vitro PDT treatment of CRC, however future studies need to confirm its tumor selectivity by comparing its uptake in normal cells.

1. Introduction

Colorectal cancer (CRC) is the world's third most prevalent malignancy and the fourth leading cause of cancer-related mortality [1]. Treatment for CRC continues to be a formidable challenge in oncology due to eminent metastatic incidence and tumour recurrence [2]. Furthermore, currently available CRC conventional treatments such as surgical excision, chemotherapy, radiation therapy, targeted and immunotherapy have rarely yielded appreciable prognosis and are hampered by undesirable side effects in patients [2]. Thus, it remains imperative to develop other therapeutic approaches with increased potency and negligible side effects.

In recent years, photodynamic therapy (PDT) has emerged as a favourable approach to obliterate different cancers [2]. It is based on the uptake of photosensitizer (PS) by tumor cells and subsequent activation of the PS by laser light at a specific wavelength. The activated PS then reacts with molecular oxygen within tumours to generate cytotoxic reactive oxygen species (ROS) [3]. PSs have minimal dark and administration toxicity [4,5]. Preferentially when PSs are administered alone, they tend to passively accumulate more in cancer cells, due to their intrinsic overexpression of low-density

lipoprotein (LDL) receptors [4,5]. However, in most cases this passive accumulation does not render a high enough PS concentration uptakes to produce significant forms of PDT induced cancer cell death [4,5]. Thus, since PDT is non-invasive, with minimal toxicity in comparison to conventional therapies, it is imperative to conduct further research in terms of improving PS accumulation in cancer cells in order to induce significant forms of tumor destruction [4].

Zinc Phthalocyanine Tetrasulfonic acid (ZnPcS_4) is a promising metallated second generation PS which has been intensely investigated for PDT cancer applications due to its remarkable photophysical and photochemical properties [6]. It contains a zinc diamagnetic central atom, which produces high quantum ROS yields within the 680 nm wavelength range with minimal dark toxicity [7]. This compound also contains a number of sulfonated thiol groups, which increase its solubility, as well as its distribution in biological tissues and volume of distribution [7]. Studies reported that $\text{ZnPcS}_{\text{mix}}$ PS and 680 nm laser irradiation at a fluency of 5 J/cm^2 , induced a significant 60% of apoptotic cell death within in vitro cultured CRC cells [4]. However, despite the many remarkable attributes PDT has had in oncology, when PSs are administered alone, they inherently are hydrophobic and so tend aggregate when subjected to aqueous conditions [8]. This aggregation profoundly hampers their quantum ROS yields, as well as their bioavailability at target sites [8]. To overcome this issue, nanoparticles (NPs) are often combined with PSs to significantly improve their solubility, through their hydrophilic properties and so enhance PS cellular uptake in cancer cells [8].

Gold nanoparticles (AuNPs) have gained a great deal of attention in PDT applications due to their remarkable photostability, highly modifiable surface chemistry, strong absorption within the near infrared region, high biocompatibility, localized plasmon resonance and high loading capacity [9]. Studies have reported that AuNPs improve PDT treatment outcomes as they protect PSs from biological barriers and so promote passive uptake [6]. Nevertheless, NP PS delivery systems cannot exclusively identify malignant cells and so PS uptake is still often too low, to induce significant forms of PDT tumor cell destruction [10]. Thus, in an effort to enhance PS accumulation in cancer cells, research has focused on the development of antibody NP-based PS delivery platforms [2,8]. Studies by Naidoo et al. (2019) have shown that by developing NP-based PS delivery platforms which have anti-antibody moieties immobilized on their surface (which can identify overexpressed antigens on the surface of malignant cells), PDT tumor cell destruction outcomes are often enhanced, since the selectively bound anti-antibodies promote improved PS uptake and retention [6].

This study combined an efficient cytotoxic oxygen generating hydrophilic tetra sulphonated metal-based Zinc Phthalocyanine Tetrasulfonic Acid PS (ZnPcS_4) with CRC-specific targeting antibodies Anti-Guanylate Cyclase (Anti-GCC Ab) on the surface of heterobifunctional PEG amine stabilized AuNPs to enhance PS uptake and retention within in vitro cultured CRC cells, in order to improve PDT tumor cell destruction.

2. Methodology

2.1. Chemical Synthesis of Final Nano Bioconjugate

1 ml of AuNP-PEG5000-SH-NH₂ (Sigma-Aldrich 765309) were added to 1 ml of 125 μM ZnPcS_4 (w/v in 0.001M PBS) (Santa Cruz® Biotechnology, sc-264509A) and vortexed overnight at room temperature at 1500rpm to promote spontaneous ligand exchange and absorption. The mixture was then purified by centrifugation (18000rpm for 1hr) and the pellet was resuspended in 1ml 0.001 PBS. To bind the Anti-GCC Ab (ab122404) to the AuNP- ZnPcS_4 nanocomposite, an amide bond was achieved using two-step coupling chemistry. The carboxylic terminus of the Anti-GCC Ab was activated with EDC N-(3-Dimethylaminopropyl)-N'-ethylcarbodiimide hydrochloride and N-Hydroxysulfosuccinimide sodium salt. 200 $\mu\text{g/ml}$ of activated Anti-GCC Ab was then added to 1 ml of AuNP- ZnPcS_4 nanocomposite and vortexed overnight to allow for the activated carboxylic moiety succinimidyl ester of the Ab to react with the amine functionalized group on AuNPs so a strong amide bond could be established. Characterization of this final nano bioconjugate (FNBC) was conducted using UV-visible spectroscopy.

2.2. Cell Culture, Dose Response, FNBC and PDT Laser Irradiation Assays

Commercially purchased CaCo-2 CRC cell line CaCo-2 (Cellonex Cat SS1402 CCAC-FL; CCAC-C) was used in this study. Cells were cultured in Dulbecco's Modified Eagle Medium (D5796, Sigma Aldrich) enriched with 10% Foetal Bovine Serum (FBS), 4mM sodium pyruvate, 4mM L-glutamine, 2.5 g/ml amphotericin B, and 100 U Penicillin 100 g/ml streptomycin solution in an 85% humidified condition at 37°C and 5% CO₂. Control and experimental culture dishes were seeded with cells at a density of 6×10^5 cells and incubated for 4hrs to allow for attachment. Dose response studies were performed to determine the lowest concentration of ZnPcS₄ PS alone, which could yield 50% cytotoxicity (ICD₅₀), in order to determine the optimum concentration PS loading required within the FNBC. Within FNBC assays control groups received ZnPcS₄ or ZnPcS₄-AuNP treatments, whereas experimental groups received FNBC treatments. After ZnPcS₄ PS dose response or FNBC additions, culture plates were incubated for an additional 20 hrs. Post 24 hrs groups which required PDT laser treatment were irradiated using a continuous semiconductor diode laser (Oriel Corporation) at wavelength of 673 nm, with a fluence of 10 J/cm². Following treatment, all control and experimental groups were further incubated for 24 hrs in fresh media, before cytotoxicity and cell death analysis assays were performed.

2.3. Subcellular Localization of FNBC

CaCo-2 cells were seeded at density of 6×10^5 cells/ml in culture dishes containing a coverslip and post attachment received ZnPcS₄, ZnPcS₄-AuNP or FNBC only without irradiation. After 24h of incubation, the cells were stained for 30min with 2 µg/ml ICAM-1 mouse monoclonal IgG1 (AbAB2213 AC: Abcam) and 5 µg/ml Goat anti-mouse IgG-FITC (AB6785 AC: Abcam) on ice, respectively. Thereafter, the cells were stained with µl of 1µg/ml DAPI for 5 min and rinsed with HBSS. The coverslips were then mounted on slides and examined using the filter settings of a Carl Zeiss Axio Z1 Observer immuno fluorescent microscope.

2.4. Cellular Cytotoxicity

CytoTox96® non-radioactive assay (Promega G1780) assay was used to measure lactate dehydrogenase (LDH) released from cellular supernatant cytosol to detect membrane damage prior and post treatment.

2.5. FNBC Cell Death Analysis

Annexin V-FITC/PI cell death detection kit (BD Scientific: BD/556570), was used for detection and quantitation of cells undergoing early or late apoptosis, cells dying from necrosis cells, or cells remaining viable post-PDT treatment using the BD Accuri™ C6 flow cytometer.

3. Results and Discussion

3.1. PS Dose Response Studies

With reference to Figure 1, cells treated with varying doses of ZnPcS₄ PS alone, showed no statistical significance in LDH release, when compared to untreated control cells. Irradiated cells incubated with 0.0625 µM to 0.25 µM ZnPcS₄ produced significant dose-dependent increases in the amount of LDH released, when compared to untreated control cells. Within irradiated cells groups treated with 0.125 µM ZnPcS₄, a significant 45% (indicated by ** in Figure 1) of LDH cytotoxicity was reported and so was the recommended ICD₅₀ concentration, which was utilized within FNBC experiments.

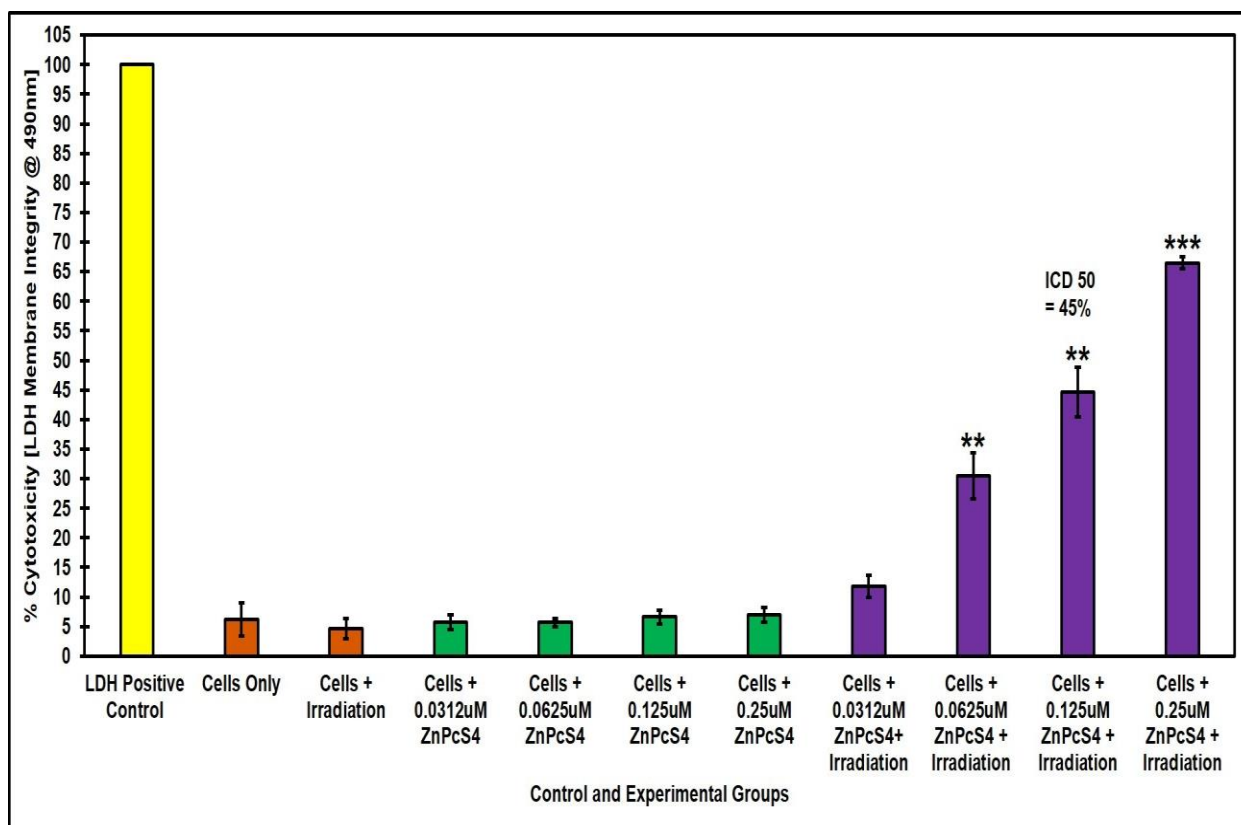


Figure 1. Varying doses of ZnPcS₄ administered to CaCo-2 cells with and without laser irradiation showing a dose-dependent increase in the amount of LDH release.

3.2. Characterization of the FBNC

With reference to Figure 2, ZnPcS₄ and AuNP-PEG5000-SH-NH₂ retained their respective visible absorption peaks after FBNC conjugation, however with some reduction in absorption, suggesting that these two compounds had successfully bound together. The FBNC noted a slight shift in the resonance peak position of AuNP at 520 nm, signifying that the Anti-GCC Ab had been successfully conjugated to its surface. Moreover, the FBNC retained its prominent ZnPcS₄ 673 nm absorbance peak, which meant that the photochemical characteristics of the PS were conserved after conjugation, suggesting that PDT experiments were possible. A slight broadening in the absorption peaks of the FBNC was seen since additional conjugates increased its overall molecular size. Furthermore, the peaks remained smooth suggesting no aggregation occurred. Overall, the FBNC consisted of 0.95×10^{15} particles/ml AuNPEG5000-SH-NH bound to 35 μ M of ZnPcS₄ in 0.001 M PBS (w/v), which was diluted to 0.125 μ M ZnPcS₄ in relation to the recommended ICD₅₀ PS dose concentration that was reported above.

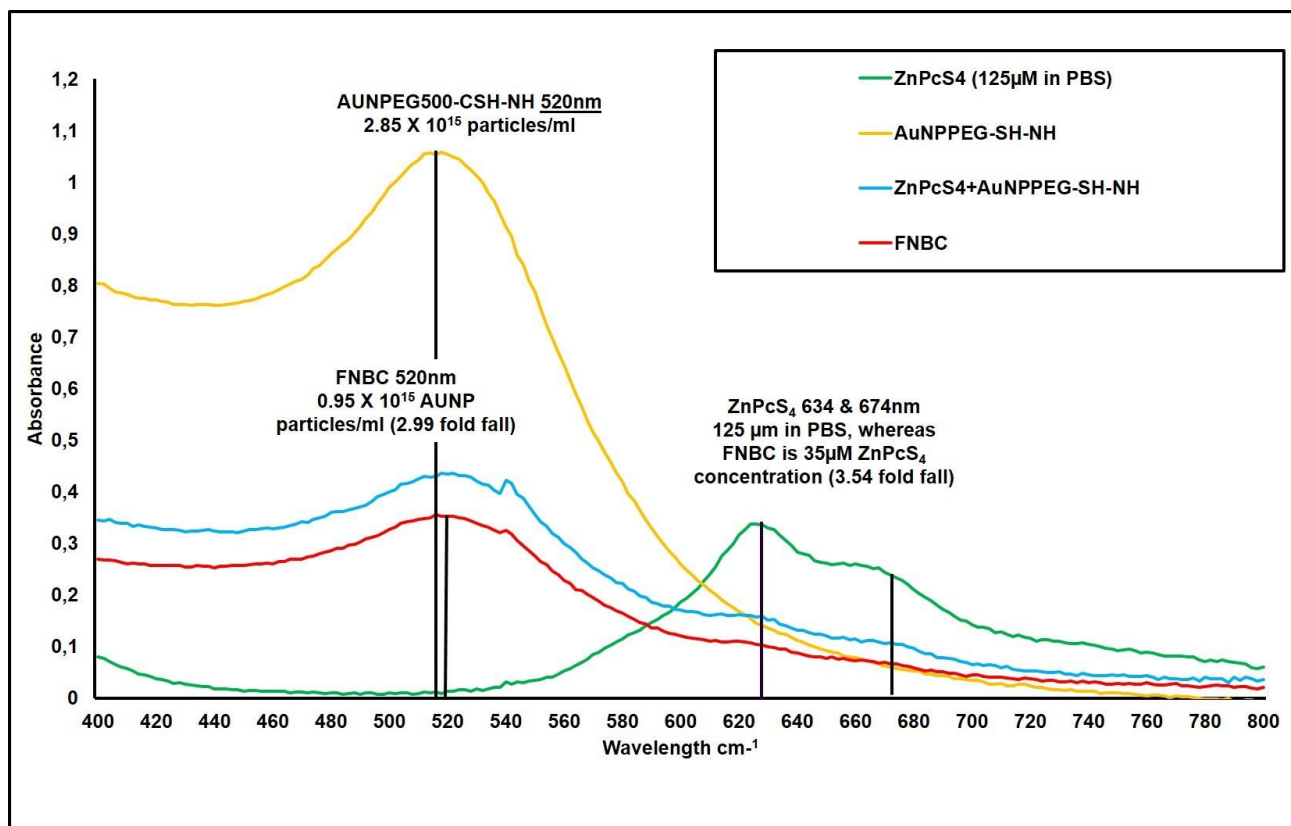


Figure 2. UV-Visible absorption spectral and fluorescence analysis of the FNBC and control groups.

3.3. Subcellular Localization Studies of the FNBC

Live cell immunofluorescent staining and imaging noted a far more improved PS bioavailability in CRC cells which received the FNBC, versus ZnPCs₄ PS or ZnPCs₄-AuNP alone control administrations (Figure 3). This improved PS accumulation in CRC cells can be observed by the increased red intensity observed in images, which received the FNBC.

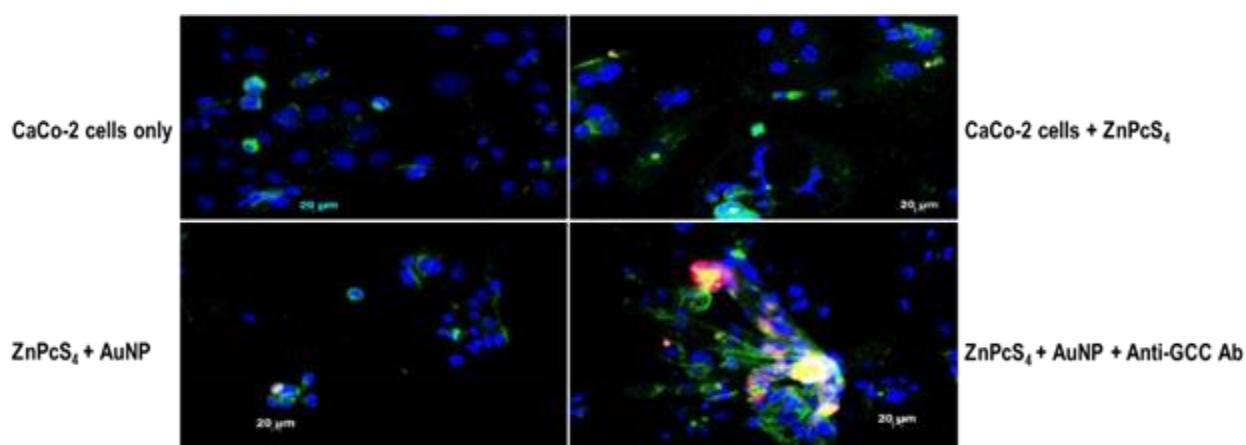


Figure 3. Subcellular localization of ZnPCs₄ PS alone, ZnPCs₄-AuNP and FNBC within CaCo-2 cells, showing blue stained DAPI nuclei, green stained cellular membrane proteins and red fluorescent ZnPCs₄ PS localization.

These findings suggest that the Anti-GCC Ab within the FNBC enhanced the ZnPcS₄ PS accumulation within CRC far more superior than its administration alone. Considering that the only difference within the experimental FNBC group versus the control groups was the fact that it contained Anti-GCC Ab, these results are suggestive that the anti-antibody must have promoted this improved PS uptake. However, in order to confirm if this enhanced FNBC PS uptake in CRC cells was due to selective tumor targeting, future research would need to be conducted in normal cells.

3.4. Cell Death Analysis of the FNBC

Annexin V-FITC/PI cell death detection kit was used differentiate between live, apoptotic, and necrotic forms of cell death in CRC cells. With reference to Figure 4, no significant differences in cell death percentages were noted in control groups which received laser irradiation, ZnPcS₄ PS, ZnPcS₄-AuNP or FNBC alone when compared to the cells only control, which received no treatment.

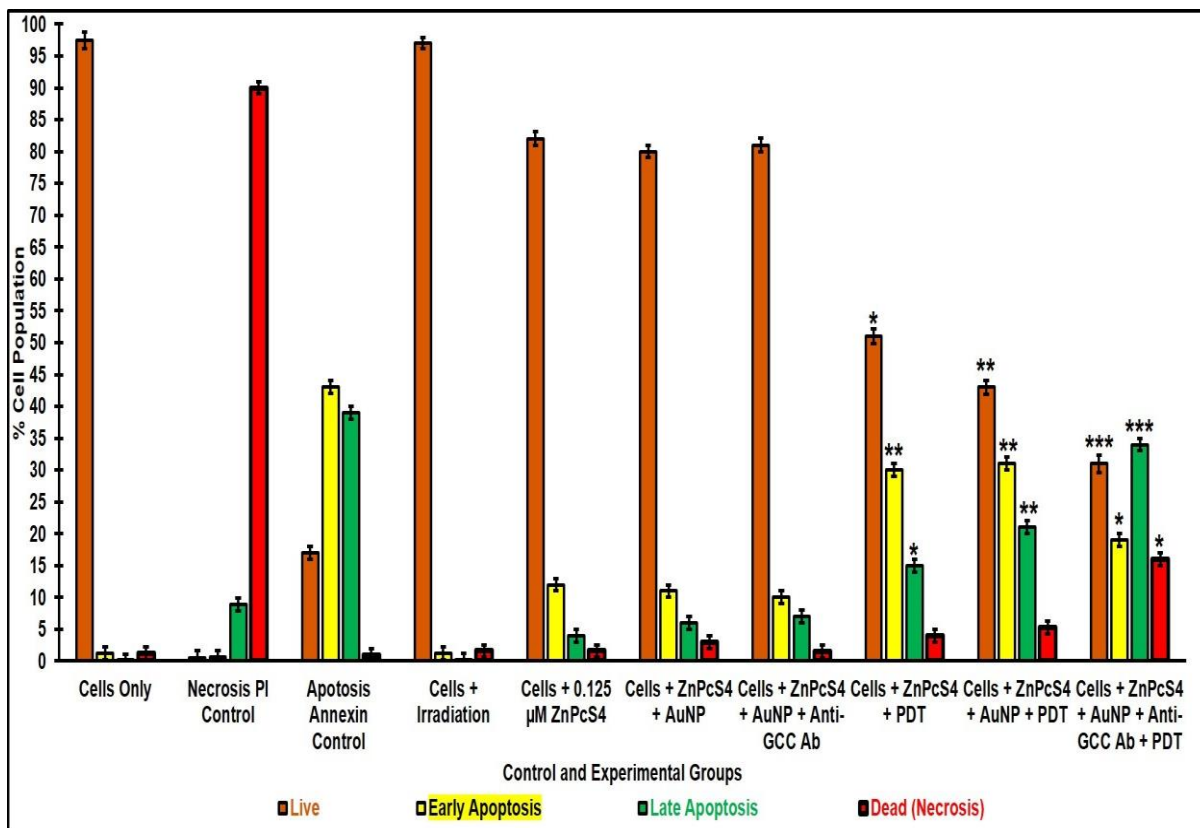


Figure 4. Cell death analysis of control and experimental groups

Irradiated experimental groups which received ZnPcS₄ PS, ZnPcS₄-AuNP or FNBC noted significant increases in apoptotic cell death, with lowered cellular viability. However, irradiated experimental groups treated with ZnPcS₄ PS alone, exhibited less significant late apoptotic cell death (15% - indicated by * in Figure 4), when compared to groups which were treated with ZnPcS₄-AuNP (21% - indicated by ** in Figure 4). Furthermore, when comparing these two experimental groups to irradiated FNBC treated cells, a highly significant apoptotic cell death (34% - indicated by *** in Figure 4), with a significant increase in necrotic cell death (16% - indicated by * in Figure 4) was found. Studies have reported that the most favored modes of cell death in relation to successful PDT treatment outcomes are late apoptosis and necrosis, since they destroy cells beyond recovery, unlike early apoptosis, whereby cells can rejuvenate causing potential tumour reoccurrence [6]. Irradiated

experimental groups which were treated with ZnPcS₄ PS alone, possibly did not exhibit as much significant late apoptotic cell death (15%), since studies have noted that when this PS is administered alone it tends to aggregate due to its hydrophobic nature, hindering its PS accumulation in cancer cells and so limits its overall PDT cell death outcomes [8]. The significant 21%** late apoptosis observed in irradiated groups treated with ZnPcS₄-AuNP, was attributed to the fact that the PS was conjugated to AuNPs and studies have reported that they improve the passive uptake of PSs in cancer cells due to their hydrophilic nature [8]. The highly significant and favorable forms of PDT induce cell death (34%*** late apoptosis and 16%* necrosis) which was found in irradiated groups which received FNBC, was possibly due to the fact that FNBC had Anti-GCC conjugated onto its surface, since previous studies have noted that antibody moieties immobilized on NP surfaces can promote improved PS uptake and retention in cancer cells [6]. However, in order to fully realize and confirm if the improved PS uptake in CRC cells was due to the FNBC selective targeting abilities future studies using comparative normal cells needs to be investigated.

4. Conclusion

ZnPcS₄ PS was successfully conjugated onto AuNP-PEG5000-SH-NH₂ NPs surface to increase its solubility and uptake in CRC cells. Furthermore, Anti-GCC Ab was immobilized onto AuNP-PS surfaces to observe if the FNBC was capable of even further enhanced PS retention in CRC cells. Subcellular localization assays revealed that the FNBC significantly increased the intracellular accumulation of ZnPcS₄ within CRC cells far more than the administration of ZnPcS₄ PS alone or when conjugated to AuNPs. Furthermore, the FNBC post PDT induced a far more significant cell death, when compared to ZnPcS₄ PS, or ZnPcS₄-AuNP treatment alone. These findings suggest that the conjugation of Anti-GCC Ab to ZnPcS₄-AuNPs, enhanced PS delivery in CRC cancer cells. Overall, FNBC showed enhanced cellular PS retention in CRC cells and so improved PDT cytotoxic treatment outcomes enormously. However, this study warrants further investigation to compare the uptake between in vitro cultured CRC and normal cells in order to determine whether the improved PS uptake in CRC cells was due to selective Anti-GCC Ab targeting.

Acknowledgements

This work is based on the research supported by the South African Research Chairs Initiative of the Department of Science and Technology and National Research Foundation of South Africa (Grant No 98337) and National Research Foundation Thuthuka Fund (Grant No TTK180409318735).

References

- [1] Mármol I, Sánchez-de-Diego C, Pradilla Dieste A, Cerrada E and Rodriguez Yoldi M J 2017 *Int. J. Mol. Sci.* **18** 197
- [2] Nkune NW, Kruger CA and Abrahamse H 2021 *Anticancer Agents in Med Chem* **2** 137-48
- [3] Muniyandi K, George B, Parimelazhagan T and Abrahamse H 2020 *Molecules* **18** 4102
- [4] Sekhejane PR, Houreld NN and Abrahamse H 2014 *Int. J. Photoenergy* **2014** 2014
- [5] Kwiatkowski S, Knap B, Przystupski D, Saczko J, Kędzierska E, Knap-Czop K, Kotlińska J, Michel O, Kotowski K and Kulbacka J 2018 *Biomed Pharmacother* **106** 98-107
- [6] Naidoo C, Kruger CA and Abrahamse H 2019 *Oncotarget* **10** 6079
- [7] Nombona N, Maduray K, Antunes E, Karsten A and Nyokong T 2012 *J Photochem Photobiol* **107** 35-44
- [8] Hong EJ, Choi DG and Shim MS 2016 *Acta Pharm Sin B* **6** 297-307
- [9] Montaseri H, Kruger CA and Abrahamse H 2021 *Pharmaceutics* **13** 296
- [10] Mokwena MG, Kruger CA, Ivan MT and Abrahamse H 2018 *Photodiagnosis Photodyn Ther* **22** 147-154

Targeted Photodynamic Diagnosis of *In Vitro* Cultured Colorectal Cancer Cells

N W N Simelane, C A Kruger and H Abrahamse¹

Laser Research Centre, Faculty of Health Sciences, University of Johannesburg, P.O. Box 17011, Doornfontein 2028, South Africa.

E-mail: cherier@uj.ac.za

Abstract. Colorectal cancer (CRC) currently remains a challenge to diagnose and is the third most diagnosed cancer worldwide. Photodynamic diagnosis (PDD) is a promising early diagnostic approach which uses photosensitizers for fluorescence detection of malignant cancer cells without inducing tumour damage. In this study, ZnPcS₄ a photosensitizer with pronounced chemical properties due to its tetra sulphonation was incorporated with specific CRC targeting antibodies (Anti-GCC Ab) on the surface of heterobifunctional aminefunctionalized and PEG stabilized gold nanoparticles (AuNPs), to form a final actively targeted PS nanoconjugate (ZnPcS₄ – AuNP-PEG5000-SH-NH₂ – Anti-GCC Ab). The final actively targeted PS nanoconjugate was successfully synthesized and characterized using spectroscopic techniques. Immunofluorescent photodiagnostic results confirmed that the final actively targeted PS nanoconjugate was able to localize within in vitro cultured CRC cells more specifically, due to its active targeting biomolecule (Anti-GCC Ab) than PS treatment alone. The final targeted PS nanoconjugate offered highly specific and sensitive absorption of the PS in CRC cells and so allowed for the successful photodynamic diagnosis of CRCs in vitro.

1. Introduction

Colorectal cancer (CRC) remains the fourth most commonly diagnosed cancer and represents about 9.4% of all estimated cancer deaths worldwide [1,2]. Additionally, CRC is the sixth leading cause of cancer death in South Africa [3]. Conventional CRC diagnostic techniques are often limited for early detection, as they lack specificity and are often invasive [4]. Moreover, the poor prognosis and decreased survival rate when CRC is identified at advanced stages raise a demand for an early diagnostic modality that can reduce cancer mortality [5].

Photodynamic diagnosis (PDD) is an emerging minimally invasive technique that may be utilized as an alternative option for the diagnosis of malignant disorders [6]. This technique offers advantages such as selective targeting and primary localized within tumor cells for specific identification [6]. The PDD technique relies on the combined use of an administered tumor targeted photosensitizer (PS), that when excited by blue light, emits a strong fluorescence signal that can be used to precisely diagnose cancer [5,7].

Zinc Phthalocyanine Tetrasulfonic acid (ZnPcS₄) is a hydrophilic metallated PS that has been found to exhibit great potential in CRC photodynamic studies, due to its prolonged lifespan and passive absorption in tumor cells [8–10]. Since, ZnPcS₄ exhibits a characteristic short-blue B absorption band, between 330 to 350 nm, this particular PS could be possibly utilized within PDD applications [9].

Nanoparticles (NPs) are attractive carriers of PSs in PDD applications for improved diagnostic outcomes, since they enhance the PS accumulation in tumor cells via the enhanced permeability and retention effect (EPR), as well as can be further modified with specific tumor receptive site biomarker targets (such as antibodies), which promote active precise PS absorption in marked tumors [11]. Gold nanoparticles (AuNPs) are the most promising PS carrier in photodynamic applications, since they have

¹ To whom any correspondence should be addressed.

a large surface area to accommodate high PS loading, as well as provide PS protection from biological barriers due to their immune biocompatibility [12]. Additionally, the large surface area of AuNPs accommodates further functionalization with various targeting moieties to deliberately enhance targeted active uptake and specific cellular localization of PSs for overall improved PDD outcomes [13].

Overall, the use of the active targeting approach that exploits the modification of NP-PS with celltargeting ligands, such as monoclonal antibodies (mAb) is a highly sought-after strategy in PDD applications, since it promotes PS internalization and accumulation and so enhanced specific and highly accurate cancer diagnosis outcomes [11]. The transmembrane receptor protein, guanylyl cyclase C (GCC) has been reported to be specifically overexpressed in CRC cells and so can be used as an active target biomarker within passive NP-PS conjugates to improve PS internalization for precise PDD [14].

Within this study, Anti-GCC monoclonal antibodies (mAbs) moieties were loaded onto AuNPs which were conjugated to ZnPcS₄ PSs, in order to construct a final targeted nanobioconjugate (BNC), that could possibly increase specific PS localization within in vitro cultured CRC and so enhance PDD precision.

2. Methodology

2.1. Chemical Synthesis and Molecular Characterization of the BNC

The final bionanoconjugate: ZnPcS₄ – AuNP-PEG5000-SH-NH₂ – Anti-GCC mAb (BNC) was synthesized according to Naidoo and co-workers [15]. Briefly, the ZnPcS₄ PS was conjugated onto the surface of AuNP-PEG5000-SH-NH₂ (Sigma-Aldrich: 765309), using spontaneous ligand exchange (between Au and PS tetra sulphides) and adsorption (disulphide bond between PEG and PS) techniques. 200µg/ml of Anti-GCC mAb (Abcam: ab122404) were activated using covalent mode carbodiimide crosslinker two-step coupling and bound to the surface of the already conjugated ZnPcS₄ PS - AuNP-PEG5000-SH-NH₂, using EDC and NHS chemistry. The BNC was then subjected to UV Visible, DLS and ZP characterization, as well as immunofluorescent staining.

2.1.1. UV-Visible Spectroscopy

The BNC contained ZnPcS₄ PS, which is known to absorb at 350nm (Soret Band) and emits at 583, 634 and 674nm (Q band) ranges in PBS [9]. The photostability of the BNC and its characteristic Soret and Q bands values were measured and confirmed using UV-Vis spectroscopy over the duration of experimental assays (8 weeks).

2.1.2. Light Scattering (DLS) and Zeta potential

Particle size and zeta potential (ZP) of the BNC were measure by dynamic light scanning (DLS) on a Malvern Zetasizer Nano ZS (Malvern Instruments, Malvern UK), equipped with a 4mW He-Ne laser at a 633nm wavelength at 25°C, in triplicate, with all appropriate controls.

2.2. Cell Culture

Human colon cancer CaCo-2 (CaCo-2 Cellonex Cat SS1402) and normal human fibroblasts WS1 (ATTC CRL-1502) cell lines were cultured in DMEM Media or MEM media, respectfully, supplemented with 10% Foetal Bovine Serum (FBS), 4mM sodium pyruvate, 4mM L-glutamine, 2.5g/ml amphotericin B, and 100U Penicillin 100g/ml streptomycin solution. The cells were maintained in a humidified incubator with atmosphere of 5% CO₂ at 37°C. Upon confluency, the cells were harvested using TrypleSelect™ and seeded into a 3.4cm culture plates at a density of 6 x 10⁵ cells, which contained a sterile coverslip. Culture plates were incubated for 4hrs to allow for cellular attachment.

2.3. Photo Diagnostic Assays

To determine if the BNC could be selectively absorbed by CRC cells only (and not by normal fibroblast cells), in order to be utilized as a fluorescent marker for the early CRC PDD, intercellular cell adhesion

molecule-1 (ICAM-1) immunofluorescent membrane staining and fluorescent microscopy imaging assays were performed. Post 4hrs attachment culture plates received a predetermined effective dose of $0.125\mu\text{M}$ ZnPcS₄ PS only, ZnPcS₄ – AuNP-PEG5000-SH-NH₂ and BNC in 3ml of supplemented culture media to form various control and experimental groups. The culture plates were then incubated in the dark at 37°C overnight. Thereafter, the cells in the culture plates were rinsed using PBS and fixed with 3.7% paraformaldehyde for 10min at room temperature. The cells were then incubated with $2\mu\text{g/ml}$ ICAM-1 mouse monoclonal IgG1 (AbAB2213 AC: Abcam) and $5\mu\text{g/ml}$ Goat anti-mouse IgG-FITC (AB6785 AC: Abcam) on ice, for 30min at room temperature. After incubation, the cells were rinsed with HBSS, and the coverslips were mounted into microscope slides. Immuno fluorescent microscopic images were captured with a Carl Zeiss Axio Z1 Observer with FITC green (cell membranes) and DAPI blue (ZnPcS₄ PS) detection filter fluorescent settings, at 400x magnification.

3. Results

3.1. Molecular Characterization of the BNC

3.1.1. UV-Visible Spectroscopy

The UV-vis spectra of the BNC, noted no significant changes or deformations over an 8 week period, suggesting that it remained photostable (Figure 1). Additionally, the 340nm Soret band for the ZnPcS₄ PS within the final BNC remained high and prominent suggesting it conserved its photochemical properties, without any quenching and so could be utilized within PDD CRC *in vitro* assays fairly successfully.

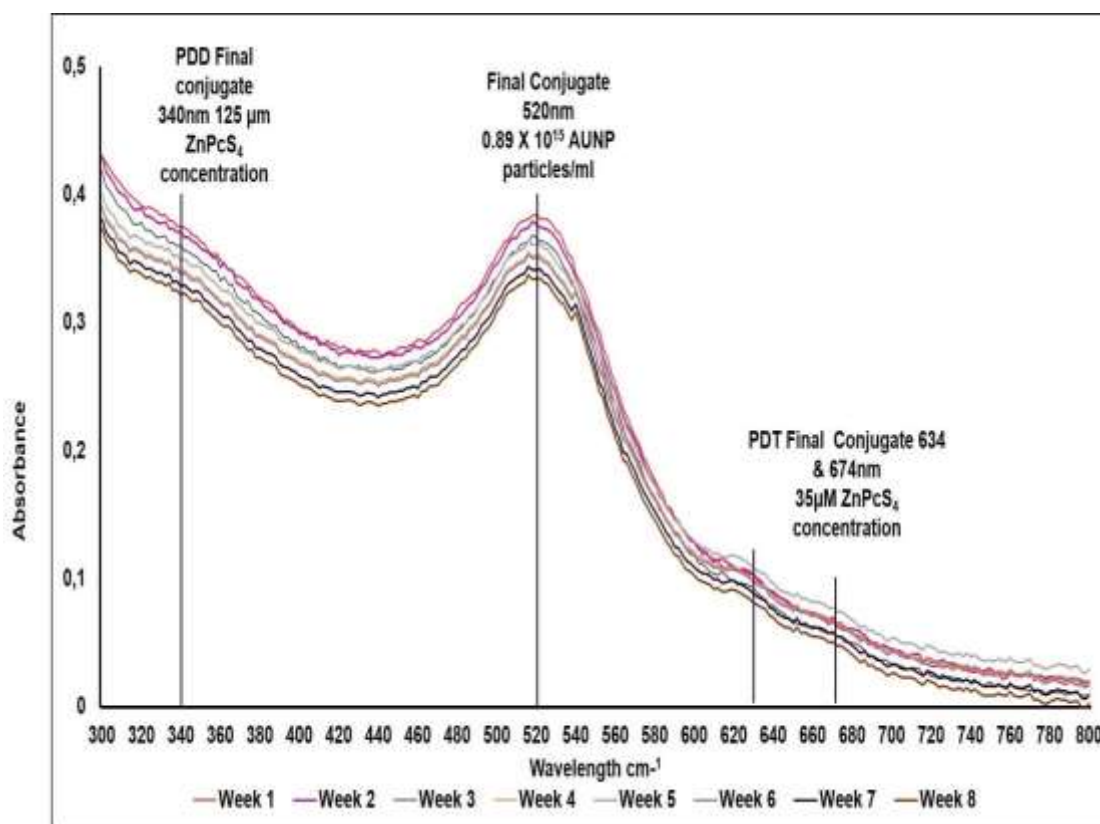


Figure 1. UV-vis spectroscopy measurements. Absorption spectra with respect to the ZnPcS₄ PS contained within the final BNC.

3.1.2. Dynamic Light Scattering (DLS) and Zeta Potential (ZP)

Within dynamic light scattering studies, the BNC reported one single major peak with a narrow width and no additional smaller side peaks, when repeated in triplicate (Figure 2). These findings demonstrated that a components of the final BNC were successfully bound [16]. Additionally, the DLS Polydispersity Index (PDI) value of the final BNC was found to be 0.353, reporting that it was a single monodisperse homogenously pure molecule, that had no aggregation. ZP results reported the BNC had a mean hydrodynamic diameter of $57.18 \pm 3.04\text{nm}$, suggesting it was small enough for cellular absorption [17]. The final BNC had a ZP value $36.5 \pm 2.6\text{ mV}$, noting it was highly stable with a slight positively charge and should so would remain intact within an *in vivo* environment, as well as be retained more selectively by tumour cells which are negatively charged [16,18].

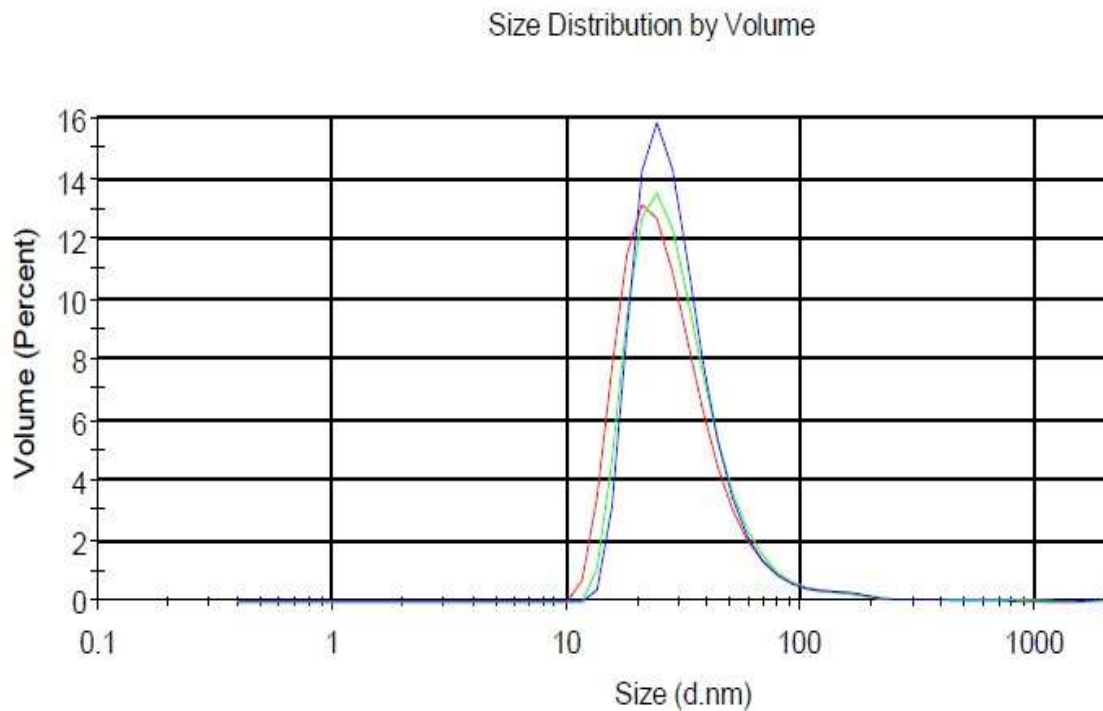


Figure 2. DLS hydrodynamic radius distribution graph of the final BNC.

3.2. Photo Diagnostic Assays

Fluorescent microscopy imaging was performed within various control and experimental groups to confirm the specific and targeted ZnPcS₄ PS absorption within CRC Caco-2 versus normal WS1 human fibroblast cells. Green immunofluorescent ICAM-1 / FITC membrane staining and ZnPcS₄ PS blue 340 nm fluorescence signals from the images were captured and examined. With reference to the first row of CRC images in Figure 3, the blue fluorescence intensity of ZnPcS₄ PS was far higher within the BNC experimental group than when compared to the other control groups. The control group of ZnPcS₄ PS alone reported less blue fluorescence intensity in CRC cells than when compared to the control group which received AuNP-PEG5000-SH-NH₂ - ZnPcS₄. These observations suggest that the AuNPs were responsible for improved passive localization of the PS in CRC cells than compared to when it is administered in singular form [19]. Nevertheless, the CRC experimental group which received the final BNC, noted the highest blue fluorescence intensity, suggesting the most significant uptake of ZnPcS₄.

PS was found. These observations suggest that the conjugated Anti-GCC mAbs, within the final BNC, successfully facilitated an active up-take of the PS, directed towards GCC overexpressed cellular surface receptors and so a far higher retention of the PS was found [14,20). With reference to the second row of WS1 normal human fibroblast images in Figure 3, the experimental cells which received the final BNC showed no selective or active accumulation retention of the blue stained ZnPcS₄ PS, in comparison to the control groups which received ZnPcS₄ PS alone or AuNP-PEG5000-SH-NH₂ - ZnPcS₄.

These observations suggest that the final BNC had no specific targeting affinity for normal human cells and so could be successfully utilized in PDD application to distinguish between normal and in vitro cultured CaCo-2 CRC cells, however if ZnPcS₄ PS was to be administered alone or in conjugation with AuNPs its cellular uptake would not be specific enough to differentiate between in vitro normal and CRC cultured cells.

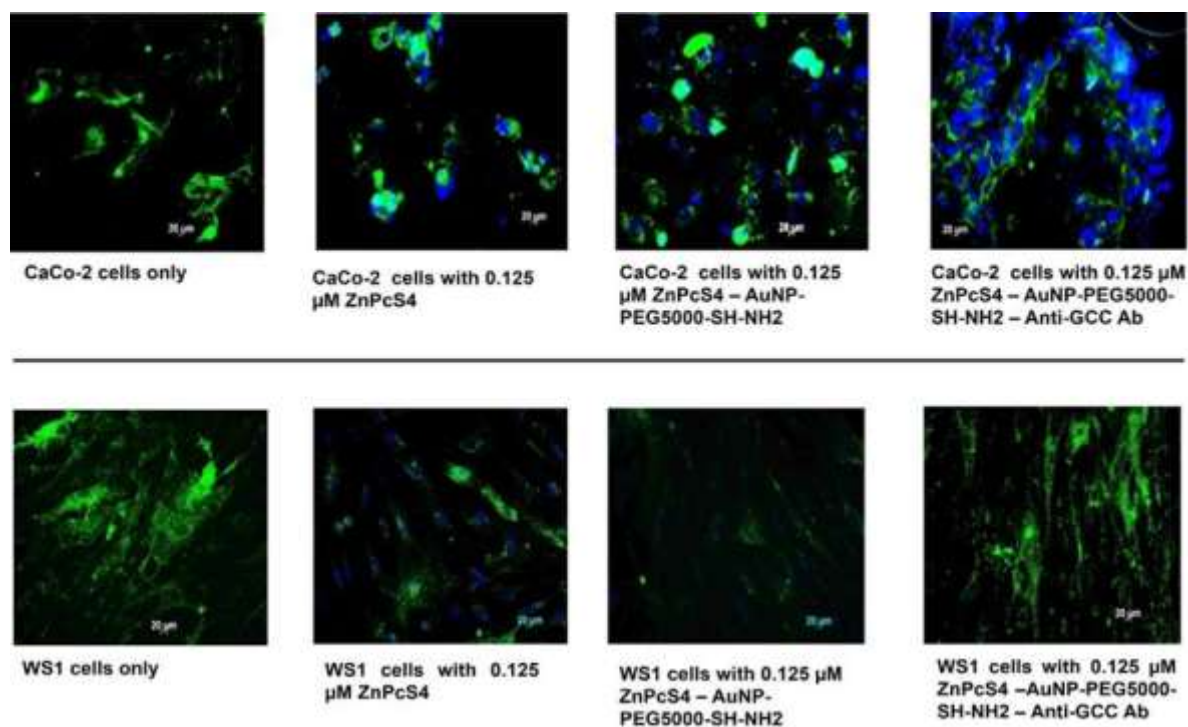


Figure 3. PDD fluorescent microscopy images comparison of ZnPcS₄ PS uptake in CRC CaCo-2 versus normal WS1 fibroblast cells, treated with ZnPcS₄ PS alone, AuNP-PEG5000-SH-NH₂ - ZnPcS₄, and the final BNC. Cellular ICAM membrane proteins (GREEN stain), and ZnPcS₄ PS localization (BLUE stain).

4. Conclusion

In conclusion, a novel final BNC, consisting of ZnPcS₄ PS with CRC specific targeting Anti-GCC mAbs conjugated to PEGlated AuNP was successfully synthesized. Molecular characterization assays confirmed that all components within the final BNC were successfully bound and that it displayed its signature Soret ZnPcS₄ PS PDD band at 340 nm. DLS and ZP results reported the final BNC was stable, monodisperse and of an acceptable size for cellular nano-targeting. Control groups which consisted of ZnPcS₄ PS bound to AuNP-PEG5000-SH-NH₂, did note an improved passive uptake of the PS for PDD in CRC, however owing to the attachment of the Anti-GCC mAbs within the final BNC, it reported a highly active, localized, and enhanced uptake of the ZnPcS₄ PS and so was capable of the specific and

targeted PDD identification of CRC, since it showed no affinity for normal human WS1 fibroblast cells. Overall, this study demonstrated that the final BNC could be a promising platform for early targeted photodynamic diagnosis of CRC and so requires *in vivo* investigation.

5. Acknowledgements

This work is based on the research supported by the South African Research Chairs Initiative of the Department of Science and Technology and National Research Foundation of South Africa (Grant No 98337), Cancer Association of South Africa (CANSA) Research Funding Grant and National Research Foundation Thuthuka Fund (Grant No TTK180409318735).

6. References

- [1] Rawla P, Sunkara T and Barsouk A 2019 *Prz Gastroenterol.* **14** 89–103
- [2] Sung H, Ferlay J, Siegel RL, Laversanne M, Soerjomataram I, Jemal A and Bray F 2021 *CA: Cancer J. Clin.* **71** 209-49
- [3] Brand M, Gaylard P and Ramos J 2018. *SAMJ.* **108** 118-22
- [4] Naidoo C, Kruger CA and Abrahamse H 2019 *Molecules* **24** 3153
- [5] Simelane NWN, Kruger CA and Abrahamse H 2020. *RSC Adv.* **10** 41560-76
- [6] Agostinis P, Berg K, Cengel KA, Foster TH, Girotti AW, Gollnick SO, Hahn SM, Hamblin MR, Juzeniene A, Kessel and D, Korbely M 2011 *CA: Cancer J. Clin.* **61** 250-81
- [7] dos Santos AF, de Almeida DR, Terra LF, Baptista MS and Labriola L 2019 *JCMT* **5**
- [8] Nombona N, Maduray K, Antunes E, Karsten A and Nyokong T 2012 *J Photochem Photobiol* **107** 35-44
- [9] Brozek-Pluska B, Orlikowski M, Abramczyk H, Kadish KM, Smith KM and Guillard R 2016 *Handbook of Porphyrin Science* **36** 1-49
- [10] Brozek-Pluska B, Jarota A, Kania R and Abramczyk H 2020 *Molecules* **25** 2688
- [11] Kruger CA and Abrahamse H 2018 *Molecules* **23** 2628
- [12] Dube E and Nyokong T 2019 *J. Lumin* **205** 532-9
- [13] Calavia PG, Bruce G, Pérez-García L and Russell DA 2018 *Photochem. Photobiol. Sci.* **17** 153452
- [14] Danaee H, Kalebic T, Wyant T, Fassan M, Mescoli C, Gao F, Trepicchio WL and Rugge M 2017 *PLoS One* **12** e0189953
- [15] Naidoo C, Kruger CA and Abrahamse H 2019 *Oncotarget* **10** 6079
- [16] Patel VR and Agrawal YK 2011 *J. Adv. Pharm. Technol. Res* **2** 81–7
- [17] Yu X, Trase I, Ren M, Duval K, Guo X and Chen Z 2016 *J. Nanomater* **2016**
- [18] Bhattacharjee S 2016 *J. Control. Release* **235** 337-51
- [19] Hong EJ, Choi DG and Shim MS 2016 *Acta Pharm. Sin. B.* **6** 297-307
- [20] Hodgkinson N, Kruger CA and Abrahamse H 2017 *Tumor Biol.* **10** 1010428317734691.

Photobiomodulated Differentiation of Adipose-derived Stem Cells into Osteoblasts.

D Da Silva¹, A Crous² and H Abrahamse²

^{1/2}Laser Research Centre, Faculty of Health Sciences, University of Johannesburg,
P.O. Box 17011, Doornfontein, Johannesburg, South Africa, 2028

²Email: habrahamse@uj.ac.za

Abstract. Osteoporosis is a progressive, metabolic bone disease affecting millions across the globe. Stem cell (SC) regenerative therapy has demonstrated potential in treating osteoporosis, particularly when using Adipose-derived Mesenchymal Stem Cells (ADMSCs). Photobiomodulation (PBM) has gained international momentum due to its ability to aid in the proliferation and differentiation of stem cells. Additionally, PBM when combined with differentiation growth factors has revealed enhanced proliferation and ADMSC differentiation into osteoblasts. This *in vitro* study combined the use of osteogenic differentiation inducers and PBM at a near-infrared (NIR) wavelength of 825 nm, a green wavelength of 525 nm and their combination wavelengths (825 nm and 525 nm) using a single fluence of 5 J/cm² to determine the proliferation and differentiation effectivity of ADMSCs into osteoblasts. The cells were characterised via the use of flow cytometry. Morphology was investigated and the biochemical assays performed include proliferation, viability, and cytotoxicity. The successful outcome of this study provides relevant scientific knowledge and a standardization for osteogenic differentiation *in vitro* using PBM.

1. Introduction

Osteoporosis is known as the most progressive mitochondrial bone disease in humans [1]. Osteoporosis is characterized by the increase in bone fragility leading to the increase in fracture occurrence [2]. Regenerative Medicine (RM) is currently the most promising branch of medical science used to repair or heal tissues and organs damaged by severe injuries, chronic disease or age [3]. At the frontline of RM stands SC therapy due to the characteristics of SCs including self-renewal and trans-differentiation into various cell types [4]. Adipose-derived Mesenchymal Stem Cell (ADMSC) transplantation can facilitate the development and strength of new bones, increase bone consistency and decrease the risk of fractures [5]. ADMSCs are easily isolated and harvested from adipose tissues via minimally invasive surgery, providing low risk of morbidity, a high abundance and a high yield in cell numbers [6]. The successful trans-differentiation of ADMSCs into osteogenic lineages *in vitro*, requires the addition of biological and chemical growth factors (GFs) within the cell culture medium [7]. However, ADMSCs have a tendency of favouring adipogenic lineages despite GF presence [8]. Therefore, lineage specific differentiation control is required via a combinational use of GF presence and a mechanical stimulant such as photobiomodulation (PBM) [9]. The use of visible and NIR light by coherent or incoherent light sources on cells and tissues is known as PBM [10]. Once endogenous chromophore absorption occurs, the light within various ranges brings about photophysical and photochemical responses. PBM is understood to aid in cell function, proliferation, migration and tissue regeneration due to the increased mitochondrial oxidative metabolism [11]. The potential stimulatory and inhibitory outcomes of PBM

on ADMSCs are wavelength and fluence dependant [12]. Cell proliferation has been suggested when stimulated by PBM using a wavelength of/between 660–850 nm and a fluence of/between 5 – 10 J/cm² [13], whereas wavelengths of 495–570 nm had been seen to affect differentiation [14]. The aim of this *in vitro* study was to combine the use of osteogenic differentiation inducers and PBM at a near-infrared (NIR) wavelength of 825 nm, a green wavelength of 525 nm and their combination wavelengths (825 nm and 525 nm) using a single fluence of 5 J/cm² to determine the proliferation and differentiation effectivity of ADMSCs into osteoblast cell lineages.

2. Materials and Methodology

Immortalized ADMSCs (ASC52telo hTERT, ATCC®SCRC-4000™) were cultured for one week in osteogenic differentiation media comprised of Dulbecco's Modified Eagle Media (DMEM) media, 10% Fetal Bovine Serum, 0.5% Penicillin-Streptomycin, 0.5% Amphotericin B solution, 50 nM Dexamethasone, 10 nM Beta-glycerol phosphate disodium and 0.2 mM Ascorbic acid. All cultured cells were kept in Corning® cell culture flasks and incubated at 37°C in 5% CO₂ and 85% humidity. The cultured immortalized ADMSCs were seeded at 1 x 10⁵ cells into treated culture dishes with a radius of 1,75 cm with 2 mL of osteogenic differentiation media. Prior to irradiation, the osteogenic differentiation media was refreshed. Cells were irradiated from above in the dark at room temperature with the petri dish lid taken off prior to irradiation to avoid negligible factors. The time of irradiation was calculated as follows:

$$mW/cm^2 = \frac{mW}{\pi \times (r^2)}$$

$$W/cm^2 = \frac{mW/cm^2}{1000}$$

$$Time (s) = \frac{J/cm^2}{W/cm^2}.$$

This study included an experimental standard whereby cells did not receive osteogenic growth factors nor PBM treatment and an experimental control of which cells received osteogenic trans-differentiation growth factors but weren't exposed to PBM treatment. The laser parameters are shown in Table 1. The cell samples were collected at 24 hours, 48 hours and 7 days post-irradiation. Cell characterization, via the use of flow cytometry as a qualitative assay, identified SC protein markers CD44 and CD166 presence on the immortalized ADMSCs. Morphology was identified by inverted light microscopy and biochemical assays such as Adenosine triphosphate (ATP) proliferation (Promega, G9241) [15], Trypan blue viability (Invitrogen™, T10282) and Lactate dehydrogenase (LDH) cytotoxicity (Promega, G1780) were performed. For statistical analysis, biochemical assays included n=3 biological repeats with technical duplicates. Statistical analysis was performed using SigmaPlot version 12 and the data was evaluated by a student t-test and one-way ANOVA. The statistical variances amongst the experimental groups were denoted on the figures as P < 0.05 (*), P < 0.01 (**) and P < 0.001 (***).

Table 1. Laser Parameters

Laser Parameters	Near infra-red (NIR)	Green (G)
Light Source	Diode Laser	Diode Laser
Wavelength (nm)	825	525
Power Output (mW)	515	553
Power Density (mW/cm ²)	53.53	57.47
Area (cm ²)	9.62	9.62
Emission	Continuous Wave	Continuous Wave
Fluence (J/cm ²)	5	5
Irradiation Time (sec)	93	86

3. Results

Flow cytometry characterisation was used to detect the expression of stem cell and neuronal markers, where detection is represented by a histogram peak. An increased percentage to the right or right shift is indicative of increased expression and a left shift a decrease. Flow cytometry analysis (Figure 1) demonstrated a left shift, CD44 and CD166 SC protein marker expression by all experimental groups at 7 days post-PBM treatment. This implies the effective use of PBM to reduce stem-ness and be an efficient tool for trans-differentiation of immortalized ADMSCs into osteoblasts.

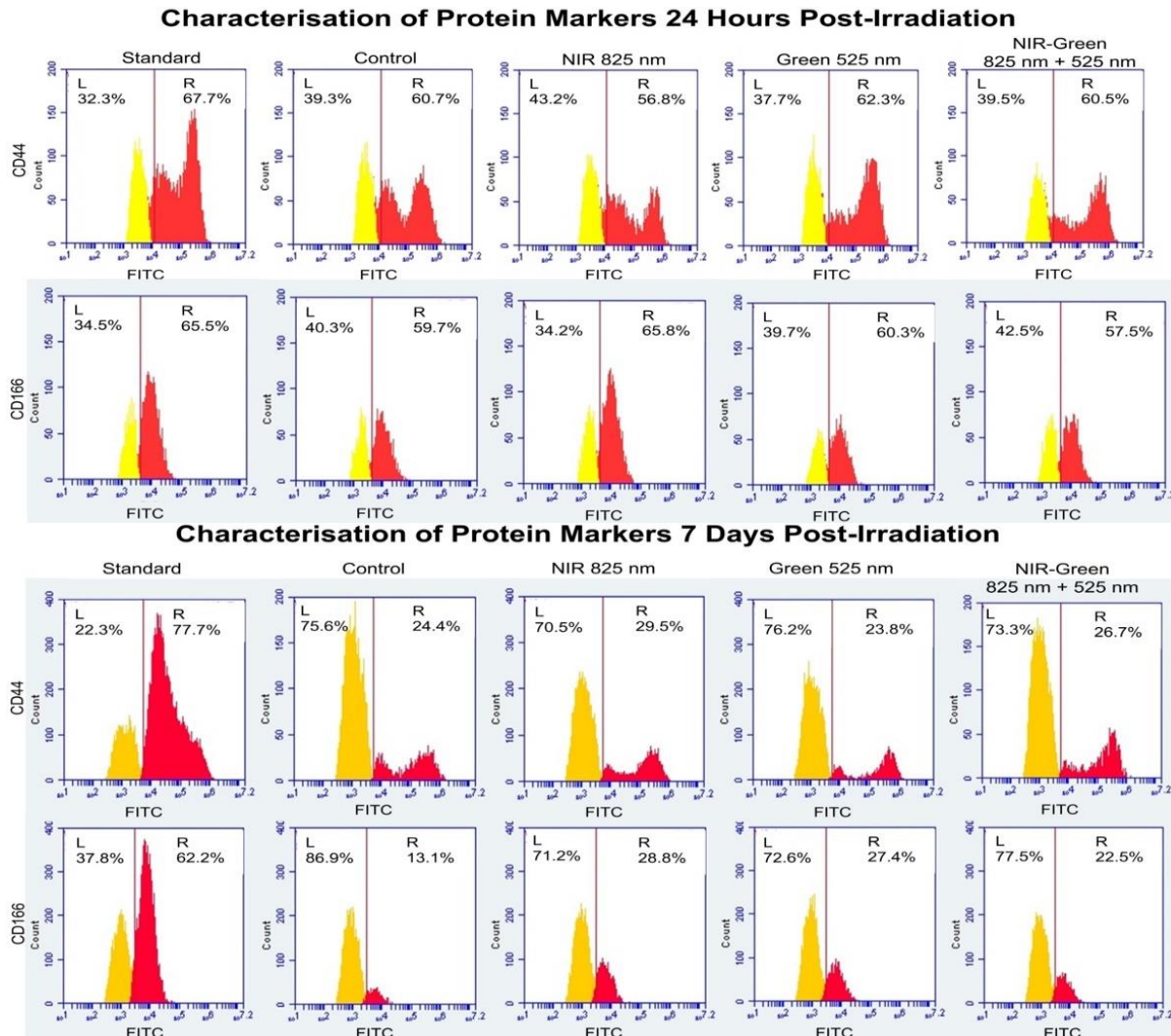


Figure 1. Flow cytometry characterization of immortalized ADMSC CD44 marker and CD166 markers at 24 hours and 7 days post-irradiation treatment. The red histogram is indicative of a right shift and increase in protein marker expression and the yellow histogram is indicative of a left shift, a decrease in protein marker expression.

Immortalized ADMSCs are characteristically thin and spindle in shape. A noticeable change in cell morphology (Figure 2) occurred amongst the Green treated cell groups at 24 hours, the Green and NIR-Green treated cell groups at 48 hours and amongst the NIR, Green and NIR-Green treated cell groups at 7 days post-PBM treatment. The cell shape had become rounded in appearance similarly to that of osteoblasts and a loss in the visibly thin and longitudinal initial ADMSC cell shape.

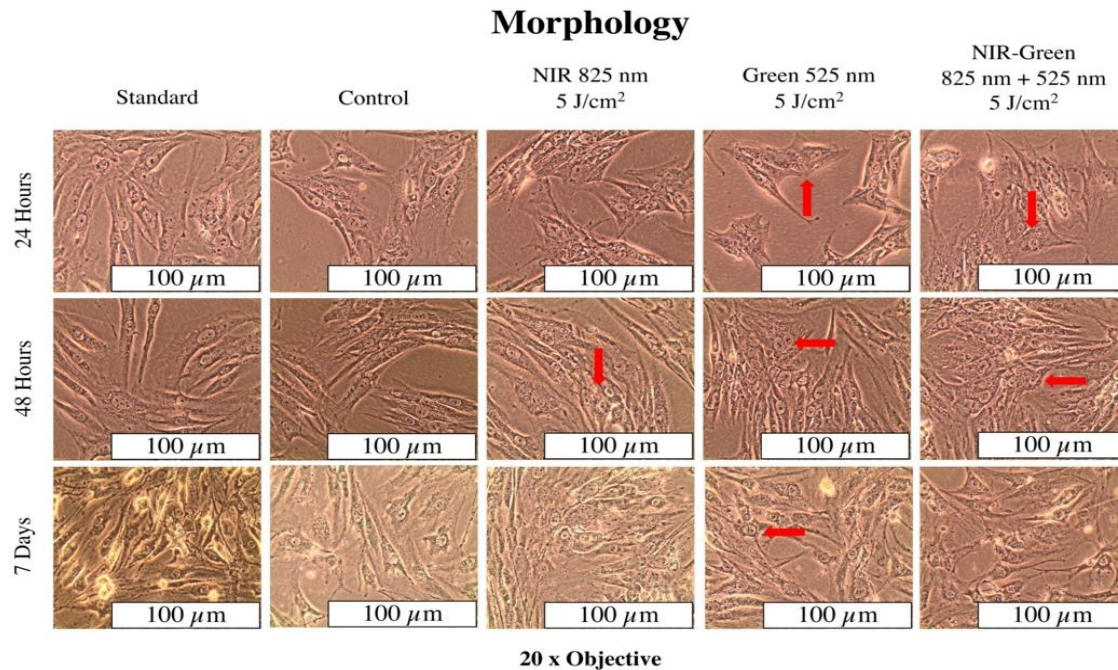


Figure 2. Morphology of immortalized ADMSC differentiation post-PBM treatment using Inverted Light Microscopy.

A statistically significant decrease in ATP (Figure 3A) was identified for all experimental groups compared to the standard, at 24 hours and in the Green and NIR-Green experimental groups at 48 hours post-PBM treatment. Proliferation was decreased for all experimental groups compared to the standard at 7 days, albeit insignificant. The overall decrease in proliferation seen may suggest that ATP is being redirected for cell differentiation instead of cell proliferation [16]. The viability assay (Figure 3B) suggested a consistent cell percentage viability over time implying that PBM does not negatively impact cell health instead maintains the overall health of cells. LDH results (Figure 3C) showed no significant increase in LDH production at 24 hours and 48 hours post-PBM treatment, however, a significant increase in LDH production did occur amongst the control and all the experimental groups at 7 days post-PBM treatment. Despite the significant increase when compared to the standard, these increases are not of toxic concentrations in comparison to the cytotoxic positive control which represents a hundred percent cell toxicity and cell death. As the cell viability was seen to be maintained over time. The slight LDH leakage identified may be explained by changes in cell membrane permeability due to trans-differentiation [17], or due to contact inhibition and nutrient depletion within the cell culture medium after an extended cell culture period [18].

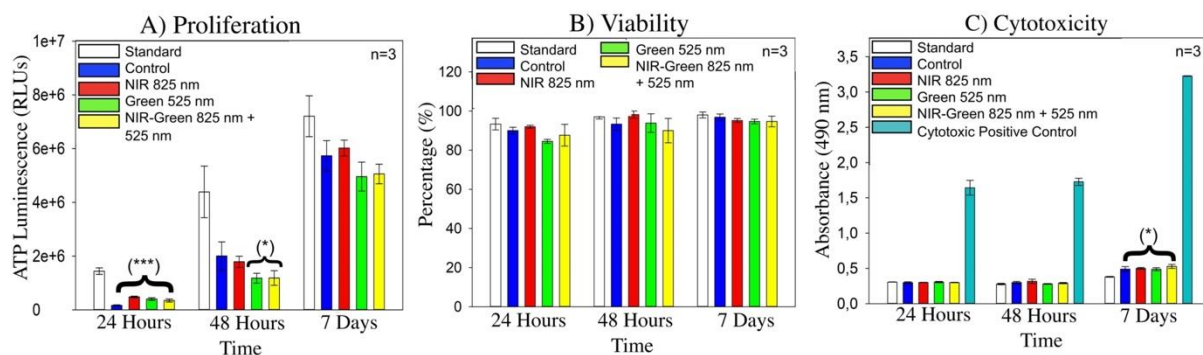


Figure 3. Biochemical Analysis of immortalized ADMSC differentiation at 24 hours, 48 hours, and 7 days post-PBM treatment.

4. Discussion and Conclusion

Osteoporosis is the consequence of a decline in bone-forming mature osteoblast populations [19] instigated by changes in the biology of Mesenchymal Stem Cells (MSCs), insufficient osteoblast progenitor proliferation, a rise in apoptosis and an upsurge in the accumulation of adipocytes within the marrow [20]. The development, strength, and consistency of new bones can be aided by the transplantation of ADMSCs [5] because ADMSCs are an ample multipotent cell source capable of differentiation into osteoblast, adipocyte, and chondrocyte cell lineages [21]. PBM has been recognized to assist in cell function, proliferation, migration, and the regeneration of tissue [11]. The effects of PBM on ADMSCs have shown to be dependent based on the wavelength and fluency applied [12]. Previous studies have identified the effect of PBM at a single wavelength on ADMSCs [22–24], however, limited studies have explored the outcome of combining PBM wavelengths to aid multiple cellular functions [25].

Flow cytometry analysis indicated a reduction in CD44 and CD166 immortalized ADMSC stem-ness protein markers at 7 days post-PBM treatment, implying the transition of stem cell into cell lineage. The data identified Green PBM to have a greater outcome in reducing CD44 and NIR-Green PBM to have a greater outcome in reducing CD166. This suggests Green PBM and NIR-Green PBM influence different cellular pathways, yet both are an effective aid in the trans-differentiation of immortalized ADMSCs. Wang et al. concluded their findings on the detection of trans-differentiated ADMSCs into osteogenic lineages with the aid of Green PBM after 7 days post-PBM treatment [14].

Immortalized ADMSCs are typically identified as thin and spindle in cell shape, however, cellular morphology depicted noticeable cell shape rounding as early as 24 hours post-PBM treatment amongst the Green PBM experimental group. At 48 hours post-PBM treatment, both Green and NIR-Green PBM experimental groups presented with rounded cell and/or shorter spindle shaped cell morphology. An osteoblast is characteristically rounded in cell morphology as identified by previous research [26]. This change in cell morphology suggests cell differentiation of immortalized ADMSCs into osteoblasts.

Analysis of biochemical assays identified a statistically significant decrease in cell proliferation at 24 hours post-PBM treatment amongst all experimental groups. At 48 hours post-PBM treatment, a decreased cell proliferation occurred amongst the Green PBM and NIR-Green PBM experimental groups. However, the decrease in proliferation is suggestive that ATP had been redirected for the use of cellular differentiation instead of cellular proliferation as suggested by the findings of a study which intended for the differentiation of human embryonic stem cells into neural cells [27]. The viability assay presented with a consistent cell percentage viability of cells amongst all experimental groups at 24 hours, 48 hours and 7 days post-PBM treatment. This indicates that PBM treatment assists in the maintenance of cell health without a negative outcome [24]. Lastly, a significant increase in LDH production had been identified amongst the control group and all three experimental groups 7 days post-PBM treatment, however, these concentrations were not toxic to the cell population. In comparison to a hundred percent cell toxicity and death, the cytotoxic positive control, the increases of LDH were not a result of plasma membrane damage induced by PBM and thus, not harmful to the cells [28]. This is further supported by the proliferative and viability assays performed.

In conclusion, this study has indicated promising early osteogenic differentiation of immortalized ADMSCs using a combination of growth trans-differentiation inducers and PBM treatment. The results of this study suggest that both Green PBM and NIR-Green PBM possess the greatest potential for the differentiation of immortalized ADMSCs into osteoblasts as identified by the significant decrease of CD44 and CD166 protein markers, suggesting a loss of immortalized ADMSC stem-ness into osteogenic cell lineage and the identifiable changes in cell morphology into rounded cells characteristic of osteoblast cells. These findings further imply that Green PBM has the ability to prime immortalized ADMSCs for cellular differentiation into osteogenic cell lineages. However, further analysis such as early and late osteogenic protein marker characterisation, additional biochemical assays and genetic expression using Real Time-PCR and ELISA will offer confirmation of efficient immortalized ADMSC differentiation into osteoblasts via the aid of PBM treatment.

Acknowledgments

The authors sincerely thank the South African Research Chairs Initiative of the Department of Science and Technology and National Research Foundation of South Africa (SARChI/NRF-DST) [Grant No. 98337], received by Daniella Da Silva and Prof Heidi Abrahamse, the National Research Foundation (NRF) S&F -Scarce Skills Postdoctoral Fellowship [Grant no: 120752] received by Dr Anine Crous, the University of Johannesburg and the Laser Research Centre for their facilities.

References

- [1] Phetfong J, Sanvoranart T, Nartprayut K, Nimsanor N, Seenprachawong K, Prachayasittikul V and Supokawej A 2016 *Cell. Mol. Biol. Lett.* **21** 1–20
- [2] Sozen T, Ozisik L and Calik Basaran N 2017 *Eur. J. Rheumatol.* **4** 46–56
- [3] Mason C and Dunnill P 2008 *Regen. Med.* **3** 1–5
- [4] Polak J M and Bishop A E 2006 *Ann. N. Y. Acad. Sci.* **1068** 352–66
- [5] Hu L, Yin C, Zhao F, Ali A, Ma J and Qian A 2018 *Int. J. Mol. Sci.* **19**
- [6] Frese L, Dijkman P E and Hoerstrup S P 2016 *Transfus. Med. Hemotherapy* **43** 268–74
- [7] Trentz O A, Ariketh D, Sentilnathan V, Hemmi S, Handschin A E, de Rosario B, Mohandas P and Mohandas P V A 2010 *Eur. J. Trauma Emerg. Surg.* **36** 457–63
- [8] Lee S Y, Lee J H, Kim J Y, Bae Y C, Suh K T and Jung J S 2014 *Cell. Physiol. Biochem.* **34** 1339–50
- [9] Akyol U K, Sipal S, Demirci E and Gungormus M 2015 *Lasers Med. Sci.* **30** 1141–6
- [10] Anders J J, Arany P R, Baxter G D and Lanzafame R J 2019 *Photobiomodulation, Photomedicine, Laser Surg.* **37** 63–5
- [11] De Freitas L F and Hamblin M R 2016 *IEEE J. Sel. Top. Quantum Electron.* **22** 1–37
- [12] Soleimani M, Abbasnia E, Fathi M, Sahraei H, Fathi Y and Kaka G 2012 *Lasers Med. Sci.* **27** 423–30
- [13] Escudero J S B, Perez M G B, de Oliveira Rosso M P, Buchaim D V, Pomini K T, Campos L M G, Audi M and Buchaim R L 2019 *Injury* **50** 1853–67
- [14] Wang Y Y, Huang Y Y, Wang Y Y, Lyu P and Hamblin M R 2016 *Sci. Rep.* **6** 1–9
- [15] Crouch, S.P.M., Kozlowski, R., Slater, K.J. & Fletcher J 1993 *J. Immunol. Methods* **160** 81–8
- [16] Vander Heiden M G, Cantley L C and Thompson C B 2009 *Science (80-.)*. **324** 1029–33
- [17] Ahn H, Lee K, Kim J M, Kwon S H, Lee S H, Lee S Y and Jeong D 2016 *PLoS One* **11** 1–13
- [18] Pavel M, Renna M, Park S J, Menzies F M, Ricketts T, Füllgrabe J, Ashkenazi A, Frake R A, Lombarte A C, Bento C F, Franze K and Rubinsztajn D C 2018 *Nat. Commun.* **9**
- [19] Coipeau P, Rosset P, Langonn A, Gaillard J, Delorme B, Rico A, Domenech J, Charbord P and Senseb L 2009 *Cytotherapy* **11** 584–94
- [20] Li C, Cheng P, Liang M, Chen Y, Lu Q, Wang J, Xia Z, Zhou H, Cao X, Xie H, Liao E and Luo X 2015 *J. Clin. Invest.* **125** 1509–22
- [21] Dai R, Wang Z, Samanipour R, Koo K I and Kim K 2016 *Stem Cells Int.* **2016**
- [22] Mvula B, Mathope T, Moore T and Abrahamse H 2008 *Lasers Med. Sci.* **23** 277–82
- [23] Wang Y, Huang Y-Y, Wang Y, Lyu P and Hamblin M R 2017 *Biochim. Biophys. Acta - Gen. Subj.* **1861** 441–9
- [24] Bölükbaşı Ateş G, Ak A, Garipcan B and Gülsoy M 2020 *Cytotechnology* **72** 247–58
- [25] Fekrazad R, Asefi S, Eslaminejad M B, Taghiar L, Bordbar S and Hamblin M R 2019 vol 34
- [26] Hong D, Chen H X, Yu H Q, Liang Y, Wang C, Lian Q Q, Deng H T and Ge R S 2010 *Exp. Cell Res.* **316** 2291–300
- [27] Birket M J, Orr A L, Gerencser A A, Madden D T, Vitelli C, Swistowski A, Brand M D and Zeng X 2011 *J. Cell Sci.* **124** 348–58
- [28] Hwang M H, Kim K S, Yoo C M, Shin J H, Nam H G, Jeong J S, Kim J H, Lee K H and Choi H 2016 *Lasers Med. Sci.* **31** 767–77

***Dicoma anomala* enhances the zinc phthalocyanine tetrasulphonic acid ZnPcS_4 mediated photodynamic therapy in breast cancer cells**

A Chota¹, B P George¹ and H Abrahamse¹

Laser research Centre, Faculty of Health Sciences, University of Johannesburg P. O. Box 17011, Doornfontein 2028, South Africa

E-mail: blassang@uj.ac.za

Abstract. Globally, cancer has been identified as one of the leading causes of death in both men and women. Breast cancer is the common type of cancer that affects women, and it is the second leading cause of cancer-related death. To completely eradicate cancer, multiple therapeutic options that target distinct disease processes must be applied. For many years, combination treatment has remained a therapeutic option for resistant cancers. In this research, we investigated the enhanced effect of zinc phthalocyanine tetrasulphonic acid (ZnPcS_4) mediated photodynamic therapy by using *Dicoma anomala* methanol root extract in breast cancer cells. *D. anomala* root methanol extract and ZnPcS_4 Photosensitizer (PS) was used to treat MCF-7 breast cancer cells at different concentrations (25, 50, and 100 $\mu\text{g/mL}$ of *D. anomala* and 5, 10, 20, 40, and 60 μM of ZnPcS_4) in photodynamic therapy (PDT) using a diode laser of 680 nm at 10 J/cm² fluency. After 24 h of treatment, MCF-7 cells were analyzed for possible morphological changes, adenosine triphosphate (ATP) proliferation, and lactate dehydrogenase (LDH) cellular cytotoxicity. ATP proliferation rates and LDH cytotoxicity were analyzed to determine the anticancer effects of *D. anomala* and ZnPcS_4 mediated photodynamic therapy in monotherapy as well as in combination therapy. All experiments were performed 4 times ($n=4$) and results obtained were analyzed using SPSS statistical software version 27 at a 0.95 confidence interval. The outcomes from this study show that *D. anomala* significantly enhances the cytotoxic effects of ZnPcS_4 mediated PDT in breast cancer cells. In monotherapy, *D. anomala* root extract induced MCF-7 cell death, while in combination with ZnPcS_4 , the plant extract significantly enhanced the PDT efficacy. Furthermore, the outcome from this research suggests the use of *D. anomala* root extract as a natural anticancer agent for the treatment of breast cancer.

1. Introduction

Cancer is a condition characterized by the unregulated proliferation of tumor cells. Despite the invention of new diagnostic, and treatment modalities, cancer has continued to be the leading cause of morbidity and mortality in both males and females [1]. Breast cancer is the most common and frequently diagnosed cancer in women. According to the 2020 GLOBOCAN report, the incidence rate of breast cancer is expected to increase from 2.63 million cases in 2020 to 3.19 million new cases by 2040 [2]. However, an increase in the incidence rate is attributed to many risk factors which may be intrinsic or extrinsic. Examples of intrinsic factors include mutations and random error during deoxyribonucleic acid (DNA) replication while extrinsic risk factors include radiation, chemicals, and smoking. There are various treatment modalities employed in the treatment of breast cancer. These include chemotherapy, immunotherapy, surgery, and radiotherapy. Although these therapies have been used in the treatment of various cancers, they are also known to elicit different side effects [3]. The increased side effects have led to the development of novel combination treatments [4].

Photodynamic therapy (PDT) is one of the emerging modalities that has shown potential in the treatment of various cancers such as breast cancer. This form of cancer therapy uses chemical compounds known as photosensitizers to initiate the generation of reactive oxygen species (ROS). When generated within tumor cells, ROS targets and induce oxidative stress of different organelles of the cells such as the nucleus, and the mitochondria [5]. In addition, many researchers are exploring the use of plant-derived anticancer compounds as a source of bioactive compounds as well as photosensitizers to

be used in the treatment of different forms of cancer. *D. anomala* is an African medicinal plant that has been used in the treatment of various ailments [4]. Photodynamic therapy and plant-derived bioactive compounds may induce tumor cell death through various mechanisms which might be autophagy, apoptotic, necrotic, and cell cycle checkpoint arrest [6]. Most cancer studies are now concentrating on combining one or two therapeutic modalities to maximize efficacy with less side effects [7]. This study is aimed at evaluating the enhanced anticancer effects of zinc phthalocyanine tetrasulphonic acid (ZnPcS₄) mediated PDT with *D. anomala* on MCF-7 cancer cell line.

2. Methodology

2.1. Cell culture, and treatment

A breast cancer cell line (MCF-7) (ATCC® HTB 22) used in this research was obtained from American Type Culture Collection (ATCC). MCF-7 cells were cultured in a T175 culture flask containing Dulbecco's Modified Eagle's Medium (DMEM), supplemented with 10% Fetal Bovine Serum (FBS), 1% Amphotericin B, 1% Penicillin-streptomycin, and incubated at 37°C, 85% humidity, and 5% CO₂. Experimental cells were seeded at a seeding density of 5×10^5 in 3.4 cm² diameter culture plates. The IC₅₀ for *D. anomala* plant extract was determined by treating cells with different concentrations of the extract (i.e., 25, 50, and 100 µg/mL), whereas IC₅₀ concentration of ZnPcS₄ was calculated following 24 h treatment using 5, 10, 20, 40, and 60 µM concentrations of PS. Photodynamic therapy experiments were performed using the IC₅₀ concentrations of PS with a 680 nm laser diode at the fluency 10 J/cm².

2.2. Cell morphology

Morphological changes of the cells were evaluated after 24 h of treatment with different concentrations of *D. anomala*, and ZnPcS₄ by using an inverted light microscope (Wisan Olympus CKX 41).

2.3. Adenosine triphosphate (ATP) proliferation assay

The CellTiter-Glo® 3D luminescence reagent (Promega, G968A) was used to determine cellular proliferation and the amount of ATP in viable cells. To initiate cell lysis, 50 µL of reconstituted reagent was added to an equal volume of cell suspension and thoroughly mixed. The mixture was later incubated in the dark at room temperature for 10 min. After 10 min incubation, ATP luminescence was read by using PerkinElmer, VICTOR Nivo™.

2.4. Lactate dehydrogenase (LDH) cytotoxicity assay

Cyto Tox 96® Non-Radioactive Cytotoxicity assay (Promega, G179A) kit was used to measure the amount of cytosolic LDH released by cells with a damaged cell membrane. To estimate the levels of LDH, 50 µL of reconstituted reagent was added to an equivalent amount of cell suspension, mixed thoroughly, and incubated at room temperature in the dark for 30 min. The colorimetric mixture was read by using PerkinElmer, VICTOR Nivo™.

2.5. Statistical analysis

MCF-7 passage numbers between 16 and 21 were used to conduct all experiments. All sets of experiments were performed four times ($n=4$). Throughout the study, all the mean values of experimental groups were compared with the mean value of untreated MCF-7 cells. One-way ANOVA was performed with the aim of determining statistical significance between the control and experimental groups at 0.95 confidence interval. Statistical significances between the control and experimental groups in graphs are shown as $p < 0.05$ (*), $p < 0.01$ (**), and $p < 0.001$ (***). All statistics were analysed by using SPSS statistical software version 27.

3. Results and discussion

3.1. Morphological changes

Morphological alterations in MCF-7 treated, and untreated cells are shown in Figure 1. Untreated MCF-7 cells (Fig. 1 A) displayed no aberrant changes in morphology. MCF-7 cells that only received laser (10 J/cm²) treatment (Fig. 1 B) clearly suggests that laser alone does not have cytotoxic effects on MCF-

7 cells. When compared to untreated cells, various concentrations (25, 50, and 100 $\mu\text{g/mL}$) of *D. anomala* treated cells (Fig. 1 C-E) showed significant morphological changes. On the other hand, cells that were treated with different concentrations (10, 20, 40, and 60 μM) of ZnPcS₄ only (Fig. 1 F-J) displayed no morphological changes while cells that were treated with ZnPcS₄ + laser (Fig. 1 K-O) demonstrated significant morphological changes when compared to the control cells. Cells that were treated with ZnPcS₄ IC₅₀ + laser (Fig. 1 P), *D. anomala* IC₅₀ (Fig. 1 Q), *D. anomala* IC₅₀ + laser (Fig. 1 R), and ZnPcS₄ IC₅₀ + laser + *D. anomala* IC₅₀ (Fig. 1 S) demonstrated changes in morphology when compared to untreated and laser only treated MCF-7 cells. Morphological changes observed 24 h post treatment include cell shrinkage, loss of membrane integrity, and cell detachment from culture plates. These morphological changes observed in the treatment groups of this study are suggestive of apoptotic activities.

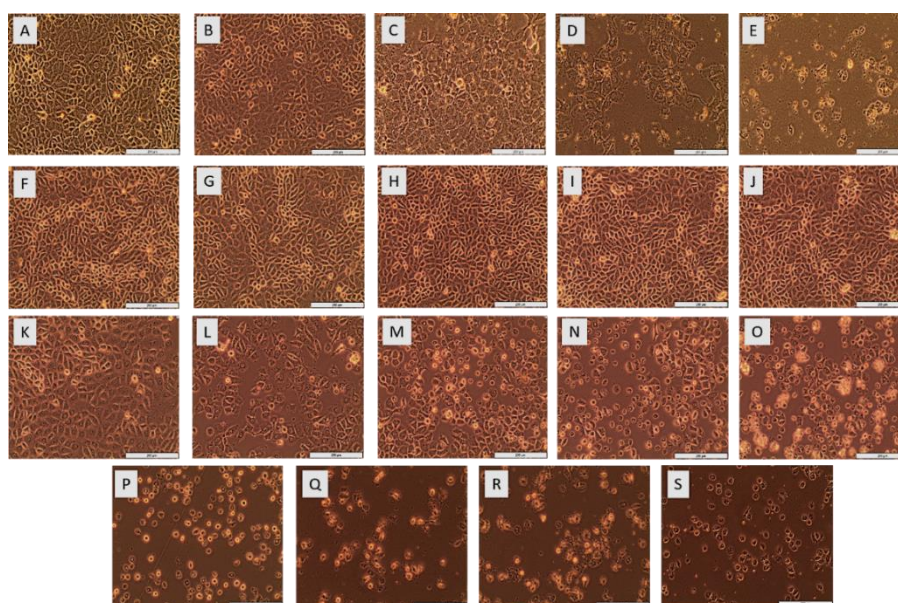


Figure 1. Morphological changes in MCF-7 cells after 24 h treatments. A) MCF-7 untreated cells; B) MCF-7 cells + laser; C) 25 $\mu\text{g/mL}$ *D. anomala*; D) 50 $\mu\text{g/mL}$ *D. anomala*; E) 100 $\mu\text{g/mL}$ *D. anomala*; F) 5 μM of ZnPcS₄; G) 10 μM of ZnPcS₄; H) 20 μM of ZnPcS₄; I) 40 μM of ZnPcS₄; J) 60 μM of ZnPcS₄; K) 5 μM of ZnPcS₄ + laser; L) 10 μM of ZnPcS₄ + laser; M) 20 μM of ZnPcS₄ + laser; N) 40 μM of ZnPcS₄ + laser; O) 60 μM of ZnPcS₄ + laser; P) ZnPcS₄ IC₅₀ + laser; Q) *D. anomala* IC₅₀; R) *D. anomala* IC₅₀ + laser; S) ZnPcS₄ IC₅₀ + laser + *D. anomala* IC₅₀.

3.2. ATP proliferation assay

The level of metabolic activity of cells was determined by measuring cellular ATP concentration. The CellTiter-Glo® 3D luminous assay was used to assess the ability of cells to proliferate. All metabolically active cells contain ATP, which is a marker for cell viability and proliferation. Studies showed that, ATP can initiate cell differentiation and proliferation [8]. The levels of ATP in MCF-7 cells only remained high as shown in (Fig. 2 A-C). In comparison to control cells, cells treated with *D. anomala* methanol root extract and ZnPcS₄ mediated PDT demonstrated significant decrease in cellular proliferation. In *D. anomala* treatment model, all the three treatment groups demonstrated a significant decrease in ATP levels when compared to the untreated cells. The cells treated with increasing doses of *D. anomala* (25, 50, and 100 $\mu\text{g/mL}$) showed a dose-dependent significant decrease in ATP levels (Fig. 2 A). On the other hand, ZnPcS₄ alone treated cells showed no significant ATP levels. This suggests that ZnPcS₄ alone does not have cytotoxic effects when compared to ZnPcS₄ treated cells that received laser (680 nm) at 10 J/cm². MCF-7 cells treated with increasing doses of ZnPcS₄ (10, 20, 40, and 60 μM) showed a strong dose-dependent significance with p value < 0.001 when compared to untreated cells (Fig. 2 B). This suggests that the cytotoxicity effects of ZnPcS₄ is dependent on the exposure of MCF-7 cells treated

with ZnPcS₄ to a diode laser of 680 nm. In monotherapy, the two IC₅₀ (*D. anomala* and ZnPcS₄ mediated PDT) concentrations demonstrated a strong significance with *p* value (<0.001) when compared to the untreated cells that showed higher ATP levels as shown in Fig. 2 C. The combination of the two IC₅₀ (*D. anomala* and ZnPcS₄ mediated PDT) showed a significant decrease in ATP levels when compared to the control group (Fig. 2 C). Metabolically active cells undergoing proliferation produce high levels of ATP. The major source of cellular ATP occurs in the mitochondria via different metabolic processes such as beta-oxidation [9]. ATP levels drastically drop in cells which are in the late stages of apoptosis. In most cases, this is due to the loss of mitochondrial activities and increased activity of ATP dependent proteolytic enzymes [10]. This suggests that all cellular metabolic activities are dependent on the synthesis of ATP.

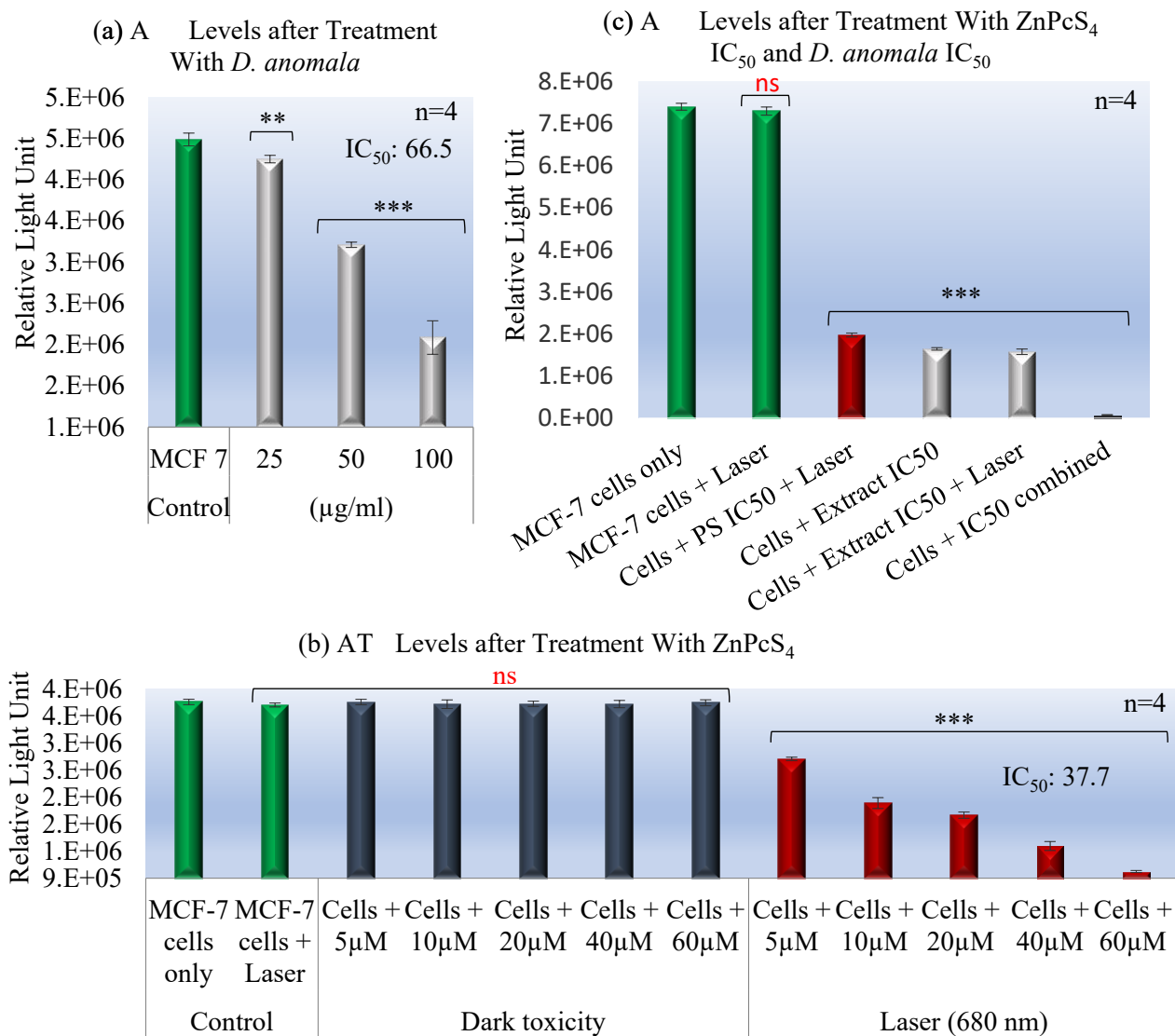


Figure 2. ATP proliferation effects of *Dicoma anomala* and ZnPcS₄ on MCF-7 cells. a) MCF-7 control cells showed a highest ATP levels while *D. anomala* root extract-treated cells showed a significant decrease in ATP levels and IC₅₀ established was 66.5 µg/mL. b) MCF-7 control cell, laser only treated and ZnPcS₄ only treated cells showed a significant increase in ATP proliferation while ZnPcS₄ treated and laser irradiated cells showed a significant decrease in ATP proliferation and the IC₅₀ established was 37.7 µM. c) A decrease in ATP proliferation was observed in IC₅₀ (*D. anomala* and ZnPcS₄) treated MCF-7 cells as well as in combination of the two IC₅₀ when compared to the control cells. The values depicted are mean plus or minus standard deviations (n=4). **p* < 0.05, ***p* < 0.01, and ****p* < 0.001 indicate significant differences between the control and experimental groups.

3.3 LDH cytotoxicity assay

Lactate dehydrogenase (LDH) cytotoxicity assay is a colorimetric assay that determines cellular cytotoxicity by measuring the levels of LDH in a culture medium. LDH is an enzyme found in the cytoplasm of all living cells. It acts as a marker for cell membrane damage and is released into culture medium of cells undergoing apoptosis. In addition, the release of LDH into the culture media is directly proportional to the number of dead cells [6]. Cell membrane integrity of *D. anomala* and ZnPcS₄ treated MCF-7 cells was measured by using PerkinElmer, VICTOR Nivo™. The control cells and laser only (10J/cm²) treated cells showed low levels of LDH when compared to cells that were treated with various concentrations of *D. anomala* and ZnPcS₄ mediated PDT. *D. anomala* treated MCF-7 cells induced the release of higher levels of LDH when compared to the control cells and laser (10J/cm²) only treated cells. A dose-dependent significant increase in LDH levels was observed in *D. anomala* concentrations (25, 50, and 100 µg/mL) as shown in Table 1. In another experimental model, ZnPcS₄ treated cells that did not receive laser showed less LDH levels when compared to ZnPcS₄ treated cells that received laser (680 nm) at 10 J/cm². This suggests that the cytotoxic effects of ZnPcS₄ is dependent on concentration and exposure to laser light. MCF-7 cells that were treated with increasing doses of ZnPcS₄ (10, 20, 40, and 60 µM) showed high release in LDH levels when compared to the control cells as shown in Table 2. In monotherapy, the two IC₅₀ (*D. anomala* and ZnPcS₄ mediated PDT) concentrations provoked a high release in LDH levels with a strong significance (*p* value <0.001) when compared to the untreated cells. The combination of two IC₅₀ (*D. anomala* and ZnPcS₄ mediated PDT) showed a very strong significant increase in LDH levels when compared to the control group as shown in Table 3.

Table 1: LDH levels after treatment with *D. anomala*. Standard error ± of mean.

Groups	LDH levels
LDH positive control	1.004 ± 0.0220
MCF-7 control	0.54775 ± 0.0179
<i>D. anomala</i> (25 µg/mL)	0.6035 ± 0.0084 *
<i>D. anomala</i> (50 µg/mL)	0.75975 ± 0.0013 ***
<i>D. anomala</i> (100 µg/mL)	0.88275 ± 0.0194 ***

Table 2: LDH levels after treatment with ZnPcS₄. Standard error ± of mean.

Groups	LDH levels	
LDH positive control	1.1027 ± 0.023	
MCF-7 control	0.556 ± 0.020	
MCF-7 + Laser	0.5832 ± 0.014	
<i>ZnPcS₄</i> concentrations	Dark Toxicity	680 nm Laser (10J/cm ²)
5 µM	0.5585 ± 0.016	0.669 ± 0.007 **
10 µM	0.5562 ± 0.020	0.7935 ± 0.024 ***
20 µM	0.5662 ± 0.0186	0.8487 ± 0.018 ***
40 µM	0.5585 ± 0.017	0.9745 ± 0.019 ***
60 µM	0.564 ± 0.019	1.0362 ± 0.042 ***

Table 3: LDH levels after treatment with ZnPcS₄ IC₅₀ and *D. anomala* IC₅₀. Standard error ± of mean.

Groups	LDH levels
LDH positive control	1.9147 ± 0.0156
MCF-7 control	0.4625 ± 0.0177
MCF-7 + Laser	0.465 ± 0.0174
ZnPcS ₄ + Laser	0.6167 ± 0.0086 ***
<i>D. anomala</i> IC ₅₀	0.6287 ± 0.0166 ***
<i>D. anomala</i> IC ₅₀ + Laser	0.6325 ± 0.0109 ***
ZnPcS ₄ IC ₅₀ + Laser + <i>D. anomala</i> IC ₅₀	0.955 ± 0.0255 ***

4. Conclusion

Plants used in traditional medicine have been proven to have pharmacological properties and offer strong therapeutics, making complementary medicine essential to the medical sector. In conclusion, *Dicoma anomala* methanol root extract has demonstrated to have anticancer effects when administered in monotherapy as well as in combination with zinc phthalocyanine tetrasulfonate (ZnPcS₄) photosensitizer mediated photodynamic therapy in MCF-7 breast cancer cells. Furthermore, the cell death mechanism analysis will be warranted to explore the exact mechanisms of *D. anomala* in monotherapy as well as the combination therapy. This combination might potentially lower the effective therapeutic dosages of commercially prepared photosensitizers, lowering dose dependence in PDT. In drug development and cancer research, many natural chemicals serve as lead anticancer compounds. However, scientific validation is required for the discovery of anticancer properties in traditional medicinal plants and natural products.

Acknowledgments

The authors sincerely thank the Department of Science and Technology and National Research Foundation (NRF) of South Africa, Laser Research Centre (LRC), University of Johannesburg, and the African Laser Centre (ALC) for their support.

Funding

This work is supported by the South African Research Chairs initiative of the Department of science and technology and National Research Foundation of South Africa (Grant No 98337), as well as grants received from the University Research Committee (URC), University of Johannesburg, and Council for Scientific and Industrial Research (CSIR)-National Laser Centre (NLC), and African Laser Centre (ALC).

References

- [1] Sharma GN, Dave R, Sanadya J, Sharma P, and Sharma KK. 2010. Various types and Management of Breast Cancer: An Overview. *J Adv Pharm Technol Res* **1**, 109–126.
- [2] WHO, 2020. Cancer Tomorrow. Available at: <https://gco.iarc.fr/tomorrow/en/>
- [3] Guimarães*, I. dos S, Daltoé* RD, Herlinger AL, Madeira KP, Ladislau T, Valadão IC, Junior PCML, FernandesTeixeira S, Amorim GM, Santos DZ dos, Demuth KR, and Rangel LBA. 2013. Conventional Cancer Treatment, Cancer Treatment - Conventional and Innovative Approaches. *IntechOpen*.
- [4] Chota A, George B, and Abrahamse H. 2020. Potential Treatment of Breast and Lung Cancer Using *Dicoma anomala*, an African Medicinal Plant. *Molecules* **25**, 4435.
- [5] Das K, and Roychoudhury A. 2014. Reactive oxygen species (ROS) and response of antioxidants as ROS-scavengers during environmental stress in plants. *Front. Environ. Sci.* **2**.
- [6] George B, and Abrahamse H. 2016. A Review on Novel Breast Cancer Therapies: Photodynamic Therapy and Plant Derived Agent Induced Cell Death Mechanisms. *Anti-cancer agents in medicinal chemistry* **16**, 793–801.
- [7] Eric Chekwube A, George B, and Abrahamse H. 2019. Cell death induced by combination of Phthalocyanine photosensitizer and Doxorubicin on MCF-7 breast carcinoma cells. *SA Institute of Physics*, 194–198.
- [8] Plackal Adimuriyil George B, Tynga IM, and Abrahamse H. 2015. In Vitro Antiproliferative Effect of the Acetone Extract of *Rubus fairholmianus* Gard. Root on Human Colorectal Cancer Cells. *BioMed Research International* **2015**, e165037.
- [9] Balaban S, Lee LS, Varney B, Aishah A, Gao Q, Shearer RF, Saunders DN, Grewal T, and Hoy AJ. 2018. Heterogeneity of fatty acid metabolism in breast cancer cells underlies differential sensitivity to palmitate-induced apoptosis. *Mol Oncol* **12**, 1623–1638.
- [10] Zhou Y, Tozzi F, Chen J, Fan F, Xia L, Wang J, Gao G, Zhang A, Xia X, Brasher H, Widger W, Ellis LM, and Weihua Z. 2012. Intracellular ATP Levels are a Pivotal Determinant of Chemoresistance in Colon Cancer Cells. *Cancer Res* **72**, 304–314.

Effects of photodynamic therapy on A375 Melanoma cells using aluminium phthalocyanine photosensitizer

B Mkhobongo, R Chandran¹ and H Abrahamse

Laser Research Centre, Faculty of Health Sciences, University of Johannesburg
P.O. Box 17011, Doornfontein, South Africa, 2028

E-mail: rahulc@uj.ac.za

Abstract. Metastatic Melanoma (MM) is highly aggressive and is among cancers causing major global deaths annually. It is imperative to find therapies that can eliminate MM and has become a major concern due to the potential for cancer relapse and metastasis, as well as the disease being accounted to be resistant to multiple forms of therapy. This *in vitro* study explores the effect of Photodynamic Therapy (PDT) using an Aluminium Phthalocyanine Photosensitizer (AlPcS₄Cl) at 673 nm and a fluency of 5 J/cm², in targeting Melanoma cells (A375). Dose dependent response of AlPcS₄Cl was studied on both A375 and fibroblast (WS1) cell lines and the IC₅₀ calculated from this. Significant post-irradiation signs of cell death were detected using microscopy and biochemical assays. An increased release of Lactate Dehydrogenase (LDH) content due to cytotoxicity with increasing doses of AlPcS₄Cl was measured. Cell viability testing showed increased damaged cells taking up Trypan Blue Dye. The study suggested an effective treatment against Melanoma cells. Enhanced capabilities of PDT for MM could possibly be achieved through gold nanoparticle (AuNP) activated increased uptake of AlPcS₄Cl photosensitizer, targeting their quiescent cancer stem cells.

1. Introduction

Melanoma typically arises in the skin and is a malignant tumour of melanocytes that is highly life-threatening with an increasing incidence worldwide [1]. Advanced or Metastatic Melanoma (MM) treatment can be difficult as patients are highly prone to cancer relapse and disease progression despite treatment due to developing resistance to treatment [2].

PDT uses the combination of a photosensitizer, intracellular molecular oxygen, and light for the destruction of cancer cells [3]. Phthalocyanines (PS) retain a vigorous absorbance near the infrared region and maintain high chemical levels in tissue and photo-stability with deeper tissue region *in vivo* activation [4]. Additional properties are longer absorption wavelengths in the region of 650–750 nm with high extinction coefficients, and elevated singlet oxygen quantum yields [5].

Intracellular localisation of a PS into targeted cells is one of the factors that determine the success of PDT as it assists in establishing the system and effectiveness of photo-induced cell death [6]. The localisation of a PS in the mitochondria commonly initiates apoptosis due to the high levels of ROS production as the mitochondria are sites of high oxygen levels and cytochrome c which causes the activation of caspases [7,8]. Lysosomal PS localisation leads to the leakage of catalytic hydrolases such as cathepsin D post PDT and membrane destabilisation [9], while in the endoplasmic reticulum (ER) implications are calcium instability and the accumulation of misfolded proteins [10].

2. Methods and materials

2.1. Cell culture and maintenance

Human Malignant Melanoma cell line A375, commercially purchased from the European Collection of Authenticated Cell Cultures (ECACC no: 88113005), was grown in a complete liquid medium DMEM (Dulbecco's Modified Eagle Medium). Fibroblast WS1 cells, obtained from the American Type Culture Collection (WS1, ATCC®, CRL-1502™), were grown in a complete liquid medium MEM (Minimum Essential Medium) and both cell lines were incubated at 37°C, 5% CO₂ and a humidity of 85%. Cell

confluent monolayers were detached and cellular suspensions seeded at 5×10^5 in 3.4 cm diameter cell culture dishes and incubated for a further 24 hours to adhere to the surface.

2.2. Aluminium phthalocyanine and irradiation dose response

A low-intensity diode laser (Oriel Corporation, USA, LREBT00-ROITHI) emitting at a wavelength of 673 nm, fluency 5 J/cm^2 supplied by the National Laser Centre of South Africa was used for this study. Cells were incubated for 4 hours with different ALPcS₄Cl concentrations (dose 1: 4 μM , dose 2: 10 μM , dose 3: 15 μM , dose 4: 20 μM) and controls. Post-irradiation signs of cell death were determined after 24 hours of incubation. The lowest inhibitory concentration (IC₅₀) was established for A375 through calculation, using biochemical assay data.

2.3. Post-irradiation analyses

Cellular morphological changes were observed at 200 \times magnification using an inverted microscope (Wirsam, Olympus CKX41) with an attached digital camera.

A Lactate dehydrogenase (LDH) kit (CytoTox96® Non-Radioactive Cytotoxicity Assay - Promega G1780) was used for cytotoxicity determination. The LDH excreted from the cytosol into the cell culture media upon membrane destruction was evaluated by measuring the calorimetric compound spectrophotometrically at 490nm using a microplate reader (Perkin Elmer, Victor³).

Trypan blue dye viability exclusion assay measured the percentage of viable cells present in the categorised cell suspensions. Equal parts of 0.4% (w/v) trypan blue dye (Invitrogen, Trypan Blue Stain Thermo Fisher-T10282) was added to cell suspensions and counted on an automated cell counter.

2.4. Subcellular localisation of ALPcS₄Cl PS in A375 cells

A375 cells seeded at 2.5×10^5 cells/ml were incubated with added ALPcS₄Cl PS for 4 hours in the dark for PS localisation. Post incubation and washing with PBS (Phosphate-buffered saline), cells were stained with an ER-tracker, Mitotracker, and LysoTracker for each respective group. Cells were washed with PBS and counterstained with 4'-6-diamidino-2-phenylindole (DAPI). After washing again with PBS, coverslips were mounted onto slides and viewed for PS organelle localisation under a fluorescent microscope.

2.5. Statistical analysis

Graphs represent the mean, and standard error of biochemical assays using Sigma Plot version 14.0. The Dunnett's method was used for non-normally distributed data, whereas the one-way analysis of variances (ANOVA) was used for normally distributed data. These tests were used to determine the significant difference between control and experimental groups where values in the 95% confidence interval ($p < 0.05^*$, $p < 0.01^{**}$ or $p < 0.001^{***}$) were accepted as statistically different.

3. Results and discussion

3.1. Light microscopy cell morphological changes

Dark toxicity WS1 and A375 cells, denoted as C - F in Figure 1 and 2 respectively, that received doses 5 μM – 20 μM ALPcS₄Cl photosensitizer alone without laser irradiation did not display significant morphological changes. This group resembled that of the cells only control group that received no treatment, shown in A. No morphological changes were seen in B, indicating irradiation of cells alone had no effect. Cells that received doses 5 μM – 20 μM PS and laser suggested morphological changes with increasing doses; however, non-significant cell death was seen in WS1 cells receiving dose 20 μM . A375 cells in Figure 2: J were noted to show the most significant cytotoxic effects. Signs of blebbing, vacuolisation, and cell shrinkage could be seen.

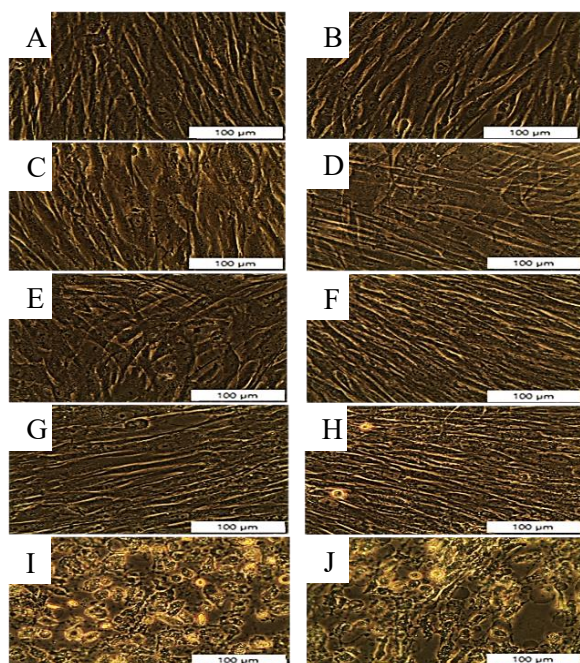


Figure 1. Morphological analysis post irradiation of WS1 cells at 200x magnification: A - Cells only; B - Cells + irradiation; C - Cells + AlPcS₄Cl dose 1 (4 μM); D - Cells + AlPcS₄Cl dose 2 (10 μM); E - Cells + AlPcS₄Cl dose 3 (15 μM); F - Cells + AlPcS₄Cl dose 4 (20 μM); G - Cells + AlPcS₄Cl dose 1 (4 μM) + PDT; H - Cells + AlPcS₄Cl dose 2 (10 μM) + PDT; I - Cells + AlPcS₄Cl dose 3 (15 μM) + PDT; J - Cells + AlPcS₄Cl dose 4 (20 μM) + PDT.

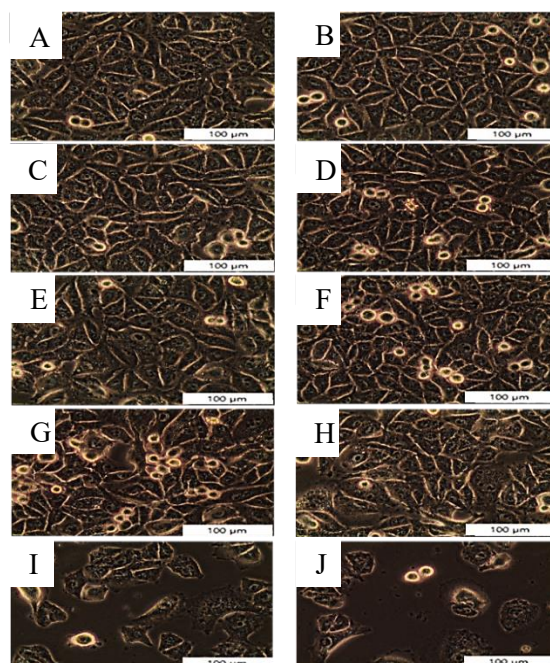


Figure 2. Morphological analysis post irradiation of A375 cells at 200x magnification: A - Cells only; B - Cells + irradiation; C - Cells + AlPcS₄Cl dose 1 (4 μM); D - Cells + AlPcS₄Cl dose 2 (10 μM); E - Cells + AlPcS₄Cl dose 3 (15 μM); F - Cells + AlPcS₄Cl dose 4 (20 μM); G - Cells + AlPcS₄Cl dose 1 (4 μM) + PDT; H - Cells + AlPcS₄Cl dose 2 (10 μM) + PDT; I - Cells + AlPcS₄Cl dose 3 (15 μM) + PDT; J - Cells + AlPcS₄Cl dose 4 (20 μM) + PDT.

3.2. Cytotoxicity

A non-significant increase in LDH was observed for dose dependant dark toxicity groups for both WS1 and A375 cell lines, indicating that AlPcS₄Cl PS dispensation to cells without light exposure has no cytotoxic effects. WS1 treatment groups showed no statistically significant results as seen in Figure 3. Treatment groups for A375 cells as seen in Figure 4, with doses 4, 10, 15 and 20 μM indicated statistically significant results of $p < 0.001$ (***)

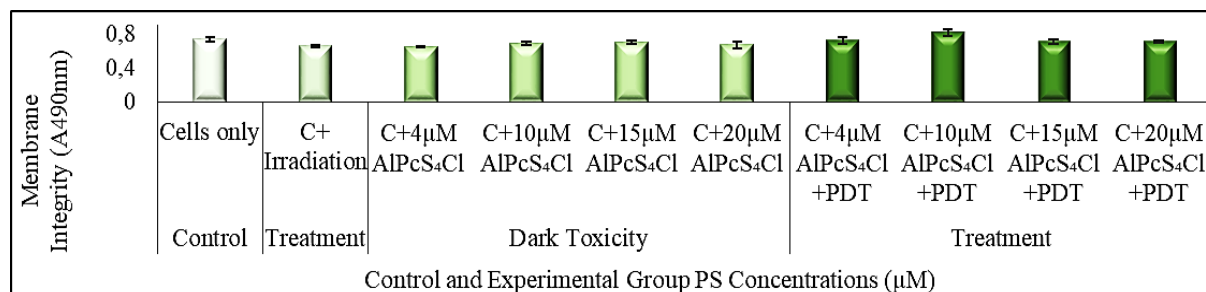


Figure 3. Post-irradiation cytotoxicity analysis on WS1 using LDH assay for control, treatment, and dark toxicity cell groups with increasing AlPcS₄Cl dose and laser irradiation at 673nm, fluency: 5 J/cm². No significant results from sample groups.

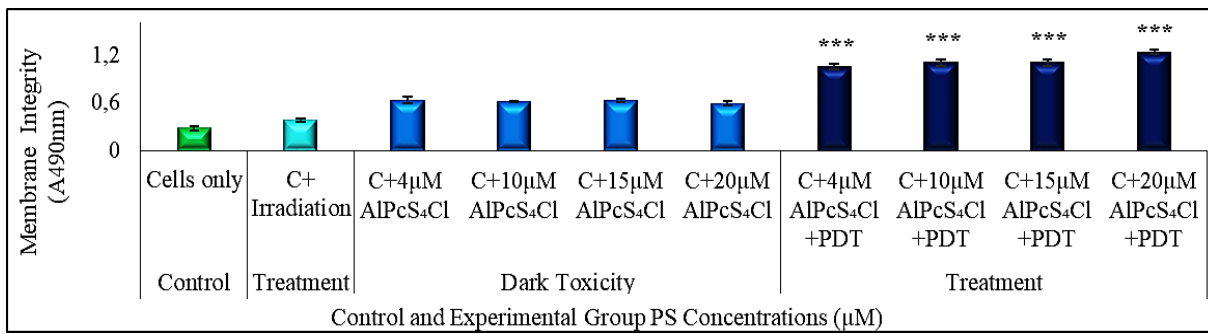


Figure 4. Post-irradiation A375 cells LDH cytotoxicity analysis for control, treatment, and dark toxicity cell groups with increasing AlPcS₄Cl dose and laser irradiation at 673nm, fluency: 5 J/cm². A high significance of $p < 0,001$ (***) was established from treatment doses 4, 10, 15 and 20 μM.

3.3. Cellular viability

Trypan blue dye viability exclusion assay showed no statistically significant results for WS1 treatment group cells when compared to the control in Figure 5. This suggested that PDT was non-lethal at these doses. Treatment groups were compared to cells only (control) and cells with laser only groups that showed a high viability count. The dark cytotoxicity group showed insignificant decreased in viability for cells subjected to the dose of 15 μM. Significant results for A375 (Figure 6) cells when collated against the control were $p < 0.05$ (*) for the treatment group cells at doses 4 μM and $p < 0,01$ (**) for dose 15 μM and 20 μM. The A375 dark toxicity group showed no significant decrease in viability.

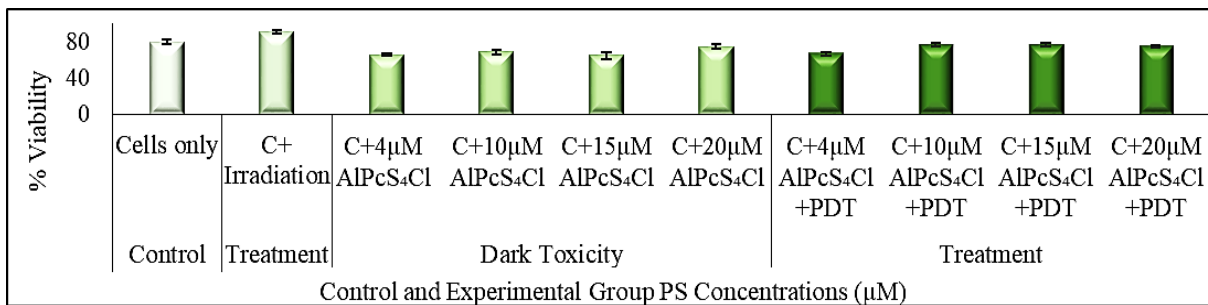


Figure 5. WS1 Trypan blue dye viability exclusion assay results for control, treatment and dark toxicity groups of increasing AlPcS₄Cl dose and laser irradiation at 673nm, fluency: 5 J/cm². No significant results were noted.

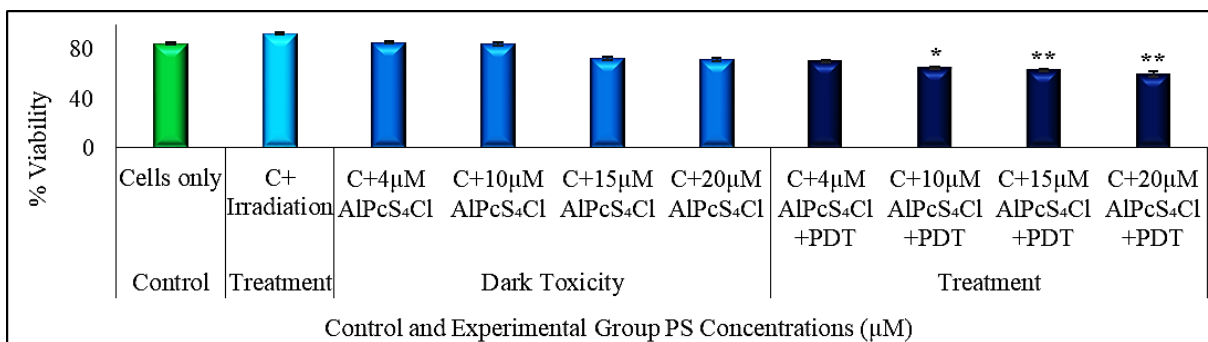


Figure 6. A375 Trypan blue dye viability exclusion assay results for control, treatment and dark toxicity groups of increasing AlPcS₄Cl dose and laser irradiation at 673nm, fluency: 5 J/cm². Significant results were noted for dose 10 μM: $p < 0,05$ (*), dose 15 μM, and 20 μM: $p < 0,01$ (**).

3.4. IC₅₀ Calculation

The lowest inhibitory concentration (IC₅₀) was established by calculations, using data from the Trypan Blue viability biochemical assay conducted. The optimal IC₅₀ concentration of AlPcS₄Cl after PDT treatment that induced approximately 50% cytotoxicity was found to be 35 µM.

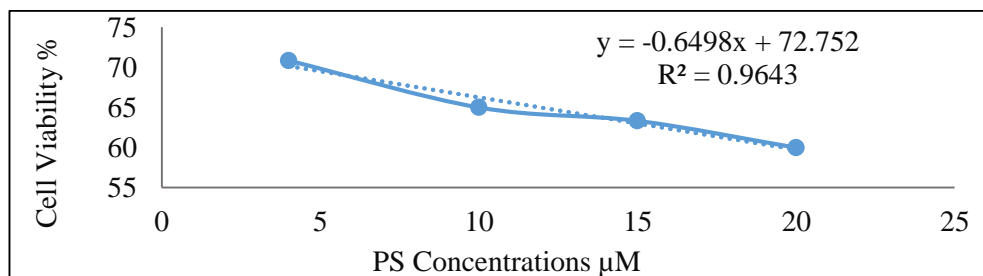


Figure 7. Trypan Blue viability IC₅₀ calculation: 35,01385 µM.

3.5. Subcellular Localisation of AlPcS₄Cl in A375 cells

Findings in Figure 8 suggest that there is passive uptake and localisation of AlPcS₄Cl PS in the mitochondria and lysosomes of cultured A375 cells. Intermediate yellow-orange is seen in image D and H, where the merged green fluorescence from the mitochondrion and red fluorescence from the PS are seen overlapping. No overlapping is seen for the ER in image L which fluoresces blue-white when merged with the PS that fluoresces red.

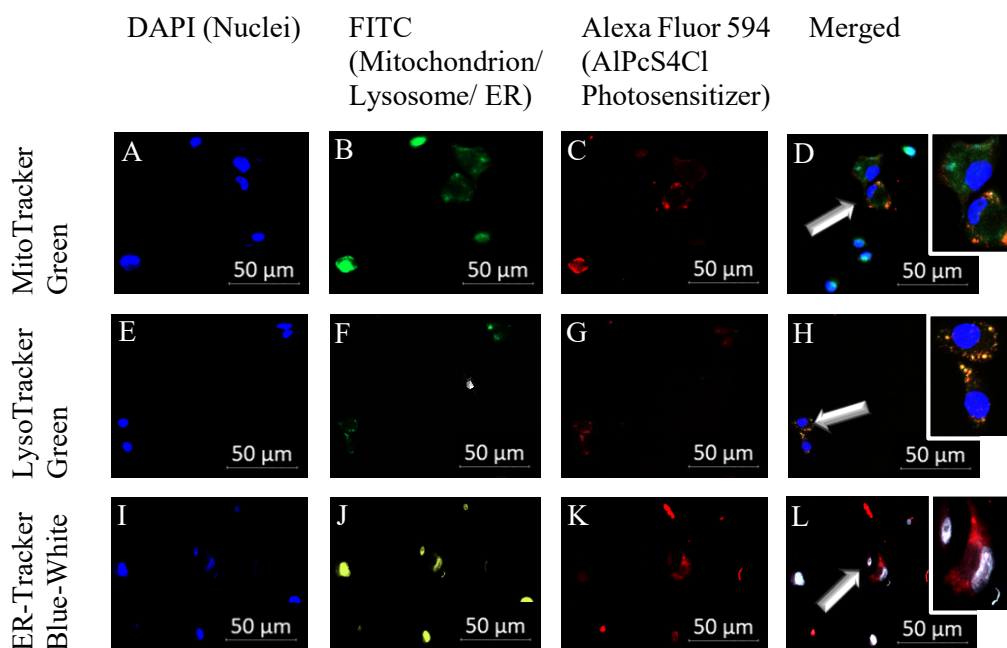


Figure 8. Subcellular localisation live cell imaging of AlPcS₄Cl PS in A375 cells: A, E, I - Control stained blue with DAPI (nuclei); B, F, J - Mitochondrion/ Lysosome fluoresces green and ER fluoresces blue-white (FITC); C, G, K - AlPcS₄Cl fluoresces red (A594). (200x magnification).

4. Conclusion

The efficiency of AlPcS₄Cl PDT on A375 cells was realised through the successful cellular uptake and accumulation of the PS in the mitochondria and lysosomes with subsequent tumour cell cytotoxicity. The cell viability and cytotoxicity study results attained from treated A375 cells demonstrated a decrease

in cell viability with an IC_{50} of 35 μ M dose of AlPcS₄Cl irradiated at 673 nm with fluency of 5 J/cm². An increasing dose concentration of the PS renders high phototoxicity for the *in vitro* PDT of melanoma A375 cells. Cell death or cytotoxic indications were not observed from the WS1 cells, those treated with PS doses and incubated in the dark as well as those without PS treatment exposed to laser irradiation. Characteristics of a good photosensitizing agent are denoted to have no dark toxicity, (Zeng et al., 2011). This can be attributed to AlPcS₄Cl, which may however show toxicity to WS1 fibroblast (normal) cells at higher dose concentrations. Moreover, the results have indicated an idea on the dose optimization of AlPcS₄Cl PS and agents that can deliver targeted therapy to accomplish future research objectives. Strategies developing and enhancing multiplex photosensitizer drug targeting systems that will deliver desired concentrations only in precisely targeted cells are progressing with an alarming interest.

Acknowledgements and Funding

This work is supported by the CSIR-DSI Council for Scientific and industrial Research) Inter-Bursary Support Programme (IBS) and the Faculty of Health Sciences Supervisor Linked Bursary (FHSSLB). The authors also thank and acknowledge the financial support by the South African Research Chairs Initiative of the Department of Science and Technology and National Research Foundation of South Africa (Grant No 98337), as well as grants received from the University of Johannesburg (URC), the National Research Foundation (NRF), and the CSIR (Council for Scientific and industrial Research) – NLC (National Laser Centre) Laser Rental Pool Programme.

Conflicts of interest

The authors declare no conflict of interest. The funders had no role in the design of the study; in the collection, analyses, or interpretation of data; in the writing of the manuscript, or in the decision to publish the results.

References

- [1] Pillaiyar T, Namasivayam V, Manickam M, Jung S H 2018 Inhibitors of melanogenesis: an updated review *J. Med. Chem.* **61** (17) 7395-7418
- [2] Holderfield M, Deuker M M, McCormick F, McMahon M 2014 Targeting RAF kinases for cancer therapy: BRAF-mutated melanoma and beyond. *Nat. Rev. Cancer* **14** (7) 455–467
- [3] Domingues B, Lopes J M, Soares P, Pópulo H 2018 Melanoma treatment in review *Immunotargets Ther.* **7** 35-49
- [4] Sekkat N, van den Bergh H, Nyokong T, Lange N 2011 Like a bolt from the blue: phthalocyanines in biomedical optics. *Molecules* **17** Basel, Switzerland 98-144
- [5] Ranyuk E, Cauchon N, Klarskov K, Guérin B, van Lier J 2013 Phthalocyanine-peptide conjugates: receptor-targeting bifunctional agents for imaging and photodynamic therapy *J. Med. Chem.* **56** 1520–1534
- [6] Oliveira C S, Turchiello R A, Kowaltowski A J, Indig G L, Baptista M S 2011 Major determinants of photoinduced cell death: subcellular localization versus photosensitization efficiency *Free Radic. Biol. Med.* **50** (4) 824-833
- [7] Mahalingam S M, Ordaz J D, Low P S 2018 Targeting of a Photosensitizer to the mitochondrion enhances the potency of photodynamic therapy *ACS Omega* **3** (6) 6066-6074
- [8] Sekhejane P R, Houreld N N, Abrahamse H 2014 Multiorganelle localisation of metallated phthalocyanine photosensitizer in colorectal cancer cells (DLD-1 and CaCo2) enhances efficacy of photodynamic therapy. *Int. J. Photoenergy.*
- [9] Emert-Sedlak L, Shangary S, Rabinovitz A, Miranda M B, Delach S M, Johnson D E 2005 Involvement of cathepsin D in chemotherapy-induced cytochrome c release, caspase activation, and cell death. *Mol. Cancer Ther.* **4** (5) 733-742
- [10] Marchal S, Francois A, Dumas D, Guillemin F, Bezdetnaya L 2007 Relationship between subcellular localisation of Focsan and caspase activation in photosensitised MCF-7 cells *Br. J. Cancer* **96** (6) 944-951

Inhibition of Lung Cancer Migration and Invasion Using a Gold Nano Photosensitizer Conjugate

Anine Crous¹, and Heidi Abrahamse²

^{1,2} Laser Research Centre, Faculty of Health Sciences, University of Johannesburg, PO Box 17011, Johannesburg 2028, South Africa

¹E-mail: acrous@uj.ac.za

Abstract. Despite advances in cancer treatment, lung cancer remains one of the leading causes of cancer deaths worldwide. Lung cancer can spread through the blood and lymphatic systems, as well as infiltrate healthy tissues underlying the lung, resulting in both distant and local metastasis. The most common causes of death are cancer metastasis and the threat of secondary tumours. The ability of cells to invade, which is largely controlled by cell motility, is an essential aspect of metastases. Photodynamic therapy (PDT), a minimally invasive cancer treatment, is based on the concept of light stimulation of a photosensitizing agent at a certain wavelength, which, combined with an optimum energy density of light activation, induces the photosensitizer (PS) to reach their triplet state, where oxidants causing tumour cell death can form in the presence of molecular oxygen. Due to their physicochemical and optical properties, gold nanoparticles have been shown to improve the effectivity of PDT by increasing the loading potential of the PS within cancer cells, are biocompatible and non-toxic, and give improved permeability and retention. The use of gold nanoparticles in nano-mediated PDT has been shown to cause lung cancer cell death. Several physiological studies, including migration, cell cycle analysis and the extracellular matrix cell invasion assay were carried out in this study to determine whether PDT using a gold nano sensitizer inhibits lung cancer migration and invasion. The results show that nano mediated PDT treatment of lung cancer inhibits lung cancer migration and invasion, causes cell cycle arrest, and reduces lung cancer proliferative abilities, elaborating on the efficacy of nano mediated PDT treatment of lung cancer.

1. Introduction

Lung cancer continues to be the top cause of cancer death globally, with an estimated 1.8 million fatalities [1]. Despite considerable diagnostic and therapeutic improvements, overall survival remains poor. About 70% of lung cancer patients have advanced-stage illness, which contributes to its high death rate [2]. Cancer metastasis is the spread of cancer cells to different organs and tissues, as well as the creation of new tumours [3]. Lung cancer treatment options vary based on the cancer's stage, size, and location in the lung. Treatment is also based on whether the cancer has spread and the patient's general condition. However, most conventional lung cancer treatments have drawbacks [4].

Photodynamic therapy (PDT), is a non-invasive, sophisticated technique of cancer treatment that is generally conducted as an outpatient operation [5]. PDT is founded on the notion of a photoexcited photosensitizer (PS) interacting with oxygen to create oxidants, resulting in the death of tumour cells. PDT follows a Type I and Type II mechanism. In type I interactions, the PS interacts with biomolecules in its excited triplet state, exchanging hydrogen atoms through the radical process.

It produces free radicals and radical ions, which combine with oxygen to produce reactive oxygen species (ROS). Triplet–triplet annihilation is the basis for Type II reactions. The excited PS interacts with oxygen resulting in the formation of reactive and cytotoxic singlet oxygen [6]. The PS's characteristics affects its pharmacokinetics and biodistribution allowing for either selective accumulation and/or selective retention preferentially in cancerous cells [7]. PDT advantages over conventional therapy includes repeatability, decreased adverse effects, no PDT-related morbidity or mortality, bio interactivity and compatibility and low cost [8]. Aluminium (III) Phthalocyanine Chloride Tetra sulphonate (AlPcS₄Cl) has been extensively studied and proven to be a PS with excellent PDT properties including high molar absorption coefficient in the red to NIR spectrum [9]. Its sulphate functional groups allow for thermal stability and solubility, along with increased oxidant production [10], is amphiphilic and has little or no dark toxicity [9].

There is still opportunity for development in PDT by improving PS delivery and making the PS target selective. Incentives for using nanoparticles (NPs) include their polydispersity, stability, and biocompatibility. Gold nanoparticles (AuNPs) have exact physicochemical and optical characteristics, are biocompatible and non-toxic, and have increased permeability and retention (EPR) [11]. AuNPs loaded with AlPcS₄ can enhance PS binding affinity and tumour selectivity, as well as EPR-induced singlet oxygen generation. It also inhibits non-specific protein binding through PEGylation of AuNPs [12]. In this study we aimed to evaluate whether nanoPDT, using a gold nano sensitizer, inhibits lung cancer metastatic abilities.

2. Materials and methods

2.1. Cell culture

Complete media composed of Rosewell Park Memorial Institute 1640 medium (RPMI), supplemented with 10% foetal bovine serum and antibiotics consisting of 0.5% penicillin/ streptomycin and 0.5% amphotericin B were used to grow lung cancer cells (A549; ATCC® CCL-185™). Cells were placed in a humidifying incubator set at RH 85%, 37°C and CO₂ of 5%.

2.2. Photodynamic treatment

An AlPcS₄Cl-goldnano bioconjugate was used where the PS using a predetermined [IC₅₀] concentration of 20 μ M AlPcS₄Cl (Frontier Scientific, AlPcS-834) [13] was adsorbed onto 20 ppm AuNP-PEG-COOH (Sigma-Aldrich, 765465) [14]. The cells were divided into four experimental groups, a control receiving no treatment, cells receiving photobiomodulation (PBM)/ irradiation alone, PDT and nanoPDT groups. The cells were irradiated with a 660 nm Light Emitting Diode (LED) plate illuminator, using the Keithley 2200-32-3 power supply (PSU). To eliminate nuisance variables, all experiments were done in the dark at ambient temperature. The parameters of irradiation are listed in Table 1 below.

Table 1. LED well plate illuminator parameters.

λ nm	V (volts)	A (amps)	Power (mW)	Intensity (mW/cm ²)	Fluence (J/cm ²)
659.4	22.913	3.02	33.130	117.17	10

2.3. Migration

The migration of cells was determined using the 'central scratch' technique. Cells were grown overnight in 6-well cell culture plates and incubated. A central scratch was made using a sterile P-200 pipette tip prior to irradiation. At 0, 24, and 48 hours after irradiation, migration was examined using an inverted light microscope (Wirsam, Olympus CKX41) and captured using a SC30 Olympus Camera.

2.4. Cell cycle analysis

DNA content was quantified using flow cytometry as a measure of cell cycle. Cells were fixed using 70% ethanol and washed, followed by treatment with 50 μ l RNase (stock 100 μ g/ml) and stained with 200 μ l Propidium iodide (PI) (stock solution 50 μ g/ml). For analysis using a flow cytometer (BD Accuri Flow Cytometer C6) the cell population was gated and applied to a scatter plot, where the gated samples were then applied to a PI histogram plot describing the cell phases.

2.5. Proliferation and Toxicity

The effect of PDT and nanoPDT on the metabolism of lung cancer cells was evaluated by the quantity of ATP present in the cells following treatment. Intracellular ATP was quantified using a Multilabel Counter (Perkin Elmer, VICTOR3TM, 1420) in conjunction with the CellTiter-Glo[®] luminous cell proliferation assay (Promega, G7570). To ascertain the degree of toxicity, the quantity of LDH produced from cells because of membrane damage and cell death was determined. Where formazan generation was determined using a multilabel counter at 490 nm, the CytoTox96[®] nonradioactive cytotoxicity assay (Promega, G400) was employed.

3. Results

3.1. Migration

The scratch test is conducted by creating a "scratch" in a monolayer of cells and photographing the cells at the start and at regular intervals throughout cell migration as the scratch closes. Figure 1 shows the migration of lung epithelial carcinoma cells (A549) at 0, 24 and 48 hours post PDT treatment. Untreated a) control cells and b) cells receiving PBM show a similar trend in migration where the cells move towards the central scratch and the cell density increases. Cells treated with c) PDT and d) nanoPDT show a decreased migration rate and were not able to close the scratch over time, where dead cells and cell debris were seen floating in the culture medium due to cell arrest.

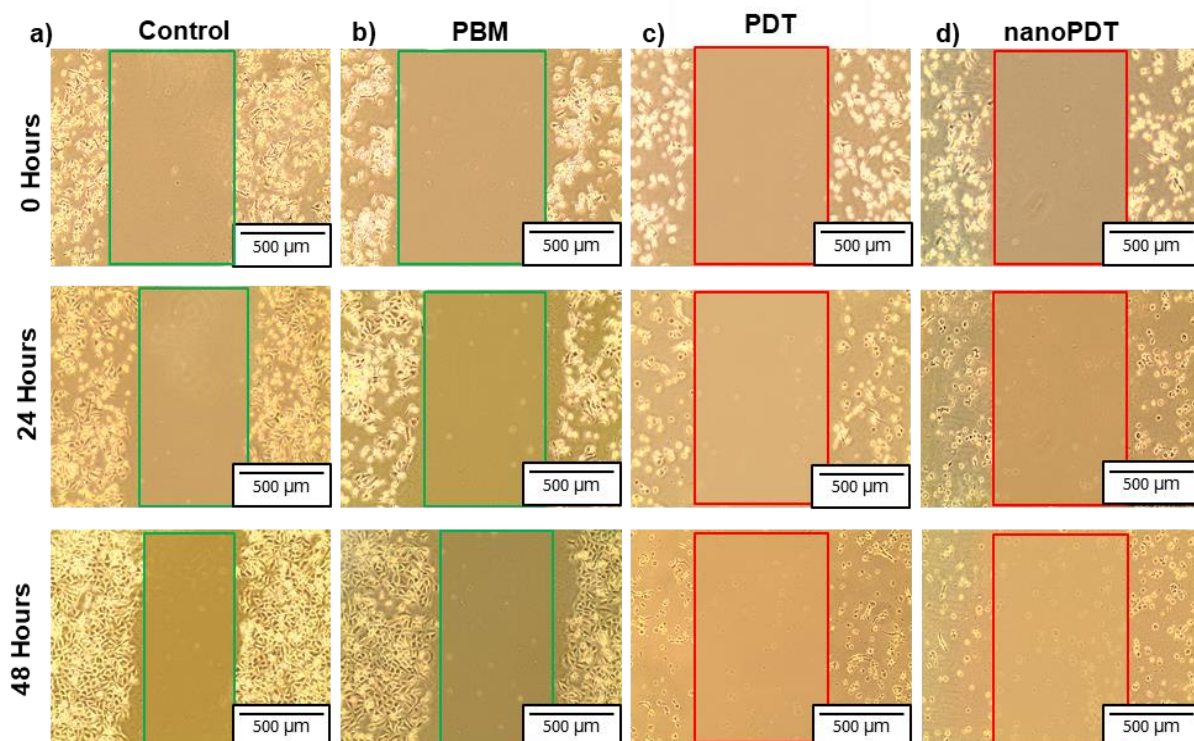


Figure 1. Migration of lung epithelial carcinoma cells (A549) at 0, 24 and 48 hours post PDT treatment.

3.2. Cell cycle analysis

The cell cycle phases were identified by quantifying cellular DNA. The cell cycle is a multiple process during which cells proliferate. It consists of the gap 1, or G1, stage where cells mature. The S phase where the cell copies its DNA, the G2 phase where cells prepare to divide and does DNA checks and the M phase where cells undergo mitoses. Cells can also move in to the G0 phase indicative of cell cycle arrest or cell death. Results in figure 2 show that the a) control cells and b) PBM treated cells are predominantly in the G1 and S phase. Whereas c) PDT treated samples show many cells entering G0, where the percentage of cells in G1 decreased, as well as the cells moving out of S phase. Cell treated using d) nanoPDT shows an even greater cell cycle arrest with no cells seen in S phase and less cells in G1, compared to PDT.

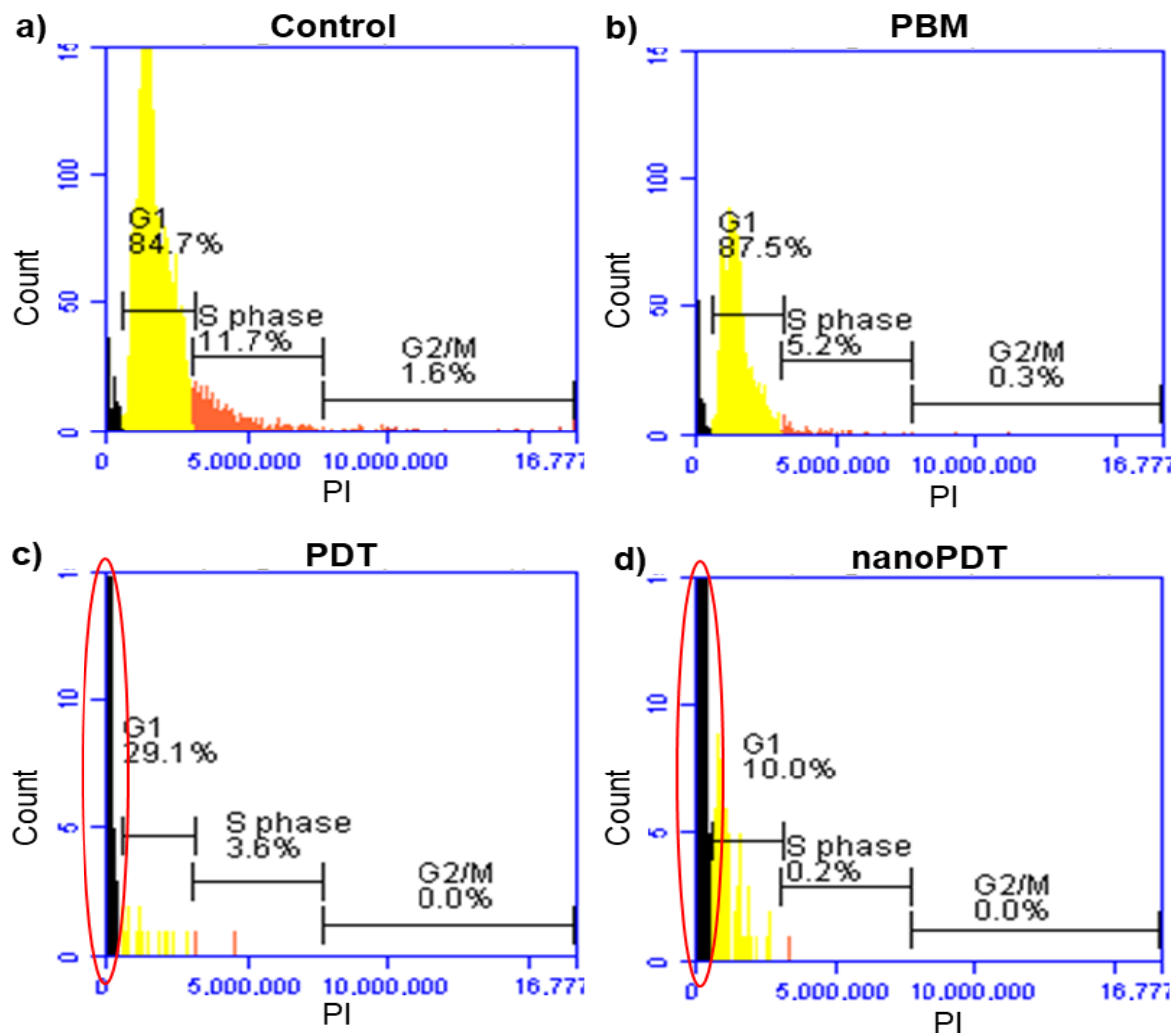


Figure 2. Cell cycle analysis through DNA quantification of lung epithelial carcinoma cells (A549) 24 hours post PDT treatment.

3.3. Proliferation and toxicity

Cell proliferation was measured using ATP luminescence in relative light units and cytotoxicity was measured as the amount of LDH leakage caused by membrane damage and cell death, where it was

read using an absorbance of 490 nm. Proliferation results (figure 3 a) show that control cells and PBM treated cells had an increased proliferation rate with PBM cells having a significant increase in proliferation. Cells treated with PDT and nanoPDT had a significant decrease in proliferation compared to the control and cells treated with PBM alone. There is a slight decrease seen in cells treated with nanoPDT compared to PDT, however this decrease is not significant. Cytotoxicity results (figure 3 b) show that control cells and PBM-treated samples released little LDH into the environment, cells treated with PDT and nanoPDT both released significant amounts of LDH. Additionally, nanoPDT treated samples show a higher increase in LDH release when compared to PDT-treated samples.

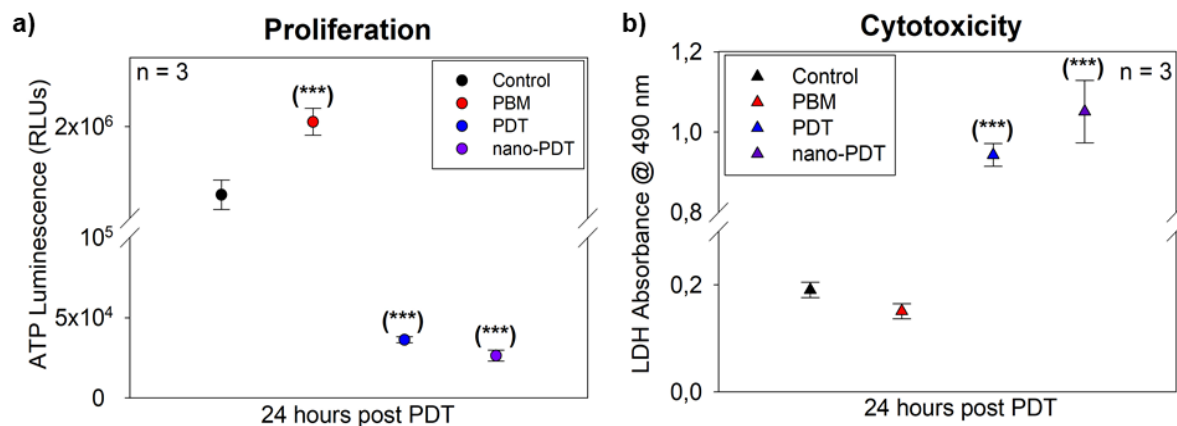


Figure 3. Proliferation and cytotoxicity of lung epithelial carcinoma cells (A549) 24 hours post PDT treatment.

4. Discussion and Conclusion

Considering lung cancers ability to metastasize, cancer treatments need to be effective at reducing cell motility and their proliferative abilities, which can reduce cancer relapse and enhance prognosis. The interruption of normal biological function followed by disseminating tumour cells causes mortality and morbidity in individuals with cancers. Cancer metastasis is thought to be caused by tumour cell motility. The importance of tumour cell migration in metastatic development has been demonstrated experimentally and empirically through fundamental and clinical studies. Cell motility is seldom targeted clinically, and adjuvant treatment to prevent cancer cell spread is severely restricted [15]. The purpose of this study was to determine the effect of nanoPDT on lung cancer cells. NanoPDT was shown to limit migration because of cell death. Cancer cells must be both proliferative and invasive to infiltrate and metastasize. Whereas lung cancer's proliferative, invasive, and migratory properties are correlated to the cell cycle phase they are in [16]. Cancer cell cycle arrest in the G1 phase is required for cell invasion [17] and cells in the S phase are indicative of proliferative activity [18]. Cells that are in the G0 phase or are senescent are unable to begin the cycle due to DNA damage and self-destruction [19]. NanoPDT, more than PDT, induces lung cancer cell cycle arrest, in which cells exit the G1/S stages of invasion and proliferation and enter irreversible G0 owing to DNA damage and degradation. The regulatory criteria for cancer treatment include the need that the drug be cytostatic, producing antiproliferation and toxicity in the cancer, as research indicates that therapy-induced senescence offers a unique functional target that may enhance cancer therapy [20]. The results of this study suggest that nanoPDT is an effective cytostatic treatment for lung cancer cells, as demonstrated by a significant reduction in proliferation and an increase in toxicity. In conclusion, the impacts of PDT and nanoPDT on lung cancer cell motility demonstrated substantial reductions in cell migration and proliferation, an increase in cell cycle arrest, and a large rise in membrane damage, all of which

facilitated lung cancer cells' anti-metastatic capacities. In general, nanoPDT demonstrated increased anti-metastatic activity.

Acknowledgments

The authors sincerely thank the University of Johannesburg and the Laser Research Centre for their facilities and use of equipment. This work was supported by the National Research Foundation (NRF) S&F -Scarce Skills Postdoctoral Fellowship (Grant no: 120752) received by Anine Crous and the South African Research Chairs Initiative of the Department of Science and Technology and National Research Foundation of South Africa (SARChI/NRF-DST) (Grant no: 98337) received by Heidi Abrahamse.

References

- [1] Sung H, Ferlay J, Siegel R L, Laversanne M, Soerjomataram I, Jemal A and Bray F 2021 *CA Cancer J Clin* **71** 209-49
- [2] Martins D, Mendes F and Schmitt F 2021 *Pathobiology* **88** 198-207
- [3] Martin T A, Ye L, Sanders A J, Lane J and Jiang W G 2013 *Madame Curie Bioscience Database [Internet]*: Landes Bioscience
- [4] Wang W, Hao Y, Liu Y, Li R, Huang D B and Pan Y Y 2021 *Wiley Interdiscip Rev Nanomed Nanobiotechnol* **13** e1654
- [5] Arruebo M, Vilaboa N, Saez-Gutierrez B, Lambea J, Tres A, Valladares M and Gonzalez-Fernandez A 2011 *Cancers (Basel)* **3** 3279-330
- [6] Castano A P, Demidova T N and Hamblin M R 2004 *Photodiagnosis Photodyn Ther* **1** 279-93
- [7] Castano A P, Demidova T N and Hamblin M R 2005 *Photodiagnosis Photodyn Ther* **2** 91-106
- [8] Giuliano E A 2015 *Robinson's Current Therapy in Equine Medicine*, ed K A Sprayberry and N E Robinson (St. Louis: W.B. Saunders) pp 624-9
- [9] Amin R M, Hauser C, Kinzler I, Rueck A and Scalfi-Happ C 2012 *Photochemical & photobiological sciences : Official journal of the European Photochemistry Association and the European Society for Photobiology* **11** 1156-63
- [10] Sekkat N, Bergh H v d, Nyokong T and Lange N 2012 *Molecules* **17** 98
- [11] Ben Tahar I, Fickers P, Dziedzic A, Ploch D, Skora B and Kus-Liskiewicz M 2019 *Microb Cell Fact* **18** 210
- [12] Jang B, Park J Y, Tung C H, Kim I H and Choi Y 2011 *ACS Nano* **5** 1086-94
- [13] Crous A, Dhilip Kumar S S and Abrahamse H 2019 *J Photochem Photobiol B* **194** 96-106
- [14] Crous A and Abrahamse H 2020 *Int J Mol Sci* **21** 3742
- [15] Palmer T D, Ashby W J, Lewis J D and Zijlstra A 2011 *Adv Drug Deliv Rev* **63** 568-81
- [16] Huang B, Cohen J R, Fernando R I, Hamilton D H, Litzinger M T, Hodge J W and Palena C 2013 *Cell Death Dis* **4** e682
- [17] Bayarmagnai B, Perrin L, Pourfarhangi K E and Gligorijevic B 2018 *bioRxiv* 412916
- [18] Eymin B and Gazzeri S 2010 *Cell Adh Migr* **4** 114-23
- [19] Malumbres M 2014 *Abeloff's Clinical Oncology*, ed J E Niederhuber, *et al.* (Philadelphia: Churchill Livingstone) pp 52-68.e6
- [20] Ewald J A, Desotelle J A, Wilding G and Jarrard D F 2010 *J Natl Cancer Inst* **102** 1536-46

**DIVISION D –
ASTROPHYSICS & SPACE
SCIENCE**

Kinematics and star formation histories of brightest cluster galaxies

S A Nkosi^{1*} and S I Loubser¹

¹Centre for Space Research, North-West University, Potchefstroom 2520, South Africa

E-mail: 27201732@nwu.ac.za

Abstract. We present a study on the kinematics and star formation histories of brightest cluster galaxies (BCGs) in a sample of clusters over a 3.4 Gyr time period ($0.3 < z < 0.8$). We analyze the spectroscopic data of Brightest cluster galaxies Evolution with AdvACT, MeerKAT and SALT (BEAMS) BCGs observed on the Southern African Large Telescope (SALT). We focus on stacking the clusters as a function of redshift, to increase the signal-to-noise ratios. We fit the stacked BCG spectra using full-spectrum fitting to measure kinematics and stellar populations, from which star formation histories can be inferred. For the example stack that we present here it is found to have ages in the range 2.74 - 9.12 Gyr, and metallicities in the range $-1.17 < [Z/H] < 0.06$ depending on the model used. The spectra also indicates the presence of a younger component although with varying contribution, depending on the model used. The results are highly dependent on the stellar models and libraries chosen, emphasising the need to fit multiple models and interpret their difference.

1. Introduction

Brightest cluster galaxies (BCGs) are the most massive and luminous galaxies in the Universe. A typical BCG is located near the centre of its parent cluster and well-aligned with the cluster galaxy distribution suggesting that it lies at the bottom of the cluster's gravitational potential well [4, 9]. Their origin and evolution is intimately linked with the evolution of their host cluster, and therefore can provide direct information on the formation and history of large-scale structures in the Universe.

BCGs Evolution with AdvACT, MeerKAT and SALT (BEAMS)¹ is a new spectroscopic survey of BCGs in massive clusters detected by the Advanced Atacama Cosmology Telescope (AdvACT). The goal is to trace the evolution of Active galactic nucleus (AGN)

¹ BEAMS - <https://acru.ukzn.ac.za/~beams/>

feedback (both radio and quasar mode), stellar populations, and the growth of central galaxies in clusters over a 3.4 Gyr time period ($0.3 < z < 0.8$). The clusters are detected using the redshift-independent Sunyaev-Zel'dovich (SZ) effect [13, 14], and the targets are selected from within the Dark Energy Survey (DES) [12] footprint which ensures excellent quality deep imaging.

A fraction of the BCGs exhibit recent star formation and therefore have evolutionary histories that are in stark contrast with the conventional expectation that giant elliptical galaxies in the cluster environment are all quiescent, passively evolving, ‘red and dead’ systems [2, 8]. We are particularly interested in the star formation histories of the BCGs, and we investigate full-spectrum fitting to derive the stellar populations, first on single BCG spectra, and then on BCG spectra stacked in redshift bins. Here we describe some preliminary results from the BEAMS project.

2. Optical spectroscopy and data reduction

2.1. The cluster sample

The AdvACT SZ cluster survey is a sample of > 4000 optically confirmed clusters with both spectroscopic and photometric redshifts [6, 7]. The data in this study utilise a large sample of BEAMS optical selected clusters, with a well-defined selection function that is relatively independent of cluster mass across a wide range of redshifts. The following selection criteria were used to select a sample of clusters to be observed with SALT (2019-1-LSP-001, PI: Matt Hilton):

- (i) firstly, a signal-to-noise ratio (S/N) $> 5\sigma$ cut was made in the AdvACT SZ detection significance;
- (ii) restricted the redshift range to $0.3 < z < 0.8$;
- (iii) the clusters are required to be within the footprint of DES.

Of the 186 clusters satisfying these criteria, 89 of them have been observed on the Robert Stobie Spectrograph (RSS) using the longslit spectroscopy mode over a period of three observing semesters.

2.2. Data reduction and the BCG slit

The data reduction was performed with the RSSMOSPipeline² [6], including wavelength calibration, and extraction of one dimensional (1D) spectra. The slit was positioned to observe more than one galaxy, and we needed to identify which of the extracted 1D spectra contained the BCG. The identification of the BCG slit was made via a visual inspection of the DES imaging with the aid of finder charts and region files. In Figure 1 given as an example, the long-slit data contains spectra for four galaxies. The BCG is located at the centre of the finder’s chart where the green vertical and horizontal lines meet (see Fig. 1b), overlaying the region file on the DES imaging allowed us to approximate the slit that had the BCG. The BCG given in this example corresponds to the 1D spectra marked “slit 2”. This process was repeated for all clusters in the survey.

² <https://github.com/mattyowl/RSSMOSPipeline>

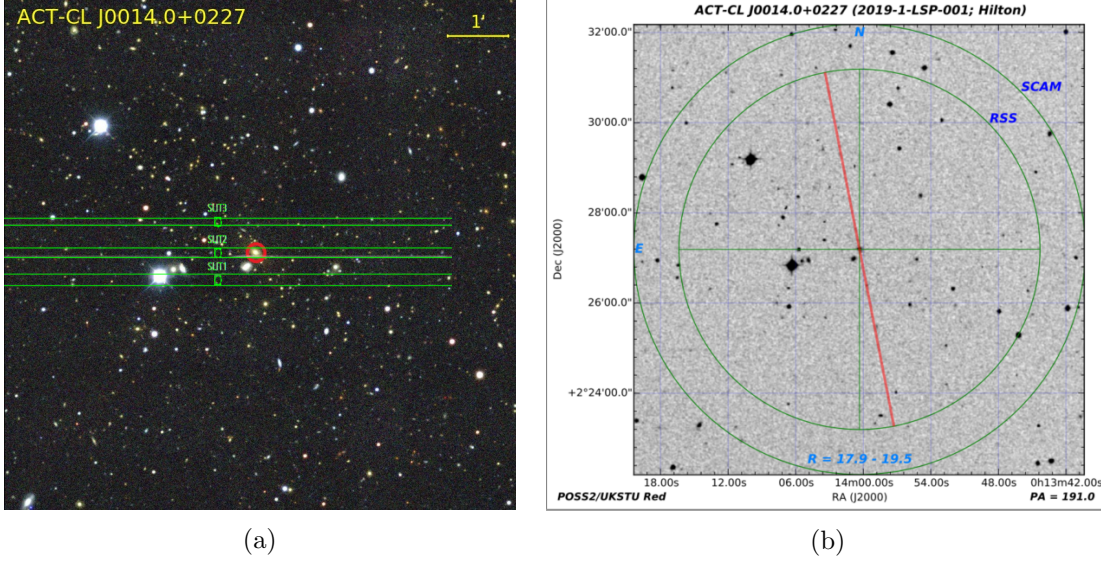


Figure 1: (a) DES cluster image of ACT-CL J0014.0+0227 ($z = 0.337$). The BCG is circled in red. (b) SALT finder chart of J0014.0+0227, used in the identification process of the BCG. The green slit lines (not shown to scale) is the region file of J0014.0+0227, used in the identification process of the slit in which the BCG is located. The BCG is this scenario was in slit 2.

3. Spectral analysis

We used Penalized Pixel-Fitting (PPXF)³ [1, 16] to find the stellar kinematics (velocity, V , and line-of-sight velocity dispersion, σ) and to measure any emission lines present. We first attempted to fit model spectra to the spectra of individual BCGs. In Figure 2, we can see that the S/N is too low, as PPXF struggled to fit the model spectra and the kinematics measured were not accurate. We used χ^2 statistics to determine the best fitting template.

In order to make improvements in the fit to the model spectra and to make accurate measurements of kinematic properties we stacked the spectra of BCGs of similar redshifts (see Figure 3), using *SPECSTACK*⁴ [15]. The BCGs were firstly grouped into five groups, these were $0.3 \leq z < 0.4$, $0.4 \leq z < 0.5$, $0.5 \leq z < 0.6$, $0.6 \leq z < 0.7$ and $0.7 \leq z < 0.8$ and from these groups so-called “stacking groups” were derived by taking BCGs with redshift at ± 0.05 of each other. The stacked spectra varied from 3 spectra to as much as 7 spectra per stacking group. From using *SPECSTACK* we can observe that the model fit to the spectra is much improved (see Figure 4), and thus the various measurements can be made more accurately, such as the velocity dispersion.

We use Fitting iteratively for relative likelihood analysis (FIREFLY)⁵ [3, 5, 10, 11, 17] to fit the stacked spectra in order to derive the stellar population properties of BCGs (i.e.,

³ <https://www-astro.physics.ox.ac.uk/~mxc/software/>

⁴ <https://specstack.readthedocs.io/en/latest/>

⁵ <https://www.icg.port.ac.uk/firefly/>

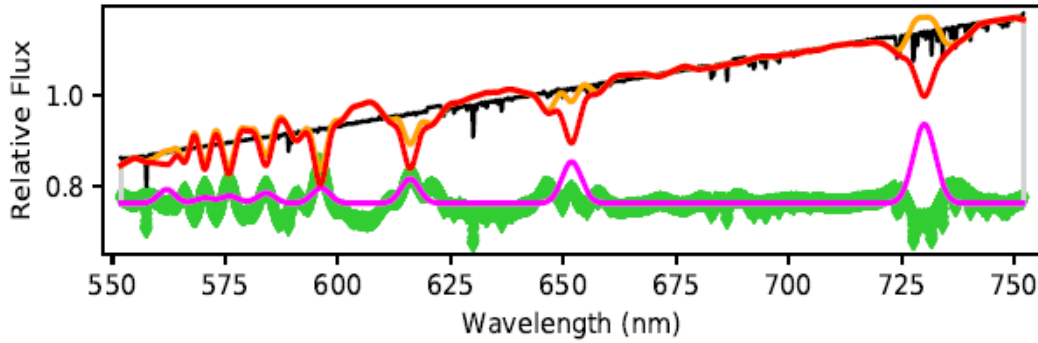


Figure 2: Spectra of ACT-CL J0014.0+0227 at $z = 0.337$, before stacking. The S/N of a single BCG is too low to fit with stellar templates. The black line is the relative flux of the observed spectrum. The red line is the pPXF fit for the stellar component, while the orange line is a fit to the gas emission lines. The green symbols at the bottom are the fit residuals, while the blue line is the gas only best-fitting spectrum.

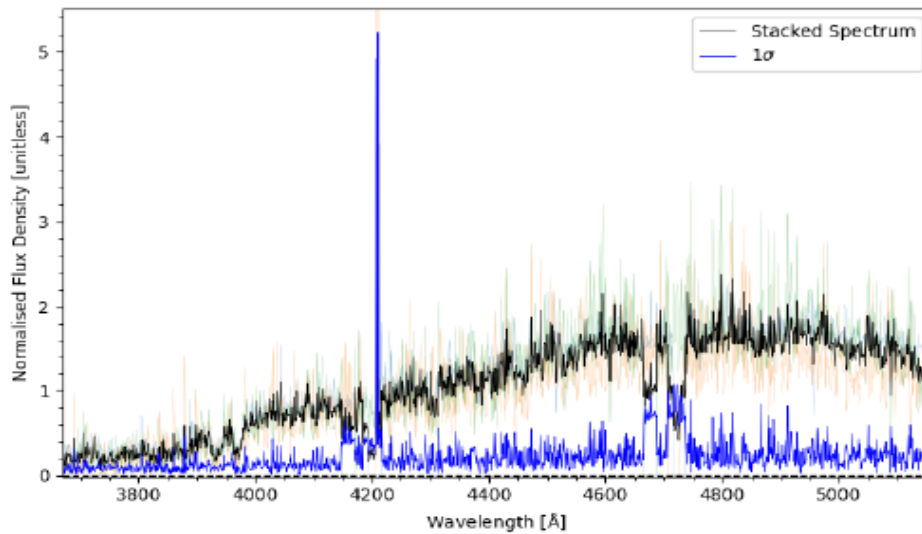


Figure 3: Stacked spectra of ACT-CL J0257.7-2209, ACT-CL J0405.9-4915 and ACT-CL J0014.0+0227 at $z = 0.323$, 0.325 and 0.337 . The black line represents the stacked spectra. Green, orange and cyan are the three individual spectra that were stacked together. The blue line at the bottom is the residual.

age, metallicity and dust extinction).

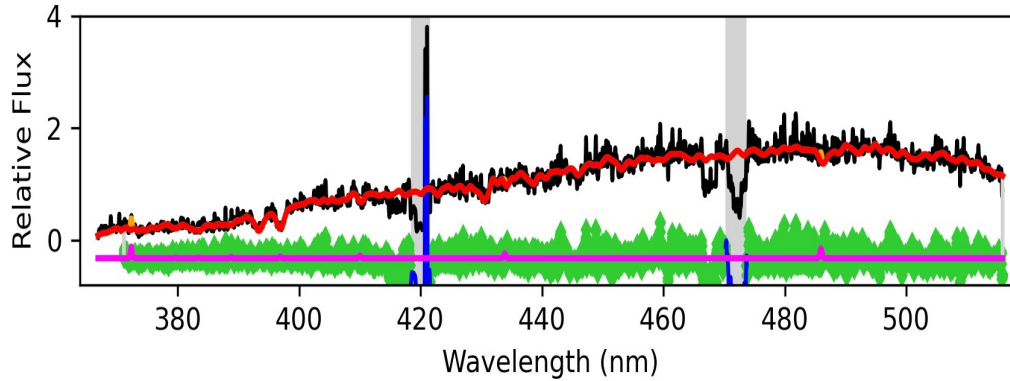


Figure 4: Stacked spectra model fit. The grey lines represent the masked regions of the “SALT chip gaps” in order to improve the model fit of the spectra. The red line is the pPXF fit for the stellar component, while the orange line is a fit to the gas emission lines. The green symbols at the bottom are the fit residuals, while the blue line is the gas only best-fitting spectrum.

4. Results

We show preliminary results from the FIREFLY analysis of the stacked spectra of ACT-CL J0257.7-2209, ACT-CL J0405.9-4915 and ACT-CL J0014.0+0227 as an example. We fit different libraries, i.e., the MaStar library [11] and the M11 library [10] together with different initial mass functions (IMFs). This is done to quantify the systematic uncertainties on the ages and metallicities measured using different stellar population model ingredients. The M11 library contains the MILES and STELIB models. The MILES model has spectra of 985 stars with a wavelength range of 3500 - 7430 Å covering most evolutionary stages based upon what can be expected to exist in our Galaxy at all metallicities down to $[\text{Fe}/\text{H}] \sim -2.0$ [10]. The STELIB model has spectra of 249 stars with a wavelength range of 3200 - 9300 Å, most spectral types and luminosity classes are included, with a fair coverage in metallicity. The MaStar library comprises of ~ 9000 , high S/N spectra, and has the E-MaStar and Th-MaStar models both models have a wavelength range of 3621.6 - 10352.3 Å [11].

We show for example the results from the E-MaStar model (see Figure 5) given here for the Kroupa (KR) IMF, STELIB model (see Figure 6) given here for both the KR and Salpeter (SS) IMFs and the MILES model (see Figure 7) given here for the KR IMF. For the STELIB model both IMFs show that the stacked spectra has an average age of 6.02 Gyrs and a metallicity of 0.05 dex. The MILES model for the SS IMF showed an age of 9.08 Gyrs and a metallicity of -1.08 dex and for the KR IMF an age of 9.12 Gyrs and metallicity of -1.01 dex. The E-MaStar produced an age of 3.82 Gyrs and a metallicity of -1.16 dex for the SS IMF and for the KR IMF an age of 2.74 Gyrs and a metallicity of -0.82 dex.

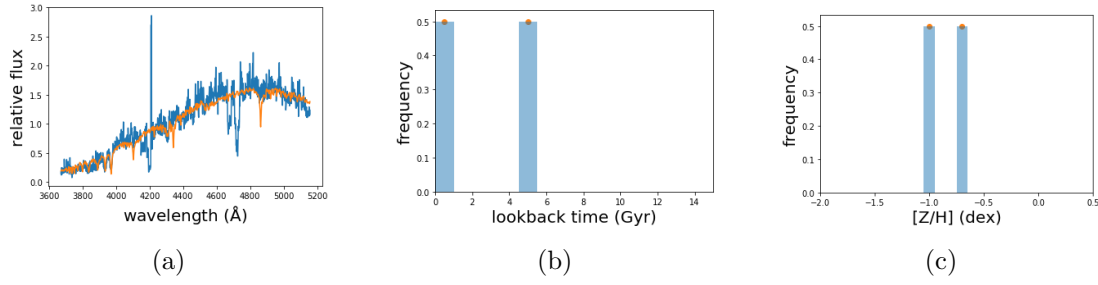


Figure 5: E-MaStar model. (a) The fitted spectra (b) Lookback time (age) (c) and the metallicity of the stacked spectra. The orange line represents the FIREFLY best fit. In (b) it can be seen that this stacked spectrum can be fitted by two stellar components (a young ~ 5 Gyr component, and a much younger stellar component).

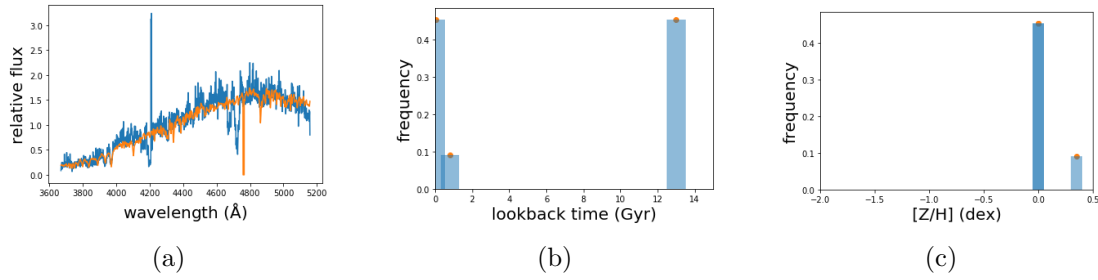


Figure 6: STELIB Model (a) The fitted spectra, (b) Lookback time (age) (c) and the metallicity of the stacked spectra. The orange line represents the FIREFLY best fit. In (b) it can be seen that this stacked spectrum can be fitted by three stellar components (an old ~ 13 Gyr component, a bigger and much young stellar component and a much smaller younger stellar component).

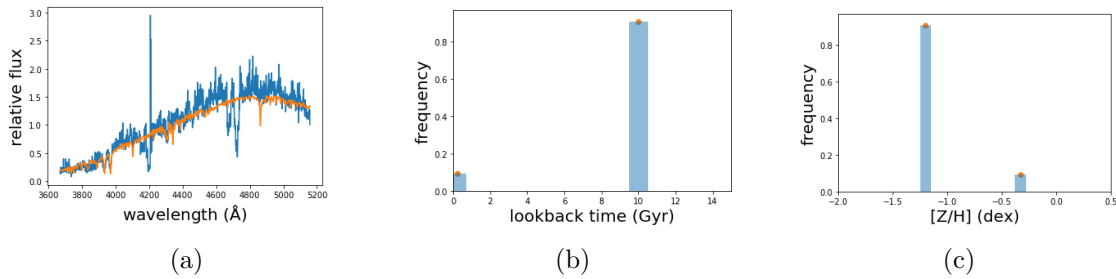


Figure 7: MILES model (a) The fitted spectra, (b) Lookback time (age) (c) and the metallicity of the stacked spectra. The orange line represents the FIREFLY best fit. In (b) it can be seen that this stacked spectrum can be fitted by two stellar components (an old 10 Gyr component, and a much smaller, younger stellar component).

5. Conclusions

We investigate the kinematics and star formation histories in BCGs drawn from the Advanced Atacama Cosmology Telescope (AdvACT) Sunyaev–Zel’dovich (SZ) cluster survey at redshift $0.3 < z < 0.8$. From the preliminary results, we observe that single BCG spectrum does not have enough S/N to fit with spectral fitting software (i.e., PPXF and FIREFLY) as the fit fails. We use *SPECSTACK* to stack spectra in redshift bins to achieve enough S/N. We measure stellar kinematics with PPXF. We measure stellar populations using FIREFLY for different models, stellar libraries and IMFs to determine the ages and metallicities of the stacked spectra (and systematic errors). For the example stack that we present here we find that the MILES model is a poorer fit compared to the other two based on the continuum level. The STELIB and E-MaStar models both give ‘intermediate’ age stellar components and indicate the presence of a younger component (although with varying contributions). The results are highly dependent on the stellar models and libraries chosen, emphasising the need to fit multiple models and interpret their differences. Stacking spectra enables us to investigate BCG evolution with redshift.

6. Acknowledgements

This work is based on the research supported by the National Research Foundation of South Africa (SIL: Grant number 120850). Opinions, findings and conclusions or recommendations expressed in this publication is that of the author(s), and that the NRF accepts no liability whatsoever in this regard. SAN wishes to thank the National Astrophysics and Space Science Programme (NASSP) for financial support.

References

- [1] Cappellari M 2017 *Mon. Not. R. Astron. Soc.* **466** 798-811
- [2] Cavagnolo K W, Donahue M, Voit G M and Sun M 2008 *Astrophys. J.* **683** L107
- [3] Comparat J *et al.* 2017 Stellar population properties for 2 million galaxies from sdss dr14 and deep2 dr4 from full spectral fitting *Preprint* arXiv:1711.06575
- [4] De Propriis R *et al.* 2021 *Mon. Not. R. Astron. Soc.* **500** 310-18
- [5] Goddard D *et al.* 2017 *Mon. Not. R. Astron. Soc.* **466** 4731-58
- [6] Hilton M 2018 *et al. Astrophys. J.* **235** 20
- [7] Hilton M *et al.* 2021 *Astrophys. J.* **253** 3
- [8] Loubser S I, Babul A, Hoekstra H, Mahdavi A, Donahue M, Bildfell C and Voit G M 2016 *Mon. Not. R. Astron. Soc.* **456** 1565-78
- [9] Loubser S I, Babul A, Hoekstra H, Bahé Y M, O’Sullivan E and Donahue M 2020 *Mon. Not. R. Astron. Soc.* **496** 1857-80
- [10] Maraston C and Strömbäck G 2011 *Mon. Not. R. Astron. Soc.* **418** 2785-811
- [11] Maraston C *et al.* 2020 *Mon. Not. R. Astron. Soc.* **496** 2962-97
- [12] Perez S J A *et al.* 2018 *Astrophys. J.* **239** 2
- [13] Sunyaev R A and Zeldovich Ya B 1970 *Astrophys. Space Sci.* **2** 66
- [14] Sunyaev R A and Zeldovich Ya B 1972 *Astrophys. Space Sci.* **4** 173
- [15] Thomas R 2019 *Astrophysics Source Code Library* 1904
- [16] Vazdekis A, Sánchez-Blázquez P, Falcón-Barroso J, Cenarro A J, Beasley M A, Cardiel N, Gorgas J and Peletier R F 2010 *Mon. Not. R. Astron. Soc.* **404** 1639-71
- [17] Wilkinson D M, Maraston C, Goddard D, Thomas D and Parikh T 2017 *Mon. Not. R. Astron. Soc.* **472** 4297-326

Probing dark matter in the Madala model using radio observations

R K Temo¹ and G M Beck

School of Physics and Centre for Astrophysics, University of the Witwatersrand,
Johannesburg, Wits 2050, South Africa

E-mail: temokhilly@gmail.com

Abstract. The Madala (or 2HDM+S) model was introduced to explain several anomalies observed at the Large-Hardon-Collider. This model introduces an extra Higgs doublet (2HDM) and an additional scalar boson S . Furthermore, a dark matter candidate can be accomodated, coupling to the standard model via the S boson. Using the 2HDM+S dark matter parameter space previously found to fit the AMS-02 cosmic ray, and Fermi-LAT gamma-ray excesses we make synchrotron emission predictions and compare it with radio observations in variety of targets. The regions of interest for the predictions are M31 (or Andromeda galaxy) as well as the Coma and Ophiuchus galaxy clusters. The 3σ exclusion limits produced in this work do not exclude the Madala model that best fits the cosmic-ray and gamma-ray excesses.

1. Introduction

Madala model extends the Higgs-sector of the standard model (SM) by introducing bosons heavier than the SM Higgs boson h . The bosons introduced are the Madala boson H and a Higgs-like scalar mediator S . Parameters of the model are fixed such that $m_H = 270 \text{ GeV}$, $m_S = 150 \text{ GeV}$ and assuming the dominance of the decay mode $H \rightarrow Sh, SS$ [1]. In essence the model was postulated to explain the anomalous features seen in Run-1 [1, 2] and Run-2 data [3] at the LHC. The particular anomalies include the Higgs boson's transverse momentum p_T and the event excesses in the multi-leptons final states [1, 2, 4, 5, 6]. Interestingly, the model also provides a dark matter (DM) candidate χ . In this work, we try to constrain χ from an astrophysical standpoint.

The regime for using radio-band for indirect DM search was prominently advocated in Ref. [7], and the field has been active ever since. For example, Ref. [8] performed a radio-frequency indirect DM search using the Australian Compact Telescope Array (ATCA) instrument, and highly competitive constraints were placed on the DM annihilation cross-section of DM particles (model-independent). However, in this work, we employ a model-dependent approach for the indirect DM searches.

In this work we extend the previous work in [9], where χ was constrained using the cosmic-ray (positrons and anti-protons) excesses observed by the Alpha Magnetic Spectrometer (AMS-02) [10, 11] and the excesses seen by Fermi-LAT [12] in gamma-ray fluxes from the Milky-Way's galactic centre. The parameter space that best fits the aforementioned excesses is employed to make radio emission predictions for the sources, M31, Coma cluster and Ophiuchus cluster. The predicted DM synchrotron fluxes, from the 2HDM+S model, are compared to radio data in M31

as well as the Coma and Ophiuchus galaxy clusters to produce the 3σ level exclusion limit. We find that the radio data for the sources considered in this work do not exclude the 2HDM+S model. This is the case when both Einasto and NFW halo are considered for the 2HDM+S parameter space. It is worth highlighting that M31 place more robust limits as compared to the Coma and Ophiuchus cluster.

This paper is structured as follows; Section 2 describes the synchrotron emission from DM annihilations. Section 3 discusses the DM halos environment that governs our DM targets. Finally in Section 4 results are depicted and discussed.

2. Synchrotron Emission from Dark Matter Annihilation

Since the regime of interest is the radio band, we consider the synchrotron emission from the DM annihilation induced positrons. We consider the DM annihilation through S according to $2 \rightarrow 2$ scattering. The cascade of the scattering process follows $\chi\bar{\chi} \rightarrow S \rightarrow x$ (where x corresponds to some SM product). The source function for the SM products i (positrons or electrons) with energy E is given by,

$$Q_i(E, \vec{x}) = \frac{1}{2} \langle \sigma V \rangle_f \sum_f \frac{dN_i^f}{dE} B_f \left(\frac{\rho_\chi}{M_\chi} \right)^2, \quad (1)$$

where $\langle \sigma V \rangle$ denotes the thermally velocity-averaged DM annihilation cross-section at 0 K, f denotes the kinematically allowed annihilation states with the branching ratio B_f , dN_i^f/dE denotes the production spectra for the SM products taken from the 2HDM+S model [9], the factor $(\rho/M_\chi)^2$ (where M_χ , ρ_χ denote the dark matter mass and density respectively) yields the dark matter pair density at the given position \vec{x} within the galactic halo. The average power per positron with energy E is given by [13],

$$P_{\text{synch}}(\nu, E, r, z) = \int_0^\pi \frac{\sin^2 \theta}{2} 2\pi \sqrt{3} r_e m_e c \nu_g F_{\text{synch}} \left(\frac{\kappa}{\sin \theta} \right) d\theta, \quad (2)$$

where ν denotes the observed frequency, r denotes the position within the halo, z denotes the redshift of the source of interest, r_e denotes the electron's classical radius, m_e denotes the electron's mass, c is the speed of light in vacuum, and finally, ν_g denotes the gyro-frequency for the non-relativistic case. Then the parameters κ and F_{synch} are further defined by,

$$\kappa = \frac{2\nu(1+z)}{3\nu_g \gamma^2} \left(1 + \left(\frac{\gamma \nu_p}{\nu(1+z)} \right)^2 \right)^{\frac{3}{2}}, \quad (3)$$

with the ν_p denoting the plasma frequency which turns out to be directly proportional to $\sqrt{n_e}$, and γ denotes the Lorentz factor of the positron. Additionally, the synchrotron kernel is given by,

$$F_{\text{synch}}(x) = x \int_x^\infty K_{5/3}(y) dy \approx 1.25 x^{\frac{1}{3}} e^{-x} (648 + x^2)^{\frac{1}{12}}. \quad (4)$$

Then the emissivity of synchrotron radiation is given by,

$$j_{\text{synch}}(\nu, r, z) = \int_{m_e}^{M_\chi} \left(\frac{dn_{e^-}}{dE} + \frac{dn_{e^+}}{dE} \right) P_{\text{synch}}(\nu, E, r, z) dE, \quad (5)$$

where dn_{e^+}/dE and dn_{e^-}/dE are positron and electron equilibrium distributions respectively (see below for their explanation). By integrating over the volume of interest then we have the

flux density spectrum within the halo radius r given by,

$$S_{\text{synch}}(\nu, z) = \int_0^r \frac{j_{\text{synch}}(\nu, r', z)}{4\pi (D_L^2 + (r')^2)} d^3r', \quad (6)$$

where the D_L denotes the luminosity distance to the DM halo of interest.

To account for diffusion and energy loss by electrons/positrons from DM annihilation, for an assumption where the processes of reacceleration and convection are negligible, the diffusion-loss equation is given by,

$$\frac{\partial}{\partial t} \frac{dn_e}{dE} = \nabla \left(D(E, \mathbf{x}) \nabla \frac{dn_e}{dE} \right) + \frac{\partial}{\partial E} \left(b(E, \mathbf{x}) \frac{dn_e}{dE} \right) + Q_e(E, \mathbf{x}), \quad (7)$$

where $D(E, \mathbf{x})$ denotes the spatial diffusion function and $b(E, \mathbf{x})$ denotes the energy loss rate. A fully detailed analysis of the solutions to equation (7) can be found in [14]. The spatial diffusion is given by [14],

$$D(E) = D_0 \left(\frac{d_0}{1 \text{ kpc}} \right)^{\frac{2}{3}} \left(\frac{\bar{B}}{1 \mu G} \right)^{-\frac{1}{3}} \left(\frac{E}{\text{GeV}} \right)^{\frac{1}{3}}, \quad (8)$$

where the diffusion constant $D_0 = 3.1 \times 10^{28} \text{ cm}^2 \text{ s}^{-1}$, \bar{B} denotes the average magnetic field and d_0 denotes the smallest scale where the magnetic field is found to be homogenous. The energy loss rate is given by [7],

$$b(E) = b_{\text{IC}} E^2 [1 + z]^4 + b_{\text{synch}} E^2 \bar{B}^2 + b_{\text{coul}} \bar{n} \left[1 + \frac{1}{75} \log\left(\frac{\gamma}{\bar{n}}\right) \right] + b_{\text{brem}} \bar{n} \left[\log\left(\frac{\gamma}{\bar{n}}\right) + 0.36 \right], \quad (9)$$

where \bar{n} denotes the average electron density, $\gamma = E/m_e c^2$ denotes the electron Lorentz factor, while b_{IC} , b_{synch} , b_{Coul} and b_{brem} are inverse-Compton, synchrotron, Coulomb and bremsstrahlung energy loss factor. These take values 0.25, 0.0254, 6.13 and 1.51 in units $10^{-16} \text{ GeVs}^{-1}$ respectively.

3. Dark Matter Halos Environment

In this section we discuss the halo environments that characterise M31, Coma and Ophiuchus. More attention is given to the magnetic field and thermal electron density distribution for sources under consideration.

3.1. M31

For M31 we assume the halo data from [15] at a distance 770 kpc. For the virial mass of $1.04 \times 10^{12} M_\odot$ the halo density profile is given by Navarro-Frenk-White (NFW) profile [16],

$$\rho_{\text{NFW}}(r) = \frac{\rho_s}{\frac{r}{r_s} \left(1 + \frac{r}{r_s} \right)^2}, \quad (10)$$

where ρ_s denotes the characteristic density and r_s denotes the scale radius. For the magnetic field profile we follow [17],

$$B(r) = \frac{4.6r_1 + 64}{r_1 + r} \mu G, \quad (11)$$

where $r_1 = 200 \text{ kpc}$ as suggested by fittings in [17]. For $r = 14 \text{ kpc}$ the magnetic field strength is taken to be $B = 4.6 \pm 1.2 \mu G$. The thermal electron density distribution follows an exponential profile from [17],

$$n_e(r) = n_0 \exp\left(-\frac{r}{r_d}\right), \quad (12)$$

where central density is taken to be $n_0 = 0.06 \text{ cm}^{-3}$ and r_d is the disk scale radius which is approximately 5 kpc [17]. We predict synchrotron emission fluxes for frequencies between $50 - 10^9 \text{ MHz}$ for M31. Subsequently, this is compared to the low frequency 408 MHz point flux [18] for a rather optimistic region of interest (50 arcminutes).

3.2. Coma Cluster

For the Coma cluster the virial mass is $1.33 \times 10^{15} M_\odot$ and virial concentration $c_{\text{vir}} = 10$, at the redshift $z = 0.0231$. Similar to M31 we use NFW density profile for Coma. For the thermal electron density distribution in Coma we follow [19, 20],

$$n_e(r) = n_0 \left(1 + \left[\frac{r}{r_s} \right]^2 \right)^{-q_e}, \quad (13)$$

where $n_0 = 3.49 \times 10^{-3} \text{ cm}^{-3}$ and $q_e = 0.981$. The magnetic field profile in Coma is given by [21],

$$B(r) = B_0 \left(\frac{n_e(r)}{n_0} \right)^{q_b}, \quad (14)$$

where $B_0 = 4.7 \mu\text{G}$ and $q_b = 0.5$. The fittings from [21] suggest a magnetic field with a Kolmogorov power spectrum characterised by a minimal coherence length $\Lambda_{\text{min}} \approx 2 \text{ kpc}$. We predict $50 - 10^9 \text{ MHz}$ synchrotron emission fluxes for Coma. For a region of interest of about 30 arcminutes, the Coma radio fluxes data from [22] with a frequency range $30.9 - 4850 \text{ MHz}$ was compared with the predicted radio fluxes.

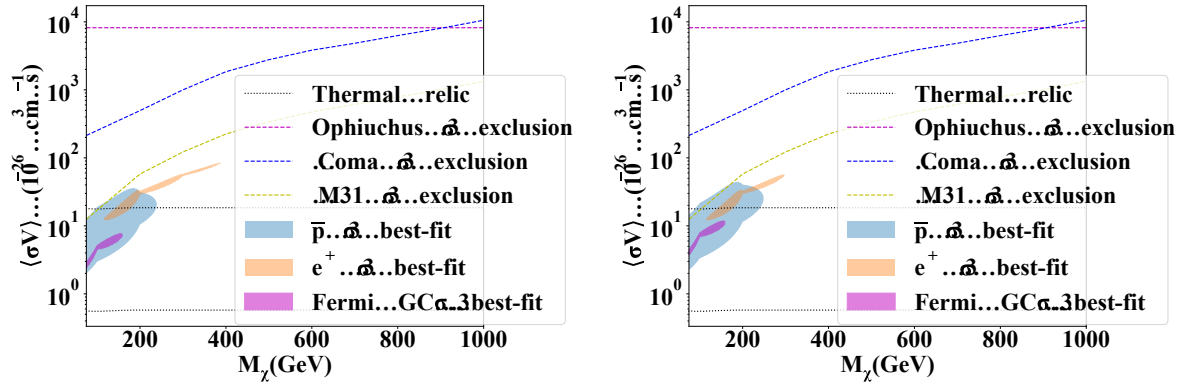


Figure 1. Depicts $2 \rightarrow 2$ best-fit parameter space to the AMS-02 positron, anti-proton spectra and Fermi-LAT galactic excesses. The contours are 3σ confidence intervals on the M_χ and $\langle\sigma V\rangle$ plane. The thermal relic [23] is denoted as a band to account for uncertainties in the local DM density and halo profile. Dashed lines denote 3σ exclusion limits for M31 (yellow), Coma (blue) and Ophiuchus (Magenta). Left: For Einasto halo profile. Right: For NFW halo profile.

3.3. Ophiuchus Cluster

For the Ophiuchus cluster we assume halo data from [24]. The virial mass is $1.1 \times 10^{15} M_\odot$ and virial radius is given by $r_{\text{vir}} = 2.1 \text{ Mpc}$ at the redshift $z = 0.0296$. Even here we will employ the NFW density profile. In terms of the magnetic field and the thermal electron density distribution we adhere to the formalism in [25] which assumes that Ophiuchus follows profiles similar to that in Coma, where $B_0 = 5.225 \mu\text{G}$, $q_b = 0.74$, $n_0 = 0.29614$ and $q_e = 0.412725$.

Even here, we predict $50 - 10^9$ MHz synchrotron emission fluxes for Ophiuchus. Subsequently, this is compared to the 153, 240 and 1477 MHz, radio fluxes from [26] for a region of interest of about 7 arcminutes.

4. Results and Discussion

We make use of the parameter space that best-fits the cosmic-ray and gamma-ray excesses produced in [9] for both NFW and Einasto halos. This parameter space gives annihilating DM through the Madala model to induce highly energetic positrons, which in the presence of a magnetic field emits synchrotron emission in M31, Coma and Ophiuchus. Following the recipe delineated in both Section 2 and 3, synchrotron emission predictions were made. Comparing the predicted synchrotron emission fluxes with M31 [18], Coma [22] and Ophiuchus [26] radio observation data, 3σ exclusion limits were produced to match our previous work parameter space. The M31 radio data used here have been highly constraining in other DM models (see e.g [27]). In figure 1, we observe that M31 has better constraining limits transcending those of Coma and Ophiuchus. Significantly, all the exclusion limits do not exclude our Madala DM model. With the radio DM-search regime entering a new era of high sensitivity and resolution, this will aid to place more stringent limits on the Madala model in near future. MeerKAT is one of the exciting detectors that may be able to probe the DM interpretation offered by the Madala model as elucidated in [9]. More interestingly, the full-SKA has the potential of probing the parameter space of the Madala model at 5σ confidence level within 100 hours observation time [9].

Acknowledgments

We acknowledge Elias Malwa, Mukesh Kumar and Bruce Mellado for useful insights regarding the Madala model. This work was supported by South African National Research Foundation, and the South African Research Chair Initiative of the Department of Science and Technology and National Research Foundation. GB acknowledges the funding of the National Research Foundation through Thuthuka grant number 117969.

References

- [1] Von Buddenbrock S, Chakrabarty N, Cornell A S, Kar D, Kumar M, Mandal T, Mellado B, Mukhopadhyaya B, Reed R G and Ruan X 2016 *Eur. Phys. J. C* **76** 1–18
- [2] Von Buddenbrock S, Chakrabarty N, Cornell A S, Kar D, Kumar M, Mandal T, Mellado B, Mukhopadhyaya B and Reed R G 2015 The compatibility of LHC run 1 data with a heavy scalar of mass around 270 GeV *Preprint hep-ph/1506.00612*
- [3] Von Buddenbrock S, Cornell A S, Mohammed A F, Kumar M, Mellado B and Ruan X 2018 *J. Phys. G Nucl. Part. Phys.* **45** 115003
- [4] Kumar M, von Buddenbrock S, Chakrabarty N, Cornell A S, Kar D, Mandal T, Mellado B, Mukhopadhyaya B and Reed R G 2017 The impact of additional scalar bosons at the LHC *Journal of Physics: Conf. Series* vol 802 (IOP Publishing) p 012007
- [5] von Buddenbrock S, Cornell A S, Kumar M and Mellado B 2017 The Madala hypothesis with run 1 and 2 data at the LHC *Journal of Physics: Conf. Series* vol 889 (IOP Publishing) p 012020
- [6] von Buddenbrock S 2017 Exploring LHC run 1 and 2 data using the Madala hypothesis *Journal of Physics: Conf. Series* vol 878 (IOP Publishing) p 012030
- [7] Colafrancesco S, Profumo S and Ullio P 2007 *Phys. Rev. D* **75** 023513
- [8] Regis M, Richter L and Colafrancesco S 2017 *J. Cosmol. Astropart. Phys.* **2017** 025
- [9] Beck G, Temo R, Malwa E, Kumar M and Mellado B 2021 Connecting multi-lepton anomalies at the LHC and in astrophysics and the prospects of MeerKAT/SKA *Preprint astro-ph.HE/2102.10596*
- [10] Aguilar M, Cavasonza L A, Ambrosi G, Arruda L, Attig N, Azzarello P, Bachlechner A, Barao F, Barrau A, Barrin L *et al.* 2019 *Phys. Rev. Lett.* **122** 041102
- [11] Aguilar M, Cavasonza L A, Alpat B, Ambrosi G, Arruda L, Attig N, Aupetit S, Azzarello P, Bachlechner A, Barao F *et al.* 2016 *Phys. Rev. Lett.* **117** 091103

- [12] Ackermann M, Ajello M, Albert A, Atwood W, Baldini L, Ballet J, Barbiellini G, Bastieri D, Bellazzini R, Bissaldi E *et al.* 2017 *Astrophys. J.* **840** 43
- [13] Longair M S 2010 *High energy astrophysics* (Cambridge University Press)
- [14] Colafrancesco S, Profumo S and Ullio P 2006 *Astron. Astrophys.* **455** 21–43
- [15] Tamm A, Tempel E, Tenjes P, Tihhonova O and Tuvikene T 2012 *Astron. Astrophys.* **546** A4
- [16] Navarro J F 1996 The structure of cold dark matter halos *Symp.-Int. astronomical union* vol 171 (Cambridge University Press) pp 255–258
- [17] Ruiz-Granados B, Rubiño-Martín J, Florido E and Battaner E 2010 *Astrophys. J. Lett.* **723** L44
- [18] Ficarra A, Grueff G and Tomassetti G 1985 *Astron. astrophys., Suppl. ser. (Print)* **59** 255–347
- [19] Lokas E L and Mamon G A 2003 *Mon. Notices Royal Astron. Soc.* **343** 401–12
- [20] Chen Y, Reiprich T, Böhringer H, Ikebe Y and Zhang Y Y 2007 *Astron. Astrophys.* **466** 805–12
- [21] Bonafede A, Feretti L, Murgia M, Govoni F, Giovannini G, Dallacasa D, Dolag K and Taylor G 2010 *Astron. Astrophys.* **513** A30
- [22] Thierbach M, Klein U and Wielebinski R 2003 *Astron. Astrophys.* **397** 53–61
- [23] Steigman G, Dasgupta B and Beacom J F 2012 *Phys. Rev. D* **86** 023506
- [24] Durret F, Wakamatsu K i, Nagayama T, Adami C and Biviano A 2015 *Astron. Astrophys.* **583** A124
- [25] Beck G 2020 *Mon. Notices Royal Astron. Soc.* **494** 1128–32
- [26] Murgia M, Eckert D, Govoni F, Ferrari C, Pandey-Pommier M, Nevalainen J and Paltani S 2010 Gmrt observations of the ophiuchus galaxy cluster *Preprint astro-ph.CO/1002.2332*
- [27] Beck G 2019 *J. Cosmol. Astropart. Phys.* **2019** 019

Diffusing assumptions in astroparticle physics

M Sarkis¹ and G Beck¹

¹ Department of Physics, University of the Witwatersrand, Private Bag 3, WITS-2050, Johannesburg, South Africa

E-mail: michael.sarkis@students.wits.ac.za

Abstract. Previous calculations of diffuse synchrotron radio emissions from dark matter annihilations have made use of a semi-analytical solution method for the diffusive cosmic ray transport equation. This method requires that various halo properties like the magnetic field and thermal gas density are spatially independent. We evaluate the physical accuracy of this approximation by calculating the expected synchrotron flux from three astrophysical sources, the Coma galaxy cluster, the M33 galaxy and the Reticulum II dwarf spheroidal galaxy. We find that for large structures, where diffusion effects are less significant to the output flux, using an average weighted with the dark matter halo density for magnetic field and gas density profiles results in a lower observed flux. We note that prescription is more accurate to the physical scenario than the conventionally used unweighted average and indicates that results dependent on such averages may be optimistic. Additionally, we explore other common approximations and detail their effects.

1. Introduction

There have been many studies in the literature that calculate the expected radio emissions from dark matter (DM) residing in astronomical structures. These studies typically calculate the synchrotron flux from secondary electrons, produced by DM annihilations, with the goal of constraining various DM properties via radio observations. For a review of these methods, see [1, 2, 3] and references therein. With the MeerKAT project and the upcoming Square Kilometre Array in mind, this important avenue of DM hunting will likely play an even larger role in future indirect DM detection studies.

A rigorous calculation of the radio emissions from DM secondary electrons involves the solution of a general cosmic-ray transport equation with diffusion and energy loss effects, which is a second-order partial differential equation that depends on the spatial structure of the host environment. Several simplifying assumptions have thus been utilised by authors when studying these radio emissions in order to find a tractable and analytic solution. One of the assumptions commonly used in the literature is that the magnetic field permeating the host DM halo is spatially independent. This form allows one to find a semi-analytical formula for the solution to the diffusive transport equation, allaying the need for full numerical methods. Since real magnetic fields in large structures will have some kind of spatial dependence, this assumption is generally carried out in two separate ways. The first is to take a simple spatial average of an assumed/observed magnetic field profile, and the second is to assume a constant or ‘flat’ magnetic field strength throughout the entire region of interest. Another assumption that could be made to drastically simplify the calculation of the synchrotron flux is that diffusion effects

can be neglected altogether, and that the synchrotron flux is determined entirely by the peak energy of the emission, leading to the so-called monochromatic approximation.

Here we aim to evaluate the impact of some of these assumptions on the observed flux from various astronomical sources ranging from dwarf spheroidal galaxies (dSphs) to galaxy clusters. To do this, we calculate the synchrotron flux for three astronomical targets using a variety of often-used assumptions and approximations.

2. Halo and DM particle models

2.1. Halo properties

The formulation of halo properties in this work closely resembles that of [4]. For any further details, we therefore refer the reader to [4] and references therein. We consider two density profiles, the NFW [5] and Einasto [6], to characterise the DM halos in the targets considered here. These profiles are given as:

$$\rho_{\text{NFW}}(r) = \frac{\rho_s}{\frac{r}{r_s} \left(1 + \frac{r}{r_s}\right)^2}, \quad \rho_{\text{Ein}}(r) = \rho_s \exp \left[-\frac{2}{\alpha} \left(\left[\frac{r}{r_s} \right]^\alpha - 1 \right) \right] \quad (1)$$

where r_s and ρ_s are the halo scale radius and density respectively, and α is the Einasto parameter. The thermal gas density (n_e) and magnetic field (B) are chosen to have the following profiles:

$$n_{e,\text{PL}}(r) = n_0 \left(1 + \left[\frac{r}{r_d} \right]^2 \right)^{-q_e}, \quad B_{\text{PL}}(r) = B_0 \left(\frac{n_e(r)}{n_0} \right)^{q_b} \quad (2)$$

$$n_{e,\text{Exp}}(r) = n_0 \exp \left(-\frac{r}{r_d} \right), \quad B_{\text{Exp}}(r) = B_0 \exp \left(-\frac{r}{r_d} \right) \quad (3)$$

where $q_e = 1.125$, $q_b = 0.5$, as in [4]. A list of properties for the DM density, magnetic field and thermal gas profiles of each source target is shown in Table 1.

Table 1: List of astronomical source targets and their halo properties.

Target name	ρ_χ profile	$n_e(r)$ profile	$B(r)$ profile	n_0 (cm ⁻³)	B_0 (μG)	r_d (kpc)
Coma	NFW	PL	PL	3.44×10^{-3}	4.7	290.0
M33	NFW	Exp	Exp	0.03	13.34	5.0
Reticulum II	Ein ($\alpha = 0.4$)	Exp	Exp	1.0×10^{-6}	~1.0	0.015

2.2. Spatial dependence of magnetic field and thermal gas density

When analytically solving for the electron equilibrium distribution with the transport equation (see Equation 5 below), a common simplifying assumption made in the literature is that the diffusion and energy loss coefficients have no spatial dependence. Since this assumption requires a spatially independent magnetic field and thermal gas density, simple ‘flat’ averages of these quantities have been used – notably in the code package RX-DMFIT [7] (see also [8, 9] and references therein). Since the rate of annihilation of WIMPs is strongly dependent on the density profile of the halo, as in [4] we consider a weighted average for the magnetic field or thermal gas density that uses the squared DM density of the halo as a tracer for the regions in the halo that have a more significant impact on the total observed flux. This weighting factor is taken from the dependence of the annihilation particle source function (see Equation 4 below) on halo density. We argue that this is a more realistic modelling scenario than a flat average over the entire halo, which takes into equal account those regions in which there may be very little or negligible contributions to the overall flux (typically in the outer edges of the halo).

2.3. Particle Source function

The annihilation of WIMPs inside a DM halo is expected to lead to the production of a set of kinematically-accessible SM products. The following particle source function,

$$Q(E, r) = \frac{1}{2} \langle \sigma v \rangle \sum_f \frac{dN_e^f}{dE} B_f \left(\frac{\rho_\chi(r)}{m_\chi} \right)^2, \quad (4)$$

describes the distribution of particles formed by a single annihilation. Here $\langle \sigma v \rangle$ is the velocity-averaged annihilation cross-section, dN_e^f/dE is the particle energy spectrum (obtained from [10]), B_f is the branching ratio for the channel indexed by f and m_χ is the WIMP mass. In this work, as is common in indirect DM detection studies, we consider each channel individually and set B_f to 1 for each channel of interest. We also only consider a representative WIMP mass of $m_\chi = 100$ GeV, as we are studying environmental effects that will not scale with WIMP mass.

Page: 316

3. Radio emissions from DM annihilation

The electrons and positrons produced by WIMP annihilations are expected to interact with magnetic fields and the thermal electron population within the halo environment. The radiative and cooling effects are usually encapsulated in a transport equation, here given by

$$\frac{\partial}{\partial t} \frac{dn_e}{dE} = \nabla \cdot \left(D(E, \mathbf{x}) \nabla \frac{dn_e}{dE} \right) + \frac{\partial}{\partial E} \left(b(E, \mathbf{x}) \frac{dn_e}{dE} \right) + Q_e(E, \mathbf{x}), \quad (5)$$

where $D(E, \mathbf{x})$ and $b(E, \mathbf{x})$ are the diffusion and energy loss coefficients respectively, and would in general depend on the position \mathbf{x} within the halo. In this work we take these to be:

$$D(E) = D_0 \left(\frac{d_0}{1 \text{ kpc}} \right)^{\frac{2}{3}} \left(\frac{\langle B \rangle}{1 \mu\text{G}} \right)^{-\frac{1}{3}} \left(\frac{E}{1 \text{ GeV}} \right)^{\frac{1}{3}}, \quad (6)$$

and

$$b(E) = b_{\text{IC}} \left(\frac{E}{1 \text{ GeV}} \right)^2 + b_{\text{synch}} \left(\frac{E}{1 \text{ GeV}} \right)^2 \langle B \rangle^2 + b_{\text{coul}} \langle n_e \rangle \left(1 + \frac{1}{75} \log \left(\frac{\gamma}{\langle n_e \rangle} \right) \right) + b_{\text{brem}} \langle n_e \rangle \left(\frac{E}{1 \text{ GeV}} \right). \quad (7)$$

Here D_0 is the diffusion constant, d_0 is the magnetic field coherence length, γ is the electron Lorentz factor, and b_{IC} , b_{synch} , b_{coul} and b_{brem} are the energy loss coefficients for Inverse Compton, synchrotron, Coulomb scattering and bremsstrahlung effects. As in [4], we use the following values for each in units of 10^{-16} GeV s $^{-1}$, respectively: 0.25, 0.0254, 6.13, 4.7. The quantities $\langle B \rangle$ and $\langle n_e \rangle$ are calculated by the description in Section 2.2.

The solution of Equation 5 can be found via the semi-analytic method described in [8]. If the DM halo and thermal electron population are considered spherically symmetric and the diffusion and energy loss coefficients are spatially independent, the equilibrium electron distribution is

$$\frac{dn_e}{dE}(r, E) = \frac{1}{b(E)} \int_E^{m_\chi} dE' G(r, E, E') Q(r, E'), \quad (8)$$

where $G(r, E, E')$ is a Green's function. For the full derivation of this solution, and details about the form of this function, we refer the reader to [8].

The average power of synchrotron radiation produced by electrons/positrons with energy E and at a redshift z , at an observed frequency of ν , is then calculated using the following equation [11]:

$$P_{\text{synch}}(\nu, E, r, z) = \int_0^\pi d\theta \frac{\sin^2 \theta}{2} 2\pi \sqrt{3} r_e m_e c \nu_g F_{\text{synch}} \left(\frac{\kappa}{\sin \theta} \right). \quad (9)$$

Here m_e , $r_e = e^2/m_e c^2$ and $\nu_g = eB/2\pi m_e c$ are the mass, classical radius and gyro-radius of an electron respectively. The value of κ is given by

$$\kappa = \frac{2\nu(1+z)}{3\nu_g \gamma^2} \left[1 + \left(\frac{\gamma \nu_p}{\nu(1+z)} \right)^2 \right]^{3/2}, \quad (10)$$

where $\nu_p \propto \sqrt{n_e}$ is the plasma frequency, and the synchrotron kernel function $F_{\text{synch}}(x)$ is calculated with

$$F_{\text{synch}}(x) = x \int_x^\infty dy K_{5/3}(y) \approx 1.25 x^{1/3} e^{-x} (648 + x^2)^{1/12}. \quad (11)$$

Combining the average power emitted per electron/positron in Equation 9 with the equilibrium spectral distribution of electrons/positrons, we finally calculate the synchrotron flux at frequency ν to a target at a luminosity distance of D_L as

$$S(\nu, z) = \frac{1}{4\pi D_L^2} \int_0^r \int_{m_e}^{m_\chi} d^3 r' dE \left(\frac{dn_{e^-}}{dE} + \frac{dn_{e^+}}{dE} \right) P_{\text{synch}}(\nu, E, r', z), \quad (12)$$

where $dn_{e^-,+}/dE$ are the equilibrium spectral distributions of electrons, positrons respectively.

3.1. Monochromatic approximation

If we assume a simplifying monochromatic form for the synchrotron kernel function [1, 3, 12], *i.e.* that the peak electron energy corresponds to the frequency of the emitted radiation, then $F_{\text{synch}}(x) \sim \delta(x - 0.29)$ and the peak energy can be determined by $E(\nu) \simeq 0.463 \nu^{1/2} B^{-1/2}$ GeV, with the frequency ν in Mhz and the magnetic field strength B in μG . Under the additional assumption of a constant magnetic field strength B , the synchrotron flux can then simply be approximated using the formula

$$S_{\text{mono}}(\nu) \approx \frac{1}{4\pi D_L^2} \left[\frac{9\sqrt{3}\langle\sigma v\rangle}{2m_\chi^2(1+C)} E(\nu) Y(\nu, m_\chi) \int d^3 x \rho_\chi(\mathbf{x})^2 \right], \quad (13)$$

where $Y(\nu, m_\chi) = \int_{E(\nu)}^{m_\chi} dE' (dN_e/dE')$ (and dN_e/dE is the particle energy spectrum from Equation 4) and C is the ratio of synchrotron to Inverse Compton scattering energy loss coefficients.

4. Results and discussion

We have calculated and plotted the fluxes from three source targets using various approximate formulae, including different forms for the magnetic field and gas density, and in the case of the Coma galaxy cluster, different synchrotron flux equations. These are shown in Figure 1, which shows the results for the Coma galaxy cluster (top), the M33 galaxy (bottom-left) and Reticulum II dSph (bottom-right). In each plot we have shown the flux, $S(\nu)$, for the case of a radially-dependent magnetic field profile, $B(r)$, that has been spatially averaged with both flat and ρ_χ^2 weights. We also show fluxes calculated with a flat magnetic field profile that has a strength B_x , with the subscript denoting the value in μG in each case. We consider WIMPs of mass 100 GeV that annihilate entirely into the $b\bar{b}$ channel, and assume a thermal relic annihilation cross section of $\langle\sigma v\rangle = 3.0 \times 10^{-26} \text{cm}^3 \text{s}^{-1}$.

In the Coma galaxy cluster we first note that diffusion effects, represented by the dashed curves, are almost negligible. This is an expected feature of fluxes calculated for large structures like galaxy clusters where diffusion timescales are small compared to other energy-loss

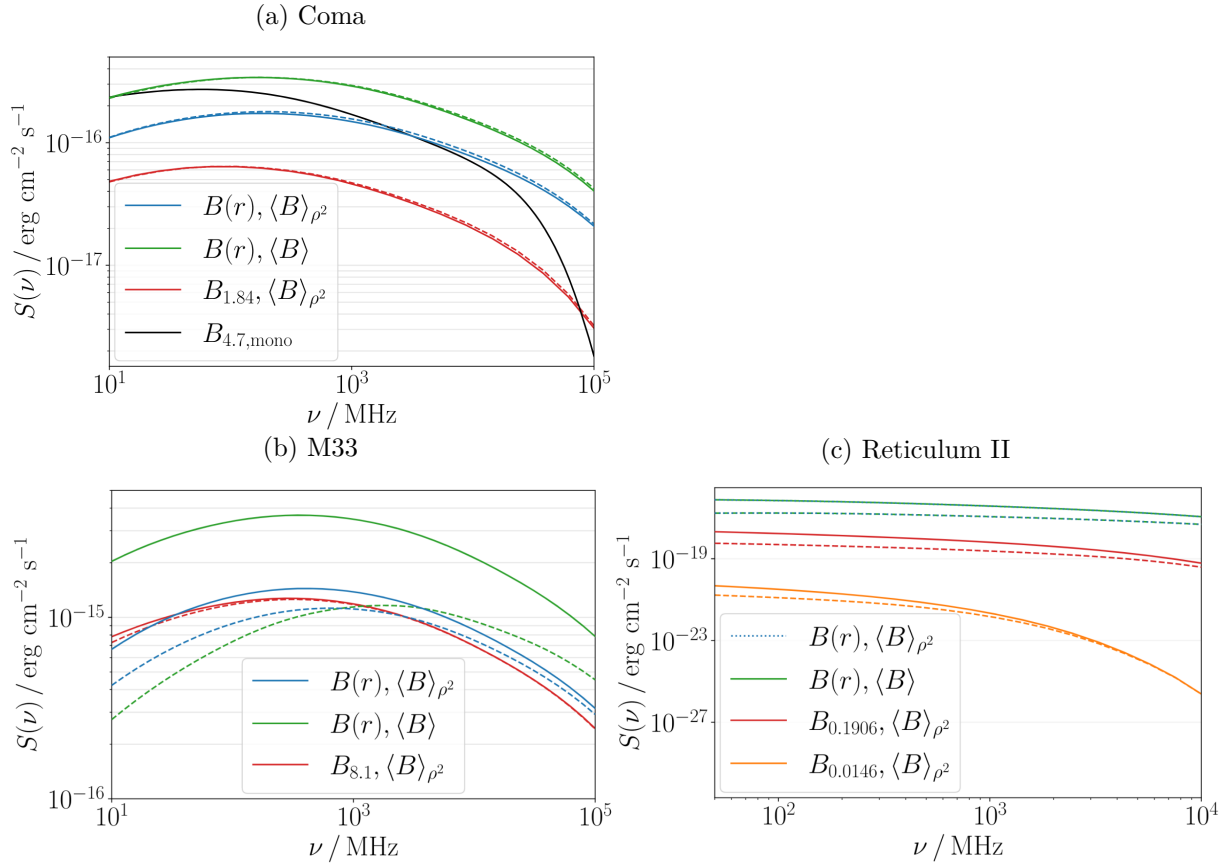


Figure 1: Expected radio synchrotron flux output from (a): the Coma galaxy cluster, (b): the M33 galaxy and (c): the Reticulum II dSph. Each solid curve represents a calculation with a different treatment of halo parameters (see text) and without diffusion effects. The dashed curves of each colour show the same calculation with diffusion included in the calculation.

mechanisms (for a detailed analysis of diffusion in galaxy clusters, we refer the reader to [8]). Using a ρ^2 weighted average for the spatially dependent functions results in a flux that is roughly a factor of 2 lower than using a flat average, and using a flat magnetic field profile further lowers the output flux by roughly a factor of 6. For all targets, we see that the flux output from a flat magnetic field profile is highly dependent on the strength of the field, which highlights the importance of accuracy when choosing this value. In this source we have also calculated the flux using the monochromatic approximation, given by Equation 13. The flux obtained with this calculation has a very steep drop-off at higher frequencies, which may lead to an unnecessary over-emphasis on low frequency data sets. This is caused by the dependence of the flux on the peak frequency and the assumption of a monochromatic synchrotron kernel function. We also note that this approximation does not account for diffusion effects within the halo, which could motivate its use in galaxy cluster approximations but not in smaller structures wherein diffusion effects are generally more significant.

In the M33 galaxy, we see that the inclusion of diffusion effects in the case of an unweighted magnetic field can reduce the output flux by a factor of ~ 1.5 at higher frequencies, and up to a factor of ~ 7.5 at lower frequencies. In the case of a weighted magnetic field, diffusion effects still reduce the expected flux by up to a factor of ~ 1.5 at lower frequencies. The significance of diffusion in these results contrasts with the formulation of radio flux models in [13, 12], where

the flux from the M33 (and M31) galaxy is found from the monochromatic approximation which neglects diffusion completely.

In the Reticulum II dSph, we firstly note that the use of a flat or ρ^2 weighted average for a spatially dependent magnetic field has no discernible effect on the output flux. This could be explained by the relatively small size of the dSph DM halo, which equalises the two averaging techniques. However, we see that the flux has a very strong dependence on the magnetic field strength under the assumption of a flat profile. In the cases shown here, for two values of the magnetic field strength calculated using a flat and weighted average of a fully spatially dependent profile (0.0146 and 0.1906 μG respectively), we see a relative difference of at least 2 orders of magnitude, which increases drastically with higher frequencies. Since this value is typically calculated using an unweighted average of a full magnetic field profile, its use in radio flux approximations may lead to significant uncertainties – especially for smaller structures like the dSph modelled here.

5. Conclusion

We have found that the various assumptions used when calculating the radio synchrotron flux from astronomical DM can have a significant effect on the expected flux from these sources. In particular, we see that the use of flat magnetic field profiles can drastically alter the output flux, especially in the case of smaller structures like the Reticulum II dSph. We also note that the inclusion of diffusion effects in M33, neglected in previous studies, can lead to a noticeable reduction in the expected flux. For larger structures like the Coma galaxy cluster, we find that using a spatial average of the magnetic field weighted with the DM density – which should provide a more realistic estimate of the rate of DM annihilations in different regions of the halo – results in a flux that is lower than when using a flat average by a factor of ~ 2 . With the upcoming boost in radio observation capabilities with MeerKAT and the SKA, the assumptions used when hunting for DM with radio synchrotron fluxes should be evaluated carefully for each source target and host environment in order to maximise accuracy.

Acknowledgments

This work is based on the research that was supported by the National Research Foundation of South Africa (Bursary No. 112332). G.B acknowledges support from a National Research Foundation of South Africa Thuthuka grant no. 117969.

References

- [1] Profumo S and Ullio P 2010 *Particle Dark Matter: Observations, Models and Searches* (Cambridge, UK: Cambridge University Press)
- [2] Beck G 2019 *Galaxies* **7**
- [3] Chan M H 2019 *Galaxies* **9** 11
- [4] Beck G 2021 *JCAP* **2021** 007
- [5] Navarro J, Frenk C and White S 1997 *ApJ* **490** 493–508
- [6] Einasto J 1968 *Publications of the Tartuskoj Astrofizika Observatory* **36** 414–41
- [7] McDaniel A, Jeltama T, Profumo S and Storm E 2017 *JCAP* **2017** 027
- [8] Colafrancesco S, Profumo S and Ullio P 2006 *A & A* **455** 21–43
- [9] Colafrancesco S, Marchegiani P and Beck G 2015 *JCAP* **2015** 032
- [10] Cirelli M, Corcella G, Hektor A *et al.* 2011 *JCAP* **2011** 051
- [11] Longair M 1994 *High Energy Astrophysics* (Cambridge, UK: Cambridge University Press)
- [12] Chan M H, Cui L, Liu J and Leung C S 2019 *ApJ* **872** 177
- [13] Chan M H 2017 *Phys. Rev. D* **96**(4) 043009

Studying patched spacetimes for binary black holes

J Tarrant¹ and G Beck¹

¹ School of Physics, University of the Witwatersrand, Johannesburg, WITS-2050, South Africa

E-mail: justine.tarrant@wits.ac.za

Abstract. Circumbinary accretion disks have been examined, theoretically, for supermassive and intermediate mass black holes, however, disks for black hole masses in the LIGO regime are poorly understood. Assuming these binaries possess such a disk initially, the question we want to answer is: are they dissipated by outflows or accretion prior to inspiral? To study this problem we propose a novel approach, whereby we consider an approximate, analytic spacetime and solve the geodesic equation for particles in this spacetime so that we can determine the likely fate of particles coming from the accretion disk. Preliminary indications suggest a likelihood of accretion prior to inspiral.

1. Introduction

An interesting astrophysical problem to consider is the treatment of circumbinary accretion disks (hereafter, disks) around binary black holes. Currently, in the literature, supermassive ($10^5 - 10^9 M_\odot$) and intermediate ($10^2 - 10^5 M_\odot$) mass black holes have been considered with disks. The case of disks around binaries in the LIGO (Laser Interferometer Gravitational wave Observatory) regime (tens of solar masses) are more obscure. It is worth noting that circumbinary disks have not been observed for any mass regime. Examining these problems comes with numerical challenges since one generally employs hydrodynamical and magneto-hydrodynamical simulations which are computationally expensive and may be impractical [1]. To date, numerical relativity remains one of the most powerful probes used to study the strong regime in general relativity around extreme environments such as binary black holes and their mergers [2].

Numerical simulations must proceed from initial data which is tricky to produce [3]. One way to calculate the initial data is to construct an approximate, analytic, global metric as calculated in [4, 5]. This method makes use of a mathematical technique called asymptotic matching. Alvi [4, 5] was the first person to attempt such a construction. The four-dimensional global metric is subdivided into four regions, each with their own approximation schemes for solving the Einstein equations, which are then ‘glued’ together in a *buffer zone* in which two adjacent metric approximations are valid. The work by Alvi is based on earlier research by Manasse [6] and D’Eath [7, 8].

The main goal of the broader project we consider is to determine whether a mechanism exists that will describe the fate of particle trajectories existing in a spacetime around merging binary black hole systems. We want to identify potential mergers before inspiral. Therefore, we want to find a characteristic signal unique in its identity that could alert one to the stage at which the particles are ejected, engulfed or has become faint and inactive. This would consequently give us an early warning of gravitational wave emission from the inspiral. In this proceeding we

tackle only part of the problem. We ignore, leaving to future research, the angular momentum accompanying spinning black holes.

Making use of the analytical spacetime from [4, 5], we propose to study the geodesics living on this spacetime. Geodesics are simple to study and they allow us to track the movement of particles in the spacetime. This will allow us to determine how many particles are falling into the inner zone of the binary and eventually the black holes.

The structure of this paper is as follows: Section 2 concerns the structure of the spacetime we use and its limitations. Section 3 deals with the problem of computing and using geodesics in a numerical simulation. Then, Section 4 deals with the discussion of our results. Finally, we end with the conclusion.

2. Spacetime structure

Our project begins by considering two equal mass ($m_1 = m_2 = 30M_\odot$) Schwarzschild black holes, each of them perturbed by the other, i.e. each black hole exerts a tidal force on the other. They are widely separated ($\sim 14M$ in geometric units where $M = m_1 + m_2$), this allows for the subdivision of the spacetime. For $14M$ separation, the black hole speeds are $\frac{v}{c} \approx 0.13$, thus being on the very edge of the slow-motion regime. The analytic metric of [4, 5] generates a space-like hypersurface from the full spacetime. The global metric on each hypersurface is made up of 4 individual regions (see Figure 1), all held together by asymptotically *patching* in the buffer zones, which cover the space where two adjacent regional metrics overlap and are simultaneously valid. In patching, one sets the metrics in the buffer zone equal to each other at a point, i.e. set approximate solutions to the Einstein equations equal to each other on specified 2-surfaces [9].

In regions I and II, the inner zones, the perturbed black hole metrics are patched to region III, the near zone. Region III is described by a post-Newtonian approximation which holds for the weak-field ($GM/(rc^2) \ll 1$) and slow-motion ($v/c \ll 1$) limit¹ [10]. A post-Minkowski metric describes region IV, the far zone. Alvi considers the near and far zones as already patched by construction.

In order to study geodesics, we need to produce a full spacetime from these hypersurface slices. The slicing that allows for the production of the hypersurfaces remains valid when the separation is $> 10M$ (along with the regional decomposition) [1]. Thus, our approach is to generate a full spacetime out of a collection of space-like hypersurfaces each corresponding to a given time. The evolution of the binary itself provides the evolutionary linkage between each hypersurface. This is because the analytic metric depends on the separation and speed of the binary, on a given hypersurface, and we impose these evolutions via the relations from [11] according to the time assigned to that hypersurface.

3. Calculating geodesics

Our results are based on the calculation of geodesics. This is a very useful probe, since it provides a relatively simple way to study the motion of particles on different trajectories as well as their fate. As mentioned already, the metric we used to get our geodesics was an analytic metric by Alvi. To obtain geodesics, we needed to compute the Christoffel symbols in this spacetime first. We compute these symbols using finite differencing techniques up to second order. Our geodesics were computed with the time coordinate as a parameter since this formalism is useful

¹ Here c and G are the speed of light and Newton's gravitational constant, whilst v , M , r are the characteristic velocity, mass and separation of the system [9].

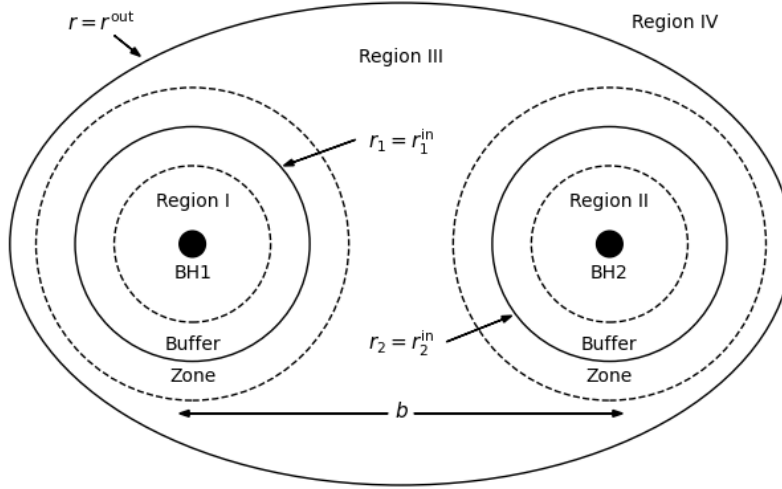


Figure 1. Global metric displaying all regions following (gr-qc/991211).

in numerical computations:

$$\frac{d^2 x^\mu}{dt^2} = -\Gamma_{\alpha\beta}^\mu \frac{dx^\alpha}{dt} \frac{dx^\beta}{dt} + \Gamma_{\alpha\beta}^0 \frac{dx^\alpha}{dt} \frac{dx^\beta}{dt} \frac{dx^\mu}{dt}. \quad (1)$$

Furthermore, we did this using the Runge–Kutta–Fehlberg [12] method. Then, using the geodesic equation, we can produce acceleration maps which provide insight into where electromagnetic radiation would be most intense. However, the actual geodesics themselves belong to the particles in the spacetime. Thus, we can observe the forces acting on particles in the disk without employing fluid dynamic methods.

4. Results and discussion

In this work we have computed the trajectories of particles in a four-dimensional, subdivided spacetime made up of four regions held together by asymptotic patching in the buffer zones containing adjacent metrics. This means that adjacent metrics are set equal to each other at a point, rather than in the entire buffer zone region [9]. This means that the global metric is mildly discontinuous and errors may be introduced.

These analytic metrics were designed to calculate initial data for binary black hole simulations. Hence, we note that Alvi mentions that before one extracts initial data using this metric, the discontinuities need to be smoothed out. Yunes et. al. [13] found a way to deal with the issues in Alvi by creating transition functions [14] which broke the discontinuities and allowed transitions from one region to its adjacent region without the introduction of errors.

Let us begin by addressing Figure 1. This shows the full global metric in Alvi [4] and allows one to visualize how the regions are related. One thing we need to be cautious about is that Figure 1 is somewhat misleading. In that figure all regions seem to be connected and even appear to have smooth transitions between each of the zones. However, the full metric contains discontinuities at the boundaries between regions. Despite this, Figure 2 shows no visible signs of discontinuity in the accelerations.

Next, we consider each region of the global metric separately. The acceleration maps produced allow one to visualise the areas of the region where electromagnetic radiation is likely to be most intense.

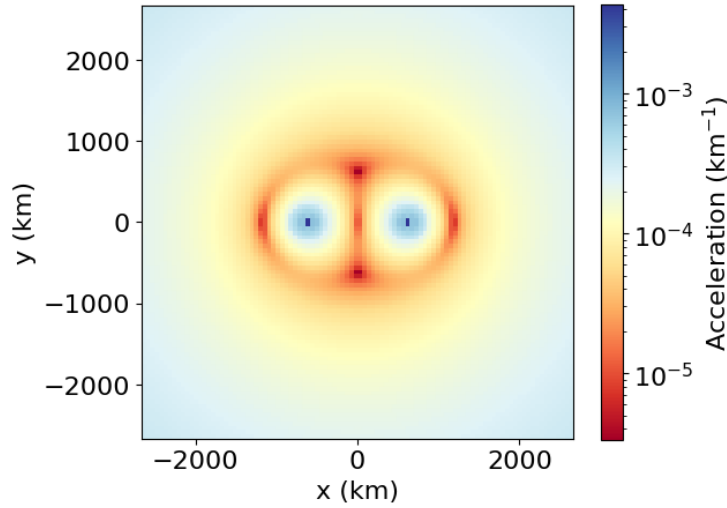


Figure 2. Acceleration map of the whole global metric.

4.1. Regions I and II

The left panel of Figure 3 shows the inner regions around black hole 1 and black hole 2. The black holes are of equal mass. We have excised regions that we are not discussing (masked in white). For the case we now consider, we see that the acceleration is larger nearer to the black holes. This is expected since the gravitational pull is larger there. Additionally, the contour lines circularize as they move away from the black holes due to the perturbation.

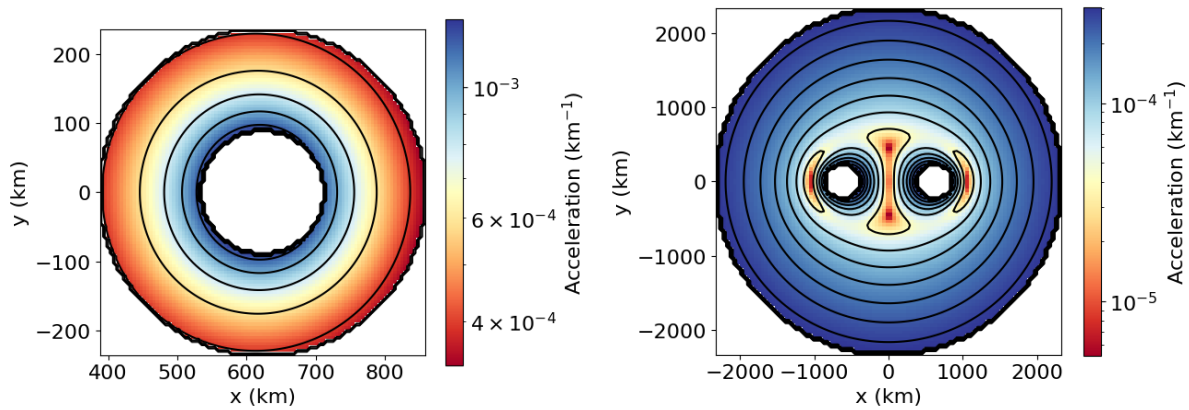


Figure 3. Left: the acceleration map covering Regions I and II which surround BH 1 and 2, respectively. Right: acceleration map covering Region III.

4.2. Region III

This region, also called the near zone, shows how particles accelerate around both black holes when dealing with a centre of mass problem. Here, in the right panel of Figure 3, we have excised the inner regions and the far zone. The centre shows several nodal regions where the acceleration is very small relative to the rest of the space. We point out that the acceleration gets larger as we move away from the centre, excised regions. This is due to the use of co-rotating coordinates. Note that we validated our algorithm on a Schwarzschild black hole metric to ensure this effect was not spurious.

4.3. Geodesics

We display geodesics for 100 initially stationary particles starting in region III, they have a maximum simulation time of ≈ 0.1 s. This duration is such that the binary remains widely separated throughout, the time where the Schwarzschild radii would cross being ≈ 0.89 s. To justify our choice of stationary initial conditions, we note the particles of interest are coming from a circumbinary, accretion disk. Therefore, the maximum initial speed of these particles is the speed of sound in the disk: $v_s = \sqrt{\frac{3}{8}}\omega z_0$ [15], where $z_0 \approx 1M$ [16] is half the disk thickness and we have assumed a polytropic disk with index $4/3$ [16]. In the co-rotating coordinates, the initial speed of a stationary particle is $\sim \omega r$. Comparing this to v_s we find $\frac{v_s}{\omega r} \approx 0.035$ when $r \sim 1000$ km. Thus, an initial orbital velocity is a small correction which we ignore as a first order approximation. In our plots geodesic origin points are given by ‘star’ markers. We will use a black ellipse surrounding the geodesics to give the border of the near zone.

Figure 4 shows both the geodesics that will potentially accrete onto the black holes and those that do not within the maximum simulation time of ≈ 0.1 s. It is notable that around 24% of the particles fall into the black holes within the simulation time.

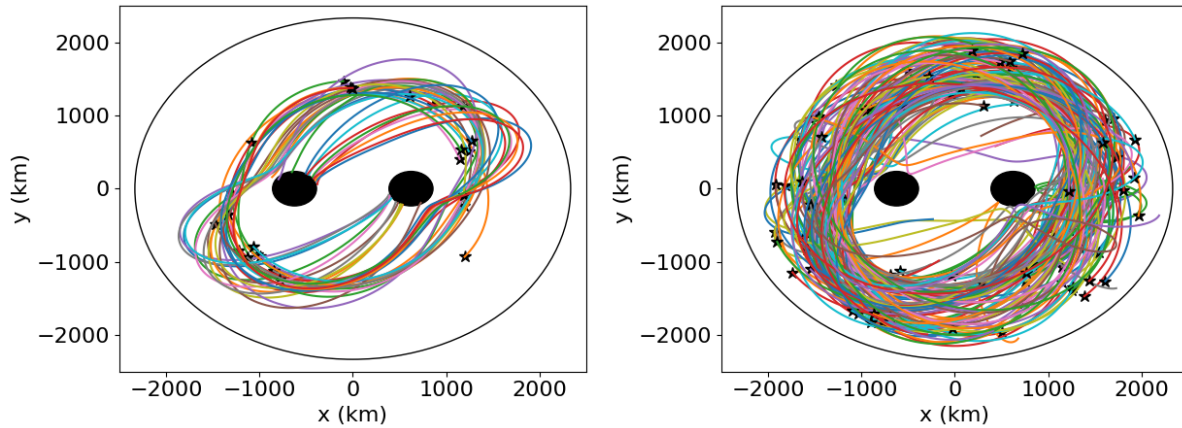


Figure 4. Geodesics for potentially accreting geodesics (left) and those that do not accrete (right).

5. Conclusions

Studying geodesics, computationally, provides a unique means to search for precursor electromagnetic signals that would herald the release of gravitational waves prior to the tight inspiral phase of the binary. If the environment around the black holes is magnetised, synchrotron radiation is likely to occur with any flow of particles towards the black holes,

producing radio emissions which may be detectable by MeerKAT. Though this is more probable for larger black holes than studied here as such small regions may not be resolvable. Magnetized environments will also require additional dynamical corrections, as strong magnetic fields will affect the particle geodesics. The effect of such fields will be considered in future work.

We have assumed that a disk, straddling the near zone [17], exists. It is contained within a spacetime described by an analytic metric. We observed the motion of individual particles by computing the geodesics of each particle in the spacetime and found initial indicators that if the particles begin from rest in the near zone, they can be rapidly swallowed up by the black holes. In addition, the orbits within the near zone appear to be unstable. The instability observed does not occur due to effects resulting from the individual black holes as the particles starting closest to an inner zone can be found at $r \gtrsim 3r_{\text{ISCO}}$ from that black hole.

6. Acknowledgements

We thank the referee, whose comments greatly improved the presentation of this work. JT acknowledges the support of the SARAo post-doctoral fellowship initiative. GB acknowledges the financial support of the National Research Foundation of South Africa via Thuthuka grant no. 117969.

References

- [1] Mundim B C, Nakano H, Yunes N, Campanelli M, Noble S C and Zlochower Y 2014 *Phys. Rev. D* **89** 084008
- [2] Baumgarte T and Shapiro S 2010
- [3] Cook G B 2000 *Living Rev. Rel.* **3** 5
- [4] Alvi K 2000 *Phys. Rev. D* **61**(12) 124013
- [5] Alvi K 2003 *Phys. Rev. D* **67**(10) 104006
- [6] Manasse F K 1963 *J. Math. Phys.* **4** 746–761
- [7] D'Eath P D 1975 *Phys. Rev. D* **11**(6) 1387–1403
- [8] D'Eath P D 1975 *Phys. Rev. D* **12**(8) 2183–2199
- [9] Yunes N, Tichy W, Owen B J and Brügmann B 2006 *Phys. Rev. D* **74**(10) 104011
- [10] Blanchet L 2014 *Living Rev. Rel.* **17** 2
- [11] Isoyama S, Sturani R and Nakano H 2020
- [12] Fehlberg E 1969 *NASA* **315**
- [13] Yunes N and Tichy W 2006 *Phys. Rev. D* **74** 064013
- [14] Yunes N 2007 *Clas. and Quant. Grav.* **24** 4313–4336
- [15] Pringle J E 1981 *Annu. Rev. Astron. Astrophys* **19** 137–160
- [16] Gold R, Paschalidis V, Etienne Z B, Shapiro S L and Pfeiffer H P 2014 *Phys. Rev. D* **89** 064060
- [17] Khan A, Paschalidis V, Ruiz M and Shapiro S L 2018 *Phys. Rev. D* **97**(4) 044036

Simulating the enrichment of cosmological gas: incorporating a new chemical enrichment model in Simba

R T Hough¹, D Rennehan², S I Loubser¹, A Babul² and R Davé³

¹ Centre for Space Research, North-West University, Potchefstroom 2520, South Africa

² Department of Physics & Astronomy, University of Victoria, Victoria BC V8P 5C2, Canada

³ School of Physics and Astronomy, University of Edinburgh, Edinburgh EH9 3HJ, U.K.

E-mail: renierht@gmail.com

Abstract. Large-scale, state-of-the-art cosmological simulations allow us to follow the evolution of various galaxies, and since these contain detailed knowledge of e.g. the metal content of the stars in each galaxy, it can then be compared to galaxies in the real Universe. In our work, we are improving the implementation of a stellar feedback model for the cosmological simulation Simba. This simulation is the merged product of GIZMO's public and Mufasa/Simba codes to create realistic large-scale environments. Specifically, we are improving the current instantaneous recycling of the metals model, with a more accurate cosmic chemical enrichment, called the Chem5 model. This will improve the stellar evolutionary tracks, allow the tracing of more individual elements, and treat each gas particle as an evolving particle rather than instantaneously giving away its metals. This will lead to a better understanding how the metallicities impact the gas and stellar metallicities in galaxies and the Circumgalactic medium.

1. Introduction

In modern large-scale structure cosmology, there is a drive to understand the formation and the evolution of galaxies, based on their environment. However, due to the extremely long time-scales over which these events occur, it can become very difficult to understand their evolutionary paths [1]. Therefore, trying to create an evolutionary track can be incomplete. There are two main methods used to get an idea about these evolutionary paths.

The first method is statistical observations. The idea behind this method is to get observational data from as many sources as possible [1]. These sources will need to have similar properties. For example, observing a certain mass galaxy with a certain star formation rate. Since their basic key properties are the same, it is assumed that their evolutionary track will be the same. If they are formed at different epochs in the cosmic age, they will be at different stages in their evolution. We can then use each object's evolution point to create an evolutionary track. However, this method can lead to gaps being formed in this track if there is a lack of observational data [1]. Therefore, trying to come to conclusions about their evolution can lead to a distorted view of how they form and evolve.

The second method is to use cosmological computer simulations [1, 2, 3]. By this we mean, create a simulated galaxy, by using physics laws. The basic idea is that you start with the initial conditions of the Universe (or a certain volume of it), namely those suggested by the Cosmic Microwave Background (CMB) radiation, and the computer simulation will evolve this mock

Universe, galaxy, stars, accounting for physics. It does this by evolving gas, stellar and dark matter particles through time, while determining how they interact with each other.

In this work we will be looking specifically at the second method. We are incorporating a new metal-enrichment model into one of these cosmological simulations to improve the metal production in certain events that will occur with these particles. This will enable us to better understand the star formation histories, since these simulations can enable a detailed data analysis of each particle's metal component and how it evolved.

1.1. Cosmological simulations

Before we can discuss this new model's functions and which simulation we will be using, we need to understand how these simulations work. The first step is the initial conditions, i.e. the CMB. Then we need physics models. These models include [1, 2]:

- Gravity \sim Gravity solvers are needed, since they control the formation of large-scale objects, structure, halos and mergers. Fundamentally, these models need to be able to determine the force on each mass element from all others by solving Poisson's equation. After computing the gravitational forces on these particles the system evolves forward in discrete time-steps.
- Hydrodynamics \sim Solving the equations of hydrodynamics is required for modelling gas particle interactions. This needs to be solved concurrently with the gravity solver. There are two main methods: Firstly, the Lagrangian method, for example the Smoothed Particle Hydrodynamics (SPH) and the Meshless Finite-Mass (MFM) solvers, where the particles themselves carry the information about the fluid, which is obtained via a kernel-weighted sum over neighbouring particles. Secondly, the Eulerian method is where you discretize the fluid onto grid cells and then compute the advection of properties across the cell boundaries.
- Thermal evolution \sim Radiative cooling and photo-ionization heating of the gas particles via radiative processes found in baryons.
- Chemical evolution \sim Tracking the enrichment of heavy elements in gas particles are required for the cooling calculations, as well as for predictions of galactic chemical evolution. Early models tracked only Type II supernovae (SN) enrichments due to its relation with the Oxygen abundance. Later models also track asymptotic giant branch (AGB) stars, since they are required to understand the abundances of Carbon (their ejecta dominate the present-day Carbon observations), while Type Ia SN models are required to produce Iron.
- Sub-grid/sub-resolution models \sim These are processes which occur on scales smaller than the resolution of a single grid space and therefore, cannot be directly modelled. They are treated using heuristic models. For example, two of many different sub-grid models are [3]:
 - Star and black hole formation \sim The accumulated gas particles due to gravity, must be able to create stars and black holes to be able to form galaxies.
 - Feedback processes \sim These models are required to re-heat the cooling flow gas particles. The reason for this re-heating is due to the fact that cooling gas particles form stars, since it is observed that stars form in the dense, cold, molecular phase of the interstellar medium (ISM). So if the gas continues to cool it will form stars at an increasing rate. However, it is observed that at around $z \sim 2$, namely Cosmic High Noon, this star formation rate is at its highest and is quenched after this epoch [4]. It is, therefore, assumed that some feedback processes re-heat the gas. Feedback consist out of two general classes, preventive (stopping the gas from accreting into the ISM) and ejective (removing gas from the ISM after it has been accreted). Some feedback processes are: Photo-ionization suppression, star formation via stellar winds or supernovae, and Active Galactic Nuclei (AGB) feedback from black holes.

1.2. Observational confirmation

All of the aforementioned models will be used to evolve the initial conditions into a “Mock Universe”. This simulated Universe’s properties can then be compared to known global and structural properties to determine whether or not the simulation was successful in creating a “realistic approximation” of the Universe [2]. These observational tests include testing the global distribution functions, which refers to the comoving number density of galaxies as a function of global properties, such as luminosity or stellar mass. Some known distribution functions are the colour-luminosity function which tells us whether a galaxy is star forming (blue cloud - younger stellar populations) or are quiescent (red-sequence - older stellar populations).

Other observational tests include global scaling relations, such as the mass-metallicity relation (galaxies with a given mass has a lower gas-phase metallicity at high redshift) or structural scaling relations, such as the correlation of galaxies’ stellar mass with their radial size. We can also test the simulated galaxy’s demographics against known galaxy morphology.

Taking all of these into account there is an abundance of different global and structural property tests that we can use to determine whether the simulation succeeded. Other global and structural property tests are further discussed in-depth in [1, 2, 3].

2. The Simba simulation

2.1. GIZMO-Simba

From the description above, it follows that there is a lot of preparational work to create this type of simulations. Therefore, we will not be creating a new simulation from scratch, but rather improve on a current simulation. There exist a lot of different cosmological simulations, each trying a different approach to solving this problem. According to [1], these simulations can be separated into four different categories: 1) Zoomed simulation/dark matter-only e.g. Aquarius simulation, 2) Zoomed simulations/dark matter + baryons e.g. FIRE simulation, 3) Large volume/dark-matter only e.g. Millennium simulation, and lastly 4) Large Volume/dark matter + baryons e.g. Simba simulation. In this categorization it comes down to whether only gravity models are needed for dark matter halos, or whether hydrodynamics are also needed for the baryonic particle interactions. A simulation best suited to the problem should be chosen. This will also determine which known global and structural observational tests can be used to test the simulation.

Since we want to look at how a new metals production model improves the current simulation, we would firstly need baryons. Secondly, we want to see whether it improves our current statistics, therefore the 4th category. Specifically, we will be using the Simba simulation developed by [5]. There are other simulations in this category e.g. EAGLE, Illustris, Romulus25, that we also could have used. The Simba simulation is the successor of the Mufasa simulation [6] and gives updated sub-resolution star formation and feedback models. The Simba simulation consists out of 2 different components, namely GIZMO (a cosmological gravity plus hydrodynamics MFM solver [7]) and Simba. GIZMO is based on the simulation “GALaxies with Dark matter and Gas intERacT 3” or GADGET3 [8] and it evolves dark matter and gas elements together. In essence this is the backbone of Simba, since it controls the large-scale structure formation and particle interactions.

The second component, namely Simba itself controls the sub-grid/resolution models as discussed in section 1.1. Therefore, Simba will control the star and black hole formation (just two of many different processes) and the way they interact with their environments. Even though chemical/thermal evolution is part of the hydrodynamics part of the simulations, they are also controlled via Simba, since for example a SN occurs, metals and energy are produced on this sub-resolution scale and then distributed through the entire system. In figure 1, we show a small volume example run based on the default parameter values for the Simba simulation.

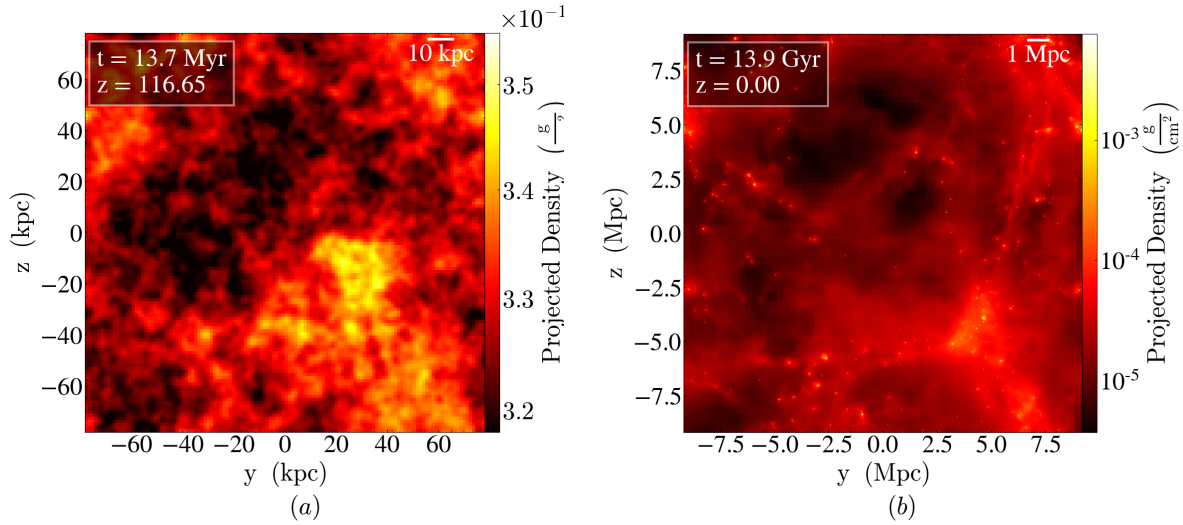


Figure 1. GIZMO-Simba simulation [5] at 2 different epochs ($z \sim 116, 0$) displaying the large-scale evolution of a 12.5 Mpc volume box size and a resolution of 128^3 particles. (a) Contains mostly diffused cooling gas left over from the Big Bang. (b) At present day these gas particles are accumulated through gravity to form the large-scale structure, called the “Cosmic Web”.

2.2. Chem5 metals model

From figure 1, it is clear that the large-scale structure component of the simulation do in fact represent a realistic idea of the large-scale evolution. So we do not want to change this part of the simulation, rather improve the small details in the metals production. You may ask why the metal production? The answer comes down to the fact that the chemical enrichment evolution of the gas particles influences the formation of stars and how they evolve, since it mediates how efficiently gas cools by impacting the stellar metallicities in galaxies and the Circumgalactic medium, and therefore influencing the following generation of stars being formed [9]. Therefore, we need to be able to accurately simulate the metal production to create more realistic galaxies.

However, due to the computationally expensive nature of these simulations, assumptions are made [5]. For example, in Simba only 11 elements (H, He, C, N, O, Ne, Mg, Si, S, Ca, Fe) are tracked from SN Ia/II and AGB stars. This still results in a somewhat “realistic” galaxy formation, since more than 90% of the Universe’s metal mass come from these 11 elements and they are the most important elements in star formation and feedback systems. Furthermore, Simba uses an instantaneous recycling of the distributed metals approximation. Therefore, we would want to add more elements into the system to obtain knowledge about how the less abundant elements influence the star formation histories, while also wanting to remove the instantaneous recycling of the distributed metals approximation.

This is where the Chem5 model comes in to play. The Chem5 model was developed by [10] and continued improvements since [11], and it is a self-consistent 3D Chemodynamical model. This model can track 32 elements (H, He, Li, Be, B, C, N, O, F, Ne, Na, Mg, Al, Si, P, S, Cl, Ar, K, Ca, Sc, Ti, V, Cr, Mn, Fe, Co, Ni, Cu, Zn, Ga, Ge), meaning that we can obtain a much more detailed description on how the metals influence the formation and evolution of the stars. This model also does not use the instantaneous recycling approximation method, rather treating each star particle as evolving stellar population which eject thermal energy, gas mass and heavy elements from stellar winds, SN Ia, SN II and Hypernovae (HNe) (previously not taken into account) as a function of time [10]. Other physical processes that it takes into account are radiative cooling, star formation, and photometric evolution.

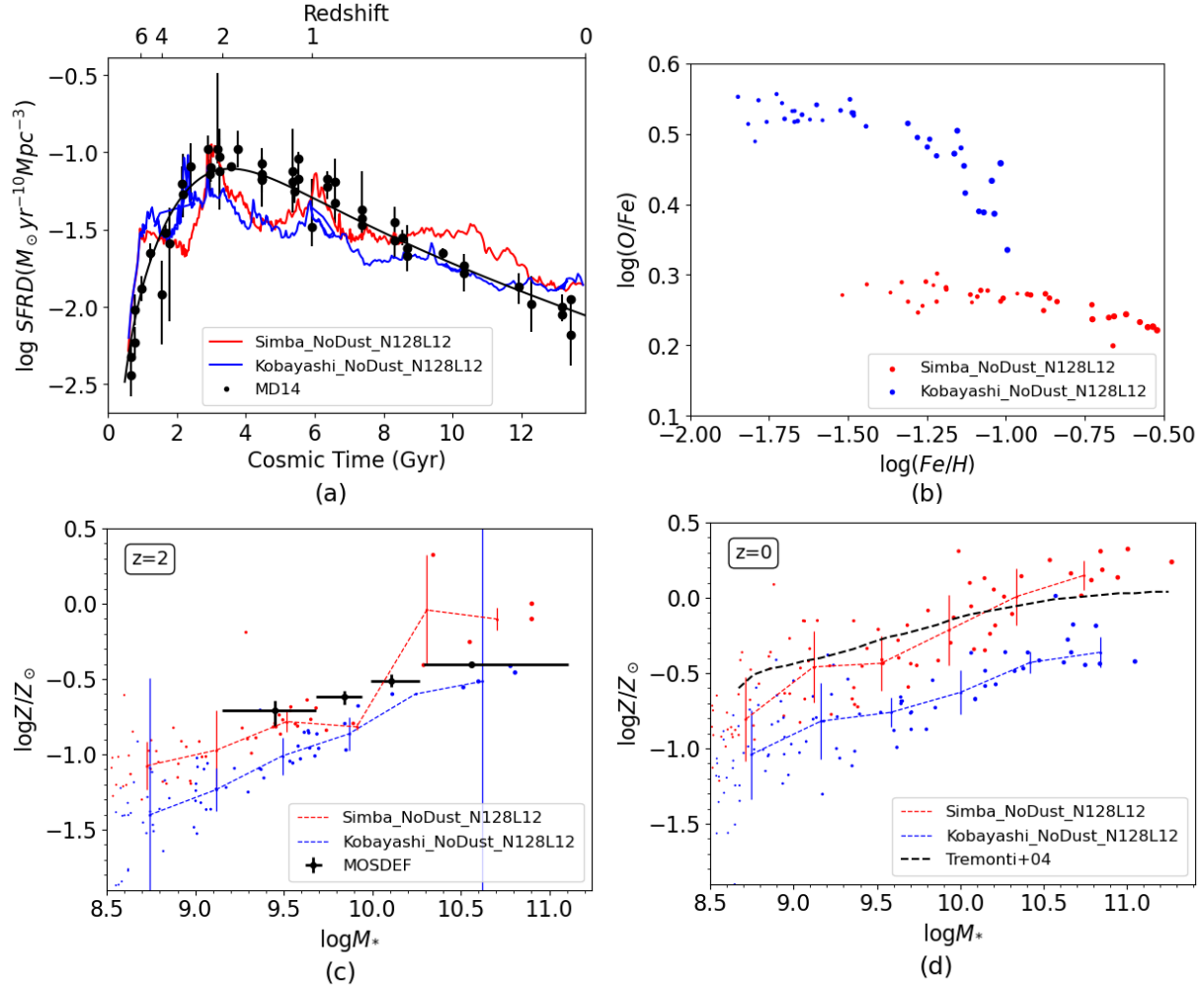


Figure 2. In (a), we show the star formation rate over the Cosmic Time. We compare both the resultant simulations for the Simba instantaneous model (red) and the Chem5 model (blue) against observations from [4]. In (b), we show the chemical abundance ratio's for the galaxies in the samples. In (c) and (d), we show the mass-metallicity relation evolution from these simulated galaxies and compare it to the observation made by [12] as part of the MOSDEF survey and [13]. It should be noted that all three these tests were done without the dust models.

2.3. Simba simulation with the new metal production model

For this work, we incorporated this new metals model into the Simba simulation without disrupting the current set-up. We had to create the program in such a way that the user can still use the old instantaneous model if they do not have a need for accuracy in the chemical enrichment of the gas particles and therefore helping with the computationally expensive nature of these simulations. We had to take into account that events can happen across different computer nodes, therefore just looping through all neighbouring particles that will receive the distributed metals, will lead to the same “event” needing to be calculated more than once, leading to the ejected energy/mass/metals being erroneously subtracted more than once. At this stage we are also not yet including the dust models from the Simba simulation, since it requires information about the metallicity structure. We will incorporate this after the integration phase. We present three early integration phase test plots to show the state of the integration in figure 2. This is once again for the 12.5 Mpc volume box size and a particle resolution of 128^3 . We also compare it to some well known observations, as well as against the original Simba simulation.

In figure 2, the star formation rates between simulations are similar, with the chem5 function obtaining a slightly more favourable comparison to the data. We also see in the abundance ratio graph that only the chem5 function obtained the know plateau of 0.5 and the “*bend*” close to -1 [11]. This is an improvement over Simba. But the Chem5 model still struggles with the total metallicity values, being under the observations and Simba in the mass-metallicity relation. Therefore, the integration phase is not yet complete.

3. Conclusions and future work

In this work, we introduced different ways to determine the evolutionary paths of celestial objects, such as galaxies, namely statistical observations and computer simulations. We then had a more in-depth look into how to create these computer simulations. We also discussed the Simba simulation and how we can use it for the research that we want to achieve. We briefly discussed the new Chem5 model and how it improves on the simplified nature of the current instantaneous recycling of the metals model in the Simba simulations. We then showed some integration phase plots, namely the star formation rate graph and the mass-metallicity relation plot. Both were compared to the Simba simulation and to observations.

For future work, we can see from figure 2, that some improvements are still necessary, but we are in a position to start incorporating the Chem5 model to work concurrently with the dust models and hopefully this will improve some of these results. We do have at least one improvement over Simba already, with the top R. H. S. panel obtaining $[O/Fe] \sim 0.5$, which is much closer to the observed values than Simba, but the “*bend*” that it obtained at $[Fe/H] \sim -1.3$ is yet not correct and it should be closer to -1.

For future science applications, we can e.g. study the less abundant elements, look at the mass-metallicity relation’s evolution for these new elements, or we can also track the metallicity of the intragroup and intracluster gas more accurately due to the larger element sample, which can give us clues into their formation history. We can also look at the detailed chemical abundances (e.g. alpha-enhancements) in the galaxies to better understand the star formation timescales. We will use papers like [5] to test improvements over Simba.

Acknowledgements

I acknowledge funding through a National Research Foundation (NRF) Grand Holder-linked Ph.D scholarship (Grant number 120850). I also acknowledge the help of the Compute Canada team for the usage of the Cedar supercomputer which were are using to run the simulations. I also acknowledge the Simba collaboration for the usage of the simulation.

References

- [1] Vogelsberger M, Marinacci F, Torrey P and Puchwein E 2020 *Nat. Rev. Phys.* **2** 42-66
- [2] Somerville R C and Davé R 2015 *ARA&A* **53** 51-113
- [3] Naab T and Ostriker J P 2017 *ARA&A* **55** 59-109
- [4] Madau P and Dickinson M 2014 *ARA&A* **52** 415-86
- [5] Davé R, Anglés-Alcázar D, Narayanan D, Li Q, Rafieferantsoa M H and Appleby S 2019 *MNRAS* **486** 2827-49
- [6] Davé R, Thompson R and Hopkins P F 2016 *MNRAS* **462** 3265-84
- [7] Hopkins P F 2015 *MNRAS* **450** 53-110
- [8] Springel V 2005 *MNRAS* **364** 1105-34
- [9] Tumlinson J, Peebles M S and Werk J K 2017 *ARA&A* **55** 389-432
- [10] Kobayashi C, Springel V and White S D M 2007 *MNRAS* **376** 1465-79
- [11] Kobayashi C, Karakas A I and Lugaro M 2020 *ApJ* **900** 179
- [12] Sanders R L, Shapley A E, Kriek M, Reddy N A, Freeman W R , Coil A L, Siana B, Mobasher B, Shivaiei I, Price S H *et al.* 2015 *ApJ* **799** 138
- [13] Tremonti C A, Heckman T M, Kauffmann G, Brinchmann J, Charlot S, White S D M, Seibert M, Peng E W, Schlegel D J, Uomoto A *et al.* 2004 *ApJ* **613** 898-913

Galaxy evolution in the local universe: studying the complete local-volume groups sample (CLoGS)

CD Stevens¹, K Kolokythas¹, SI Loubser¹

1. Centre for Space Research, NWU, Potchefstroom, 2520, South Africa

E-mail: 28850696@nwu.ac.za

Abstract. More than half of all galaxies within the local Universe are found in group environments. Therefore, galaxy groups are excellent laboratories for studying galaxy evolution. The Complete Local-Volume Groups Sample (CLoGS) is the first statistically complete galaxy group survey in the optical, X-ray and radio bands, consisting of 53 galaxy groups and 1427 member galaxies in total. The properties of the member galaxies, such as their star-formation rates (SFR_{FUV} , SFR_{W3}), stellar masses ($M_{*,K}$), radio emission ($P_{1.4\text{ GHz}}$) and WISE colours (W1-W2 and W2-W3) have been determined. The relation between the properties of the group member galaxies and their X-ray environment has been examined. The trends we have found suggest that star-formation relates to each group's dynamical age, X-ray halo and radio emission from each group's brightest group elliptical (BGE). We have found that within the majority (over 80%) of the dynamically young and X-ray bright groups of the CLoGS High Richness subsample, the SFR_{W3} of the member galaxies tend to increase the closer they are to the BGEs of their respective groups. Furthermore, we have found that within X-ray bright groups, the $P_{1.4\text{ GHz}}$ of the member galaxies tend to increase the closer they are to the BGEs of their respective groups, while their SFR_{FUV} tends to decrease. As a continuation of this research, a detailed optical spectroscopic study of these BGEs using data obtained on SALT (Southern African Large Telescope) is currently underway. The determined statistical relations and latest spectroscopy results are presented here.

1. Introduction

Galaxies co-evolve in gravitationally bound structures such as groups. More than half, roughly 60%, of all galaxies in the local Universe are found within group environments [1]. By studying the properties of galaxies within nearby groups, galaxy evolution in the local Universe can be better understood. Typically, groups span 0.5 Mpc across in diameter and contain less than 100 galaxies, each galaxy with a stellar mass between $\sim 10^{11} M_{\odot}$ and $\sim 10^{14} M_{\odot}$ [2]. However, there is not a single precise definition for the boundaries of a galaxy group.

CLoGS is the first statistically complete sample of galaxy groups in the local Universe ($< 80\text{ Mpc}$) observed in the radio, X-ray and optical bands [3]. CLoGS selects groups optically to avoid the X-ray detection bias for cool-core groups [4] and performs a follow-up X-ray study to determine which of these groups have extensive haloes to circumvent false detection. CLoGS consists of 1427 member galaxies distributed throughout 53 galaxy groups [3]. These groups are further divided into the high-richness (HRS) subsample and low-richness (LRS) subsample based on the richness parameter 'R' of these groups. 'R' is defined as the amount of optically bright galaxies with a luminosity of $\log(L_B) \geq 10.2 L_{\odot}$. The HRS subsample consists of groups

with $4 \leq R \leq 8$ and the LRS subsample of groups with $R = 2$ or $R = 3$. In more detail, the HRS subsample consists of 26 groups with 766 member galaxies and the LRS subsample consists of 27 groups with 661 member galaxies in total.

The X-ray properties of the HRS subsample have been studied [3]. Additionally, the radio properties of the central radio galaxies of the HRS [5] and LRS subsamples [6] have been studied in detail. To relate the properties of the HRS subsample member galaxies with their group environment, the groups are divided into 6 categories. These categories are: X-ray bright, X-ray faint, dynamically young, dynamically old and with- or without radio jets. In terms of scale, X-ray bright groups have extensive X-ray haloes ($> 65 kpc$) and X-ray faint groups have galaxy-like or point-like haloes [5]. The dynamical age of the groups is determined by their fraction of spiral (late-type) galaxies f_{sp} . Groups with $f_{sp} \geq 0.75$ are defined as dynamically young and groups with $f_{sp} < 0.75$ as dynamically old [5]. The BGE of each group may or may not possess active galactic nuclei (AGN) with outflowing radio jets and the groups are categorised accordingly [6].

2. Method

2.1. Determining the properties of the CLoGS member galaxies

The fundamental galaxy properties that we examine in order to better understand how galaxy evolution works in nearby groups are stellar mass ($M_{*,K}$), star-formation rates (SFR_{FUV} and SFR_{W3}), radio power ($P_{1.4 GHz}$) and WISE colours (W1-W2 and W2-W3).

The stellar mass of a galaxy can be gauged from the luminosity of its evolved stellar population using stellar mass to luminosity (M/L) ratios. In particular the K-band ($2 \mu m - 3 \mu m$) is insensitive to dust and is dominated by infrared emission from the evolved stellar populations. For this purpose the 2MASS extended source catalog (XSC) which has data available for $\sim 60\%$ of the CLoGS member galaxies was chosen to estimate their stellar masses. The stellar masses were estimated with the following M/L ratio calibrated to the extended K-band (k_{m_ext}) of 2MASS [7]:

$$\log\left(\frac{M_{*,K}}{L_K}\right) = -0.206 + 0.135 \times E(B - V), \quad (1)$$

where $E(B-V)$ is the corresponding Galactic reddening of each galaxy.

The star-formation rate of a galaxy can be estimated from the luminosity of its young stellar population. The light from newly formed stars can either be measured indirectly from the dust reflecting light from them (dust-obscured star-formation) or directly from the stars themselves (unobscured star-formation).

The W3-band ($12 \mu m$) from the AllWISE survey which observed all of the CLoGS member galaxies, is sensitive to dust-obscured star-formation [8] and was used to estimate their star-formation rates with the following relation [9]:

$$\log(SFR_{W3}[M_{\odot}.yr^{-1}]) = 0.873(\pm 0.021) \times \log(\nu L_{W3}[L_{\odot}]) - 7.62(\pm 0.18), \quad (2)$$

where νL_{W3} is the normalised spectral luminosity of each galaxy in the W3-band.

The FUV-band ($100 nm - 200 nm$) from the GALEX survey, which observed $\sim 85\%$ of the CLoGS member galaxies, is sensitive to unobscured star-formation [10] and was similarly used to estimate their star-formation rates with the following relation [10]:

$$SFR_{FUV}[M_{\odot}.yr^{-1}] = 1.08 \times 10^{-28} L_{FUV}[erg.s^{-1}.Hz^{-1}], \quad (3)$$

where L_{FUV} is the luminosity of each galaxy in the FUV-band in cgs units.

To have an indication of each galaxy's degree of star-formation and AGN activity, the $P_{1.4\text{ GHz}}$ of the CLoGS member galaxies were determined using data from the NRAO VLA Sky Survey (NVSS) [11], which observed all of the CLoGS member galaxies. The 1.4 GHz band is sensitive to synchrotron radiation from electrons accelerated either by the observed galaxy's central black hole (possible AGN) or supernovae remnants [12]. To classify the CLoGS member galaxies by colour, the same classification method developed by Jarrett et al. [8] is used. This method relies on the W1 ($3.35\text{ }\mu\text{m}$), W2 ($4.6\text{ }\mu\text{m}$) and W3 ($12\text{ }\mu\text{m}$) magnitude measurements of the AllWISE survey and divides galaxies into 4 possible colour regions based on the infrared properties of their bulges and discs (their W1-W2 and W2-W3 colours) [8].

The 4 possible WISE colour regions, as shown in Figure 1, are [8]:

- Spheroid-dominated (Spheroids): With $W2 - W3 < 1.5$ and $W1 - W2 < 0.8$. Galaxies in this colour region are identified by their prominent bulges and strong mid-infrared emission from its central evolved stellar population. These galaxies are typically spheroidal, although not necessarily.
- Star-formation dominated (Star forming discs): With $W2 - W3 > 3$ and $W1 - W2 < 0.8$. Galaxies in this colour region are significantly bright in W3 and have notable ongoing star-formation. These galaxies are typically discs, although not necessarily.
- Intermediate: With $1.5 \leq W2 - W3 \leq 3$ and $W1 - W2 < 0.8$.
- Infrared-AGN and extrema: With $W1 - W2 \geq 0.8$. A high W1 measurement may indicate AGN activity within the galaxy and such galaxies are classified accordingly.

It should be noted this method does not strictly determine the morphology of the galaxies, for such a task visual inspection would be required. This method merely states what the most likely morphology of each galaxy would be based on their WISE colours, star-formation activity and AGN activity. The galaxies are further divided into 3 star-formation types based on their far-ultraviolet (FUV) and infrared (IR) colours provided by GALEX and AllWISE, as similarly done by Gil de Paz et al. [13]. The 3 star-formation types are [13]:

- Dust-obscured star-forming (IR bright), with colours: $FUV - K_s > 8.8$ and $W3 - W4 > 2$.
- Star-forming (FUV bright) with colour: $FUV - K_s \leq 8.8$.
- Non-star-forming, with colours: $FUV - K_s > 8.8$ and $W3 - W4 \leq 2$.

2.2. Relating the HRS member galaxies to their group environment

To study the galaxy evolution of the CLoGS group sample, we examine the properties of the HRS member galaxies with respect to their group environment. To achieve this, we study the most prevalent type of the CLoGS member galaxies: those within the WISE colour region: $W2 - W3 > 3$ and $W1 - W2 < 0.8$. We note how their properties change with distance from the brightest group ellipticals (BGEs) of their groups. Here we only consider galaxies within R_{500} of each group, where $R_{500} = 500\rho_c$ (ρ_c : critical density of the Universe), which is a rough estimation of each group's size. We simply inspect and note whether the properties of the member galaxies $P_{1.4\text{ GHz}}$, SFR_{FUV} , SFR_{W3} and $M_{*,K}$ increase or decrease towards the centres of the groups, where each group's BGE is roughly located.

3. Results

Only the results for the HRS subsample are shown. The results for the LRS subsample are qualitatively the same with a slightly different WISE colour distribution. The stellar masses and star-formation rates of the LRS subsample galaxies are of the same order of magnitude.

3.1. The properties of the CLoGS HRS member galaxies

The WISE colour distribution of the 766 HRS member galaxies are shown Figure 1. Figure 1 shows the 4 different WISE colour regions as defined in Section 2. The member galaxies are shown in terms of their star-formation types (FUV and IR colours) as described in Section 2.

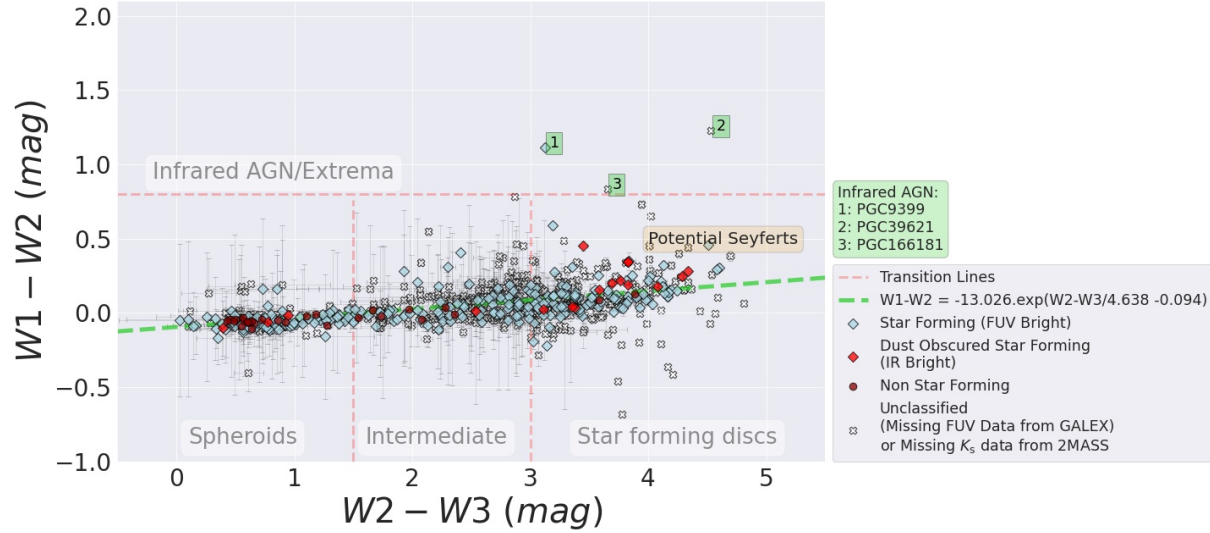


Figure 1. The $W1 - W2$ and $W2 - W3$ colours of the member galaxies are fitted with an exponential function which shows the general trend in star-formation. Galaxies which deviate from this trend are classified as potential Seyfert galaxies (or other). The star-formation types of the galaxies with missing data from GALEX or 2MASS are left as unclassified. The infrared AGN are numbered and their Principal Galaxies Catalog (PGC) names shown.

The $W3$ -star-formation rates and K -band estimated stellar masses of the 766 HRS subsample member galaxies are shown in Figure 2. The members are once again categorised according to their WISE colour region and their star-formation type as discussed in Section 2.

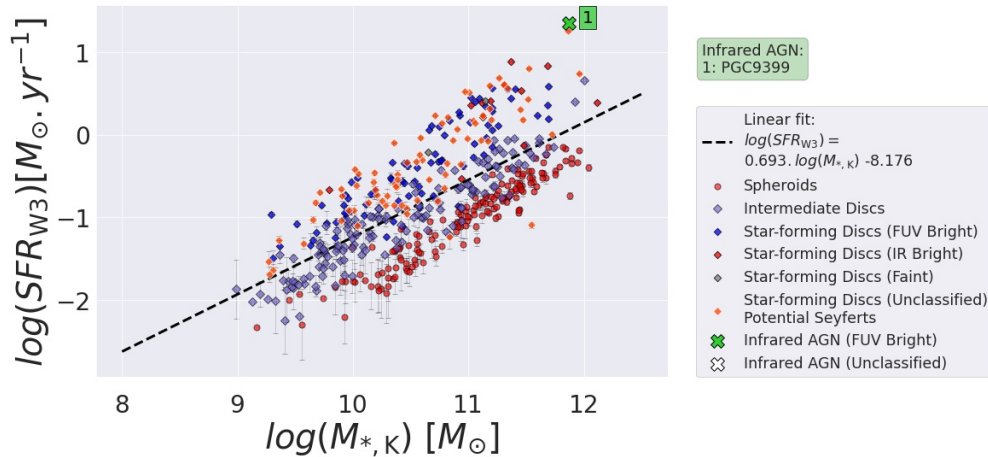


Figure 2. It can clearly be seen that the star-formation rates (SFRs) increase with stellar mass and change with WISE colour region. In ascending order, the SFRs of the member galaxies change in terms of their WISE colour regions as: spheroid-dominated, intermediate, star-formation dominated and Infrared-AGN.

3.2. Relationship between the HRS member galaxy properties and their group environment

The property trends of the HRS member galaxies, with $W2 - W3 > 3$ and $W1 - W2 < 0.8$ are shown in Table 1. Only galaxies within R_{500} of each group are selected as discussed in Section 2.2. The groups are divided by category as discussed in Section 1. These trends were determined by treating each group individually, with each member galaxy a data point (further binned to every 0.25 kpc). Linear regression lines were fitted to determine if the member galaxies within each group had an increase or a decrease in each property the closer they were to the BGEs of their respective groups. However these trends are not necessarily linear, other functions may be more accurate. A larger sample of member galaxies within each group would be required to fit these.

Table 1. \uparrow indicates an increase in the property and \downarrow indicates a decrease. For example, the first cell reads: Within 80% of the X-ray bright groups (4 out of the 5 groups), the member galaxies had an increase in $P_{1.4 \text{ GHz}}$ the closer they were to their group's BGE.

Group Category	$P_{1.4 \text{ GHz}}$	SFR_{FUV}	SFR_{W3}	$M_{*,\text{K}}$
X-ray Bright (5 groups)	\uparrow (80%)	\uparrow (40%) \downarrow (40%)	\uparrow (80%)	\uparrow (80%)
X-ray Faint (1 group)	-	-	-	-
With Jet (6 groups)	\uparrow (66.7%)	\downarrow (66.7%)	\uparrow (83.3%)	\uparrow (83.3%)
Without Jet (0 groups)	-	-	-	-
Dynamically Young (3 groups)	\uparrow (66.7%)	\downarrow (66.7%)	\uparrow (100%)	\uparrow (100%)
Dynamically Old (3 groups)	\uparrow (66.7%)	\downarrow (66.7%)	\uparrow (66.7%)	\uparrow (66.7%)
All (6 groups)	\uparrow (66.7%)	\downarrow (66.7%)	\uparrow (83.3%)	\uparrow (83.3%)

3.3. Current work: spectroscopy of the CLoGS brightest group ellipticals (BGEs)

We have already analysed long-slit spectra for 32 BGEs from the Hobby-Eberly Telescope [15]. At present, the BGEs observable from the Southern Hemisphere have been observed with the Southern African Large Telescope (SALT) and an in-depth optical spectroscopic study of these galaxies is in progress. We are studying the spatially resolved stellar kinematics of these galaxies by analysing their spectra, such as Figure 3. Furthermore, we are studying the stellar populations of these galaxies and deriving their star-formation histories.

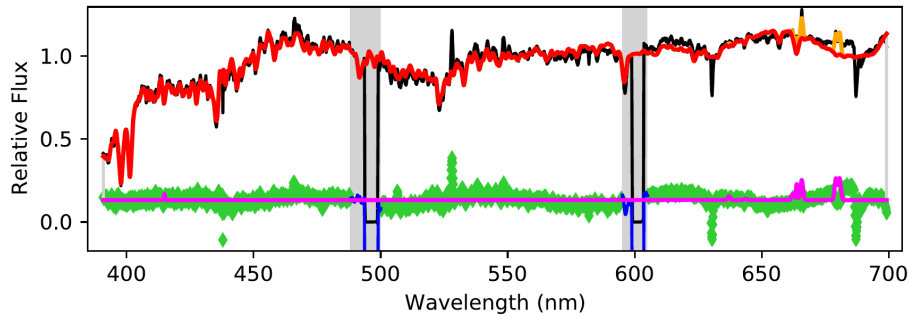


Figure 3. The observed SALT spectrum for NGC7377 is shown in black. The masked chipgaps of SALT is shown in grey and blue. The fitted spectrum, generated with the penalised pixel fitting method (pPXF) of Cappellari [14], is shown in red. The baseline fit is shown in pink. The deviations between the data and model spectra is shown in green and the identified spectral lines are shown in orange.

Clear $H\alpha$ (656 nm), $[SII]$ (6716 nm and 6731 nm), $[OI]$ (6300 nm) and $[NII]$ (6583 nm) emission can be seen on the spectrum of NGC7377, as shown in Figure 3. Similar spectra were observed and fitted for all the CLoGS BGEs, with minor differences in shape and emission lines.

4. Concluding Remarks

Within each group, the member galaxies with $W2 - W3 > 3$ and $W1 - W2 < 0.8$ in the CLoGS HRS subsample have several of their properties related to their distance from the BGEs of their respective groups. Within the majority (over 80%) of the dynamically young and X-ray bright groups, the SFR_{W3} of the member galaxies tend to increase the closer they are to the BGEs of their respective groups. Furthermore, within 80% (4 out of 5) of the X-ray bright groups, the $P_{1.4\text{ GHz}}$ of these member galaxies tend to increase the closer they are to the BGEs of their respective groups, whilst their SFR_{FUV} tends to decrease. This increase in $P_{1.4\text{ GHz}}$ and decrease in SFR_{FUV} is found to be more frequent in X-ray bright groups than in any other group category. However, a larger and more statistically significant number of groups need to be observed to verify these trends. Additionally, more member galaxies need to be observed within each group to determine the exact function of these trends, which may be linear or otherwise. The CLoGS BGEs are currently being studied more closely using optical spectroscopy obtained on SALT. These results will provide more clues to galaxy evolution in groups in the local Universe.

5. Acknowledgements

This work is based on the research supported wholly by the National Research Foundation of South Africa (CDS: Grant Number 134198; KK SIL: Grant number 120850). Opinions, findings and conclusions or recommendations expressed in this publication is that of the author(s), and that the NRF accepts no liability whatsoever in this regard.

References

- [1] Eke VR, Baugh CM, Cole S, Frenk CS and Navarro JF 2006 Galaxy groups in the 2dF Galaxy Redshift Survey: the number density of groups *Mon. Not. R. Astron. Soc.* **370** 1147-58
- [2] Sparke L and Gallagher S 2007 *Galaxies in the Universe: An Introduction* 273
- [3] O'Sullivan E, Ponman TJ, Kolokythas K, Raychaudhury S, Babul A, Vrtilek JM, David LP, Giacintucci S, Gitta M and Haines CP 2017 The Complete Local-Volume Groups Sample -I. Sample selection and X-ray properties of the high-richness subsample *Mon. Not. R. Astron. Soc.* **472** 1482-505
- [4] Eckert D, Molendi S and Paltani S 2018 The cool-core bias in X-ray galaxy cluster samples I: method and application to HIFLUGCS *A&A* **526** A79
- [5] Kolokythas K, O'Sullivan E, Raychaudhury S, Giacintucci S, Gitti M and Babul A 2018 The Complete Local-Volume Groups Sample - II. A study of the central radio galaxies in the high-richness subsample *Mon. Not. R. Astron. Soc.* **481.2** 1550-77
- [6] Kolokythas K, O'Sullivan E, Intema H, Raychaudhury S, Babul A, Giacintucci S and Gitti M 2019 The Complete Local-Volume Groups Sample - III. Characteristics of group central radio galaxies in the local Universe *Mon. Not. R. Astron. Soc.* **489.2** 2488-504
- [7] Bell EF 2003 The optical and near-infrared properties of galaxies. I. Luminosity and stellar mass functions *ApJS* **149** 289-312
- [8] Jarrett TH, Cluver ME, Brown MJI, Dale DA, Tsai CW and Masci F 2019 The WISE extended source catalog (WXSC) I: The 100 largest galaxies *ApJS* **245** -63
- [9] Cluver ME, Jarrett TH, Dale DA, Smith J-DT, August T and Brown MJI 2017 Calibrating star-formation in WISE using total infrared luminosity *ApJ* **850** 67-91
- [10] Salim S *et al.* 2007 UV star-formation rates in the local universe *ApJS* **173** 267-92
- [11] Condon JJ, Cotton WD, Greisen EW and Yin QF 1998 The NRAO VLA sky survey *AJ* **115** 1693-716
- [12] Condon JJ 1992 Radio emission from normal galaxies *Annu. Rev. Astron. Astrophys.* **30** 575-611
- [13] Gil de Paz AB *et al.* 2007, *ApJS*, **173**, 185
- [14] Cappellari M 2016 Improving the full spectrum fitting method: accurate convolution with Gauss-Hermite functions *Mon. Not. R. Astron. Soc.* **466** 798-811
- [15] Loubser SI, Hoekstra H, Babul A and O'Sullivan E 2018 Diversity in the stellar velocity dispersion profiles of a large sample of brightest cluster galaxies $z \leq 0.3$ *Mon. Not. R. Astron. Soc.* **477** 335-58

A study of the lobes of the radio galaxy Hydra A using MeerKAT observations

M A Naidoo¹, D A Prokhorov^{2,1}, P Marchegiani^{3,1}, A W Chen¹, S Makathini¹, P Serra⁴ and W J G de Blok^{5,6,7}

¹ School of Physics, University of the Witwatersrand, Johannesburg, Wits 2050, South Africa

² GRAPPA, Anton Pannekoek Institute for Astronomy, University of Amsterdam Science Park 904, 1098 XH Amsterdam, The Netherlands

³ Sapienza Universita' di Roma, Piazzale Aldo Moro 5, Roma RM,00185, Italy

⁴ INAF- Osservatorio Astronomico di Cagliari Via della Scienza 5, I-09047 Selargius (CA), Italy

⁵ Netherlands Institute for Radio Astronomy (ASTRON), Oude Hoogeveensedijk 4, 7991 PD Dwingeloo, the Netherlands

⁶ Dept. of Astronomy, Univ. of Cape Town, Private Bag X3, Rondebosch 7701, South Africa

⁷ Kapteyn Astronomical Institute, University of Groningen, PO Box 800, 9700 AV Groningen, The Netherlands

E-mail: 1678178@students.wits.ac.za

Abstract. The radio galaxy Hydra A hosts a pair of hundred-kiloparsec diameter radio lobes that are being powered by one of the most powerful AGN outbursts known to date. Observations in the radio band provide us with an excellent probe for studying a high-energy electron population residing in the lobes. Using the MeerKAT observations of Hydra A, we computed the flux densities of these giant lobes at several frequencies and combined them with previous results from VLA observations at lower frequencies. We found that the spectrum in the MeerKAT frequency range is well described by a power law, while the overall spectrum indicates a steepening with frequency. We set constraints on the magnetic field strength and the age of the giant lobes through modelling of the temporal evolution of electron spectra under the influence of synchrotron losses.

1. Introduction

The powerful radio galaxy Hydra A lies at the center of the galaxy cluster Abell 780, which is located at a redshift of $z = 0.054$. Hydra A is classified as a type I Fanaroff-Riley (FRI)[1] radio galaxy, which is characterised by a high surface brightness near the center and a lower surface brightness further out. When matter accretes onto a central supermassive black hole (SMBH), a large amount of energy is expelled into the ambient medium in the form of highly collimated, highly relativistic jets. When these jets encounter the intracluster medium (ICM), they inflate giant radio lobes. This expulsion of energy can occur more than once during the lifetime of the radio galaxy resulting in multiple generations of outbursts. Depressions in the X-ray emission surrounding Hydra A have been discovered [2,3] and are coincident with the radio lobes. This suggests that the inflation of radio lobes is the driving mechanism responsible for the displacement of the X-ray emitting gas in the ICM. Hydra A has experienced three

generations of outbursts, indicated by the three pairs of X-ray cavities [3] and radio bubbles of different ages and energetics[4].

The energetics involved in an AGN outburst can be huge, even exceeding 10^{61} erg, which corresponds to the amount of energy released in tens of billions of supernovae explosions [5]. The most powerful AGN outbursts are found in MS 0735+7421, Hercules A, and Hydra A[5]. The bubbles in these systems have ages of about 100 million years. Their energy content is determined using arguments of pressure balance between the thermal ICM and the relativistic plasma within the bubbles. The energy required to expand bubbles with volume V into a surrounding ICM with pressure p ranges from $2pV$ to $4pV$ [3]. However, the nature of the principal component responsible for the pressure support and which fills the bubbles in the ICM is not known to date. Among the possibilities for the pressure support in the bubbles are cosmic-ray hadrons or electrons, hot plasmas, or magnetic fields. While gamma-ray observations allow us to test a hadronic model [6,7] and measurements of the Sunyaev-Zel'dovich effect are a tool to test hot plasmas [8] and non-thermal electrons [9] inside the bubbles, observations in the radio band provide us with a probe of magnetic fields.

Synchrotron radiation and inverse Compton scattering cause energy losses of high-energy electrons. The former is dominant if the magnetic field strength is above several μG . The radiative cooling of electrons results in time evolution of an electron spectrum. As electrons lose energy, the radio spectrum steepens, a phenomenon known as spectral aging [10, 11, 12]. A theory of synchrotron aging has been applied to the lobes of FRI radio galaxies (e.g., Fornax A [13]) and FRII radio galaxies (e.g., Cygnus A [14]). The previous detection of the giant Hydra A lobes at 74 MHz, 327 MHz, and 1415 MHz [4] suggested that the spectrum steepens in this frequency range. In these proceedings, we report the preliminary results obtained from our spectral analysis of MeerKAT observations of Hydra A between 960 MHz and 1525 MHz.

2. Observations and analysis

Hydra A was observed with the MeerKAT radio telescope on 30 May 2019 (Proposal ID: SCI-20190418-PA-01; PI: Prokhorov). The observations were made using the entire array which is made up of 64 antennas, each 13.5 m in diameter. MeerKAT is equipped with L-band receivers and a correlator with 4096 channels. For this study, we used 30 minutes of these observations accumulated over a frequency range of 856 MHz - 1712 MHz. We reduced the data using the Containerised Automated Radio Astronomy Calibration (CARACal) pipeline [15]. To derive the flux densities from the radio maps obtained with CARACal, we used the radioflux routine by M J Hardcastle (<https://www.extragalactic.info/mjh/radio-flux.html>).

3. Results

We produced four radio maps of Hydra A at four frequencies, 1000 MHz, 1100 MHz, 1330 MHz and 1485 MHz with a bandwidth of 80 MHz and in units of Jy/beam. These maps shown in Figure 1 reveal two bright inner lobes extending in the northern and southern directions and two larger outer lobes. The morphology of these spatial structures is in good agreement with that obtained from the observations of the Very Large Array (VLA) telescope (Figure 1 in [4]) at 1415 MHz. The MeerKAT and VLA radio maps display similar spatial structures. However, the MeerKAT observations for the first time reveal finer details such as the bridge at (RA, Dec)=(9h18m8s, -12d03m28s) between the bright central source and the northern outer lobe.

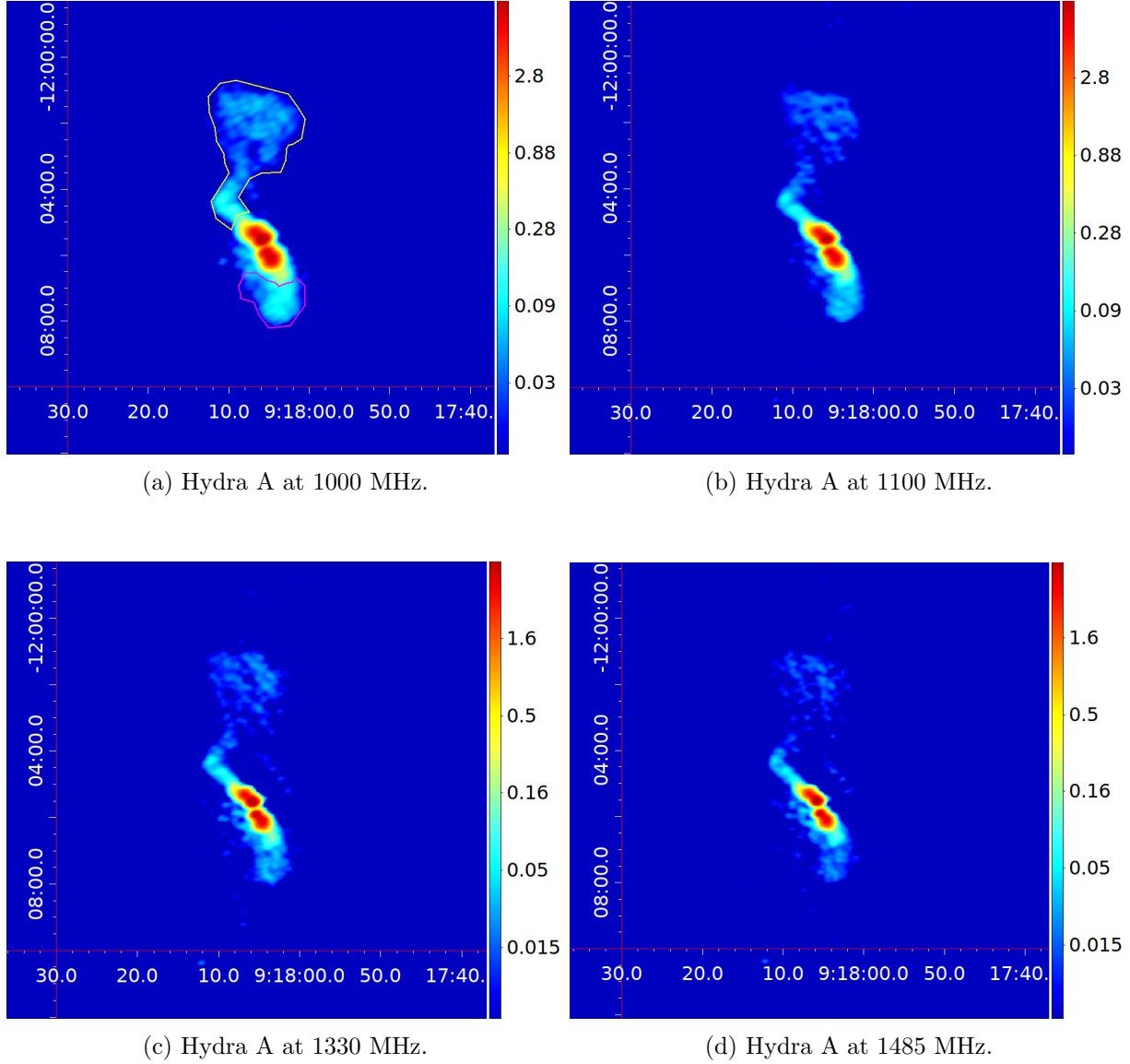


Figure 1: Radio maps of Hydra A between 1000 MHz and 1485 MHz shown in equatorial coordinates of right ascension (hours) and declination (deg.). The colour bar represents the radio intensity in units of Jy/beam. The size of the beam is 20×12 arcsec² at 1000 MHz, 18×11 arcsec² at 1100 MHz, 15×9 arcsec² at 1330 MHz, and 13×8 arcsec² at 1485 MHz.

To study the spectral behaviour between 960 MHz and 1525 MHz, we computed the flux densities and corresponding uncertainties for the outer lobes using the MeerKAT observations. The regions that we have defined as the outer lobes are indicated in Figure 1a. The fluxes are computed from the regions which significantly exceed in size the synthesized beams at the four frequencies.

We combined our data points with the two low-frequency data points at 74 MHz and 327 MHz adopted from [3, 15] to produce the multi-frequency radio spectrum of Hydra A shown in Figure 2. We checked and found that the fluxes obtained from the VLA maps do not depend strongly on the template selection, this will be addressed in a future journal paper. The spectrum in the

MeerKAT frequency range is well described by a steep power law with a spectral index of 2.05 with a statistical error of 0.04. Extrapolating the derived power law to the 74 MHz frequency, assuming a best fit spectral index of 2.05 gives a flux density of ~ 500 Jy which is significantly higher than the measured flux density given by 221 ± 30 Jy. This suggests that a spectral break is present in the overall spectrum. The most likely mechanism to produce this break is spectral aging.

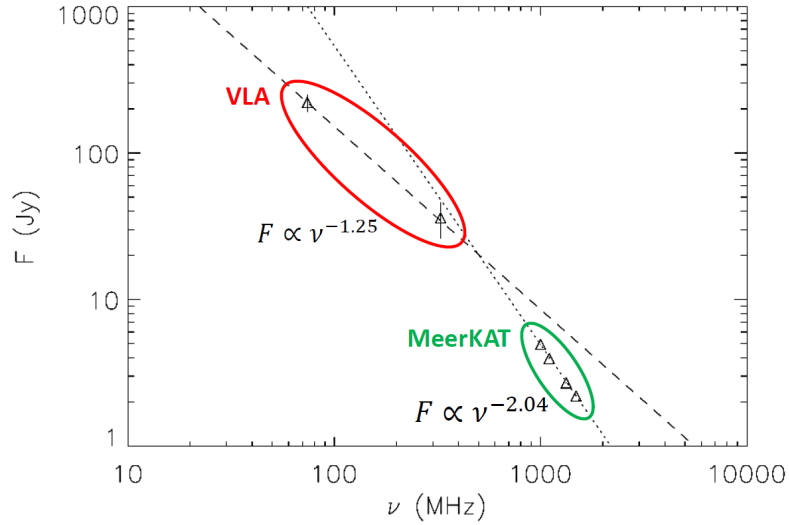


Figure 2: The radio spectrum of Hydra A using our four MeerKAT data points combined with the two low-frequency data points at 327 MHz and 74 MHz.

We find that the Kardashev-Pacholczyk model [9,10] for spectral aging satisfactorily describes the overall spectrum. To model the spectral steepening (see Figure 3), we assumed values for the age and magnetic field strength of 35 million years and $18 \mu\text{G}$, respectively. The best-fit values are found using automated χ^2 minimization.

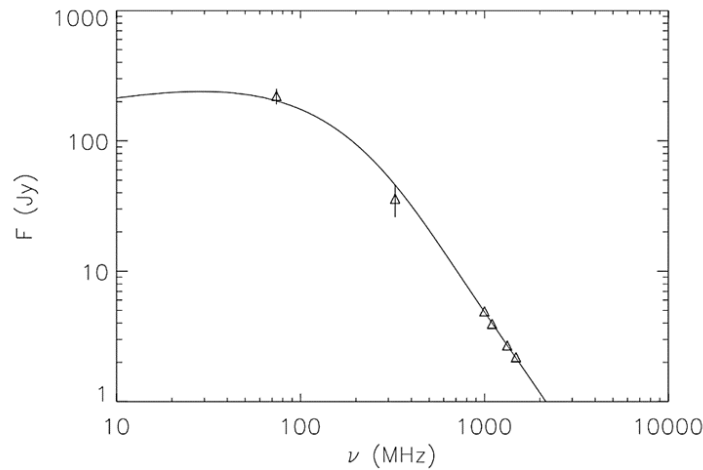


Figure 3: An illustrative model for the overall radio spectrum of the outer lobes of Hydra A. The values of the magnetic field strength and age of the outer lobes are derived from the modelling.

4. Conclusion

We present four MeerKAT radio maps of Hydra A at 1000, 1100, 1330 and 1485 MHz. These radio maps reveal an extended radio structure that consists of two bright inner radio lobes and two giant outer radio lobes. The entire spatial structure is consistent with previous observations. We computed the flux densities and combined them with those from the previous low-frequency VLA observations. We found that the spectrum for the giant lobes in the MeerKAT frequency range is well described by a steep power law with a spectral index $\alpha = 2.05 \pm 0.04$. The MeerKAT data, in conjunction with the low frequency VLA observations, reveal the presence of a spectral break. To explain this spectral break, we used the Kardashev-Pacholczyk model for spectral aging due to synchrotron losses of high-energy electrons.

Acknowledgments

This study has made use of data obtained from the MeerKAT telescope that has been provided by the South African Radio Astronomy Observatory (SARAO) which is a facility of the National Research Foundation, an agency of the Department of Science and Technology. The data published here have been reduced using the CARACal pipeline, partially supported by ERC Starting grant number 679627 “FORNAX”, MAECI Grant Number ZA18GR02, DST-NRF Grant Number 113121 as part of the ISARP Joint Research Scheme, and BMBF project 05A17PC2 for D-MeerKAT. Information about CARACal can be obtained online under the URL: <https://caracal.readthedocs.io>. M A Naidoo acknowledges support from the South African National Space Agency (SANSA).

References

- [1] Fanaroff B L and Riley J M 1974 The morphology of extragalactic radio Sources of high and low Luminosity *MNRAS* **167** 31P-36P
- [2] Nulsen P E J, McNamara B R, Wise M W and David L P 2005 The cluster-scale AGN outburst in Hydra A *ApJ* **628** 629-36
- [3] Wise M W, McNamara B R, Nulsen P E J, Houck J C and David L P 2007 X-Ray supercavities in the Hydra A cluster and the outburst history of the central galaxy’s active nucleus *ApJ* **659** 1153-58
- [4] Lane W M, Clarke T E, Taylor G B, Perley R A and Kassim N E 2004 Hydra A at low radio frequencies *AJ* **127** 48-52
- [5] McNamara B R and Nulsen P E J 2007 Heating hot atmospheres with active galactic nuclei *ARA&A* **45** 117-75
- [6] H.E.S.S. collaboration et al. 2012 Constraints on the gamma-ray emission from the cluster-scale AGN outburst in the Hydra A galaxy cluster *A&A* **545** id.A103
- [7] Prokhorov D A and Churazov E M 2017 Confinement and diffusion time-scales of CR hadrons in AGN-inflated bubbles *MNRAS* **470** 3388-94
- [8] Prokhorov D A, Moraghan A, Antonuccio-Delogu V and Silk J 2012 Simulating Sunyaev-Zel’dovich intensity maps of giant active galactic nucleus cocoons *MNRAS* **425** 1753-62
- [9] Colafrancesco S 2005 The SZ effect from cluster cavities *A&A* **435** L9-L12
- [10] Kardashev N S 1962 Nonstationarity of spectra of young sources of nonthermal radio emission *SvA* **6** 317
- [11] Pacholczyk A G 1970 *Radio Astrophysics: Nonthermal Processes in Galactic and Extragalactic Sources* vol XXI+269 (San Francisco: Freeman)
- [12] Jaffe W and Perola G 1973 Dynamical models of tailed radio sources in clusters of galaxies *A&A* **26** 423-35
- [13] Maccagni F M, Murgia M, Serra P, Govoni F, Morokuma-Matsui K, Kleiner D, Buchner S, Józsa G I G, Kamphuis P, Makhathini S et al. 2020 The flickering nuclear activity of Fornax A *A&A* **634** A9
- [14] Carilli C L, Perley R A, Dreher J W and Leahy J P 1991 Multifrequency radio observations of Cygnus A: spectral aging in powerful radio galaxies *ApJ* **383** 554-73
- [15] Józsa G I G, White S V, Thorat K, Smirnov O M, Serra P, Ramatsoku M, Ramaila A J T, Perkins S J, Molnár D C, Makhathini S et al. 2020 *ASPC* **527** 635
- [16] Bîrzan L, McNamara B R, Nulsen P E J, Carilli C L, and Wise M W. 2008 Radiative efficiency and content of extragalactic radio sources: toward a universal scaling relation between jet power and radio power *ApJ* **686** 859-80

Optical emission line properties of some little-known Narrow Line Seyfert 1 galaxies

Bynish Paul^{1,2}, Hartmut Winkler¹ and Stephen B Potter^{1,2}

¹ Department of Physics, University of Johannesburg
P.O. Box 524, 2006 Auckland Park, Johannesburg, South Africa

² South African Astronomical Observatory (SAAO)
P.O. Box 9, 7935 Observatory, Cape Town, South Africa

E-mail: bynish@saa.ac.za, hwinkler@uj.ac.za, sbp@saa.ac.za

Abstract. We analyse medium resolution optical spectra of six Active Galactic Nuclei (AGN) with iron emission spectra and characteristics associated with the class referred to as Narrow-Line Seyfert 1 galaxies (NLS1). These were observed using the 1.9 m telescope at the South African Astronomical Observatory (SAAO) in Sutherland. The objects are among the brighter sources of that description accessible from the southern hemisphere: Fairall 265, NPM1G –15.0297, CTS J03.19, EUVE J0414–59.6, A0644–1, and HE 2116–3609. For each target we performed multiple integrations totalling between 1 and 2.5 hours, yielding spectra in the range $\sim 3700\text{--}6000\text{ \AA}$ with relatively high signal-to-noise ratios. This enabled us to locate multiple spectral emission features, including the strong Fe II bands in the range $4000\text{--}5400\text{ \AA}$ as well as other prominent emission lines associated with the Balmer series, helium and the [O III] nebular doublet. Our measurements include the flux, width and peak wavelength shifts of the lines, which sometimes displayed multiple components. We summarize some of the properties found for our sample, compare these to other representatives of the NLS1 class and interpret the results in the context of AGN theory.

1. Introduction

Narrow Line Seyfert 1 (NLS1) galaxies are a type of active galactic nuclei (AGN) that form a subclass of Seyfert 1 galaxies in which they exhibit unusually narrow broad emission lines compared to their broad-line counterparts and many of them also display strong optical Fe II lines in their spectra. The defining features of this subclass include that the $H\beta$ full width at half maximum (FWHM) must be less than 2000 km s^{-1} , and the flux ratio $[O\text{ III}]/H\beta$ must be smaller than 3 [1]. Though NLS1s were initially also required to have strong optical Fe II emission [2], there are quite a few AGN referred to as NLS1 that only have weak or moderate strength Fe II lines.

Emission line properties such as the width, strength and profile are affected by the system dynamics, geometry, central gravitational field, temperature of emitting clouds, excitation mechanisms, etc. The random motion and possible inflow, outflow and orbital trajectories of the gas clouds leads to line broadening due to the Doppler effect [3]. Emission line variability is a common feature in AGN, but there are suggestions that these variations are much less significant in NLS1, see for example Hu et al. [4].

In this paper, we present a preliminary analysis of the optical spectra of six little known AGN for which previous spectra suggested they might be NLS1. These sources were amongst

the brighter known or suspected NLS1 that were initially considered (but ultimately not chosen) for regular monitoring. Our measurements include emission line ratios and widths of Fe II lines and other major emission lines. We also compare the spectra with previously published ones to establish the extent of line variations and explore the significance of our findings.

2. Observation, data reduction and emission line fits

Table 1: The sample of AGN observed. Column 4 shows the angular diameter of the source taken from the NED. Column 5 shows the V magnitude of the AGN from the SIMBAD database (<https://simbad.u-strasbg.fr>). Column 7 lists the date of observation and the number of 20 minute exposures (in brackets) taken on that night.

AGN Name	RA J(2000.0)	Dec J(2000.0)	Diameter (arcsec)	V (mag)	Redshift z	Date (exposures)
EUVE J0414–59.6	04 14 19	–59 41 31	21	16.50	0.071	19 Jan 2016 (3)
Fairall 265	06 56 29	–65 33 37	45	14.55	0.030	14 Dec 2016 (7)
A0644–1	08 17 39	–07 33 09	17	16.69	0.073	19 Jan 2016 (5)
NPM1G–15.0297	09 06 48	–15 17 44	33	16.58	0.054	13 Jan 2016 (3)
CTS J03.19	10 15 56	–20 02 27	38		0.054	13 Jan 2016 (3)
HE 2116–3609	21 19 20	–35 56 25		16.64	0.092	08 Jul 2018 (5)

The AGN in this study were observed with the 1.9 m telescope at the SAAO’s Sutherland Observatory using the SpUpNIC optical spectrograph [5]. We performed between three and seven integrations of 20 minutes for each object, which were then averaged to secure better signal-to-noise ratios. The details of the targets and observations are given in Table 1.

We used grating 6 set at an angle of 12.5° to obtain a medium resolution of $\approx 1.4 \text{ \AA}$ per pixel and the spectra covering the wavelength range $\sim 3700\text{--}6000 \text{ \AA}$. Each target was placed at the centre of the slit, set to a width of 0.9 arcsec, smaller than the typical seeing, which allowed the light to be recorded from the nucleus, while minimising photons originating from the surrounding host galaxy. For wavelength calibration, we took an emission spectrum using a Cu-Ar lamp before and after each AGN spectrum. Well-known spectrophotometric standard stars were also observed for flux calibration purpose [6].

All observed data were processed and calibrated for wavelength and flux using standard packages in IRAF. This included applying Doppler corrections to shift the spectra of the redshifted AGN to the rest frame. We used the task `onedspec.continuum` in IRAF to remove the continuum flux contribution in the spectra. An Fe II template [3] was used to model the strong Fe II lines in the range $4000\text{--}5400 \text{ \AA}$ (see Figure 1). The template fits a single Gaussian function to each Fe II line and hence determines the strengths and widths of each set of Fe II lines. Other emission lines in the spectra were investigated after subtracting the fitted Fe II lines from the original spectra. Emission line profiles are the result of multiple components originating from different emission regions in AGN. The line profiles in NLS1 galaxies may be represented as a combination of Gaussian functions [3, 7, 8]. Multiple Gaussian functions were used for fitting other major emission lines in the spectra (see Figure 2, and Figure 3 and also Table 2). The area under the overall line fit was taken to be the total flux for each emission line.

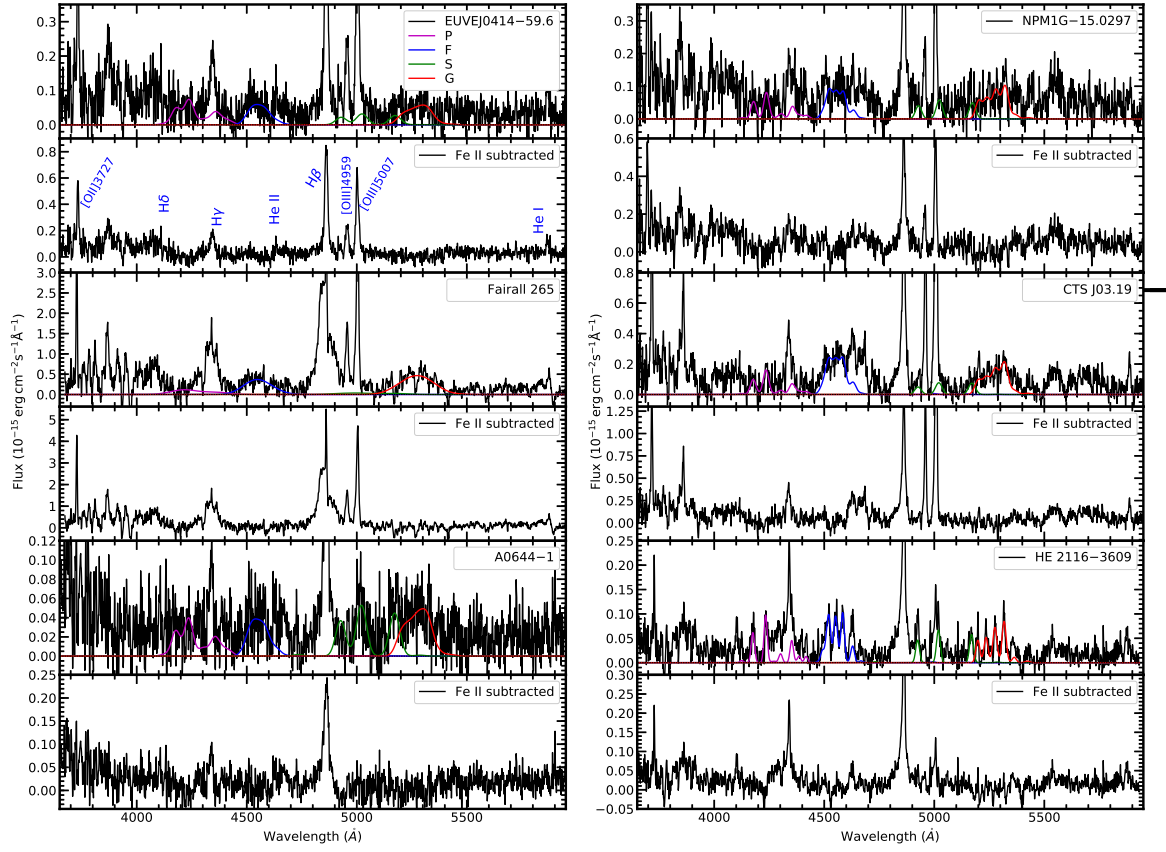


Figure 1: The FeII fitted spectra followed by the FeII subtracted spectra of the six AGN analysed in this study. The fit for different FeII bands (P, F, S and G) are highlighted in colours. The lines of interest in the spectra other than the FeII lines are marked in the second spectrum of the left plot.

3. Analysis and Discussion

Few studies have been undertaken for the objects investigated in this paper. Not all turned out to be NLS1 as expected. Fairall 265, originally discovered with the same telescope [9], is a Seyfert 1 galaxy at $z = 0.0295$ with broad Balmer lines and a $[\text{O II}]/[\text{O III}] 5007 \text{ \AA}$ ratio of 0.76 [10], while this ratio measured for the spectrum in this sample is 0.40. The broad Balmer lines measured for $\text{H}\beta$ for the spectrum in this study is 2912 km s^{-1} and this was measured to have a width of 2800 km s^{-1} [11]. This corresponds to a black hole mass of $10^{7.33} M_{\odot}$ [12]. This AGN is not considered as an NLS1 galaxy as the width of its broad Balmer line is greater than the upper limit by which the NLS1 subclass is defined, which confirms in this study as well. The line ratios relative to $[\text{O III}] 5007 \text{ \AA}$ of different emission lines in the spectra are given in Table 2. Fairall 265 has a relatively strong $[\text{O III}] 5007 \text{ \AA}$ line, but helium is almost absent. Its Balmer lines have an asymmetric profile with thin emission line peaks, which may be a sign of a superimposed H II region near the AGN.

EUVEJ0414-59.6 was identified as an X-ray emitter, and its optical spectral observation yielded a redshift of $z = 0.071$ [13]. It was incorrectly classified as a Seyfert 2 galaxy in its discovery paper, whereas its spectrum is characteristic of NLS1. Its $\text{H}\beta$ profile is asymmetric, its helium lines are weak and it displays an abnormally strong $[\text{O II}] 3727 \text{ \AA}$ line.

HE 2116-3609 has the comparatively strongest FeII lines in the sample, while its $\text{H}\beta$ line is also much stronger than $[\text{O III}]$. Its helium lines are weak and the $\text{H}\beta$ shows hints of a

broad component at its base. The $[\text{O II}] 3727 \text{ \AA}$ line is the strongest in this sample relative to $[\text{O III}] 5007 \text{ \AA}$ with a ratio of $[\text{O II}] 3727 \text{ \AA}/[\text{O III}] 5007 \text{ \AA} = 0.97$.

NPM1G–15.0297 is an NLS1 with weak Fe II lines. The FWHM was measured as 390 km s^{-1} for $[\text{O III}]$ and 1181 km s^{-1} for the $\text{H}\beta$ broad component of this object [14], while these values measured in this sample are 558 km s^{-1} and 1308 km s^{-1} respectively, consistent with the FWHM criteria defined for NLS1 galaxies. The $\text{H}\beta$ line is mostly symmetric in shape, while, unlike other AGNs in this sample, its $[\text{O III}] 5007 \text{ \AA}$ also has more of a symmetric shape.

CTS J03.19 is an NLS1 galaxy with $\text{H}\beta$ FWHM of 560 km s^{-1} and 1932 km s^{-1} for the narrow and broad components respectively, a $[\text{O III}] 5007 \text{ \AA}$ FWHM of 570 km s^{-1} [15] and a $[\text{O II}]/[\text{O III}] 5007 \text{ \AA}$ ratio of 0.163 [10]. In this sample those values for the $\text{H}\beta$ components turned out to be 538 km s^{-1} and 1890 km s^{-1} respectively, while a $[\text{O III}] 5007 \text{ \AA}$ FWHM of 520 km s^{-1} and $[\text{O II}]/[\text{O III}] 5007 \text{ \AA}$ ratio of 0.28. Its $\text{He II } 4686 \text{ \AA}$ is the strongest in the sample, and is also much broader than the $\text{H}\beta$ line. The total $[\text{O III}] 5007 \text{ \AA}$ strength is much greater than that for total $\text{H}\beta$.

A0644–1 was identified as a NLS1 by Martini et al. [16] and their spectrum displayed rich Fe II emission. In the observation reported here, the $\text{H}\beta$ profile is visible and this is the only AGN in the sample with no clear sign of $[\text{O III}]$ or other forbidden lines in the spectra, while a $\text{He II } 4686 \text{ \AA}$ line is visible. Compared to $\text{H}\beta$, almost all other emission lines in its spectra are very weak or not visible. If the apparent weakness of Fe II is not due to high noise levels in our spectrum then this would be a rare instance of a NLS1 that has experienced long term major changes in its iron line spectrum. This warrants further investigation requiring higher quality data.

It has previously been noted that NLS1 show an anti-correlation between $[\text{O III}]$ and Fe II strengths [17]. We can also confirm this from the AGN examined by us. Among the sources in the sample, HE 2116–3609 has strong Fe II lines, while $[\text{O III}]$ lines are less prominent. On the other hand, CTS J03.19 has the strongest $[\text{O III}]$ lines in the sample, but Fe II emission is relatively weak. Asymmetric profiles associated with $[\text{O III}]$ emission lines in AGN have been identified in many studies [3, 8, 18, 19]. NPM1G–15.0297 has an almost symmetric $[\text{O III}]$ shape, while for A0644–1 $[\text{O III}]$ is too weak to establish the existence and nature of any asymmetry. The $[\text{O III}]$ profiles of Fairall 265, CTS J03.19 and HE 2116–3609 have clear asymmetric blue wings. In contrast, there is asymmetry in the form of a red $[\text{O III}]$ wing in EUVE J0414–59.6. The two-component modelling of the $[\text{O III}]$ profile gives the indication of two distinct locations in the Narrow Line Region (NLR) in these AGN in which the broader asymmetric component of the $[\text{O III}]$ line could be a sign of the presence of emitting gas clouds turbulent in nature due to its location in the NLR closer to the accretion disc, and the asymmetry is caused as a result of strong wind and outflows from the accretion disc [7, 8, 19, 20, 21, 22].

NLS1 galaxies usually do not show large variations in the optical compared to many other classes of AGN, and their variability is often considered lower than that of other Seyfert 1 galaxies. To understand the scale of variability, two spectra found in the literature were compared with our spectra for NPM1G–15.0297 and CTS J03.19 (see Figure 4). We detect no significant differences in the emission lines.

4. Summary

- We confirm that five of the six AGN investigated here are indeed NLS1. This includes EUVE J0414–59.6, which had previously been misclassified as a Seyfert 2. Fairall 265 has Balmer lines that are broader than 2000 km s^{-1} and that are furthermore currently displaying asymmetric profiles. It is hence a normal Seyfert 1 rather than a NLS1.
- The asymmetric blue wing is evident in three AGN in the sample (Fairall 265, HE 2116–3609 and CTS J03.19) and is presumably a result of outflowing gas from the central nucleus. EUVE J0414–59.6 exhibits a clear red wing $[\text{O III}]$ profile, while NPM1G–15.0297 mostly

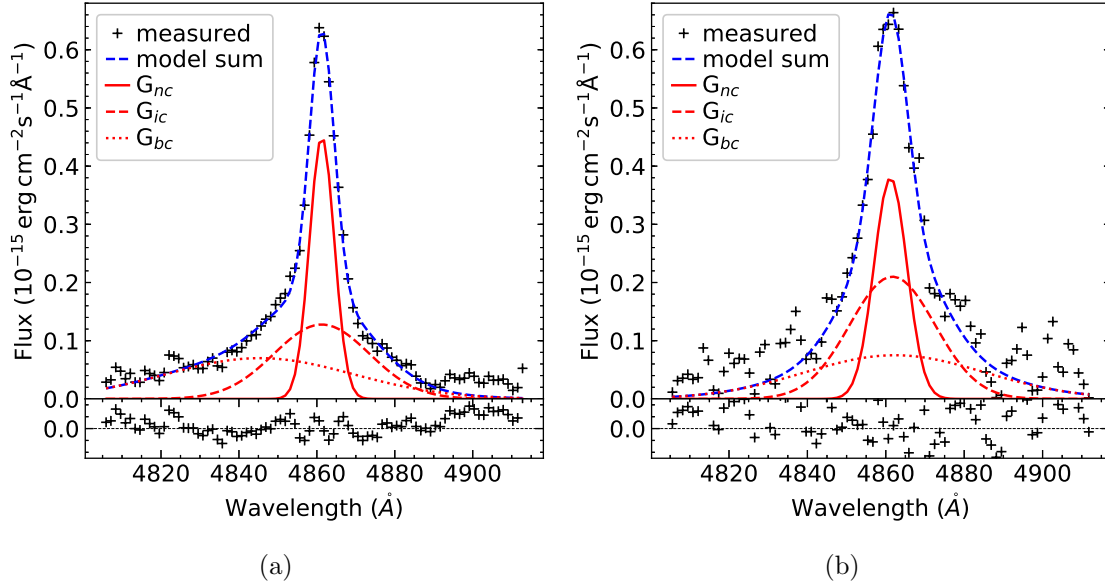


Figure 2: Examples of the $H\beta$ profile fitted as the sum of three Gaussian functions for HE 2116–3609 (a) and NPM1G–15.0297 (b) respectively. The observed data is represented using crosses. The Gaussian components, *narrow*, *intermediate* and *broad*, are shown in *solid*, *dashed* and *dotted* red lines respectively and the fitted sum is shown as *dashed* blue line. The residual of the fitted sum is shown at the bottom.

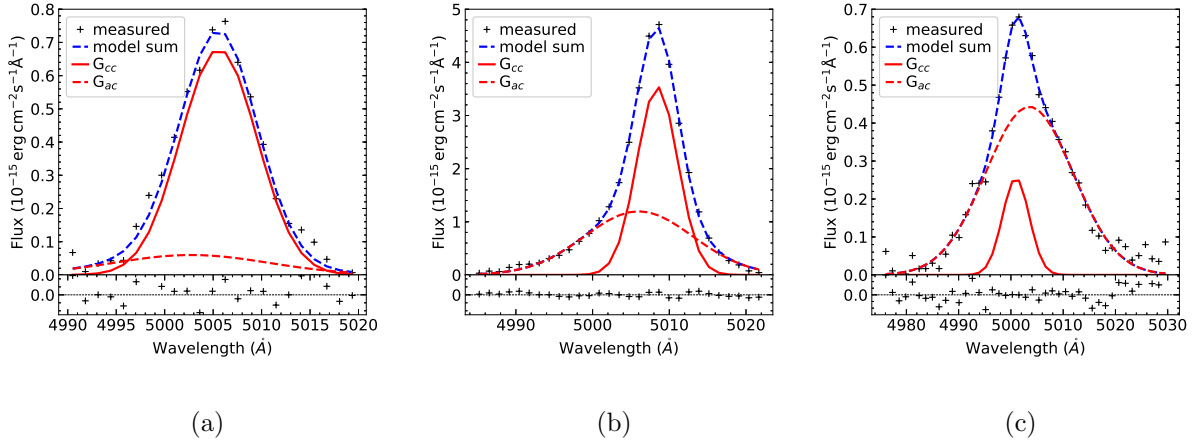


Figure 3: Different $[O\ III]\ 5007\ \text{\AA}$ profiles: A symmetric shape for NPM1G–15.0297 (a) and asymmetric blue and red wings for CTS J03.19 (b) and EUVE J0414–59.6 (c) respectively. The spectral line is fitted as a combination of two Gaussians.

shows a symmetric shape. The $[O\ III]\ 5007\ \text{\AA}$ is not evident for A0644–1.

- When comparing with older spectra from the literature, the spectra collected in this study (i.e. for NPM1G15.0297 and CTS J03.19) usually do not show much change in emission line strength or shape, in line with previous findings.

Table 2: Flux ratios relative to total [O III] 5007 Å: Columns 2 to 8: ratios of total strength for the line relative to [O III]. Column 9 is the ratio of total Fe II strength relative to [O III] in the range 4000–5400 Å. The table excludes A0644–1 and some ratios in other targets, as the lines there are either too weak to measure reliably or seem to be absent in the spectra.

AGN Name	H β	H γ	H δ	He II 4686 Å	He I 5876 Å	[O III] 4959 Å	[O II] 3727 Å	Fe II
EUVE J0414–59.6	1.73	0.34				0.32	0.53	3.69
Fairall 265	1.56	0.27			0.10	0.38	0.40	3.64
NPM1G–15.0297	1.76	0.36				0.30		5.72
CTS J03.19	0.68	0.14		0.13	0.06	0.34	0.28	2.18
HE 2116–3609	8.12	2.38	0.83				0.97	20.29

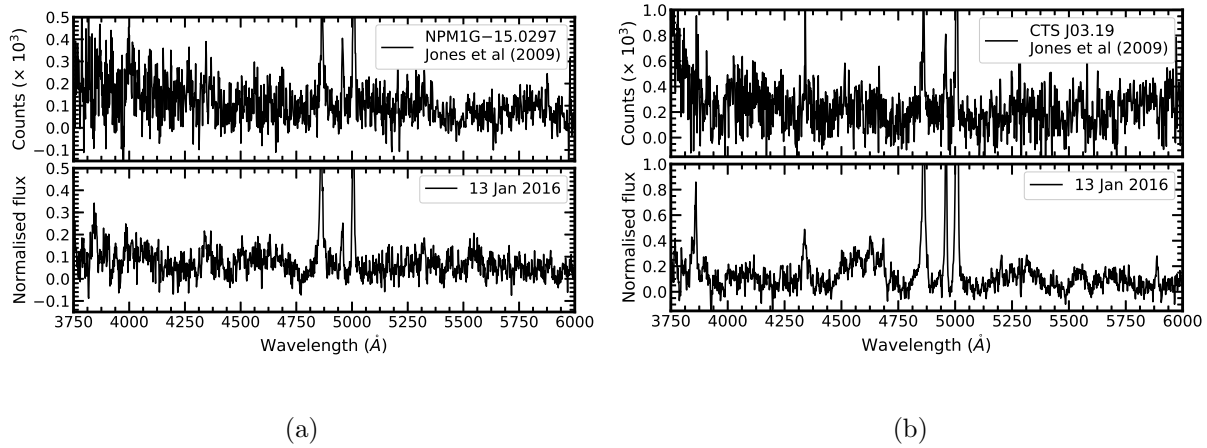


Figure 4: Comparison of continuum subtracted spectra for NPM1G–15.0297 (a) and CTS J03.19 (b) respectively with earlier spectra from the literature [23].

Acknowledgments

Byniah Paul acknowledges the receipt of a PhD bursary through the South African Astronomical Observatory from the National Research Foundation of South Africa. We thank Francois van Wyk for occasional assistance at the telescope.

References

- [1] Goodrich R W 1989 *Astrophys. J.* **342** 224–34
- [2] Osterbrock D E and Pogge R W 1985 *Astrophys. J.* **297** 166–76
- [3] Kovačević J, Popović L Č and Dimitrijević M S 2010 *Astrophys. J. Suppl.* **189** 15–36
- [4] Hu C *et al.* 2015 *Astrophys. J.* **804** 138–51
- [5] Crause L A *et al.* 2019 *J. Astron. Telesc. Instrum. Syst.* **5** 024007
- [6] Hamuy M, Suntzeff N B, Heathcote S R, Walker A R, Gigoux P and Phillips M M 1994 *Publ. Astron. Soc. Pac.* **106** 566–89
- [7] Zhang K, Dong X B, Wang T G and Gaskell C M 2011 *Astrophys. J.* **737** 71–93
- [8] Schmidt E O, Oio G A, Ferreiro D, Vega L and Weidmann W 2018 *Astron. Astrophys.* **615** A13
- [9] Fairall A P 1980 *Mon. Not. R. Astron. Soc.* **192** 389–97
- [10] Nagao T, Murayama T and Taniguchi Y 2001 *Astrophys. J.* **546** 744–58
- [11] Winkler H 1992 *Mon. Not. R. Astron. Soc.* **257** 677–88

- [12] Wang J M and Zhang E P 2007 *Astrophys. J.* **660** 1072–92
- [13] Craig N and Fruscione A 1997 *Astron. J.* **114** 1356–64
- [14] Ho L C and Kim M 2009 *Astrophys. J. Suppl.* **184** 398–415
- [15] Rodríguez-Ardila A, Binette L, Pastoriza M G and Donzelli C J 2000 *Astrophys. J.* **538** 581–93
- [16] Martini P, Kelson D D, Kim E, Mulchaey J S and Athey A A 2006 *Astrophys. J.* **644** 116–32
- [17] Boroson T A and Green R F 1992 *Astrophys. J. Suppl.* **80** 109–35
- [18] Boroson T A and Oke J B 1987 *Publ. Astron. Soc. Pac.* **99** 809–15
- [19] Véron-Cetty, M-P, Véron, P and Gonçalves, A C 2001 *Astron. Astrophys.* **372** 730–54
- [20] Bian W, Yuan Q and Zhao Y 2005 *Mon. Not. R. Astron. Soc.* **364** 187–94
- [21] Komossa S, Xu D, Zhou H, Storchi-Bergmann T and Binette L 2008 *Astrophys. J.* **680** 926–38
- [22] Cracco V, Ciroi S, Berton M, Di Mille F, Foschini L, La Mura G and Rafanelli P 2016 *Mon. Not. R. Astron. Soc.* **462** 1256–80
- [23] Jones D H *et al.* 2009 *Mon. Not. R. Astron. Soc.* **399** 683–98

SALT spectroscopy to measure the abundances of gas-rich galaxies in Fornax A

K Mosia¹ and S I Loubser¹

¹ Centre for Space Research, North West University, Potchefstroom 2520, South Africa

E-mail: Katleho.Mosia@nwu.ac.za

Abstract. The Fornax cluster is currently undergoing mass assembly. It has a lower-density group surrounding the radio galaxy NGC1316 (Fornax A) currently falling into the cluster. Infalling groups are ideal environments to study the transformation in the properties of the multi-phase gas due to e.g. tidal interactions and ram pressure stripping due to the velocity change at the boundary between the group and cluster. We have optical and H α imaging of Fornax A, and also obtained MeerKAT data, which for the first time resolved HI emission in different substructures in the subgroup, often coinciding with detections in H α . We then obtained spectroscopy of 11 gas-rich galaxies on SALT (Southern African Large Telescope). In this study, a combination of spectral fitting routines are used to accurately separate stellar continuum and absorption lines from the ionized gas emission in the observed SALT spectra, and to measure gas as well as stellar population properties. We present our latest results from the SALT spectral analysis, which will ultimately be combined with the information obtained from the various other multi-wavelength observations to fully understand the physical processes and the multi-phase gas. We illustrate our methodology by presenting results for NGC 1310 as an example. Our preliminary measurements of the gas abundances in NGC 1310 suggest that warm gas is photo-ionised by star formation.

1. Introduction

The Fornax cluster, the nearest massive cluster in the Southern sky, is actively assembling mass which makes it an ideal laboratory for studying the evolution of galaxy clusters, the physics of gas accretion and stripping of infalling galaxies, and the connection between these processes and the neutral medium in the cosmic web. Numerous observational campaigns have focused on the Fornax cluster; these include the deep optical imaging from the Fornax Deep Survey (FDS; [1]), optical integral field unit observations of selected targets [2, 3], the Atacama Large Millimeter Array (ALMA) observations of the cold molecular gas [4, 5], far-infrared Hershel imaging [6], and HI surveys with MeerKAT [7]. Studying the physical processes that drive the evolution of galaxies in galaxy clusters will help in answering questions as; how do these galaxies lose their cold gas, and why they stop accreting new gas? To answer these questions, we need optical spectroscopy to study the composition and kinematics of the warm ionised gas, in addition to the other wavelength observations. Figure 1 shows the HI velocity field from [8] where the known galaxies and previously detected clouds and tails in the Intragroup Medium (IGM) have been labeled. We can combine our SALT spectroscopy with previous studies, e.g. the study by [8] to investigate the pre-processing and HI morphology, including the gas (atomic and molecular) scaling relations in the Fornax A group. Studies from several observational campaigns will also

provide an understanding of the processes of gas accretion or removal.

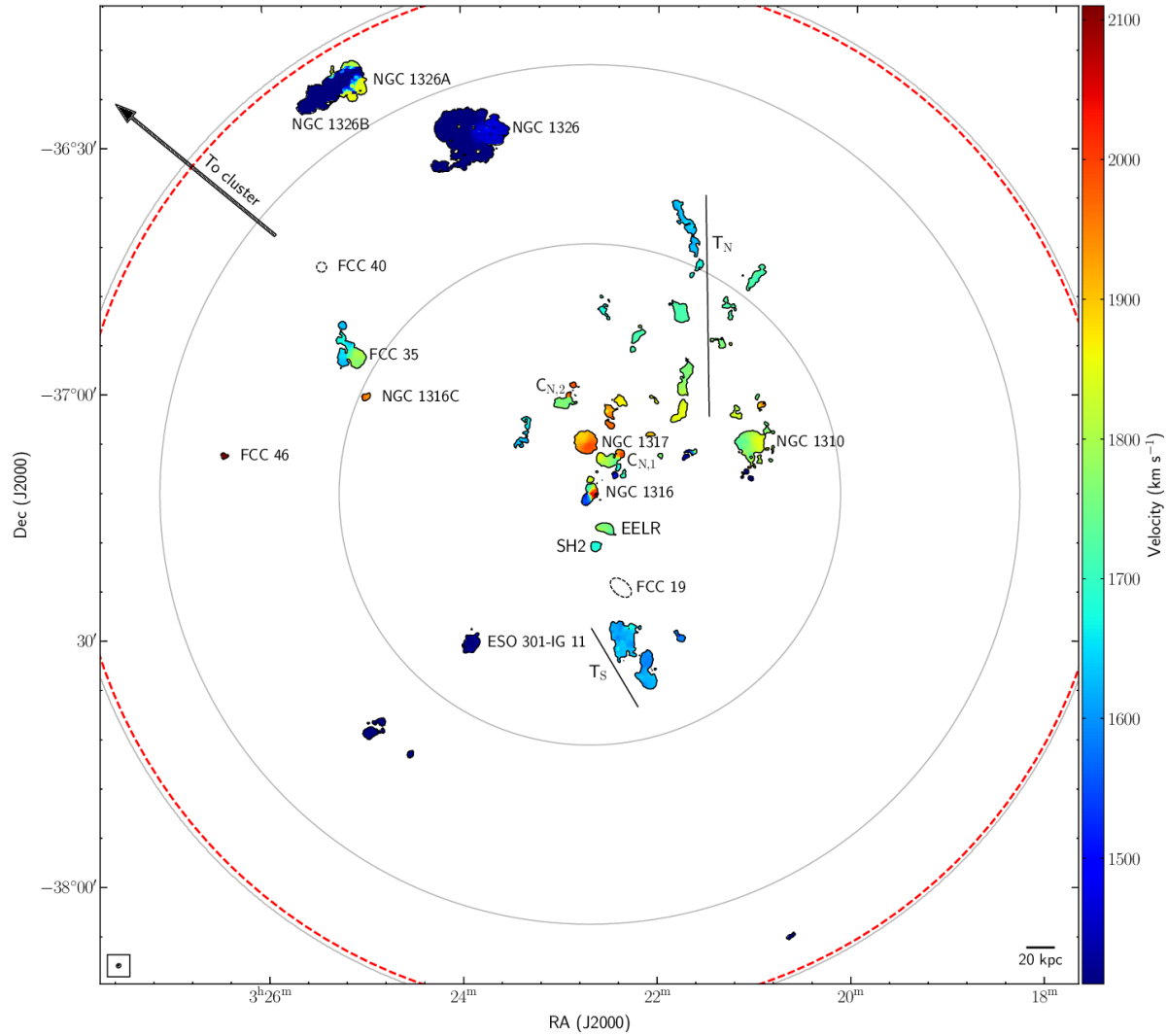


Figure 1. The HI velocity field of Fornax A from [8] showing the known galaxies and previously detected clouds and tails (T_N and T_S denotes the Northern and Southern tails respectively). The grey circles represent the sensitivity of the primary beam at 50, 20 and 2%. The red dashed circle indicates the 0.38 Mpc virial radius of the group.

2. Observations and Data Reduction

The 11 galaxies in the Fornax A group were observed with the South African Large Telescope (SALT) during November and December 2019 with more observations allocated for the remainder of 2021 (SALT Proposal ID: 2019-2-MLT-002 and 2020-2-SCI-029, PI: Ilani Loubser). To measure the strong emission lines of interest, the PG1300 grating was used at an angle of 44.5° which corresponds to a spatial scale of $0.127''$ and a spatial resolution of 0.33 \AA .

A series of reduction steps were carried out to reduce and analyze the SALT spectral data. First, a cosmic ray correction was applied to clean the images of bad pixels and cosmic rays. Interpolation was then applied to the images to mask the chip gaps. Wavelength calibration, which includes identifying emission lines in the arc lamp spectrum and taking the wavelength solution

and performing it up and down across the 2D spectrum was performed. The final 2D wavelength solution that will be applied to the actual science image was created. Figure 2 shows the 2D spectrum of NGC 1310 after interpolation and wavelength calibration. Background subtraction was done to remove skylines and any residual sky background flux followed by generating a variance image from the combined science images. Next, an extinction correction and primary aperture extraction was done and finally, flux calibration using a spectrophotometric standard star was performed to get a calibrated spectrum. All the data reduction steps were carried with the Image Reduction and Analysis Facility¹ (IRAF; [9, 10, 18] and Pyraf (a Python-based alternative to IRAF)).

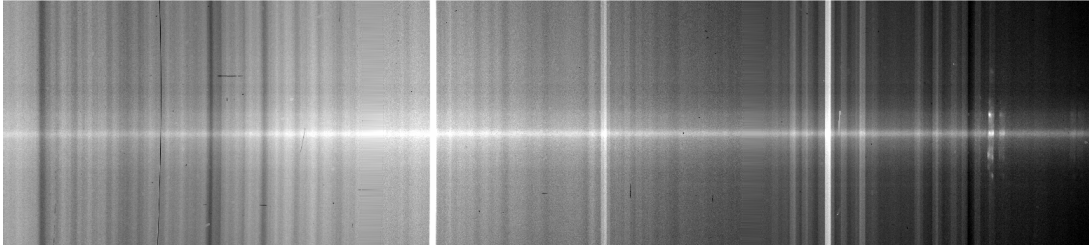


Figure 2. A 2D spectrum of NGC1310 after interpolation and wavelength calibration.

A combination of fitting routines, pPFX (Penalized Pixel-Fitting; [11, 19]) and FIREFLY [12], are used to accurately separate stellar continuum and absorption lines from the ionized gas emission in the observed SALT spectra. FIREFLY² is a fitting code that derives stellar population properties of stellar systems, be these observed galaxy or star cluster spectra or model spectra for simulations. FIREFLY uses an iterative best-fitting approach controlled by the Bayesian Information Criterion to fit combinations of single-burst star population models to spectroscopic data. There are no priors applied; instead, all solutions inside a statistical group are retained with their arbitrary weight, thus allowing one to map out the effect of intrinsic spectral energy distribution (SED) degeneracies on stellar population parameters, including age, metallicity, and dust reddening [12]. The routine was applied on the reduced spectra while changing parameters such as the Initial Mass Function (IMF; Kroupa [17] and Salpeter [13]) and models (M11 [16] and MaStar [15]). The equivalent age and metallicities, along with their uncertainties, were derived by calculating the average and standard deviation of the results.

The Python implementation of [11] freely accessible penalized Pixel Fitting (pPXF³) software, which includes the improvement described in [19], was used to derive stellar kinematics. After logarithmically rebinning the spectrum in the wavelength direction, the pPXF procedure recovers the line-of-sight velocity distribution (LOSVD) by fitting an optimized template to an observed galaxy spectrum directly in pixel space. By binning all spatial pixels within 5 arcseconds of the object's center, we first retrieved a high S/N spectrum for each galaxy. We calculated the best-fitting template spectrum, systemic velocity, and central velocity dispersion from these high S/N spectra. The higher-order Gauss-Hermite moments, h_3 and h_4 , were also fitted.

¹ More information about the pipeline and installation can be found on <https://iraf-community.github.io/>.

² The code can be found from the dedicated Github repository https://github.com/FireflySpectra/firefly_release.

³ See <https://www-astro.physics.ox.ac.uk/~mxc/software/> for a full guide on installation and usage examples.

3. Results and Discussion

In this section, we present the preliminary results obtained from FIREFLY and pPXF for NGC 1310. Figure 3 represents the 1D spectrum of this galaxy where the Salpeter Initial Mass Function (IMF; [13]) was utilized. The black spectrum represents the model that best fit the data (as determined from minimising the χ^2 residuals), which in this case was the STELIB model [14].

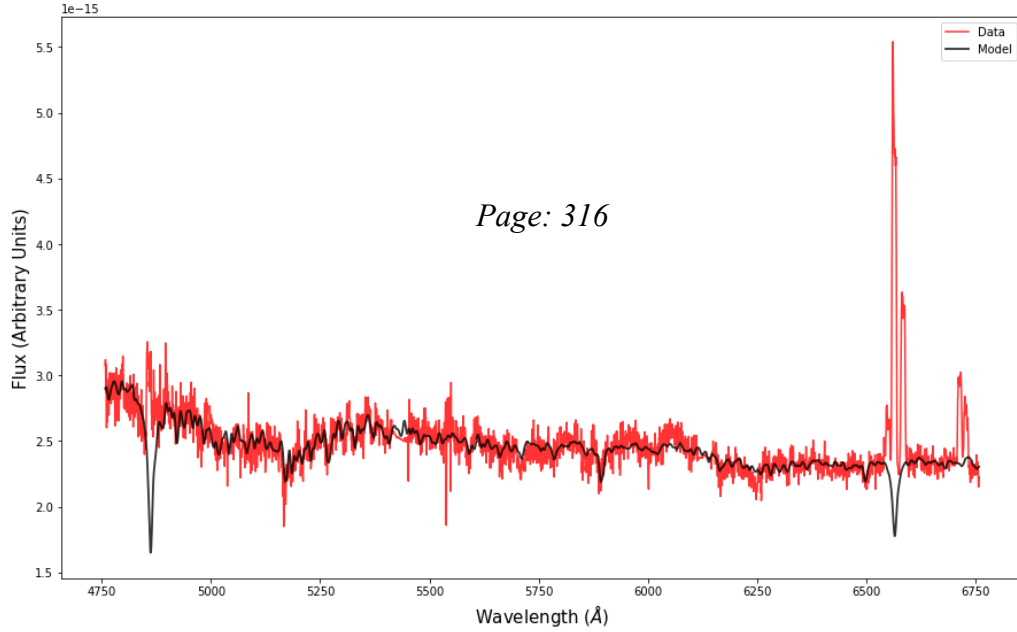


Figure 3. A 1D spectrum of NGC 1310 from FIREFLY for the extraction of star formation histories. The red spectrum represents the data with the black representing the fitted model which in this case is the STELIB model with the Salpeter IMF.

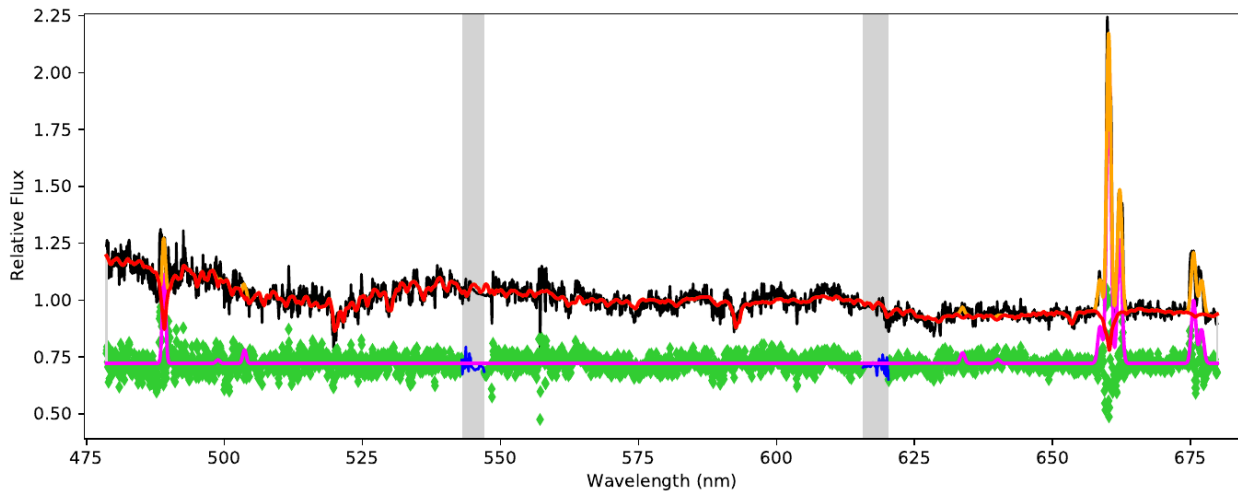


Figure 4. A 1D spectrum of NGC 1310 from pPXF where the grey regions indicate the masked chip gaps. The emission line ratios, e.g. $H\alpha/[NII]$ is indicative of photo-ionisation by star formation.

Figure 4 also shows a 1D spectrum from pPXF where the H α , [NII] and [SII] emission lines are clearly visible $> 6500 \text{ \AA}$. The grey regions indicate the masked chip gaps and black line is the relative flux of the observed spectrum. The red line is the pPXF fit for the stellar component, while the orange line is a fit to the gas emission lines. The green symbols at the bottom are the fit residuals, while the blue lines is the gas-only best-fitting spectrum.

The FIREFLY routine automatically fits multiple stellar populations (e.g. including a young stellar component in cases where the galaxy experienced a recent star formation episode). From the fitted model, we find that the galaxy has an approximate Single Stellar Population (SSP) equivalent age of $2.86 \pm 0.55 \text{ Gyr}$, and a metallicity $([Z/H]) = -0.07 \pm 0.03 \text{ dex}$. Since the dominant errors in stellar population analysis for high S/N spectra are systematic errors which stem from different stellar population model ingredients, we are currently repeating the analysis with various different stellar population models, e.g. MaStar [15] and M11 [16], for both a Kroupa [17] and a Salpeter IMF. This will allow us to determine the combination of stellar libraries and population models that are most consistent for this type of galaxy, and also allow us to quantify the systematic errors caused by using different stellar population models. This will consequently allow us to discard models that produce bad fits and inconsistent results. Once the FIREFLY analysis is complete, we will proceed to extract the stellar and gas kinematics from pPXF which will give us a clear picture of the star formation rates, kinematics and formation histories of the galaxies in our sample.

4. Conclusion

In this project we have displayed the techniques used in reducing SALT spectral data and explored the fitting routines applied to extract stellar properties of the observed galaxies. Our preliminary measurements of the gas abundances in NGC 1310 suggest that warm gas is photo-ionised by star formation.

5. Acknowledgements

KM and SIL acknowledges funding through the National Astrophysics and Space Science Program (NASSP) on behalf of the National Research Foundation (NRF) scholarship (Grant number 134202).

References

- [1] Iodice E, Capaccioli M, Grado A, Limatola L, Spavone M, Napolitano N R, Paolillo M, Peletier R, Cantiello M, Lisker T *et al.* 2016 The Fornax Deep Survey with VST. I. The Extended and Diffuse Stellar Halo of NGC 1399 out to 192 kpc *ApJ* **820**, 42
- [2] Mentz J, La Barbera F, Peletier R, Falc3n-Barroso J, Lisker T, van de Ven G, Loubser S, Hilker M, S3nchez-Janssen R, Napolitano N *et al.* 2016 Abundance ratios and IMF slopes in the dwarf elliptical galaxy NGC 1396 with MUSE *MNRAS* **463**, 2819-2838
- [3] Sarzi M, Iodice E, Coccato L, Corsini E, de Zeeuw P, Falc3n-Barroso J, Gadotti D, Lyubenova M, McDermid R, van de Ven G *et al.* 2018 Fornax3D project: Overall goals, galaxy sample, MUSE data analysis, and initial results *A&A* **616**, A121
- [4] Zabel N, Davis T A, Smith M W, Maddox N, Bendo G J, Peletier R, Iodice E, Venhola A, Baes M, Davies J I *et al.* 2019 The ALMA Fornax Cluster Survey I: stirring and stripping of the molecular gas in cluster galaxies *MNRAS* **483**, 2251-2268
- [5] Hatsukade B, Tominaga N, Hayashi M, Konishi M, Matsuda Y, Morokuma T, Morokuma-Matsui K, Motogi K, Niinuma K and Tamura Y 2018 Obscured star formation in the host galaxies of superluminous supernovae *ApJ* **857**, 72
- [6] Davies J, Bianchi S, Baes M, Boselli A, Ciesla L, Clemens M, Davis T, De Looze I, Alighieri S d S, Fuller C *et al.* 2013 The Herschel Fornax Cluster Survey–I. The bright galaxy sample *MNRAS* **428**, 834–844
- [7] Serra P, De Blok W, Bryan G, Colafrancesco S, Dettmar R J, Frank B, Govoni F, J3zsa G, Kraan-Korteweg R, Loubser S *et al.* 2017 The MeerKAT Fornax Survey *arXiv preprint arXiv:1709.01289*
- [8] Kleiner D, Serra P, Maccagni F, Venhola A, Morokuma-Matsui K, Peletier R, Iodice E, Raj M, de Blok W, Comrie A *et al.* 2021 A MeerKAT view of pre-processing in the Fornax A group *A&A* **648**, A32

- [9] Tody D 1986 The IRAF Data Reduction and Analysis System Instrumentation in Astronomy VI *SPIE* **627**, 733–748
- [10] Tody D, Hanisch R, Brissenden R and Barnes J 1993 Astronomical data analysis software and systems II, *ASP Conf. Ser.* **52**
- [11] Cappellari M and Emsellem E 2004 Parametric recovery of line-of-sight velocity distributions from absorption-line spectra of galaxies via penalized likelihood *PASP* **116**, 138
- [12] Wilkinson D M, Maraston C, Goddard D, Thomas D and Parikh T 2017 FIREFLY (Fitting Iteratively For Likelihood analysis): A Full Spectral Fitting Code *MNRAS* **472**, 4297–4326
- [13] Salpeter E E 1955 The luminosity function and stellar evolution *ApJ* **121**, 161
- [14] Le Borgne J F, Bruzual G, Pelló R, Lançon A, Rocca-Volmerange B, Sanahuja B, Schaerer D, Soubiran C and Vélchez-Gómez, R R 2003 STELIB: A library of stellar spectra at $R \sim 2000 \text{ Å}$ *A&A* **402**, 433–442
- [15] Yan R, Chen Y, Lazarz D, Bizyaev D, Maraston C, Stringfellow G S, McCarthy K, Meneses-Goytia S, Law D R, Thomas D *et al.* 2019 SDSS-IV MaStar: A Large and Comprehensive Empirical Stellar Spectral Library—First Release *ApJ* **883**, 175
- [16] Maraston C and Strömbäck G 2011 Stellar population models at high spectral resolution *MNRAS* **418**, 2785–2811
- [17] Kroupa P 2001 On the variation of the initial mass function *MNRAS* **322**, 231–246
- [18] Iraf.net. 2021. iraf.net - User Support and IRAF Software. [Accessed 3 June 2021]
- [19] Cappellari M 2017 Improving the full spectrum fitting method: Accurate convolution with Gauss–Hermite functions *MNRAS* **466** 798–811

Spatio-kinematics of the massive star forming region NGC6334I during an episodic accretion event

*J M Vorster¹, J O Chibueze^{1,2}, T Hirota^{3,4}

¹Centre for Space Research, Potchefstroom campus, North-West University, Potchefstroom 2531, South Africa

²Department of Physics and Astronomy, Faculty of Physical Sciences, University of Nigeria, Carver Building, 1 University Road, Nsukka 410001, Nigeria

³National Astronomical Observatory of Japan, National Institutes of Natural Sciences, 2-21-1 Osawa, Mitaka, Tokyo 181-8588, Japan.

⁴Department of Astronomical Sciences, SOKENDAI (The Graduate University for Advanced Studies), Osawa 2-21-1, Mitaka-shi, Tokyo 181-8588, Japan

E-mail: 28570057@nwu.ac.za

Abstract. Episodic accretion in massive protostars is an exciting and upcoming field of study. In this paper we report multi-epoch very long baseline interferometry (VLBI) observations of 22 GHz water masers before and during the recent accretion burst in NGC6334I. We traced proper motions before and during the accretion burst, showing significant variability in the water maser flux densities and number of detections due to the variable radiation field from the bursting high mass young stellar object. We calculated an average proper motion of $82 \pm 38 \text{ km s}^{-1}$ before and $85 \pm 36 \text{ km s}^{-1}$ during the accretion burst. The average proper motions were not expected to change as the dynamical timescale of the system is of the order of decades. On the other hand, we did see significant variability in the number and position of proper motions in CM2, MM1-W1, UCHII-W1, UCHII-W2 and UCHII-W3. In CM2, the water masers flared, as seen in previous studies, and new maser features were excited. In MM1-W1 and UCHII-W1, pre-burst maser features dropped below detection limits during the burst and new features were re-excited $\sim 10 \text{ AU}$ from previous detections. The simultaneous flaring and dampening of water masers due to an increase in infrared flux has not been adequately discussed in maser modelling, and we discuss possible explanations for this phenomenon. The VERA observations continue the campaign to understand this important accretion bursting source.

1. Introduction

Massive ($M > 8M_{\odot}$) stars play an important role in galactic evolution. They are an important source of heavy elements and feedback due to the type II supernovae they cause at the end of their lifetimes [1]. They have also contributed greatly to the ionization in galaxies on different scales [2] and cosmic times [3]. Yet, their early stages are difficult to observe due to their short lifetimes and their formation in embedded clusters with high dust extinction [4]. Radio interferometric arrays, combined with Very Long Baseline Interferometry (VLBI) and long term single dish monitoring have played a pivotal role in studying star forming regions at different angular scales, wavelengths and time scales [5]. The study of NGC6334I is a prime example of this multi-instrument approach. At a distance of 1.3 kpc [6], the region harbours multiple possible protostars in the millimetre peaks MM1-MM9 detected by the Atacama Large

Millimetre/Submillimetre Array (ALMA) [7]. NGC6334I-MM1 harbours multiple outflows, a ~ 0.5 pc NE-SW jet [8], a N-S jet and the blueshifted half of a NW outflow has been detected [5]. These jets indicated at least three previous ejection events. An important discovery was the observation and confirmation of an accretion burst in this region [9]. Simulations have shown that high mass young stellar objects (HMYSOs) gain significant portions of their mass in episodic periods of high accretion due to the infalling of fragments from the protostellar disc [10]. As the HMYSO absorbs the fragment, its natal region heats up significantly. Observationally, an accretion burst is most clearly shown by the significant increase in the region's dust temperature. Due to the dust temperature increase, various maser species and chemical line emission may flare significantly [11]. It was found that NGC6334I-MM1 had a luminosity increase of a factor of 16.3 ± 4.4 [12]. Significant flaring in the 6.7 GHz methanol masers, and the 22 GHz water masers was also found co-temporal with the dust temperature increase [10]. Interferometric observations with the Karl Jansky Very Large Array (JVLA) of 22 GHz water masers showed interesting behaviour, close to the accreting HMYSO (MM1B) the water masers were dampened close to the HMYSO, but had an order of magnitude flare in a region ~ 3000 AU from the source, CM2 [5]. High resolution multi-epoch VLBI observations using KaVA, a collaboration between the Korean VLBI network (KVN) and the Japanese VLBI Exploration of Radio Astrometry (VERA) of 22 GHz water masers relative proper motions measured an average proper motion of 86 km s^{-1} , tracing a major outflow with a position angle of -79.4° [13]. This measurement of another NW-SE jet, separate from the N-S jet, shows that the HMYSO/HMYSOs driving the jets in MM1 have had multiple previous accretion bursts leading to ejection events. As there have only been few observations of accretion bursts, the effects of the burst on the natal environment on the HMYSO is still poorly understood. In this paper we present preliminary results of multi-epoch 22 GHz water maser observations with VERA, as a continuation of a multi-epoch and multi-instrument campaign to probe the region. This data set is unique in that it traces water maser proper motions before and during the burst.

2. Observations and data reduction

We used the 4-antenna VERA array to undertake 7 epochs of observation of the 22 GHz water masers associated with NGC6334I. The pointing centre was $(\alpha, \delta) = (17^h 20^m 53.377^s, -35^\circ 46' 55.808'')$ in the J2000.0 epoch. The data reduction procedure and proper motion calculations were similar to the procedure described in [13]. To be able to compare the proper motions before and during the burst, we split the seven epochs into pre-burst epochs (4 epochs 2014.72-2015.28) and burst epochs (3 epochs 2015.88-2016.19). We then traced the proper motions for the pre-burst and burst epochs respectively. Individual maser detections (2D Gaussian fits in an individual channel), which we call “maser spots”, were averaged into “maser features”. Maser features are regions assumed to be moving together due to similar motion and to be in the same channel with equal V_{LSR} . The positions in (α, δ) of the maser features over time were fit linearly to time to calculate the proper motion $(\mu_x, \mu_y) = (\Delta\alpha \cos \delta, \Delta\delta)$ mas yr $^{-1}$. We performed self-calibration on the maser maps by choosing the brightest feature in UCHII-W1 as a reference maser. We did not perform phase referencing to obtain absolute position information on this feature, so our water maser positions are relative to the position of the reference maser. The same reference maser was used in all epochs. As the proper motions are relative in the reference maser's velocity frame, they can, therefore be shifted by adding a constant vector $\vec{\mu}_R$, the proper motion of the reference maser. To be able to compare the proper motions with previous KaVA results, we shifted the VERA proper motions by a constant velocity vector $\vec{\mu}_R = (-1.94 \pm 0.3, 17.3 \pm 0.4) \text{ mas yr}^{-1}$ and position $\vec{P}_R = (-0.68921, 5.28800) \text{ arcsec}$. This shift was calculated by calculating the vector so that the proper motion and position of the VERA reference maser corresponds to the proper motion and position of the same maser region in the KaVA observation (ID: 70-73 of Table 1 of [13]). The uncertainty in the proper motion of

Table 1: General characteristics of water maser proper motions detected by VERA before and during the burst. Columns 2, 3 and 4 are the number of detections, average transverse velocity (in km s^{-1}) and the error of the velocity (in km s^{-1}) before the burst (4 epochs, 2014.72-2015.28). Columns 5, 6 and 7 are the same quantities for the water maser proper motions during the burst (3 epochs, 2015.88-2016.19).

Region	#Detections	\bar{v}	$\delta\bar{v}$	#Detections	\bar{v}	$\delta\bar{v}$
All	125	82	38	102	85	36
CM2	49	112	26	55	111	23
MM1-W1	14	95	24	7	81	22
UCHII-W1	44	48	24	20	48	20
UCHII-W2	10	52	9	13	39	6
UCHII-W3	4	97	29	7	74	4

the VERA reference maser is known as it was previously derived in the KaVA observations and was taken into account. The error on the KaVA reference maser induces an error $< 10\%$ in our VERA proper motions in the KaVA velocity/position frame. This shift gives us good ground to compare the proper motions measured using the two instruments, noting that VERA has worse angular resolution and sensitivity.

3. Results

Table 1 shows the most general results for the water maser proper motions. The average proper motions stayed the same before and during the burst although the number of detections dropped by 19.4%. Figure 1 shows the proper motion positions, orientations and magnitudes. CM2 showed little variation in the number of detections and average proper motions but new maser features were excited in CM2 during the burst on both edges of the bow shape. MM1-W1 had northerly point proper motions both before and during the burst. The number of detections halved, and the average proper motion dropped by 10%. Notably, all the water masers detected pre-burst dropped below detection limits in the burst epochs and new masers were detected in a region 12 AU to the north-east. UCHII-W1 had almost half of the detections, although the average proper motion was completely unchanged. The region has a group of maser detections which also dropped below detection limits before the burst and new detections were made 12 AU to the north-east, similar to MM1-W1. UCHII-W2 had 3 more detections (from 10) and had a reduced average proper motion, although the orientations and magnitudes of the proper motions stayed relatively constant before and during the burst. UCHII-W3 had 3 more detections (from 4), and a reduction of 24% in average proper motion, with a notable decrease in the error on the mean from $\delta\bar{v} = 29 \rightarrow 4 \text{ km s}^{-1}$. The maser features detected before the burst in UCHII-W3 were not detected during the burst, and two new features were excited during the burst ~ 100 AU to the east.

4. Discussion

4.1. VERA and KaVA proper motions

The water maser proper motions traced with VERA can be compared with water maser proper motions observed with KaVA [13]. The VERA observations, although less sensitive and with lower angular resolution, covers a longer time. We also detected some proper motions not detected by KaVA. UCHII-W2 and some features in UCHII-W1 were not detected by KaVA. The VERA results further confirm the KaVA results. The proper motions calculated in CM2 align very well. The following discrepancies should be noted: With the VERA observations, we detected quite clear upward motion with $\bar{v} \sim 90 \text{ km s}^{-1}$ in MM1-W1, while in the KaVA observations we detected complicated motions with $\bar{v} \sim 43 \text{ km s}^{-1}$. In UCHII-W1 the average

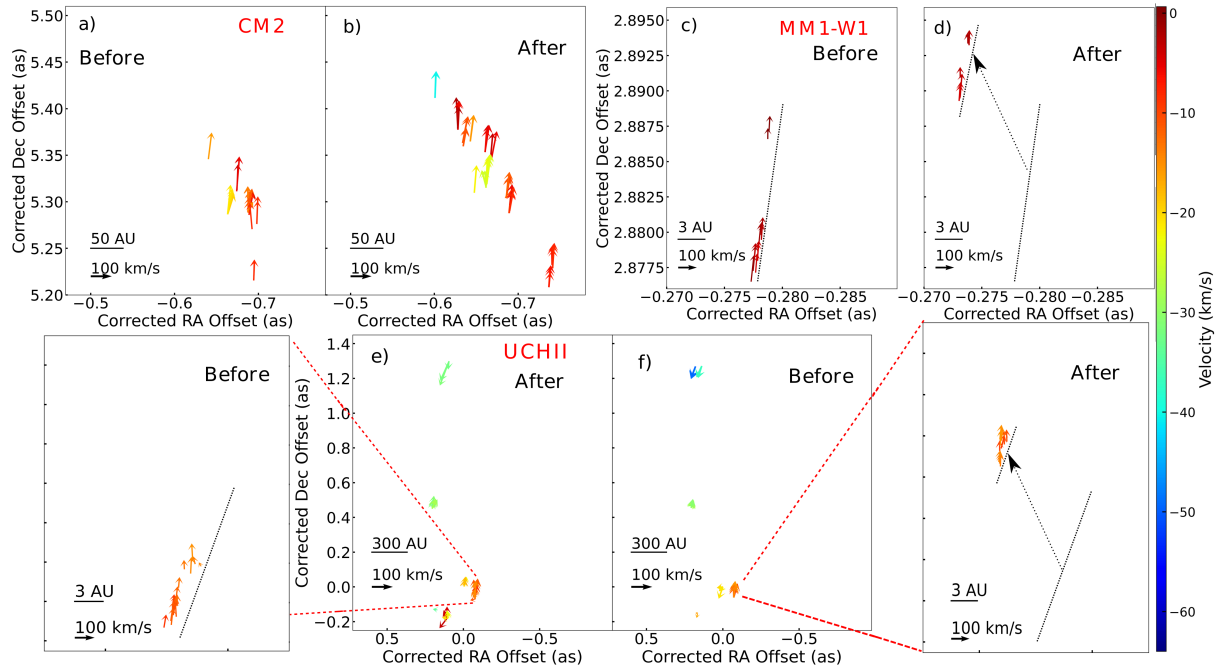


Figure 1. The panels on the left (a,c,e) are the pre-burst proper motions and the panels on the right (b,d,f) are the proper motions during the burst. The name of each region is written in red using the same naming convention of [13]. Panels e and f also contain zoom-ins of a region in UCHII-W1, note the different distance scales of the different regions. For clarity, the panels before and after the peak of the accretion burst were labelled “before” and “after”. The positions and orientation of the arrows indicate the positions and orientations of the proper motions. The colour scale indicate the radial velocity. On the bottom left of each plot is the linear distance scale, and the linear velocity scale for the arrows.

proper motion differs by 16 km s^{-1} during the burst between VERA and KaVA. In both regions the water maser spatial distribution was very complicated, and errors in the calculation in the maser features might be the cause of the discrepancy. Note that due to the three additional short baselines in KaVA, it has significant improvements in sensitivity over VERA. VERA detected significantly less proper motions during the burst in both regions than KaVA, and the high velocity northward motions in MM1-W1 is visible in Figure 5 of [13], although proper motions derived from fainter spots point in other directions, changing the average. In UCHII-W1 the same can be noted. In summary: The differences are due to selection effects due to the sensitivity and angular resolution differences in the instruments.

4.2. Insights into water maser variability

22 GHz water masers are famously variable [14], and this causes a lot of difficulty in the interpretation of their proper motions. Observationally, there is no difference between a newly excited maser spot with the disappearance of another spot, and a real proper motion. If water masers in a region are variable in a timescale of multi-epoch observations, discerning real proper motions from re-excitations is a difficult task. It is therefore imperative to constrain water maser variability to reduce false detections in water maser proper motions. In the case of NGC6334I, we have an excellent testing ground to refine water maser interpretations. The accretion burst did not cause changes in gas kinematics of most of the water maser regions (for a fast jet of 400 km s^{-1} , it would take decades for the material from the burst to reach most regions we observe).

Therefore, the abrupt differences in the spatial distribution of the water masers must be due to *radiative* changes in the maser environment. In NGC6334I, both *dampening* and *amplification* of water masers has been seen [15]. Dampening of water masers due to increases in the external radiation has been seen by [5], and we see the anti-correlation with radiation in the destruction of the water maser regions MM1-W1 and UCHII-W1. This can be explained by a heat wave that caused unfavourable masing conditions as was already seen in this region by [5]. On the other hand, *amplification* of water masers due to an increase in external radiation has not been adequately explained. 22 GHz water masers are seen as collisionally pumped, as they typically form in environments with high kinetic temperatures such as shock fronts or turbulent regions. This is contrary to 6.7 GHz methanol masers, which are radiatively pumped. Co-spatial water and methanol masers have been found to be anti-correlated [16]. In NGC6334I it is not clear if this was the case. CM2 brightened significantly [5] due to an increase in external radiation associated to the accretion burst. This observation stands contrary to the “collisionally pumped” paradigm. Two realistic alternatives to explain this phenomenon have recently come to the fore. One explanation is an unpublished possible “radiatively pumped” 22 GHz water maser that occurs at high densities and low kinetic temperature (Gray M., 2021, private communication). This can be tested by seeing if there are co-spatial correlated 6.7 GHz methanol and 22 GHz water masers. There are 6.7 GHz methanol masers in CM2 [9]. Figure 9 of [15] shows a time series of 22 GHz water, 6.7 GHz methanol and other maser species close to the systemic velocity of the source (-7.6 km s^{-1}). They found a clear correlation between the 6.7 GHz methanol and water maser fluxes. From VLA K band observations of [5] it is known that CM2 is by far the brightest source of 22 GHz water masers at that velocity. [17] imaged the 6.7 GHz methanol masers with VLA, and showed that the brightest methanol masers at that velocity are not in CM2, but about 1200 AU north from the probable source of the accretion burst MM1B. There are faint 6.7 GHz methanol masers in CM2. VLA K and C band observations from 2019 (Project ID: 19A-256) can be used to test the radiatively pumped water maser hypothesis by comparing the water and methanol maser maps to 2017 observations. This data is publicly available at the time of writing. The 2019 6.7 GHz CH_3OH results are planned to be presented early in 2022 (Hunter T., private communication), while the 2019 K band data is still being processed. The second hypothesis is that the water masers stay “collisionally pumped”, but that the simple correlation/anti-correlation to radiation for 22 GHz water masers is a simplification. Modelling of formaldehyde masers show a complex relationship between maser gain and the radiation field, where the maser gain in a certain part of parameter space (density and kinetic temperature) is dampened by external radiation, while other parts of parameter space seems to be undergoing a flare. This means that an observer might observe a flare of one maser spot and a dampening of another in the same radiation field if the spots are in regions of different kinetic temperatures and densities (van der Walt J., 2021, private communication). This hypothesis can be tested by more detailed modelling of water masers using variable background radiation. A consequence of this hypothesis is that the temporal variation in water masers might be used to constrain the time dependence of densities, kinetic temperatures and radiation fields.

5. Conclusion

We have reported high-resolution water maser proper motions in the accretion bursting source NGC6334I before and during the burst. We detected proper motions in CM2, MM1-W1 and the southern UCHII region. We found proper motions consistent with previous studies, and have found destruction and re-excitation of two water maser regions: MM1-W1 and UCHII-W1. We have also discussed possible ways to test new insights into water maser pumping models. Future studies with JVLA water maser maps could test these models. Accretion bursts in massive protostars are showing to be interesting phenomena in themselves, and also helpful test beds for other physical phenomena.

Acknowledgements

JMV acknowledges the National Research Foundation of South Africa for funding this research (Grant Number: 134192). JOC acknowledges support from the Italian Ministry of Foreign Affairs and International Cooperation (MAECI Grant Number ZA18GR02) and the South African Department of Science and Technology's National Research Foundation (DST-NRF Grant Number 113121) as part of the ISARP RADIOSKY2020 Joint Research Scheme. T. Hirota is financially supported by the MEXT/JSPS KAKENHI Grant Number 17K05398. This research made use of NASA's Astrophysics Data System Bibliographic Services. VERA is operated by Mizusawa VLBI Observatory, a branch of the National Astronomical Observatory of Japan.

References

- [1] Tsujimoto T, Nomoto K, Yoshii Y, Hashimoto M, Yanagida S and Thielemann FK 1995 Relative frequencies of type Ia and type II supernovae in the chemical evolution of the galaxy, LMC and SMC, *MNRAS* **277** 945–58
- [2] Dale JE, Ercolano B and Bonnell IA 2012 Ionizing feedback from massive stars in massive clusters - II. Disruption of bound clusters by photoionization, *MNRAS* **424** 377–92
- [3] Haehnelt MG, Madau P, Kudritzki R and Haardt F 2001 An Ionizing ultraviolet background dominated by massive stars, *ApJ* **549** L151–4
- [4] Zinnecker H and Yorke HW 2007 Toward understanding massive star formation, *ARAA* **45** 481–563
- [5] Brogan CL, Hunter TR, Cyganowski CJ, Chibueze JO, Friesen RK, Hirota T, MacLeod GC, McGuire BA and Sobolev AM 2018 The extraordinary outburst in the massive protostellar system NGC 6334I-MM1: flaring of the water masers in a north-south bipolar outflow driven by MM1B, *ApJ* **866** 87–102
- [6] Chibueze JO, Omodaka T, Handa T, Imai H, Kurayama T, Nagayama T, Sunada K, Nakano M, Hirota T and Honma M 2014 Astrometry and spatio-kinematics of H₂O masers in the massive star-forming region NGC 6334I(North) with VERA, *ApJ* **784** 114–22
- [7] Brogan CL, Hunter TR, Cyganowski CJ, Chandler CJ, Friesen R and Indebetouw R 2016 The massive protostellar cluster NGC 6334I at 220 au resolution: discovery of further multiplicity, diversity, and a hot multi-core, *ApJ* **832** 187–205
- [8] Qiu K, Wyrowski F, Menten KM, Gusten R, Leurini and, Leinz C 2011 APEX CO (9-8) Mapping of an extremely high velocity and jet-like Outflow in a high-mass star-forming region, *ApJ* **743** L25–30
- [9] Hunter TR, Brogan CL, MacLeod G, Cyganowski CJ, Chandler CJ, Chibueze JO, Friesen R, Indebetouw R, Thesner C and Young KH 2017 An extraordinary outburst in the massive protostellar system NGC6334I-MM1: quadrupling of the millimeter continuum, *ApJ* **837** L29–35
- [10] Meyer DMA, Vorobyov EI, Kuiper R and Kley W 2017 On the existence of accretion-driven bursts in massive star formation, *MNRAS* **464** L90–4
- [11] Caratti o Garatti A, Stecklum B, Garcia Lopez R, Eisloffel J, Ray TP, Sanna A, Cesaroni R, Walmsley CM, Oudmaijer RD, de Wit WJ, Moscadelli L, Greiner J, Krabbe A, Fischer C, Klein A and Ibáñez JM 2017 Disk-mediated accretion burst in a high-mass young stellar object, *Nature Physics* **13** 276–9
- [12] Hunter TR, Brogan CL, De Buizer JM, Towner APM, Dowell CD, MacLeod GC, Stecklum B, Cyganowski CJ, El-Abd SJ and McGuire BA 2021 The extraordinary outburst in the massive protostellar system NGC 6334 I-MM1: strong increase in mid-infrared continuum emission, *ApJ* **912** L17–25
- [13] Chibueze JO, MacLeod GC, Vorster JM, Hirota T, Brogan CL, Hunter TR and van Rooyen R 2021 The extraordinary outburst in the massive protostellar system NGC 6334 I-MM1: spatiokinematics of water masers during a contemporaneous flare event, *ApJ* **908** 175–84
- [14] Felli M, Brand J, Cesaroni R, Codella C, Comoretto G, Di Franco S, Massi F, Moscadelli L, Nesti R, Olmi L, Palagi F, Panella D and Valdetaro R 2007 Water maser variability over 20 years in a large sample of star-forming regions: the complete database, *A&A* **476** 373–664
- [15] MacLeod GC, Smits DP, Goedhart S, Hunter TR, Brogan CL, Chibueze JO, van den Heever SP, Banda PJ and Paulsen JD 2018 A masing event in NGC6334I: contemporaneous flaring of hydroxyl, methanol, and water masers, *MNRAS* **478** 1077–92
- [16] Szymczak M, Olech M, Wolak P, Bartkiewicz A and Gawronski M 2016 Discovery of periodic and alternating flares of the methanol and water masers in G107.298+5.639, *MNRAS* **459** L56–60
- [17] Hunter TR, Brogan CL, MacLeod GC, Cyganowski CJ, Chibueze JO, Friesen R, Hirota T, Smits DP, Chandler CJ and Indebetouw R 2018 The extraordinary outburst in the massive protostellar system NGC 6334I-MM1: emergence of strong 6.7 GHz methanol masers, *ApJ* **854** 170–86

Optical spectropolarimetry monitoring of flaring blazars

J Barnard¹, B van Soelen¹, J Cooper¹, R J Britto¹, J P Marais¹, I P van der Westhuizen¹, D A H Buckley^{1,2}, H M Schutte³, M Böttcher³, B Vaidya⁴, S Acharya⁴ and A Martin-Carrillo⁵

¹Department of Physics, University of the Free State, Bloemfontein, 9300, South Africa

²South African Astronomical Observatory, PO Box 9, Observatory, Cape Town, 7935, South Africa

³Centre for Space Research, North-West University, Potchefstroom 2520, South Africa

⁴Discipline of Astronomy Astrophysics and Space Engineering, Indian Institute of Technology Indore, Khandwa Road, Simrol, Indore 453552, India

⁵ Space Science Group, School of Physics, University College Dublin, Belfield, Dublin 4, Ireland

E-mail: ElsJ@ufs.ac.za

Abstract. Blazars are a subclass of radio-loud active galactic nuclei, with relativistic jets closely aligned with the line of sight. These sources are highly variable across all time-scales, and emit non-thermal emission across all wavelength regimes. Blazar-emission is characterised by a double-humped structure in its spectral energy distribution, indicating different emission mechanisms at play. At optical wavelengths, there is an underlying thermal component from the accretion disc, broad line region, and dusty torus, making it difficult to separate the different emission components. As part of a long term campaign, we are undertaking spectropolarimetric observations of flaring blazars, using the Southern African Large Telescope. This could be used to help disentangle the thermal from the non-thermal emission. We present results on the degree of linear polarisation of a selection of fourteen blazars observed between April 2016 and June 2021, with emphasis on five sources of interest. Three sources, namely 4FGL J0231.2-4745, PKS 0537-441, and PKS 2023-07 were observed during/around periods of increased activity. The degree of linear polarisation for all three of the above sources was observed to be higher close to the peak of activity, and decreased as it returned to quiescence. Two sources, AP Lib (a BLL) and PKS 1034-293 (an FSRQ) was observed continually over a period spanning roughly one year. Both of these sources showed some variability in polarisation over the period in question.

1. Introduction

Active galactic nuclei (AGN), the central active cores of some galaxies, are believed to be powered by accretion of material onto a central supermassive black hole (SMBH). They display broad-band emission across the entire electromagnetic spectrum which, in some cases, outshines the host galaxy itself [1]. AGN present unique observational signatures across the different wavelength bands, which led to many different classes of AGN being identified [2]. The unified model suggests all AGN consist of a central SMBH and an accretion disc, a dusty absorber or torus, broad- and narrow-line regions, and in some cases, a strong, collimated jet [3], and the type of AGN observed depends strongly on the viewing angle of the observer.

Table 1. List of FSRQs and BLLs observed with the SALT . The mean linear polarisation was measured between 4000 Å and 8000 Å.

Target	Type	Obs. Date	Mean Pol. (%)	Target	Type	Obs. Date	Mean Pol. (%)
4FGL J0231.2-4745	FSRQ	22/10/2019	27.5	PKS 0208-512	FSRQ	05/12/2019	27.4
		29/10/2019	08.7			19/12/2019	05.3
AP Lib	BLL	14/05/2020	05.3	PKS 0346-279	FSRQ	09/02/2018	18.2
		08/06/2020	05.0	PKS 0426-380	BLL	17/01/2017	10.8
		24/06/2020	03.4			20/02/2017	10.9
		07/08/2020	08.9	PKS 0447-439	BLL	21/02/2017	05.1
		04/09/2020	06.3	PKS 0537-441	BLL	14/01/2019	37.4
		18/02/2021	03.4			05/03/2019	12.6
		12/03/2021	05.2	PKS 0837+012	FSRQ	16/03/2021	10.6
		04/04/2021	08.5	PKS 0907-023	FSRQ	19/01/2017	05.1
		11/04/2021	09.1	PKS 1034-293	FSRQ	15/05/2020	16.2
		21/04/2021	11.0			08/02/2021	17.9
		02/05/2021	08.6			17/03/2021	13.8
		08/05/2021	09.6			09/04/2021	12.7
		14/05/2021	07.1			05/06/2021	19.1
		03/06/2021	06.2	PKS 2023-07	FSRQ	14/04/2016	27.5
PKS 0035-252	FSRQ	20/07/2018	02.6			04/10/2018	09.1
PKS 0131-522	FSRQ	19/11/2017	07.8	TXS 0506+056	BLL	14/10/2017	10.7
		22/11/2017	06.4			20/10/2017	08.6

Blazars are a radio-loud subclass of AGN, with relativistic jets that propagate in a direction closely aligned with the observer's line of sight (viewing angle $< 10^\circ$). As a result, the non-thermal emission originating in the jet is highly Doppler boosted, making blazars the brightest gamma-ray sources in the extragalactic sky [4]. Blazar emission is extremely variable on all time-scales (on time-scales from minutes up to several years), with dramatic variation present across the entire electromagnetic spectrum. Blazars are subdivided into two different categories, namely BL Lac type objects (BLLs) and Flat-Spectrum Radio Quasars (FSRQs). These can be distinguished by their optical spectral features: FSRQs display strong, broad emission lines, while BLLs display absorption or weak emission lines, or featureless spectra dominated by the non-thermal jet emission [2].

The spectral energy distributions (SEDs) of blazars are characterised by a double-humped structure. The lower-energy component (radio to optical/UV and sometimes soft X-rays) is powered by synchrotron emission from relativistic electrons in the jet. However, both leptonic and hadronic models have been previously postulated for the high-energy (X-ray to gamma-ray) component. The leptonic model assumes that the high-energy emission is dominated by Compton scattering of low-energy photons, whereas the hadronic model assumes that the high-energy component is produced through proton-synchrotron radiation or photomeson processes [4]. At optical wavelengths, there is also an underlying thermal contribution originating from the accretion disc, dusty torus, broad-line region (BLR) and host galaxy [5]. Since both the leptonic and hadronic models are able to reproduce blazar SEDs, separating the emission regions can be very difficult.

Polarimetry can be used as a diagnostic tool to disentangle the emission components in blazar SEDs. In the optical, it serves as a tool to separate the thermal (non-polarised) contributions from the non-thermal (polarised) contributions, allowing constraints to be placed on the jet's magnetic field structure, the non-thermal electron population, and the state of the accretion disc [5]. Here we present optical spectropolarimetry observations of a selection of blazars observed with the Southern African Large Telescope (SALT).

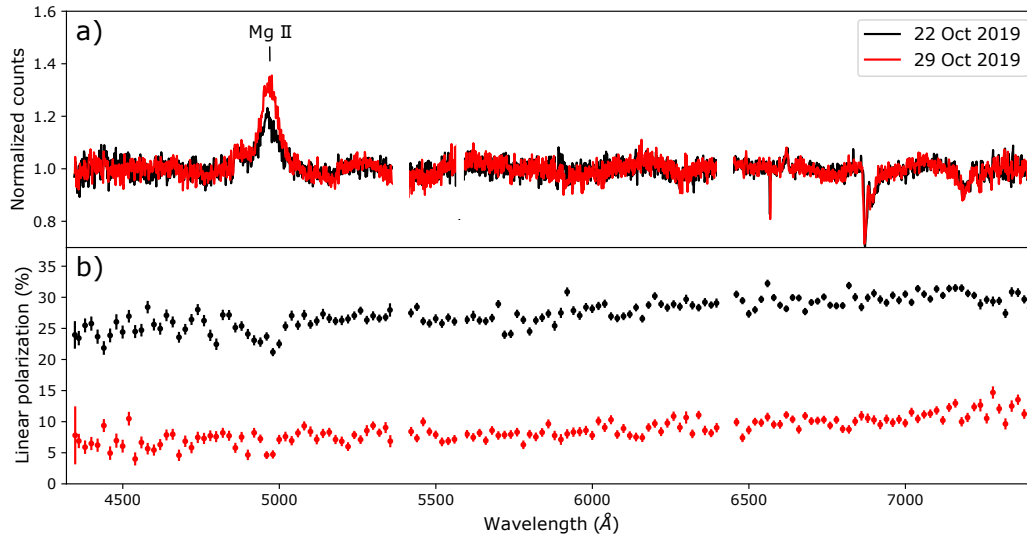


Figure 1. Spectropolarimetry observations of 4FGL J0231.2-4745 taken around a period of increased activity, where a) is the spectra and b) the observed degree of linear polarisation.

2. Observations

The spectropolarimetry observations (listed in Table 1) were taken with the SALT to observe blazars in different states, as well as track the long-term evolution of the degree of polarisation in both BLLs and FSRQs. The observations were performed using the Robert Stobie Spectrograph (RSS) in spectropolarimetry LINEAR mode to measure the degree of linear polarisation [6, 7]. The sources were observed using either the pg0300 grating (with a resolving power of $R = 190$ –560 from 3400 Å to 9867 Å) or with two orientations of the pg0900 grating ($R = 620$ –1655 from 3750 Å to 9000 Å), with either the argon or thorium-argon arc lamp used for wavelength calibration.

Data reduction was performed using a modified version of the POLSALT reduction pipeline (<https://github.com/saltastro/polsalt.git>). The modification allowed the wavelength calibration to be performed using the IRAF/NOAO package (<http://ast.noao.edu/data/software>). Additional cosmic-ray cleaning was performed in PYTHON using the LACOSMIC package (<https://github.com/larrybradley/lacosmic.git>). All other reductions followed the standard procedure given by the POLSALT pipeline. The two larger spaces in the spectra are due to gaps in the CCD detector mosaic, and the smaller missing region at ~ 5600 Å is due to the removal of a skyline.

3. Results

3.1. Flaring Blazars

Figures 1 - 3 show the spectropolarimetry results on three blazars during both flaring and/or quiescent state. The spectra are normalised with respect to counts, and the degree of linear polarisation is represented as a percentage. Using the normalised spectra allows us to show the relative change in the emission/absorption line strengths. 4FGL J0231.2-4745 (Figure 1) was observed twice around a period of increased gamma-ray, X-ray and optical emission [8, 9, 10], where the gamma-ray flux increased by a factor of ~ 60 with respect to the reported catalogue value [8] on 2019 October 19. The observations showed a significant decrease in linear polarisation from the first observation on 2019 October 22 to the second a week later (2019 October 29). There is also an increase in the equivalent width of the Mg II line, which indicates

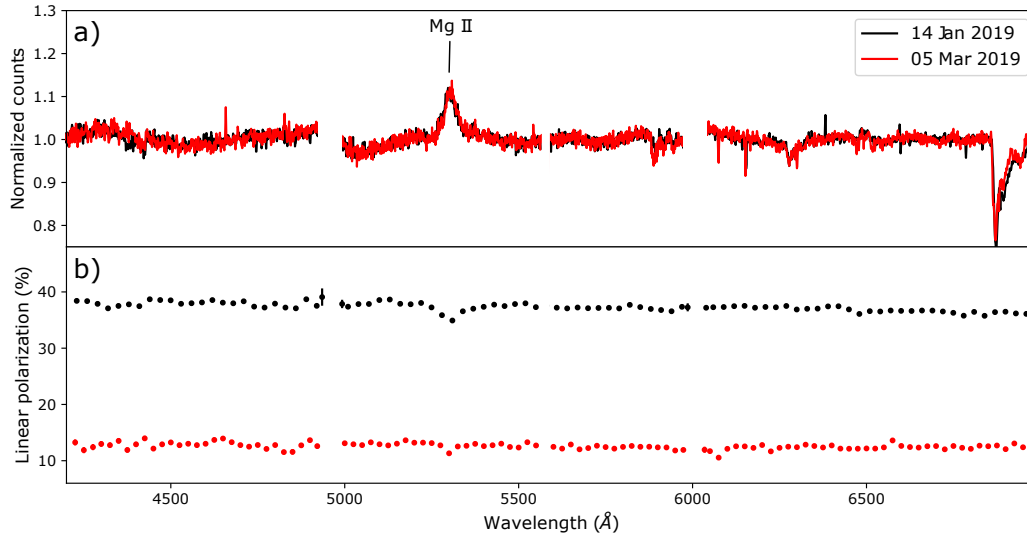


Figure 2. Spectropolarimetry observations of PKS 0537-441 taken around a period of increased activity, where a) is the spectra and b) the observed degree of linear polarisation.

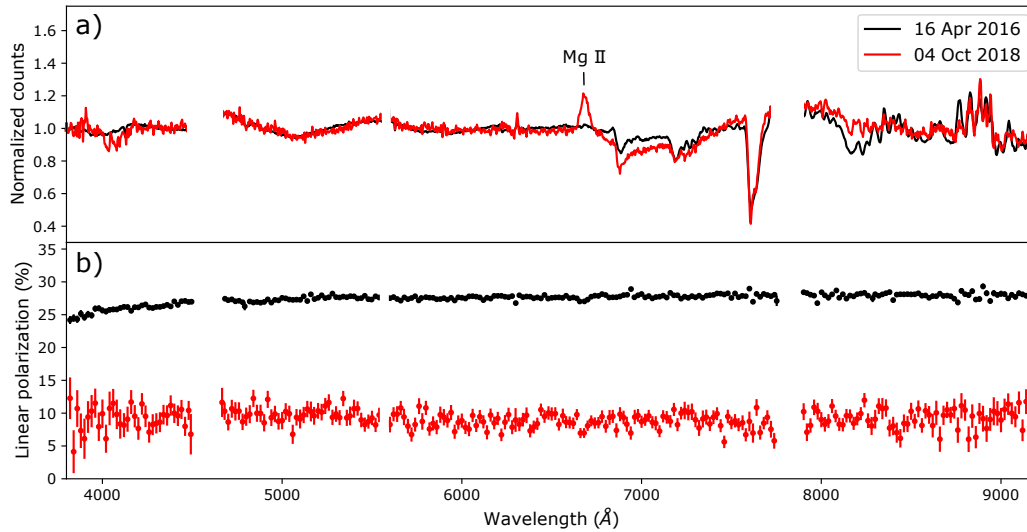


Figure 3. Spectropolarimetry observations of PKS 2023-07 taken during a flaring and non-flaring state, where a) is the spectra and b) the observed degree of linear polarisation.

a decrease of the non-thermal emission component between the two observations. In FSRQs, the non-thermal, beamed jet-emission often outshines the host galaxy, BLR, and accretion disc. Hence, a strengthening of the non-thermal component during a flare can cause the emission lines originating in these regions to appear less prominent/weaker than during quiescence [2].

PKS 0537-411 (Figure 2) was observed at the start of a period of increased activity following a quiescent period [11]. The two observations were taken 50 days apart. While the observations show no significant change in the equivalent width of the Mg II line, they show a large change in the degree of linear polarisation (decrease from 37% to 13%). The publicly available data from the monitoring of *Fermi*-LAT sources indicated that, in the weekly bins, there

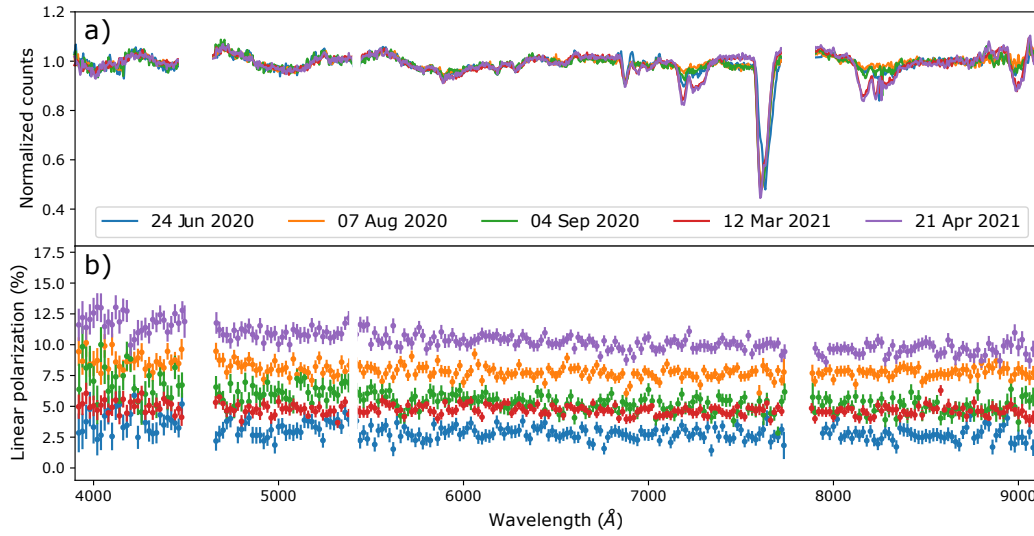


Figure 4. Long-term spectropolarimetry observations of AP Lib, a BLL. Observations were taken from 14 May 2020 to 3 June 2021. Here, only a selection of five observations are shown, with each colour representing an observation date, and a) is the spectra and b) the observed degree of linear polarisation.

was a decrease in the flux (>100 MeV) by a factor of ~ 1.8 between these two observations (<https://fermi.gsfc.nasa.gov/ssc/data/access/lat/mslhc/>).

PKS 2023-07 (Figure 3) was observed once during a flaring state in April 2016 [12], and once during a quiescent state in October 2018. The optical spectrum clearly shows the switch from being dominated by the non-thermal synchrotron emission where no emission lines are observable during the flare, to showing a Mg II emission line during the quiescent state. The degree of polarisation changed by roughly 18% between the two observations.

3.2. Long-term Monitoring

Long-term monitoring of AP Lib (a BLL) and PKS 1034-293 (an FSRQ) has been performed over approximately one year (May 2020 to June 2021) to study the long-term variation in polarisation. Although there were no large changes in the degree of linear polarisation for either of the sources, there was definite variation over time. The spectropolarimetry results are shown in Figures 4 and 5, respectively, where the spectra are normalised with respect to counts.

4. Discussion and Conclusion

To date, the degree of polarisation has been successfully measured for fourteen blazars, both BLLs and FSRQs, during both flaring and/or non-flaring states. For the two sources presented in Figures 1 - 2, observations were taken during periods of increased activity. For these sources, the degree of linear polarisation decreased substantially after the initial observations. The blazar presented in Figure 3 was observed during a flare, along with a follow-up observation taken some time later during quiescence. We expect the thermal component to contribute more at shorter wavelengths. Therefore, there should be a general decrease in the degree of linear polarisation towards the bluer end, and it appears to be the case for the three blazars in question.

For the two long-term sources, both AP Lib (BLL, Figure 4) and PKS1034-293 (FSRQ, Figure 5), displayed some variability in polarisation over the observational period. The FSRQ source had a higher mean polarisation (12-20%) than the BLL (3-12%), while the BLL showed

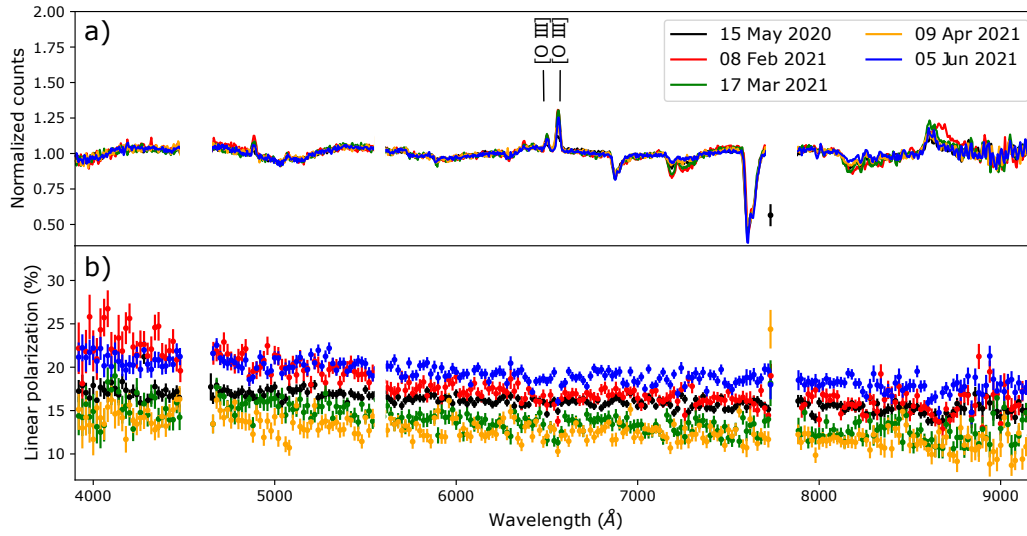


Figure 5. Long-term spectropolarimetry observations of PKS 1034-293, an FSRQ. Observations were taken from 14 May 2020 to 05 June 2021, with each colour representing an observation date, and a) is the spectra and b) the observed degree of linear polarisation.

a slightly larger range in polarisation. However, this may be due to observational bias and can only be confirmed through more observational data.

These are the initial results from an ongoing, long-term project. The variation found in the degree of linear polarisation will now be compared to the multi-wavelength behaviour of these sources. The change in the measured polarisation could be used in the modelling of the blazars' jet-behaviour.

Acknowledgments

All of the observations reported in this paper were obtained with the Southern African Large Telescope (SALT) under program 2018-2-LSP-001 (PI: DAH Buckley) and program 2019-2-MLT-001 (PI: B van Soelen).

References

- [1] Padovani P 2017 *Front. Astron. Space Sci.* **4** 12-18
- [2] Beckmann V and Shrader, C R 2012 *Active Galactic Nuclei* (Weinheim: Wiley)
- [3] Urry C M and Padovani P 1995 *PASP* **107** 803-45
- [4] Böttcher M 2019 *Galaxies* **7** 20-56
- [5] Böttcher M, van Soelen B, Britto R J, Buckley D A H, Marais J P and Schutte H 2017 *Galaxies* **5** 52-58
- [6] Burgh E B, Nordsieck K H, Kobulnicky H A, Williams T B, O'Donoghue D, Smith M P and Percival J W 2003 *SPIE* **4841** 1463-71
- [7] Kobulnicky H A, Nordsieck K H, Burgh E B, Smith M P, Percival J W, Williams T B and O'Donoghue D 2003 *SPIE* **4841** 1634-44
- [8] Principe G and Angioni, R 2019 *ATel* **13209**
- [9] D'Ammando F, Principe G and Angioni, R 2019 *ATel* **13212**
- [10] Pursimo T, Martikainen J and Ojha R 2019 *ATel* **13248**
- [11] Nesci R and Ojha R 2019 *ATel* **12357**
- [12] Emery G, Jankowsky F, Lenain J P, Marais J P, Mbonani T, Romoli C, van Soelen B, Wierzcholska A, Zacharias M and Meyer M 2019 *Proc. of the 36th Int. Cosmic Ray Conf. (Madison)* PoS(ICRC2019) 669

Investigating the orbital parameters of the gamma-ray binary HESS J0632+057

N Matchett¹, B van Soelen¹ and R O Gray²

¹ Department of Physics, University of the Free State, Bloemfontein, 9300, South Africa

² Department of Physics and Astronomy, Appalachian State University, Boone, NC 28608, USA

E-mail: MatchettN@ufs.ac.za

Abstract. Gamma-ray binaries are a small (<10) subclass of high mass binary systems that display non-thermal emission peaking in the gamma-ray regime (≥ 1 MeV). All known systems contain an O/Oe or B/Be star and a compact object in the mass range of a black hole or neutron star. In order to interpret how the non-thermal emission is produced, the orbital parameters need to be determined. HESS J0632+057 is a gamma-ray binary comprising of a Be star and an unknown compact object with an orbital period of ~ 317 days. Two previous studies by Casares et al. 2012 and Moritani et al. 2018 obtained two different and incompatible orbital solutions. We are undertaking a long-term observational campaign with the High Resolution Spectrograph on the Southern African Large Telescope to establish the radial velocities in order to differentiate between the two proposed orbital solutions. The initial results, from the first observing semester, of Voigt profile fitting to the $H\alpha$, $H\beta$ and $H\gamma$ Balmer emission lines show changes over the observation period, indicating variation within the circumstellar disc, while the radial velocities display a general trend of decreasing with time that is consistent with the Moritani et al. solution.

1. Introduction

Gamma-ray binaries are a rare subclass of high mass binaries displaying multiwavelength non-thermal emission that peaks at energies greater than 1 MeV in a νF_ν representation. Currently less than 10 systems have been identified. All comprise of a compact object, in the mass range of a black hole or neutron star, orbiting an O/Oe or B/Be companion star (see e.g. [1] or [2] and reference therein). The nature of the compact object remains unconfirmed for all but two of the systems, where a young pulsar is observed in both PSR B1259-63/LS 2883 [3] and PSR J2032+4127/MT91 213 [4]. Two scenarios have been proposed to explain the source of the gamma-ray emission, namely the pulsar-wind scenario and the microquasar scenario. In the pulsar-wind scenario, the compact object is a rotationally powered young pulsar. The interaction between the stellar and pulsar wind produces a termination shock wherein particle acceleration will take place. It has been suggested that this scenario would occur during a brief period in the binary evolution of High Mass X-ray Binaries (HMXBs), before the neutron star has spun down enough to allow accretion to occur. Alternatively, in the case of a black hole compact object, the microquasar scenario would occur. Energy from an accretion disc around the compact object powers a relativistic jet, wherein particle acceleration will take place. In both scenarios the non-thermal emission arises from synchrotron and inverse Compton emission of the accelerated

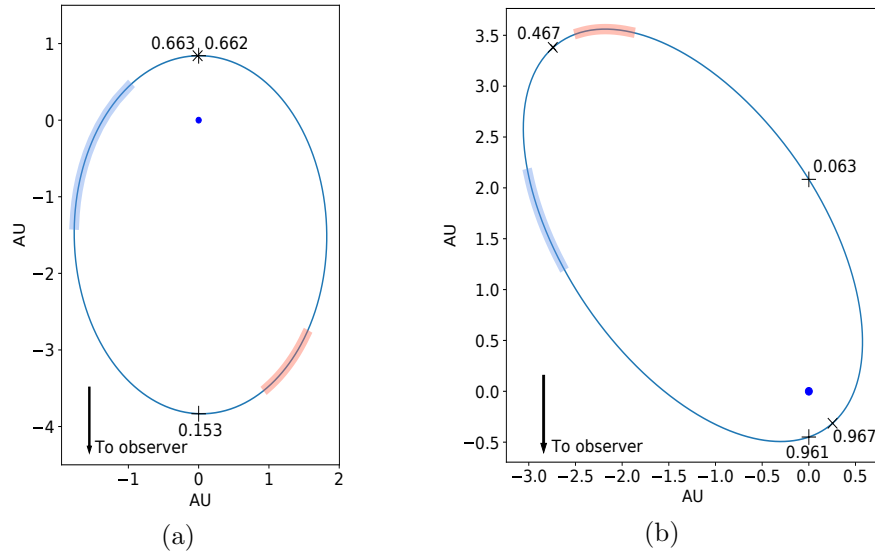


Figure 1: The binary geometry as determined by the Moritani et al. (a) and Casares et al. solution (b) for orbital periods of 313 and 321 days, respectively. Superior conjunction and inferior conjunction, as well as apastron and periastron are indicated on the orbital paths. The phases for the maxima in the X-ray and TeV light curves are indicated by the broad red (phases 0.3-0.4) and blue (phases 0.7-0.8) lines. The observer views both systems from the bottom of the page as indicated by the arrow.

electrons. A key aspect in modelling and interpreting the observed emission from these systems, is knowing the orbital parameters of the system.

The gamma-ray binary HESS J0632+057 is composed of the Be type star MWC 148 and an unknown compact object, in a ~ 317 day orbit (see recent studies by Malyshev et al. 2019 [5] and Adams et al. 2021 [6]). The Be star is surrounded by a circumstellar disc, as evident by the emission lines in the optical spectrum. The observed X-ray and TeV emission displays two maxima in their light curves, at orbital phase 0.3-0.4 and 0.7-0.8 [7]. Two previous studies, by Casares et al. 2012 [8] and Moritani et al. 2018 [9], have previously undertaken radial velocity measurements to determine the orbital parameters of HESS J0632+057. However, they obtained two incompatible solutions. Casares et al. determined the orbital parameters from radial velocity measurements obtained from the faint He I 4471 Å, 4731 Å and 5048 Å photospheric absorption lines, whereas Moritani et al. measured the radial velocity from the wings of the H α emission line. The orbital geometry for the two solutions is shown in Figure 1. Moritani et al. proposed that the maxima in the X-ray and TeV light curves could be attributed to the compact object passing through the Be star's circumstellar disc, tilted with respect to the orbital plane of the system. The inclined disc model has also been discussed by Malyshev et al. 2019 [5], where they used this interpretation to constrain parameters for the position of periastron and the eccentricity which are compatible with the Moritani et al. solution. They also obtained an orbital period of $316.8^{+1.2_{stat}+1.4_{sys}}_{-0.4_{stat}-1.0_{sys}}$ days from analysis of the Swift-XRT data. Spectral energy distribution modelling of the X-ray and TeV observations by Archer et al. 2020 [10] favour a pulsar-wind scenario; this is consistent with the Moritani et al. solution. An analysis of long-term X-ray and gamma-ray observations reported by Adams et al. 2021 [6] found orbital periods of $317.3 \pm 0.7_{stat} \pm 1.5_{sys}$ days (X-ray) and $316.7 \pm 4.4_{stat} \pm 2.5_{sys}$ days (gamma-ray). In addition, an independent solution for the binary parameters (which are within range of the proposed solution by Moritani et al.) has been proposed by Tokayer et al. 2021 [11], based on modelling

the Swift-XRT light curve.

Although there appears to be some consistency in the various different studies with the Moritani et al. solution, optical radial velocity measurements provide a model-independent method to determine the binary parameters. While the method used in Moritani et al. has previously been applied to other binary systems containing Be stars (see [12], and reference therein), it would be preferable to obtain consistent radial velocities from both the emission and absorption lines.

Here we discuss the initial results from a long-term observation campaign to observe HESS J0632+057 using the High Resolution Spectrograph [13] on the Southern African Large Telescope [14], presenting the radial velocity measurements obtained from the Balmer emission lines.

2. Observations, data reduction and analysis

Five spectroscopic observations were obtained with the HRS in High Resolution mode ($R \sim 65000$ - 74000) on SALT between December 2020 and February 2021. Each observation consisted of three 600 s exposures. The CCD reduction, spectral extraction, wavelength calibration and flat fielding was performed using the HRS pipeline described in Kniazev et al. 2016 [15]. The merging of the different orders was performed in PYTHON. The three observations taken for each night were averaged together, continuum corrected and adjusted to the barycenter. The change in the Balmer emission lines over the observations is shown in Figure 2.

As a first step, we have measured the radial velocity from the Balmer emission lines, $H\alpha$, $H\beta$ and $H\gamma$, similar to Moritani et al. For each line we fit a Voigt profile to the wings of the emission feature, which was taken as where the emission decreased below half of the peak intensity. An example of the profile fits are shown in Figure 3. The difference between the centre of the fitted lines and the rest wavelength was used to calculate the radial velocity.

3. Results and discussion

Over the observation period, the emission lines show a clear variation. The $H\alpha$ does not show a clear double peak structure, but the line does shift from single peaked, to an indication of a double peak on 2020 December 25, to be single peaked again. The $H\beta$ and $H\gamma$ lines are double peaked in all observations. The $H\beta$ line shows a stronger component in the blue, which shifts through the observations, while similarly, the $H\gamma$ lines show small shift in the V/R variation. This variation indicates changes in the circumstellar disc, including any change to the symmetry of the disc or regions of higher density (see e.g. [16]).

In order to minimize the influence of the changing shape of the emission lines, when measuring the radial velocity, the Voigt profiles were fit to the wings of the lines, as stated above. Since the circumstellar discs of Be stars are Keplerian (see e.g. [17]) the region of the disc closest to the star will have the highest rotation velocity, contributing more light to the wings of the emission lines. The radial velocity measurements for these observations are compared to the orbital solutions presented by Casares et al. and Moritani et al. is shown in Figure 4. For consistency, we have used the orbital periods of 321 and 313 days, given by Casares et al. and Moritani et al. respectively, to phase fold the radial velocities obtained in this work. The difference between these orbital periods and the recent orbital period estimate of ~ 317 days, should not significantly impact our analysis. The radial velocities show a general trend of decreasing with orbital phase, and are more consistent with the Moritani et al. solution. There is a systematic difference between the different radial velocities measured for the different lines, but this is on the order of a few $\times \text{km s}^{-1}$ and the errors shown are statistical, derived from the goodness of fit of the Voigt profile.

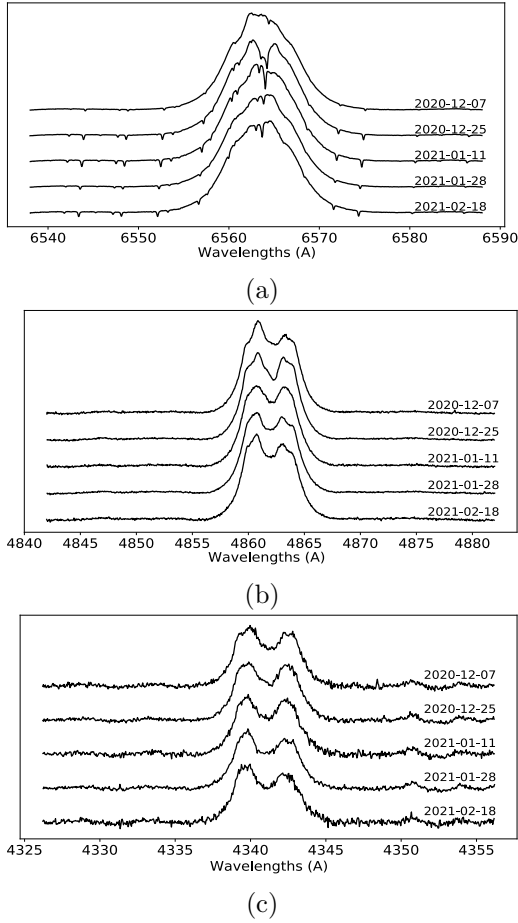


Figure 2: The variation of the H α (a), H β (b) and H γ (c) Balmer emission lines over the observation period. Spectra are normalized and offset for clarity.

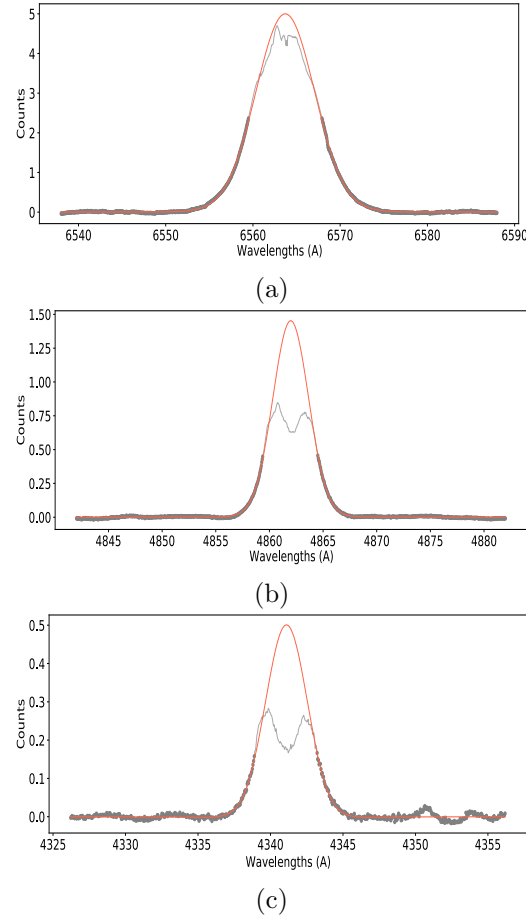


Figure 3: Examples of the Voigt profile (red line) fit to the wings of the Balmer lines (thick dotted region). The average of the H α (a), H β (b) and H γ (c) Balmer lines (thin gray line) is shown for illustration.

4. Conclusions

Initial results from spectroscopic observations obtained from SALT showed the emission line profiles changed over the observation period (Figure 2), indicating variations within the circumstellar disc, while the radial velocities display a general trend of decreasing radial velocity with time for all the Hydrogen emission line fits (Figure 4). These results are more consistent with the Moritani et al. solution. In future work the analysis will be performed for the weaker absorption lines originating from the Be star's photosphere. Further observations are proposed to increase the signal-to-noise and obtain full orbital phase coverage to accurately determine the orbital parameters of the binary.

Acknowledgments

All of the observations reported in this paper were obtained with the Southern African Large Telescope (SALT) under program 2020-2-MLT-007 (PI: B van Soelen).

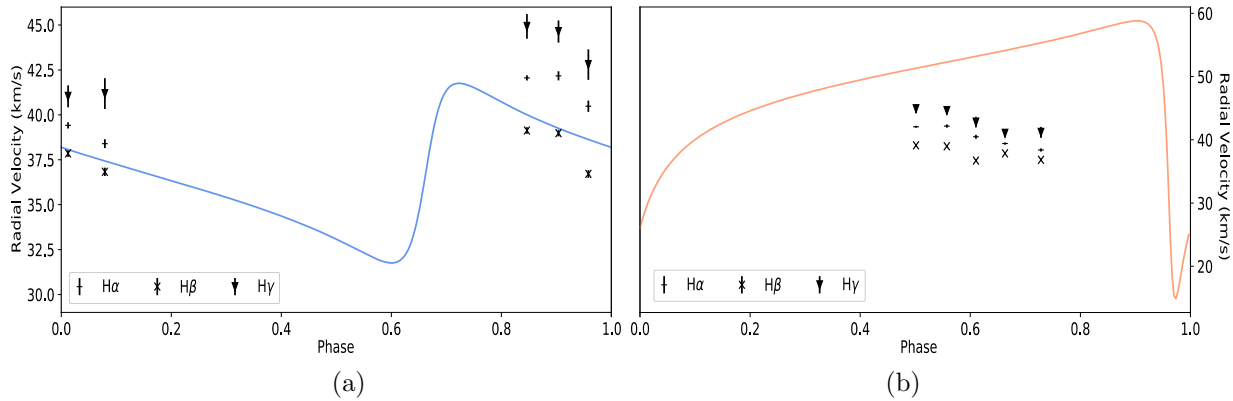


Figure 4: The radial velocity measurements of the Balmer emission lines obtained in this work (black data points), plotted against the phase relative to the Moritani et al. (a) and Casares et al. (b) models of their orbital solutions. The error shown in the radial velocities are purely statistical, derived from the goodness of fit from the Voigt profile fits to the wings of the $H\alpha$, $H\beta$ and $H\gamma$ Balmer emission lines.

References

- [1] Dubus G. 2013 *A&ARv* **21** 64-134
- [2] Chernyakova et al. 2019 *A&A* **631** A177
- [3] Johnston S et al. 1992 *ApJ* **387** L37-41
- [4] Lyne A G et al. 2015 *MNRAS* **451** 581-7
- [5] Malyshev D., Chernyakova M., Santangelo A., Pühlhofer G. 2019 *AN* **340** 465
- [6] Adams C. B., Benbow W., Brill A., Buckley J. H., Capasso M., Chromey A. J., Errando M., et al. 2021 *arXiv* **2109.11894**
- [7] Aliu E, Archambault S, Aune T, Behera B, Beilicke M, Benbow W, Berger K, et al. 2014 *ApJ* **780** 168-81
- [8] Casares J, Ribó M, Ribas I, Paredes J M, Vilardell F and Negueruela I 2012 *MNRAS* **421** 1103-12
- [9] Moritani et al. 2018 *PASJ* **70** 61
- [10] Archer A., Benbow W., Bird R., Brill A., Brose R., Buchovecky M., Christiansen J. L., et al. 2020 *ApJ* **888** 115
- [11] Tokayer Y. M., An H., Halpern J. P., Kim J., Mori K., Hailey C. J., Adams C. B., et al. 2021 *arXiv* **2110.01075**
- [12] Dulaney N et al. 2017 *ApJ* **836** 112-6
- [13] Crause L A, Sharples R M, Bramall D G et al. 2014 *SPIE* **9147** 2138-51
- [14] Buckley D A H, Swart G P and Meiring J G 2006 *SPIE* **6267** 333-47
- [15] Kniazev A Y, Gvaramadze V V and Berdnikov L N 2016 *MNRAS* **459** 3068-77
- [16] Telting J H and Kaper L 1994 *A&A* **284** 515-29
- [17] Carciofi A *The circumstellar discs of Be stars* Proc. of the International Astronomical Union 2010 **6(S272)** 325-36

A multi-band view on the evolution of group central galaxies

K Kolokythas,¹ E O’Sullivan,² I Loubser,¹ A Babul,^{3,4}
S Raychaudhury^{5,6} and S Vaddi⁷

¹Centre for Space Research, North-West University, Potchefstroom 2520, South Africa

²Center for Astrophysics | Harvard & Smithsonian, 60 Garden Street, Cambridge, MA 02138, USA

³Department of Physics and Astronomy, University of Victoria, Victoria, BC V8P 1A1, Canada

⁴Center for Theoretical Astrophysics and Cosmology, Institute for Computational Science, University of Zurich, Winterthurerstrasse 190, 8057 Zurich, Switzerland

⁵Inter-University Centre for Astronomy and Astrophysics, Pune University Campus, Ganeshkhind, Pune, Maharashtra 411007, India

⁶School of Physics and Astronomy, University of Birmingham, Birmingham B15 2TT, UK

⁷Arecibo Observatory, NAIC, HC3 Box 53995, Arecibo, Puerto Rico, PR 00612, USA

Abstract. Nearby galaxy groups are the place in which non-secular processes have the greatest impact on galaxy formation and evolution. We examine, using multiple wavebands, the processes that play a significant role in galaxy evolution in the central brightest group early-type galaxies (BGEs) of an optically selected, statistically complete sample of 53 nearby groups (<80 Mpc; CLoGS sample). The CLoGS sample has been observed in radio 235/610 MHz (GMRT), CO (IRAM/APEX) and X-ray (Chandra and XMM-Newton) frequencies and also has a wealth of archival Far-UV and mid-infrared data. Characterizing the BGEs based on their X-ray group environment and radio properties we examine the relations between i) radio-AGN activity and X-ray intra-group gas and ii) between the molecular gas content, its morphology and the status of their star formation. We suggest that active star formation is promoted by the presence of cold gas in the form of disks whereas AGN radio jet activity mainly emanates from an X-ray bright Intra-group medium (IGrM), with AGN feedback in galaxy groups manifested either as a smooth continuous thermal regulation, or also as an extreme outburst that may affect the group gas dramatically.

1. Introduction

More than half of all galaxies reside in galaxy groups [1]. Groups are a diverse class, ranging from spiral-dominated systems rich in *HI* and molecular gas, to more massive, evolved systems dominated by early-type galaxies, with little cold gas but often hosting an extended hot X-ray emitting intra-group medium (IGrM). The shallow potential wells of groups bring galaxies close together at low velocities, making interactions and mergers common, and making groups perhaps the most important environment for studies of galaxy evolution. The transition in gas properties, as groups increase in mass, is related to the evolution of the galaxy population, with some intermediate systems showing intergalactic structures of cold gas, or even a cold *HI* IGrM [2].

X-ray bright groups are also a key environment for the study of Active Galactic Nuclei (AGN) feedback, having almost universally short central cooling times and low entropies [3]. Evidence of repeated cycles of AGN activity is relatively common, in the form of nested radio sources or multiple sets of X-ray cavities. While most group-central radio galaxies conform to the known relationship between the cooling luminosity of the IGrM and jet power (as measured from X-ray

cavities, e.g., [4], there are cases where the AGN appears to be dramatically over-powered [5] and recent studies have shown that groups can host larger radio galaxies than clusters [6]. It is believed that these group-central AGN are fuelled by material cooled from the IGrM, often observed in clusters as H α and CO filaments (e.g., [7]). The amount of cooled material in X-ray bright groups is typically smaller than in clusters (e.g., [8]) perhaps indicating, in combination with the short cooling times, a more rapid cycling of the AGN.

At present, our understanding of the impact of the group environment on member galaxies is largely based on optical and *HI* studies of low-mass compact groups, while studies of AGN feedback have focused on relatively small numbers of well-known, highly X-ray luminous galaxy groups. Selecting representative samples of groups is difficult, with both X-ray and optical selection having important flaws. The wide variety of data needed to trace star formation, different gas phases, and AGN activity is often only available in moderate redshift survey fields where detailed analysis of the groups is impossible. We use one of the few samples of nearby groups that is both representative and has the requisite supporting data at multiple frequencies (X-ray, CO, radio and archival mid-IR, FUV and K band) to investigate in detail the relative balance of different processes operating to transfer energy from the AGN and the IGrM, and the role of star formation in the cooling gas.

As AGN in galaxy groups dominate feedback in the Universe as a whole, the detailed study of the properties of cold gas and its link to star formation, will also have implications on our global understanding of structure formation and galaxy evolution.

2. The sample: CLoGS

The Complete Local-Volume Groups Sample (CLoGS, [3]) is a statistically complete, optically-selected set of 53 groups within 80 Mpc, with declinations $>-30^\circ$. The groups cover a range of mass, richness and galaxy population, but all contain at least one large early-type galaxy, since the original goal of the sample was to investigate AGN feedback. The sample has an exceptionally rich supporting dataset: GMRT 235 and 610 MHz observations to trace continuum emission from AGN and star formation ([9],[5]); *XMM-Newton* and/or *Chandra* X-ray observations to provide information on their IGrM [3]; IRAM 30m or APEX CO mass measurements for the dominant galaxies ([10],[8]); and a wealth of optical imaging and spectroscopy, including (for subsets) MUSE IFU maps and long-slit spectra of the dominant galaxies, and wide-field H α imaging of the groups. In addition, due to its proximity CLoGS is ideal for the study of star formation using catalog data in the FUV (GALEX), and mid-infrared (WISE).

Another benefit of CLoGS proximity, is that it provides also the opportunity to study in detail the AGN outburst properties and energetics of individual strong radio jet sources (e.g., NGC 4261, [11]) as well as the examination of galaxy interactions and their important role in the development of a galaxy group and its formation history (see e.g., NGC 5903, [12] and NGC 1550, [13]).

3. Results from multiple bands

3.1. X-rays, radio-AGN and gas content in group dominant galaxies

X-ray observations reveal that more than half (55%) of the CLoGS groups are X-ray luminous, presenting a full scale X-ray halo; their hot gas halo extends >65 kpc (26/53; [3], O'Sullivan 2022 in prep), with the remaining systems having only limited or no hot intra-group medium being generally spiral rich. The X-ray bright groups were misidentified as single galaxies or not detected at all in the Rosat All Sky Survey prior to our observations, which implies that about 30% of the X-ray bright groups in the local universe might still be not known. On the other hand, using GMRT radio observations at 235/610 MHz and archival VLA data, the radio-AGN population of the central CLoGS group dominant galaxies appears at a high detection rate (87%; 46/53) with the dominant galaxies presenting a wide range in radio power ($10^{20} - 10^{25}$ W Hz $^{-1}$) and projected size (~ 3 kpc to 2 Mpc). Roughly half of the radio detected dominant galaxies (53%) present point-like radio emission, followed by 19% having jets with non-detections at 13%. The mean spectral index α_{235}^{610} is ~ 0.68 with only 3.8% of the radio sources presenting ultra-steep spectra (>2.5). Radio morphology is seen to correlate with the dynamical youth of the groups as radio point sources are more common in the dominant galaxies of spiral-rich systems whereas jet sources show no preference of their close environment ([9],[5]) and can emanate from a range ($2-50 \times 10^8 M_\odot$) of black hole masses.

Adding to the picture examination of the cold gas content in CLoGS groups' dominant galaxies, a relatively high detection rate is found for CO ($\sim 40\%$). However the galaxies are found to present short depletion times, suggesting that group-central galaxies must replenish their molecular gas reservoirs on timescales of ~ 100 Myr. The majority of the dominant galaxies present signs of AGN (instead of star formation) dominance with at least half of them containing HI as well as molecular gas ([10],[8]).

3.2. AGN feedback in group dominant galaxies

Combining radio and X-ray observations shows that 11/26 ($\sim 42\%$) of X-ray bright groups host jet systems with the radio non-detections appearing in groups which either possess a galaxy scale X-ray halo or not one at all (X-ray faint groups). This suggests that gas cooling availability is more likely to feed the central engine and give rise to radio jet sources, in contrast to X-ray faint systems. The jet occurrence in X-ray bright groups implies an AGN duty cycle $> 1/3$ with these central jet sources seen in systems that possess cool cores with short central cooling times ($t_{cool} < 7.7$ Gyr; [3]) and low entropies in their cores (jet activity hasn't increased significantly the entropy in their central region).

Examining the balance in CLoGS groups between heating from AGN jet systems and cooling from X-rays (cooling X-ray luminosity), it is found that AGN feedback in galaxy groups can manifest as expected, as a smooth near-continuous thermal regulation without excessive cooling, but in addition we have identified two systems (NGC 193 and NGC 4261) whose exceptionally powerful AGN outbursts are delivering $100\times$ more power into the intra-group medium than is being lost by radiative cooling. Therefore, AGN feedback in galaxy groups can also manifest as an extreme outburst which could potentially shut down cooling in the group for much longer periods of time [9].

3.3. Star formation in galaxy groups

With all relevant information from multi-band wavelengths at hand for CLoGS groups (Far-UV, and mid-infrared), we examine the star formation (star-formation rate -SFR-, specific star-formation rate, stellar mass) and central AGN properties (e.g., radio power) of the dominant early-type galaxies in relation to their gas content and the large-scale environment they reside in. FUV magnitudes were drawn from the *Galaxy Evolution Explorer* (GALEX; [14]) GR6 data release¹ with mid-infrared ones retrieved from the *WISE* mission catalog [15] at $3.4\ \mu\text{m}$ (W1), $4.6\ \mu\text{m}$ (W2), $12\ \mu\text{m}$ (W3) and $22\ \mu\text{m}$ (W4) with an angular resolution of $6.1''$, $6.4''$, $6.5''$ and $12''$ respectively. The near-infrared K_s -band magnitudes were taken from the Two Micron All-Sky Survey (2MASS; [16]).

3.3.1. Results from SFR Diagnostics We find that the FUV star-formation rate (SFR_{FUV}) in CLoGS group dominant galaxies is low ($0.01 - 0.4\ \text{M}_{\odot}\ \text{yr}^{-1}$). Using the $[\text{FUV} - K_s] < 8.8$ mag criterion from the study of [17] to distinguish between actively star-forming and quiescent galaxies, we find that only 6/47 ($\sim 13\%$) of the dominant galaxies are currently in some form star-forming (namely NGC 252, NGC 924, NGC 940, NGC 1106, NGC 7252 and ESO507-25). All of the six FUV bright systems share some common characteristics between them: they are lenticular (S0 morphological type), cold gas rich, present low-powered radio sources ($P_{1.4\text{GHz}} < 10^{23}\ \text{W}\ \text{Hz}^{-1}$) and occupy X-ray faint groups. This suggests that, as expected, the majority of the group dominant galaxies (87%; 41/47) are FUV faint (passive) with no significant star-forming activity in agreement also with previous studies ([17],[18]).

The state of the dominant galaxies is also determined based on the mid-infrared diagnostics by [19] and [20]. Examination of the mid-infrared activity of the CLoGS dominant galaxies also reveals that the majority of the systems (87%; 46/53) occupy the spheroid region ($W2 - W3 < 1.5$ mag) having little star-formation with only one system (NGC 4956) having a very 'warm' $W1 - W2$ color, thus characterized as mid-IR bright AGN and with only one system having the reddest ($W2 - W3 > 3$ mag) color in the sample (NGC 7252) and characterized as actively star-forming disk. Five systems are classified as mid-infrared intermediate disks, namely NGC 252, NGC 940, NGC 1106, NGC 1779, and NGC 7377 with 3/5 of them being also classed as actively star-forming based on $[\text{FUV} - K_s]$ color, having the same characteristics as the FUV bright ones.

¹ <https://galex.stsci.edu/GR6><https://galex.stsci.edu/GR6>

3.3.2. Radio power in relation to SFR_{FUV} and stellar mass Examining the relation between radio power and SFR_{FUV} with stellar mass for the CLoGS group dominant galaxies, we find a lack of correlation denoting that the relation between AGN feedback and star formation is dependent on a variety of factors and can hint to multiple governing related processes. We suggest that this favors predominantly a combination of i) an external origin of gas (e.g., mergers) for some systems and ii) a stellar mass loss or cooling from the inter-stellar medium or halo for some other CLoGS dominant galaxies instead of a single origin of gas supply for the CLoGS sample that fuels the AGN and/or star formation related only with the host galaxy itself.

3.3.3. Specific star-formation rate and gas content The majority of the CLoGS group dominant galaxies exhibit low specific star-formation rates (sSFRs; $\sim 10^{-13} \text{ yr}^{-1}$) with the six FUV bright active star-forming galaxies presenting an order of magnitude higher sSFRs than the rest of the sample. Adding to the picture information on the cold gas morphology for the FUV bright systems, we find that 4/6 have gas disks suggesting that not only the presence of cold gas, but also its dynamical state plays an important role. In addition, the fact that all of these dominant galaxies are found in X-ray faint groups denotes that the cold gas is not likely originating from the cooling of gas from a hot intra-group medium, but most probably has been acquired through gas-rich mergers/tidal interactions.

On the other hand, we find that passive systems with lower sSFR values can either have AGN feedback at work in powerful radio systems suppressing or keeping star formation at low rates, or, in the case of low-radio power systems their gas deposit is not sufficient to fuel any significant star formation or a powerful AGN which is inherent to their environmental properties or linked to their groups evolutionary status/history. Examining the large scale environment of passive systems we find that radio powerful AGN reside in X-ray bright groups showing the connection between IGrM cooling and jet-mode feedback, with X-ray bright systems overall presenting a range of SFRs, but lower than the SFRs seen in the active star-forming systems -with the exception of NGC 315. This suggests that gas mass availability promotes fueling of star formation in actively star-forming systems, with the presence of a cooling IGrM on the other hand, being capable of promoting more powerful AGN, but not the fastest SFR, with mergers/interactions being important factors for both star formation fueling and AGN.

4. Conclusions

We conclude that evolution in the nearby group dominant galaxies of the CLoGS sample is driven not merely by a single process for all systems, but by a combination of secular processes and mergers/interactions, regulated also by the environment in which they reside. In the near future, observations with MeerKATs unprecedented sensitivity at L-band will allow us to examine in more detail the neutral hydrogen content of nearby galaxy groups, as well as to complement the continuum radio emission from AGN and star-forming galaxies.

5. Acknowledgments

This work is based on the research supported by the National Research Foundation of South Africa (KK & SIL: Grant number 120850). Opinions, findings and conclusions or recommendations expressed in this publication is that of the author(s), and that the NRF accepts no liability whatsoever in this regard.

References

- [1] Eke V R, Baugh C M, Cole S, Frenk C S and Navarro J F 2006 *MNRAS* **370** 1147
- [2] Verdes-Montenegro L, Yun M S, Williams B A, Huchtmeier W K, Del Olmo A and Perea J 2001 *A&A* **377** 812
- [3] O'Sullivan E, Ponman T J, Kolokythas K, Raychaudhury S, Babul A, Vrtiljek J M, David L P, Giacintucci S, Gitti M and Haines C P 2017 *MNRAS* **472** 1482
- [4] Panagoulia E K, Fabian A C and Sanders J S 2014 *MNRAS* **438** 2341
- [5] Kolokythas K, O'Sullivan E, Intema H, Raychaudhury S, Babul A, Giacintucci S and Gitti M 2019 *MNRAS* **489** 2488
- [6] Pasini T, Bruggen M, de Gasperin F, Brzan L, O'Sullivan E, Finoguenov A, Jarvis M, Gitti M, Brighenti F, Whittam I H, Collier J D, Heywood I and Gozaliasl G 2020 *MNRAS* **497** 2163

- [7] Olivares V, Salome P, Combes F, Hamer S, Guillard P, Lehnert M D, Polles F L, Beckmann R S, Dubois Y, Donahue M, Edge A, Fabian A C et al. 2019 *A&A* **631** 22
- [8] O'Sullivan E, Combes F, Salome P, David L P, Babul A, Vrtillek J M, Lim J, Olivares V, Raychaudhury S and Schellenberger G 2018a *A&A* **618** 126
- [9] Kolokythas K, O'Sullivan E, Raychaudhury S, Giacintucci S, Gitti M and Babul A 2018 *MNRAS* **481** 1550
- [10] O'Sullivan E, Combes F, Hamer S, Salome P, Babul A and Raychaudhury S 2015 *A&A* **573** 111
- [11] Kolokythas K, O'Sullivan E, Giacintucci S, Raychaudhury S, Ishwara-Chandra C H, Worrall D M and Birkinshaw M 2015 *MNRAS* **450** 1732
- [12] O'Sullivan E, Kolokythas K, Kantharia N G, David L P, Raychaudhury S, David L P and Vrtillek J M 2018b *MNRAS* **473** 5248
- [13] Kolokythas K, O'Sullivan E, Giacintucci S, Worrall D M, Birkinshaw M, Raychaudhury S, Horellou C, Intema H and Loubser I 2020 *MNRAS* **496** 1471
- [14] Martin D C, Fanson J, Schiminovich D, Morrissey P, Friedman P G, Barlow T A, Conrow T, Grange R, Jelinsky P N, Milliard B et al. 2005 *ApJ* **619** L1
- [15] Wright E L, Eisenhardt P R M, Mainzer A K, Ressler M E, Cutri R M, Jarrett T, Kirkpatrick J D, Padgett D, McMillan R S, Skrutskie M et al. 2010 *AJ* **140** 1868
- [16] Jarrett T H, Chester T, Cutri R, Schneider S E and Huchra J P 2003 *AJ* **125** 525
- [17] Gil de Paz A, Boissier S, Madore B F, Seibert M, Young J H, Boselli A, Wyder T K, Thilker D, Bianchi L et al. 2007 *ApJS* **173** 185
- [18] Vaddi S, ODea C P, Baum S A, Whitmore S, Ahmed R, Pierce K and Leary S 2016, *ApJ* **818** 182
- [19] Jarrett T H, Cluver M E, Magoulas C, Bilicki M, Alpaslan M, Bland-Hawthorn J, Brough S, Brown M J I et al. 2017 *ApJ* **836** 182
- [20] Jarrett T H, Cluver M E, Brown M J I, Dale D A, Tsai C W and Masci F 2019 *ApJ* **245** 25

Potential of the MeerKAT telescope to detect the stimulated decay of axion-like particles

A Ayad and G Beck

School of Physics, University of the Witwatersrand, Private Bag 3, WITS-2050, Johannesburg, South Africa

E-mail: ahmed@aims.edu.gh

Abstract. A prominent aspect of the hunt for cold dark matter is looking for light scalar candidates such as axion-like particles (ALPs). The coupling between ALPs and photons allows for the spontaneous decay of ALPs into pairs of photons. It has been previously shown that stimulated ALP decay rates can become significant on cosmic time scales. Furthermore, it has been claimed, in several recent works, that ALPs can gravitationally thermalize and form macroscopic condensates. Consequently, the photon occupation number of ambient populations (like the cosmic microwave background) can receive Bose enhancement in dense ALP clumps and grows exponentially. For cold dark matter ALPs, this can lead to radio emissions produced from this process and could be observed by the forthcoming radio telescopes. In this work, we investigate the detectability of such a radio signature from some astrophysical targets using the MeerKAT radio telescopes. The results show that the MeerKAT telescope is able to probe the ALPs parameter space with limits reaching the current level of the CAST experiment and the potential level of the IAXO experiment with an arcminute visibility taper.

1. Introduction

Large amounts of stable cold dark matter are required to explain many astrophysical and cosmological observations [1]. These include the rotation curves of galaxies [2], gravitational lensing by galaxy clusters [3], and the power spectrum of the cosmic microwave background [4]. However, the nature of this dark matter is still one of the most perplexing unsolved problems in cosmology and particle physics. This problem can potentially be explained by the presence of non-baryonic dark matter candidates such as axions and axion-like particles (ALPs). Axions [5] are pseudo-scalar bosons arising in the Peccei-Quinn mechanism proposed to solve the problem of charge-parity invariance of the strong interactions in quantum chromodynamics (QCD) [6]. While ALPs are similar particles often predicted by a variety of string-theoretic extensions to the standard model of particle physics [7]. Axions and ALPs have the same characteristics that are determined by their coupling with two photons. The main difference between them is that the coupling parameter for the QCD axions is directly related to the axion mass, however, this is not necessarily the case for the generic ALPs. These axions and ALPs are believed to be very light and weakly interacting with most of the standard model particles, see reference [8]. Because of these properties, it is suggested that the total content of the cold dark matter in the universe, or at least a portion of it, may well consist of axions and ALPs [9, 10, 11].

In recent years, the search for dark matter particles in the form of axions and ALPs has grown enormously, for simplicity we will use the term ALPs to refer to both axions and ALPs.

Most of the current search for direct detection of ALPs depends essentially on their coupling with photons via a two-photon vertex [12]. This coupling can allow for the conversion of ALPs into single photons $a \rightarrow \gamma$ through the Primakoff effect in the presence of an external magnetic field, see recent works [13, 14]. This coupling may also allow for the decay of ALPs into pairs of photons $a \rightarrow \gamma + \gamma$, see recent works [15, 16]. While the first process received more attention in the research, we are now focusing on deepening our understanding of the second process. In our previous work [15], we studied the stimulated decay of ALPs and the influence of plasma effects on this process. Then we compared the predicted fluxes produced from this process with the sensitivity of the Square Kilometer Array (SKA) and the MeerKAT radio telescopes. We found that the point source sensitivity of the MeerKAT telescope had very limited potential for probing the ALP coupling-mass parameter space. In this work, we study the possibility of using different taper scales as an effective tool to improve the limits that the MeerKAT telescope can put on the coupling parameter between ALPs and photons. This tapering approach has been used for indirect radio detection of dark matter in a previous work [17]. We find that the use of taper calculations is able to improve the MeerKAT limits on the ALP-photon coupling by about an order of magnitude.

The structure of this paper is as follows. In Sections 2, we briefly discuss the spontaneous and stimulated decay of ALPs into pairs of photons. Then, we discuss the sensitivity of the MeerKAT telescope and the use of the tapering approach to improving it in Section 3. Next, in Section 4, we check the capability of the MeerKAT telescope to put new limits on the coupling parameter between ALPs and photons. Finally, our conclusion is provided in Section 5.

2. Spontaneous and stimulated decay of ALPs

The fundamental process that describes the phenomenology of ALPs is the interaction between them and photons through the ALP-two-photon vertex. The Lagrangian equation that describes the electromagnetic field in interaction with the ALP field is given by [12]

$$\ell_{a\gamma} = -\frac{1}{4}g_{a\gamma}F_{\mu\nu}\tilde{F}^{\mu\nu}a = g_{a\gamma}\mathbf{E} \cdot \mathbf{B}a. \quad (1)$$

Here a is the ALP field, $F_{\mu\nu}$ is the electromagnetic field strength, $\tilde{F}^{\mu\nu}$ is its dual, and $g_{a\gamma}$ is the ALP-photon coupling parameter. While \mathbf{E} and \mathbf{B} represent the electric and magnetic fields respectively. The presence of the ALP-two-photon interaction vertex makes possible the spontaneous decay of an ALP with mass m_a into pair of photons, each with a frequency $\nu = m_a/4\pi$. The decay time of ALPs can be expressed as inverse of their decay rate in terms of the ALP mass and the ALP-photon coupling as in [18]

$$\tau_a \equiv \Gamma_{\text{pert}}^{-1} = \frac{64\pi}{m_a^3 g_{a\gamma}^2}. \quad (2)$$

For the typical QCD axion with mass $m_a \sim 10^{-6}$ eV and coupling with photons $g_{a\gamma} \sim 10^{-12}$ GeV⁻¹, the lifetime τ_a is about 1.32×10^{47} s. This lifetime for axions is large enough comparing to the current age of the universe 4.3×10^{17} s to say that this type of particle is very stable on the cosmological scale. This might be the main reason for not focusing on searching for a detectable signal produced from the spontaneous decay of ALPs in the literature. However, this is ignoring the fact that ALPs are bosons. They have very low mass and accordingly they may exist with very high occupation numbers forming a Bose-Einstein condensate with only short-range order. These condensates may thermalize due to their gravitational attraction and self-interactions to spatially localized clumps comprising the dark matter halos around galaxies [19, 20]. In the presence of background photon population with high occupation number f_γ , the stimulated decay of ALPs condensate is highly likely with an effective decay rate expressed as

$$\Gamma_{\text{eff}} = \Gamma_{\text{pert}}(1 + 2f_\gamma). \quad (3)$$

Such systems with very high occupation numbers are well described by a classical field approximation [21]. Using the classical equation of motion; the stimulated decay time of ALPs was calculated to be just about 10^{-7} s, which is dramatically small comparing to the spontaneous decay time. This is problematic because theoretically ALPs are expected to be left-over from the early universe and their very short lifetime implies that they must decay so rapidly. Therefore according to this scenario, ALPs must have vanished a long time ago, and we can not hope for any current observable signal to remain due to their stimulated decay. The expansion of the universe and the plasma effects slow down the decay rate of ALPs and explain the huge discrepancy between the classical and the standard calculations [22]. Considering that the mass range m_0 – m_1 (these masses were placeholders for the range allowed by the cosmic plasma) will be able to sustain large populations into the present epoch while undergoing stimulated decay [23], we estimate the radio emissions which can be produced from the stimulated decay of ALPs if they form the total dark matter content of galactic halos. Then, we compare the predicted fluxes with the sensitivity of the MeerKAT telescope in order to determine the region of the mass-coupling parameter space that is accessible to MeerKAT.

3. The MeerKAT radio telescope and the taper sensitivity calculations

The MeerKAT radio telescope is a precursor for the SKA system in South Africa which would be the most sensitive radio telescope ever upon its completion [24]. This project has the potential to produce a high-performing contribution to obtain new cosmological constraints from a large sky survey. This makes it the most aspirant radio telescope to detect the possible emissions produced from the stimulated decay of ALPs and probe their parameter space.

In our analysis, we determine the MeerKAT sensitivities via the Stimela [25] software package. This allows us to find the rms image noise after simulating MeerKAT observations with the NVSS source catalog as a sky model [26]. To do this, Stimela makes use of CASA [27] for observation simulation, RFIMasker¹ to mask out frequency channels with static interference, Meqtrees [28] for calibration and visibility simulation, and WSClean [29] for imaging (at robust weighting 1). All our sensitivities apply to the MeerKAT L-band (890 MHz to 1.65 GHz) and assumed a channel width of 1 MHz for the simulation. To improve the MeerKAT sensitivity we employ different taper scales on the visibilities. The use of a taper has been reported in [17] in ATCA observations of dwarf galaxies to probe WIMP dark matter. The calculations of the effect of tapering are drawn from [30] and make use of the Stimela package [25] to realistically simulate MeerKAT sensitivities. A UV taper acts to down-weight the contribution of long baselines to interferometric observations. The consequence of which is the reduction in the contribution of small-scale sources [31]. This is of great use in hunting for ALP emissions as they should be diffuse, emanating from an extended halo around the center of observed cosmic structures. Here we will examine the effect of the chosen taper scale on MeerKAT's sensitivity to ALP emissions.

4. Results and discussion

The stimulated decay of ALPs would lead to an exponential growth in the photon occupation number, and therefore we expect to produce a large flux of photons with a frequency of about half the ALP mass. Hence, we hunt for a signal that would appear as a narrow spectral line broadened by the ALPs velocity dispersion. The radio emissions per unit surface area can be given by the following expression

$$S_{\text{SB}} = \frac{\Gamma_{\text{eff}}}{4\pi} \frac{\Delta\nu}{\nu} \int_R^\infty \frac{\rho_a(r)}{\sqrt{r^2 - R^2}} dr. \quad (4)$$

Here the factor $\Delta\nu/\nu$ describes the effect of line broadening, ρ_a is the density of the dark matter halo, R is the radius at which we determine the surface brightness. In our analysis,

¹ <https://github.com/bennahugo/RFIMasker>

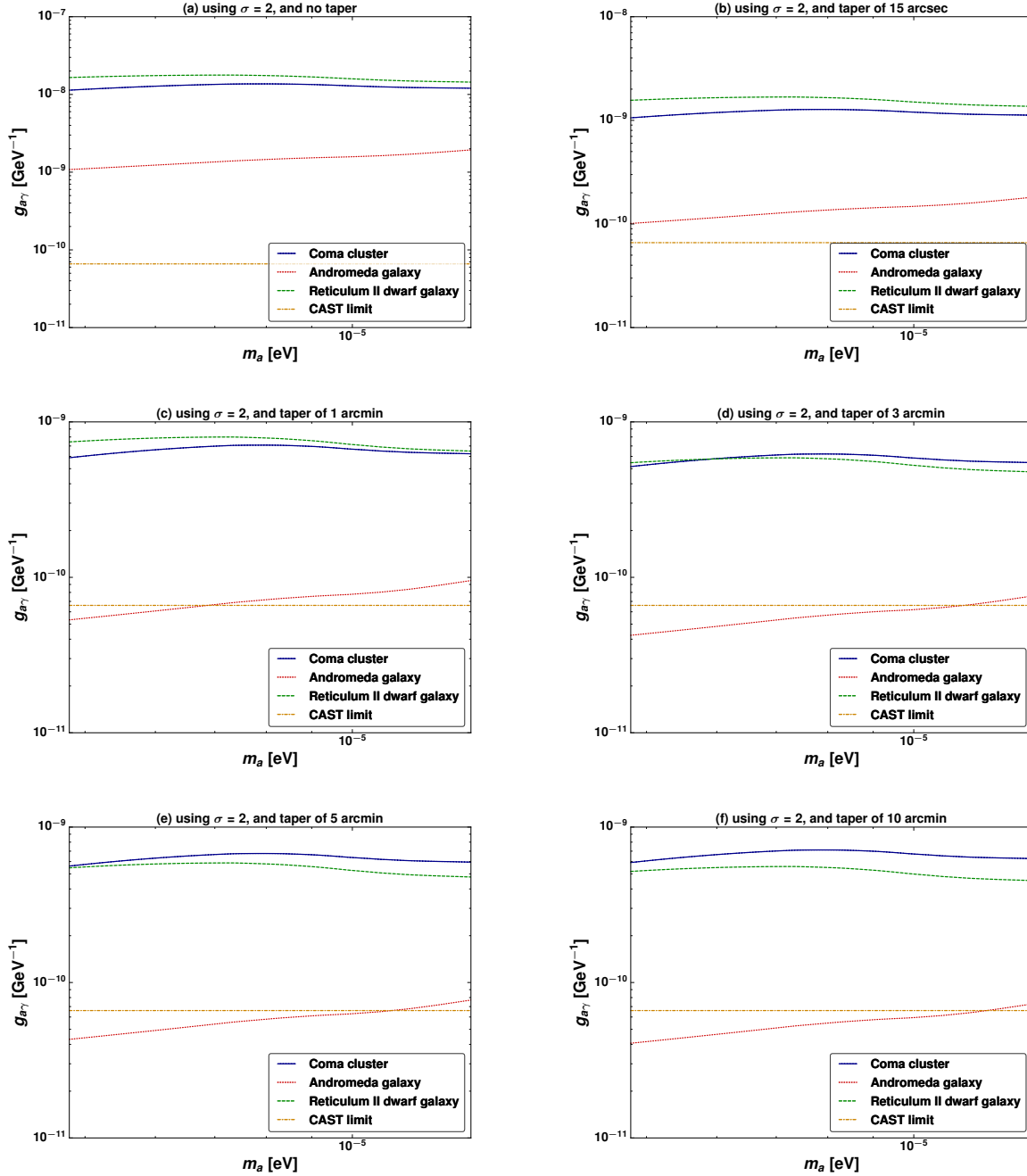


Figure 1: The potential non-observation constraints with the MeerKAT telescopes for 2σ confidence interval using halo surface brightness from ALP decay. In this plot, taper with different scales is employed on the visibilities. The CAST limit is taken from [32].

in order to determine the dark matter density in the galaxy halos, we use the NFW profile for the Coma cluster [33] as well as for the Andromeda galaxy [34] and we use the Einasto profile for the Reticulum II dwarf galaxy [17]. The MeerKAT is currently equipped with receivers that are sensitive to cover a frequency range from 890 MHz to 1.65 GHz [35]. This range of frequencies corresponds to photons produced from the decay of ALPs in the mass range 4.80×10^{-6} – 1.36×10^{-5} eV. With this range of ALPs masses, we find that the radio

Table 1: Summarizing the limits of the minimum ALP-photon coupling that can be probed by the MeerKAT radio telescope with the 2σ and 5σ confidence intervals within the MeerKAT sensitivity range for the ALP mass and using tapered sensitivities with different scales.

Taper scale	Minimum coupling g_{\min} with $\sigma = 2$	Minimum coupling g_{\min} with $\sigma = 5$
untapered	$1.09 \times 10^{-9} \text{ GeV}^{-1}$	$1.71 \times 10^{-9} \text{ GeV}^{-1}$
15 arcsec	$1.01 \times 10^{-10} \text{ GeV}^{-1}$	$1.60 \times 10^{-10} \text{ GeV}^{-1}$
1 arcmin	$5.33 \times 10^{-11} \text{ GeV}^{-1}$	$8.42 \times 10^{-11} \text{ GeV}^{-1}$
3 arcmin	$4.24 \times 10^{-11} \text{ GeV}^{-1}$	$6.70 \times 10^{-11} \text{ GeV}^{-1}$
5 arcmin	$4.31 \times 10^{-11} \text{ GeV}^{-1}$	$6.81 \times 10^{-11} \text{ GeV}^{-1}$
10 arcmin	$4.07 \times 10^{-11} \text{ GeV}^{-1}$	$6.43 \times 10^{-11} \text{ GeV}^{-1}$

emissions per unit surface are quite difficult to detect considering the point-source sensitivity of the MeerKAT telescope². In panel (a) of Figure 1, we illustrate the potential non-observation constraints with the MeerKAT telescope for 2σ confidence interval using point source sensitivities. This point source sensitivity produces weak limits on the values of the coupling strength $g_{a\gamma} \sim 1.09 \times 10^{-9} \text{ GeV}^{-1}$, comparing to the current limits put by the CAST experiment, i.e. $g_{a\gamma} \lesssim 6.6 \times 10^{-11} \text{ GeV}^{-1}$ [32], and the potential limits of the IAXO experiment, i.e. $g_{a\gamma} \lesssim \text{few} \times 10^{-11} \text{ GeV}^{-1}$ [36]. In panels (b) to (f) of Figure 1, we improve these results using tapering effects with different scales on the visibilities on the MeerKAT sensitivity with 2σ confidence interval. The results showing the taper effect are summarized in Table 1 using 2σ confidence interval as well as 5σ confidence interval. We remark that the use of the 2σ confidence interval allows us to estimate the exclusion limits in the event of non-observation, whereas 5σ confidence interval demonstrates the discovery potential. From the table, we find that the benefits of a taper saturate around scales of 1 arcminute, but provide a sensitivity gain of around an order of magnitude. The projected limits now are stronger as about $g_{a\gamma} \sim 4.09 \times 10^{-11} \text{ GeV}^{-1}$ in the most promising case, and in general overlapping now with the limits of the IAXO and CAST experiments.

It is worth noting here that future works might address more reasons responsible for boosting these radio emissions and that the MeerKAT telescope will also receive an upgrade of 20 additional dishes by 2023 which will enhance its sensitivity. Hence, the MeerKAT telescope will be able to play a more important role in parallel with other experiments such as CAST and IAXO experiments to rule out new regions of the parameter space of ALPs.

5. Conclusion

Axion-like particles can form the total abundance of the cold dark matter in the universe. In this work, we illustrated that the MeerKAT radio telescope will be capable of probing the parameter space of ALPs by hunting for the radio emissions produced from their stimulated decay. The potential non-observation limits from this study are superior to the current limits put by the CAST experiment and comparable to the expected limits that can be reached by the IAXO experiment in future. In particular, the MeerKAT sensitivity can reach lower limits of the ALP-photon coupling as strong as $4.07 \times 10^{-11} \text{ GeV}^{-1}$. To obtain these results we had to use a visibility taper to improve the limits on the minimum detectable coupling. The taper provides an improvement on the limits by around an order of magnitude across the studied

² For the MeerKAT sensitivity calculations, see the online sensitivity calculator at: <https://skaafrica.atlassian.net/wiki/spaces/ESDKB/pages/41091107/Sensitivity+calculators>.

mass ranges. Indeed, increasing the sensitivity reach of the next-generation radio telescopes such as the MeerKAT telescope on probing the ALP-photon coupling will allow it to play a strong complementary role to experiments like CAST and IAXO in exploring the ALP parameter space. This undoubtedly should have a lot of influence in our search for direct evidence of the presence of cold dark matter in the form of ALPs using the next-generation of radio telescopes which are expected to receive more attention within the coming years.

Acknowledgments

This work is based on the research supported by the South African Research Chairs Initiative of the Department of Science and Technology and National Research Foundation of South Africa (Grant No 77948). A. Ayad acknowledges support from the Department of Science and Innovation/National Research Foundation (DSI/NRF) Square Kilometre Array (SKA) post-graduate bursary initiative under the same Grant. G. Beck acknowledges support from a National Research Foundation of South Africa Thuthuka grant no. 117969. The authors would like also to offer special thanks to Prof. S. Colafrancesco, who, although no longer with us, continues to inspire by his example and dedication to the students he served over the course of his career.

References

- [1] Komatsu E, Smith K, Dunkley J *et al.* 2011 *Astrophys. J., Suppl. Ser.* **192** 18
- [2] Rubin V C and Ford Jr W K 1970 *Astrophys. J.* **159** 379
- [3] Blandford R and Narayan R 1992 *Annu. Rev. Astron. Astrophys.* **30** 311–58
- [4] Fixsen D, Cheng E, Gales J, Mather J C, Shafer R and Wright E 1996 *Astrophys. J.* **473** 576
- [5] Peccei R D and Quinn H R 1977 *Phys. Rev. Lett.* **38** 1440–1443
- [6] Peccei R D 2008 *The strong CP problem and axions* (Berlin: Springer) pp 3–17
- [7] Anselm A and Uraltsev N 1982 *Phys. Lett. B* **114** 39–41
- [8] Asztalos S J, Rosenberg L, van Bibber K, Sikivie P and Zioutas K 2006 *Annu. Rev. Nucl. Part. Sci.* **56** 293–326
- [9] Preskill J, Wise M and Wilczek F 1983 *Phys. Lett. B* **120** 127–32
- [10] Abbott L and Sikivie P 1983 *Phys. Lett. B* **120** 133–6
- [11] Dine M and Fischler W 1983 *Phys. Lett. B* **120** 137–41
- [12] Raffelt G and Stodolsky L 1988 *Phys. Rev. D* **37** 1237
- [13] Ayad A and Beck G 2020 *J. Cosmol. Astropart. Phys.* **2020** 055
- [14] Ayad A and Beck G 2019 *arXiv preprint arXiv:1911.10075*
- [15] Ayad A and Beck G 2020 *arXiv preprint arXiv:2010.05773*
- [16] Ayad A and Beck G 2020 *arXiv preprint arXiv:2007.14262*
- [17] Regis M, Richter L and Colafrancesco S 2017 *J. Cosmol. Astropart. Phys.* **2017** 025
- [18] Kelley K and Quinn P 2017 *Astrophys. J. Lett.* **845** L4
- [19] Sikivie P and Yang Q 2009 *Phys. Rev. Lett.* **103** 111301
- [20] Hertzberg M and Schiappacasse E 2018 *J. Cosmol. Astropart. Phys.* **2018** 028
- [21] Guth A, Hertzberg M and Prescod-Weinstein C 2015 *Phys. Rev. D* **92** 103513
- [22] Alonso-Álvarez G, Gupta R, Jaeckel J and Spannowsky M 2020 *J. Cosmol. Astropart. Phys.* **2020** 052
- [23] Madau P and Dickinson M 2014 *Annu. Rev. Astron. Astrophys.* **52** 415–86
- [24] Booth R and Jonas J 2012 *African Skies* **16** 101
- [25] Makhathini S 2018 *Advanced radio interferometric simulation and data reduction techniques* Ph.D. thesis
- [26] Condon J, Cotton W, Greisen E, Yin Q, Perley R, Taylor G and Broderick J 1998 *Astron. J.* **115** 1693
- [27] McMullin J, Waters B, Schiebel D, Young W and Golap K 2007 *Astronomical data analysis software and systems XVI* vol 376 p 127
- [28] Noordam J and Smirnov O 2010 *Astron. Astrophys.* **524** A61
- [29] Offringa A, McKinley B, Hurley-Walker N *et al.* 2014 *Mon. Notices Royal Astron. Soc.* **444** 606–19
- [30] Beck G and Makhathini S in prep Just a meerkat, or a dark matter machine?
- [31] Wilson T 2011 *Planets, Stars and Stellar Systems* **2** 283–323
- [32] Anastassopoulos V, Aune S, Barth K *et al.* 2017 *Nat. Phys.* **13** 584
- [33] Lokas E L and Mamon G A 2003 *Mon. Notices Royal Astron. Soc.* **343** 401–12
- [34] Tamm A, Tempel E, Tenjes P, Tihhonova O and Tuvikene T 2012 *Astron. Astrophys.* **546** A4
- [35] Braun R, Bonaldi A, Bourke T, Keane E and Wagg J 2019 *arXiv preprint arXiv:1912.12699*
- [36] Armengaud E, Attié D, Basso S *et al.* 2019 *J. Cosmol. Astropart. Phys.* **2019** 047

Dark coupling: cosmological implications of interacting dark energy and dark matter fluids

M A van der Westhuizen¹, A Abebe²

¹Centre for Space Research, North-West University, Potchefstroom 2520, South Africa

² Centre for Space Research, North-West University, Mahikeng 2735, South Africa

E-mail: marcelvdw007@gmail.com

Abstract. In this study, cosmological models are considered where dark matter and dark energy are coupled and may have non-gravitational interactions with each other. These dark energy couplings are introduced to potentially alleviate both the Hubble tension and the cosmic coincidence problem (regarding the current observed ratio of dark matter to dark energy today). Assuming two different linear dark energy couplings, the conservation and Friedmann equations are used to predict how these couplings affect crucial events in the expansion history of the universe. These events include the big bang and cosmic acceleration, as well as the radiation-matter and matter-dark energy equality. These results are compared with the standard uncoupled Λ CDM model where dark energy is assumed to be a cosmological constant. Cosmological parameters for this study are obtained from Type-Ia Supernovae data using a previously developed Markov Chain Monte-Carlo (MCMC) simulation.

1. Problems with the Λ CDM model

The expansion of the universe has thus far been well described by the Λ CDM model, where the energy budget of the universe is divided between $\approx 5\%$ baryonic matter (standard model particles), $\approx 25\%$ non-baryonic cold dark matter (which keeps galaxies from flying apart) and $\approx 70\%$ dark energy in the form of the cosmological constant Λ (which explains late-time accelerated expansion). This model has proven to be very successful [1], but problems with the Λ CDM model remain, which include:

The Cosmological Constant Problem or vacuum catastrophe, which refers to the measured energy density of the vacuum being over 120 orders of magnitude smaller than the theoretical prediction. This has been referred to as the worst prediction in the history of physics and casts doubt on dark energy being a cosmological constant, motivating research into alternative dark energy models [2].

The Cosmic Coincidence Problem, which alludes to the dark matter and dark energy densities having the same order of magnitude at the present moment of cosmic history, while differing with many orders of magnitude in the past and predicted future [3].

The Hubble Tension, which concerns the 4.4σ level difference between values of the Hubble constant H_0 as measured from the Cosmic Microwave Background (CMB) versus the value obtained from Type Ia Supernovae using a calibrated local distance ladder [4].

2. Dark coupling models

These problems motivate research beyond the Λ CDM model. One possible approach is to investigate cosmological models in which there are non-gravitational interactions between the dark sectors of the universe. This allows the two dark sectors to exchange energy (and/or momentum) while dark matter and dark energy are not separately conserved, but the energy (and

momentum) of the total dark sector is conserved. This coupling between dark matter and dark energy modifies the continuity equations into [4, 5, 6, 7]:

$$\dot{\rho}_{\text{dm}} + 3H\rho_{\text{dm}} = Q \quad ; \quad \dot{\rho}_{\text{de}} + 3H\rho_{\text{de}}(1 + \omega) = -Q, \quad (1)$$

where $H = (\dot{a}/a)$ is the Hubble parameter, with a the scale factor which denotes the relative size of the universe. $\rho_{\text{dm/de}}$ is the dark matter/dark energy density, ω is the equation of state of dark energy ($\omega_{\text{dm}} = 0$ since dark matter is assumed to be pressureless) and Q is the rate of energy exchange, which defines the direction of energy flow between the dark sectors such that:

$$Q = \begin{cases} > 0 & \text{Dark Energy} \rightarrow \text{Dark Matter} \\ < 0 & \text{Dark Matter} \rightarrow \text{Dark Energy} \\ = 0 & \text{No interaction (\Lambda CDM case)} \end{cases} \quad (2)$$

The behaviour of coupled models may be understood by how the interaction affects the effective equations of state, relative to the uncoupled background equations ($Q = 0$) in (1) such that:

$$\omega_{\text{dm}}^{\text{eff}} = -\frac{Q}{3H\rho_{\text{dm}}} \quad ; \quad \omega_{\text{de}}^{\text{eff}} = \omega_{\text{de}} + \frac{Q}{3H\rho_{\text{de}}}. \quad (3)$$

Thus, the effects of an interaction may be understood to imply that if:

$$\begin{aligned} Q > 0 &\rightarrow \begin{cases} \omega_{\text{dm}}^{\text{eff}} < 0 & \text{Dark matter redshifts slower (less DM in past)} \\ \omega_{\text{de}}^{\text{eff}} > \omega_{\text{de}} & \text{Dark energy has less accelerating pressure (older universe)} \end{cases} \\ Q < 0 &\rightarrow \begin{cases} \omega_{\text{dm}}^{\text{eff}} > 0 & \text{Dark matter redshifts faster (more DM in past)} \\ \omega_{\text{de}}^{\text{eff}} < \omega_{\text{de}} & \text{Dark energy has more accelerating pressure (younger universe)} \end{cases} \end{aligned}$$

When $Q = 0$, the effective equations of state reduce back to the case for the Λ CDM model, where dark matter is pressureless ($\omega_{\text{dm}} = 0$) and dark energy has a constant negative pressure.

Since there is currently no fundamental theory for these couplings, they are purely phenomenological and must be tested against observations. Two models will be considered which have interactions proportional to the Hubble parameter [4, 5, 6, 7]. Solving the conservation equations (1) for both models shows how the energy densities evolve, such that:

Model 1: $Q_1 = \delta H \rho_{\text{dm}}$

$$\rho_{\text{dm}} = \rho_{(\text{dm},0)} a^{(\delta-3)} \quad (4)$$

$$\rho_{\text{de}} = \rho_{(\text{de},0)} a^{-3(1+\omega_{\text{de}})} + \rho_{(\text{dm},0)} \frac{\delta}{\delta + 3\omega} \left[a^{-3\omega} - a^{\delta} \right] a^{-3}, \quad (5)$$

with $\left(0 < \delta < -\frac{3\omega}{(1+r_0)}\right)$ to ensure $\rho_{\text{dm/de}} > 0$ throughout evolution.

Model 2: $Q_2 = \delta H \rho_{\text{de}}$

$$\rho_{\text{dm}} = \rho_{(\text{dm},0)} a^{-3} + \rho_{(\text{de},0)} \frac{\delta}{\delta + 3\omega} \left[1 - a^{-(\delta+3\omega)} \right] a^{-3} \quad (6)$$

$$\rho_{\text{de}} = \rho_{(\text{de},0)} a^{-(\delta+3\omega+3)}, \quad (7)$$

with $\left(0 < \delta < -\frac{3\omega}{(1+1/r_0)}\right)$ to ensure $\rho_{\text{dm/de}} > 0$ throughout evolution.

Here $r_0 = (\rho_{(\text{dm},0)}/\rho_{(\text{de},0)})$ is the ratio of dark matter to dark energy today; and δ is a dimensionless coupling constant which determines the strength of the interaction between dark matter and dark energy. Furthermore, when $Q = 0$, both models reduce to the Λ CDM case where $\rho_{\text{dm}} \propto a^{-3}$ and $\rho_{\text{de}} = \text{constant}$.

Negative couplings ($\delta < 0$) are often used in the literature for these models [4, 6, 7], which are problematic since this leads to negative energy densities in the future. Therefore it is very important to take note of these positive energy density conditions for δ , as they ensure that the energy density for both dark matter and dark energy is not only positive for the past expansion history, but for the future as well.

3. Cosmological parameters

The present cosmological parameters for these models are obtained from a data set of 359 low and intermediate redshift Type-Ia Supernovae (obtained from the SDSSII/SNLS2 Joint Light-curve Analysis (JLA)). This data is used with a previously developed Markov Chain Monte-Carlo (MCMC) simulation for a flat FRLW universe to obtain cosmological parameters for each model from its corresponding Friedmann equation (15). The contribution of $\Omega_{(\text{rad},0)}$ on the expansion and the MCMC model is negligible, but has been chosen as $\Omega_{(\text{rad},0)} = 9 \times 10^{-5} = 9\text{e-}5$ (notation used throughout) for further calculations [1]. Details of this MCMC model may be found in [8, 9].

The limit $\omega > -1$ has been imposed for all models, while applying the positive energy conditions ($0 < \delta < -\frac{3\omega}{(1+r_0)}$) and ($0 < \delta < -\frac{3\omega}{(1+1/r_0)}$) for Q_1 and Q_2 respectively. The priors of these parameters are the results from the Λ CDM case. This gives the following results:

Table 1: Cosmological parameters from type Ia Supernovae

Model	$\Omega_{(\text{dm},0)}$	$\Omega_{(\text{bm},0)}$	H_0	ω	δ
Λ CDM	$0.213^{+0.037}_{-0.037}$	$0.055^{+0.031}_{-0.030}$	$69.7^{+0.5}_{-0.5}$	$-1.000^{+0.000}_{-0.000}$	$0.000^{+0.000}_{-0.000}$
$Q_1 = \delta H \rho_{\text{dm}}$	$0.234^{+0.036}_{-0.024}$	$0.043^{+0.022}_{-0.016}$	$68.0^{+0.9}_{-0.9}$	$-0.949^{+0.057}_{-0.036}$	$0.296^{+0.146}_{-0.184}$
$Q_2 = \delta H \rho_{\text{de}}$	$0.232^{+0.031}_{-0.022}$	$0.044^{+0.021}_{-0.017}$	$69.4^{+0.5}_{-0.5}$	$-0.948^{+0.059}_{-0.037}$	$0.257^{+0.161}_{-0.167}$

with $\Omega_{(\text{de},0)} = 1 - \Omega_{(\text{dm},0)} - \Omega_{(\text{bm},0)}$ since a spatially flat universe is assumed. Here it can be seen that H_0 is slightly lower and closer to the CMB value for both Q_1 and Q_2 , which slightly alleviates the Hubble Tension [4]. It should be noted that since the conditions to avoid early time instabilities [6] have not yet been considered, these results should be taken as preliminary.

4. Evolution of energy densities

Universe models will be considered which contain radiation (rad), baryons (bm), dark matter (dm) and dark energy (de). In order to avoid fifth force constraints, it is assumed that radiation and baryons are separately conserved and uncoupled [5] such that:

$$\dot{\rho}_{\text{rad}} + 3H\rho_{\text{rad}}(1 + \omega_{\text{rad}}) = 0 \quad ; \quad \dot{\rho}_{\text{bm}} + 3H\rho_{\text{bm}}(1 + \omega_{\text{bm}}) = 0, \quad (8)$$

where $\omega_{\text{rad}} = 1/3$; $\omega_{\text{bm}} = 0$. Solving these equations, it is found that radiation evolves as $\rho_{\text{rad}} = \rho_{(\text{rad},0)}a^{-4}$ and baryonic matter as $\rho_{\text{bm}} = \rho_{(\text{bm},0)}a^{-3}$. If the density parameter $\Omega = \rho/\rho_c$ (where $\rho_c = (3H^2/8\pi G)$ and G is the universal gravitational constant) is introduced, the corresponding density parameter for each component may be obtained. This may then be

expressed in terms of redshift z through the transformation $1/a = (1+z)$. Therefore the various energy densities ρ_i are transformed into the following density parameters Ω_i :

$$\Omega_{\text{rad}} = \frac{H_0^2}{H^2} \Omega_{(\text{rad},0)} (1+z)^4 \quad (9)$$

$$\Omega_{\text{bm}} = \frac{H_0^2}{H^2} \Omega_{(\text{bm},0)} (1+z)^3 \quad (10)$$

$$Q_1 : \Omega_{\text{dm}} = \frac{H_0^2}{H^2} \Omega_{(\text{dm},0)} (1+z)^{-(\delta-3)} \quad (11)$$

$$\Omega_{\text{de}} = \frac{H_0^2}{H^2} \left[\Omega_{(\text{de},0)} (1+z)^{3(1+\omega)} + \Omega_{(\text{dm},0)} \frac{\delta}{\delta + 3\omega} \left[(1+z)^{3\omega} - (1+z)^{-\delta} \right] (1+z)^3 \right] \quad (12)$$

$$Q_2 : \Omega_{\text{dm}} = \frac{H_0^2}{H^2} \left[\Omega_{(\text{dm},0)} (1+z)^3 + \Omega_{(\text{de},0)} \frac{\delta}{\delta + 3\omega} \left[1 - (1+z)^{(\delta+3\omega)} \right] (1+z)^3 \right] \quad (13)$$

$$\Omega_{\text{de}} = \frac{H_0^2}{H^2} \Omega_{(\text{de},0)} (1+z)^{(\delta+3\omega+3)}. \quad (14)$$

The Λ CDM equations for Ω_{dm} , Ω_{de} are obtained by setting the interaction strength $\delta = 0$ in equations (11) - (14). The evolution of these energy densities may be seen in Figure 1:

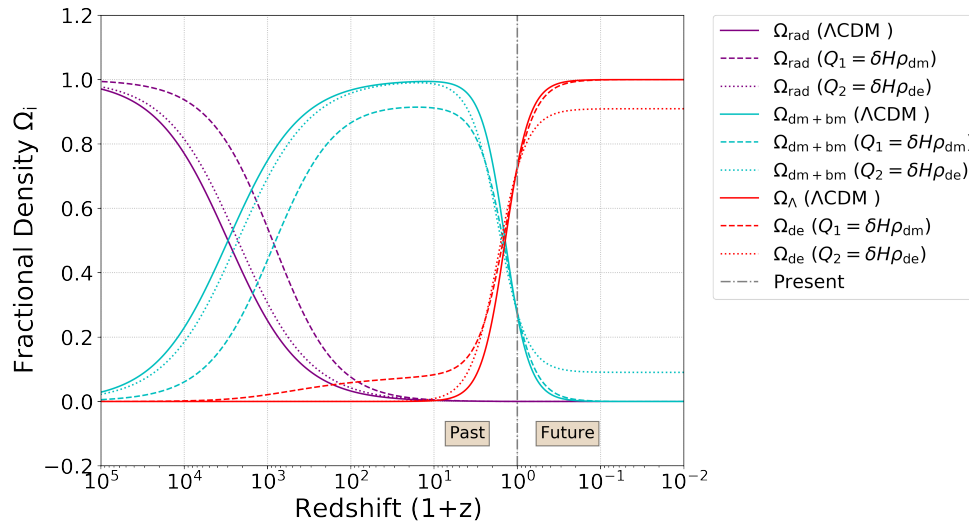


Figure 1: Fractional energy densities vs. redshift.

In all cases, there is an early time radiation domination followed by matter domination, which finally gives way to the the current era of dark energy domination. Here it may be seen that since $\delta > 0 \rightarrow Q > 0$ for both coupled models, that there is less dark matter in the past and that the matter-radiation equality therefore happened later (smaller redshift) in cosmic evolution, while the matter-dark energy equality happens earlier (larger redshift). The energy densities ρ_i (in Joule.m^{-3}) throughout cosmic evolution can be seen in Figure 2. These results are summarised in Tables 2, 3 and 4.

The previously mentioned cosmic coincidence problem may now be addressed by considering how the ratio of dark matter to dark energy $r = (\rho_{\text{dm}}/\rho_{\text{de}})$ evolves with redshift z in Figure 3. Here it can clearly be seen that for the Λ CDM case, the current value of $r_0 \approx (\frac{3}{7})$ seems fine tuned and coincidental in comparison to Q_1 and Q_2 , where r converges and becomes constant in the past and the future respectively. Thus, alleviating the cosmic coincidence problem [3].

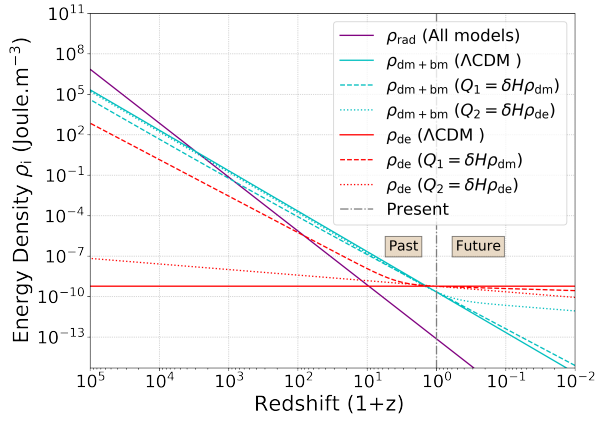


Figure 2: Energy densities vs redshift.

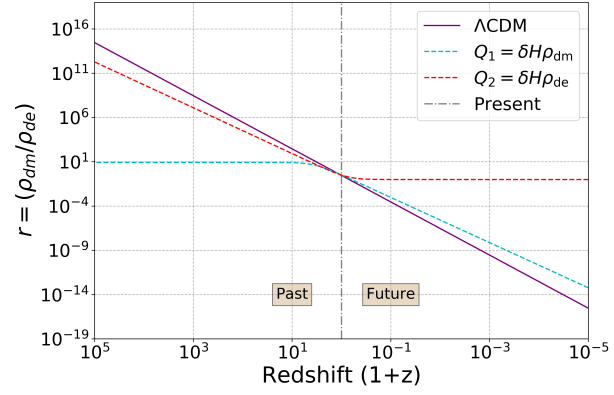


Figure 3: Cosmic Coincidence Problem.

5. Expansion history of universe models

The expansion of these universe models may be described by the Friedmann equation for a flat FLRW universe (15) and the deceleration parameter q (16), with the constituents (9)-(14):

$$\left(\frac{\dot{a}}{a}\right)^2 = \frac{8\pi G}{3} (\rho_{\text{rad}} + \rho_{\text{bm}} + \rho_{\text{dm}} + \rho_{\text{de}}) , \quad (15)$$

$$q = \Omega_{\text{rad}} + \frac{1}{2} (\Omega_{\text{dm}} + \Omega_{\text{bm}}) + \frac{1}{2} \Omega_{\text{de}} (1 + 3\omega) . \quad (16)$$

The Friedmann equation may be numerically integrated, which alongside the deceleration parameter q yields the total expansion histories of the universe models:

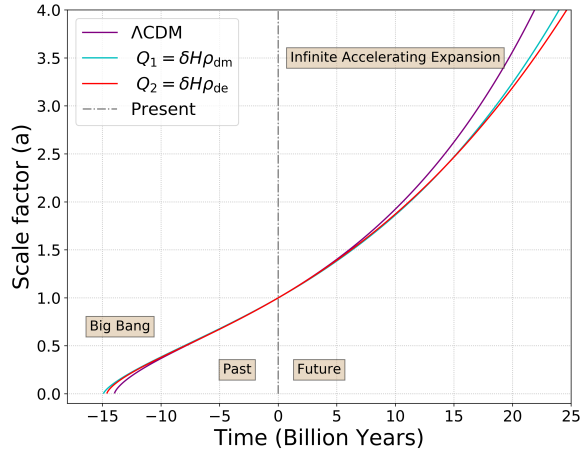


Figure 4: Expansion history of universe models.

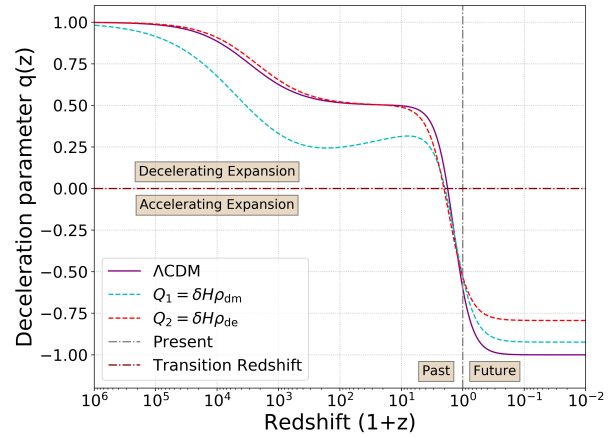


Figure 5: Deceleration parameter vs redshift.

These models all start with a big bang singularity (at $a = 0$) which leads to a period of decelerating expansion during the radiation and matter dominating epochs (the latter starting when $\rho_{\text{rad}} = \rho_{\text{dm+bm}}$), followed by an infinite accelerating expansion (starting at $q = 0$ when $\rho_{\text{dm+bm}} \approx 2\rho_{\text{de}}$) and a final era of dark energy domination (starting when $\rho_{\text{dm+bm}} = \rho_{\text{de}}$). Tables 2, 3 and 4 show the redshift z , time and energy densities (ρ_{rad} , $\rho_{\text{dm+bm}}$ and ρ_{de}) at the start of these crucial events in cosmic history for each of the models. It should be noted that cosmological parameters from Table 1 are used for the Λ CDM model instead of Planck CMB parameters [1].

Table 2: Λ CDM (Supernovae data from [8])

Event	Redshift z	Time (Gyr)	ρ_{rad}	$\rho_{\text{dm+bm}}$	ρ_{de} (J/m ³)
Big bang singularity	∞	13.96	∞	∞	∞
Radiation-matter equality	2976	13.63	5.7	5.7	5.9e-10
Cosmic acceleration ($q = 0$)	0.76	6.76	7.0e-13	1.2e-9	5.9e-10
Matter-dark energy equality	0.40	4.32	2.8e-13	5.9e-10	5.9e-10

Table 3: $Q_1 = \delta H \rho_{\text{dm}}$

Event	Redshift z	Time (Gyr)	ρ_{rad}	$\rho_{\text{dm+bm}}$	ρ_{de} (J/m ³)
Big bang singularity	∞	14.90	∞	∞	∞
Radiation-matter equality	831.97	14.90	3.5e-2	3.5e-2	1.7e-3
Cosmic acceleration ($q = 0$)	0.94	7.79	1.0e-12	1.4e-9	7.6e-10
Matter-dark energy equality	0.48	5.07	3.5e-13	6.6e-10	6.6e-10

Table 4: $Q_2 = \delta H \rho_{\text{de}}$

Event	Redshift z	Time (Gyr)	ρ_{rad}	$\rho_{\text{dm+bm}}$	ρ_{de} (J/m ³)
Big bang singularity	∞	14.61	∞	∞	∞
Radiation-matter equality	2266	14.61	1.9	1.9	1.4e-8
Cosmic acceleration ($q = 0$)	1.02	8.05	1.2e-12	1.4e-9	7.8e-10
Matter-dark energy equality	0.57	5.60	4.4e-13	7.0e-10	7.0e-10

6. Conclusions

Interacting dark energy models may alleviate the cosmic coincidence problem by stabilising the ratio of dark matter to dark energy in both the past and future (Figure 3). These models also predict a slightly lower value for H_0 , thereby showing potential as a candidate for relieving the Hubble tension (Table 1). This lower H_0 value leads to crucial events in cosmic history occurring longer ago with slightly different conditions relative to the Λ CDM model (Tables 2, 3 and 4). These results only hold for energy flow from dark energy to dark matter ($\delta > 0$) since flow from dark matter to dark energy ($\delta < 0$) causes negative energy densities. Finally, since early time instability conditions [5, 6] and other data constraints from the CMB and large-scale structure [1, 4, 7] have not yet been considered, these results should be seen as preliminary.

Acknowledgements

MvdW and AA acknowledges funding for this work through the National Astrophysics and Space Science Program (NASSP) and the National Research Foundation (with grant number 112131).

References

- [1] Planck Collaboration 2018 *Astron. Astrophys.* **641** A6
- [2] Weinberg S 1989 *Rev. Mod. Phys.* **61** 1-23
- [3] del Campo S, Herrera R and Pavon D 2009 *J. Cosmol. Astropart. Phys.* **2009** 020
- [4] Di Valentino E, Melchiorri A, Mena O and Vagnozzi S 2020 *Phys. Dark Universe* **30** 100666
- [5] Valiviita J, Majerotto E and Maartens R 2009 *J. Cosmol. Astropart. Phys.* **2008** 020
- [6] Gavela M B, Hernandez D et al. 2009 *J. Cosmol. Astropart. Phys.* **07** 034
- [7] Lucca M, Hooper D C 2020 *Phys. Rev. D* **102** 123502
- [8] Hough R T 2020 *Constraining modified gravity models with cosmological data* Master's thesis North-West University
- [9] Hough R T, Abebe A and Ferreira S E S 2020 *Eur. Phys. J. C* **80** 787

The Effect of Dark Matter During the Cosmic Dawn

M Kgoadi¹ and G Beck¹

¹ Department of Physics, University of the Witwatersrand, Private Bag 3, WITS-2050, Johannesburg, South Africa

E-mail: kgoadimpho16@gmail.com; geoffrey.beck@wits.ac.za

Abstract. The global 21 cm signal provides rich information about the thermal and ionization history of the universe. In this work we explore how the inclusion of annihilating dark matter, specifically the Weakly Interacting Massive Particle (WIMPs) alters the global signal. To do this, we study three different WIMP masses with each having maximum allowed annihilation cross-section according to the WMAP7 observations, motivated by previous studies on this work. In our model we use updated efficiency functions as well as up-to-date temperature and ionization histories. Our model shows that DM has reduced heating effects during the cosmic dark ages and induces an absorption trough at $z \sim 25$, in distinct contrast to previous works whose results were based on earlier energy deposition efficiency models which are now believed to be substantially flawed.

1. Introduction

Dark matter (DM) forms a fundamental part of the current standard model of the Universe known as the Λ -Cold Dark Matter (Λ CDM). In this theory, about 5 % of the energy content of the Universe is made of baryonic matter, 68 % is in the form of Dark Energy and dark matter only accounts for 27 % [1]. Although the nature of DM still remains unknown, there has been numerous observations that have indirectly confirmed its existence [2, 3, 4, 5]. In this work, we focus our attention on the global 21 cm background, which is one of many ways we could constrain the nature of DM. In this scenario, DM annihilation and decay products, through the injection of high energy photons into the intergalactic medium (IGM) could heat and ionize the gas thus leaving a mark on the global signal which could be observed directly [6, 7].

In this paper we explore, in particular, the effects of WIMPs on the global 21 cm signal, with specific focus on three candidates motivated by Ref.[8]. These are 10 GeV, 200 GeV and 1 TeV WIMPs annihilating via the $b\bar{b}$ channel and have the annihilation cross-section that is compatible with the CMB observations. To get the full scope of the DM impact on the global signal, it is very important look into the details of the energy deposition from DM annihilations. Earlier studies found that a relatively small fraction of the energy deposited by DM is absorbed by the IGM and goes to ionization and heating [9]. However, recent studies have shown that DM annihilation as WIMPs can have substantial changes from the fiducial scenario with some models having twice as much heating effects as the baseline [8]. This ultimately comes down to the modelling of the energy deposition mechanisms and specifically the fraction of energy from DM that is released to or absorbed by the IGM.

We make use of a publicly available python package called Darkhistory to compute the effects of DM on the temperature and ionization history of the Universe [10]. Darkhistory allows

for fast and accurate computation of the energy deposition efficiency function $f_c(z)$ into any deposition channel $c = (\text{excitation, heating, ionization})$. On top of this, computing the efficiency functions with Darkhistory allows us to perform consistent calculations of the ionization and temperature histories with both exotic energy injection processes and reionization. Previous studies that have investigated the effects of DM annihilation/decay on the ionization history during the cosmic dark ages and recombination generally assumed that the injected energy from DM annihilation/decay is deposited with some redshift-independent efficiency [7, 11, 12]. It is worth noting that the calculations of these efficiency functions are very involved and we direct the readers to Refs.[10, 13, 14] for a careful and detailed analysis. To summarize, Darkhistory keeps track of the amount of the total energy from low and high energy photons and electrons deposited into the channel c . This allows the energy deposition fraction $f_c(z)$ to be calculated by normalizing the total energy deposited into the channel within a certain redshift step $1+z$ by the total injected energy. The annihilation byproducts will then transfer their energy into ionization and excitation of atoms, heating of the IGM and free-streaming photons to be added to the CMB continuum. The improved $f_c(z, \mathbf{x})$ functions from Darkhistory are mostly due to the fact that they are calculated with the full z and \mathbf{x} -dependency which was previously not done, where \mathbf{x} is the ionization fractions of the relevant species in the gas denoted as $\mathbf{x} \equiv (x_{\text{HII}}, x_{\text{HeII}}, x_{\text{HeIII}})$. This work will not indulge in the technical details and derivations of the efficiency functions but will present the equations and discuss the implications.

The structure of this paper is as follows: in section 2 we give a brief description of the 21 cm physics, in section 3 we explain in detail the DM effects on the IGM with basic equations provided. The results are provided and discussed in section 4 and we finally conclude and discuss future work in section 5.

2. 21 cm physics

The redshifted 21 cm line of hydrogen is a great probe of the epoch of reionization, this line is caused by the hyperfine transition between the singlet and triplet levels of the hydrogen ground state. The global signal is commonly described in terms of the brightness temperature and it is given by the following equation [15]

$$\delta T_b = 23 x_{\text{HI}}(z) \left(\frac{0.15}{\Omega_m} \right)^{1/2} \left(\frac{\Omega_b h}{0.02} \right) \left(\frac{1+z}{10} \right)^{1/2} \left[1 - \frac{T_R(z)}{T_S(z)} \right] \text{ mK}, \quad (1)$$

where x_{HI} is the neutral fraction of the gas, Ω_m is the matter energy density and Ω_b is the baryon energy density. h is the hubble parameter and $T_R(z)$ is the radiation temperature, typically assumed to be the CMB. $T_S(z)$ is the spin temperature and is given by the ratio of the number density of hydrogen atoms in the higher energy triplet state to the lower energy singlet state which is expressed as,

$$\frac{n_1}{n_0} = \frac{g_1}{g_0} e^{-T_*/T_S}, \quad (2)$$

where n_0 and n_1 are the number densities of electrons in the singlet and triplet states respectively. The statistical weights of the energy levels are given by $g_1 = 3$ and $g_0 = 1$. $T_* = 0.0681$ K is the temperature associated with the 21 cm wavelength. In order for a signal to be detected, the spin temperature needs to deviate from the radiation background. There are three main ways that T_S can be determined; via the absorption or emission of 21 cm photons against the CMB, through resonant scattering of Lyman- α photons which cause downward transitions from the triplet state to the singlet state via the Wouthuysen-Field effect and lastly, through the collisions with electrons and other hydrogen atoms (See [16] for an extensive overview). The spin temperature at these limits can be written as [17]

$$T_S^{-1} = \frac{T_{\text{CMB}}^{-1} + x_\alpha T_\alpha^{-1} + x_c T_K^{-1}}{1 + x_\alpha + x_c}, \quad (3)$$

where T_{CMB} is the background temperature, T_α is the color temperature associated with the Lyman- α radiation field and is closely coupled to the kinetic temperature T_K [18]. The coupling coefficients for collisions and scattering of Lyman- α photons are given by x_c and x_α respectively and are given by the following expressions:

$$x_\alpha = \frac{16\pi\sigma_\alpha T_* J_\alpha}{27A_{10}T_k E_\alpha}, \quad (4)$$

$$x_c = \frac{(k_{10}n_{\text{HI}} + n_e\gamma_e)T_*}{A_{10}T_k}, \quad (5)$$

where $A_{10} = 2.85 \times 10^{-15} \text{ s}^{-1}$ is the coefficient for spontaneous emission of the 21 cm line, J_α is the Lyman- α emissivity, k_{10} is the tabulated temperature data from [19]. The coupling coefficients determine whether collisions or Lyman- α photons affect the signal and provides information about how strongly coupled is the spin temperature to the gas temperature. This means that the signal will appear as absorption or emission if either the collisions or the Lyman- α radiation couples the spin temperature to the kinetic temperature. The equation that has a contribution from DM annihilation is given by,

$$J_{\alpha,\text{DM}} = \frac{hcn_{\text{H}}^2(z)}{4\pi H(z)} f_{c,\alpha} \frac{E_{\text{DM}}}{n_{\text{H}}E_\alpha}, \quad (6)$$

where $f_{c,\alpha}$ is the fraction of annihilation energy that goes into Lyman- α excitation, n_{H} represents the hydrogen atom number density, E_α is the Lyman- α excitation energy and E_{DM} is the energy rate from DM annihilation. The next section will address the significance of the efficiency fractions in the context of energy deposition by DM into the IGM.

3. Exotic energy injection on the IGM

Next, we shift our focus on the implications of DM annihilations on the thermal and ionization evolution of the IGM, which directly determines the changes of the global 21 cm signal. It is thought that DM annihilation in the early Universe can act as a source of X-rays which lead to ionization, heating and other processes [20]. DM annihilation rate scales as the square of the density, n_{DM}^2 , this indicates that it rises with the onset of structure formation and that the collapse of DM into halos can have a significant energy injection in the process of reionization. The rate of energy injection from DM annihilation or decay is given by [10]

$$\left(\frac{dE}{dVdt} \right)^{\text{inj}} = \begin{cases} \rho_{\chi,0}^2 (1+z)^6 \langle \sigma v \rangle / m_\chi, & \text{annihilation,} \\ \rho_{\chi,0} (1+z)^3 / \tau, & \text{decay,} \end{cases} \quad (7)$$

where m_χ is the mass of DM, $\langle \sigma v \rangle$ is the velocity averaged cross-section, τ is the decay lifetime and $\rho_{\chi,0}$ is the mass density of DM today. Annihilation and decay products have the potential to alter the levels of ionization, can heat up neutral gas and increase the production of Lyman- α photons. The evolution of the free electron fraction and the matter temperature is given by [11]

$$-\frac{dx_e}{dz} = \frac{1}{H(z)(1+z)} [R_s(z) - I_s(z) - I_x(z)], \quad (8)$$

and

$$(1+z)\frac{dT_k}{dz} = 2T_k - \kappa_s(z) - \kappa_x(z), \quad (9)$$

where R_s , I_s are the standard recombination and ionization rates. The standard heating is given by κ_s . I_x and κ_x are the dark matter contributions to the ionization and heating. The ionization rate I_x and heating κ_x from DM are given by

$$I_x(z) = f_{c,\text{ion}}(z) \frac{m_{\text{DM}}}{E_0} n_{\text{DM}}^2 \langle \sigma V \rangle, \quad (10)$$

and

$$\kappa_x(z) = \frac{f_{c,\text{heat}}(z) m_{\text{DM}} n_{\text{DM}}^2 \langle \sigma V \rangle}{3 k_B H(z) (1 + f_{\text{He}} + x_e(z))}, \quad (11)$$

where m_{DM} is the mass of the DM particle, $E_0 = 13.6$ eV is the threshold ionization of hydrogen, k_B is the Boltzmann factor, $\langle \sigma V \rangle$ is the annihilation cross-section, $H(z)$ is the Hubble parameter and f_{He} is the helium fraction. The functions $f_{c,\text{ion}}(z)$ and $f_{c,\text{heat}}(z)$ are the fractions of annihilation energy that go into ionization and heating respectively. The energy deposited into any channel c can be parametrized as [10]

$$\left(\frac{dE}{dV dt} \right)_c^{\text{dep}} = f_c(z, x) \left(\frac{dE}{dV dt} \right)^{\text{inj}}, \quad (12)$$

with all the complicated physics condensed into a factor that depends on redshift and the ionization fraction of all the relevant species in the gas. Darkhistory goes into all the details needed to calculate the efficiency function $f_c(z, x)$ but provides the resulting modifications to T_k and x_e with DM energy injection as

$$T_k = \frac{2f_{\text{heat}}(z, x)}{3(1 + F_{\text{He}} + x_e)n_{\text{H}}} \left(\frac{dE}{dV dt} \right)^{\text{inj}}, \quad (13)$$

$$x_e = \left[\frac{f_{\text{H,ion}}(z, x)}{R_{\text{nH}}} + \frac{(1 - C)f_{\text{exc}}(z, x)}{0.75R_{\text{nH}}} \right] \left(\frac{dE}{dV dt} \right)^{\text{inj}}, \quad (14)$$

where R_{nH} is the hydrogen ionization potential, $F_{\text{He}} = n_{\text{He}}/n_{\text{H}}$ is the helium abundance, n_{H} is the number density of hydrogen, $f_{\text{exc}}(z, x)$ is the fractions of annihilation energy that go into excitation and C is the Peebles-C factor which is the probability of HI in the $n = 2$ state decaying to the ground state. The results of Darkhistory are then used to compute the global 21 cm signal following equations Equation 1 - Equation 6.

4. Results

We present the results obtained for the three DM models in section 1. The associated masses have the maximum allowed values according to the CMB observations; for 200 GeV the annihilation cross-section is $\langle \sigma v \rangle_{\text{max}} = 1.2 \times 10^{-24} \text{ cm}^3 \text{s}^{-1}$, for 10 GeV the annihilation cross-section is $\langle \sigma v \rangle_{\text{max}} = 1 \times 10^{-25} \text{ cm}^3 \text{s}^{-1}$ and for 1 TeV the annihilation cross-section is $\langle \sigma v \rangle_{\text{max}} = 1.4 \times 10^{-23} \text{ cm}^3 \text{s}^{-1}$. These were chosen to see how the DM predictions change with the efficiency functions from Darkhistory, the models were kept the same as [8] for the purpose of comparison. We compare our results to the baseline, which is the default signal without DM. It is worth pointing out that our analysis does not include the astrophysical sources below $z \sim 30$, this follows the analysis of Ref.[6]. This is done so that we can easily study the DM effects on the global signal. The baseline model uses reionization models from [21] and is consistent with rapid reionization. This model provides photoheating and photoionization rates as functions of redshift.

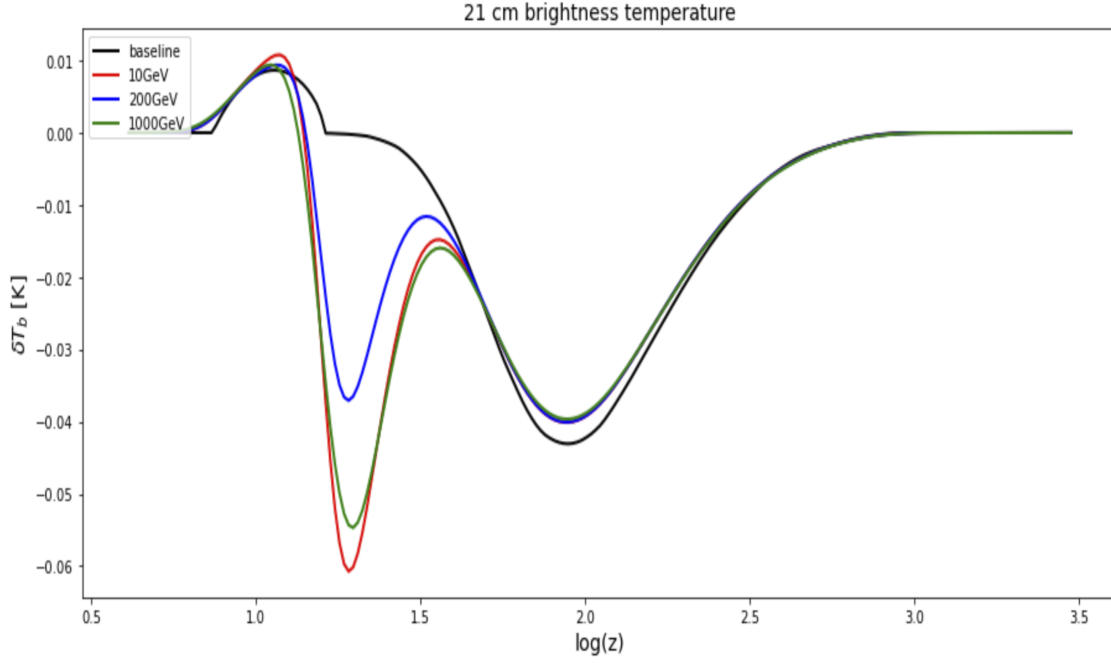


Figure 1. The brightness temperature as a function of redshift in a \log_{10} scale, for all the considered DM models. The baseline case without any injected energy from DM annihilation is depicted in the black line. The red line is for a 10 GeV DM mode with a $b\bar{b}$ channel, the blue line depicts the 200 GeV DM with W^+W^- channel and finally the green line is the 1000 GeV DM with $\mu^+\mu^-$ annihilation channel.

Before we dive into the analysis, we note that in Figure 1, the smoothing of the plots is not a DM related effect. We also notice that the results do not scale up with mass. Another important factor is that the models chosen have different annihilation channels which suggests that there is more at play than just $\langle\sigma v\rangle$ and m_χ . The efficiency functions vary depending on the nature of the annihilation products. Varying the mass will change the composition of the products and complicate naive expectations. Now looking at $z \sim 100$, during the Cosmic Dark Ages, we see that there is a reduction in the absorption trough for the DM case compared to the baseline because DM is heating the neutral hydrogen at this period and this causes emission, albeit very small. This is because the kinetic temperature at these redshifts is increasing since there is a high density of DM and therefore higher chance of annihilations. It is worth noting that in [8], the various DM models they use reduce this trough quite substantially compared to ours. Looking at one example; 10 GeV WIMP, we see that the difference of our model compared to the baseline is about 5 mK whereas in [8], they produce a difference of about 10 mK, this is twice as much as what we produce for the same mass. This is due to the updated efficiency function f_c that is provided by Darkhistory. When we look to $z \sim 30$, we notice that instead of heating and reducing the absorption trough as seen in [8], we are inducing an absorption feature in the case of DM. The 10 GeV model produces lower energy products, compounded by the smaller cross-section, this reduces heating efficiency. The 1 TeV model experiences a far larger cross-section but is suppressed by reduced number density. The 200 GeV case benefits from a larger cross-section than 10 GeV and doesn't carry as large a number density suppression as 1 TeV. Now moving to the onset of reionization, we see that our model, especially 10 GeV increases the emission very slightly at $z \sim 10$. This means that the efficiency functions we used produces opposite effects to previous studies in this topic, as can be seen with the surprisingly

strong absorption features.

5. Conclusion and future work

In this work we presented an argument for the use of a comprehensive approach of investigating the effect of dark matter in the early universe using the redshifted 21 cm hydrogen line. It is important to note that the work done here has limitations in a sense that there were no astrophysical sources included at $z \leq 30$, meaning that the results obtained are for optimistic cases. We have seen that studying the early universe with particular focus on the global 21 cm signal is a great probe of exotic energy injection. However, this requires precise modelling of the energy deposition especially the efficiency functions and the physics within them. Our results have shown that previous assumptions of f_c were highly over-estimated and Darkhistory lets us correct this.

The early results are promising but more work still needs to be done. Firstly, we need to add the astrophysical sources of Lyman- α and X-rays at the on-set of the Cosmic Dawn. This will allow us to have a full picture of the global 21 cm signal. Further work will investigate the potential for detecting or constraining DM annihilation effects using single-dish experiments and potentially interferometers.

Acknowledgments

M.K acknowledges support from a National Research Foundation of South Africa Thuthuka grant no. 117969.

References

- [1] Aghanim N, Akrami Y, Ashdown M, Aumont J, Baccigalupi C, Ballardini M, Banday A, Barreiro R, Bartolo N, Basak S *et al.* 2020 *Astronomy & Astrophysics* **641** A6
- [2] Ade P A, Aghanim N, Arnaud M, Ashdown M, Aumont J, Baccigalupi C, Banday A, Barreiro R, Bartlett J, Bartolo N *et al.* 2016 *Astronomy & Astrophysics* **594** A13
- [3] Blumenthal G, Faber S, Primack J and Rees M 1985 *Nature* **313** 72
- [4] Clowe D, Gonzalez A and Markevitch M 2004 *The Astrophysical Journal* **604** 596
- [5] Schramm D N and Turner M S 1998 *Reviews of Modern Physics* **70** 303
- [6] Valdes M, Ferrara A, Mapelli M and Ripamonti E 2007 *Monthly Notices of the Royal Astronomical Society* **377** 245–52
- [7] Furlanetto S R, Oh S P and Pierpaoli E 2006 *Physical Review D* **74** 103502
- [8] Valdés M, Evoli C, Mesinger A, Ferrara A and Yoshida N 2013 *Monthly Notices of the Royal Astronomical Society* **429** 1705–16
- [9] Ripamonti E, Mapelli M and Ferrara A 2007 *Monthly Notices of the Royal Astronomical Society* **374** 1067–77
- [10] Liu H, Ridgway G W and Slatyer T R 2020 *Physical Review D* **101** 023530
- [11] Chen X and Kamionkowski M 2004 *Physical Review D* **70** 043502
- [12] Mapelli M, Ferrara A and Pierpaoli E 2006 *Monthly Notices of the Royal Astronomical Society* **369** 1719–24 ISSN 1365-2966 URL <http://dx.doi.org/10.1111/j.1365-2966.2006.10408.x>
- [13] Slatyer T R, Padmanabhan N and Finkbeiner D P 2009 *Physical Review D* **80** 043526
- [14] Slatyer T R 2013 *Physical Review D* **87** 123513
- [15] Zaldarriaga M, Furlanetto S R and Hernquist L 2004 *The Astrophysical Journal* **608** 622
- [16] Pritchard J R and Loeb A 2012 *Reports on Progress in Physics* **75** 086901
- [17] Furlanetto S R, Oh S P and Briggs F H 2006 *Physics reports* **433** 181–301
- [18] Field G B 1959 *The Astrophysical Journal* **129** 536
- [19] Allison A and Dalgarno A 1969 *The Astrophysical Journal* **158** 423
- [20] Liu H, Slatyer T R and Zavala J 2016 *Physical Review D* **94** 063507
- [21] Puchwein E, Haardt F, Haehnelt M G and Madau P 2019 *Monthly Notices of the Royal Astronomical Society* **485** 47–68 ISSN 1365-2966 URL <http://dx.doi.org/10.1093/mnras/stz222>

Remote Sensing of Aerosol Optical Depth (AOD) over Pretoria, South Africa.

Z Faniso¹, E Magimisha¹ and T Malatji¹

CSIR, Defense and Security, Meiring Naude Road, Brummeria, Pretoria 0001

E-mail: ZFaniso@csir.co.za

Abstract. This paper presents the analysis of Aerosol Optical Depth (AOD) level data monitored through the Cimel CE 318A Sun-photometer over the year seasons of 2014. The data was collected at the Council for Scientific and Industrial Research (CSIR), Department of Defence and Security (D&S) in Pretoria (PTA), South Africa. The Aerosol Robotic Network (Aeronet) instrument was placed at the roof-top of a building and has been recording and providing continuous atmospheric AOD data from 2011 until 2018. The atmospheric aerosols contribute to atmospheric scattering and absorption within the Visible to Near-Infrared (VISNIR) band and can severely affect the performance of remote sensing imaging systems. The AOD measurement data can therefore be used as an input in the performance of the calibration validation process of Earth Observation (EO) sensors and other long-range target detection and recognition systems. The Optronic Sensor Systems (OSS) of the Defence and Security (D&S) cluster focuses on building optical imaging systems for satellites EO, short-range and long-range surveillance applications. The reported data is an extract of measurements obtained over a year when the instrument was in operation at the D&S. This work provides the necessary exposure in building the capability and confidence in the evaluation of the performance of remote sensing systems.

1. Introduction

Spaceborne remote sensing of aerosol particles, evaluation of the aerosols' climatic effects, and atmospheric corrections of imageries from Earth Observation (EO) systems mainly involves the understanding of the spectral Aerosol Optical Depth (AOD). AOD is the measure of aerosols (e.g., urban haze, smoke particles, desert dust, sea salt, etc) distributed within a column of air from the instrument (Earth's surface) to the top of the atmosphere [1]. It is a degree by which the aerosols prevent the transmission of light from reaching the earth's surface by absorbing and scattering the light. The Aerosol Radiative Forcing's (ARF) is one of the largest uncertainties in climate change. They are known to significantly influence the radiative budget of the Earth's atmosphere, both directly by scattering and absorbing radiation and indirectly by affecting cloud properties [1]. Precise and consistent measurements of aerosol optical properties, such as AOD, single scattering albedo, and phase function are key parameters to the aerosol direct effect [8]. The study will analyse AOD measurements from Pretoria (PTA), South Africa where the Aeronet instrument was previously installed.

Pretoria is an inland area that can be easily affected by large amounts of aerosols that contribute massively to the climate and radiative transfer over the area. The major industries in PTA includes those which manufacture motorcycles, chemicals, pharmaceuticals, engineering products, construction materials, steel industries, and cement factories. In addition to the industrial emissions, other anthropogenic sources that include vehicular emissions from main highways, coal combustion, agricultural and biomasses burning are the major local sources of aerosols in this capital city of South Africa [5]. To monitor the aerosols levels, various radiometric systems have been used to measure AOD which include Micro tops II Sun photometer a handheld analog instrument that measures AOD.

However, the accurate knowledge of the spatial and temporal extent of aerosol concentrations and properties has been a limitation for assessing their influence on satellite remotely sensed data and climate forcing [2][9]. Hence the National Aeronautics and Space Administration (NASA) developed an

Aeronet (Aerosol Robotic Network), a UNIX-based near real-time processing, display, and analysis system providing internet access to the emerging global database [2]. This global network installs CIMEL Sun-photometers for monitoring AOD and aerosol optical properties for AOD trend analysis, optical properties characterisation, and validation of satellite retrievals see Figure 1[3]. The Cimel systems data require validation and monitoring to ensure stability and use for calibration and validation of space sensors.



Figure 1: Aeronet ground based remote sensing instrument installations

The Council for Scientific and Industrial Research (CSIR) is the host to one of the Aeronet ground-based sun photometers (Cimel-318 Sunphotometer) that is used to monitor the atmospheric AOD distribution levels. The current study reviews the Cimel-318 AOD data captured in 2014. The instrument had captured full data(for all the months) for the year 2014. The other years encountered interruptions which lead to the instrument missing data. The 2014 data is analysed for all the seasons (Summer, Autumn, Winter and Spring) to evaluate the data stability for future validation of optical space sensors.

2. Methodology

2.1. Cimel-318 Sunphotometer Installation at CSIR

The Council for Scientific and Industrial Research (CSIR) Aeronet Cimel-318 Sunphotometer was installed at the roof-top of building 44, that is at 1449 m above sea level with a clear spatial view of the surrounding areas and no obstructions from nearby objects. The system was installed at -25.756611° S latitude and 28.279722° E longitude (see Figure 2). Some estimates suggest that anthropogenic aerosols and biomass burning have climate forcing enough to offset the warming caused by Green House Gases (GHGs) such as carbon dioxide [4]. Ground-based remote sensing has become a powerful method for characterising atmospheric aerosols as it can present a clear picture of the optical properties of each of the aerosol species [4]. OSS Aeronet Cimel-318 Sunphotometer installation contributes to the calibration and validation of space optical surveillance systems, Satellites sensors, Air quality and climate change research study sensors etc.

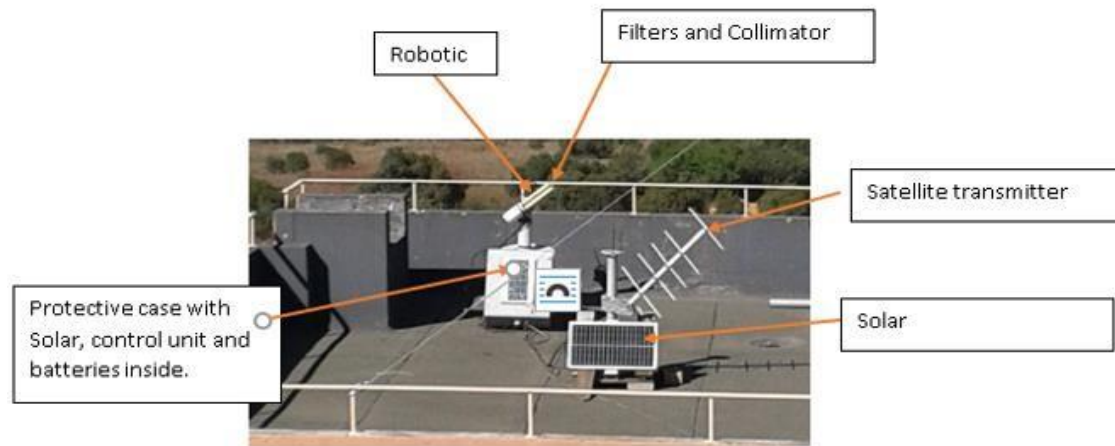


Figure 2: Cimel 318 Sunphotometer installation at CSIR/D&S Building

For more than 25 years, the project has provided a long-term, continuous, and readily accessible public domain database of aerosol optical, microphysical, and radiative properties for aerosol research and characterization, validation of satellite retrievals, and synergism with other databases [3]. The CIMEL318 Sunphotometer makes direct spectral solar radiation measurements within a 1.2° full field of view at a typical temporal repetition interval of 15 min. The solar radiance is sampled at 8 standard band filters from 340 nm, 380 nm, 440 nm, 500 nm, 675 nm, 870 nm, 1020 nm, and 1640 nm [5]. These filter bands are contained by the robotic part of the system, and each region from visible to short wave is represented by at least two filters. The Satellite transmitter data sends the data automatically to 4 Satellites: GOES East, GOES West, Meteosat and Geostationary Meteorological Satellite GMS using Data Collection Platform (DCP). Data are transferred from satellites to Aeronet processing server via several receiving stations. The case is the component where the Control Unit (CU) and the pair of batteries are placed. The solar panel that powers the system is incorporated in the case. The output plug of the solar panel is a RJ11 connector. The instrument batteries supply power to the CU. The battery is 8AH. The YUASA battery is furnished when the satellite transmitter is used. The battery is 24AH. The Mascot 2240 battery charger is used only in case of solar panel breakdown [5].

Figure 3 shows the atmospheric scenario that generally explains what the Cimel instrument is exposed to while in operation. Various aerosol types are suspended in the atmosphere affecting the sun radiation propagation towards the earth surface. The Cimel sun photometer employs the sun as reference in determining the atmospheric AOD from aerosols floating in the path between the Sun and the instrument.

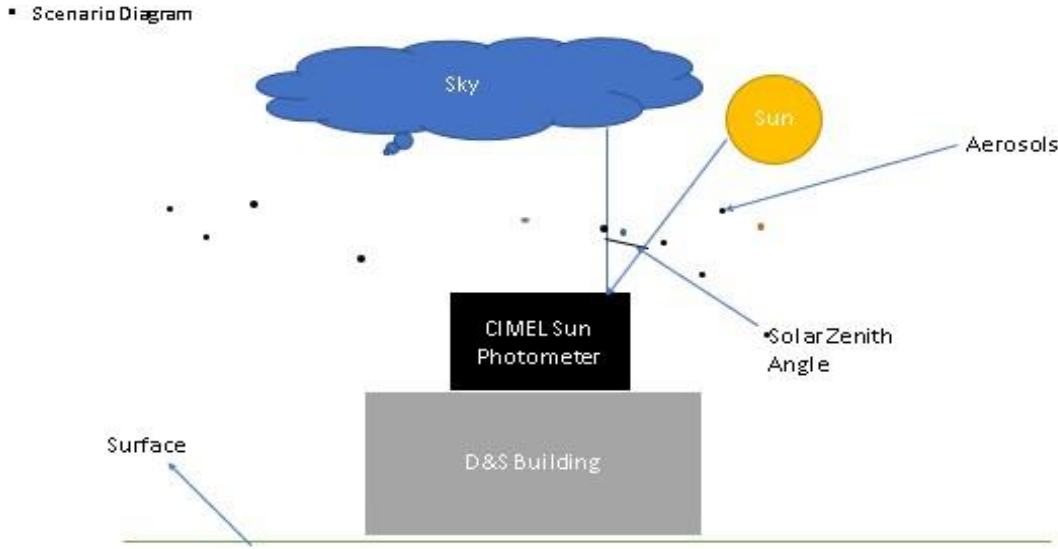


Figure 3: Atmospheric scenario for the Cimel-318 Sunphotometer at CSIR/D&S building

Depending on the abundance of the atmospheric aerosols, the solar radiation can either be absorbed, reflected and some transmitted to the earth surface.

2.2 AOD Measurements

The city has a humid subtropical climate with long hot and rainy summers, and short cool and dry winters [5]. The data from the PTA station can be found on the AERONET website (<http://aeronet.gsfc.nasa.gov/>). AOD data are computed for three data quality levels, Level 1.0 (unscreened), Level 1.5 (cloud-screened and quality controlled), and Level 2.0 (quality assured) [3]. The version 2.0/level 2.0 of the quality assured daily points' format data of direct sun and inversion products are used for the study period of the year 2014.

The effect of radiative transfer is proportional to the amount of particles present in the column and depends on their intrinsic optical properties. The spectral variation of AOD provides useful information on columnar size distribution and can be best represented by Ångström power law relationship, given by Ångström (1964) [4].

$$\tau_a(\lambda) = \beta \lambda^{-\alpha} \quad (1)$$

Where $\tau_a(\lambda)$ is the AOD at wavelength λ (in micrometers), β is the turbidity coefficient, indicating total aerosol loading, which equals to τ_a at $\lambda = 1 \mu\text{m}$, and α is widely known as the Angstrom exponent (AE), which is a good indicator of aerosol particle size [4]. AE largely depends on aerosol size distribution and is a measure of the ratio of coarse- to fine-mode aerosols [4].

$$\alpha = -\frac{\beta \lambda}{\tau_a} \quad (2)$$

with higher values representing the increased abundance of fine-mode aerosols and lower values representing the increased abundance of coarse-mode aerosols. Aerosol size distribution in turn depends on their production mechanism, e.g. particles formed by gas-to-particle conversion are small particles whereas particles formed by mechanical actions such as wind lifting of dust, wave-breaking, etc. are bigger[4].

3. Results and Discussion

The aerosol optical depth is representative of the airborne aerosol loading in the atmospheric column. For this current study seven of the eight bands AOD data has been analysed. Figure 4 illustrates the average mean of the retrieved AOD data while Figure 5 illustrates the $AE_{(440\alpha-870)}$ average mean data for each month of the year 2014 in PTA. All the seasons of the year are shown, however seasons of the year vary in temperatures with winter consisting of dry, cool to low-temperature experiences while summer experiences high temperatures with heavy rainfalls. The Aeronet AOD data showed an increase in the AOD rate from January with a maximum of ± 0.3 and swiftly drops in May to a minimum of ± 0.10 (see Figure 4). May is the first month of the winter season and PTA winter season mostly shows clear and uncloudy sky with the soft wind that contributes to the transfer of dust particles in the atmosphere. An AOD growth is observed from the end of May which spreads along to June and July with a maximum between ± 0.2 and ± 0.23 still lower than the Autumn season (February, March, and April). The winter season is followed by another drop at the mid-spring season (August, September, and October) and shows an increase again in the summer season with a maximum of ± 0.35 .

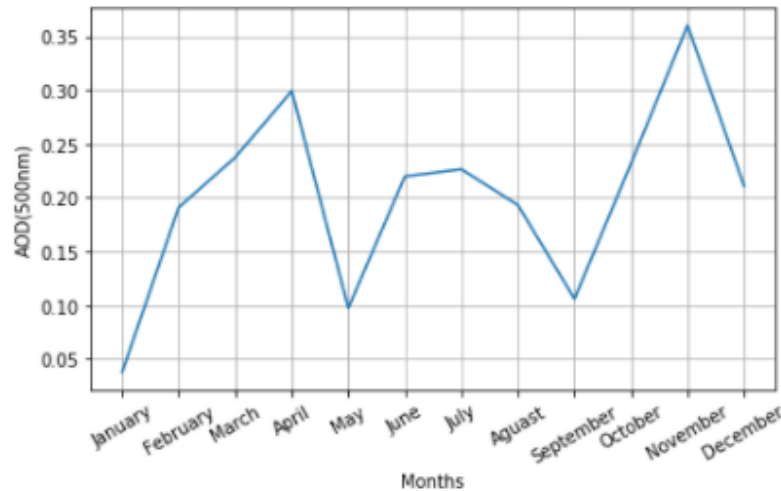


Figure 4: AOD average mean data from January to December 2014

A comparison between the AOD (Figure 4) and AE (Figure 5) has been performed. It has been observed that the two data sets project the same trend for all the seasons of the year. The AE (Angstrom Exponent) shows the increase from January and decrease in May with an increase in winter season followed by a drop in mid-Autumn season and a huge increase in the summer season. The AE has shown that it is dependable to the AOD rate.

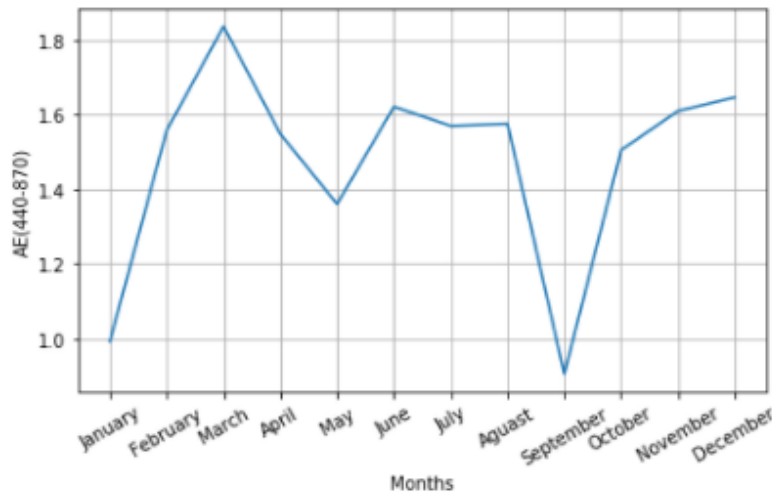


Figure 5: The Angstrom Exponent data for the year 2014.

In terms of monthly variations Figure 6 and 7 filter variations between Cimel sensors from visible to infrared range.

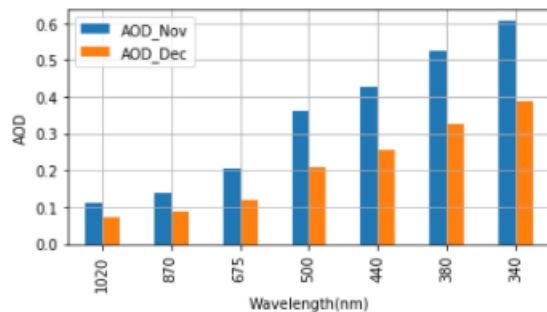


Figure 6: Comparison of AOD for the summer season (AOD_November and December). Of 2014.

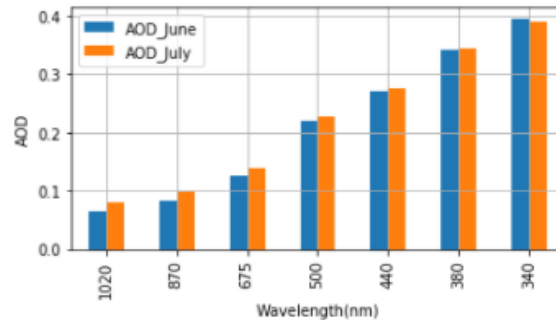


Figure 7: Comparison of AOD for the winter season (AOD_June and July) of 2014.

The summer season commences with November where there is a high peak in AOD with ± 0.6 , followed by December (see Figure 6) with a maximum of ± 0.39 . December experiences high temperatures accompanied by heavy rainfalls. These heavy rainfalls may contribute to shutting the Cimel sensor since it only performs measurements when the Sun is actively radiating the Earth surface without interruptions. The occurrence of high value in urban regions was also related to the anthropogenic pollution and local prevailing meteorological condition. This implies that there were Aerosols over PTA within the winter season (June/July) see Figure 7. The two months show almost equal amount of AOD in each sensor. This is because the winter season experiences almost the same temperatures without drastic changes as compared to summer (see Figure 4 and 6).

4. Summary

The analysis of Aerosol Optical Depth profile and Angstrom exponent (AE) data from the Aeronet Cimel-318 Sun photometer based at the CSIR in PTA was performed. A year data (from January to December) of the year 2014 has been used in the present study. The data was downloaded from the AERONET webpage to analyse the AOD of the aerosol loading in association with local aerosol conditions behaviour and estimated the atmospheric radiative forcing around the area. The aerosol

optical depth (AOD) showed the highest rate occurring in November and December respectively, while the lowest was noticed in June and July. In the PTA city, the summer season is known to experience heavy rainfalls with dry winter seasons with mostly uncloudy days. It is significant to continuously monitor aerosol properties to assess more accurately and characterize the annual cycle since only one year of data has been used in the present study.

References

- [1] K.K Raghavendra, S Venkataraman, R. R Rajuru and R.G Kotalo, SPIE, 2016, Remote sensing of atmospheric aerosols in South Africa.
- [2] B.N Holben, T.F.Eck, I.Slutsker, D.Tanre, J.P.Buis, A.Setzer, E.Vermote, J.A.Reagan, Y.Kaufman, T.Nakajima, F.Lavenu, I.Jankowiak and A.Smirnov,1998:AERONET Afederated instrument network and data archive for aerosol characterisation, Rem.Sens. Environ.,66,1-16.
- [3] <https://aeronet.gsfc.nasa.gov>
- [4] A.J. Adesina, K.R Kumar, V.Sivakumar, and D.Griffith, 2014, Direct radiative forcing of urban aerosols over Pretoria(25.75 D,2828 E) using AERONET Sunphptometer data First Scientific results environmental impact Journal of Environmental Sciences, 26(12), pp.2459-2474.
- [5] Multiband and photometer CE318-T User's Manual(rev.January 2018).
- [6] Y.J.Kaufman, 1993. Aerosol optical thickness and atmospheric path radiance. Journal of Geophysical Research:Atmospheres, 98(D2), PP.2677-2692.
- [7] X.Y. Zhang, Y.X.Xiong, J.J.Qu,and H.Che,2011. Validation of MODIS aerosol optical depth product over China using CARSNET measurements. Atmospheric Environment, 45(33), pp.5970-5978.
- [8] B.N Holben, T.I.Eck, I.Slutsker:D.Tar&',6 J.P Buis,II A.Setxer, J.E Vemte,' J.A Reagan, F.Y.J Kaufman, T.Nakajima,l:F.Lavenu,qqI.Jankowiak and A.Smirnozit, 1998. ELSEVIER AERONET A Federated Instrument Network and Data Achirve for Aerosol Characterisation.
- [9] Kumar, P., Choudhary, A., Singh, A.K., Prasad, R. and Shukla, A., 2020. Aerosol parameters during winter and summer seasons and meteorological implications. In EPJ web of conferences (Vol. 237). EDP Sciences.

Daily global solar radiation estimation using artificial intelligence approach

Y T Olorunfemi^{1*}, O B Wojuola¹ and J A Adesina^{2,3}

¹ Dept. of Physics, Faculty of Natural and Agricultural Sciences, NWU, Mafikeng Campus, South Africa.

² School of Geo- and Spatial Science, Unit for Env. Sc. and Management, NWU, Potchefstroom Campus, South Africa.

³ EPPEI Specialisation Centre for Emissions Control, NWU, Potchefstroom Campus, South Africa.

*E-mail: olorunfemiyetundet@gmail.com

Abstract. Daily global solar radiation (DSR) is sparsely measured in meteorological stations in South Africa. The prediction of DSR is crucial to solar energy conversion systems (modelling, design and operation) and decision-making of potential energy policies. The need for these solar system designs varies from the use of power and water supply for industrial purposes to agricultural and domestic services. This paper employed the use of three artificial intelligence models, which are artificial neural networks (ANN), adaptive neuro-fuzzy inference system (ANFIS), and support vector regression (SVR) in predicting DSR from the Capes of South Africa using NASA satellite data for 30 years. Daily values of minimum and maximum temperatures, relative humidity, precipitation, wind speed, atmospheric pressure and earth's temperature were used as independent variables and the solar radiation as dependent variable when training the model. Statistical metrics such as root mean squared error (RMSE), mean absolute percentage error (MAPE) and coefficient of determination were used to evaluate the model performance. The result shows that the ANFIS algorithm has the least MAPE values ranging from 9.82 – 13.18 and lowest RMSE values ranging 0.70 – 0.78 which outperforms the SVR model (MAPE ranging 11.53 – 14.89 and RMSE values ranging 0.78 – 0.94) and ANN model (MAPE ranging 11.41 – 27.34 and RMSE values ranging 0.79 – 1.57), making it a better technique for estimating solar radiation.

1. Introduction

The potential contribution of renewable energy technology to power generation is enormous. The building of solar energy systems in a specific area is highly dependent on knowledge about that region's sun radiation [1]. High-quality measurements done by pyranometers are the best sources of data on daily global solar radiation (DSR). Unfortunately, the high price, maintenance, and calibration criteria of these devices, as well as the necessity for a skilled professional make it challenging to measure in many regions [2].

Artificial intelligence (AI) has become highly popular in virtually all technical areas in recent decades as a result of technological advancements [3]. Numerous AI approaches, such as deep learning (DL), support vector machine (SVM), artificial neural networks (ANN), kernel nearest neighbour (k-NN), genetic algorithms (GA), adaptive neuro-fuzzy inference system (ANFIS), and others, have begun to be widely used models [4]. Previous research has found that AI algorithms have several benefits over traditional modelling. The benefits include the capacity to handle huge volumes of outliers from dynamic and unpredictable systems. This provides more precise outcomes than empirical models when it comes to predicting solar radiation.

A review of the literature revealed that no study has investigated and compared the accuracy of support vector regression (SVR), ANFIS and ANN, incorporating the earth's temperature as one of the inputs in DSR estimation in the Capes of South Africa. The goal of this research is to study and to compare the performance of these techniques in modelling DSR from three locations in the Capes of South Africa. Comparisons and performance assessments are carried out based on various commonly used statistical indicators.

2. Methodology

2.1. Areas of case study and data source

Daily measurements of atmospheric pressure, minimum and maximum temperatures, wind speed, precipitation, relative humidity, earth's temperature and solar radiation for a period of thirty years (1990-2020) for selected cities in the Western Cape, Eastern Cape, and Northern Cape of South Africa were considered in this study. These measurements were obtained from the NASA satellite in RETScreen Expert Software. Each model used in this study was trained using data for the period of January 1990 to September 2011, while data for October 2011 to December 2020 were used for testing. The cities' geographical coordinates and locations in a geospatial map are presented in Table 1 and Figure 1 respectively.

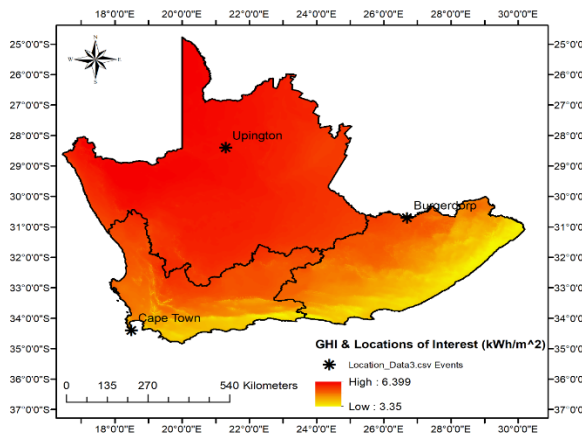


Figure 1: The geospatial mapping of the Cape cities (South Africa) used in this study.

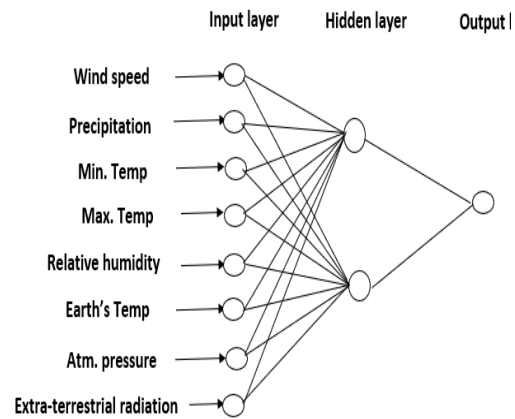


Figure 2: Schematic diagram of ANN model for the present work.

Table 1. Climate data locations.

Province	Location	Latitude (°S)	Longitude (°E)	Altitude (m)
Western Cape	Cape point	34.4	18.5	42
Eastern Cape	Burgersdorp	30.7	26.7	1518
Northern Cape	Upington	28.4	21.3	838

2.2. Support vector regression

The support vector regression (SVR) used for modelling the DSR for each chosen city was built according to a supervised learning approach. Meteorological variables formed the inputs to the model, and the solar radiations constituted the models' output.

In the SVR model, the Gaussian function was used as the kernel function for model training. The Gaussian kernel with an automatic kernel scale was used, and this selection was due to the efficiency of the Gaussian function:

$$K(x, y) = (x^T y + c)^d, \quad (1)$$

where x and y are feature vectors derived from training or testing data, and c is a constant that optimizes the effect of higher-order against lower-order polynomial components.

2.3. Artificial Neural Network

A back-propagation ANN was utilized to generate the intended output properly with an optimal network topology. Figure 2 above shows the schematic diagram of the ANN model.

2.4. Adaptive Neuro-Inference System

The ANFIS model combines ANN with the Fuzzy Inference System (FIS) to provide the best membership function distribution from feedback mapping [5]. The fuzzy layer, product layer, normalized layer, de-fuzzy layer, and total output layer in layers one to five respectively make up a typical ANFIS network [5, 6], as can be seen in Figure 3 and in equations (2) – (7).

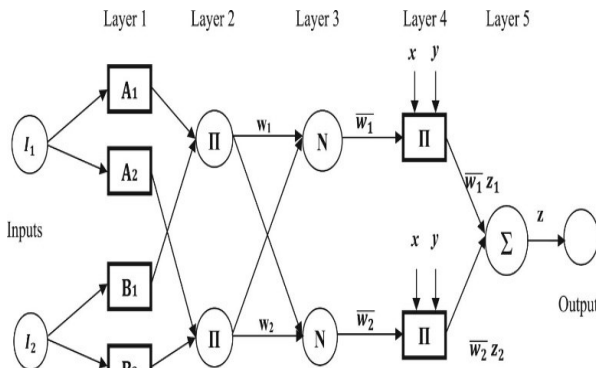


Figure 3: ANFIS structure

$$O_m^1 = \mu_{A_m}(x), m = 1, 2 \quad (2)$$

$$O_m^1 = \mu_{B_m}(y), m = 1, 2 \quad (3)$$

$$O_m^2 = w_m = \mu_{A_m}(x) \cdot \mu_{B_m}(y), m = 1, 2 \quad (4)$$

$$O_m^3 = \bar{w}_i = \frac{w_m}{w_1 + w_2}, m = 1, 2 \quad (5)$$

$$O_k^4 = \bar{w}_i(p_m x + q_m y + r_m), m = 1, 2 \quad (6)$$

$$O_m^5 = \sum_m \bar{w}_i z_m, m = 1, 2 \quad (7)$$

Figure 3 shows the fuzzy rules of the first order Takagi-Sugeno fuzzy model, which have the following structure:

Rule 1: if I_1 is A_1 AND I_2 is B_1 then $f_1 = p_1 I_1 + q_1 I_2 + r_1$

Rule 2: if I_1 is A_2 AND I_2 is B_2 then $f_2 = p_2 I_1 + q_2 I_2 + r_2$

where x and y are the crisp inputs to node, A_m and B_m are the fuzzy sets in the antecedent, f_i is the output inside the fuzzy area defined by the fuzzy rule, m is the adaptive node, \bar{w}_i is the normalized third layer firing strength, O_m^i is the output of adaptive node m in layer $i = 1, 2, \dots, 5$ and p_m, q_m , and r_m are the design criteria decided during the training phase.

2.5. Evaluation of the model's performance

Mean absolute percentage error and root mean square error were used for evaluating the performance of the models. The mean absolute percentage error (MAPE) reflects the mean absolute percentage variation between observed and expected values, whereas the root mean square error (RMSE) compares the variance between predicted and the actual data to assess the model's accuracy. The RMSE always has a positive value. The coefficient of determination (R^2) is a metric that indicates the strength of the linear connection between the predicted and measured values. It is important to note that lower MAPE and RMSE values indicate greater precision in the global solar radiation prediction, and in an ideal situation, they are both zero. The R^2 is a number that ranges from 0 to 1. The presence of a perfect linear relationship is indicated by R^2 values around 1. The performance of the model was evaluated using the MAPE, RMSE, and R^2 as expressed in the following equations:

$$MAPE = [\sum(s_i - t_i)]/n \quad (6)$$

$$RMSE = \left[\sum (s_i - t_i)^2 / n \right]^{1/2} \quad (7)$$

$$R^2 = 1 - \frac{\sum(s_i - t_i)^2}{\sum(t_i)^2 - \frac{\sum(t_i)^2}{n}} \quad (8)$$

where s_i and t_i are observed and predicted values, respectively, n is the observation number. The MLP model script for this study was written using MATLAB (R2021a) software.

3. Results

Figure 4-6 depict the scattering diagrams of measured DSR estimated using three AI models for the location of Burgersdorp, Upington, and Cape Point located in the South African provinces of Eastern Cape (EC), Northern Cape (NC), and Western Cape (WC) respectively. The prediction accuracy of DSR differed significantly among the various model types. Based on the statistical values of the three AI models, the ANFIS model has the least MAPE values ranging from 9.82 – 13.18, and least RMSE values ranging from 0.70 -0.78 , if compared to the other models. However, the SVR model has the highest R^2 value of 0.89 amidst the three AI models, with a better model forecast ranging from 85.11% to 88.47 % when compared to the ANN model.

SVR model (MAPE ranging 11.53-15.52, RMSE ranging 0.78 - 0.94 and R^2 ranging 0.77 - 0.89) performed better than the ANN model (MAPE ranging 11.41-27.34, RMSE ranging 0.79 – 1.57 and R^2 ranging 0.60 - 0.83). In general, the ANFIS model outperformed the other two AI models in the testing stage, with reduced data dispersion and better fitting of predicted data to actual values, especially in the Northern Cape (Upington).

The results demonstrate the ability of SVR, ANFIS, and ANN models to adapt to existing conditions in the Capes of South Africa. The lowest value of MAPE and highest value of the coefficient of determination at the study's sites are comparable those found by other researchers [7, 8].

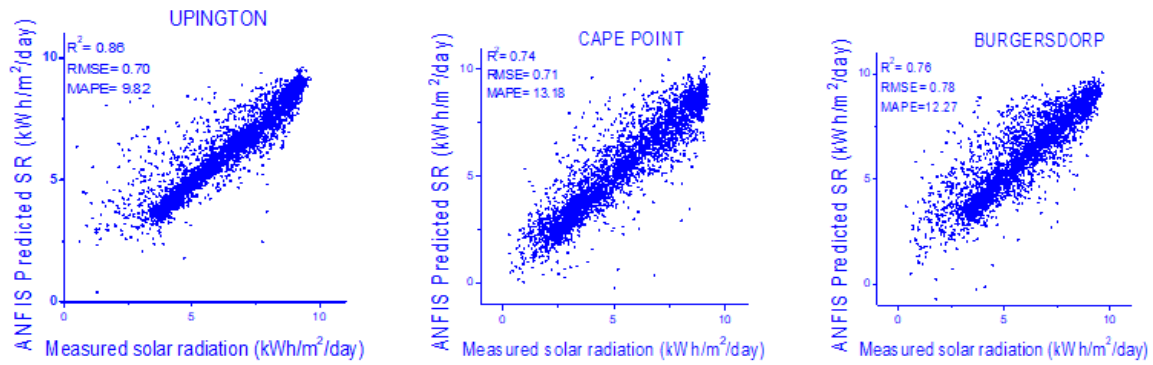


Figure 4: Scattering diagrams of measured DSR estimated using ANFIS model for Upington, Cape point and Burgersdorp.

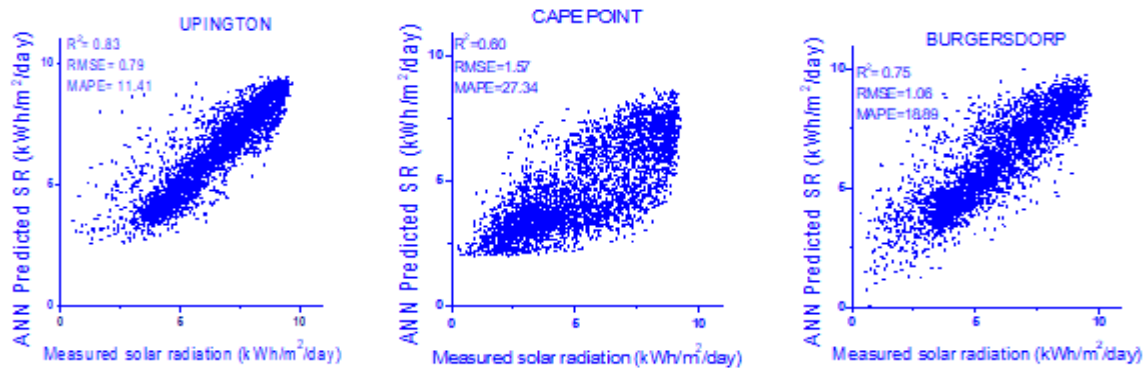


Figure 5: Scattering diagrams of measured DSR estimated using ANN model for Upington, Cape point and Burgersdorp.

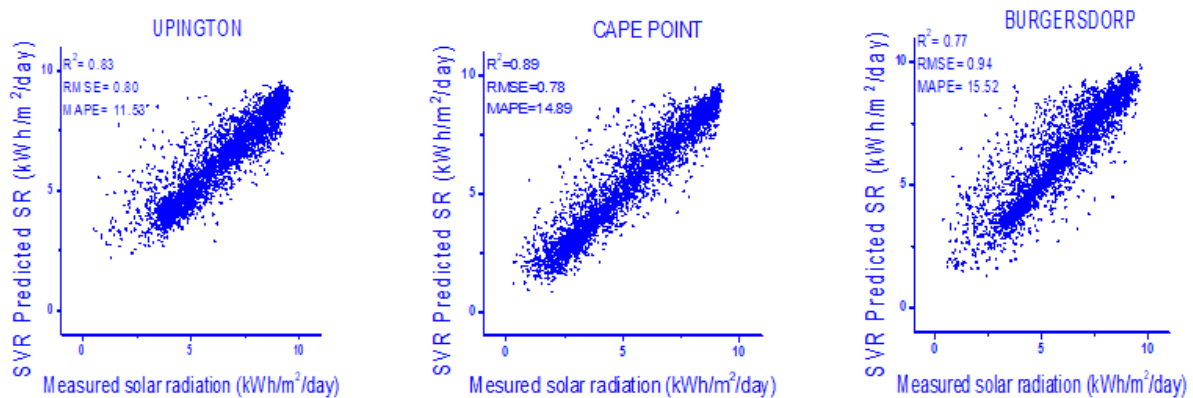


Figure 6: Scattering diagrams of measured DSR estimated using SVR model for Upington, Cape point and Burgersdorp.

Table 2. Model performance evaluation

	SVR			ANFIS			ANN		
	WC	EC	NC	WC	EC	NC	WC	EC	NC
R ²	0.89	0.77	0.83	0.74	0.76	0.86	0.60	0.75	0.83
RMSE	0.78	0.94	0.80	0.71	0.78	0.70	1.57	1.06	0.79
MAPE	14.89	15.52	11.53	13.18	12.27	9.82	27.34	18.89	11.41

4. Conclusions

The possibility of employing three artificial intelligence models (artificial neural networks (ANN), adaptive neuro-fuzzy inference system (ANFIS), and support vector regression (SVR) to predict the horizontal daily global solar radiation using meteorological information was investigated in this study. Three cities in South Africa's Cape that serve as the country's solar centres were chosen as case studies. Aside from using the models for forecasting the daily global solar radiation, the three artificial intelligence models were further verified and compared. Statistical metrics, (MAPE, RMSE, and R², were used to evaluate the models' performance. Findings show that ANFIS give the best estimation of daily global solar radiation.

References

- [1] Bakirci K, Kirtiloglu Y. Effect of climate change to solar energy potential: a case study in the Eastern Anatolia Region of Turkey. *Environmental Science and Pollution Research*. 2021;1-14.
- [2] Yıldırım HB, Çelik Ö, Teke A, Barutçu B. Estimating daily Global solar radiation with graphical user interface in Eastern Mediterranean region of Turkey. *Renewable and Sustainable Energy Reviews*. 2018;82:1528-37.
- [3] Kuo P-H, Huang C-J. A green energy application in energy management systems by an artificial intelligence-based solar radiation forecasting model. *Energies*. 2018;11(4):819.
- [4] Long H, Zhang Z, Su Y. Analysis of daily solar power prediction with data-driven approaches. *Applied Energy*. 2014;126:29-37.
- [5] Jang J-S. ANFIS: adaptive-network-based fuzzy inference system. *IEEE transactions on systems, man, and cybernetics*. 1993;23(3):665-85.
- [6] Adedeji P, Madushele N, Akinlabi S, editors. Adaptive Neuro-fuzzy Inference System (ANFIS) for a multi-campus institution energy consumption forecast in South Africa. *Proceedings of the International Conference on Industrial Engineering and Operations Management Washington DC, USA, September 27-29; 2018*.
- [7] Alizamir M, Kim S, Kisi O, Zounemat-Kermani M. A comparative study of several machine learning based non-linear regression methods in estimating solar radiation: Case studies of the USA and Turkey regions. *Energy*. 2020;197:117239.
- [8] Quej VH, Almorox J, Arnaldo JA, Saito L. ANFIS, SVM and ANN soft-computing techniques to estimate daily global solar radiation in a warm sub-humid environment. *Journal of Atmospheric and Solar-Terrestrial Physics*. 2017;155:62-70.

**DIVISION E –PHYSICS
FOR DEVELOPMENT,
EDUCATION AND
OUTREACH**

Polarising questions in the Force Concept Inventory

Anna Chrysostomou¹, Emanuela Carleschi¹, Alan S. Cornell¹ and Wade Naylor^{1,2}

¹ Department of Physics, University of Johannesburg, PO Box 524, Auckland Park 2006, South Africa

² Immanuel Lutheran College, PO Box 5025, Maroochydore 4558, Australia

E-mail: ecarleschi@uj.ac.za, annachrys97@gmail.com, acornell@uj.ac.za, naylorw@immanuel.qld.edu.au

Abstract. The Force Concept Inventory (FCI) is a well-established physics education assessment tool used to evaluate students' comprehension of elementary mechanics principles. While it can be used to analyse the effectiveness of instruction if deployed as a pre- and post-test, we utilise the FCI here as pre-test only, to extract insights into first-year students' (mis)conceptions of Newtonian mechanics as they enter university. In this preliminary study, we tested 353 students enrolled at the University of Johannesburg in 2021, across six introductory physics courses. We focus on their responses to six “polarising” questions, for which the presence of a correct and a mostly-correct answer allows for a clear demonstration of persistent misconceptions.

1. Introduction

Physics pedagogy has become a topic of interest in recent decades, with a particular focus on confronting persistent misconceptions generally held by incoming undergraduate students [1–7]. While the development of these misconceptions may arise from a number of sources beyond the control of the educator, Bani-Salameh has suggested that these flaws in understanding should be diagnosed as early as possible if effective teaching is to take place [6]. To identify these misconceptions, a number of diagnostic tools have been developed for the various physics sub-disciplines. A subset of these have been designed to gauge student comprehension at the onset of an introductory university course, and then to assess their progress at the end of the course.

One such tool is the *Force Concept Inventory* (FCI) [8–10], a 30-minute multiple-choice test comprised of 30 questions on elementary principles and applications of classical mechanics *viz.* circular motion, Newton's three laws, etc. The recommended means of administering this assessment tool is as a strictly closed-book test held at the beginning of the semester, to provide instructors with an indication of their students' baseline mechanics skills. Note that students are not expected to prepare for the assessment. This is known as the “pre-test”. Once the pre-test is completed it is not reviewed in class and students receive no feedback on their attempts. At the end of the semester the same FCI test is administered once again to students, without their prior knowledge of the re-testing. This is the “post-test” phase. A common statistical measurement used to quantify student progress is the normalised gain G [11], defined as

$$G = \frac{\langle \%S_f \rangle - \langle \%S_i \rangle}{100 - \langle \%S_i \rangle}, \quad (1)$$

where $\%S_f$ and $\%S_i$ are the final and initial FCI test scores, respectively.

Another way to interpret FCI data is to investigate individual questions, as recently performed by Alinea and Naylor [12–14]. In these works, a breakdown of the type of response to each of the 30 questions demonstrated a “polarisation” between a correct and a partially-correct answer within several questions (specifically, questions: 5, 11, 13, 18, 29, and 30). Students who choose the incorrect answer may unwittingly reveal that they suffer from one of the commonly held misconceptions outlined in references [4, 6, 7]. Our preliminary investigations conducted with the first-year engineering and physics students at the University of Johannesburg in 2020 [15] seemed to support this, where one particularly popular incorrect response was that “a force in the direction of motion” was partially responsible for the action described in the question. The belief that “motion requires an active force” was flagged as a misconception as identified in references [4, 6, 7].

In our present study, we have performed this question-by-question analysis on the FCI pre-test responses from six first-year physics classes, with a total of $N = 353$ students. We begin with a description of the student participants and the manner in which their responses were collected in section 2. We then present our results in section 3, with a focus on the polarising questions provided in table 2. Conclusions and future avenues of pursuit are presented in section 4.

2. Methodology and data collection

Due to the ongoing nature of the COVID-19 pandemic, South African institutions of tertiary education were expected to function mostly – if not entirely – online. The delayed release of the 2020 Grade 12 results further derailed the 2021 academic programme, with first-year academic activities only beginning on March 8th at the University of Johannesburg, leading to a first semester shortened by several weeks.

To allow for first-year students to adjust to online learning, the authors of this study were forced to delay the deployment of the FCI test to the beginning of April. With the permissions of the various lecturers involved in each of the six courses that participated in this study (see table 1 for details), we launched the FCI test via the Blackboard interface and made it available to students for a total of five days, using the module page corresponding to each of the six courses. Through this platform, we were able to track student activity (to determine whether test-takers left the browser page during the course of the test), time their test attempt, and force submission after an allotted time. We were also able to make a test visible for a set period of time. For our data collection, we enabled these features to reduce cheating and to ensure students submitted their responses after 30 minutes.

Once the deployment period was over and each class had completed the assignment, the data was downloaded and processed within a single Excel spreadsheet for each of the six individual classes. All data was anonymised in accordance with the requirements of the protection of personal information act.

In what follows we will present some preliminary analyses for FCI pre-test data for the 2021 cohort at the University of Johannesburg. The analyses break down the responses for each question to look for dominant misconceptions [4]. This can be very useful in gauging how an initial cohort and indeed different subgroups need different teaching pedagogies.

3. Pre-test analyses and results

The preliminary analyses of the pre-tests for the 2021 cohort at the University of Johannesburg, for each of the 30 questions, is summarised in figure 1. The green shaded % shows the percentage of students who got the correct answer, with the black outline showing the % for the most commonly chosen answer. For example, questions 1-4 have the majority correct and this being the most chosen response. The choices where the majority response was incorrect correspond

Table 1. Course codes, their associated entry-level requirements (Grade 12 mathematics and physical sciences scores), FCI deployment period, number of student responses per class, and average scores for the six first-year classes involved in the 2021 FCI pre-testing. Note that Ext. refers to the extended courses, where students who do not meet entry-level requirements for introductory physics classes can complete a four-year Bachelor of Science in which the traditional first-year physics course is taught over a three-semester period.

Course (Physics for...)	Ent. % Math.	Ent. % Phys. Sci.	Deployment period	Responses/ class	Mean (%)
PHYS1A1 (Majors)	70	60	13/04 - 17/04	19/70	33.2
PHY1EA1 (Physics Ext.: Sem1)	60	50	09/04 - 13/04	187/306	30.1
PSFT0A1 (Education)	50	50	05/04 - 09/04	62/91	29.9
PHYG1A1 (Earth Sci.)	60	50	05/04 - 09/04	13/17	28.2
PHYL1A1 (Life Sci.)	70	60	07/04 - 11/04	32/64	28.6
PHE3LA1 (Life Sci. Ext.: Sem3)	60	50	13/04 - 17/04	40/87	38.2

to those questions with a larger red % difference showing that more students chose the wrong question – for this cohort of students this corresponded to questions 5, 11, 17, 19, 26, and 30, respectively.

These questions appear to show what Martin-Blas *et al.* call “dominant misconceptions”* [4]. For example, question 5 focuses on circular motion and we can see here that this question was not well understood by most of the cohort. Given that this information was collected at the pre-test stage, the course instructors could attempt to adjust the teaching and learning to try to reinforce such a concept.

We will now turn our attention to the “polarising” questions 5, 11, 13, 18, 29, and 30, which we observe to line up well with some of the dominant misconceptions found in figure 1. The responses to these questions are summarised in table 2 for each of the six classes. The interest in these particular questions lies in the fact that the “polarising answer” is mostly correct but contains within it one intentionally misleading statement. For example, question 5 asks students to identify the forces driving an object’s circular motion. The correct answer is B; the polarising choice of D lists the same forces as B but also includes “a force in the direction of motion”. As mentioned in section 1, the polarising answer therefore reveals the students’ misconception.

We see this polarising effect to be most pronounced in classes where physics comprehension is assumed to be greatest – the physics and life science majors, where the course prerequisites are higher, as well as the third-semester life sciences students, who have had the most exposure to Newtonian mechanics. However, it is concerning that the proportion of students polarised towards the wrong choice remains fairly high and even overtakes the correct answer (especially for questions 13 and 30, where more of these students favour the polarising rather than the correct answer).

The polarising effect remains fairly consistent for questions 18, 29, and 30 within the other studied classes; for questions 5, 11, and 13, the answers are far more scattered. These questions each concern motion in a frictionless environment, in the absence of a contact force. Again, it became apparent students struggled to understand the forces at play when objects are in motion.

* Note that the majority wrong answer questions – where the red shading % is greater than the green shading % – lines up quite well with the “polarising” questions [12]: 5, 11, 13, 18, 29 and 30.

Table 2. A summary of the responses from the six participating classes to the polarising questions. Here, green [grey] and blue [light-grey] represent the correct and polarising choice [14], respectively, while orange [dark-grey] denotes responses more or equally popular.

Course	Answer	Q5	Q11	Q13	Q18	Q29	Q30
PHYS1A1	A	10.5	10.5	15.8	5.3	0.0	0.0
	B	26.3	5.3	5.3	31.6	73.7	5.3
	C	26.3	63.2	36.8	15.8	5.3	21.1
	D	15.8	15.8	26.3	21.1	10.5	5.3
	E	21.1	0.0	5.3	21.1	0.0	47.4
	none	0.0	5.3	10.5	5.3	10.5	21.1
	total	100.0	100.0	100.0	100.0	100.0	100.0
PHY1EA1	A	16.0	15.5	20.3	5.3	12.3	4.8
	B	13.9	26.7	26.7	23.5	56.7	19.8
	C	40.6	36.9	23.5	16.0	2.7	13.4
	D	8.0	10.7	20.9	25.1	10.2	6.4
	E	17.6	4.8	3.2	21.4	3.2	35.3
	none	3.7	5.3	5.3	8.6	15.0	20.3
	total	100.0	100.0	100.0	100.0	100.0	100.0
PSFT0A1	A	12.9	11.3	22.6	4.8	16.1	4.8
	B	14.5	40.3	27.4	21.0	50.0	11.3
	C	41.9	25.8	19.4	16.1	8.1	14.5
	D	11.3	9.7	24.2	29.0	9.7	12.9
	E	17.7	11.3	3.2	27.4	4.8	41.9
	none	1.6	1.6	3.2	1.6	11.3	14.5
	total	100.0	100.0	100.0	100.0	100.0	100.0
PHYG1A1	A	7.7	7.7	23.1	15.4	7.7	0.0
	B	15.4	23.1	23.1	15.4	53.8	0.0
	C	30.8	30.8	23.1	23.1	0.0	7.7
	D	15.4	7.7	23.1	30.8	15.4	23.1
	E	23.1	7.7	0.0	7.7	0.0	46.2
	none	7.7	23.1	7.7	7.7	23.1	23.1
	total	100.0	100.0	100.0	100.0	100.0	100.0
PHYL1A1	A	25.0	9.4	15.6	3.1	9.4	15.6
	B	6.3	12.5	18.8	28.1	65.6	0.0
	C	31.3	43.8	34.4	12.5	0.0	21.9
	D	12.5	15.6	25.0	31.3	6.3	6.3
	E	21.9	6.3	0.0	18.8	0.0	34.4
	none	3.1	12.5	6.3	6.3	18.8	21.9
	total	100.0	100.0	100.0	100.0	100.0	100.0
PHE3LA1	A	7.5	22.5	5.0	5.0	7.5	0.0
	B	30.0	17.5	17.5	42.5	60.0	22.5
	C	30.0	35.0	37.5	7.5	10.0	32.5
	D	20.0	22.5	37.5	27.5	7.5	2.5
	E	10.0	0.0	2.5	15.0	5.0	30.0
	none	2.5	2.5	0.0	2.5	10.0	12.5
	total	100.0	100.0	100.0	100.0	100.0	100.0

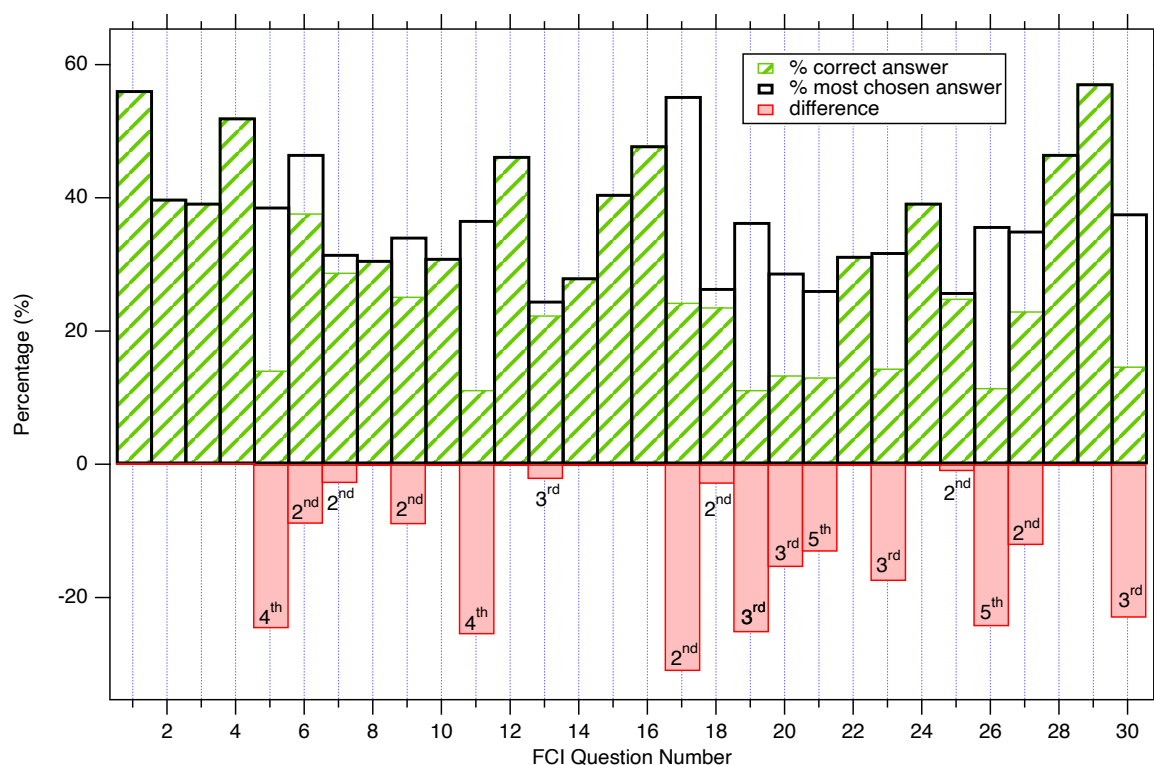


Figure 1. Breakdown of pre-test questions for the 2021 University of Johannesburg students sitting an introductory physics course, $N = 353$. The labels on the red % differences, such as 4th, 2nd etc., label the most commonly chosen (incorrect) response.

4. Concluding remarks

In these proceedings, we have used the pre-test part of the FCI to evaluate the baseline comprehension of Newtonian mechanics presented to first-year students enrolled in six introductory physics courses. We have demonstrated that misconceptions are more easily identified in students with a higher mechanics aptitude (considered to be the physics and life sciences majors in this study), but remain persistent despite extensive training (as in the case of the life sciences students in the third semester of the extended programme).

Although this is only a preliminary study, we hope to extend our data taking across future years (to eliminate any transient biases which may exist in this current cohort), where it would also be interesting to look at data not just from the University of Johannesburg, but also to extend the research by including other universities in South Africa that have similar demographics.

Acknowledgements

EC and ASC are supported in part by the National Research Foundation of South Africa (NRF). AC is supported by the NRF and Department of Science and Innovation through the SA-CERN programme. WN would like to thank Margaret Marshman (University of the Sunshine Coast, Australia) for useful comments and suggestions.

References

- [1] Hammer D 1996 *Am. J. Phys.* **64** 1316.
- [2] Obaidat I M and Malkawi E 2008 *Int. J. Scholarship Teach. Learn.* **3** 19.

- [3] Bayraktar S 2009 *Int. J. Sci. Math. Educ.* **7** 273.
- [4] Martin-Blas T, Seidel L and Serrano-Fernandez A 2010 *Eur. J. Eng. Educ.* **35** 597.
- [5] Savinainen A and Viiri J 2008 *Int. J. Sci. Math. Educ.* **6** 719.
- [6] Bani-Salameh H N 2016 *Phys. Educ.* **5** 2014003.
- [7] Bani-Salameh H N 2016 *Phys. Educ.* **5** 2015006.
- [8] Halloun I. A. and Hestenes D *Am. J. Phys.* **53** 1043.
- [9] Hestenes D, Wells M and Swackhamer G 1992 *Phys. Teach.* **30** 141.
- [10] Hestenes D 1998 *Am. J. Phys.* **66** 465.
- [11] Hake R 1998 *Am. J. Phys.* **66** 64.
- [12] Alinea A L and Naylor W 2015 *Phys. Educ.* **50** 210.
- [13] Alinea A L and Naylor W 2015 *Phys. Educ.* **33**.
- [14] Alinea A L 2020 *Eur. J. Phys.* **41** 065707.
- [15] Carleschi E, Chrysostomou A, Cornell A S and Naylor W 2021 *arXiv preprint*: 2101.09908 [physics.ed-ph].

Classification of sound conceptions

D B Fish¹, T R Anderson², S Aalih³ and N Pelaez⁴

¹ Director: Unizulu Science Centre, University of Zululand, KwaDlangezwa

² Department of Chemistry, Purdue University, West Lafayette, USA.

School of Biochemistry, Genetics and Microbiology, University of KwaZulu-Natal (Pietermaritzburg)

³ Department of Physics, University of Cape Town

⁴ Department of Biological Sciences, Purdue University, West Lafayette, USA

E-mail: thefish@iafrica.com

Abstract. Experience and other studies show that students come to our Science Centres with pre-existing ideas of how the world works (often called prior-, naïve- or mis-conceptions). When confronted with conflicting ideas from science they are forced to make a “border crossing” [1] from the familiar territory of their cherished beliefs into the “unknown country” of science. How difficult this crossing is and how comfortable a student feels to remain in this new country depends on many factors both internal and external to the student. The challenge for our Science Centres is to assist students to cross these borders more easily and to remain in their new country without feeling threatened. An example will be given of student prior conceptions with regard to sound and waves: a brief literature survey will outline pre-existent conceptions noted around the world. The 4 level framework [2] is used to classify these conceptions and modify them in the light of data gathered. Student responses to a questionnaire provide multiple mode (MCQ, written and drawings) feedback into this process. The result is a modified table of local students’ prior conceptions with regard to sound and waves. This is a useful resource when designing (and improving) science shows, exhibits and other programme materials in this area. While the specific example of sound and waves will be the focus of this presentation, suggestions will be made of how this resource can be used in other subject areas.

1. Review of Research into Student Conceptions of Sound (Summary and comments)

Most of the literature on this topic starts with the comment that little work has been done on students’ conceptions of sound [3], [4], or that even in higher level Physics courses, sound is often treated superficially as a simple example of wave-physics [5]. The studies all continue to assert that sound is not a straightforward topic, based on findings of clear gaps in students’ conceptual understanding of the subject material [6]. This review was undertaken using Pfundt and Duit’s [7] Database of student and teacher conceptions and science education, and further searches, which revealed only a few relevant papers.

Linder [5], on summarising the findings of Linder and Erickson [8], reported the following types of understanding of sound expressed by students: Firstly, sound is sometimes seen as an entity carried by individual molecules as they move through a medium. This entity is transferred from one molecule to another through the medium. For others, sound is a traveling bounded substance with impetus, usually

represented in the form of flowing air. Another understanding was that sound is a bounded substance in the form of some traveling pattern. Finally, for many students, sound is linked to the concept of waves as part of a mathematical physics modelling system (but students' wave conceptualization is often divorced from their conceptualization of sound).

Hrepic et al [6] expanded on Linder's idea of the "entity model" with the notion of blend models. They identified the entity model as the usual starting point for naïve students (as would be expected in the present study), and the wave model as the scientifically accepted, or community consensus model. In addition to these two main models he enumerated models which were conceptual blends of these two, incorporating ideas from both of them. His studies showed that most students begin with an entity model of sound, but after instruction move closer to the wave model, but often finishing somewhere in between in a blend model. Linder [5] also discusses at length the confusion caused by representing longitudinal sound waves with transverse sinusoidal waves, and the problems associated with the "water-wave analogy", which is inappropriate at best, incorrect and profoundly misleading. From my very first pilot tests this factor came through very strongly, so was worth a detailed follow-up. He stresses later [9] that students' conceptions can be classified into two perspectives: a mental model (inside the head)-based perspective and an experientially-based one. My experience has shown that sophisticated, urban students tend towards more abstract mental model perspectives, while rural students living simpler lives often maintain a perspective based on their life experiences. This was tested especially in the written answers and drawings.

In a later study, Linder [9] identified three conceptualizations of the factors which university students believe affect the speed of sound, namely: a sound-resistance factor based on the physical size or density of the molecules; a separation factor based on molecular separation as a function of medium density and a compressibility factor based on a (confused) understanding of the elasticity of the medium. Wittman et al. [4] found similar problems with conceptualizations of wave-speed, whereby students believed that the force used to create a wave would determine its speed. In other studies Watt and Russel [10] found that students perceived sound as an invisible object with dimensions which required some space in order to move, echoing Linder's finding of sound as an entity. Similarly, Wittman et al [4] encountered student problems when they focused purely on the object-like properties of sound waves, rather than other properties relating to their propagation. Boyes and Stannistreet [11] uncovered an unusual belief – especially in younger students - in a reverse pathway whereby sound travels from the hearer to the source, rather than source to hearer. We have never encountered that particular notion in many years of teaching Physics, so were interested to see if it surfaced in the present study.

Eshach and Schwartz [3] used the 11 substance schema of Reiner et al [12] to investigate whether students would use these properties to explain sound phenomena. They found that Reiner et al.'s [12] properties were not all applicable, but that some of them did apply. They too cautioned teachers to be careful when describing sound as waves because of the confusion caused between longitudinal, transverse and water waves, echoing Linder's findings and my anecdotal experience. Houle and Barnett [13], in an interesting study using Urban Bird Communication to teach sound topics, found three main student conceptions, that: sound travels in a sinusoidal wave fashion (as mentioned above and by Linder), sound is a material or a substance and sound is a vibration (the "shaking model" of Hrepic et al [6]). Caleon and Subramaniam [14] identified eleven student conceptions of sound, eight of which had featured in at least two previous studies. Huey-Por Chang et al. [15] found similarly that students attributed sound leaving a container carried by the air which escaped through small holes in the container-wall. In addition students in Caleon and Subramaniam's [14] study asserted that sound, unlike light, cannot be refracted and that wave speed is dependent on wave properties such as frequency or amplitude, with a resulting confusion as to whether pitch is associated with amplitude or frequency. Again many of their students imagined sound as propagating like a (transverse) sine-wave.

My anecdotal experience from teaching and performing this show for many years is that students do indeed confuse frequency and amplitude (and pitch and volume), so in the present study questions were designed to test this.

Calik [16] compared different conceptual change pedagogies and their effectiveness and found that a combination of different methods (e.g. the use of analogies, computer animations and conceptual change text) was most effective in producing conceptual change in sound-related topics. Finally, Hapkiewicz [17] compiled a list of 17 Student Conceptions of sound (“Sound Misconceptions”) in the Michigan Science Teachers’ Association newsletter, based on teaching experience, which formed the main basis for my list.

2. Synthesis and Classification of student difficulties with sound

The goal of this study was to perform a comprehensive synthesis and classification of students’ difficulties with the phenomenon of sound based on both the Hapkiewicz list [17] and other relevant literature. The initial synthesis was taken mostly from the literature with some input from teaching experience. This was then modified in the light of the data *we* gathered and reflected in the final table, table 1. The four-level framework [2] was used to classify the conceptions at different levels, according to the insight one has from research or experience into the nature of the difficulty. Those difficulties firmly established by multiple studies with different groups are classified with a 4 at the top level as ***established***. These were confidently used in devising questions and distracters. Those shown in a single study or in limited studies as only ***partially established*** were classified as 3, and those merely suspected from anecdotal information mentioned in single studies (and which *we* have personally not encountered), or from personal experience (teaching science *or presenting* this show for 20 years) were classified at level 2, as ***suspected***. It is expected that this study will produce some as yet ***unanticipated*** conceptions, which *we* will then add at level 1. Finally the difficulties will be reclassified in the light of the results and data, possibly resulting in some of them moving up the list as being more firmly established.

A simple study of 117 Grade 9 students from three different schools (urban, township and rural) was conducted using pre and post tests administered before and after a science show on sound and waves at the Unizulu Science Centre. Students answered the same 10 multiple choice questions before and after the show and then more comprehensive questions after, including written explanations and drawings. The questions were carefully structured to cover all the difficulties in the table below and data analysed to probe for evidence of students displaying these difficulties. Having done the data analysis of the mixed-mode student questionnaires, table 1 was established: with the following columns:

OR LEV – the initial 4 level classification of the difficulty based on experience and literature survey alone

FIN LEV – the revised 4-level classification amended in the light of data

LIT REF – the number of different literature references mentioning this difficulty

SEEN IN DATA: the prevalence of this difficulty in my student data, ranked from 0 (not present) to 5 (present across all groups)

The student difficulties are numbered from 1 through 19 and will hereafter be referred to as “d 1” etc.

Table 1: Summary of student difficulties evident: level, literature references and prevalence.

NO.	DIFFICULTY	OR LEV	FIN LEV	LIT REF	SEEN IN DATA
1	Sound travels as a transverse sine wave	4	4	8	4
2	Sound is a microscopic entity either carried by or transferred between molecules	4	(4)	4	0
3	Sound is a macroscopic entity with impetus like flowing air or a traveling pattern	4	(4)	5	0
4	Speed of sound-wave is affected by: force, sound-resistance, molecule separation	4	(4)	5	0
5	Sound can be trapped in a container if the air is trapped-needs holes to escape	4	4	4	3
6	Sound can travel through a vacuum and therefore through space	4	4	4	3
7	Sound waves cannot be refracted or bent like light	3	(3)	2	0
8	Confusion between volume and pitch (and amplitude and frequency) and their units	3	4	2	5
9	Sound only travels if air is present (therefore can't travel through liquids or solids)	3	4	2	5
10	A human has many different vocal cords to produce different sounds	2	(2)	1	0
11	Ultrasounds are very loud sounds	2	(2)	1	0
12	Sound travels from the hearer to the source (Reverse sound)	2	(2)	1	0
13	Music has low volume (small amplitude) & noise has high volume (large amplitude)	2	2		3
14	Longer objects vibrate faster, or produce higher notes	2	2		1
15	The sound box on a musical instrument is to make the sound clearer	2	2		1
16	Vibrations and waves are the same thing	2	2		3
17	Sound travels as electromagnetic Waves	1	2		3
18	Sound is unaffected by solid obstacles, passing right through them	1	2		4
19	Sound waves turn towards a hearer	1	2		5

In general it is apparent from table 1 that the difficulties experienced by South African students were not the same as those found overseas. We did not experience any students displaying difficulties d2, d3 or d4, but these are deeper level explanations which would be more likely to come out in interviews than in the simple tests we used. Similarly, we didn't experience d7 either, but again we are not sure if it would have come out in our simple tests. d8 and d9 came out consistently across all school groups and one should consider reclassifying these at level 4 (as they also come from the literature). From all the data, we found no evidence of d10, 11 or 12, and indeed have never found any evidence of these while doing this show, so would not suggest raising them to a level 3. None of d13 – d16 was found in all the groups and we would not want to elevate these to level 3 without finding some more evidence of their regular occurrence. The new student difficulties d17 – d19 were fairly consistent across all the schools (although slightly less so for the rural group) and in future studies we would certainly raise them to a level 2. These suggested changes to the level are reflected in the fourth column in table 1, but could certainly be revised following further studies. The above discussions allowed table 1 to be modified into a condensed table which better shows local students difficulties with sound (but space does not allow it to be displayed). This table would reflect the final level we came to, rather than the original level and would omit difficulties not encountered locally (those with the final level in parentheses)

3. Conclusion

In conclusion this study yielded some interesting insights into local student difficulties in sound. Starting with a difficulties table drawn from the literature, this was refined and focussed on a particular group of South African students. Our students' difficulties were not unlike those in the literature, although it was interesting that a few difficulties in the table above were not found in this group. It was also interesting to discover strong evidence of 3 new difficulties not found in the literature and to add these as d 17, 18 and 19. The final, refined table will be very useful in designing and evaluating science shows on sound. Indeed a similar method could be employed for any section of the Physics curriculum and could be adapted to guide teaching at school or tertiary level. This research was limited to the evaluation of a single science show in one subject area. Much work has been done in attempting to evaluate the impact of Science Centres in general (for example Perrson [18]) but this is a much more complex issue and beyond the scope of this study.

References

- [1] Aikenhead, G. (1996). "Science Education: Border crossing into the subculture of science." *Studies in Science Education* **27**: 1-52
- [2] Grayson, J., Anderson, T. R., Crossley, L. G. (2001). "A four-level framework for identifying and classifying student conceptual and reasoning difficulties." *International Journal of Science Education* **23**(6): 611-622
- [3] Eshach, H., and Schwartz, J. L. (2006). "Sound stuff? Naive materialism in middle-school students' conceptions of sound." *International Journal of Science Education*, **28**(7), 733-764 // g6, P, S, GC
- [4] Wittmann, M. C., Steinberg, R. N., Redish, E. F. (2003). "Understanding and affecting student reasoning about sound waves." *International Journal of Science Education*, **25**(8), 991-1013
- [5] Linder, C. J. (1992). "Understanding sound: so what is the problem?" *Physics Education*, **27**(5), 258-264
- [6] Hrepic et al (2010). "Identifying students' mental models of sound propagation: The role of conceptual blending in understanding conceptual change." *Physics Education Research* **6**, 020114 _2010
- [7] Pfundt, H and Duit, R (1988) "*Bibliography: Students' Alternative Frameworks and Science*

Education." Kiel. IPN

- [8] Linder, C. J., Erickson, G. L. (1989). "A study of tertiary physics students' conceptualizations of sound." *International Journal of Science Education*, **11**, 491-501
- [9] Linder, C. J. (1993). "University physics students' conceptualizations of factors affecting the speed of sound propagation." *International Journal of Science Education*, **15**(6), 655-662
- [10] Watt, D., and Russell, T. (1990). "Sound, primary SPACE project research report." Liverpool, England: Liverpool University Press
- [11] Boyes, E., and Stanisstreet, M. (1991). "Development of pupils' ideas about seeing and hearing—The path of light and sound." *Research in Science and Technology Education*, **9**, 223–251
- [12] Reiner, M., Slotta, J. D., Chi, M. T. H., and Resnick, L. B. (2000). "Naïve physics reasoning: A commitment to substance-based conceptions." *Cognition and Instruction* **18**(1), 1–34
- [13] Houle and Barnett (2008). "Students' Conceptions of Sound Waves Resulting from the Enactment of a New Technology-Enhanced Inquiry-Based Curriculum on Urban Bird Communication." *Journal of Science Education and Technology* (2008) **17**:242-251
- [14] Caleon and Subramaniam, (2010). "Development and Application of a Three-Tier Diagnostic test to Assess Secondary Students' Understanding of Waves." *International Journal of Science Education*, **32**(7), 939-961
- [15] Huey-Por Chang et al (2007): "Investigating Primary and Secondary Students' Learning of Physics Concepts in Taiwan." *International Journal of Science Education*, **29**(4), 465-482
- [16] Calik, M et al. (2011). "A Comparison of Different Conceptual Change Pedagogies Employed Within the Topic of 'Sound Propagation'." *Journal of Science Education and Technology* (2011) **20**:729–742
- [17] Hapkiewicz, A. (1992). "Finding a List of Science Misconceptions." *MSTA Newsletter*, **38**(Winter '92), pp.11-14
- [18] Persson, P. E. (2000). "Science centers are thriving and going strong!" *Public understanding of science*, **9**(4), 449-460

Grade 11 Physical Sciences learners' perceptions of scientific inquiry

R Zunga and S Ramaila

Department of Science and Technology Education
University of Johannesburg, South Africa

E-mail: samr@uj.ac.za

Abstract. This study explored South African Grade 11 Physical Sciences learners' perceptions of scientific inquiry within the context of science classrooms. The study adopted a mixed method approach as part of an exploratory descriptive survey design and involved 50 purposively selected Grade 11 physical sciences learners from 3 South African township schools. Quantitative data was collected by administering a validated Learner Perceptions of Classroom Inquiry (LPCI) instrument with the participants. Qualitative data was collected through semi-structured interviews. The study revealed that the learners held mixed conceptions about the nature of scientific inquiry. A substantial number of learners held naïve and incoherent views about the nature of scientific inquiry. Lack of practical laboratory lessons, lack of well-equipped science laboratories, inadequate teacher professional competence when conducting scientific investigations, and limited opportunities for meaningful engagement in inquiry-based learning activities were perceived to be contextual factors that serve to hinder meaningful enactment of scientific inquiry in science classrooms. The findings have profound implications for meaningful enactment of contemporary pedagogic approaches such as inquiry-based learning in diverse contexts. Theoretical implications for coherent development of scientific literacy through meaningful enactment of scientific inquiry within the broader South African educational context are discussed.

1. Introduction

The Curriculum and Assessment Policy Statement (CAPS) promulgated by the South African Department of Basic Education (DBE) advocates that the teaching and learning of science ought to engage learners to perform scientific investigations, identify, analyse and solve problems, design and evaluate solutions and then apply the knowledge in new contexts [1]. Scientific inquiry provides opportunities to enhance understanding in a process of testable illustrations and explanations that learners can utilize to guess the outcome of subsequent investigations. This empowers learners or scientists to acquire a greater perception of the subject or topic they may be studying thereby making use of the understanding in other science topics by following the science process. Scientific inquiry is widely accepted as a method of science teaching. Understanding the characteristics of the Nature of Scientific Inquiry (NOSI) is also necessary for a whole conception of scientific inquiry [2]. This study explored Grade 11 Physical Sciences learners' perceptions of their experiences of scientific inquiry within the context of science classrooms at three South African township schools.

In the knowledge-based economy, “learning-by-doing” is paramount, and inquiry-based learning activities could encapsulate experiences that develop thinking skills needed in the workplace. These new demands from the workplace and the technological advancements of the world in which we live served to stimulate much change in national curricula throughout the world [3]. In terms of the Next Generation Science Standards (NGSS), students are expected to demonstrate understanding by developing and constructing models, planning and carrying out investigations, constructing explanations, analyzing and interpreting data sets, providing evidence, and using argumentation to substantiate findings [4]. Hence, scientific inquiry is synonymous with a vision of scientific literacy that encompasses skills and knowledge related to scientific and engineering practices [5].

2. Research design and methodology

The study adopted a mixed method approach as part of an exploratory descriptive survey design. Population and sampling. For this study, the target population comprised of Physical Sciences learners from three township schools in the Gauteng West District located in the Gauteng Province of South Africa. The study involved 50 purposively selected Grade 11 Physical Sciences learners as participants. Grade 11 Physical Sciences learners constituted a representative sample of a cohort of Physical Sciences learners as a target population. Quantitative data was collected through the administration of Learner Perceptions of Classroom Inquiry (LPCI) instrument with the participants. Qualitative data was collected through semi-structured interviews. Table 1 below provides a breakdown in terms of the number of participants from each school.

Table 1. Number of participants from each school.

School	Type of school	Number of participants
A	Township School	16
B	Township School	17
C	Township School	17

3. Results

3.1 Findings emanating from quantitative data

Table 2 below provides the distribution of responses to the questionnaire. The counts (frequencies) are determined for each of the items based on participants’ responses. Majority of the learners (58%) indicated that they were afforded opportunities to ask frame research questions in a science classroom while 42% of the learners indicated that they have not been afforded such opportunities. While 54% of the learners were not exposed to formulation of questions which can be answered by investigations, 46% of the learners were exposed to such an activity as part of the enactment of scientific inquiry. The learners provided varied responses to the item “My research questions are used to determine the direction and focus of the lab”. Responses to this item indicate that learners’ research questions were not taken into account when determining the direction and focus of the laboratory activities. A considerable number of learners (68%) appreciated the importance of framing their own questions when conducting scientific investigations. The learners devoted time to refine their questions so that they can be answered by the investigation. This sentiment was expressed by 52% of the learners. the findings emanating from quantitative data demonstrated that when enacting scientific inquiry, Physical Sciences learners at selected schools were afforded limited meaningful opportunities to ask framing research questions in the science classroom, design investigations in the science classroom, conduct investigations in the science classroom, collect data in the science classroom, and draw conclusions in the science classroom. This deficiency in teacher professional practice can be attributed to teacher

commitment to traditional instruction which is not compatible with the dictates of meaningful enactment of scientific inquiry. These findings point the need for sustainable teacher professional development interventions which are geared towards the enhancement of professional practice on meaningful enactment of contemporary pedagogical approaches such as inquiry-based learning. The development of scientific literacy would be severely restricted if appropriate systems are not put in place to implore teachers as key agents of educational change to fully embrace pedagogic innovation with a view to create conducive, dynamic and intellectually stimulating teaching and learning environments. Coherent realization of this key strategic imperative requires commitment on the part of South African Department of Basic Education to provide meaningful platforms which promote transformation of teacher professional practice in its broadest sense.

Table 2. Distribution of responses .

Items	Frequencies				
	Almost never	Seldom	Sometimes	Often	Almost always
Learners ask framing research questions in the science classroom					
<i>I formulate questions which can be answered by investigations</i>	13	14	12	6	5
<i>My research questions are used to determine the direction and focus of the lab</i>	14	13	5	13	5
<i>Framing my own questions is important</i>	7	9	10	8	16
<i>Time is devoted to refining my questions so that they could be answered by investigations</i>	11	13	8	11	7
Learner designs investigations in the science classroom					
<i>I am given stepwise instructions before they conduct investigations</i>	3	5	15	10	17
<i>I design my own procedures for investigations</i>	23	7	18	12	0
<i>We engage in the critical assessment of the procedures that we employ when conducting investigations</i>	10	5	13	19	3
<i>We justify appropriateness of the procedures that are employed when we conduct investigations</i>	10	5	7	24	4
Conducting investigations in the science classroom					
<i>I conduct my own procedures of an investigations</i>	17	13	3	13	4
<i>The investigation is conducted by the teacher in from of class</i>	4	11	8	8	19
<i>I actively participate in investigations as they are conducted</i>	7	16	7	11	9
<i>I have a role as investigations are conducted</i>	23	3	9	7	8
Collecting data in the science classroom					
<i>I determine which data to collect</i>	27	3	18	2	0
<i>I take detailed notes during each investigation along with other data I collect</i>	8	7	9	19	7
<i>I understand why the data I am collecting is important</i>	10	5	7	24	4
<i>I decide when data should be collected in an investigation</i>	12	13	14	5	6

Drawing conclusion in the science classroom

<i>I develop my own conclusion for investigation</i>	4	12	11	6	17
<i>I consider a variety of ways of interpreting evidence when making conclusions</i>	9	15	8	11	7
<i>I connect conclusions to scientific knowledge</i>	21	5	7	7	10
<i>I justify my conclusions</i>	2	5	12	13	18

3.3 Findings emanating from qualitative data

Findings emanating from qualitative data are clustered according to the themes that emerged during data analysis. The themes are: enactment of scientific inquiry, available infrastructure and resources, and contextual factors influencing the enactment of scientific inquiry in science classrooms.

Theme 1: Enactment of scientific inquiry in science classrooms

The enactment of scientific inquiry at the selected schools appeared to be teacher-centred. Limited opportunities were provided for learners to design investigations in the science classroom. Learners were not at liberty to design their own procedures for investigations as required by the nature of scientific inquiry. This sentiment is reflected in the following excerpt.

“We are not given the chance to be imaginative and creative when doing investigations in the classroom. The teacher does everything”

At another pragmatic level, learners bemoaned lack of meaningful opportunities to ask framing research questions in the science classroom when performing scientific investigations. Yet, framing research questions is central to the design of scientific investigations. These concerns are captured in the following excerpt.

“Sometimes it is difficult to understand the research questions informing the scientific investigation performed in class. This understanding is important for us as learners.”

While learners appreciated the importance of data collection as an integral part of scientific investigations, they bemoaned lack of opportunities to independently determine the type of data to collect. Learner autonomy is a key ingredient for fostering the development of investigation skills. Concerns expressed in this regard are encapsulated in the following excerpt.

“The teacher tells us everything about data collection and the scientific phenomenon to be investigated. We follow the recipe approach when performing scientific investigations in our classroom.”

Theme 2: Available infrastructure and resources

Township schools are generally under-resourced and this state of affairs adversely affects provision of quality education within the broader South African context. More specifically, general lack of resources has a detrimental impact on meaningful enactment of inquiry in science classrooms. Sentiments expressed by the participants in relation to this state of affairs are reflected in the following excerpt.

“We don’t have any labs at school, usually Mam does the experiments. Teachers improvise with little resources that we have. We don’t have labs, often chemicals used are outdated. Teachers try to involve us and set apparatus as groups.”

Theme 3: Contextual factors influencing the enactment of scientific inquiry in science classrooms

The implementation of scientific inquiry at the selected township schools appeared to be influenced by a myriad of contextual factors. These factors included general lack of infrastructure and resources, lack of teacher professional competence on the enactment of scientific inquiry, adoption of teacher-centred approaches, language as a barrier in science learning, and lack of meaningful opportunities for learners to engage in deep learning. Concomitant sentiments expressed in this regard are captured in the following excerpt.

“The teacher does not give us chance to actively participate when doing scientific investigation. We want to be imaginative and creative when we take part in the activities. Sometimes working in groups is not nice because you cannot do the investigation independently. But, lack of laboratory resources is a problem.”

4. Discussion

The study uncovered inadequacies associated with the enactment of scientific inquiry at selected South African township schools. General lack of resources at township schools appears to have a detrimental impact on meaningful enactment of inquiry in science classrooms. In most schools, poor infrastructure and resources limit learners' engagement in inquiry-based activities and by extension the opportunity to understand the nature of scientific inquiry [6]. The use of language appeared to be a barrier to meaningful enactment of inquiry in science classrooms. Instructional language serves as a barrier to students' performances in Physical Sciences [7]. Meaningful enactment of inquiry-based learning as a contemporary pedagogic approach remains a fundamental challenge to teachers as key agents of educational change within the broader South African context. The views expressed by learners about the nature of scientific inquiry point to extensive exposure to instructional settings providing limited opportunities for learner autonomy when performing scientific investigations. Such instructional settings essentially serve to stifle meaningful development of inquiry skills required to perform plausible scientific investigations. The development of learners' knowledge about scientific inquiry remains a key science education curriculum goal. Yet, many secondary school learners continue to demonstrate naive understandings about scientific inquiry [8]. Meaningful enactment of scientific inquiry was largely hampered by a myriad of contextual factors. These factors included general lack of infrastructure and resources, lack of teacher professional competence on the enactment of inquiry, adoption of teacher-centred approaches, language as a barrier in science learning, and lack of meaningful opportunities for learners to engage in deep learning.

By its very nature, enactment of inquiry provides learners with opportunities to grapple with scientific data, make observations, draw conclusions, provide explanations for evidence and communicate findings [9]. However, it must not be assumed that when learners engage in or do scientific inquiry, they automatically understand the NOSI [10]. Teachers should not only engage learners in investigations, but should also provide them with explicit/reflective instruction on the rationale for every inquiry action for learners to understand the process through which scientists generate knowledge [11]. It is believed that such an approach essentially serves to develop learners' scientific inquiry skills as well as the understanding of the nature of scientific evidence and knowledge.

5. Conclusion

The study demonstrated that learners at selected township schools held fragmented and mixed views about the nature of scientific inquiry as a result of the inadequacy of traditional instruction. The enactment of scientific inquiry was largely characterized by the adoption of teacher-centred approaches which are not compatible with the development of scientific inquiry skills. There is a

critical need to enhance teacher professional capacity required for meaningful implementation of contemporary pedagogic approaches such as inquiry-based learning.

6. References

- [1] Department of Basic Education 2011 *CAPS* Pretoria Government Printer
- [2] Leblebicioglu G, Metin D, Capkinoglu E, Cetin PS, Eroglu Dogan E and Schwartz R 2017 Changes in students' views about nature of scientific inquiry at a science camp *Sci. & Ed.* doi:10.1007/s11191-017-9941-z
- [3] Ramnarain U and Hlatwayo M 2018 Teacher beliefs and attitudes about inquiry-based learning in a rural school district in South Africa *S.A. Afric. J. Ed.* **38** 1
- [4] Jorgenson O, Vanosdall R, Massey V and Cleveland J 2014 *Doing Good Science in Middle School*, Expanded 2nd Edition: A Practical STEM Guide. NSTA Press
- [5] Lederman JS, Lederman NG, Bartos SA, Bartels SL, Meyer AA and Schwartz RS 2014 Meaningful assessment of learners' understandings about scientific inquiry – The views about scientific inquiry (VASI) questionnaire *J. Res. Sci. Teach.* **51** 65
- [6] Bantwini B 2017 Analysis of teaching and learning of natural sciences and technology in selected Eastern Cape Province primary schools S.A. J. Ed. **67** 39
- [7] Mosoeunyane MG 2001 The Relationship between Language Scores and Science Scores of 538 Junior Certificate Students in Lesotho
- [8] Abd-El-Khalick F and Lederman NG 2000 Improving science teachers' conceptions of nature of science: A critical review of the literature *Int. J. Sci. Ed.* **22** 665
- [9] Crawford B 2014 From Inquiry to Scientific Practices in the Science Classroom. In 1141 *Handbook of Research on Science Education*, vol. II, edited by N. Lederman and S Abell, 515–544. New York: Taylor and Francis Group
- [10] Lederman NG and Lederman JS 2004 Project ICAN: A Professional Development Project to Promote Teachers' and Students' Knowledge of Nature of Science and Scientific Enquiry The 11th annual SAARMSTE conference, Cape Town, SA
- [11] Lederman JS, Lederman NG, Bartels S, Jimenez J, Akubo M, Aly S and Bao C 2019 An international collaborative investigation of beginning seventh grade students' understandings of scientific inquiry: Establishing a baseline *J. Res. Sci. Teach.* **56** 486

Music, context-based inquiry, and computer simulation as engagement strategy

Grace Djan¹ and Miriam Lemmer¹

Northwest University, Potchefstroom South Africa

E-mail: gdjan@hotmail.com

Abstract. The standard of engagement in science classes is fundamental for effective learning. Creating an active learning environment is essential for engaging learners. However, implementing engagement is a critical problem that teachers face. Due to the large variety of engagement strategies teachers often do not know what strategy to use or make use of. This paper attends to the factors that could influence the choice of an appropriate engagement strategy. The objective of this research study was to explore music, context-based inquiry, and computer simulation as engagement strategies as well as the impact of these strategies on the four components (behavioural, affective, cognitive, and authentic) of engagement. The application of mixed methods comprised of a pre-test and post-test questionnaire (quantitative), video recording and semi-structural interviews (qualitative). The general results that follow from this research is that the choice of an appropriate engagement strategy does not only depend on the topic that is taught, but also on other factors namely teachers' acquaintance with the strategy, the learning environment, the background of the learners, the engagement components that need attention as well as the amount of time available. A combination of the three engagement strategies is proven to enhance learning engagement.

1. Introduction

Engagement is viewed as active involvement, curiosity, and the drive to learn and achieve. Learning, that involve active participation of students using different learning strategies creates active learning. [1] found that a combination of technology-infused strategies and online approaches such as Google Classroom and "flipped classrooms" using a variety of well-planned activities promote engagement. With the normal South-African context in mind, we focused instead on learner engagement through three engagement teaching strategies that can be used in face-to-face classrooms. Namely music, context-based inquiry, and computer simulations.

The purpose of this paper is to determine the impact of these three engagement strategies on the four components of engagement, namely cognitive, affective, behavioural, and authentic engagement. Given its wider scope, this paper serves to examine factors that affect science teachers' choice of strategy based on how these strategies influence learner engagement. Therefore, the research questions are: what is the impact of music, context-based inquiry, and computer simulation as engagement strategies on the four components of engagement? What factors may affect the choice of a teaching strategy?

1.1 Music and its importance to learning

Music is a pedagogical approach to science education that is appropriate to provide an alternative science teaching and engagement strategy [2]. Firstly, it activates prior knowledge, promote critical thinking which is a crucial aspect of learning [2], [3]. Secondly music may promote engagement, excitement, and creativity, although the excitement may sway learners from complying to class discipline [4], [5].

1.2 Context-based and its importance to learning

Context-based strategies bridge the gap between learning in class and everyday life which include solving problems that are relevant to students [6], [7]. This strategy promotes meaningful science learning and successful transfer of knowledge across different contexts as well as between the classroom and the real-world [8], [9]. The use of the context-based strategy may promote learner engagement with content, learner responsibility to learn, and active involvement [10], [11].

1.3 Computer simulation and its importance to learning

Computer simulation was pioneered as a scientific tool in meteorology and nuclear physics immediately after World War II and has now expanded into a number of research disciplines [12]. Even though computer simulation can slow down learners' interpersonal skills [13], it can be used to teach complex physics [14]. Additionally, it may provide positive contribution and significant improvement in the performance of students [14], [13], [15].

2. Design and method of empirical study

Fifty in-service secondary school science educators of the North-West province participated in two Saturday's workshops. The intervention entailed the use of music, context-based inquiry, and computer simulation to engage the participants to learn basic concepts of the Periodic Table. In order to accomplish this, a reliable questionnaire with valid constructs was compiled by the researcher. The questionnaire served as pre and post-test; followed-up by semi-structured interviews.

The application of sequential explanatory mixed method in this study procedure provided the opportunity for the researcher to combine elements of quantitative and qualitative research approaches for breadth and depth of understanding, validation, corroboration, and verification [16], [17].

The questionnaires used in the pre-test and post-test contained different groupings of questions that formed constructs. All questions were categorised into phases: Phase 1 music, Phase 2 context-based inquiry, and Phase 3 computer simulation. Each phase was assessed with questions in four constructs that relate to the four components of engagement, namely cognitive, affective, behaviour and authentic. Each construct contained five sub-questions in the form of a statement with four Likert scale options. Options 1 and 2 correspond to strongly disagree or disagree with the statement, while options 3 and 4 indicate agree and strongly agree respectively. A statistical analysis was done to determine the reliability and validity of the constructs, to produce frequency tables and compare pre- and post-test results.

Though all fifty participants took part in completing the questionnaire, six participants were interviewed after completion of the interventions. Six is a convenient and manageable number to represent the sample of teachers in the semi-structural interview. The results were transcribed, and trends were determined.

3. Results

3.1 Reliability and validity of constructs

To answer the first research question, the pre- and post-test results were compared with the aid of Cohen's effect sizes. This requires reliability and validity of the questionnaire which were respectively established by Cronbach's alpha coefficients and factor analysis. Table 1 gives the Cronbach's alpha coefficient for the sets of questions pertaining to each phase (or strategy). Phase 1 questions relate to

music, phase 2 to context-based inquiry and phase 3 to computer simulation as engagement strategy. Three participants did not complete phase 1 questions while four did not complete phases 2 and 3.

Table 1. Reliability of sets of questions per phase.

Sets of questions	N	Cronbach's Alpha	Internal consistency
Phase 1 Music	47	0.87	Very good
Phase 2 Context-based inquiry	46	0.86	Very good
Phase 3 Computer simulation	46	0.89	Very good

All the sets of questions on the strategies proved to have been answered consistently with a high Cronbach's alpha value between 0.85 and 0.9. Each of these sets were then divided into the 4 constructs of 5 sub-questions, each pertaining to a component of engagement. All constructs also yielded Cronbach alpha values larger than 0.8 and are thus reliable.

Construct validity was determined with the aid of a factor analysis. According to the results, the number of factors retained by the Mineigen criterion was 1 for each of the constructs. Low variation in communalities confirmed that the constructs contained valid, interrelated questions.

3.2 Cohen's effect size

Cohen's effect size, d , for dependant groups, were used to compare the averages of the constructs before and after the intervention. The two matched groups were the pre and post-test averages obtained for each construct. The descriptive statistics includes interpretation of comparisons between the group means as illustrated in Table 2. Practical significance, which indicates the degree to which the difference is large enough to have an impact in practice, follows from Cohen's d -values, namely small effect: $d = |0.2|$; medium effect (noticeable with the naked eye): $d = |0.5|$; large effect (practically significant): $d \geq |0.8|$. The constructs with noticeable d -values are marked in bold in Table 2.

Table 2. Descriptive statistics of constructs for pre- and post-tests.

Constructs		N	Pre-test Average %	Post-test Average %	Cohen's effect sizes (d)
MUSIC	Cognitive	47	80.50	88.25	0.58*
	Affective	45	84.25	85.75	0.24
	Behaviour	45	80.75	87.00	0.51*
	Authentic	47	83.50	85.50	0.21
CONTEXT-BASED	Cognitive	45	84.75	84.50	0.10
	Affective	46	81.50	84.50	0.13
	Behaviour	46	85.75	85.75	0.02
	Authentic	47	83.50	84.25	0.01
COMPUTER SIMULATION	Cognitive	47	87.25	93.25	0.51*
	Affective	46	83.75	88.50	0.29
	Behaviour	46	85.25	88.50	0.24
	Authentic	45	82.25	90.00	0.23

For all constructs, except context-based cognitive, the average scores were higher in the post-test than the pre-test. This implies that the teachers' perception after the intervention changed positively. A general shift towards the Strongly Agree option was observed in the post-test results.

The interventions had a medium effect that is noticeable with the naked eye on the following constructs (with $0.5 \leq d \leq 0.8$): Music cognitive, Music behaviour, and Computer cognitive. For example, for the cognitive construct of music there was a difference in average of nearly 8% in pre and post-test scores. The d-value ($d=0.58$) indicates that the music intervention had a medium effect on the perceptions of the teachers regarding cognitive engagement through music, while the effects on affective and authentic were small ($0.2 \leq d \leq 0.5$).

The constructs under context-based inquiry showed no significant difference between pre and post-test responses, with a consequent low d-value ($d < 0.2$). On the other hand, computer simulations impacted positively with small to medium effect on all four engagement components.

3.3 Factors that influence the choice of strategy

Both the questionnaire and interview results contributed to answering the second research question. The quantitative results showed the impact of the interventions on teachers' perceptions regarding the association of three teaching strategies with four components of engagement (Table 2). The factors characteristic to the components of engagement with the largest percentage change from the pre to the post-test for each strategy are described in Table 3.

Table 3. Description of some factors related to teaching strategies that enhance learner engagement.

Teaching strategy	Engagement component	Description
Music	Cognitive	Aid learning scientific concepts. Useful for enhancing understanding of relationships.
	Behaviour	Enhance participation in class. Promote concentration on content.
Context-based inquiry	Affective	Arouse interest to learn and promote enjoyment. Create an environment with a pleasant working climate.
Computer simulation	Cognitive	Useful for promoting conceptual understanding and mastering of content. Create opportunity to visualize abstract concepts. Assist students to engage in science problem solving in a meaningful way.
	Affective	Improve classroom environment by creating a friendly working climate. Promote enjoyment and passion to pursue STEM career.
	Authentic	Create opportunity to use variety of resources with activities that match real world tasks. Enhance collaboration and teamwork.

According to Table 3, music strategy mostly enhances cognitive learning of scientific concepts and is useful for understanding relations amongst concepts. Music also accomplished behavioural factors such as concentration and active participation. Context-based inquiry only yielded a positive change in favour of affective engagement. This entailed arousing interest and creating a pleasant working climate. The interventions further increased teachers' perceptions that cognitive, affective, and authentic engagement can be achieved with the aid of computer simulations. Prominent factors include visualisation of abstract concepts (cognitive), a friendly working climate (affective) and enhancement of collaboration and teamwork (authentic).

With regard to the qualitative results, the following interview quotes by the interviewees provide examples that confirm quantitative results shown in Table 3 concerning the engagement components relevant to the different strategies.

- ⊙ Music: “music helps with memorisation of facts, definition and things like that”
- ⊙ Context-based: “It is also helpful with concept of the content and abstract.”
“Experiment brought out the interest.” “Doing practical fascinates learners.”
- ⊙ Computer simulation: “Much easier to use.” “Do not need lots of preparation.”
“Do not need a lot of resources.”

Apart from the effect of engagement, the interviewees also brought out the following factors that may determine the strategy that teachers use:

- ⊙ Teachers’ acquaintance and knowledge of the strategy:
“You need to know it yourself of how you must maneuver it from one side to the other, so you do not flop.”
- ⊙ Content to be taught:
“How do one put those calculations of formulae in terms of music?”
- ⊙ Time available:
“It can work ... but the time to create the music will take all your time.”
- ⊙ Learner background and personality
“...the very shy person who you thought was not interested in reading or ... they even have more knowledge than those who actually pass.”
- ⊙ Learning environment
“It arouses and creates interest and enjoyment, participation. The group was very inquisitive”.

4. Discussion of results

The quantitative results showed that the three teaching strategies impacted at differing intensities on the four components of engagement. The use of music has the highest practical, and noteworthy impact on both cognitive and behaviour engagement followed by affective engagement and the least on authentic engagement. It enhances understanding and application of scientific concepts, more specifically of basic facts and definitions. Furthermore, it promotes concentration and active participation in class.

With regard to context-based inquiry, the teacher participants’ perceptions that affective engagement can be achieved, was enhanced by the intervention. This was described by terminology such as interest, enjoyment, and fascination. However, context-based inquiry only had minor effects on perceptions regarding cognitive, authentic engagement and little effect on behaviour engagement. The reason might be that participants, being science teachers, were already accustomed to the application of context-based inquiry and the intervention consequently did not change their perceptions regarding the value of this engagement strategy.

Computer simulation was successful in enhancing cognitive engagement to a medium effect and affective, authentic, and behavioural engagement to a lesser effect. Mastering of content and visualisation of abstract concepts are prominent factors. It also requires less resources than context-based inquiry.

Although engagement was the main focus of the investigation, other factors that could affect the choice of the teaching strategy came to the fore, namely the teacher’s acquaintance and knowledge of the strategy, the topic of the lesson, amount of time available, the learning environment and the background and personalities of students.

5. Conclusions and recommendations

In conclusion, it can be postulated that teachers should use all three strategies, music, context-based inquiry, and computer simulation as each has its own beneficial impact on the different components of

engagement. For instance, music can be used in an introductory lesson, for learning basic concepts and definitions, in order to enhance cognitive and behavioural engagement. Additionally, context-based inquiry can be used for learning concepts and application problems and to enhance affective engagement. Computer simulation is ideal for all topics, especially abstract content, and may enhance all the four components of engagement.

In order to engage students, we must be able to understand our students, to select an appropriate engagement strategy for each specific context. A solid understanding of the links between how students engage in learning and how to help students to engage in learning should be further investigated.

References

- [1] Nueva N G C and Calica J 2018 Technology-infused approach to learning science: an examination of students learning experiences and academic achievement. *Asia-Pacific Soc. Sci. Rev.* **18** 114-126
- [2] Crowther G J, McFadden T, Fleming J S and Davis K 2016 Leveraging the power of music to improve science education *J. Sci. Educ.* **38** 73-95
- [3] Miché M 2002 Weaving music into young minds (Albany, NY: Delmar Thomson Learning) p304
- [4] Kuśnierek A 2016 The role of music and songs in teaching english vocabulary to students. *World Sci. News.* **43** 1-55.
- [5] Murphey T 2013 Music and song-resource books for teachers Oxford University Press.
<https://books.google.co.za/books?hl=en&lr=&id=rfCdBgAAQBAJ&oi=fnd&pg=PT15&ots=bIHBB38KsP&sig=jTf1RXPfJ0-PA9lj6cCgeXbea3U&> Date of access: 21 Dec.2019
- [6] Duran M and Dökme I 2016 The effect of the inquiry-based learning approach on student's critical-thinking skills. *Eurasia J. Math, Sci. & Tech. Edu.*, **12** 2887-2908
- [7] Walan S and Rundgren S C 2015 Student responses to a context-and inquiry-based three-step teaching model *J. Teach. Sci.* **61** 31-39
- [8] Herranen J, Kousa P, Fooladi E and Aksela M 2019 Inquiry as a context-based practice a case study of pre-service teachers' beliefs and implementation of inquiry in context-based science teaching. *J. Sci. Educ.* **41** 1977-98
- [9] Gilbert J K, Bulte A M W and Pilot A 2011 Concept development and transfer in context-based Sci Edu. *J. Sci. Educ.* **33** 817-837
- [10] Trudel L and A Mētioui 2015 Conditions of implementation of an inductive learning sequence about the Periodic Table in high school chemistry *UMAT.* **3** 529-544
- [11] Minne D D, Levy A J and Century J 2010 Inquiry-based science instruction what is it and does it matter? Results from a research synthesis years 1984 to 2002. *J. Res in Sci. Teach* **47** 474-496
- [12] Winsberg E 2019 Computer simulations in science, *The Stanford Encyclopedia of Philosophy* (Winter 2019 Ed), Edward N Z (ed.) <https://plato.stanford.edu/win2019/>
- [13] Guy R S and Lownes-Jackson M 2015 The use of computer simulation to compare student performance in traditional versus distance learning environments. *J. Inf. Sci and Inf. Tech.* **12** 95-109
- [14] Kunnath B J 2017 *The effect of computer simulations on grade 12 learners' understanding of concepts in the photoelectric effect.* University of South Africa: UNISA. (Dissertation- Master of science in mathematics, science and technology education)
- [15] Udo M and Etiubon R 2011 Computer-based science simulations, guided-discovery and students' performance in chemistry *Mod. Appl. Sci.* **5** 211-7
- [16] Johnson R B Onwuegbuzie A J and Turner L A 2007 Toward a definition of mixed methods research. *Mixed Methods Res.* **1** 112-133
- [17] Tashakkori A and Teddlie C 2010 *Overview of contemporary issues in mixed methods research* (In Tashakkori A and Teddlie C eds. Mixed methods in social and behavioural research. 2nd ed. London: SAGE Publications (pp1-45)

Science teachers' beliefs about the impact of 4IR on their classroom practices

L Mavuru¹

Department of Science and Technology Education, *University of Johannesburg, B Ring 404A, Cnr Kingsway Ave and University Rd, Auckland Park, Johannesburg, South Africa*

E-mail: lydiam@uj.ac.za

Abstract. Embracing the Fourth Industrial Revolution (4IR) in the education system has become mandatory considering the COVID-19 pandemic. Because this is a 'revolution' many science teachers have been caught off guard and may harbour mixed feelings regarding their roles and what the future has in store. The current qualitative study sought to establish newly qualified science teachers' beliefs about their roles in science classrooms where 4IR is embraced. An online questionnaire was administered to 60 participants to establish their preparedness and competencies, resource availability, and future professional prospects. Data was subjected to content analysis and three themes emerged: 1. Teachers believed that the government and the Department of Basic Education's stance to embrace 4IR is a vehicle that promotes unequal education opportunities for science learners. 2. Most of the science teachers believed they were not technologically prepared to embrace 4IR tools such as Artificial Intelligence (AI), coding and robotics. 3. The science teachers believed that too much utilisation of technology in a science classroom demeans the actual teaching and learning of scientific concepts. The findings contribute towards the call to change the status quo on the disparities between urban, rural, township and suburban schools in terms of resource distribution and teacher professional development.

Key words: Classroom practices, science teacher beliefs, 4IR.

1 Introduction

Because of the current global pandemic many countries have embraced 4IR in their education system and South Africa is part of the change. As such 4IR affects every human facet let alone science teaching and learning [1]. It has also been found that sometimes there is a mismatch between teachers' beliefs about the affordances of technology and the actual practices in the classrooms due to contextual factors. Because this is a 'revolution' many science teachers have been caught off guard and they harbour mixed feelings regarding their roles and what the future has in store for them.

1.1. Problem statement

The onset of the COVID-19 pandemic has necessitated that schools embark on online or remote teaching and learning mode. Such a scenario required teachers' competencies in technology use though such a call has been made previously regarding the need for teachers to be equipped with digital skills. It is however inevitable to establish teachers' preparedness because the success of an

¹ To whom any correspondence should be addressed.

innovation in the classroom is dependent on the teachers' willingness and ability to implement it. Researchers have indicated that a crucial factor for successful technology integration into the classroom is the teacher [2]. On the other hand, teachers' beliefs are a revelation of their thought processes which are more influential than the teachers' knowledge when it comes to lesson planning, decision-making and ultimately on how they teach [3]. Hence teachers' beliefs about their role should help to shed light on how they make technology integration decisions [4].

1.2. Purpose of study

The study was premised on the reality that embracing 4IR tools in the science classroom is inevitable, but also on the knowledge that the way in which teachers perceive an innovation impacts on the successes of its implementation. It is against this backdrop that the current study sought to establish newly qualified science teachers' perspectives on their roles due to the call to embrace 4IR tools in their classrooms. The study was guided by the research question: What are science teachers' beliefs about their roles in science classrooms where 4IR is embraced?

2. Literature review

Teaching should develop learners for survival in an environment for which Reaves coined the term VUCA: "volatility, uncertainty, complexity, ambiguity" [5] (p. 1). Researchers acknowledge the importance of developing learners to be flexible, adaptable, creative and innovative [6] [7] which are some of the 21st-century skills. To achieve such skills science learning should embrace 4IR, which prepares learners for the unforeseen future [8].

2.1. 4IR as the conceptual framework: The need to embrace 4IR in the science classroom

4IR has been defined as the fusion of technologies which blurs the lines between the physical, digital, and biological worlds [9]. 4IR has been found to provide and cause significant influence on instructional and learning opportunities and education policies [10]. As such, the future prospects afforded by 4IR motivate teachers and researchers to search for more knowledge and skills to prepare science learners [11]. During 4IR teachers co-teach, team teach and collaborate with others rather than teach in isolation [12]. Teaching should involve 4IR technologies, such as mobile and augmented reality (AR) and virtual reality (VR) and 5G [5].

2.2. Science teacher beliefs about technology integration

From a philosophical perspective, beliefs are defined as "psychologically held understandings, premises, or propositions about the world that are felt to be true" [13] (p.103). From an educational standpoint, beliefs are one's convictions and opinions about teaching and learning [14]. Whilst beliefs are considered to be persistent, they however change with experience [15]. Studies have shown that teachers' beliefs are consistent with their classroom practices [16] [17]. This said, science teachers' beliefs about technology integration is vital as this will have implications on how they embrace 4IR in their classrooms [18].

3 Methodology

Located within the interpretive paradigm [19] which enabled the researcher to make sense of the science teachers' beliefs, the study adopted a qualitative case study research design. A qualitative study allows the assessment of the lived experiences of participants [20]. A case study allowed the exploration of a phenomenon [21] and in this case the teachers' beliefs about how their practices could be impacted in science classrooms where 4IR is embraced. The case in this study was newly qualified science teachers who had just completed a four-year teacher professional development programme at a University in South Africa. The unit of analysis, therefore, was the science teachers' beliefs about their levels of preparedness in terms of competencies, resource availability and management, and future

professional prospects in order to examine the teachers' beliefs about their roles in science classrooms where 4IR is embraced.

Using purposive sampling technique [22] 60 science teachers were selected as participants. The participants were ideal considering their relative young age which is 'the digital age' group [23]. An online questionnaire designed by the researcher was administered to the teachers who had just qualified to teach science. The questionnaire specifically sought science teachers' levels of preparedness in terms of competencies, resource availability and management, and future professional prospects. Data was analysed using content analysis [24] wherein codes and categories were identified leading to relational analysis. Through content analysis the researcher carefully reviewed the teachers' responses to identify pertinent information from non-pertinent information and to make sure the information was organised into categories related to the research questions [25].

4 Research findings

The findings are presented under three themes which depict the science teachers' beliefs about their roles in classrooms that embrace 4IR. Their beliefs were centred on issue of 4IR promotion of unequal education opportunities (73%); their lack of confidence and fear of the unknown (81%); and the teachers questioning the efficacy of 4IR in making science concepts comprehensible to learners (57%).

4.1. Theme 1: *The majority of teachers (73%) believed that the government and the Department of Basic Education's stance in embracing 4IR is a vehicle that promotes unequal education opportunities for science learners.* The teachers' argument was that whilst it is a welcome development, there has not been parity in resource distribution in schools because learners come from diverse socioeconomic backgrounds. Their point was that those from disadvantaged backgrounds even struggled with acquisition of simple calculators, which means that the acquisition of electronic gadgets for use in the classroom learning could even be out of reach for many. To show the gravity of the matter, one of the science teachers said, "Will the government and the Department of Basic Education provide for the poor orphan to acquire a laptop yet struggling to get the next meal?"

The teachers' beliefs are that whilst 4IR integration in the science classrooms may be beneficial to the elite (referring to learners coming from advantaged backgrounds and schools), this may not be the case for learners from township and rural backgrounds. The majority of the teachers painted a gloomy picture on the possibilities of equal education opportunities for science learners as encapsulated in what one science teacher said,

Technology integration does not only require the acquisition of electronic gadgets but other services such as availability of internet connectivity, availability of electricity, and let alone skilled manpower to assist teachers and learners in case of technology failure in the science classrooms.

The teachers pointed out that because 4IR changes the frame of science education, if a school is not technically advanced then learners will be left behind, which is likely to increase the disparities in schools in different school environments. Some of the science teachers strongly believed that the integration of 4IR will exacerbate the inequality in the South African education system which they blamed on the irregular provision of resources in schools, primarily caused by corruption and lack of financial assistance to accommodate all the needs of the schools.

4.2. Theme 2: *Most of the science teachers (81%) showed lack of confidence as they believed they were not technologically prepared to embrace 4IR tools such as AI, coding and robotics.* As such, they expressed fears and insecurities when it comes to their competencies to deliver

technology led classroom teaching and learning of science. To show the teachers' fears of the unknown, the following are some of the responses.

Teacher 1: What if the robot replaces me and I'm left without a job?

Teachers 2: If learning can happen over a video call streaming, one teacher can teach as many as 100 learners in one session meaning job opportunities for teachers will be diminished because of 4IR.

Teacher 3: I fear that those robots may know more than me and the learners would enjoy the time with the robot more than with me as the human teacher.

A point to note is that whilst some science teachers welcomed and embraced 4IR in the education system, others were hesitant as the issue of job securities came into play. They feared machines would replace them in the classroom as one teacher said, "Because robots can be programmed to teach relevant content without any errors, myself on the other hand sometimes make mistakes when explaining some science concepts". The teachers believed they were not well equipped to embrace 4IR tools in their science classrooms as attested by the following excerpt:

Teacher: I lack the digital knowledge and skills to ensure innovative and creative science classrooms using technology.

The teachers believed they did not receive adequate training during their teacher development programmes at university because of various constraints which included the lack of facilities, and the nature of the curriculum which did not make 4IR integration mandatory. The teachers' bone of contention is that how then are they expected to implement an innovation without being equipped.

4.3. Theme 3: *The science teachers (57%) believed that too much utilisation of technology in a science classroom will demean the actual teaching and learning of scientific concepts.*

In this case the teachers questioned the effectiveness of technology in providing meaningful learning of science.

Some of the teachers welcomed the benefits of being relieved from working extra hours with the introduction of artificial intelligence (AI). In this way they considered that learners will be more involved in technology and information will be shared easily. As such, they believed the teaching and learning process will be done speedily. To this one of the teachers said, "My fear on the 4IR is that most teachers will abuse the use of technology, they will just relax with the hope that technology will do the work". The teachers argued that machines do not provide prompt responses to learners regarding issues arising in the science classroom.

This belief is shared by many who argued that the human input is needed in the actual teaching and learning since teaching is a social human endeavor, where interaction is inevitable. They cautioned other science teachers to desist from renegading their duties to technology but rather utilise technology to enhance the teachers' efforts. The teachers argued that learners need both worlds, advanced technologies provided by robots, and the irreplaceable social/emotional quality of humans.

5 Discussion

Teachers believed that the government and the Department of Basic Education's stance to embrace 4IR is a vehicle that promotes unequal education opportunities for science learners. The lack of pedagogical adaptation, and the poor teacher development were also found to be challenges that

schools and societies face due to 4IR in a study by Kayembe and Nel [26]. The science teachers believed that they were not technologically prepared to embrace 4IR tools such as AI, coding and robotics hence they lacked confidence. Because teachers are the agents of change in the 4IR, the way in which they perceive technology can be either developmental or destructive when it comes to developing learners' 21st Century skills [27]. Thus said, science teachers should be developed so that they can be competent to integrate 4IR in their classrooms.

The science teachers questioned the efficacy of 4IR tools if used alone in making science concepts more comprehensible to the learners. Such beliefs bring in the role of pedagogy of care which is pertinent particularly considering the current COVID-19 pandemic, that machines cannot provide. The teachers' beliefs resonate with the call made in the previous study that teachers need to demonstrate acts of caring as ultimate goals of teaching [28]. The teachers in the current study believed that too much utilisation of technology in a science classroom would demean the actual teaching and learning of scientific concepts. In a previous study [10] pre-service science teachers were found to also display very low perceptions with regards to the human element required between the interactions of teachers and learners as they believed that robots and artificial intelligence only execute the input data but do not have emotional skills to understand attitudes and values.

6 Conclusion and recommendations

Whilst some of the science teachers indicated in their responses that they were not ready for 4IR as an innovation because of poor digital skills, unavailability of resources and insecurities, there is need to move with the times and adopt the innovation. A point to note from the findings is that nothing points to the teachers' negative attitude towards the integration of 4IR per se as an innovation but instead their beliefs emanated from the issues regarding its implementation. Based on the teachers' beliefs, the study suggests that if schools, teachers and learners are equipped with the necessary resources (e.g. electronic gadgets, necessary facilities, connectivity), and competencies, embracing 4IR in the science classrooms would be well received. The findings suggest the need to change the status quo on the disparities between urban and rural, as well as township and suburban schools in terms of resource distribution. Teacher professional development programmes are needed for continued technological knowledge and skills development of science teachers.

References

- [1] Deloitte Global Business Coalition for Education. Preparing tomorrow's workforce for the Fourth Industrial Revolution. Deloitte: London, UK (pp. 1–58). 2020 May; <https://www.voced.edu.au/content/ngv:85595>.
- [2] Rhema A, Miliszewska I. Towards e-learning in higher education in Libya. *Iss. in Informing Sci. and Info. Tech.* 2010 Jan; 7: 423-436.
- [3] Gilakjani AP, Sabouri NB. Teachers' beliefs in English language teaching and learning: a review of the literature. *Eng. Lang. Teaching.* 2017 March; 10(4): 78–8. <https://doi.org/10.5539/elt.v10n4p78>
- [4] Ertmer PA. Teacher pedagogical beliefs: the final frontier in our quest for technology integration? *Educ. Tech. Research and Dev.* 2005 Feb; 53: 25-39.
- [5] Reaves J. 21st-century skills and the fourth industrial revolution: a critical future role for online education. *International J. on Innovations in Online Educ.* 2019 Jun; 3(1): 1- 21
- [6] Gray A. The 10 skills you need to thrive in the Fourth Industrial Revolution. 2016 Dec; Available online: <https://www.weforum.org/agenda/2016/01/the-10-skills-you-need-to-thrive-in-the-fourth-industrial-revolution/>
- [7] Education Design Lab. 21st century skills badges. 2018 December; Available online: <https://eddesignlab.org/the-labs-21st-century-skills-badges/>

- [8] Davis N. What is the Fourth Industrial Revolution? World Economic Forum: Geneva, Switzerland, 2016; p. 11. Available online: <https://www.weforum.org/agenda/2016/01/what-is-the-fourth-industrial-revolution/> (accessed on 5 May 2020).
- [9] Shava E, Hofisi C. Challenges and opportunities for public administration in the Fourth Industrial Revolution. *African J. of Public Affairs*. 2018 Jan; **9**: 203–215.
- [10] Eleyyan S. The future of education according to the Fourth Industrial Revolution. *Journal of Educ. Tech. & Online Learning*. 2021 Jan; **4**(1): 23-30.
- [11] Schwab K. The Fourth Industrial Revolution. *Academic J. of Manufacturing Eng.* 2016 Jan; **14**: 5.
- [12] Doucet A, Evers J, Guerra E, Lopez N, Soskil M, Timmers K. Teaching in the Fourth Industrial Revolution: standing at the precipice. London: Routledge Taylor & Francis Group. 2018 Feb; <https://doi.org/10.4324/9781351035866>.
- [13] Richardson V. The role of attitudes and beliefs in learning to teach. In J Sikula (Ed.) *Handbook of Research on Teacher Education* (2nd ed.). New York: Macmillan. 1996. p. 102-119.
- [14] Haney JJ, Lumpe AT, Czerniak CM. Constructivist beliefs about the science classroom learning environment: perspectives from teachers, administrators, parents, community members, and students. *School Sci. and Math.* 2003 Dec; **103**(8): 366-377.
- [15] Savaşçı-Açıklan F. Teacher beliefs and practice in science education. *Asia-Pacific Forum on Sci. Learning and Teaching*. 2009 Jan; **10** (1): 12.
- [16] Pajares MF. Teachers' beliefs and educational research: cleaning up a messy construct. *Rev. of Edu. Research*. 1992 Sept; **62**(3): 307-332.
- [17] Haney JJ, McArthur J. Four case studies of prospective science teachers' beliefs concerning constructivist teaching practices. *Sci. Edu.* 2002 Nov; **86**: 783-802.
- [18] Razak NA, Alakrash H, Sahboun Y. English language teachers' readiness for the application of technology towards fourth industrial revolution demands. *Asia-Pacific J. of Info. Tech. and Multimedia*. 2018 Dec; **7** (2-2): 89- 98.
- [19] Bertram C, Christiansen I. Understanding research: an introduction to reading research. Pretoria: Van Schaik Publishers. 2015.
- [20] Creswell J. Research design. Thousand Oaks: Sage Publications. 2014.
- [21] Sturman A. Case study methods. In J. P. Keeves (ed.). *Educational research, methodology and measurement: an international handbook* (2nd ed.) Oxford: Pergamon. 1997. p. 61–66.
- [22] Patton MQ. Qualitative research and evaluation methods (3rd ed.). Thousand Oaks, CA: Sage. 2002.
- [23] Smith C, Crespo-Dubie D. What is the Digital Age and the Internet of Things? Smith & Associates. 2018. Accessed Dec 11 on: <https://www.linkedin.com/pulse/what-digital-age-internet-things-daniel-crespo-dubie>.
- [24] Marshall M, Firth S. My revision notes: AQA A level psychology. London: Hodder Education. 2017 Jan.
- [25] Bowen G. Document analysis as a qualitative research method. *Qual. Research J.* 2009 Aug; **9** (2): 27-40. <https://doi.org/10.3316/QRJ0902027>.
- [26] Kayembe C, Nel D. Challenges and opportunities for education in the Fourth Industrial Revolution. *African J. of Public Affairs*. 2019 Sept; **11** (3): 79-93.
- [27] Sinha N. The importance of teachers in a technology-driven world. 2018. Retrieved from: <https://www.valuewalk.com/2018/02/teachers-vs-technology-learning/>
- [28] Owusu-Ansah A, Kyei-Blankson L. Going back to the basics: demonstrating care, connectedness, and a pedagogy of relationship in education. *World J. of Edu.* 2016 March; **6**(3): 1-9.

Quantum technology: A potential tool for development in Africa

Mhlambululi Mafu¹ and Makhamisa Senekane²

¹Department of Physics and Astronomy, Botswana International University of Science and Technology, P/Bag 16, Palapye, Botswana

²Institute for Intelligent Systems, University of Johannesburg, South Africa

E-mail: mafum@biust.ac.bw, smakhamisa@uj.ac.za

Abstract.

The first quantum revolution started in the early 1900s and was characterized by the exploration of physics at the sub-atomic level. This was followed by a second revolution around the 1970s, which witnessed the application of quantum physics to develop quantum technology. Currently, quantum technology is gaining traction in most parts of the world. However, besides having a history of innovation in quantum physics, Africa has fallen behind in each quantum revolution. Therefore, this paper highlights challenges relating to quantum technologies and points to the opportunities that quantum technologies present to close the gap and drive economic growth and development in Africa. The latter can be achieved through capacitation and the democratization of quantum technology knowledge. This initiative will, in turn, ensure that Africa is adequately represented in the second quantum revolution. Finally, in this paper, we introduce a new development framework, namely quantum technology for development (QT4D), and explore how Africa could deploy this framework to advance the adoption and use of quantum technology and become part of mainstream computing landscape. This will allow Africa to apply these technologies in space communications, finance, drug development, and material science, thus solving some everyday challenges and opening new opportunities for industries leading to economic growth and development.

1. Introduction

Quantum technology is poised to revolutionize the technological world. In essence, quantum technology makes use of quantum-mechanical concepts and principles in order to process information [1, 2, 3]. The field of quantum technology has various sub-fields. These sub-fields include quantum communication, quantum cryptography, quantum computing, quantum sensing, and quantum imaging.

The advent of quantum technology can be traced back to the 1970s [1, 4]. Since its inception in the 1970s, quantum technology has gained some traction across the globe. However, Africa is still lagging behind in the adoption of quantum technology [5]. In this paper, we discuss the opportunities and challenges related to the adoption of quantum technology in Africa. Furthermore, this paper proposes and explores a new quantum technology framework, namely the Quantum Technology for Development (QT4D) framework.

The remainder of this paper is structured as follows. The next section provides the background information on quantum technology and the development theory. This is then followed by Section 3, which outlines the quantum technology initiatives in Africa. Additionally,

this section highlights the opportunities and challenges facing Africa in the adoption of quantum technology. Furthermore, Section 4 outlines the Quantum Technology for Development framework that is proposed in this paper. The *QT4D* framework proposed in this paper can serve as a handy tool towards providing an assistance in the closing of the quantum technology adoption gap, especially in Africa and other low-resource regions of the worlds. Finally, Section 5 concludes this paper.

2. Background Information

2.1. Quantum Technology

Quantum technology is also referred to as the second Quantum Revolution [6, 7]. It uses the laws of quantum physics in order to enable information processing in a manner that offers some advantages over the conventional, non-quantum information processing paradigm. Therefore, it is envisaged that quantum technology should offer some advantage over the current non-quantum technology. Quantum concepts that enable quantum technology to offer advantages over its conventional counterpart include entanglement, superposition, interference, tunneling, and no-cloning Theorem [1, 7].

Analogous to the conventional information processing paradigm; which uses a binary digit (bit) as a unit of information, quantum technology uses a quantum bit (qubit) as a unit of information [1, 2]. Unlike a bit, which can only exist in either state 0 or state 1, a qubit can exist in superposition of both states. Mathematically, a qubit is represented as [1]:

$$|\psi\rangle = \alpha|0\rangle + \beta|1\rangle, \quad (1)$$

where α and β , which are referred to as probability amplitudes, satisfy the condition [1]:

$$|\alpha|^2 + |\beta|^2 = 1. \quad (2)$$

2.2. Theory of Development

In essence, development is associated with a positive change in the society [8, 9]. That is, the objective of development is to implement technical and/or economic interventions that are intended to bring about a positive change in a society [10]. This positive change can either be physical, social, environmental, or economic.

The positive change can be brought about in a way that is sustainable; that is, without irreversibly depleting resources. In such a case, the development is referred to as the sustainable development [9, 11]. The United Nations (UN) has been responsible for developing and overseeing the implementation of the seventeen Sustainable Development Goals (SDGs) for the duration of fifteen years; from 2015 to 2030. These SDGs are pictorially depicted in Figure 1.

Technology can be used as a tool to drive a positive change in a society. The use of technological tools in development is referred to as Technology for Development (*Tech4Dev*). Different technological tools can be used to address various developmental challenges. Examples of these tools include Information and Communication Technology for Development (*ICT4D*) [12, 13] and Artificial Intelligence for Development (*AI4D*) [14].

3. Quantum Technology Initiatives in Africa: Opportunities and Challenges

As stated earlier in this paper, Africa is lagging behind in the adoption of quantum technology. However, some African countries have already started some initiatives geared towards the adoption of this technology. For instance, South Africa has already drafted a quantum technology framework document [5]. Furthermore, South Africa has various research groups that work on quantum technology [5]. Egypt and Tunisia also have research groups working on quantum technology, and Rwanda is pursuing quantum technology research through the



Figure 1. The seventeen UN Sustainable Development Goals The picture courtesy of <https://www.un.org/sustainabledevelopment/news/communications-material>.

AIMS (African Institute of Mathematical Sciences)-based “Quantum Leap Africa” initiative. AIMS is an institute that is responsible for the promotion of mathematical sciences in Africa. through its “Quantum Leap Africa” initiative, AIMS intends to promote data analytics, machine intelligence, smart systems, and quantum technology in Africa¹.

Another approach that is being used in Africa to fast-track the adoption of quantum technology is by partnering with the international organizations. For instance, the University of Witwatersrand has partnered with IBM in order to pursue quantum computing research². Through this partnership, researchers who are based at any member of the African Research Universities Alliance (ARUA) can have access to the IBM quantum computing facilities through the University of Witwatersrand.

Furthermore, through citizen-led initiatives, some African countries have partnered with an international organization called QWORLD³ in order to promote quantum computing in their respective countries. QWORLD is an organization that has the objective of promoting quantum technology across the globe. The African countries that have partnered with QWORLD are: Tunisia, Egypt, Morocco, and Zimbabwe.

Another international organization that African countries have partnered with (through citizen-led initiatives) is OneQuantum⁴. OneQuantum is an organization that brings together quantum technology researchers and enthusiasts world-wide. So far, the African countries that have partnered with OneQuantum are South Africa and Kenya.

¹ <https://quantumleapafrica.org>

² <https://research.ibm.com/blog/south-africa-quantum-ready>

³ <https://qworld.net/>

⁴ <https://onequantum.org/>

3.1. Challenges Facing the Adoption of Quantum Technology in Africa

The key challenge facing the adoption of quantum technology in Africa is the availability of funds. To date, virtually all African countries spend less than 1% of their Gross Domestic Product (GDP) on research and development [15]. This lack of funding in turn leads to the second challenge, namely the ‘brain drain’ [16, 17]. African countries lose their quantum technology researchers to the countries that are relatively more resourced. As a consequence of ‘brain drain’, African countries are left with another challenge, namely the dearth of quantum technology skills-base.

Another challenge facing the adoption of quantum technology in Africa is the lack of intra-continental collaboration. This lack of collaboration then leads to the uneven access to quantum technology resources; with the African countries which are relatively well-off having access to such resources while the relatively low-resourced do not. Finally, like most STEM (Science, Technology, Engineering, and Mathematics) fields; where gender disparity is a challenge [18], the field of quantum technology in Africa is still male-dominated.

3.2. Quantum Technology Opportunities in Africa

Although Africa has a wealth of natural resources [19], this wealth does not equally translate to developed economies in Africa. In this regard, quantum technology can be used to spur both technological and economic developments in Africa. Potential applications of quantum technology in Africa are [5, 19]:

- quantum machine learning;
- quantum chemistry;
- quantum finance; and
- quantum metrology.

4. Quantum Technology for Development (QT4D) Framework

The QT4D framework is intended to guide the adoption of quantum technology so as to address the developmental challenges. In Africa, the framework can be used to ensure that when it comes to quantum technology, no-one is left behind.

The pictorial representation of the Quantum Technology for Development framework is shown in Figure 2. This framework can be summarized as follows. First, the developmental challenge that affects the society is identified. Then the identified problem is probed in order to assess whether it is amenable to the quantum solution. If the problem is amenable to the quantum solution, it is further probed in order to ascertain if the potential solution is sustainable. Finally, the societal impact of the potential quantum-driven solution is assessed. If the potential solution has a potential have an impact to the society, then such as quantum approach (which is referred to as ‘quantum solution’ in the figure) could be explored.

Based on the sustainability theory of development, the potential use-cases for the Quantum Technology for Development are provided in Table 1.

5. Conclusion

In this paper, we have explored the quantum technology initiatives in Africa. Additionally, we have discussed the challenges facing the adoption of quantum technology in Africa, and the potential technological and economic development benefits that the adoption of quantum technology can bring to Africa. Furthermore, we have introduced the Quantum Technology for Development framework. The Quantum Technology for Development framework is intended to guide the adoption of quantum technology in order to address the developmental challenges. This framework can be deployed in Africa, in order to address the developmental challenges in

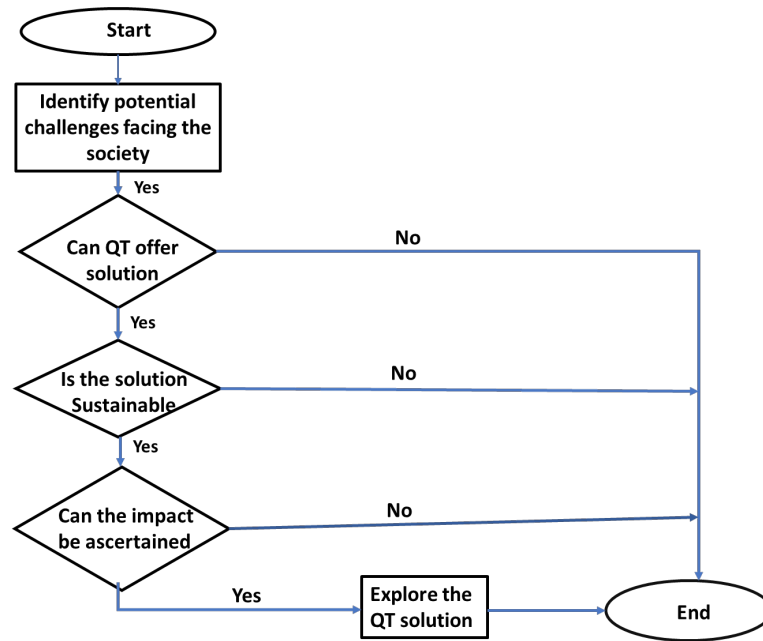


Figure 2. A pictorial representation of the Quantum Technology for Development Framework.

the continent. Future work will focus on the adoption by individual African states of the QT4D framework proposed in this paper.

Acknowledgments

Mhlambululi Mafu is grateful for the support he received from his colleagues in the Department of Physics and Astronomy, at the Botswana International University of Science and Technology. Makhamisa Senekane acknowledges the support he received from the Institute for Intelligent Systems at the University of Johannesburg, and the National Institute for Theoretical and Computational Science.

References

- [1] Nielsen M A and Chuang I 2010 *Quantum Computation and Quantum Information* (Cambridge University Press)
- [2] Wilde M M 2017 *Quantum Information Theory* (Cambridge University Press)
- [3] Kasirajan V 2021 *Fundamentals of Quantum Computing: Theory and Practice* (Springer)
- [4] Aaronson S 2013 *Quantum computing since Democritus* (Cambridge University Press)
- [5] National Working Group S Q 2020 Framework for quantum technology driven research and innovation in south africa Tech. rep. Department of Science and Innovation, Technical Report
- [6] Dowling J P and Milburn G J 2003 *Philosophical Transactions of the Royal Society of London. Series A: Mathematical, Physical and Engineering Sciences* **361** 1655–74
- [7] Senekane M, Maseli M and Taele M B 2020 *The Disruptive Fourth Industrial Revolution* (Springer) pp 205–225
- [8] Hopper P 2018 *Understanding Development* (John Wiley & Sons)
- [9] Blewitt J 2018 *Understanding Sustainable Development* (Routledge)
- [10] Rabie M 2016 *A Theory of Sustainable Sociocultural and Economic Development* (Springer) pp 7–15
- [11] Ki-moon B 2016 *UN General Assembly*
- [12] Unwin P 2009 *ICT4D: Information and Communication Technology for Development* (Cambridge University Press)
- [13] Samoilenko S V and Osei-Bryson K M 2017 *Creating Theoretical Research Frameworks Using Multiple Methods: Insight from ICT4D Investigations* (CRC Press)

Table 1. The QT4D Potential Use Cases.

Mhlambululi Mafu is grateful for the support he received from his colleagues in the Department of Physics and Astronomy, at the Botswana International University of Science and Technology. Makhamisa Senekane acknowledges the support he received from the Institute for Intelligent Systems at the University of Johannesburg, and the National Institute for Theoretical and Computational Science.

SDG	Potential use case
SDG1	Data analysis using quantum computers.
SDG2	Quantum machine learning to predict climate-resistant crops. Quantum computers for analysis of big data for land use, agricultural drought, <i>etc.</i> Quantum sensing for imagery. Quantum machine learning for yield forecasting.
SDG3	Quantum computers for health big data analytics. Quantum cryptography for health data protection. Quantum machine learning for drug discovery.
SDG4	Quantum machine learning to identify at-risk students. Equitable QT training (skills development).
SDG5	Inclusive and equitable representation in QT. Female-friendly QT environment.
SDG6	Quantum sensing to identify water sources. Quantum dots to test water quality.
SDG7	Quantum machine learning for energy forecasting.
SDG8	Intensive QT up-skilling.
SDG9	Innovation in QT. QT industrialization and entrepreneurship for inclusive job creation. Fair and equitable access to QT infrastructure.
SDG10	Inclusive access to QT tools.
SDG11	Quantum computers for big data analytics.
SDG12	Quantum computers for big data analytics.
SDG13	Quantum computers for climate modeling. Quantum machine learning for forecasting extreme weather event.
SDG14	Quantum computers for big data analytics.
SDG15	Quantum computers for big data analytics.
SDG16	Quantum cryptography to combat cyber-terrorism.
SDG17	Strategic partnerships for equitable access to QT resources; ensuring that no-one is left behind.

[14] Mann S and Hilbert M 2018 *Available at SSRN 3197383*

[15] Schneegans S, Straza T and Lewis J 2021 *UNESCO Science Report: the Race Against Time for Smarter Development* (UNESCO Publishing)

[16] Docquier F and Rapoport H 2012 *Journal of economic literature* **50** 681–730

[17] Brock G and Blake M 2014 *Debating Brain Drain: May Governments Restrict Emigration?* (Oxford University Press)

[18] Baskaran A 2017 *Institutions and Economies* 125–127

[19] Akhalwaya I and Saib W 2021 *The African Physics Newsletter* **1** 1–5

The global Gender Gap project: fair treatment, and some recommendations for South Africa

I M A Gledhill^{1,5,6}, G Butcher², S Ponce-Dawson³, R Ivie⁴ and S White⁴

¹Flow Research Unit, School of Mechanical, Industrial and Aeronautical Engineering, Wits University, South Africa

E-mail: Igle.Gledhill@wits.ac.za

²Space Research Centre, Department of Physics and Astronomy, University of Leicester, United Kingdom

³Departamento de Física, Facultad de Ciencias Exactas y Naturales, Universidad de Buenos Aires, and Instituto de Física de Buenos Aires (Consejo Nacional de Investigaciones Científicas y Técnicas), Argentina

⁴Statistical Research Center, American Institute of Physics, College Park, Maryland, United States of America

Abstract. This short paper describes selected results from an international project on the gender gap in science, with a focus on fair treatment at work in physics in South Africa. The three-year project was a collaboration of eight international unions, including the International Union of Pure and Applied Physics, and three global organisations. Among the tasks was a worldwide survey, to which there were 32 346 respondents. The most significant difference was seen in reporting on sexual harassment, with 29% of women and 2% of men in physics indicating that they personally encountered sexual harassment at school or work. In physics there is a significant gender gap in response to the statement “My employer treats everyone fairly”, with which 62% of women and 73% of men agreed. Recommendations from the final project conference offered to combat harassment include significantly improved campus security for women, to which we add the development of a culture in physics that combats harassment and violence. In terms of fairness at work, several recommendations from the conference are offered. These include replacing the usual method of assessing an individual’s output by counting published papers by nomination of their best papers. We also recommend recognising the contributions of men in attaining gender equality in physics.

1. Introduction

The design of initiatives for reducing the gender gap should be based on evidence. The resolution on which the International Union of Pure and Applied Physics (IUPAP) Working Group on Women in Physics was founded was to “to survey the situation of women physicists in IUPAP member countries, to analyze and report the data collected along with suggestions on how to improve the situation...”. A major step in this direction was the Global Survey of Physicists of 2010 [1].

However, changes occur in the global academic, scientific and social environment, and in 2016 a successful application was made to the International Science Council for the project “A Global

⁵ This project was funded as described in the Acknowledgements

⁶ To whom all correspondence should be addressed

Approach to the Gender Gap in Mathematical, Computing, and Natural Sciences: How to Measure It, How to Reduce It?”. This project disaggregated results across the disciplines involved, and across geographical regions. The aim of this paper is to consider selected responses relevant to fair treatment, relevant to physics and to Africa and South Africa, and to prioritise recommendations which are relevant to the physics community of practice.

1.1. The Gender Gap project and the South African context

The project involved eight international unions: mathematics (lead partner), chemistry (co-lead), physics through IUPAP, astronomy, industrial and applied mathematics, biosciences, history and philosophy of science, and computing machinery, together with three international organisations: UNESCO, GenderInSITE, and OWSD⁷. The project undertook three tasks: a global survey, a data-backed study of publication patterns, and the collection of initiatives known to have successfully addressed the gender gap in science [2]. An important aspect was the collaboration of social scientists and mathematical, computing, and natural scientists to ensure that the social science aspects of the project were professionally undertaken, and to introduce concepts of social science to their colleagues.

In terms of the South African context, it is said that South African women experience the highest levels of Gender-Based Violence (GBV) in the world (Dlamini, 2021 [3]). Many positive actions have been taken, but the problem persists. In an environment and context where GBV is so prevalent, and femicide and assault have occurred at universities, it is important to take note of data that may indicate whether sexual harassment takes place in the workplace of physicists.

The South African physics community has taken a highly participative view of its own transformation. This ranges from the community prompting of a nation-wide review when the discipline was in crisis [4], to the generation of a benchmark curriculum statement in which almost all physics departments in the country participated, to transformative actions in terms of race and gender. Although a specific study was not found in the literature, it is possible that a strong physics identity [5] may exist among many South African physicists. A physics identity is understood as a self-view that includes recognition within the community, self-efficacy, and self-determination. These aspects of self-awareness may be helpful both in countering harassment, and in refraining from harassing.

2. Methodology: Gender Gap project

The survey was carried out by the American Institute of Physics Statistical Research Center. The interested reader is referred to the description by Ivie and White, 2020 [6]. The term “gender gap” describes any difference “between women and men in terms of their levels of participation, access, rights, remuneration or benefits” [7]. The research questions are: to improve understanding of scientists’ development of interest in science, experiences in education and careers, work-life balance, family support, demographics, access to resources needed to conduct science, and opportunities to contribute to the scientific enterprise, and the survey covered early years, university studies, doctoral studies, and careers. Among the dimensions investigated were contrasts across disciplines, regions, and Human Development Index (HDI) [8]. The questionnaire [9] was based largely on the previously used Global Survey of Physicists [1] and the UNESCO SAGA⁸ framework. The first draft of the questionnaire was provided at workshops in 2017 in Bogotá, Cape Town and Taipei, reviewing specific questions to collect feedback on regional implications of wording and topics, apply special consideration to ensure that the questions work for the region and for all disciplines, and to outline the

⁷ IMU, the International Mathematical Union; IUPAC, the International Union of Pure and Applied Chemistry; IUPAP; IAU, the International Astronomical Union; ICIAM, the International Council of Industrial and Applied Mathematics; IUBS, the International Union of Biological Sciences; IUHPST, the International Union of History and Philosophy of Science and Technology; ACM, the Association for Computing Machinery; UNESCO, the United Nations Educational, Scientific and Cultural Organisation; GenderInSITE, Gender in Science, Innovation, Technology and Engineering and OWSD, the Organisation of Women in Science for the Developing World.

⁸ UNESCO STEM and Gender Advancement; STEM: Science, Technology, Engineering and Mathematics

distribution plan. The questionnaire was translated by a professional service, with advice from scientists, into Spanish, Russian, French, Chinese, Japanese, and Arabic. Given the absence of a single method of contacting and sampling scientists across the globe, the snowball sampling method was used, in which the eleven partnering organisations distributed the survey, and participants provided referrals through their networks to recruit further participants. Because this is not a probabilistic sampling method, results apply only to the respondents. Ivie and White [6] conducted multivariate analyses that allow the inclusion of potential confounding factors, such as HDI, employment sector, discipline, geographic region, and age. Because of the large number of models tested, a difference was considered statistically significant if the p -value⁹ was less than 0.002 [6].

3. Responses

The total number of respondents was 32 346, identifying themselves as from 150 countries. In physics 7 570 responses were received. In astronomy 2 597 responses were received. In Africa, the total response from all disciplines was 1 265, of whom 61% identified themselves as women and 39% as men. This response was somewhat disappointing in view of the fact that the African workshop discussed distribution methods. Given these numbers it is not worthwhile to disaggregate physics in terms of Africa or South Africa.

In the following figures and tables, green and orange indicate that a statistically significant gender gap was found in the multivariate model which accounts for confounding factors including age, geographic region, employment sector, HDI, and academic discipline. The results quoted in sections 3.1 to 3.3 are among those published to date [6]. Of the results across eight disciplines, only “Physics” is shown as a discipline, for all regions, in the present short paper. Of results across twelve geographical regions, only “Africa”, for all disciplines, is shown here. These specific results were selected for a short paper as potentially illustrative for South Africa in exploring fair treatment at work, in the context of a country plagued by gender violence, but in which the physics community is seeking active transformation in terms of gender.

3.1. Harassment

For the question “Have you ever encountered sexual harassment at school or work?”, responses for “yes, it happened to me” are shown in figure 1. Given these data, it is likely that women in physics in Africa are likely to encounter sexual harassment more frequently than men. Global figures for astronomy, considered as a separate discipline, were 30% for women and 3% for men. Further analysis has recently been published [10] which provides comparison of the data on harassment across the dimensions of discipline, region, HDI and employment. The evidence shows that significant numbers of women in physics are experiencing harassment.



(a) Physics discipline, global

(b) Africa, all disciplines

Figure 1. Respondents indicating that they personally encountered sexual harassment at school or work.

⁹ Probability that the dependent variable of interest is 1 in a binary test.

3.2. Fair treatment in the Doctoral Programme and in the Workplace

Table 1 shows respondents' agreement with statements [6] about the doctoral programme and the workplace. In a separate question, respondents from physics were more likely to agree that they had respectful co-workers than any of the other disciplines studied.

In the analysis for the region Africa, it is possible that a significant gender gap was not identified either due to the relatively small number of respondents, or due to a relatively small existing gender gap. To investigate this, we show the results for countries with HDI ≥ 0.7 ("high HDI") and those with HDI < 0.7 "lower HDI" (table 2). South Africa, at the time of the study, had HDI = 0.704.

Table 1. Responses to questions on fair treatment in terms of Physics and Africa.

Statement	Dimension	Agree		Neutral		Disagree	
		w	m	w	m	w	m
"My program treated everyone fairly"	Physics	63%	76%	19%	14%	18%	11%
	Africa	65%	62%	18%	22%	18%	16%
"My employer treats everyone fairly"	Physics	62%	73%	17%	14%	22%	14%
	Africa	53%	60%	20%	15%	27%	21%
"My co-workers are respectful of everyone"	Physics	68%	79%	16%	12%	15%	9%
	Africa	68%	70%	15%	15%	17%	15%

Table 2. Responses to questions on fair treatment in terms of Human Development Index.

Statement	HDI	Agree		Neutral		Disagree	
		w	m	w	m	w	m
"My program treated everyone fairly"	High	62%	74%	18%	14%	20%	12%
	Lower	64%	70%	19%	17%	18%	13%
"My employer treats everyone fairly"	High	60%	71%	17%	15%	23%	15%
	Lower	52%	60%	21%	19%	28%	21%
"My co-workers are respectful of everyone"	High	68%	78%	14%	12%	18%	10%
	Lower	61%	69%	19%	18%	21%	13%

While other factors, for example race and class, may be embraced by the term "everyone", significantly more men (69%) than women (61%) in lower HDI countries agreed that "My co-workers are respectful of everyone": this constitutes a gender gap in the response from men and women, in the sense that respondents who are women are indicating that less respect (in a general sense) is exercised in their environment than is indicated by men. A significant gender gap in responses exists in both high HDI and in lower HDI countries in terms of fair treatment at work, and respect between co-workers. Because over 80% of African countries fall in the lower HDI category, this may be indicative of a gender gap in Africa.

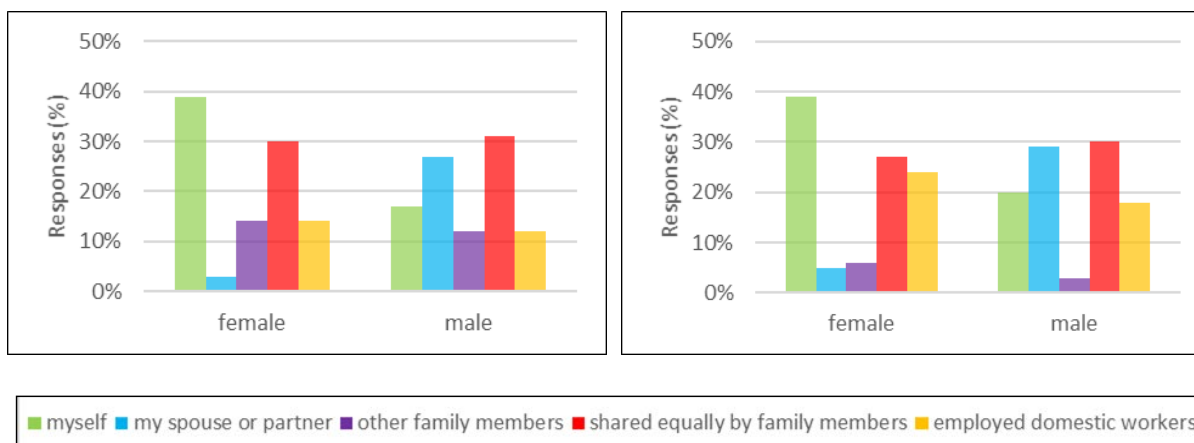
3.3. Access to resources

Access to resources was considered through a series of questions covering office space, laboratory space, equipment, travel funds, clerical (administrative) support, employees or students, computing capability, technical support, access to data, access to scientific literature, and support as a working parent. While detailed data exist for each of these resources, a simple single proxy is the average number of these resources available. In the global study of all disciplines, the average number of the listed resources per year for women is 7.2 and for men is 7.6, with a statistically significant gender gap in the multivariate model accounting for confounding factors including age, geographic region, employment sector, academic discipline, and HDI. A difference of this kind is likely to have an effect

of cumulative disadvantage that grows exponentially over the years of a career, as well as providing a source of discouragement, as discussed by Valian [11].

3.4. Housework

Further light may be thrown on fair treatment and work-life balance among physicists by a question asked both in the global survey of physicists [1] and the global survey of scientists [6, 14]: “Who is responsible for the majority of the housekeeping in your household?” Responses are shown in figure 2. Because the 2010 survey used $HDI > 0.8$ as the cut-off to distinguish very highly developed countries from less developed, we have used the same cut-off in Figure 2. All countries in Africa had $HDI < 0.8$. It is possible that more men in physics may be undertaking more household work themselves in 2018 than in 2010 (the years of the surveys). However, it is difficult to be certain because the same respondents did not necessarily answer both surveys. There appears to be more employment of domestic workers apparent in the 2018 survey.



(a) 010 Physicists, $HDI < 0.8$ [1]

(b) 2018 Physicists, $HDI < 0.8$ [14]

Figure 2. Household work in responses from physicists only. Colours indicate the same responses in (b) as in (a).

4. Conclusions and recommendations

We have shown some results which are relevant to fair treatment of physicists and of people in Africa from the Gender Gap project global survey of scientists. About a quarter of women in physics (29%) and in Africa (22%) report that they have encountered sexual harassment at first hand at school or at work. Given South Africa's history of gender-based violence, it is critical to overcome this problem, or to pre-empt it. The Gender Gap book contains a number of recommendations made at the final conference [2], from which, in the South African context, we select improved provision of safety for women on campus and at work, especially in circumstances where wi-fi is needed for study. The provision of both physical safety, and reliable bandwidth, in libraries, laboratories, offices and residences is vital in protecting women without compromising their education or work. From the same source, we recommend an ombudsperson, within universities or companies, who is a woman. Given the transformative nature of the physics community in South Africa and the concept of physics identity, we recommend building a culture within the physics community that combats harassment and violence of any kind.

It is heartening to note that in the survey of multiple disciplines, physicists reported the highest levels of respect from their colleagues. At the same time, women in physics are less likely than men to report that they are treated fairly in the doctoral programme or in employment, and less likely to report fair treatment by, and respect from, their co-workers. This extends to a reported lower availability of resources for women. Straightforward measures are recommended: monitor support, wellbeing,

mentoring and progress of female academics and students; make the selection processes transparent; noting that both female and male representatives on recruitment committees may have unconscious bias in favour of men, provide unconscious bias training; and make the gender lens the responsibility of a dedicated person on each selection or allocation committee. We recommend replacing the assessment of publications using a count of the papers of an individual by nomination of her or his 5 best papers [12]. In addition, charters and accreditations have proved to be successful aids to a welcoming departmental atmosphere [13], and the exploration of the concept of gender budgeting, which has already been used in sub-Saharan Africa by governments [3], should be encouraged.

Comparison of the 2010 and 2018 surveys for physicists indicate that, for lower HDI countries, there is a slightly larger percentage of men in 2018 indicating that they do their own housework. While the respondents may not be the same individuals in the two surveys, the evidence suggests a shift in the approach of male physicists to household responsibilities. The contributions of men in all aspects of improving the environment for women in physics are welcomed.

Acknowledgments

Figure 1 and tables 1 and 2 are adapted from the final report which appeared under a Creative Commons Attribution 4.0 International License. All authors were part of the project team. The funding for this project was provided by the ISC, IMU, IUPAC, IUPAP, IAU, IUBS, ICIAM, IUHPST, UNESCO, GenderInSITE, OWSD, and ACM⁷. The African Workshop was enabled by the African Institute of Mathematical Sciences and the ISC Regional Office for Africa. The authors thank their friends and colleagues across many countries who made this project possible.

References

- [1] Ivie R and Tesfaye T L 2012 *Physics Today* **65** 47–50 <http://dx.doi.org/10.1063/PT.3.1439>
- [2] Roy M-F et al. 2020 *A Global Approach to the Gender Gap in Mathematical, Computing, and Natural Sciences: How to Measure It, How to Reduce It?* (Berlin: IMU) DOI https://zenodo.org/record/3882609#.YQ_u-4gzY2w [Accessed 9 June 2020]
- [3] Dlamini NJ 2021 *Critical Sociology* **474** 583–590
- [4] Hellberg MA et al. 2004 *Report of the International Panel appointed by the Department of Science and Technology, the National Research Foundation, and the SA Institute for Physics, (Shaping the Future of Physics in South Africa)* (NRF: Pretoria)
- [5] Hazari Z, Sonnert G, Sadler P M and Shanahan M-C 2010 *Journal of Research in Science Teaching* **47** 978–1003
- [6] Ivie R and White S 2020 Measuring and analyzing the gender gap in science through the global survey of scientists, in [2] (Berlin: IMU) Chapter 2 pp 39–81
- [7] World Economic Forum 2020 *The Global Gender Gap Index 2020* (Geneva: WEF) <http://reports.weforum.org/global-gender-gap-report-2020/the-global-gender-gap-index-2020/>
- [8] United Nations Development Programme 2018 *United Nations Human Development Index* (New York: UNDP) <http://hdr.undp.org/en/content/human-development-index-hdi>
- [9] Gender Gap in Science 2020 *Task 1: Global Survey of Mathematical, Computing, and Natural Scientists* <https://gender-gap-in-science.org/work-packages/global-survey/>
- [10] White S and Ivie R 2021 *Pure and Applied Chemistry* <https://doi.org/10.1515/pac-2021-0304>
- [11] Valian V 1998 *Why So Slow? The Advancement of Women* (Cambridge Mass: The MIT Press)
- [12] Bjorkquist R, Gabrys B J and Gledhill I 2019 AIP Conference Proceedings **2109** 040003
- [13] Working Group 5 IUPAP 2021 *The Waterloo Charter for Women in Physics* <https://iupap.org/strategic-plan/diversity-in-physics-2/waterloo-charter-for-women-in-physics/>
- [14] Ivie R and White S 2021 Global Survey of Scientists: Results for Physics. Presented at 7th Int. Conf. on Women in Physics 11-16 July 2021 Melbourne, Australia

South Africa and the joint data-backed study of publication patterns of the Global Gender Gap project

I M A Gledhill

Flow Research Unit, School of Mechanical, Industrial and Aeronautical Engineering,
University of the Witwatersrand, South Africa

E-mail: Igle.Gledhill@wits.ac.za

Abstract. As the level of participation of women in physics changes, it is of interest to understand whether a gender gap exists in publication, and what trends can be observed. This paper quotes data from the joint data-backed study of publication patterns that was undertaken as a task within the Gender Gap in Science project initiated through the International Science Council. The study was based on metadata available through publication databases, which allow inference of author gender from name strings using services that provide access to databases of names. Five such services were benchmarked. Results have been made available in an interactive online tool, from which the data available from South Africa have been drawn. Within the Astrophysics Data System, the rise in South African publications in the field can be observed, together with the evolution of the proportion of authorships by women. A global result from this project is also very relevant to South Africa: fractional authorships by women in high-impact journals in theoretical physics show average percentages of women near 10%, with little or no tendency to rise since 1999, while top journals in astrophysics and astronomy show steadily rising fractional authorships which have approximately doubled since 1999. The implications for South Africa are explored.

1. Introduction

Peer-reviewed publications are the basis of the body of scientific knowledge and of acknowledgement of contributions to science. In many countries, authorship is also used in the evaluation of individual performance and institutional achievement, and has become a part of hiring and promotion practices.

This is the case in South Africa, and is particularly relevant in building a strong base in basic sciences as the community of practice transforms itself towards a more equitable gender balance. Major projects in South Africa include co-hosting of the SKA¹, particle physics at CERN², and the National Institute of Theoretical and Computational Sciences. In the wider context relevant to this study lie theoretical physics, astronomy and astrophysics, and the many domains of physics and applied physics in South Africa.

There is a known gender gap in publication practices, and a known under-representation of women as authors in high-ranked journals. This short paper describes results from the Gender Gap in Science

¹ Square Kilometre Array Telescope

² European Organization for Nuclear Research

project [1] in the context of two questions relevant to South Africa. Firstly, how do publication patterns among women in astrophysics and astronomy compare with publication patterns in theoretical physics - what can South Africa learn from global data? Secondly, what data can be obtained from the project's study of bibliometrics for women in physics in South Africa?

A scientometric study of physics, including astronomy [2], has recently been completed in South Africa. The data are drawn from the South African Knowledgebase, which captures the self-identified gender of authors. Evidence of positive change of the community of physics with respect to women is captured. Nevertheless, the discipline lags the other basic sciences in percentages of women.

Of papers authored in physics and astronomy in 2016, 83% were co-authored with at least one international researcher [2]. Collaboration appears to foster authorships by women in physics [3].

Contrasts across subdisciplines may exist. A concept of specific relevance to this paper is the “field-specific ability beliefs hypothesis” put forward by Leslie et al. [4], whose formulation indicates that the extent to which practitioners “believe that success depends on sheer brilliance” is a good predictor of under-representation of women in that field.

1.1. The Gender Gap in Science project

This project, “A Global Approach to the Gender Gap in Mathematical, Computing, and Natural Sciences: How to Measure It, How to Reduce It?”, was a 3-year collaboration of eleven scientific unions and global organisations³. Three major tasks were undertaken: a global survey, a data-backed study of publication patterns, and the formulation of a databases of initiatives known to have successfully addressed the gender gap in science. The project book [1] provides a complete report on the three tasks and on recommendations arising from the study.

2. The Joint Data-Backed Study of Publication Patterns

The objectives of the study of publication patterns included the provision of insights into the proportions of women as publication authors, and the presence of women as authors in top journals (“top” journals in each field were identified by members of the discipline participating in the study) [3]. While other aspects, such as author drop-out rates of men and women, were covered, these are not included in the present brief study.

In a study of this kind, expertise is required across data science, scientometrics, gender studies and sociology, and in the Gender Gap project domain experts were available to collaborate and to check the methodologies used.

3. Methodology of the Joint Data-Backed Study of Publication Patterns

A full description of the methodology [3] will be found in the project publication [1]. In this study, an instance of *authorship* refers to a one-to-many pair of a publication and an author. A *fractional authorship* of a paper with n authors is defined as $1/n$.

Data for physics and astronomy were sourced from the Astrophysics Data System (ADS) [5] and the arXiv [6]. The limitations and rationale is provided by Mihaljević and Santamaría [3]. Geoinformation was extracted from affiliation where possible using the Stanford Named Entity Recogniser NER, GeoNames, and CERMINE [7]. Authorships and author profiles were extracted; gender inference was performed using Gender API, genderize.io, Python gender guesser, and Russian surname suffices [8]. All author names were assigned an identifier of ‘female’, ‘male’, or ‘unknown’. The method was benchmarked [9] and it was shown that unknown names more likely to be associated with men, and

³ IMU, the International Mathematical Union; IUPAC, the International Union of Pure and Applied Chemistry; IUPAP, the International Union of Pure and Applied Physics; IAU, the International Astronomical Union; ICIAM, the International Council of Industrial and Applied Mathematics; IUBS, the International Union of Biological Sciences; IUHPST, the International Union of History and Philosophy of Science and Technology; ACM, the Association for Computing Machinery; UNESCO, the United Nations Educational, Scientific and Cultural Organisation; GenderInSITE, Gender in Science, Innovation, Technology and Engineering and OWSD, the Organisation of Women in Science for the Developing World.

therefore that fractions of women in the final analysis are likely to be upper bounds. A public interactive database was built which has been used as the data source for the present paper.

Automated inference of gender is a sensitive and complex subject. The methodology and its limitations were discussed in a critical paper by Mihaljević et al., 2019 [10]. Automatically inferred gender may contrast with internal perception of gender. In the present study, only binary gender was inferred. Statements about societal issues based on publication meta-data may be subject to error. Fairness, Accountability and Transparency in Machine Learning is a critical element of the field [10]. Selection bias may be present due to the datasets that are available; in the present study this primarily affects names from certain regions. The removal of authors classified as “unknown” from the dataset may cause exclusion bias favouring groups for whom gender inference is easier.

Usage of the research may change the system being observed. One or another group may become objectified, to the detriment of the scientific field. The logical misuse of publication data to justify the lack of women professors or grant holders is not unknown [10].

Given these limitations, why should publication pattern analysis be attempted? The answer is at least partially that physics is experiencing a well-defined problem in gender balance, and the gender gap needs to be understood and remedied based on the evidence available. This short paper addresses two useful aspects emerging from the data-backed study of publications in the Gender Gap project, concerning a global gap between astronomy and physics, and specific data available on the publication patterns of women in South Africa.

4. Global findings

The database is publicly available [11]. From the ADS, data from 1970 to March 2018 were drawn, with selection of publications in “Astro” only. From 777 270 documents, 181 172 author profiles were extracted. Gender could be assigned to 93 608 of which 15% could be classified as female and 60% as male. From the arXiv, data from 1991 to July 2019 were drawn, with selection of the theoretical physics subfield only (noting that High Energy Physics has its own platform, not on arXiv). Of 1 667 512 documents, 458 485 author profiles were extracted. Gender could be assigned to 281 602 of which 17% could be classified as female and 83% as male. The first result that is evident is that the fraction of female authorships in astronomy/astrophysics contrasts with other physics subfields in arXiv (figure 1).

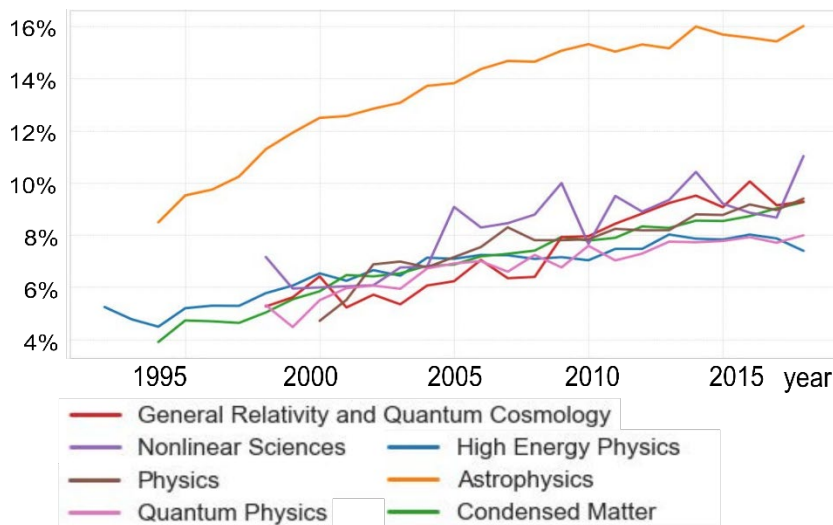


Figure 1. Global fractions of authorships by women per physics subfield and year in publications indexed in the arXiv. Reproduced under CC-BY 4.0 [3].

From “top” journals identified by participants in the project, the percentages of authorships by women in astronomy and astrophysics, and in theoretical physics, have been derived and are shown in figures 2 and 3.

It is of interest to note that in the Global Survey of Scientists, to which there were 32 346 respondents from 159 countries, of whom there were 7 570 in physics and 2 597 in astronomy/astrophysics, the

question was asked “During the last five years, how many articles have you submitted to journals that are top-ranked in your field?”. A model indicated that the self-perceptions of men and women of their rate of submissions to highly ranked journals are similar [3].

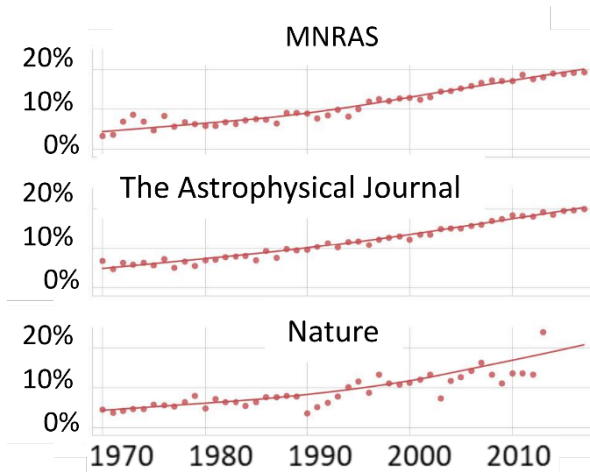


Figure 2. Percentage of fractional authorships from women in three top astronomy and astrophysics journals per year since 1970. MNRAS: Monthly Notices of the Royal Astronomical Society. The journals *Astronomy and Astrophysics*, *The Astronomical Journal*, and *Science* follow similar trends. Reproduced under CC-BY 4.0 [3].

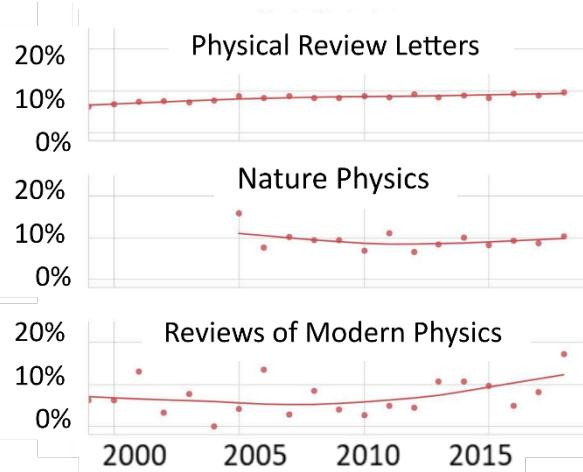


Figure 3. Percentage of fractional authorships from women in top theoretical physics journals per year since 1999. *Physical Review D*, *Journal of Physics A*, and *Journal of Mathematical Physics* show similar trends. Reproduced under CC-BY 4.0 [3].

5. South Africa

Within the Gender Gap publication database [11], the available data relevant to physics are from ADS only. The last year shown in each study does not include all papers published in that year.

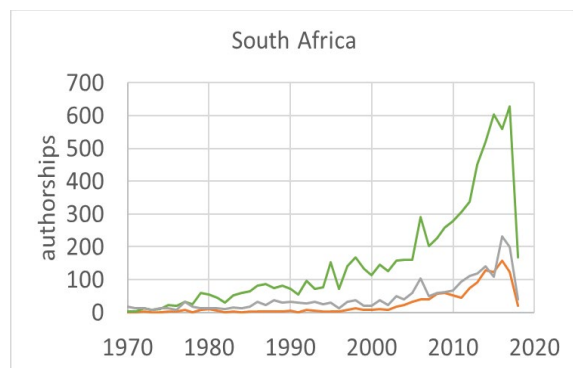


Figure 4. Chronology of absolute numbers of authorships extracted from ADS, [11].

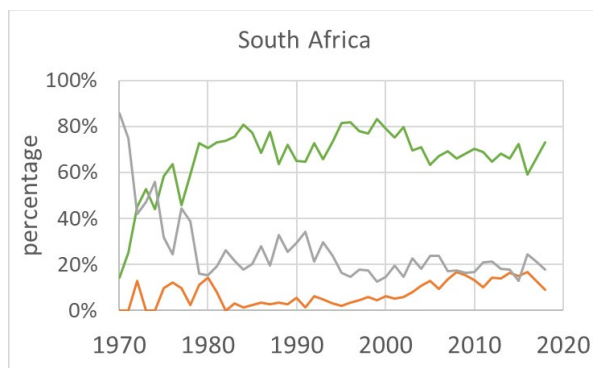


Figure 5. Chronology of percentages of authorships extracted from ADS, [11].

Figure 4 shows that South Africa experienced steady growth in the number of papers accessible through ADS, and figure 5 indicates that the percentage of authorships identified within this study as those of women rose from 6% in 2000 to 13% in 2017.

In figures 6 and 7, the same data [11] are compared with authorships identified from a recent South African scientometric study of physics [2]. These author profiles are based on self-identification of gender in the South African Knowledgebase. Only binary gender is available in the results [2]. It is observed that the number of authorships assigned through the Gender Gap publication pattern study [11] is between $\frac{1}{8}$ and $\frac{1}{3}$ of those available to the scientometric study. Figure 7 shows the percentages of authorships by gender in the two studies. The fraction of authors identified as women is very similar in the two studies. Trends with time are similar for the percentage of authors who are men. The automated gender assignment benchmark study [9] indicated that unknown names are more likely to be those of men, and it is not impossible that this is supported by figure 7.

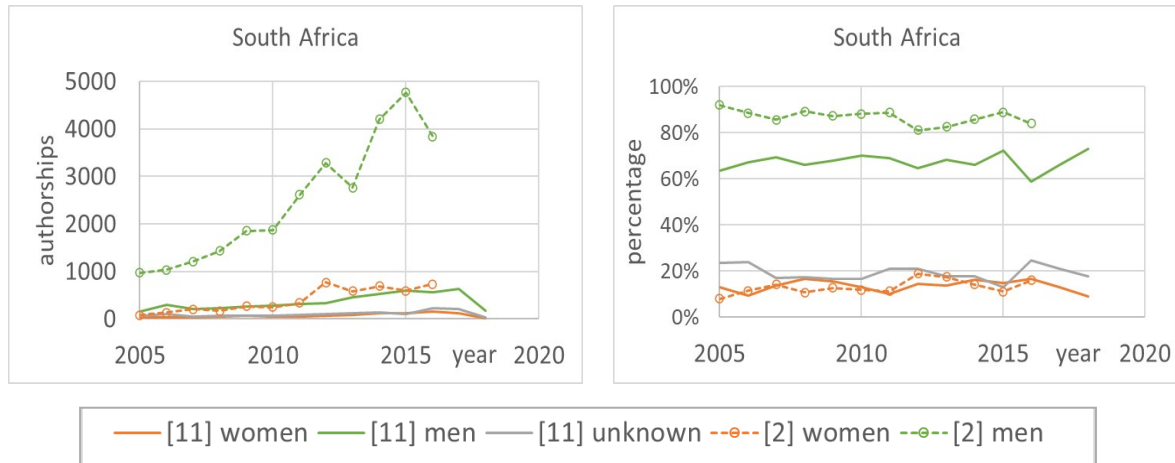


Figure 6. Numbers of authorships, [2], [11]

Figure 7. Percentages of authorships, [2], [11]

Profiles for two additional countries were drawn for comparison with South Africa. Egypt was chosen as an African country in which significant publication in physics is taking place. The data for Egypt show a surge in publications after 2010, and the percentage of authorships by women dropped from 9% (2000) to 7% (2017). Brazil was chosen as a country perhaps close to South Africa in science infrastructure. The percentage of authorships by women was 15% in 2000 and 17% in 2017, a slow rise.

6. Conclusions and recommendations

In global trends within publication patterns of women, the difference in authorships between astrophysics/astronomy ($\approx 20\%$) and theoretical physics ($\approx 10\%$) is both striking and relevant in the context of South Africa, which has significant success and investment in both these fields. In the database of publication patterns, top journals in astronomy and astrophysics exhibit rising percentages of female authorships, while percentages in some of the top theoretical physics journals appear to be stagnating or rising more slowly. Understanding the successes visible in astronomy may help theoretical physics.

A starting hypothesis is that there is a higher percentage of women in astronomy and astrophysics than in theoretical physics. As an illustrative example, data from the USA for 2017 [12] indicate that women earned 40% of astronomy doctorates, and 20% of physics doctorates. The Gender Gap project was not designed to measure percentages of women across the disciplines studied, and the data from the scientometric study do not provide gender disaggregation in subfields. If the fraction is indeed higher, this would contribute to explaining the lower publication rate in physics.

However, we should then ask why physics is less attractive to women, or loses women faster, than astronomy [3]. In terms of culture or bias, is the field-specific ability belief hypothesis [4] that “success depends on sheer brilliance” useful in explaining lower numbers, and stagnating publication rates, within theoretical physics? It is recommended that testing whether such beliefs are present may provide useful insight, and may lead to cultural changes which attract and retain women in theoretical physics.

Collaboration, in general, fosters higher publication rates by women [3]. Both astronomy and high energy physics are highly collaborative fields. However, the latter has its own preprint platform and is not well-represented on the arXiv database, and papers with more than 100 authors may not have been captured in the South African scientometric study due to rules governing the data collection process. Collaboration may be assisting women to publish, but the accessible data do not allow the effect to be definitively seen in these studies for South Africa.

South Africa experienced significant growth in the percentages of female authorships illustrated in publications accessible through ADS: the percentage of authorships identified within the publication pattern study as those of women rose from 6% in 2000 to 13% in 2017. The percentages of authorships by women in the publication pattern analysis using ADS [11] are similar to the percentages of authorships by women in the South African scientometric study of physics [2], although the two source datasets each have limitations.

Astronomy has run active development programmes in Southern Africa, and both the physics community and university departments have specific initiatives targeted at closing the gender gap. The outcomes of an intense effort to build an equitable physics culture may be evident in the fact that South Africa has a much greater rate of increase in physics publication by women than the two countries with which comparisons were made, Egypt and Brazil.

Acknowledgments

Images are reproduced from the final report which appeared under a CC-BY 4.0 International License [3]. The funding for this project was provided by the ISC and the eleven participating Unions and organisations³. The African Workshop was supported by the African Institute for Mathematical Sciences and the ISC Regional Office for Africa. The author thanks Helena Mihaljević, Lucía Santamaría and Christian Steinfeldt for their impactful research and for providing Open Access to the project data.

References

- [1] Roy M-F *et al.* 2020 *A Global Approach to the Gender Gap in Mathematical, Computing, and Natural Sciences: How to Measure It, How to Reduce It?* (Berlin: IMU)
- [2] Mouton J *et al.* 2020 *A scientometric assessment of Physics in South Africa* (Pretoria: Department of Science and Innovation, Republic of South Africa)
- [3] Mihaljević H and Santamaría L 2020 *Measuring and analysing the Gender Gap in science through the Joint Data-Backed Study of Publication Patterns in Roy M-F et al. [1]* (Berlin: IMU) pp 85–152
- [4] Leslie S-J, Cimpian A, Meyer M and Freeland T 2015 Expectations of brilliance underlie gender distributions across academic disciplines *Science* **347** pp 262–265
- [5] Smithsonian Astrophysical Observatory-NASA <https://ui.adsabs.harvard.edu>
- [6] arXiv <https://arxiv.org>
- [7] Stanford Named Entity Recogniser NER <https://nlp.stanford.edu/software/CRF-NER.html>
GeoNames <http://www.geonames.org/>
CERMINE <https://github.com/CeON/CERMINE>
- [8] Gender API <https://gender-api.com>
genderize.io <https://genderize.io>
Python gender guesser <https://github.com/lead-ratings/gender-guesser>
Wikipedia List of Surnames in Russia https://en.wikipedia.org/wiki/List_of_surnames_in_Russia
- [9] Santamaría L and Mihaljević-Brandt H 2018 Comparison and benchmark of name-to-gender inference services *PeerJ Computer Science* **4**:e156; DOI 10.7717/peerj-cs.p156 pp 1–29
- [10] Mihaljević H, Tullney M, Santamaría L and Steinfeldt C 2019 Reflections on Gender Analyses of Bibliographic Corpora *Frontiers in Big Data* **2** 29 pp1–6
- [11] Gender Gap in Publications <https://gender-publication-gap.f4.htw-berlin.de/>
- [12] Porter A M and Ivie R 2019 *Women in Physics and Astronomy, 2019* (American Institute of Physics, College Park MD USA)

Inaugural Quantum Computing School in Lesotho: Its impact and the Lessons Learnt

Naleli Matjelo¹ and Makhamisa Senekane²

¹Department of Physics and Electronics, National University of Lesotho, Roma, Lesotho

²Institute for Intelligent Systems, University of Johannesburg, South Africa

E-mail: nj.matjelo@nul.ls, smakhamisa@uj.ac.za

Abstract.

This paper reports the events and impact of a two-day Physics Without Frontiers (PWF) quantum computing School that took place on the 14th and 15th of November 2020 at the National University of Lesotho (NUL). Sponsored by the International Centre for Theoretical Physics (ICTP) and aimed to run annually, the School was intended to introduce quantum computing; using existing open-source quantum computing platforms, to undergraduate students in Lesotho as well as to highlight how quantum computing can be used as a driver for the Fourth Industrial Revolution (4IR). The School was also intended to encourage students to consider furthering their study in quantum computing and related disciplines. This (hoped-to-be annual) event will potentially unite the NUL, the Lesotho government and the ICTP in a long-term relationship; to the benefit of young Basotho scientists and students. The November 2020 event was, in and of itself, a success on several response measures including good and consistent attendance over the two days, as well as being influential based on several students' requests for postgraduate reference letters following this event. The outreach approach used here can be replicated elsewhere, especially in Africa, in order to capacitate students with quantum computing skills. Challenges encountered in this event will also be discussed in the paper.

1. Introduction

The first quantum revolution started in the early 1900s; with the birth of quantum mechanics. Quantum mechanics probes the world at a sub-atomic level. During the second half of the 20th century; in the 1970s, the second quantum revolution was born [1]. The second quantum revolution is characterized by the use of concepts from quantum physics in order to process information. This use of quantum mechanical concepts in order to process information is referred to as quantum information processing (QIP) [1, 2, 3].

Some of the sub-fields of QIP include quantum cryptography [4] and quantum computing [5]. Quantum cryptography uses quantum mechanical concepts such as the *no-cloning theorem* and Heisenberg's *uncertainty principle* in order to enable secure communication of information. On the other hand, quantum computing makes use of quantum mechanical concepts such as *interference* and *superposition* in order to perform computations in a manner that offers computational advantage over conventional computing paradigm [1]. Coincidentally, in addition to being one of the sub-fields of the second quantum revolution, quantum computing is also one of the driving technologies of the fourth industrial revolution (4IR) [6, 7]. As a consequence, quantum computing has gained some traction beyond the academia.

Despite the growing popularity of quantum computing in other parts of the world [8], there are other parts of the world where the awareness of quantum computing is still limited. These parts are predominantly in the global South. This limited awareness of quantum computing in the global South can be addressed through science communication approaches such as outreach and public engagement activities [9].

In this paper, we provide a report on the two-day quantum computing outreach activity that was held in Lesotho in November 2020. The goals of this outreach activity were:

- to introduce quantum computing to undergraduate students in Lesotho; and
- to encourage these students to consider pursuing their studies in quantum computing.

The remainder of this paper is structured as follows. The next section provides the background information on quantum computing and science communication. This is followed by Section 3, which outlines how the quantum computing outreach activity discussed in this paper was conducted. Furthermore, Section 4 discusses the outputs of the outreach activity, including the lessons learnt from this quantum computing outreach. Finally, Section 5 concludes this paper.

2. Background Information

2.1. Quantum Computing

As already stated earlier in this paper, quantum computing uses quantum mechanical concepts in order to perform computation. Additionally, in order to process information, quantum computing uses a quantum bit (qubit) as a unit of information [1]. A qubit is analogous to a binary digit (bit) in conventional computing paradigm. Additionally, a qubit can exist in superposition of two quantum computational basis states, namely $|0\rangle$ and $|1\rangle$.

Mathematically, a qubit can be represented as [1, 10, 11]:

$$|\psi\rangle = \alpha|0\rangle + \beta|1\rangle, \quad (1)$$

where α and β , which are known as probability amplitudes, satisfy the condition:

$$|\alpha|^2 + |\beta|^2 = 1. \quad (2)$$

In order to implement quantum computing on the existing noisy, intermediate-scale quantum (NISQ) computing devices [12], various quantum computing software frameworks can be used. These frameworks include [7, 13, 14]:

- QuTiP;
- IBM's Qiskit;
- Google's Cirq and TensorFlow Quantum;
- Amazon's BraKet; and
- Xanadu's Strawberry Fields and PennyLane.

2.2. Science Communication

Besides communicating with peers through the publication in scientific journals, scientists can also communicate directly with the general public [9, 15]. Various approaches can be used by scientists to engage with the general public. These approaches include [9]:

- outreach activity;
- public engagement;
- diversity and inclusion promotion activity; and
- knowledge exchange.

The communication approach that was used in the work reported in this paper is the outreach activity. The details of this outreach activity will be provided in the next section.

Table 1. Summary of Topics Covered on Day 1.

Topic	Speaker
Introduction to Quantum Computing	Makhamisa Senekane
Quantum Computing and the 4IR	Makhamisa Senekane
Introduction to Python	Makhamisa Senekane
Navigating Through Google Colab	Naleli Matjelo
Hands-on Introduction to QuTIP	Makhamisa Senekane

Table 2. Summary of Topics Covered on Day 2.

Topic	Speaker
Hands-on Intro. to QISKit	Makhamisa Senekane (MS)
Hands-on Intro. to Cirq and TensorFlow Quantum	Naleli Matjelo (NM)
Hands-on Intro. to BraKet	MS
Hands-on Intro. to PennyLane and Strawberry Fields	NM
Careers Opportunities in Quantum Computing	MS and NM

3. The Quantum Computing Outreach Activity

The two-day quantum computing outreach activity was held at the National University of Lesotho's Roma Campus, Lesotho, from the 14th November 2020 to the 15th November 2020. This outreach activity was organized by the International Centre for Theoretical Physics (ICTP) Physics Without Frontiers (PWF) and the National University of Lesotho (NUL). The ICTP PWF provided both the technical and the financial support, while the NUL hosted the event and prepared the learning material for this activity.

As already stated, this outreach activity was intended to introduce quantum computing to undergraduate students studying in Lesotho. Therefore, in order to prepare for the event, invitations were sent out to the three universities in Lesotho; namely the NUL, Botho University, and Limkokwing University of Technology. Students who were familiar with computing and/or physics were requested to apply for the event electronically, and successful candidates were notified via an e-mail. Consequently, 34 students were invited to attend this event.

The topics that were covered on the first day of the quantum computing outreach activity are provided in Table 1. In essence, the first day was intended to introduce the students to Python programming language [16] and quantum computing. Additionally, students were exposed to cloud-based programming environment using Google Colaboratory/colab [17]. Finally, they were briefly introduced to one of the quantum computing frameworks, namely QuTiP framework.

On the other hand, the topics covered on the second day are provided in Table 2. These topics were mainly geared towards exposing the students to different types of quantum computing frameworks. Finally, the students were exposed to the career opportunities in quantum computing. Originally, more speakers were invited to give lessons in this School. However, due to various challenges, especially owing to the fact that the School took place on a weekend, ultimately, only two speakers were able to give lessons in this School.

Through-out this two-day event, the students were using their own computing devices and using Google Colab to run their codes, while the free internet access was provided by the National University of Lesotho. Furthermore, the students were permitted to discuss the quantum computing exercises provided with their colleagues. Figure 1 shows students sharing ideas during one of the exercises.



Figure 1. Students engaging with the exercises during the quantum computing outreach event.

4. Outreach Activity Outputs

In total, 34 students registered for the quantum computing outreach activity. These students came from two of the three universities in Lesotho, namely the NUL and Botho University. Figure 2 provides an overview of the students who attended, and their institutions. As can be observed from the figure, majority of the participants were from then National University of Lesotho. This might be due to the publicity that this event received within the National University of Lesotho, as opposed to two other universities.

Figure 3 shows participants when dis-aggregated by gender. It can be observed from the data that when dis-aggregated by gender, the list of participants paints a very gloomy picture. This gender disparity underlines the necessity to pay attention to gender representation during the admission process of the participants. Furthermore, the disparity underlines the need to further mainstream gender equality, especially in the quantum computing community.

At the end of the event, the students who successfully attended all the sessions of this two-day event were awarded with certificates of participation. Of the 34 students who were invited to attend the quantum computing event, 32 were awarded with the certificates of successful completion. Figure 4 shows the design of the certificate of participation that was awarded to the students upon successful completion of all the activities.

The first goal of the quantum computing outreach activity was to introduce the undergraduate students in Lesotho to quantum computing. This goal was met, even though the attendance of the students was dominated by one university. Furthermore, the attendees were predominantly male.

On the other hand, the second goal of the outreach activity was to encourage students to consider pursuing a career in quantum computing. After the completion of the event, several students have approached the event organizers (the authors of this paper), requesting reference letters for postgraduate studies.

As stated earlier, this quantum computing outreach initiative was a result of a collaboration of the ICTP PWF and the National University of Lesotho. This collaboration underlines the necessity of the resource-constrained countries to explore the possibility of joining hands with

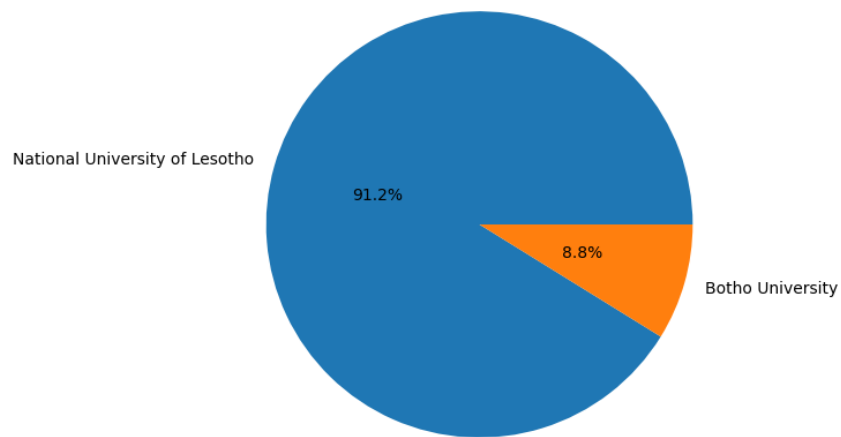


Figure 2. Quantum computing outreach activity participants, by institution.

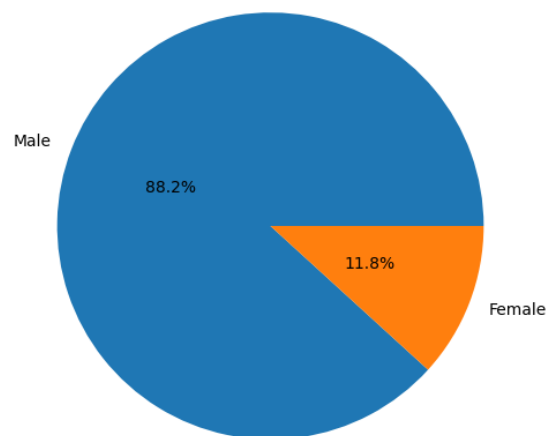
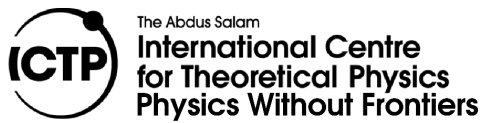


Figure 3. Quantum computing outreach activity participants, by gender.

the established entities in order to up-skill and develop their communities. Furthermore, the learning material produced in this collaborative work can be used by other resource-constrained countries as a tool to introduce quantum computing to the undergraduate students.



This is to certify that

 attended the
 ICTP Physics Without Frontiers
School on Quantum Computing.
 National University of Lesotho
 14th - 15th November 2020

Prof. Bobby Acharya
 Co-Coordinator of PWF

Dr. Molefe Makhele
 Head of the Department of Physics

Figure 4. Upon the successful completion of all the sessions of the event, the students were awarded with certificates of participation.

5. Conclusion

In this paper, we have discussed the details concerning the two-day quantum computing activity that was held in Lesotho in November 2020. Additionally, we have discussed the challenges that this activity faced, and the lessons learnt from hosting the activity. We have also reported on the impact of the event. Finally, we have argued that the approach used in organizing and hosting this activity can be replicated elsewhere in a resource-constrained country, especially in Africa.

Acknowledgements

Both authors would like to thank ICTP PWF in general and Dr. Kate Shaw in particular, for both technical and financial assistance provided, in order to make this quantum computing outreach activity a success. Naleli Matjelo would like to thank the National University of Lesotho for the support. Makhamisa Senekane thanks the Institute for Intelligent Systems in the University of Johannesburg and the National Institute for Theoretical and Computational Science, for the support.

References

- [1] Nielsen M A and Chuang I 2010 *Quantum Computation and Quantum Information* (Cambridge University Press)
- [2] Aaronson S 2013 *Quantum Computing Since Democritus* (Cambridge University Press)
- [3] Wilde M M 2017 *Quantum Information Theory* (Cambridge University Press)

- [4] Gisin N, Ribordy G, Tittel W and Zbinden H 2002 *Reviews of modern physics* **74** 145
- [5] Scherer W 2019 *Mathematics of Quantum Computing* (Springer)
- [6] Schwab K 2017 *The Fourth Industrial Revolution* (Currency)
- [7] Senekane M, Maseli M and Taele M B 2020 *The Disruptive Fourth Industrial Revolution* (Springer) pp 205–225
- [8] Asfaw A *et al.* 2021 *arXiv preprint arXiv:2108.01311*
- [9] Illingworth S and Allen G 2020 *Effective Science Communication* (IOP Publishing Limited)
- [10] Wittek P 2014 *Quantum Machine Learning: What Quantum Computing Means to Data Mining* (Academic Press)
- [11] Schuld M and Petruccione F 2018 *Supervised Learning with Quantum Computers* (Springer)
- [12] Preskill J 2018 *Quantum* **2** 79
- [13] Johansson J R, Nation P D and Nori F 2012 *Computer Physics Communications* **183** 1760
- [14] Asfaw A *et al.* 2020 *Learn Quantum Computation Using Qiskit* (IBM) URL <http://community.qiskit.org/textbook>
- [15] Moore B *et al.* 2021 Ten simple rules for organizing a bioinformatics training course in low-and middle-income countries
- [16] Van Rossum G and Drake F 2009 *Python 3 Reference Manual* (Scotts Valley, CA: CreateSpace) ISBN 1441412697
- [17] Nelson M J and Hoover A K 2020 *Proceedings of the 2020 ACM conference on innovation and Technology in Computer Science Education* pp 533–534

Leveraging Artificial Intelligence and Quantum Machine Learning for economic growth in Africa

Keaotshepha Karabo and Mhlambululi Mafu

Department of Physics and Astronomy, Botswana International University of Science and Technology, P/Bag 16, Palapye, Botswana

E-mail: keaotshepha.karabo@studentmail.biust.ac.bw

Abstract. Artificial Intelligence (AI) and Quantum Machine Learning (QML) have become the most promising significant tools for addressing the challenges of the Fourth Industrial Revolution (4IR). Besides its use in understanding physical and complex systems, these tools have demonstrated unmatched potential applications in numerous research disciplines and sectors such as banking, finance, social networks, cybersecurity, and health. Most importantly, recently, they have played a critical role in addressing challenges related to the Covid-19 pandemic. While these developments are remarkable, Africa has been lagging. Therefore, this paper aims to identify opportunities behind the challenges of implementing AI and MLA in addressing this technology gap, especially in earlier sectors, and fully participate in the 4IR. While the quantumness presents various opportunities, especially for industries and stakeholders, we examine which intelligent tools can address these challenges. Thus, this will allow the proper application of these techniques to solve Africa's long-standing problems.

1. Introduction

Artificial Intelligence (AI) has driven development in technology in many societies and economies of developing countries to enforce sustainable human development. AI has been defined as the “science and engineering of making intelligent computer systems” to enhance learning and decision making for solving problems [1]. Many countries have benefited from applications of AI, which provided faster performance and efficiency in conducting tasks better than humans. At present, AI systems can understand human expressions, recognise images, predict traffic, and many others. It has aided technological innovation as digitalised data continued to grow, and thus many economies depended on its applications in order to expand the digital revolution that addresses challenges of the Fourth Industrial Revolution (4IR) [2]. Quantum machine learning (QML) is an emerging field encompassing systems learning without being programmed or modified. As data grows massively, better computing storage and performance are required to achieve accurate results faster. Therefore, QML enhances systems through superposition and entanglement tools to solve complex systems and perform operations on large data. It has also been successful in optimising classical machine learning algorithms [3].

Such applications of AI and QML are transparent across sectors such as banking, finance, social networks, cybersecurity, and health and are currently addressing the Covid-19 pandemic, as discussed in this paper. Since AI and QML are the elementary technology of the 4IR, various developing countries have been committed to developing their competencies. AI and QML have

both aimed at sustaining human development in many countries; however, there is a wide variation between developing countries and Africa in applying these tools. Africa has been falling behind with visions of accessing these 4IR tools due to some challenges; among them is poor growth of human capital, which leads to poor productivity as per Amankwah-Amoah [4]. On the other hand, these tools can bring industrialisation opportunities that have considerable potential to improve the economies in Africa so it could be more efficient and competitive in its industrial processes. As Africa leans towards the acquisition of these tools, it will address various challenges which impact the implementation of the 4IR, which are necessary for technological progress in order to achieve a successful transformation in the sectors as mentioned earlier [5].

Against this background, we explore ways in which Africa can benefit from the Fourth Industrial Revolution to solve some challenges, bringing some development in some countries in the various stated sectors. We show how AI and QML can impact these sectors to close the technological gap between Africa and other developed countries. Moreover, we demonstrate how these tools can impact these various sectors. Therefore, we organise this work according to the following. First, section 2 examines the impact of AI and QML in developing countries' economies, especially its relevance in Africa. Second, in section 3, we identify opportunities available for the continuous development of economies in Africa. Third, in section 4, we demonstrate the advantage of the quantumness (i.e., the condition of being quantum in nature), especially in performing high-end tasks faster and efficiently then; finally, in section 5, we conclude.

2. Impact of AI and QML in economies of developing countries

AI has been successful in various developing countries at performing different tasks that assist people. Nowadays, many intelligent assistant software can understand human behaviour based on a pattern from data collected by that software. Various industries use this data to give better comfort of using the software to their customers, thus driving the economies. QML, on the other hand, utilises superposition and entanglement to give a better computational performance and is expected to revolutionise the future. Since it has successfully optimised classical machine learning algorithms to solve complex systems, it will also escalate the development of AI-based systems. This is on account of qubits being able to occupy two simultaneous states $|0\rangle$ and $|1\rangle$ at once. Thus QML suffices up to the task of solving computationally-intensive operations. QML has shown its unmatched potential by solving algebraic computational problems such as the problem of factoring large integers using Shor's algorithm, which improves computational speed and data storage over a range of computer systems [6]. Moreover, the advance of AI and ML have resulted in the need to pay more attention to the provision of privacy to the data being analyzed [7, 8].

The 4IR promotes the implementation of AI and QML for efficient industrialization. However, Africa has fallen behind in technological development, and the challenges are poor human development which involves poverty, youth unemployment, poor health, and education. Another motive for Africa being undeveloped is due to lack of technical education across various countries, thus stagnating the economies [9]. Nevertheless, AI and QML can increase opportunities offered by technology to transform Africa and bring innovative ideas over numerous sectors. These tools can enable Africa to close the technological gap with developed countries and encourage economic growth. Failing to exploit the opportunities of 4IR will consequently urge additional risks on African stakeholders, with no attempts to find new innovative ideas for digital growth. This will additionally weaken global competitiveness as Africa risk falling behind.

3. Opportunities available for continuous development of economies in Africa

3.1. Banking & Finance

AI and QML are significant in interacting with people such that they acquire data to perform cognitive activities such as learning, understanding, and giving feedback on the best course of action. As such, they enhance software capabilities, and due to this, many software nowadays can automate some banking processes that involve customer accounting, making payments, or cash handling. Therefore, customers could enjoy faster services at the comfort of staying home instead of forming long queues at banks. Customers can also benefit from using straightforward assistant services from their devices to make financial plans, whereby the software analyze their behavior and best interests for better well-planned and cost-effective actions [10].

QML can be used in communication to manage information and insist on better encryption methods. For example, through quantum key distribution (QKD), an untrusted party is prevented from eavesdropping on the information shared by, in context Alice (client) and Bob (server) [11]. Thus this demonstrates the capability of cryptographic algorithms securing data from attack or leaking, which will be a successful application in banking and finance [12]. Furthermore, since AI and QML can fluently analyze data and give accurate results through algorithms, it can help to forecast risks in loans which can improve the long-term growth of industries [13], thus developing the economy.

3.2. Social networks

These tools have demonstrated the ability to drive the economy through social networking primarily, as Africa can acquire needed skills to understand its customer trends, offer preferred product or service (through recommendation systems) [14], based on the data accumulated. This will help industries to effectively manage resources through citizen participation, thus promoting the market growth. Nowadays, the same knowledge and technology are used in popular software, such as LinkedIn and Facebook, to suggest preferable connections and serve users with specific posts of interest in their feed. QML can also create a secure network by merging with the Internet of Things (IoT) and Blockchain [15], which will improve efficiency in systems that contain large data and also provide reliable data protection schemes. Distribution of marketing content will also be faster and monitored easily across most social media platforms, with shortened links and some auto-scheduled shares. Industries in Africa could also use these technologies to recognize emerging customer trademarks and keep track of social mentions to identify approaches for better social media promotions [16].

3.3. Cybersecurity

AI can be used in the 4IR to strengthen cybersecurity in Africa by detecting data breaches to remove unwanted data or malware from systems being developed to lower the cyber-attack. This is done through analyzing patterns from input data and recognizing unusual patterns of behavior. These could enable quality protection through QML in systems or accessories when using artificial neural networks and data mining techniques such as classification, clustering and regression-to- to ultimately give better security services [17]. Through QML, it could be relatively easy and faster to determine how vulnerable or exposed the system is, guided by how the pattern behaves to recognize the infiltration points. This will therefore alert authorities much sooner to protect sensitive data from being swindled from their computers [18]. Nowadays, AI provides more intelligent biometric authentication systems such as face or voice recognition and fingerprint scanning across various devices. As a result, authentication is improved; for example, in voice recognition, tone, accent, and pitch are analyzed much faster, and biometric systems can identify unique voice impressions accurately [19]. According to Perdomo-Ortiz *et al.* (2018), QML will assist in storage and performance challenges, wherever systems contain large data, and also build systems that will transform current security initiatives, such as quantum

sensors, quantum radars, and location detection, which cannot be interfered with easily [20]. Furthermore, since these systems also use communication systems, they will be secured through quantum encryption.

3.4. Health

Digital technology will play a significant role in making cost-effective algorithms to diagnose patients effectively by learning from past cases or reports to enhance clinical decisions. This technology can also monitor multiple patients at the same time through medical algorithms. These algorithms can also offer self-service to patients with health-related inquiries and thus save time, effort, and most importantly, lives [21]. Moreover, AI machines are capable of analyzing data from past surgeries recorded, and they could be more precise at detecting illnesses and even discover some new surgical procedures, which could improve the health facilities in Africa. Finally, in battling current medical concerns, AI and QML can track the spread of Covid-19 by effectively evaluating existing data to make predictions on infection rates across countries [22]; this provides viable information and meaningful future guidance across Africa.

4. Simulation of Grover's algorithm

Grover's algorithm enables one to find a specific element of interest within an unordered set of elements, with probability greater than $\frac{1}{2}$. Quadratic speedup needs to optimize classical algorithms. However, its applications can be considered in various and broad disciplines. We simulate Grover's search algorithm, with several items as $N = 2000$ for two input qubits. The amplitude is obtained as:

$$\sin \theta = \frac{1}{\sqrt{N}} = \frac{1}{2}$$

$$\text{where } \theta = \sin^{-1}\left(\frac{1}{2}\right) = \frac{\pi}{6} \quad (1)$$

with the probability of $\frac{1}{4}$. If we consider the element $'0, 1'$ to be part of the database we wish to perform a search on, then it would be an input register $|x\rangle = |01\rangle$. Then we reference the winner item as $|k\rangle$; therefore, oracle U_f will act as follows:

$$U_f|k\rangle = \frac{1}{2}(|00\rangle - |01\rangle + |10\rangle + |11\rangle),$$

or

$$U_f = \begin{bmatrix} 1 & 0 & 0 & 0 \\ 0 & -1 & 0 & 0 \\ 0 & 0 & 1 & 0 \\ 0 & 0 & 0 & 1 \end{bmatrix} \quad (2)$$

and it will distinguish the element 01 from the rest of the other elements. The winner item is obtained following the condition:

$$f(x) = \begin{cases} 1 & x = k \\ 0 & \text{otherwise} \end{cases} \quad (3)$$

for all $N = 2000$ items.

The input qubits and target qubits are then passed through a Toffoli gate (using a conditional

NOT gate) as a control to flip the amplitude of the winner state, which ensures it is converted to 1s. Next, the conditional phase flips are obtained using a combination of CNOT, X and H gates. The final step is to restore the winner state to 1, and therefore obtain the results.

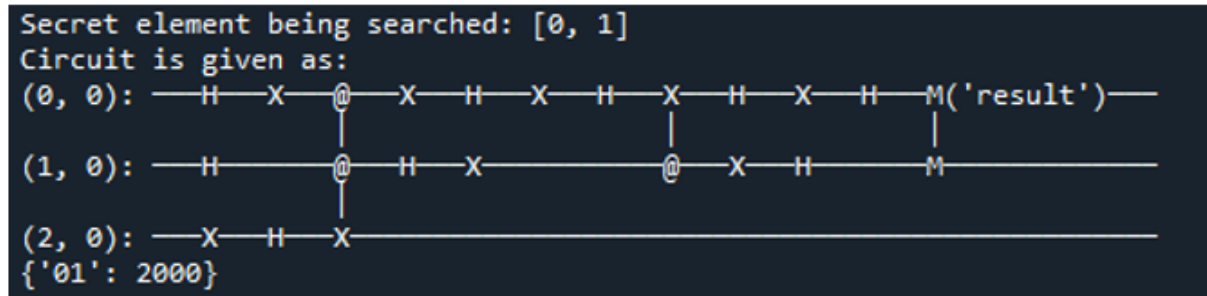


Figure 1: Results after performing the Grover's algorithm search

From Figure 1, Grover's algorithm is thus significant in optimizing classical machine learning algorithms to perform high-end tasks faster and efficiently. This shows how much QML and AI can enhance some daily computational tasks; this makes it powerful in the applications mentioned above. Furthermore, since 'big data' is the most concerning challenge, especially in the classical computing era, QML can thus increase chances of acquiring more excellent computational performance, speedups and ultimately provide many secure networks against cyber attacks. Therefore, all this knowledge can improve the standard of technology for the 4IR implementation in Africa, hence contributing to the growth of economies.

5. Conclusion

We have evaluated and illustrated how AI and QML can become powerful tools in implementing the 4IR and how these tools can address some significant challenges that prohibit full industrialization. The significance of these tools has proven effective in sectors such as banking, finance, social networks, cybersecurity, and health. Hence, it is significant that these technologies contribute to closing the gap in the mentioned sectors between Africa and other developed countries.

References

- [1] Cioffi R, Travaglioni M, Piscitelli G, Petrillo A and De Felice F 2020 *Sustainability* **12** 492
- [2] Butler-Adam J 2018 *South African Journal of Science* **114** 1–1
- [3] Schuld M, Sinayskiy I and Petruccione F 2015 *Contemporary Physics* **56** 172–185
- [4] Amankwah-Amoah J 2019 *Sustainable Development* **27** 910–922
- [5] Naudé W 2018 *Journal of International Affairs* **72** 143–158
- [6] Monz T, Nigg D, Martinez E A, Brandl M F, Schindler P, Rines R, Wang S X, Chuang I L and Blatt R 2016 *Science* **351** 1068–1070
- [7] Senekane M, Mafu M and Taele B M 2017 *2017 IEEE AFRICON* 1432–1435
- [8] Senekane M, Mafu M, Maseli M and Taele B M 2021 *2021 IEEE AFRICON* 1–6
- [9] Chemhuru M 2021 *African Values, Ethics, and Technology* (Springer) pp 17–33
- [10] Caron M S 2019 *Banking & Finance Law Review* **34** 169–214
- [11] Xi-Han L, Chun-Yan L, Fu-Guo D, Ping Z, Yu-Jie L and Hong-Yu Z 2007 *Chinese Physics* **16** 2149
- [12] Sheng Y B and Zhou L 2017 *Science Bulletin* **62** 1025–1029
- [13] Bissoondoyal-Bheennick E and Treepongkaruna S 2011 *Australian Journal of Management* **36** 405–424
- [14] Hoens T R, Blanton M and Chawla N V 2010 *2010 IEEE Second International Conference on Social Computing* (IEEE) pp 816–825
- [15] Kaarathi P A and Sathiyabama S 2021 *Annals of the Romanian Society for Cell Biology* 58–72
- [16] Ng C and Law K M 2020 *Computers & Industrial Engineering* **139** 106180
- [17] Wu X 2004 *IEEE/WIC/ACM International Conference on Web Intelligence (WI'04)* pp 7–7

- [18] Wachter S and Mittelstadt B 2019 *Colum. Bus. L. Rev.* 494
- [19] Fang H, Qi A and Wang X 2020 *IEEE Network* **34** 24–29
- [20] Perdomo-Ortiz A, Benedetti M, Realpe-Gómez J and Biswas R 2018 *Quantum Science and Technology* **3** 030502
- [21] Ngiam K Y and Khor W 2019 *The Lancet Oncology* **20** e262–e273
- [22] Shah P, Kendall F, Khozin S, Goosen R, Hu J, Laramie J, Ringel M and Schork N 2019 *NPJ Digital Medicine* **2** 1–5

Evolution of the 3rd Year Physics Major Project at WITS

Jonathan M Kearthland

School of Physics, University of the Witwatersrand, WITS2050, South Africa

Jonathan.Kearthland@wits.ac.za

Abstract. The Major Project has been an important component of the 3rd Year Physics curriculum at WITS for many decades. It has proven very popular with the students and has allowed academic staff to identify students with research potential as early as the final year undergraduate level. In the original model each student chose a project offered by a member of the academic staff, and completed the work required during one of the first three quarters of the academic year. In 2015 the student numbers increased dramatically from approximately 25 students to approximately 50 students, and it became increasingly difficult to run the projects in their existing form. In 2018 the major project underwent a transformation, and since then students have completed an Independent Research Essay (IRE) under supervision of a member of the academic staff, with a student teaching assistant acting as a mentor for a small group of students. This report provides a description of the evolution of the Major Project, paying particular attention to the components of the IRE as it is at present. In particular, it will be shown how the IRE may be used to inculcate or enhance essential skills for budding scientists, be they enrolled students or graduate student tutors.

1. Introduction

The final year physics undergraduate curriculum in institutions of higher learning should be designed to equip students with sufficient background to proceed to post-graduate study, and should also take note of the number of students that will not continue with their studies following successful completion of a bachelor's degree. Examination of the literature in Physics Education Research (PER) shows that the vast majority of studies are aimed at addressing teaching and learning at first year level. This is understandable, as students in the first year of study often arrive from secondary schooling with critical misconceptions that hamper their ability to succeed at tertiary level. While PER studies of higher-level courses are rare, studies that focus on laboratory curricula are even less common. In the recent past, reports by Zwickl *et al* [1, 2] have attempted to provide laboratory coordinators with guidance as to the design and implementation of innovative higher-level laboratory programmes.

A description of the Physics III curriculum at WITS has been provided previously [3]. In brief, the curriculum comprises five modules, for a total of 72 points (this a standard points allocation for a 3rd Year course at WITS). There are four modules that are presented by way of lectures (11 points each), and the Advanced Experimental Physics and Project (PHYS3006) module which is worth 28 points. At present there are three components of the module: Set Experiments, An Introduction to Electronics, and the Major Project. The Major Project contributes approximately 50% of the final mark for the module. This activity therefore contributes a significant portion of the final mark for Physics III. Moreover, the activity has always been extremely popular with the students, who have cited it as the most stimulating component of PHYS3006 in several course surveys over the years [3]. Any changes

that are made to the format of the Major Project should not negatively affect the existing learning goals and outcomes of the activity. Any implemented changes should also be designed to enhance the skills required for graduating students who are proceeding to post-graduate study, and those who will be making their way into the workforce [1].

This report seeks to provide the reader with a description of the evolution of the Major Project component of PHYS3006 for the period 2011-2021. While it is clear that the initial impetus for considering and implementing changes is the remarkable increase in student numbers (see Fig. 1), it will be shown that the changes that were made provide the students with the opportunity to develop certain high-level skills that will benefit their future careers. The opportunity for the teaching assistants, who support small groups of students, to develop supervision skills, is a useful by-product of the changes that were made to the Major Project.

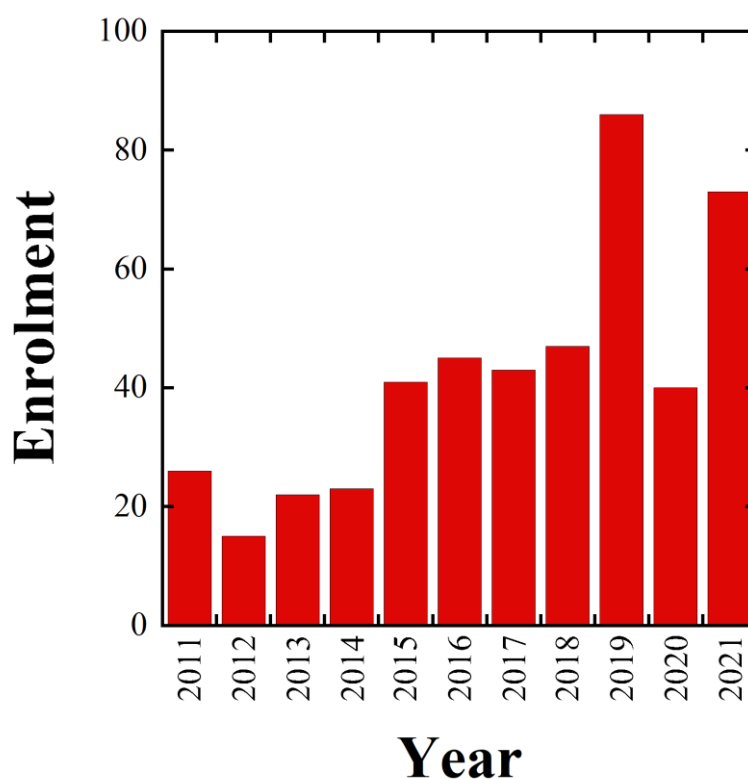


Figure 1. Student enrolment for PHYS3006 for the period 2011 – 2021. This corresponds to the period for which the author was the coordinator of the PHYS3006 module. The data show that for the period prior to 2015 student numbers were stable at approximately 25 students. A sudden increase in student enrolment for the period 2015 – 2017 placed severe strain on the existing model for the Major Project (see Section 2.), and changes were implemented for 2018 and subsequent years. The Independent Research Essay was introduced and is described in detail in Section 3 of this report.

2. The Physics III Major Project prior to 2018

The Major Project has been described in some detail previously [3]. Fig. 2 shows a flow diagram of the Major Project, which indicates that the student and supervisor are in essentially a one-to-one relationship for the duration of the project. Some members of the academic staff were able to rely on a cohort of graduate students that were under their supervision to assist with 3rd Year project supervision, but this was by no means the case for all supervisors. The activity was designed to develop the following essential scientific skills: critical reading of scientific literature, written and oral communication, and the ability to develop analytical thinking. Students were introduced to some of

the research interests of the academic staff in the School of Physics, albeit in projects that were designed to be didactic, rather than directly related to the supervisor's research programme. As was pointed out in the Introduction, students reported that the activity stimulated their interest in physics, and it was rated as the most valuable part of PHYS3006 by a majority of students in formal course surveys.

The increase in student numbers, which was first seen in 2015, placed increased pressure on supervisors and their research groups. From having to supervise one project per year, they were now being asked to supervise two or three projects. The inevitable result was “supervisor fatigue”, and the activity was no longer a pleasurable experience for the research-active academic staff. It was clear that the Major Project could not continue in its present model, and alternative activities were considered.

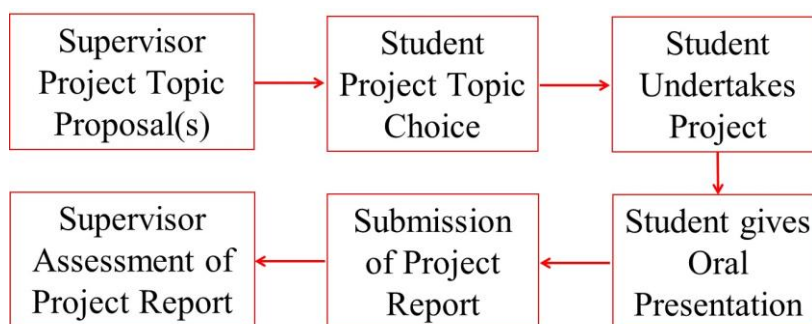


Figure 2. A flow diagram for the Major Project for the period 2011 – 2017. Further detail is provided in Section 2. As can be seen, this model is dependent on a one-to-one relationship between the supervisor and the student. With the approximately two-fold increase in student numbers first encountered in 2015, offering the Major Project in this form became increasingly onerous for supervisors. The Independent Research Essay was introduced in 2018.

3. The Independent Research Essay (IRE)

The coordinator of the module was reluctant to replace the Major Project with alternative activities. Firstly, it was clear that the essential skills that the project was able to inculcate could not be imparted by some of the suggestions that were made. A proposal for an Independent Research Essay (IRE) was prepared and presented to the School of Physics Teaching and Learning Committee, and this was accepted for implementation in 2018. The activity was designed to retain many of the desirable aspects of the previous model for the project, but to ensure that the aforementioned “supervisor fatigue” was minimized. While the IRE runs throughout the year, the contact time required from the supervisor, even if more than one essay is supervised, is designed to be less than, or equivalent to, supervision of an experimental, computational, or theoretical project. To this end, responsibilities were devolved from the supervisor to teaching assistants. For the purposes of the activity, the job description of the teaching assistants is Essay Tutor. Each tutor was allocated a small group of students (between five and ten) and asked to act as mentors. Details of the responsibilities of supervisors and essay tutors are provided below.

A flow diagram of the IRE is shown in Fig. 3. It is immediately obvious that continuous assessment is part of the model, as each student is required to submit a minimum of two and a maximum of three documents for assessment, in addition to the assessment of their oral presentation (known as the Oral Defence in this case). Readers that are familiar with the procedures for Higher Degrees will notice that the activity is designed to introduce the 3rd Year students to the scientific process of doing research. Each student is required to prepare a Research Proposal, which must contain a Literature Review and a Work Plan. More details of this phase of the IRE are provided below. It is recommended to the students that they submit both a First Draft and a Final Draft of the

IRE, so that they can respond to the comments made by the supervisor on the First Draft. Some students decide to only submit a First Draft, or only to submit a Final Draft.

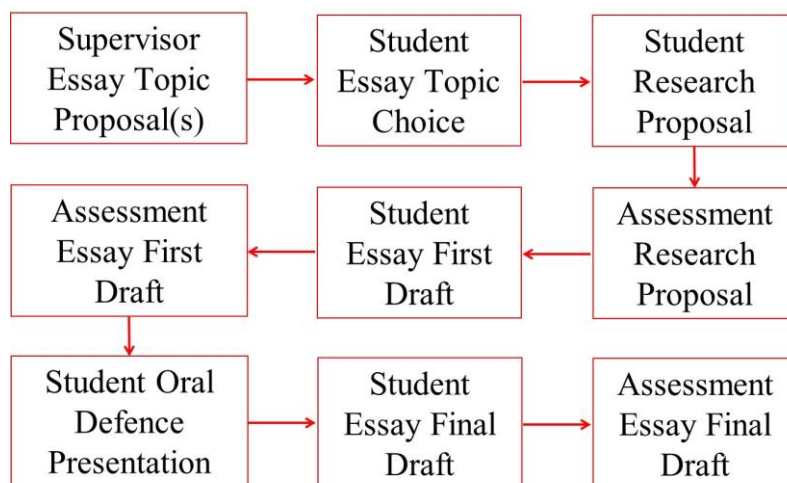


Figure 2. A flow diagram for the Major Project for the period 2018 – 2021. Further detail is provided in Section 3. In this model the time demands on supervisors are significantly reduced. Much of the day-to-day support is provided by the essay tutors. The essay tutors benefit by learning how to supervise a small group of students.

3.1. Supervisor Essay Topic Proposals

Every research-active member of the academic staff is required to submit at least one Essay Topic Proposal. It is suggested that the essay topic be sufficiently broad so that more than one distinct essay is possible (for example, the broad title of “Superconductivity” will allow the supervisor to offer several distinct essays). The proposal consists of supervisor details, a short synopsis of the essay as envisaged by the supervisor, and a short list of readily accessible introductory reading references. These proposals are posted on the Learning Management System web page for PHYS3006.

3.2. Student Essay Topic Choice

Students are divided into three groups. Each group receives a tailored list of prospective supervisors and their proposed essay topics. Students are required to make a shortlist of essay topics that interest them, and to make (and attend) appointments to meet with at least three potential supervisors before making their final choice of topic. The final choice is signed off by both the student and the supervisor.

3.3. Research Proposal: preparation and assessment

Supervisors are requested to provide additional references (if necessary) once they have accepted a student for supervision. The student is expected to use the reading suggested to seek additional references, and to prepare a Research Proposal of six pages which includes a Literature Review and a Work Plan. The final document must go through plagiarism detection software before it is submitted to an online submission portal. A rubric for assessment is provided to both the student body, and the supervisors. The Essay Tutors assist their group of students throughout this process, meeting once a week with their group. Their role is to mentor the students, to ensure that the students are making reasonable progress, to provide electronic copies of references, and to assist with referencing style and other presentation issues. Supervisors are only consulted by their student if scientific understanding issues arise, and the students are required to make an appointment if they need to consult their supervisor.

3.4. Student Oral Defence Presentation: preparation and assessment

Approximately three weeks before the date of the Oral Defence the students attend a session that provides them with tips and suggestions for the preparation and delivery of a successful Oral Defence. Each presentation is limited to 15 minutes, which includes 3 minutes for questions. Essay tutors ensure that their small group of students has at least one practice run before their presentation. The number of enrolled students has meant that the presentations are given in several parallel sessions, with the supervisors, the essay tutors, and the relevant small group of students in attendance. The essay tutors chair one half of each these sessions, and so gain session chair experience. Every person attending an oral presentation is required to assess the presentations according to a simple rubric. The policy at present is to take the average of the peer assessors, the average of the instructor assessors, and for the final mark to be the average of those two.

3.5. First and Final Draft: preparation and assessment

The student is expected to use their Research Proposal, and the comments made by their supervisor on the proposal, to do additional reading and research. The results of the reading, research, and writing will be the First (or Final) Draft of the essay. The final document, which should be between 20 and 30 typewritten pages, must go through plagiarism detection software before it is submitted to an online submission portal. A rubric for assessment is provided to both the student body, and the supervisors. The Essay Tutors assist their group of students throughout this process as before. The responsibilities of the essay tutors and supervisors are essentially the same as for the Research Proposal phase of the IRE. If a student decides to submit a First Draft, then they may use the feedback provided by their supervisor to improve the document and submit a Final Draft, or they may decide that they will accept the mark for the First Draft as their Final Draft mark.

4. Conclusion

A precipitous increase in student numbers has persuaded the School of Physics at WITS to review the model for the Physics III Major Project that has been in use for decades. The previous model required a large time commitment from research-active academic staff members during the duration of the project. In the past this was concentrated in one quarter of the academic year, but the increased numbers meant that this commitment was extending to two, and even three quarters in some cases.

A model involving an Independent Research Essay (IRE) was introduced in 2018. The IRE is intended to retain some of the best characteristics of the previous model, including an oral presentation and final written submission. In addition, the IRE allows for a continuous assessment of a student's written skills. The process goes through stages that mimic the development of a real research project (proposal, two drafts, oral presentation), and therefore provide skills that are useful to all early-career scientists.

The introduction of teaching assistants into the project, with the title of essay tutor, greatly reduces the time demands on the essay supervisor. This also allows the teaching assistant to gain invaluable experience of the process of successful supervision.

The previous Major Project model allowed students to encounter experimental apparatus, or a computational model, or a theoretical calculation. This experience cannot be offered using the IRE model, but the additional positive aspects of the IRE model are fair recompense for the lost experience.

References

- [1] Zwickl B M, Finkelstein N and Lewandowski H J 2012 *Am. J. Phys.* **81** 63-70
- [2] Zwickl B M, Finkelstein N and Lewandowski H J 2012 *AIP Conf. Proc.* **1413** 391-394
- [3] Kearthland J M 2014, *Proceedings of SAIP2012: the 57th Annual Conference of the South African Institute of Physics* 412-417 ISBN: 978 1-77592-070-0

Modular logic gate emulator for on-line laboratory

Marco Mariola

University of KwaZulu-Natal, University Road, Durban 4000, South Africa

E-mail: mariolam@ukzn.ac.za

Abstract. The pandemic year represented a challenging time for educators, a time where the classical way of teaching change from contact to remote learning. While contact lectures can be replaced by videos or video conferences, the laboratory can be replaced with simulations or by instructing the students to buy and build ad hoc systems by supplying the essential instructions. A remote assisted experiment requires to be conducted safely, the components readily available, and possibly low-cost. Technical High Schools and universities teach the logic gates and how to assemble a circuit to solve a specific function. Several licensed and free software are available for simulation, and for a hypothetical real experiment, it is necessary to supply the students with several components and tools. This project proposes performing several digital electronics experiments by using a building block, a logic gate emulator. This device can be modified according to the teacher's needs and sent to the students to do remote experiments.

1. Introduction

During the pandemic year, the teaching activities move from contact to online, and what was established in the past years suddenly change. As videos can replace the contact lessons, the laboratory activity ensures that students are familiar with the experimental tools. The simulation software does not guarantee that students face the real challenge present in a natural practical environment. The students can replicate the mechanic's experiments using fortune components, but more complex activities, such as electronics, can be challenging. In this manuscript, a low-cost method is proposed to experiment with digital electronics for high school and potentially for tertiary institutions. Minimal laboratory equipment for digital electronics requires one breadboard, one logic probe, several digital IC, switches and one power supply¹. Provides the students with the components cited above can result in costly and dangerous for less-skilled students. The proposed board only requires a smartphone power supply and a set of jumpers. The lecturer can program the board according to his needs and send the students two or more boards. A datasheet designed by the lecturer is provided for a specific board. The board can emulate up to 32 digital functions.

2. Board description

A minimal combinational digital electronic experiment requires integrated circuits, switches to emulate input and a logic probe. The board is represented in Figure 1 embed what is necessary for an electronic experiment. Through the picture is possible to identify the block of the board. The core of the board is the EEPROM AT28C64b [1], which contains the logic function to be emulated. A detailed description of the components of the board is give here below:

¹ The student can use the power supply improperly.

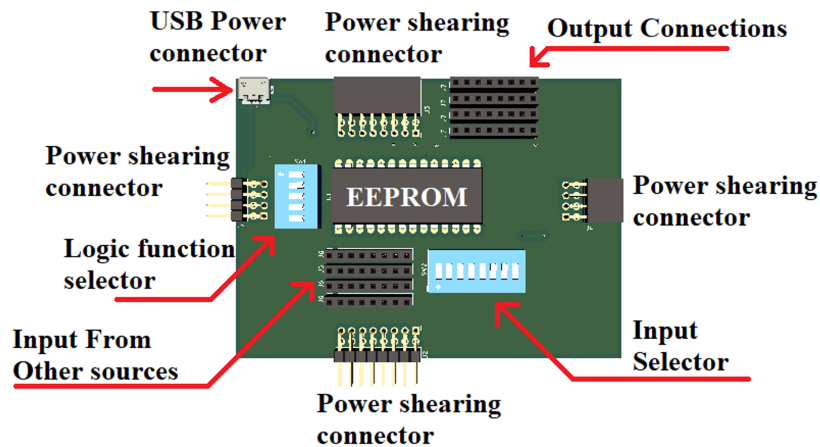


Figure 1. On the picture are represented the main accessible parts of the board. EEprom can be removed or placed into the board through a Dual In-line Package (DIP) socket. An integrated circuit buffer is placed on the back of the board to ensure an appropriate fan-out.

- **USB Power connector:** the power connector is a USB standard. This connector can be easily substitute with another.
- **Output Connections:** the female pin header is an 8 bit output port. The Most Significant Bit (MSB) is the first bit on the left. The other pin header in parallel serves to connect a single bit to other 3 node of the circuit. Input and Output connections can be done by the Jumper leads 40W, Male- Male.
- **Input selector port:** If the user needs to control the input manually through the switches, the pin-header must be disconnected. If the output of another logic device must control the input, the switches must be set at logic level zero by placing the switch in the off position which is normally indicated on the body of the component. The first bit starts from the left of the DIP switches, while in the input pin header, the Most Significant Bit starts from the right of the female pin header².
- **Logic Function Selector:** the switches named selector are used to define the programmed logic function to used. For our purposes only the switches can manually define the logic function, but the reader can modify the schematic by placing a pin header in parallel to the switch, to change the logic function by any digital external device.
- **Power shearing connector:** these pins only serve to connect another board and share the power. This kind of configuration permits to create a complex circuit by using only one power point. One of the possible configuration is represented in Figure 2.

3. Programmer

The system was thought to allow the lecturer to design a specific experiment for the students. In particular, the lecturer must be able to program the board with a series of logic functions. In this section, the programmer used will be discussed. The programmer scheme is depicted in Figure 3. For simplicity, the realisation of the programmer can be designed as an Arduino shield. In our case, an Arduino Uno was used since it can be directly applied to the socket [2]. In our case, an Arduino Uno was used since it can be directly applied to the socket. The Arduino Uno is based on the microcontroller Atmega328 and does not have many digital pins

² This was decided to simplify the PCB of the board.

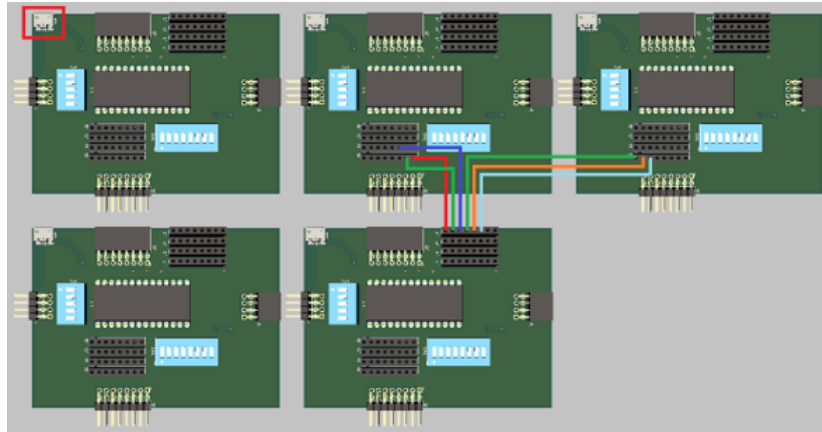


Figure 2. Possible connection between boards.

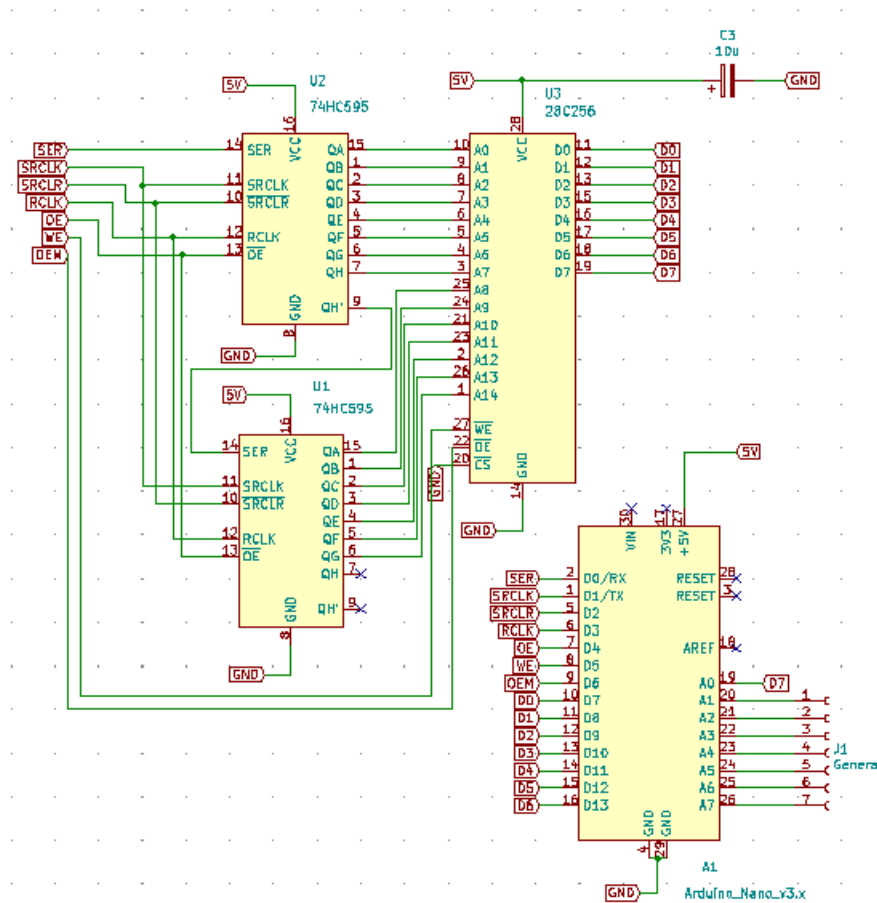


Figure 3. Scheme of the programmer.

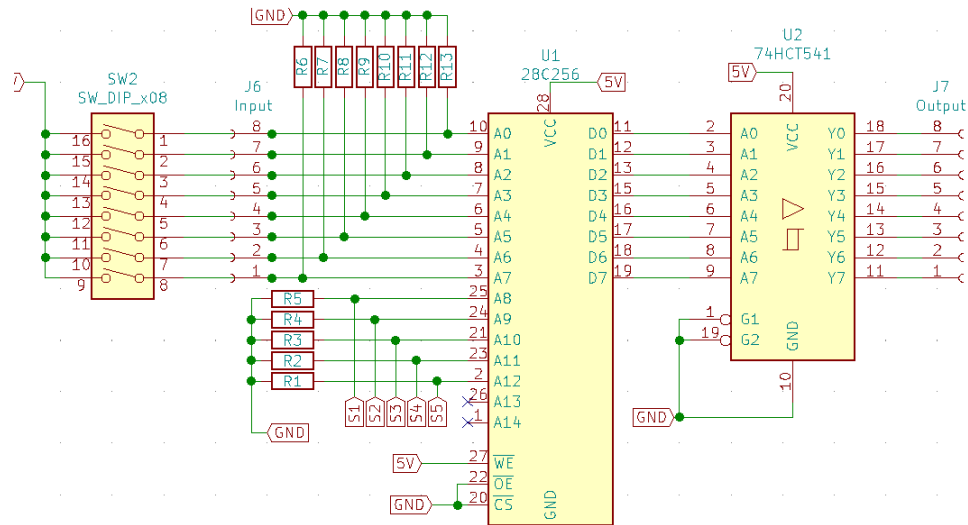


Figure 4. Universal board

to program the memory [3]. To program the memory is necessary to design a simple serial to parallel converter with the IC 74hc595[4]. The connector J1 is connected to the Digital to Analog Converter (DAC) of Arduino in case the user wants to save EEPROM an analog signal in the memory ³.

4. The board

The board's purpose is to prepare a specific experiment for digital electronics and send the programmed boards to the students. By a video conference the lecturer can teach the students how to assemble the circuit emulating an in-person laboratory experience. This philosophy follows what was done in a similar project to teach how robotic harm works[5]. The board is represented in Figure 4. The switch SW2 is connected to a pull down resistors and in parallel to the pin-header. The left side of the DIP switch SW2 is connected to 5 V. This particular configuration is used to set the input by the switch or by mean of an external signal. The Fan out of the memory may not be sufficient to drive the input of other universal boards, and the buffer 74HCT541 is used [6]. To monitor the output it is possible connect a string of LED, connected to the output pin-header.

5. Testing and limitation

In this section we expose the limit of the board by using a latch S-R as example. This circuit consists of two NAND ports closed in a loop as represented in Figure 5. These two ports are programmed in one board. The output *O1* is physically connected to the input *I3*, while the output *O2* is connected to the input *I2*. The latch S-R in this test is used as debouching circuit, and the change from 5V to 0V of the output should follows a step function without intermediate oscillations. By changing the input state of *I1* and *I4*, the output *O1* begins to oscillate and the circuit clearly does not work. For a functional debouching circuit it is necessary to use no less than two boards, in other words for each NAND gate a separate board must be used. The instability is reported in Figure 5. If for the same circuit two boards are used, the debouching circuit perfectly work with no output oscillations, as represented in Figure 6.

³ This can be useful if the lecturer wants to do an experiment with a primitive Direct Digital Synthesis (DDS) function generator.

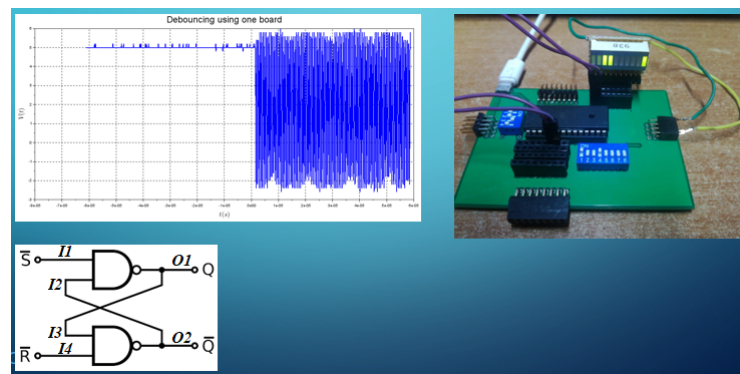


Figure 5. debounce circuit with only one board. On the bottom left of the Figure is represented the latch S-R. On the top left of the Figure is presented the output of the circuit.

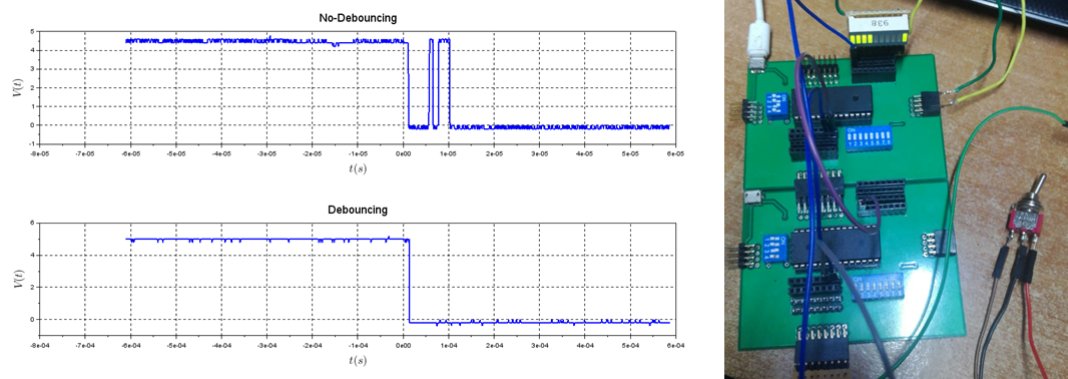


Figure 6. Debounce circuit using two different boards. The plot on the top represents the typical ON-OFF switch response, while the plot on the bottom represent the response of the Latch S-R.

5.1. Some example of logic function

The power of the board is given by the possibility to emulate any combinational logic function, previously programmed by the lecturer or the students. The prototype shown in this manuscript can emulate a 7-segment display driver, full-adder and all the basic logic functions, for example: the gate NOT, AND, XOR and OR. Many other functions can be implemented but, as was stated previously, the loops in the same board must be avoided.

6. Conclusion

This board aims to be an alternative system for laboratory activity in the field of digital electronics. Each board can emulate up to 32 digital logic functions programmed ad-hoc from the lecturer. Two or more boards can be given to the students and experiments can be monitored on-line by the lecturer or teacher. The structure of the board permits 8 inputs and 8 output, which permits to emulate more than one logic gate in a single board, but no closed-loops are allowed on a single board as shown in section 5. Approximately the cost for one board is 110 ZAR and is easy to repair. Using this system the students will learn how to read a data sheet, how a memory works, and how several parts of the circuit should be connected.

Acknowledgements

This work is based on research supported by the South African Research Chair Initiative of the Department of Science and Technology and National Research Foundation and the Technology Innovation Agency, South Africa.

References

- [1] Atmel 2009 *AT28C64B, 64K (8K x 8) Parallel EEPROM with Page Write and Software Data Protection* (San Jose, CA 95131, USA: Microchip) URL <https://ww1.microchip.com/downloads/en/DeviceDoc/doc0270.pdf>
- [2] Banzi M and Shilon M 2014 *Make: Getting Started with Arduino, 3rd Edition* 3rd ed (Sebastopol, California: Maker Media, Inc)
- [3] Williams E 2014 *Make: AVR Programming* 1st ed (Sebastopol, CA 95472. United states of America: Maker Media, Inc.)
- [4] Instrumen T 2015 *SNx4HC595 8-Bit Shift Registers With 3-State Output Registers* URL <https://www.arduino.cc/en/Tutorial/Foundations/ShiftOut>
- [5] Benitez V H, Symonds R and Elguezabal D E 2020 *HardwareX* **8** e00158 ISSN 2468-0672 URL <https://www.sciencedirect.com/science/article/pii/S2468067220300675>
- [6] Nexperia *74hc541, Octal buffer/line driver; 3-state* URL https://assets.nexperia.com/documents/data-sheet/74HC_HCT541.pdf

The South African Institute of Physics (SAIP) Benchmark Statement and physics graduate preparedness: A case study of the University of the Western Cape

Bako Nyikun Audu and Delia Marshall

Department of Physics and Astronomy, University of the Western Cape, South Africa

Email: 3699756@myuwc.ac.za

Abstract. Worldwide, there is a growing focus on physics graduate preparedness, with physics bodies such as the IOP (UK), the APS (USA) and the AIP (Australia) listing the skills and attributes that graduates should develop during their undergraduate education. In South Africa, similarly, the SAIP Benchmark Statement was developed in 2015 to address concerns about the quality and skills of physics graduates. The Benchmark Statement identified important skills for physics graduates in South Africa but left it up to individual institutions to implement. This study examines the extent to which espoused physics graduate attributes (as specified in the SAIP and other institutional documents) are embedded in the University of the Western Cape (UWC) undergraduate physics module descriptors. The study found that key graduate attributes are scantily embedded, with many skills gaps revealed. Implications for curriculum review and the mapping of graduate attributes across the curriculum are discussed.

1. Introduction

Internationally there is renewed debate on the purposes of higher education in contemporary times. One important function of higher education is to develop the skills needed for economic growth (this is referred to as human capital theory); another is the aim of developing citizenship, and the capacity to lead a meaningful life [1, 2, 3]. In a developing country context like South Africa, it is argued that university graduates also need to be equipped to address inequalities and social justice in society [4].

Universities are increasingly concerned with the quality of graduates they produce and how these graduates are equipped with the skills and attributes that would enable them to be active at work and be good citizens in the society at large [5, 6]. Many universities address this through drafting charters of generic attributes which outline the attributes and skills (which transcend disciplinary knowledge) that the institutions expect their students to have acquired upon the completion of their studies. A comprehensive and well-used definition of graduate attributes is as follows:

‘the qualities, skills and understandings a university community agrees its students should develop during their time with the institution. ... These attributes include but go beyond the disciplinary expertise or technical knowledge that has traditionally formed the core of most university courses. They are qualities that also prepare graduates as agents of social good in an unknown future.’ [7]

Graduate attributes are broad and generic, and are often developed at a university-wide level, but then need to be adapted for specific disciplines.

2. Graduate attributes in the context of physics

In Physics worldwide, there has been a greater emphasis on the skills that physics graduates are able to demonstrate. International physics organisations, such as the Institute of Physics (IOP) in the UK, the American Physical Society (APS) in the USA, the European Physical Society (EPS) and the Australian Institute of Physics (AIP), have listed the skills and attributes that physics graduates should develop during their undergraduate education [8, 9, 10]. These include problem solving, investigative skills, analytical skills, communication skills, ICT (information and communication technology) skills, ethical behaviour and personal skills, technology aptitude, etc (see table 1).

There is a recognition that physics graduates require a range of physics-specific knowledge and skills, as well as broader skills. For example, the report *Preparing Physics Students for 21st-Century Careers* [11] argues that preparation of physics students currently needs to go beyond the ‘standard model’ of getting them ready for graduate school. The report recommends ways to improve physics programmes to prepare students for the diverse careers they will embark on. Such preparation would include working well in teams, understanding how science and technology are used in real-world settings, writing and speaking well, and understanding the workplace context.

In South Africa, the South African Institute of Physics and Council for Higher Education (SAIP-CHE) report [12] raised concerns about the quality and skills of physics graduates, and this in turn yielded the Benchmark Statement of Physics for South Africa, which was published in 2015 [13]. The SAIP Benchmark Statement sets out the core content aspects of an undergraduate physics Bachelor of Science (BSc) degree, and acknowledges that ‘Physics is a universal discipline: content is largely a ‘given’ and all universities are more or less aligned with the ‘international’ curriculum’. However, it then goes on to argue that ‘in addition to acquiring insights into the working of the physical world’ physics students should also develop ‘a wide range of competence in generic and subject-specific skills’ [13]. These skills are listed as follows:

1. **Physics skills**
2. **Generic skills**
 - Problem-solving
 - Analytical skills
 - Investigative skills
 - Communication skills
 - ICT
 - Personal skills (work independently and in groups)
3. **Ethical behaviour**

Although the SAIP Benchmark Statement sets out this list of suggested skills to be developed in the BSc Physics degree, the document notes that ‘...it is up to each institution to formulate the precise and measurable indicators that apply to its situation in the context of various national policies, including the Higher Education Qualifications Framework (HEQF), Level Indicators, and the generic Qualification Standard for the Bachelor of Science degree, as well as the respective university rules’ [15].

3. A framework for Physics Graduate Attributes (PGAs)

In developing a framework of desired physics graduate attributes, I examined documents from international physics bodies that specified the sorts of capabilities, skills and attributes to be developed in physics graduates (for example, from IOP (UK), AIP (Australia), APS (USA)). I also drew on the South African Quality Agency (SAQA) Critical cross-field outcomes for South African higher education

[14], and the UWC Charter of Graduate Attributes. Absent in the SAIP Benchmark Statement were some attributes in the SAQA and UWC documents (eg. teamwork, technology aptitude, social/civic awareness and environmental awareness). These were therefore combined with the skills specified in the SAIP Benchmark Statement, to form a broader framework for Physics Graduate Attributes (PGAs) – see Table 1 below.

Table 1. A framework for Physics Graduate Attributes
(collated from physics organisations internationally,
SAQA and the UWC Charter of Graduate Attributes)

Physics Graduate Attribute	
Category	Specific Skill
Transferable skills	Problem Solving skills
	Investigative skills
	Analytical skills
	Technology aptitude
	ICT skills
	Practical skills
	Ethical behaviour
	Personal skills
	Teamwork
	Communication skills
Citizen skills (Graduate Attributes)	Social/Civic awareness
	Environment awareness

4. Graduate attributes in the undergraduate curriculum – espoused or enacted

Graduate attributes can be said to be *espoused* (for example, in institutional documents, such as a Charter of Graduate Attributes or the SAIP Benchmark Statement) or *enacted* (through being embodied in teaching and learning activities and assessment). In other words, sometimes graduate attributes might be espoused in institutional mission statements or even module descriptors, without actually being enacted in the curriculum. Alignment between attributes espoused and attributes enacted in the curriculum is difficult to ensure [15]. As a starting point, this study looked at the *espoused graduate attributes* (through analysis of physics module descriptors from first year to Honours level). Espoused graduate attributes were examined first, because if graduate attributes are not espoused, then they are unlikely to be enacted; or the enactment in the teaching and assessment will likely be dependent on individual lecturers, rather than being formally specified [15].

5. Research design and methodology

The research question that framed this study was “How are espoused physics graduate attributes (as specified by SAIP and UWC graduate documents) embedded in the UWC undergraduate physics curriculum?”. Document analysis was undertaken of the UWC Physics programme module descriptors (using the Physics Graduate Attributes framework as analytical tool).

6. Findings

Table 2 displays the extent to which physics graduate attributes are explicitly embedded in the module descriptors (which act as a guide or compass for both lecturers and other team players in framing an undergraduate physics programme). The academic year is scheduled in 2 semesters across all levels for all taught courses. A total of 18 physics modules were examined (Extended Curriculum Programme PHY 151 and PHY 152 captured as one module) and the First Year (PHY 111 and PHY 121 captured as one module). Others constitute the modules of the undergraduate programme and honours programmes respectively.

Table 2: Mapping of Physics graduate attributes as identified in undergraduate module descriptors

Category	Specific Skill	Undergraduate										Hons										Total (indicator)
Physics Graduate Attributes	Modules: PHY	151/152	111/121	212	222	217	227	312	322	317	327	709	720	721	722	723	724	725	726			
Generic skills	Problem Solving skills	√	√*	√	√			√*	√*				√	√		√						9
	Investigative skills								√*													1
	Analytical skills	√*		√*				√*	√*						√*		√*	√*	√*			8
	Communication skills	√		√	√	√*	√	√		√*	√*	√	√*	√*	√*		√*		√*			14
	ICT skills	√	√	√	√			√*	√		√	√	√				√		√			11
	Practical skills	√	√	√	√		√	√		√			√			√	√		√			11
	Ethical behaviour	√														√						2
	Personal skills																					0
	Teamwork																					0
	Technology aptitude	√										√	√						√			4
Citizen skills	Social/Civic awareness	√																				1
	Environment awareness	√					√															2
Summary	Total	9	3	5	4	1	2	5	4	2	3	2	5	2	2	3	4	1	5			

Where: √ represents a stated attribute/skill in the module descriptor

√* represents an inferred attribute/skill in the module descriptor.

The furthest right-hand column indicates the number of times a physics graduate attribute (PGA) is stated in module descriptors over the undergraduate modules from year 1 to year 3. Out of the 12 PGAs, only ICT skills (10 indicators) and Practical skills (11 indicators) were stated frequently in the module descriptors and followed by Problem solving skills (6) and Communication skills (6). Table 3 summarises the PGAs in Table 2 for the BSc and BSc (Hons) levels. Broadly, the following trend was evident:

Most embedded: ICT skills, Practical skills

Somewhat embedded: Problem solving, Communication skills

Scantily embedded: Ethical behaviour, Technology aptitude, Social awareness, Environmental awareness

Absent/not embedded: Analytical Skills, Investigative skills, Team work, Personal skills

The bottom row of Table 2 indicates the *range* of PGAs evident in the module descriptor of each module. There is only one module, PHY151/152 that had a significant range of PGAs stated in the module descriptor (eight physics graduate attributes), followed by three other modules with 4 stated PGAs. In summary, of a total of 18 modules, all but one could be said to have a scanty range of PGAs listed in the module descriptors.

In summary, this curriculum mapping gives a reflection of how the espoused physics graduate attributes (as specified by SAIP and UWC graduate documents) are embedded in the module descriptors of this case-study Department. The analysis shows that there are gaps in the physics graduate attributes and skills embedded, with skills such as investigative skills, analytical skills, teamwork, social and environmental awareness not explicitly embedded much in the module descriptors. Despite the SAIP Benchmark Statement being published in 2015, the case study Department had not adapted the module descriptors based on this.

It is important to note that this does not imply that a pedagogical focus on these attributes and skills is absent from these modules; rather, it shows that these are not *explicitly* embedded in the module descriptors and learning outcomes of a module. In this case, their presence or absence could be lecturer-dependent and vary from year to year.

7. Discussion

The SAIP Benchmark Statement arose out of concerns about the quality and skills of physics graduates, and how to best prepare students for changing world of work and society. To address these concerns, the SAIP Benchmark Statement identified important skills for physics graduates in South Africa but left it up to individual institutions to implement. This case study suggests that leaving ‘it up to each institution to formulate the precise measurable indicators that apply to its situation’ [13] could have led to universities not engaging adequately with the Benchmark Statement. Would it have been beneficial to specify some basic implementation standards and processes?

A threshold for the embedding of the physics graduate attributes in the physics curriculum or module descriptors might offer a baseline to which various departments of physics could aim. For example, a minimum threshold might suggest that a specific skill (eg. communication) be embedded in several modules as various stages of an undergraduate programme (because skills take time to develop, across years of study, and cannot be ‘fixed’ in a single module). It might also be useful to look to other professional bodies for implementation guidance (for example, the Engineering Council of South Africa). Such professional bodies require the mapping of graduate attributes across modules in a programme as part of their accreditation processes.

For the case-study Department, the findings from this study suggest that a ‘graduate attribute mapping’ [16] or ‘backward design’ process [17] might be useful. This would entail starting with the skills and attributes required in a physics graduate (as specified in the SAIP Benchmark statement and UWC framework) and then mapping these backwards from the Honours level modules, into 3rd year, 2nd year and 1st year modules. A further step for implementation and for research would be to examine how *espoused* graduate attributes are actually *enacted* in the curriculum through teaching activities and assessment.

8. Conclusion

The SAIP Benchmark Statement identified important skills for physics graduates to develop. This case-study examined the extent to which espoused physics graduate attributes (as specified in the SAIP and other institutional documents) are embedded in the UWC undergraduate physics module descriptors. The study found that only practical skills, ICT skills, problem solving skills and communication skills

were well-embedded, with skills such as investigative skills, analytical skills, teamwork, social and environmental awareness largely absent. This case-study suggests that the SAIP's stance of leaving the implementation of the Benchmark Statement up to individual institutions could have led to universities not engaging adequately with it. Instead, it is suggested that implementation guidelines be developed (as with other professional bodies) and that measurable indicators or thresholds of skills embeddedness be formulated for undergraduate physics programmes.

References

- [1] Boni A and Walker M 2016 *Universities and Global Human Development: Theoretical and Empirical Insights for Social Change (Journal of Human Development and Capabilities.* (Abingdon: Routledge Press)
- [2] Marginson S 2011 *Higher Education and Public Good (Higher Education Quarterly 65)*
- [3] Griesel H and Parker B 2009 *Graduate Attributes: A baseline Study on South African Graduates from the Perspectives of Employers* (Pretoria: Higher Education South Africa & SAQA)
- [4] Walker M and Fongwa S 2017 *Universities, Employability and Human Development* (London: Palgrave Macmillan)
- [5] Clegg S, Stevenson J and Willott J 2010 *Staff Conceptions of Curricular and Extracurricular Activities in Higher Education (Higher Education, vol 59 5)*
- [6] Bitzer E and Withering M 2020 *Graduate attributes: How some university students experience and learn them (South African Journal of Higher Education, vol 34 3)*
- [7] Bowden J, Hart G, King B, Trigwell K and Watts O 2000 *Generic capabilities of ATN University Graduates.* (Canberra: Australian Government Department of Education, Training and Youth Affairs)
- [8] AIP and AAS 2012 *Underpinning Australia's Future Excellence in Physics Part 2* (Sydney: AIP & AAS)
- [9] APS and AAPT 2013 *Graduate Education in Physics: The Path Ahead* (Maryland: AAPT & APS)
- [10] IOP 2014 *The Physics Degree: Graduate Skills Base and the Core of Physics.* 1st edn. (London: IOP)
- [11] McNeil, L. and Heron, P. 2017 'Preparing physics students for 21st-century careers', (*Physics Today* vol 70 11), (Maryland; AAPT & APS)
- [12] CHE and SAIP 2013: *Review of Undergraduate Physics Education in Public Higher Education Institutions.* (Pretoria: CHE)
- [13] SAIP 2015 *Benchmark Statement for Physics in South Africa* (Pretoria: SAIP)
- [14] SAQA 2011 *Critical Cross-field outcomes (CCFOs).* (Pretoria: eDegree)
- [15] Bath D, Smith C, Stein S and Swann R. 2004 *Beyond Mapping and Embedding Graduate Attributes: Bringing together Quality Assurance and Action Learning to Create a Validated and Living Curriculum (Higher Education Research and Development vol 23 3)*
- [16] Lowe K and Marshall L 2004 *Proc. the 21st ASCILITE Conf.* In R. Atkinson, C. McBeath, D. Jonas-Dwyer & R. Phillips (Eds), *Beyond the comfort zone* (Australia: ASCILITE)
- [17] Wiggins G and McTighe 2005 *Backward Design.* In *Understanding by Design* (expanded 2nd ed.). (Alexandria :Association for Supervision and Curriculum Development)

DIVISION F – APPLIED PHYSICS

The development of a real-time Monitoring system for the ATLAS Tile Calorimeter Phase-II Upgrades

M G D Gololo¹, F C Argos¹ and B Mellado^{1,2}

¹ School of Physics and Institute for Collider Particle Physics, University of the Witwatersrand, Johannesburg, Wits 2050, South Africa

² iThemba LABS, National Research Foundation, PO Box 722, Somerset West 7129, South Africa

E-mail: `mpho.gift.doctor.gololo@cern.ch`

Abstract. A major upgrade to the High Luminosity Large Hadron Collider (LHC) will increase the instantaneous luminosity by a factor 5 compared to the LHC. A complete redesign of the electronic system is required for new radiation levels, data bandwidth as well as the clock distribution. This new design is called the A Toroidal LHC ApparatuS (ATLAS) Tile Calorimeter (TileCal) Phase-II upgrade system. This is an integration of the front-end and back-end electronics to meet technical requirements of the design. Numerous sensors will be used to monitor the status of the ATLAS TileCal Phase-II upgrade system. This paper presents a real-time monitoring system that will be used to read data from the sensors of the TileCal electronic system that will be used by the Detector Control System (DCS). The real-time monitoring system includes an implementation of a server on the System-on-Chip (SoC) Zynq Field Programmable Gate Array known as Tile Computer-on-Module (TileCoM). This server will read data and publish it to the clients of the DCS. A test bench that includes an Avnet Ultra96-V2 ZYNQ UltraScale+ MPSoC evaluation board and Tile Gigabit Ethernet switch that serves as a basis for the TileCoM mezzanine board as part of the Tile PreProcessor (TilePPr).

1. Introduction

For the discovery of the Higgs boson, the Large Hadron Collider (LHC) [1] collide protons at a centre of mass energy of 14 TeV with a luminosity of $1 \times 10^{-34} \text{ cm}^{-2} \text{ s}^{-1}$. The LHC is upgraded to the High-Luminosity Large Hadron Collider (HL-LHC) [2] to reach an instantaneous luminosity of $7.5 \times 10^{-34} \text{ cm}^{-2} \text{ s}^{-1}$. The HL-LHC will produce about 200 proton to proton collisions per bunch crossing at an integrated luminosity ($3000\text{--}4000 \text{ fb}^{-1}$). ATLAS is one of the four experiments for the HL-LHC. The basic principle of this experiment involves the collision between two proton beams at the center of the ATLAS detector generating particles in all directions. To detect the ionising radiation, the Pixel detector and the semiconductor tracker (SCT) utilizes silicon and microstrips. The trajectories of the charged particles are bent by the magnetic field produced from Inner Detector. Figure 1 shows the ATLAS detector which is a general-purpose particle detector for the LHC [3]. The Tile Calorimeter (TileCal) [4] is a sampling calorimeter with steel as an absorber and scintillator tiles as active medium. The TileCal detector is divided into a long inner barrel and two extended barrels on both sides of the

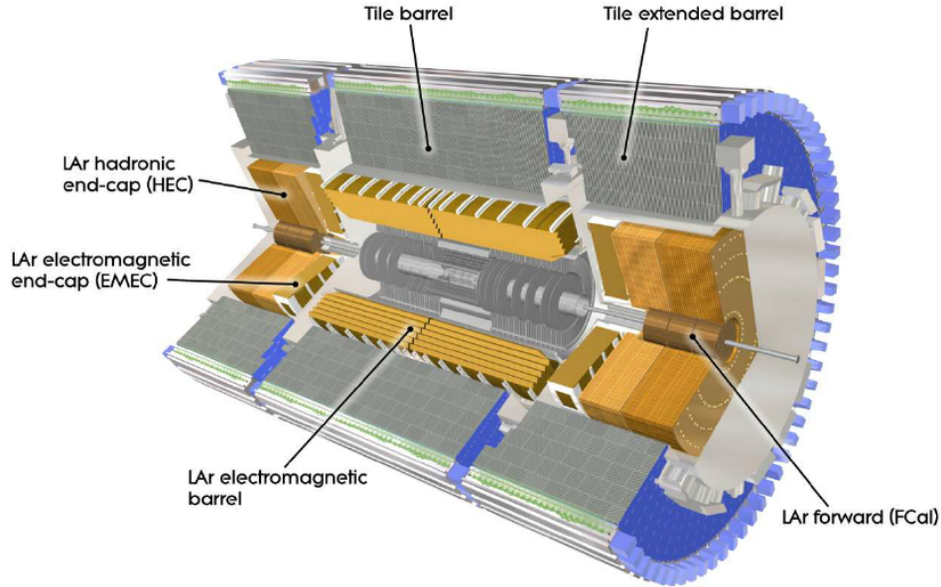


Figure 1. *The ATLAS detector* [3].

detector. Due to the new requirements of the HL-LHC, the ATLAS TileCal Phase II upgrades redesign the ATLAS TileCal readout electronic chain. The TileCal detector modules consists of the wavelength-shifting (WLS), scintillators and the photomultiplier tubes (PMT). The On-detector electronics takes snapshots of the ultraviolet scintillation light in nano seconds (ns) using Photo-Multipliers (PMT). These PMT signals are digitized by Front-End (FE) electronics, serialized and sent to the Back-End (BE) electronics. This is a project in instrumentation for particle physics.

2. The Atlas Tile Calorimeter Phase II Upgrade

Figure 2 shows the proposed redesign of the electronic system [5] to read-out data from the detector. The system is divided into FE electronics that are on the detector and BE electronics. The analog signals from the FENICS board are then converted into digital signals by the ADCs on the Main board. The Daughter Board transmits digital data from the FE to the BE through GBT protocol. These data is transmitted at the HL-LHC frequency of 40 Mhz. The BE electronics consists of the TileCal Pre-Processor (TilePPr) [6] that receives digital data and process it in a pipeline memories of the FPGA. The Trigger Data Acquisition Interface (TDAQi) [7][8] communicates with the TilePPr. All the TilePPr electronics are housed inside the Advanced Telecommunication Computing Architecture (ATCA) [9] that can be remotely configured and controlled through the Gigabit Ethernet. The TileCoM is one of the TilePPr modules and it is used for three main functionalities. Section 3 presents one of the main functionalities of TileCoM.

3. The TilePPr-DCS communication system

All the boards that are installed on the ATLAS TileCal Phase II upgrade electronics readout chain have sensor components. These sensor components measures temperature, voltage, current, humidity, etc. A software functionality is implemented to integrate with these sensors to be able to remotely control and monitor the electronic readout chain.

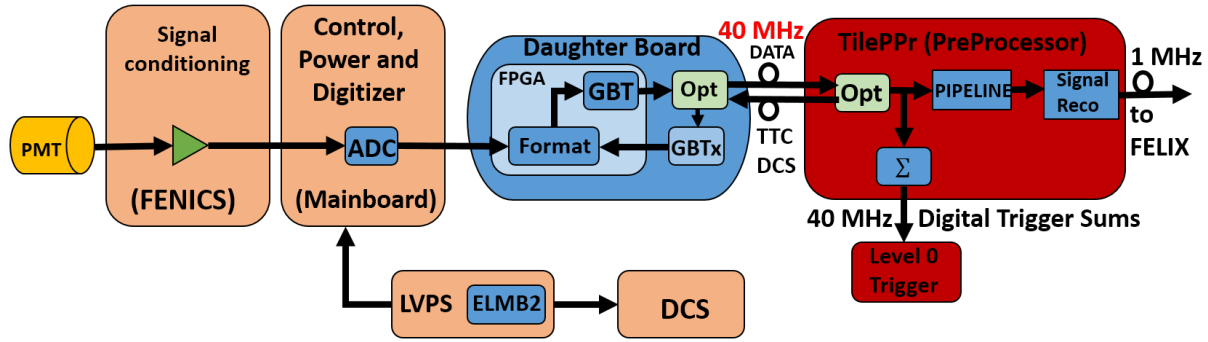


Figure 2. The ATLAS Tile Calorimeter Phase II Upgrade electronic readout system [5].

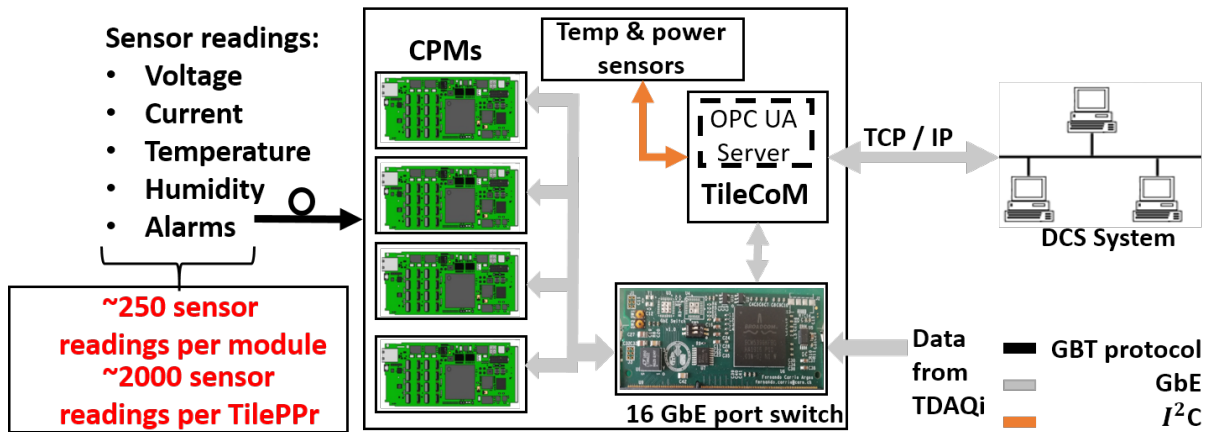


Figure 3. The ATLAS Tile Calorimeter TilePPr-DCS communication system.

This functionality is implemented to ensure healthy operation of the electronics at all times. This functionality is implemented in the TileCoM on the BE electronics. Gigabit Ethernet (GbE) and Inter-Integrated Circuit (I²C) are used as communication protocols between the TileCoM and the BE electronics. Figure 3 shows the general block diagrams of the TilePPr and the DCS [10] interface functionality. This block diagram shows the connection of all the components of the FE and BE electronics. The TilePPr and the DCS interface functionality will read data from approximately 2000 sensors from the FE electronics into the BE electronics. This data from the FE electronics is transferred through the Gigabit Transceiver (GBT) protocol to the BE electronics. In order to implement this functionality and to remotely monitor this data, two server applications are implemented on the TileCoM to readout data sensor data and publishes this data to the DCS client.

These two server applications are implemented using the open source and stable framework called the Quick OPC UA server generation framework (Quasar) framework [11]. This framework is used to efficiently implement OPC UA servers in a short period of time with precise data reading from the sensors. This is achieved by allowing the developer to create design files using XML documents with minimal C++ development. The XML files are also used for configuration purposes in order to publish to the client and to also act as a lightweight data-interchange format between the hardware and the software applications. The first server (OpcUATileXADC) readout XADC sensor data from the TilePPr modules. This server access the low-level ADC device tree, IIO library and the Linux virtual file system to be able to interface with the

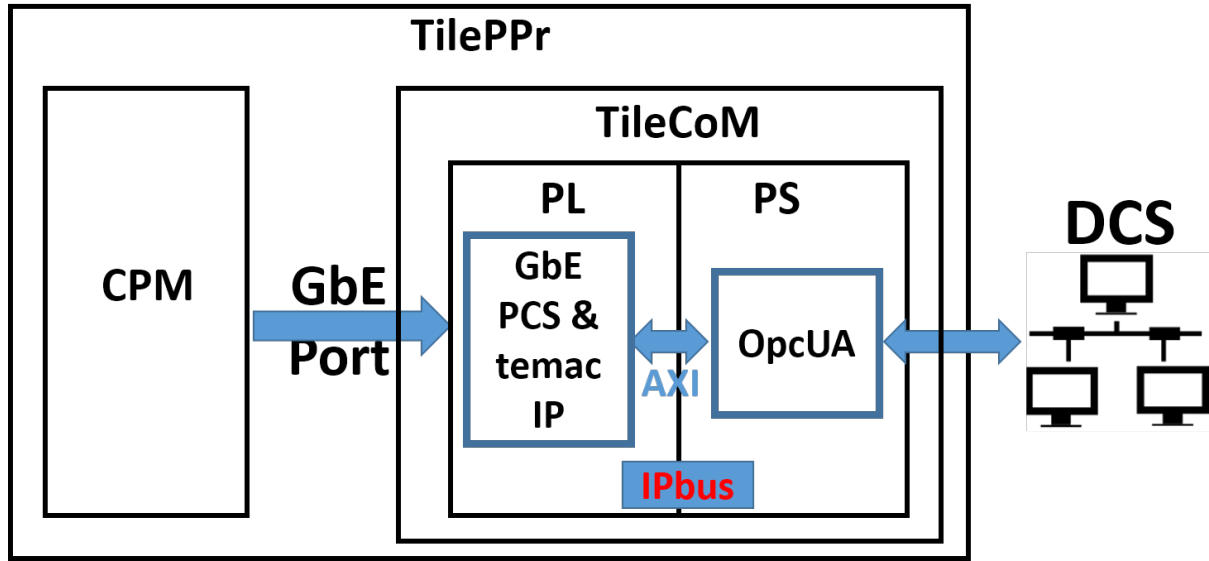


Figure 4. The second OpcUA server block diagram for the TilePPr-DCS system.

hardware. When the server is executed on the TileCoM, it reads sensor data and publishes this data to the Supervisory Control and Data Acquisition (SCADA). Figure 4 shows a block diagram of the second server (OpcUATile) block diagram for the TilePPr-DCS system. An IPbus implementation is integrated with the quasar framework to read sensor data. This IPbus is implemented using the Ironman [12] open source framework. The IPbus enables flexible integration and reading of data between the CPM and the TileCoM. This functionality will also be used to read sensor data from the ATCA carrier. For this sensor data acquisition, the server will use the I²C protocol to interface with the ATCA carrier sensors.

4. The implementation of OpcUA servers for TilePPr-DCS communication system

4.1. Test-bench to readout sensor data from the readout electronic chain

The main objective of this software development and the TileCoM functionality is to remotely control and to monitor the readout electronic chain. Figure 5 shows an integration of the first prototype for the TilePPr-DCS communication system. This test-bench resembles the readout architecture as shown in Figure 3. The CPM emulator board is used to resemble the CPM for the ATLAS TileCal Phase II upgrade readout electronic chain. The computer is used to serially connect the embedded Linux running on the TileCoM. The power supply is used to power the CPM and the TileCal GbE Ethernet Switch motherboard. The Network router enables remote connection to the whole test-bench together with the TileCal GbE Ethernet Switch. The Avnet Ultra96-V2 ZYNQ UltraScale+ MPSoC TileCoM evaluation board is used to run the OpcUaXADC server. The CPM Emulator board is a Xilinx Virtex-7 FPGA VC707 Evaluation Kit that is used for test purposes. This evaluation board implements a similar VHDL firmware code that is used to readout sensor data from the FE electronics. The TileCal GbE Ethernet Switch motherboard has 24 ports to allow as many boards to be connected to the network as possible. These boards are powered with 12V power supply which is the same voltage that will be used for the final design of the BE electronics components.

4.2. Progress results for the OpcUA servers

This contribution is a work in progress of the implementation of OpcUA servers. For this contribution and test purposes, presentation results for the first server are discussed. Only

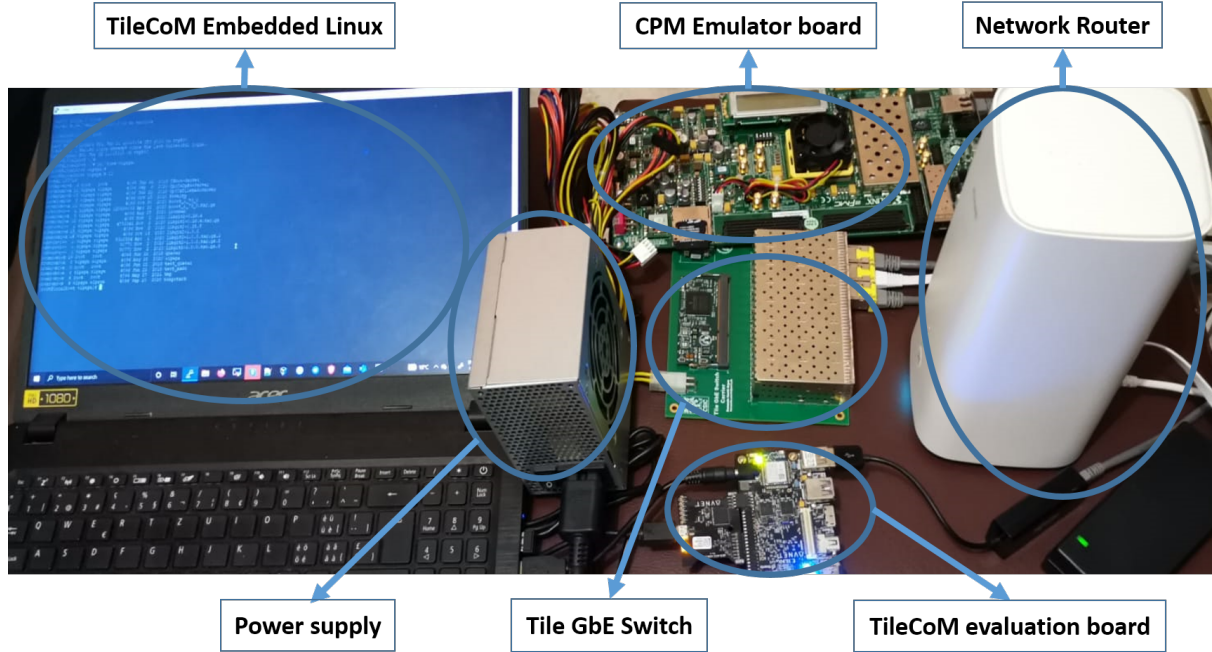


Figure 5. *Server and client communication test-bench.*

voltages and temperatures sensor readings are acquired from the OpcUATileXADC server running on the TileCoM. This server is running on the CentOS embedded Linux shown on the left side of figure 5. An executable is used to run the server on the embedded Linux terminal. Only the XADC values were acquired from the OpcUATileXADC. Figure 6 shows the results for the OpcUATileXADC server. The figure shows the results for the vcc ps batt, Vcc aux, vcc ps ddr, vcc int and vcc bram sensors. The voltage values obtained for each sensor are 2.89 for vcc ps batt, 2.88 for Vcc aux, 1.76 for vcc ps ddr, 1.35 for vcc int and 1.35 for vcc bram sensors. However, according to the datasheet of the TileCoM evaluation board used for the test, the results obtained are not exact values. The exact values according to the datasheet [13] are 2.80 for vcc ps batt, 2.80 for Vcc aux, 1.80 for vcc ps ddr, 1.40 for vcc int and 1.40 for vcc bram sensors. Thus, the error analysis between the measured results and the expected results is 0.09 for vcc ps batt, 0.08 for Vcc aux, 0.04 for vcc ps ddr, 0.05 for vcc int and 0.05 for vcc bram sensors.

5. Conclusion

This contribution is based on real-time control and monitoring for the ATLAS Calorimeter Phase-II upgrade electronic system. This is a project in instrumentation for particle physics. It is part of the electronic system for the ATLAS Calorimeter Phase-II upgrade. Two servers are implemented on the TileCoM to connect to read out on- and off-detector electronics. The acquired sensor data is published to the UA expert or SCADA for DCS to monitor the system. This software application is vital for the electronics readout chain to be able to remotely control and monitor all the sensors on the system. As this is the first stage of integration test for the TilePPr-DCS communication system, this functionality is tested using commercial boards for the TileCoM and the CPM to readout XADC sensor data. Results for the first server (OpcUATileXADC) are discussed and the second server (OpcUATile) is a work-in progress.

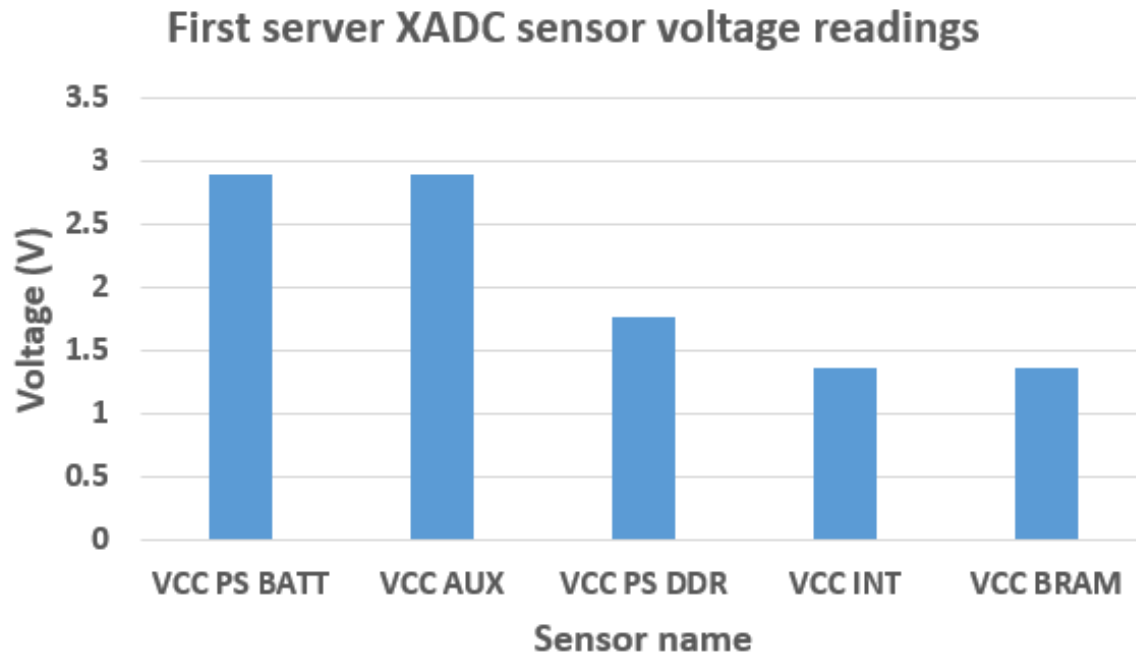


Figure 6. The ATLAS TileCal OpcUA server XADC results.

References

- [1] Aad G *et al.* (ATLAS) 2008 *JINST* **3** S08003
- [2] Barton A (ATLAS) 2021 *PoS BEAUTY2020* 061
- [3] Izzo V (ATLAS) 2021 *PoS LHCP2020* 094
- [4] Clement C (ATLAS) 2021 *Phys. At. Nucl.* **84** 368–372
- [5] Santurio E V 2020 Performance of the ATLAS Hadronic Tile Calorimeter Demonstrator system for the Phase-II upgrade facing the High-Luminosity LHC era *22nd IEEE Real Time Conference (Preprint 2010.14980)*
- [6] Carrió F and Valero A (ATLAS Tile Calorimeter) 2020 *Nucl. Instrum. Meth. A* **958** 162487
- [7] Yue X 2019 Tile TDAQ interface module for the Phase-II Upgrade of the ATLAS Tile Calorimeter *2019 IEEE Nuclear Science Symposium (NSS) and Medical Imaging Conference (MIC)* pp 1–4
- [8] Gololo M G D, Argos C F, Martins F and Mellado B G 2020 *J. Phys. Conf. Ser.* **1690** 012054
- [9] Tang F (ATLAS Tile Calorimeter System) 2018 *Springer Proc. Phys.* **213** 22–30
- [10] Martins F (ATLAS) 2016 The ATLAS tile calorimeter DCS for run 2 *2016 IEEE Nuclear Science Symposium and Medical Imaging Conference* p 8069837
- [11] Nikiel P P, Farnham B, Filimonov V and Schlenker S 2015 *J. Phys. Conf. Ser.* **664** 082039
- [12] Stark G 2021 ironman documentation Tech. rep.
- [13] Xilinx 2018 7 series fpgas and zynq-7000 soc xadc dual 12-bit 1 msp/s analog-to-digital converter Tech. rep.

Integration of the ALTI module in the ATLAS Tile Calorimeter system

Humphry Tlou¹ and Bruce Mellado^{1,2}

¹ School of Physics and Institute for Collider Particle Physics, University of the Witwatersrand, Johannesburg, Wits 2050, South Africa

² iThemba LABS, National Research Foundation, PO Box 722, Somerset West 7129, South Africa

E-mail: humphry.tlou@cern.ch

Abstract. The Tile Calorimeter of the ATLAS experiment is currently preparing for Run 3 data-taking period. As part of the ongoing Phase I upgrades, the Tile Calorimeter is replacing a part of the Timing, Trigger and Control system. The legacy Timing, Trigger and Control system is being replaced with a new advanced electronic board. The new ATLAS Local Trigger Interface module, is a 6 unit Versa Module Europa board which integrates the functionalities of four legacy modules currently used in the experiment: Local Trigger Processor, Local Trigger Processor interface, Timing, Trigger and Control Versa Module Europa bus interface and the Timing, Trigger and Control emitter. The ATLAS Local Trigger Interface module will provide the interface between the Level-1 Central Trigger Processor and the Timing, Trigger and Control optical broadcasting network, to the Front-End electronics for each of the ATLAS sub-detectors. The implementation and validation of the data acquisition software for the ATLAS Local Trigger Interface module in a Tile Calorimeter test station is complete. The TileCal Back-End electronics consists of four legacy Timing, Trigger and Control partitions, and the integration of the ATLAS Local Trigger Interface module in the Tile Calorimeter requires the insertion of four new ATLAS Local Trigger Interface modules in the Timing, Trigger and Control crates. Calibrations and data quality validations are performed in order to certify the readiness of the new trigger system for Run 3 data-taking period in early 2022.

1. Introduction

The ATLAS experiment [1] is a multipurpose particle physics experiment at the Large Hadron Collider (LHC) [2]. It is designed to study a large range of physics at a TeV scale. In 2012, the ATLAS experiment was one of the two experiments that contributed to the discovery of the Higgs boson. It is made of several sub-detectors and the Tile Calorimeter (TileCal) being the central hadronic calorimeter, is responsible for providing the energy and position of hadrons [3]. TileCal is made out of iron plates and plastic scintillators. It is divided into three cylinders along the beam axis and each cylinder is azimuthally segmented into 64 wedge-shaped modules, staggered in the ϕ direction. It has one central long barrel (LB), consisting of two partitions LBA and LBC side. The other two short extended barrels consist of two partitions EBA and EBC side. The Front-End (FE) electronics are housed inside the outermost part of the wedge-shaped modules, and are connected to the Back-End (BE) read-out electronics through optical Timing, Trigger and Control (TTC) distribution network. These four partitions are controlled by their corresponding TTC crates in the BE electronics. The TileCal utilises the ATLAS

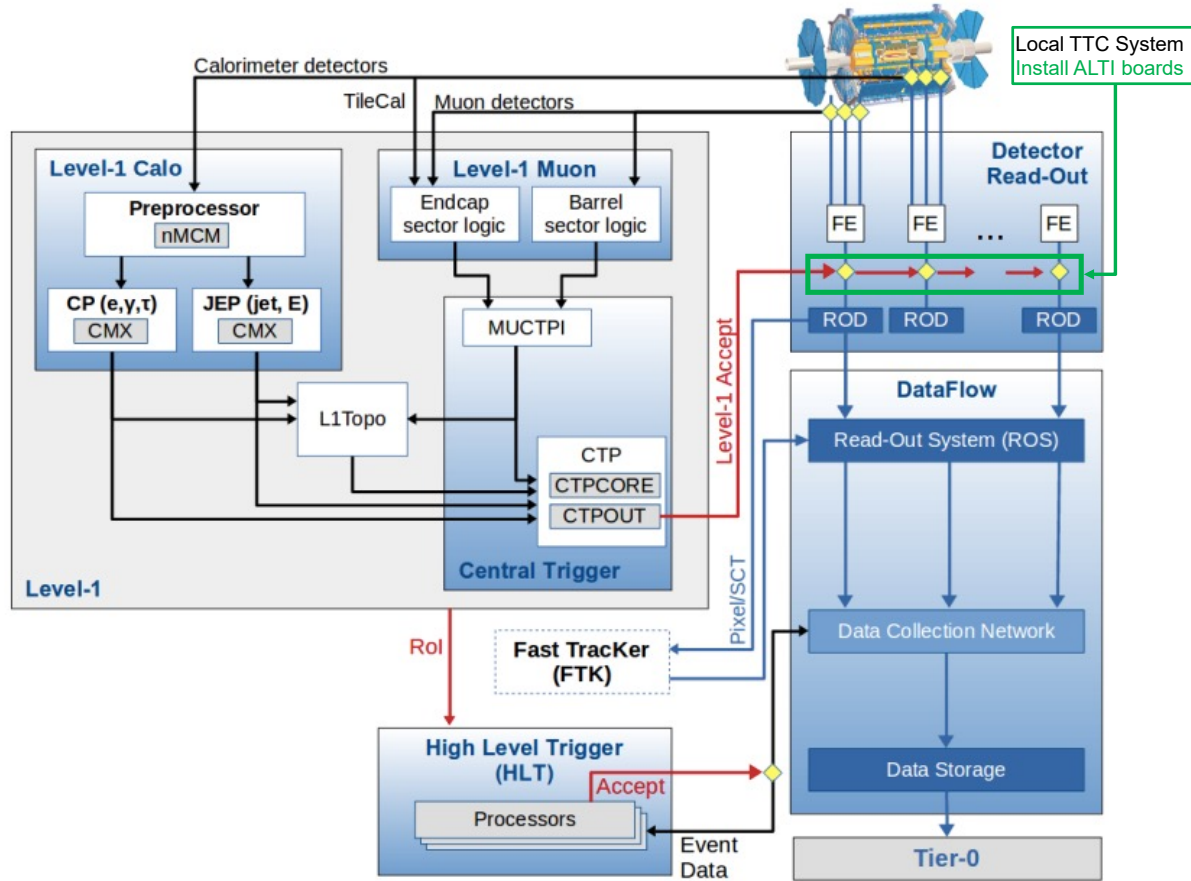


Figure 1: The schematic diagram of the ATLAS TDAQ system, with emphasis on the upgrade of the local TTC system [7].

Trigger and Data Acquisition (TDAQ) system for data collection. The TDAQ system, shown in figure 1 selects events with distinguishing characteristics that might be interesting for physics analyses. It is structured in a 2-level architecture, hardware Level-1 and High Level trigger (HLT) system. The Level-1 trigger (Level-1 Calo and Level-1 Muon) gives a fast identification of interesting events based on specific inputs from the muon detectors and the calorimeters. It uses the Central Trigger Processor (CTP) to reduce the accepted events from an input rate of 40 MHz (25 ns) to 100 kHz [4, 5]. The corresponding event signal produced by the CTP is called Level-1 Accept (L1A). The rate of accepted events is further processed in the HLT, to reduce the rate of recorded events from 100 kHz to 1 kHz [4]. The ATLAS experiment is upgrading the TTC system hardware with new electronics. The ALTI module is being integrated into the TileCal TTC system, in preparation for Run 3 data-taking period commencing in 2022. In order to operate the ALTI module in the TileCal, the TileCal online software,¹ has been adapted to integrate the new ALTI libraries provided by the ATLAS TDAQ group [6].

¹ The TileCal online software is a set of TDAQ software, used for the operation of the TileCal. Its main purpose is to readout, transport and store physics data originating from collisions at the LHC.

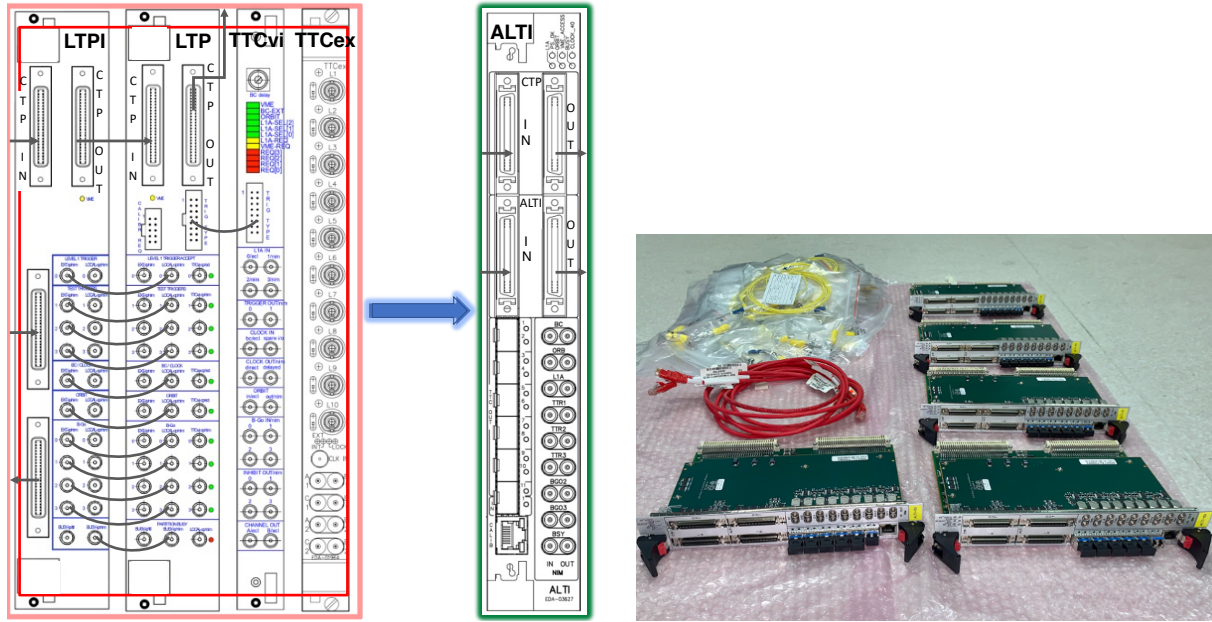


Figure 2: The four legacy TTC modules (LTPI, LTP, TTCvi and TTCex) will be replaced by the ALTI module (left). ALTI modules with new optical fibres, ready to be installed in the TTC crates of the BE electronics (right).

2. The ALTI project

The ALTI module is a new electronic board designed for the ATLAS experiment at CERN as part of the TTC system [8]. It integrates the functionalities of the four existing modules shown in figure 2 (left), which are currently used in the local TTC system of experiment: Local Trigger Processor (LTP), Local Trigger Processor interface (LTPI), TTC VME bus interface (TTCvi) and the TTC emitter (TTCex). The primary function of the ALTI board is to provide interface between the Level-1 CTP and the local TTC system of the sub-detector. It is made of state-of-the-art components and the logic is implemented in a single FPGA, which allows for more flexibility and added functionalities. During the operation of the detector, the ALTI module receives the TTC signals from the CTP through parallel twisted-pair of low voltage differential signaling cables and distributes them to the sub-detector electronics through the optical TTC distribution network. The full LHC turn consists of 3564 bunch crossings (BCs). The signals received from the CTP are the bunch clock, orbit signal, L1A with 8-bit trigger type and the event counter reset. The bunch clock is the main timing signal produced by the LHC and has a frequency of 40 MHz and the orbit signal is the second timing signal that indicates the start of a new LHC turn and allows the identification of the BCs.

3. Installation of ALTI modules

Five ALTI modules shown in figure 2 (right) were prepared for the installation in the BE electronics counting room in ATLAS USA15 cavern shown in figure 3 (left). Additional material include forty 0.5m Lucent Connector (LC) to Straight Tip (ST) patch fibres with forty ST-ST connectors, five TTC loop fibres for the TTC decoder and four calibration request cables. The connection scheme shown in figure 3 (right) was prepared prior the installation to properly configure the ALTI modules. All the LTP, TTCvi and the TTCex modules in EBA, LBA, LBC and EBC TTC crates and the laser crate were removed and replaced with the five ALTI modules.

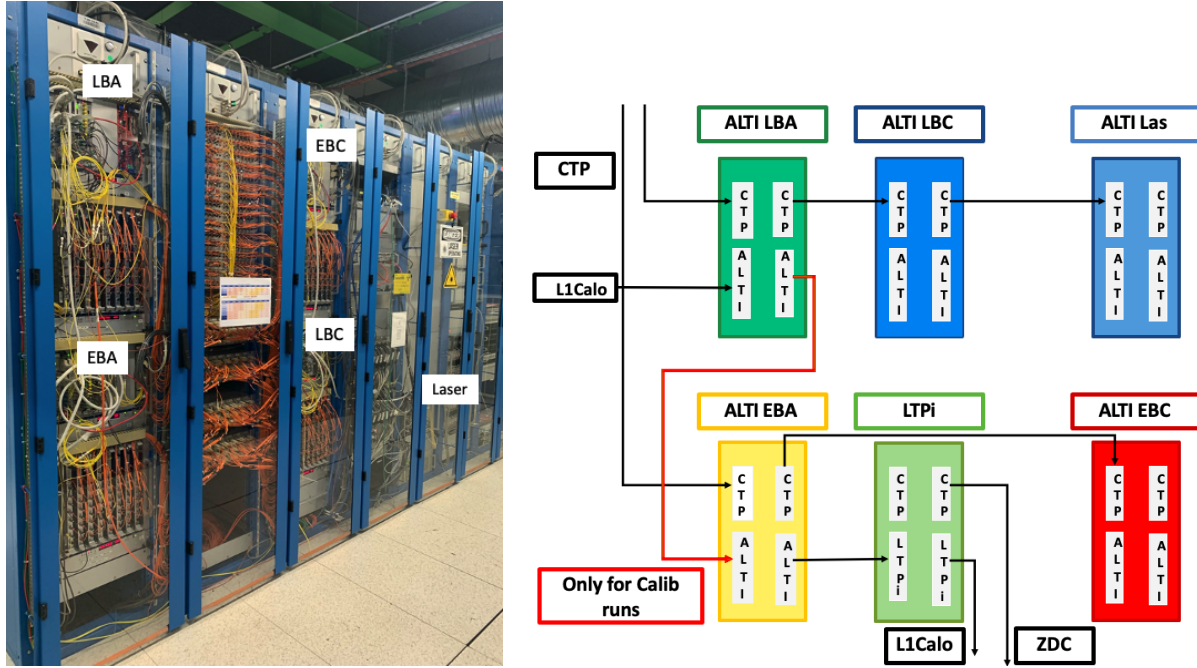


Figure 3: The TileCal TTC crates are located above the read-out driver crates in the BE electronics (left). The connection scheme shows the distribution of the TTC signals from the CTP and Level-1 Calo, to the ALTI modules in the TTC crates (right).

The ALTI modules are configured to use two different configurations for physics and calibration runs. During physics runs, all the ALTI modules are configured to be in slave mode and receive the CTP input. During the calibration runs, the LBA ALTI module is configured as the master and it generates the signals through the pattern generator and propagates them to the other TTC crates. EBA ALTI module is configured as the slave to the LBA ALTI module. All the other ALTI modules in LBC, EBC and the laser crate are configured as slaves to receive the CTP input. The database, OKS (Object Kernel Support), an object-oriented database with storage based on XML (Extensible Markup Language), has been modified to include new configuration objects.

4. Calibration systems and the Diagnostics and Verification System

The implementation of the new TileCal ALTI software involved the upgrade of the calibration systems [9] and the Diagnostics and Verification System (DVS) [10]. These systems have been extensively validated in relation to the legacy TTC system.

4.1. The Calibration systems

The TileCal uses highly accurate and precise calibration systems to achieve good energy determination and to account for changes in the readout electronics, which might be due to irradiation, ageing, and electronic failures. The calibration systems are the Cesium system, Laser system, Charge Injection Scan (CIS) and the Minimum Bias System. Each system tests a specific element in the readout electronics chain, as shown in figure 4. A combination of these tests provides the overall calibration of each readout channel. The tests are taken using seven data samples per event, which means that the read-out window is $25 \text{ ns} \cdot 7 = 175 \text{ ns}$. The calibration runs are taken during beam interruption periods. These calibration systems require a special handling of their calibration signal requests, which has been adapted for the ALTI

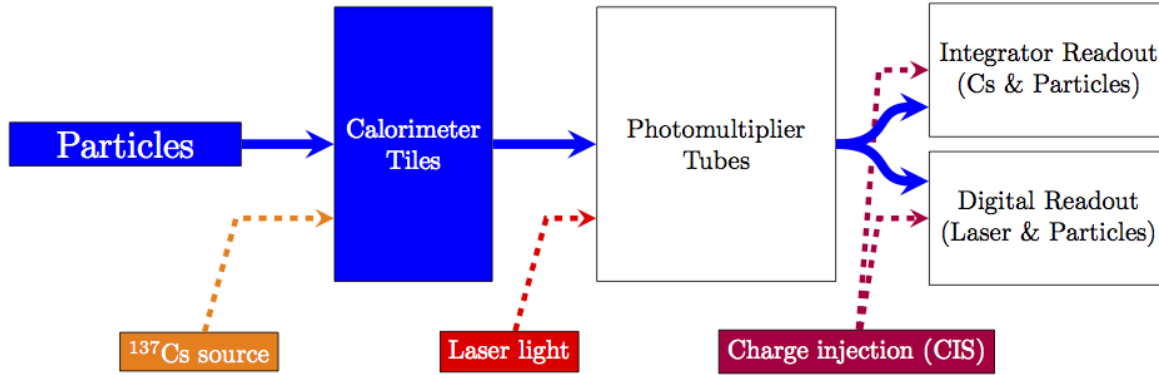


Figure 4: Flow diagram of the signal readout chain of different calibration systems in TileCal [9].

system.

4.1.1. The Laser system The Laser calibration system sends laser pulses to the PhotoMultiplier Tubes (PMTs), allowing for calibration with respect to each PMT's response. This allows for the calculation of corrections to the optical gain of the PMT and a test for the stability of each PMT over time. Laser pulses are also sent during empty bunch crossings of the LHC and the events are used in monitoring the evolution in time of the time calibration.

4.1.2. The Charge Injection Scan This calibration system consists of the simulation of physics signals through the injection of known charge values into the readout electronics. This is achieved by using dedicated capacitors (5 pF and 100 pF) plus a 4096 Digital Analog Converter controlled by an Analogue-to-Digital Converter (ADC). The relation of the peak amplitude in the response of the electronics (measured in ADC counts) to the value of charge injected (in pC) gives the calibration of each ADC in units of ADC counts/pC. This enables verification and identification of errors with the readout chains and allows for calibration of single ADC outputs of each PMT.

4.1.3. Minimum Bias System The proton-proton collisions denoted as “Particles” in figure 4 are dominated by soft parton interactions, known as Minimum Bias (MB) events. The MB readout system identifies response to Minimum Bias events over a time window of approximately 10 ms. Data produced by the integrator are continuously recorded during proton-proton collisions. The response of the TileCal to signals induced by the MB interactions, provides an estimation of instantaneous luminosity [11]. The MB system monitors the stability of the full optical chain and provides an independent cross-check of the Cesium calibration [12].

4.2. Diagnostics and Verification System

The DVS is part of the ATLAS TDAQ online software packages used for configuring and executing tests for TDAQ components [10]. The DVS software package has been modified for the TileCal ALTI system. In the TileCal system the tests are a set of checks for the digital read-out of the super-drawers and gives immediate results. CIS and pedestal are the two main types of tests. CIS checks the existence of the pulse reconstructed with the seven samples shown in figure 5 (left). Noise for a given channel is defined as the standard deviation of the signal in pedestal events.² For a given channel, the signal in a pedestal event is sampled seven times and

² Empty events where no physics signal is expected in the calorimeter

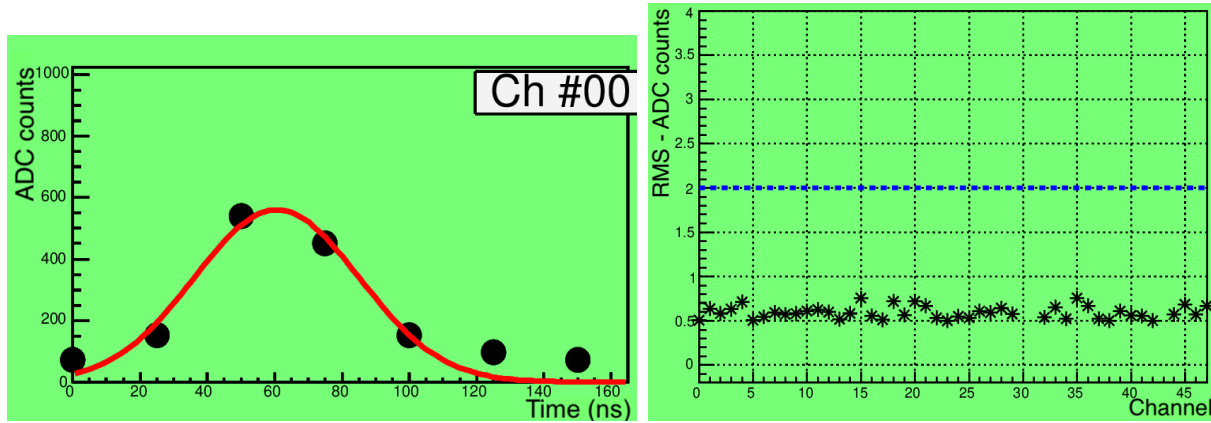


Figure 5: The CIS DVS test taken for one read-out module in good working condition, shows a good reconstructed pulse of the ADC counts against time, for seven samples per channel (left). The pedestal DVS test shows the RMS ADC counts against the channel number and the electronics noise level is below the threshold for all read-out channels (right).

the standard deviation of the samples is averaged over all events and termed “high frequency noise”. Likewise, for a given channel, the value of the first of the seven samples is recorded for all pedestal events and the standard deviation of this distribution is called the “low frequency noise”. The pedestal test can be run in ATLAS mode (seven samples with auto-gain at 100 kHz) performing the analysis in the read-out drivers, discarding all the events and reading results out at the end of the test. Figure 5 shows part of the DVS test results taken with the ALTI system.

5. Conclusions

During the Long shutdown 2 period (2019-2021), the TileCal has been undergoing maintenance and Phase-I upgrades, in preparation for the Run-3 (2022-2025) data-taking period. As part of the ATLAS Phase-I upgrade, TileCal replaces its local legacy TTC system with the new local ALTI system. The ALTI module integrates the functionalities of four legacy TTC modules: LTP, LTPi, TTCvi and the TTCex. The TileCal ALTI online software has been developed and tested in the test station and is being fully validated for the ATLAS detector at CERN. Five ALTI modules have been installed and configured for physics and calibration runs in the counting room in ATLAS USA15 cavern. The ALTI system is being tuned for data taking.

References

- [1] Aad G *et al.* (ATLAS) 2008 *JINST* **3** S08003
- [2] Alici A, Bomben M, Dawson I and Sonneveld J 2021 *CERN Yellow Rep. Monogr.* **1** 23–34
- [3] Hrynevich A (ATLAS) 2017 *JINST* **12** C06021
- [4] Vazquez Schroeder T (ATLAS) 2017 *PoS EPS-HEP2017* 525
- [5] Abolins M *et al.* (ATLAS TDAQ) 2016 *JINST* **11** P06008
- [6] Tlou H 2020 *J. Phys. Conf. Ser.* **1690** 012055
- [7] Aaboud M *et al.* (ATLAS) 2017 *Eur. Phys. J. C* **77** 317 (*Preprint* 1611.09661)
- [8] Ask S *et al.* 2008 *JINST* **3** P08002
- [9] Aaboud M *et al.* (ATLAS) 2018 *Eur. Phys. J. C* **78** 987 (*Preprint* 1806.02129)
- [10] Barczyk M *et al.* 2003 *eConf C0303241* TUGP005 (*Preprint* hep-ex/0305106)
- [11] Aad G *et al.* (ATLAS) 2013 *Eur. Phys. J. C* **73** 2518 (*Preprint* 1302.4393)
- [12] Blanchot G *et al.* 2020 *JINST* **15** P03017 (*Preprint* 2002.12800)

Quality control software development for testing the next generation of upgraded low voltage power supplies for the ATLAS Tile Calorimeter

E Nkadameng¹, R Mckenzie¹, R van Rensburg¹, N Njara¹, T Lepota¹, O Moaune¹ and B Mellado^{1,2}

¹ School of Physics and Institute for Collider Particle Physics, University of the Witwatersrand, Johannesburg, Wits 2050, South Africa

² iThemba LABS, National Research Foundation, PO Box 722, Somerset West 7129, South Africa

E-mail: edward.khomotso.nkadameng@cern.ch

Abstract. The High Luminosity Large Hadron Collider (LHC) will deliver five times the LHC nominal instantaneous luminosity, after a series of upgrades scheduled to take place in 2025 - 2027 during the long shutdown. The ATLAS TileCal will require the complete replacement of the readout electronics in order to accommodate its acquisition system to the increased radiation levels, trigger rates, and high pile-up conditions during the HL-LHC era. A major replacement of the on- and off detector electronics is required. The drawer electronics are powered by custom switching power supplies, called the Finger Low Voltage Power Supply. This contribution provides details on the ongoing development of quality assurance test benches that use custom built software packages to interface, monitor and verify parameters for check-out of the LVPS bricks. The strict procedure required for brick checkout during production constitutes of a series of highly automated tests that provides information about the general conditions of the brick and subsequently ensure the reliability and quality of the upgraded LVPS brick which will power the next generation of the upgraded readout system of ATLAS TileCal at CERN. The quality control procedure will be used as An initial virtual Instrument (VI) was written in LabVIEW to scan and read out voltages and current measurements and monitor the parameters in real-time. The tested LVPS bricks were monitored over a period of a day and were observed to fall within the required specification criteria of the TileCal Phase-II upgrade.

1. Introduction

At the European Laboratory, CERN, A Toroidal Large Hadron Collider Apparatus (ATLAS) is one of 2 multi-purpose experiments at the Large Hadron Collider (LHC) [1]. The Tile calorimeter (TileCal) is the central region of the ATLAS detector and designed to absorb most of the particles coming from a collision, forcing them to deposit all of their energy and stop within the detector [2]. The calorimeter is composed of alternating layers of steel absorber and scintillating tiles as the active medium. Light produced in the scintillators is routed into the photo-multiplier tubes (PMTs) using wavelength-shifting (WLS) fibers. The TileCal is divided into four cylindrical readout sections along the beam axis: one central long barrel (LBA, LBC) and two extended barrels (EBA, EBC). Each barrel is segmented azimuthally into 64 wedge-shaped TileCal modules. Power is supplied to the front-end electronics of a single

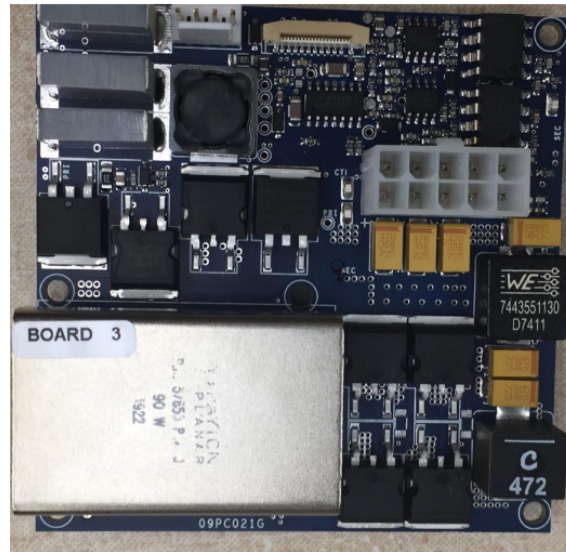


Figure 1: Custom built Wits University low voltage power supply brick.

super-drawer by means of a low-voltage power supply (LVPS) source, which is positioned in an external steel box mounted just outside the electronics drawer also referred to as a super-drawer. Each power supply provides power to one module, and resides on the outside of the drawer in a special metallic shielding called a “finger”. Each supply is a package that consists of eight power supply “bricks,” providing a range of currents and voltages as required by a module.

2. Upgraded Tile Low Voltage Power Supply

The basic topology of the brick is a transformer-coupled buck converter. Each brick receives + 200 VDC at low current, and converts it using switching techniques to low voltage at the required currents. The heart of the design is the LT1681 controller chip [6]. It is a pulse width modulator (PWM) that operates at a fundamental frequency of 300 kHz. The LT1681 provides an output clock to the FET Drivers. These are transistor drivers that have sufficient current and voltage to drive the high-side and low-side power Field Effect Transistors (FETs) that perform the switching on the primary side. The upgraded design uses synchronous switching, for switching on the high-side and low-side transistors turn on and conduct for the duration that output clock signal oscillates between a high and a low state and both are in the off state when the clock is low. The transformer is a custom planar design with turn ratios suitable for the 10 V brick. The buck converter is implemented on the secondary side of the transformer. The output side also contains an additional LC stage for noise filtering. The design also incorporates a shunt resistor for measuring the output current, the voltage fed back using an opto-isolator. The brick has three types of protection circuitry built in as part of the design. There is a over-voltage protection (OVP) and over-current protection (OCP). Both of these circuits are on the primary side of the brick. These send facsimile analog voltages to the ELMB that represent the input and output voltage, the input and output current, and readings from two temperatures located on the brick. The upgraded version of the LVPS bricks are all identical with the same converted output of +10 VDC. This greatly reduces the complexity with regards to design, production and testing of the bricks. The LVPS brick (see figure 1) has a 4 pin connector, with two pins for +200 V and two pins for the signal return line. There is a 10 pin output connector to deliver the 10 V output of the brick to the Harting connector on the LVPS box. There is also a small 20 pin connector, which connects the brick to the Embedded Local Monitor Board (ELMB)

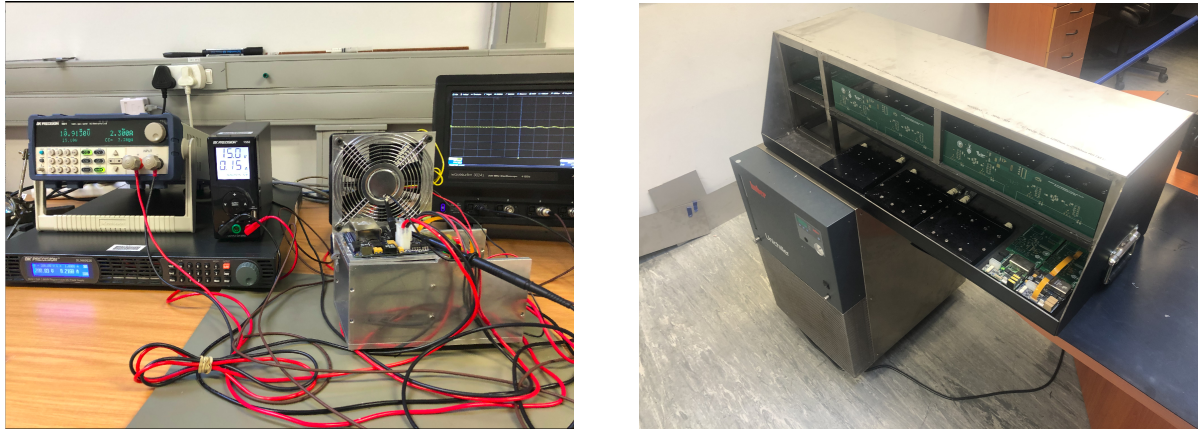


Figure 2: The initial test bench setup (left) consists of a test fixture providing support for both the LVPS brick and the interface card, a + 200 VDC power supply used for the input to the low voltage power supply, an electronics load meter to measure and display the output current and voltage, oscilloscope to measure the switching frequency of the converter and a PC computer. The Burn-In test bench (right) utilizes a programmable high voltage power supply for the input + 200 VDC, eight mounted DC/DC bricks with corresponding interface boards, two dummy-load boards, a mainboard for interface with all custom boards and water cooling station for cooling the LVPS bricks.

motherboard with a ribbon cable. This connector is used to receive the control signals from the Auxilliary board used to generate all auxiliary signals and power voltages for the fLVPS via the ELMB motherboard, and send the monitoring signals in differential analog format to the ELMB motherboard.

3. Production checkout and test bench designs for quality control

The first checkout procedure is visual inspection consisting of: checking the soldering of each part and the cleanliness of the brick, as well as verifying the correct assembly of components. During the visual inspection the brick receives an identification serial number. At this point the brick is logged into the database.

3.1. Initial test bench

The next step is the initial tests, which consists of a series of highly automated tests (see figure 2). The tests provide information about the general conditions of the brick (voltages and currents output, clock efficiency, start-up and shut-down of the brick) and checks the correct functioning of the protection and monitoring circuits. The initial test bench is based on a computer, for the control and readout of several commercial equipment and custom built interface printed circuit boards (PCB) which perform the tests; a metal case that acts as brick and PCB support and provides the interface to the computer as well as the ground connections [5]. The data acquisition card can digitize eight channels simultaneously and has in/out registers for control purposes. If the brick fails one or more tests a technician and/or an engineer proceeds to identify the causes and to fix the problem. After that the brick will be fully retested, with the initial test results, repairs and final acceptance inserted into the database.

3.2. Burn-In test bench

The power supply is then subjected to a the burn-in procedure. This comprises of a 7 hours test during which the brick runs at an upper limit current to stress components and solder

Parameter	Value
Threshold for Stable Load	2.3 A
Over Voltage Protection	12.5 V
Over current Protection	7 A
Duty Cycle at Nominal Load	> 45 %
Frequency at Nominal Load	300 kHz
Efficiency at Nominal Load	75 %
Input Current at Nominal Load	0.2 A
Over Temperature Protection	72 °C

Table 1: Specification parameters used to ensure uniformity of individual bricks in the test station software.

joints that are on the edge of failure. The burn-In test bench consisting of an aluminum chassis and custom built printed circuit boards to interface and read out several parameters using a desktop computer. Interfaced with a LabVIEW 2020 framework, external 200 V DC power supply, and a water cooling circuit utilized to cool the bricks and internal electronics. The circulating water temperature in the test-benches is stabilized between 17 - 19 °C. During the burn-in, bricks are thermally coupled to a water-cooled plate to mimic during standard working conditions and thermal grease applied under the posts to help the coupling. Temperatures from the burn-in are registered along with several parameters of the brick (voltages, currents and temperatures) [5]. The brick efficiency rating is also verified which is the power output to those components divided by the wattage drawn by the front-end electronics. Any wrong functioning of the monitoring circuits on the LVPS bricks in response to the front-end electronics may prevent the detection of critical malfunctioning therefore preventing any possible response in the detector. It is also important to note that a malfunctioning in the electronic components of a module, would undoubtedly involve a severe data loss from the module.

4. Software architecture for monitoring and control

The LVPS system and all subsequent components are integrated with various software packages to allow for advanced monitoring and control in a graphical manner from a LabVIEW framework. The Framework allows for live monitoring of sensors, (hardware control), automated recovery and more. The use of custom built interface boards do all the data acquisition and further multiplex and parse the data to the desktop personal computer (PC). The central software is used on the desktop PC, which communicates all the interface boards and graphically displays and logs data points. Parts of the legacy software, an old and outdated program that is still used to perform a task for a user at CERN was recycled for the front-panel graphics as seen in figure 3. Several custom LabVIEW drivers were also created to communicate with the high voltage source via the virtual instrument software architecture (VISA) communications layer over ethernet and to test and measure the standard communication API (Application Programming Interface) for use with any testing and measurement devices. The VISA libraries enables communication for many interfaces such as General Purpose Interface Bus (GPIB), Universal serial bus (USB), and Ethernet. [4] In the control software the main functions and parameters of the bricks are verified to be correct. The required accuracy of all parameters need to be within the 3σ limit from the nominal specification values for all tests, where the measured data is within three standard deviations from the mean.

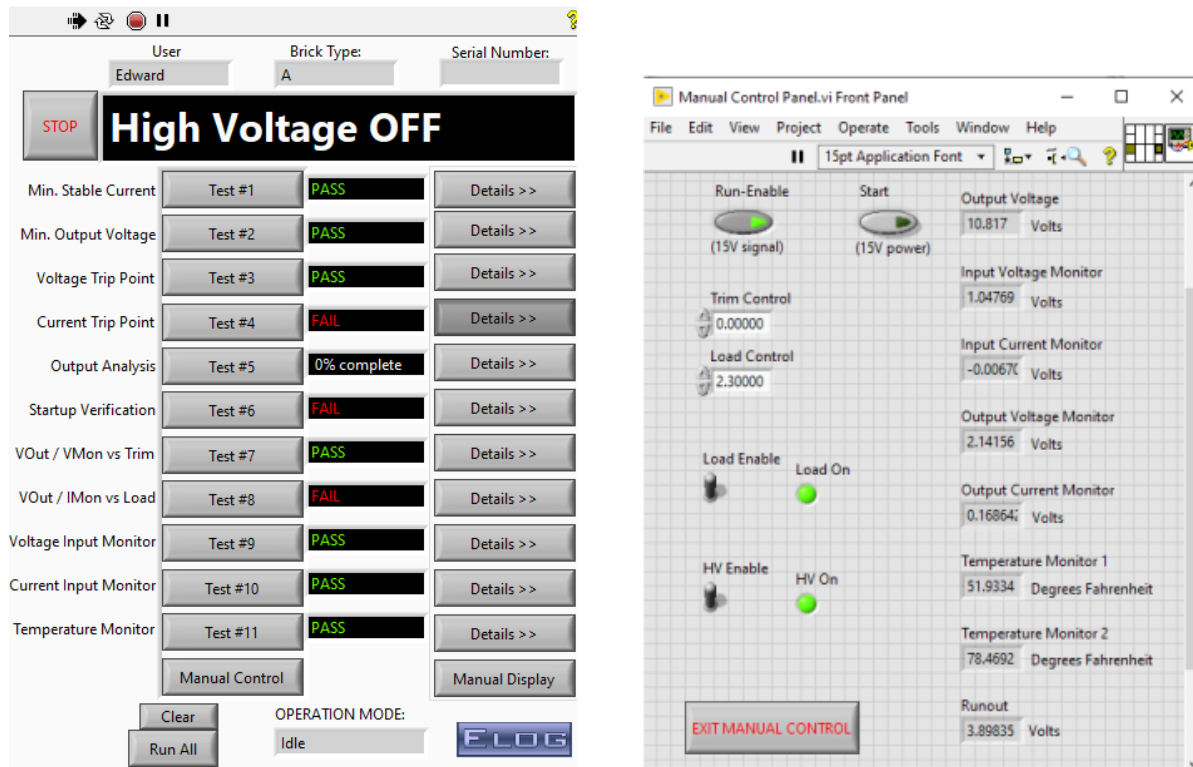


Figure 3: Programme test panel used to perform various tests to guard against over temperature, over current and over voltage. These also include tests such as startup verification to start the brick and minimum stable current when the brick is on (left). The manual control panel displays parameters such as output voltage in real-time on a graphical user interface (GUI) (right).

5. Performance testing of latest version of power supply

The initiation of a test is straight forward with the user executing the desired test, where the software automatically configures all relevant parameters and follows the specific algorithm associated with the test. Following the test, the software renders a binary pass or fail and displays the outcome alongside the respective test as shown in figure 3. The software is also able to export the resulting data as a text file and/or display plots and other graphical representations of the test data, depending on the test run involved. For the completion of a test sequence, by an operator, all tests need to be successfully completed without any error messages. The test measures the stability of the voltage over a long period as seen in figure. For a brick to receive an overall pass status all eleven tests on the test panel as seen in figure 3 must have yielded results within the allowed parameter distribution.

The most notable metrics measured is the feedback signal where the test checks the correct functioning of the monitor circuit of output voltage and input current (see results in figure 4 and 5) to be distributed to the front-end electronics of the TileCal. The brick is started at a nominal load of 2.3 A. The manual control feature is a new addition, which allows the brick to be monitored at any period interval through the data acquisition card. To determine this value, the brick is connected to the nominal load and the clock output from the LT1681 controller chip [6] read with an oscilloscope. The load is then decreased until missing clock cycles are registered, and the load value recorded. Permitted values for all the bricks should be within the 3σ range as summarized in table 1. Any values outside the 3σ of the specified values are considered as a failure of a brick. The expected voltage of the power supply should not exceed 12.5 V which can

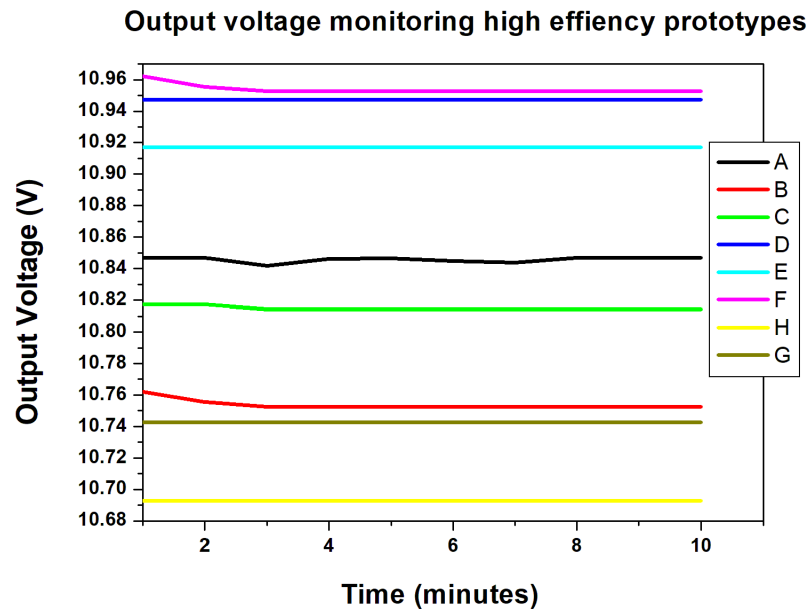


Figure 4: The output voltage monitored over elapsed time during initial testing of LVPS brick. All eight bricks tested fall within the acceptable tolerance range between 9 V to 12.5 V. The difference in monitoring data is due to electronic components of a given type not being identical. Even for components made from the same materials and by the same processes, differences still exist due to noise factors such as microscopic material defects or variations within a single manufacturing process. Therefore, the strength of a component is considered to be a random variable. Thus, statistical distributions are usually used to describe any anomalies in data.

be observed from figure 4 where both the upper and lower bounds of the tested brick are with the required specifications. The same can be observed for the input current of the brick which should not exceed a value of 0.220 A as seen in figure 5.

6. Conclusion

The ATLAS collaboration has planned a huge upgrade for the next phase that will allow the collaboration to fully exploit the LHC physics opportunities. The quality assurance testing station has been commissioned at the University of the Witwatersrand's electronics laboratory. These test benches will ensure high quality and reliability of the hardware that will be delivered to CERN. Each LVPS brick will undergo a long list of tests and compliance with set parameters are to ensure correct functioning of bricks and of components powered. Any departure will cause severe consequences for the Calorimeter module electronics such as the front end electronics powered by the LVPS bricks. If the output (voltage or current) or the temperature of the brick exceeds the allowed range during operation, measures will be put in place to protect the front-end electronics. However a failure in a brick may result in the loss of data in a mini-drawer.

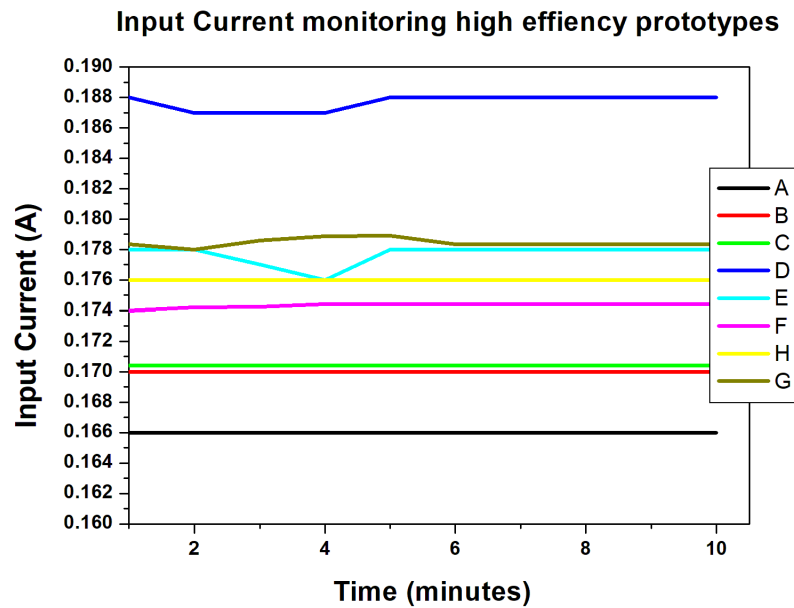


Figure 5: The Input current monitored over time of the LVPS brick. All eight bricks tested, fall within the acceptable tolerance range between 0.15 A to 0.22 A.

References

- [1] ATLAS Collaboration. (2008) The ATLAS Experiment at the CERN Large Hadron Collider. JINST. vol **3** p 150.
- [2] Ryan Mckenzie. (2021) The ATLAS Tile Calorimeter performance and its upgrade towards the High Luminosity Large Hadron Collider. Technical report. p 1-4.
- [3] Nkadameng E. (2019) *Proc. SAIP Conf. (Venda)* p 257 - 262
- [4] Lepota T. (2019) *Proc. SAIP Conf. (Venda)* p 251 - 256
- [5] Nkadameng E and Mellado B. (2020) *Proc. Int. Conf. on Particle Physics and Astrophysics (Moscow)* JPCS Ser. **201** p 589
- [6] LT1681 datasheet, *Technical datasheet* p 1 - 16

Programming the load readout board micro-controllers used in the development of a Burn-In test bench for the ATLAS TileCal Phase-II Upgrade

Nkosiphendule Njara¹, Bruce Mellado^{1,2}, Edward Nkadimeng¹,
Thabo Lepota¹, Ryan Mckenzie¹ and Roger van Rensburg¹

¹School of Physics and Institute for Collider Particle Physics, University of the
Witwatersrand, Johannesburg, Wits 2050, South Africa

²iThemba LABS, National Research Foundation, PO Box 722, Somerset West 7129, South
Africa

E-mail: nkosiphendule.njara@cern.ch

Abstract. The University of the Witwatersrand will be producing over 1024 Low Voltage Power Supplies (LVPS) "Bricks" to power the on-detector electronics of the Tile Calorimeter (TileCal) of the ATLAS detector in preparation for the Phase-II upgrade. A brick is a DC/DC converter. The ATLAS Phase II upgrade will increase the instantaneous luminosity of the Large Hadron Collider (LHC) by at least a factor of five. Burn-in type test stations are currently being developed in the Wits high-throughput electronics laboratory for testing the Bricks. Burn-in test station is made up of various Printed Circuit Board (PCBs) with different functions. Each PCB contains a PIC16F883 microcontroller which must be programmed in order for the PCBs to perform their respective functions. The burn-in test station setup consists of a Load readout/interface board used to read and control/adjust parameters of four channels of the dummy load board. This paper discusses how different commands for each PIC microcontroller are written and used to shift bits into the register of the Digital to Analog converter (DAC) contained on the dummy load to control the current and voltage load. A hexadecimal (hex) source file is generated and used by programmable logic devices which provides general information of the configured functions.

1. Introduction

The LHC is a high energy particle accelerator. ATLAS (A Toroidal LHC ApparatuS) as shown in figure 1 is a general purpose detector designed for probing proton-proton (pp) collisions, it is sensitive to a wide range of signatures left by particles. The ATLAS detector is scheduled for an upgrade during the long shutdown between the year 2025 and 2027 in anticipation of the LHC Phase-II upgrade. The High Luminosity LHC (HL-LHC) project will increase the instantaneous luminosity by at least a factor of five compared to the nominal luminosity of $10^{34} \text{ cm}^{-2} \text{ s}^{-1}$ [1].

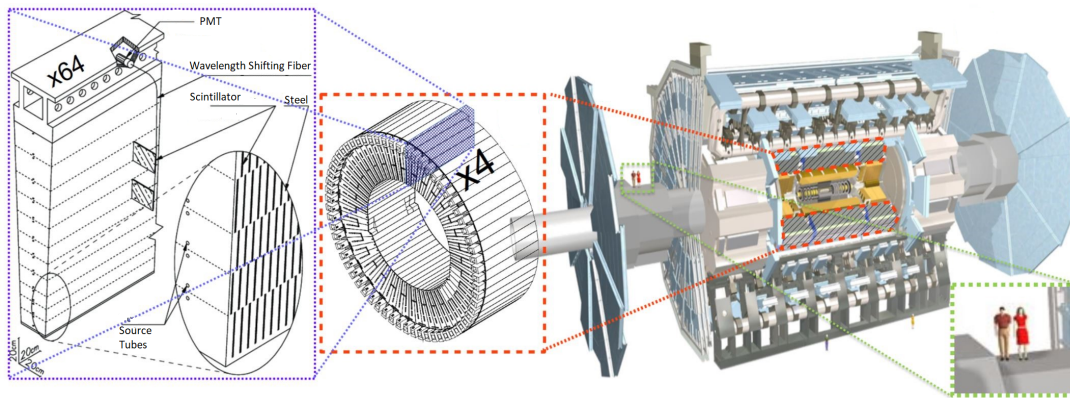


Figure 1. The ATLAS detector [2].

The Tile Calorimeter (TileCal) of the ATLAS detector is the central region of the detector [3]. TileCal is a sampling detector constructed of steel and plastic scintillator plates consisting of 256 wedge shaped modules arranged around the beam axis. The scintillating tiles are placed in the plane perpendicular to the colliding beams and are radially staggered in depth, this is illustrated in figure 1. It consists of 500000 scintillator tiles and TileCal barrels [3]. The TileCal barrels are segmented azimuthally into 64 modules, each serviced by electronics housed in a water-cooled "drawer" at the outer radius of the module. Power is supplied to the drawers by the "finger" low-voltage power supplies (LVPS) located at the outer end of each drawer [3].

2. Low Voltage Power Supply (LVPS) Brick

The LVPS Brick form part of the electronics for the TileCal. They are positioned inside of an electronics drawer. These "Bricks" are DC/DC converters. They convert a 200 VDC input to 10 VDC output required by the front-end electronics of a TileCal module [4]. The switching frequency of the brick is 300 kHz. The brick receives an Enable signal and a start-up pulse from Embedded Local Monitor Board motherboard. The start-up pulse provides temporary power to the control circuits of the brick to power it on [4]. Each brick will be tested using specific procedures and it must pass different criteria. One of the procedures used to test the Bricks is the Burn-in procedure.

3. Burn-In test station

The University of the Witwatersrand is currently developing two Burn-In test stations. Burn-In test station is used to perform endurance type test on the LVPS brick to detect early failures on the components of the brick, thus improving the reliability of these LVPS Bricks. In the burn-in procedure, the LVPS bricks are subjected to high load and elevated temperature. In this environment we expect the operational life of the Brick to be reduced. This allow components to fail immediately within the Burn-in station so that the failed components can be replaced or repaired. The Burn-in test station is made up of a programmable high voltage power supply (200 V), chassis, cooling system, LabView control program, PC and custom built PCBs (Mainboard, Dummy load boards, Brick interface and load interface boards). Figure 2 shows the connections between the different PCBs of the burn-in test station and the high voltage power supply. These proceedings concentrate on programming the load readout board Peripheral Interface Controller (PIC) microcontrollers. This board also consists of an Analog to Digital Converter (ADC).

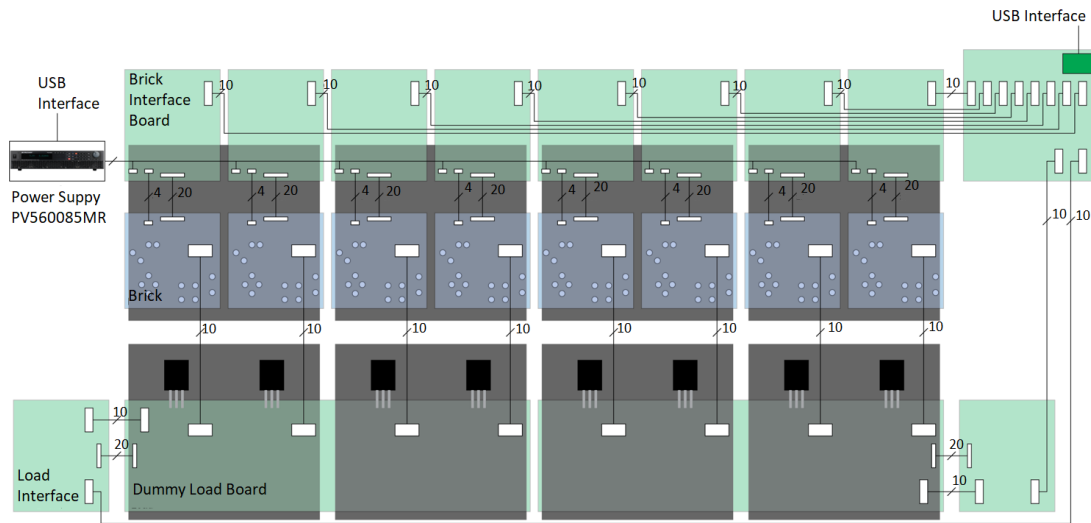


Figure 2. Burn-In test station interconnection block diagram [5]

3.1. Load interface board

The Load interface board communicates with two PCBs, the mainboard and the electronic load. This connection is shown in figure 2 using a block diagram. The electronic load and load interface PCBs are shown in figure 3. The load interface reads the brick differential voltages and currents from the four channels of the electronic load. These values are read as analog signals and a 10 bit 16-channel ADC is used to convert this signal into digital format. A PIC16F883 microcontroller processes this data from the ADC. This information is then passed into the mainboard which acts as a multiplexer. The mainboard is connected to the PC using a high-speed USB 2.0 interface. In order for PCBs to perform their respective functions the PIC microcontroller must be programmed to give the commands for each PCB.

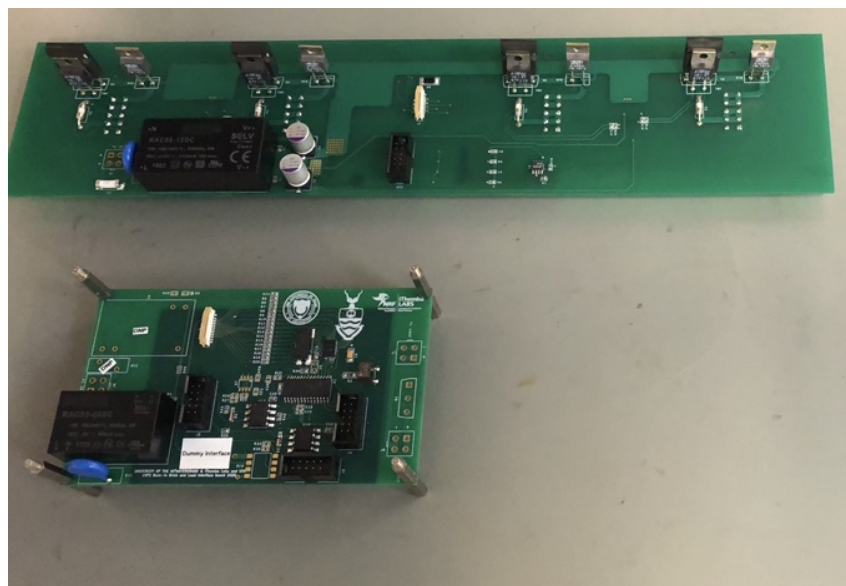


Figure 3. Dummy load (top) and load interface (bottom).

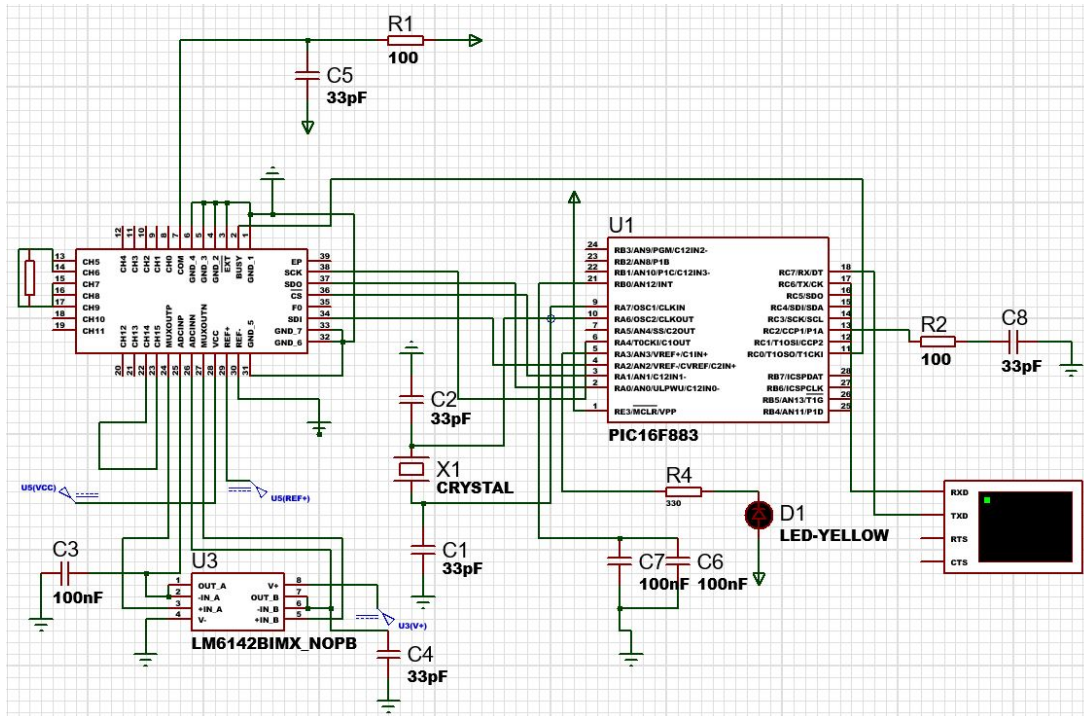


Figure 4. Load interface circuit designed in Proteus for the simulation of the PIC C microcontroller firmware.

3.2. Proteus Simulation

The Proteus software is used for designing, drawing and simulation of electronic circuits. It is beneficial to run simulations of circuits in proteus before you make them practically. One of these benefits is that there is no possibility of burning or damaging of any of the electronic components. Our firmware is compiled in MPLABX IDE using a CCS compiler. A hexadecimal (hex) format source file is generated when compiling in MPLABX IDE. This file contain machine code, these are the commands used to program the PIC microcontroller. The hex file is used in the simulation of the load interface board in proteus ISIS by uploading this file on the PIC microcontroller component of the circuit. The purpose of this simulation is to confirm that our firmware works efficiently before programming the hardware. It is important to set all the properties of the components to emulate the hardware properties i.e. both the frequency for the PIC16F883 and the crystal oscillator must be set to 16MHz. In our simulation of the interface board PIC C code we use ASCII characters used in the switch statement of the firmware to turn the LED ON and OFF. The ASCII character used for switching on the LED is "h" and "l" is used to switch off the LED. We can also send the ASCII character "q" on the virtual terminal of the proteus software to read back module address, the address should change and be unique for each module 1-63. We also designed the load interface circuit in Proteus to be able to read analog signals i.e the brick differential voltages and currents from the 8-differential channels of the LTC2449 ADC. This is done by sending an analog signal (voltage/current) through the ADC channels and the ADC converts the analog signal into binary information and sends it to the microcontroller. The microcontroller processes this information and displays it as digital information on the virtual terminal.

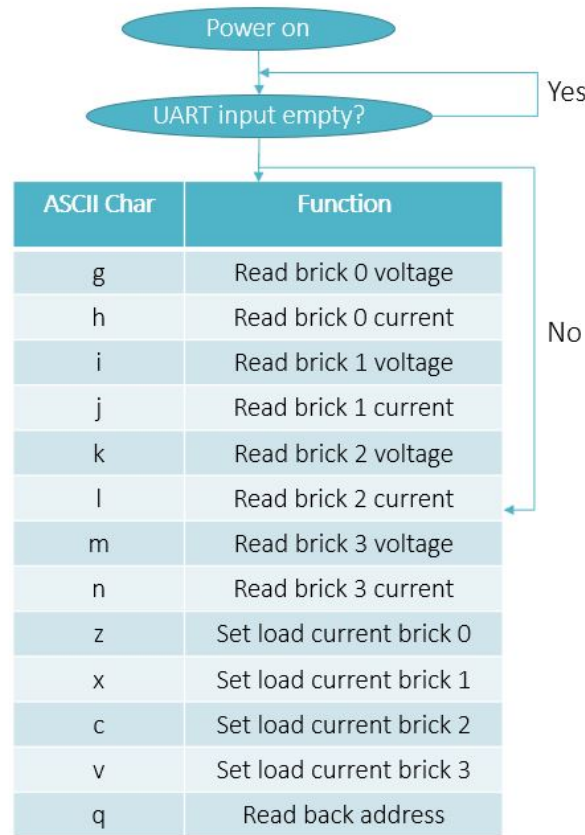


Figure 5. Load interface state machine [2].

Programming the load interface board - To program the PIC16F883 microcontroller PICKit 4 debugger is used. For this setup we require a breadboard, breadboard wires, PICKit 4 debugger, rs232 serial communication cables, PIC16F883 microcontroller and a PC running MPLABX Integrated Programming Environment (IPE) programmer. This MPLABX debugger communicates with the PICKit 4 programmer and it is used for uploading the the hex file containing the commands for the PCBs. When the programming process of the PIC microcontrollers of the PCBs is completed, the boards must be validated using a Real-Time serial capture software. To validate the load interface we can use the ASCII characters just like in the simulation. This means we can send ASCII characters and be able to read the differential voltages and current values from the LTC2449 ADC of the load interface. These are the analog values sampled from the electronic load of the burn-in test station.

In Figure 5 the state machine of the load interface board is shown. The state machine is a structured approach to programming. This is a useful tool for getting a clear and structured code. The state machine of the load interface board works as follows, when the board is turned on the UART input is checked whether it is empty or not. If the UART input is empty nothing happens but if you send the ASCII character, for example character g which is written on the switch statement on the C code, the board will read the brick differential voltage in position 0. All the ASCII character functions are shown on the state machine with their respective functions.

4. Conclusion

Two burn-in test station are currently under development at the University of Witwatersrand. This is in preparation of the pre-production and main production of the Low Voltage Power Supply Bricks. The burn-in test station consists of various PCBs with different functions. These PCBs contains a PIC16F883 microcontroller which must be programmed to allow the boards to perform their respective functions. The PIC C code is written in MPLABX IDE using CCS compiler for microcontrollers. The hex file generated after compiling the C code was used in the simulation of the load interface circuitry. We did this simulation to check whether our firmware works efficiently. The results of the simulation were successful as the firmware works as expected in the Proteus simulation. The PIC16F883 microcontrollers for all the PCBs has been successfully programmed using MPLABX IPE software. The load interface board was validated successfully by sending different ASCII characters using a Real-Time serial communication program and received back the the current and voltage values from each channel of the 16 channels analog to digital converter.

References

- [1] ATLASCollaboration 2008 *JINST* **3** S08003. 437 p also published by CERN Geneva in 2010
- [2] Hibbard M J 2018 *ACCELERATED AGING OF A SWITCHING POWER SUPPLY PROTOTYPE* Ph.D. thesis URL <http://hdl.handle.net/10106/27761>
- [3] 2017 Technical Design Report for the Phase-II Upgrade of the ATLAS Tile Calorimeter Tech. rep. CERN Geneva URL <https://cds.cern.ch/record/2285583>
- [4] Nkadimeng E, Mellado B, Lepota T and Sandrock C (eds) 2019 *Low Voltage Power Supply production, hardware upgrade and testing for the ATLAS TileCal Front-End Electronics system* (The Proceedings of the 64th Annual Conference of the South African Institute of Physics, edited by Prof. Makaiko Chithambo) URL <https://events.saip.org.za/event/144/images/34-43.pdf>
- [5] Mckenzie R P (ATLAS Collaboration) 2020 *5th International Conference on Particle Physics and Astrophysics (ICPPA)* URL <https://cds.cern.ch/record/2741103/files/ATL-TILECAL-SLIDE-2020-380.pdf>

The characterization and functionality of the interface boards used in the burn-in test station for the ATLAS Tile Calorimeter Low Voltage Power Supplies Phase-II upgrade

T J Lepota¹, E Nkadimeng¹, R Mckenzie¹, N Njara¹, R Van Rensburg¹ and B Mellado^{1,2}

¹ School of Physics and Institute for Collider Particle Physics, University of the Witwatersrand, Johannesburg, Wits 2050, South Africa

² iThemba LABS, National Research Foundation, PO Box 722, Somerset West 7129, South Africa

E-mail: thabo.james.lepota@wits.ac.za

Abstract. The Wits Institute of Particle Physics and iThemba LABS are responsible for developing and manufacturing over thousand of the transformer-coupled buck converters, known as bricks, for the Low Voltage Power Supply (LVPS) system. The bricks that pass this test are sent to CERN to be installed in the ATLAS detector in order to turn ON/OFF the front-end electronics. As part of the quality assurance test for these bricks, the burn-in test station is necessary. We describe the Brick Interface (BI) boards on the burn-in station, their operation, and characterize the main aspects of the board, as well as their importance to the entire system.

1. Introduction

The start of the operation of High Luminosity Large Hadronic Collider (HL-LHC) [1] is planned for 2026 with a foreseen integrated luminosity of 4000 fb^{-1} . The ATLAS Tile Calorimeter also known as TileCal [2] is a sampling calorimeter which forms the central region of the Hadronic calorimeter of the ATLAS experiments [1]. TileCal is responsible for the measurement of jet and missing transverse energies, jet-substructure and triggering (including muon information). An individual module (see figure 1) consists of alternating steel (absorber) tiles and plastic scintillators (active medium) tiles and a Super Drawer (SD) which houses the front-end (FE) electronics as well as Photo-Multiplier Tubes (PMTs). When Particles pass through and interact with active tile, it produce light. This light is then transmitted to PMTs located in SDs via wavelength shifting fibers. TileCal must be upgraded to maintain high performance in the new HL-LHC environment. There is a widespread of upgrades on the TileCal, however in this article we will focus on the Low-Voltage (LV) system.

2. LVPS bricks

A brick in figure 2 is a transformer-coupled buck converter, it functions to step down 200 VDC to 10 VDC, which is then distributed to the FE electronics [1]. With its twin transistor forward converter [4], the LT1681 controller chip is at the heart of its design. The chip can switch frequencies up to 300 kHz. The LT1681 controls the switching of the primary side by providing a clock signal to the Field Effect Transformer (FET) drivers. When the FETs conduct, current flows through the primary windings

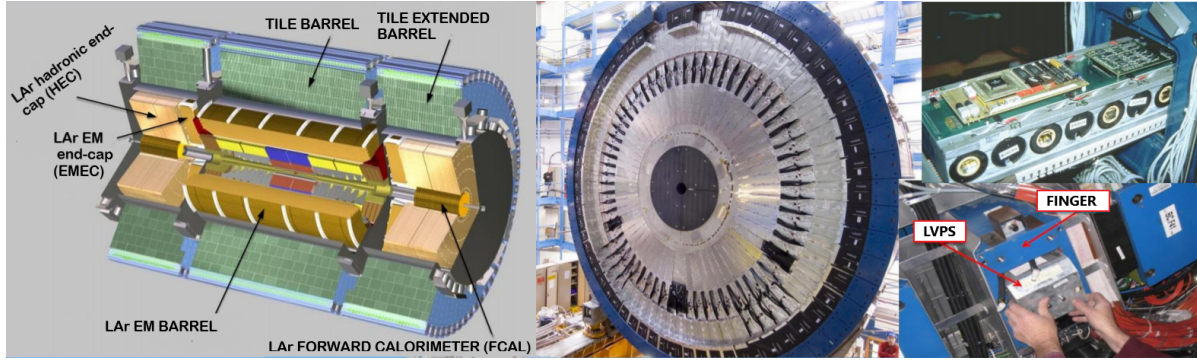


Figure 1: Shows the cross sectional view of the inner barrel (left), modules (middle), electronic drawer and the LVPS system (right) [3].

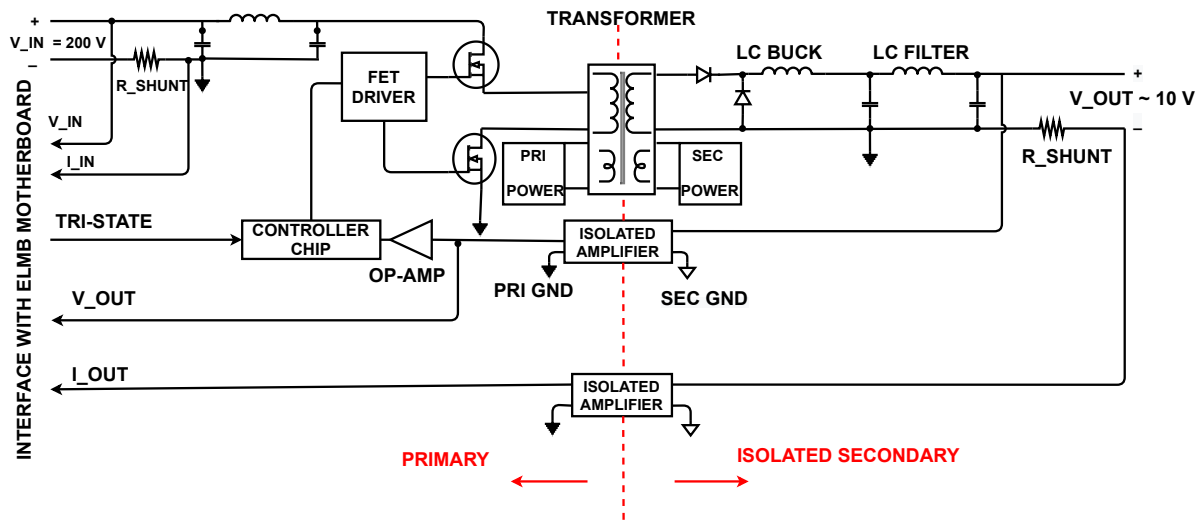


Figure 2: Functional block diagram of the LVPS brick V 8.4.2 produced in RSA [4].

of the transformer, sending energy to the secondary windings. On the output side, an additional inductor-capacitor stage for noise filtering is incorporated when the buck converter is used on the secondary side. The brick includes a built-in remote control and measures that delivers six analog signals (input/output voltages, input/output currents, and two temperatures) to the Embedded Local Monitoring Board (ELMB) is a plug-on board used in LHC detectors for front-end control and monitoring tasks. It communicates using the CAN field bus protocol and provides analog read-out, digital input/outputs and a serial interface to the hardware it is connected to.

3. Burn-in testing

This is a form of accelerated ageing of electronics components. We use this burn-in testing to improve reliability of the LVPS bricks by trying to stimulate a failure mechanism which the bricks experience when they are on normal operation within the TileCal. We use elevated temperature and load to facilitate accelerated ageing. A hardware test station is developed for that purpose. The burn-in electronics, which



Figure 3: BI board prototype for burn-in station.

include a Main board, eight BI boards, two Dummy load boards, and two Load interface boards, with the focus being on the BI boards. Finally, LabVIEW control programme is used to handle the electronics, high voltage power supply, and data monitoring. The BI communicates with each brick to deliver enable and start-up orders, as well as monitor and read all of the measured analog signals, including as voltages, current, and temperature. The other functionality is to receive 200 V from the power supply and deliver it to the bricks; it acts as a switch for the high voltage power supply. We also have a Universal Asynchronous Receiver-Transmitter (UART) interface with the main board and we have a programmable microcontroller on this board with the same dedicated connector as the main board. Furthermore, the board's local power is provided by AC/DC modules and is used within the board.

4. Simulation and Validation of the BI boards

Programming of PIC16F883 for BI boards: The microcontroller (MCU) PIC16F883 plays a vital role whereby it takes signals received from board mounted Analogical/Digital Converter (ADC) chip and transmits the data to main board. The PIC also received digital communication for the Main boards and by extension the LabVIEW control software. This communication allows for the control of the aforementioned functions of the Brick interface boards. It does this by interpreting data it receives from its Input/Output (I/O) peripherals using its central processor. The BI boards provides the control and data acquisition of a brick and its automated process by the LabVIEW control programme. The temporary information that the microcontroller receives is stored in its data memory, where the processor accesses it, uses instructions stored in its program memory to decipher and apply the incoming data. It then uses its I/O peripherals to communicate and execute the appropriate action. To program an MCU, you'll need multiple software packages, including MPLAB X. An Integrated Development Environment (IDE) is used for writing and configuring code. It works in tandem with the Custom Computer Services (CCS) software compiler, which constructs and compiles the code into a Hexadecimal (HEX) source file. The HEX file contains

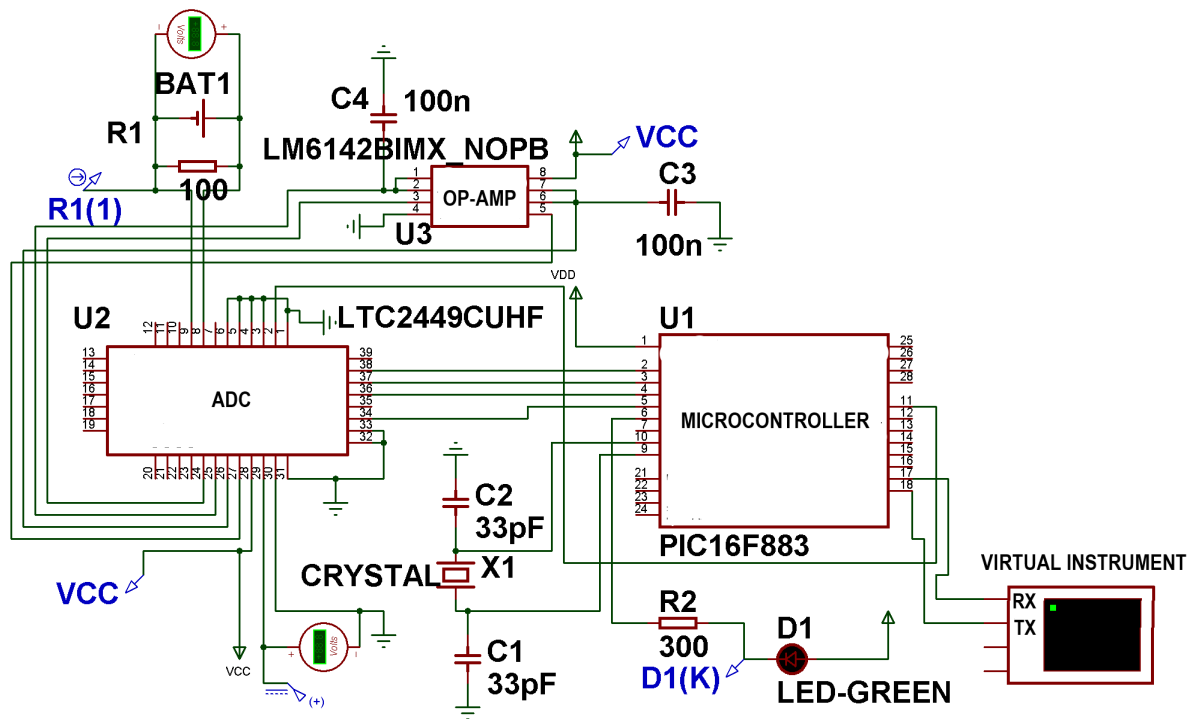


Figure 4: Proteus diagram for the BI boards [6].

settings, configuration information and other data. The MCU only recognises the hex file as a machine code, whereby it carries commands to/from other components. Once the hex file is generated, it is then flashed onto PIC16f883 MCU using the MPLAB X Integrated Programming Environment and PICKIT 4, which allows for debugging and programming of the Microchip PIC [5].

The Proteus framework [6], is used for design, simulation and debugging of a firmware circuit. We used this framework to convert a schematic of the BI board to functional diagram whereby a simulation was carried out to debug the circuits connections. This process is important as it helps in resolving issues that arises on the Printed Circuit Board (PCB) before it is populated. The simulation is also used to check the signal flow and functionality of the PIC as it is the main component on the PCB. In figure 4 we show a simulation of the BI board, whereby I/O peripherals lines of the MCU were checked to observe whether they received or transmitted data.

Validation of BI boards: After the population of the BI PCBs we also perform test on the actual firmware to validate it and draw a correlation as to what was observed on the Proteus simulations. The American Standard Code For Information Interchange (ASCII) characters shown in table 1, are used to request signals from a particular channel of interest. We use the circuit in figure 4 and table 1 and send an arbitrary values to emulate signals that would come from the bricks, a similar test would be carried out on the actual firmware. Before being read and processed by the MCU, the outputs are eventually transformed to digital form. Each sample is assigned a digital value by the ADC, which samples the analog waveform at consistent time intervals. The digital value appears in a binary coded format on the converter's output, which is subsequently

Table 1: ASCII characters sent to ADC to check functionality of each channels

ASCII characters	Function	ADC Channels
1	Brick 15V on	CH0-CH1
2	Brick 15V off	CH2-CH3
3	Brick 200V on	CH4-CH5
4	Brick 200 off	CH6-CH7
g	Read brick input current	CH8-CH9
i	Read brick output current	CH15-CH16
t	Read brick input voltage	CH0-CH1
p	Read brick output voltage	CH2-CH3
e	Read brick temp 1	Ch4-CH5
f	Read brick temp 2	CH6-Ch7
q	Read back address	CH8-CH9

read and processed by the MCU. The terminal program sends out ASCII data in UART format. When you type out a character, the ASCII equivalent is transmitted. The characters are transmitted according to the rate at which you type them. They are not sent at fixed intervals. The ADC, which is at the heart of this BI board, receives and translates all behavioural parameters including voltages, current, and temperature so that the MCU can read and distribute them.

The PC LabVIEW [7] software communicates with all eleven microprocessors in the burn-in station through a single UART layer link passed over a USB bus. UART communication is suitable for embedded system to PC-based microprocessor communications [8]. A Future Technology Devices International (FTDI) integrated circuit is a USB to UART interface used to connect main board with a computer. Only the Main Board physically communicates directly with the PC, and communicates itself directly to every other interface board. Its primary function is to multiplex between the PC and the ten other interface boards. This way, the LabView software on the PC communicates with only one microprocessor at a time. Each interface board for the brick and load contains a 16 bit PIC 16F883 microcontroller. The BI boards provides control and data acquisition of bricks through automated process executed by the LabVIEW control programme. The execution flow diagram shown on figure 5 indicates how the program carries out the tasks as per the users requests, when they're using the GUI of the LabVIEW control programme. The programme enables the user to control and monitor the entire process of the burn-in and record all the information regarding the behaviour of the LVPS bricks. Currently, we are improving the design, structure, and implementation of the LabVIEW control, while preserving its functionality.

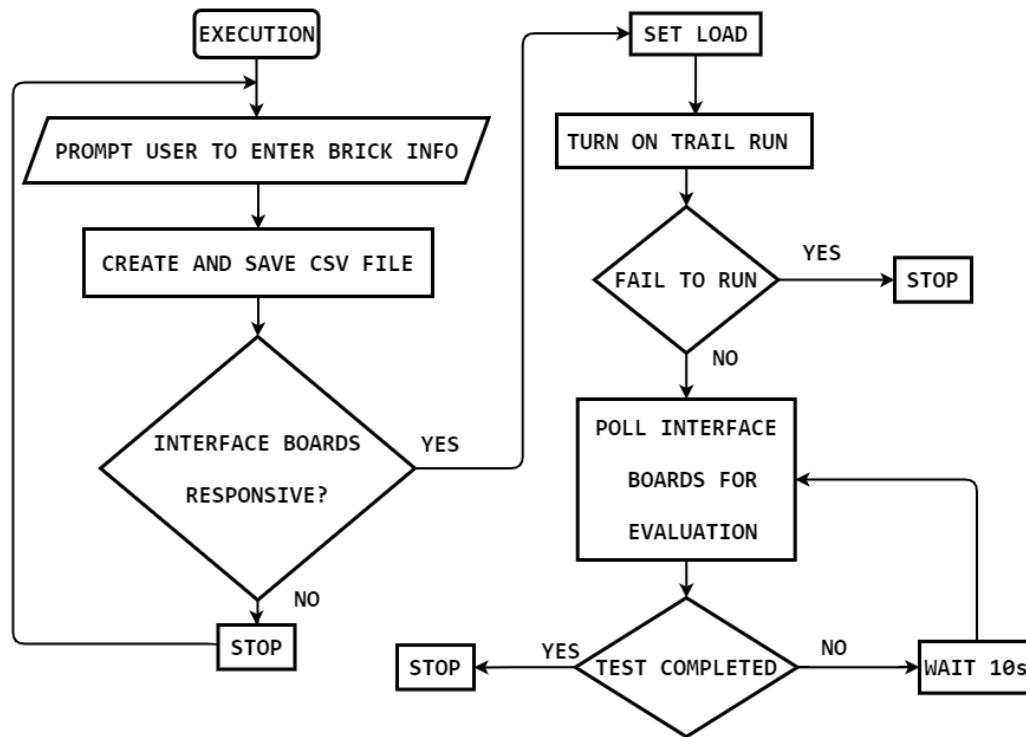


Figure 5: LabView execution flow diagram [9].

5. Summary

The Wits Institute of Particle Physics and iThemba LABS are entrusted with developing and manufacturing over 1000 LVPS bricks for the ATLAS Tile Calorimeter, which will power the detector's front-end electronics during Run 3. Testing mechanisms are necessary for quality assurance to ensure that the design, construction, and production techniques of the bricks are reliable before they are transported to CERN. The burn-in is currently being finalized, with all the boards undergoing functionality testing as well as a review of how they interact with the LabVIEW control programme. An extensive study will be conducted to see how the findings from simulations correlate with the physical firmware outcomes.

References

- [1] ATLAS C (ATLAS Collaboration) 2017 Technical design report for the phase-ii upgrade of the atlas tile calorimeter Tech. Rep. CERN-LHCC-2017-019, ATLAS-TDR-028 CERN Geneva
- [2] Aad G *et al.* (ATLAS) 2008 *JINST* **3** S08003
- [3] Lepota T and Mellado B 2019 *Proc. of the 64th Conf. SAIP* (University of Venda, South Africa: SAIP) pp 256–261
- [4] Nkadimeng E *et al.* 2019 *Proc. of the 64th Conf. SAIP* (University of Venda, South Africa: SAIP) pp 262–267
- [5] Smolnikar M and Mohorcic M 2008 *WSEAS Transactions on Advances in Engineering Education* **5** 83–91
- [6] Lin W M C and Meng C 2008 *Microcomputer Information* **16** 098
- [7] Bitter R, Mohiuddin T and Nawrocki M 2006 *LabVIEW: Advanced programming techniques* (Crc Press)

- [8] Machacek J and Drapela J *2008 Int. Conf. on Modern Technique and Technologies* (IEEE) pp 36–40
- [9] Hibbard M J 2018 *Accelerated Aging of a switching power supply prototype*. Master's thesis
University of Texas - Arlington, USA

A Burn-in test station for the ATLAS Tile-calorimeter low-voltage power supply transformer-coupled buck converters

R Mckenzie¹, E Nkadimeng¹, R Van Rensburg¹, T Lepota¹, N Njara¹
and B Mellado^{1,2}

¹Wits, School of Physics and Institute for Collider Particle Physics, Johannesburg, South Africa

²iThemba LABS, National Research Foundation, PO Box 722, Somerset West 7129, South Africa

E-mail: ryan.peter.mckenzie@cern.ch

Abstract. The Tile Calorimeter (TileCal) is a sampling calorimeter that forms the central region of the hadronic calorimeter of the ATLAS experiment. This detector is to undergo its Phase-II upgrade during Long-Shutdown in preparation for the start of operation of the High Luminosity Large Hadron Collider. The TileCal phase-II upgrade consists of numerous elements such as the Low-Voltage Power Supplies (LVPS) which reside on-detector. A total of 256 LVPSs provide the TileCal on-detector electronics with +10 VDC power. They contain eight transformer-coupled buck converters (Bricks) among other electronics. Access to the Bricks is limited to only once per year due to their location within the inner-barrel. If a Brick experiences a failure it can be offline for up to a year resulting in the front-end electronics that it services being offline for this extended period as well. Therefore, the reliability of the Bricks is a key concern that needs to be addressed during their production. To this end, all Bricks will be required to undergo Burn-in testing. This testing is a form of accelerated aging which allows for the reduction of Brick early-life failures once installed on-detector.

1. Introduction

The TileCal is a sampling calorimeter that forms the central section of the Hadronic calorimeter of the ATLAS experiment [1]. It performs several critical functions within ATLAS such as the measurement and reconstruction of hadrons, jets, hadronic decays of τ -leptons, and missing transverse energy. It also contributes to muon identification and provides inputs to the Level 1 calorimeter trigger system. The sub-detector is located in the pseudorapidity region $|\eta| < 1.7^1$ and is partitioned into four barrel regions. Each barrel region consists of 64 wedge-shaped modules which cover $\Delta\phi \sim 0.1$ rad and are composed of plastic scintillator tiles, functioning as the active media, inter-spaced by steel absorber plates. A Super Drawer (SD) housing the Front-End (FE) electronics is located inside the widest section of each TileCal Module. In the third quarter of 2027, the start of the operation of the High-Luminosity Large Hadron Collider is planned with a foreseen peak luminosity of $5 \times 10^{34} \text{ cm}^{-2} \text{ s}^{-1}$. The resulting environment has necessitated the development of new electronics, both on- and off-detector, to ensure the

¹ The pseudorapidity (η) is defined in terms of the polar angle θ as $\eta = -\ln \tan(\theta/2)$.

Table 1. V8.4.2 Brick protection circuitry trip parameters.

Protection circuitry	Trip parameters
Over voltage protection	11.50 V - 12.00 V
Over current protection	10.24 A - 10.75 A
Over temperature protection	$70^{\circ}\text{C} \geq$

continued peak performance of the detector under high pileup conditions and increased radiation exposure. The development of these electronic components falls under the ATLAS TileCal Phase-II upgrade [2].

2. The Low-voltage power supply (LVPS)

The upgrade of the LVPS falls under the TileCal Phase-II upgrade. The LVPSs form the second stage of a three stage Low-Voltage (LV) system which provides LV power to the FE electronics of the TileCal. The first stage of the LV system resides off-detector and is comprised of Auxiliary boards, that provide on/off control of the individual Bricks within a Low Voltage Power Supply (LVPS), as well as 200 VDC power supplies. An LVPS, of which one is located on the end of every SD, is comprised of eight transformer-coupled buck converters (Bricks), an Embedded Local Monitoring Board (ELMB), an ELMB Mother Board (ELMB-MB), a fuse board, and a cooling plate to which the Bricks are affixed. The Bricks function to step down the 200 VDC power, received from the off-detector power supplies to 10 VDC. The 10 VDC power is then routed to point-of-load regulators located on the FE electronics which perform the final stepping down of the voltage [3].

3. Bricks

A Brick, of which there are 2048 within TileCal, provides a nominal output current of 2.3 A at 10 VDC. At the centre of its design is the LT1681 controller chip. It is a pulse width modulator that operates at a fundamental frequency of 300 kHz. The pulse width is controlled via two inputs, the first of which is a slow feedback path that monitors the feedback voltage with a bandwidth of approximately 1 kHz. The second input is a fast feedback path that monitors the current through the low-side transistor on the primary side. The LT1681 provides an output clock to the Field Effect Transformer (FET) drivers, which perform the switching on the primary side. The design utilizes synchronous switching, That is, both the high-side and low-side transistors turn on and conduct for the duration that the output clock is in the high state, and both are off when the clock is in the low state. When the FETs conduct, current flows through the primary windings of the transformer, which then transfers energy to the secondary windings. A buck converter is implemented on the secondary side of the transformer. The output side also contains an additional inductor-capacitor stage for the filtering of noise. Voltage feedback for controlling the output voltage is provided. The V8.4.2 brick utilizes the same protection circuitry implemented on previous iterations of the Brick. The purpose of this circuitry is to initiate a trip of the Brick if operating parameters exceed a specified range from nominal. The design utilizes three types of inbuilt protection circuitry, Over-Voltage Protection (OVP), Over-Current Protection (OCP), and Over-Temperature Protection (OTP). These circuits, if activated, initiated an immediate shutdown of the brick. Their activation depends on preset thresholds which are stated in Table 1. A trip should be initiated within the given thresholds for the OVP and OCP and above 70°C for the OTP.

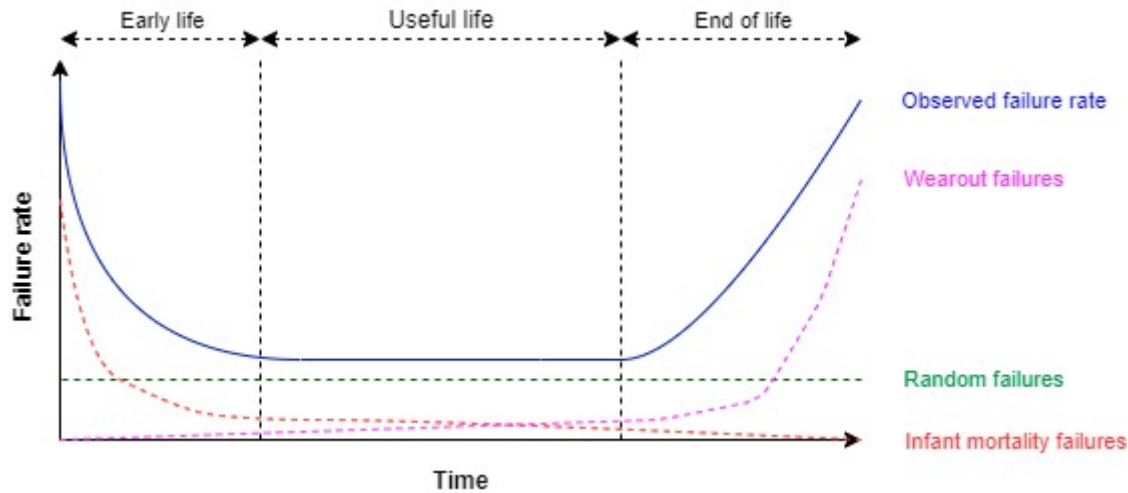


Figure 1. A generalized Bathtub-curve illustrating the failure rate as a function of time as experienced by electronic components.

4. Motivation for Burn-in testing

Access to the LVPS Bricks is of the order of once per year as they are located within the Inner-barrel of the ATLAS detector. Therefore, any Bricks which fail will result in a portion of the Module to which they provide power being offline for the same period of time. Due to this, the reliability of the Bricks is of the utmost importance. The Bricks failure rate and reliability are inversely proportional. This failure rate can be approximated by what is known as a generalized electronics Bathtub-curve which is illustrated in figure 1. We can observe the undesirable high failure rate within the Early-life (Infant-mortality) region. Failures experienced in this region are known as Early-life (Infant-mortality) failures. These failures occur due to unavoidable manufacturing inconsistencies at both the device and component levels as well as numerous other sources such as mechanical damage during transport. Burn-in testing serves to actively address the former sources of Early-life failure and in doing so improves the reliability of the Bricks once installed on-detector. This is achieved by artificially ageing the Bricks towards the more desirable Useful-life region. The accelerated aging causes Bricks that would fail during their Early-lifetime to fail during the Burn-in procedure thereby allowing for them to be repaired before installation. This results in the Brick population obeying an approximately constant failure rate from their time of installation as the Early-life failures have been screened out. A Burn-in station achieves the accelerated aging of the Bricks by implementing a Burn-in procedure.

Table 2. Preliminary Brick Burn-in parameters and nominal Brick operating parameters.²

Parameter	Burn-in	Nominal operation
Brick operating temperature	60° C	35° C
Applied load	5 A	2.3 A
Run-time	8 hours	-

5. The Burn-in procedure

The Burn-in procedure subjects the Bricks to sub-optimal operating conditions which function to stimulate failure mechanisms within the Bricks. These conditions need to fall within the

extrema allowed for by the Brick design and operation. There are two reasons for this. The first of which is related to effective Burn-in and the second is related to the implementation of the Burn-in procedure. Firstly, the failure mechanisms stimulated must be of the kind that can be experienced during operation within TileCal. Inducing failures by the application of excessive operating conditions such as impossibly high loads serves no purpose. This as these failures will not be due to unavoidable manufacturing inconsistencies but are rather a result of the Bricks being operated outside of their design specifications. The second reason for limiting the Burn-in parameters¹ provided in Table 2 to within the Bricks final operating extrema is due to the Bricks inbuilt protection circuitry. A Brick will initiate a trip if the OCP, OVP or OTP trip parameters are met. If the operating parameters are set to within the variance of the trip points maxima intermittent Brick trips would occur during the Burn-in procedure. Whereas, if the parameters are set higher than this variance the Bricks will start and immediately trip.

6. The Burn-in test station

The Burn-in station is of a fully custom design. This was necessitated by the unique design of the Bricks and also allows for the fine-tuning of the applied Burn-in parameters. It consists of six distinct elements namely the test-bed, hardware, cooling system, control software, custom PCB Programmable Integrated Circuit (PIC) firmware, and custom instrumentation drivers.

6.1. Test-bed

The Test-bed is primarily responsible for housing the Burn-in station electronic hardware, heat sinks, water manifolds (housed externally) and the 8 Bricks undergoing the burn-in procedure. Secondary roles include providing electrical and thermal insulation which function to provide a safety measure for the operators and to provide a temperature-controlled environment for the Bricks, respectively.

6.2. Hardware

The Burn-in station hardware is composed of a programmable DC power supply (BK precision XLN600-26), a PC, and custom Printed Circuit Boards (PCBs) as illustrated in figure 2. The custom electronic boards are subdivided into four types. These are the Main Board (MB), Brick-Interface (BI) board, Dummy-Load (DL) board, and the Dummy-load Interface (DI) board.

Mainboard: There is one MB per Burn-in station. It functions purely as a multiplexer to each individual interface board [4]. This allows the LabVIEW control software on the PC to communicate via UART to each individual PIC located on the interface boards.

Brick-interface boards: There are eight BI boards per Burn-in station with one associated with each of the Bricks undergoing the burn-in procedure. These boards provide control, digitization, and transmission functions to their respective Bricks. The control functions can be subdivided into two. The first function allows for the Brick to be powered on or off via the Tri-state signal line as in an LVPS. The second allows for the on/off control of the input 200 VDC provided to the Brick by the DC power supply. The BI board digitizes the analog behavioral parameter signals received from the Brick by use of a 16-bit analog-to-digital converter. These parameters are the input voltage, input current, output voltage, output current, and two temperatures. The now digitized signals are transmitted to the PC via the MB.

Dummy-load boards: A Burn-in station contains two DL boards with each containing four independent current loads which receive the output power from four Bricks. The output power is shunted through a MOSFET operating in the ohmic region thereby converting it to heat to be

¹ These are considered to be preliminary parameters as the Brick design has yet to be finalized due to pending radiation studies. Changes to the design of the Brick will impact the Burn-in parameters.

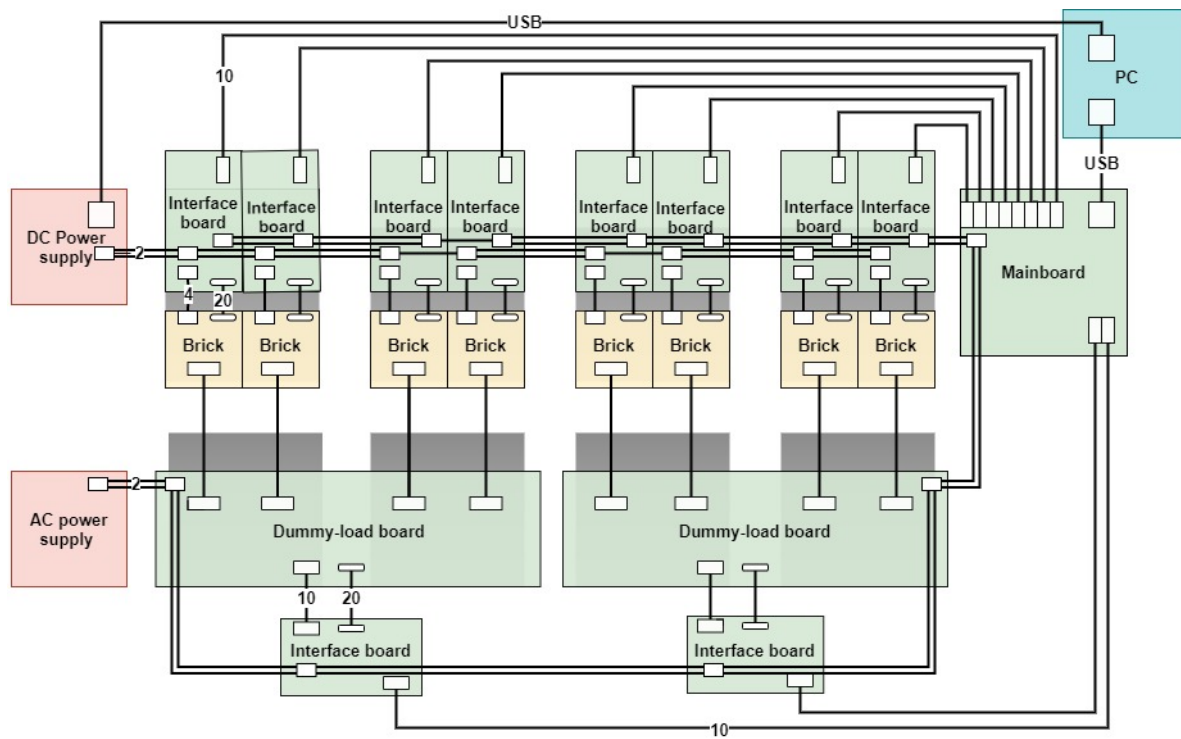


Figure 2. A block diagram of the Burn-in station hardware.

dissipated. The applied load to the Bricks is controllable allowing for the application of different loads if need be. This provides flexibility in the Burn-in station operation.

Dummy-load interface boards: There are two DI boards per Burn-in station, one per Dummy-load board. These interface boards provide control, digitization, and transmission functions to their associated Dummy-load board. An individual DI board is responsible for shifting bits into a digital-to-analog converter located on the DL board in order to control the load current applied to each of the four Bricks. The LI board digitizes the output Brick voltage and current sampled at the DL board. This is done for each of the four Bricks attached to the associated DL board.

6.3. Cooling system

Active cooling of the Burn-in station is required due to the presence of two heat sources within the test-bed. The first source consists of the 8 Bricks. Heat is generated by the Bricks as a result of the inefficiency of the step-down process. The second heat source consists of the two Dummy-Load boards which convert the output power received from the eight Bricks into heat. The heat produced by these two sources is sunk into water cooled plates which are identical to those within a TileCal LVPS. This replication of the cooling hardware, and in particular the cooling hardware which comes into contact with the Bricks, creates an identical thermal distribution throughout a Brick during Burn-in.

The cooling system topology consists of four independent cooling channels, arranged in parallel, each of which is composed of two cooling plates connected in series. The four Brick cooling plates comprise the first row of cooling plates. They receive the cooled water from the water-chiller via a 1-to-4 intake manifold. It is important that these cooling plates receive the coolant first. This as the temperature of the Bricks which is controlled by the water chiller is a key parameter of the Burn-in procedure. The intake coolant temperature can be calibrated

to produce the desired Brick Burn-in operating temperature. The now warmer coolant flows to the second row of cooling plates. A single DL board has its four MOSFETs directly attached to two cooling plates in this row with the other DL board occupying the second pair of cooling plates. The now hot coolant merges into a 4-to-1 manifold after which it travels to the water chiller to be cooled and recirculated.

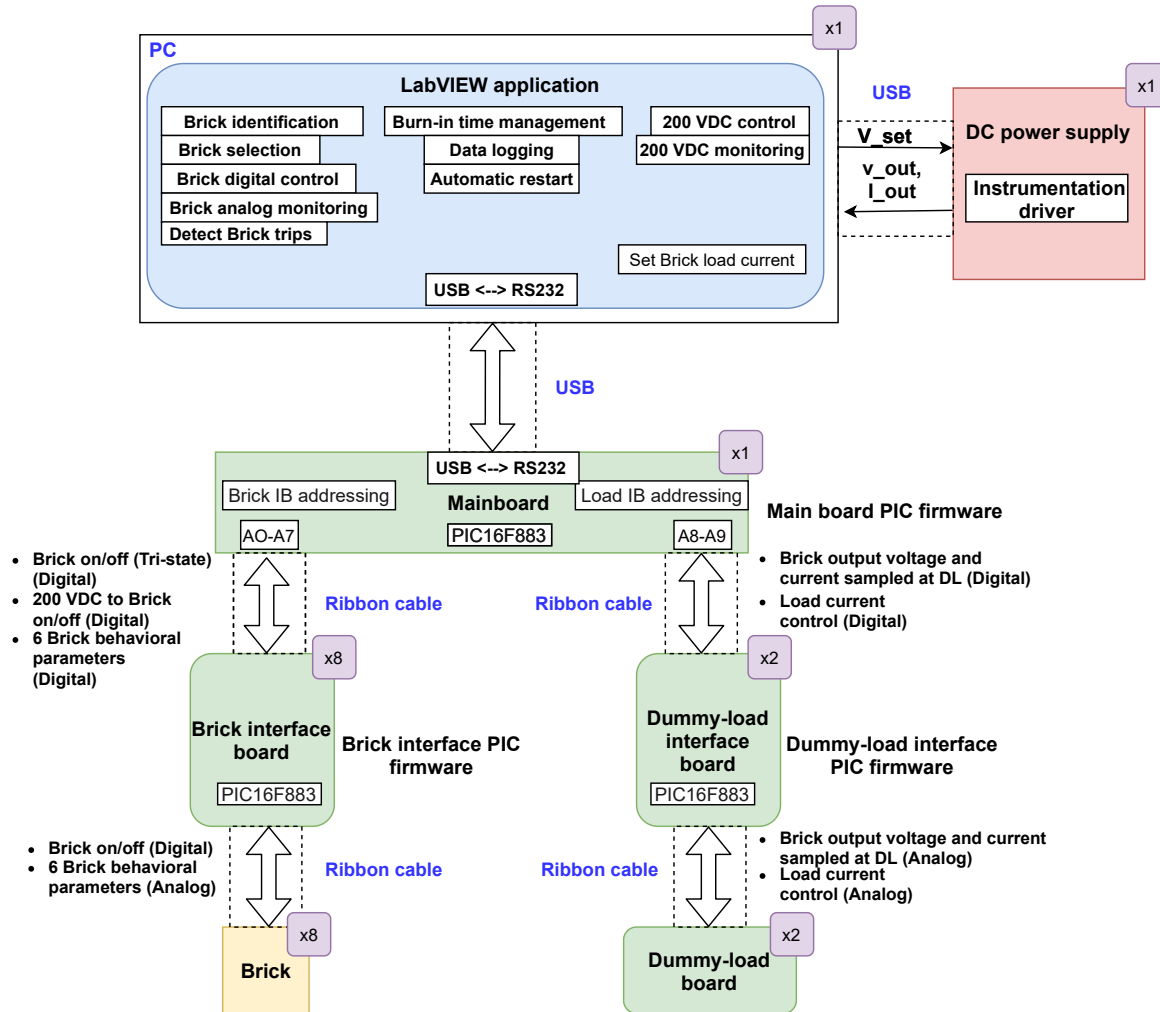


Figure 3. A simplified block diagram illustrating the Burn-in station data flow.

6.4. Software

The software required for the operation of a Burn-in station can be divided into three categories. These are the LabVIEW control and monitoring application, the PCBs (PIC) firmware, and high voltage power supply instrumentation drivers. The relationships between these three categories can be observed in figure 3.

LabVIEW application: A custom application for the Burn-in station has been developed utilizing the LabVIEW graphical development suit. This application provides control, monitoring, and data collection capabilities. It allows for the automated implementation of the Burn-in procedure with minimal input from the user.

PIC firmware: All of the Burn-in station PCBs, excluding the DL boards, make use of a PIC. The PIC (PIC16F883) is a microcontroller which has the capability to be programmed with

customized firmware. The function of the PIC is determined by the specific firmware which is programmed which is dependant on the PCB type. Therefore, a Burn-in station requires specific firmware for the MD, BI board, and DI board. With the BI board a DI board containing a subset of firmware due to each of these PCBs possessing a unique address (AO-A7 and A8-A9 respectively).

Instrumentation driver: A custom LabView driver was also created to communicate with the DC power supply via the LabVIEW VISA communications layer, over Ethernet.

7. Burn-in station development status

Two Burn-in stations are currently undergoing construction. The Test-beds for both stations have been completed with the cooling system having been fully commissioned. The hardware for the first station is currently undergoing testing before its installation within a Test-bed. The control software is the final outstanding deliverable and is in an advanced state of development.

8. Conclusions

The context of TileCal LVPS Brick Phase-II upgrade was provided with a detailed circuit overview of an LVPS Bricks also having been covered. An emphasis was placed on the Bricks in-built protection circuitry and the associated trip parameters. The motivation for and application of Burn-in testing was discussed in detail. This was followed by a concise breakdown of the Burn-in station hardware and software required to implement the Burn-in procedure. The proceedings then culminated with the current Burn-in station development status.

References

- [1] The ATLAS collaboration 2008 Tech. Rep. 08 URL <https://doi.org/10.1088/1748-0221/3/08/s08003>
- [2] The ATLAS collaboration The ATLAS Tile Calorimeter performance and its upgrade towards the High Luminosity Large Hadron Collider Tech. rep. CERN
- [3] The ATLAS collaboration Technical Design Report for the Phase-II Upgrade of the ATLAS Tile Calorimeter Tech. rep. CERN
- [4] Hibbard M J 2018 *ACCELERATED AGING OF A SWITCHING POWER SUPPLY PROTOTYPE* Master's thesis University of Texas Arlington URL <https://rc.library.uta.edu/uta-ir/handle/10106/27761>

Heat Transfer Enhancement of a Thermal Interface Material for Heat Sink Applications Using Carbon Nanotubes

O Mouane¹, E Nkadimeng¹, R Mckenzie¹, R Van Rensburg¹, E Sideras-Haddad¹ and B Mellado¹

¹ School of Physics and Institute for Collider Particle Physics, University of the Witwatersrand, Johannesburg, Wits 2050, South Africa

E-mail: othmane.mouane@cern.ch

Abstract. A functional material of carbon nanotubes composite is investigated to be utilised as a thermal interface material in the low voltage power supply electronics as part of the upgrade of the ATLAS detector at CERN. These electronics, located inside the detector, produce heat by Joule heating and it is important to dissipate the generated heat in order to maintain the continuous full operation of the detector. The thermal interface material is a composite in a paste form, based on carbon nanotubes and Silicone heat transfer compound. The goal behind the implementation of the carbon nanotubes in the thermal interface material was to increase the thermal transfer from the electronics to the heat sink by the intermediary of the aluminium oxide (Al_2O_3) posts. The temperature of the thermal posts was read by means of an automated test stand built in house and controlled with a LabVIEW interface. The composite of carbon nanotubes and silicone compound were prepared by simple process in order to achieve a homogeneous mixture. Also, the study included the investigation of the effect of the carbon nanotubes in the nano-composite from which it is found that the optimum heat transfer is reported for a thermal interface material of 1% of carbon nanotubes.

1. Introduction

As part of the phase-II upgrade of the ATLAS detector at CERN, a new Low Voltage Power Supply (LVPS) brick is being manufactured at the University of Witwatersrand (figure 1) [1–3]. The LVPS brick is a six squared layer board with a dimension of 80.26 mm^2 , and comprises electronic components such as transformers, transistors, and inductors. In these electronics, the flowing electrical current coupled with the resistance cause the generation of heat. Hence, the main electronic components are bonded to cylindrical ceramic posts (Al_2O_3), by means of a thermal compound, in order to sink the heat. The important role of the LVPS is the generation of the power (voltage and current) to the Tile Calorimeter (TileCal is a part of ATLAS) distributed front-end electronics [4]. The accelerator is designed to host the electronics inside the particle detector [2,3] and therefore, the electronics operate in extreme conditions; exposure to radiation, direct current magnetic field, limitation of the space, and with a cooling system based on water [4]. Hence, for a proper functioning of the detector, it is mandatory to protect the electronics operating under a such condition from damage, overheating, and to expand their life-span.

The most practical way to solve the issue of overheating within the electronic devices is to employ thermal conductors used in thermal applications such as thermo-electric devices [5] and functional

materials [6]. In order to dissipate the heat, as it is the case with the LVPS brick, it is required to use a functional Thermal Interface Materials (TIMs).

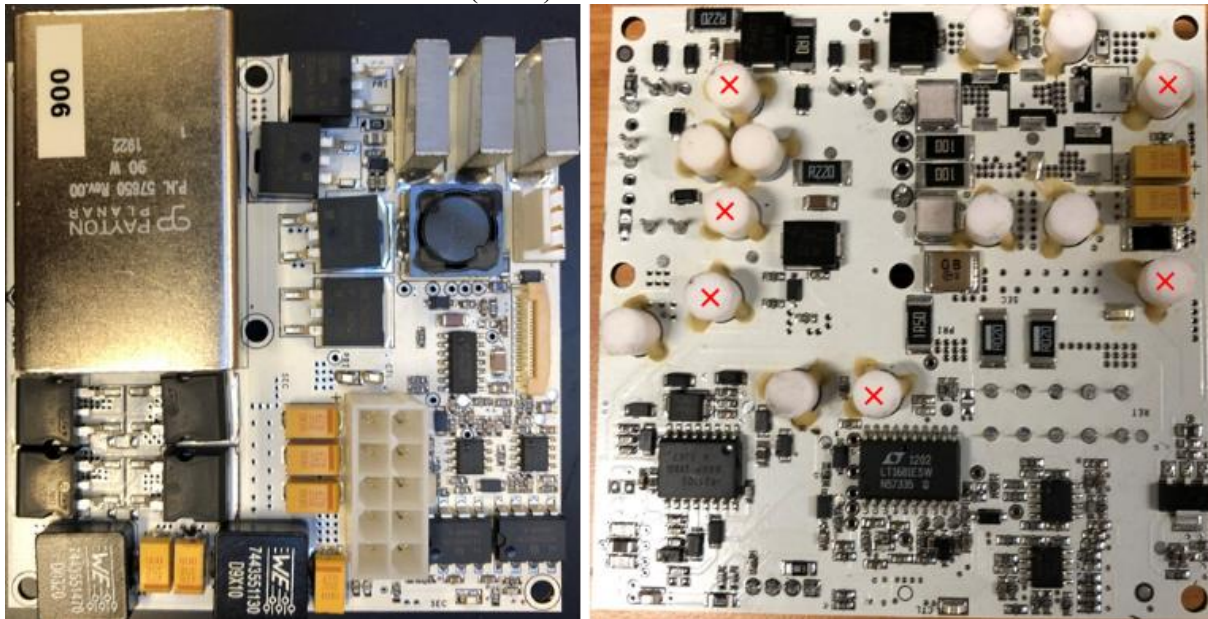


Figure 1. The LVPS brick manufactured at Wits. The marks (x) locate the cylindrical Al_2O_3 posts that conduct the generated heat to the sink. A thermal compound is applied between the interfaces of the electronics and the posts to maintain a good thermal conduction.

TIMs are materials with high thermal conductivity placed between a heat source and a heat sink to dissipate the heat effectively, increase the contact area and reduce the air gaps [7]. The conventional and commercial TIMs are made of polymer-based material (silicone) impregnated with highly thermally conductive particles, mainly alumina, zinc oxide, graphite, silver. As far as the technological development is concerned, the heat transmission offered by the commercial TIMs is still considered to be inefficient for many contemporary applications either in micro or nano-electronics [8,9].

In this proceedings, we report on the enhancement of the heat transfer of a commercial TIM by incorporating Carbon Nanotubes (CNTs) impregnation. The implementation of CNTs in heat sink applications are motivated by their good thermal conductivity of $4840\text{--}5300 \text{ W}\cdot\text{m}^{-1}\cdot\text{K}^{-1}$ [6,9] and also by their mechanical properties needed since the TIMs have to be molded between two interfaces and under high pressure. In this study, we use an experimental setup that simulates the operating of the LVPS brick in order to improve the heat transfer. A simple process to prepare the TIMs was developed and the effect of the amount of CNTs on the heat transfer was investigated as well.

2. Experimental methods

The investigated TIMs in this study is a composite of CNTs and a thermal epoxy. The CNTs were synthesized by chemical vapour deposition in the department of chemistry, University of Witwatersrand. For more details in regard to the synthesis method, one can refer to [10,11]. The commercially purchased thermal epoxy (Unick Chemical Corp.) is a silicone based compound in which zinc oxide particles were diffused.

The preparation of the TIM based on CNTs follows a precisely developed protocol (figure 2), which is considered simple in comparison to methods reported in the literature [12–16]. First, the conglomerated CNTs in a powder form were dispersed in acetone by sonication at room temperature for 30 minutes, then, the thermal epoxy was added. The solution comprised CNTs, epoxy and acetone and was sonicated for a second time for a duration of not less than 60 minutes at 55°C . At a such temperature, the diffusion of the CNTs in the epoxy can be facilitated together with the evaporation of the acetone in order to fabricate the TIM in a required paste (greasy) form. Also in order to investigate the effect of the

CNTs on the heat transfer improvement, the amount of CNTs was varied in a range between 0 to 10 % of CNTs within the TIMs.

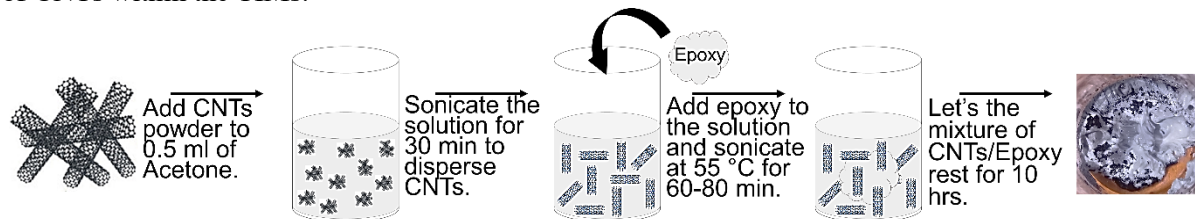


Figure 2. The different steps for the preparation of TIM based on CNTs. The picture shows the TIM of CNTs ready for use. The black spots are non-dispersed CNTs that were hanging on the acetone surface before evaporation.

In order to test the improvement of heat transfer, an experimental setup that simulates the functioning of the LVPS brick was designed, as shown in figure 3. The setup is composed of resistors for heat generation and an aluminum plate as heat sink. The conduction of the heat from the resistors to the heat sink was maintained by means of ceramic posts (Al_2O_3), as in the LVPS brick. The temperature was measured using of thermocouples connected to the posts throughout the experiment and recorded by a Data Acquisition system which is controlled by LabVIEW software.

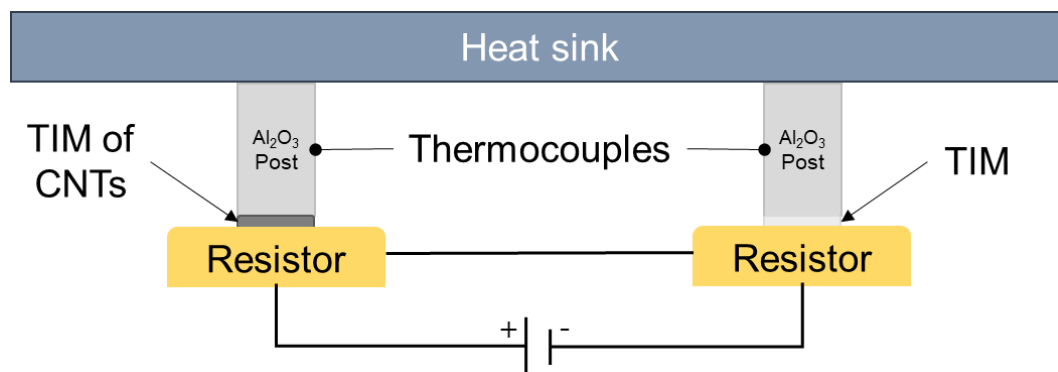


Figure 3. The experimental setup in use to mimic the LVPS bricks to test the TIMs. It consists of two identical resistors, aluminum plate, Al_2O_3 posts, thermocouples, and power supplies. In order to compare the heat transfer, the TIM of CNTs was applied on one post and the commercial TIM non-containing CNTs on the second post. The temperatures were recorded continuously with a data acquisition system for more than 8 hours.

3. Results and discussion

The recorded temperatures of the posts are presented in figure 4. The plots show the progress of temperatures in the posts for a duration of over 8 hours using TIMs with composition of 0 (without CNTs), 0.5, 1, 5, and 10 % of CNTs.

In figure 4, all the curves have similar trend and are characterised by a temperature rise during the first hours, after which a visible plateau is reached. In fact, the steady behaviour of the temperature was preserved over the 24 hours of measurements, as reported in figure 5 (graph on the left).

In addition, the plots show a temperature gap between the two posts (between the orange and blue lines). It is shown clearly that the temperatures of the posts with TIMs containing CNTs are lower by comparison to temperatures of posts with TIMs only (0% of CNTs), except for the TIM with 10% of CNTs. These results are highly reproducible and consistent as confirmed by a large number of measurements. Moreover, this temperature gradient, noted T_{diff} , varied as a function of the amount of CNTs incorporated in the TIM, as summarized in the right graph of figure 5.

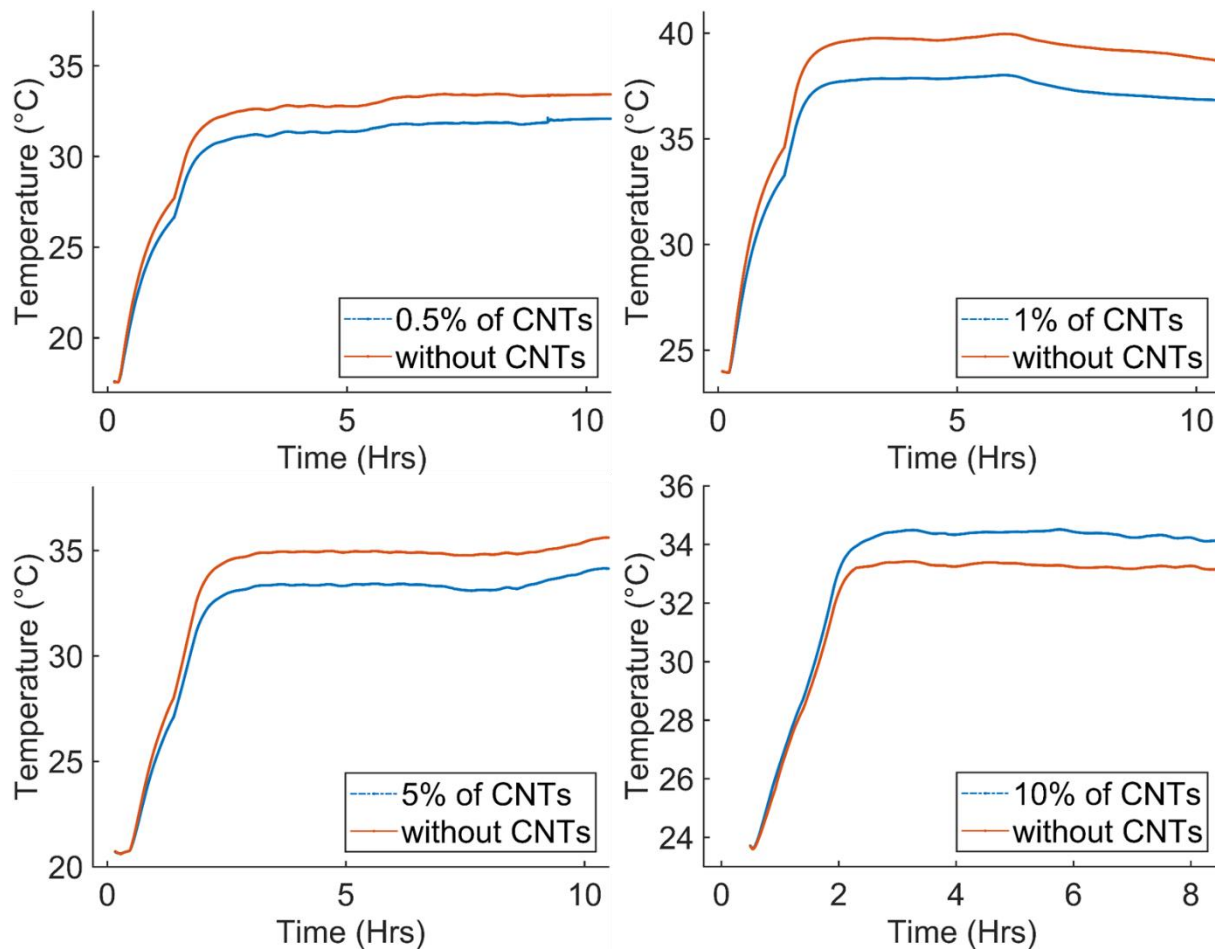


Figure 4. The measured temperatures of the two posts by the use of the setup described in figure 3. The plots show the dependence of the temperature gradient to the amount of CNTs in the TIMs. The gradient temperature is observed to be positive except for TIM with 10 % of CNTs.

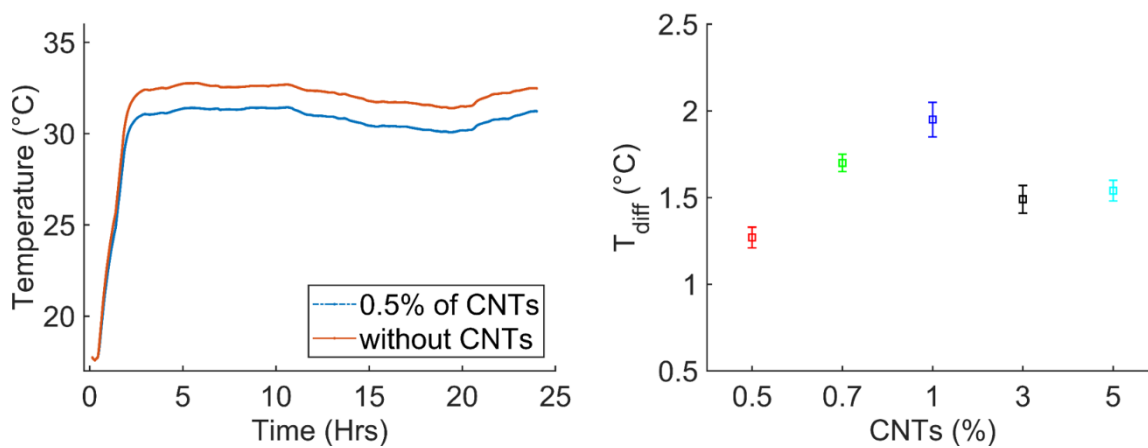


Figure 5. The measured temperatures for over 24 hours for TIM with (0.5%) and without CNTs (left). The plot shows the steady temperature gradient over the flat part of the curve. On the right, the temperature gradients T_{diff} ($T_{diff} = T_{without\ CNTs} - T_{CNTs}$) for different TIMs. The calculated T_{diff} is the average along the plateau of the curve.

From the results reported above, the heat transfer is found to improve substantially by incorporating CNTs in the thermal compound. This claim is supported by the proportionality between the heat transfer (Q) and the temperature difference ΔT ($\Delta T = T_{in} - T_{out}$) over the posts. Thus, by comparing the temperatures of the posts, noted as T_{out} , one can deduce whether an improvement of the heat transfer takes place. The amount of offered heat to the post corresponding to temperatures T_{in} was equal at the interfaces (resistors and applied voltage were identical while running the experiment), which means a lower temperature T_{out} implies a higher heat transfer Q .

Based on figure 4, the integration of CNTs in the thermal epoxy to a certain amount (<5%) showed an increase in the heat transfer from the heat source to the heat sink. The increase reached a maximum with the use of TIMs with 1% of CNTs (figure 5). The improvement of the heat transfer can be due to a homogenous dispersion of the CNTs within the TIMs, as well as to the coupling between the CNTs and thermal epoxy which results in the enhancement of the thermal conductivity of the prepared TIMs. Also, it was observed that by the use of a large amount of CNTs, it became difficult to mix and disperse the carbon nanomaterials in the epoxy homogeneously, and the outcome was mostly a TIM in a solid state. The fabricated TIM with 10% of CNTs was a clear example of the late observation which explains the deterioration of the heat transfer.

4. Conclusions

In this work, the enhancement of the thermal properties of a commercial compound by CNTs impregnation was presented. The preparation of the TIM with CNTs followed a simple process based on sonication. The results showed the improvement of the heat transfer due the application of TIMs containing CNTs at the interface of the posts. Also, the achieved experiments revealed the increase of the heat transfer in function of the amount of CNTs injected and the reproducibility of the results. In addition, it was deduced that the optimum heat transfer was observed for TIMs with 1% of CNTs. Moreover, the fabricated TIM offers a potential use in applications to protect expensive components from overheating such as micro and nano-electronics. The use of the fabricated TIM in the LVPS brick will increase the transfer of the heat to the sink and protect the electronics from overheating and damage, which will maintain the detector in a constant full operation. In a future work, different types of carbon nanomaterials will be investigated, as well the increase of their homogeneous dispersion in the epoxy.

Acknowledgments

We thank Prof. Neil Coville and his group (department of Chemistry, University of Witwatersrand) for providing the carbon nanotubes.

References

- [1] Nkadameng E, Lepota T, Van Rensburg R, Sandrock C and Mellado B 2019 Low Voltage Power Supply production, hardware upgrade and testing for the ATLAS Tile-Cal Front-End Electronics System *2019 64th Annual Conference of the South African Institute of Physics (SAIP)* pp 257–62
- [2] Mckenzie R 2021 The ATLAS Tile Calorimeter performance and its upgrade towards the High Luminosity Large Hadron Collider *2021 XXVIII International Workshop on Deep-Inelastic Scattering and Related Subjects (SciPost Physics)*
- [3] Nkadameng E 2021 Performance of the Tile Calorimeter Demonstrator system for the ATLAS Phase-II Upgrade *2021 9th Annual Large Hadron Collider Physics (LHCP 2021) (Proceedings of Science)*
- [4] Palan B and Hruska I 2007 Radiation-tolerant custom made low voltage power supply system for ATLAS/TileCal detector *Topical Workshop on Electronics for Particle Physics (CERN)* p 55
- [5] He R, Schiering G and Nielsch K 2018 Thermoelectric devices: a review of devices, architectures, and contact optimization *Advanced Materials Technologies* **3** 1700256
- [6] Kumanek B and Janas D 2019 Thermal conductivity of carbon nanotube networks: A review *Journal of materials science* **54** 7397–427

- [7] Demko M T, Yourey J E, Wong A, Lin P-Y, Blackman G S, Catlin G C and Yahyazadehfir M 2017 Thermal and mechanical properties of electrically insulating thermal interface materials 2017 16th IEEE Intersociety Conference on Thermal and Thermomechanical Phenomena in Electronic Systems (ITherm) (IEEE) pp 237–42
- [8] Chu K, Wu Q, Jia C, Liang X, Nie J, Tian W, Gai G and Guo H 2010 Fabrication and effective thermal conductivity of multi-walled carbon nanotubes reinforced Cu matrix composites for heat sink applications *Composites Science and Technology* **70** 298–304
- [9] Hsieh C-T, Lee C-E, Chen Y-F, Chang J-K and Teng H 2015 Thermal conductivity from hierarchical heat sinks using carbon nanotubes and graphene nanosheets *Nanoscale* **7** 18663–70
- [10] Deshmukh A A, Mhlana S D and Coville N J 2010 Carbon spheres *Materials Science and Engineering: R: Reports* **70** 1–28
- [11] Qin L 1997 CVD synthesis of carbon nanotubes *Journal of materials science letters* **16** 457–9
- [12] Khaleed A A, Bello A, Dangbegnon J K, Madito M, Olaniyan O, Barzegar F, Makgopa K, Oyedotun K O, Mwakikunga B W, Ray S, and others 2017 Solvothermal synthesis of surfactant free spherical nickel hydroxide/graphene oxide composite for supercapacitor application *Journal of Alloys and Compounds* **721** 80–91
- [13] Roro K T, Mwakikunga B, Tile N, Yalisi B and Forbes A 2012 Effect of Accelerated Thermal Ageing on the Selective Solar Thermal Harvesting Properties of Multiwall Carbon Nanotube/Nickel Oxide Nanocomposite Coatings ed M S Abdel-Mottaleb *International Journal of Photoenergy* **2012** 678394
- [14] Khaleed A, Bello A, Dangbegnon J, Madito M, Ugbo F, Akande A, Dhonge B, Barzegar F, Momodu D, Mwakikunga B, and others 2017 Gas sensing study of hydrothermal reflux synthesized NiO/graphene foam electrode for CO sensing *Journal of Materials Science* **52** 2035–44
- [15] Taziwa R, Meyer E L, Sideras-Haddad E, Erasmus R M, Manikandan E and Mwakikunga B W 2012 Effect of Carbon Modification on the Electrical, Structural, and Optical Properties of TiO₂ Electrodes and Their Performance in Labscale Dye-Sensitized Solar Cells ed L Menon *International Journal of Photoenergy* **2012** 904323
- [16] Saasa V, Mokwena M, Dhonge B, Manikandan E, Kennedy J, Murmu P P, Dewar J, Erasmus R, Whaley M F, Mukwevho E, and others 2015 Optical and structural properties of multi-wall-carbon-nanotube-modified ZnO synthesized at varying substrate temperatures for highly efficient light sensing devices *Sensors & Transducers* **195** 9

Digital data acquisition system for neutron metrology

Chloé Sole¹, Andy Buffler¹, Tanya Hutton¹, Tom Leadbeater¹,
Vincent Gressier² and Richard Babut²

¹Department of Physics, University of Cape Town, Rondebosch, South Africa

²Neutron Metrology and Dosimetry Laboratory, Institut de Radioprotection et de Sûreté Nucléaire, Cadarache, France

E-mail: andy.buffler@uct.co.za

Abstract. Within the neutron metrology and spectrometry community digital pulse processing systems are being developed for measurements of fast neutron fields in a wide variety of contexts. Investigations have been completed into the suitability of a CAEN DT5730 digitiser unit as an alternative to a traditional analogue system for data acquisition for fast neutron metrology. Experiments were undertaken at the fast neutron facilities of AMANDE using a BC501A scintillation detector and both the DT5730 digitiser and an analogue system based on NIM electronics and an MPA-3 multichannel analyser acquisition unit, under identical conditions using a broad range of beam conditions available at the AMANDE facility. The measurements covered an energy range from 0.5 MeV to 20 MeV, over a large range of intensities allowing for the digital system to be benchmarked against the metrology standard acquisition system for a large range of contexts. The results of the study indicate that digital data acquisition systems have matured, such that they may be considered for neutron metrology measurements in the laboratory and in field.

1. Introduction

Metrology is the science of measurement, and fundamentally has as its focus the activity of counting with reference to a set of standards. Neutron metrology may be understood as the process of counting free neutrons, with the two main quantities of interest being the number of neutrons (either crossing a region of interest or emitted by a source), and the energy distribution of these neutrons. The measurement result is often presented as a fluence rate (number of neutrons per unit time), which can further be presented as a function of the neutron energy. This process is often complicated by the energy dependent fluence being influenced by the directionality of the neutron source [1].

Neutron fields can vary widely with respect to context, energy and fluence [2], with each of these aspects introducing an additional degree of complexity. The energy of neutron fields can range from cold neutrons produced at facilities like CNRF [3] and HANARO [4], below the meV range, to very high energy (on the order of GeV) neutrons produced in accelerator facilities or by cosmic rays interacting with the atmosphere. Similarly, the possible intensities span from a few neutrons $\text{cm}^{-2} \text{s}^{-1}$, having importance to radiation protection, to 10^{15} neutrons $\text{cm}^{-2} \text{s}^{-1}$, occurring at the core of high intensity nuclear fission reactors.

The way in which neutrons are detected varies greatly with energy and intensity. Neutron interaction cross-sections are highly dependent on the material type and the energy of the irradiating neutrons [5, 6]. On the higher end of the intensity range, detecting individual

neutron events becomes more difficult and estimating the number of neutrons interacting with the material often relies on a calculation rather than direct measurement [1].

Direct measurements of neutron energy and fluence requires well characterised response functions for the detector used if spectrum unfolding is required. Unfolding relies on convolving the response functions to fit the measurement to determine the fluence distribution as a function of energy [7]. For these measurements pulse shape discrimination techniques are required to separate the events associated with incident neutrons and gamma-rays.

Metrology laboratories such as the IRSN (France), PTB (Germany), NPL (UK) and iThemba LABS (South Africa), use a BC501A organic liquid scintillator coupled to an analogue pulse processing acquisition system as the reference for measurements of neutron fields. These reference systems are based on NIM-standard pulse processing modules and an analogue ADC-based multi-parameter analyser (MPA) [8]. These systems are expensive, difficult to use outside of the laboratory and have a limited technological horizon.

The advent of digital data acquisition systems (dDAQs) for nuclear radiation measurements has brought several new approaches to the acquisition and analysis of data. However, rigorous benchmarking is required before such a system can be deployed in a neutron metrology scenario. A comparison of an off-the-shelf CAEN DT5730 digitiser [9] to the metrology standard analogue acquisition system is presented.

The measurements, made at the AMANDE facility [10], were taken with a BC501A detector coupled with either the standard analogue metrology acquisition system (MPA-3) [11, 8] or an off-the-shelf CAEN DT5730 digitiser [9]. The measurements covered an energy range from 0.5 MeV to 20 MeV, over a large range of intensities giving an effective range for the neutron fluence rates at the position of the detector of $10^3 \text{ cm}^{-2} \text{ s}^{-1}$ to $10^4 \text{ cm}^{-2} \text{ s}^{-1}$. Unfortunately the detector is also sensitive to gamma photons, and mixed neutron-gamma fields always occur within the contexts studied. To account for this, responses for both neutron and gamma events are recorded, and pulse shape discrimination (PSD) is used to differentiate between neutron (proton recoil) and gamma (electron recoil) events. The results for the measurements of the 7.000(6)MeV neutron field at the standard beam current of 0.57 μC are presented.

The energy and intensity response for both systems and digital configurations were investigated based on the unfolding of measured light output spectra using an existing neutron response matrix for the detector. The quality of the measured neutron spectra were compared through uncertainty budgets designed for both systems.

2. Results and Analysis

The analogue acquisition system determines the light output parameter (L) through the integration of the slow output (dynode) of the detector. The analogue pulse shape parameter (S) is determined using the zero cross over method [12, 13, 14] and implemented using a FAST Comtec 2160A PSD unit [11]. The digital measurements consisted of sampling the anode waveform and determining the analysis parameters post acquisition. The light output parameter was calculated as the integral of the sampled waveform for an integration time of 500 ns, and the pulse shape parameter was determined through the charge comparison method [15, 16, 17]. The digital pulse shape parameter was defined as the ratio of an integral over 30 ns to L .

The measurements of events as a function of S and L allow for the neutron events to be selected for through pulse shape discrimination (PSD) techniques [11, 18]. The events as a function of S and L can be seen in figure 1 for the MPA-3 and DT5730 acquisition systems, where L is presented in a MeV_{ee} scale defined by the units of MeV for recoil electrons. The measurements are in good agreement with each other and exhibit the same features. The only significant difference being related to pile up event management which is attributed to the difference in the definition of S .

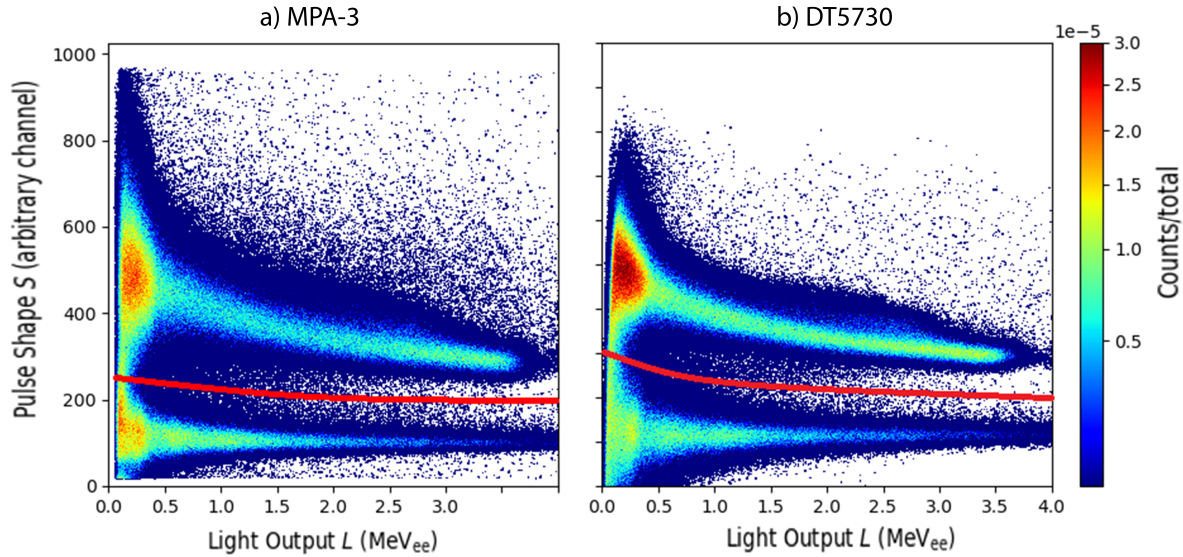


Figure 1. Events as a function of S and L (MeV_{ee}) for (a) the MPA-3 acquisition system and (b) the DT5730 CAEN digitiser for the 7.000(6) MeV neutron field measurement. The neutron-gamma cuts are indicated by the red lines where the neutron events have a higher S value.

The separation of the loci associated with neutron and gamma-ray events can be determined through a Figure-of-Merit (FoM) value, which is defined as:

$$FoM = \frac{|\mu_p - \mu_e|}{FWHM_p + FWHM_e} \quad (1)$$

where $\mu_{p,e}$ and $FWHM_{p,e}$ refer to the mean and full width half maximum of the proton and electron recoil loci respectively. The distributions presented in figure 1 can then be compared using the FoM as a function of light output, as seen in figure 2. Below a FoM value of one, the loci are considered inseparable. The quality of separation is equivalent for the two acquisition systems, with their lower energy limits in agreement with each other.

From these measurements neutron cuts are applied (indicated in red in figure 1), selecting for events which are only associated with neutrons. The neutron light output spectra can be seen in figure 3(a) along with the associated neutron energy spectra 3(b). The normalised neutron light output spectra are in good agreement indicating that the shape of the spectra behave as expected. The neutron energy spectra seen in figure 3(b) exhibit the same features, with the smaller secondary peaks in good agreement across the two acquisition systems. The disagreement in the primary neutron energy peak is attributed to the small difference in the edge of the neutron light output spectra seen in figure 3(a) due to differences in the light output parameters.

The results for the measurements of the primary energy peak for the 1.200(3) MeV, 2.500(4) MeV, 5.000(3) MeV and 7.000(6) MeV neutron fields are presented in table 1 with their associated standard uncertainties. The results all agree with the expected values, calculated from beam conditions, within 2σ .

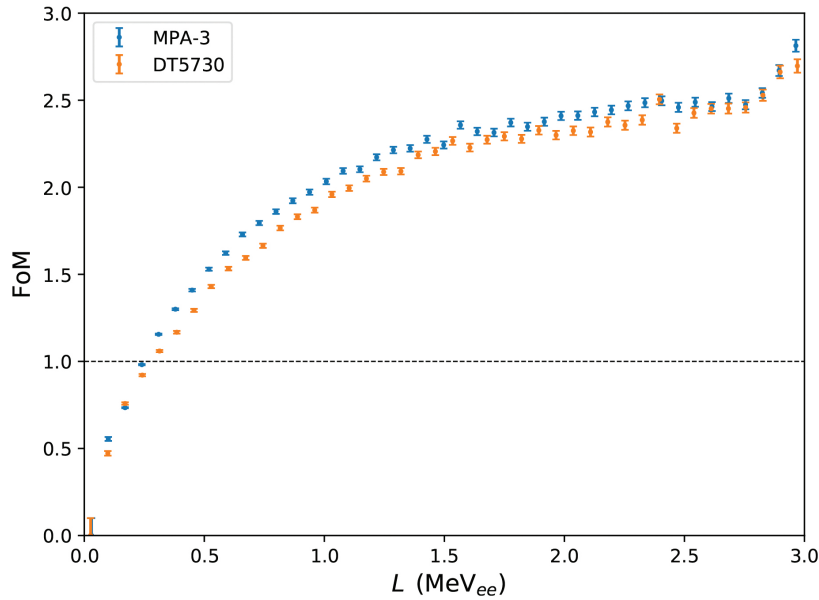


Figure 2. Figure-of-Merit (FoM) as a function of L (MeV_{ee}) for the 7.000(6) MeV neutron field measurement for both acquisition systems, indicating equivalent PSD quality for the two acquisition systems. FoM values were calculated from slices along the L -axis of width 0.1 MeV_{ee} .

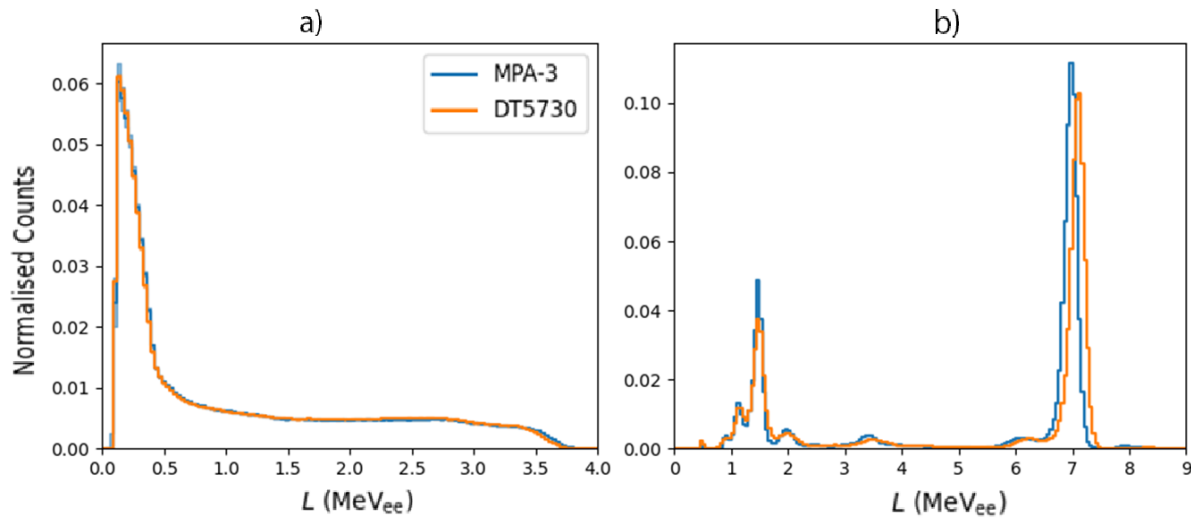


Figure 3. The (a) neutron light output spectra and (b) the associated neutron energy spectra, normalised by the total counts, as measured by the MPA-3 acquisition system (blue) and the DT5730 CAEN digitiser (orange) for the 7.000(6) MeV neutron field measurement.

3. Conclusion

In conclusion, the measurements reported here made with a CAEN DT5730 system suggest that modern digital systems are now offering a reliable alternative to the well characterized reference acquisition systems based on analogue NIM modules. The measurements demonstrated similar quality PSD separation, with good agreement in unfolded energy distributions between the two data acquisition systems for the four measured neutron energies. Present measurements were made with the DT5730 module connected by USB-2 cable to a regular laptop. Further improvements in stability, reliability, and performance are expected by utilising the optical cable connection between the DT5730 and an appropriate desktop PC. Rate related measurements and characterisation are required to fully investigate dead time effects and stability.

Table 1. Neutron energy measurements for the 1.200(3) MeV, 2.500(4) MeV, 5.000(3) MeV and 7.000(6) MeV neutron fields for the analogue and digital systems along with the expected values of the neutron energies calculated from beam conditions.

Expected Neutron Energy [MeV]	1.200(3)	2.500(4)	5.000(3)	7.000(6)
MPA-3				
Measured Energy [MeV]	1.145(26)	2.515(42)	4.994(82)	6.98(11)
DT5730				
Measured Energy [MeV]	1.160(30)	2.582(63)	5.053(97)	7.10(14)

Further investigations on a large range of beam conditions will enable a comparison of neutron energy spectra determined from both neutron time-of-flight and unfolding techniques. For a larger range of applicability, analysis of measurements taken with other detectors and at other facilities (UCT and iTL) will be completed.

The present investigations have demonstrated that there is now value in seriously considering implementation of a digital acquisition system for fast neutron metrology in a laboratory setting. Furthermore, a compact digital unit, such as the DT5730, offers the advantage of deploying the same metrology reference system in both laboratory and field environments.

Acknowledgements

Thanks to the staff of the AMANDE facility for assisting with beam time.

This work was funded by the IRSN (France) and National Research Foundation of South Africa (grant ID 118506).

References

- [1] Thomas D, Nolte R and Gressier V 2011 *Metrologia* **48** 225–38
- [2] Nolte R, Allie M, Böttger R, Brooks F, Buffler A, Dangendorf V, Friedrich H, Guldbakke S, Klein H, Meulders J, Schlegel D, Schuhmacher H and Smit F 2004 *Radiation Protection Dosimetry* **110** 97–102 ISSN 0144-8420
- [3] Arif M, Dewey M, Greeneand G and Snow W 1993 *Journal of research of the National Institute of Standards and Technology* **98(1)** 135–144
- [4] Kim Y K, Lee K H and Kim H R 2008 *Nuclear Engineering and Design* **238** 1664–9 ISSN 0029-5493
- [5] Block R, Danon Y, Gunsing F and Haight R 2010 *Neutron Cross Section Measurements* (Boston, MA: Springer US) pp 1–81 ISBN 978-0-387-98149-9
- [6] Carlson A 2011 *Metrologia* **48** S328
- [7] Beni M, Krstic D, Nikezic D and Yu P 2019 *Nuclear Science and Techniques* **30**
- [8] FastComtec *Model MPA-3, PC-card Multiparameter Multichannel Analyzer System*
- [9] DT5730 / DT5730S - 8 Channel 14 bit 500 MS/s Digitizer - CAEN - Tools for Discovery online: <https://www.caen.it/products/dt5730/> (Accessed on 02/09/2020)
- [10] Gressier V, Guerre-Chaley J, Lacoste V, Lebreton L, Pelcot G, Pochat J, Bolognese-Milstajn T and Champion D 2004 *Radiation Protection Dosimetry* **110** 49–52 ISSN 0144-8420
- [11] 2160a <https://www.fastcomtec.com/nim/2160a> (Accessed on 02/09/2020)
- [12] Roush M, Wilson M and Hornyak W 1964 *Nuclear Instruments and Methods* **31** 112–24 ISSN 0029-554X
- [13] Sperr P, Spieler H, Maier M and Evers D 1974 *Nuclear Instruments and Methods* **116** 55–9 ISSN 0029-554X
- [14] Onge R, Galonsky A, Jolly R and Amos T 1975 *Nuclear Instruments and Methods* **126** 391–5 ISSN 0029-554X
- [15] Moszynski M, Bizard G, Costa G, Durand D, El Masri Y, Guillaume G, Hanappe F, Heusch B, Huck A, Peter J, Ring C and Tamain B 1992 *Nuclear Instruments and Methods in Physics Research Section A: Accelerators, Spectrometers, Detectors and Associated Equipment* **317** 262–72 ISSN 0168-9002

- [16] Kaschuck Y and Esposito B 2005 *Nuclear Instruments and Methods in Physics Research Section A: Accelerators, Spectrometers, Detectors and Associated Equipment* **551** 420–8 ISSN 0168-9002
- [17] Esposito B, Kashchuk Y, Rizzo A, Bertalot L and Pensa A 2004 *Nuclear Instruments and Methods in Physics Research Section A: Accelerators, Spectrometers, Detectors and Associated Equipment* **518** 626–8
- [18] Brooks F 1979 *Nuclear Instruments and Methods* **162** 477–505 ISSN 0029-554X

Development of ^{18}F Radiochemistry for Positron Emission Particle Tracking (PEPT)

A Camroodien¹, M van Heerden¹, S Nair² and T Leadbeater¹

¹ Department of Physics, University of Cape Town, South Africa

² Radiation Biophysics Division, iThemba LABS, Somerset West, Africa

E-mail: CMRAME001@myuct.ac.za

Abstract. Positron Emission Particle Tracking (PEPT) is a radioactive tracer technique used to track the trajectory of a radioactively labelled macroscopic particle using a variant of Positron Emission Tomography (PET). The primary application of PEPT is to study dynamic flow systems under varying conditions; including a wide range of particle size distributions, physical, and chemical properties, with applications across the science disciplines. For radiochemical tracer particle production, we are interested in utilising ion-exchange techniques to label small phase-representative resin particles (diameter < 1 mm). For physical activation we will primarily be looking at the novel reaction $^{16}\text{O}(\alpha, \text{pn})^{18}\text{F}$ to produce positron emitters in-situ for larger particles (diameter > 5 mm). This work will develop iThemba LABS specific tracer particle production mechanisms using ^{18}F for the first time, and will provide insight into the effects of tracer particle properties in PEPT applications including optimisation of the PEPT technique and enhanced tracer production mechanisms.

1. Introduction

Positron emission particle tracking (PEPT) is a non-invasive technique used to obtain dynamic information within multiphase dynamic systems. Of particular value to science and engineering, this technique obtains information on the motion and flow fields of fluids and/or granular materials in three dimensions and often in dense and opaque media. PEPT enables tracking of a single tracer particle moving within the field-of-view of a modified Positron Emission Tomography (PET) scanner. The basis of the technique is to radiolabel a tracer particle with a suitable positron emitting radionuclide. Positrons that originate from the tracer radionuclide annihilate with local electrons and produce back-to-back 511 keV gamma photon pairs. When both gamma photons are detected simultaneously (defined as coincident with a typical 12 ns time window), a line of response (LOR) can be formed with the tracer particle located somewhere along that line. Multiple LORs are used to calculate the tracer location as shown in figure 1; an iterative location algorithm is employed to calculate the position of the particle based on the detection of a consecutive series of back-to-back gamma photons, within limits set by the spatial resolution of the camera.

In principle, only two lines of response are necessary, but a larger number (100s – 1000s) of measured LORs are required in practice as the acquired data contains a certain fraction of corrupt LORs, due to scatter, attenuation, and random coincidences [1].

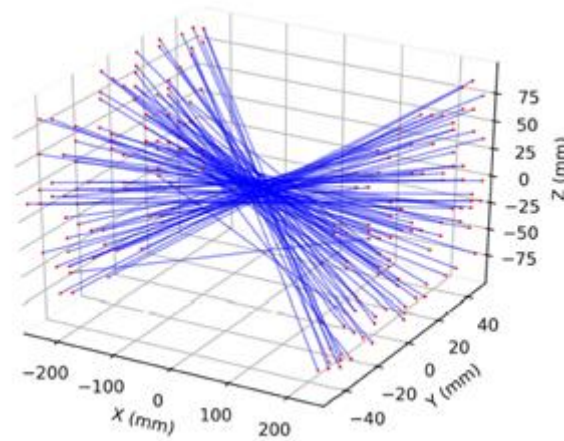


Figure 1. Example LORs from a point source of positron activity placed at the origin. The majority of lines converge at the source position, forming the basis of the technique. Some outliers are visible, being corrupt LORs from scatter or random coincidences.

The acquisition rate of LORs depends upon the emission rate of positrons from the tracer particle (itself a function of activity and the branching ratio for positron decay), multiplied by the sensitivity for detecting coincidence pairs of annihilation photons (proportional to the square of the intrinsic efficiency for detecting single photons). Typical sensitivities for the detector systems at PEPT Cape Town are of the order 5 – 10 % absolute (including solid angle terms) [2]. The data acquisition rate, and hence location reconstruction rate, primarily depends on the tracer particle activity for a fixed geometry. For low activity, the rate of event detection is insufficient to measure a continuous trajectory, and dynamic information is lost. Conversely, with activity too high, effects of pulse pileup and acquisition deadtime degrade the measurement [3]. To ensure that the measured PEPT data is reflective of the motion under study, the radioactivity in a single particle must be sufficient irrespective of the tracer size and physical properties of the material under study which itself must be representative of the media under study.

In addition to the instrumentation, application and data processing, a crucial aspect of the PEPT technique is the production of a suitable representative tracer particle. Currently, the primary radionuclide used at PEPT Cape Town is ^{68}Ga with a half-life of 68 minutes, produced at iThemba LABS thorough the use of $^{68}\text{Ge}/^{68}\text{Ga}$ radioisotope generators. We have extended the application of PEPT by producing ^{18}F -based tracer particles with the longer half-life of 109 minutes. Advantageously, ^{18}F is a pure β^+ emitter with no additional gamma emissions, thus its use intrinsically increases the signal to noise ratio in PEPT studies.

2. Tracer Production Mechanisms

Radiochemical and physical methods are both being explored to produce ^{18}F based tracer particles. Two methods of tracer production used are direct activation and chemical sorption, with the latter comprising surface modification and ion exchange radiolabelling, as illustrated in table 1. If the materials in the system contain natural oxygen, are thermally stable and greater than 1 mm in diameter, tracer particles may be directly produced by activation in a suitable cyclotron beam. For routine work, and for tracer particles below 1 mm in diameter, PEPT Cape Town utilises chemical sorption methods to produce tracer particles. Ion exchange radiolabelling relies on controlling the uptake of a desired radionuclide (here: ^{18}F or ^{68}Ga) by an organic or inorganic resin which exchanges

non-radioactive counterions for the required species. The Birmingham group has demonstrated that commercially available ion exchange resins of 600 μm diameter can adsorb up to 1500 μCi of ^{18}F [3]. Unfortunately, ion exchange resins are typically not representative of the particles of interest due to differences in density or surface chemistry properties; however, applying suitable coating layers to modify these properties improves representation. Figure 2 highlights a range of various PEPT Cape Town tracer particles that have been developed [5].

Table 1. A summary of different types of PEPT tracers.

	Direct Activation	Ion Exchange	Surface Modification
Typical activity (μCi)	2600	800 - 1000	± 600
Typical size range (μm)	>1000	50 - 1200	100 - 1000
Typical material	contain oxides, heat tolerant, matches bulk	ion exchange resin, tuned to match bulk density	reacts with radioisotope selective to material



Figure 2. A selection of PEPT Cape Town tracer particles from left to right: moulded, density modified, mineral coating, silica coating, coal particle, glass bead with ion-exchange inset. The images have a global scale with the tracer on the far left approximately 300 μm in diameter, up to 1 mm diameter on the far right.

2.1. Radionuclide production

Irrespective of the production method chosen to fabricate tracer particles with the required properties, nuclear activation techniques are used to produce the required radioactive species. Typical reaction pathways for oxygen bearing targets are illustrated in figure 3. Production typically utilises positive ion beams produced by cyclotron, with the majority of global ^{18}F production utilising the $^{18}\text{O}(\text{p}, \text{n})^{18}\text{F}$ reaction on an enriched ^{18}O water target with proton beam energy above 7 MeV threshold [6]. Disadvantageously, this production method requires enriched ^{18}O targets (90 – 95% is typical) and therefore cannot be used on natural oxygen bearing substances such as water or oxides. For PEPT, where activation of natural materials is required, both Birmingham and Cape Town groups [2, 3] have explored alternative pathways. Reactions on naturally occurring ^{16}O bearing targets utilise ^3He or alpha particle beams above 20 MeV. For radiochemical synthesis, ^{18}F dissolved in aqueous solution is required. In this scenario the reaction pathway does not affect the chemical properties of the produced solution, and both methods are used with Birmingham preferring the $^{16}\text{O}(^3\text{He}, \text{x})^{18}\text{F}$ reactions, and iThemba LABS using the $^{18}\text{O}(\text{p}, \text{n})^{18}\text{F}$ reaction on a dedicated 11 MeV cyclotron used for medical grade ^{18}F (^{18}F FDG) production. PEPT Cape Town has historically utilised the $^{68}\text{Ge}/^{68}\text{Ga}$ radioisotope generators produced by iThemba LABS for routine tracer particle production [4]. In these generators, the long lived (271 day half-life) ^{68}Ge is produced by (p, xn) reactions on natural Ga targets with proton beam energy 66 MeV using the iThemba LABS $k = 200$ Separated Sector Cyclotron (SSC). The ^{68}Ge is loaded into an exchange column, and decays to ^{68}Ga (68 min half-life) which can be eluted on a daily basis to form an aqueous solution. Ion exchange techniques similar to those discussed below have been developed and optimised to produce PEPT tracer particles via radiochemical means using this solution.

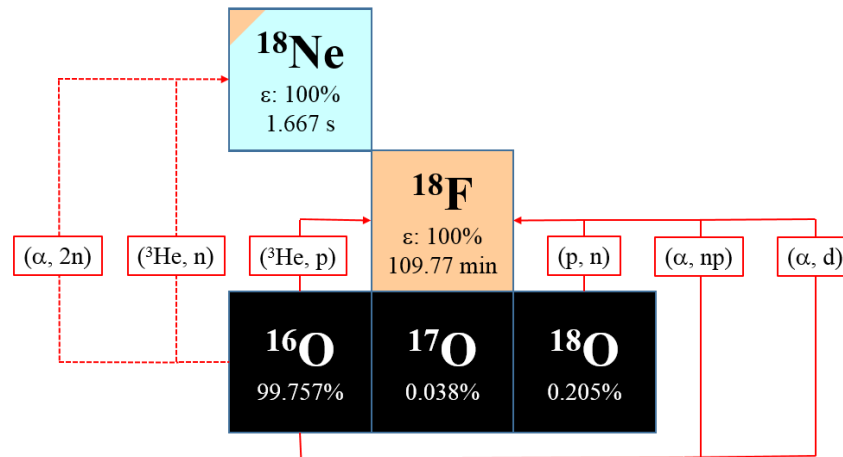


Figure 3. Typical reaction pathways for ^{18}F production from oxygen targets, using proton, ^3He and alpha particle beams. Note many competing reactions contribute to the ^{18}F end-product, sometimes through intermediate short lived stages.

2.2. Direct Activation

The physical-chemical properties of the tracer particle are of extreme importance to accurate representation of results. Ideally, an original particle of the operational bulk material is extracted and radiolabelled. In the context of iThemba LABS the reactions on natural ^{16}O bearing targets with high-energy alpha particle beams are preferred. Up to 10 silicon dioxide (SiO_2) glass spheres of diameter 5 - 10 mm were placed in an aluminium target holder with active water cooling. The target was irradiated in the “Elephant” target station [7] using a 100 MeV alpha particle beam averaging 800 nA current over approximately 2 hours. Radioisotope activation yields were characterised by half-life measurements and gamma photon spectroscopy, with the highest yield being < 3 mCi of ^{18}F on a single glass sphere. Few impurities from other nuclear reaction channels were observed, and the activity was produced firmly embedded in the matrix of the material thus negating radiological contamination issues. Figure 4 illustrates the typical cyclotron target and main conclusions, detailed analysis can be found in [8, 9]. This method complements existing techniques as a benchmark. Typical materials of interest across physics and engineering include: Glass/silica (SiO_2), Mullite ($3\text{Al}_2\text{O}_3 \cdot 2\text{SiO}_2$), Magnetite (Fe_3O_4), and Chromite (FeCr_2O_4).

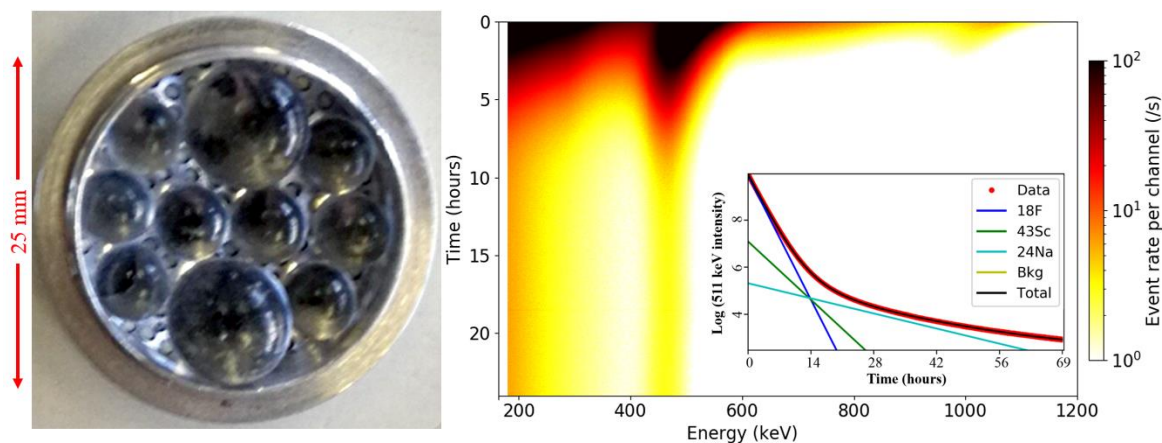


Figure 4. Left: target holder with SiO_2 glass beads of 5 – 10 mm diameter. Right: time-series spectroscopy recorded over 24 hours (vertical axis) showing the principle 511 keV photopeak from positron annihilation, there are very little contaminant species at other gamma energies. The inset shows the 511 keV peak area decaying over time, fitted to half-lives of ^{18}F and the theorised contaminants. These data are consistent with over 95% of the produced activity being due to ^{18}F .

2.3. Ion exchange radiolabelling

Two types of anion exchange resins: weak-base and strong-base, can be used as sorbent resin structures to concentrate and fix suitable radioactivity, and on which to deposit additive layers to control physical material properties. Ion exchange techniques are used to make a resin tracer when particle diameters are required below 1000 μm , and when suitable oxygen bearing substances are not available. The resins consist very small porous plastic beads with functional groups attached to the styrene divinylbenzene copolymer lattice [10]. Each fixed ion is neutralised with a counterion to preserve the overall electrical neutrality of the resin. The basis of ion exchange labelling is to then use radioactive ions to replace the counterions attached to the functional groups on the resin surface. In order for the process to occur, the radioactive ions must have a higher affinity for the resin than the counterions. The functional groups for anion resins are quaternary ammonium cations, shown in figure 5 as N^+R_3 where R is the organic backbone. The mobile counterion in the anion resin beads are chloride anions, and the resin is used in an ionic form with a lower selectivity for the functional group than the sample ions to be exchanged [8], where only ions of the same electrical sign are exchanged. The ion exchange process normally happens in aqueous solution, and here with $^{18}\text{F}^-$ ions dissolved in the high purity deionised water solution used as the cyclotron target.

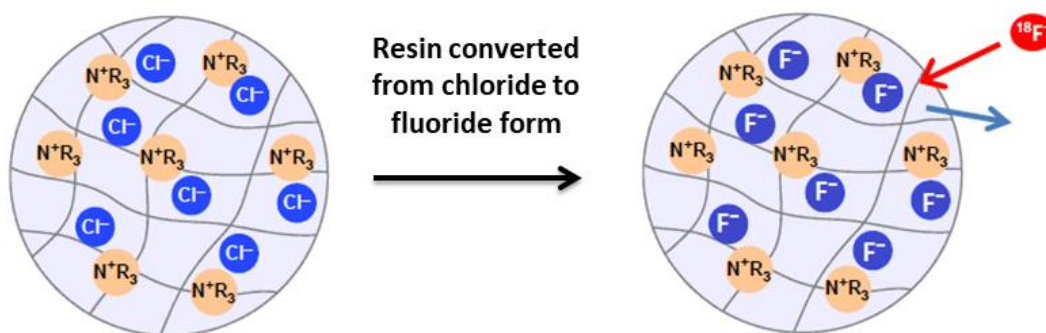


Figure 5. Schematic representation of strong-base anion exchange resin converted from chloride to fluoride form, followed by F^- ion exchange with $^{18}\text{F}^-$ in an anion resin bead to gain radioactive uptake [11].

The uptake of ^{18}F on weak-base anion exchange resins is strongly controlled by water pH. The free-base amines in the weak-base anion exchange resins, eg. $\text{RCH}_2\text{N}(\text{CH}_3)_2$, interact with water and form $\text{RCH}_2\text{N}(\text{CH}_3)_2^+\text{OH}^-$ in which the OH^- acts as a counter ion and can be exchanged by $^{18}\text{F}^-$. The dissociation of the hydroxide ions from the functional group is very weak [3]. As the process progresses, the hydroxyl concentration increases in solution causing the resin to convert back to the undissociated free-base form and inhibiting the anion exchange capacity. The affinity of ^{18}F ions to weak-base anion exchange resin is much weaker than hydroxide ions. Therefore, the use of weak-base anion exchange resins are limited as ^{18}F absorption can only perform at a low pH [3]. Alternatively, strong-base anion exchange resins are less affected by water pH or hydroxide ions since the affinity of $^{18}\text{F}^-$ ions is stronger than hydroxide ions of resins [3]. The strong-base anion exchange resins used are quaternary ammonium derivatives in chloride form: $\text{R-CH}_2\text{N}(\text{CH}_3)_3^+\text{Cl}^-$, where chloride is the counter ion. However, because the affinity of the $^{18}\text{F}^-$ ion to the functional groups is much weaker than the Cl^- ion, the resin particles must first be converted into fluoride or hydroxide form e.g. $\text{R-CH}_2\text{N}(\text{CH}_3)_3^+\text{F}^-$. The conversion is achieved by pouring a resin slurry into a column and eluting with 8 – 10 bed volumes of 1 M KF solution and rinsing with 10 bed volumes of deionised water, the converted F^- ions act as counter ions that exchange with $^{18}\text{F}^-$ ions as illustrated in figure 5.

3. Summary and outlook

We are presently improving the uptake of $^{18}\text{F}^-$ through altering the resin characteristics in which they are based using a polystyrenic or polyacrylic matrix with either gel or macroporous structures [12]. Polystyrenic based resins are hydrophobic relative to polyacrylic based resins, meaning the styrene matrix will retain organic molecules more efficiently. Gel resins offer higher activity levels as increased porosity results in easier ion diffusion through the resin bead. Novel resins under study include mixed base and ion selective functionality, with some having higher chemical and temperature stability, and others with higher capacity and easier regeneration. We have successfully pre-treated a selection of strong-base anion exchange resins for radiolabeling with ^{18}F , and we have demonstrated direct activation using iThemba LABS facilities. In future work we will produce a full kinetic model to explore the change in yield over time as the radioactive species decay and as ions exchange with the introduced media. This work will develop iThemba LABS specific tracer particle production mechanisms, and will provide insight into the effects of tracer particle properties in PEPT applications.

Acknowledgments

The authors would like to thank the National Research Foundation (NRF) for funding: A. Camroodien was supported through an MSc bursary, this work was partially supported by NRF grant number 114785 (Leadbeater). iThemba LABS is gratefully acknowledged for providing access to the SSC and PET cyclotrons.

References

- [1] Buffler A, Govender I, Cilliers J J, Parker D J, Franzidis J P, Mainza A N, Newman R T, Powell M and van der Westhuizen A 2010 PEPT Cape Town: a new positron emission particle tracking facility at iThemba LABS *In Proceedings of International Topical Meeting on Nuclear Research Applications and Utilization of Accelerators* 1-8.
- [2] Buffler A, Cole K, van Heerden M and Leadbeater, T W 2018 Positron emission particle tracking: A powerful technique for flow studies, *Int. J. Mod. Phys. Conf. Ser.* 48.
- [3] Fan X, Parker D J and Smith M D 2006 Labelling a single particle for positron emission particle tracking using direct activation and ion-exchange technique, *Nuclear Instruments & Methods in Physics Research* **562(1)** 345-50.
- [4] Cole K, Buffler A, Cilliers J J, Govender I, Heng C, Liu C, Shah U V, van Heerden M, Fan X 2014 A surface coating method to modify tracers for positron emission particle tracking (PEPT) measurements of froth flotation *Powder Technology* **263** 26–30.
- [5] PEPT Cape Town, University of Cape Town, accessed 29 August 2021, <http://www.peptcapetown.uct.ac.za/pept-cape-town/tracers>.
- [6] Cyclotron Produced Radionuclides: Guidance on Facility Design and Production of [^{18}F]Fluorodeoxyglucose (FDG) *IAEA radioisotopes and radiopharmaceuticals series no. 3*.
- [7] Mills S J, Nortier F M, Rautenbach W L, Smit H A and Steyn G F 1989 A multi-purpose target station for radioisotope production at medium energies *Proceedings of the 12th international conference on cyclotrons and their applications* Germany.
- [8] Steyn et. al. 2020 *30th World Conf. of the INTDS (International Nuclear Targets Development Society)* Germany.
- [9] Leadbeater et al 2020 *14th Int. topical meeting on nuclear applications of accelerators IAEA* Austria.
- [10] AG 1, AG MP-1 and AG 2 Strong Anion Exchange Resin Instruction Manual Biorad accessed 29 August 2021 [AG® 1, AG MP-1 and AG 2 Strong Anion Exchange Resin Instruction Manual \(googleusercontent.com\)](#).
- [11] Rohm and Haas Ion Exchange An Introduction accessed 29 August 2021 [Ion Exchange-An Introduction.pdf \(desal.co.uk\)](#)
- [12] Resins Product Guideline Purolite accessed 29 August 2021 [Strong Base Anion Exchange Resin | Purolite | www.purolite.com](#).

Solar irradiance in Gauteng during the 2020 COVID-19 lock-down – can we detect decreased aerosol loading?

Charles H Fourie¹, Hartmut Winkler¹ and Kittessa Roro²

¹ Department of Physics, University of Johannesburg, PO Box 524, 2006 Auckland Park, Johannesburg, South Africa

² Energy Centre, Council of Scientific and Industrial Research (CSIR), Building 34, Pretoria, South Africa

Corresponding author email: hwinkler@uj.ac.za

Abstract. This paper seeks to investigate the impact of aerosol loading in Tshwane (Pretoria) during the initial 35-day COVID-19 lock-down period in March-May 2020 using solar irradiance data obtained from pyranometer and spectroradiometer measurements. We seek to detect and identify possible aerosol loading reductions over that period due to lowered combustion and emissions associated with urban and industrial processes. Any such decline would manifest itself in a higher-than-average direct solar beam intensity and a lower incidence of scattered photons reaching the detector from different directions than the solar beam. We measure these irradiation components both spectroscopically and in integrated broadband form for selected days deemed free of cloud. We examine the relationship of the irradiance to the solar zenith angle, and confirm this to be well represented by a power law. A comparison of the 2020 results to similar determinations for selected days in 2018 and 2019 shows no difference between the seasonal averages, and we therefore conclude, in contrast to what would be expected in view of reduced anthropogenic activity, that the impact of the lockdown on aerosol levels was minimal.

1. Introduction

The Earth's atmosphere contains varying levels of suspended particles referred to as aerosols that by their presence reduce incoming solar radiation and decrease long distance visibility. This decreased transparency is also referred to as turbidity. While some aerosols are natural, many are also generated through human activity, which can lead to enhanced turbidity in urban areas [1].

During the early high-level lock-down linked to the COVID-19 pandemic in 2020, much of the South African industrial and economic sectors ground to a halt. The lower transport and industrial activity is well illustrated in human mobility data determined from communication device locations (see <https://www.google.com/covid19/mobility/>). This provided an opportunity to identify the role human activities have on the local contribution to aerosol emissions in Gauteng province, the most urbanized and industrialised region in South Africa, by comparing the 2020 atmospheric turbidity during that time of the year with the levels observed in prior years. This is done by measuring the solar beam strength during the lockdown months and comparing this to earlier periods.

The downscaling of activities lowers emissions due to industrial activity and transportation, but also leads to heightened domestic burning. The degree to which these processes affect aerosol concentration at a specific site furthermore depends on specific local meteorological conditions, especially wind.

2. Solar Irradiance

2.1. Solar Geometry

As the Earth orbits the Sun and the Earth rotates around its polar axis, the position of the Sun in the sky is constantly changing. As the angle of inclination of a solar beam reaching the surface changes, so does the amount of atmosphere a photon in the solar beam would pass through. The solar zenith angle (θ_z) is measured between the vertical and the incoming solar beam. This depends on the time of day, day of the year and latitude. Various procedures are available to calculate θ_z at any particular moment, the choice depending on the level of accuracy required (e.g. [2]). On any particular day, θ_z is at a minimum at solar noon, which is defined as the time when the Sun passes the meridian.

The parameter m , referred to as the airmass, equates to the amount of atmosphere a photon of light must pass through before reaching the ground. Its units are such that $m = 1$ corresponds to the vertical path from ground level to the top of the atmosphere. When ignoring distortions due to Earth curvature and refraction, airmass can be approximated by $m = \cos \theta_z$.

2.2. Radiation losses and light scattering in the atmosphere

Solar irradiance passing through the atmosphere may interact with some of its constituents, leading to a photon being absorbed or deflected into a different direction through scattering. The amount and spectral distribution of the radiation detected at ground level is influenced by numerous factors, such as the albedo (which refers to the reflected light from a surface), as well as the concentration of atmospheric gasses such as carbon dioxide, water vapour and other trace gases [3]. Different aerosols affect the spectrum of incoming solar radiation at different wavelengths. Factors determining this include particle size, as well as chemical or molecular composition, which determine energy states and the wavelengths of photons associated with atomic and molecular transitions. This results in scattering and absorption at specific wavelengths. The absorption bands for various aerosols and related radiation attenuation processes have been well documented (e.g. [4]).

2.3. Radiation components and spectral distribution

Global horizontal irradiance G is defined as the energy per unit time and per unit area collected by a horizontally placed detecting surface. There are two components contributing to this. The first is the solar beam, i.e. the sunlight reaching the surface that was not absorbed or scattered during the traverse of the atmosphere. We refer to this as the direct normal irradiance I . Given that the solar beam makes an angle of θ_z with the normal to the horizontal measuring surface, the effective detector surface area seen by the beam is reduced by a factor of $\cos \theta_z$. The second component contributing to G is the scattered radiation from the sky dome. This is referred to as the diffuse horizontal irradiance D . All these quantities are thus related to each other by the following expression:

$$G = I \cos \theta_z + D \quad (1)$$

While the accurate characterization of the global irradiance is extremely complex, there are mathematically very straightforward model formulations available that are able to approximate the actual relationship between G and θ_z quite well. One reasonably successful such formulation is a power law relationship sometimes referred to as the Adnot-Bourges-Campana-Gicquel clear-sky model (hereafter ABCG model) [5], defined by the following expression:

$$G = A(\cos \theta_z)^B \quad (2)$$

Note that the scaling parameter A corresponds to the global horizontal irradiance when the Sun is directly overhead (i.e. $\theta_z = 0 \Rightarrow \cos \theta_z = 1$). G will then be highest when radiation losses in the atmosphere are at their lowest, and hence A is an indicator of atmospheric transparency. This also applies to the majority of days when the Sun does not reach the point directly overhead at noon. The parameter B describes the deviation from a pure cosine form (which corresponds to $B = 1$). A value of $B \gg 1$ indicates enhanced irradiation when the Sun approaches the horizon, i.e. higher aerosol concentrations.

2.4. The Solar spectrum

Solar radiation is emitted by our Sun with a spectral form largely resembling a blackbody characteristic of its effective surface temperature of 5800 K. Most of the emitted sunlight is radiated in the near ultraviolet (0.28–0.40 μm ; UV), visible (0.40–0.70 μm) and infrared (0.70–3.0 μm) regions [6].

When studying the spectral properties of irradiance, it is useful to introduce another parameter, the spectral irradiance, which quantifies the irradiance per unit wavelength interval. In terms of the solar beam, this parameter is then referred to as the direct normal spectral irradiance I_λ , and is related to I by

$$I = \int_0^\infty I_\lambda d\lambda . \quad (3)$$

3. Methodology

We examine Council for Scientific and Industrial Research (CSIR) solar spectral irradiance, broadband irradiance and weather data for the period in question together with corresponding data from the two previous years. The broadband and weather data also form part of the regional Southern African Universities Radiometric Network (SAURAN) database [7].

We categorise days and months according to the measured degree of turbidity for the period April–July for 2018 and 2020 through analysis of the relationship between the measured irradiance and the solar zenith angle on cloud-free days. To eliminate the influence of cloud cover and other obstructions candidate clear-sky days were checked visually by inspecting the smoothness and morning-to-afternoon symmetry of the G vs. time plots for that day. We thus identified four days in 2018, six days in 2019 and seven days in 2020 which did not show signs of cloud interference. In the analysis later on we restrict ourselves to irradiance measurements taken when the solar zenith angle is smaller than $\theta_z = 84^\circ$, because, as with other simplistic models, the ABCG model fails when the Sun is close to the horizon.

The instrumentation used to secure the irradiance data was supplied by the CSIR, and is located on a rooftop on its main campus in Tshwane (Pretoria). The exact measurement site location is longitude 28.2787 E, latitude 25.7465 S and the altitude is 1400 m above sea level. The instruments were:

- Two pyranometers. When placed on a horizontal surface they directly measure G . The diffuse component D can also be determined with a pyranometer by obstructing the direct solar beam with a shading ball. The pyranometers we used are manufactured by Kipp & Zonen and are sensitive in the wavelength range 0.28–2.80 μm . They were set up to take measurements at a frequency of once every 30 seconds and record data every minute.
- A spectroradiometer manufactured by EKO-Weiser. It measures the direct normal spectral irradiance I_λ in the wavelength range 0.28–1.10 μm at 5 second intervals and recording data every minute.
- Weather data was gathered by a standard integrated weather sensor, which recorded wind data, temperatures, humidity and precipitation at 30 second intervals.

4. Results and analysis

4.1. Global horizontal irradiance model fits

This A and B parameters in the ABCG model are then obtained by linearising G as a function of $\cos \theta_z$ through the application of a logarithm to both sides of equation 2:

$$\log_{10} G = \log_{10} A + B \times \log_{10} (\cos \theta_z) . \quad (4)$$

Figure 1 illustrates one such plot. The best fitting line is determined by applying routine linear regression analysis, which then yields the parameters A and B . A comparison of the model for G and the actually measured data over the course of a day is shown in figure 2.

The R^2 values ranging between 0.988 and 0.999 highlight the high degree of linearity in the plots, not only confirming the suitability of the model, but also that the days chosen were indeed clear. Figure 3 is a plot of A vs. B , and there is no evidence of a systematic shift of the points for 2020 compared to the previous years.

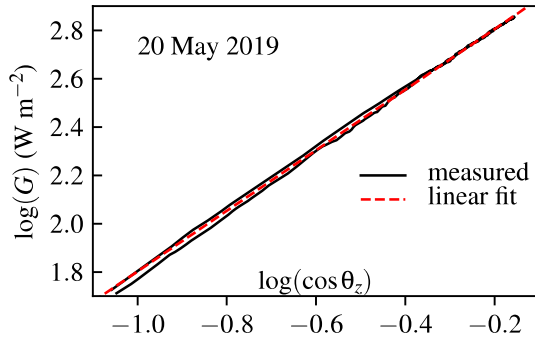


Figure 1. Example of a linearised $\log G$ vs. $\log(\cos \theta_z)$ plot.

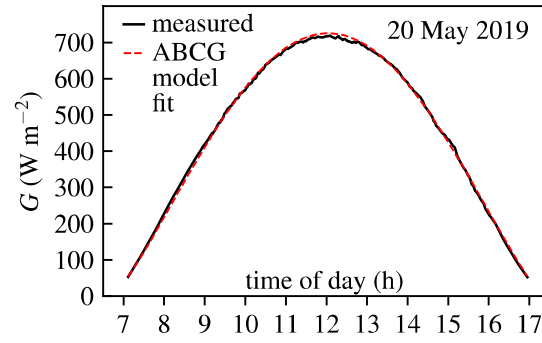


Figure 2. Comparison of the measured and model global horizontal irradiance values.

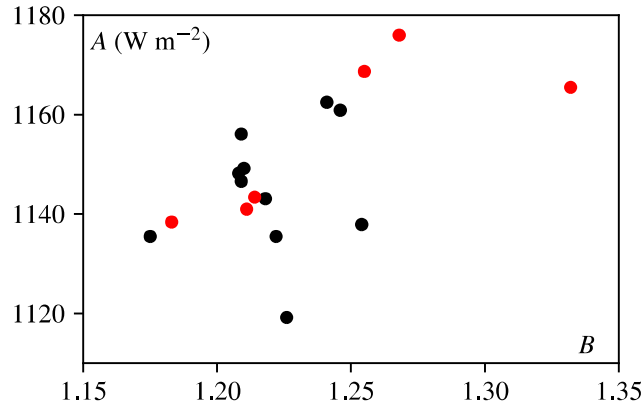


Figure 3. ABCG model A vs. B fitting parameters for selected clear days in 2018-2019 (in black) and in 2020 (in red).

The A and B fitting parameters are always higher than the values originally associated with the ABCG model. This can be attributed to differences in elevation and changed environment to the low altitude central European localities where the ABCG model was originally developed [5]. The RMSE values in table 1, were obtained by comparing the measured values of G to the values modelled using the ABCG formulation with A and B values obtained from fitting a straight line to the $\log G$ vs $\log(\cos \theta_z)$ plots analogous to the example shown in figure 2:

$$RMSE = \left(N^{-1} \sum (G(\text{model}) - G(\text{measured}))^2 \right)^{1/2}. \quad (5)$$

The number of values for each day varies as the ABCG model is restricted to $\theta_z < 84^\circ$, as measurements nearer to the horizon can be affected by shading through nearby buildings and trees. In addition to determining fitting parameters, the log-log plots can highlight variations in aerosol loading between morning and afternoon. The example shown in figure 1 is such a case.

The analysis performed in this section confirms that broadband values for 2018, 2019 and 2020 have not shown any clear evidence in a reduction in aerosol absorption, which would have resulted in an increase in the values of G and I with a corresponding decrease in D .

4.2. Solar noon irradiance comparison

As an alternative method of analysis, we compared the global horizontal, diffuse horizontal and direct normal irradiance at solar noon for the days investigated. G and D have been measured directly, while I can be calculated from these with equation 1.

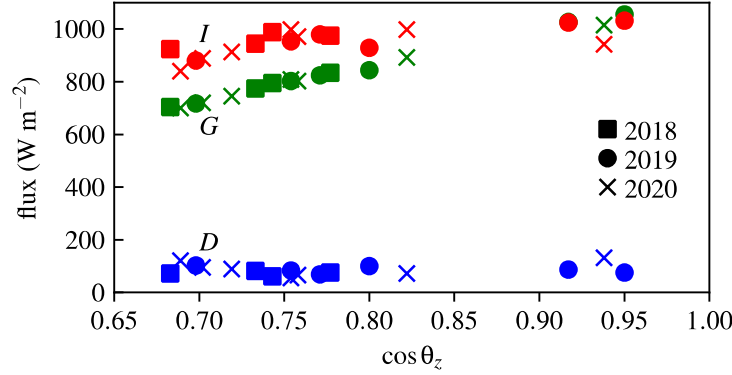


Figure 4. The measured values of G (in green) and D (in blue) at solar noon, and the corresponding values of I calculated from these using equation 1 (in red), plotted versus $\cos(\theta_z)$. The squares, circles and crosses represent the 2018, 2019 and 2020 data respectively.

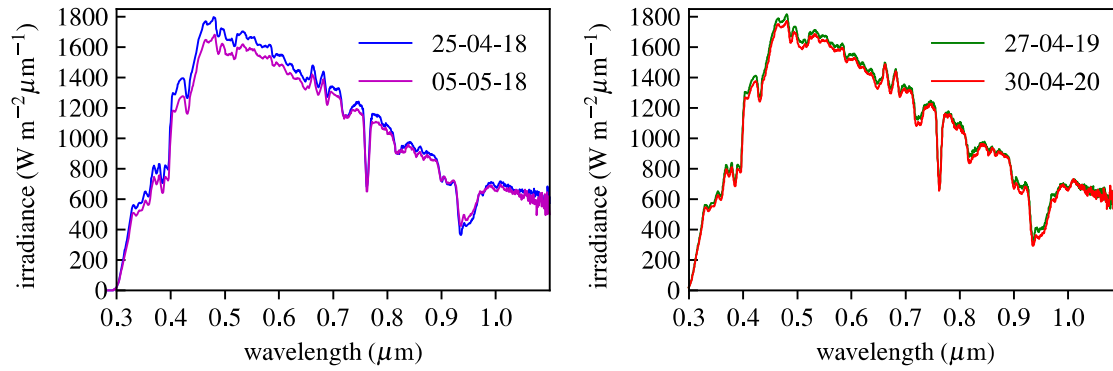


Figure 5. Spectral irradiance profiles for 2018-2020 (in $\text{W m}^{-2}\mu\text{m}^{-1}$).

Figure 4 compares the global, direct and diffuse irradiance at solar noon to the corresponding $\cos \theta_z$. The 2020 values of G and I would for a given θ_z be higher and for D be lower than those for the earlier years if the atmosphere was indeed clearer during the 2020 lockdown. There is no evidence for this. To demonstrate this, we fitted power law curves to the combined 2018-2020 data and determined the average offsets of the data points of the 2020 data. For 2020 we get: $\Delta G = -4.6 \pm 12.8 \text{ W/m}^2$, $\Delta D = +7.7 \pm 28.0 \text{ W/m}^2$ and $\Delta I = -11.6 \pm 51.1 \text{ W/m}^2$, meaning that the 2020 measurements are statistically consistent with the three-year average. If anything, there is a tendency for G and I to be lower and D to be higher in 2020, the opposite of what one would expect in the event of a clearer atmosphere.

4.3. Spectral Irradiance profile

Spectral profiles were inspected to identify possible variations in the absorption profiles in the 0.30-1.10 μm spectral range. The spectra were always taken close to solar noon, and within a week of 1 May so that the spectra all correspond to similar solar zenith angles.

All four spectral profiles in figure 5 show similar trends in spectral absorption bands for natural atmospheric aerosols. When looking at the UV region, clear signs of ozone absorption are visible, particularly in the UV spectrum, as well as the 0.45 μm to 0.75 μm region. Similarly, water vapour

absorption can be observed at 0.72 μm , 0.82 μm and 0.94 μm . Molecular oxygen exhibits absorption at 0.63, 0.69, 0.76 and 1.06 μm [3].

There is no obvious difference in the spectral shape between 2020 and the other years. The small variations between the displayed spectra can easily be explained as the result of the slow seasonal drift to larger airmass at solar noon, which leads to a slight weakening of I_λ as one moves towards mid-winter. There is also no sign of any changes to specific spectral lines. All this supports the earlier finding that the lockdown months of 2020 experienced normal aerosol loading.

5. Discussion

There are two ways to interpret the findings presented here: i) atmospheric particle concentrations at the measurement site have always been low even though this is an urban site; or ii) the methodology employed here and chosen sample are inadequate to detect changes in aerosol loading.

Looking at the first hypothesis, we note that the measurement site at the CSIR is comparatively removed from major industrial sites, so the downscaling of industrial operations during the COVID-19 lockdown would not have had a major impact there. Emissions from domestic coal fires would, if anything, have been more frequent during the lockdown due to more people being at home during the day. This could have counteracted the decrease in vehicle emissions. We also note that atmospheric transparency measurements carried out at the CSIR do not differ dramatically from those at some very remote locations [8], indicating that the CSIR site enjoyed only moderately aerosol loaded even in the pre-COVID lockdown period.

It is also possible that a larger number of daily data sets would have yielded a significant difference in sky transmission characteristics. For example, we note that the three days with the largest values of the ABCG model parameter A were all in 2020 (see figure 3). We also checked wind characteristics [9] on the days when our irradiance data was gathered, and found that there was wind with speeds of the order of 10 km h^{-1} on virtually all clear days chosen for 2018 and 2019. That would have assisted in dissipating locally polluted air on those days.

6. Conclusion

We attempted to detect whether the lockdown period at the start of the COVID-19 pandemic followed trends as seen in other major international cities of a significant decline in pollutants being emitted into the atmosphere. We find that, at least as far as average sky transparency is concerned, the urban region near our measurement site shows no evidence of lowered emission as a result of the March-May 2020 shut down of most economic and industrial activities.

References

- [1] Piketh S J, Annegarn H J and Tyson P D 1999 *Journal of Geophysical Research* **104** D1 1597
- [2] Blanco-Muriel M, Alarcon-Padilla D C, Lopez-Moratalla T and Lara-Coira M 2001 *Solar Energy* **70** 431
- [3] Patadia F, Levy R C and Mattoo S 2018 *Atmospheric Measurement Techniques* **11** 3205
- [4] Gueymard C A 2004 *Solar Energy* **76** 423
- [5] Badescu V 1997 *Solar Energy* **61** 251
- [6] Jacobson M Z 2013 *Fundamentals of Atmospheric Modelling* (Cambridge: Cambridge University Press) p 317
- [7] Brooks M J, du Clou S, van Niekerk J L, Gauche P, Leonard C, Mouzouris M J, Meyer A J, van der Westhuizen N, van Dyk E E and Vorster F 2015 *Journal of Energy in Southern Africa* **26** 2
- [8] Javu L, Winkler H and Roro K 2021 submitted to *Solar Energy*
- [9] <https://www.worldweatheronline.com>

Enhancing Zinc Oxide gas sensing device for microcontroller application

Sanele S Gumede, Lungisani Phakathi and Betty Kibirige

Department of Physics and Engineering, Faculty of sciences and Agriculture, University of Zululand, KwaDlangezwa, South Africa

E-mail: sanele.scelo.gumede@cern.ch

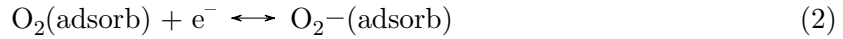
Abstract. Zinc Oxide (ZnO) gas sensors have been popular for some time now, responding with change of sensor resistivity in the presence of a reducing or oxidising gas. The presence of a reducing/oxidising gas is indicated by a measured change in resistance in a gas sensing environment developed at the University of Zululand in the physics department. The purpose of the project was to convert changes in resistance to voltage changes that lie between 0 V to 5 V, suitable for microcontroller applications. Formaldehyde (HCHO), a reducing gas was used to investigate changes in resistivity of the gas sensor in order to establish the range of measured resistance which varied from 1380 to 420 ohms in the absence or presence of the HCHO respectively. Design of a suitable circuit was done, this included the choice of Wheatstone bridge resistances in tandem with a difference operational amplifier. A P-spice simulation environment was developed and used to assess the designed circuit for its suitability for the required voltage range. Simulation results showed that the design circuit provides 3.25 V and 0.13 V in the presence and absence of the gas respectively. This results show that a microcontroller can be introduced to the circuit to give alerts.

1. Introduction

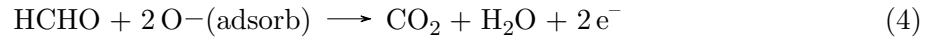
Zinc Oxide (ZnO) as a typical semiconductor metal oxide gas sensor, exhibits characteristics needed for a perfect gas sensor. These include wide band gap of 3.37 eV, large exciton energy of 60 meV, high electron mobility, photoelectric response together with excellent chemical and thermal stability [1, 2, 3, 4, 5, 6]. ZnO is low-cost, non-toxic and easy to prepare [7]. Moreover, ZnO could be a typical chemo-resistive sensing material as its gas sensing is dominantly controlled by the change in sensor resistance when gas molecules react with its surface [8]. In a surrounding atmosphere, oxygen molecules are adsorbed (attached) on the surface of ZnO which then ionizes into oxygen species by capturing electrons from the conduction band, resulting in the formation of surface depletion layer and thus increasing the sensor resistance. When a reductive gas like acetone, approaches ZnO surface, oxygen species will interplay with these gas molecules and release trapped electrons back to the conduction band, causing the sensor resistance to decrease [9, 10]. While exposure to oxidising gases like NO₂ act as electron acceptor, the sensor resistance increases instead [11, 12]. Hence, it is the variation in sensor resistance that achieves the gas sensing characteristic.

Since HCHO is a reducing gas, it will act as an electron donor when interacting with the Zinc Oxide surface. Oxygen ions will be desorbed (released) from ZnO during the interaction and OH ions physisorbed (attached) to the metal oxide (ZnO) surface. As this interaction occurs

there will be a variation of resistance in ZnO [13]. The adsorption of oxygen creates ionic species such as O^{2-} , O_2^- , and O^- , which acquire electrons from the conduction band [14]. The reaction kinetics for creation of the ionic species are as follows:



The HCHO molecules react with created oxygen species releasing trapped electrons back to the conduction band of the zinc oxide semiconductor, that will increase carrier concentration and electron mobility that will lead to a decrease in resistance of a gas sensor. The reaction is described below [15]:



For this project, the main aim was to improve the sensitivity of the electronics used to sense the small resistance changes associated with ZnO gas sensors and to convert it to an output voltage in the range of 0 to 5 V, suitable for microcontroller application. The P-spice [16] simulation (Cadence's electronic circuit simulation tool) environment was used to evaluate the design concept to provide recommendations for the next stage of development.

1.1. Synthesis Of ZnO

Zinc oxide is a known metal oxide semiconductor gas sensor, because of its wide band gap energy. Numerous processes have been used to deposit ZnO on substrates for certain applications such as spin coating, spray pyrolysis technique, thermal evaporation and DC magnetron sputtering [17]. At the department of Physics and Engineering at the University of Zululand, one of the methods used to synthesise ZnO thin films is the chemical bath technique. This method doesn't need sophisticated equipment, uses low temperature and has low cost of deposition [17]. Samples to be used for the devices being considered for this project was synthesized using this technique [18]. The samples provided for this project were ZnO thin films with gold contacts applied.

2. Design Process

2.1. Description Of a Test Chamber

The existing test chamber [18], shown in figure 1 contains the targeted gas introduction under controlled conditions taking cognizance of safety related to explosive gases. The chamber made from brass, allows constant visual monitoring (window in the chamber lid) of the sample gas sensor and controlling the temperature inside the chamber. Inside the test chamber, there is a stage that is capable to heating up to desired temperature and also a thermocouple that monitor the temperature. The chamber consists of an inlet for the introduction of the required test gas volumes, gas outlet and also nitrogen line for flushing the chamber. The test chamber circuit was replaced with a Wheatstone bridge circuit so that the output voltage can be measured instead of a resistance. All other components in the test chamber were kept the same.

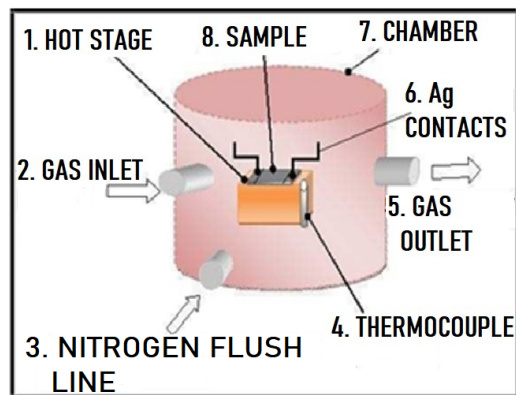


Figure 1: Schematic of the test chamber of ZnO samples as function of temperature and test gas. [18]

2.2. P-spice Circuit Simulation

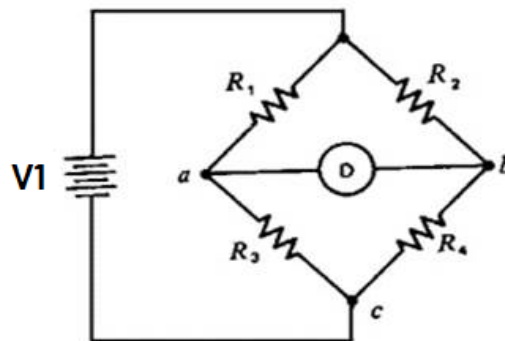


Figure 2: Schematic of a Wheatstone bridge

For the simulation a Wheatstone bridge circuit was used to convert the changing in sensor resistance into change in the output voltage of the Wheatstone bridge. The general Wheatstone bridge circuit is shown in figure 2:

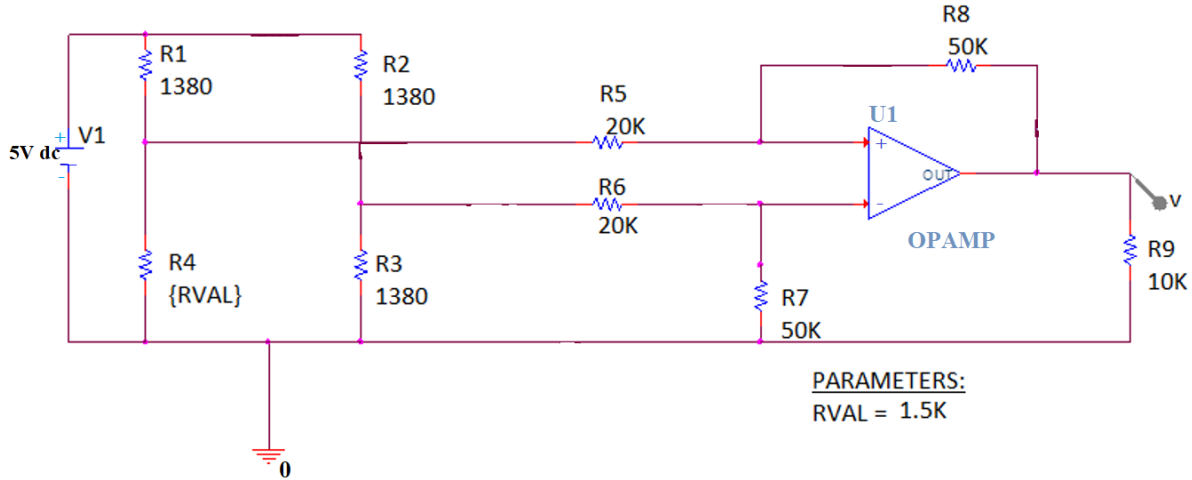


Figure 3: Proposed circuit design

In the Wheatstone bridge circuit, resistor R1 represents a sensor resistance in air and resistor R4 represents sensor resistance in a gas chamber. Resistors R2 and R3 are chosen to be equivalent to R1 in order to give zero output voltage when there is no gas according to equation (5). The difference operational amplifier (OpAmp) was introduced as shown in figure 3. Resistors, R5, R6, R7 and R8 are chosen to control amplification factor of the OpAmp circuit. The operational amplifier connected at the output port of the Wheatstone bridge amplifies the bridge output voltages to between 0 and 5 V suitable for micro controller application. The amplification factor is determined by resistor ratios R8/R5 or R7/R6. R1, the gas sensor resistance in air, has a value of 1380 ohms and R4 which is labelled as RVAL has values that varies with a gas presence.

The formulae used to calculate the output voltage of the OpAmp in Excel are shown below. Equation (5) is the output voltage of the Wheatstone bridge circuit and equation (6) is the amplification output voltage.

$$V_{th} = \left(\frac{1}{1 + \frac{R4}{R1}} - \frac{1}{1 + \frac{R2}{R3}} \right) V1 \quad (5)$$

$$V_{OpAmp} = \left(V_{th} * \frac{R8}{R5} \right) \quad (6)$$

3. Results And Discussion

3.1. Results

The graph below shows results obtained from the P-Spice simulations compared with those obtained through calculations using equation (6) in Excel:

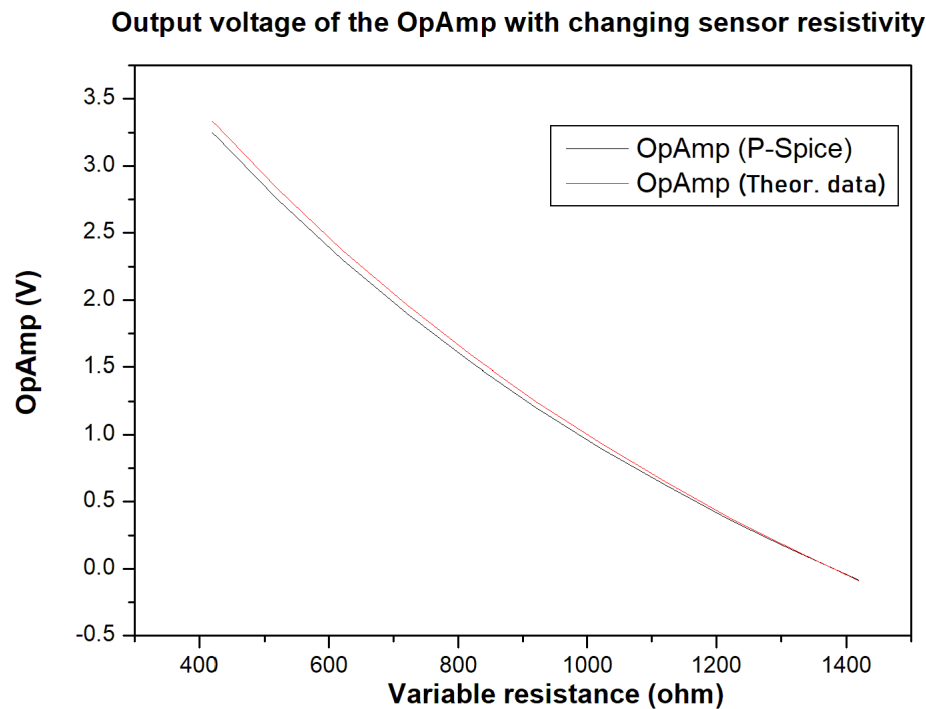


Figure 4: The graph comparing the result of Pspice and calculated data

3.2. Discussion

It was observed that the operational amplifier output voltage decreased exponentially as the gas entered the test chamber which implies the presence of a reducing gas. The resulting decrease in resistivity correspond to an increase in conductivity of the gas sensor. The output voltage magnitude of an operational amplifier lies between 0 to 3.25 V which is sufficient for microcontroller application. Figure 4 validates that the PSpice simulated results and the calculated results are very close to each other with a difference of $\pm 0.04V$.

4. Conclusion

By using a Wheatstone bridge in tandem with a difference operational amplifier, the electronic circuit simulated in P-spice was successful in providing the required output voltage, ranging from 0 to 3.25 V, that is suitable for microcontroller application. For HCHO, a reducing gas, a resistance of the ZnO gas sensor decreased in the presence of the target gas resulting in a decreasing output voltage from the simulated circuit. Results from Pspice correspond with theoretical data, therefore, the simulation was successful.

5. Future Work

In future, the respective effects from reducing and oxidizing gases will be integrated in a single design. A microcontroller will be introduced to the system to differentiate between gas types.

References

- [1] Rai P, Kim Y S, Song H M, Song M K and Yu Y T 2012 The role of gold catalyst on the sensing behavior of ZnO nanorods for CO and NO₂ gases *Sens. Actuators B* **165** 133-142

- [2] Wang Z L 2008 Splendid one-dimensional nanostructures of zinc oxide: a new nanomaterial family for nanotechnology *ACS Nano* **2** 1987-1992
- [3] Zheng J, Jiang Z Y, Kuang Q, Xie Z X, Huang R B and Zheng L S 2009 Shape-controlled fabrication of porous ZnO architectures and their photocatalytic properties *J. Solid State Chem.* **182** 115-121
- [4] Kundu S and Nithiyantham U 2014 DNA-mediated fast synthesis of shape-selective ZnO nanostructures and their potential applications in catalysis and dye-sensitized solar cells *Ind. Eng. Chem. Res.* **53** 13667-13679
- [5] Sankar Ganesh R, Durgadevi E, Navaneethan M, Patil V L, Ponnusamy S, Muthamizhchelvan C, Kawasaki S, Patil P and Hayakawa Y 2017 Low temperature ammonia gas sensor based on Mn-doped ZnO nanoparticle decorated microspheres *J. Alloys Compd* **721** 182-190
- [6] Das M and Sarkar D 2017 One-pot synthesis of zinc oxide-polyaniline nanocomposite for fabrication of efficient room temperature ammonia gas sensor *Ceram. Int.* **43** 11123-11131
- [7] Wongrat E, Chanlek N, Chueaiarrom C, Samransuksamer B, Hongstith N and Choopun S 2016 Low temperature ethanol response enhancement of ZnO nanostructures sensor decorated with gold nanoparticles exposed to UV illumination *Sens. Actuators A* **251** 188-197
- [8] Cui J, Jiang J, Shi L, Zhao F, Wang D, Lin Y and Xie T 2016 The role of Ni doping on photoelectric gas-sensing properties of ZnO nanofibers to HCHO at room-temperature *RSC Adv.* **6** 78257-78263
- [9] Jing Z and Zhan J 2008 Fabrication and gas-sensing properties of porous ZnO nanoplates *Adv. Mater* **20** 4547-4551
- [10] Liu C, Zhao L, Wang B, Sun P, Wang Q, Gao Y, Liang X, Zhang T and Lu G 2017 Acetone gas sensor based on NiO/ZnO hollow spheres: fast response and recovery and low (ppb) detection limit *J. Colloid Interface Sci.* **495** 207-215
- [11] Sonker R K, Sabhajeet S R, Singh S and Yadav B C 2015 Synthesis of ZnO nanopetals and its application as NO₂ gas sensor *Mater. Lett.* **152** 189-191
- [12] Yu L, Guo F, Liu S, Yang B, Jiang Y, Qi L and Fan X 2016 Both oxygen vacancies defects and porosity facilitated NO₂ gas sensing response in 2D ZnO nanowalls at room temperature *J. Alloys Compd.* **682** 352-356
- [13] Shankar P and Rayappan J B B 2015 Gas sensing mechanism of metal oxides: The role of ambient atmosphere type of semiconductor and gases *Sci. Lett. J.* **4** 126
- [14] Chu X, Chen T, Zhang W, Zheng B and Shui H 2009 *Sens. Actuator. B-Chem* **142** 49-54
- [15] Koo W T, Choi S J, Jang J S and Kim I D 2017 *Sci. Rep.* **7** 45074
- [16] Nguyen M A Pspice Tutorial 5-9
- [17] Nkrumah I, Ampomg F K, Kwakye-Awuah B, Nkum R K and Boakye F 2013 Synthesis and characterization of ZnO thin films deposited by chemical bath technique *International Journal of Research in Engineering and Technology* **02** 809-810
- [18] Ngqondo S T 2008 Hydrothermally grown Pb²⁺ doped ZnO nanorods for hydrogen and acetylene gas sensing

A new fast neutron facility for materials analysis at UCT

Sizwe Mhlongo^{1,*}, Andy Buffler¹, Tanya Hutton¹ and Zina Ndabeni^{1,2}

¹ Department of Physics, University of Cape Town, Private Bag X3, Rondebosch, 7701, South Africa

² Department of Subatomic Physics, iThemba LABS, PO Box 722, Somerset West 7129, South Africa

*E-mail: mhlsiz016@myuct.ac.za

Abstract. Fast neutron analysis is one of the techniques that can be used to perform qualitative and quantitative elemental analysis in a range of contexts, including the food, coal and minerals processing industries, and the detection of contraband. The technique makes use of mainly gamma rays as a characteristic signature, however, other signatures such as scattered and transmitted neutrons can be used for elemental characterisation. In 2017, the University of Cape Town (UCT) Department of Physics commissioned the n-lab, a fast neutron laboratory centred around a Thermo MP-320 deuterium-tritium Sealed Tube Neutron Generator (STNG) and a 220 GBq americium-beryllium (Am-Be) radioisotopic source. In this study, the aim is to characterise the n-lab and develop standardised analysis protocols for the elemental analysis of bulk materials. Experiments to characterise the facility have been undertaken, where the neutron yield produced by the STNG, was measured. The measured neutron yield was found to be $(1.22 \pm 0.10) \times 10^8$ neutrons s^{-1} , a value comparable to the specified yield in the STNG operation manual. Furthermore, proof-of-principle materials analysis measurements have also been made, where samples of graphite were characterised using prompt gamma ray neutron analysis. It was possible to positively identify ^{12}C using the 4.43 MeV gamma ray, which is induced by the inelastic scattering interaction between incident neutrons and the ^{12}C nuclei in the graphite sample.

1. Introduction

Fast neutrons can be used to perform elemental analyses of samples, both qualitatively and quantitatively through a range of techniques [1, 2]. A material of unknown composition is exposed to a field of neutrons for a predetermined period of time, resulting in the production of various signatures, such as gamma rays, scattered neutrons and transmitted neutrons [2, 3]. These signatures are highly characteristic of the individual constituent elements whose nuclei have interacted with the incident neutrons. In the case of gamma ray signatures, two techniques are commonly used: Prompt Gamma Neutron Activation Analysis (PGNAA) and Delayed Gamma Neutron Activation Analysis (DGNAA) [1]. Gamma rays are considered as prompt if their decay time is shorter than the resolving time (usually 10 ns to 10 μ s) of the gamma ray detector system [4]. Delayed gamma-rays are usually due to activation of target nuclei, which is due to neutron capture or other reactions that lead to the production of radioactive isotopes [1].

A neutron facility for experimental neutron physics studies requires the availability of neutron sources, neutron and gamma-ray spectrometers. The neutron facility at UCT (n-lab) was commissioned in 2017 [5] and is centered around a Thermo MP-320 Sealed Tube Neutron Generator (STNG), which is an accelerator-based source that relies on the deuterium-tritium fusion reaction to produce 14.1 MeV

monoenergetic neutrons at a rate of approximately 1×10^8 neutrons s^{-1} as per manufacturer specification. Also available is a 220 GBq americium-beryllium (Am-Be) radioisotope neutron source that produces neutrons with a broad energy spectrum, with energies ranging from thermal to 11 MeV. Irradiation of samples can be performed either in the experimental area or close to the source inside the vault by positioning the sample through the variable collimator (see figure1).

We report on recent developments at the n-lab, particularly those focused on the development of techniques for the analysis of materials in bulk using the STNG.

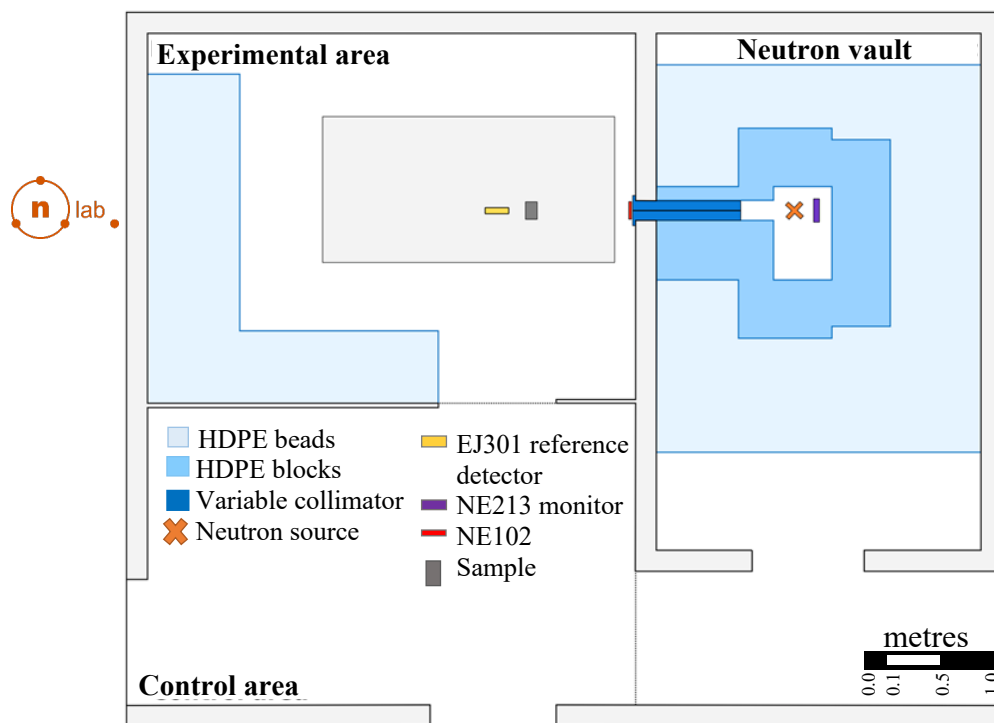


Figure 1. A schematic of the n-lab facility showing the neutron vault, where the STNG is well shielded with High Density Polyethylene (HDPE), the control area and experimental area.

2. Neutron yield measurements of the STNG

The analysis of materials using neutron techniques requires knowledge of the yield and energy distribution of the neutron field. A neutron yield and energy distribution can be measured by active methods such as using neutron spectrometers, or by passive methods, such as foil activation. At the n-lab, the foil activation method was used to measure the fast neutron yield produced by the STNG. Since this requires a material with a known cross section for specific incident neutron energy, a natural copper foil with dimensions of $2.0 \times 2.0 \times 0.1 \text{ cm}^3$ was used. The foil was placed at $12 \pm 1 \text{ cm}$ from the centre of the STNG and was irradiated at maximum operating capacity for approximately 2 hours.

Natural copper has two isotopes, ^{63}Cu and ^{65}Cu , with abundances of 69.15% and 30.85%, respectively. Both these isotopes have well-known and relatively high cross sections for (n,2n) reactions at 14.1 MeV. The $^{63}\text{Cu}(n,2n)^{62}\text{Cu}$ and $^{65}\text{Cu}(n,2n)^{64}\text{Cu}$ reactions have threshold energies of 11.03 MeV and 10.06 MeV [6], respectively, thus, 14.1 MeV neutron energies are sufficient to induce these reactions. The resulting radioactive products, ^{62}Cu and ^{64}Cu , have half-lives of 9 min and 12 h, respectively, and both decay by positron emission followed by two 0.511 MeV annihilation gamma rays.

The gamma rays were measured using a calibrated spectrometer consisting of a cerium-doped lanthanum bromide ($\text{LaBr}_3(\text{Ce})$) detector and electronics for signal processing. The measurements were taken at 30 s intervals, for a total acquisition time of 2 h. The 0.511 MeV gamma ray peak in the spectrum shown in figure 2(a) has contributions from both ^{62}Cu and ^{64}Cu . The 0.511 MeV gamma ray counts from ^{64}Cu can be obtained by summing the count rates from $t = 3030$ s to $t = 7200$ s in figure 2 (b), since the radioactivity of ^{62}Cu is low in this region. Generally, the activity of an isotope diminishes to negligible levels after a period of time that is equal or more than five times its half-life [7].

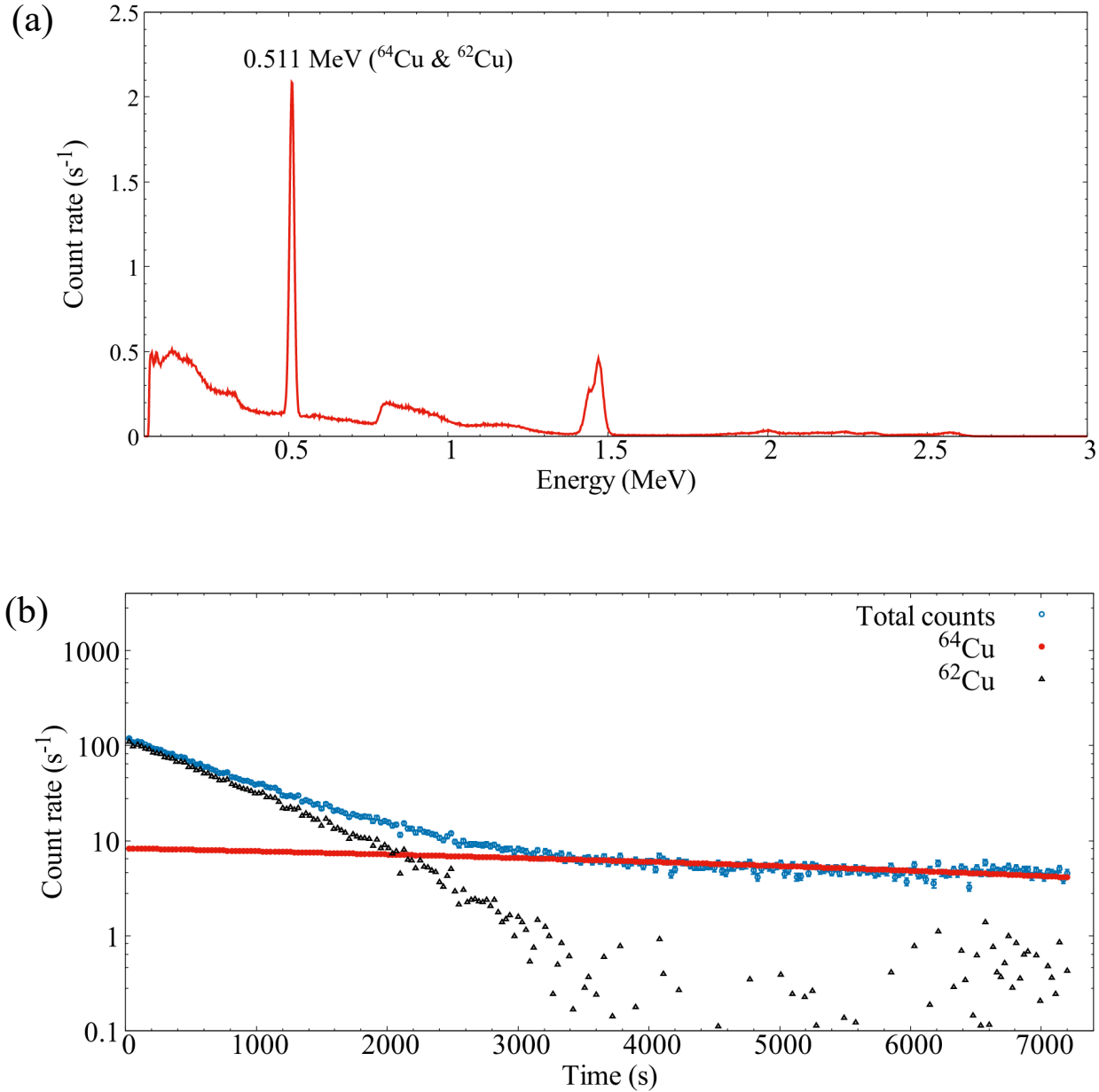


Figure 2. The figure shows (a) the gamma ray spectrum of the copper sample after irradiation with the STNG and (b) the 0.511 MeV gamma ray decay curves. The blue data points are 0.511 MeV gamma ray decays of the STNG irradiated copper. The red and black curves correspond to the decay of ^{64}Cu and ^{62}Cu , respectively.

The fitting of ^{64}Cu data in the 3030-7200 s region makes it possible to also estimate the number of counts from ^{64}Cu in the 0-3000 s region; the 0.511 MeV gamma ray counts from ^{64}Cu can be estimated by obtaining the difference between the abscissas of the ^{64}Cu and the total counts curves. The number of gamma rays attributed to ^{64}Cu , N_p , can then be used to calculate the flux using [7]

$$\Phi(E) = \frac{N_p M \lambda}{N_A m \sigma \theta I_\gamma \varepsilon (1 - e^{-\lambda t_i}) e^{-\lambda t_d} (1 - e^{-\lambda t_c})} \quad (1)$$

The parameter definitions, as well as their values used to calculate the flux are summarised in table 1.

Table 1. The summary of the parameters used in equation (1) with their definitions. The values that were used to calculate the flux are also given, with their uncertainties where possible.

Symbol	Definition	Value
N_p	Net counts in the photopeak	44720 ± 210 counts
M	Isotopic mass	64.93 g mol^{-1}
λ	Decay constant of ^{64}Cu	$1.52 \times 10^{-5} \text{ decays s}^{-1}$ ^a
N_A	Avogadro's constant	$6.02 \times 10^{23} \text{ atoms mol}^{-1}$
m	Mass of copper foil	$5.34 \pm 0.02 \text{ g}$
σ	Cross section at 14.1 MeV	$(9.61 \pm 0.14) \times 10^{-25} \text{ cm}^2$ ^a
θ	Isotopic abundance of ^{65}Cu	0.31
I_γ	Gamma ray intensity	0.352 ± 0.004 ^b
ε	Detector efficiency at 0.511 MeV	0.189 ± 0.004
t_i	Irradiation time	7260 s
t_d	Delay time before counting	3144 s
t_c	Counting time	7200 s
$\Phi(E)$	Neutron flux	$(6.75 \pm 0.13) \times 10^4 \text{ cm}^{-2} \text{ s}^{-1}$

^aAdapted from [8]

^bAdapted from [9]

Using the source-target distance of $12 \pm 1 \text{ cm}$, it was then possible to calculate the neutron yield, Y , of the STNG in $4\pi \text{ sr}$ using equation (2) given as

$$Y = 4\pi r^2 \Phi(E). \quad (2)$$

By substituting the neutron flux into equation (2) the neutron yield of the STNG was calculated to be $(1.22 \pm 0.10) \times 10^8 \text{ neutrons s}^{-1}$ in $4\pi \text{ sr}$, which is comparable to the expected value of $10^8 \text{ neutrons s}^{-1}$, as documented in the user manual.

3. Materials analysis using 14 MeV neutrons

We report on first proof-of-principle experiments to characterise graphite samples, irradiated in the experimental area with a 14.1 MeV neutron beam shaped by a $0.8 \text{ cm } \varnothing \times 100.0 \text{ cm}$ HDPE collimator. At the n-lab, a graphite block with dimensions $13.8 \times 5.9 \times 5.9 \text{ cm}^3$ was irradiated for a period of 1 hour. The gamma ray spectra were acquired during irradiation with a calibrated $3'' \text{ NaI (TI)}$ detector positioned 30 cm from the center of the sample and 90° with respect to the beam direction (see figure 3), with and without the sample present.

The results of the experiment show promise that it is possible to positively identify carbon using the 4.43 MeV gamma rays from the $^{12}\text{C}(n,n')^{12}\text{C}$ reaction, though the rates are low. Figure 4 shows gamma ray spectra acquired during the irradiation of the graphite sample (red) and when the STNG was running without the graphite sample in the sample position (blue). While the 4.43 MeV peak and the single-escape peak at 3.92 MeV are present in both the spectra, it can be seen that the count rates are higher in the red spectrum due to the presence of graphite in the sample position. The 2.20 MeV and 4.43 MeV gamma ray photopeaks in the no sample spectrum are produced from the radiative capture on hydrogen, and inelastic scattering on carbon, respectively, in the HDPE shielding around the STNG.

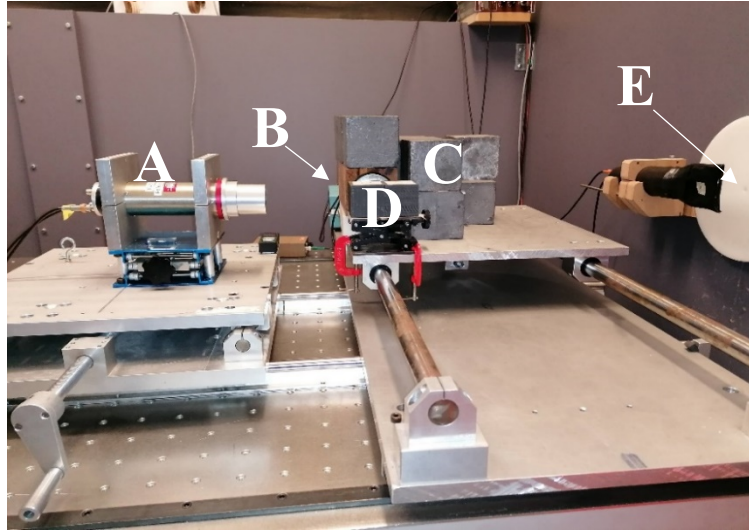


Figure 3. The experimental setup used for neutron analysis of graphite samples consisting (A) neutron detector, which was not in use, (B) 3" NaI(Tl) detector, (C) lead blocks for shielding the NaI detector from gamma rays produced in the HDPE shielding and (D) the graphite block. The detector is positioned at a 90° angle with respect to the beam direction. Neutrons exit of the collimator at (E).

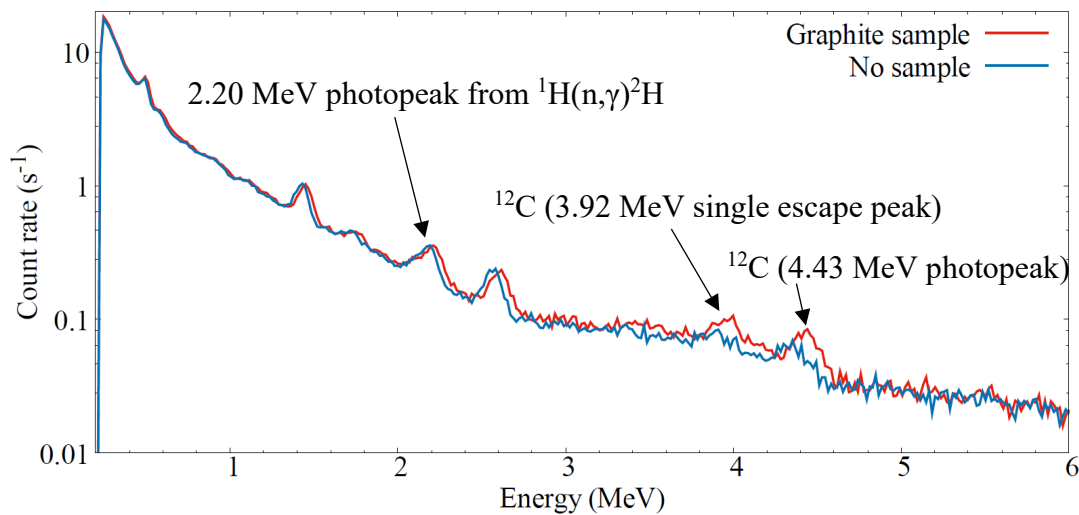


Figure 4. The spectrum acquired during the irradiation of a graphite sample (red) superimposed on the spectrum acquired during the run of the STNG without the graphite sample (blue) in the sample position.

4. Conclusion

The analysis of materials using fast neutrons requires a well characterised neutron field. At the n-lab, the maximum neutron yield from the 14.1 MeV STNG was measured to be $(1.22 \pm 0.10) \times 10^8$ neutrons s^{-1} and is in agreement with the value of 1×10^8 neutrons s^{-1} specified by the manufacturer. Furthermore, the prompt gamma neutron analysis of graphite samples shows that it is possible to qualitatively characterise carbon using the 4.43 MeV gamma rays from the $^{12}\text{C}(n,n')^{12}\text{C}$ reaction.

In the next phase of the study the experimental setup will be redesigned to improve gamma ray count rates by increasing the neutron flux and the geometric detector efficiency. This will be achieved by increasing the diameter of the collimator and by using multiple gamma ray detectors. The measurement of other signatures (scattered and transmitted neutrons) will be explored in parallel. Ultimately, the goal is to develop and demonstrate multi-modal standardised measurement techniques for elemental characterisation of samples in bulk. It is envisaged that this will improve the sensitivity and reduce or eliminate ambiguity where there are suspected interferences when analysing a multi-elemental sample.

Acknowledgements

The authors wish to acknowledge and thank the National Research Foundation for funding this study.

References

- [1] Elayi A G, 1990 *Activation Analysis* Vol 2, ed. Z B Alfassi (Florida: CRC Press) p. 74
- [2] Csikai J, 1995 *Int. conf. neutrons and their applications* (Crete) Vol 2339, ed. G Vourvopoulos and T Paradellis (Washington: SPIE) pp 318-334
- [3] Buffler A 1997, *Int. conf. neutrons in research and industry* (Crete) Vol 2867, ed. G Vourvopoulos (Washington:SPIE) pp. 192-197
- [4] Revay Z and Belgia T 2004 *Handbook of prompt gamma activation analysis*, ed Molnar G (Dordrecht: Kluwer Academic Publishers) p. 5
- [5] Hutton T and Buffler A, 2018 *Proc. of SAIP2017 (Stellenbosch)*, ed. Engelbrecht J (SAIP) pp. 324-330
- [6] Audi G and Wapstra A H, 1995 *Nucl. Phys. A* **595** P. 409
- [7] Xu X, Chang Y, Tang W, Sun Y, Lu J and Li X, 2020 *Applied Radiation and Isotopes* 156
- [8] Ghanbari F and Robertson J C, 1986 *Ann. nucl. Energy* **13** pp. 301-306
- [9] Singh B 2007 *Nuclear Data Sheets* **108** p.197

Enhancing PEPT: high fidelity analysis with augmented detection

R S van der Merwe* and T W Leadbeater

Department of Physics, University of Cape Town, South Africa

E-mail: * VMRR0B003@myuct.ac.za

Abstract. The Positron Emission Particle Tracking (PEPT) technique allows for the tracking of a radioactive tracer particle at high spatial resolution over time, from which its trajectory can be reconstructed with uncertainty. The uncertainty budget when working with higher order measurands, such as velocities and accelerations, is complex and poorly understood, which can be problematic in the case of derived quantities. The uncertainties involved in calculations with these quantities become large as numerical derivatives are computed. To solve this, an alternative filtering and data processing method is investigated, enabling numerical differentiation of the measured trajectories while maintaining useful uncertainty bounds on results. This new method is the Savitzky-Golay filter, a local polynomial least squares fitting technique which is adapted to incorporate propagation of measurement uncertainties applicable to the PEPT technique. This new method is benchmarked against systems of known motion to place confidence limits on the results obtained. These results are then compared to the existing method, and the Savitzky-Golay filter is found to outperform the existing method in both its precision and accuracy across all tested regimes of motion. This potentially improves the uncertainty budget in PEPT analysis, enabling higher precision measurements to be performed.

1. Introduction

The Department of Physics at the University of Cape Town (UCT) runs a dedicated facility for Positron Emission Particle Tracking (PEPT) at iThemba LABS, South Africa. The PEPT technique allows for the tracking of a radioactive tracer particle to high spatial and temporal resolution over an extended time, from which the trajectory (position as a function of time) of the particle can be accurately reconstructed with an associated uncertainty. PEPT enables the non-invasive study of many important dynamical systems, with applications in a range of fields from engineering to medicine [1, 2, 3]. From the trajectories of the tracer particles, first and second order time derivatives can be computed numerically to determine dynamic parameters of the motion, such as velocities and accelerations, from which bulk system behaviours can be inferred. However, the uncertainty budget involved in these calculations is complex and poorly understood, and the application of numerical differentiation is typically accompanied by a loss of dynamic information, leading to greater uncertainties in the computed results. To extend the capabilities of the PEPT technique to enable higher precision analysis, alternative filtering and data processing methods are required to allow for the numerical differentiation of the relevant trajectories while maintaining useful uncertainty bounds on results. In this paper a new differentiation method, applicable to data obtained from the PEPT technique, is formally benchmarked against systems of known motion.

2. The PEPT technique and detector systems

The mechanism of tracking used in PEPT relies on a radioactive tracer particle being a positron emitter. When a positron is emitted, it annihilates with a free electron within a short displacement of the tracer to produce two approximately back-to-back ($180^\circ \pm 0.5^\circ$) annihilation gamma photons with an energy of 511 keV each [4]. If these two photons are detected in coincidence, a line of response (LOR) can be defined linking the two detectors in three dimensional space. Ideally, an LOR can then be used to define the line along which the annihilation event occurred, which, when combined with one or more additional LORs, can be used to identify the location of the tracer at a given time. Of course, not every coincidence detection corresponds to the same annihilation event from the tracer, due to effects such as random or scattered coincidences. To deal with this, an iterative least squares minimisation (triangulation) routine [1] is used to find the most likely location of the tracer at a given time, producing the position $\langle x, y, z \rangle$ and time t with corresponding uncertainties.

Two physical systems were used for the PEPT measurements of tracer trajectories in this paper, being the Siemens HR++ PET scanner, housed at iThemba LABS, and the H3D small-animal PET system, currently housed at UCT. The HR++ camera, as described in [2], consists of 432 bismuth germanate (BGO) block detectors, each segmented into an 8 x 8 grid of independent detector elements, with a total of approximately 28000 detector elements. The block detectors are arranged into a ring in order to facilitate coincidence measurements, giving an axial field of view (FOV) of 23.4 cm with a ring diameter of 82.0 cm. The H3D PET system is comprised of four Polaris generation detector modules [5] arranged into a square, with each module containing four ($20 \times 20 \times 10$) mm CdZnTe (CZT) semiconductor crystals giving a central FOV of ($77 \times 77 \times 42$) mm. While the BGO crystals of the HR++ camera have a much greater intrinsic efficiency leading to higher event rates, the significantly improved spatial and energy resolution of the semiconductor H3D system allows for the acquisition of the tracer emissions to a higher precision. The contrast between these two systems is therefore useful in testing the limits of the applied differentiation method.

3. Differentiation methods

3.1. The 6-point method

In previous research using the PEPT technique, differentiation methods have always been required for analysis, with the most commonly used method being the 6-point method [3].

When considering the output of measurements being of the form $(t_i, \vec{P}_i, \vec{u}_i)$, with \vec{P}_i being the vector position of the particle at time t_i with three dimensional uncertainty \vec{u}_i , the simplest way to estimate the velocity \vec{v}_i of the tracer at time t_i is to use a difference quotient, which is nothing but the spatial difference between two measured positions divided by their relevant measured times. The 6-point method can be considered as a weighted average of six difference quotients, with specific weights and positions chosen for the differences.

The uncertainty on each computed velocity is then calculated by simply propagating the measured position uncertainties through the method. To determine accelerations from the calculated velocities, the 6-point method can be applied again, using the computed velocities as inputs rather than the measured positions. Since the uncertainties must be propagated again through the method, it is expected that they will rise significantly, leading to the desire for an alternative method.

A additional challenge arises when trying to numerically differentiate PEPT data, as the time resolution is low with tracked locations recorded to a precision of 1 ms, meaning that often consecutive locations have the same time stamp and division by zero issues can occur. Therefore, the 6-point method (which is symmetric about the particular point of interest) offers the benefit of increasing the statistics by using non-consecutive data points in division. This method has been shown to produce an unbiased approach, but introduces some smoothing of the

instantaneous velocity as a result of the need for consecutive locations. Under conditions of high accelerations the method also suffers, as even consecutive points can have different dynamics.

3.2. The Savitzky-Golay filter

Here, we replace the conventional numeric approach of the 6-point method with a more advanced filtering method known as the Savitzky-Golay filter [6], which is a particular type of low-pass filter historically used for data smoothing [7]. However, this filter offers the calculations of velocities and accelerations of a tracer particle with potentially significantly reduced uncertainties. The filter assumes that, at least locally in some narrow window of the data, the trajectory of the tracer can be approximated by a polynomial of some degree. Since PEPT measurements are discrete spatial positions with timestamps, a window of the data is a selection of several consecutive discrete positions along the trajectory of the tracer, with the width of the window being the number of selected positions. To apply the polynomial approximation assumption, a weighted least squares fitting routine is used over a moving window of the trajectory of the tracer to simultaneously smooth the measured positions and enable differentiation, which is made simple by the polynomial approximation. The details of this process can be seen as described in [7], and particularly useful results are quoted here.

Consider a design matrix \mathbf{X} of dimension $n \times (m + 1)$, containing all the timing information of a selection of the measured positions along the tracer's trajectory, a weight matrix \mathbf{W} of dimension $n \times n$, containing all the corresponding uncertainty information, and a position vector \vec{y} of dimension $n \times 1$, containing all the consecutive measured positions corresponding to the selections in the previous matrices. Using these matrices and vectors, an m^{th} order polynomial can be fit to a window of the data of width n using the normal equations [8] to extract the best fitting coefficients of the polynomial, given by $\hat{\beta} = (\mathbf{X}^T \mathbf{W} \mathbf{X})^{-1} \mathbf{X}^T \mathbf{W} \vec{y}$, with $\hat{\beta}$ being a vector containing each consecutive fitted polynomial coefficient. Similarly, the uncertainties on these parameters can be extracted using $E_{\beta} = (\mathbf{X}^T \mathbf{W} \mathbf{X})^{-1}$, with E_{β} defining a covariance matrix of the calculated coefficients.

On a case by case basis, the fitting polynomial degree m can be adjusted to better represent the motion of the tracer according to theoretical or experimental expectation. For example, with a tracer falling under gravity the motion is theoretically described by a second degree polynomial, but when a radial coordinate in circular motion is considered a polynomial of a greater degree may better describe the sinusoidal motion. If the calculation of acceleration is desired, the minimal polynomial degree that can be used is 2.

When implementing this filter, the design matrix is typically redefined with a coordinate transformation which places the data point central to the window at the local position $t = 0$. This is useful since with a polynomial of the form $y = \beta_1 + \beta_2 t + \dots + \beta_m t^m$, to determine any filtered value central to the window, being a smoothed version of the same data or even the m^{th} derivative, only a single coefficient needs to be extracted since all others give no contribution following the coordinate transformation. In other words, to determine the values of the m^{th} derivative of the data, the data point central to the window is replaced with the value of $m! \beta_m$, which can then be translated in time back to its absolute position along the trajectory of the tracer particle, simplifying the calculation of the filtered values and uncertainty analysis.

4. Experimental proof of concept

4.1. Interpolation

In addition to the new differentiation method, the effects of interpolation on the smoothing of noise in the data was tested as a precursor to the main filtering. In the interpolation procedure, new events were inferred from measured data, however, as the events arrive randomly in time and are not uniformly distributed in time or space, this becomes an additional source of uncertainty to be propagated carefully.

In this paper, a first step in applying interpolation was the use of a moving average to smooth the data, replacing each measured position at time t_i with the mean of the surrounding 11 events, reducing some of the variation in the data due to noise. Following this, a weighted linear least squares fitting procedure was applied to the smoothed data, using a moving timing window of selected size Δt from which the position with uncertainty at the interpolation time can be extracted. The uncertainty is of course propagated through both the moving average and the linear fitting methods in typical fashion.

A critical assumption for this interpolation is that the event rate or the spacing between the events is small relative to the changes in the motion, such that no adverse effects are seen, which can be controlled to some degree with the choice of the Δt parameter. This limits applicability in cases where the dynamics of the tracer particle are rapidly changing, with time scales on the order of Δt , for example in turbulent flow.

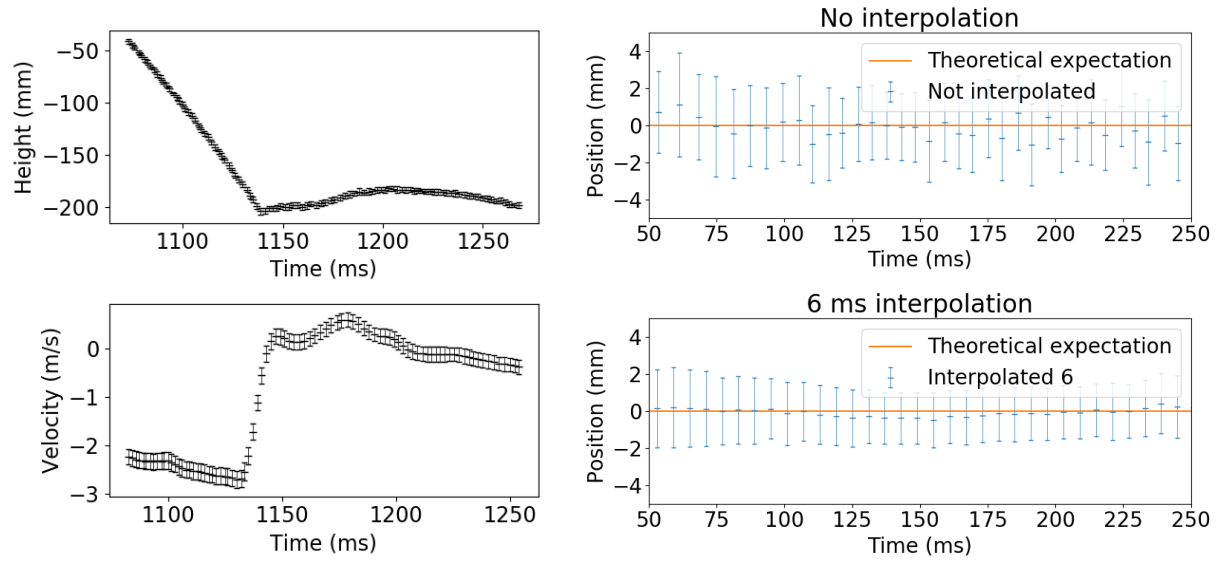


Figure 1. The height and velocity (calculated with the 6-point method) of a tracer falling and bouncing under the effects of gravity.

Figure 2. The effects of interpolation on the positions of a falling tracer, with residuals plotted showing the difference between measured values and theoretical expectation.

In testing this interpolation scheme, typical effects seen were an overall reduction in the mean uncertainties in each position, including a reduction in the overall deviation of the positions from the expected theoretical motion when working with benchmark systems of known motion. Figure 1 shows typical motion of a tracer falling under the effects of gravity, upon which a theoretical expectation for the motion can be built. Figure 2 shows the interpolation scheme applied to the falling tracer, with residuals calculated from the measured motion in figure 1 and the theoretical expectation obtained from the motion.

4.2. Results

The Savitzky-Golay filter was applied to measured data of a tracer particle undergoing standardized motion including remaining stationary, falling under the effects of gravity, and undergoing circular motion. In all cases the HR++ camera was used to perform these measurements, besides for a case of circular motion where the H3D system was used with a rotation speed of around 1 mm/s, showing its applicability to systems of small-scale motion.

The Savitzky-Golay filter was on average 30% – 50% slower than the 6-point method in computing the velocities and accelerations of the motion, but since these computation times reached only tens of seconds when applied to many hours worth of measured data, the time difference between the methods used was not considered in comparisons.

For stationary motion, in all cases the Savitzky-Golay filter was found to outperform the 6-point method, offering optimized mean uncertainty reductions for a moving window of the trajectory with a width of 25 consecutive events and a fitting polynomial degree of 2. This polynomial degree was selected as stationary motion is theoretically described by a 0th order polynomial, but to calculate the acceleration from the filter a minimum degree of 2 had to be used as to test the method itself.

In comparison with the 6-point method, a 77% reduction of the mean uncertainty was seen in the computed velocities while maintaining an equivalent representation of the theoretical motion as the 6-point method. The representation of the theoretical motion was quantified by taking the sum of the squares of the differences between the discrete computed positions, velocities or accelerations and the corresponding theoretical prediction, with a lower value better representing the theoretical model. In the accelerations, a mean uncertainty reduction of 81% was seen with a 75% reduction, or improvement, in the representation of the motion in comparison to the results of the 6-point method.

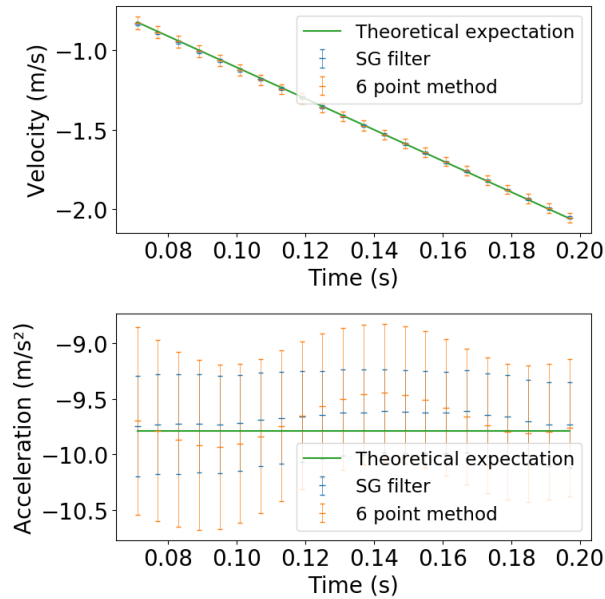


Figure 3. Velocities and accelerations of a tracer falling under gravity computed by the Savitzky-Golay filter, 6-point method, and theoretical expectation, measured by the HR++ camera. Both methods and expectation are in agreement. Note a clear reduction in uncertainties computed by the Savitzky-Golay filter.

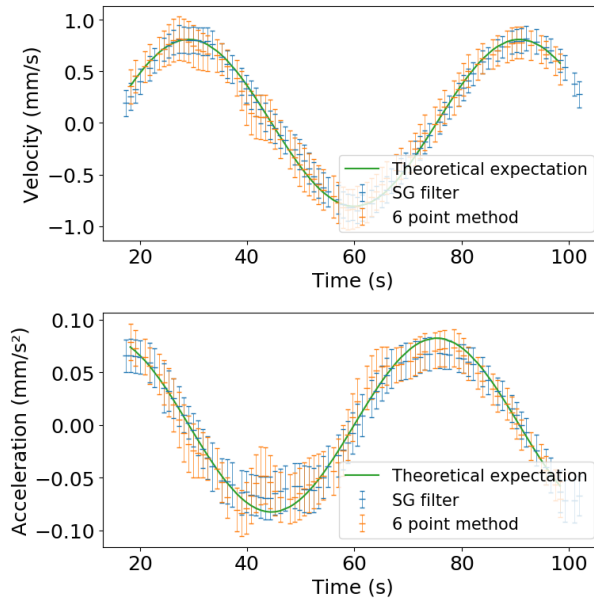


Figure 4. Velocities and accelerations of a tracer undergoing circular motion computed by the Savitzky-Golay filter, 6-point method, and theoretical expectation, measured by the H3D system. Both methods are in agreement, but a loss of accuracy at the extremes of the motion can be seen, leading to underestimates of the absolute velocities and accelerations.

When looking at the falling tracer, very similar effects were seen as in the stationary case, using the same window length and polynomial degrees, and in figure 3 the overall reduction in mean uncertainties in comparison to the 6-point method can be seen. In the case of the velocities, a 76% reduction of the mean uncertainty and a 53% improvement of the representation

of motion was seen. With accelerations, a 40% reduction of the mean uncertainty and a 50% improvement of the representation of motion was seen. Interestingly, with the improvements offered by the Savitzky-Golay filter, we note that the deviations of the accelerations from the expected theoretical motion are all in the same direction in the Savitzky-Golay filtered results of figure 3, indicating that it may be possible to discern the effects of air resistance, but further analysis would be required to confirm this.

In circular motion, rapid changes in the extremities of a particular radial coordinate, i.e. the peaks of the sinusoidal motion of a particular coordinate, were underestimated by lower order polynomials and longer timescales. In this case, the fitting window of the data was reduced in size and the polynomial degree was increased on a case by case basis to account for the more rapid changes in the motion.

Using the circular motion as measured by the H3D system as an example, shown in figure 4, we see qualitatively that the mean uncertainties of the computed velocities and accelerations are approximately of the same order, with quantitative comparisons critical for analysis. To account for the underestimates of the extremities of the motion, the window width was reduced to 21 consecutive events with a fitting polynomial degree of 3. In the velocity a reduction of the mean uncertainty by 28% was seen, with a 67% improvement of the representation of the theoretical motion. In the acceleration, a 12% reduction of the mean uncertainty was seen, with a 52% improvement in the representation of the theoretical motion.

When looking at the results of the H3D system in figure 4, we note that the velocities and accelerations being computed are small, but with the uncertainties on these quantities remaining at least a factor of 6 smaller than the maximal velocity and a factor of 3 smaller than the maximal acceleration, with the uncertainty of the acceleration being of the order of $20 \mu\text{m.s}^{-2}$. This will hopefully permit deeper analysis into small-scale systems of motion in the future.

5. Conclusions

A novel technique for PEPT, being the application of the Savitzky-Golay filter for smoothing and differentiation, was investigated to enhance the uncertainty budget involved when discussing PEPT analysis. The Savitzky-Golay filter was benchmarked, with the results from measured data compared to systems of known motion, and found to outperform existing methods on standardized data sets, offering generally decreased uncertainties on measured positions and derived velocities and accelerations, while also improving the representation of the theoretical motion by the filtered experimental results. However, this was only a proof of concept investigation, and a formal analysis of the uncertainty budget would be needed to quantify the improvements offered by the Savitzky-Golay filter on arbitrary data, but in doing this analysis the enhanced filtering method may lead to an improved quality of future PEPT analyses, particularly in terms of describing the quality of the inferences made from measured data.

References

- [1] Parker D, Broadbent C, Fowles P, Hawkesworth M and McNeil P 1993 *Nuclear Instruments and Methods in Physics Research Section A: Accelerators, Spectrometers, Detectors and Assoc. Equipment* **326** 592 – 607
- [2] Buffler A, Govender I, Cilliers J, Parker D, Franzidis J P, Mainza A, Newman R, Powell M and Van der Westhuizen A 2009 *Int. Topical Meeting on Nuclear Research Applications and Utilization of Accelerators*
- [3] Leadbeater T, Parker D J and Gargiuli J 2012 *Particuology* **10**(2) 146–153
- [4] Knoll G F 2009 *Radiation Detection and Measurement* (John Wiley) pp 12–13 3rd ed
- [5] Jin Y, Tanton P, Streicher M, Yang H, Brown S, He Z and Meng L J 2021 *J. of Nuclear Medicine* **D 62** 1129
- [6] Savitzky A and Golay M J E 1964 *Analytical Chemistry* **36** 1627–1639
- [7] Press W H and Teukolsky S A 1990 *Computers in Physics* **4** 669–672
- [8] Bohm G and Zech G 2010 *Introduction to Statistics and Data Analysis for Physicists* (Deutsches Elektronen-Synchrotron) pp 198–199

Plasma Diagnostics of Miniaturised DC Glow Discharge Thruster Concept

Maheen Parbhoo and Philippe Ferrer

School of Physics and Mandelstam Institute for Theoretical Physics, University of the Witwatersrand, Johannesburg, Wits 2050, South Africa.

E-mail: maheen.parbhoo1@students.wits.ac.za, philippe.ferrer@wits.ac.za

Abstract. The DC discharge microthruster concept is a simple, energy efficient plasma micropropulsion system that operates using an ionisation-acceleration coupling mechanism. It was developed in the hopes of addressing some of the shortcomings of many state-of-the-art electric micropropulsion systems. In this paper, measurements of the thruster's extracted ion beam current as a function of electrode aperture number are presented. The results are compared with theoretical predictions and then used to obtain estimates of the system's thrust. The paper concludes with a discussion of the system's overall efficiency based on its estimated thrust per unit of input power.

1. Introduction

Electric propulsion systems have seen much success on large satellites due to their low fuel consumption and high overall efficiencies [1]. Attempts to miniaturise these systems for applications on the small satellite platform have been physically prohibited since many of them are not scale invariant. Furthermore, power and mass budget restrictions imposed on small satellites creates an additional barrier for the implementation of propulsive mechanisms on these systems [2]. The proposed micropropulsion concept presented here draws inspiration from the popular Direct Current (DC) glow discharge tube [3]. It utilises an ionisation-acceleration coupling mechanism which eradicates the need for additional components and thus reduces the overall size and mass of the system in alignment with the constraints imposed on the CubeSat platform [4]. Additionally, different discharge regimes are obtainable by varying the potential applied between the system's electrodes. These discharge regimes would allow for various operating modes on a potential thruster leading to a system with a high versatility [5].

2. Theoretical Background

The thruster concept studied here can be viewed as a quintessential ion source consisting of a plasma and an accelerator (more commonly called an extractor). The plasma is produced through the electrical breakdown of a gas between an anode and a cathode, with the cathode acting as the ion accelerator/extractor in this context. The ions produced from the plasma flow towards the extractor, where a fraction of them are ejected out of the system through a single or multiple apertures, producing an energetic ion beam. A high voltage power supply provides the means for biasing the plasma. This power supply can also be called the accelerator supply as it determines the ion acceleration voltage V_a [6]. The anode is biased with the positive high

voltage, while the cathode is fixed at ground potential. The resulting electric field between the electrodes acts as the acceleration mechanism allowing the ions to flow to the extractor. Figure 1 illustrates this concept.

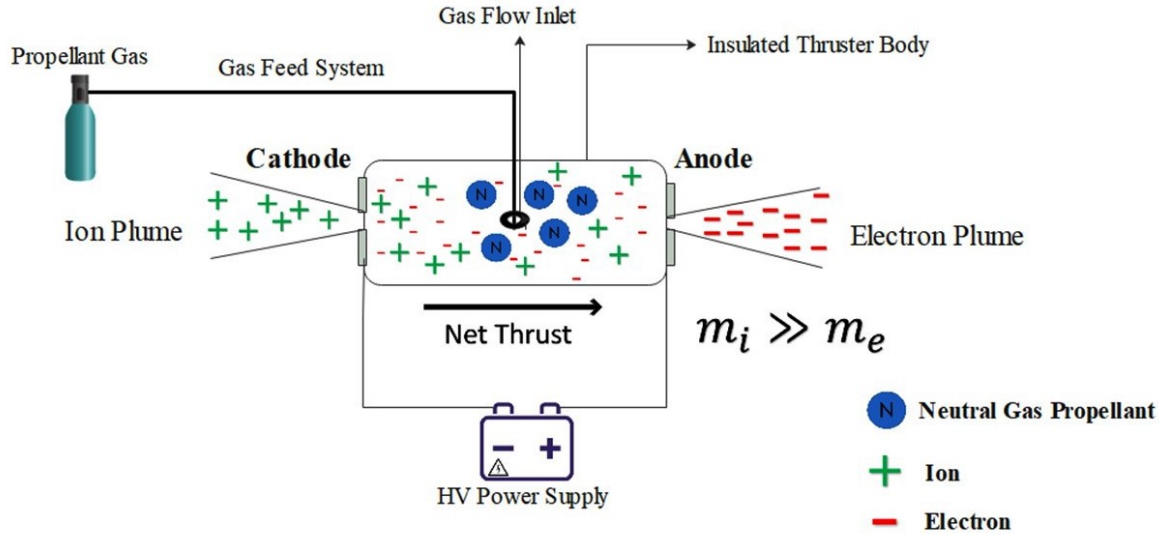


Figure 1. Schematic of the thruster concept. The cathode extracts the positive ions into a focused beam which creates a net momentum providing the desired thrust.

The net thrust T generated by the system can be deduced from the acceleration voltage V_a , and the ion current in the extracted beam I_b as follows [1]:

$$T = \gamma \sqrt{\frac{2MV_a}{e}} I_b \quad (1)$$

Where, M is the ion mass, e is the electronic charge and γ is the thrust correction factor which accounts for the presence of doubly charged ions within the beam, along with thrust dissipation due to beam divergence [1].

In a cylindrically-symmetric extraction system, the total extracted ion beam current can be calculated from the Child-Langmuir Law as follows [6]:

$$I_b = I_{CL} = \frac{4}{9} \pi \epsilon_0 \sqrt{\frac{2e}{M}} S^2 V_a^{3/2} \quad (2)$$

Equation (2) holds if the ion beam current is space charge limited and the emission area is planar and infinite [6]. Here, ϵ_0 represents vacuum permittivity. The aspect ratio S is defined as the ratio of the aperture radius to the discharge gap (distance between the electrodes) i.e., $S = r/d$. Then, for a fixed aspect ratio the extractable ion beam current will be proportional to the acceleration voltage to the three half power (i.e. $I_b \propto V_a^{3/2}$). The remaining constant of proportionality is called the perveance of the extraction system [6].

Many satellite missions implement orbital maneuvers which require an appreciable amount of thrust to be produced at set periods of time. In these situations, it is important to optimize thrust production. This can be accomplished by adding additional apertures to the extractor electrode. However, the addition of apertures will decrease the total electrode surface area and

subsequently decrease the secondary electron emission rate. Thus a higher acceleration voltage, relative to a single aperture system, will be required to generate a particular discharge current.

3. Experimental Setup

The thruster body was constructed from high temperature resistant speciality ceramic material to mitigate any undesirable effects when coming into contact with the discharge plasma. High purity (99.99%) argon was used as the working gas (propellant) for all experimental tests while high durability stainless steel was selected as the electrode material.

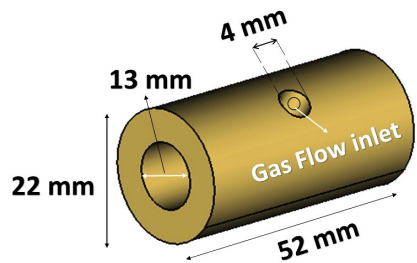


Figure 2. Ceramic thruster tube geometry.

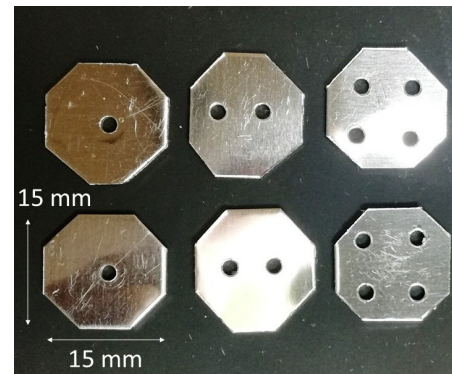


Figure 3. Different electrode aperture configurations explored:
1x2mm, 2x2mm and 4x2mm apertures.

The thruster needed to be small enough to meet the size constraints of small satellites, it also had to have a sufficiently large opening to facilitate the addition of apertures on the electrode surfaces. A length of 52 mm and inner diameter of 13 mm was found to be appropriate to meet these requirements. Additionally, a 4 mm nylon thread was securely fitted at the gas inlet opening and was used to connect a plastic tube from which propellant gas was fed into the thruster. The electrodes were attached to the open ends of the tube using a vacuum compatible adhesive. Extreme care was taken to ensure that the apertures were symmetrically aligned with each other on both ends of the thruster. The experiments were conducted using three different electrode aperture configurations (see figure 3).

4. Methodology

Figure 4 shows the general experimental setup. A 760 mm diameter x 200 mm high stainless steel ring vacuum chamber, fitted with multiple access ports, was used to simulate the ambient space environment. The chamber was pumped down to $5 \pm 1 \times 10^{-5}$ torr with the aid of an Alcatel 2012A roughing pump and a Leybold-Heraeus water cooled diffusion pump. An in-house developed mass flow measurement system, based on the orifice plate concept, was used to measure the mass flow rate of the propellant gas into the thruster (refer to [7], p.63-79 for more details on the procedure used). Mass flows as low as 10^{-7} kg/s were accurately measured using this procedure. In these experiments the mass flow rate was kept fixed at 180 ± 4 ng/s. The HV power supply was then switched on and the current was set to 1 mA.

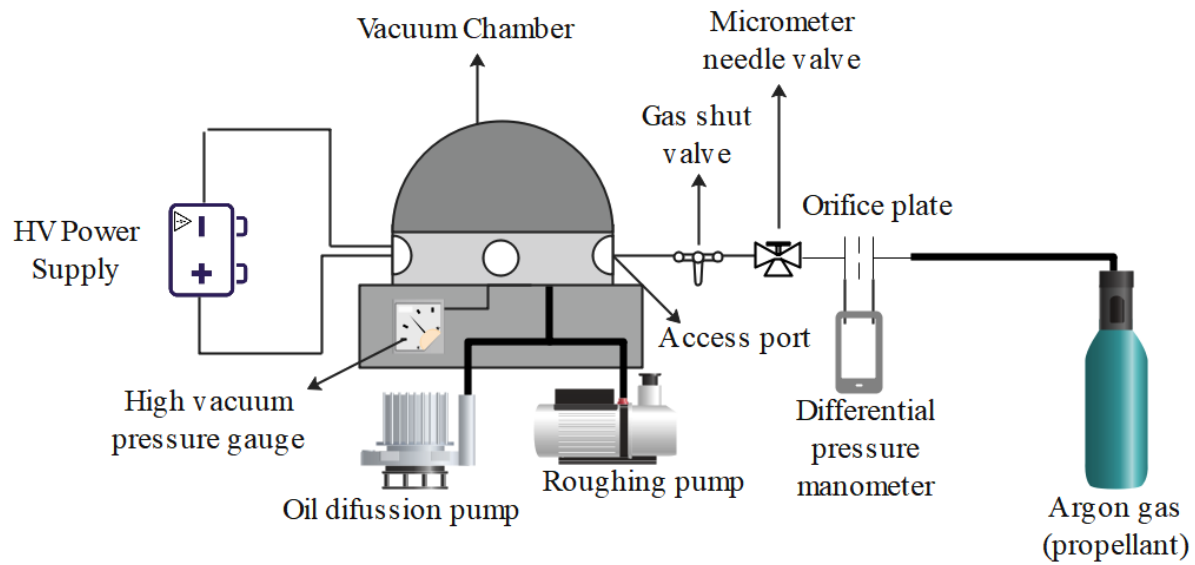


Figure 4. Schematic of the general experimental setup (outside of the vacuum chamber).

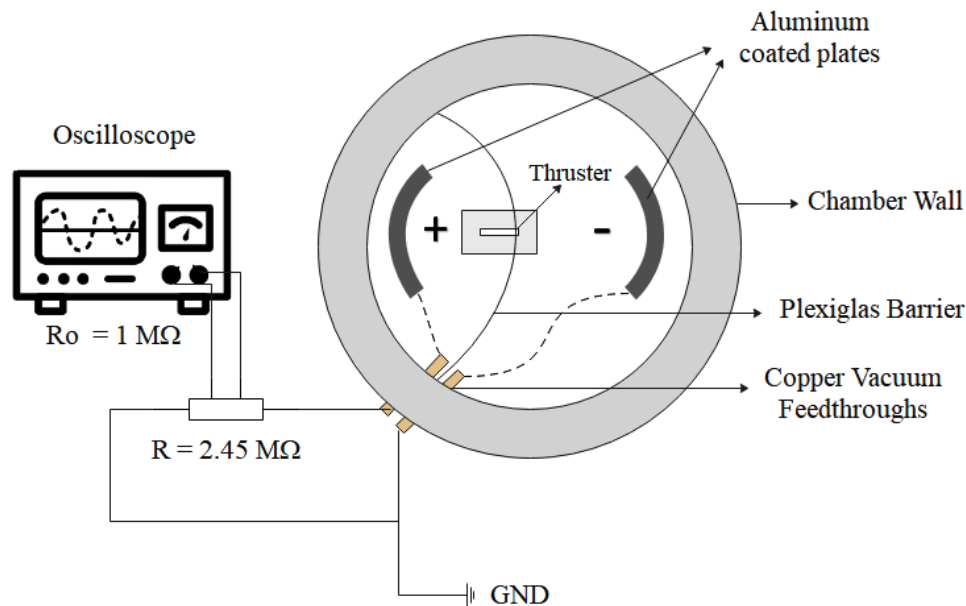


Figure 5. Schematic of the extracted ion beam current measurement setup (inside the vacuum chamber).

Figure 5 shows the experimental setup on the inside of the vacuum chamber. The electrodes on each end of the thruster were connected to the HV power supply with high voltage cables through copper vacuum feedthroughs. Two aluminum coated mylar sheets were used as collector plates to measure the extracted ion beam current. The plates were positioned 90 ± 10 mm and 180 ± 10 mm from the cathode and anode respectively and were separated by a plexiglas barrier. The plate at the anode end was connected directly to ground, while the ion beam collecting plate was connected to a 2.45 ± 0.01 MΩ terminating resistor and then to ground. An oscilloscope,

with internal impedance of $1\text{ M}\Omega$, was used to measure the voltage drop across the resistor. The oscilloscope measured the average plate voltage over 60 seconds and, from this voltage, the beam current was deduced through Ohm's law. Multiple trials were conducted for averaging and to check for repeatability.

5. Results and Discussion

The measured extracted ion beam current for a single, double and quadruple 2 mm aperture electrode configuration is shown in table 1 (the theoretically predicted ion beam currents, for multiple apertures, according to the Child-Langmuir law is given by I_b^{CL}). In each case, the discharge current was kept fixed at 1 mA for comparison. The acceleration voltage V_a corresponding to the 1 mA discharge current, for each aperture configuration, was obtained from the LCD display panel on the power supply and ranged from 1.5 ± 0.1 to 3.5 ± 0.1 kV. Ion beam currents on the order of tens to hundreds of microamps were measured from which the system's thrust was calculated using equation 1. Note however, that the thrust calculated in table 1 does not take into account the correction factor γ and is therefore only an estimate of the system's actual thrust. This is justified since the beam divergence angle, calculated from the spot size of the beam at the collector plate, was measured to be less than 0.2 rad. Thus, the thrust correction factor can be taken as unity to good approximation.

The results show that for a fixed aperture diameter of 2 mm and a discharge current of 1 mA, increasing the number of apertures increases the total extracted ion beam current as expected. However, the results obtained do not match the Child-Langmuir law and suggest that the ion beam current is much greater than theoretically predicted. A possible reason for the discrepancy is that the current measured at the plate may not be the same as the total current leaving the thruster. As noted by Brown I G 2004, the measurement of the ion beam current is affected by the presence of secondary electrons generated from ion impacts on the collector plate as well as the presence of ambient neutral gas particles along the beam path [6]. Collisions between the various particle species may have generated the excess ion current observed.

Table 1. The relationship between the number of apertures, the average ion acceleration voltage, the measured ion beam current (from the $2.45\text{ M}\Omega$ resistor) and the estimated thrust for a fixed aperture radius of 2 mm. The discharge current was kept constant at 1 mA across all aperture configurations.

Aperture No.	V_a (V)	δV_a (V)	I_b (μA)	δI_b (μA)	T (μN)	δT (μN)
1	1765	± 10	10.29	± 0.15	0.13	± 0.02
2	2340	± 10	102.98	± 1.45	1.43	± 0.12
4	3435	± 10	135.79	± 1.91	2.29	± 0.13

One may naively expect the "thrust" to increase linearly with the number of apertures, but the system is likely much more complex. These early results seem to indicate that the apertures "interact" non-trivially with each other. The experiments need to be repeated more carefully with a more sophisticated setup. Moreover, it is recommended that a much larger sample size of apertures is studied, with aperture numbers ranging from 1 to > 20 , in order to make a pattern more apparent. Additionally, one can also experiment with changes in the aperture size to identify the optimal input parameters (current, voltage etc.) for a specific aperture configuration.

6. Conclusion

Ion beam current measurements were conducted on the DC discharge based microthruster. These measurements were used to obtain estimates of the system's thrust. The measured ion current was found to be in excess of the theoretical prediction by the Child-Langmuir equation. This discrepancy may be attributed to a non-ideal experimental setup i.e. the measurement of the ion beam current may have been affected by the presence of secondary electrons generated from ion impacts on the collector plate as well as the presence of ambient neutral gas particles along the beam path. It will therefore be necessary to use a more sophisticated measuring apparatus (for example, a Faraday cup probe) to make more accurate measurements of the ion beam current. Nevertheless, this experiment has verified that a microthruster based on an ionisation-acceleration coupling mechanism can work in principle and can produce a thrust ranging from $0.13 \pm 0.02 \mu\text{N}$ to $2.29 \pm 0.13 \mu\text{N}$ depending on the number of extraction apertures used. It must be noted that the addition of multiple apertures introduces a thrust efficiency trade-off and based on the data from these experiments it may be more beneficial to use a 2x2 mm extractor aperture configuration for optimum thruster performance under these conditions. The main purpose of these experiments, namely to determine thrust production with various electrode apertures, was successfully demonstrated. The results of this paper will justify a more in depth investigation.

Acknowledgements

The financial assistance of the National Research Foundation (NRF) towards this research is hereby acknowledged. Opinions expressed and conclusions arrived at, are those of the lead author (Mr. Maheen Parbhoo) and are not necessarily to be attributed to the NRF.

References

- [1] Goebel D M and Katz I 2008 *Fundamentals of electric propulsion: ion and Hall thrusters* John Wiley & Son (Vol. 1) 21-30
- [2] Tummala A R and Dutta A 2017 An overview of cube-satellite propulsion technologies and trends *Aerospace*. **4** 58-88
- [3] Gudmundsson, J.T. and Hecimovic, A., 2017. *Foundations of DC plasma sources*. Plasma Sources Science and Technology, 26(12), p.123001.
- [4] Ferrer P and Tchonang M 2011 Miniaturization of electrostatic ion engines by ionization and acceleration coupling *J. Phys. D: Appl. Phys.* **44** 335204
- [5] Wright, W.P., 2017. Characterization of direct current discharge based electric microthrusters Doctoral thesis (University of the Witwatersrand, Johannesburg)
- [6] Brown I G 2004 *The physics and technology of ion sources* John Wiley & Sons 29-63
- [7] Krommenhoek M 2015 *Modelling of the propulsion mechanism for a miniaturized corona ionization thruster* Masters thesis (University of the Witwatersrand, Johannesburg) 63-79

Performance analysis of thin-film photovoltaic (PV) technologies in an embedded generation network

R P Roodt^{1,*}, E E van Dyk¹, J L Crozier McClelland¹ and F J Vorster¹

¹ Department of Physics, Nelson Mandela University, Port Elizabeth, 6031, South Africa

* Email: s217357709@mandela.ac.za

Abstract. Thin-film photovoltaic (PV) technology has varying performance for different technologies. Even though the efficiency of the thin-film modules are less than that of crystalline silicon modules, the thin-film modules do have advantages in certain locations, due to their spectral and thermal responses. In this study, the performance of thin-film PV modules operating in an outdoor environment is monitored and analysed. An embedded generation network has been established by the PV Research Group at the Outdoor Research Facility (ORF) located on the South Campus of Nelson Mandela University. This network contains three kW-scale grid-connected PV arrays comprising cadmium telluride (CdTe), copper indium diselenide (CIS) and amorphous silicon (a-Si) thin-film technologies. This paper presents and discusses the performance data of these three arrays over an extended period. A thorough comparison of the energy production is given, together with preliminary performance loss and degradation. From the data acquired, it is observed that the CIS and CdTe systems have higher performance ratios of the order of 85 %, while the performance ratio of the a-Si system is consistently below 75 %. It was found that the a-Si array lost 30% of its rated power in a period of 4 years, indicating that its operational lifespan is much less than that of the other thin-film modules studied.

1. Introduction

Thin-Film PV modules have lower efficiencies compared to crystalline silicon PV modules. The thin-film modules therefore need larger surface areas to produce the same peak output power as that of crystalline silicon modules. Furthermore, the thin-film modules guaranteed operational lifespan has improved significantly and has become similar to that of crystalline silicon modules. The advantages that thin film PV modules do have over crystalline silicon modules is they have a lower temperature coefficient as well as a very good response to the shorter wavelengths of the sunlight's spectrum. This means that in hotter environments the power of the thin film materials will be less effected and as well as in overcast conditions [1]. The performance of these PV modules is strongly dependent on the location; as temperature, and the spectrum of the sunlight play a big role in how the modules perform [2]. It is therefore important to monitor these modules for a significant timespan to evaluate them in an operational setting.

1.1. Performance parameters of PV systems

The in-field monitoring of the performance of thin-film PV systems is of great importance as it allows one to better understand how the systems work under real outdoor grid-tied conditions. In addition to the array parameters, the performance parameter investigated in this work is:

Performance Ratio (PR): The performance ratio is a measure used to determine the efficiency with which the PV plant handles the available radiation energy. This parameter is defined as the ratio between the final specific yield, Y_F and the reference yield, Y_R [3]:

$$PR = \frac{Y_F}{Y_R} \quad (1)$$

1.2. I-V Curve

An I-V curve (current-voltage characteristic curve) is a graphical representation of the relationship between the voltage applied across the PV module or array and the current flowing through it. The shape of the curve is also significant as one can detect any deviations from what should be observed, and the causes of these deviations can then be investigated further [4]. Another curve that is plotted together with an I-V curve is a P-V curve (power-voltage curve) which indicates the power that the module or string produces at each voltage value .

Important points on these curves are I_{sc} , I_{mp} , V_{mp} , V_{oc} and P_{max} , where I_{sc} is the short-circuit current which is the largest current that can be drawn from the PV module or string, V_{oc} is the open-circuit voltage which is the maximum voltage available from the PV module or string and I_{mp} and V_{mp} is the maximum power current and maximum power voltage respectively and these are the values that correspond to the P_{max} value, which is the maximum power point [4]. Another quantity that one can obtain from the above-mentioned points is the fill-factor (FF) which is the ratio of the maximum power and the product of V_{oc} and I_{sc} :

$$FF = \frac{I_{mp} \times V_{mp}}{I_{sc} \times V_{oc}} \quad (2)$$

Graphically, the FF is a measure of the “squareness” of the I-V curve, and it is also the largest rectangle that will fit into the IV curve [4].

2. Experimental Procedure

A grid-tied PV network, consisting of three thin-film systems of approximately 1kWp each, is installed at the Outdoor Research Facility (ORF) situated at Nelson Mandela University. The three thin-film PV arrays make use of copper indium diselenide (CIS), cadmium telluride (CdTe) and amorphous silicon (a-Si) technologies respectively. An aerial image of the three PV arrays together with diagrams illustrating how they are connected is shown in figure 1.

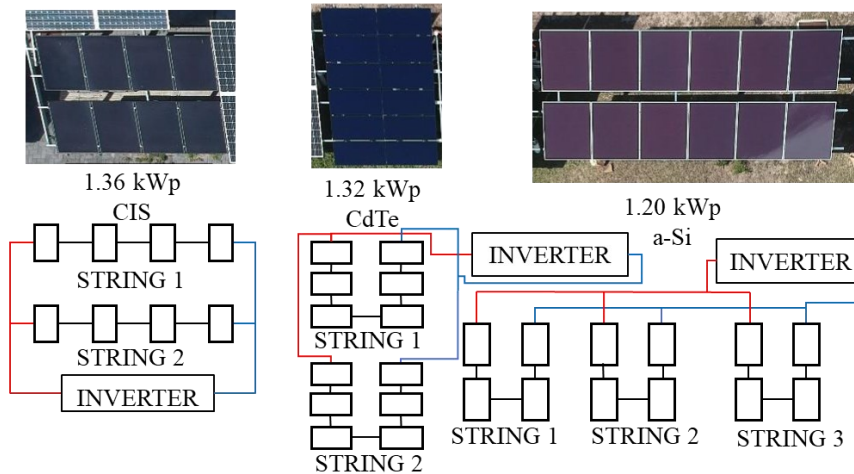


Figure 1. an Aerial image of the three thin-film PV arrays, together with a schematic of how they are connected. The peak output power of the arrays and the thin-film material of each array are also included.

2.1. Data Acquisition

The plane of array irradiance (POA) was obtained from a CMP3 Kipp & Zonen pyranometer, located above the CIS array. The DC current/voltage and power as well as AC current/voltage and power together with the module temperatures of each array was monitored by using a custom build datalogger unit for each PV array [5]. The dataloggers are programmed to collect data from the sensors every second. After every 10 seconds, the data is averaged, and the averaged value is recorded in the database on the datalogger. Every 15 minutes the data from the datalogger is transferred to the computer via an ethernet cable. The software used for acquiring the data from the data loggers is LoggerNet. The data retrieved from the datalogger is stored on the PC in a text file for the selected time interval. Due to the data being in text format, it is not easy to manipulate or perform analysis. A custom-built LabVIEW program was used to process and examine the data in the text files.

2.2. I-V curve measurements.

The I-V curves of the strings of the three arrays were taken on clear sunny days as close as possible to solar noon to minimise the uncertainty in the measurements. The first measurement is when they were installed or shortly thereafter to have the initial performance values of the arrays. The I-V curve measurements were obtained with the use of a Solmetric's PV analyser and I-V Curve Tracer, the PVA-1000S and the SolSensor 200 which measures the irradiance. The measured I-V curves were then corrected to Standard Test Conditions (STC), temperature of 25 °C and irradiance of 1000 W/m², according to the standard translation equations [6]. These equations consider the measured irradiance, temperature and uses the temperature coefficients specified by the manufacturer to obtain how the modules would have performed at STC. This is done so that I-V curves taken at different conditions could be compared to one another.

3. Results

The results illustrated in this report for the PR of the arrays are for the period of November 2019 to February 2020 and November 2020 to February 2021. The reason for the gap in between the results is due to a technical fault resulting in no data collected for that period and this fault could only be fixed after the first COVID-19 lockdown.

3.1. Performance Ratios

The monthly averaged performance ratios obtained for the three thin-film arrays for the period of November 2019 to February 2020 and November 2020 to February 2021 together with two of the array's back of module temperature is showing in figure 2.

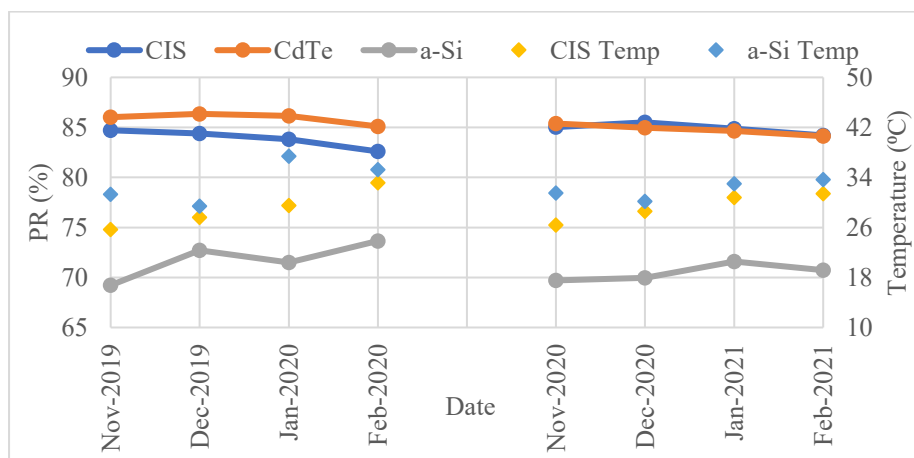


Figure 2. Monthly average performance ratios of the three PV arrays together with two of the arrays back of module temperature.

The Performance ratios obtained for the CIS and CdTe systems throughout the periods are comparable, in this first period the CdTe had a higher performance ratio but in the second period, the

performance ratios were almost the same. For the a-Si array on the other hand it was found that its performance ratio was much less, around the 70% mark. This is due to the modules in the a-Si array degrading as these modules have been in operation since 2018. One interesting trend observed with the performance ratio of the a-Si system is that as the back of module temperature increases so too does the performance ratio of the a-Si array. This is seen in both earlier and later measurements. The reason for this improvement in the performance ratio of the a-Si array is due to the thermal regeneration of the a-Si material [7]. The CIS and CdTe array's performance ratios decreased as the back of module temperatures increased, which is expected.

3.2. I-V Curves

The I-V curves obtained for one string of each of the three arrays are showing in figures 3 to 5. Figure 3 shows the I-V curves obtained for string 1 of the CIS array, figure 4 shows the I-V curves obtained for string 1 of the CdTe array and figure 5 shows the I-V curves obtained for string 2 of the a-Si array. The other strings of the various arrays show the same features as seen in these I-V curves.

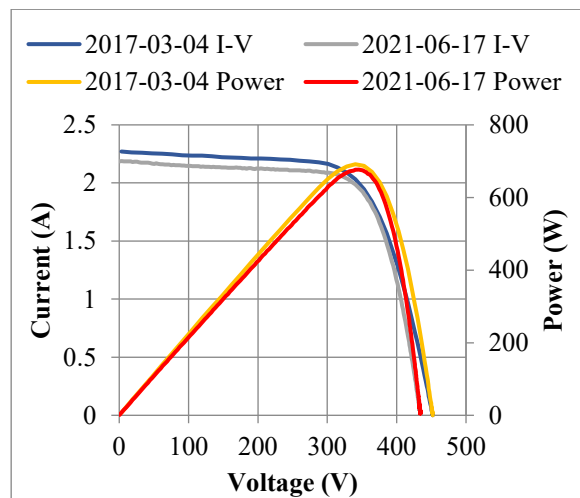


Figure 3. CIS string 1.

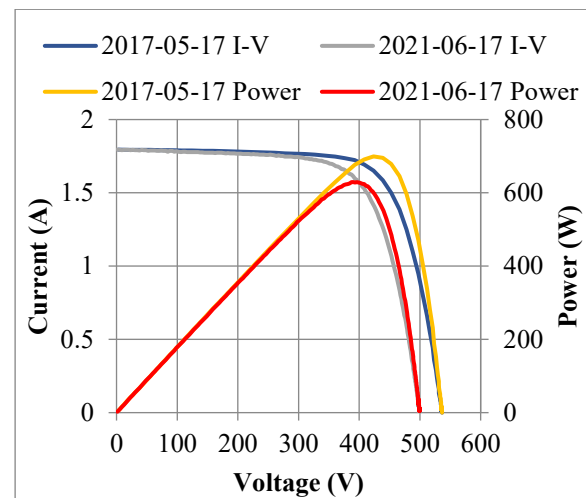


Figure 4. CdTe string 1.

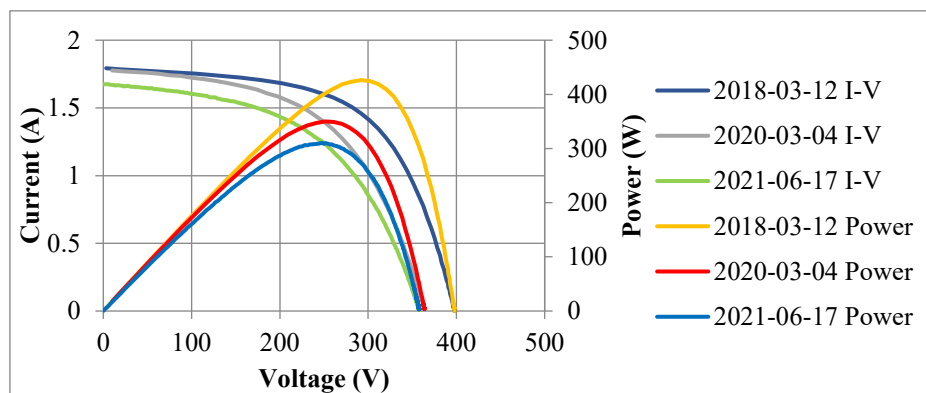


Figure 5. a-Si string 2.

The shape of the I-V curve for the CIS and CdTe strings is quite similar with regards to the knee of the curves. The shape of the I-V curve obtained for the a-Si strings differs quite significantly from those obtained for the other two arrays as it has a much "rounder" knee. These differences in the shape of the I-V curves can also be seen in the FF values for the strings of the three arrays. the CIS and CdTe strings FFs are round about 0.70 but the a-Si strings FFs starts at 0.60 and decreases to 0.50 in the last measurement. These FF values together with the P_{\max} and V_{mp} points measured for the strings of the

three PV arrays are shown in figures 6 – 8. Figure 6 shows the values obtained for the 2 CIS strings; figure 7 for the 2 CdTe strings and figure 8 for the 3 a-Si strings. In these figures the dates are replaced by alphabetical letters to make the results more visible. The initial values measured for the strings in the 3 arrays are labeled alphabetically, where “a” represents 2017-04-03, “b” represents 2017-05-17 and “c” represents 2018-03-12. The rest of the measurements for the 3 arrays were obtained on the same dates and these dates were 2019-12-05, 2020-03-04 and 2021-06-17 which are represented by the letters, “d”, “e” and “f”, respectively.

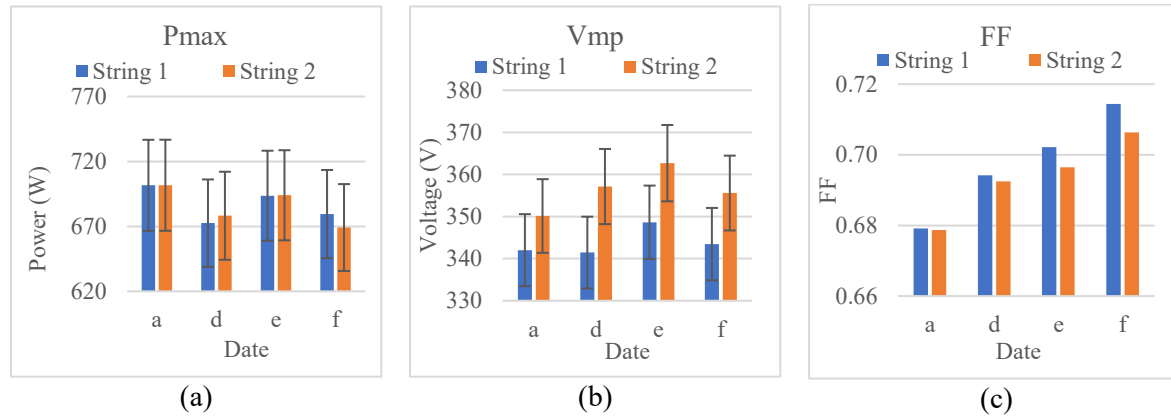


Figure 6. I-V curve parameters obtained for the 2 strings in the CIS array.

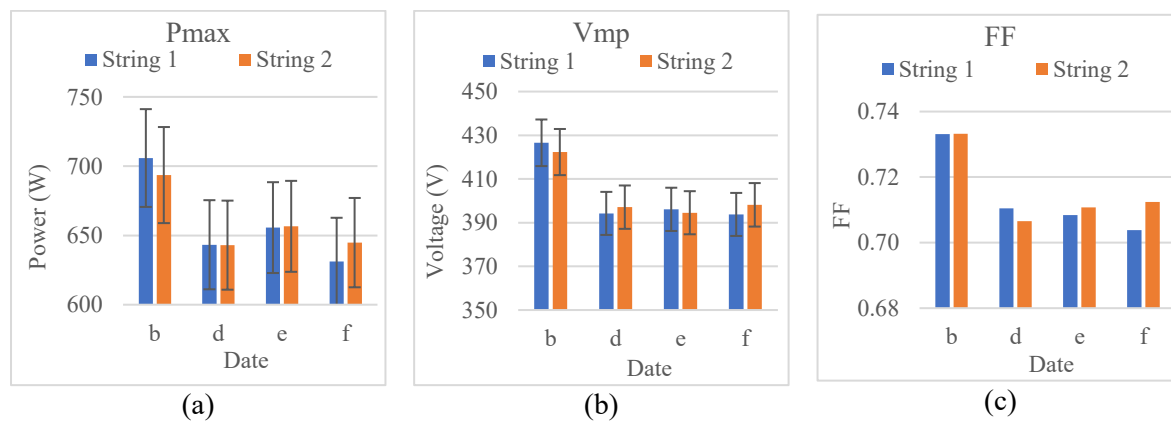


Figure 7. I-V curve parameters obtained for the 2 strings in the CdTe array.

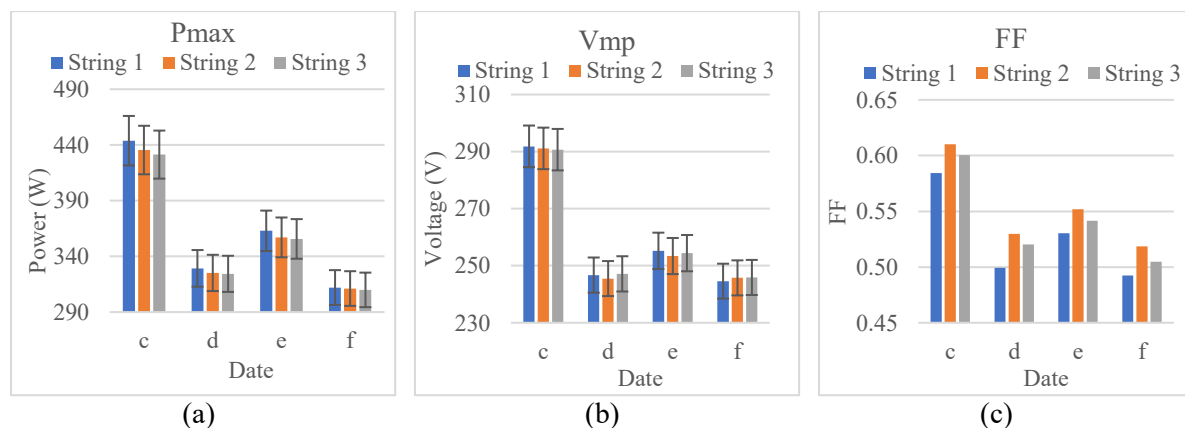


Figure 8. I-V curve parameters obtained for the 3 strings in the a-Si array.

The Power values obtained for the two strings of the CIS array are consistent from the time of installation till the last measurement, with only minor variations which all fall within the $\pm 5\%$ uncertainty. What is interesting to note is that these two strings produced the same power values, even though they have different V_{mp} and I_{mp} values. The FF of the two strings increased which is mainly due to the decrease in the V_{oc} values of the strings.

The decrease in the power values of the CdTe strings, from the first to the second measurement, is due to degradation as the period between these two measurements is 2.5 years. The reason for this degradation requires further investigation and will be looked at in future work. The power measurements decreased from the first measurement to the last measurement by 10% for string 1 and 7% for string 2. This decrease observed in the power values and the FF is mainly due to the decrease in the V_{mp} values. This decrease in voltage values of the CdTe strings was also observed in another study for a CdTe module [8].

The power of the a-Si strings decreased by 30% from the initial measurement to the last measurement, which is due to light-induced degradation. Furthermore, the power values increased by 10% from 2019-12-05 (d) to 2020-03-04 (e), which confirms the thermal regeneration seen in the performance ratio of the a-Si array [7]. This regeneration is also seen in the increase of the V_{mp} for that period.

4. Conclusion

The performance of three different thin-film PV technologies, situated at the outdoor research facility at Nelson Mandela University, was investigated. It was found that the array consisting of CdTe modules had the overall best performance ratio, around 85%. The array consisting out of CIS modules had the most consistent performance ratio and power measurements. The a-Si array performance ratio was the lowest of the three arrays but showed an increase in performance over the summer period due to thermal regeneration and this is confirmed by the increase in their power measurements in that period [7]. Comparing the results obtained here to that of a similar study done in Poland, with a similar operational time frame of 4 years, it was found that out of the thin-film materials the copper indium gallium selenide (CIGS) had the highest PR which was followed by the a-Si, which in the summer had similar PRs seen in the current study and the CdTe had the lowest PR of 42% [2]. In that study the CdTe modules have degraded. In the current study the a-Si modules have degraded and lost 30% of its rated peak power. Indicating that the operational lifetime of the a-Si modules is much less than that of the other two thin-film module types.

References

- [1] Taraba M, Adamec J, Danko M, Drgona P and Urica T 2019 Properties measurement of the thin film solar panels under adverse weather conditions *Transportation Research Procedia* **40** 535–40
- [2] Zdyb A and Gulkowski S 2020 Performance assessment of four different photovoltaic technologies in Poland *Energies* **13** 196
- [3] Quansah D A, Adaramola M S, Appiah G K and Edwin I A 2017 *Int. J. of Hydrogen Energy* **42** 4626–4635
- [4] Zhu Y and Xiao W 2020 A comprehensive review of topologies for photovoltaic I–V curve tracer *Solar Energy* **196** 346–57
- [5] Yaso A 2018 *Monitoring of Grid-Integrated and Stand-Alone Photovoltaic Systems* MSc thesis Nelson Mandela University
- [6] Solmetric PV Analyzer I-V Curve Tracer User's Guide 8.1 – 8.3
- [7] Staebler D L and Wronski C R 1977 *Appl. Phys. Lett.* **31** 292–294
- [8] Rawat R, Kaushik S C, Sastry O S, Bora B and Singh Y K 2018 *Materials Today: Proc.* **5** 23210–23217

Evaluation of PV power forecasting models using temperature data

L Masevhe¹, J K Kirui¹ and N E Maluta^{1,2*}

¹University of Venda, Department of Physics, P/Bag X5050, Thohoyandou, 0950, South Africa

²National Institute for Theoretical Physics (NITheP), Braamfontein, Johannesburg, 2000, South Africa

E-mail: Eric.Maluta@univen.ac.za

Abstract. The study is based on the temperature data of 2019 as collected from the USAid Venda, one of the South African University Radiometric Network (SAURAN) stations in Vuwani, Limpopo Province. The temperature-based Hargreaves-Samani ($H - S$) empirical model has been used to estimate the global solar radiation in order to forecast the potential solar output. The statistical parameters used for the analysis showed strong correlation between the observed and estimated solar radiation data, giving a $RMSE$ value of 1.84 W.m^{-2} , a MBE value of 1.39 W.m^{-2} , a MPE value of 1.29 W.m^{-2} and a R^2 statistics value of 0.84. The strong correlation validated the $H - S$ model as a reliable input for solar power output models. The annual average power output predicted by the two models were 51 W and 57 W based on the use of a 255-W solar panel. The efficiencies of the models agreed well with that using standard testing condition which is about 20 % of the input values of solar radiation values. The study has proven that the solar power output predictions can be conducted in areas with limited weather data for long- to short-term PV power output forecast to assist in the design of power generation system irrespective of the power of the PV and location where it is to be implemented.

1. Introduction

An electric power-system capable of meeting a prescribed demand requires a high level of prediction accuracy in the planning stage. The accurate estimation of photovoltaic (PV) power output based on the weather information of the local area of the solar panel installation is crucial in many applications. The PV -effect is an electrochemical process that generates voltage or electric current in a photovoltaic cell when exposed to sunlight [1]. The PV power output prediction depends on meteorological variables such as solar radiation, temperature, rainfall, wind speed and relative humidity at the specific site [2]. Global solar radiation (H) is an important input for estimating power output, (P_{PV}) from the PV panel. Relevant instrumentation to measure these parameters such as a pyranometer should be installed, but due to its high cost and scarcity [3], estimation of values become necessary. In such cases local temperature values can be used for estimation by employing mathematical models as an alternative to measurements [4].

The chosen temperature-based empirical model used for this study was the Hargreaves-Samani ($H - S$) Model. It has an advantage of being effective in areas where the weather data is not available, but temperatures are [5]. The estimated radiation data is validated by comparing

with observed values for the year 2019 at the USAid Venda Station located at Vuwani (Latitude of -23.13100052 and Longitude of 30.42399979) which is one of the South African Universities Radiometric Network (SAURAN) stations. SAURAN is a network of stations located across the Southern African region including South Africa, Namibia, Botswana and Reunion Island that provide ground-based solar radiometric data [6]. The estimated H was used to predict the potential power to be generated by the solar panel that has been installed at the station. Forecasting of the H is the first and most essential step in most PV power predictive systems. Numerous PV solar power forecasting methods including the physical models based on numerical weather prediction and satellite images have been reported in the literature [5].

In the current study, two global solar radiation-based PV power output generation models Skoplaki *et al.* and Ramli *et al.* were used to determine the power output were from the panels installed on site. The performance of the two models was determined by using the calculated solar radiation from equation (1) and the manufacturer's dataset of a 255-W polycrystalline silicon PV panel from the 5kW array on site. Modelling PV power output accurately is hampered by the difficulty of estimating the solar irradiance, especially when influenced by cloud cover. Output power depends also on parameters, such as the PV technology used, module temperature and panel shading as a function of sun angle, among others. The performance of these models was checked for the panel under standard testing (STC) conditions and then under the local weather conditions. A notable advantage of this approach is that it uses only weather variables that are easily obtainable [6]. Furthermore, the correlation between different meteorological data for different sites or locations and power output at any time including the future period was well demonstrated [7]. This paper lays a foundation short- to long-term forecasting of PV power output and the sizing of the system in the design phase which is adaptable to any location with limited weather data information, as well as determining the suitable panels for the site.

2. Methodology

2.1. Weather information

Figure 1 is a graphical presentation of the daily minimum, maximum and average temperature values observed at the USAid Venda SAURAN Station for a period of one year in 2019. The average monthly temperature values were used to estimate solar radiation by employing an empirical temperature-based equation.

2.2. Temperature-based estimation of solar radiation (Hargreaves-Samani Model)

The average monthly temperature values that were measured at research site in 2019 were used as input in equation (1) to estimate the global solar irradiance (H_c). The $H - S$ model uses a simple equation for estimating solar radiation (H_c); it requires only maximum and minimum temperatures (T_{min} and T_{max}) at the research site in Vuwani, and is given by [7]:

$$H_c = k_r H_0 \sqrt{\Delta T} \quad (1)$$

where k_r is an empirical constant of 0.16 for inland region [5]. The average daily extra-terrestrial irradiance H_0 (W.m^{-2}) is estimated using equation (2) [8]:

$$H_0 = \frac{1440}{\pi} H_{sc} D_f (\cos \varphi \cos \delta \sin \omega_s + \omega_s \sin \varphi \sin \delta) \quad (2)$$

where H_{sc} is the solar constant (1367 W.m^{-2}) [9], φ is latitude of location being considered (deg), δ_s is the solar declination for the month (deg), and ω_s is the mean sunrise hour angle for a given month (deg). D_f is the eccentricity correction factor of the earth's orbit on the n^{th} day of the year (Julian days from 1 January to 31 December) [10]. The expressions for D_f , δ_s and ω_s are given by equations (3) - (5) below:

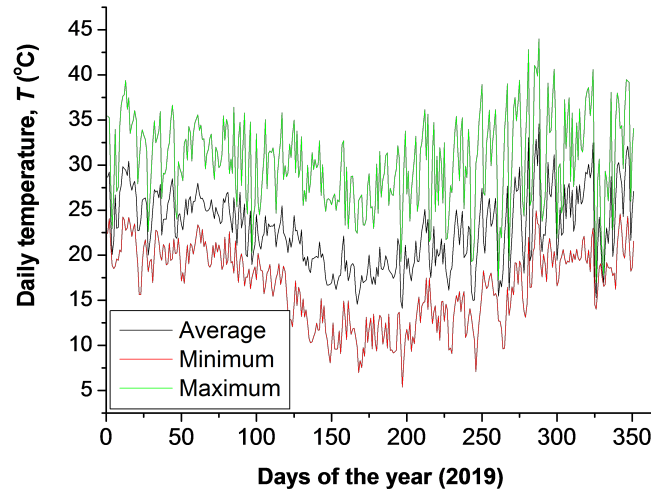


Figure 1. The observed daily temperature at Vuwani in 2019.

$$D_f = 1 + 0.033 \cos \left[2\pi \left(\frac{n}{365} \right) \right] \quad (3)$$

$$\delta_s = \frac{23.45\pi}{180} \sin \left[2\pi \left(284 + \frac{n}{365} \right) \right] \quad (4)$$

$$\omega_s = \cos^{-1} (-\tan \varphi \tan \delta) \quad (5)$$

2.3. PV power output forecast models

The average monthly solar radiation estimated by means of empirical model in equation (1) were used as inputs to determine the performance of two solar power output models given in equations (6) and (8) [10] as Skoplaki Model ($P_{PV,model1}$) and Ramli Model ($P_{PV,model2}$), respectively. Both models include the effects of radiation levels and panel temperature on the solar output power. In addition to radiation and temperature, the $P_{PV,model1}$ considers solar cell properties such as efficiency, temperature coefficient of maximum power, transmittance of the cover system and absorption coefficient of the cell [11], while $P_{PV,model2}$ relies on the theoretical short-circuit current and open-circuit voltage parameters [12] to determine PV power output.

$$P_{PV} = H_c \tau \eta A [1 - \beta_{ref} (T_c - T_{ref})] \quad (6)$$

where τ , η , β_{ref} and A respectively are the transmittance of the PV cell's outside layer, the module's electrical efficiency (0.16) at the reference temperature T_{ref} (25 °C) and H_T reference irradiance at STC (1000 W.m⁻²), the temperature coefficient (0.0045 %/°C) and the surface area of the solar panel (1.61 m²). T_c is the cell temperature given by equation (7) [8]:

$$T_c = T_a + \left[\frac{T_{NOCT} - 20}{800} \right] H_T \quad (7)$$

equation (8) defines the current-voltage relationship based on PV panel's electrical characteristics [10]:

$$P_{PV} = V_{mpp} I_{mpp} \quad (8)$$

where $V_{mpp} = V_{mpp,ref} + \mu_{V,OC}(T_c - T_{c,ref})$ and $I_{mpp} = I_{mpp,ref} + I_{SC,ref} \left(\frac{H_c}{H_T} \right) + \mu_{I,SC}(T_c - T_{c,ref})$.

The performance of a *PV* panel is based on ideal conditions or a controlled environment, which is not the case for real outdoor conditions [12]. The two power generation models were used for determining the correlation of maximum power with the dataset provided by the manufacturer of the selected *PV* panel at STC. The electric power output calculated with the help of each model was used to choose the best model for this study.

2.4. Statistical metrics for *H-S* model

The estimated solar radiation values using the *H – S* model were compared with the observed values [13]. The coefficient of determination R^2 , root mean square error (*RMSE*), mean bias error (*MBE*) and mean percentage error (*MPE*) in equations (9) to (12), were used to analyse the accuracy of the estimated values produced [14]. The metrics are:

$$R^2 = 1 - \frac{\sum (H_{oi} - H_{ci})^2}{\sum (H_{oi} - \bar{H}_o)^2} \quad (9)$$

$$RMSE = \sqrt{\frac{\sum_{n=1}^n (H_{ci} - H_{oi})^2}{n}} \quad (10)$$

$$MBE = \frac{1}{n} \sum_{n=1}^n (H_{ci} - H_{oi}) \quad (11)$$

$$MPE = \frac{1}{n} \sum_{n=1}^n \frac{|H_{ci} - H_{oi}|}{H_{oi}} \quad (12)$$

In the above relations, the subscript *i* refers to the i^{th} value of the solar irradiation and *n* is the number of the solar irradiation data. The subscripts *c* and *o* refer to the calculated and observed global solar irradiation values, respectively.

3. Results and discussion

3.1. Monthly irradiance and power output data

Figure 2 represents the estimated monthly average solar irradiance based on the calculation using the *H – S* Model and the observed data at the USAid Venda SAURAN Station for 2019. The annual average solar radiation values from the *H – S* Model and the observation were 222 W.m⁻² and 211 W.m⁻², respectively. The good correlation between the measured and calculated solar irradiance correspond to the calculated values from equations (10) to (12) giving values for *RMSE* equal to 1.84, *MAE* value of 1.39, *MBE* value of 1.29 and R^2 statistical correlation value of 0.84, which agreed with corresponding findings by other researchers [15]: $MBE \leq MAE \leq RMSE$. Therefore, the *H – S* model is suitable for estimating the irradiance due to its good fit to the measured data [12].

Solar irradiance can be difficult to model, due to cloud cover and other meteorological effects. The overestimation by equation (1) of solar radiation in October shows the 24 % deviation from the measured data due to about 13 rainy days at Vuwani. The deviation in October demonstrates the limitations of the model under cloudy, rainy days, and wind speed as the temperature hovered around 30°C, 50.94 mm of rain and approximately 13 rainy days in the month with humidity of 57%. Therefore, other empirical models based on sunshine hour, relative humidity and atmospheric pressure need to be explored in the future studies.

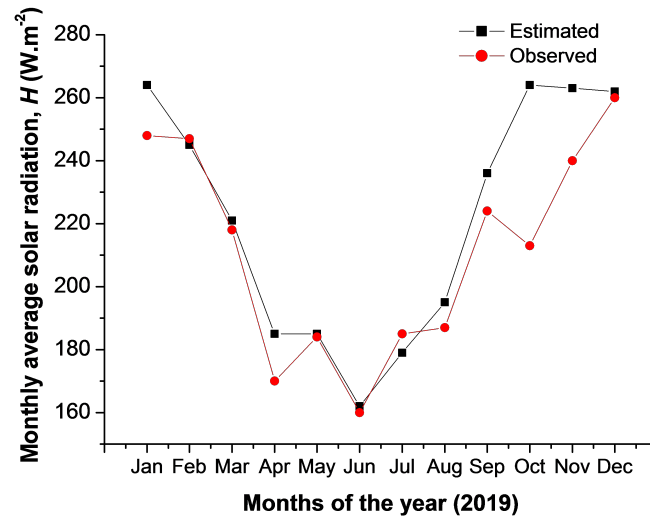


Figure 2. Estimated and observed inter-monthly global solar radiation at Vuwani for 2019.

3.2. Predicted PV power output

The results in figure 3 show that $P_{PV,model2}$ in equation (8) overestimated power output from the PV panel by 10 % as compared to $P_{PV,model1}$ in equation (6). It is also noted that the calculated annual average solar power output values for the two models are about 22 % compared to the manufacturer's supplied maximum power values of the solar panel in datasheet at *STC* conditions. This trend was consistent with that of measured solar radiation on site against the reference solar irradiance of 1000 W.m^{-2} .

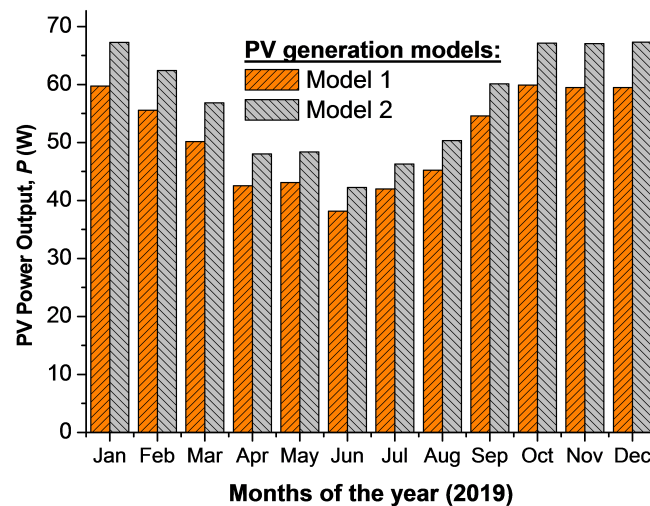


Figure 3. Monthly average power output forecasted at Vuwani for 2019 by the two models using the estimated solar radiation.

4. Conclusion

The performance of $H - S$ model for estimating H_c has been compared with observed data at Vuwani. Results suggest that the empirical model in equation (1) provides acceptable H_c estimation at any location. Accurate estimation of H_c is important for various applications including PV power forecasting during the design and sizing of a power generation system. This work aimed at examining the capability of empirical models in forecasting PV power output in areas with no other weather data except temperatures. The average measured H_o , 211 W.m^{-2} ; ranged from 160 to 260 W.m^{-2} while the empirical model gave an average H_c : 221 W.m^{-2} with values ranging from 162 to 264 W.m^{-2} . The two PV power models $P_{PV,model1}$ and $P_{PV,model2}$ predicted average annual power outputs, respectively of 51 and 57 W , hence about 22% of the maximum power output of the panel at STC. This performance was found to be consistent with the local solar radiation observed at Vuwani, which was about 21% of the reference solar radiation of 1000 W.m^{-2} .

References

- [1] Fortunato E, Gaspar D, Duarte P and Pereira L, Águas H, Vicente A, Dourado F, Gama M and Martins R 2016 *Bacterial Nanocellulose*, Elsevier 179-197
- [2] Maluta N E and Mulaudzi T S 2018 *International Energy Journal* **18**: 181 – 190
- [3] Miguntanha N P, Jayasinghe M T R and Sendanayake S 2015 *Journal of Urban and Environmental Engineering* **9**: 109 - 118
- [4] Ishiharay A K and Poolla I C 2018 *ECE, Carnegie Mellon University (SV), Moffett Field, CA*
- [5] Althoff D, Santos R A, Bazame H C, Cunha F F and Filgueiras R 2019 *Water* **11** 2272
- [6] Brooks M J, du Clou S, van Niekerk J L, Gauche P, Leonard C, Mouzouris M J, Meyer A J, van der Westhuizen N, van Dyk E E, and Voster F 2015 *Journal of Energy in Southern Africa* **26**: 2 - 10
- [7] Zhang Q 2018 *Advances in Meteorology* 1 - 22
- [8] Marwal V 2012 *Indian Journal of Science and Technology* **5**: 2729-2732
- [9] Duffie J A and Beckman W A 2006 *Solar Engineering of Thermal Process*, 3rd ed., John Wiley and Sons Inc., New York, USA
- [10] Amekudzi L K, Preko K, Aryee J, Boakye O R and Quansah E 2014 *Journal of Solar Energy*: 1 - 6
- [11] Skoplaki E, Boudouvis A G and Palyvos J A 2008 *Solar Energy Materials and Solar Cells* **92**: 1393 – 2402
- [12] Ayzvazogluyuksel O and Filik U B 2017 *Conference paper, Anadolu University, IEE Xplore*: 1253 - 1257
- [13] Mulaudzi T S, Maluta N E and Sankaran V 2015 *Turkish Journal of Physics* **39** 264 – 271
- [14] Antonanzas J, Osorio N, Escobar R and Urraca R 2016 *Sol. Energy* **136** 78 – 111
- [15] Pal R 2017 *Texas, Texas Tech University, Lubbock, TX, United States*: 83 – 107

An experimental study of a combined solar cooking and thermal energy storage system for domestic applications

K A Lentswe¹, A Mawire*¹, P Owusu¹, A B Shobo²

¹Department of Physics and Electronics, Material Science, Innovation and Modelling (MaSIM) Research Focus Area, North-West University, Private Bag X2046, Mmabatho, South Africa.

²Department of Mathematics, Science and Sports Education, University of Namibia, Private Bag 5507, Oshakati, Namibia

*E-mail: ashmore.mawire@nwu.ac.za

Abstract. In this paper, a combined solar cooker with a Sunflower oil storage tank is presented. The solar cooker consists of a 1.8 m parabolic dish that has an oil circulating copper spiral coil receiver embedded at the bottom of a metallic cooking plate. During sunny periods, cooking and charging of the storage tank take place. 1 L of water is heated up in a cooking pot that is placed on the cooking plate when solar radiation is focused on it, while oil circulating through a spiral coil receiver charges the storage tank. The receiver is connected to a 50 L Sunflower oil storage tank that is used to store heat during charging. A DC pump is used to circulate the oil during charging and discharging. Sunflower oil is the heat transfer fluid during the cooking /charging experiments. Storage tank temperatures above 100 °C are achieved in the storage tank. During the discharging cycle, the dish is defocused from the sun, and the pump is reversed to extract heat from the storage tank. 1.0 L of water is heated up with the stored heat, however, heat transfer is poor with the heated water only achieving temperatures just above 40 °C. Preliminary experiments are presented, and the charging process is seen to be more efficient than the discharging process with the charging pump reversed. The average charging and discharging efficiencies are found to be 18 % and 14 %, respectively. The system can be used to cook food as well as provide heat for indirect cooking using insulated bag slow cookers. However, cooking food directly on the cooking plate using the reverse discharging process is not efficient, and heat transfer should be enhanced to make the process more efficient and viable.

Keywords: *Combined solar cooker; Thermal energy storage; Parabolic dish; Sunflower oil*

1. Introduction

Disadvantaged communities and rural areas depend on polluting energy sources such as coal, wood, cow dung and agricultural waste for cooking. Utilizing these harmful energy sources daily increases the chances of health risks, negative environmental impacts, and disrupting the nutritional value of food [1]. To prevent these negative impacts, solar cookers that are affordable and user friendly must be introduced and be promoted to disadvantaged communities that have abundant access to solar energy. Solar cookers are suitable devices that can cook food by converting solar energy to heat energy. They can be used for pasteurization and sterilisation of food. Researchers, scientists and engineers have done extensive work on improving solar cooking systems in recent years [2-13]. Solar cooking is becoming a potential cooking option for disadvantaged communities and rural areas that cannot afford and access traditional cooking methods such as electricity or gas [14-16].

The advantages of solar cookers are that they have no running costs, they produce nutritious food, they emit no greenhouse gases, and most of them can be homemade (e.g. box solar cookers). There are three common types of solar cookers which are; (1) concentrating solar cookers, (2) box solar cookers, and (3) panel solar cookers. An appealing solar cooker must be user friendly, locally available at an affordable price, and must be able to reach high cooking temperatures in a short period of time. Concentrating solar cookers are appealing because they cook faster, reach higher cooking temperatures and can cook multiple individual meals rapidly as compared to other types of solar cookers [17]. The disadvantage of solar cookers is that they cannot be operated during off-shine periods (e.g. cloudy periods). In order to address this shortcoming, solar cookers must be integrated with thermal energy storage (TES) materials. An ideal thermal energy storage material must be readily available, easy to access and cheap. Sunflower oil is widely used in South Africa for a variety of cooking methods such as frying fast foods like chips. It is locally available in commercial stores, and it is manufactured in South Africa. Although it is mostly utilized for cooking purposes, it can also be used as thermal energy storage (TES) material [18-21].

Limited research has been done on the combination of a concentrating solar cooker and a TES system for the dual purpose of cooking and storing energy [2, 7, 22, 23]. In an attempt to understand the thermal performance of a concentrating solar cooker combined with a TES system, an experimental evaluation of a parabolic dish solar cooker combined with a Sunflower oil storage system is presented in this paper. The novelty of the study is that the concentrating solar cooker coupled with a TES system can cook and store energy simultaneously which is a different design to the other cookers with storage whereby thermal energy has to be stored first before cooking. The stored heat can be used to cook food and other domestic applications during off-shine periods. Combined solar cookers with storage are an important innovation to mitigate greenhouse gas emissions generated by the use of fossil fuels used for cooking in developing countries.

2. Experimental setup and procedure

Figure 1 shows a laboratory experimental setup of a solar parabolic dish cooker combined with a TES system. (1) An insulated 50-L cylindrical stainless steel storage tank was filled with Sunflower oil. K-type thermocouples with accuracy of $\pm 2.2^\circ\text{C}$ were fitted at five different axial positions from the top to the bottom of the storage tank. (2) A DC pump was connected to the outlet of the storage tank and was used to circulate Sunflower oil from the bottom of the storage tank to the receiver and back to the top of the storage tank

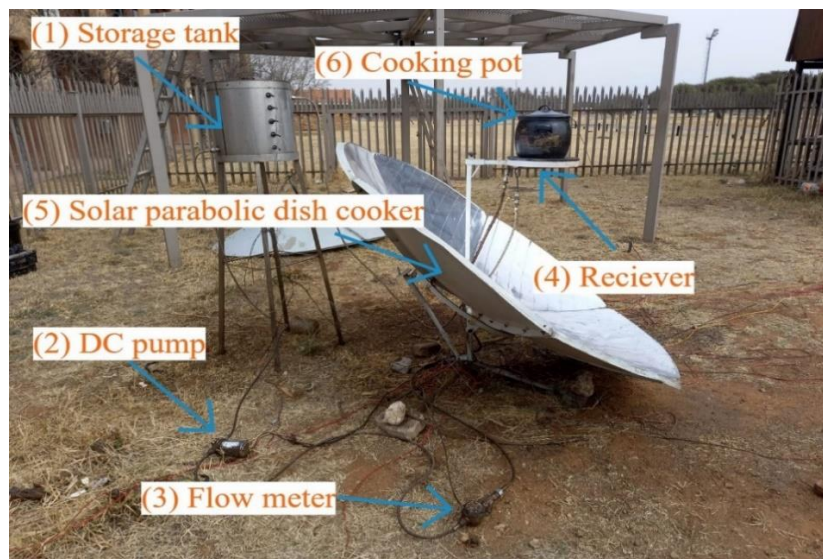


Figure 1: Experimental setup of a solar parabolic dish cooker combined with a TES system. (1) Storage tank, (2) DC pump, (3) Flow meter, (4) Receiver, (5) Solar parabolic dish cooker and (6) Cooking pot.

The flow rate of the Sunflower oil was measured with a pulse-type positive displacement flow meter (3) with an accuracy of $\pm 1\%$. The inlet and outlet pipes of the receiver (4) were coupled with thermocouples to measure the inlet and outlet receiver temperatures. The receiver which was a copper spiral coil was placed at the focal region of the solar parabolic dish (SK-14) cooker (5) to allow the heat transfer fluid to be heated thus charging the storage tank. A black cooking pot (6) filled with different test loads (water and sunflower oil of different masses) was placed on top of the receiver during experimental periods.

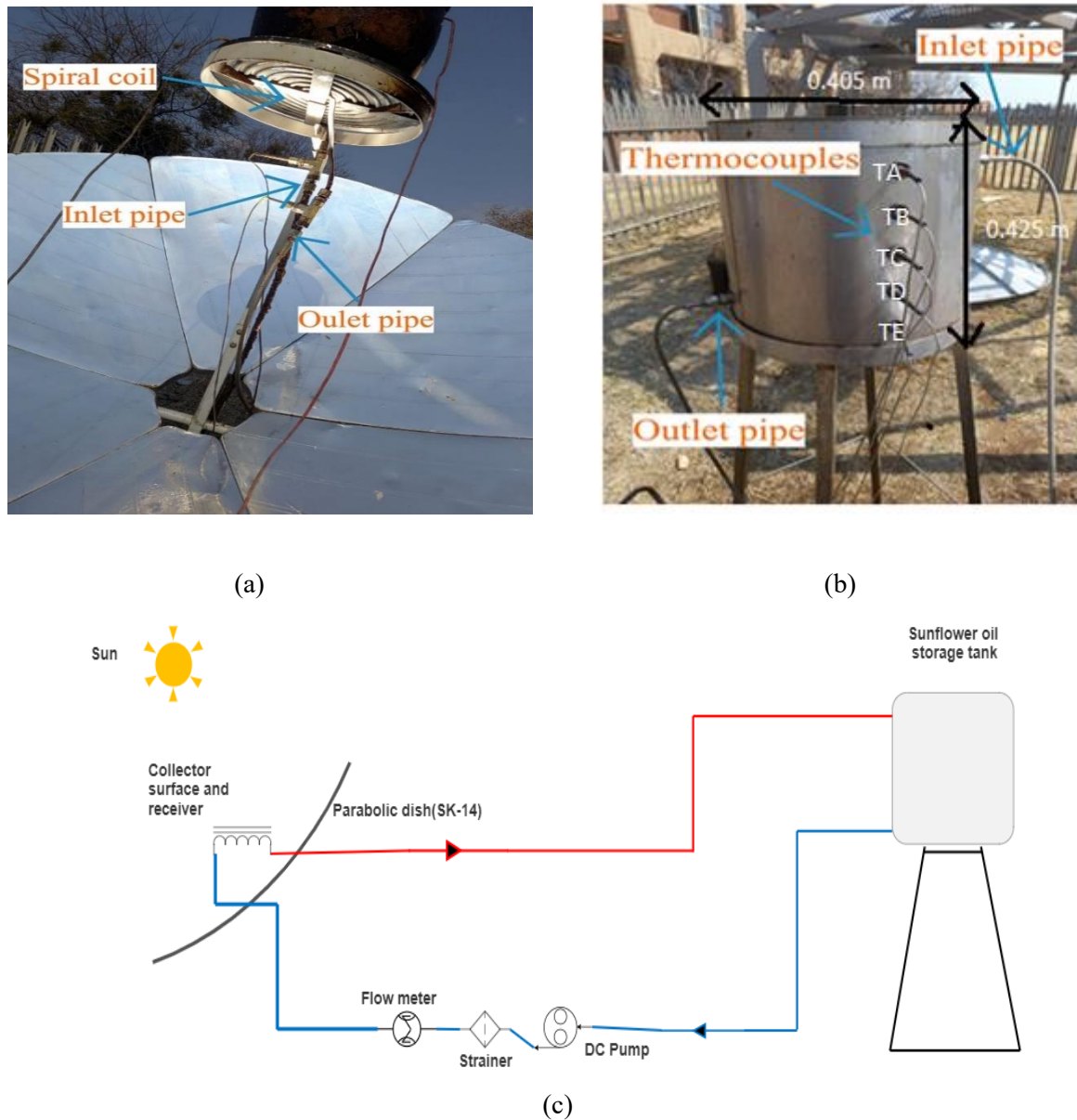


Figure 2: (a) Magnified photographs of the receiver, the (b) storage tank and, (c) schematic diagram of the experimental setup.

Figure 2 shows magnified photographs of the receiver, the storage tank and schematic diagram of the experimental setup. The receiver was composed of a black painted flat stainless steel plate, and a copper spiral coil which was connected with the inlet and outlet pipes to the storage tank. The diameter of the cooking plate was 0.310 m. The receiver was placed at the focal region of the solar parabolic dish cooker and solar radiation was reflected to it as shown in fig. 2 (a). During experiments, Sunflower oil flowed from the bottom of the storage to the inlet pipe of the receiver which was integrated with a thermocouple. Heat was absorbed from the spiral coil by Sunflower oil, and exited through the outlet

pipe to the top of the storage tank thus charging the storage tank. The storage tank was a cylindrical stainless steel fitted with 5 thermocouples (T_A - T_E) to measure the axial thermal distribution (fig. 2(b and c)). The storage tank had a diameter of 0.405 m and a height of 0.425 m. Thermocouples were placed at axial distances of 0.083 m (T_A), 0.150 m (T_B), 0.220 m (T_C), 0.285 m (T_D), and 0.355 m (T_E), respectively from the top of the storage tank. The outlet pipe of the tank was connected to a DC pump, and the inlet was connected to the receiver. The insulation of the storage tank was glass wool fitted between the inner vessel and the outer vessel of the storage tank. When conducting experiments, 50 L of Sunflower oil was filled to a level just above the top thermocouple (T_A).

3. Thermal analysis

The receiver power from the circulating oil in receiver coil to the storage tank is calculated as:

$$Pr = \rho_{av} c_{av} \dot{V} (T_{Rout} - T_{Rin}) \quad (1)$$

, where ρ_{av} is the average density, C_{av} is the average specific capacity, \dot{V} is the flowrate of the oil during the circulating period, T_{Rout} is the outlet of the receiver and T_{Rin} is the inlet of the receiver. The average density is calculated as:

$$\rho_{av} = 932.37 - 0.66T \quad (2)$$

, and the average specific capacity is:

$$c_{av} = 2115 + 3.13T. \quad (3)$$

The charging efficiency is calculated by the ratio of the receiver power to the solar collecting power, and it is expressed as:

$$\eta_{ch} = \frac{\rho_{av} c_{av} \dot{V} (T_{Rout} - T_{Rin})}{A_{ap} G} \quad (4)$$

, where the aperture area of the parabolic dish is A_{ap} , and G is the direct solar radiation that falls on the parabolic dish collector (SK-14). The discharging efficiency can be calculated from the ratio of total energy discharged to the total energy stored from the initial (t_i) to the final time (t_f), and this is expressed as:

$$\eta_{dis} = \frac{\sum_{t_i}^{t_f} \rho_{av} c_{av} \dot{V} (T_{Rout} - T_{Rin}) dt_{(dis)}}{\sum_{t_i}^{t_f} \rho_{av} c_{av} \dot{V} (T_{Rout} - T_{Rin}) dt_{(ch)}} \quad (5)$$

4. Results and discussion

Figure 3 shows the solar radiation, temperature profiles of the receiver, and storage tank temperatures on 17 May 2021 using 1.0 L of water as the load at a flow rate of 2 ml/s. The solar radiation (fig. 3(a)) during the solar cooking period (11:00-14:00 h) is seen to be around 840 W/m² for the duration of the experiment except for brief cloudy periods around 13:00 h, 13:15 h and 13:45 h., respectively. The inlet and outlet (T_{Rout} , T_{Rin}) temperatures (fig. 3(b)) of the receiver fluctuate up and down during the solar cooking period due to manual tracking of the receiver. T_{Rout} achieves maximum temperatures close to 160 °C, and T_{Rin} achieves maximum temperatures close to 70 °C during the solar cooking period. The temperature of the water in the pot reaches a maximum stagnation temperature of around 75 °C from about 12:30 h- 14:00 h during the solar cooking period thus supporting the idea of dual solar cooking and storage of thermal energy. The surface temperature at the cooking plate shows lower temperatures than the receiver outlet temperature since heat is being extracted by the fluid to charge the storage tank. Fig 3 (c) shows that the top of the storage tank (T_A) achieves maximum temperatures above 120 °C during the solar cooking period with the bottom (T_E) achieving a maximum temperature close to 80 °C. A clear stratified distribution of the thermal profiles in the storage tank is seen during charging.

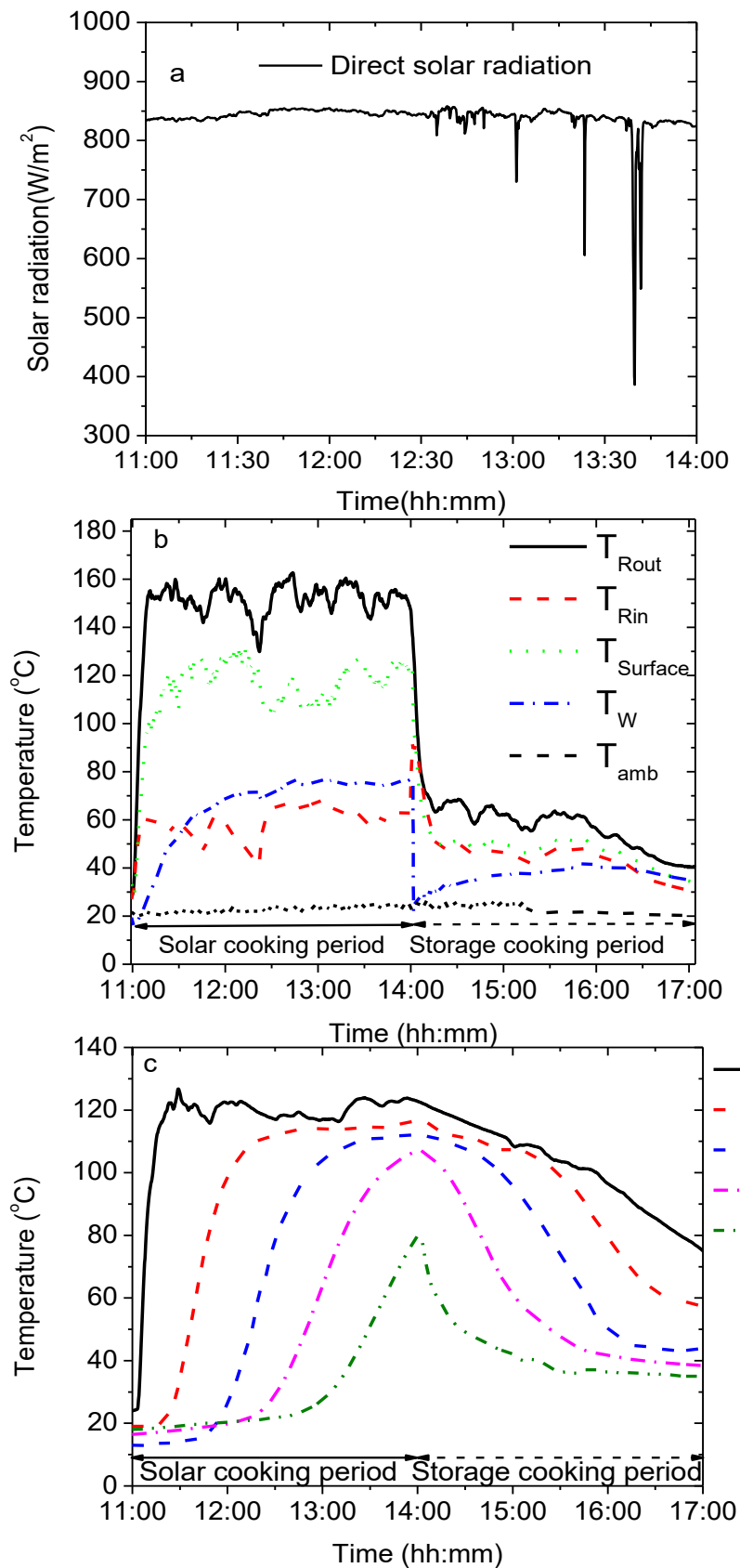


Figure 3: (a) Direct solar radiation, (b) temperature profiles of the receiver, and (c) temperature profiles of the storage tank using 1 kg of water as the test load performed on 17 May 2021 using a flow-rate of 2 ml/s.

During the storage cooking, the stored heat in the tank (fig. 3(c)) is used to heat up 1 L of water by reversing the direction of the pump and defocusing the solar receiver from the sun. During the 3 h discharging period, the maximum temperature achieved by water in a pot is around 41 °C at 16:00 which is not sufficient to cook food but enough to warm food. This is because of the long flow pipes which induced heat losses during discharging since the same charging loop was used for discharging. Introducing shorter discharging loop pipes will definitely improve the heat transfer rate during discharging. Another improvement will be an optimized receiver to extract and discharge heat efficiently. However, the stored heat can be used indirectly to cook food using slow insulated wonderbag cookers as recently reported in [3]. The storage tank temperature (fig. 3(c)) drops from around 120 °C at the top of the storage tank (T_A) to around 70 °C during the discharging the 3 h discharging period. On the other hand, the bottom storage tank temperature drops from around 80 °C to 35 °C at the end of the discharging period. As already mentioned, this discharging process can be optimized to improve the thermal performance.

Table 1 shows a summary of receiver energy efficiencies on different days (17 and 18 May 2021) using a water heating load of 1 kg. During the charging cycle, the average charging efficiencies were approximately 18 % and 17 %, which represents an average receiver power of around 367 W at a collector power of around 2100 W. This lower receiver power is expected since some of the solar energy heats up water used for cooking. This is evidence that receiver can harness energy that can cook light meals such rice, noodles and chicken. During the discharging cycle, the average discharging efficiency was found to be 14 % and 13 %, respectively, indicating poor heat transfer from the storage tank during discharging possibly due to the long connecting pipes. This shows that during the discharging cycle, the stored heat was not suitable for cooking purposes but the stored heat can be used indirectly in storage cooking pots as reported in [3]. Although the performance during discharging is unsatisfactorily, heat transfer mechanisms can be employed to make it more economically viable such it can be scaled up to cook food for at least 10 people. In addition to this, future work intends to replace Sunflower oil with water so that the system can cook as well as provide hot water for a variety of domestic applications such as bathing, cooking and washing dishes.

Table 1. A comparison of receiver charging and discharging efficiencies on different days using 1.0 kg of water

Date	Average charging efficiency (%)	Average discharging efficiency (%)
17 May 2021	18	14
18 May 2021	17	13

5. Conclusion

A combined solar cooker with a Sunflower oil storage tank was investigated experimentally. The solar cooker consisted of a 1.8 m parabolic dish that had an oil circulating copper spiral coil receiver embedded to a metallic cooking plate to charge a 50 L Sunflower oil storage tank. During charging, 1.0 L of water was heated up to around 75 °C in a cooking pot with storage tank temperatures above 100 °C being achieved. During discharging, the heat transfer was poor with the heated water only achieving temperatures just above 40 °C. Preliminary experiments showed that the charging process was more efficient than the discharging process with the charging pump reversed. The system can be used to cook food for a minimum of 3 people in the solar cooking period as well as provide heat for indirect cooking using insulated bag slow cookers. However, cooking food directly on the cooking plate using the reverse discharging process was not efficient, and heat transfer should be enhanced to make the process more efficient and viable.

6. Acknowledgement

The authors would like to thank the National Research Funding (NRF) of South Africa for funds to carry out the research under the Incentive Funding for Rated Researchers (IFRR) scheme, Grant Number:127192. Reference: RA181002364433. We acknowledge that opinions, findings and

conclusions or recommendations expressed in any publication generated by the NRF supported research are our own, and that the NRF accepts no liability whatsoever in this regard.

6. References

- [1] Iessa, L., De Vries, Y. A., Swinkels, C. E., Smits, M., & Butijn, C. A. A. (2017). What's cooking? Unverified assumptions, overlooking of local needs and pro-solution biases in the solar cooking literature. *Energy Research & Social Science*, 28, 98-108.
- [2] Omara, A. A., Abuelnuor, A. A., Mohammed, H. A., Habibi, D., & Younis, O. (2020). Improving solar cooker performance using phase change materials: A comprehensive review. *Solar Energy*, 207, 539-563.
- [3] Mawire, A., Lentswe, K., Owusu, P., Shobo, A., Darkwa, J., Calautit, J., & Worall, M. (2020). Performance comparison of two solar cooking storage pots combined with wonderbag slow cookers for off-sunshine cooking. *Solar Energy*, 208, 1166-1180.
- [4] Panwar, N. L., Kaushik, S. C., & Kothari, S. (2012). State of the art of solar cooking: An overview. *Renewable and Sustainable Energy Reviews*, 16, 3776-3785.
- [5] Cuce, E. (2018). Improving thermal power of a cylindrical solar cooker via novel micro/nano porous absorbers: A thermodynamic analysis with experimental validation. *Solar Energy*, 176, 211-219.
- [6] Aramesh, M., Ghalebani, M., Kasaeian, A., Zamani, H., Lorenzini, G., Mahian, O., & Wongwises, S. (2019). A review of recent advances in solar cooking technology. *Renewable Energy*, 140, 419-435.
- [7] Mussard, M., Gueno, A., & Nydal, O. J. (2013). Experimental study of solar cooking using heat storage in comparison with direct heating. *Solar Energy*, 98, 375-383.
- [8] Indora, S., & Kandpal, T. C. (2019). A framework for analyzing impact of potential financial/fiscal incentives for promoting institutional solar cooking in India. *Renewable Energy*, 143, 1531-1543.
- [9] Shukla, S. K., & Khandal, R. K. (2016). Design investigations on solar cooking devices for rural India. *Distributed Generation & Alternative Energy Journal*, 31, 29-65.
- [10] Ayub, H. R., Ambusso, W. J., Manene, F. M., & Nyaanga, D. M. (2021). A Review of Cooking Systems and Energy Efficiencies. *American Journal of Energy Engineering*, 9, 1-7.
- [11] Arunachala, U. C., & Kundapur, A. (2020). Cost-effective solar cookers: A global review. *Solar Energy*, 207, 903-916.
- [12] Saxena, A., Lath, S., & Tirth, V. (2013). Solar cooking by using PCM as a thermal heat storage. *MIT International Journal of Mechanical Engineering*, 3, 91-95.
- [13] Zalengera, C., Blanchard, R. E., Eames, P. C., Juma, A. M., Chitawo, M. L., & Gondwe, K. T. (2014). Overview of the Malawi energy situation and A PESTLE analysis for sustainable development of renewable energy. *Renewable and Sustainable Energy Reviews*, 38, 335-347.
- [14] Baptista, T. L., Curnow, K., Hiranaga, B. J., Magnus, B. D., & Perry, D. (2003). Solar Household Energy, Incorporated: a market-based strategy for introducing passive solar ovens in Kenya. *Ann Arbor: Michigan Business School*.
- [15] Martínez, N. N., Mäusezahl, D., & Hartinger, S. M. (2020). A cultural perspective on cooking patterns, energy transfer programmes and determinants of liquefied petroleum gas use in the Andean Peru. *Energy for Sustainable Development*, 57, 160-167.
- [16] Kumar, A. (2018). Justice and politics in energy access for education, livelihoods and health: How socio-cultural processes mediate the winners and losers. *Energy research & Social Science*, 40, 3-13.
- [17] Lahkar, P. J., & Samdarshi, S. K. (2010). A review of the thermal performance parameters of box type solar cookers and identification of their correlations. *Renewable and Sustainable Energy Reviews*, 14, 1615-1621.
- [18] Mawire, A. (2016). Performance of Sunflower Oil as a sensible heat storage medium for domestic applications. *Journal of Energy Storage*, 5, 1-9.
- [19] Sousa, L. A., Zotin, J. L., & Da Silva, V. T. (2012). Hydrotreatment of sunflower oil using supported molybdenum carbide. *Applied Catalysis A: General*, 449, 105-111.

- [20] Echarte, M. M., Puntel, L. A., & Aguirrezabal, L. A. (2013). Assessment of the critical period for the effect of intercepted solar radiation on sunflower oil fatty acid composition. *Field Crops Research*, 149, 213-222.
- [21] Jiao, J., Gai, Q. Y., Fu, Y. J., Zu, Y. G., Luo, M., Wang, W., & Zhao, C. J. (2013). Microwave-assisted ionic liquids pretreatment followed by hydro-distillation for the efficient extraction of essential oil from *Dryopteris fragrans* and evaluation of its antioxidant efficacy in sunflower oil storage. *Journal of Food Engineering*, 117, 477-485.
- [22] Li, Q., Tehrani, S. S. M., & Taylor, R. A. (2017). Techno-economic analysis of a concentrating solar collector with built-in shell and tube latent heat thermal energy storage. *Energy*, 121, 220-237.
- [23] Yadav, V., Kumar, Y., Agrawal, H., & Yadav, A. (2017). Thermal performance evaluation of solar cooker with latent and sensible heat storage unit for evening cooking. *Australian Journal of Mechanical Engineering*, 15, 93-102.

DIVISION G – THEORETICAL AND COMPUTATIONAL PHYSICS

Fitting the relic density with dimension-five contributions

L Mason^{1,2}, A S Cornell¹, A Deandrea², T Flacke^{3,4} and B Fuks⁵

¹ Department of Physics, University of Johannesburg, PO Box 524, Auckland Park 2006, South Africa,

² Université de Lyon, F-69622 Lyon, France: Université Lyon 1, Villeurbanne CNRS/IN2P3, UMR5822, Institut de Physique Nucléaire de Lyon,

³ Center for Theoretical Physics of the Universe, Institute for Basic Science (IBS), Daejeon 34126, Korea

⁴ Korea Institute for Advanced Study, Seoul 02455, Korea

⁵ Laboratoire de Physique Théorique et Hautes Energies (LPTHE), UMR 7589, Sorbonne Université et CNRS, 4 place Jussieu, 75252 Paris Cedex 05, France,

E-mail: acornell@uj.ac.za

Abstract. We investigate the behaviour of the relic density for a heavy dark matter model with a dimension-five operator added to the theory. The model features a top-philic dark matter candidate and heavy fermionic mediator which interact via a Yukawa-type term, and which in mass-degenerate set-ups results in coannihilation effects on the relic density. We present a semi-analytical fit to the relic density, modelling the interplay between the dimension-five contact term and Yukawa-type contribution, and showing that coannihilation effects should not be neglected in a naive fit. Additionally, we motivate the use of a semi-analytic fit in place of computer-intensive simulations, showing that the functional form is able to predict parameters producing the correct relic density.

1. Introduction

The dark matter puzzle is one of the foremost questions in particle physics today, and one which forms a significant part of many experimental programs. It has been well established that about 25 % of the energy in the universe is taken up by dark matter [1], so-named for its non-interaction with light [2], but its nature remains unknown. If it is a particle, it does not form part of the Standard Model (SM). Physics programmes designed to detect it include astrophysical attempts using indirect and direct detection, and experiments at colliders such as the Large Hadron Collider at CERN. None of these efforts have yet yielded conclusive discoveries.

In the following, we investigate the phenomenology of a heavy scalar dark matter candidate S which is top-philic and couples to the SM via a heavy fermionic mediator, T , via a t -channel interaction. The new physics states S and T are both odd under a Z_2 symmetry, and the masses of both resonances are constrained to lie in the range $200 \text{ GeV} \leq m_S, m_T \leq 3 \text{ TeV}$. The upper limit is chosen to match the scale of a generic composite Higgs theory, which is expected to be several TeV. We build upon a previous model studied in Refs. [3, 4], where it was shown that the next-to-leading-order (NLO) contributions to the annihilation cross section should not be neglected for heavy dark matter. Furthermore, it is a goal of this work to postulate that S and T

arise as bound states in a composite Higgs model featuring underlying fermions, and to support this we enforce that their masses lie within one order of magnitude. To further investigate this avenue, we follow an effective theory approach and add to the existing model [3, 4] an additional contact interaction $SStt$ with an unknown $\mathcal{O}(1)$ coefficient. Such a dimension-five term is a generic feature of a broad range of Beyond the Standard Model theories, including composite Higgs models, arising from strong dynamics. Following Refs. [3, 4], we add to the SM the minimal Lagrangian

$$\mathcal{L} = i\bar{T}\not{D}T - m_T\bar{T}T + \frac{1}{2}\partial_\mu S\partial^\mu S - \frac{1}{2}m_S^2 S^2 + [\tilde{y}_t S\bar{T}P_R t + h.c.] + \frac{C}{\Lambda}SSt\bar{t}, \quad (1)$$

where m_T is the mass of the mediator and m_S is the mass of the dark matter candidate. The dark matter interaction with the SM sector is achieved through the Yukawa-type operator with coefficient \tilde{y}_t and the dimension-five term with coefficient C/Λ . The parameter Λ indicates the energy scale of the effective theory, such as the range of validity of compositeness. When the masses of S and T are near to the compositeness scale, the validity of the EFT should be treated with care. However, colliders such as the LHC probe scales of 1 TeV or less in typical dark matter searches, implying these predictions may be safely trusted there.

A dark matter candidate S in the presence of mediator T with a small mass splitting between the two leads to coannihilations becoming important in the calculation of the relic density. In this case, the relic abundance of dark matter is not only controlled by the process $\sigma(SS \rightarrow \text{SM SM})$, but also by $\sigma(ST \rightarrow \text{SM SM})$. The rate of annihilation of dark matter may then also be indirectly impacted by annihilations of the mediator, $\sigma(TT \rightarrow \text{SM SM})$.

The thermally averaged cross section $\langle\sigma v\rangle$ may be non-relativistically expanded as

$$\langle\sigma v\rangle \approx a + b\langle v^2\rangle + \mathcal{O}(v^4), \quad (2)$$

with v the relative velocity between the two scattering dark matter candidates. The annihilation rate features contributions from partial waves of the scattering amplitude, where the term a on the right hand side of equation (2) corresponds to the velocity-independent s -wave term, and the second represents the p -wave contribution, and scales with v^2 . In simple dark matter models, the s -wave contribution to the annihilation cross section dominates, and higher partial waves are minimal [5].

In a phenomenon dubbed the WIMP miracle, a weak-scale particle generically undergoes thermal freeze-out within a few orders of magnitude of the correct cross section, making the measured relic density $\Omega_{DM}h^2 = 0.1186 \pm 0.0020$ [6] easily achievable. In the case without coannihilations, the relic density of S , $\Omega_{DM}h^2$ [7], is the solution to the Boltzmann equation [7]

$$\frac{dn}{dt} = -3Hn - \langle\sigma_{eff}v\rangle (n^2 - n_{eq}^2), \quad \Omega_{DM}h^2 \approx \frac{1.04 \times 10^9}{M_{Pl}} \frac{x_F}{\sqrt{g_*(x_F)}} \frac{1}{a + 3b/x_F} \quad (3)$$

where H is the Hubble constant, the number density of S is given by n , the equilibrium number density is indicated by n_{eq} , M_{Pl} is the Planck mass, g^* the number of effectively massless degrees of freedom, and $x = m_S/T_x$, with T_x the freeze-out temperature. In the case at hand, the NLO annihilation cross section for SS annihilation is a sum of tree level and virtual internal bremsstrahlung contributions¹ [4]

$$\sigma v_{NLO} \approx \sigma v_{q\bar{q}} + \sigma v_{VIB}^{(0)}, \quad \text{with } \langle\sigma v\rangle = \sigma v_{NLO} + \sigma v_{SStt}. \quad (4)$$

¹ For the full expression of the NLO cross section, the interested reader is referred to Ref. [4], and for the dimension-five cross section to Ref. [8].

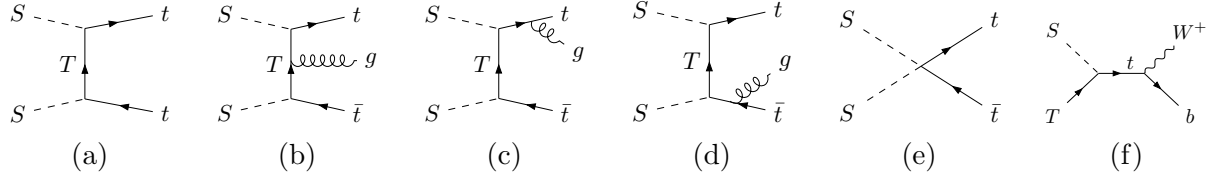


Figure 1. Relevant Feynman diagrams for the annihilation and co-annihilation (with T) of S .

From equation (3), we use that $\Omega_{DM} h^2 \sim 1/\langle\sigma v\rangle$ [9], solving for C/Λ yields

$$\frac{C}{\Lambda} = f(m_S, m_T, \tilde{y}_T) \approx \frac{1}{\sqrt{A(m_S)}} \sqrt{b'(x_F, g_*(x_F)) - B(m_S, m_T)} \tilde{y}_t^4, \quad (5)$$

with²

$$A(m_S) = \frac{\Lambda^2 \langle\sigma v\rangle_{SStt}}{C^2} = \frac{N_c}{4\pi} \left(1 - \frac{m_t^2}{m_S^2}\right)^{3/2}, \quad B(m_S, m_T) = \frac{\sigma v_{q\bar{q}} + \sigma v_{VIB}^{(0)}}{\tilde{y}_t^4}, \quad (6)$$

$$b'(x_F, g_*(x_F)) = (7.2 \times 10^{-10} \text{ GeV}^{-2}) \frac{x_F}{\sqrt{g_*(x_F)}},$$

where m_t is the mass of the top quark, and $b'(x_F, g_*(x_F))$ is fitted from the numerical result. Here, $A(m_S)$ and $B(m_S, m_T)$ are obtained by factorising the coefficients from each of the relevant cross sections, so as to use those coefficients as variables for the fit.

2. Considering coannihilations

The canonical calculation of dark matter relic density must, however, be modified when coannihilations with another relatively mass-degenerate state are possible. This is highlighted in figure 1, where diagrams (a) through (e) illustrate the SS annihilation channels, diagram (f) presents an example coannihilation channel. In the following, we present the steps for including such features in the calculation of the relic density, before presenting the fit.

Consider the case at hand, where $m_S < m_T$. The abundance of S is determined by a set of Boltzmann equations [10]

$$\frac{dn}{dt} = -3Hn - \langle\sigma_{ij}v\rangle(n^2 - n_{eq}^2), \quad (7)$$

which is of the same form as the Boltzmann equation for the single particle annihilation. It can then be solved by the same techniques, through performing the annihilation integral after solving for the freeze out temperature. More detail on this process is available in Ref. [10]. In that case, the additional state (here, the mediator T), can effect the annihilation cross section. In the general case, the effective thermally averaged cross section due to coannihilations is given by [10]

$$\sigma_{eff}(x) = \sum_{ij} \sigma_{ij} \frac{g_i g_j}{g_{eff}^2} (1 + r_i)^{3/2} (1 + r_j)^{3/2} \exp(-x(r_i + r_j)), \quad (8)$$

$$g_{eff}(x) = \sum_{i=1}^N g_i (1 + r_i)^{3/2} \exp(-x r_i), \quad \text{with } r_i = \frac{m_i}{m_S} - 1,$$

² For the full expression of $B(m_S, m_T)$ and further details of the calculation, the interested reader is referred to Ref. [8].

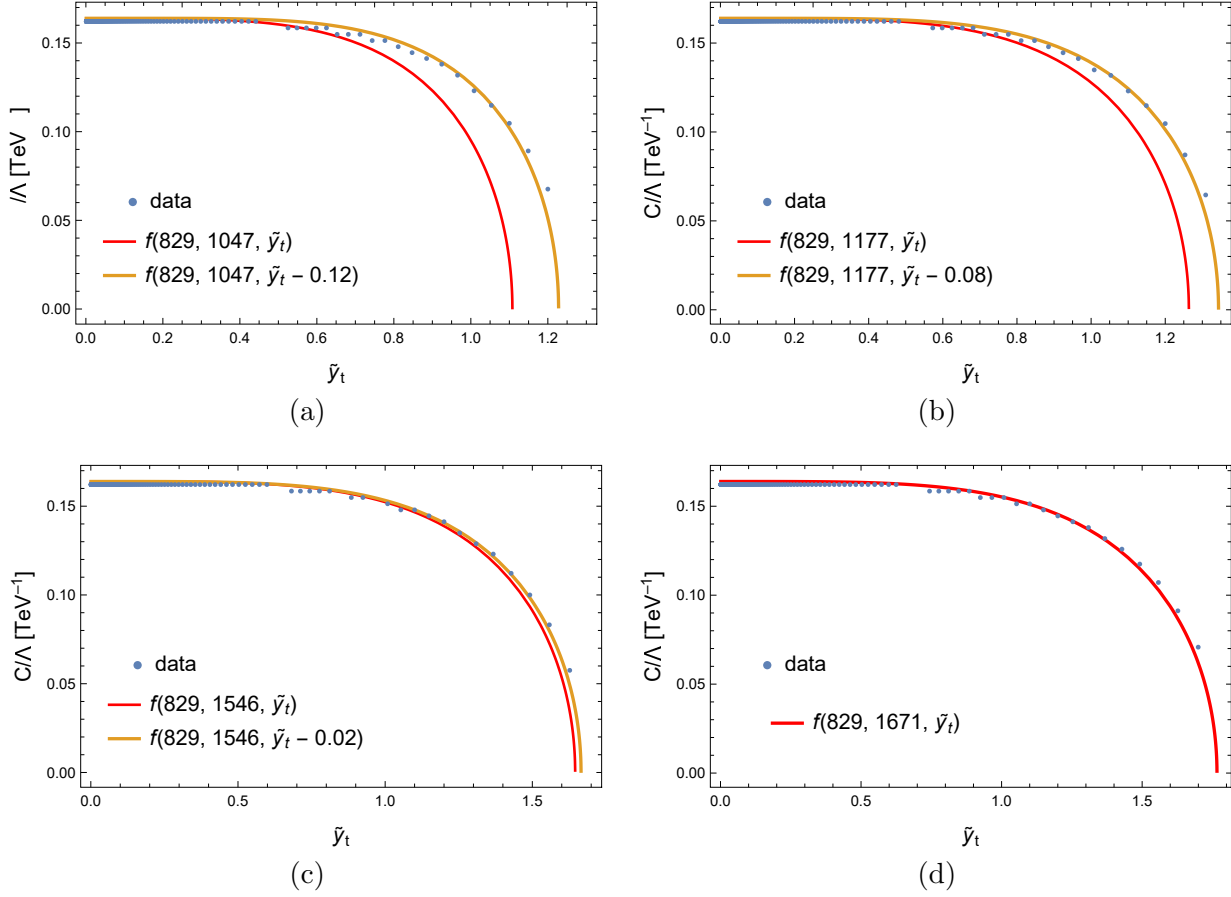


Figure 2. The shift due to coannihilations for $m_S = 829$ GeV, with mass ratios $r = 0.26$, $r = 0.42$, $r = 0.86$, and $r = 1.01$ for plots (a – d). All points yield the correct relic density.

recalling that $x = m_S/T_x$. Here, $\sigma_{ij} \equiv \sigma(\chi_i \chi_j \rightarrow \text{SM})$ for states χ_i with g_i internal degrees of freedom. In this case, with only two states $S = \chi_i$ and $T = \chi_j$ relevant, the effective annihilation cross section simplifies to

$$\sigma_{eff}(x) = \sigma_{SS} + \sigma_{ST} \frac{g_S g_T}{g_{eff}^2} \left(\frac{m_T}{m_S} \right)^{3/2} \exp(-x r), \quad (9)$$

where $\sigma_{ST} \propto \tilde{y}_t^2$. The form of equation (9) displays an exponential dependence attached to the coannihilation-induced cross section. That is, for smaller values of r , we expect to observe a larger modification to σ_{SS} (where $x > 0$ always). We now move to examining the semi-analytical fit to the relic density, bearing these contributions in mind.

3. Semi-analytical fit

The dark matter relic density is simulated using the MICROMEAS [11] framework, which allows the user full control of the cross section and numerical calculation of the relic abundance, and includes all relevant annihilation and coannihilation channels. The CalcHEP [12] model file was generated using the FeynRules [13, 14]/CalcHEP interface [13]. In this work, we have improved the estimation of $\langle \sigma v \rangle$ by including the NLO form of the cross section within the framework. The free parameters of the scan are varied with masses m_S (m_T) $\in [200 -$

3000(3500)] GeV, $\tilde{y}_t \in [10^{-4}, 6]$, and $C/\Lambda \in [10^{-3}, 10^{-5}] \text{ GeV}^{-1}$. The masses are chosen to lie above the top mass (avoiding threshold effects) and roughly below the envisioned compositeness scale, which typically lies around 3 TeV. The justification for the Yukawa parameter bounds is borrowed from previous investigations [3], where the upper limit is the limit of the perturbative regime, and the lower limit ensures that MICROMEGAS correctly handles co-annihilation effects. Finally, to establish the bounds for the contact term coefficient, the values of C/Λ which take over from the Yukawa term ($\tilde{y}_t \sim 0$) in producing the correct relic density were established, as well as the largest value of C/Λ which does not modify the relic density due to the Yukawa term.

In studying the modification of the relic density behaviour for a benchmark at hand, we study the behaviour in the $\tilde{y}_t - C/\Lambda$ plane, using as benchmark data the numerical predictions from the relic density simulations. In particular, as shown in figure 2 for $m_S = 829 \text{ GeV}$, we observe that as expected the smaller $r = m_T/m_S - 1$ values deviate from the simple fit of equation (5). The fit has been further detailed in Ref. [8], so here we will simply quote the result. The shift relevant to a mass point (m_S, m_T) which influences the Yukawa-type parameter is found to follow

$$s(m_S, m_T) = \begin{cases} 0.4k^r & m_S \leq 1.2 \text{ TeV} \\ 0.7k^r & m_S > 1.2 \text{ TeV} \end{cases}, \quad (10)$$

where $k(m_S)$ is an unconstrained dimensionless parameter. The change in behaviour at roughly 1 TeV is motivated by the appearance of NLO effects at that energy regime, which is independent of the value of Λ chosen. The value for $k(m_S)$ may be found via a fit to an exponential function

$$k(m_S) = \begin{cases} (1.9 \times 10^{-4}) (6.2 \times 10^8)^{m_S/\Lambda} & m_S \leq 1.2 \text{ TeV} \\ (3.0 \times 10^{-3}) (1.8 \times 10^4)^{m_S/\Lambda} & m_S > 1.2 \text{ TeV} \end{cases}, \quad (11)$$

for $\Lambda = 3.5 \text{ TeV}$, which yields the semi-analytic fit result

$$\frac{C}{\Lambda} \approx f(m_S, m_T, \tilde{y}_t) = \frac{1}{\sqrt{A(m_S)}} \sqrt{b' - B(m_S, m_T) \left(\tilde{y}_t - \alpha \left[\beta \gamma^{\frac{m_S}{\Lambda}} \right]^r \right)^4}. \quad (12)$$

The coefficient $b'(x_F, g_*(x_F))$ is determined by the fit as $b' = 6.0 \times 10^{-9} \pm 0.2 \times 10^{-9} \text{ GeV}^{-2}$. Additionally, we find the remaining coefficients parametrising the fit to be $(\alpha, \beta, \gamma) = (0.4, 1.9 \times 10^{-4}, 6.2 \times 10^8)$ for $m_S \leq 1.2 \text{ TeV}$, and $(\alpha, \beta, \gamma) = (0.7, 3.0 \times 10^{-3}, 1.8 \times 10^4)$ for $m_S > 1.2 \text{ TeV}$. In particular, the parameter γ has been raised to a dimensionless ratio, where $\Lambda = 3.5 \text{ TeV}$ is the maximum value for m_T used in the scan. As mentioned above, Λ provides an indicative effective scale, such as the limit of validity of the theory or the scale of compositeness.

4. Applying the shift

The fit to the relic density was performed to motivate its use over time-consuming and CPU-heavy simulations. The function obtained in equation (12) offers an alternative to performing a simulation of the relic density in this context, where the user may instead obtain the values of the \tilde{y}_t and C/Λ parameters which yield the correct relic density for a given benchmark. In order to further motivate this, we apply the functional form (without fitting) to data points to check the agreement. As displayed in figure 3, the functional form closely matches the behaviour of the data, motivating the use of the fit in place of simulation.

In particular, we note good agreement at the ‘boundaries’ of the parameter space; for large \tilde{y}_t and small C/Λ (and vice versa) the functional form matches the data well. We observe slight deviation from data in the regions where the interplay between the variables is strongest, particularly for larger m_S . This behaviour may be expected generally for t -channel dark matter theories which feature coannihilations due to small mass gaps.

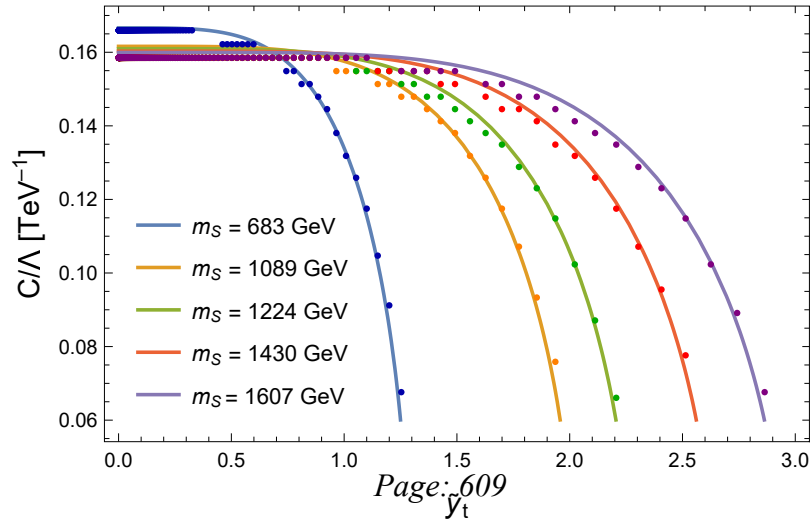


Figure 3. A number of benchmarks with a common mass ratio, $r = 0.72$ are presented, where the shift due to coannihilations is included. All points achieve the correct relic density.

5. Conclusion

This work has demonstrated that the relic density for a simple dark matter model may be modelled through a simple semi-analytical fit, which takes into account coannihilation effects. Additionally, we have motivated the possibility that a functional fit of this nature could conceivably take over from an intensive computer simulation, and may be used to access the parameters yielding the correct relic density for additional benchmarks or mass splittings.

Acknowledgements

ASC is supported in part by the National Research Foundation of South Africa. LM is supported by the UJ GES 4IR initiative.

References

- [1] Silk J *et al.* 2010 *Particle Dark Matter: Observations, Models and Searches* (Cambridge: Cambridge Univ. Press)
- [2] Adam R *et al.* (Planck) 2016 *Astron. Astrophys.* **594** A1 (*Preprint* 1502.01582)
- [3] Colucci S, Fuks B, Giacchino F, Lopez Honorez L, Tytgat M H G and VandeCasteele J 2018 *Phys. Rev.* **D98** 035002 (*Preprint* 1804.05068)
- [4] Colucci S, Giacchino F, Tytgat M H and VandeCasteele J 2018 *Phys. Rev. D* **98** 115029 (*Preprint* 1805.10173)
- [5] Das A and Dasgupta B 2017 *Phys. Rev. Lett.* **118** 251101 (*Preprint* 1611.04606)
- [6] Aghanim N *et al.* (Planck) 2020 *Astron. Astrophys.* **641** A6 (*Preprint* 1807.06209)
- [7] Kong K and Matchev K T 2006 *JHEP* **01** 038 (*Preprint* hep-ph/0509119)
- [8] Cornell A S, Deandrea A, Flacke T, Fuks B and Mason L 2021 *JHEP* **07** 026 (*Preprint* 2104.12795)
- [9] Lisanti M 2016 Lectures on Dark Matter Physics *Theoretical Advanced Study Institute in Elementary Particle Physics: New Frontiers in Fields and Strings* (*Preprint* 1603.03797)
- [10] Griest K and Seckel D 1991 *Phys. Rev. D* **43** 3191–3203
- [11] Bélanger G, Boudjema F, Goudelis A, Pukhov A and Zaldivar B 2018 *Comput. Phys. Commun.* **231** 173–186 (*Preprint* 1801.03509)
- [12] Belyaev A, Christensen N D and Pukhov A 2013 *Comput. Phys. Commun.* **184** 1729–1769 (*Preprint* 1207.6082)
- [13] Alloul A, Christensen N D, Degrande C, Duhr C and Fuks B 2014 *Comput. Phys. Commun.* **185** 2250–2300 (*Preprint* 1310.1921)
- [14] Christensen N D, de Aquino P, Degrande C, Duhr C, Fuks B, Herquet M, Maltoni F and Schumann S 2011 *Eur. Phys. J. C* **71** 1541 (*Preprint* 0906.2474)

Quasinormal modes in the large angular momentum limit: an inverse multipolar expansion analysis

A Chrysostomou¹ and A S Cornell²

Department of Physics, University of Johannesburg, PO Box 524, Auckland Park 2006, South Africa.

E-mail: ¹annachrys97@gmail.com, ²acornell@uj.ac.za

Abstract. The quasinormal modes (QNMs) of a black hole (BH) may be identified as a class of damped, classical oscillations in spacetime, emergent as part of the late-stage response to a perturbation of the BH. In a recent paper, we utilised the inverse multipolar expansion method proposed by Dolan and Ottewill to investigate the quasinormal frequencies of 4D Schwarzschild, Reissner-Nordström, and Schwarzschild de Sitter BHs within the eikonal limit for fields of spin $s = \{0, 1/2, 1, 3/2, 2\}$. Here, we extend this method to the calculation of the radial component of the QNM wavefunctions within the Schwarzschild BH spacetime for each of these fields, investigating specifically the behaviour of these wavefunctions within the large- ℓ regime.

1. Introduction

The regular detection of binary black hole (BH) mergers has provided us with a wealth of data against which we may test our extant models of gravitational-waves (GWs) and their BH sources [1]. The demonstrable consensus between GW data and modelling [2] validates our understanding of BH mergers as three-phase events successfully described using (i) the post-Newtonian approximation, (ii) numerical relativity, and (iii) BH perturbation theory. These phases are, respectively, (i) inspiral, a long adiabatic stage as the orbit shrinks and GW emission increases; (ii) merger, a violent coalescence of these compact bodies into a single BH such that GW emission peaks; (iii) ringdown, where the final BH emits damped GWs as it relaxes into a stationary state [3, 4].

The damped oscillations in spacetime from which ringdown is comprised are known as the quasinormal modes (QNMs). Their corresponding quasinormal frequencies (QNFs) may be decomposed into a real and imaginary part, where the former represents the physical oscillation frequency and the latter is related to the decay timescale of the BH's perturbation. Unlike the oscillations within the inspiral and merger phases, the QNFs are independent of the initial conditions; they depend exclusively on the characteristics of the final BH [5]. This, as well as their relationship to gauge-gravity duality [6] and possibly even BH area quantisation [7], had led to immense interest in QNFs within the field of BH physics and beyond.

However, the computation of BH QNFs is wrought with technical difficulty due to the inherently dissipative nature of the BH system. This is a consequence of the boundary conditions thereof: in BH spacetimes with a cosmological constant $\Lambda \geq 0$, energy is irrevocably lost at the BH event horizon and at spatial infinity (or at the cosmological horizon of the de Sitter (dS) cases denoted by $\Lambda > 0$). As such, QNMs do not form a complete set in these contexts (see Ref. [8] for

further discussion). Finally, QNMs may be shown to be non-normalisable in asymptotically-flat and dS spacetimes (but can be normalisable in anti-de Sitter (AdS) spacetimes) [9].

To contend with these technical challenges, a number of methods have been developed within the QNM literature (concisely reviewed in Refs. [5, 9]). As explained in Ref. [10], the computational method applied to solve for QNFs must be chosen carefully such that the specifics of the BH spacetime and wave equation dependencies are accommodated, for a certain approach may fail under conditions where another proves more accurate. Here, we utilise a method derived directly from the BH context: the inverse multipolar expansion method put forth by Dolan and Ottewill in Ref. [11]. The “Dolan-Ottewill” method involves the introduction of a novel ansatz for the QNM wave equation (described in section 2) constructed from the circular null geodesics of a spherically-symmetric BH in non-AdS spacetime. The QNF can then be solved for through an iterative process, and emerges as an expansion in inverse powers of the multipolar number (ℓ). Consequently, the method is explicitly useful in exploring large- ℓ asymptotics [12].

In this work, we expand upon our paper, Ref. [13], by explaining the application of the Dolan-Ottewill method in greater detail. We then demonstrate how the method can be extended to the computation of QNM wavefunctions of spin $s = \{0, 1/2, 1, 3/2, 2\}$ for the 4D Schwarzschild BH. Finally, we impose the large- ℓ limit on the wavefunctions and assess their behaviour therein.

2. QNM effective potentials in the 4D Schwarzschild BH spacetime

A non-rotating, spherically-symmetric, 4D BH may be described in its most general terms by

$$ds^2 = g_{\mu\nu}dx^\mu dx^\nu = -f(r)dt^2 + f(r)^{-1}dr^2 + r^2(d\theta^2 + \sin^2\theta d\phi^2) . \quad (1)$$

The Schwarzschild metric function is given by $f(r) = 1 - r_H/r$, with the event horizon located at $r_H = 2M$ (setting $\hbar = G = c = 1$). To analyse the perturbation of such a BH, we may decompose the spacetime into a background metric $g_{\mu\nu}^{BG}$ and a small perturbing term $h_{\mu\nu}$,

$$g'_{\mu\nu} = g_{\mu\nu}^{BG} + h_{\mu\nu} , \quad h_{\mu\nu} \ll g_{\mu\nu}^{BG} . \quad (2)$$

We then solve the consequent system of linear differential equations that satisfy Einstein’s vacuum field equations [14]. If we consider a scalar test field Φ as a perturbing field on this linearised gravitational background, it may be shown that $h_{\mu\nu}$ and Φ decouple such that the metric perturbations described by $h_{\mu\nu}$ can be set to zero (see Ref. [5] for details). With the tortoise coordinate $dx/dr = 1/f(r)$, we can isolate the radial behaviour of the QNM as

$$\frac{d^2}{dx^2}\Phi(x) + [\omega^2 - V_{eff}(r)]\Phi(x) = 0 , \quad (3)$$

where ω represents the QNF. The effective QNM potentials associated with fields of integer spin s within the Schwarzschild BH spacetime can be concisely expressed through

$$V_{eff}(r) = \frac{f(r)}{r^2} \left[\ell(\ell+1) + \frac{2M(1-s^2)}{r} \right] , \quad (4)$$

$$s = \begin{cases} 0 , & \text{scalar perturbations} & \Rightarrow (1-s^2) = 1 \\ 1 , & \text{electromagnetic perturbations} & \Rightarrow (1-s^2) = 0 \\ 2 , & \text{gravitational perturbations: vector-mode} & \Rightarrow (1-s^2) = -3 . \end{cases}$$

On the basis of the isospectrality of the spin-2 scalar- and vector-modes [15], here we shall consider only the vector-modes. For half-integer fields, the QNM potentials can be cast as isospectral supersymmetric partners through

$$V_{eff} = \pm f(r) \frac{d}{dr} W + W^2 , \quad W = \frac{\sqrt{f(r)}}{r} \kappa z , \quad (5)$$

where the superpotential W is dependent on $\kappa \equiv j + 1/2$, the spinor eigenvalue on the 2-sphere, and

$$\kappa z = \begin{cases} \kappa, & \kappa = \ell + 1, \text{ Dirac perturbations} & s = 1/2 \\ \kappa \frac{\kappa^2 - 1}{\kappa^2 - f(r)}, & \kappa = \ell + 2, \text{ Rarita-Schwinger perturbations} & s = 3/2. \end{cases} \quad (6)$$

respectively [19]. Note that there exists a distinction between the definition of κ : while $j = \ell \pm 1/2$ for Dirac cases [16], $j = \ell \pm 3/2$ for Rarita-Schwinger fields [17, 18]. Here, as in Ref. [13], we define the spinor eigenvalue on the 2-sphere in terms of ℓ (where ℓ is an integer).

3. The Dolan-Ottewill method: Schwarzschild QNFs

The primary objective of the multipolar expansion method is to express the QNF as a linear expansion in inverse multipolar numbers,

$$\omega = \sum_{k=-1} \omega_k L^{-k}, \quad L = \ell + 1/2, \quad (7)$$

where each ω_k of the summation is computed iteratively. The procedure begins by defining the novel ansatz,

$$\Phi(r) = e^{i\omega z(x)} v(r), \quad z(x) = \int^x \rho(r) dx, \quad (8)$$

where the ansatz must adhere to the non-AdS boundary conditions,

$$f(r) \rightarrow 0, \quad b_c k_c(r) \rightarrow -1 \quad \text{as } x \rightarrow -\infty, \quad (9)$$

$$f(r)/r^2 \rightarrow 0, \quad b_c k_c(r) \rightarrow +1 \quad \text{as } x \rightarrow +\infty. \quad (10)$$

These convey the fact that the event horizon is encountered as $x \rightarrow -\infty$ and an asymptotically-flat region or cosmological horizon is approached as $x \rightarrow +\infty$. The ansatz may be substituted into equation (3) to obtain

$$f(r) \frac{d}{dr} \left(f(r) \frac{dv}{dr} \right) + 2i\omega \rho(r) \frac{dv}{dr} + \left[i\omega f(r) \frac{d\rho}{dr} + (1 - \rho(r)^2) \omega^2 - V(r) \right] v(r) = 0. \quad (11)$$

Though not obvious by inspection, this equation is simpler to solve than equation (3) as it lends itself with greater ease to the iterative procedure of Dolan and Ottewill.

We may then define $\rho = b_c k_c(r)$. The ansatz therefore depends on the impact parameter $b = r/\sqrt{f(r)}$ and the newly-defined function $k(r) = b^{-2} - f(r)/r^2$, both of which are evaluated at the critical orbit $r = r_c$. This r_c can be derived using the metric function, $r_c = 2f(r)/\partial_r f(r)|_{r=r_c}$. Finally, we may define the function $v(r)$ as a further expansion in L^{-k} , namely

$$v(r) = \exp \left\{ \sum_{k=0} S_k(r) L^{-k} \right\}. \quad (12)$$

For the Schwarzschild BH spacetime, where we opt to set $M = 1$, the components of the ansatz are given by $r_c = 3$, $b_c = \sqrt{27}$, and thus $\rho(r) = (1 - 3/r)(1 + 6/r)^{1/2}$. We substitute these into equation (11), in conjunction with equations (7) and (12) expanded to our order of choice. Here, we select $\mathcal{O}(L^{-6})$. Lastly, we substitute the potential corresponding to our perturbing field of interest.

The procedure then involves collecting powers of L , setting the coefficient to zero, and solving for ω_k and $S'_k(r)$ for monotonically increasing values of k . The process can become fairly

Table 1: The inverse multipolar expansions for the effective QNFs of spin s at order $\mathcal{O}(L^{-k})$, from Ref. [13]. Odd (even) values of k correspond to real (imaginary) expansion terms. While the lowest-order terms remain constant for each field, we find that for each $k \geq 0$, the magnitude of the L^{-k} coefficients increases with s . Note that for QNFs of half-integer spin, we parametrise the multipolar number as $L \rightarrow \bar{L} = \kappa$, using the values of κ specified in equation (6).

s	$b_c \sum_{k=-1}^6 \omega_k L^{-k}$
Perturbations of integer spin	
0	$L - \frac{i}{2} + \frac{7}{216L} - \frac{137}{7776L^2}i + \frac{2615}{1259712L^3} + \frac{590983}{362797056L^4}i - \frac{42573661}{39182082048L^5} + \frac{11084613257}{8463329722368L^6}i$
1	$L - \frac{i}{2} - \frac{65}{216L} + \frac{295}{7776L^2}i - \frac{35617}{1259712L^3} + \frac{3374791}{362797056L^4}i - \frac{342889693}{39182082048L^5} + \frac{74076561065}{8463329722368L^6}i$
2	$L - \frac{i}{2} - \frac{281}{216L} + \frac{1591}{7776L^2}i - \frac{710185}{1259712L^3} + \frac{92347783}{362797056L^4}i - \frac{7827932509}{39182082048L^5} - \frac{481407154423}{8463329722368L^6}i$
Perturbations of half-integer spin	
1/2	$\bar{L} - \frac{i}{2} - \frac{11}{216\bar{L}} - \frac{29}{7776\bar{L}^2}i + \frac{1805}{1259712\bar{L}^3} + \frac{27223}{362797056\bar{L}^4}i + \frac{23015171}{39182082048\bar{L}^5} - \frac{6431354863}{8463329722368\bar{L}^6}i$
3/2	$\bar{L} - \frac{i}{2} - \frac{155}{216\bar{L}} + \frac{835}{7776\bar{L}^2}i - \frac{214627}{1259712\bar{L}^3} + \frac{25750231}{362797056\bar{L}^4}i - \frac{2525971453}{39182082048\bar{L}^5} + \frac{292606736465}{8463329722368\bar{L}^6}i$

straightforward with the aid of the `Coefficient` and `Solve` functions within the MATHEMATICA environment. In this manner, we may compute the ω_k terms of equation (7), evaluate them at $r = r_c$, and express the QNF through the L^{-k} -dependent expansions provided in table 1. The lowest order terms are as follows:

$$\begin{aligned}
L^2: \quad 27\omega_{-1}^2 - 1 = 0 &\Rightarrow \omega_{-1} = \pm \frac{1}{\sqrt{27}}; \\
L^1: \quad 2i\omega_{-1} \left(1 + \frac{6}{r}\right)^{1/2} \left(1 - \frac{3}{r}\right) S'_0 + \frac{54\omega_{-1}\omega_0}{r^2} + \frac{27i\omega}{r^3} \left(1 + \frac{6}{r}\right)^{-1/2} &= 0 \\
&\Rightarrow \omega_0 = -\frac{i}{2\sqrt{27}} \\
&\Rightarrow S'_0(r) = \frac{\sqrt{27}}{r(r+6)(r-3)} \left[\left(1 + \frac{6}{r}\right)^{1/2} - \frac{\sqrt{27}}{r} \right].
\end{aligned}$$

Thus, for every ω_k ($k \geq 0$) of table 1, we solve also for a $S'_k(r)$ term. These latter expressions are more complicated, and become undefined if $r = r_c$ is naively imposed. However, through integrating the $S_k(r)$ derivatives, we obtain the necessary terms to define $v(r)$. We may then substitute these various components of the ansatz into equation (8). The subsequent functions are plotted in figure 1 for spin $s = \{1/2, 1, 3/2, 2\}$, to order $\mathcal{O}(L^{-6})$ for $\ell = 4$.

Certain behaviours are consistent for all radial wavefunctions explored here, such as the divergence at the boundaries and the shift of $\pi/2$ between real and imaginary components. We observe, however, a decrease (an increase) in the amplitude for increasing s for integer (half-integer) cases. Irrespective of the spin, an increase in ℓ corresponds to an increase in the amplitude and a decrease in the wavelength of these radial profiles, as demonstrated in figure 2. Furthermore, there is notable shifting from one wavefunction to the next, with Dirac and gravitational wavefunctions shifted ahead of their Rarita-Schwinger and electromagnetic counterparts.

Despite these features, it was noted in Ref. [11] that the radial profile does not offer much in terms of physical insight. It is important to remember that our starting point of equation

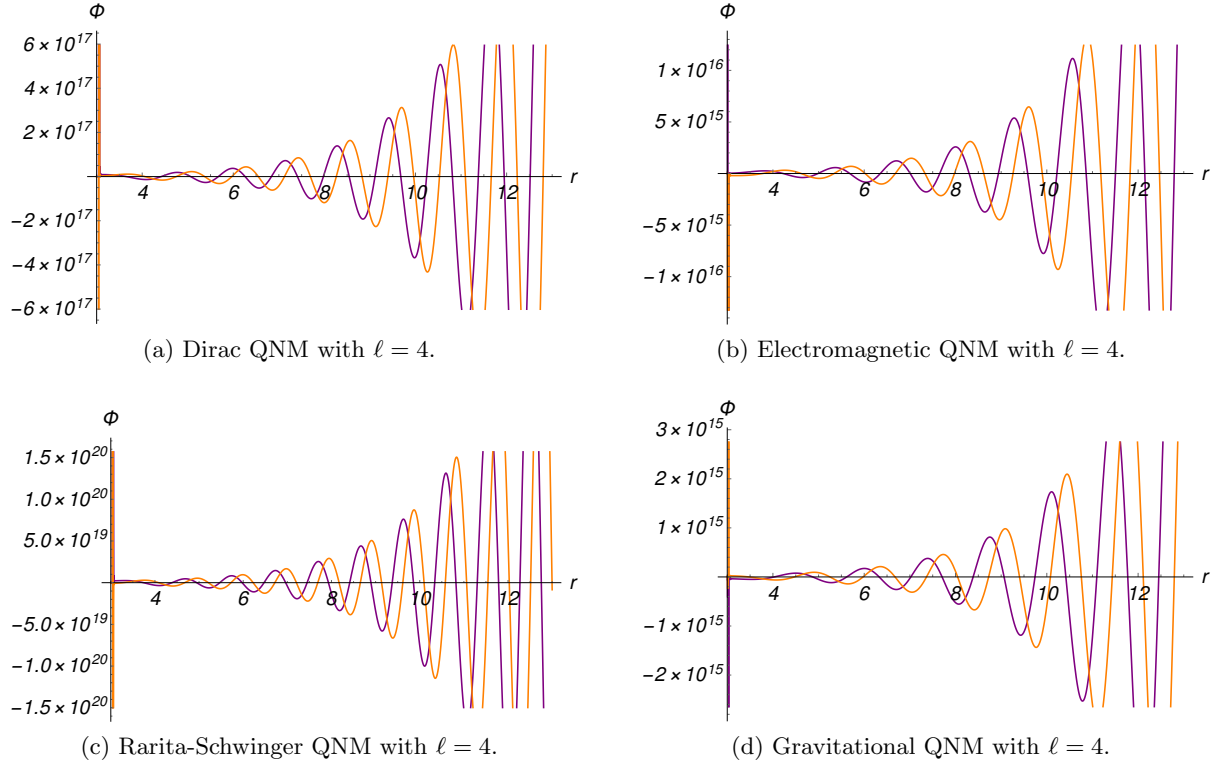


Figure 1: The radial wavefunctions for QNMs of spin $s = \{1/2, 1, 3/2, 2\}$ for Schwarzschild BHs with $\ell = 4$. Real and imaginary components are denoted by purple and orange, respectively.

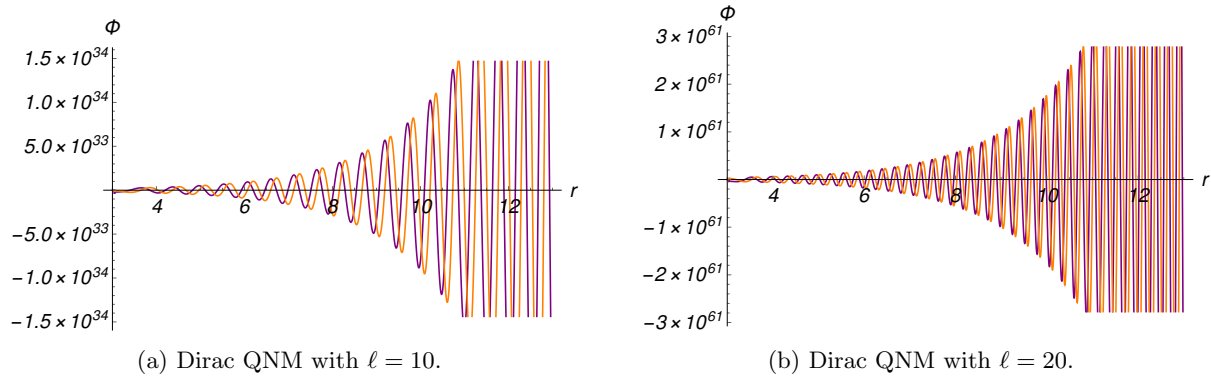


Figure 2: The radial wavefunctions for QNMs of spin $s = 1/2$ for Schwarzschild BHs with $\ell = 10$ and $\ell = 20$. Real and imaginary components are denoted by purple and orange, respectively.

(3) represents the isolated radial behaviour. However, understanding the radial component is a necessary first step into calculating the full waveform in any 4D Schwarzschild application.

4. Conclusions

The Dolan-Ottewill method is an efficient, economical method that allows for the computation of QNFs to high orders in L^{-k} with relative ease. As a physically-motivated method, it is easy to match the method with the appropriate context, and therefore avoid the limitations discussed

in Ref. [10]. An especially interesting aspect of the method is its flexibility: here, we have demonstrated the simple means by which it can be extended to the computation of radial QNM wavefunctions; in Ref. [13], we explored the various non-rotating, spherically-symmetric BH spacetimes to which the Dolan-Ottewill method may also be applied. Since focus in the literature has been concentrated on the development of computational methods for QNFs [5, 9], the Dolan-Ottewill method becomes especially valuable for its use in the calculation of the relatively underexplored QNM wavefunctions.

Further extensions, however, are highly desirable *viz.* through an incorporation of temporal and angular components into our assessment of the QNM wavefunction. Studies into physically relevant aspects of the QNM contribution through the use of the Dolan-Ottewill method is already underway: in Ref. [12], Dolan and Ottewill combined their expansion method with a WKB analysis in order to compute the “QNM excitation coefficient” from the residues of the poles in the Green function for the scalar field within the 4D Schwarzschild context. This aids in the establishment of a more complete description for the QNM response in the wake of a BH perturbation. To explore these computations beyond the scalar field and Schwarzschild BH spacetime would be interesting.

Moreover, an investigation into the application of the Dolan-Ottewill method to higher-dimensional BHs may be possible. This was demonstrated in Ref. [11], where Dolan and Ottewill computed the lowest terms in the QNF expansion for the gravitational perturbations of a d -dimensional Schwarzschild BH. Whether this can be extended to AdS BH spacetimes remains an open question. Rotating BH spacetimes, however, may be accommodated. This was suggested in Ref. [20], where an additional expansion was introduced via the angular eigenvalue. We reserve exploration into these various avenues for future works.

Acknowledgments

ASC is supported in part by the National Research Foundation (NRF) of South Africa; AC is supported by the NRF and Department of Science and Innovation through the SA-CERN programme. The authors wish to thank Prof. Hing-Tong Cho and Dr. Chun-Hung Chen for their insightful discussions during the production of this short note.

References

- [1] Isi M, Giesler M, Farr W M, Scheel M A and Teukolsky S A 2019 *Phys. Rev. Lett.* **123** 111102.
- [2] Abbott B P *et al.* 2016 *Phys. Rev. Lett.* **116** 061102.
- [3] Ching E S C, Leung P T, Suen W M and Young K 1995 *Phys. Rev. D* **52** 2118.
- [4] Berti E, Cardoso V, Gonzalez J A, Sperhake U, Hannam M, Husa S and Bruegmann B 2007 *Phys. Rev. D* **76** 064034.
- [5] Berti E, Cardoso V and Starinets A O 2009 *Class. Quant. Grav.* **26** 163001.
- [6] Chruściel P T, Costa J L and Heusler M 2012 *Living Rev. Relativ.* **15**.
- [7] Hod S 1998 *Phys. Rev. Lett.* **81** 4293.
- [8] Nollert H P 1999 *Class. Quant. Grav.* **16** R159 (1999).
- [9] Konoplya R A and Zhidenko A 2011 *Rev. Mod. Phys.* **83** 793.
- [10] Konoplya R A, Zhidenko A and Zinhailo A F 2019 *Class. Quant. Grav.* **36** 155002.
- [11] Dolan S R and Ottewill A C 2009 *Class. Quant. Grav.* **26** 225003.
- [12] Dolan S R and Ottewill A C 2011 *Phys. Rev. D* **84** 104002.
- [13] Chen C H, Cho H T, Chrysostomou A and Cornell A S 2021 *Phys. Rev. D* **104** 024009.
- [14] Regge T and Wheeler J A 1957 *Phys. Rev.* **108** 1063.
- [15] Chandrasekhar S and Detweiler S L 1975 *Proc. Roy. Soc. Lond. A* **344** 441.
- [16] Cho H T, Cornell A S, Doukas J and Naylor W 2007 *Phys. Rev. D* **75** 104005.
- [17] Chen C H, Cho H T, Cornell A S, Harmsen G and Naylor W 2015 *Chin. J. Phys.* **53** 110101.
- [18] Chen C H, Cho H T, Cornell A S and Harmsen G 2016 *Phys. Rev. D* **94** 044052.
- [19] Cooper F, Khare A and Sukhatme U 1995 *Physics Reports* **251** 267.
- [20] Dolan S R 2010 *Phys. Rev. D* **82** 104003.

Generating function approach to Open Quantum Walks

Ayanda Zungu¹, Ilya Sinayskiy^{2,3}, Francesco Petruccione^{2,3}

¹Centre for Space Research, North-West University, Mahikeng, 2745, South Africa

²Quantum Research Group, School of Chemistry and Physics, University of KwaZulu-Natal
Durban, 4001, South Africa

³National Institute for Theoretical and Computational Sciences (NITheCS), South Africa

E-mail: ¹arzngu@gmail.com

Abstract. Open quantum walks (QWs) have been introduced as a type of quantum walk that is entirely driven by the dissipative interaction with external environments and defined as completely positive trace-preserving maps (CPTP) on graphs. In this work, we study the continuous-time QW master equation that simulates an QW on \mathbb{Z}^+ in the quantum optical setting. The physical system realizing this QW is a two-level atom interacting with a quantized mode of electromagnetic radiation at zero temperature in the dispersive regime. We solve this QW analytically using generating functions. We use the obtained solution for arbitrary initial conditions to explicitly construct the moments of this quantum walk. As an example, the dynamics of the observables (mean, variance) are presented for various parameters.

1. Introduction

Open quantum walks (QWs) are a class of quantum walks (QWs) which are exclusively based on the non-unitary dynamics induced by the interaction with an environment [1–3]. Mathematically, the non-unitary dynamics are described by the completely positive trace preserving (CPTP) maps [4,5]. Unlike QWs where the probability of finding the walker results from the quantum interference over the vertices of a graph [6–8], the QW probability to find the quantum walker on a particular node depends on the structure of the underlying graph, and also on the inner state of the walker. In QWs, the evolution of the walker is strictly driven by the dissipative interaction with a local environment. As a new framework, it has been suggested that QWs can be used to perform dissipative quantum computation and to create complex quantum states [9]. The detailed description of the formalism of QWs can be found in [1–3].

Recently, a quantum optical scheme for the experimental realization of QWs was proposed [10]. In the proposed quantum optical scheme, a two-level atom plays the role of the “walker” and the Fock states of the cavity mode correspond to the lattice sites of the QW. Using the small unitary rotations approach [11] the effective dynamics of this system was shown to be an QW. The presence of spontaneous emission in the system was an essential ingredient for obtaining an QW. Although this scheme leads to QW, the dynamics of the walker is not covering all possible behaviors, especially in comparison to the traditional microscopic approaches [12].

The main motivation for performing the research presented in this paper is to solve analytically the QW master equation developed in [10], use the solution to construct the moments of this quantum walk explicitly and derive the exact solution for the mean and the variance.

The paper is structured as follows: in Sec. 2 we introduce the model, with reference to [10]; Sec. 3 contains the analytical solution of the OQW master equation and discussions; finally, in Sec. 4 we present the conclusion.

2. Model

As suggest by [10], we consider the following quantum optics set-up: a two-level atom (qubit) interacting with a quantized mode of the electromagnetic radiation at zero temperature. The qubit correspond to the “walker” and the Fock states of the cavity mode with the nodes of the graph. The jumps between different nodes is associated with the action of the annihilation or creation operator on a Fock state. In an experiment setting, there will be processes which lead to dissipative losses. In our model, the only dissipative process considered is the spontaneous emission. The master equation for the system has the following form [4, 13] ($\hbar = 1$):

$$\frac{d}{dt}\hat{\rho}(t) = -i[\hat{H}_{\text{int}}, \hat{\rho}] + \gamma\mathcal{L}[\hat{\sigma}_-, \hat{\sigma}_+]\hat{\rho}, \quad (1)$$

where $\mathcal{L}[\hat{X}, \hat{Y}]\hat{\rho} = \hat{X}\hat{\rho}\hat{Y} - (1/2)(\hat{\rho}\hat{Y}\hat{X} + \hat{Y}\hat{X}\hat{\rho})$ is the standard Gorini-Kossakowski-Sudarshan-Lindblad (GKSL) dissipator [14, 15]. The interaction Hamiltonian [16] for the model in the rotation wave approximation (RWA) can be written as

$$\hat{H}_{\text{int}} = \Delta\hat{a}^\dagger\hat{a} + g(\hat{a}\hat{\sigma}_+ + \hat{a}^\dagger\hat{\sigma}_-). \quad (2)$$

Here Δ denotes the frequency detuning between the qubit and the field, g is their interaction strength, $\hat{\sigma}_\pm$ are the Pauli raising and the lowering operators for the qubit, satisfying $[\hat{\sigma}_+, \hat{\sigma}_-] = \hat{\sigma}_z$. The operators \hat{a}^\dagger and \hat{a} are the creation and annihilation operators for the cavity photons. The constant γ is the coefficient of spontaneous emission. With this experimental setting and moving the system into the dispersive regime ($\frac{g}{\Delta} \ll 1$) one can physically implement an OQW. By applying the small unitary rotations method [11] to the quantum optical master equation (1), then apply the RWA, using $\hat{\rho} = \sum_n \hat{\rho}_n \otimes |n\rangle\langle n|$, one can obtain the following continuous-time OQW master equation (see [10] for the full derivation)

$$\begin{aligned} \frac{d}{dt}\hat{\rho}_n(t) = & i\frac{g^2}{\Delta} \left[n\hat{\sigma}_z + \frac{\hat{\sigma}_z}{2} + \frac{1}{2}, \hat{\rho}_n \right] + \gamma \left(1 - \frac{2g^2}{\Delta^2} (2n+1) \right) \mathcal{L}[\hat{\sigma}_-, \hat{\sigma}_+]\hat{\rho}_n \\ & + \frac{\gamma g^2}{\Delta^2} \left((n+1)\hat{\sigma}_z \hat{\rho}_{n+1} \hat{\sigma}_z - n\hat{\rho}_n \right), \end{aligned} \quad (3)$$

where $|n\rangle$ is the Fock state of the cavity mode and $\hat{\rho}_n$ is the positive operator describing the state of the two-level system. In the next section, we solve this OQW master equation (3) analytically using generating functions.

3. Derivation of moments

In this section we derive the exact expression for the observables, the mean and the variance. The OQW master equation (3) can be written as

$$\begin{aligned} \dot{P}_n(t) &= \frac{\gamma g^2}{\Delta^2} ((n+1)P_{n+1} - P_n), \\ \dot{X}_n(t) &= \frac{g^2}{\Delta} (2n+1)Y_n - \frac{A_n}{2}X_n - \frac{\gamma g^2}{\Delta^2} ((n+1)X_{n+1} + nX_n), \\ \dot{Y}_n(t) &= -\frac{g^2}{\Delta} (2n+1)X_n - \frac{A_n}{2}Y_n - \frac{\gamma g^2}{\Delta^2} ((n+1)Y_{n+1} + nY_n), \\ \dot{Z}_n(t) &= -A_n(P_n + Z_n) + \frac{\gamma g^2}{\Delta^2} ((n+1)Z_{n+1} - nZ_n), \end{aligned} \quad (4)$$

where $A_n = \gamma \left(1 - \frac{2g^2}{\Delta^2}(2n+1)\right)$ and the index n runs from 0 to ∞ . The functions P_n, \dots, Z_n are defined as $P_n(t) = \text{Tr}[\hat{\rho}_n(t)]$ and $K_n(t) = \text{Tr}[\hat{\sigma}_K \hat{\rho}_n(t)]$ i.e., $K_n \in (X_n, Y_n, Z_n)$ ($\hat{\sigma}_K$ is the corresponding Pauli matrix). Using this system of differential equations (4), one can easily obtain a corresponding system of differential equations for P_s, X_s, Y_s and Z_s from the generating function $K_s(x, t) = \sum_{n=0}^{\infty} x^n K_n(t)$,

$$\begin{aligned}\frac{\partial P_s}{\partial t} &= \frac{\gamma g^2}{\Delta^2}(1-x) \frac{\partial P_s}{\partial x}, \\ \frac{\partial X_s}{\partial t} &= \frac{g^2}{\Delta} Y_s + 2x \frac{g^2}{\Delta} \frac{\partial Y_s}{\partial x} + \gamma \left(\frac{g^2}{\Delta^2} - \frac{1}{2} \right) X_s + \frac{\gamma g^2}{\Delta^2}(x-1) \frac{\partial X_s}{\partial x}, \\ \frac{\partial Y_s}{\partial t} &= -\frac{g^2}{\Delta} X_s - 2x \frac{g^2}{\Delta} \frac{\partial X_s}{\partial x} + \gamma \left(\frac{g^2}{\Delta^2} - \frac{1}{2} \right) Y_s + \frac{\gamma g^2}{\Delta^2}(x-1) \frac{\partial Y_s}{\partial x}, \\ \frac{\partial Z_s}{\partial t} &= 2\gamma \left(\frac{g^2}{\Delta^2} - \frac{1}{2} \right) P_s + 4x \frac{\gamma g^2}{\Delta^2} \frac{\partial P_s}{\partial x} + 2\gamma \left(\frac{g^2}{\Delta^2} - \frac{1}{2} \right) Z_s + \frac{\gamma g^2}{\Delta^2}(3x+1) \frac{\partial Z_s}{\partial x}.\end{aligned}\quad (5)$$

The first equation for this system at $x = 1$ reduces to $P_s(1, t) = \sum_{n=0}^{\infty} (1)^n P_n(t) = \sum_{n=0}^{\infty} P_n(t)$, where P_n is the probability of finding the walker on the node n , and $\sum_{n=0}^{\infty} P_n(t)$ is the total probability. This implies that $P_s(1, t) = 1$. If we assume that at $t = 0$ the walker is localized at site k ($k \in \mathbb{Z}$) with $\hat{\rho}(0) = \begin{pmatrix} a & z \\ \bar{z} & b \end{pmatrix} \otimes |k\rangle\langle k|$, where $a + b = 1$, $(a, b) \in \mathbb{R}_{\geq 0}$ and $z \in \mathbb{C}$, one can show that $P_s(x, 0) = x^k$. Using the method of characteristics and initial condition, one can show that the formal solution for P_s has the form

$$P_s(x, t) = \sum_{n=0}^k \binom{k}{n} x^n (1 - e^{-\frac{\gamma g^2}{\Delta^2} t})^{k-n} e^{-\frac{\gamma g^2}{\Delta^2} nt}, \quad (6)$$

where $\binom{k}{n}$ denotes the binomial coefficient and the expression for P_n reads

$$P_n(t) = \begin{cases} \binom{k}{n} (1 - e^{-\frac{\gamma g^2}{\Delta^2} t})^{k-n} e^{-\frac{\gamma g^2}{\Delta^2} nt}, & k \geq n \\ 0, & \text{otherwise.} \end{cases} \quad (7)$$

The probability to find the walker at site n (7) is shown in figure 1 for various parameters. Following the same steps with initial conditions $X_s(x, 0) = 2x^k$ and $Y_s(x, 0) = 2x^k$, we derive and solve for the real part X_n and the imaginary part Y_n of the population coherences

$$\begin{aligned}X_n(t) &= 2e^{\beta t} \binom{k}{n} \text{Re} \left\{ \bar{z} e^{-(i\delta + k\lambda)t} \left[\frac{\alpha}{\bar{\lambda}} (1 - e^{\lambda t}) \right]^{k-n} \right\}, \\ Y_n(t) &= 2e^{\beta t} \binom{k}{n} \text{Im} \left\{ z e^{(i\delta - k\bar{\lambda})t} \left[\frac{\alpha}{\bar{\lambda}} (1 - e^{\bar{\lambda}t}) \right]^{k-n} \right\}.\end{aligned}\quad (8)$$

Here $\lambda = 2i\delta + \alpha$, $\alpha = \frac{\gamma g^2}{\Delta^2}$, $\delta = \frac{g^2}{\Delta}$ and $\beta = 2\gamma \left(\frac{g^2}{\Delta^2} - \frac{1}{2} \right)$ ($(g, \Delta, \gamma) \in \mathbb{R}_{\geq 0}$). The term $\bar{\eta}$ represent the complex conjugate i.e., $\eta \in (\lambda, z)$. The behavior of equation (8) is shown in figure 2 for various parameters. Using the explicit solution of the function P_s (6) and the initial condition $Z_s(x, 0) = x^k(a - b)$, one can derive the solution for the function Z_s

$$Z_s(x, t) = \beta \sum_{m=0}^k x^m f(m, t) + 4\alpha k \sum_{m=1}^k x^m g(m-1, t) + x^k(a-b)e^{\beta t}, \quad (9)$$

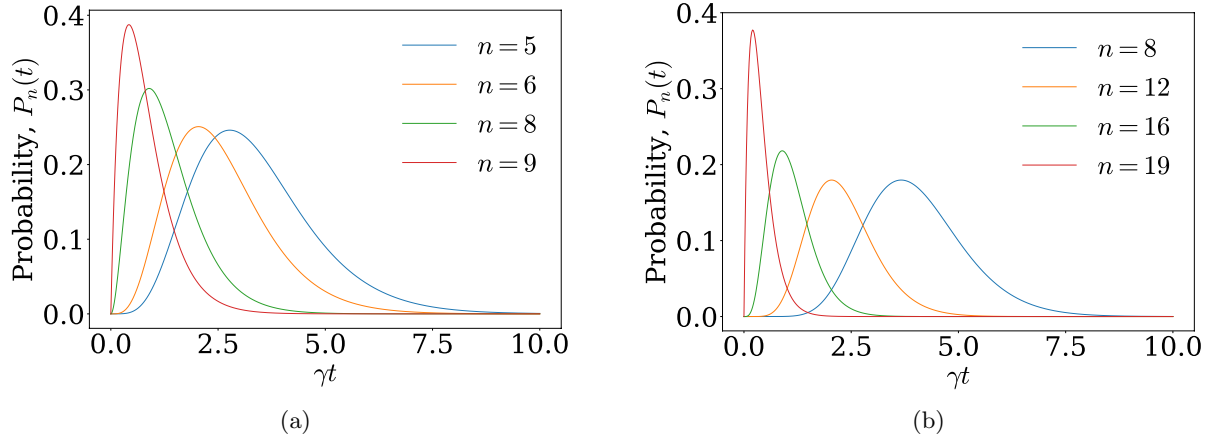


Figure 1: (Color online) The probability $P_n(t)$ to find a walker at site n as a function of dimensionless time γt for different initial Fock states (stated in the legend). The initial sites are $k = 10$ (a) and $k = 20$ (b). Other parameters are set as $\gamma = 0.1$, $g = 0.5$ and $\Delta = 1$.

where

$$f(m, t) = \sum_{n=m}^k \binom{k}{n} \binom{n}{m} (-1)^{n-m} \frac{e^{\beta t}}{r_n} \{e^{r_n t} - 1\},$$

$$g(m-1, t) = \sum_{n=m}^k \binom{k-1}{n} \binom{n}{m-1} (-1)^{n-m+1} \frac{e^{\beta t}}{r'_n} \{e^{r'_n t} - 1\}. \quad (10)$$

Here $r_n = -\alpha n - \beta$ and $r'_n = -\alpha(n+1) - \beta$. Other parameters are the same as defined earlier. Using the generating function Z_s (9) one can derive the solution for the population inversion $Z_n(t)$. We are going to consider three solutions for Z_s ; (i) the population in the vacuum Fock state $m = 0$, (ii) the population in the intermediate site $1 \leq m \leq k-1$ and (iii) the population in the initial site $m = k$. The solution for the vacuum Fock state $m = 0$ has the form

$$Z_0(t) = \beta \sum_{n=0}^k \binom{k}{n} (-1)^n \frac{e^{\beta t}}{r_n} \{e^{r_n t} - 1\}. \quad (11)$$

The population in the intermediate site $1 \leq m \leq k-1$ has the form

$$Z_{1 \leq m \leq k-1}(t) = \beta f(m, t) + 4\alpha k g(m-1, t), \quad (12)$$

where $f(m, t)$ and $g(m-1, t)$ are given by equation (10). Lastly, one can show that the population in the initial site $m = k$ has the form

$$Z_k(t) = \beta f(k, t) + 4\alpha k g(k-1, t) + (a-b)e^{\beta t}$$

$$= \frac{e^{\beta t}}{r_k} (e^{r_k t} - 1)(\beta + 4\alpha k) + (a-b)e^{\beta t}, \quad (13)$$

where $r_k = -\alpha k - \beta$. The expressions (11), (12) and (13) conclude the derivation of the solution of $Z_n(t)$. These results are illustrated in figure 3 for various parameters.

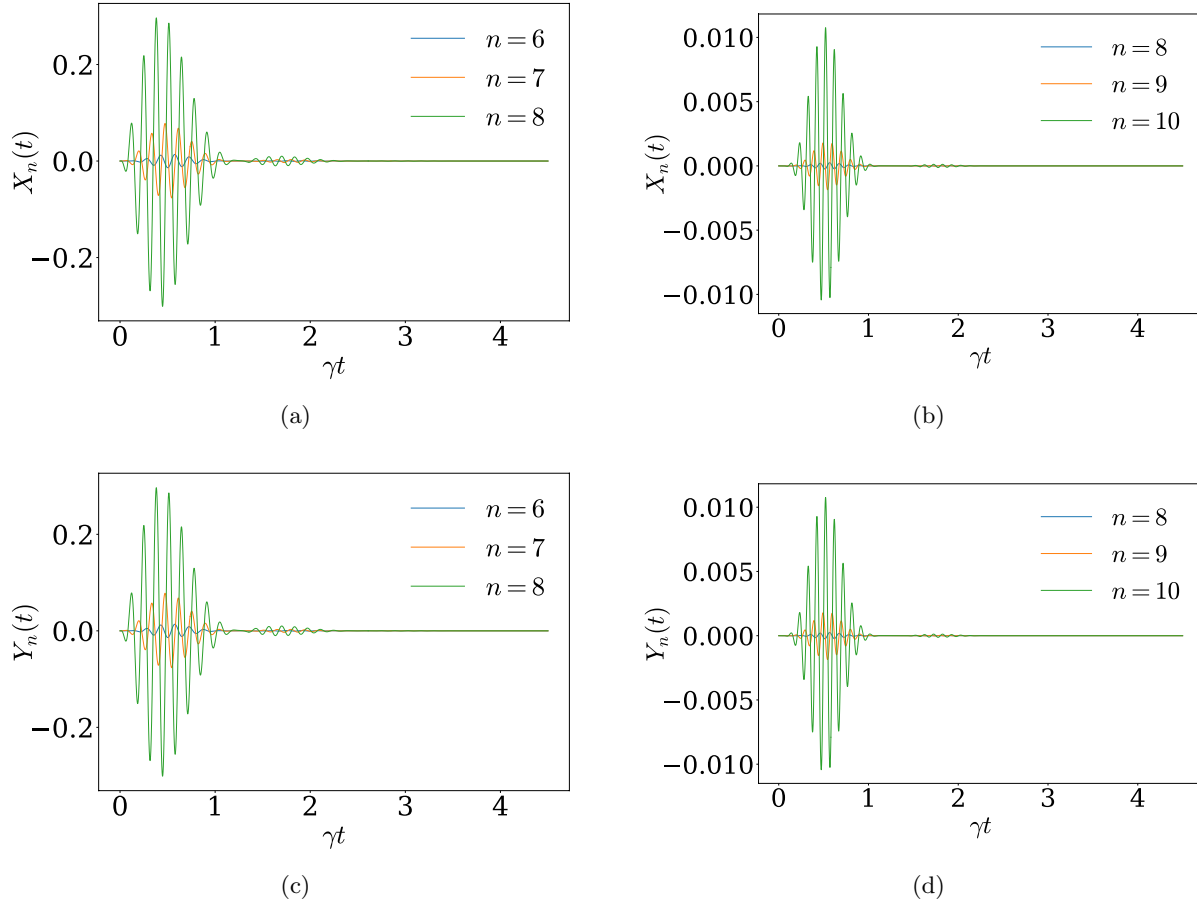


Figure 2: (Color online) The real part $X_n(t)$ (a-b) and the imaginary part $Y_n(t)$ (c-d) of the coherences are shown as a function of the dimensionless time γt for different initial Fock states (stated in the legend). The initial sites are $k = 10$ (a-c) and $k = 15$ (b-d). Other parameters are $\gamma = 0.1$, $g = 0.5$ and $\Delta = 1$.

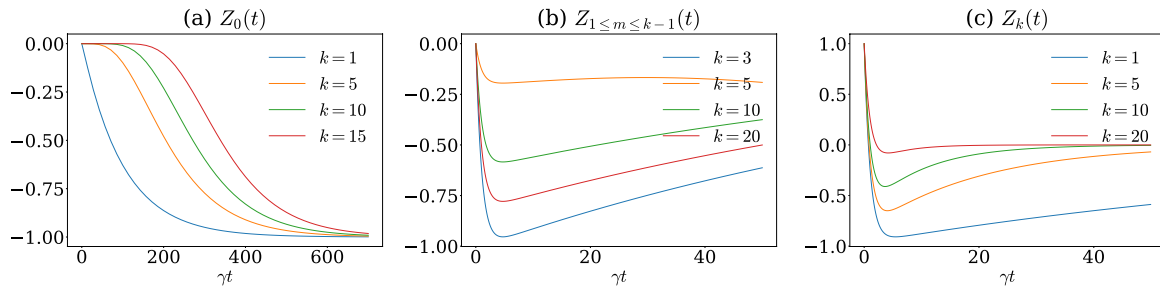


Figure 3: (Color online) The population inversion $Z_n(t)$ is shown as a function of dimensionless time γt for different initial sites k (stated in the legend). The figures correspond to (a) the population in the vacuum Fock state, (b) the population in the intermediate site and (c) the population in the initial site, respectively. Other parameters are $\gamma = 0.1$, $g = 0.1$ and $\Delta = 1$.

In the next step, we are going to derive the exact expression for the mean $\mu(t) = \langle P \rangle$ and the variance $\sigma^2(t) = \langle \langle P \rangle \rangle - \langle P \rangle^2$ of the position of the “walker”. Using the explicit solution for $P_n(t)$ (6), the expression for the variables $\langle P \rangle$ and σ^2 reads

$$\begin{aligned} \langle P \rangle(t) &= \sum_{n=0}^k n P_n(t, \xi)|_{\xi=1} & \sigma^2(t) &= \sum_{n=0}^k (n^2 P_n(t, \xi)|_{\xi=1} - \mu^2(t)) \\ &= k e^{-\alpha t} & &= k e^{-\alpha t} (1 - e^{-\alpha t}). \end{aligned} \quad (14)$$

It is clear that at asymptotic time $t \rightarrow \infty$ $\langle P \rangle, \langle \langle P \rangle \rangle \rightarrow 0$ due to the collapse to the vacuum state. With the help of equation (14), one can derive the velocity distribution V_μ and the velocity spread V_σ^2 (see equation (15)). In the transient regime, for sufficiently large times $t \gg 1$, but still satisfying $|\alpha t| < 1$, the position of the walker obey the central limit theorem with parameters given by

$$V_\mu = \frac{\langle P \rangle(t)}{t} \approx -k\alpha, \quad V_\sigma^2 = \frac{\sigma^2(t)}{t} \approx k\alpha. \quad (15)$$

4. Conclusion

In this contribution, we solved analytically the OQW master equation derived in [10] using generating functions. We use the obtained solution for arbitrary initial condition to construct the moments of this quantum walk explicitly. The exact solution allowed us to analyze the behavior of the observables of interest for various parameters. An interesting quantum feature (collapse-revival) was observed on the scaled time evolution of the real part and imaginary part of the coherences (see figure 2). This quantum feature provides direct evidence of the field quantization in the cavity. Furthermore, with the help of the analytical solution for the probability $P_n(t)$, the exact solution for the mean and the variance are derived and investigated for transient time.

Acknowledgements

This work is based upon research supported by the South African Research Chair Initiative, Grant No. 64812 of the Department of Science and Innovation and the National Research Foundation of the Republic of South Africa. AZ acknowledge support in part by the National Research Foundation of South Africa (Grant No. 129457).

References

- [1] S. Attal, F. Petruccione, C. Sabot, and I. Sinayskiy, 2012 *J. Stat. Phys.* **147**, 832.
- [2] S. Attal, F. Petruccione, and I. Sinayskiy, 2012 *Phys. Lett. A* **376**, 1545.
- [3] I. Sinayskiy and F. Petruccione, 2012 *Phys. Scr.* **T 151**, 014077.
- [4] H. Breuer and F. Petruccione, 2002 *The Theory of Open Quantum Systems* (Oxford University Press, Oxford).
- [5] K. Kraus, 1983 *States, Effects and Operations: Fundamental Notions of Quantum Theory* (Springer-Verlag, Berlin).
- [6] Y. Aharonov, L. Davidovich, and N. Zagury, 1993 *Phys. Rev. A* **48**, 1687.
- [7] J. Kempe, 2003 *Contemp. Phys.* **44**, 307.
- [8] S. E. Venegas-Andraca, 2012 *Quant. Inf. Proc.* **11**, 1015.
- [9] I. Sinayskiy and F. Petruccione, 2019 *Eur. Phys. J. Spec. Top.* **227**, 1869-1883.
- [10] I. Sinayskiy and F. Petruccione, 2014 *Int. J. Quantum Inform.* **12**, 1461010.
- [11] A. B. Klimov and S. M. Chumakov, 2009 *A Group-Theoretical Approach to Quantum Optics* (Wiley-VCH, Darmstadt).
- [12] I. Sinayskiy and F. Petruccione, 2015 *Phys. Rev. A* **92**, 0321205.
- [13] H. J. Carmichael, 2002 *Statistical Methods in Quantum Optics 1: Master Equations and Fokker-Planck Equations* (Springer, Berlin).
- [14] G. Lindblad, 1976 *Commun. Math. Phys.* **48**, 119-130.
- [15] V. Gorini, A. Kossakowski, and E. C. G. Sudarshan, 1976 *J. Math. Phys.* **17**, 821.
- [16] E. T. Jaynes and F. W. Cummings, 1963 *Proc. IEEE* **51**, 89.

GHZ state generation via projected squeezed states with dephasing

B Alexander and M Tame

Department of Physics, SU, Stellenbosch 7600, South Africa

E-mail: byron.alexander@alumni.uct.ac.za

Abstract. Emerging quantum technologies rely principally on quantum phenomena such as superposition and entanglement for their unique capabilities. To this end, it is essential to develop well-defined and efficient protocols to produce and further exercise control over states of quantum bits that exhibit desired quantum mechanical traits. From a pure separable multipartite state, a control sequence, which includes rotation, spin squeezing via one-axis twisting, quantum measurement and post-selection, generates a highly entangled multipartite state, which we refer to as a Projected Squeezed (*PS*) state. Through an optimization method, we then identify parameters required to maximize the overlap fidelity of the *PS* state with the maximally entangled Greenberger-Horne-Zeilinger (*GHZ*) state. This method leads to an appreciable decrease in state preparation time of N -qubit *GHZ* states when compared to preparation through unitary evolution only. The efficiency of the *PS* state protocol is studied in non-ideal experimentally relevant settings by employing numerical methods to simulate dephasing channels.

1. Introduction

Multipartite entangled quantum states play a central role in quantum information and related subareas. As such, there is already an established class of applications in quantum sensing [1], quantum computing [2], quantum communication [3], quantum cryptography [4] and quantum metrology [5]. This highlights the importance of the basic quantum control theoretic task, which seeks to establish well-defined methods for producing highly entangled multipartite states from initial pure separable states. In reference [6], we proposed such a protocol for producing highly entangled *GHZ*-type states which we denote as *Projected Squeezed* states (*PS* states). Using the protocol, we are able to produce *PS* states with *GHZ* overlap fidelity $\mathcal{F} > 0.99$. Essential steps in the protocol include spin-squeezing [7], which generates correlations between qubits, and quantum measurement (see equation (6) in reference [6]), which requires post-selection for obtaining the desired measurement outcome.

In reference [6], we considered the ideal case without decoherence, hence our computational modelling of the protocol was restricted to the symmetric subspace (known as the Dicke-basis [8]). This subspace is no longer suitable when including decoherence, since as a consequence of decoherence the state can in a sense migrate out of the subspace. Note that the dimension of the full Hilbert state space (computational basis) scales exponentially with qubit system size ($\sim 2^N$), while the dimension of the symmetric subspace spanned by the Dicke-basis has linear scaling ($\sim N + 1$). Due to the resultant increased computational complexity, only systems in the approximate range $N \leq 10$ are viable for modelling using standard computational resources.

In this work we consider a low system size example of $N = 4$ (as opposed to the original study [6] where we considered a larger spread of system size N). We now consider the efficacy and robustness of the protocol in experimentally relevant settings, by including decoherence using numerical methods [9]. Our focus will be on dephasing, since this has been the dominant form of decoherence [10] when utilizing trapped-ion systems for spin-squeezing (our proposed experimental setup) [11].

2. PS State Protocol

The N -qubit Greenberger-Horne-Zeilinger state (GHZ state) [12] reads as

$$|GHZ\rangle := \frac{|0\rangle^{\otimes N} + |1\rangle^{\otimes N}}{\sqrt{2}}. \quad (1)$$

Our protocol for producing highly entangled GHZ -type states can be summarised by the following sequential steps [6]:

Step 1: For an N -qubit multipartite system, we initialize to an all spin-up state

$$|\psi(0)\rangle = \underbrace{|\uparrow\rangle \otimes \cdots \otimes |\uparrow\rangle}_{N\text{-qubits}}. \quad (2)$$

Step 2: To form the coherent spin state $|CS\rangle$, we execute a $\pi/2$ -collective $\hat{J}_x := \frac{1}{2} \sum_{i=1}^N \hat{\sigma}_i^x$ rotation of the initial all-spin up state (2), i.e.,

$$|\psi(0)\rangle \mapsto \exp\left(-i\frac{\pi}{2}\hat{J}_x\right)|\psi(0)\rangle =: |CS\rangle, \quad (3)$$

where $\hat{\sigma}_i^x$ is the Pauli- \hat{x} spin operator acting on the i -th component of the state tensor product (see Figure 1(a)). In our analysis, we use the Husimi representation as it is more intuitive for visualizing symmetric states like the PS state (see Figure 1 and Figure 2). In principle, any phase space distribution could be used.

Step 3: The coherent spin state then undergoes spin-squeezing by the unitary operator

$$\hat{U}_{Sq}(\chi t) := \exp\left(-i\chi t \hat{J}_z^2\right), \quad (4)$$

where $\hat{J}_z := \frac{1}{2} \sum_{i=1}^N \hat{\sigma}_i^z$ and χt denotes the squeezing magnitude (see Figure 1(b)).

Step 4: The squeezed coherent spin state then undergoes a $-\pi/2$ -collective $\hat{J}_x := \frac{1}{2} \sum_{i=1}^N \hat{\sigma}_i^x$ rotation (see Figure 1(c)), i.e.,

$$\hat{U}_{Sq}(\chi t)|CS\rangle \mapsto \exp\left(i\frac{\pi}{2}\hat{J}_x\right)\hat{U}_{Sq}(\chi t)|CS\rangle. \quad (5)$$

Step 5: We now execute a Gaussian quantum measurement, characterized by Kraus operators, which reads as

$$\hat{A}_c := \sum_{m=0}^N \sqrt{\Pr(N-m|c)} \sum_{\{\underline{M}\}} \underbrace{|\uparrow \cdots \downarrow_{j_1} \cdots \downarrow_{j_m} \cdots \uparrow\rangle}_{N\text{-qubits}} \langle \uparrow \cdots \downarrow_{j_1} \cdots \downarrow_{j_m} \cdots \uparrow |, \quad (6)$$

where $(\sum_{\{\underline{M}\}} \cdot)$ denotes the summation over all binary permutations (of length N) with m -spin down qubits. A modification of the Kraus measurement operators described in the

original study (equation (6) in [6]) is required, since the PS state can, as a result of the dephasing channel (see equations (10)-(12) later on), migrate out of the symmetric subspace spanned by the Dicke basis. As such, the full Hilbert space should be considered. There is some level of freedom in choosing how to distribute the projector weightings, denoted $\sqrt{\text{Pr}(\cdot|c)}$, without compromising the required completeness condition of Kraus operators, i.e., $\int \hat{A}_c \hat{A}_c^\dagger dc = \mathbb{1}$ (see [13]). Equation (6) is a natural extension of the Kraus measurement operators (equation (6) in [6]) such that the completeness condition extends to the full Hilbert space. Additionally, we consider equation (6) as it produces favourable GHZ overlap fidelity values for $N = 4$, about measurement outcome $c = 0$. The projector weightings, in summation (6), are characterized by the Gaussian probability distribution

$$\text{Pr}(x|c) := \frac{1}{\sqrt{2\pi\sigma^2}} \exp \left[-\frac{(x-c)^2}{2\sigma^2} \right], \quad (7)$$

where $\{c\}_{c \in \mathbb{R}}$ denotes the set of measurement outcomes (with cardinality of the continuum). The post-measurement state is given by

$$\frac{\hat{A}_c \rho \hat{A}_c^\dagger}{\text{Tr}[\hat{A}_c^\dagger \hat{A}_c \rho]}, \quad (8)$$

for measurement outcome c , which occurs with probability $\text{Tr}[\hat{A}_c^\dagger \hat{A}_c \rho]$ [13]. Since the quantum measurement is a stochastic process, a chosen result is post-selected. The numerical models yield optimal results for the measurement outcome value $c = 0$ (for $N = 4$).

Step 6: Finally, in sequence, we execute collective \hat{J}_x and \hat{J}_y rotations (by $-\pi/7$ and $\pi/2$ respectively for $N = 4$), for the purposes of generating a PS state ρ_{PS} , which has a maximal GHZ overlap fidelity \mathcal{F} (see Figure 2). The overlap fidelity between the PS and GHZ state density operators is given by

$$\mathcal{F}(\rho_{PS}) := \left(\text{tr} \sqrt{\sqrt{\rho_{PS}} \rho_{GHZ} \sqrt{\rho_{PS}}} \right)^2, \quad (9)$$

where $\sqrt{\cdot}$ now denotes the matrix square root.

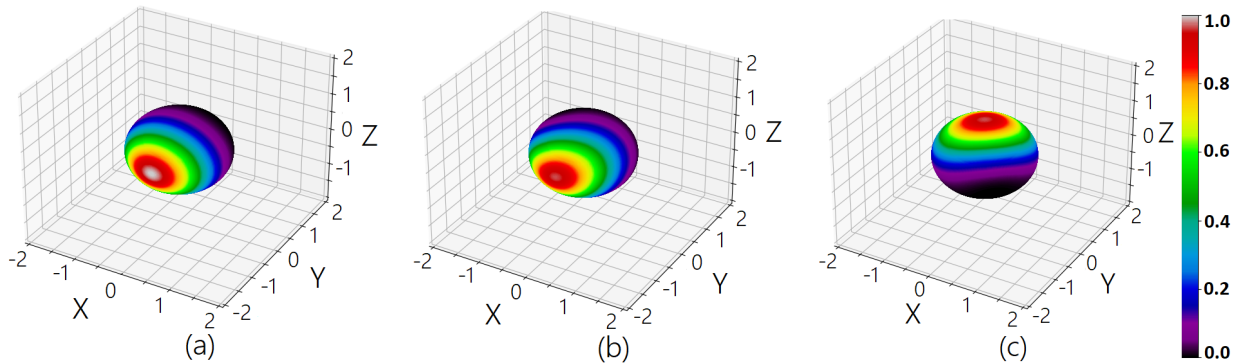


Figure 1. ($N = 4$) Husimi representations [17] (projections onto a rotated coherent spin state) of (a) step 2 - forming the $|CS\rangle$ state, (b) step 3 - spin squeezing by $\chi t = .15$, (c) step 4 - collective \hat{J}_x rotation by $-\frac{\pi}{2}$.

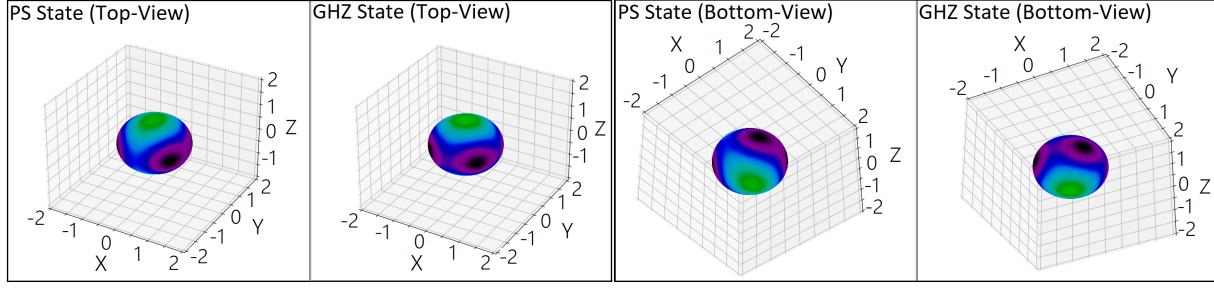


Figure 2. ($N = 4$) Husimi representations of the *PS* state vs the *GHZ* state.

As in [6], a numerical optimization method (random walk–Markov chain Monte Carlo type regime) is employed to find, respectively, the measurement operator variance $\sigma^2 > 0$ (see equation (7)) and squeezing magnitude $\chi t > 0$, which maximizes the overlap fidelity (denoted \mathcal{F}) of the *PS* state and *GHZ* state (1). For $N = 4$, we find that the optimal squeezing magnitude and operator measurement variance are respectively $\chi t = .15$ and $\sigma^2 = 1$.

3. Numerical Methods

To model the evolution of the density operator in the presence of decoherence, we utilize the (Kraus) operator sum formalism [9] given by

$$\rho(t + dt) = \sum_{\mu=0}^{\mathcal{M}} \hat{M}_{\mu}(dt) \rho(t) \hat{M}_{\mu}^{\dagger}(dt), \quad (10)$$

for infinitesimal time steps dt . For computational purposes, we approximate the infinitesimal increments dt with small finite increments hereafter denoted as Δt . The dephasing channels are characterized by the Kraus operators

$$\hat{M}_0 = \begin{pmatrix} \sqrt{1-p} & 0 \\ 0 & \sqrt{1-p} \end{pmatrix} \quad (11)$$

and

$$\hat{M}_1 = \begin{pmatrix} \sqrt{p} & 0 \\ 0 & -\sqrt{p} \end{pmatrix}, \quad (12)$$

with the decoherence rate given by $\Gamma := \frac{p}{\Delta t}$, for qubit decay probability p during time Δt .

The analysis which follows assumes negligible dephasing for non-squeezing steps of the protocol, whilst during the squeezing step, the dephasing operators, given by (11) and (12), act locally on each qubit. This is in line with envisioned experimental applications, utilizing ion-traps in particular [10, 11, 16]. In step 3, for finite time increments Δt , we interlace unitary squeezing $\hat{U}_{Sq}(\chi \Delta t)$ with dephasing characterized by equations (10)-(12), for varied qubit decay probability values $p = \Gamma \Delta t$. During the squeezing step, the total dephasing time for the *PS* and *GHZ* protocols, are respectively $n_{PS} \Delta t = .15/\chi$ and $n_{GHZ} \Delta t = \pi/2\chi$, where n_{PS} and n_{GHZ} are the number of $\chi \Delta t$ - squeezing increments (for our numerical methods we assume $\chi = 1$ and $\Delta t = 1e^{-3}$). Therefore, given decay probability p , the corresponding dephasing rate is

$$\Gamma = \frac{p \chi n_{PS}}{.15} = \frac{2p \chi n_{GHZ}}{\pi}. \quad (13)$$

As in reference [6], the measurement outcome $c \approx 0$ is post-selected (with operator variance $\sigma^2 = 1$) as it yields a state with distinct probability lobes on opposing sides of the multipartite Bloch sphere (see Figure 2); this is a characteristic feature of the maximally entangled *GHZ* state (1).

4. Dephasing Results

To study the efficacy of the *PS* state protocol with a given dephasing rate Γ , we compare it with *GHZ* state generation with $\pi/2$ -squeezing of the coherent spin state (this yields the state $\hat{U}_{Sq}(\pi/2)|CS\rangle$). This state is LU-equivalent (equivalent under local unitary operations) to the *GHZ* state (1). More specifically, a collective \hat{J}_x rotation by $\pi/2$, followed by a local phase gate (commonly denoted by $S := \begin{pmatrix} 1 & 0 \\ 0 & i \end{pmatrix}$) acting on the N -th qubit, yields the *GHZ* state (1). As such, the unitary $\pi/2$ -squeezing only version of the *GHZ* generation serves as a benchmark. We stress again the usefulness of the *PS* state protocol in that it requires a much shorter squeezing time compared to this benchmark, and therefore, in principle, should perform better in the presence of noise.

In Figure 3 and Figure 4, we respectively compare the quantum Fisher information (QFI) [14] (denoted by $\mathcal{Q}(\rho, \hat{A})$ for a chosen operator \hat{A}) with respect to the \hat{J}_z operator, and *GHZ* overlap fidelity \mathcal{F} , of the *PS* state protocol with the $\pi/2$ -squeezing only *GHZ* state generation protocol for varying dephasing rates Γ .

The QFI is studied because entanglement bounds known as the *Heisenberg* and *Shot-Noise* bounds, are respectively the maximum attainable QFI (for the collective operator \hat{J}_z), and a separable upper bound (the violation of which implies entanglement). The aforementioned Heisenberg upper bound is saturated for the *GHZ* state (hence simply labeled ‘*GHZ*’ in Figure 3). All states which violate the upper shot-noise bound are entangled [15].

As shown in Figure 3 and Figure 4, the *PS* state protocol obtains maximum QFI and *GHZ* overlap fidelity values for measurement result $c = 0$. From these figures, we can also observe the robustness of the protocol by noting the range of measurement outcomes for which it maintains an advantage over the *GHZ* protocol (in the presence of noise). Since the quantum measurement is a stochastic process, it is important to note that the post-selected results $B(c = 0, 1e^{-3})$ (where B denotes an open interval, more generally an open-ball, centered about measurement result $c = 0$) occur with probability $\approx 1/20$. This means that the improvement in preparation time is at the expense of the success probability of the protocol. Further work is needed to ascertain the trade-off between the overlap fidelity and preparation time of the *PS* state protocol and *GHZ* state squeezing only protocol.

Lastly, in Figure 4 the entanglement bound labelled ‘GME-Wit’ represents a sufficient condition (in terms of entanglement witnesses [15]) for genuine multipartite entanglement (GME). More specifically, the *GHZ* overlap fidelity $\mathcal{F} > 1/2$ implies GME.

5. Discussion

As shown in Figure 3 and Figure 4, there are experimentally relevant ranges of dephasing (see [16]), for which the reduced squeezing time of the *PS* protocol, allows the generation of states with significantly larger QFI and *GHZ*-overlap fidelity values \mathcal{F} than that generated by unitary $\pi/2$ -squeezing only (*GHZ* protocol). The trend suggests that the *PS* state maintains an advantage for increased dephasing beyond a given qubit decay rate (for example consider $p \in \{1e^{-3}, 1e^{-4}\}$).

For a larger system size N , the exponential increase in computational complexity can be suppressed by utilizing numerical methods, such as the quantum trajectory method [9]; together with computational schemes such as parallel computing. We leave the implementation of this for a future study.

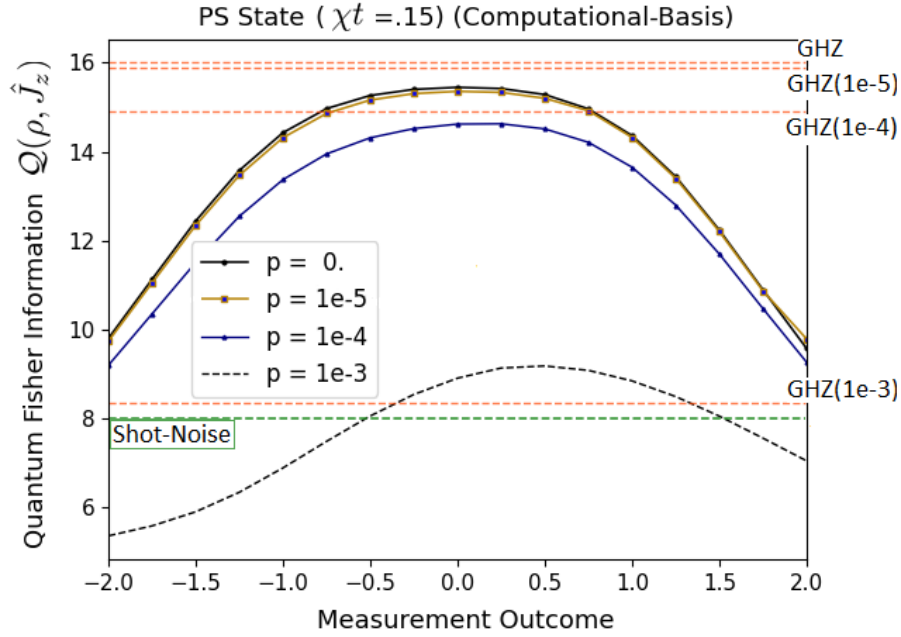


Figure 3. ($N = 4$) QFI of the *PS* State protocol vs the squeezing only *GHZ* protocol (for varied dephasing rate p); the latter is represented by dashed horizontal line plots (orange). The Shot-Noise upper bound (green) denotes the maximum QFI (with respect to \hat{J}_z) for separable N -qubit systems.

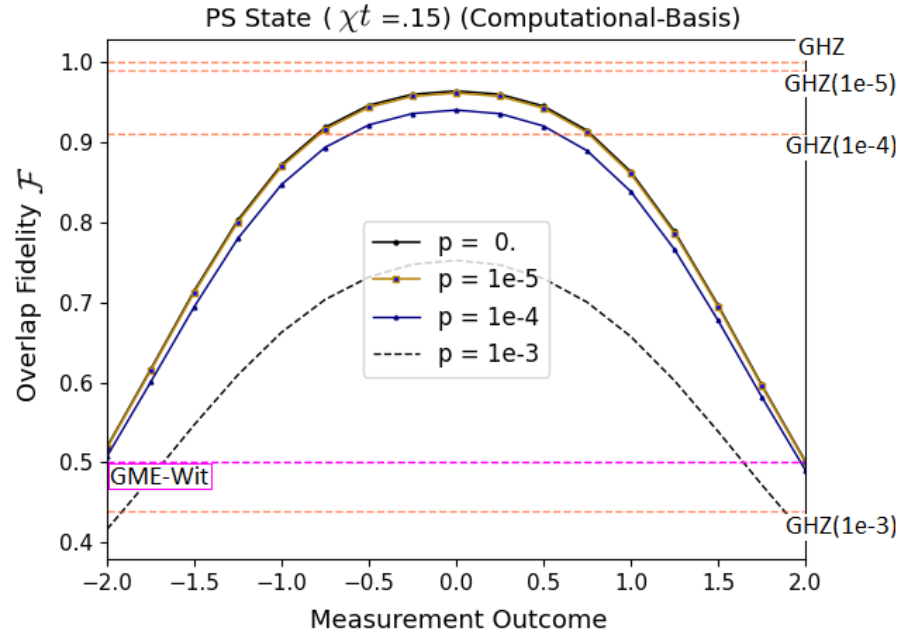


Figure 4. ($N = 4$) Overlap fidelity of the *PS* State protocol vs the squeezing only *GHZ* protocol (for varied dephasing rate p); the latter is represented by dashed horizontal line plots (orange). The GME-Wit lower bound (purple) denotes a sufficient condition for GME (with respect to the *GHZ* overlap fidelity \mathcal{F}).

Acknowledgments

We acknowledge the Council of Scientific and Industrial Research (CSIR) and the Department of Science and Technology for funding this project. Much appreciated collaborative support from the National Institute of Standards and Technology (NIST). A special note of thanks to Prof. Hermann Uys and Dr. John Bollinger for their guidance in developing the project at its inception.

References

- [1] Degen C L, Reinhard F and Cappellaro P 2017 *Rev. Mod. Phys.* **89** 035002
- [2] Gottesman D and Chuang I L 1999 *Nature* **402** 390-93
- [3] Hillery M, Bužek V and Berthiaume A 1999 *Phys. Rev. A* **59** 1829
- [4] Jennewein T, Simon C, Weihs G, Weinfurter H and Zeilinger A 2000 *Phys. Rev. Lett.* **84** 4729
- [5] Shettell N and Markham D 2020 *Phys. Rev. Lett.* **124** 110502
- [6] Alexander B, Bollinger J J and Uys H 2020 *Phys. Rev. A* **101** 062303
- [7] Kitagawa M and Ueda M 1993 *Phys. Rev. A* **47** 5138
- [8] Dicke R H 1954 *Phys. Rev.* **93** 99
- [9] Carlo G G, Benenti G, Casati G and Mejia-Monasterio C 2004 *Phys. Rev. A* **69** 062317
- [10] Foss-Feig M, Hazzard K R, Bollinger J J and Rey A M 2013 *Phys. Rev. A* **87** 042101
- [11] Uys H, Biercuk M, Britton J and Bollinger J J 2012 *AIP Conf. Proc.* **1469** pp 108-121
- [12] Greenberger D M, Horne M A and Zeilinger A 1989 vol 37, ed Kafatos M (Dordrecht: Springer) pp 69-72
- [13] Jacobs K 2014 *Quantum Measurement Theory and its Applications* (Cambridge University Press) p 24
- [14] Tóth G and Apellaniz I 2014 *J. Phys. A* **47** 424006
- [15] Tóth G and Gühne O 2005 *Phys. Rev. A* **72** 022340
- [16] Bohnet J G, Sawyer B C, Britton J W, Wall M L, Rey A M, Foss-Feig M and Bollinger J J 2016 *Science* **352** 1297-01
- [17] Husimi K 1940 *Proc. of the Physico-Mathematical Society of Japan 3rd Series* **22** pp 264-314

Investigating a New Approach to Quasinormal Modes: Physics-Informed Neural Networks

A M Ncube¹, G E Harmsen² and A S Cornell³

Department of Physics, University of Johannesburg, PO Box 524, Auckland Park 2006, South Africa.

E-mail: ¹ncubeanele4@gmail.com, ²gerhard.harmsen5@gmail.com, ³alanc76@gmail.com

Abstract. Physics-informed neural networks (PINNs) hold the potential for supplementing the existing set of techniques for solving differential equations that emerge in the study of black hole quasinormal modes. The present research investigated them by studying black hole perturbation equations with known analytical solutions and thus could be framed as inverse problems in PINNs. Our main goal was to test the accuracy of PINNs in computing unknown quasinormal frequencies within the differential equations. The black hole perturbation scenarios that we considered included near extremal Schwarzschild-de Sitter and Reissner-Nordström-de Sitter black holes, and a toy problem resembling them. For these cases, it was shown that PINNs could compute the QNFs with up to 4 digit decimal accuracy for the lowest multipole number, l , and lowest mode number, n .

1. Introduction

A black hole responds to test field perturbations by producing quasinormal modes (QNMs) that dissipate over time as the black hole returns to its initial state of equilibrium [1]. Similar to the well-known phenomenon of standing waves, these QNMs oscillate with a set of discrete resonant frequencies, known as quasinormal frequencies (QNFs), which are represented by complex-valued scalars. The real part is the physical oscillation frequency of the QNM and the imaginary part is proportional to its damping rate. Since these frequencies depend only on the physical parameters of their source, they are ideal for probing the characteristics of black holes [3, 2].

Mathematically, black hole QNMs are solutions to second-order differential equations describing the space-time evolution of perturbing fields in the vicinity of a black hole. Given that many of these equations are analytically intractable, several approximation techniques have arisen to solve them over the past decades. These methods have been outlined concisely in recent review articles such as Ref. [3] and include a modified form of the asymptotic iteration method [5] initiated by one of the authors of this proceeding.

This proceeding, however, is focused on investigating physics-informed neural networks (PINNs) to determine whether they could compute black hole QNMs. PINNs were recently introduced in the literature and are derived from traditional artificial neural networks. These machine learning algorithms are known for their capabilities as universal function approximators [6]. We have considered them in our study of black hole perturbation equations because of their capacity to solve differential equations. The key to their operation is the inclusion of physical constraints in the loss function, which are used to steer them towards accurate solutions. Note that PINNs have been shown to be more effective at solving inverse problems

than forward-modelling problems where they are currently surpassed by existing numerical mesh-based techniques [7]. Inverse problems are differential equations with unknown parameters that can be determined from observational data of the solution. On the other hand, forward problems are well-posed differential equations that require only the boundary and/or initial conditions of a given physics problem for the PINNs to solve them.

2. Perturbations of spherically symmetric black holes

To arrive at the differential equations of black hole perturbations, we begin by considering the space-times of spherically symmetric black holes given generally as [8]:

$$ds^2 = -f(r)dt^2 + f(r)^{-1}dr^2 + r^2(d\theta^2 + \sin^2\theta d\phi^2). \quad (1)$$

Here r is the radial distance from the centre of the black hole and $f(r)$ is a metric function which, for Schwarzschild-de Sitter (SdS) and Reissner-Nordström-de Sitter (RNdS) black holes is [8, 9]:

$$f(r) = 1 - \frac{2M}{r} + \frac{Q^2}{r^2} - \frac{\Lambda r^3}{3}, \quad (2)$$

where M and Q are the mass and electric charge of the black hole in geometrical units, and Λ is the cosmological constant. The SdS black hole has no electric charge; thus, the term Q in the metric function vanishes. For de-Sitter black holes, the cosmological constant is positive as these space-times have positive curvature as $r \rightarrow +\infty$.

Building on these black hole space-times, the perturbation equations for given perturbing fields are derived from the equations of motion of these fields. For example, the perturbation equation for an electromagnetic test field in the vicinity of a black hole is obtained from the source-free Gauss-Ampère law of Maxwell's equations [10, 11]:

$$F^{\mu\nu}{}_{;\nu} = \frac{1}{\sqrt{|g|}}\partial_\nu \left(\sqrt{|g|} F^{\mu\nu} \right) = 0. \quad (3)$$

Here $F^{\mu\nu}$ is the electromagnetic field tensor and $|g|$ is the determinant of the metric tensor of the curved space-time around the black hole. When we consider metric tensors of spherically symmetric black holes, the equations of motion for perturbing fields simplify to “Schrödinger-like” black hole perturbation equations given generally as [8]:

$$\frac{d^2\psi(r)}{dx^2} + (\omega^2 - V(r))\psi(r) = 0, \quad (4)$$

where x is the “tortoise” coordinate that is related to r by the relation: $dr/dx = f(r)$ [3]. The black hole effective potential, $V(r)$, for massless scalar perturbations of SdS and RNdS black holes is given as [5, 9]:

$$V(r) = f \left[\frac{l(l+1)}{r^2} + \left(\frac{2M}{r^3} - \frac{2Q^2}{r^4} - \frac{2\Lambda}{3} \right) \right], \quad (5)$$

where l is the multipole number and $Q = 0$ for a SdS black hole. When black hole QNMs have negative temporal dependence they satisfy the boundary conditions given by $\psi(x) \sim \exp(\pm i\omega x)$ as $x \rightarrow \pm\infty$. Physically, this implies that the QNMs can only radiate inward at the horizon and outward at spatial infinity [12, 13] at a time $t > 0$.

Due to the nature of the effective potential $V(r)$, equation (4) is generally difficult to solve analytically except for some special cases such as those considered here for simplicity. These space-times are the SdS and RNdS black holes in the near extremal limit where the cosmological horizons of the space-times are very close (in the r coordinate) to their event horizons.

Ref. [9] demonstrated that for any de-Sitter black hole space-time in the near extremal limit, the metric function $f(r)$ can be written as:

$$f(r(x)) = \frac{(r_2 - r_1)\kappa_1}{2\cosh^2\kappa_1 x} + \mathcal{O}(\delta^3), \quad (6)$$

where $\delta = (r_2 - r_1)/r_1$, κ_1 is the surface gravity at the horizon, r_1 and r_2 are two consecutive positive roots of $f(r)$, and x is the tortoise coordinate whose domain lies within (r_1, r_2) . For both the SdS and RNdS, r_1 and r_2 are the event and cosmological horizons, respectively, with $r_2 > r_1$. Consequently, in the near extremal limit the two black holes share the same mathematical expression for the metric function, which in turn results in a single expression for the effective potential valid for both SdS and RNdS black holes [8, 9]:

$$V(x) = \frac{V_0}{\cosh^2(\kappa_b x)}. \quad (7)$$

Here $V_0 = \kappa_b^2 l(l+1)$ for massless scalar perturbations and κ_b is the surface gravity associated with the black hole horizon. With the effective potential in this form, the black hole perturbation equations yield analytic solutions.

In the case of massless scalar perturbations of SdS and RNdS black holes, the exact analytic expressions for the QNMs (denoted by $\psi(x)$) and QNFs (denoted by ω) are, respectively [8, 9, 14]:

$$\psi(x) = [\xi(\xi - 1)]^{i\omega/2\kappa_b} \cdot {}_2F_1\left(1 + \beta + i\frac{\omega}{\kappa_b}, -\beta + i\frac{\omega}{\kappa_b}; 1 + i\frac{\omega}{\kappa_b}; \xi\right), \quad (8)$$

$$\frac{\omega}{\kappa_b} = \sqrt{\left(l(l+1) - \frac{1}{4}\right) - i\left(n + \frac{1}{2}\right)}, \quad n = 0, 1, 2, \dots \quad (9)$$

where $\xi^{-1} = 1 + \exp(-2\kappa_b x)$ and $\beta = -1/2 + (1/4 - V_0/\kappa_b^2)^{1/2}$.

With these exact solutions, a dataset was generated to provide “observational biases” [7] for training the PINNs to solve the perturbation equations given as inverse problems.

Another problem similar to the perturbations of SdS and RNdS black holes, which was discussed in Ref. [5], involves a simpler form of the inverted Pöschl-Teller potential given as:

$$V(x) = \frac{1}{2\cosh^2(x)}. \quad (10)$$

The aforementioned boundary conditions of black hole QNMs are also satisfied by the QNMs of this problem. In this case, the exact form of the QNMs, obtained in Ref. [15] using quasi-exactly solvable theory, are:

$$\psi(x) = (\cosh(x))^{(i+1)/2} \chi_n(\sinh(x)), \quad (11)$$

$$\omega_n = \pm \frac{1}{2} - i\left(n + \frac{1}{2}\right), \quad (12)$$

where χ_n is a polynomial of degree n in $\sinh(x)$. This problem and the previously mentioned one pertaining to near extremal SdS and RNdS black holes were used to test the accuracy of PINNs in computing QNFs.

3. Computing QNMs with PINNs

The PINN algorithm, and the steps taken to implement it on black hole perturbation equations, have two components [7]:

- (i) A physics-uninformed artificial neural network of a particular architecture, such as a feed-forward neural network (FNN). It represents the neural network solution to the differential equation (figure 1 (left)).
- (ii) A *loss-function* that measures the deviation of the neural network solution from the physical constraints of the problem (figure 1 (right)). During the training phase, these constraints force the PINN solution to satisfy the boundary and initial conditions of the problem in addition to a labelled training dataset. At the same time, the neural network is forced to minimise a residual associated with the differential equation.

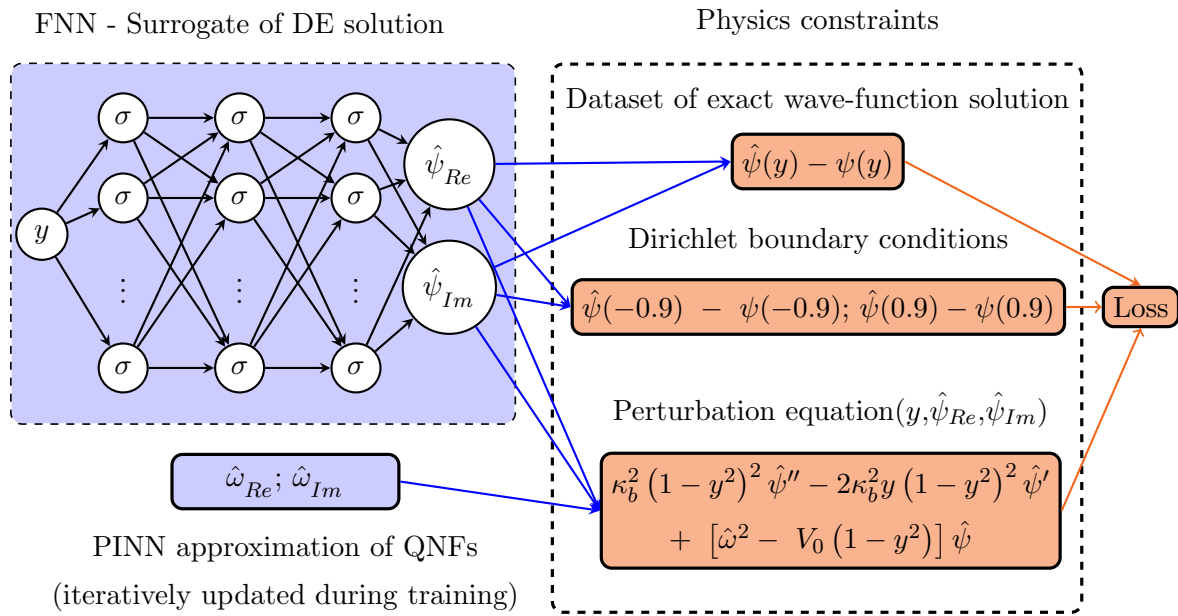


Figure 1. A schematic of the PINN set-up that was built to solve the perturbation equation with the effective potential given by an inverted Pöschl-Teller potential.

The algorithm for building PINN models is outlined in figure 2. Initially, the physics equations governing the problem are all defined and included as arguments for `deepxde.data.PDE(...)`. The neural network part is set up by defining the specific neural network architecture, the number of hidden layers, nodes per layer and the non-linear activation function used in the nodes. The PINN model is the sum of the neural network (denoted by `net` in figure 2) and the physical constraints (denoted by `data` in figure 2) set as arguments for `deepxde.Model`. The parameters for training, such as the specific choice for the optimiser, are set up using the function `Model.Compile(...)`. Thereafter, the PINN model can be run for a specified number of training epochs using the command `Model.Train(...)`.

The same steps were followed in customising PINNs to solve our inverse problem involving massless scalar perturbations of SdS and RNdS black holes with an inverted Pöschl-Teller potential. Since the domain of the problem in the original form is infinite, a new co-ordinate, $y = \tanh(x)$, was used to give a finite domain $(-1,1)$ which is easier to implement in code.

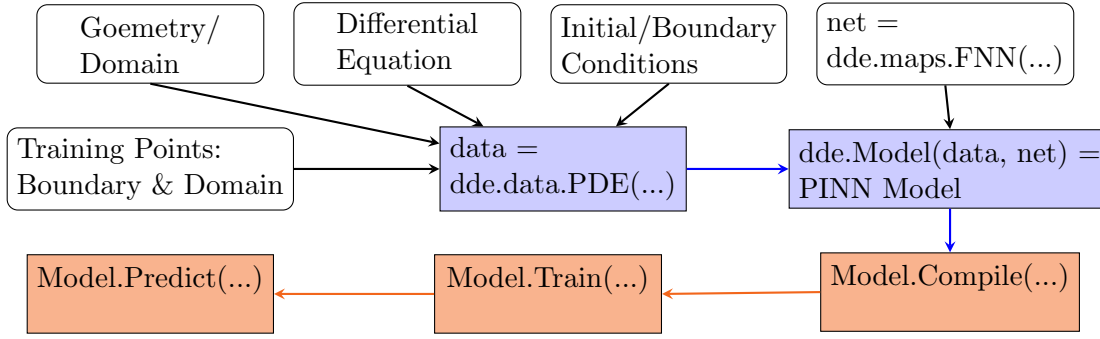


Figure 2. The PINN algorithm in DeepXDE [16].

Consequently, the QNM boundary conditions become $\psi(y) = (1 \mp y)^{-i\omega/2}$, as $y \rightarrow \pm 1$. Thus, in terms of y , the perturbation equations for the near extremal SdS and RNdS black holes are:

$$\kappa_b^2(1-y^2)^2 \cdot \frac{d^2\psi(y)}{dy^2} - 2\kappa_b^2 y(1-y^2) \cdot \frac{d\psi(y)}{dy} + [\omega^2 - V_0(1-y^2)] \psi(y) = 0. \quad (13)$$

This equation takes the same form in the case of the problem with an effective potential given by equation (10), except that $\kappa_b = 1$ and $V_0 = 1/2$. For easier implementation within the DeepXDE package the equations were split into real and imaginary parts. Figure 1 illustrates the PINN that was used to solve the perturbation equations.

The training hyperparameters used in all our computations were the following: FNN with 3 hidden layers, 20 nodes per layer; *tanh* as a non-linear activation function; Adam optimiser, which is a standard optimisation method in neural networks [17]; 20 000 training epochs; training data consisting of 100 domain points, and a dataset with 50 uniformly distributed true values of the QNMs ($\psi(y)$) in the “spatial” domain $[-0.9, 0.9]$.

4. Results

The results for the first inverse problem with the SdS and RNdS black holes, and the second inverse problem with an inverted Pöschl-Teller potential given by equation (10) are listed in tables 1 and 2, respectively. To measure the accuracy of the PINN approximations, we used the L2 relative as a metric [16]. For the SdS and RNdS cases, we obtained at most 4 digit decimal accuracy with errors increasing with higher values of l . As seen in table 2, the accuracy of the PINN model for the other problem decreased with higher values of n .

Table 1. PINN approximations of the QNFs (in geometrical units) for massless scalar perturbations of SdS and RNdS black holes.

n	l	PINN approximation		Exact [8, 9]		L_2 relative error
		ω_{Re}/κ_b	ω_{Im}/κ_b	ω_{Re}/κ_b	ω_{Im}/κ_b	
0	1	1.32287	-0.49997	1.32288	-0.50000	0.00214%
	2	2.39790	-0.50002	2.39792	-0.50000	0.00106%
	3	3.42761	-0.50032	3.42783	-0.50000	0.01105%
	4	4.44096	-4.98165	4.44410	-0.50000	0.08128%
	5	5.43513	-0.50716	5.45436	-0.50000	0.37463%

Table 2. PINN approximations of the QNFs (in geometrical units) for the “Schrödinger-like” equation with the simple effective potential given by equation (10).

n	PINN approximation		Exact [5, 15]		L_2 relative error
	ω_{Re}	ω_{Im}	ω_{Re}	ω_{Im}	
0	0.49984	-0.50002	0.50000	-0.50000	0.02270%
1	0.49961	-1.49877	0.50000	-1.50000	0.08174%
2	0.49807	-2.49714	0.50000	-2.50000	0.13540%
3	5.01544	-3.53140	0.50000	-3.50000	0.88922%

5. Conclusion

This proceeding has investigated the accuracy of PINNs in solving perturbation equations with effective potentials expressed in the form of inverted Pöschl-Teller potentials. This work was preliminary to the larger goal of our project, which is to implement PINNs for differential equations of more general black hole perturbation scenarios. So far, our results indicate that PINNs can accurately compute QNFs, for a readily implementable set of hyperparameters. Further work on more general space-times will entail fine-tuning our choice of hyperparameters using a grid-search algorithm similar to the technique employed in Ref. [18]. Increasing the performance of our PINN models may ultimately require us overcoming the spectral bias that is inherent in fully connected neural networks, an attribute that renders them less accurate for higher frequency solution functions [19].

Acknowledgments

AMN is supported by the Faculty of Science at the University of Johannesburg. GEH was supported by the GES, and ASC is partially supported by the National Research Foundation South Africa.

References

- [1] Dey S and Chakrabarti S 2019 *Eur. Phys. J. C* **79** 504.
- [2] Iyer S and Will C M 1987 *Phys. Rev. D* **35** 3621.
- [3] Konoplya R A and Zhidenko A 2011 *Rev. Mod. Phys.* **83** 793.
- [4] Chandrasekhar S and Detweiler S 1975 *Proc. Roy. Soc. Lond. A* **344** 441.
- [5] Cho H T, Cornell A S, Doukas J, Huang T R and Naylor W 2012 *Adv. Math. Phys.* **2012** 281705.
- [6] Raissi M, Perdikaris P and Karniadakis G E 2019 *J. Comput. Phys.* **378** 686.
- [7] Karniadakis G, Kevrekidis Y, Lu L, Perdikaris P, Wang S and Yang L 2021 *Nat. Rev. Phys.* **3** 422.
- [8] Cardoso V and Lemos J P S 2003 *Phys. Rev. D* **67** 084020.
- [9] Molina C 2003 *Phys. Rev. D* **68** 064007.
- [10] d’Inverno R A 1992 *Introducing Einstein’s Relativity* (Oxford: Clarendon Press) p 159.
- [11] Carroll S M 2004 *Spacetime and Geometry*, ed A Black and N Benton (San Francisco: Addison-Wesley).
- [12] Leaver E W 1985 *Proc. Roy. Soc. Lond. A* **402** 285.
- [13] Stein L C 2019 *J. Open Source Softw.* **4** no. 42 1683.
- [14] Ferrari V and Mashhoon B 1984 *Phys. Rev. D* **30** 295.
- [15] Cho H and Ho C 2007 *J. Phys. A* **40** 1325.
- [16] Lu L, Meng X, Mao Z and Karniadakis G E 2021 *J. Soc. Ind. Appl. Math.* **63** 208.
- [17] Kingma D P and Ba J 2015 *3rd Int. Conf. on Learning Representations (San Diego)* ed Y Bengio and Y LeCun.
- [18] Kadeethum T, Jørgensen T M and Nick H M 2020 *PLoS ONE* **15** 1932.
- [19] Wang S, Yu X and Perdikaris P 2020 *Preprint* arXiv:2007.14527.

Random number generation using IBM quantum processors

C Strydom and M S Tame

Department of Physics, SU, Matieland 7602, RSA

E-mail: conradstryd@gmail.com

Abstract. Random numbers are used extensively in both cryptography and simulation, but are difficult to generate reliably using classical methods. We investigate random number generation on the *ibmq_16_melbourne* quantum processor, a 15-qubit superconducting quantum computer. By applying simple post-processing techniques to the random bits generated, we were able to extract a sample of random bits which passed the NIST Statistical Test Suite. This shows that, with some post-processing, solid-state quantum computers such as IBM quantum processors can be used to generate random numbers of sufficient quality for cryptographic applications.

1. Introduction

Random numbers are used extensively in cryptography, the simulation of economic, traffic and agricultural models, as well as coordination in computer networks [1]. True random numbers are hard to generate using classical methods, as the unpredictability relies on an incomplete knowledge of a system, which can introduce ordered features. On the other hand, the inherent randomness central to quantum mechanics makes quantum systems ideal for generating true random numbers. A number of quantum random number generation schemes have been realised experimentally over the past two decades, many of which rely heavily on photonics [2, 3, 4, 5, 6]. Several photonic integrated circuits [7, 8, 9], as well as implementations on superconducting systems [10], have also recently been demonstrated.

In this paper, we further investigate random number generation on superconducting quantum computers. To this end, we generated a sample of random bits using the *ibmq_16_melbourne* quantum processor. Just as previous samples generated using IBM quantum processors [10], our sample showed a small bias towards zero. However, once we removed the bias by employing the von Neumann scheme [11, 12], the processed bits passed all 15 NIST tests [13], allowing us to show the successful generation of high quality randomness. The bits of Ref. [10] did not pass any NIST tests due to a lack of post-processing. After completion of the study, we were made aware that IBM recently released their own quantum random number generator with post-processing available via the University of Cambridge, which has also passed the NIST Statistical Test Suite.

2. Implementation

Bits of a classical computer can take only two values, namely 0 or 1. In contrast, qubits of a quantum computer can be prepared in either of two computational basis states, namely $|0\rangle$ or $|1\rangle$, or in any linear combination or superposition of these states. A random bit can be

generated using a qubit, by first applying a Hadamard to the qubit and then measuring it in the computational basis. Since all qubits are initialised in the state $|0\rangle$ on IBM processors, applying a Hadamard to a qubit prepares the qubit in the state $|+\rangle = (|0\rangle + |1\rangle)/\sqrt{2}$. The state $|+\rangle$ has the property that measurements in the computational basis result in $|0\rangle$ with probability $\frac{1}{2}$ and in $|1\rangle$ with probability $\frac{1}{2}$. Thus, in the absence of noise, computational basis measurements generate uniformly distributed random bits.

The *ibmq_16_melbourne* quantum processor is a 15-qubit superconducting quantum computer and used to be accessible via the IBM cloud service [14], but has recently been decommissioned. By executing a circuit with Hadamards applied to all 15 qubits and computational basis measurements on all 15 qubits 200 times on the *ibmq_16_melbourne* quantum processor, with 8000 shots each, we were able to generate a sample of 24 million random bits. In what follows, we will refer to this sample of 24 million bits as the raw sample.

3. Results

3.1. Quality analysis

To determine if the raw sample has the expected properties of a true random bit sequence, we applied a number of standard tests [2, 3]. What follows is a brief description of each test as well as the results obtained for the raw sample.

In a true random bit sequence, the bits should be uncorrelated. To detect short-ranged correlations and periodicity in the raw sample, we calculate the Pearson correlation coefficient [15] of the full bit sequence with 1-bit to 40-bit delays of the sequence. The results are shown in figure 1.

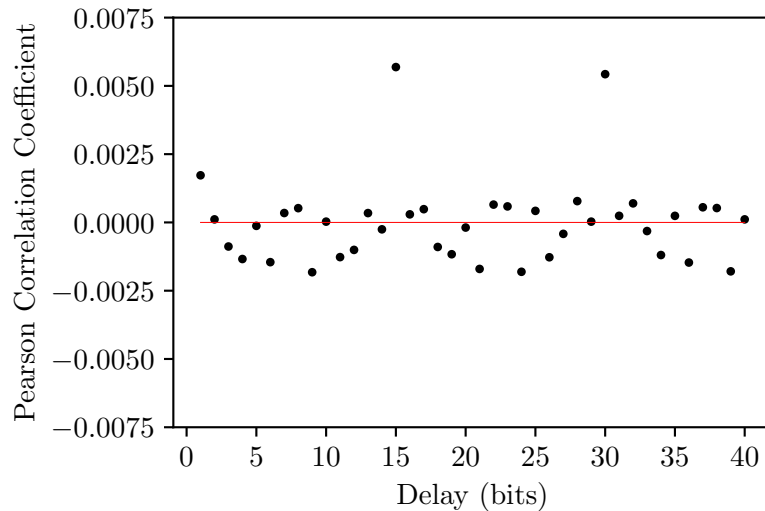


Figure 1. Pearson correlation coefficient of the full bit sequence of the raw sample (blue dots) and a true random sample (red line) with 1-bit to 40-bit delays of the sequence.

The Pearson correlation coefficient ranges from -1 to 1, where -1 implies perfect anti-correlation, 0 implies no correlation and 1 implies perfect correlation. Thus the results indicate that the bits in the raw sample are mostly uncorrelated, with small correlations present between bits at 15-bit intervals. This is likely because these bits were generated by the same qubit in the *ibmq_16_melbourne* quantum processor. Since each qubit has a unique error rate, bits generated by the same qubit show larger correlations than bits generated by different qubits.

All possible n -bit combinations should occur with equal probability in a true random bit sequence. We first consider single bits, for which we expect to find an approximately equal proportion of zeros and ones in a large enough sample. In the raw sample, the relative frequency of zeros and ones is 0.5262 and 0.4738 respectively. Hence the data shows a bias towards zero. As a result of decoherence of the qubits and errors that occur when gates are applied and

measurements are made, the two different computational basis measurement outcomes do not occur with a probability of exactly $\frac{1}{2}$ each. To investigate 8-bit blocks, we convert each 8-bit block in the bit sequence to an unsigned integer in the range $[0, 255]$. For a true random bit sequence, these integers should be uniformly distributed over the interval $[0, 255]$ and they should have an average of 127.5. Figure 2 shows the distribution of integers for the raw sample and their average is 120.87. The small average can be attributed to the bias towards zero.

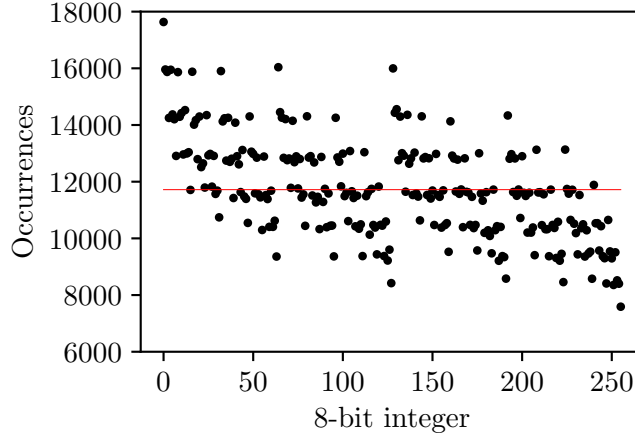


Figure 2. Distribution of integers for the raw sample (blue dots) and a true random sample (red line).

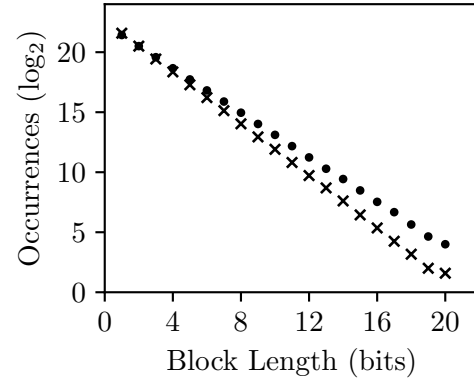


Figure 3. Run length distributions for zeros (blue dots) and ones (blue crosses) for the raw sample.

A run in a sequence of bits is a block of consecutive zeros or ones. In a true random bit sequence, a n -bit run of zeros or ones should occur with probability 2^{-n} , since zeros and ones each occur with probability $\frac{1}{2}$. The run length distributions for zeros and ones for the raw sample are shown in figure 3. The gradient of the best fit line is (-0.925 ± 0.002) and (-1.076 ± 0.005) for runs of zeros and ones respectively. For a true random bit sequence, we should have a gradient of $-\log_2(2) = -1$ for both zeros and ones. The deviations in the data can be explained as follows — since the zeros occur with a higher frequency than ones, runs of zero occur with a higher frequency than runs of one of the same length.

Entropy quantifies irregularity or randomness. The Shannon entropy is defined as

$$H = - \sum_i p_i \log_2 p_i \quad (1)$$

where $i \in \{0, 1\}^n$ is an n -bit string and p_i is the probability of obtaining i . The Shannon entropy should be n bits for a true random source of n -bit strings. The Shannon entropy for 8-bit strings in the raw sample is 7.98403 bits. This was calculated using relative frequencies obtained from the distribution in figure 2. The entropy is slightly smaller than for a perfectly random source as a result of order introduced by the bias towards zero and the 15-bit interval correlations.

Finally, we test the raw sample on a practical problem in simulation — estimating the value of π using a Monte Carlo method. Since the area of a circle of radius r divided by the area of a square of side length $2r$ is $\frac{\pi}{4}$, the value of π can be estimated by randomly placing points in a square of side length r which contains a quarter-circle of radius r . An estimate for π is calculated by dividing the number of points inside the quarter-circle by the total number of points used and multiplying by 4. Considering $r = 255$, and obtaining random positions for points using the unsigned integers extracted from the raw sample when investigating the distribution of 8-bit blocks, we obtain an estimate of 3.282 for π . This is larger than the true value of π , because the bias towards zero results in a larger proportion of points being placed inside the quarter-circle than for randomly placed points.

3.2. Post-processing

The quality analysis of the raw sample shows that the bias towards zero greatly reduces its quality. We therefore employ the von Neumann scheme [11, 12] to remove the bias and improve the quality. Given a biased sample of independent bits (say, in which 0 occurs with probability p and 1 occurs with probability q , where $p \neq q$), the von Neumann algorithm yields an unbiased sample of random bits. Provided that the bits are independent, the pairs 01 and 10 both occur with a probability pq in the biased sample and can thus be used as an unbiased source of random bits. Hence an unbiased sample is obtained from the biased sample by replacing occurrences of 01 by 0, occurrences of 10 by 1 and removing occurrences of 00 and 11. Applying the von Neumann algorithm reduces the size of the sample by a fraction pq of its original length. However, this large reduction can be avoided by applying the recursive von Neumann algorithm [12]. Instead of simply removing occurrences of 00 and 11, they are used to generate additional biased bit sequences, to which the von Neumann algorithm is then applied. This is repeated recursively, each time appending the output to the previous. The number of unbiased bits produced by the recursive von Neumann algorithm is arbitrarily close to the entropy bound [12], and so the algorithm is optimal in terms of output size.

Although some non-negligible correlations are present between bits in the raw sample, it is clear from figure 1 that these are generally small enough so that the bits can be considered independent and the von Neumann scheme can be applied. Applying the recursive von Neumann algorithm to the raw sample, we obtain a debiased sample of 23,795,395 bits. We applied the same five standard tests to this debiased sample. The Pearson correlation coefficients are much smaller for the debiased sample, as shown in figure 4, indicating that the 15-bit interval correlations have been removed by the rearrangement of bits which occurred when applying the recursive von Neumann algorithm.

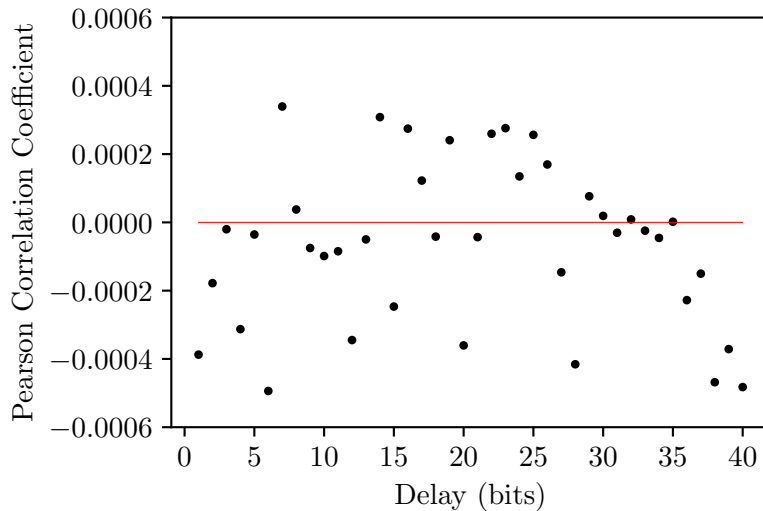


Figure 4. Pearson correlation coefficient of the full bit sequence of the debiased sample (blue dots) and a true random sample (red line) with 1-bit to 40-bit delays of the sequence.

The relative frequency of zeros and ones in the debiased sample is 0.5001 and 0.4999 respectively, which shows that the bias towards zero has indeed been removed. The distribution of integers is much closer to a uniform distribution, as can be seen in figure 5, and their average is 127.46 reflecting the removal of bias. The run length distributions for zeros and ones for the debiased sample are shown in figure 6 and also reflect the removal of bias. The gradient of the best fit line is (-1.004 ± 0.008) and (-1.007 ± 0.005) for runs of zeros and ones respectively, both of which are closer to the expected result for a true random bit sequence. Furthermore, we find that the Shannon entropy for 8-bit strings is 7.99994 bits and obtain 3.134 for an estimate of π , both of which show improvement in the quality of the random bits.

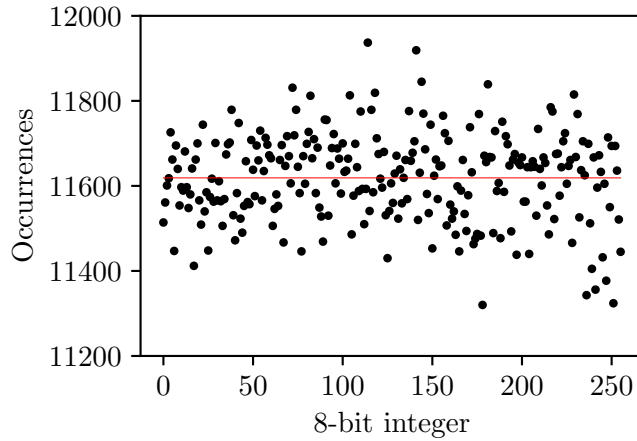


Figure 5. Distribution of integers for the debiased sample (blue dots) and a true random sample (red line).

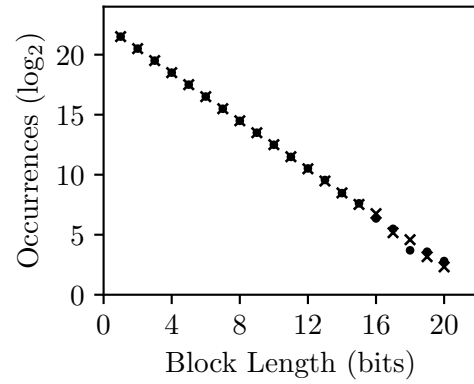


Figure 6. Run length distributions for zeros (blue dots) and ones (blue crosses) for the debiased sample.

Table 1. Summary of NIST test results for the debiased sample. A sequence passes a test if the p-value (the probability that a true random number generator would generate the given bit sequence or a less random bit sequence) is greater than 0.01. ‘Required’ is the required number of sequences which must pass a test for the sample to pass and ‘Proportion’ is the number of sequences which passed. The p-values quoted in the final column arise via applying a χ^2 test to the p-values obtained for the individual sequences and can be used to assess their uniformity. When a test consists of more than 5 separate tests (indicated with *) averages were taken.

Statistical Test	Required	Proportion	p-value
Frequency	230	234	0.231016
Block Frequency	230	234	0.735559
Cumulative Sums 1	230	233	0.236279
Cumulative Sums 2	230	232	0.043540
Runs	230	236	0.158711
Longest Run of Ones	230	235	0.247079
Binary Matrix Rank	230	234	0.547343
Discrete Fourier Transform	230	233	0.609979
Non-overlapping Template*	230	234.36	0.420221
Overlapping Template	21	22	0.392456
Universal Statistical	21	23	0.788728
Approximate Entropy	230	236	0.565084
Random Excursions*	10	12	0.358879
Random Excursions Variant*	10	11.89	0.344683
Serial 1	21	23	0.105618
Serial 2	21	23	0.484646
Linear Complexity	21	23	0.105618

3.3. NIST Statistical Test Suite

For a more stringent test of the quality, we applied the NIST Statistical Test Suite [13] to the debiased sample. This is an industry standard test suite for random number generators, aimed

at assessing their suitability for use in cryptographic applications. The debiased sample passed all 15 NIST tests at the required 1% significance level. The results are presented in table 1. The Overlapping Template, Universal Statistical, Random Excursions, Random Excursions Variant, Serial and Linear Complexity tests were run with 23 sequences, each consisting of one million bits. The other tests were run with 237 sequences, each consisting of one hundred thousand bits. The block length was adjusted to 1128 and 1000 in the Block Frequency and Linear Complexity tests respectively. Default values were used for the block length in the other tests.

The NIST test results for the debiased sample clearly demonstrate the importance of post-processing, since previous implementations on superconducting systems, in which no post-processing was done, did not pass any NIST tests [10]. Photonic quantum random number generators also generally require post-processing to pass the NIST Statistical Test Suite [1, 2, 9].

4. Conclusion

We generated a sample of 24 million bits using the *ibmq_16_melbourne* quantum processor. This raw sample showed a small bias towards zero, which was removed by applying the recursive van Neumann algorithm [12]. The resulting debiased sample passed the NIST Statistical Test Suite [13]. We therefore conclude that, with post-processing, solid-state quantum computers such as IBM quantum processors can be used to generate random numbers of sufficient quality for cryptographic applications.

Acknowledgments

We acknowledge the use of IBM Quantum services for this work. The views expressed are those of the authors, and do not reflect the official policy or position of IBM or the IBM Quantum team. We thank Taariq Surtee and Barry Dwolatzky at the University of Witwatersrand and Ismail Akhalwaya at IBM Research Africa for access to the IBM processors through the Q Network and Africa Research Universities Alliance. This research was supported by the South African National Research Foundation, the University of Stellenbosch, and the South African Research Chair Initiative of the Department of Science and Technology and National Research Foundation.

References

- [1] Herrero-Collantes M and Garcia-Escartin J C 2017 *Rev. Mod. Phys.* **89** 015004
- [2] Francis J T, Zhang X, Özdemir S K and Tame M S 2017 *Quantum Sci. Technol.* **2** 035004
- [3] Jennewein T, Achleitner U, Weils G, Weinfurter H and Zeilinger A 2000 *Rev. Sci. Instrum.* **71** 1675
- [4] Nie Y Q, Zhang H F, Zhang Z, Wang J, Ma X, Zhang J and Pan J W 2014 *Appl. Phys. Lett.* **104** 051110
- [5] Nie Y Q, Huang L, Liu Y, Payne F, Zhang J and Pan J W 2015 *Rev. Sci. Instrum.* **86** 063105
- [6] Shi Y, Chng B and Kurtsiefer C 2016 *Appl. Phys. Lett.* **109** 041101
- [7] Abellan C, Amaya W, Domenech D, Muñoz P, Capmany J, Longhi S, Mitchell M W and Pruneri V 2016 *Optica* **3** 989–94
- [8] Raffaelli F, Ferranti G, Mahler D H, Sibson P, Kennard J E, Santamato A, Sinclair G, Bonneau D, Thompson M G and Matthews J C 2018 *Quantum Sci. Technol.* **3** 025003
- [9] Bai B, Huang J, Qiao G R, Nie Y Q, Tang W, Chu T, Zhang J and Pan J W 2021 *Appl. Phys. Lett.* **118** 264001
- [10] Tamura K and Shikano Y 2021 *Int. Symp. on Mathematics, Quantum Theory, and Cryptography, Mathematics for Industry 2019 (Fukuoka)* vol 33 (Singapore: Springer) pp 17–37
- [11] von Neumann J 1951 *Natl Bur. Stand. Appl. Math. Ser.* **12** 36–8
- [12] Peres Y 1992 *Ann. Stat.* **20** 579–90
- [13] <https://nvlpubs.nist.gov/nistpubs/Legacy/SP/nistspecialpublication800-22r1a.pdf> Accessed on 5 November 2020
- [14] <https://quantum-computing.ibm.com/> Accessed on 5 November 2020
- [15] Edwards A L 1976 *An Introduction to Linear Regression and Correlation* (San Francisco, CA: Freeman) chapter 4 pp 33–46

Effect of Ti content on the magnetic and mechanical properties of B2 FeCo alloy: a DFT study

T M Ledwaba, R G Diale, P E Ngoepe and H R Chauke

University of Limpopo, Materials Modelling Centre, Private Bag x1106, Sovenga, 0727

E-mail: tebogo.ledwaba@ul.ac.za

Abstract. Iron-cobalt alloys are considered a good candidate for high-temperature applications due to their high saturation magnetization and Curie temperature. These alloys are applicable in the automotive industry as actuators, however, suffer low levels of ductility at room temperature. In this study, ternary alloying is used to investigate the strength of the alloys. Titanium is chosen as the alloying element since it has the potential to enhance the ductility of the alloy system. A density functional theory study applying the supercell approach was used to investigate the stability and magnetic behaviour of B2 Fe₅₀Co_{50-X}Ti_X ($0 \leq X \leq 50$) structures. Full structural optimization have been performed and provided equilibrium ground-state properties for both binary and ternary system in good agreement with previous studies to within 1 %. The stability of Fe₅₀Co_{50-X}Ti_X is evaluated from the formation energies, elastic properties, magnetic properties and phonon dispersion curves. We find that the thermodynamic stability increases with an increase in Ti content. Furthermore, the calculated Pugh's and Poisson's ratios showed that alloying with Ti effectively enhances ductility. Moreover, Fe₅₀Co_{50-X}Ti_X systems showed positive shear modulus for the entire concentration range, a condition of mechanical stability. It was also revealed that the Ti addition does not compromise the magnetic properties of the alloy greatly. Thus, the results suggest that the B2 Fe₅₀Co_{50-X}Ti_X alloy can be used for the development of magnetic components with good strength that can be used for actuator applications.

1. Introduction

Fe-Co alloys represent a crucial group of soft magnetic materials [1, 2, 3] which provides remarkable magnetic properties due to their scarce combination of good properties such as high mechanical strength, low coercivity, high permeability, and highest saturation magnetization. [4]. These alloys find application in pole tips for high field magnets, data storage, and high-performance transformers [5]. They also have the potential for use in the manufacturing of aircraft and jet engines, but they are rarely used due to their low levels of ductility at room temperature [6]. The workability of these alloys can be improved by ternary additions which may lead to higher tensile strength and elongation at room temperature.

Ternary alloying with Pd was investigated previously to improve the ductility of FeCo [7]. However, no information was given on how this affected the magnetic properties of the material since Pd reduced a considerable amount of Fe, which may lead to weak magnetic properties. In another study, it was reported that the addition of vanadium on the B2 Fe-Co alloy relieved the poor ductility and facilitated hot rolling in the disordered state by up to 90 %. Comparable to other alloying elements, adding vanadium to Fe-Co alloy weakens its magnetic properties [4]. In this study, we have used the plane-wave implementation of density functional theory (DFT) to investigate how ternary alloying can

improve the ductility of a typical bimetallic alloy, i.e. FeCo. Titanium was chosen as the alloying element since it has the potential to enhance the ductility of the alloy system without compromising the magnetic strength [8]. Furthermore, structural, mechanical, and thermodynamic properties were evaluated to ascertain the influence of Ti addition in the FeCo system.

2. Methodology

The calculations were carried out using the Vienna ab initio simulation package (VASP) code [9] based on density functional theory [10, 11] along with the projector augmented wave (PAW) pseudopotential [12]. We have used the generalized gradient approximation (GGA) of the Perdew-Burke-Ernzerhof (PBE) exchange-correlation functional [13] since it provided better results compared to other functionals. An energy cut-off of 500 eV was used, to achieve a good convergence of the parameters. The k-spacing of 0.2 1/Å (12X12X12) for B2 FeCo was used according to Monkhorst and Pack [14]. A 2x2x2 B2 Fe₅₀Co₅₀ supercell was used to generate different compositions (6.25, 18.75, 25, 31.25 and 43.75 at. % Ti). The most favorable Co substitution-sites were chosen based on the lowest possible total energy values i.e. the structure with the lowest energy was considered for each concentration. Note that the Pm-3m symmetry was maintained in all calculations since there was no significant difference with the results of the P1 symmetry. The structures were fully relaxed with respect to the volume, shape and internal atomic positions until the atomic forces were less than 0.01 eV/Å. Their stability was evaluated using heats of formation and the Born elastic stability criteria [17,18]. All calculations were subjected to spin polarization to take account of the magnetization. The PHONON [26] code was used to determine the phonon dispersion curves of both binary and ternary systems. The atomic arrangements of pure FeCo and supercell are shown in figure 1.

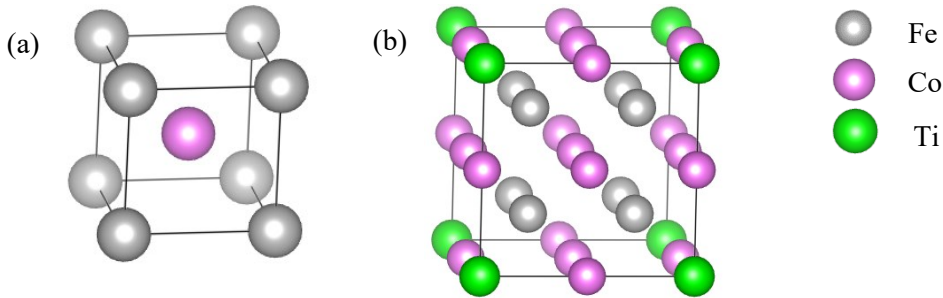


Figure 1. The atomic arrangements of the unit cell (a) binary B2 FeCo (b) B2 FeCo-Ti (2x2x2 supercell) with the space group Pm-3m.

3. Results and discussions

3.1. Structural and thermodynamic properties

Figure 2 shows the equilibrium lattice parameters for the Fe₅₀Co_{50-x}Ti_x (0 ≤ x ≤ 50) alloys. The equilibrium lattice parameter of binary B2 FeCo was predicted to be 2.844 Å (2.840 Å [16]) which agrees very well with experimental data to within 1 %. It was noted that the lattice parameter of the Fe₅₀Co_{50-x}Ti_x decreases as Ti content is increased (see figure 2). This is due to the large atomic radius of Ti (1.76 Å [27]) compared to Co (1.52 Å [28]). The thermodynamic stability of Fe₅₀Co_{50-x}Ti_x is argued through the predicted heats of formation (ΔH_f). ΔH_f was calculated by subtracting the individual atomic energies (Fe, Co, Ti) from that of the bulk system:

$$\Delta H_f = E_C - \sum_i x_i E_i, \quad (1)$$

where E_C is the calculated total energy of the compound and E_i is the calculated total energy of the element in the compound. Note that for a structure to be stable, the heat of formation must have the lowest negative value ($\Delta H_f < 0$) otherwise, a positive value implies instability. In figure 3, we show the heats of formation for the B2 Fe₅₀Co_{50-x}Ti_x systems for concentrations 0 ≤ x ≤ 50. The heats of formations for the binary B2 Fe₅₀Co₅₀ was found to be -0.057 eV/atom (-0.065 eV/atom [25]) which is in good

where E_C is the calculated total energy of the compound and E_i is the calculated total energy of the element in the compound. Note that for a structure to be stable, the heat of formation must have the lowest negative value ($\Delta H_f < 0$) otherwise, a positive value implies instability. In figure 3, we show the heats of formation for the B2 $\text{Fe}_{50}\text{Co}_{50-x}\text{Ti}_x$ systems for concentrations $0 \leq x \leq 50$. The heats of formations for the binary B2 $\text{Fe}_{50}\text{Co}_{50}$ was found to be -0.057 eV/atom (-0.065 eV/atom [25]) which is in good agreement with the theoretical value in parenthesis to within 3%. It was found that the ΔH_f decreases as Ti content is increased, which implies that the structure becomes thermodynamically stable.

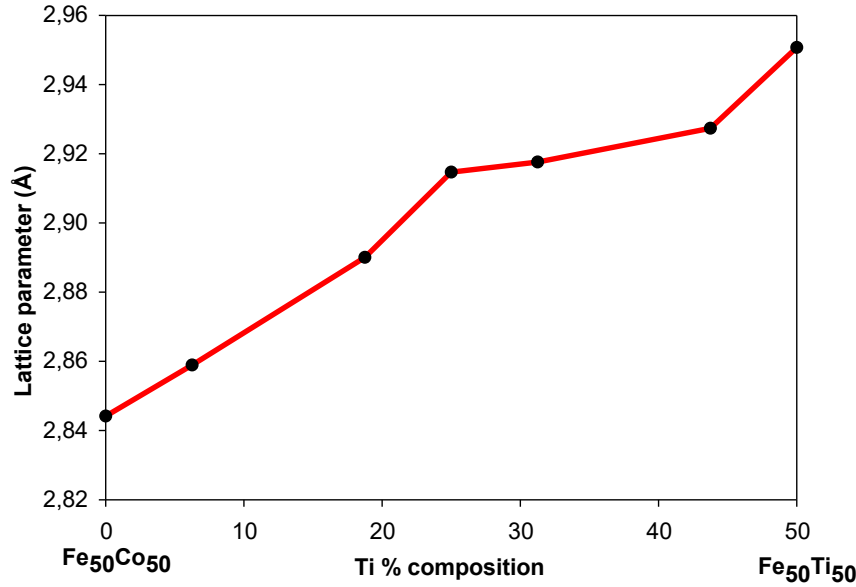


Figure 2. Lattice parameter (Å) against atomic percent Ti for $\text{Fe}_{50}\text{Co}_{50-x}\text{Ti}_x$ alloys ($0 \leq x \leq 50$).

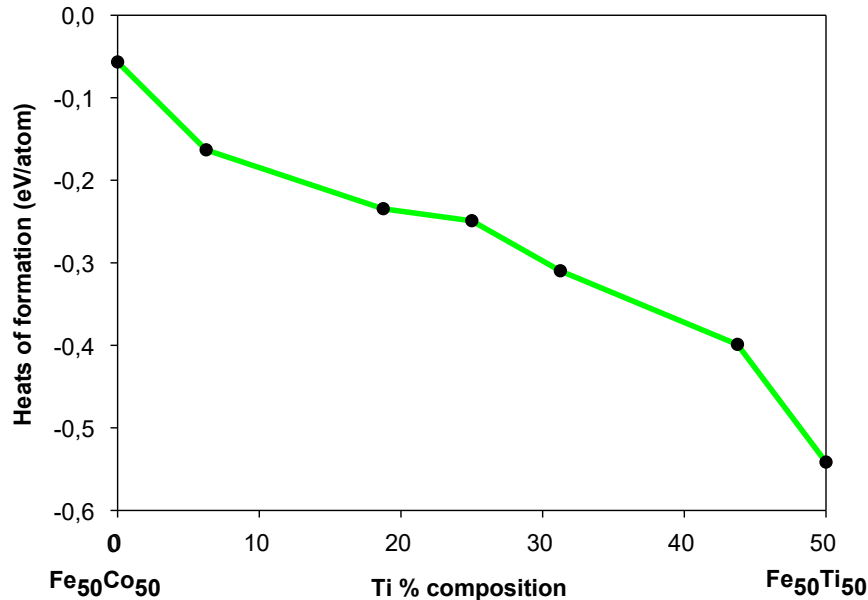


Figure 3. Heats of formation, ΔH_f against atomic percent Ti for $\text{Fe}_{50}\text{Co}_{50-x}\text{Ti}_x$ alloys ($0 \leq x \leq 50$).

3.2. Elastic and magnetic properties

The elastic properties give important information about the mechanical stability of compounds. For a cubic crystal structure (i.e B2 $\text{Fe}_{50}\text{Co}_{50-x}\text{Ti}_x$), there are three independent elastic constants (C_{11} , C_{12} and C_{44}), in which case the structure is considered stable if it satisfies the cubic stability criterion as described elsewhere [17, 18]:

The elastic properties give important information about the mechanical stability of compounds. For a cubic crystal structure (i.e B2 $\text{Fe}_{50}\text{Co}_{50-x}\text{Ti}_x$), there are three independent elastic constants (C_{11} , C_{12} and C_{44}), in which case the structure is considered stable if it satisfies the cubic stability criterion as described elsewhere [17, 18]:

$$C_{11} > C_{12}, C_{44} > 0, \text{ and } C_{11} + 2C_{12} > 0, \quad (2)$$

$$C' = \frac{1}{2}(C_{11} - C_{12}) > 0$$

In figure 4, it is seen that all the independent elastic constants are positive, confirming that the $\text{Fe}_{50}\text{Co}_{50-x}\text{Ti}_x$ alloys are stable in the entire composition range. More importantly, the C' is positive ($C' > 0$) which indicates mechanical stability. The C' is slowly varying (at low concentration) and increases slightly with the increase in Ti concentration above 25 at.%. This trend is similar to that of C_{11} , however, the C_{11} plot is higher. We also observe a coupling of C' and C_{44} at about 35 at. % Ti, while C' coincide with C_{12} at about 43.75 at. % Ti. This is attributed to a possible phase transformation from B2 to B19, similar observations were reported previously [24].

To measure the ductility of the materials, we have calculated the Pugh (B/G) and Poisson's ratios as shown in Figure 5 (a) and (b), respectively. Note that a structure is considered ductile if the B/G ratio is greater than 1.75 and otherwise brittle as noted elsewhere [19]. The structures (see figure 5(a)) were observed to be ductile for the entire concentration range since all ratios were greater than the critical value of 1.75.

Poisson's ratio (σ) was also evaluated to confirm the ductility of the material. Note that the structure is considered ductile when σ is greater than 0.26 otherwise brittle [20]. As the content of Ti is increased, the σ values were found to be greater than 0.26 in the entire concentration that is a condition of ductility (see figure 5 (b)).

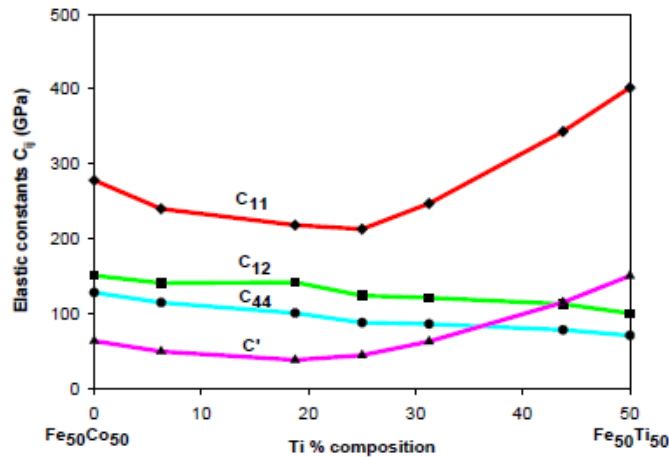


Figure 4. Elastic constants (GPa) against atomic percent Ti for $\text{Fe}_{50}\text{Co}_{50-x}\text{Ti}_x$ alloys ($0 \leq x \leq 50$).

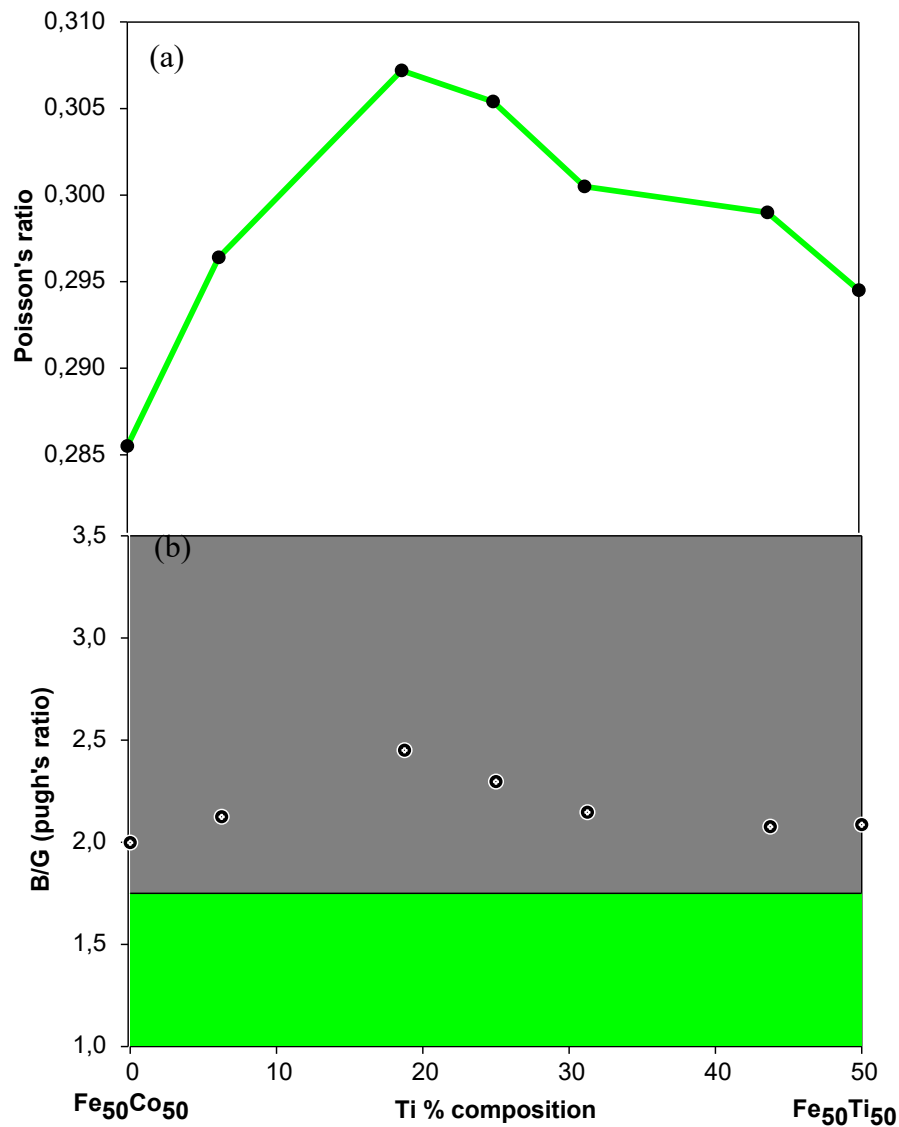


Figure 5. (a) B/G ratio and (b) Poisson's ratio against atomic percent Ti for Fe₅₀Co_{50-x}Ti_x alloys (0 ≤ x ≤ 50).

The total magnetic moments were calculated to check the magnetic strength of both binary Fe₅₀Co₅₀ and ternary Fe₅₀Co_{50-x}Ti_x systems. A positive value of total magnetic moment indicates good magnetic strength. The initial magnetic moments were defined for every atom by assigning a chosen value for Fe (3 μ B) and Co (2 μ B). Figure 6 shows the total magnetic moments of Fe₅₀Co_{50-x}Ti_x alloys as a function of Ti atomic composition. The contributions for each element in the system are also shown and indicate poor magnetic strength for Ti (low magnetic moments), and highest for Fe. The total magnetic moment of the binary B2 Fe₅₀Co₅₀ alloy was found to be 4.530 μ B in good agreement with the theoretical value of 4.479 μ B [25]. It can be seen that the total magnetic moment decrease with an increase in Ti composition. At 43.75 at. % Ti (0 μ B), the structure transition from ferromagnetic to diamagnetic, similar observations were discussed elsewhere [29, 30].

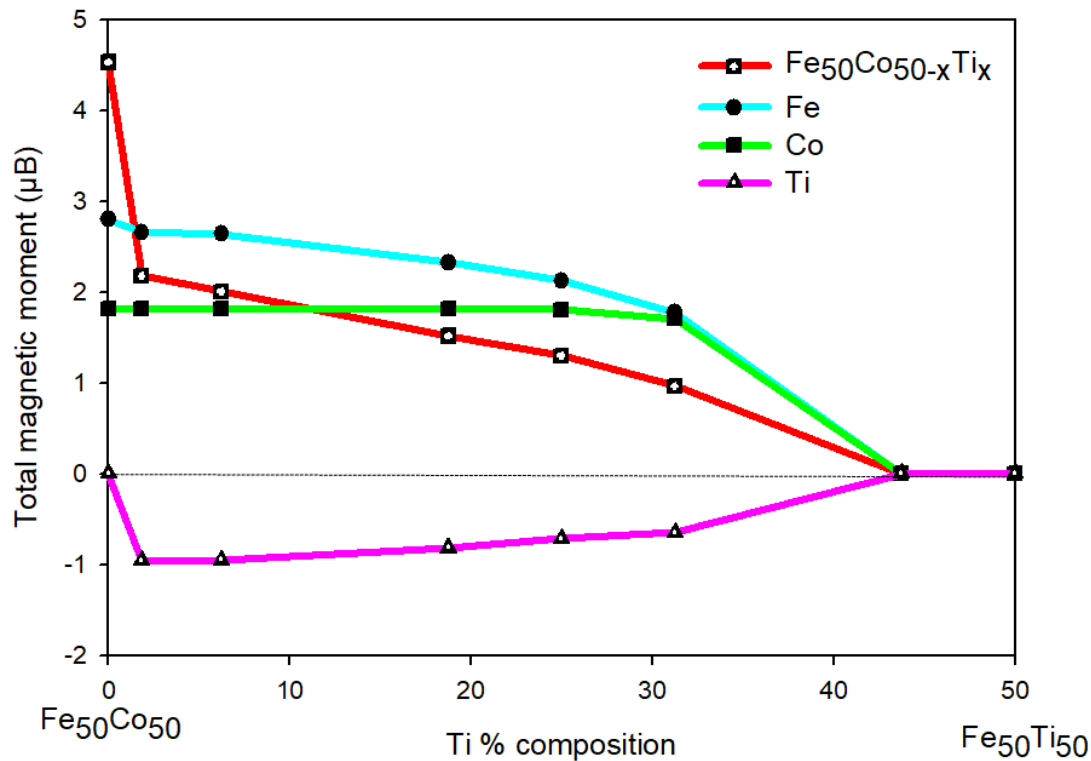


Figure 6. Total magnetic moments against atomic percent Ti for $\text{Fe}_{50}\text{Co}_{50-x}\text{Ti}_x$ alloys ($0 \leq x \leq 50$). The contributions of the individual elements (Fe, Co, Ti) are also included for reference.

3.3. Phonon dispersion curves

The Phonon dispersion curves were calculated to determine the structural stability of B2 $\text{Fe}_{50}\text{Co}_{50-x}\text{Ti}_x$ alloys and are illustrated in figure 7. It can be seen that the phonon dispersion curves of B2 $\text{Fe}_{50}\text{Co}_{50-x}\text{Ti}_x$ are vibrational stable for the entire concentration range ($0 \leq x \leq 50$) due to the absence of soft modes (i.e., negative frequency) along all the Brillouin zone directions. This observation suggests that Ti addition does not compromise the stability of the B2 $\text{Fe}_{50}\text{Co}_{50}$ structure, and this prediction is consistent with the elastic moduli C_{ij} that are given in figure 4.

3. Conclusion

The DFT results revealed a significant effect of Ti content on the structural, magnetic, and mechanical properties of B2 FeCo alloy. The results showed that $\text{Fe}_{50}\text{Co}_{50-x}\text{Ti}_x$ is thermodynamically stable at high concentrations displaying the lowest heats of formation value. It was found that $\text{Fe}_{50}\text{Co}_{50-x}\text{Ti}_x$ alloys are mechanically stable for the entire concentrations according to the cubic stability criteria. Furthermore, the ductility is enhanced due to an increased tendency in the Pugh (B/G) and Poisson's ratio with an increase in Ti concentration above the critical point. The phonon dispersion curves showed mechanical stability for the entire concentration of $\text{Fe}_{50}\text{Co}_{50-x}\text{Ti}_x$ ($0 \leq x \leq 50$). Ternary addition of Ti slightly reduces the total magnetic moments of B2 FeCo, however, maintained the magnetic strength as well as the mechanical stability. The present findings may guide the future development of Ferromagnets made up of new $\text{Fe}_{50}\text{Co}_{50-x}\text{Ti}_x$ alloys.

Acknowledgments

The authors would like to appreciate the computing resources offered by the Materials Modelling Centre (MMC) at the University of Limpopo and the Center for High-Performance Computing (CHPC). The

support from the Titanium Centre of Competence (TiCoC) and the South African Research Chair Initiative of the Department of Science and Innovation is highly appreciated.

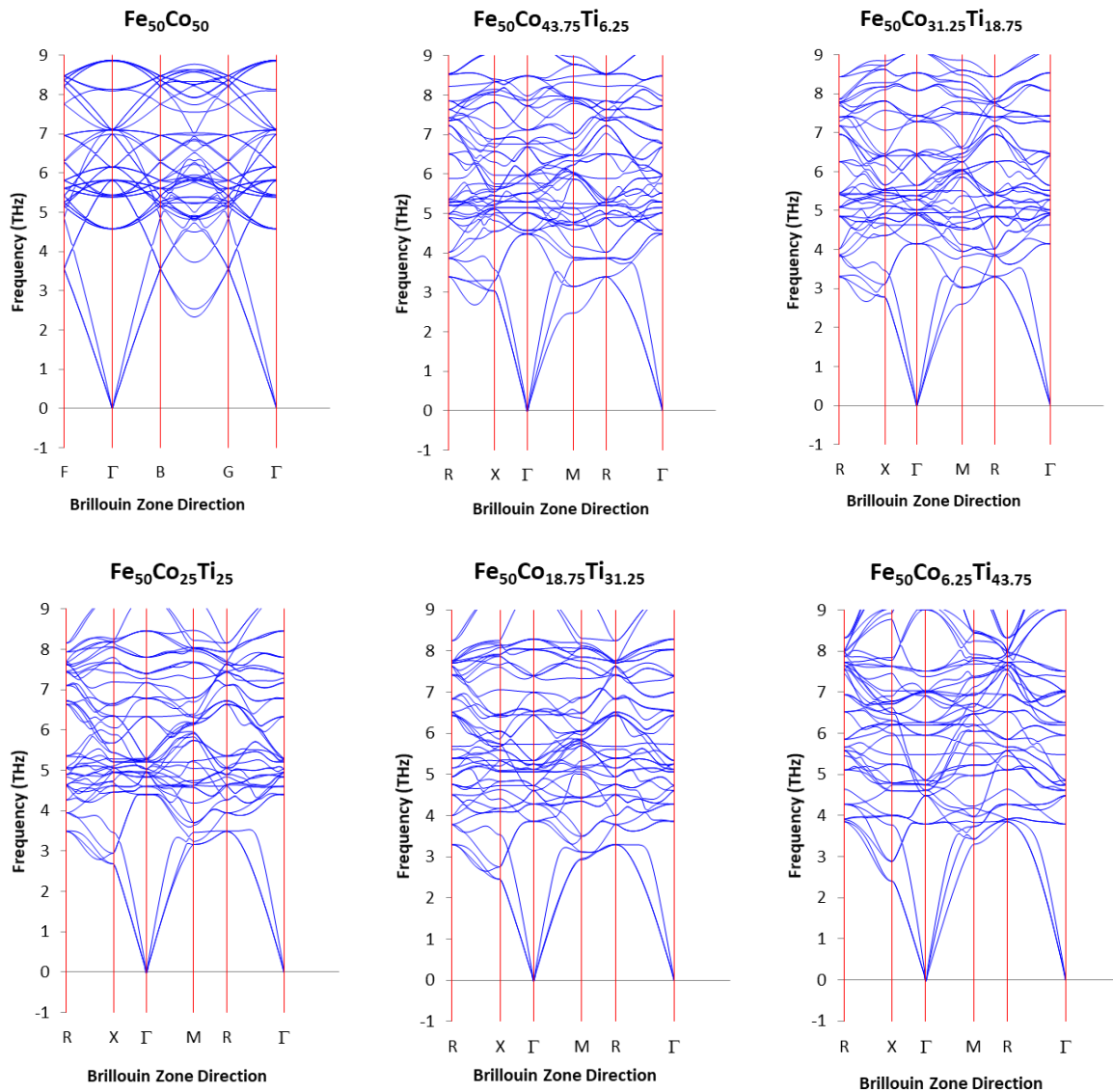


Figure 7. Phonon dispersion curves for B2 $\text{Fe}_{50}\text{Co}_{50-x}\text{Ti}_x$ alloys, where $0 \leq x \leq 43.75$ and the Γ (000) denote the center of the Brillouin zone.

References

- [1] Fingers R T and Kozlowski G 1997 *J. Appl. Phys.* **81** 4110-4111.
- [2] Sundar R S and Deevi S C 2013 *Int. Mat. Rev.* **50** 157-192.
- [3] Hasegawa T, Kanatani S, Kazaana M, Takahashi K, Kumagi K, Hirao M and Ishio S 2017 *Sci. Rep.* **7** 13215.
- [4] Sourmail T 2005 *Prog. Mat. Sci.* **50** 816-880.
- [5] Diaz-Ortiz A, Drautz R., Fahnle M, Dosch H and Sanchez J M 2006 *Phys. Rev. B.* **73** 1-15.
- [6] Matsuda M, Yamashita K, Sago R, Akamine K, Takashima K and Nishida M 2012 *Mater. Trans.* **53** 1826-1828.
- [7] Matsuda M, Sago R, Akamine K, Tsurekawa S, Takashima K and Nishida M 2016 *J. Alloys*

- Compd.* **682** 1-8.
- [8] Boyer R R 2010 *JOM*. **62** 35-43.
 - [9] Hohenberg P and Kohn W *Phys. Rev. B*. **136** 864-871.
 - [10] Kohn W and Sham L J *Phys. Rev. A*. **140** 1133-1138.
 - [11] Kresse G and Hafner J *Phys. Rev. B*. **47** 558-561.
 - [12] Blöchl P E 1994 *Phys. Rev. B*. **50** 17953-17979.
 - [13] Perdew J P, Burke K and Ernzerhof M 1996 *Phys. Rev. Lett.* **77** 3865-3868.
 - [14] Monkhorst H J and Pack J D *Phys. Rev. B*. **13** 5188-5192.
 - [15] Hasegawa T, Niibori T, Takemasa Y and Oikawa M 2019 *Sci. Rep.* 5248.
 - [16] Wang J H, Yip S, Phillpot S R and Wolf D 1993 *Phys. Rev. Lett.* **71** 4182-4185.
 - [17] Patil S K R, Khare S V, Tuttle B R, Bording J K and Kodambaka S, 2006 *Phys. Rev. B*. **73** 104118.
 - [18] Mayer B, Anton H, Bott E, Methfessel M, Sticht J and Schmidt P C 2003 *intermetallics*. **11** 23.
 - [19] Pugh S F 1954 *Philos. Mag.* **45** 843.
 - [20] Frantsevich I N and Voronov S A 1983 *Naukova Dumka, Kiev*. **1** 60-180.
 - [21] Pettifor G D 1992 *Mater. Sci. Technol.* **8** 345-349.
 - [22] White J H and Wahl C V 1932 *US patent*. **1** 559.
 - [23] Persiano A I and Rawlings R D 1991 *J. Mater. Sci.* **26** 4026-4032.
 - [24] Ren X, Miura N, Taniwaki L, Otsuka K, Suzuki T, Tanaka K, Chumlyakov Y I and Asai M 1999 *Mater. Sci. Eng. A* **273-275** 190-194.
 - [25] Persson, Kristin, and Project, Materials, "Materials Data on FeCo by Materials Project.," United States: N, 2020.
 - [26] Parlinski K, Li Z Q and Kawazoe Y 1998 *Phys. Rev. Lett* **81** 3298.
 - [27] Duwez P E 1952 *J. Inst. Met.* **80** 525-527.
 - [28] Syukri, Ban T, Ohya Y and Takahashi Y K 2003 *Mater. Chem. Phys.* **78** 645-649.
 - [29] Li J, Jiang Y, Li Y, Yang D, Xu Y and Yan M 2013 *Appl. Phys. Lett.* **102** 072406.
 - [30] Kapilashrami M, Xu J, Strom V, Rao K V and Belova L 2009 *Appl. Phys. Lett* **95** 033104.

Bianchi Type-V model in R^n -gravity: A dynamical systems approach

T Tsabone¹ and A Abebe²

^{1,2} Center for Space Research, North-West University, Mahikeng 2745, South Africa.

E-mail: ¹ tsabonethato@gmail.com

E-mail: ² amare.abbebe@gmail.com

Abstract. The accelerated expansion of the universe and the rotational dynamics of galaxies have become part of the mysteries of the physical world and have had theorists working tirelessly in the past years. There is no consensus on what is causing these observable effects: whether it is the yet-to-be-discovered dark energy and dark matter or it is the breaking down of our currently accepted theory of gravity, General Relativity, on larger scales. In this paper, we assume it is the latter and analyze R^n -gravity - a type of modified theory of gravity - in the Bianchi Type-V spacetime. Numerous accelerating solutions are found and their stability is analyzed. There is one particular solution that was found to be stable for a wide range of values of n and it makes for a possible solution for the accelerated expansion anomaly.

1. Introduction

The dynamics of the cosmos at large are nothing like any system we have encountered in the solar system. Experimental evidence indicate that galaxies are moving apart instead of pulling together as gravity would have them [1, 2]. To account for this, an energy density with a negative pressure is included into the energy budget of the universe when calculations are being carried out in the standard model of cosmology [3]. This energy cannot be accounted for using any of our most successful theoretical tools, in fact, the results are disastrous. In the frame work of quantum field theories, the expansion was attributed to the vacuum energy which observations have shown to have a density of not more than 10^{-29} g/cm³ [4]. The theoretical calculations, however, exceeds this bound by 55 orders of magnitude [4].

There is a search for a theory that contains the undisputed General Relativity as a subset and, at the same time, explain why is spacetime expanding. Various candidates have been put forward, ranging from quantum field theories to the so-called modified theories of gravity [5]. One of the promising of the modified theories is R^n -gravity, obtained from replacing the Ricci scalar R in the Einstein-Hilbert action (in normalized units) [6, 7, 8, 9]

$$S_{EH} = \frac{1}{2} \int dx^4 \sqrt{-g} (R + 2\mathcal{L}_M), \quad (1)$$

with R^n such that the generalized action is

$$S = \frac{1}{2} \int dx^4 \sqrt{-g} (R^n + 2\mathcal{L}_M). \quad (2)$$

Here g is the determinant of the metric tensor and \mathcal{L}_M is the matter Lagrangian. Varying the action (2) with respect to the metric, performing a 1+3 covariant decomposition to the resulting field equations, and imposing the Bianchi V group of isometries onto the underlying spacetime, we obtain the field equation for R^n -gravity in Bianchi Type V spacetime for a non-tilted fluid:

$$\begin{aligned} \dot{a} &= -\frac{1}{3}a\Theta, \\ \dot{\sigma} &= -\Theta\sigma - (n-1)\frac{\dot{R}}{R}\sigma, \\ \dot{\Theta} &= \frac{R}{2n} + (n-1)\frac{\dot{R}}{R}\Theta - \frac{\rho}{nR^{n-1}} - \frac{1}{3}\Theta^2 - 2\sigma^2, \\ \dot{\rho} &= -\Theta(1+\omega)\rho, \\ 0 &= \frac{1}{3}\Theta^2 - 3a^2 - \sigma^2 - \frac{(n-1)}{2n}R - \frac{\rho}{nR^{n-1}} + (n-1)\frac{\dot{R}}{R}\Theta. \end{aligned} \quad (3)$$

Here σ is the shear scalar, ρ is the matter density, Θ is the rate of expansion scalar, ω is the equation of state parameter, and a is a parameter related to the spatial curvature scalar, \tilde{R} , by the formula $\tilde{R} = -6a^2$ [3, 10, 11].

2. Analysis

Defining the expansion-normalized variables [7, 9]:

$$\begin{aligned} d\tau &:= \Theta dt, & \Sigma &:= \frac{3\sigma^2}{\Theta^2}, & W &:= \frac{9a^2}{\Theta^2}, \\ x &:= \frac{3\dot{R}}{R\Theta}(n-1), & y &:= \frac{3R}{2n\Theta^2}(n-1), & z &:= \frac{3\rho}{nR^{n-1}\Theta^2}, \end{aligned} \quad (4)$$

and substituting into (3), we obtain the dimensionless equations:

$$\begin{aligned} W' &= \frac{2W}{3} \left(1 - \frac{n}{n-1}y - W + \Sigma \right), \\ \Sigma' &= -\frac{2\Sigma}{3} \left[\left(\frac{2n-1}{n-1} \right) y + z - 2W \right], \\ y' &= \frac{y}{3(n-1)} [(3-2n)W + (2n-1)\Sigma - (2n-1)y + z + (4n-5)], \\ z' &= \frac{z}{3} \left[-z + (2-3\omega) - 3W + \Sigma - \left(\frac{3n-1}{n-1} \right) y \right]. \end{aligned} \quad (5)$$

For brevity we focus our attention on the vacuum solutions, $z = 0$. The fixed points and the corresponding solutions are summarized in tables 1 and 2, respectively. Of all the obtained solutions, only the solution at the fixed point \mathcal{B} could produce an accelerating spacetime depending on the value of n . Mathematically, the slope, $\dot{l}(t)$, and the concavity, $\ddot{l}(t)$, of the scale factor, $l(t)$, are always positive for accelerating solutions. For the scale factor in \mathcal{B} , this is true for $n \in \left(-\infty, \frac{1-\sqrt{3}}{2}\right) \cup \left(\frac{1+\sqrt{3}}{2}, 2\right)$.

Stability analysis [12, 13] show that this fixed point is a stable node for $n \in \left(-\infty, \frac{1-\sqrt{3}}{2}\right) \cup \left(\frac{1}{2}, 1\right) \cup \left(\frac{1+\sqrt{3}}{2}, \infty\right)$, a saddle for $n \in \left(\frac{1-\sqrt{3}}{2}, \frac{1}{2}\right) \cup \left(\frac{5}{4}, \frac{1+\sqrt{3}}{2}\right)$ and an unstable node for $1 < n < \frac{5}{4}$. Comparing the values of n such that \mathcal{B} is stable and those which result in accelerating solutions, it is

Table 1. Local fixed points for the vacuum solutions.

	(Σ_i, W_i, y_i)
Point \mathcal{A}	$(0, 1, 0)$
Point \mathcal{B}	$\left(0, 0, \frac{4n-5}{2n-1}\right)$
Point \mathcal{C}	$[0, -2n^2 + 2n + 1, 2(n-1)^2]$
Point \mathcal{D}	$\left[-\frac{n(4n-5)}{2(2n-1)}, -\frac{n-2}{2}, -\frac{(n-1)(n-2)}{2n-1}\right]$
Line \mathcal{L}_1	$(\Sigma_*, 0, 0), \Sigma_* \geq 0$

Table 2. Vacuum solutions at each fixed point.

	$a(t)$	$\sigma(t)$	$R(t)$	$l(t)$
Point \mathcal{A}	$a = a_0(t - t_0)^{-1}$	0	0	$l(t) = l_0(t - t_0)$
Point \mathcal{B}	0	0	$R = \frac{6n(4n-5)(n-1)(2n-1)}{(n-2)^2 t^2}$	$l(t) = l_0(t - t_0)^{\frac{(2n-1)(1-n)}{n-2}}$
Point \mathcal{C}	$a = a_0(t - t_0)^{-1}$	0	$R = \frac{12n(n-1)}{t^2}$	$l(t) = l_0(t - t_0)$
Point \mathcal{D}	$a = a_0(t - t_0)^{-1}$	$\sigma = \sigma_0(t - t_0)^{2n-5}$	$R = \frac{6n(2-n)}{(2n-1)t^2}$	$l(t) = l_0(t - t_0)$
Line \mathcal{L}_1	0	$\sigma = \sigma_0(t - t_0)^{-\frac{2+\Sigma_*}{1+2\Sigma_*}}$	0	$l(t) = l_0(t - t_0)^{\frac{1}{1+2\Sigma_*}}$

seen that \mathcal{B} is stable for all values of n that result in accelerating solutions. This implies that any initial conditions in the vicinity of \mathcal{B} will have solutions which qualitatively behave like those of \mathcal{B} [12]. Roughly speaking, this means that a universe which has an initial state similar to that described by the solutions of \mathcal{B} , will evolve to have characteristics which are similar to those of \mathcal{B} .

The phase space is unbounded and asymptotic fixed points must be considered to complete the analysis. Performing the following change of variables:

$$\begin{aligned}\Sigma &= \bar{r} \cos \phi \sin \theta, \\ W &= \bar{r} \sin \phi \sin \theta, \\ y &= \bar{r} \cos \theta,\end{aligned}\tag{6}$$

where $\bar{r} = \frac{r}{1-r}$ [7, 14], $0 < \phi \leq \frac{\pi}{2}$ and $0 < \theta < \pi$, and taking the limit $\bar{r} \rightarrow \infty$ ($r \rightarrow 1$) the equations in (5) reduce to:

Table 3. Asymptotic fixed points and solutions for the scale factor.

Point	(ϕ_i, θ_i)	Scale factor
\mathcal{A}_∞	$(0, 0)$	$ \tau - \tau_\infty = \left[C_1 \pm C_0 \left \frac{n-1}{2n-1} \right (t - t_0) \right]^{\frac{2n-1}{n-1}}$
\mathcal{B}_∞	$(0, \frac{\pi}{2})$	$\tau - \tau_\infty = C_1 \ln t - t_0 + C_2$
\mathcal{C}_∞	$(\frac{\pi}{2}, 0)$	$ \tau - \tau_\infty = \left[C_1 \pm C_0 \left \frac{n-1}{2n-1} \right (t - t_0) \right]^{\frac{2n-1}{n-1}}$
\mathcal{D}_∞	$(\frac{\pi}{2}, \frac{\pi}{2})$	$ \tau - \tau_\infty = \left[C_1 \pm \frac{1}{2} C_0 (t - t_0) \right]^2$
\mathcal{E}_∞	$\left[\arctan\left(\frac{1}{3}\right), \frac{\pi}{2} \right]$	$ \tau - \tau_\infty = \left[C_1 \pm \frac{1}{2} C_0 (t - t_0) \right]^2$

Table 4. Asymptotic fixed points and solutions for the scale factor.

Point	$a(\tau)$	$\sigma(\tau)$	$R(\tau)$
\mathcal{A}_∞	0	0	$R = R_0 \frac{n}{2n-1} \tau - \tau_\infty ^{\frac{1}{2n-1}}$
\mathcal{B}_∞	0	$\sigma = \sigma_0 e^{\tau - \tau_\infty}$	0
\mathcal{C}_∞	0	$\sigma = \sigma_0 \sqrt{\frac{n-1}{2n-1}} \tau - \tau_\infty ^{\frac{1}{2(2n-1)}}$	$R = R_0 \frac{n}{2n-1} \tau - \tau_\infty ^{\frac{2n}{2n-1}}$
\mathcal{D}_∞	a_0	0	0
\mathcal{E}_∞	a_0	σ_0	0

$$r' = -\frac{\sin^2 \theta}{3} \left\{ 2 \cos^2 \phi [\cos \theta + (\cos \phi - 3 \sin \phi) \sin \theta] + \frac{1}{n-1} [\cos \theta + (\sin \phi + \cos \phi) \sin \theta] \right\} \\ + \frac{1}{3} \left[\frac{3-2n}{n-1} \sin \phi \sin \theta + \frac{2n-1}{n-1} \cos \phi \sin \theta - \frac{2n-1}{n-1} \cos \theta \right], \quad (7)$$

$$\theta' = -\frac{\sin 2\theta}{6(1-r)} \left\{ 2 \cos^2 \phi [\cos \theta + (\cos \phi - 3 \sin \phi) \sin \theta] + \frac{1}{n-1} [\cos \theta + (\sin \phi + \cos \phi) \sin \theta] \right\}, \quad (8)$$

$$\phi' = \frac{\sin 2\phi}{3(1-r)} [\cos \theta + (\cos \phi - 3 \sin \phi) \sin \theta]. \quad (9)$$

The fixed points and the solutions are given in tables 3 and 4. The stability of the fixed points is summarized in table 5 and none of them are stable as can be seen therein.

Table 5. Stability of the asymptotic fixed points in vacuum

Point	Eigenvalues	r'	$n < 1/2$	$1/2 < n < 1$	$n > 1$
\mathcal{A}_∞	$\left[\frac{2}{3}, -\frac{2n-1}{3(n-1)}\right]$	$-\frac{2n-1}{3(n-1)}$	Saddle	Saddle	Saddle
\mathcal{B}_∞	$\left[\frac{2}{3}, \frac{2n-1}{3(n-1)}\right]$	0	Unstable	Saddle	Unstable
\mathcal{C}_∞	$\left[-\frac{2}{3}, -\frac{1}{3(n-1)}\right]$	$-\frac{2n-1}{3(n-1)}$	Saddle	Saddle	Saddle
\mathcal{D}_∞	$\left[2, \frac{1}{3(n-1)}\right]$	$-\frac{2}{3}$	Saddle	Saddle	Unstable
\mathcal{E}_∞	$\left[-\frac{\sqrt{10}}{5}, \frac{2\sqrt{10}}{15(n-1)}\right]$	$\frac{2\sqrt{10}}{15}$	Stable	Stable	Saddle

3. Conclusion

Although Bianchi models are generally anisotropic, the accelerating solution discussed describe a spatially flat and anisotropic universe . And since this is a vacuum solution, the acceleration is not influenced by any energy but is an intrinsic property of spacetime. Furthermore, due to the stability of the solution, the universe whose gravitational interaction is governed by R^n -gravity is more likely to asymptotically approach a flat, isotropic and expanding state. This is indeed our own universe. It was shown in [8] that for $n = 1.4$ and $n = 0.6$ the R^n model does mimic the real universe in the context of the FLRW metric, however. The model discussed in this paper allows for anisotropies in the early universe and thus is more general than the model discussed in [8].

Acknowledgements

TT and AA acknowledge that this work is based on the research supported in part by the NRF of South Africa with respective grant numbers 117318 and 112131.

References

- [1] Perlmutter S, Aldering G, Goldhaber G, Knop R, Nugent P, Castro P G, Deustua S, Fabbro S, Goobar A, Groom D E *et al.* 1999 *The Astrophysical Journal* **517** 565
- [2] Riess A G, Filippenko A V, Challis P, Clocchiatti A, Diercks A, Garnavich P M, Gilliland R L, Hogan C J, Jha S, Kirshner R P *et al.* 1998 *The Astronomical Journal* **116** 1009
- [3] Ellis G F, Maartens R and MacCallum M A 2012 *Relativistic cosmology* (Cambridge University Press)
- [4] Rugh S E and Zinkernagel H 2002 *Studies in History and Philosophy of Science Part B: Studies in History and Philosophy of Modern Physics* **33** 663–705
- [5] Capozziello S and De Laurentis M 2011 *Physics Reports* **509** 167–321
- [6] Sotiriou T P and Faraoni V 2010 *Reviews of Modern Physics* **82** 451
- [7] Leach J A, Carloni S and Dunsby P K 2006 *Classical and Quantum Gravity* **23** 4915
- [8] Capozziello S, Cardone V F, Carloni S and Troisi A 2003 *International Journal of Modern Physics D* **12** 1969–1982
- [9] Carloni S, Dunsby P K, Capozziello S and Troisi A 2005 *Classical and Quantum Gravity* **22** 4839
- [10] Ellis G, Siklos S and Wainwright J 1997 *Dynamical Systems in Cosmology* 11–50
- [11] Ellis G F and Van Elst H 1999 *Cosmological models Theoretical and Observational Cosmology* (Springer) pp 1–116
- [12] Perko L 2013 *Differential equations and dynamical systems* vol 7 (Springer Science & Business Media)
- [13] Strogatz S H 2018 *Nonlinear dynamics and chaos with student solutions manual: With applications to physics, biology, chemistry, and engineering* (CRC press)

- [14] Clifton T and Barrow J D 2005 *Physical Review D* **72** 103005

Three-party reference frame independent quantum key distribution with an imperfect source

Comfort Sekga^{1*} and Mhlambululi Mafu¹

¹Department of Physics and Astronomy, Botswana International University of Science and Technology, P/Bag 16, Palapye, Botswana

E-mail: *comfort.sekga@gmail.com

Abstract. We propose a reference frame independent quantum key distribution (RFI-QKD), allowing three legitimate parties to share a common secret key without aligning reference frames in their quantum channels. Furthermore, we relax the perfect state preparation assumption by employing a loss tolerant technique, making the proposed protocol suitable for practical applications. The results show that the proposed RFI-QKD with an imperfect source is comparable to the RFI-QKD with a perfect source. Moreover, we investigate the impact of reference frame misalignment on the stability of our protocol when the reference frames drift by various misalignment angles. Also, we demonstrate that our protocol is not heavily affected by an increase in misalignment of reference frames and it finds immediate applications in quantum networks.

1. Introduction

Quantum key distribution (QKD) provides information-theoretically secure communication by exploiting the laws of quantum mechanics to detect an eavesdropper [1, 2]. Since the inception of the primitive BB84 protocol [3], considerable theoretical and experimental efforts have been accomplished to improve the security and implementation of QKD. However, several challenges remain for QKD to become fully adopted in securing communication. One of the challenges in the practical implementation of QKD is a requirement for an aligned reference frame between the communicating parties [4, 5, 6]. However, Laing et al. (2010) proposed the reference frame independent (RFI) protocol to address this problem of alignment [4]. Typically, various QKD security proofs assume perfect state preparation. But, in practical implementations, this is impossible due to inherent deficiencies of photon sources [7]. Thus, Tamaki et al. (2014) recently proposed a loss-tolerant protocol that is robust against channel losses due to state preparation flaws and capable of attaining key rates comparable to a protocol that assumes perfect encoding [8]. Furthermore, considering that this protocol is resource-efficient, we employ the loss tolerant technique in our security proof, making the proposed protocol suitable for practical applications.

Against this background, we harness the loss tolerant protocol and derive the security bounds under the imperfect state preparation for the three-party RFI protocol. Also, we demonstrate that the number of communicating parties can be further extended and still achieve a secret key rate and transmission distance comparable to the traditional two-party QKD.

2. Operation of the proposed protocol

State preparation

In each run i , Alice prepares a two-photon entangled state using a Spontaneous Parametric Down Conversion source (SPDC). She then randomly selects the basis $a_i \in \{X, Y, Z\}$ with

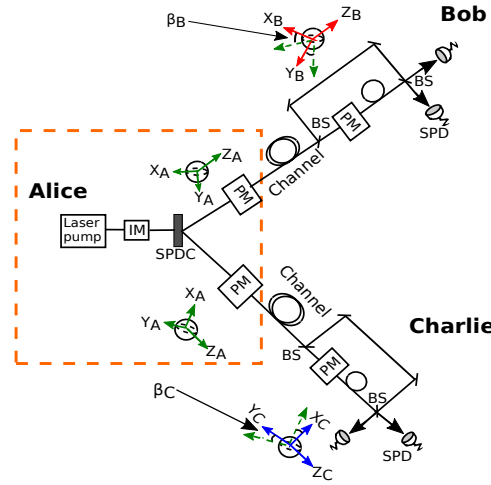


Figure 1: The schematic diagram of the three-party RFI-QKD protocol. Alice starts by preparing a two-photon entangled state using an SPDC source. The acronyms IM, BS and SPD stand for intensity modulators, beam splitter, and single-photon detectors.

probabilities p_z and $p_c = 1 - p_z$, respectively. Here, Z basis is chosen with probability $p_z > \frac{1}{2}$ and the complementary bases, $\{X, Y\}$ with probability $p_c = 1 - p_z$. She applies phase modulation $\theta_A \in \{0, \frac{\pi}{2}\}$, $\theta_A \in \{\frac{\pi}{4}, \frac{3\pi}{4}\}$ and $\theta_A \in \{\pi, \frac{3\pi}{2}\}$ when she selects the Z , X and Y basis, respectively. Here the phase values $\theta_A \in \{0, \frac{\pi}{4}, \pi\}$ and $\theta_A \in \{\frac{\pi}{2}, \frac{3\pi}{4}, \frac{3\pi}{2}\}$ are assigned bit values $r_i = 0$ and $r_i = 1$, respectively. Note that for each run i , Alice performs the same phase shift to both entangled photons, i.e., both photons are prepared in the same state, therefore she keeps one bit value r_i corresponding to that state. The two photons are delivered to Bob and Charlie via insecure quantum channels.

Measurement

Upon receipt of photons, Bob and Charlie measure them using the basis $b_i \in \{X, Y, Z\}$ and $c_i \in \{X, Y, Z\}$, respectively, with probabilities p_z and p_c . They choose uniform random bits $r'_i \in \{0, 1, \emptyset\}$ and $r''_i \in \{0, 1, \emptyset\}$ to store their outcomes. Here the symbol \emptyset corresponds to inconclusive result and is assumed the same for all bases. In this protocol, Alice, Bob, and Charlie share a common aligned measurement basis $Z_A = Z_B$, $Z_A = Z_C$ while other measurements bases X and Y are allowed to vary by an arbitrary angle β slowly (See Figure 1). Due to drift in reference frames, the measurement bases complementary to the Z basis are given by $X_B = \cos \beta X_A + \sin \beta Y_A$, $X_C = \cos \beta X_A + \sin \beta Y_A$, and $Y_B = \cos \beta Y_A - \sin \beta X_A$, $Y_C = \cos \beta Y_A - \sin \beta X_A$.

Sifting

Alice, Bob and Charlie publish their basis choices over an authenticated classical channel. We define the set $\mathcal{Z} := \{i : a_i = b_i = c_i, r'_i \neq \emptyset, r''_i \neq \emptyset\}$. The first steps are repeated as long as $|\mathcal{Z}| < n$. Here n corresponds to the required number of bit strings to form a raw key. The raw key is extracted from cases where Alice prepared her states in the Z basis while Bob and Charlie measured their received qubits in the Z direction.

3. Security Analysis

After the sequential transmission and measurement of optical pulses, Alice, Bob, and Charlie possess partially correlated bit strings. They proceed with the parameter estimation step to deduce the bit error rate in the key basis. The quantum bit error rate is given by $E_{ZZZ} = \frac{1 - \langle Z_A Z_B Z_C \rangle}{2}$, where Z_A represents that Alice prepared two states in the Z basis while Z_B and Z_C denote that Bob and Charlie's measure received states in the Z direction, respectively. The measurement results in the complementary bases are used to estimate the information that has leaked to Eve. To compute Eve's knowledge on the key, we consider a depolarising channel

where $E_{ZZ} \leq 15.9\%$ [4]. The bound is given by [6]

$$kgI_E = (1 - E_{ZZZ})h\left(\frac{1 + u_{\max}}{2}\right) - E_{ZZZ}h\left(\frac{1 + v(u_{\max})}{2}\right) + E_{ZZZ}\log_2 7, \quad (1)$$

where $u_{\max} = \min\left[\frac{1}{1-E_{ZZZ}}\sqrt{C/4}, 1\right]$ and $v(u_{\max}) = \sqrt{\frac{49}{19}\left[C/4 - (1 - E_{ZZZ})^2 u_{\max}^2\right]}/E_{ZZZ}$. The statistical quantity C defined as

$$C = \langle X_A X_B X_C \rangle^2 + \langle X_A Y_B X_C \rangle^2 + \langle X_A X_B Y_C \rangle^2 + \langle Y_A X_B X_C \rangle^2 + \langle Y_A Y_B X_C \rangle^2 + \langle Y_A X_B Y_C \rangle^2 \\ + \langle Y_A Y_B Y_C \rangle^2 + \langle X_A Y_B Y_C \rangle^2, \quad (2)$$

C is independent of β , $\langle \Gamma_A \Gamma_B \Gamma_C \rangle$ (with $\Gamma \in \{X, Y\}$), corresponds to the expectation that Alice prepares two states in the basis Γ_A while Bob and Charlie measure received states in basis Γ_B and Γ_C , respectively. To estimate C , the angle β is assumed to vary slowly in time short enough to allow for the exchange of keys. The expression in Equation 2 can be rewritten as

$$C = (1 - 2E_{XX})^2 + (1 - 2E_{XY})^2 + (1 - 2E_{YY})^2 + (1 - 2E_{XX})^2 + (1 - 2E_{YY})^2 \\ + (1 - 2E_{XY})^2 + (1 - 2E_{XY})^2 + (1 - 2E_{YY})^2. \quad (3)$$

To compute C , we employ a loss tolerant technique which takes into consideration the imperfections in the phase modulation of photons [8]. The actual states that Alice prepares are $|\phi_{0Z}\rangle = |0_Z\rangle$, $|\phi_{1Z}\rangle = \sin\frac{\delta_1}{2}|0_Z\rangle + \cos\frac{\delta_1}{2}|1_Z\rangle$, $|\phi_{0X}\rangle = \cos\left(\frac{\pi}{4} + \frac{\delta_2}{4}\right)|0_Z\rangle + \sin\left(\frac{\pi}{4} + \frac{\delta_2}{4}\right)|1_Z\rangle$, and $|\phi_{0Y}\rangle = \cos\left(\frac{\pi}{4} + \frac{\delta_3}{4}\right)|0_Z\rangle + i\sin\left(\frac{\pi}{4} + \frac{\delta_3}{4}\right)|1_Z\rangle$. These signal states can be written in terms of an identity and Pauli matrices and their density matrix representation is given by $\rho_{j\alpha} = |\phi_{j\alpha}\rangle\langle\phi_{j\alpha}| = \frac{1}{2}(\mathbb{1} + \mathbf{n}_X^{j\alpha}\sigma_x + \mathbf{n}_Y^{j\alpha}\sigma_y + \mathbf{n}_Z^{j\alpha}\sigma_z)$. Here $\mathbf{n}_\alpha^{j\alpha}$ denotes the coefficient of the Bloch vector of $\rho_{j\alpha}$ where $\alpha \in \{X, Y, Z\}$ and $j \in \{0, 1\}$. From this representation of signal states, one can obtain the joint probability, $Y^{\omega j\alpha; k_\beta m_\beta}$ ($\omega \in \{X, Y, Z\}$), that Alice prepares any of the states $|\phi_{j\alpha}\rangle$ while Bob and Charlie measure them in the basis β and obtain bit values s and t . This can be realized through exploitation of transmission rate of the Pauli operators. Subsequently the joint probability, $Y^{\omega j\alpha; k_\beta m_\beta}$ can be used to estimate error rates in Equation 3 in order to obtain the value of C . Here, we show how to estimate the phase error rate E_{XX} ; other parameters can be obtained similarly. The parameter E_{XX} is computed by considering a virtual protocol where Alice prepares entangled state $|\Psi_Z\rangle = \frac{1}{\sqrt{2}}(|0\rangle_A |\phi_{0Z}\rangle_{B(C)} + |1\rangle_A |\phi_{1Z}\rangle_{B(C)})$, (B and C denote the subsystems sent to Bob and Charlie), and then Alice, Bob and Charlie measure their subsystems in the X basis. The error rate is expressed as

$$E_{XX} = \left(Y_{0_X;0_X1_X}^{Z,\text{vir}} + Y_{0_X;1_X1_X}^{Z,\text{vir}} + Y_{1_X;0_X1_X}^{Z,\text{vir}} + Y_{1_X;0_X0_X}^{Z,\text{vir}} + Y_{1_X;1_X0_X}^{Z,\text{vir}} + Y_{0_X;1_X0_X}^{Z,\text{vir}} \right) \\ \div \left(Y_{0_X;0_X1_X}^{Z,\text{vir}} + Y_{0_X;1_X1_X}^{Z,\text{vir}} + Y_{1_X;0_X1_X}^{Z,\text{vir}} + Y_{1_X;0_X0_X}^{Z,\text{vir}} + Y_{1_X;1_X0_X}^{Z,\text{vir}} + Y_{0_X;1_X0_X}^{Z,\text{vir}} \right) \\ + Y_{0_X;0_X0_X}^{Z,\text{vir}} + Y_{1_X;1_X1_X}^{Z,\text{vir}} \quad (4)$$

where $Y_{j_X; k_X m_X}^{Z,\text{vir}}$ denotes the joint probability that Alice, Bob and Charlie measured $|j_X\rangle$, $|k_X\rangle$ and $|m_X\rangle$, respectively. In this hypothetical protocol, the state of pulses received by Bob (Charlie) can be expressed as $\hat{\sigma}_{B(C);j_X}^{\text{vir}} = \text{Tr}_A[\hat{P}(|j_X\rangle_A) \otimes \mathbb{1}_{B(C)} \hat{P}(|\Psi_Z\rangle_{AB(C)})]$. Here, $\hat{P}(|x\rangle) = |x\rangle\langle x|$ corresponds to a projection operator for a particular pure state $|x\rangle$. The normalized state can be defined as $\hat{\sigma}_{B(C);j_X}^{\text{vir}} = \hat{\sigma}_{B(C);j_X}^{\text{vir}} / \text{Tr}(\hat{\sigma}_{B(C);j_X}^{\text{vir}})$. The joint probability that Alice, Bob and Charlie measure $|j_X\rangle$, $|k_X\rangle$ and $|m_X\rangle$, respectively is given by

$$Y_{j_X; k_X m_X}^{Z,\text{vir}} = p(j_X) \text{Tr}(\hat{D}_{k_X} \hat{\sigma}_{B;j_X}^{\text{vir}}) \text{Tr}(\hat{D}_{m_X} \hat{\sigma}_{C;j_X}^{\text{vir}}) \\ = p(j_X) Y_{j_X; k_X}^{Z,\text{vir}} Y_{j_X; m_X}^{Z,\text{vir}} \quad (5)$$

where $\hat{D}_{k_X(m_X)}$ is the operator that contains Eve's operation and Bob (Charlie)'s POVM measurement, $p(j_X)$ represents the probability that Alice chooses X basis and $Y_{j_X;k_X(m_X)}^{Z,\text{vir}}$ denotes yields of the states sent to Bob (Charlie). Since the virtual state $\hat{\sigma}_{B(C);j_X}^{\text{vir}}$ can also be expressed in terms of identity and Pauli operators as $\hat{\sigma}_{B(C);j_X}^{\text{vir}} = \frac{1}{2}(\mathbb{1} + \sum_{s(t)=x,y,z} \mathbf{n}_{s(t)}^{j_X} \hat{\sigma}_{s(t)}^{j_X})$, it follows that Equation 5 can be rewritten as $Y_{j_X;k_X(m_X)}^{Z,\text{vir}} = p(j_X) \sum_{s=X,Y,Z} \mathbf{n}_s q_{k_X|s} \sum_{t=X,Y,Z} \mathbf{n}_t q_{m_X|t}$. Therefore, to obtain $Y_{j_X;k_X(m_X)}^{Z,\text{vir}}$, it suffices to calculate the transmission rate of Pauli operators defined by $q_{k(m)_X|s(t)} = \text{Tr}(\hat{D}_{k(m)_X} \sigma_{s(t)})/2$ with $s, t \in \{1, X, Y, Z\}$. The parameter $\mathbf{n}_{s(t)}$ denotes the coefficient of Pauli matrices. To evaluate the yield of these states we employ the entanglement description where Alice prepares state $|\Psi_Z\rangle = \frac{1}{\sqrt{2}}(|0_Z\rangle_A |\phi_{0Z}\rangle_{B(C)} + |1_Z\rangle_A |\phi_{1Z}\rangle_{B(C)})$ in the Z basis and likewise the preparation of optical pulses in the complementary bases can be described as a process where Alice generates $|\Phi_X\rangle = |0_X\rangle_A |\phi_{0X}\rangle_{B(C)}$ or $|\Phi_Y\rangle = |0_Y\rangle_A |\phi_{0Y}\rangle_{B(C)}$. By using the same method previously described for the yield of virtual states, we obtain the expression for the yield of actual states as

$$\begin{aligned} Y_{j_\alpha;k_\beta m_\beta}^\omega &= p(j_\alpha) \text{Tr}(\hat{D}_{k_\beta} \rho_{j_\alpha}) \text{Tr}(\hat{D}_{m_\beta} \rho_{j_\alpha}) = p(j_\alpha) \sum_{s=X,Y,Z} \mathbf{n}_s q_{k_\beta|s} \sum_{t=X,Y,Z} \mathbf{n}_t q_{m_\beta|t} \\ &= p(j_\alpha) Y_{j_\alpha;k_\beta}^\omega Y_{j_\alpha;m_\beta}^\omega \end{aligned} \quad (6)$$

with $p(j_\alpha)$ denoting probability that Alice measures her subsystems as state j_α . The state ρ_{j_α} corresponds to one of the four states defined in Equation 3. The parameters $Y_{j_\alpha;k_\beta}^\omega$ and $Y_{j_\alpha;m_\beta}^\omega$ correspond to the yields of states sent to Bob and Charlie, respectively. We consider the cases where Bob (Charlie) measured the states sent by Alice in the X basis to determine the transmission rate of Pauli operators as follows

$$[Y_{0_Z;k_X(m_X)}^Z, Y_{1_Z;k_X(m_X)}^Z, Y_{0_X;k_X(m_X)}^X, Y_{0_Y;k_X(m_X)}^Y]^T = \frac{1}{64} \mathbf{A} [q_{k_X(m_X)|1}, q_{k_X(m_X)|x}, q_{k_X(m_X)|y}, q_{k_X(m_X)|z}]^T \quad (7)$$

where $\mathbf{A} = \begin{bmatrix} 1 & 0 & 0 & 1 \\ 1 & \sin(2\delta_1) & 0 & -\cos(2\delta_1) \\ 1 & \cos(2\Theta_2) & 0 & \sin(2\Theta_2) \\ 1 & \sin(2\Theta_3) & 0 & 0 \end{bmatrix}$. Here, $\Theta_2 = \frac{\pi}{4} + \frac{\delta_2}{2}$ and $\Theta_3 = \frac{3\pi}{4} + \frac{\delta_3}{2}$. The same logic can be applied to determine the yield of virtual states in terms of transmission rate as follows

$$[Y_{0_X;k_X(m_X)}^{Z,\text{vir}}, Y_{1_X;k_X(m_X)}^{Z,\text{vir}}]^T = \frac{1}{48} \mathbf{B} [q_{k_X(m_X)|1}, q_{k_X(m_X)|x}, q_{k_X(m_X)|y}, q_{k_X(m_X)|z}]^T \quad (8)$$

where

$$\mathbf{B} = \begin{bmatrix} (1 + \sin \delta_1) & \sin \delta_1 (1 + \sin \delta_1) & \cos \delta_1 (1 + \sin \delta_1) & 0 \\ (1 - \sin \delta_1) & -\sin \delta_1 (1 - \sin \delta_1) & -\cos \delta_1 (1 - \sin \delta_1) & 0 \end{bmatrix}. \quad (9)$$

By combining the results of Equations 7 and 8 we can deduce the yield of virtual states sent to Bob and Charlie. The results can then be used to obtain the virtual yield in Equation 5 and subsequently obtain the expression for error rate E_{XX} .

4. Estimation of key rate

The key generation rate for our proposed RFI QKD protocol is given by

$$r = Q_{ZZZ}^{\mu,1} (1 - I_E^U) - f_{EC} Q_{ZZZ}^\mu h(E_{ZZZ}^\mu). \quad (10)$$

To estimate the above parameters, we consider the channel model proposed in [6], where the yield of actual states is expressed as

$$\begin{aligned} Y_{j_\alpha;k_\beta m_\beta}^\omega &= \sum_{n=0}^{\infty} p(n|\gamma) \sum_{i=0}^n C_i^m (\eta_B t)^i (1 - \eta_B t)^{n-i} (\langle \phi_{k_\beta} | \phi_{j_\alpha} \rangle)^2 \chi(n) \sum_{n=0}^{\infty} p(n|\gamma) \sum_{i=0}^n C_i^n (\eta_C t)^i \\ &\quad \times (1 - \eta_C t)^{n-i} (\langle \phi_{m_\beta} | \phi_{j_\alpha} \rangle)^2 \chi(n), \end{aligned} \quad (11)$$

where $\chi(n) = \begin{cases} 1 - Y_0 & \text{if } n > 0 \\ Y_0(1 - Y_0) & \text{if } n = 0 \end{cases}$ and $C_i^n = n!/[i!(n-i)!]$ is the binomial coefficient. The term $p(n|\gamma) = (n+1)(\frac{\gamma}{2})^n/(1+\frac{\gamma}{2})^{n+2}$ denotes probability that the source emits n -photon pulse when modulated with intensity γ . The parameter $\eta_{B(C)}$ represents efficiency of Bob (Charlie)'s detection system and t denotes the total transmittance of the quantum channel. Y_0 corresponds to the background count rate. According to the decoy-state theory, the overall gain is [9]

$$Q_{j_\alpha; k_\beta m_\beta}^{\omega, \gamma} = \sum_{n=0}^{\infty} Y_n \frac{\mu^n}{n!} e^{-\mu} = \frac{1}{2} \left\{ [1 + (1 - e_d)[e^{(-\eta_B t + a\eta_B t)\gamma} - e^{-a\eta_B \gamma t} - (1 - e_d)e^{\eta_B \gamma t}]] \right. \\ \left. \times [1 + (1 - e_d)[e^{(-\eta_C t + b\eta_C t)\gamma} - e^{-b\eta_C \gamma t} - (1 - e_d)e^{\eta_C \gamma t}]] \right\}, \quad (12)$$

where $a = (\langle \phi_{k_\beta} | \phi_{j_\alpha} \rangle)^2$, $b = (\langle \phi_{m_\beta} | \phi_{j_\alpha} \rangle)^2$ and e_d corresponds to the erroneous detection. Additionally, the overall gain in the Z basis is expressed as

$$Q_{ZZZ}^\mu = (Q_{0Z;0Z0Z}^{Z,\mu} + Q_{0Z;0Z1Z}^{Z,\mu} + Q_{0Z;1Z0Z}^{Z,\mu} + Q_{0Z;1Z1Z}^{Z,\mu} + Q_{1Z;0Z0Z}^{Z,\mu} + Q_{1Z;0Z1Z}^{Z,\mu} + Q_{1Z;1Z0Z}^{Z,\mu} \\ + Q_{1Z;1Z1Z}^{Z,\mu}) \quad (13)$$

and the corresponding quantum bit error rate is $E_{ZZZ}^\mu = (Q_{0Z;0Z1Z}^{Z,\mu} + Q_{0Z;1Z0Z}^{Z,\mu} + Q_{0Z;1Z1Z}^{Z,\mu} + Q_{1Z;0Z0Z}^{Z,\mu} + Q_{1Z;0Z1Z}^{Z,\mu} + Q_{1Z;1Z0Z}^{Z,\mu})/Q_{ZZZ}^\mu$. The gain for single photon components in the Z basis is expressed as $Q_{ZZZ}^{\mu,1} = \mu e^{-\mu} (Y_{0Z;0Z0Z}^{Z,1} + Y_{0Z;0Z1Z}^{Z,1} + Y_{0Z;1Z0Z}^{Z,1} + Y_{0Z;1Z1Z}^{Z,1} + Y_{1Z;0Z0Z}^{Z,1} + Y_{1Z;0Z1Z}^{Z,1} + Y_{1Z;1Z0Z}^{Z,1} + Y_{1Z;1Z1Z}^{Z,1})$. The parameter I_E^U is estimated from value of C and upper bound on the error rate, $E_{ZZZ}^{1,U}$ from single-photon contributions as shown in Equation 1. The parameter $E_{ZZZ}^{1,U}$ is estimated from the yield of single photons as follows

$$E_{ZZZ}^{1,U} = (E_{ZZZ}^\mu Q_{ZZZ}^\mu - e_0 Y_0 e^{-\mu}) \div (e^{-\mu} (Y_{0Z;0Z0Z}^{1,L} + Y_{0Z;0Z1Z}^{1,L} + Y_{0Z;1Z0Z}^{1,L} + Y_{0Z;1Z1Z}^{1,L} \\ + Y_{1Z;0Z0Z}^{1,L} + Y_{1Z;0Z1Z}^{1,L} + Y_{1Z;1Z0Z}^{1,L} + Y_{1Z;1Z1Z}^{1,L})), \quad (14)$$

where $Y_{j_\alpha; k_\beta m_\beta}^{1,L} = \frac{\mu}{\mu\nu - \nu^2} [Q_{j_\alpha; k_\beta m_\beta}^\nu - Q_{j_\alpha; k_\beta m_\beta}^\mu \frac{\nu^2}{\mu^2} - \frac{\mu^2 - \nu^2}{\mu^2} Q_0]$. The values $Q_{j_\alpha; k_\beta m_\beta}^\mu$, $Q_{j_\alpha; k_\beta m_\beta}^\nu$ are gains obtained on conditional probabilities that Alice prepares the state j_α , while Bob and Charlie measure the states k_α , m_β , and Q_0 is the background gain.

5. Simulation results

We simulate the performance of the proposed protocol on a fiber-based QKD system model. The plots in Figure 2a were obtained with $\delta = 0.35$, $\delta = 0.20$ and $\delta = 0.10$, which correspond to deviation of 20.05° , 11.46° and 5.73° from the desired phase angle, respectively. For comparison, we plotted the curve for $\delta = 0$, which corresponds to a perfect encoding scenario. The characterization of parameter δ is based on its relation to the extinction ratio according to the definition; $|\tan(\delta/2)|^2 = \eta_{ex}$ [11]. The non-zero extinction ratio is mainly due to imperfections in phase modulators and is of order 10^{-3} in typical experiments. The results demonstrate that the key rates achieved are comparable to the perfect encoding scenario despite increased encoding flaws. In Figure 2b, we simulate the secret key rate for three-party RFI protocol as a function of transmission distance for fixed misalignment degree $\beta = 0, \pi/5, \pi/6$ and $\pi/7$. Despite the increase in misalignment of reference frames, the achievable key rates are comparable to when there is no misalignment in reference frames (when $\beta = 0$). Also, we simulate the key rate for the two-party RFI protocol (red lines) for the same parameters in Figure 2a and Figure 2b. It is evident from both figures that the two-party RFI protocol outperforms our proposed three-party RFI protocol in terms of achievable secret key rate for different encoding source flaws and misalignment degrees of β . Nevertheless, our proposed protocol is more resourceful for secure communication tasks involving multiple parties since a secret key for each party is generated

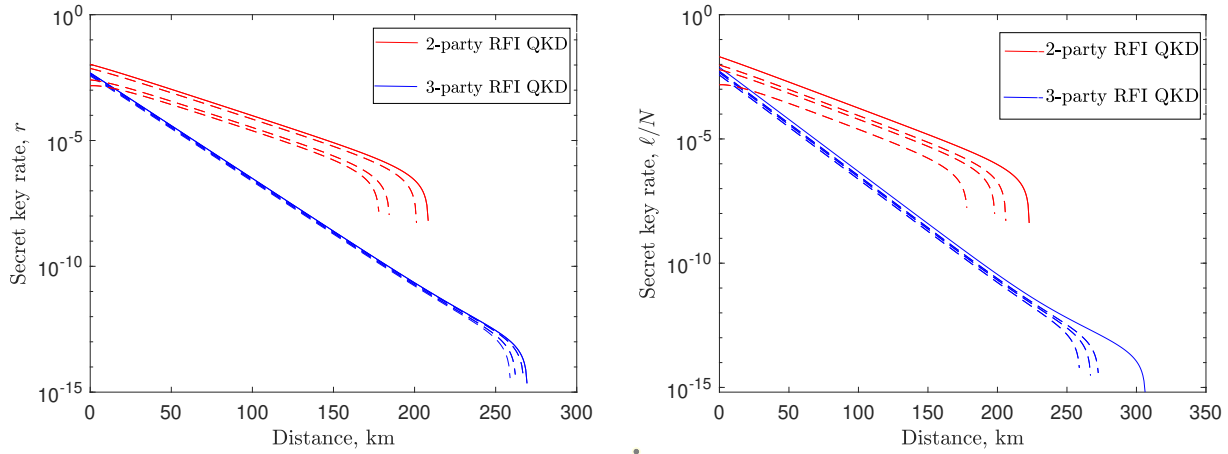


Figure 2: Comparison of our protocol with the two-party RFI QKD protocol, (red lines). (a) Expected secret key rate (in logarithmic scale) for the proposed protocol (blue lines) as a function of distance measured in km, for the fixed encoding source flaws δ . From left to right, the curves represent $\delta = 0.35$, $\delta = 0.20$, $\delta = 0.10$ and $\delta = 0$ (blue solid line). The relative rotation of reference frames is set at $\beta = \pi/5$. (b) Expected secret key rate for the proposed protocol (blue lines) as a function of distance measured in km, for the fixed misalignment degree β . From left to right, the curves represent $\beta = \pi/5$, $\beta = \pi/6$, $\beta = \pi/7$ and $\beta = 0$ (blue solid line). The encoding source flaws are fixed at $\delta = 0.10$, dark counts rate, $P_d = 1.7 \times 10^{-6}$, loss channel coefficient $= 0.2$ km/dB, detection efficiency $\eta = 14.5\%$, error correction efficiency, $f_{EC} = 1.22$ and expected photon number for signal states, $\mu = 0.6$, and optimal probability, $p_z = 0.95$ [10].

from a single execution of the protocol. On the contrary, if the two-party QKD protocol is employed in a multiparty communication scenario, multiple protocols need to be performed to establish a secret key for each party.

6. Conclusion

We presented a three-party RFI QKD protocol to be implemented without alignment between the parties. We investigated the performance of our proposed protocol for encoding flaws, and despite the state preparation flaws, the key rates achieved are comparable to those of perfect encoding scenarios. Furthermore, we performed a simulation for the variation of the secret key rate concerning transmission distance for different misalignment degrees ($\beta = \pi/6, \pi/8$) to investigate the impact of the shift in the reference frames on statistical quantity C and stability of the protocol. We demonstrated that our protocol is affected only moderately by an increase in misalignment of reference frames.

References

- [1] Gisin N, Ribordy G, Tittel W and Zbinden H 2002 *Rev. Mod. Phys.* **74**(1) 145–195
- [2] Mafu M 2013 *Security in quantum key distribution protocols* Ph.D. thesis
- [3] Bennett C H and Brassard G 2014 *Theoretical Computer Science* **560** 7–11
- [4] Laing A, Scarani V, Rarity J and O'Brien J 2010 *Physical Review A* **82** 012304
- [5] Sekga C and Mafu M 2021 *Journal of Physics Communications* **5** 045008
- [6] Sekga C and Mafu M 2021 *Chinese Physics B* **30** 120301
- [7] Mafu M, Sekga C and Senekane M 2021 *Scientific African* e01008
- [8] Tamaki K, Curty M, Kato G, Lo H K and Azuma K 2014 *Physical Review A* **90** 052314
- [9] Lo H K, Ma X and Chen K 2005 *Physical Review Letters* **94** 230504
- [10] Wei Z, Wang W, Zhang Z, Gao M, Ma Z and Ma X 2013 *Sci. Rep.* **3** 2453
- [11] Tamaki K, Lo H K, Fung C H F and Qi B 2012 *Physical Review A* **85** 042307

B and D meson Suppression and Azimuthal Anisotropy in a Strongly Coupled Plasma at $\sqrt{s_{NN}} = 5.5$ TeV

B A Ngwenya¹ and W A Horowitz¹

¹Department of Physics, University of Cape Town, Rondebosch 7700, South Africa

E-mail: ngwble001@myuct.ac.za, wa.horowitz@uct.ac.za

Abstract. We present predictions for the suppression and angular distribution of B and D mesons in $\sqrt{s} = 5.5$ TeV Pb+Pb collisions at the LHC for central, semi-central and peripheral collisions. We assume that the QGP produced at the LHC is strongly coupled and that the heavy quarks are strongly coupled to the QGP, and we employ the Langevin energy loss model with parameters from AdS/CFT. To account for the theoretical systematic uncertainties related to how the diffusion is computed across the two theories (i.e. QCD and $\mathcal{N} = 4$ SYM), we use a momentum dependent and momentum independent diffusion coefficient. We also estimate theoretical systematic uncertainties due to the mapping of parameters between the two theories, by using two sets of parameters; one where the temperature of the plasmas in the two theories is equated, and another where the energy densities of the plasmas are equated. We show that the $R_{AA}(p_T)$ increases with centrality and that the $v_2(p_T)$ is largest in semi-central collisions.

1. Introduction

Heavy-ion collisions have been successful in recreating the conditions of the early universe [1, 2], thus allowing us to probe and build our understanding of the hot-QCD matter that filled the universe shortly after the Big Bang. During a heavy-ion event, some of the incident partons experience hard perturbative interactions and result in the production of high- p_T particles [1]. These high- p_T particles are the most direct probe of the relevant degrees of freedom in a QGP [3]; they lose energy as they propagate through the QGP medium [4], and studying this energy loss allows us to measure the physics of QGP. In particular, we focus on heavy quarks (HQ) since they are produced very early in the collision and act as identifiable test particles (ideal probes), navigating the whole evolution of the QGP medium as they participate in and are affected by its dynamics, but remain conserved [5].

One way of conceptualising how high- p_T particles interact with the medium is via the weak coupling picture, tackled using pQCD techniques [6]. As the HQ propagate through the QGP medium, they scatter off the various constituents of the medium, leading to radiative and collisional energy loss [7, 8]. Weak coupling energy loss models have had success in describing RHIC and LHC data for both light and heavy flavoured particles [6].

In this paper, we will take the strong coupling view (i.e. the heavy quark is strongly coupled to a plasma that is also strongly coupled) to study this HQ energy loss. Since the relevant scale for HQ energy loss is the typical momentum transfer during interactions [7, 9] (which also

informs the HQ diffusion in the QGP), weak coupling techniques can't be applied in processes involving a small momentum transfer since non-perturbative corrections become important, but are impossible to calculate using weak coupling techniques [10]. This regime where the momentum transfer is small, is the regime where QCD matter is strongly coupled [11], and we resort to AdS/CFT techniques to perform energy loss calculations [12, 13]. AdS/CFT energy loss has previously shown a massive over-suppression of high- p_T light/heavy flavour compared to data [3, 14]; however, more recent work [15, 16] shows a jet nuclear modification factor that is quantitatively consistent with preliminary CMS data.

In addition to the energy loss, the heavy quarks propagate through a 'different looking' medium depending on the angle in which they are produced; for example, the quark travels a different distance depending on its production angle for the various centrality classes, and experiences a different temperature profile. This difference in the medium results in the suppression of these heavy quarks having an azimuthal dependence, and we will also present results for this azimuthal dependence.

2. Langevin energy loss model

The energy loss model that we have employed was developed in [13] and a further discussion and application of the model can be found in [17, 18]. We obtain the production spectrum of the heavy quarks from FONLL calculations [19, 20] for $Pb + Pb$ collisions at $\sqrt{s_{NN}} = 5.5$ TeV and $|y| < 1$. The heavy quarks are assumed to be produced in the transverse plane (with the production angles following a uniform distribution) at an initial time, t_0 . This production procedure is described by the Optical Glauber model [21], and for our purposes, we have used ^{208}Pb nuclei and the corresponding parameters can be found in [22].

Once the heavy quark has been produced in the geometry, at thermalisation time ($t \sim 0.6$ fm/c), the hydrodynamic background forms and the heavy quark propagates through it while interacting with the medium. These hydrodynamic backgrounds (used for medium evolution) are generated by VISHNU 2+1D viscous relativistic hydrodynamics [23, 24]. Then the dynamics of the heavy quark interacting with the QGP medium (hydrodynamic background) as it propagates through it, are described by the Langevin equation,

$$\frac{dp_i}{dt} = -\mu p_i + F_i^L + F_i^T, \quad (1)$$

in the fluid's rest frame, where p^i is the three-momentum of an on-shell heavy quark that is moving with constant velocity in the plasma and μ is the drag loss coefficient of a heavy quark [25]. The stochastic forces (diffusion terms) F_i^L and F_i^T are the longitudinal and transverse momentum kicks with respect to the quark's direction of propagation.

In computing the strongly coupled energy loss, we employ results from AdS/CFT [11, 12, 26]. However, there arise theoretical systematic uncertainties related to how the diffusion is computed across the two theories (i.e. QCD and $\mathcal{N} = 4$ SYM). In [25], it is shown that the diffusion coefficient grows as $\sim \gamma^{5/2}$ in the longitudinal direction, where γ is the Lorentz gamma factor. This result comes from forcing the heavy quark to move at a constant velocity by use of an external force, and the work of [27] suggests instead, that the diffusion coefficient should be momentum independent in the case where the heavy quark does not experience this forced motion. In order to account for these uncertainties, we use two different diffusion coefficients; one that is dependent on momentum, $D(p)$, and one that does not depend on the heavy quark momentum, $D = const.$

In the scenario where the diffusion coefficient is dependent on momentum, the drag (μ) and diffusion (D) are given by [13],

$$\mu = \frac{\pi\sqrt{\lambda}T^2}{2M_Q}, \quad D = \frac{2T^2}{\kappa_L}, \quad (2)$$

where M_Q is the mass of the heavy quark in a plasma of temperature T , λ is the 't Hooft coupling constant, $\kappa_L = \pi\sqrt{\lambda}T^3\gamma^{5/2}$ is the mean squared longitudinal momentum transfer per unit time, and carries the momentum dependence of the diffusion. Note that this construction of parameters does not obey the fluctuation-dissipation theorem [13] and the transport scheme only leads to thermalization in the $p_T \rightarrow 0$ limit where the fluctuation-dissipation theorem is satisfied.

On the other hand, in the scenario where the diffusion coefficient does not depend on the heavy quark's momentum, the drag (μ) and diffusion (D) are given by [11, 27]:

$$\mu = \frac{\pi\sqrt{\lambda}T^2}{2E}, \quad D = \frac{T}{M_Q\mu} = \frac{2T^2}{\kappa}, \quad (3)$$

where in this scenario, $\kappa = \pi\sqrt{\lambda}T^3$ does not contain a momentum dependence and E is the energy of the heavy quark in the local fluid rest frame. In this scenario, the momentum fluctuations are required to obey the fluctuation-dissipation theorem and the drag and diffusion are related by the Einstein relations.

The drag and diffusion coefficients in both the $D(p)$ and $D = \text{const}$ cases have a temperature and 't Hooft coupling dependence. The mapping of these parameters between the two theories (i.e. QCD and $\mathcal{N} = 4$ SYM) also introduces theoretical systematic uncertainties to our energy loss calculation. To account for these uncertainties, we have used two sets of parameters as outlined below [13, 28]:

- (i) **Equal Temperature and Parameters (ET):** $T_{SYM} = T_{QCD}$, $\lambda = 4\pi \times 0.3 \times 3 \simeq 11.3$.
- (ii) **Equal Energy Density and HQ Potential (EE):** $T_{SYM} = \frac{1}{3^{1/4}}T_{QCD}$, $\lambda = 5.5$.

The ET parameters compare QCD to $\mathcal{N} = 4$ SYM theory at the same temperature and the 't Hooft coupling is fixed by equating the coupling in the two theories. On the other hand, for EE parameters, the energy densities between the two plasmas (i.e. QCD and $\mathcal{N} = 4$ SYM plasma) are equated, resulting in the temperature relation given in (ii). The 't Hooft' coupling is then computed by comparing the static force between a quark and antiquark between the two theories, which yields $\lambda = 5.5$ [12]. Further discussions on the energy loss model and the various parameters we have employed can be found in [13, 17, 27, 29].

3. Results

The results of this paper are the comparison of the nuclear modification factor, $R_{AA}(p_T)$, and the $v_2(p_T)$ for B and D mesons at $\sqrt{s_{NN}} = 5.5$ TeV, $|y| < 1$ for $Pb + Pb$ collisions in central, semi-central and peripheral collisions. The $R_{AA}(p_T)$ and $v_2(p_T)$ are defined as follows:

$$R_{AA}(p_T) = \frac{dN^{AA}/dp_T}{\langle N_{coll} \rangle dN^{pp}/dp_T} \quad (4)$$

$$R_{AA}(p_T, \phi) = R_{AA}(p_T) [1 + 2v_2(p_T) \cos(2\phi)]. \quad (5)$$

The results will compare the four different scenarios discussed in the previous section, i.e. a momentum dependent and independent diffusion coefficients, $D(p)$ and $D = \text{const}$ respectively, as well as the ET and EE parameters. The horizontal bars represent the bin widths, while the vertical bars represent the statistical uncertainties.

In Figure 1, we show the centrality (a measure of how far apart the centres of two colliding nuclei are) dependence of $R_{AA}(p_T)$ for the EE, $D(p)$ parameters for B and D mesons. There is less suppression as we move from central to peripheral collisions (for both B and D mesons). This is due to the initial geometry of the colliding nuclei; in peripheral collisions, less QGP is produced and the heavy quarks spend less time in the QGP medium and lose less energy

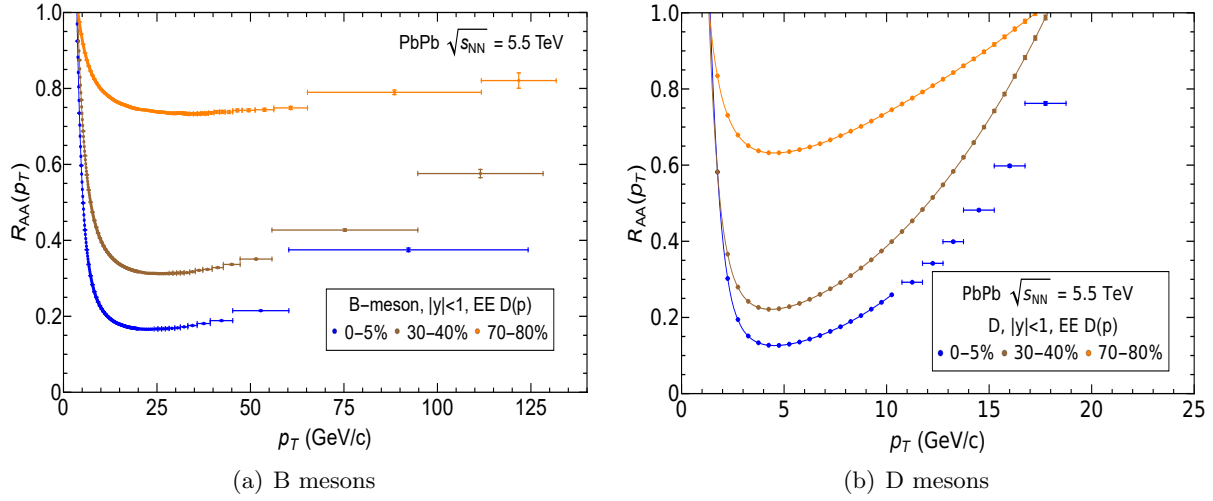


Figure 1. $EE, D(p)$ $R_{AA}(p_T)$ at $\sqrt{s_{NN}} = 5.5$ TeV for centrality classes 0-5% up to 70-80%.

compared to central collisions. The centrality dependence for the rest of the other parameters behaves similarly and is discussed in [29] for B mesons.

We then compare the $R_{AA}(p_T)$ for the different parameters we have employed for B and D meson semi-central collisions in Figure 2. Notice that the models employing $D(p)$ parameters break down around $p_T \sim 15$ GeV/c for D mesons due to the fluctuations growing rapidly with p_T (this can also be seen in Figure 1 for the various centrality classes). These fluctuations are more pronounced for D mesons compared to B mesons due to the low mass of charm quarks, thus these parameters have a limit of $p_T \sim 15$ GeV/c for D mesons. Despite the rapidly growing fluctuations in the $D(p)$ case for B mesons, the models employing $D = const$ parameters show a stronger momentum dependence due to the drag being extracted from the fluctuation-dissipation theorem, which results in a μ that is inversely proportional to the energy of the heavy quark as shown in Equation 3.

The drag coefficient, μ , has the largest contribution to the energy loss, in the EE prescription, the 't Hooft coupling is smaller by ~ 2 and T is lower, so the drag for EE parameters is smaller compared to ET parameters and results in less suppression. This difference in μ between the two parameters is clearly reflected in our results shown in Figure 2 as the EE curves show a higher $R_{AA}(p_T)$ compared to ET curves for the same diffusion coefficient.

In Figure 3, we show the centrality dependence of the $v_2(p_T)$ for B and D mesons respectively. The $v_2(p_T)$ is low for central collisions and increases as we move up in centrality to semi-central collisions as a result of the increase in the geometrical asymmetry in the collision overlap region. The $v_2(p_T)$ is largest in semi-central collisions where the spatial anisotropy is largest and converts to a large momentum anisotropy and consequently large v_2 . Generally, for the $D(p)$ scenario shown in Figure 3, the $v_2(p_T)$ is larger at low p_T for D mesons compared to B mesons at fixed centrality, and this is related to the strong fluctuations experienced by charm quarks due to their lower mass compared to bottom.

We have also shown the B and D meson comparison of the $v_2(p_T)$ predictions for each set of parameters for semi-central collisions (where we obtain the largest v_2) in Figure 4. Notice the anti-correlation of these $v_2(p_T)$ predictions to the $R_{AA}(p_T)$ results shown in Figure 2. We obtain the largest $v_2(p_T)$ for $ET, D(p)$ parameters, which corresponds to the $R_{AA}(p_T)$ and vice-versa. This anti-correlation is understood as follows: a larger energy loss implies that quarks are more sensitive to changes in geometry and thus results in a larger v_2 .

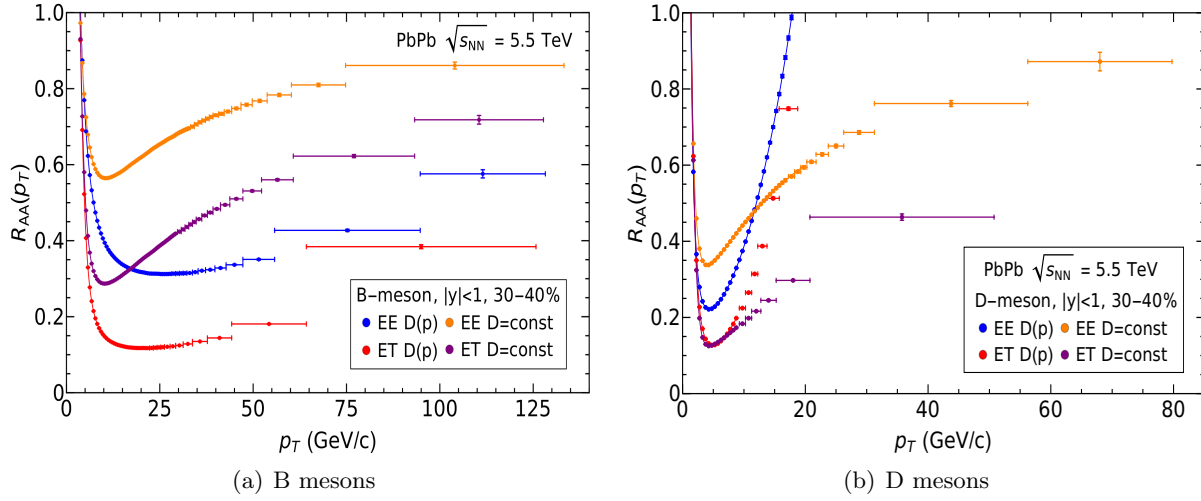


Figure 2. B and D-meson $R_{AA}(p_T)$ for various parameters at $\sqrt{s_{NN}} = 5.5$ TeV for the 30-40% centrality class.

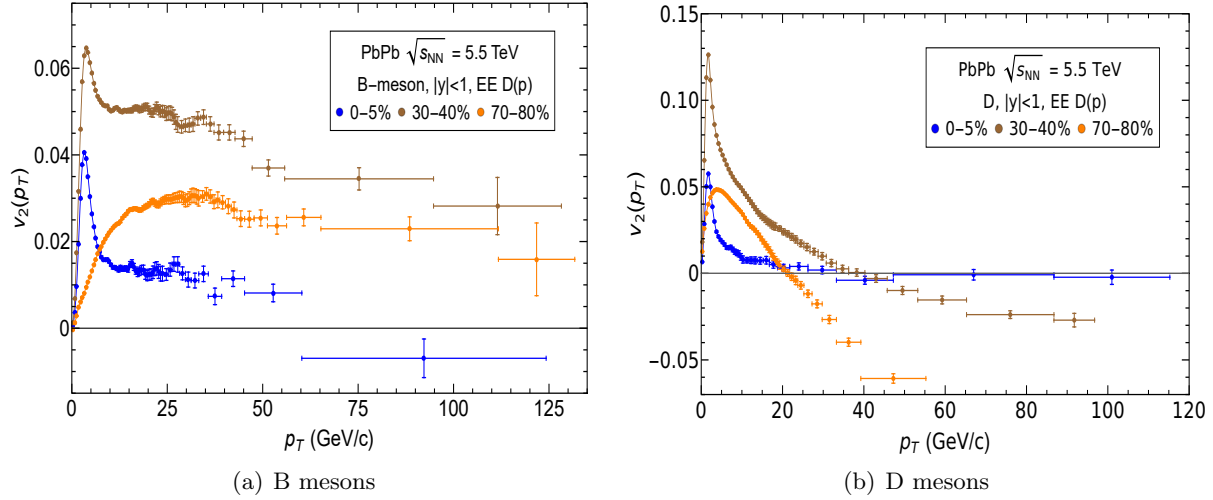


Figure 3. EE , $D(p)$ $v_2(p_T)$ at $\sqrt{s_{NN}} = 5.5$ TeV for various centrality classes.

4. Conclusions

We have presented quantitative predictions for the $R_{AA}(p_T)$ and $v_2(p_T)$ for B and D mesons at $\sqrt{s_{NN}} = 5.5$ TeV for central, semi-central and peripheral collisions assuming a strongly coupled plasma and employing AdS/CFT techniques. These predictions have been made using four different sets of parameters to account for the theoretical systematic uncertainties due to the mapping of parameters in QCD and $\mathcal{N} = 4$ SYM.

We showed that the $R_{AA}(p_T)$ increases with centrality for both B and D mesons, which is expected as a result of the changing geometry with centrality. The model employing $D(p)$ parameters breaks down at high- p_T due to the growing fluctuations and is unreliable for D mesons for $p_T \gtrsim 15$ GeV/c, and EE parameters show less suppression compared to ET parameters due to the lower T and λ . We also showed that the $v_2(p_T)$ is largest in semi-central collisions where the geometrical asymmetry is largest, and is anti-correlated with the $R_{AA}(p_T)$. The peak in v_2 is larger for D mesons compared to B mesons, both for fixed centrality and fixed parameter

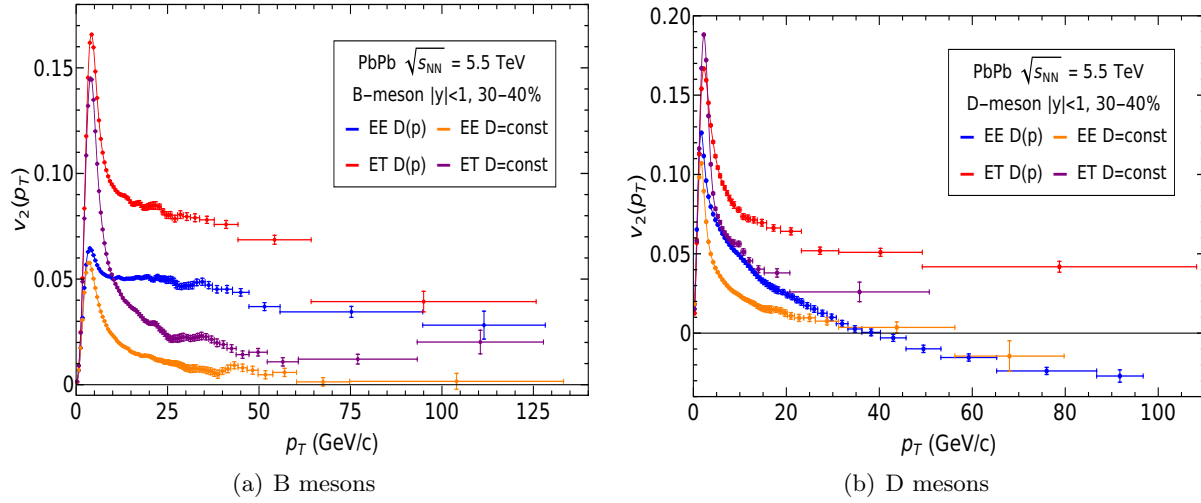


Figure 4. B and D-meson $v_2(p_T)$ at $\sqrt{s_{NN}} = 5.5$ TeV for the 30-40% centrality class.

set, which is a result of the lower mass of charm quarks that makes them more sensitive to the medium flow. A further discussion on B meson results at $\sqrt{s_{NN}} = 5.5$ TeV for other centralities and parameters can be found in [29].

One can also perform these calculations for other collision systems such as $Xe + Xe$ and this is left for future work. We would also like to incorporate pre-thermalisation energy loss effects (possibly following a pQCD approach), which could provide insights on the motion of the heavy quark prior the applicability of hydrodynamics.

Acknowledgments

The authors would like to acknowledge the SA-CERN Collaboration and the South African National Research Foundation (NRF) for their generous financial contributions towards this work.

References

- [1] Busza W, Rajagopal K and van der Schee W 2018 *Ann. Rev. Nucl. Part. Sci.* **68** 339–376 (*Preprint* 1802.04801)
- [2] Toia A (ALICE) 2011 *J. Phys. G* **38** 124007 (*Preprint* 1107.1973)
- [3] Horowitz W A 2013 *Nucl. Phys. A* **904-905** 186c–193c (*Preprint* 1210.8330)
- [4] Bjorken J D 1982 Energy loss of energetic partons in quark-gluon plasma: possible extinction of high p_T jets in hadron-hadron collisions Tech. rep. FERMILAB Batavia, IL
- [5] Dong X, Lee Y J and Rapp R 2019 *Ann. Rev. Nucl. Part. Sci.* **69** 417–445 (*Preprint* 1903.07709)
- [6] Djordjevic M, Djordjevic M and Blagojevic B 2014 *Phys. Lett. B* **737** 298–302 (*Preprint* 1405.4250)
- [7] Berrehrah H, Bratkovskaya E, Cassing W, Gossiaux P B, Aichelin J and Bleicher M 2014 *Phys. Rev. C* **89** 054901 (*Preprint* 1308.5148)
- [8] Wu B 2015 Radiative energy loss and radiative p_\perp - broadening of high-energy partons in QCD matter *7th International Conference on Hard and Electromagnetic Probes of High-Energy Nuclear Collisions* (*Preprint* 1509.07483)
- [9] Kharzeev D E 2009 *Eur. Phys. J. C* **61** 675–682 (*Preprint* 0809.3000)
- [10] Snellings R 2011 *New J. Phys.* **13** 055008 (*Preprint* 1102.3010)
- [11] Casalderrey-Solana J and Teaney D 2006 *Phys. Rev. D* **74** 085012 (*Preprint* hep-ph/0605199)
- [12] Gubser S S 2006 *Phys. Rev. D* **74** 126005 (*Preprint* hep-th/0605182)
- [13] Horowitz W A 2015 *Phys. Rev. D* **91** 085019 (*Preprint* 1501.04693)
- [14] Horowitz W A 2012 *AIP Conf. Proc.* **1441** 889–891 (*Preprint* 1108.5876)
- [15] Morad R and Horowitz W A 2014 *JHEP* **11** 017 (*Preprint* 1409.7545)
- [16] Akamatsu Y, Hatsuda T and Hirano T 2009 *Phys. Rev. C* **79** 054907 (*Preprint* 0809.1499)

- [17] Hambrock R and Horowitz W A 2017 *Nucl. Part. Phys. Proc.* **289-290** 233–236 (*Preprint* 1703.05845)
- [18] Hambrock R and Horowitz W A 2018 *EPJ Web Conf.* **171** 18002 (*Preprint* 1802.02442)
- [19] Cacciari M, Greco M and Nason P 1998 *JHEP* **05** 007 (*Preprint* hep-ph/9803400)
- [20] Cacciari M, Frixione S, Houdeau N, Mangano M L, Nason P and Ridolfi G 2012 *JHEP* **10** 137 (*Preprint* 1205.6344)
- [21] Miller M L, Reygers K, Sanders S J and Steinberg P 2007 *Ann. Rev. Nucl. Part. Sci.* **57** 205–243 (*Preprint* nucl-ex/0701025)
- [22] Loizides C, Kamin J and d’Enterria D 2018 *Phys. Rev. C* **97** 054910 [Erratum: *Phys.Rev.C* 99, 019901 (2019)] (*Preprint* 1710.07098)
- [23] Shen C, Heinz U, Huovinen P and Song H 2011 *Phys. Rev. C* **84** 044903 (*Preprint* 1105.3226)
- [24] Qiu Z, Shen C and Heinz U 2012 *Phys. Lett. B* **707** 151–155 (*Preprint* 1110.3033)
- [25] Gubser S S 2008 *Nucl. Phys. B* **790** 175–199 (*Preprint* hep-th/0612143)
- [26] Herzog C P, Karch A, Kovtun P, Kozcaz C and Yaffe L G 2006 *JHEP* **07** 013 (*Preprint* hep-th/0605158)
- [27] Moerman R W and Horowitz W A 2016 (*Preprint* 1605.09285)
- [28] Gubser S S 2007 *Phys. Rev. D* **76** 126003 (*Preprint* hep-th/0611272)
- [29] Ngwenya B A and Horowitz W A 2020 (*Preprint* 2011.07617)

Factorisation in Heavy Ion Collisions

W. A. Horowitz

Department of Physics, University of Cape Town, Private Bag X3, Rondebosch 7701, South Africa

E-mail: wa.horowitz@uct.ac.za

Abstract. We present our latest findings on the status of factorisation in heavy ion collisions. We show that energy loss calculations that assume factorisation yield results consistent with factorisation: the leading order in energy asymptotics for the mean transverse momentum squared picked up by a high energy particle propagating through a quark-gluon plasma is double logarithmic. Further, the leading order behaviour for the difference in jet sizes in medium vs. in vacuum is negative; i.e. we predict jet narrowing in heavy ion collisions. This qualitative result is consistent with recent experimental measurements.

1. Introduction

A microsecond after the Big Bang the universe cooled to a chilly trillion degrees, at which point all of space was filled with a novel state of matter: the quark-gluon plasma (QGP). As the universe continued to cool and expand, the dynamics of this early stage of its history imprinted itself; further dynamics then propagated these initial conditions to the large-scale structure of the universe as we know it today.

From a theoretical perspective, the non-trivial, emergent many-body dynamics of quantum field theories is an active and interesting open area of research [1–4]. Even “simple” systems that depend only on the Abelian electromagnetic force show a wealth of extremely important behaviours that are currently not well understood from first principles: e.g. the phase structure of water [5] or high temperature superconductivity [6]. We’re naturally led to consider the non-Abelian generalisation of many-body dynamics in quantum field theories in order to compare and contrast with the Abelian case and also because the non-Abelian case may be in some ways richer and in some ways simpler than the Abelian one [1–4, 7].

Experimentally, incredibly, we have the ability to probe these non-trivial, emergent, many-body dynamics of a non-Abelian theory and also the physics of the early universe through heavy ion collisions at the Relativistic Heavy Ion Collider (RHIC) and the Large Hadron Collider (LHC). One of the most important experimental tools for investigating the properties of the QGP produced in these heavy ion collisions is known as “hard probes” [8]. Hard probes are particles with a large scale (mass or energy) that are produced in the initial overlap of nuclei in these nuclear collisions. These particles subsequently propagate through the medium created by the collisions. The idea is that measuring the difference in distribution of these particles in heavy ion collisions compared to the distribution of these particles when produced in much smaller collision systems (in angle, momentum, etc.) will provide insight into the properties of the QGP.

In order to connect the measured distribution of particles to properties of the QGP, we need theoretical calculations. For the particular case of hard probes, one avenue is to assume that the hard probes is weakly coupled to a weakly coupled QGP medium. One then derives expressions for the amount of energy lost from the hard probe to the QGP as the probe propagates through the medium [9–17]. Phenomenological models built on these energy loss calculations have shown great success in describing experimental data [18–20]. One important avenue for research going forwards is to put these energy loss derivations on more solid theoretical footing. In particular, it's important to understand how the corrections to the current leading order results might scale with, e.g., the energy of the probe.

2. Factorisation in QCD

In many simpler QCD systems, e.g. deep inelastic scattering (DIS), semi-inclusive deep inelastic scattering (SIDIS), Drell-Yan production (DY), etc., theoretical predictions are known to be of a *factorised* form [21]. These factorised formulae share two important aspects. First, the high-energy (or hard scale), short distance physics is factorised from the low-energy, non-perturbative physics. Second, it's known that the corrections to these factorised formulae are down by a very large energy scale $\sim 1/Q^2$, $Q \gg \Lambda_{QCD}$, where Λ_{QCD} characterises the energy scale at which non-perturbative physics sets in in QCD. What we would like to do, then, is work towards a factorised form for energy loss calculations in heavy ion collisions.

As a first step in that programme, we would like to compare a result computed within the factorised approach and one within the energy loss approach. One such observable is the mean transverse momentum squared picked up by the hard probe as it propagates through the medium, $\langle p_T^2 \rangle$. The factorised approach to this SIDIS-type calculation has been computed to next-to-leading order accuracy [22, 23], which is to say up to corrections including radiative (energy loss) emissions. Similar to other factorised DIS and SIDIS calculations [21], this factorised approach yields a type of parton distribution function with DGLAP-like evolution equations induced by the NLO contributions. Since the leading order contribution is from elastic scattering and should grow like $\log(E)$, we expect that the evolution equations will lead to an additional logarithmic growth in energy. While an explicit calculation has not been performed yet, we thus expect an overall $\log^2(E)$ dependence from the factorised approach for $\Delta \langle p_T^2 \rangle$, the *difference* in transverse momentum squared picked up by the parton in medium minus the transverse momentum picked up by the parton through vacuum radiation emissions. In the following, we investigate the leading energy asymptotics of $\langle p_T^2 \rangle$ as computed within the energy loss approach.

3. Energy Loss at High Energy

In the limit of massless particles and the soft and collinear emission of gluon radiation off of a high-energy parton propagating through a weakly-coupled QGP, the single inclusive distribution of emitted radiation in medium (minus the radiation emitted by a hard scattering in vacuum) is given by [11]:

$$\frac{dN^g}{dx d^2\mathbf{k}_T d^2\mathbf{q}_T} = \frac{C_R \alpha_s L}{2\pi^2} \frac{1}{\lambda} \frac{1}{k_T^2} \frac{\mu^2}{\pi(q_T^2 + \mu^2)^2} \frac{2\mathbf{k}_T \cdot \mathbf{q}_T (\mathbf{k}_T - \mathbf{q}_T)^2}{(4xE/L)^2 + (\mathbf{k}_T - \mathbf{q}_T)^4}, \quad (1)$$

where C_R is the colour Casimir relevant for the gluon or quark parton, \mathbf{q}_T is the transverse momentum picked up by the parton from the medium, x is the (lightcone plus) momentum fraction taken by the emitted gluon from the parton, \mathbf{k}_T is the transverse momentum of the emitted gluon, $L \sim 5$ fm is the length of the plasma traversed by the parton, $\lambda \sim 1$ fm is the mean free path of a gluon in the plasma, and $\mu \sim 0.5$ GeV is the Debye mass of the plasma. The upper bound of the \mathbf{q}_T integration is set to $q_{max} \equiv \sqrt{3\mu E}$, which is the kinematic bound for elastic $2 \rightarrow 2$ scattering of two massless particles, one with energy E and one with a thermal

momentum of $\sim 3\mu$. The upper bound of the \mathbf{k}_T integration is $k_{max} \equiv 2x(1-x)E$, which ensures that the emission of the radiation is approximately collinear.

Note that because equation (1) is a *difference* in radiation distributions, there are regions of phase space for which $dN^g/dxd^2\mathbf{k}_Td^2\mathbf{q}_T < 0$, indicating the importance of quantum mechanical destructive interference in the QGP case: the presence of the QGP medium *suppresses* the emission of radiation in some cases, leading to less overall radiation than when the medium is not present.

Since equation (1) is a single inclusive distribution, the number of emitted gluons is not fixed (CITE multigluon). (For the typical values of μ , L , and λ quoted above, the total number of emitted gluons is ~ 3 .) Thus when we compute the $\Delta\langle p_T^2 \rangle$ of the emitted parton, we should simply compute:

$$\Delta\langle p_T^2 \rangle \equiv \langle p_T^2 \rangle_{QGP} - \langle p_T^2 \rangle_{vacuum} = \int dx d^2\mathbf{k}_T d^2\mathbf{q}_T (\mathbf{k}_T - \mathbf{q}_T)^2 \frac{dN^g}{dx d^2\mathbf{k}_T d^2\mathbf{q}_T}. \quad (2)$$

4. Asymptotic Analysis

Numerical evaluation of equation (2) is difficult. While the integral converges, the integral only barely converges. The reason the integral only barely converges is that the integrand is composed of several terms. If the separate terms are integrated individually, they diverge. Only when the terms are integrated together are there the correct, delicate cancellations needed for the total integral to converge. It's generally difficult for numerical integration routines to fully capture such a delicate cancellation. An analytic handle on the result is therefore desirable. One approach to approximating equation (2) is to perform a change of variables to $\mathbf{q}' \equiv \mathbf{k}_T - \mathbf{q}_T$. This shift in integration variables significantly simplifies the integrand at the cost of complicating the integration region. The integral is broken up into three regions:

$$\begin{aligned} \Delta\langle p_T^2 \rangle = & \int_0^{x_{min}} dx \int_0^{k_{max}(x)} d^2\mathbf{k}_T \int_0^{q_{max}^+(\mathbf{k}_T)} d^2\mathbf{q}' I \\ & + \int_{x_{min}}^1 dx \int_0^{q_{max}} d^2\mathbf{k}_T \int_0^{q_{max}^+(\mathbf{k}_T)} d^2\mathbf{q}' I \\ & + \int_{x_{min}}^1 dx \int_{q_{max}}^{k_{max}(x)} d^2\mathbf{k}_T \int_{q_{max}^-(\mathbf{k}_T)}^{q_{max}^+(\mathbf{k}_T)} d^2\mathbf{q}' I, \end{aligned} \quad (3)$$

where the integrand I is the same in all three regions and is given by:

$$I \equiv \frac{C_R \alpha_s}{2\pi^2} \frac{L}{\lambda} \frac{1}{k_T^2} \frac{\mu^2}{\pi((\mathbf{k}_T - \mathbf{q}')^2 + \mu^2)^2} \frac{2\mathbf{k}_T \cdot (\mathbf{k}_T - \mathbf{q}') q'^4}{(4xE/L)^2 + q'^4}. \quad (4)$$

The \mathbf{q}' integration limits are given by:

$$q_{max}^\pm \equiv k_T \cos(\theta_{kq}) \pm \sqrt{(q_{max})^2 - k_T^2 \sin^2(\theta_{kq})}, \quad (5)$$

where θ_{kq} is the angle between the \mathbf{k}_T and \mathbf{q}' vectors, and $x_{min} \equiv \sqrt{3\mu/4E}$.

In order to make our job of analysing equation (2) easier, we will take $k_{max} = 2xE$. Since spin-1 radiative emissions are dominated by small x , we expect this to be a good approximation.

Numerical investigation of the three regions shows that the first two contributions grow with $\log^2(E)$ while the third region grows only with $\log(E)$. The overall $\log^2(E)$ growth is reassuring as it should match what we believe will be the leading double logarithmic energy dependence from the factorised approach as noted above.

To derive analytic expressions from the first two integrals of equation (3), it's useful to approximate the upper bound on the \mathbf{q}' integrals as infinity. Numerical investigation shows that this approximation makes little difference in the overall results, especially as one increases in energy. Intuitively, one can understand this insensitivity as follows: the dominant contribution to the integrals comes when $\mathbf{k} \sim \mathbf{q}'$, since these values minimise the denominator in equation (4). Physically, the greatest transverse momentum transfer to the parton from the radiation occurs when the parton has the smallest momentum transfer from the medium.

Once the \mathbf{k} dependence is gone from the \mathbf{q} integration, we may readily analytically integrate equation (4) over $k_T = |\mathbf{k}|$ and θ_{kq} . (A trivial 2π falls out of the extra angular integral, as per usual.) The integration over x is less easy, but still analytically tractable; the expression is long and not insightful. Clever rearrangement of terms leads to analytically tractable integrands that numerical investigation show grow with energy and terms that do not. The final result, correct to leading logarithms in energy is:

$$\Delta\langle p_T^2 \rangle = -\frac{C_R\alpha_s}{4} \frac{L}{\lambda} \mu^2 \left[\log^2 \left(\frac{4E}{\mu^2 L} \right) + \frac{5\pi^2}{12} \right]. \quad (6)$$

5. Conclusions

One can see from equation (6) that the leading double logarithmic term for the change in the mean transverse momentum squared picked up by a parton emerging from nuclear collisions is negative, which is to say that jets are *narrowed* by the presence of the QGP medium. Further, the effect scales as one might expect. Higher energy jets are narrowed more by the QGP than less high energy jets, and the narrowing increases with increasing pathlength and Debye screening and for gluon vs. quark jets; i.e. the greater the quantum interference—from a greater amount of induced radiation—the more the jet is narrowed. The leading double logarithmic energy dependence is also what one expects if factorisation should hold for the system: elastic energy loss leads to a logarithmic dependence on energy and DGLAP-like evolution will add an additional log.

This qualitative prediction of the narrowing of jets is consistent with preliminary results from the ALICE Collaboration at the LHC [24].

Interesting further work includes quantifying the differences between the energy loss approach and the factorisation approach, and considering higher order effects such as from small path lengths [25], small system sizes [26, 27], or the flow of the medium [28].

Acknowledgements

The author gratefully acknowledges generous support from the South African National Research Foundation and the SA-CERN Collaboration. The author further gratefully acknowledges extensive valuable discussions with Matthew D. Sievert and Hannah Clayton.

References

- [1] Gyulassy M and McLerran L 2005 *Nucl. Phys. A* **750** 30–63 (*Preprint nucl-th/0405013*)
- [2] Jacak B and Steinberg P 2010 *Phys. Today* **63N5** 39–43
- [3] Accardi A *et al.* 2016 *Eur. Phys. J. A* **52** 268 (*Preprint 1212.1701*)
- [4] Abdul Khalek R *et al.* 2021 (*Preprint 2103.05419*)
- [5] Kapil V, Schran C, Zen A, Chen J, Pickard C J and Michaelides A 2021 The first-principles phase diagram of monolayer nanoconfined water (*Preprint 2110.14569*)
- [6] Aghasheh A *et al.* 2015

- [7] Casalderrey-Solana J, Liu H, Mateos D, Rajagopal K and Wiedemann U A 2014 *Gauge/String Duality, Hot QCD and Heavy Ion Collisions* (Cambridge University Press) ISBN 978-1-139-13674-7 (*Preprint* 1101.0618)
- [8] Majumder A and Van Leeuwen M 2011 *Prog. Part. Nucl. Phys.* **66** 41–92 (*Preprint* 1002.2206)
- [9] Bjorken J D 1982
- [10] Baier R, Dokshitzer Y L, Mueller A H, Peigne S and Schiff D 1997 *Nucl. Phys. B* **484** 265–282 (*Preprint* hep-ph/9608322)
- [11] Gyulassy M, Levai P and Vitev I 2001 *Nucl. Phys. B* **594** 371–419 (*Preprint* nucl-th/0006010)
- [12] Wang X N and Guo X f 2001 *Nucl. Phys. A* **696** 788–832 (*Preprint* hep-ph/0102230)
- [13] Djordjevic M and Gyulassy M 2004 *Nucl. Phys. A* **733** 265–298 (*Preprint* nucl-th/0310076)
- [14] Salgado C A and Wiedemann U A 2003 *Phys. Rev. D* **68** 014008 (*Preprint* hep-ph/0302184)
- [15] Armesto N, Salgado C A and Wiedemann U A 2004 *Phys. Rev. D* **69** 114003 (*Preprint* hep-ph/0312106)
- [16] Arnold P B, Moore G D and Yaffe L G 2003 *JHEP* **05** 051 (*Preprint* hep-ph/0302165)
- [17] Wicks S, Horowitz W, Djordjevic M and Gyulassy M 2007 *Nucl. Phys. A* **784** 426–442 (*Preprint* nucl-th/0512076)
- [18] Armesto N *et al.* 2012 *Phys. Rev. C* **86** 064904 (*Preprint* 1106.1106)
- [19] Horowitz W A 2013 *Nucl. Phys. A* **904-905** 186c–193c (*Preprint* 1210.8330)
- [20] Cao S *et al.* (JETSCAPE) 2021 *Phys. Rev. C* **104** 024905 (*Preprint* 2102.11337)
- [21] Collins J 2013 *Foundations of perturbative QCD* vol 32 (Cambridge University Press) ISBN 978-1-107-64525-7, 978-1-107-64525-7, 978-0-521-85533-4, 978-1-139-09782-6
- [22] Kang Z B, Wang E, Wang X N and Xing H 2014 *Phys. Rev. Lett.* **112** 102001 (*Preprint* 1310.6759)
- [23] Kang Z B, Wang E, Wang X N and Xing H 2016 *Phys. Rev. D* **94** 114024 (*Preprint* 1409.1315)
- [24] Adam J *et al.* (ALICE) 2015 *JHEP* **09** 170 (*Preprint* 1506.03984)
- [25] Kolbe I and Horowitz W A 2019 *Phys. Rev. C* **100** 024913 (*Preprint* 1511.09313)
- [26] Mogliacci S, Kolbé I and Horowitz W A 2020 *Phys. Rev. D* **102** 116017 (*Preprint* 1807.07871)
- [27] Kitazawa M, Mogliacci S, Kolbé I and Horowitz W A 2019 *Phys. Rev. D* **99** 094507 (*Preprint* 1904.00241)
- [28] Sadofyev A V, Sievert M D and Vitev I 2021 (*Preprint* 2104.09513)

Cosmological Models in Gravitational Scalar-Tensor Theories

Heba Sami* and Amare Abebe

Center for Space Research, North-West University, Mahikeng 2745, South Africa

E-mail: hebasami.abdulrahman@gmail.com

Abstract. In this work, a brief review of a new form of scalar-tensor theories of gravity, known as gravitational scalar-tensor theories in which the action is composed of the Ricci scalar and its first and second derivatives is made. Some of the cosmological applications in these new theories are discussed considering different models corresponding to the first non-trivial extensions of general relativity possessing $2 + 2$ degrees of freedom. We show that the resulting cosmological behavior is in agreement with observations.

1. Introduction

Despite the success of the standard cosmological model based on the theory of General Relativity (GR), the recent developments in observational cosmology and astronomy led to the statement that this model is inadequate to explain many phenomena in the Universe [1]. The Universe has experienced two phases of cosmic acceleration. The first one is the inflation phase which is an early-time accelerated phase and it is believed to have happened a fraction of second after the Big Bang and prior to the radiation-dominated epoch. The second phase is the accelerated expansion in the present universe which is considered to have started since the Universe entered its dark-energy-dominated epoch [2]. The two phases of accelerated expansion are very challenging however, there are recent attempts and alternatives to the standard Big Bang model proposed to explain these phenomena. Some of those attempts are within the framework of GR and some focused on the possibility of modifying GR, by modifying the gravitational sector of the theory. Extending the work done in [3], this particular piece of literature is aimed at studying a new form of scalar-tensor theories of gravity, known as gravitational scalar-tensor theories. There has been some recent work on the scalar-tensor theories of gravity on how to construct a gravitational modification without presenting ghosts behavior or any instabilities which normally arise due to the extra degrees of freedom introduced in such modification. In 1974, Horndeski [4] was able to construct the single-scalar field theory with second-order equations of motion with respect to the scalar field and the metric which involves $2 + 1$ propagating degrees of freedom, and thus without ghosts. This theory is further extended as in [5–10] with the same $2 + 1$ propagating degrees of freedom. In [11], the authors managed to construct a gravitational modification namely gravitational scalar-tensor theories, which possess $2 + 2$ degrees of freedom that propagate without introducing ghost nor Ostrogradski instabilities [12] under a specific choice of the Lagrangian. They considered a theory of gravity with an action that is composed of the Ricci scalar and its first and second derivatives. [3, 11]

$$S = \frac{1}{2} \int d^4x \sqrt{-g} f\left(R, (\nabla R)^2, \square R\right), \quad (1)$$

where $\square R = g^{ab} \nabla_a \nabla_b R$. The action of these theories can be transformed to an action of multi-scalar fields coupled to gravity, by using double Lagrangian multipliers. E.g., if we have $f(R)$ and $f(\phi)$, we introduce a new variable λ called a Lagrangian multiplier and it is defined $\mathcal{L}(R, \phi, \lambda) = f(\phi) - \lambda(\phi - R)$, so in case of $f(R, (\nabla R)^2, \square R)$, we introduce a set of Lagrange

multipliers $(\tilde{\lambda}, \tilde{\Lambda}_1, \tilde{\Lambda}_2)$ and the associated auxiliary fields (ϕ, X, B) in order to reduce the order of derivatives [3]:

$$f(R, (\nabla R)^2, \square R) = f(\phi, X, B) - \tilde{\lambda}(\phi - R) - \tilde{\Lambda}_1(X - (\nabla R)^2) - \tilde{\Lambda}_2(B - \square R), \quad (2)$$

where

$$\tilde{\lambda} = \lambda + \nabla^\rho [\tilde{\Lambda}_1 \nabla_\rho (\phi + R)] - \square \tilde{\Lambda}_2, \quad \tilde{\Lambda}_1 = \Lambda_1, \quad \tilde{\Lambda}_2 = \Lambda_2. \quad (3)$$

By using Eq. (2) and Eq. (3) and by replacing all the derivatives of R with the derivatives of ϕ , one can rewrite the action in Eq. (1) as follows [11]

$$S = \int d^4x \sqrt{-g} \left[f(\phi, X, B) - \lambda(\phi - R) - \Lambda_1(X - (\nabla \phi)^2) - \Lambda_2(B - \square \phi) \right]. \quad (4)$$

This action does not involve any derivative terms of those two variables Λ_1 and Λ_2 which implies that the variation of the action with respect to these two variables results in constraint equations [11]. Therefore, the action in Eq. (4) can be written as

$$S = \int d^4x \sqrt{-g} \left[f(\phi, (\nabla \phi)^2, \square \phi) - \lambda(\phi - R) \right]. \quad (5)$$

This action has derivative terms of ϕ , which implies a dynamical equation of ϕ . Since the higher derivatives terms except for λR come from $\square \phi$, therefore λ is also treated as a dynamical field. In order to reduce the order of derivatives, in [11], another Lagrangian multiplier and the associated auxiliary field have been introduced for $\square \phi$ as

$$f(\square \phi) = f(B) - \Lambda(B - \square \phi), \quad (6)$$

therefore, the action in Eq. (5) is now written as

$$S = \int d^4x \sqrt{-g} \left[f(\phi, (\nabla \phi)^2, B) - \lambda(\phi - R) - \Lambda(B - \square \phi) \right]. \quad (7)$$

By varying this action with respect to B , given that this action is independent of the derivative of B [11], therefore we have

$$\delta S = \int d^4x \sqrt{-g} [f_B - \Lambda]. \quad (8)$$

Since the action is independent of the derivative of B , δS yields a constraint equation, $f_B = \Lambda$, where f_B denotes partial derivative of f with respect to B . By replacing this constraint back into the action in Eq. (7), and by varying the action with respect to B , the resulting action is

$$\delta S = \int d^4x \sqrt{-g} [-f_{BB}(B - \square \phi)]. \quad (9)$$

- 1- If $f_{BB} = 0$, B does not enter linearly in the Lagrangian and under a conformal transformation where $g_{ab} = \frac{1}{2} e^{-\sqrt{\frac{2}{3}} \mathcal{X}} \hat{g}_{ab}$, the action of the new gravitational scalar-tensor is given as [3]

$$S = \int d^4x \sqrt{-\hat{g}} \left[\frac{1}{2} \hat{R} - \frac{1}{2} \hat{g}^{ab} \left(\partial_a \mathcal{X} \partial_b \mathcal{X} + e^{-\sqrt{\frac{2}{3}} \mathcal{X}} \partial_a \varphi \partial_b \phi \right) - \frac{1}{4} \left(e^{-\sqrt{\frac{2}{3}} \mathcal{X}} \phi + e^{-2\sqrt{\frac{2}{3}} \mathcal{X}} \left(\varphi B(\phi, (\hat{\nabla} \phi)^2, \varphi) - f \right) \right) \right]. \quad (10)$$

- 2- If $f_{BB} \neq 0$, B enters linearly in the Lagrangian, and the function f can be rewritten as

$$f(R, (\nabla R)^2, \square R) = \mathcal{K}(R, (\nabla R)^2) + \mathcal{G}(R, (\nabla R)^2) \square R. \quad (11)$$

The action of the new gravitational scalar-tensor is given by [3, 11]

$$S = \int d^4x \sqrt{-\hat{g}} \left[\frac{1}{2} \hat{R} - \frac{1}{2} \hat{g}^{ab} \partial_a \mathcal{X} \partial_b \mathcal{X} - \frac{1}{\sqrt{6}} e^{-\sqrt{\frac{2}{3}} \mathcal{X}} \hat{g}^{ab} \mathcal{G} \partial_a \mathcal{X} \partial_b \phi \right. \\ \left. + \frac{1}{4} e^{-2\sqrt{\frac{2}{3}} \mathcal{X}} \mathcal{K} + \frac{1}{2} e^{-\sqrt{\frac{2}{3}} \mathcal{X}} \mathcal{G} \hat{\square} \phi - \frac{1}{4} e^{-\sqrt{\frac{2}{3}} \mathcal{X}} \phi \right], \quad (12)$$

where

$$\mathcal{K} = \mathcal{K}(\phi, B), \quad \mathcal{G} = \mathcal{G}(\phi, B), \quad B = 2e^{\sqrt{\frac{2}{3}} \mathcal{X}} g^{ab} \partial_a \phi \partial_b \phi. \quad (13)$$

As shown in [11], despite the higher derivative nature of the Lagrangian, this new theory does not introduce any ghost under an appropriate choice of the Lagrangian.

2. Field equations in the gravitational scalar-tensor theories

In [3], the authors investigated the cosmological behavior in gravitational scalar-tensor theories to study the late-time evolution of a universe governed by these theories. They introduced the action of the matter sector S_m , and considered a homogeneous and isotropic geometry in the Einstein framework such that the total action is $S = S + S_m$. We consider the following flat Friedmann-Lemaître-Robertson-Walker (FLRW) spacetime metric where the two scalar fields are time-dependent only:

$$ds^2 = -dt^2 + a(t)^2 \delta_{ij} dx^i dx^j. \quad (14)$$

Therefore, the Friedmann equations and the evolution equations are given as [3],

$$3H^2 - \rho_m - \frac{1}{2} \dot{\mathcal{X}}^2 + \frac{1}{4} e^{-2\sqrt{\frac{2}{3}} \mathcal{X}} \mathcal{K} + \frac{2}{3} \dot{\phi}^2 \left(\dot{\phi} (\sqrt{6} \dot{\mathcal{X}} - 9H) - 3\ddot{\phi} \right) \mathcal{G}_B \\ - \frac{1}{2} e^{-\sqrt{\frac{2}{3}} \mathcal{X}} \left(\dot{B} \dot{\phi} \mathcal{G}_B + \frac{1}{2} \phi + \dot{\phi}^2 (\mathcal{G}_\phi - 2\mathcal{K}_B) \right) = 0, \quad (15)$$

$$3H^2 + 2\dot{H} + p_m + \frac{1}{2} \dot{\mathcal{X}}^2 + \frac{1}{4} e^{-2\sqrt{\frac{2}{3}} \mathcal{X}} \mathcal{K} + \frac{1}{2} e^{-\sqrt{\frac{2}{3}} \mathcal{X}} \left(\dot{B} \dot{\phi} \mathcal{G}_B - \frac{1}{2} \phi + \dot{\phi}^2 \mathcal{G}_\phi \right) = 0, \quad (16)$$

$$\varepsilon_{\mathcal{X}} = \ddot{\mathcal{X}} + 3H\dot{\mathcal{X}} - \frac{1}{3} \dot{\phi}^2 \left(\dot{\phi} (3\sqrt{6}H - 2\dot{\mathcal{X}}) + \sqrt{6}\ddot{\phi} \right) \mathcal{G}_B \\ + \frac{1}{2\sqrt{6}} e^{-\sqrt{\frac{2}{3}} \mathcal{X}} \left(2\dot{B} \dot{\phi} \mathcal{G}_B - \phi + 2\dot{\phi}^2 (\mathcal{K}_B + \mathcal{G}_\phi) \right) + \frac{1}{\sqrt{6}} e^{-2\sqrt{\frac{2}{3}} \mathcal{X}} \mathcal{K} = 0, \quad (17)$$

$$\varepsilon_\phi = \frac{1}{3} e^{-\sqrt{\frac{2}{3}} \mathcal{X}} \left(\dot{\phi} (-9H + \sqrt{6}\dot{\mathcal{X}}) - 3\ddot{\phi} \right) \mathcal{K}_B + \frac{1}{6} \dot{B} \left\{ 3e^{-\sqrt{\frac{2}{3}} \mathcal{X}} \dot{B} + 4\dot{\phi} \left(\dot{\phi} (9H - \sqrt{6}\dot{\mathcal{X}}) + 3\ddot{\phi} \right) \right\} \mathcal{G}_{BB} \\ + \frac{1}{3} e^{-\sqrt{\frac{2}{3}} \mathcal{X}} \left(\dot{\phi} (9H - \sqrt{6}\dot{\mathcal{X}}) + 3\ddot{\phi} \right) \mathcal{G}_\phi \left\{ e^{-\sqrt{\frac{2}{3}} \mathcal{X}} \dot{B} \dot{\phi} + \frac{2}{3} \dot{\phi}^2 \left(\dot{\phi} (9H - \sqrt{6}\dot{\mathcal{X}}) + 3\ddot{\phi} \right) \right\} \mathcal{G}_{B\phi} \\ - e^{-\sqrt{\frac{2}{3}} \mathcal{X}} \dot{\phi}^2 \mathcal{K}_{B\phi} + \frac{1}{2} e^{-\sqrt{\frac{2}{3}} \mathcal{X}} \dot{\phi}^2 \mathcal{G}_{\phi\phi} - e^{-\sqrt{\frac{2}{3}} \mathcal{X}} \dot{B} \dot{\phi} \mathcal{K}_{BB} + \left\{ \frac{4}{3} \dot{\phi} (9H - 2\sqrt{6}\dot{\mathcal{X}}) \ddot{\phi} \right. \\ \left. - \frac{1}{\sqrt{6}} e^{-\sqrt{\frac{2}{3}} \mathcal{X}} \dot{B} \dot{\mathcal{X}} + \dot{\phi}^2 \left(18H^2 + 6\dot{H} - 3\sqrt{6}H\dot{\mathcal{X}} - \frac{2}{3} \dot{\mathcal{X}}^2 - \sqrt{6}\ddot{\mathcal{X}} \right) \right\} \mathcal{G}_B \\ \left. - \frac{1}{4} e^{-2\sqrt{\frac{2}{3}} \mathcal{X}} \mathcal{K}_\phi + \frac{1}{4} e^{-\sqrt{\frac{2}{3}} \mathcal{X}} \right\} = 0. \quad (18)$$

Here $B(t) = -2e^{\sqrt{\frac{2}{3}} \mathcal{X}} \dot{\phi}^2$, and dots denote differentiation with respect to time and the subscripts refer to the partial differentiations with respect to the corresponding argument. The Friedmann equations presented in Eqs. (15) and (16) can be written as

$$H^2 = \frac{1}{3} (\rho_{DE} + \rho_m), \quad 2\dot{H} + 3H^2 = -(p_{DE} + p_m), \quad (19)$$

where ρ_{DE} and p_{DE} represent an effective dark energy sector with energy density and pressure respectively:

$$\rho_{DE} = \frac{1}{2}\dot{\chi}^2 - \frac{1}{4}e^{-2\sqrt{\frac{2}{3}}\chi}\mathcal{K} - \frac{2}{3}\dot{\phi}^2\left(\dot{\phi}(\sqrt{6}\dot{\chi} - 9H) - 3\ddot{\phi}\right)\mathcal{G} + \frac{1}{2}e^{-\sqrt{\frac{2}{3}}\chi}\left(\dot{B}\dot{\phi}\mathcal{G} + \frac{\phi}{2} + \dot{\phi}^2(\mathcal{G}_\phi - 2\mathcal{K}_B)\right), \quad (20)$$

$$p_{DE} = \frac{1}{2}\dot{\chi}^2 + \frac{1}{4}e^{-2\sqrt{\frac{2}{3}}\chi}\mathcal{K} + \frac{1}{2}e^{-\sqrt{\frac{2}{3}}\chi}\left(\dot{B}\dot{\phi}\mathcal{G}_B + \dot{\phi}^2\mathcal{G}_\phi - \frac{\phi}{2}\right), \quad (21)$$

with the dark-energy equation of state parameter $w_{DE} = \frac{p_{DE}}{\rho_{DE}}$.

3. Cosmological applications in gravitational scalar-tensor theories

In [3], the authors have considered different functional forms of \mathcal{K} and \mathcal{G} to study the late-time evolution of a universe governed by these new theories considering different models. In this subsection, we will investigate the cosmological application of the new gravitational scalar-tensor by considering two different models by choosing particular functional form of \mathcal{K} and \mathcal{G} .

Model 1: $\mathcal{K}(\phi, B) = \frac{\phi^2}{2} - \frac{\zeta}{2}B$ and $\mathcal{G}(\phi, B) = 0$

Here ζ is the corresponding coupling constant. We apply a transformation to any time derivative function f and H into a redshift z derivative as follows

$$\dot{f} = -H(1+z)H\frac{df}{dz}, \quad (22)$$

$$\ddot{f} = H(1+z)^2\frac{dH}{dz}\frac{df}{dz} + H^2(1+z)\frac{df}{dz} + H^2(1+z)^2\frac{d^2f}{dz^2}. \quad (23)$$

The redshift is given in terms of the scale factor as $z = (-1 + \frac{a_0}{a})$, with the normalized coefficient represented by a_0 and consider the matter sector to be dust i.e., $p_m \simeq 0$. In this model, the Friedmann and the evolution equations Eqs. (15) - (18) and the effective dark-energy energy density and pressure Eqs. (20) - (21), in the redshift space become:

$$\mathcal{X}'' + \left(\frac{1}{H}\frac{dH}{dz} - \frac{2}{(1+z)}\right)\mathcal{X}' + \frac{1}{2\sqrt{6}}\zeta e^{-\sqrt{\frac{2}{3}}\chi}\phi'^2 - \frac{(1 - e^{-\sqrt{\frac{2}{3}}\chi}\phi)}{2\sqrt{6}H^2(1+z)^2}e^{-\sqrt{\frac{2}{3}}\chi}\phi = 0, \quad (24)$$

$$\zeta\phi'' + \zeta\left(\frac{1}{H}\frac{dH}{dz} - \frac{2}{(1+z)}\right)\phi' - \frac{\sqrt{6}}{3}\zeta\phi'\mathcal{X}' + \frac{1}{2H^2(1+z)^2}(1 - e^{-\sqrt{\frac{2}{3}}\chi}\phi) = 0, \quad (25)$$

$$\frac{1}{6}\left(\mathcal{X}'^2 + \frac{1}{2}\zeta e^{-\sqrt{\frac{2}{3}}\chi}\phi'^2\right)(1+z)^2 - \frac{2(1+z)}{3H}\frac{dH}{dz} - \frac{(1 - \frac{1}{2}e^{-\sqrt{\frac{2}{3}}\chi}\phi)}{12H^2}e^{-\sqrt{\frac{2}{3}}\chi}\phi = 0, \quad (26)$$

$$\Omega_m = 1 - \frac{1}{6}\left(\mathcal{X}'^2 + \frac{1}{2}\zeta e^{-\sqrt{\frac{2}{3}}\chi}\phi'^2\right)(1+z)^2 - \frac{1}{12H^2}e^{-\sqrt{\frac{2}{3}}\chi}\left(1 - \frac{1}{2}e^{-\sqrt{\frac{2}{3}}\chi}\phi\right)\phi, \quad (27)$$

$$q = \frac{3\Omega_m}{2} + \frac{1}{2}\left(\mathcal{X}'^2 + \frac{1}{2}\zeta e^{-\sqrt{\frac{2}{3}}\chi}\phi'^2\right)(1+z)^2 - 1, \quad (28)$$

$$\omega_{DE} = \frac{1}{3\Omega_{DE}}\left(\mathcal{X}'^2 + \frac{1}{2}\zeta e^{-\sqrt{\frac{2}{3}}\chi}\phi'^2\right)(1+z)^2 - 1, \quad (29)$$

$$\Omega_{DE} = \frac{1}{6}\left(\mathcal{X}'^2 + \frac{1}{2}\zeta e^{-\sqrt{\frac{2}{3}}\chi}\phi'^2\right)(1+z)^2 + \frac{1}{12H^2}e^{-\sqrt{\frac{2}{3}}\chi}\left(1 - \frac{1}{2}e^{-\sqrt{\frac{2}{3}}\chi}\phi\right)\phi. \quad (30)$$

We solve the whole system of equations for this model numerically and we present the cosmological evolution for the matter, dark energy density parameters, the dark-energy equation of state parameters, as well as the evolution of the deceleration in Figs. 1 - 4 for the parameters choice $\zeta = 10$, $\Omega_{m0} = \frac{\rho_{m0}}{3H^2} \simeq 0.3$ and $\Omega_{DE0} = \frac{\rho_{DE0}}{3H^2} \simeq 0.7$.

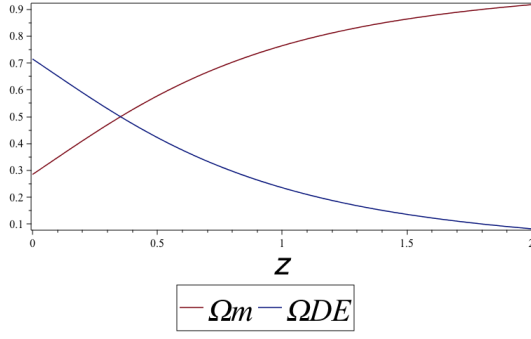


Figure 1. The evolution of Ω_m and Ω_{DE} versus the redshift z for model 1.

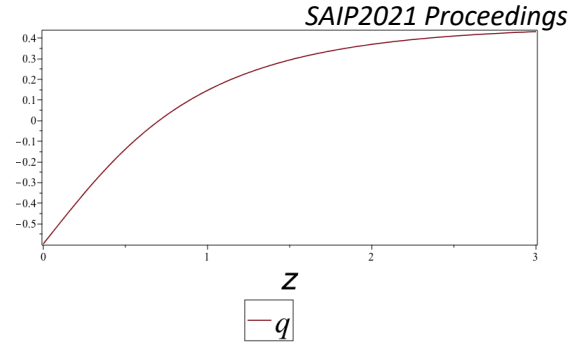


Figure 2. The evolution of the deceleration parameter q versus the redshift z for model 1.

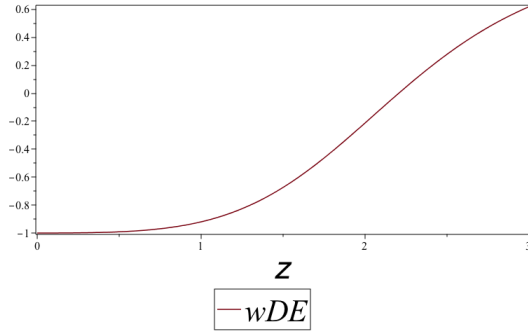


Figure 3. The evolution of the dark-energy equation of state parameter ω_{DE} versus the redshift z for model 1.

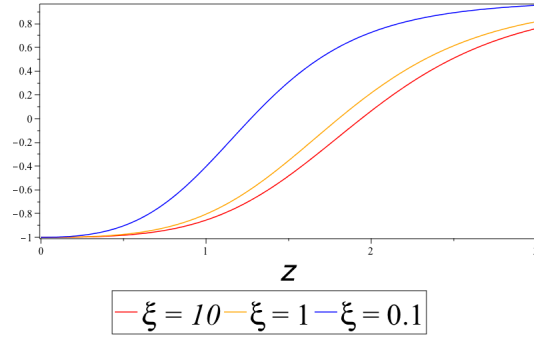


Figure 4. The evolution of ω_{DE} versus the redshift z for and different values of the model parameter ζ for model 1.

Model 2: $\mathcal{K}(\phi, B) = \zeta B$ and $\mathcal{G}(\phi, B) = \frac{\zeta \phi^2}{2}$

In this model, the Friedmann and the evolution equations Eqs. (15) - (18) and the effective dark-energy energy density and pressure Eqs. (20) - (21), in the redshift space become:

$$\mathcal{X}'' + \left(\frac{1}{H} \frac{dH}{dz} - \frac{2}{(1+z)} \right) \mathcal{X}' - \frac{1}{\sqrt{6}} e^{-\sqrt{\frac{2}{3}} \mathcal{X}} \zeta (1-\phi) \phi'^2 - \frac{1}{\sqrt{6} H^2 (1+z)^2} e^{-\sqrt{\frac{2}{3}} \mathcal{X}} \phi = 0, \quad (31)$$

$$\zeta \phi'' + \zeta \left(\frac{1}{H} \frac{dH}{dz} - \frac{2}{(1+z)} \right) \phi' - \frac{\sqrt{6}}{3} \zeta \phi' \mathcal{X}' + \frac{1}{4 H^2 (1+z)^2} \left(1 - 2 \zeta H^2 (1+z)^2 \phi'^2 \right) = 0 \quad (32)$$

$$-2H(1+z) \frac{dH}{dz} + 3H^2 + \frac{1}{2} \left(\mathcal{X}'^2 - (1-\phi) \zeta e^{-\sqrt{\frac{2}{3}} \mathcal{X}} \phi'^2 \right) H^2 (1+z)^2 - \frac{1}{4} e^{-\sqrt{\frac{2}{3}} \mathcal{X}} \phi = 0, \quad (33)$$

$$\Omega_m = 1 - \frac{1}{6} \left(\mathcal{X}'^2 - (1-\phi) \zeta e^{-\sqrt{\frac{2}{3}} \mathcal{X}} \phi'^2 \right) (1+z)^2 - \frac{1}{12 H^2} e^{-\sqrt{\frac{2}{3}} \mathcal{X}} \phi, \quad (34)$$

$$q = \frac{3\Omega_m}{2} + \frac{1}{2} \left(\mathcal{X}'^2 - (1-\phi) \zeta e^{-\sqrt{\frac{2}{3}} \mathcal{X}} \phi'^2 \right) (1+z)^2 - 1, \quad (35)$$

$$\omega_{DE} = \frac{1}{3\Omega_{DE}} \left(\mathcal{X}'^2 + (1-\phi) \zeta e^{-\sqrt{\frac{2}{3}} \mathcal{X}} \phi'^2 \right) (1+z)^2 - 1, \quad (36)$$

$$\Omega_{DE} = \frac{1}{6} \left(\mathcal{X}'^2 - (1-\phi) \zeta e^{-\sqrt{\frac{2}{3}} \mathcal{X}} \phi'^2 \right) (1+z)^2 + \frac{1}{12 H^2} e^{-\sqrt{\frac{2}{3}} \mathcal{X}} \phi. \quad (37)$$

We solve the whole system of equations for this model numerically for the parameters choice $\zeta = -1$, we present the cosmological evolution for the matter, dark energy density parameters, the dark-energy equation of state parameters and the deceleration parameter in Figs. 5 - 7.

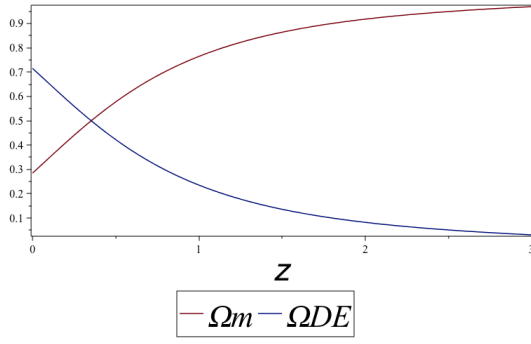


Figure 5. The evolution of Ω_m and Ω_{DE} versus the redshift z for model 2.

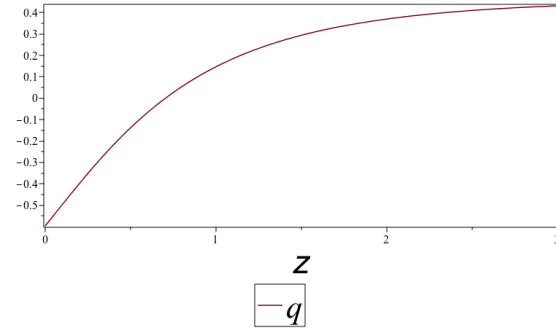


Figure 6. The evolution of the deceleration parameter q versus the redshift z for model 2.

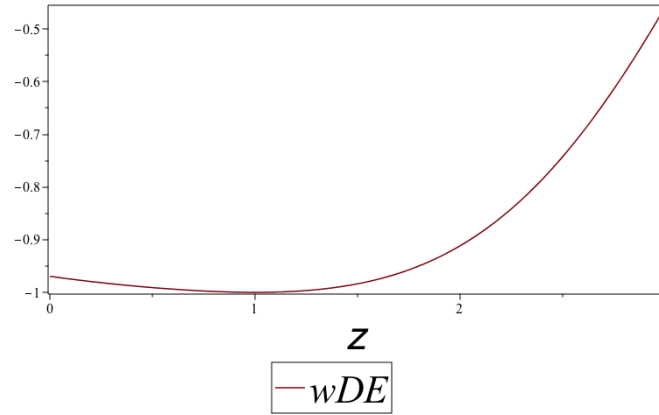


Figure 7. The evolution of the dark-energy equation of state parameter ω_{DE} versus the redshift z for model 2.

4. Conclusion

We investigated the cosmological application of the new gravitational scalar-tensor by considering two different models by choosing particular functional form of \mathcal{K} and \mathcal{G} . We noticed from the plots for both models 1 and 2 that the evolution of the matter and dark energy density parameters Ω_m and Ω_{DE} shows the transition from the matter to the dark energy epoch. The evolution of the deceleration parameter q also show the transition from deceleration ($q > 0$) to acceleration ($q < 0$). The evolution of the dark-energy equation of state parameter ω_{DE} almost stabilizes in a value very close to the cosmological constant, however it seems to be affected by both the model we consider and the coupling constant ζ .

Acknowledgments

HS gratefully acknowledges the financial support from the Mwalimu Nyerere African Union scholarship and the National Research Foundation (NRF) free-standing scholarship with a grant number 112544. AA acknowledges that this work is based on the research supported in part by the NRF of South Africa with grant number 112131.

References

- [1] Oikonomou V 2021 *Physical Review D* **103** 044036
- [2] Nojiri S, Odintsov S and Oikonomou V 2017 *Physics Reports* **692** 1–104
- [3] Saridakis E N and Tsoukalas M 2016 *Physical Review D* **93** 124032
- [4] Horndeski G W 1974 *International Journal of Theoretical Physics* **10** 363–384
- [5] Nicolis A, Rattazzi R and Trincherini E 2009 *Physical Review D* **79** 064036
- [6] Deffayet C, Gao X, Steer D A and Zahariade G 2011 *Physical Review D* **84** 064039
- [7] Gleyzes J, Langlois D, Piazza F and Vernizzi F 2015 *Physical Review Letters* **114** 211101
- [8] Langlois D and Noui K 2016 *Journal of Cosmology and Astroparticle Physics* **2016** 034
- [9] Gleyzes J, Langlois D, Piazza F and Vernizzi F 2014 *arXiv preprint arXiv:1404.6495*
- [10] Lin C, Mukohyama S, Namba R and Saitou R 2014 *Journal of Cosmology and Astroparticle Physics* **2014** 071
- [11] Naruko A, Yoshida D and Mukohyama S 2016 *Classical and Quantum Gravity* **33** 09LT01

- [12] Motohashi H and Suyama T 2015 *Physical Review D* **91** 085009

Corrigenda to The Proceedings of SAIP2021

Effect of Gold Nanoparticle-Hypericin Mediated Photodynamic Therapy in MCF-7 Breast Cancer Cells.

DR Mokoena¹, BP George¹ and H Abrahamse^{1,2}

¹Laser Research Centre, Faculty of Health Sciences, University of Johannesburg, P.O. Box: 17011, Johannesburg 2028, South Africa

²NRF SARCHI: Laser Applications in Health, South Africa

E-mail: habrahamse@uj.ac.za

Abstract. Cancer is a global emergency that needs instant intervention. Breast cancer is the second most common cancer after lung and the most common cancer amongst women. Current treatments are linked with adverse side effects, treatment failure, and cancer relapse. Photodynamic therapy (PDT) is one of the emerging cancer treatment options that is highly selective and specific towards cancer cells. Consequently, the use of gold nanoparticles (AuNP) further enhances the efficacy of PDT. In this study, gold-nanoparticle (AuNP) conjugated Hypericin (Hyp) mediated PDT was used for the treatment of MCF-7 human breast cancer cells by inducing cell death, *in vitro*. Cellular responses after 24 h post-PDT, and at 10 J/cm² were observed. The morphological changes, viability, cytotoxicity, and cell death mechanism analysis by Annexin V/PI staining was performed. The results showed activation of the apoptotic pathway with characteristic morphological features and biochemical responses of dying cells. Hence this study provided an insight into the application of advanced PDT in breast cancer treatment by actively targeting the apoptotic cell death pathway *in vitro*.

1. Introduction

Breast cancer begins when there is an uncontrolled growth of breast cells, leading to lump formation, inflammation, and metastasis to other parts of the body. Several different types of breast cancers have been identified. Such as those that begin from the ducts of the breast referred to as ductal carcinoma in situ or the ones that are in the lobules of the breast known as lobular carcinoma in situ [1]. Another uncommon yet increasing form of breast cancer is inflammatory breast cancer which is characterized by the warm, red, and swollen appearance of the breast. Breast cancer is a heterogeneous disease, and its treatment varies depending on the location of the tumour and whether it is benign or malignant. Current treatments are associated with several undesirable side effects such as poor prognosis, poor survival rate, drug resistance, and cytotoxicity to normal cells resulting in poor quality of life. In Africa, the five-year survival rate is less or equal to 60% for low and middle-income countries [2].

Photodynamic therapy (PDT) is a novel therapy due to its selective cytotoxicity and much reduced invasive quality [3]. It utilizes the use of a Photosensitiser (PS), visible light at a specific wavelength, as well as molecular oxygen to abolish cancer cells and disease causing bacteria [4]. It has the potential to meaningfully improve the quality of life and lengthen the survival rates in cancer patients. In PDT the PS plays a vital role in cancer cell destruction by entering the cell and activation with a specific wavelength light. Some PSs like hypericin, are hydrophobic and require a carrier molecule such as nanoparticles to enter the cell. Thus, increasing their movement across the cell membranes as a result of

increased aqueous solubility, stability, and bioavailability [5, 6]. PS and nanoparticle conjugates have proven to improve PDT efficiency. Using gold nanoparticles Portilho et al., 2013 observed an increased triplet lifetime of PS than unconjugated PS [7]. Some studies have demonstrated increased PS drug delivery and preservation using nanoparticles [8]. Nanoparticles have also been observed to disguising the PS from biological barricades and enzymes, resulting in improved cellular uptake with augmented ROS synthesis [9].

2. Materials and Methods

Hypericin (Sigma-Aldrich, 1MG-56690) was prepared in Dimethyl sulfoxide (DMSO), to a final stock concentration of 0.02 M. It was then conjugated with gold nanoparticles (AuNPs) (Sigma-Aldrich, 1ML-765457) by sonication for 2 h at room temperature. UV-Vis Spectrophotometry was used to determine the activation wavelength of Hypericin, AuNP, and the conjugate from 200 – 800 nm wavelengths. Dynamic Light Scattering (DLS), Zeta potential, and Fourier-transform infrared (FTIR) spectroscopy were used to characterize the conjugate. MCF-7 Breast cancer cells were commercially purchased from the ATCC, (ATCC® HTB-22™) and seeded in Dulbecco's Modified Eagle's Medium (DMEM) supplemented with 10% Foetal Bovine Serum, 1% amphotericin B, 1% pen-strep and incubated at 37 °C, 85% humidity and 5% CO₂. For PDT experiments, 3×10^5 cells were seeded in 3.4 cm² cell culture plates and treated with Hypericin-AuNP conjugate at concentrations of 3.8, 7.6, and 15.2 μ M per plate. After 12 h of incubation to allow maximum absorption of the PS by the cells, the cells were washed 3 times using pre-warmed Hank's Balanced Salt Solution (HBSS) to eliminate unabsorbed PS. The treated cells were then irradiated using a 594 nm diode laser (Oriol Corporation), supplied by the National Laser Center (NLC) of South Africa. Cells were irradiated at a fluence of 10 J/cm² as shown in table 1 below.

Table 1. Laser Parameters for PDT

Variable	Value/Description
Wavelength	594 nm
Laser type	Diode laser
Wave release	Continuous wave
Energy density	10 J/cm ²
Power output	91.1 mW
Power density	10 mW/cm ²
Spot size	9.1 cm ²
Irradiation time	16 min 42 sec

Following irradiation, cells were placed in the incubator for 24h and the morphology was checked using an inverted light microscope (Wirsam, Olympus CKX41). The cell proliferation assay was done using the CellTiter-Glo Luminescence Cell Viability Assay (Promega, G7570) to check the amount of ATP present in the cells. The luminescence signal produced from the conversion of ATP to adenosine monophosphate (AMP) by the enzyme luciferase was read out in relative light units (RLU) on the Victor-3 multi-plate reader ((Perkin Elmer, VICTOR Nivo Multimode Microplate Reader). The signal is directly proportional to the amount of ATP in the cells, which represents the number of metabolically active cells. Cellular cytotoxicity was analyzed using the spectrophotometric analysis of Lactate Dehydrogenase, LDH at 490 nm ((Perkin Elmer, VICTOR Nivo Multimode Microplate Reader). The CytoTox 96® Non-Radioactive Cytotoxicity Assay (Anatech: Promega, PRG1780) was utilized to detect the amount of LDH in the media. Annexin V- fluorescein isothiocyanate (FITC) apoptosis detection kit1 (BD Biosciences, BD Pharmingen™) was used to analyze the apoptotic or necrotic cell death pathways and the flow cytometric analysis was performed using the BD Accuri C6 (BD

Biosciences). All experiments were repeated three-times ($n=3$). The SPSS software version 27 was used for statistical analysis. Dunnett with a Confidence interval of 0.95% was used between the control (cells only) and experimental groups at significance levels $p < 0.05$ (*), $p < 0.01$ (**) and $p < 0.001$ (***)

3. Results

The results indicated damage to Hyp-AuNP PDT treated cells compared to the untreated control cells. The morphology images (Figure 1) distinctly show the rounding up of cells and detachment from the culture dish surface. The higher the concentration of the conjugate, more number of cells showed rounding up, detachment from the culture dish, and thus cell death in PDT treated cells. Cellular responses also showed a dose-dependent cell death. LDH levels were increased with the increasing concentration of conjugate ($p < 0.01$) in experimental PDT groups (3.8, 7.6 and 15.2 μM at 10 J/cm²) (Figure 2) while ATP levels decreased when compared to the untreated cells ($p < 0.05$). There was no significant difference when control cells were compared to the Hyp-AuNP conjugate only treated group (Figure 3). The Annexin V/PI flow cytometry results (Figure 4) indicate the early and late apoptotic cell death after the treatments.

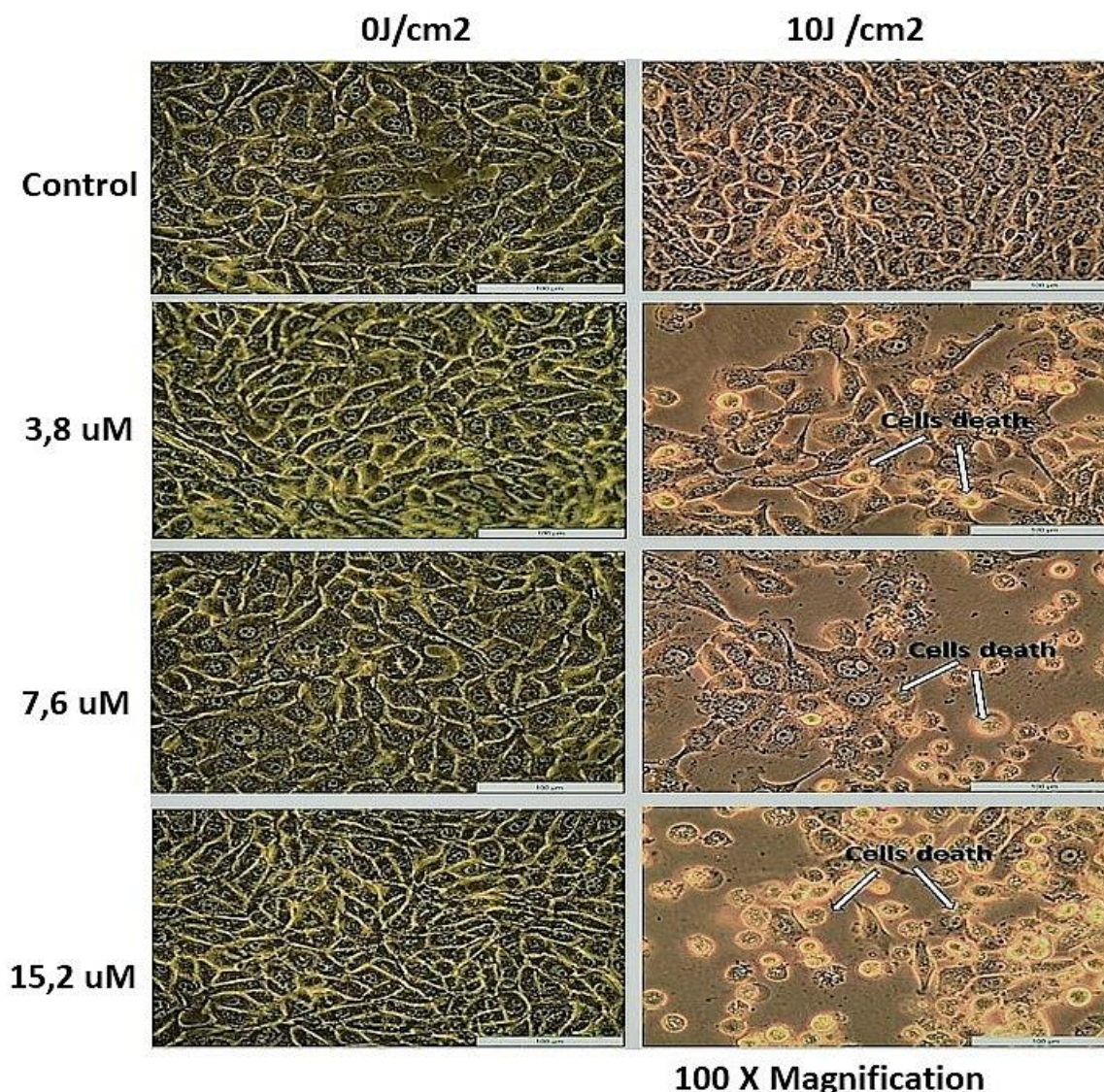


Figure 1. Morphology of MCF-7 cells pre- and post-PDT at 594 nm.

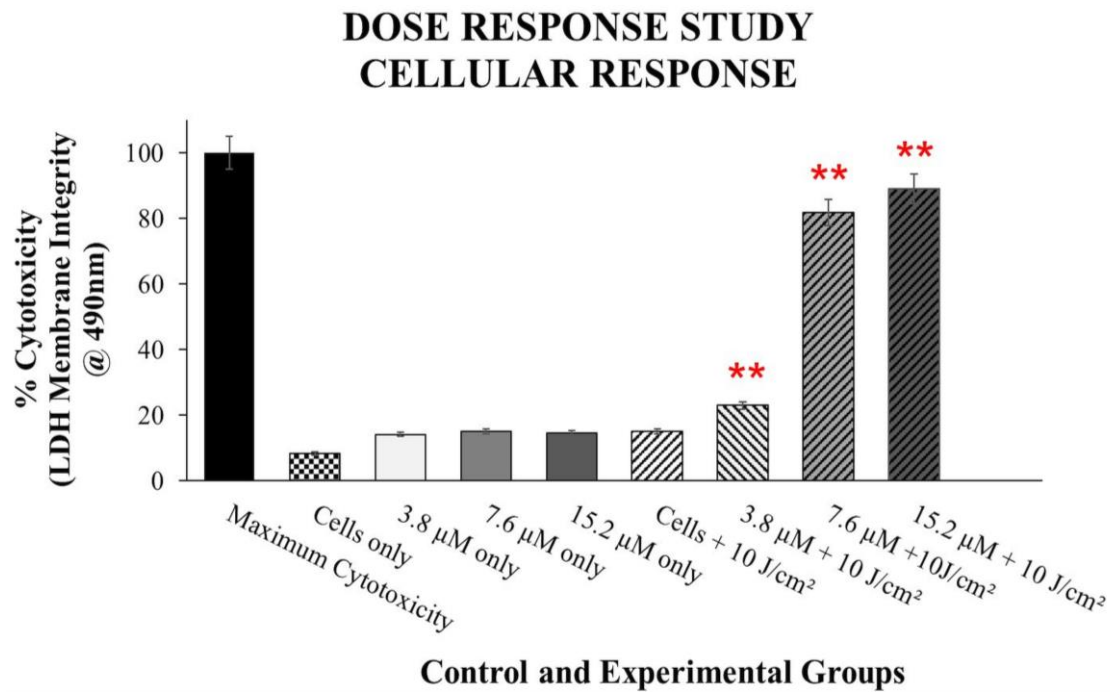


Figure 2. Lactate dehydrogenase hydrogenase (LDH) cytotoxicity assay indicated a significant ($p < 0.01$) ** increase in LDH levels in Hyp-AuNP PDT treated cells compared to the control cells.

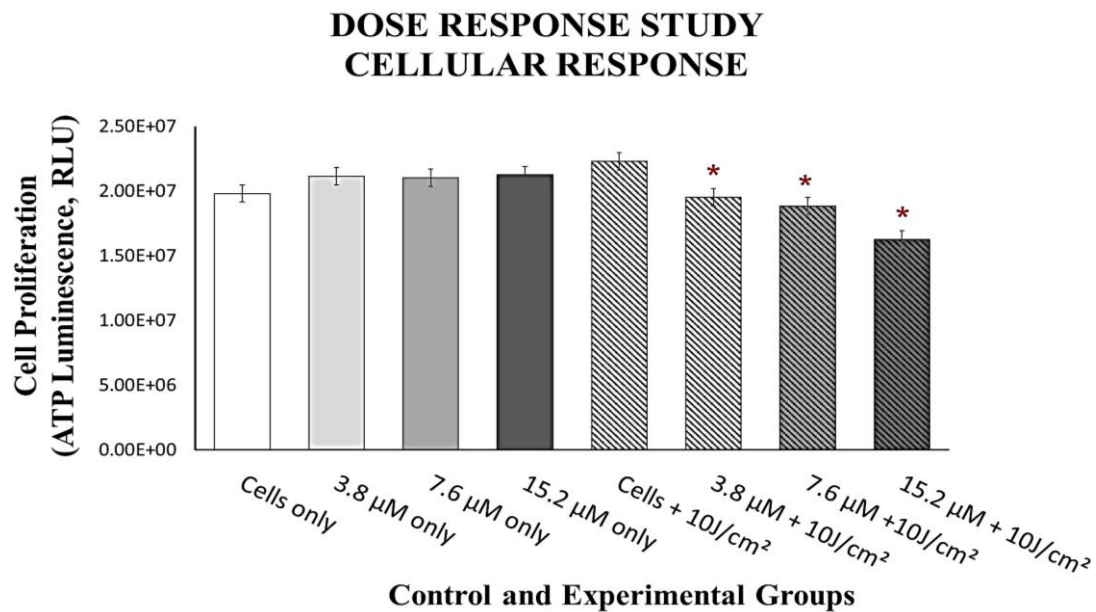


Figure 3. ATP Luminescence of cells indicating the rate of proliferation. Control cells in comparison to PDT treated groups showed a significant ($p < 0.05$)* decrease in ATP proliferation after 24 h. No significance was observed when control cells were compared with groups that only received the Hyp-AuNP conjugate.

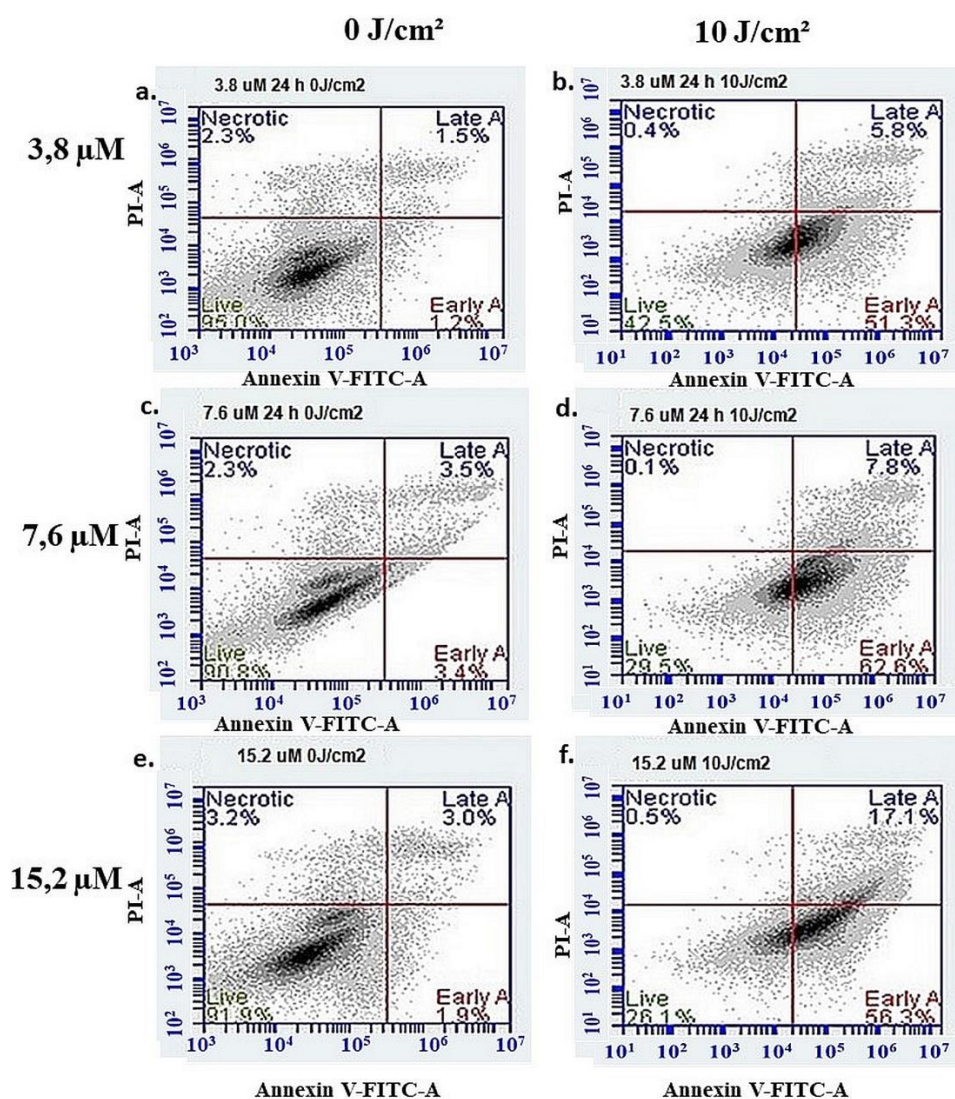


Figure 4. Annexin V/PI Flow cytometry results demonstrating early and late stage apoptosis at 24h post irradiation, where early apoptosis is shown as a percentage of the total population in the lower right quadrant and late-stage apoptosis shown as a percentage in the upper right quadrant. Plots a, c and e are non-irradiated control groups, while plots b, d and f are the PDT treated experimental groups.

4. Discussion and Conclusion

PDT prompts cell death by the production of reactive oxygen species resulting in oxidative damage to the cells, which results in cell death via apoptosis, necrosis, or autophagy [10]. In this study, the varying concentrations of the nano-PS conjugate resulted in significant photodamage to cells following laser irradiation at 594 nm. The morphology of conjugate PDT treated cells showed distinct damage compared to the untreated cells. This was further confirmed by the significantly decreased levels of ATP in proliferation assay results which indicated the decrease in cell proliferation in comparison to the cells only and cells treated with the nano-conjugate alone. There was an increase in the LDH levels in treated cells as compared to the untreated cells this indicates the damage to the cell membrane in treated cells following PDT and incubation at 24 h. The Annexin V/PI results indicate the oxidative cell damage in treated cells was due to the induction of early and late apoptosis.

Several studies have demonstrated the effects of Hypericin in PDT [11, 12]. However, its hydrophobicity has always been an issue, leading to the reduced cellular uptake and localization due to reduced movement through the cellular membrane of cancer cells. Conjugation of Hypericin to nanoparticles proves to be more effective and leading to an enhanced PDT efficacy than when used alone [13]. Hyp-AuNPs conjugate has demonstrated the desired therapeutic effects in MCF-7 cells in *in-vitro*. However, more studies need to be performed on normal breast cells to ensure the specificity of the treatment with no side effects to normal cells.

Acknowledgments

This work is based on the research supported by the South African Research Chairs Initiative of the Department of Science and Technology and the National Research Foundation of South Africa (Grant No 98337). The authors sincerely thank the University of Johannesburg, the National Research Foundation for their financial grant support, and the National Laser Centre for providing use of their lasers

References

- [1] What Is Breast Cancer? | Breast Cancer Definition [Internet]. [cited 2021 Aug 26]. Available from: <https://www.cancer.org/cancer/breast-cancer/about/what-is-breast-cancer.html>
- [2] Vanderpuye V, Grover S, Hammad N, PoojaPrabhakar, Simonds H, Olopade F, et al. 2017. *Infect. Agents Cancer* **12** 13.
- [3] Agostinis P, Berg K, Cengel KA, Foster TH, Girotti AW, Gollnick SO, et al. 2011 *CACancer J Clin* **61** 250–81.
- [4] Abrahamse H and Hamblin MR 2016 *Biochem J* **473** 347–64.
- [5] Jia X and Jia L 2012 *Curr Drug Metab* **13** 1119–22.
- [6] Plenagl N, Duse L, Seitz BS, Goergen N, Pinnapireddy SR, Jedelska J, et al. 2019 *Drug Deliv* **26** 23–33.
- [7] Portilho FA, Cavalcanti CE deOliveira, Miranda-Vilela AL, Estevanato LLC, Longo JPF, Almeida Santos M deFátimaMenezes, et al. 2013 *J Nanobiotechnol* **11** 41.
- [8] Stuchinskaya T, Moreno M, Cook MJ, Edwards DR and Russell DA 2011 *Photochem Photobiol Sci* **10** 822–31.
- [9] Zhu J, Zheng L, Wen S, Tang Y, Shen M, Zhang G, et al. 2014 *Biomaterials* **35** 7635–46.
- [10] Kubiak M, Łysenko L, Gerber H and Nowak R 2016 *Postepy Hig Med Dosw* **70** 735–42.
- [11] Kiro N and Abrahamse H (MCF-7). *SAIP Proceeding*:5.
- [12] Ali SM and Olivo M 2002 *Int J Oncol* **21** 531–40.
- [13] Yermak PV, Gamaleia NF, Shalamay AS, Saienko TV and Kholin VV 2010 *Exp Oncol* **4**.

Comparison of Indoor Radon Levels measured with three different Detectors (Passive and Active)

C G Sethabela¹, A R Ocwelwang^{1,2}, M Mathuthu¹ and A M Maheso³

¹Centre for Applied Radiation Science and Technology, North-West University
Mahikeng Campus, Corner of Albert Luthuli and University Drive Mmabatho. Private
Bag X2046 Mmabatho, 2745.

²Centre for Nuclear Safety and Security (CNSS), National Nuclear Regulator (NNR), Eco
Glades 2 Block G, 420 Witch Hazel Avenue, Highveld, Centurion. PO Box 7106 Centurion,
0046.

³Department of Physics, University of Stellenbosch-49 Victoria Street, Stellenbosch.
Private Bag X1, Matieland 7602, South Africa.

E-mail: csethabela@gmail.com

Abstract. Radon is a non-reactive, naturally occurring gas that emanates during the decay of uranium-238 (^{238}U) to radium-226 (^{226}Ra) then radon-222 (^{222}Rn). This radioactive gas is colourless, odourless and invisible. It is present in air, soil, water and building materials. Radon gas can be measured using two different measurement techniques, active and passive techniques. In this study, three types of radon detectors were deployed in two rooms at CARST to measure the indoor radon concentration. The detectors used were the AlphaGUARD model PQ 2000 detector, Airthings wave monitor and Solid-State Nuclear Track Detector (SSNTD). The detectors were deployed for three months. Results from the waste room showed that the SSNTD measured a radon concentration of $77 \pm 13 \text{ Bq/m}^3$. The AlphaGUARD and Airthings monitors recorded an average radon concentration of $37 \pm 10 \text{ Bq/m}^3$ and $35 \pm 18 \text{ Bq/m}^3$, respectively. Results from the CARST office showed that the SSNTD measured a radon concentration of $68 \pm 12 \text{ Bq/m}^3$. The AlphaGUARD and Airthings monitors recorded an average radon concentration of $19 \pm 11 \text{ Bq/m}^3$ and $12 \pm 3 \text{ Bq/m}^3$, respectively. The average radon levels obtained from the Airthings wave plus monitor and the AlphaGUARD are within a close range compared to the passive SSNTD results. However, results from all measurement techniques did not display alarming levels as they are below the recommended World Health Organization (WHO) national reference level of 100 Bq/m^3 .

1. Introduction

Radon (^{222}Rn) is a chemically inert, radioactive gas that occurs naturally in the earth's crust. This gas has a half-life of 3.8 days. It is colourless, odourless and tasteless, and it tends to accumulate to high concentration levels inside buildings [1]. Radon emanates from the radioactive decay series of uranium-238 (^{238}U). It is formed by the emission of an alpha particle from its parent radionuclide radium-226 (^{226}Ra). Radon is also an alpha emitter; it emits alpha particles when it decays to its progeny, polonium-218 (^{218}Po) and polonium-

214 (^{214}Po) [1]. Sources of indoor radon include soil, rocks, and groundwater. Radon accumulates in buildings by moving from soil and rocks into the air and seeping into buildings by advection and diffusion. Buildings without airbricks or ventilation systems and buildings with cracks are more at risk of high radon accumulation [2, 3].

Studies have shown that building materials can also be a source of indoor radon if they contain certain radioactive elements, including uranium [4]. Meteorological factors such as temperature, air pressure, and humidity have also influenced indoor radon levels. Radon has been listed as the second leading cause of lung cancer by International Agency for Research on Cancer (IARC) [5]. Thus, knowing the level of ionising radiation and indoor radioactivity in buildings where people spend most of their time is of great importance; this includes homes and workplaces such as schools, universities and offices.

1.1. Description of the study area

The Centre for Applied Radiation Science and Technology (CARST) is one of the North-West University Mafikeng Campus departments under the Natural and Agricultural Sciences faculty. The CARST facilities consist of three buildings, and measurements were taken in two of these buildings, the lecturer's office and the waste room. The two rooms are built with the same type of building materials and floor type. Ventilation in these rooms is different; the office has a window. It is frequently opened and occupied during the week but closed over weekends. The waste room does not have a window but a door that is closed 90% of the time. This door is opened only when there is an activity in the waste room.

The radioactive waste room stores low-level radioactive waste, mainly from environmental samples, like soil, water, rock and plants. There are also beakers, gloves and paper towels used by the researchers and students in the facility. All these materials were used for research. Samples stored in this room are collected from mine dams and waste rocks, Tailing Facilities Storage (TFS) and areas near mines. The lack of ventilation in the waste room makes the waste room and ultimately the laboratory conducive for radon gas accumulation. It is thus essential to measure and monitor the ^{222}Rn concentration levels in this waste room. Due to the risks associated with exposure to ionising radiation, radioactive waste materials cannot be disposed of as regular waste. Standard procedures need to be followed according to the type of waste (high level, medium level and low-level radioactive waste) classified by the IAEA and regulated by the NNR. Therefore, every facility that generates radioactive waste should follow regulatory procedures to effectively isolate, store, and dispose of waste [6]. According to the WHO, measuring and monitoring ^{222}Rn in dwellings and public buildings is the most effective way to protect people from potential health risks [7].

2. Method and Material

2.1. Description of instruments used

Many detectors are used to measure radon concentration; detectors used are either passive or active techniques. They can detect alpha particles emitted when ^{222}Rn decay to its progenies. Each method is best depending on the application. Integrative, passive radon detectors do not require electrical power to operate, while continuous active radon detectors require electrical power [8]. This study employed three different detectors to measure indoor radon concentration. The solid-state nuclear track detector (SSNTD), also called "etched track detector", is a passive technique. The AlphaGUARD and Airthings Waves radon detectors are active techniques.

2.1.1. Integrated Passive Radon Detector: Solid-State Nuclear Track Detectors (SSNTD). Figure 1 displays the SSNTD that was used in this study. The SSNTD comprises a thin plastic film (Figure 2) of materials capable of recording alpha tracks emitted by radon and its progenies. Track detectors exist in open and closed types, and sampling is done in passive mode. The plastic film usually comes in two types, the LR115 (cellulose nitrate) and CR-39 (polyallyl diglycol carbonate). After exposure of the detector for a specified period, the plastic material is etched in NaOH or KOH solution to reveal any track damages (Figure 2). The exposure period is usually long enough to get representative data [9].



Figure 1. PARC RGM Solid State Nuclear Track Detector [10].

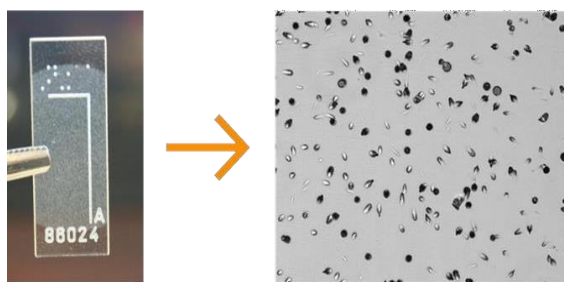


Figure 2. Alpha tracks viewed under the microscope [10].

2.1.2. Continuous Active Radon Detectors: AlphaGUARD and Airthings. The AlphaGUARD. (Figure 3) is a continuous active radon detector with an ionisation chamber and uses alpha spectrometry for radon detection. The time required for radon diffusion into the ionisation chamber cause a lag in the signal [11]. The device has an internal battery that can operate for roughly ten days. The measurement ranges from 2 Bq/m³ to 2 MBq/m³ with an operating temperature of 10 - 100° C. The operating pressure ranges between 700 to 1100 mbar [12]. The working principle of this device is that when radiation passes through gas-filled space or air, molecules get ionised, and a signal is generated [11].

A signal is generated from the alpha detection and converted to a digital output that the computer can read. DataEXPECT software installed in the computer is used to retrieve results from the AlphaGUARD [13]. The Airthings wave radon detector (Figure 4) is a disc sized radon detector operated by a pair of AA batteries. This detector uses a preinstalled three-colour light system to indicate the radon level detected. When the detected radon is high, the light turns red, and it can also beep. The green light indicates low concentration, and the yellow indicates high but not alarming radon levels. Airthings radon detector uses a smartphone connecting via Bluetooth to download the average radon concentration and temperature, air pressure, and humidity measured every 60 minutes [14].



Figure 3. AlphaGUARD Professional Radon Monitor [13].



Figure 4. Airthings Waves Radon Detector [14].

2.2. Radon Measurements

The three devices were deployed in the waste room that contains low-level radioactive waste generated from research activities. The study was conducted for three months using active and passive radon measurement techniques. AlphaGUARD had a power supply throughout the exposure period to avoid technical errors due to the instrument switching off. Detectors were placed on top of a shelf approximately 1.5 m above the floor and 150 cm from the wall and door as recommended by the International Atomic Energy Agency (IAEA) [15]. The two active devices also measured the room temperature, pressure, and humidity hourly, corresponding to the measured radon concentration.

However, this study did not focus on these parameters. The measurement interval was set to 60 minutes in both active detectors and measured in Bq/m^3 . Microsoft excel data analysis tool was used to analyse the data to obtain the three months indoor radon concentration average (mean). This is a sum of the hourly measured average concentrations divided by the total number of hours of the measurement period (i.e., 245 hours equivalent to 10 days of measurement in the CARST office). The descriptive analysis also gave the minimum, maximum and standard deviation of the data from each active detector. With the passive detector, laboratory analyses (i.e., chemical etching and counting of tracks) was conducted by the supplier (PARC RGM Laboratories). Results were provided as average indoor radon concentration in Bq.h/m^3 and the corresponding standard deviation for the measurement period. The radon concentration was converted to Bq/m^3 by dividing radon exposure in Bq.h/m^3 by 2208 hours, equivalent to the three-month measurement period ($[\text{Rn}]/\text{Bq/m}^3 = \text{Bq.h/m}^3/2208 \text{ hrs.}$).

3. Results and Discussions

3.1. CARST Radioactive waste room indoor radon results from the three detectors

Table 1 presents indoor radon levels measured with three devices in the CARST waste room. The three radon detectors were deployed for three months (November 2020 - January 2021). The table also presents the calculated annual effective exposure dose to the students and lecturers at the CARST facility.

According to the ICRP, the reference level of indoor radon is 100 Bq/m^3 . Table 1 also indicates that indoor radon concentration levels in the CARST waste room are lower than the recommended levels of 100 Bq/m^3 [16]. Measurements from radon detectors agree with the concentration of $35 \pm 18 \text{ Bq/m}^3$ and $37 \pm 10 \text{ Bq/m}^3$ from Airthings and the AlphaGUARD radon detectors, respectively. The difference between the two active detectors was expected because they both use the same detection technique. The passive SSNTD measured a radon concentration level of $77 \pm 13 \text{ Bq/m}^3$, a level twice that recorded by the active devices. Results show that indoor radon concentration levels in the radioactive waste are below the ICRP recommended reference levels between $100\text{--}300 \text{ Bq/m}^3$.

Table 1. Indoor radon concentration levels from the waste room using three different detectors.

Instrument	Type of measurements	^{222}Rn Concentration (Bq/m^3)	Standard Deviation (Bq/m^3)	Annual Effective Dose (mSv)
SSNTD	Passive	77	13	0.55
AlphaGUARD	Active	37	10	0.27
Airthings	Active	35	18	0.25

Figures 6 show the fluctuation of radon gas from two active detectors in the waste room. Radon gas can fluctuate hourly, daily and seasonally in the same space, only in 59% of cases where AlphaGUARD results were greater than that of the Airthings. The highest peak observed in figure 6 presents a radon concentration of 217 Bq/m^3 by Airthings radon active at 01:31 am on day 52 of the measurements (661 hrs.); at this time, AlphaGUARD measured 53 Bq/m^3 . This large difference may be because radon gas does not reach or interact with the detectors simultaneously. This trend is expected since radon gas is not uniformly distributed and stable in the same space [13].

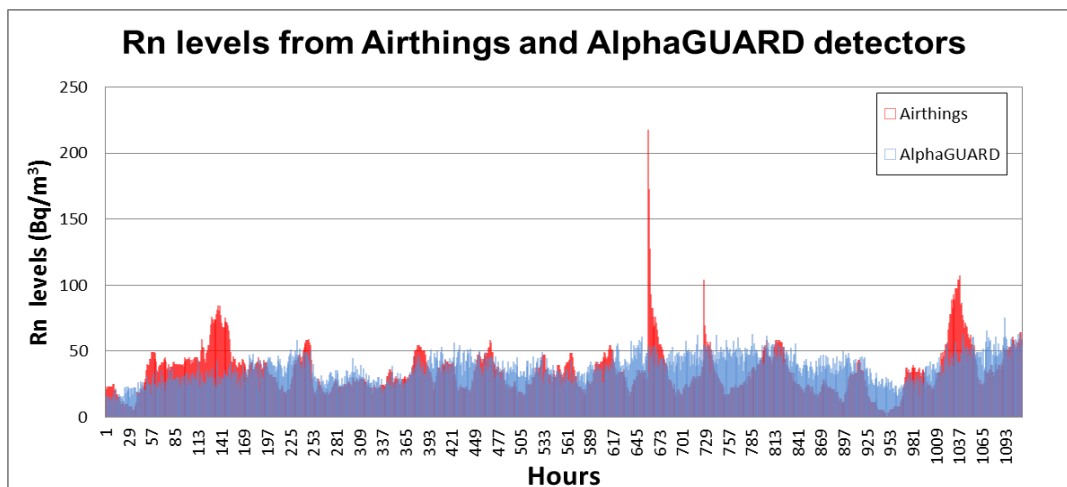


Figure 6. Fluctuations of indoor radon concentration in CASRT radioactive waste room.

3.2. CARST office indoor radon results from the three detectors.

Table 2 presents indoor radon results from a well-ventilated office at the CARST facilities measured with the passive and active detectors. The highest concentration detected from this room is 68 ± 12 Bq/m³ by SSNTD (Passive) detector. The SSNTD radon concentration in the office is lower than the level measured in the waste room. This may be because the level of radon gas in naturally ventilated environments are always substantially lower than those detected in non-ventilated environments measured by SSNTDs. Indoor radon concentrations measured for two weeks by the two active devices (Airthings and AlphaGUARD) ranged between 10 - 20 Bq/m³, significantly below the estimated world average of 40 Bq/m³ [15].

Table 2. CARST office indoor radon concentrations from three different detectors

Instrument	Type of measurements	²²² Rn Concentration (Bq/m ³)	Standard Deviation (Bq/m ³)	Annual Effective Dose (mSv)
SSNTD	Passive	68	12	0.49
AlphaGUARD	Active	12	3	0.09
Airthings	Active	19	11	0.14

The WHO and the IAEA [7, 15] have reported that ventilation is one of the methods to reduce indoor radon concentrations. This study shows that ventilation plays an important role in indoor radon concentration. A well-ventilated office measured lower radon concentration. Air circulation and ventilation dilute the radon gas after it enters the building. It also reduces the pressure difference between the soil and the occupied spaces, as indicated by the WHO [7].

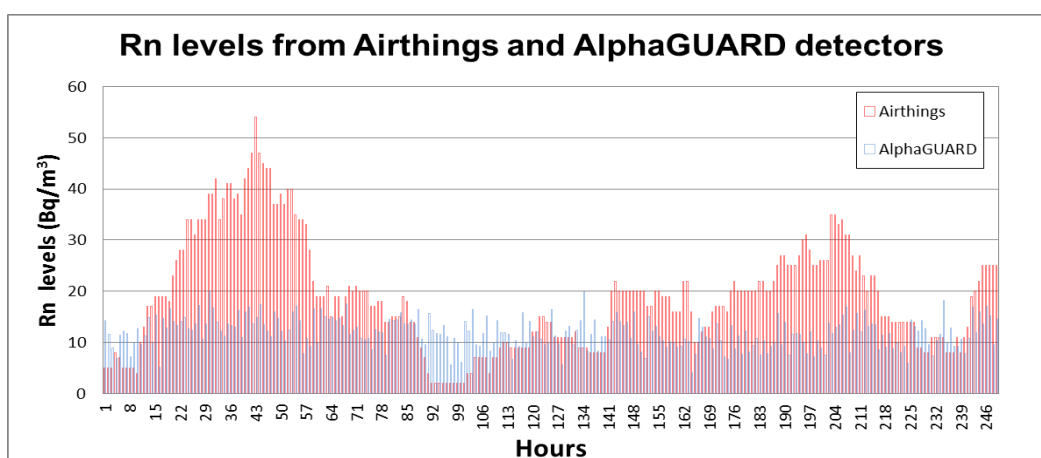


Figure 7. Fluctuations of indoor radon concentration in CARST office.

Figure 7 shows radon gas fluctuation from the two active detectors deployed in the CARST office. AlphaGUARD measured a minimum radon concentration of 4 Bq/m³ at 23:56 am day 6 of the measurements (165 hrs.). For Airthings, the minimum concentration measured was 2 Bq/m³, and this was constant from 22:56 to 07:56 am on days 3 and 4 of the measurements (93-102 hrs.). The maximum recorded concentration is 54 Bq/m³ at 08:55 pm (44 hrs.) from Airthings. The maximum concentration measured by the AlphaGUARD is 20 Bq/m³ at 07:55 am on day 2 of the measurements (31 hrs.).

It has been shown in some studies and reported by the IAEA that indoor radon concentration is higher at night than during the day due to low ventilation because doors and windows are closed. However, from this study, such a trend was not observed. Results show radon concentration varies throughout; both active detectors measured the maximum and minimum concentrations during the night. In the office, 72% of the time, Airthings results were greater than that of the AlphaGUARD. However, the difference in the average concentrations of the two active detectors is 7 Bq/m³ (23%).

Results of the passive detectors deployed in the two rooms (waste room and office) displayed elevated radon concentrations compared to the results of the active detectors. These observations may be attributed to the two techniques operating differently. As mentioned in 2.1.1, AlphaGUARD and Airthings have ionising chambers, and there is a lag/fall back in the detectors because of the time required for radon to get into the ionising chamber to be diffused [13]. SSNTDs are time-integrated detectors with no lag or measurement delays. Another factor that influenced the difference in the measured concentrations is the sensitivity of the instruments.

The low concentration detected by passive detectors (AlphaGUARD and Airthings) could be due to the fluctuation of atmospheric parameters since both detectors are sensitive to temperature, humidity and air pressure; these parameters; the passive detector (SSNTD) is not sensitive to any meteorological parameters [7]. High temperature, humidity and low air pressure are typically associated with non-ventilated places, resulting in higher radon gas detection. This agrees with the obtained results; the non-ventilated waste room has a higher radon concentration. This is due to the accumulation of radon gas. In the well-ventilated office, temperature and humidity are lower due to air circulation and subsequently reduce the accumulation of radon gas.

The annual effective dose was calculated to get the level that CARST occupants might be exposed to. Active detectors in this study detected the alpha particles from radon in 60 minutes intervals. The annual effective dose due to inhalation of radon was estimated using the following equation:

$$E_{Rn} (mSv.y^{-1}) = DCF_{Rn} \times F_{Rn} \times A_{Rn} \times T_{Rn} \times 10^{-6} \quad (1)$$

Where E_{Rn} is the annual effective dose of inhaled radon, DCF_{Rn} is the radon conversion factor through inhalation (assumed to be 9 mSv/Bq m³h) [17]. F_{Rn} is the indoor equilibrium factor between radon and its progeny (assumed to be 0.4) [18]. A_{Rn} is the radon activity concentration in Bq/m³, T_{Rn} is the exposure time (assumed to be 2000 hours/yr. for workers).

The estimated annual effective dose calculated from the three devices for the office and waste room is below the ICRP recommended occupational dose limit of 20 mSv/yr. [11, 17]. The calculated annual effective dose in the waste room and office ranged between 0.09-0.55 mSv/yr., below the recommended dose limit. The passive detector measurements indicate that CARST staff and students might be exposed to unsafe doses. However, these results contrast those recorded by active radon monitors, which showed that the calculated effective dose is acceptable.

4. Conclusion

This paper used three different radon detectors to measure radon gas in the waste room and office in two buildings at CARST. Overall results show that there is currently no cause for concern at two CARST buildings due to indoor radon gas. Passive detectors deployed in the waste room and the office recorded a ²²²Rn concentration above the WHO reported global average indoor radon of 40 Bq/m³ [9]. The active devices recorded a lower concentration in both the rooms.

The results from active radon detectors in both the waste room are close to each other, with a difference of 2 Bq/m^3 and a larger difference of 7 Bq/m^3 which was unexpected. The results obtained from the passive radon detector were relatively higher than those from active detectors in both rooms. From these observations, it can be concluded that the two techniques are different regardless of whether they are in the same room, same exposure time and same environmental parameters, suggesting that one technique must be employed to evaluate the effective dose. The overall indoor radon concentration levels were below the recommended WHO national reference level of 100 Bq/m^3 and the ICRP recommended radon exposure range of $100\text{--}300 \text{ Bq/m}^3$. According to the IAEA and the WHO, the active techniques are excellent for limited surveys, screening and analysing the fluctuation of radon over a short exposure period. Meanwhile, passive techniques are ideal for long-term measurements. They give an overall average radon concentration over a long time. This method is also excellent for determining the annual effective dose received by the students and CARST staff members. However, in this study, it is observed that passive technique Airthings detector agrees with the corresponding standard deviation in both rooms; $35 \pm 18 \text{ Bq/m}^3$ and $19 \pm 11 \text{ Bq/m}^3$, respectively. Airthings radon detector can be trusted and used for long-term and short-term measurements. The use both active and passive detectors for verification purposes. The passive detector is trustworthy because long-term measurements give a good estimate of the radon concentration. Active detectors measured very low concentrations levels that could be representing the background radon.

References

- [1] Cothorn CR and James JE 2013 *Environmental Science Research*. 35
- [2] Moshupya P, Abiye T, Mouri H, Levin M, Strauss M and Strydom R 2019 *Geosciences*. 9(11) 466
- [3] Sahu P, Panigrahi DC and Mishra DP 2014 *Journal of Sustainable Mining* 13(3)11-18
- [4] Kulali F, Günay O and Aközcan S 2019 *International Journal of Environmental Science and Technology*. 16(9)5281-5284
- [5] World Health Organization 2001 Evaluation of Carcinogenic Risk to Humans. Ionizing Radiation, part 2: Some Internally Deposited Radionuclides. International Agency for Research on Cancer Press. France
- [6] Pule J 2015 South African perspective for radon in dwellings and the anticipated regulatory control measures. SARPA conference. 2015. Villa Paradiso, South Africa: National Nuclear Regulator (NNR)
- [7] World Health Organization 2010 WHO guidelines for indoor air quality: selected pollutants
- [8] Sethi TK, El-Ghamry MN and Kloecker GH 2012 *Clin Advanced haematology-oncology*. 10(3)157-164
- [9] World Health Organization 2009 WHO handbook on indoor radon: a public health perspective
- [10] Parc RGM 2021 (Radon gas monitoring) (pty) Ltd, (www.parcrgm.co.za).
<https://www.parcrgm.co.za/analysis-and-quantification/>
- [11] Kasar S, Mishra S, Omori Y, Sahoo SK, Kavasi N, Arae H, Sorimachi A and Aono A 2020 *Journal of Soils and Sediments*. 20(1)392-403
- [12] Kamunda C, Mathuthu M and Madhuku M 2017 *Journal of Environmental and Toxicological Studies*. 1(1)
- [13] McMurdy., G., *Interfacing the AlphaGUARD Radon Monitor with Campbell Scientific's CR1000 Datalogger*, S. GmbH, Editor. 2009, Campbell Scientific Inc.: Logan, UT p. 753-2342.
- [14] Moon B 2019 *Airthings Wave smart radon detector review*. <https://blog.bestbuy.ca/smart-Home/airthings-wave-smart-radon-detector-review#>.
- [15] IAEA 2013 National and regional surveys of radon concentration in dwellings: Review of methodology and measurement techniques
- [16] Harrison, J and J Marsh 2020 *ICRP recommendations on radon. Annals of the ICRP*. 49 68-76
- [17] ICRP 2018 ICRP Publication 139: Occupational Radiological Protection in Interventional Procedures
- [18] Nader AF 2019 *IOP Conf. Series: Journal of Physics: Conf. Series*, 1258 (2019) 012032

On the advantages of relative phase Toffoli gates

Unathi Skosana¹ and Mark Tame

Department of Physics, SU, Matieland 7602, South Africa

E-mail: ¹unathiskosana@protonmail.com

Abstract. Many of the quantum algorithms that make theoretical guarantees on computational speedups are well beyond the capabilities of currently existing noisy intermediate-scale quantum (NISQ) hardware. The requisite resource demands of these algorithms (*e.g.* qubits, quantum gates, circuit repetitions etc) make their implementation impractical on such hardware. For some algorithms, various approaches exist to reduce these demands. We consider one such approach here. This approach uses relative phase Toffoli gates, advantageous over regular Toffoli gates due to their smaller circuit size. As a proof-of-concept demonstration of the utility of relative phase Toffoli gates, we have used a configuration of these gates in constructing the compiled quantum phase estimation routine to achieve a complete factoring of $N = 21$.

1. Introduction

In classical computation the reversible Toffoli gate is a universal logic gate, *i.e.* any logic circuit L which computes a Boolean function of the form $f : \{0, 1\}^n \rightarrow \{0, 1\}$ can be decomposed into a reversible logic circuit L' , equivalent in operation, made up of only Toffoli gates. The truth table and circuit diagram for a Toffoli gate are shown in figure 1.

Inputs			Outputs		
a	b	c	a'	b'	c'
0	0	0	0	0	0
0	0	1	0	0	1
0	1	1	0	1	1
1	0	0	1	0	0
1	0	1	1	0	1
1	1	0	1	1	1
1	1	1	1	1	0

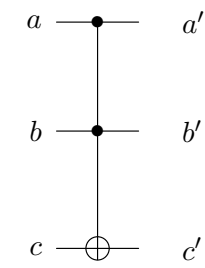


Figure 1. Truth table and circuit for a Toffoli gate.

The reversibility of a Toffoli gate implies that its operation can be realized as a unitary quantum logic gate ($U^{-1} = U^\dagger$), making reversible Boolean arithmetic reproducible on a quantum computer. The Toffoli gate, which is a doubly-controlled NOT (CCX) gate, is described by the following map on a quantum state,

$$\text{CCX}_{abc} : |a, b, c\rangle \mapsto |a, b, c \oplus a \cdot b\rangle, \quad (1)$$

where \oplus is modulo 2 addition, \cdot is the bitwise inner product and qubit Hilbert spaces are separated by commas. Notwithstanding their apparent importance, current quantum hardware do not natively support Toffoli gates but rather physically implement a universal gate-set made up of single-qubit gates (*e.g.* \sqrt{X} , X , RZ) and a single two-qubit entangling gate (*e.g.* CX , CZ , $\sqrt{i\text{SWAP}}$) with high fidelity ($\gtrsim 99\%$ for superconducting qubits, see Ref. [1]). A Toffoli gate is then decomposed into single and two-qubit gates from this native gate-set [2]. Due to the effects of decoherence, there is an upper limit on the number of two-qubit gates over a set of qubits that can be in a circuit, this makes the study of Toffoli gates a subject of interest for practical quantum computing. It has been shown that a three-qubit Toffoli gate (CCX) cannot be implemented with less than five two-qubit gates [3, 4], the traditional three-qubit decomposition into six controlled-NOT (CX) and seven T/T^\dagger gates is shown below

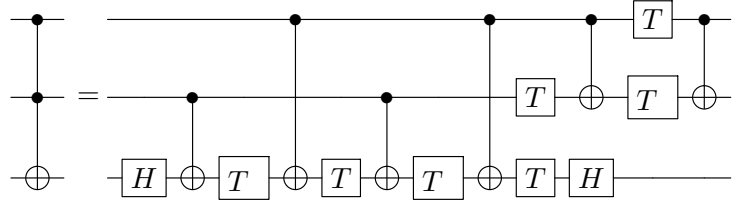


Figure 2. Circuit diagram showing the decomposition of a Toffoli gate in terms of elementary gates; six controlled-NOT (CX) and seven T/T^\dagger gates.

where H is a Hadamard gate and $T = \text{diag}(1, e^{i\frac{\pi}{4}})$. However, there exists variants of the Toffoli gate, smaller in circuit size, collectively called ‘relative phase’ Toffoli gates due to their operation being equivalent to that of a Toffoli modulo a relative phase shift. Maslov [5] showed that the utility and application of these relative phase variants extends beyond specific and commonly conceived scenarios, leading to a reduction in gate count of known configurations of multiply-controlled Toffolis while preserving functional correctness. Our recently published scheme [6] represents such a specific application of relative phase Toffoli gates, where we employed them for carrying out a demonstration of Shor’s quantum algorithm [7] for factoring $N = 21$ on IBM Q’s quantum processors. Hence, we introduce the relative phase Toffoli gate and characterize its performance.

2. Generation of entanglement with relative phase Toffoli gates

The relative phase variant which implements a three-qubit Toffoli gate up to a relative shift ($|101\rangle \mapsto -|101\rangle$) is the one considered. The decomposition of such a gate by Margolus [8], as shown in figure 3, optimally uses three CX gates and four single-qubit gates [9]. We label this gate as RCCX . If in the use of a Toffoli gate such a relative phase shift is permitted, the CX count is significantly reduced in comparison to the full Toffoli shown in figure 2. Consider such an example scenario where we seek to generate entanglement from a state prepared in a three-qubit register:

$$|\psi\rangle = X_0 H_1 |0\rangle_0 |0\rangle_1 |0\rangle_2 = |1\rangle_0 |+\rangle_1 |0\rangle_2, \quad (2)$$

where X is a bit-flip ($|0\rangle \mapsto |1\rangle, |1\rangle \mapsto |0\rangle$) and H is a Hadamard gate ($|0\rangle \mapsto |+\rangle, |1\rangle \mapsto |-\rangle$).

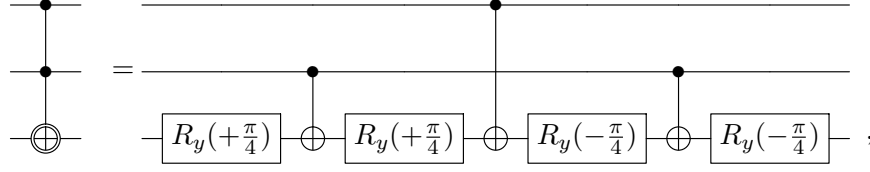


Figure 3. Circuit diagram showing the decomposition of a Margolus gate in terms of elementary gates; three controlled-NOT (CX) and four $R_y(\pi/4)$ single qubit gates, where $R_y(\pi/4) = e^{-i\pi/8} SHTHSZ$, $S = \text{diag}(1, i)$ and $Z = \text{diag}(1, -1)$.

Applying a CCX_{012} to the above state controlled by qubits 0,1 and targeted on qubit 2, we produce the state

$$\begin{aligned} \text{CCX}_{012} |\psi\rangle &= \text{RCCX}_{012} |\psi\rangle = \frac{1}{\sqrt{2}} |1\rangle_0 (|0\rangle_1 |0\rangle_2 + |1\rangle_1 |1\rangle_2), \\ &= |1\rangle_0 |\Phi^+\rangle_{12}, \end{aligned} \quad (3)$$

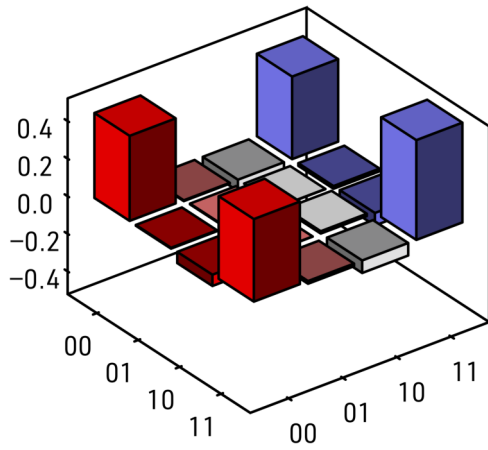
$|\Phi^+\rangle = 1/\sqrt{2}(|0\rangle|0\rangle + |1\rangle|1\rangle)$ is one of the maximally entangled two-qubit Bell states. In such a scenario, one observes that the state $|101\rangle_{012}$ never arises in the register and thus the operation of CCX and RCCX gates are equivalent. We characterize the performance of these two gates by performing state tomography of qubits 1 and 2 on the state in (3), experimentally prepared on IBM Q's seven-qubit quantum processor *ibmq_casablanca* [10] through the software development kit Qiskit [11]. A typical measured density matrix from the ensemble of measured density matrices is shown in figure 4. To quantitatively evaluate the performance of the two gates in generating the Bell state in (3), we measure the fidelity for two quantum states ρ and σ , defined as $F(\rho, \sigma) = \text{tr}(\sqrt{\sqrt{\rho}\sigma\sqrt{\rho}}^2)$ [12]. We measured (within 95% confidence intervals) the fidelities to be $F(|\Phi^+\rangle\langle\Phi^+|, \sigma_{\text{CCX}}) = 0.929 \pm 0.003$ and $F(|\Phi^+\rangle\langle\Phi^+|, \sigma_{\text{RCCX}}) = 0.972 \pm 0.008$ for measured density matrices with a CCX and a RCCX gate, respectively. Each measurement performs 8192 circuit repetitions and all other subsequent measurements. The fidelity ranges between 0 and 1, a fidelity equal to 1 means the measured state is equal to the ideal state $\rho = |\Phi^+\rangle\langle\Phi^+|$ and fidelity less than 1 indicates how “far away” the state is from ideal. In a larger circuit where more than one Toffoli gate is replaced in such a manner the overall functionality of the circuit would be unaltered, and the difference between the performance of the two gates would be much more discernible.

As further characterization of the two gates concerned, we perform quantum process tomography and reconstruct the χ matrix representation of a quantum channel \mathcal{E} that describes the operation of a circuit. We do this for circuits on the aforesaid quantum processor; *ibmq_casablanca*, which prepared the states shown in figure 4. How closely a quantum channel \mathcal{E} approximates U (the ideal circuit) is described by the average gate fidelity given by:

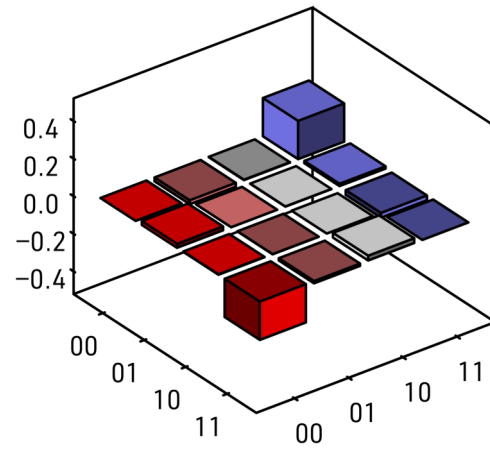
$$\bar{F}(\mathcal{E}, U) = \int d\psi \langle \psi | U^\dagger \mathcal{E}(|\psi\rangle\langle\psi|) U | \psi \rangle, \quad (4)$$

where the integration is over the uniform Haar measure on the state space, and $\mathcal{E}(\cdot)$ is an evolution with respect to the quantum channel \mathcal{E} . The χ -matrix representation of \mathcal{E} is a matrix χ such that a density matrix ρ under the action of quantum channel \mathcal{E} evolves as such:

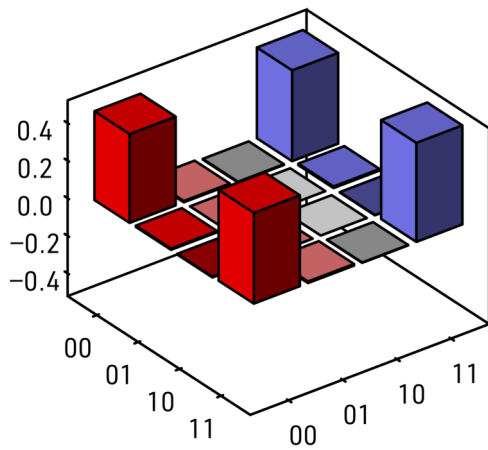
(a)



(b)



(c)



(d)

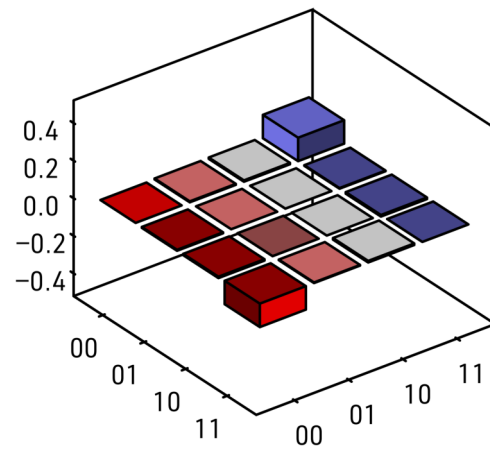
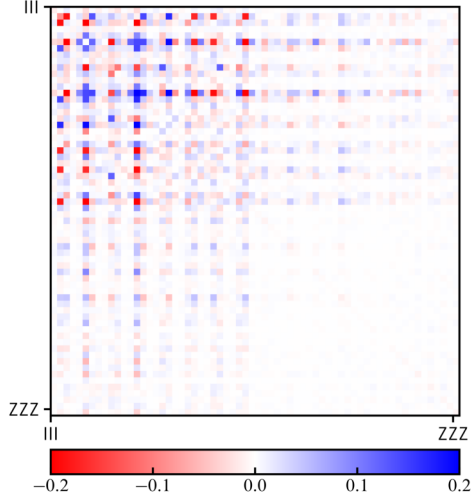
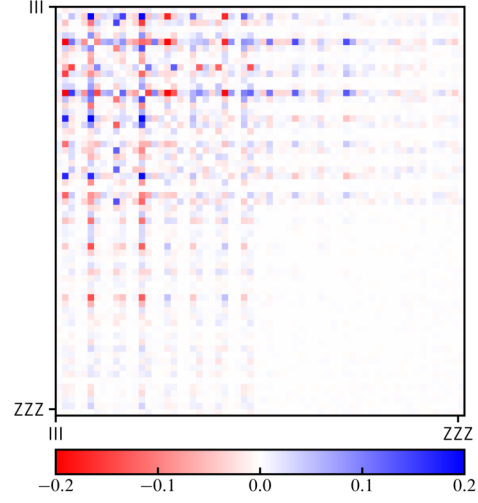


Figure 4. (a) Real and (b) imaginary parts of the measured density matrix of the state of qubits 1 and 2 in (3) prepared with a CCX gate on IBM Q's *ibmq-casablanca*. Similarly, (c) and (d) are real and imaginary parts, respectively, of the same state prepared with a RCCX gate.

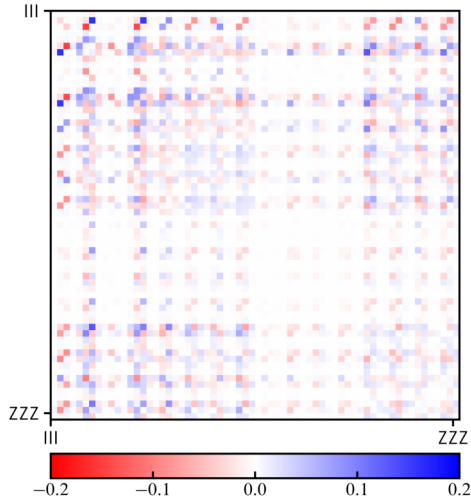
(a)



(b)



(c)



(d)

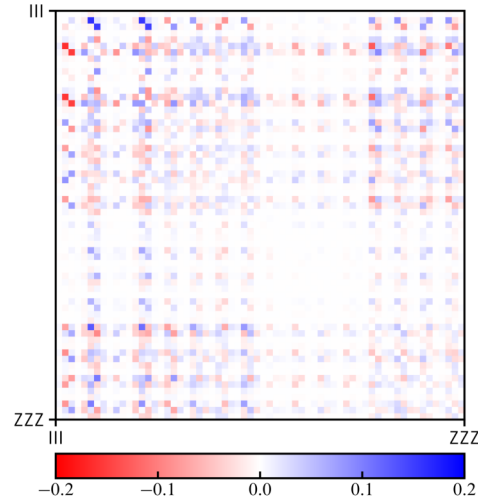


Figure 5. (a) Real and (b) imaginary part of the difference between experimentally measured and the ideal χ -matrix matrix presentation of the quantum channel prepared with a CCX gate on IBM Q's *ibmq_casablanca*, $\mathcal{E}_{\text{ideal}} - \mathcal{E}_{\text{CCX}}$; The largest element differences are 0.254 and 0.322, respectively. Similarly, (c) and (d) are real and imaginary parts, respectively, of the difference the measured and the ideal χ -matrix matrix presentation of the quantum channel prepared with a RCCX gate on IBM Q's *ibmq_casablanca*, $\mathcal{E}_{\text{ideal}} - \mathcal{E}_{\text{RCCX}}$. The largest element differences are 0.163 and 0.163, respectively. In all figures the color bar is rescaled to a range between -0.2 and 0.2 for visual clarity.

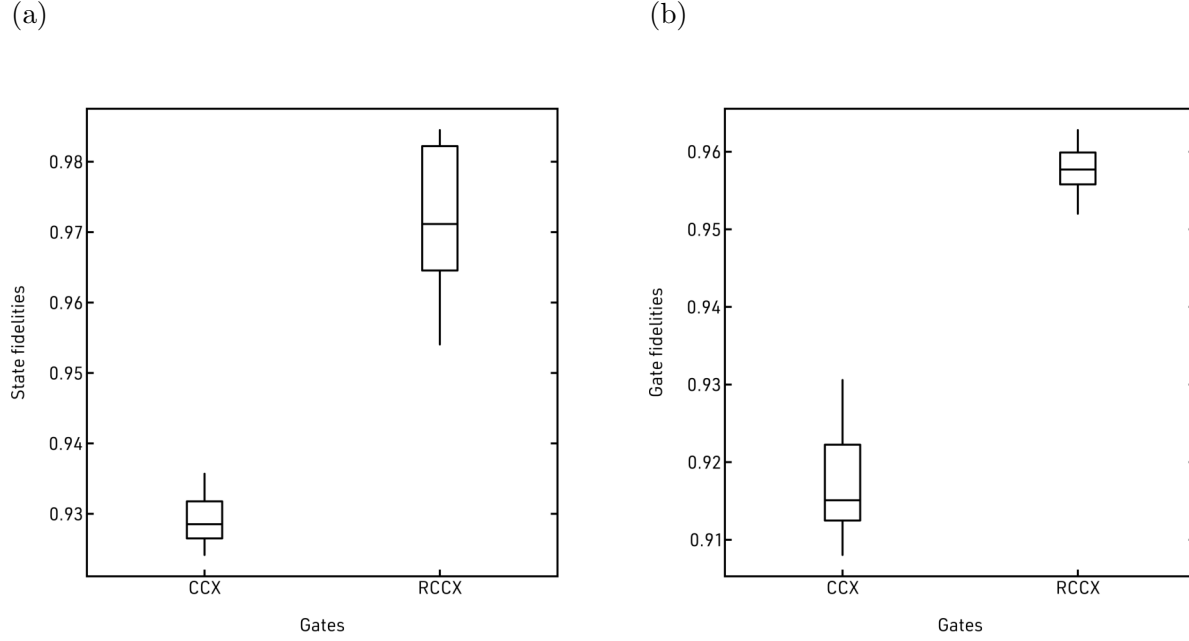


Figure 6. (a) State fidelities between the ideal Bell state $|\Phi^+\rangle\langle\Phi^+|$ and the members of the measured ensemble of density matrices σ_{CCX} and σ_{RCCX} respectively, and (b) average gate fidelities of the quantum channels that prepare the state in (3) with a CCX and RCCX gate respectively.

$$\mathcal{E}(\rho) = \sum_{i,j} \chi_{ij} E_i \rho E_j^\dagger, \quad (5)$$

here the E_i 's are n -fold tensor products of all 3^n combinations of Pauli matrices X, Y, Z plus the 2×2 identity matrix I (e.g. $E_0 = I \otimes I \otimes I$). See references [13, 14] for closed-form expressions of (4). We measured the average gate fidelities to be $\bar{F}_{\text{CCX}}(\mathcal{E}, U) = 0.917 \pm 0.005$ and $\bar{F}_{\text{RCCX}}(\mathcal{E}, U) = 0.958 \pm 0.002$ respectively, and show differences between the respective measured and ideal χ -matrices in figure 5. In the case of using a RCCX gate, the target unitary preparing the state in (3) is better reconstructed than a CCX gate on the respective processor; the measured χ -matrix for the quantum channel $\mathcal{E}_{\text{RCCX}}$ shows a smaller maximum element-wise difference from its respective ideal χ -matrix than the measured χ -matrix for the quantum channel \mathcal{E}_{CCX} . This is also corroborated by Figure 6, which shows boxplots of state fidelities and average gate fidelities, respectively. We see that comparatively the RCCX gate prepares a Bell state with a higher state fidelity than a CCX gate. Similarly, due to the RCCX gate being comparatively smaller than the CCX gate in terms of its circuit size, it has an overall better average gate fidelity on the IBM Q's *ibmq-casablanca* processor.

3. Relative phase Toffoli gates for quantum factoring

In 2012, the integer $N = 21$ was factored using a small-scale quantum processor, setting the record for the largest integer factored with Shor's quantum factoring algorithm [15]; Similarly in 2019, the integer $N = 21$ was factored again [16]. These two schemes adopt an iterative version of Shor's algorithm which employs a single qubit in the control register that is recycled

through feed forward operations to reduce the qubit overhead of the algorithm. However, at the time of writing, real-time conditional feed forwards operations are not widely supported among current quantum hardware, which the latter implementation [16] circumvented by splitting up the iterations of the algorithm into separate circuits. Moreover, upon further scrutiny, the former implementation [15] fell one iteration short of achieving full factoring.

Building upon the implementation of [15], we identified that Toffoli gates in the algorithm's construction could be replaced with the relative phase Toffoli gate studied here while leaving the operation of the circuit unaltered. As we have seen the latter gate decomposes into fewer elementary gates than the former, and hence improving the fidelity of the output state. As a result, we were able to add a further iteration to the algorithm while maintaining a clear resolution in algorithmic output, from which we were able to successfully extracted the factors of $N = 21$. Our scheme is based on the non-iterative version of Shor's algorithm which uses three qubits for the control register. Notwithstanding the increase in number of qubits in comparison to the aforesaid implementation [15], we were able to successfully factor the integer $N = 21$, and additionally verify the presence of entanglement across the quantum registers in the circuit, See Ref. [6] for details.

4. Summary

Through the use of relative phase Toffoli gates studied in this paper, we were able to go beyond the demonstration of Ref. [15] in fully factoring $N = 21$. In the aforementioned reference, they implemented a compiled and iterative version of Shor's quantum algorithm to factor $N = 21$, and their scheme uses full Toffoli gates to realize Shor's quantum algorithm. Due to this, they were only able to implement two iterations of the algorithm, which falls one iteration short of the minimum number of iterations to be able to extract the factors $N = 21$ from the algorithmic output. Our scheme [6] replaces the full Toffoli gates with relative phase Toffoli gates, while remaining functionally correct (relative phase shifts introduced by gate do not affect the circuit's correctness). This replacement significantly reduces the number of elementary gates in the circuit, allowing our scheme to implement the minimum number of iterations of the algorithm for the full factorization of $N = 21$. We implemented the algorithm on IBM quantum processors using only 5 qubits, successfully verifying the presence of entanglement between the control and work register qubits, which is a necessary condition for the algorithm's speedup in general. Future work in this direction would explore whether the use of relative phase Toffoli gates may be viable in carrying out Shor's algorithm for larger integers, or other algorithms in systems with a limited number of noisy qubits.

Acknowledgments

We acknowledge the use of IBM Quantum services for this work. The views expressed are those of the authors, and do not reflect the official policy or position of IBM or the IBM Quantum team. We thank Taariq Surtee and Barry Dwolatzky at the University of the Witwatersrand and Ismail Akhalwaya at IBM Research Africa for access to the IBM processors through the Q Network and African Research Universities Alliance. This research was supported by the South African National Research Foundation, the South African Council for Scientific and Industrial Research, and the South African Research Chair Initiative of the Department of Science and Technology and National Research Foundation.

References

- [1] Kjaergaard M, Schwartz M E, Braumüller J, Krantz P, Wang J I J, Gustavsson S and Oliver W D 2020 *Annu. Rev. Condens. Matter Phys.* **11** 369–395
- [2] Barenco A, Bennett C H, Cleve R, DiVincenzo D P, Margolus N, Shor P, Sleator T, Smolin J A and Weinfurter H 1995 *Phys. Rev. A* **52** 3457–3467
- [3] Yu N, Duan R and Ying M 2013 *Phys. Rev. A* **88** 010304
- [4] Shende V V and Markov I L 2009 *Quantum Inf. Comput.* **9** 461–486
- [5] Maslov D 2016 *Phys. Rev. A* **93** 022311
- [6] Skosana U and Tame M 2021 *Sci. Rep.* **11** 16599
- [7] Shor P W 1997 *SIAM J. Comput.* **26** 1484–1509
- [8] Margolus N 1994 *Unpublished manuscript (circa 1994)*
- [9] Song G and Klappenecker A 2003 *Quantum Inf. Comput.* **3** 139–156
- [10] IBM Quantum 2021 <https://quantum-computing.ibm.com>
- [11] Abraham H *et al.* 2019 Qiskit: An open-source framework for quantum computing
- [12] Nielsen M A and Chuang I L 2011 *Quantum Computation and Quantum Information: 10th Anniversary Edition* 10th ed (USA: Cambridge University Press)
- [13] Nielsen M A 2002 *Phys. Lett. A* **303** 249–252
- [14] Magesan E, Blume-Kohout R and Emerson J 2011 *Phys. Rev. A* **84**
- [15] Martín-López E, Laing A, Lawson T, Alvarez R, Zhou X Q and O’Brien J L 2012 *Nature Photonics* **6** 773–776
- [16] Amico M, Saleem Z H and Kumph M 2019 *Phys. Rev. A* **100** 012305